

OCEAN OPTICS XIII

Steven G. Ackleson
Robert Frouin
Convenors/Editors

22-25 October 1996
Halifax, Nova Scotia, Canada

DISTRIBUTION STATEMENT A

Approved for public release
Distribution Unlimited

Sponsors
Office of Naval Research (USA)
NASA (USA)
Russian Academy of Sciences
SPIE—The International Society for Optical Engineering

Associate Sponsors
American Geophysical Union
The Oceanography Society (USA)
American Society of Limnology & Oceanography
Bedford Institution of Oceanography (Canada)
Defense Research Establishment Valcartier (Canada)
Alliance for Marine Remote Sensing (Canada)

DTIC QUALITY INSPECTED 3



SPIE Volume 2963

19970619 052

OCEAN OPTICS XIII

Steven G. Ackleson

Robert Frouin

Convenors/Editors

22–25 October 1996

Halifax, Nova Scotia, Canada

Sponsors

Office of Naval Research (USA)

NASA (USA)

Russian Academy of Sciences

SPIE—The International Society for Optical Engineering

Associate Sponsors

American Geophysical Union

The Oceanography Society (USA)

American Society of Limnology & Oceanography

Bedford Institution of Oceanography (Canada)

Defense Research Establishment Valcartier (Canada)

Alliance for Marine Remote Sensing (Canada)

Published by

SPIE—The International Society for Optical Engineering



SPIE Volume 2963

SPIE is an international technical society dedicated to advancing engineering and scientific applications of optical, photonic, imaging, electronic, and optoelectronic technologies.

The papers appearing in this book comprise the proceedings of the meeting mentioned on the cover and title page. They reflect the authors' opinions and are published as presented and without change, in the interests of timely dissemination. Their inclusion in this publication does not necessarily constitute endorsement by the editors or by SPIE.

Please use the following format to cite material from this book:

Author(s), "Title of paper," in *Ocean Optics XIII*, Steven G. Ackleson, Robert Frouin, Editors, Proc. SPIE 2963, page numbers (1997).

ISSN 0277-786X

ISBN 0-8194-2367-X

Published by

SPIE—The International Society for Optical Engineering

P.O. Box 10, Bellingham, Washington 98227-0010 USA

Telephone 360/676-3290 (Pacific Time) • Fax 360/647-1445

Copyright ©1997, The Society of Photo-Optical Instrumentation Engineers.

Copying of material in this book for internal or personal use, or for the internal or personal use of specific clients, beyond the fair use provisions granted by the U.S. Copyright Law is authorized by SPIE subject to payment of copying fees. The Transactional Reporting Service base fee for this volume is \$10.00 per article (or portion thereof), which should be paid directly to the Copyright Clearance Center (CCC), 222 Rosewood Drive, Danvers, MA 01923. Payment may also be made electronically through CCC Online at <http://www.directory.net/copyright/>. Other copying for republication, resale, advertising or promotion, or any form of systematic or multiple reproduction of any material in this book is prohibited except with permission in writing from the publisher. The CCC fee code is 0277-786X/97/\$10.00.

Printed in the United States of America.

Contents

xv *Conference Committee*

RADIATIVE TRANSFER THEORY

- 2 **Ocean optics: a perspective and a prognosis (Invited Paper)**
R. W. Spinrad, Consortium for Oceanographic Research and Education (USA)
- 10 **Inverse radiative transfer problems in environmental optics (Invited Paper)**
H. R. Gordon, G. Boynton, T. Zhang, Univ. of Miami (USA)
- 16 **Effects of absorption and boundary conditions on the utility of diffusion theory**
C. D. Mobley, R. A. Maffione, Sequoia Scientific, Inc. (USA)
- 21 **Absorption and scattering coefficient estimation with asymptotic apparent optical properties**
R. A. Leathers, N. J. McCormick, Univ. of Washington (USA)
- 26 **Angular structure of underwater light field: importance for ocean color models**
S. Sathyendranath, Dalhousie Univ. (Canada) and Bedford Institute of Oceanography (Canada);
T. Platt, Bedford Institute of Oceanography (Canada)
- 32 **Approximation to beam propagation in ocean water**
G. R. Fournier, Defence Research Establishment Valcartier (Canada)
- 38 **Coastal optical water type 2: modeling and minerogenic scattering**
R. H. Stavn, Univ. of North Carolina/Greensboro (USA); A. D. Weidemann, Naval Research
Lab. (USA)
- 49 **Light scattering on turbulence and on particulates**
D. Bogucki, A. Domaradzki, D. Stramski, Univ. of Southern California (USA); J. R. V. Zaneveld,
Oregon State Univ. (USA)
- 54 **Polarimetric lidar returns in the ocean: a Monte Carlo simulation**
J. T. Adams, G. W. Kattawar, Texas A&M Univ. (USA)
- 60 **Models of light pulse propagation in water and determination of inherent optical properties
from parameters of the transmitted pulse**
L. S. Dolin, Institute of Applied Physics (Russia)
- 66 **Effect of Raman scattering on the asymptotic average cosine in the ocean**
J. Berwald, D. Stramski, D. A. Kiefer, Univ. of Southern California (USA); C. D. Mobley, Sequoia
Scientific, Inc. (USA)
- 72 **Calculation and implementation of 2-flow radiative transfer equations including the effects
of fluorescence using MARAS data**
D. Buckton, E. O'Mongain, Univ. College Dublin (Ireland); S. Danaher, Leeds Metropolitan
Univ. (UK)
- 78 **Effects of the wind direction on the light field reflected from a wind-roughened sea surface**
F. Fell, R. Preusker, Freie Univ. Berlin (FRG)

- 84 **Modeling of the influence of environmental factors on solar irradiance reflectance and transmittance through the wind-ruffled sea surface**
S. B. Woźniak, Institute of Oceanology (Poland)
- 90 **Method for retrieval of the aerosol particle size distribution (APSD) in the marine atmosphere boundary layer (MABL) from optical measurement data**
K. S. Shifrin, I. G. Zolotov, Oregon State Univ. (USA)
- 95 **Atmospheric correlation algorithm for satellite ocean color sensors**
J. E. Davies, M. J. Lynch, Curtin Univ. of Technology (Australia)
- 101 **Atmospheric correction of the ocean color observations of the medium resolution imaging spectrometer (MERIS)**
D. Antoine, A. Morel, Univ. Pierre et Marie Curie (France)

OPTICAL PROPERTIES

- 108 **Optical properties of oceanic case 1 waters revisited (Invited Paper)**
A. Morel, Univ. Pierre et Marie Curie (France)
- 115 **Photobiology of the deep twilight zone and beyond (Invited Paper)**
T. H. Waterman, Yale Univ. (USA)
- 120 **Yellow substances in the coastal waters of the Gulf of Maine: implications for ocean color algorithms**
C. S. Yentsch, D. A. Phinney, Bigelow Lab. for Ocean Sciences (USA)
- 132 **Seasonal variation of CDOM in the Middle Atlantic Bight: terrestrial inputs and photo-oxidation**
A. Vodacek, N. V. Blough, Univ. of Maryland/College Park (USA)
- 138 **Spectral irradiance, radiance, and polarization in blue western Mediterranean waters**
N. K. Højerslev, Niels Bohr Institute of Astronomy (Denmark); E. Aas, Univ. of Oslo (Norway)
- 148 **Variation in incident light with time of day and cloud conditions at Hurst Spit, UK South Coast**
V. Byfield, J. Cook, S. R. Boxall, Univ. of Southampton (UK)
- 154 **Recent measurements of the spectral backward-scattering coefficient in coastal waters**
R. A. Maffione, D. R. Dana, Sequoia Scientific, Inc. (USA)
- 160 **Remote sensing reflectance and inherent optical properties of oceanic waters derived from above-water measurements**
Z. Lee, K. L. Carder, R. G. Steward, T. G. Peacock, Univ. of South Florida (USA); C. O. Davis, Naval Research Lab. (USA); J. L. Mueller, San Diego State Univ. (USA)
- 167 **Model for seawater optical characteristics in the UV spectral region**
O. V. Kopelevich, P.P. Shirshov Institute of Oceanology (Russia); S. Ershova, Moscow Institute of Physics and Technology (Russia)

- 173 **Optical characteristics of seawater in the North Pacific Ocean**
M. Kishino, RIKEN—Institute of Physical and Chemical Research (Japan); J. Ishizaka, National Institute for Resources and Environment (Japan); H. Satoh, K. Kusaka, Tokyo Univ. of Fisheries (Japan); S. Saitoh, T. Miyoi, Hokkaido Univ. (Japan); K. Kawasaki, National Research Institute of Fisheries Science (Japan)
- 179 **Spatial variability in the chlorophyll-specific absorption coefficients of phytoplankton and photosynthetic pigments in the equatorial Pacific**
K. Allali, A. Bricaud, H. Claustre, Univ. Pierre et Marie Curie (France)
- 185 **Optical spectral signatures of marine sediments**
W. E. McBride III, Planning Systems Inc. (USA); V. I. Haltrin, C. D. Kennedy, A. D. Weidemann, Naval Research Lab. (USA)

IN-SITU AND REMOTE SENSING SENSORS AND SYSTEMS

- 192 **Absorption coefficients of the ocean: their measurement and implications for remote sensing (Invited Paper)**
J. T. O. Kirk, CSIRO Plant Industry (Australia)
- 198 **Three-parameter optical studies in Scottish coastal waters**
D. McKee, A. Cunningham, Univ. of Strathclyde (UK); K. Jones, Dunstaffnage Marine Lab. (UK)
- 204 **Estimation of irradiance just below the air-water interface**
H. M. Dierssen, R. C. Smith, Univ. of California/Santa Barbara (USA)
- 210 **Laboratory development of a lidar for measurement of sound velocity in the ocean using Brillouin scattering**
Y. Emery, E. S. Fry, Texas A&M Univ. (USA)
- 216 **Bio-optical drifters: scales of variability of chlorophyll and fluorescence**
M. R. Abbott, R. M. Letelier, Oregon State Univ. (USA)
- 222 **Remote sensing reflectance of case 2 waters**
R. A. Arnone, Naval Research Lab. (USA); M. Sydor, Univ. of Minnesota/Duluth (USA);
R. A. Gould, Jr., Planning Systems Inc. (USA)
- 228 **Optimal selection of spectral channels for remote sensing of optically active matters in the ocean: application of the experimental design theory**
I. M. Levin, I. V. Zolotukhin, P.P. Shirshov Institute of Oceanology (Russia)
- 234 **Application of a multispectral interpretation algorithm to remote sensing data over the Baltic Sea**
H. Krawczyk, A. Neumann, T. Walzel, M. Hetscher, DLR (FRG); H. Siegel, Baltic Sea Research Institute Warnemuende (FRG)
- 240 **Coral fluorescence characteristics: excitation-emission spectra, fluorescence efficiencies, and contribution to apparent reflectance**
C. H. Mazel, Massachusetts Institute of Technology (USA)
- 246 **Whitecaps: spectral reflectance in the open ocean and their contribution to water-leaving radiance**
K. D. Moore, K. J. Voss, H. R. Gordon, Univ. of Miami (USA)

PROCESS STUDIES

- 254 **Decade of interdisciplinary process studies (Invited Paper)**
T. D. Dickey, Univ. of California/Santa Barbara (USA); B. H. Jones, Univ. of Southern California (USA)
- 260 **Observations of a *Synechococcus*-dominated cyclonic eddy in open-oceanic waters of the Arabian Sea**
R. R. Bidigare, M. Latasa, Univ. of Hawaii (USA); Z. Johnson, R. T. Barber, Duke Univ. (USA); C. C. Trees, San Diego State Univ. (USA); W. M. Balch, Bigelow Lab. for Ocean Sciences (USA)
- 266 **Solar-stimulated inelastic light scattering in clear seawater**
C. Hu, K. J. Voss, Univ. of Miami (USA)
- 272 **Relationship between near-surface chlorophyll and solar-stimulated fluorescence: biological effects**
J. J. Cullen, Á. M. Ciotti, R. F. Davis, Dalhousie Univ. (Canada); P. J. Neale, Smithsonian Environmental Research Ctr. (USA)
- 278 **Small scale optical structure measured via images of fluorescence emission**
J. S. Jaffe, P. J. S. Franks, Scripps Institution of Oceanography (USA)
- 284 **Depth and wavelength dependence of phytoplankton photosynthesis: implications for the remote sensing of marine primary production**
O. Ulloa, Univ. of Copenhagen (Denmark); N. Hoepffner, Space Applications Institute (Italy); D. Larkin, DJL Software Consultancy Ltd. (UK)
- 290 **Photosynthetic action spectrum: estimation from phytoplankton absorption spectrum**
M. N. Kyewalyanga, Dalhousie Univ. (Canada) and Univ. of Dar-es-Salaam (Tanzania); T. Platt, Bedford Institute of Oceanography (Canada); S. Sathyendranath, Dalhousie Univ. (Canada) and Bedford Institute of Oceanography (Canada)
- 296 **In-water algorithms for estimation of chlorophyll *a* and primary production in the Arabian Sea and the eastern Indian Ocean**
T. Hirawake, H. Satoh, T. Morinaga, T. Ishimaru, Tokyo Univ. of Fisheries (Japan); M. Kishino, RIKEN—Institute of Physical and Chemical Research (Japan)
- 302 **Primary production and irradiance during an intermonsoon cruise to the Arabian Sea (November 1995)**
J. Marra, Columbia Univ. (USA); R. T. Barber, Duke Univ. (USA); C. C. Trees, San Diego State Univ. (USA); Z. Johnson, Duke Univ. (USA); C. Kinkade, Columbia Univ. (USA)
- 308 **Bermuda bio-optics project (BBOP)**
D. A. Siegel, M. C. O'Brien, S. Garver, E. Brody, J. C. Sorensen, Univ. of California/Santa Barbara (USA); A. F. Michaels, E. Caporelli, N. B. Nelson, Bermuda Biological Station for Research
- 314 **Photoacclimation strategy of *Prochlorococcus* sp. and consequences on large scale variations of photosynthetic parameters**
M. Babin, Univ. Pierre et Marie Curie (France) and ACRI S.A. (France); N. Sadoadi, Univ. Pierre et Marie Curie (France); L. Lazzara, Vegetale dell'Univ. (Italy); J. Gostan, F. Partensky, A. Bricaud, Univ. Pierre et Marie Curie (France); M. Veldhuis, Netherlands Institute for Sea Research; A. Morel, Univ. Pierre et Marie Curie (France); P. G. Falkowski, Brookhaven National Lab. (USA)

- 320 **Tidal influences on optical variability in shallow water**
A. D. Weidemann, Naval Research Lab. (USA); W. S. Pegau, Oregon State Univ. (USA);
L. A. Jugan, T. E. Bowers, Planning Systems Inc. (USA)
- 326 **Diffuse attenuation in optically shallow water: effects of bottom reflectance**
S. G. Ackleson, Office of Naval Research (USA)
- 331 **Radiative transfer within seagrass canopies: impact on carbon budgets and light requirements**
R. C. Zimmerman, Univ. of California/Los Angeles (USA); C. D. Mobley, Sequoia Scientific, Inc. (USA)

POSTER SESSION: OPTICAL PROPERTIES

- 338 **UVR attenuation in lakes: relative contributions of dissolved and particulate material**
L. M. Ayoub, B. R. Hargreaves, D. P. Morris, Lehigh Univ. (USA)
- 344 **Absorption spectra reconstruction using Voigt profiles**
R. Aguirre-Gómez, A. R. Weeks, S. R. Boxall, Univ. of Southampton (UK)
- 353 **Retrieving chlorophyll and nonchlorophyllous matter from ocean color satellite data in Baltic case 2Y waters**
J.-F. Berthon, Baltic Sea Research Institute Warnemünde (FRG) and Space Applications Institute (Italy); M. Dowell, Univ. of Southampton (UK); N. Hoepffner, S. Grossi, Space Applications Institute (Italy)
- 358 **Pigment packaging and chlorophyll-a-specific absorption in high-light oceanic waters: a method, an algorithm, and validation**
W. Bissett, J. Patch, K. L. Carder, Z. Lee, Univ. of South Florida (USA)
- 375 **Validation of in-situ inherent optical properties in the Sargasso Sea**
E. Brody, M. C. O'Brien, D. A. Siegel, Univ. of California/Santa Barbara (USA); E. A. Caporelli, N. B. Nelson, Bermuda Biological Station for Research
- 380 **Influence of phytoplankton size structure on the spectral attenuation coefficient in the upper ocean**
Á. M. Ciotti, J. J. Cullen, Dalhousie Univ. (Canada); C. S. Roesler, Univ. of Connecticut (USA); M. R. Lewis, Dalhousie Univ. (Canada)
- 386 **Upwelled spectral radiance distribution in relation to yellow substance absorption in the example of case 2 waters (Baltic Sea)**
M. Darecki, P. Kowalczyk, Institute of Oceanology (Poland)
- 392 **Angular scattering functions of algae and silt: an analysis of backscattering to scattering fraction**
A. G. Dekker, H. J. Hoogenboom, H. Volten, R. Schreurs, J. F. de Haan, Vrije Univ. (Netherlands)
- 401 **Absorption modeling in case 2 waters: the need to distinguish colored dissolved organic matter from nonchlorophyllous particulates**
M. Dowell, Univ. of Southampton (UK); J. Berthon, Baltic Sea Research Institute Warnemünde (FRG) and Space Applications Institute (Italy); N. Hoepffner, S. Grossi, Space Applications Institute (Italy)

- 408 **Retrieval of chlorophyll concentration via inversion of ocean reflectance: a modeling approach**
P. R. C. S. Fearn, M. J. Lynch, Curtin Univ. of Technology (Australia)
- 414 **SCATTERLIB: light scattering codes library**
P. J. Flatau, Scripps Institution of Oceanography (USA)
- 417 **Variation in the specific absorption of dissolved organic carbon in northern Ontario lakes**
E. A. Gallie, Laurentian Univ. (Canada)
- 423 **Classification of phytoplankton in Lake Constance by modeling the albedo**
P. Gege, DLR (FRG)
- 429 **First look at the particulate absorption coefficient in the surface water of the subtropical East China Sea in spring**
G.-C. Gong, National Taiwan Ocean Univ.
- 435 **Estimation of specific absorption coefficients of turbid coastal water constituents using the AC-9 and asymptotic attenuation coefficients**
H. Hakvoort, R. Doerffer, GKSS Research Ctr. Geesthacht (FRG)
- 440 **Simulation of medium-resolution imaging spectrometer (MERIS) performance for detecting chlorophyll a over turbid inland waters**
H. J. Hoogenboom, A. Dekker, Vrije Univ. (Netherlands)
- 448 **Neural network to extract size parameter from light scattering data**
P. G. Hull, Tennessee State Univ. (USA); M. S. Quinby-Hunt, Lawrence Berkeley Lab. (USA)
- 455 **New technique for the determination of spectral reflectance of individual and bulk particulate suspended matter in natural water samples**
R. H. Iturriaga, J. Berwald, Univ. of Southern California (USA); G. J. Sonek, Beckman Laser Institute and Medical Clinic (USA)
- 461 **Bypass method for estimating backward scattering coefficient**
Y. Jodai, T. Oishi, Y. Saruya, Tokai Univ. (Japan); M. Kishino, RIKEN—Institute of Physical and Chemical Research (Japan)
- 466 **Seawater optical characteristics near the Ryukyu Islands in Japan**
K. Kawasaki, National Research Institute of Fisheries Science (Japan)
- 471 **Estimating new production from the quantum yield of nitrate uptake**
R. M. Kudela, F. P. Chavez, Monterey Bay Aquarium Research Institute (USA)
- 477 **Optical inverse problem in turbid waters**
T. Kutser, H. Arst, S. Mäekivi, Estonian Marine Institute; A. Blanco-Sequeiros, Univ. of Helsinki (Finland)
- 483 **Remote sensing reflectance measured with and without a vertical polarizer**
Z. P. Lee, K. L. Carder, T. G. Peacock, R. G. Steward, Univ. of South Florida (USA)
- 489 **Comparison of measured inherent optical properties with estimates determined from reflectance in coastal waters off Cape Hatteras, North Carolina, USA**
S. E. Lohrenz, D. G. Redalje, K. M. Matulewski, J. E. Ivey, Univ. of Southern Mississippi (USA); A. D. Weidemann, Naval Research Lab. (USA)

- 495 **Bio-optical relationships in the southwest Atlantic sector of the Antarctic Ocean**
K. Mahapatra, Tokai Univ. (Japan); S. Matsumura, S. Kawaguchi, National Research Institute of Far Seas Fisheries (Japan); Y. Senga, Tokai Univ. (Japan)
- 502 **Remote sensing reflectance: preliminary comparisons between in-water and above-water measurements and estimates modeled from measured inherent optical properties**
J. L. Mueller, San Diego State Univ. (USA); J. R. V. Zaneveld, S. Pegau, Oregon State Univ. (USA); E. Valdez, H. Maske, S. Alvarez-Borrego, R. Lara-Lara, Ctr. de Investigación Científica y de Educación Superior de Ensenada (Mexico)
- 508 **Distribution of colored dissolved organic matter (CDOM) in the equatorial Pacific**
W. S. Pegau, Oregon State Univ. (USA)
- 514 **Short-period photophysiological responses of *Thalassiosira pseudonana* during photoacclimation to near-surface irradiance**
R. E. Reed, North Carolina State Univ. (USA); G. J. Kirkpatrick, Mote Marine Lab. (USA); D. Kamykowski, North Carolina State Univ. (USA)
- 520 **Calculation of the Q factor for case 2 waters**
S. J. Shimwell, Univ. of Southampton (UK); M. R. Wernand, Netherlands Institute for Sea Research; S. R. Boxall, Univ. of Southampton (UK)
- 526 **Variation of specific optical properties and their influence on measured and modeled spectral reflectances in the Baltic Sea**
H. Siegel, M. Gerth, M. Beckert, Baltic Sea Research Institute Warnemünde (FRG)
- 532 **Optical determination of phytoplankton floristic composition**
P. S. D. Smith, D. G. Bowers, E. G. Mitchelson-Jacob, Univ. of Wales (UK)
- 538 **Role of pigments and species composition in modifying the absorption spectra of natural phytoplankton populations**
V. Stuart, Dalhousie Univ. (Canada); S. Sathyendranath, Dalhousie Univ. (Canada) and Bedford Institute of Oceanography (Canada); T. Platt, Bedford Institute of Oceanography (Canada); H. Maass, Dalhousie Univ. (Canada); B. D. Irwin, Bedford Institute of Oceanography (Canada)
- 543 **Spatial variability in optical properties of the waters around the Ambrose Light Tower**
A. Subramaniam, K. Waters, E. Armstrong, J. Brock, NOAA Coastal Services Ctr. (USA); R. Ranheim, New York City Dept. of Environmental Protection (USA)
- 549 **Effects of suspended sediment concentration on the absorption and scattering coefficients**
G. E. Terrie, Naval Research Lab. (USA); S. Ladner, R. A. Gould, Jr., Planning Systems Inc. (USA)
- 554 **How do coccoliths affect light in the sea?**
T. Tyrrell, P. M. Holligan, Univ. of Southampton (UK)
- 560 **Optical parameters of the Black Sea waters: long term variability and present status**
V. L. Vladimirov, V. I. Mankovsky, M. V. Solov'ev, A. V. Mishonov, Marine Hydrophysical Institute (Ukraine); S. Besiktepe, E. Ozsoy, Middle East Technical Univ. (Turkey)
- 566 **Aspects of the point spread function in the coastal zone**
K. J. Voss, B. J. Frew, Univ. of Miami (USA)

- 570 **Optical properties of the upper ocean in the Arabian Sea in August 1994**
A. R. Weeks, Southampton Institute (UK); D. Ballesterio, I. S. Robinson, Univ. of Southampton (UK)
- 579 **Scattering phase function of very large particles in the ocean**
W. Hou, K. L. Carder, D. K. Costello, Univ. of South Florida (USA)
- 585 **Prediction of euphotic depths and diffuse attenuation coefficients from absorption profiles: a model based on comparisons between vertical profiles of spectral absorption, spectral irradiance, and PAR**
J. R. V. Zaneveld, W. S. Pegau, A. H. Barnard, Oregon State Univ. (USA); J. L. Mueller, San Diego State Univ. (USA); H. Maske, E. Valdez, R. Lara-Lara, S. Alvarez-Borrego, Ctr. de Investigación Científica y de Educación Superior de Ensenada (Mexico)

POSTER SESSION: RADIATIVE TRANSFER THEORY

- 592 **Comparison of model of sea-surface reflectance incorporating Raman scattering by water**
J. S. Bartlett, Dalhousie Univ. (Canada)
- 597 **Modeling of elastic and inelastic scattering effects in oceanic optics**
V. I. Haltrin, Naval Research Lab. (USA); G. W. Kattawar, Texas A&M Univ. (USA); A. D. Weidemann, Naval Research Lab. (USA)
- 603 **Four-channel color sensor to measure chlorophyll and carotenoid concentration**
S. Kratzer, Univ. of Wales (UK); P. B. Tett, Napier Univ. (UK); R. Wilton, Univ. of Wales (UK)
- 609 **Atmospheric correction over case 2 waters using an iterative fitting algorithm including relative humidity**
P. E. Land, J. D. Haigh, Imperial College of Science, Technology, and Medicine (UK)
- 614 **Toward optical closure in coastal waters**
J. Schwarz, Univ. of Southampton (UK); A. R. Weeks, Southampton Institute (UK); K. J. Trundle, I. S. Robinson, Univ. of Southampton (UK)

POSTER SESSION: IN-SITU AND REMOTE SENSING SENSORS AND SYSTEMS

- 622 **Polychromatic in-situ transmissometer for measurements of suspended particles and yellow substance in water**
H. Barth, R. Reuter, U. Stute, Univ. Oldenburg (FRG)
- 631 **New instrument for simultaneous measurement of daylight field optical properties above and under water**
K. Bochter, C. Wallhäußer, DLR (FRG)
- 637 **Hi-Star: a spectrophotometer for measuring the absorption and attenuation of natural waters in-situ and in the laboratory**
E. J. Bruce, M. J. Borgerson, C. Moore, WET Labs., Inc. (USA); A. D. Weidemann, Naval Research Lab. (USA)
- 643 **Measurements of the attenuation coefficient of a lidar in the Southern California Bight**
J. H. Churnside, NOAA Environmental Technology Lab. (USA)

- 648 **Modular optoelectronic scanner (MOS): a study of its capabilities for optically active parameter estimation by means of an ocean color model**
P. Cipollini, Univ. of Southampton (UK); G. Corsini, Univ. of Pisa (Italy)
- 654 **Remote sensing of a pigment patch in the southeastern Bering Sea**
R. F. Davis, G. Lazin, J. S. Bartlett, Á. M. Ciotti, Dalhousie Univ. (Canada); P. Staben, National Oceanic and Atmospheric Administration (USA)
- 658 **Instrument for underwater high-angular resolution volume scattering function measurements**
P. W. Dueweke, J. L. Bolstad, D. A. Leonard, H. E. Sweeney, EOO, Inc. (USA); P. A. Boyer, E. M. Winkler, Global Associates, Ltd. (USA)
- 664 **Submersible UV-B spectroradiometer using an acousto-optic tunable fiber**
V. G. Egorov, S. E. Nalivaiko, V. S. Pavlenko, O. S. Rzshevsky, E. B. Gordon, Institute for Energy Problems of Chemical Physics (Russia); L. W. Cooper, J. M. Grebmeier, L. R. Shugart, Oak Ridge National Lab. (USA)
- 670 **SeaWiFS ocean color products and services at the NASA Goddard Distributed Active Archive Center (DAAC)**
R. A. Farr, George Mason Univ. (USA); R. Kartan, Research and Professional Services (USA); A. W. Li, Research and Data Systems Corp. (USA); R. B. Simmon, Research and Professional Services (USA)
- 674 **SeaShark and StarFish operational data processing schemes for AVHRR and SeaWiFS**
R. J. Flowerdew, A. M. Corlyon, W. A. D. Greer, S. J. Newby, C. P. Winder, VEGA Group plc (UK)
- 678 **Influence of late-summer storms on the horizontal variability of phytoplankton pigment determined by coastal zone color scanner images in the Gulf of St. Lawrence, Canada**
C. Fuentes-Yaco, UQAR (Canada); A. F. Vézina, Maurice Lamontagne Institute (Canada); M. Gosselin, UQAR (Canada); Y. Gratton, INRS-Océanologie (Canada); P. Larouche, Maurice Lamontagne Institute (Canada)
- 684 **Submarine lidar for the detection of chemical pollutants on the seafloor**
S. Harsdorf, M. Janssen, R. Reuter, Carl von Ossietzky Univ. Oldenburg (FRG)
- 691 **Simultaneous retrieval of oceanic and atmospheric properties using satellite remote sensing measurements**
T. Heinemann, J. Fischer, Freie Univ. Berlin (FRG)
- 697 **Bio-optical time series collected in coastal waters for SeaWiFS calibration and validation: large structure shadowing considerations**
E. Kearns, R. Riley, Computer Sciences Corp. (USA); C. Woody, National Oceanic and Atmospheric Administration (USA)
- 703 **Ocean color measurements from low-flying aircraft: atmospheric and surface glint correction**
G. Lazin, R. F. Davis, Á. M. Ciotti, M. R. Lewis, Dalhousie Univ. (Canada)
- 708 **Field evaluation of antibiofouling compounds on optical instrumentation**
S. McLean, B. Schofield, Satlantic Inc. (Canada); G. Zibordi, Space Applications Institute (Italy); M. R. Lewis, Dalhousie Univ. (Canada); S. Hooker, NASA Goddard Space Flight Ctr. (USA); A. D. Weidemann, Naval Research Lab. (USA)

- 714 **Ocean optics in the California current: observations and theory**
B. G. Mitchell, P. J. Flatau, M. Kahru, Scripps Institution of Oceanography; C. D. Mobley, Sequoia Scientific, Inc. (USA)
- 725 **WET Labs ac-9: field calibration protocol, deployment techniques, data processing, and design improvements**
C. Moore, E. J. Bruce, WET Labs, Inc. (USA); W. S. Pegau, Oregon State Univ. (USA); A. D. Weidemann, Naval Research Lab. (USA)
- 731 **Modulated pulse lidar for enhanced underwater detection**
L. Mullen, V. Contarino, Naval Air Warfare Ctr. (USA)
- 737 **Method for removing a majority of the error in PUV attenuation coefficients due to spectral drift in response with depth in the water column**
K. W. Patterson, R. C. Smith, Univ. of California/Santa Barbara (USA); C. R. Booth, Biospherical Instruments, Inc. (USA)
- 743 **Relationship between remote sensing reflectance and optically active substances in case 1 and case 2 waters**
D. A. Phinney, D. I. Phinney, C. S. Yentsch, Bigelow Lab. for Ocean Sciences (USA)
- 753 **Algorithms for path radiance and attenuation to provide color corrections for underwater imagery, characterize optical properties, and determine bottom albedo**
P. D. Pratt, K. L. Carder, D. K. Costello, Z. Lee, Univ. of South Florida (USA)
- 760 **Influence of ship shadow on underwater irradiance fields**
Y. Saruya, T. Oishi, Tokai Univ. (Japan); M. Kishino, RIKEN—Institute of Physical and Chemical Research (Japan); Y. Jodai, K. Kadokura, A. Tanaka, Tokai Univ. (Japan)
- 766 **Development of a bio-optical algorithm for ocean color remote sensing in the sub-Arctic North Pacific Ocean**
S. Saitoh, T. Miyoi, Hokkaido Univ. (Japan); M. Kishino, RIKEN—Institute of Physical and Chemical Research (Japan)
- 772 **SeaWiFS quality monitor: a portable calibration light source**
P. S. Shaw, National Institute of Standards and Technology (USA); S. Hooker, NASA Goddard Space Flight Ctr. (USA); D. Lynch, Reyer Corp. (USA)
- 777 **Oceanographic bio-optical profiling system II**
R. C. Smith, D. W. Menzies, Univ. of California/Santa Barbara (USA); C. R. Booth, Biospherical Instruments Inc. (USA)
- 790 **Laser line scan fluorescence and multispectral imaging of coral reef environments**
M. P. Strand, Naval Surface Warfare Ctr. (USA); B. Coles, Raytheon Co. (USA); A. J. Nevis, Naval Surface Warfare Ctr. (USA); R. F. Regan, Raytheon Co. (USA)
- 796 **Long-time series of turbid coastal water using AVHRR: an example from Florida Bay, USA**
R. P. Stumpf, M. L. Frayer, U.S. Geological Survey (USA)
- 802 **Valuation of perspective application of lidar methods for sea monitoring**
I. V. Aleshin, S.I. Vavilov State Optical Institute (Russia); V. K. Goncharov, Krylov Shipbuilding Research Institute (Russia); V. G. Lyskov, E. A. Tsvetkov, S.I. Vavilov State Optical Institute (Russia)

- 808 **Generation of high-resolution ocean color information from five particular bands: a case 2 water approach**
M. R. Wernand, Netherlands Institute for Sea Research; S. J. Shimwell, Univ. of Southampton (UK); J. C. de Munck, Netherlands Institute for Sea Research
- 815 **System for maritime surveillance aid**
K. Yamamoto, K. Yamada, Electronic Navigation Research Institute (Japan); N. Kiriya, Ship Research Institute (Japan)
- 821 **Variation of aerosol optical thickness and moisture content of the atmosphere in the area of the Canary Islands**
V. E. Zuev, D. M. Kabanov, S. Sakerin, Institute of Atmospheric Optics (Russia)

POSTER SESSION: PROCESS STUDIES

- 828 **Chlorophyll maximums controlled by underwater current and solar irradiation**
I. Asanuma, Japan Marine Science and Technology Ctr.; K. Matsumoto, T. Kawano, C. Saitoh, Japan Marine Science and Technology Ctr.; M. R. Lewis, S. McLean, Dalhousie Univ. (Canada)
- 834 **Ground truthing modeled k_{PAR} and on-deck primary productivity incubations with in-situ observations**
R. T. Barber, L. Borden, Z. Johnson, Duke Univ. (USA); J. Marra, C. Knudson, Columbia Univ. (USA); C. C. Trees, San Diego State Univ. (USA)
- 840 **Pump-during-probe fluorometry of phytoplankton: group-specific photosynthetic characteristics from individual cell analysis**
A. M. Chekalyuk, R. J. Olson, H. M. Sosik, Woods Hole Oceanographic Institution (USA)
- 846 **Variations in the water column photosynthetic cross section for Antarctic coastal waters**
H. Claustre, Univ. of California/Santa Barbara (USA) and Univ. Pierre et Marie Curie (France); M. Moline, B. Prezelin, Univ. of California/Santa Barbara (USA)
- 850 **Variability of remote sensing reflectance and absorption spectra in the western Arabian Sea**
R. A. Gould, Jr., Planning Systems Inc. (USA); R. A. Arnone, Naval Research Lab. (USA); D. A. Phinney, Bigelow Lab. for Ocean Sciences (USA); C. O. Davis, Naval Research Lab. (USA)
- 856 **Modeling the environmental-optical relation in near shore regions**
D. R. Johnson, R. W. Meridith, Naval Research Lab. (USA)
- 862 **Modeled inherent scattering properties of small light-limited phytoplankton: implications for deep phytoplankton size class distributions**
Z. Johnson, Duke Univ. (USA)
- 868 **Phytoplankton quantum yield measured on minute time scales in situ**
G. J. Kirkpatrick, Mote Marine Lab. (USA); D. Kamykowski, R. E. Reed, North Carolina State Univ. (USA)
- 874 **Measurements of photophysiological parameters and primary production in the central North Pacific Ocean**
M. E. Ondrusek, R. R. Bidigare, Univ. of Hawaii (USA)

- 880 **Spatial variations of photosynthetic parameters in equatorial Pacific: forcing by vertical mixing and light penetration**
N. Sadoudi, Univ. Pierre et Marie Curie (France); M. Babin, Univ. Pierre et Marie Curie (France) and ACRI S.A. (France); K. Allali, Univ. Pierre et Marie Curie (France); M. Behrenfeld, Brookhaven National Lab. (USA); H. Claustre, A. Morel, Univ. Pierre et Marie Curie (France)
- 886 **High-throughput-volume particle in-flow imaging system**
C. K. Sieracki, M. E. Sieracki, Bigelow Lab. for Ocean Sciences (USA)
- 892 **Satellite assessment of hurricane-induced ocean turbidity for the southern U.S. coastline**
K. Waters, Technology Planning and Management Corp. (USA); J. Brock, NOAA Coastal Services Ctr. (USA); A. Subramaniam, Technology Planning and Management Corp. (USA); R. P. Stumpf, U.S. Geological Survey (USA); E. Armstrong, Technology Planning and Management Corp. (USA)
- 898 **Solitary coastal lee waves observed from space**
Q. Zheng, X.-H. Yan, V. Klemas, Z. Wang, Univ. of Delaware (USA); C. Ho, N. Kuo, National Taiwan Ocean Univ.
- 904 *Author Index*

Conference Committee

Convenors

Steven G. Ackleson, Office of Naval Research (USA)
Robert Frouin, NASA (USA)

Planning Committee

John Cullen, Dalhousie University (Canada)
Oleg Kopelevich, Russian Academy of Sciences
Marlon Lewis, Dalhousie University (Canada)
Terry Montonye, SPIE—The International Society for Optical Engineering (USA)
Shubha Sathyendranath, Dalhousie University (Canada) and Bedford Institute of Oceanography (Canada)

Session Chairs

Radiative Transfer Theory

Steven G. Ackleson, Office of Naval Research (USA)
David A. Siegel, University of California/Santa Barbara (USA)
Annik Bricaud, Université Pierre et Marie Curie (France)
Iosif M. Levin, P.P. Shirshov Institute of Oceanology (Russia)

Optical Properties

Kenneth John Voss, University of Miami (USA)
Motoaki Kishino, RIKEN—Institute of Physical and Chemical Research (Japan)
W. Scott Pegau, Oregon State University (USA)

In-Situ and Remote Sensing Sensors and Systems

Vladimir E. Zuev, Institute of Atmospheric Optics (Russia)
Kendall L. Carder, University of South Florida (USA)
Hans Hakvoort, GKSS Research Center Geesthacht (FRG)

Process Studies

Heidi M. Sosik, Woods Hole Oceanographic Institution (USA)
Trevor Platt, Bedford Institute of Oceanography (Canada)
Richard T. Barber, Duke University (USA)
William M. Balch, Bigelow Laboratory for Ocean Sciences (USA)

Radiative Transfer Theory

Ocean optics: a perspective and a prognosis

Richard W. Spinrad

Consortium for Oceanographic Research and Education, 1755 Massachusetts Avenue NW,
Washington, DC 20036, USA

ABSTRACT

The field of ocean optics is characterized by an evolution of driving forces, primarily within the last half of this century. In the 1970s, the field was a source of new information on the scales of variability of ocean dynamics, in terms of surface productivity and deep ocean sediment transport. Subsequent remote sensing developments dictated the development of more sophisticated understanding of radiative transfer and the measurements of optical properties *in situ*. By the late 1980s, US Navy operations and an ever-quieting submarine fleet demanded increased investment in non-acoustic technologies for antisubmarine warfare. Now the oceanographic community is being redirected and trends for ocean research point toward new applications: improved interannual forecasts relevant on global scales; hazard mitigation, especially in the coastal zone, where weather, anthropogenic, and natural processes are to be dealt with, and; new concerns for national security. Optics should play a key role in the development of global ocean observation systems: optical sensors are now recognized as standard indicators of change in the chemistry, biology and physics of the sea, and the marine boundary layer. Modeling efforts tied to prediction of thermal dynamics will require treatments of radiative transfer theory on temporal and spatial scales heretofore underserved.

1. BACKGROUND

The field of ocean optics is relatively new, even by oceanographic standards. While work was first performed in the 19th century, and there were initial discoveries of the variability of water clarity¹, the real growth in underwater optical observations began in the first half of the 20th century. During this age of discovery, new photographic capabilities lent themselves well to measurement of deep water characteristics², such as detection of the deep nepheloid layer, and qualitative assessments of the profile of surface irradiance.

Subsequent to the end of World War II optical oceanography was seen as a potential tool for Naval applications. Specifically, early studies hinted at the potential role for optics in antisubmarine warfare and general surveillance. This promising area of development spawned a range of observational capabilities which were then applied to a diverse set of basic research applications.

1.1 Sediment transport

Earlier studies with photographic nephelometers indicated that more quantitative techniques exploiting the stability and resolution of new light sources (e.g. light emitting diodes and lasers) were at hand. The Sea Tech transmissometer³, as just one example, was developed in response to a need for deep ocean measurements of total suspended load and sediment transport. During the High Energy Benthic Boundary Layer Experiment (HEBBLE) of the late 1970s, the measurement of beam attenuation at depths of more than 4000 meters proved to be the initial indication of the

amazing volume of sediment being transported by the western bottom current in the Atlantic⁴. The same measurement was also used to characterize the nature of particle resuspension during coastal upwelling (Coastal Upwelling Ecosystem Analysis experiment off Oregon and Peru). It was also during this time that the measurement of beam attenuation was introduced as one of the most sensitive indicators of the presence of ocean hydrothermal vents⁵.

1.2 Sedimentation

Optical techniques were also developed in conjunction with new sediment traps. Concerns about the degradation of 'preserved' sediment samples from sediment traps could best be addressed using a variety of time-series based optical characterizations⁶.

1.3 Productivity

It was also during the 1960s through the 1980s that optical techniques became the primary tool for assessing biological productivity. Traditional Secchi disk assessments of surface water turbidity and color were replaced with silicon photodetector-based measurements of the up- and down-welling radiance and irradiance fields⁷. These, coupled with the explosion of spectral remote sensing capabilities gave way to whole new realizations of the temporal and spatial nature of biological productivity.

1.4 Radiative transfer theory

Simultaneous to the observational developments described above were the improvements being made in hydrological optics theory. Through new approaches to numerical modeling, the applications of the theory of radiative transfer were broadened considerably⁸. Similarly, improved observational resolutions in space, time and the electromagnetic spectrum bolstered the need for renewed analytical treatments of the theories of optical variability in the sea.

2.0 DRIVERS OF CHANGE

The changes in sensing or modeling capability were driven by a range of new capabilities and new scientific interests.

2.1 Technology

One of the critical drivers of improvement in underwater optics was the general need to ground-truth the ever increasing set of measurements being made with remote sensors. The Coastal Zone Color Scanner (CZCS) of the late 1970s and early 1980s demanded capabilities for measuring ocean color over large areas and through the full measure of the photic zone (or at least to one optical depth).

The ability to make these kinds of measurements rested strongly in the development of new sources and detectors. Whereas the photographic and visual systems of the first half of this century proved important in giving us a sense of the qualitative nature of optical variability, the explosion of quantitative sensing and new generations of light sources allowed for the development of quality instrumentation. Stable, low power sources, such as light emitting diodes and laser diodes replaced the power-hungry wide band incandescent sources. Dye lasers provided wavelength selection and multispectral measurement heretofore unseen. Silicon based detection systems, including SIT cameras and supercooled detectors allowed for sensing down to the single

photon levels, thus permitting characterization of the natural light field at ever increasing ocean depths. It is important to note that as the sources were becoming more stable and less power hungry, the improvements in electronic design also resulted in smaller packages. This had the clear advantage of ease and diversification of use. For example, where earlier radiometers relied on one detector and a series of filters, the newer generation of these sensors could be built with a series of detectors, each tuned for a different spectral band, and often in a much smaller box. Other electronic and mechanical improvements (e.g. surface mount board configurations and computer aided machining) also worked to the great advantage of the seagoing optical oceanographer.

From the analytical and theoretical perspective the explosions in computational science were enormously valuable in accelerating our knowledge of ocean optics. Numerical modeling via Monte Carlo simulations, once the bailiwick of large mainframe time-shared systems, could now reside on dedicated, inexpensive desk top workstations, thus allowing much more flexibility in model design and testing. Similarly, parallel computing capabilities opened up a new opportunity for processing large volumes of data. Also notable were the improvements in data communication which resulted from the development of impressive networks and databases.

But not all of the drivers were based on new technologies. There were also changes in the focus of research in the ocean. Interdisciplinary studies in a range of new oceanographic problems strongly influenced the trends in optical oceanography.

2.2 Disciplinary focus

Global climate change became a critical area for research starting in the 1960s, but not fully attended to until the middle of the 1980s. At this time several multinational, interdisciplinary programs emerged. One such example, the Joint Global Ocean Flux Study focussed on the budget, transport and process studies associated with a range of parameters, including carbon and carbon dioxide. The role of marine primary productivity was recognized early on as critical in these studies. Simultaneously, the oceanographic community identified a central role for the use of optics, specifically ocean color as a key indicator of both the distribution and intensity of marine organic material worldwide. It is also worth noting that, in a related sense, the role of ocean circulation, as embodied in the World Ocean Circulation Experiment, was simultaneously defined relative to transport of marine carbon, and, again, optical parameters were quickly identified as independent variables to be included in standard measurements.

More recently, a range of global research advisory bodies have highlighted concerns about diminishing marine biodiversity. Since the days of microscopy-based taxonomy are long gone, new and more accurate techniques for quantifying species diversity and biogeography are in demand. A range of optical methodologies based on particulate scattering functions (e.g. flow cytometry) and fluorescence spectra were developed to provide rapid identification of planktonic species in the oceans.

Of course there were many other focal points for new research in the ocean, and this list is hardly comprehensive. The point is that both technology and research interests provided the driving forces for increased attention to optical oceanography in the last several decades. The numbers are impressive. Between 1986 and 1996, the investment in basic research in ocean optics by the US Navy alone increased by more than an order of magnitude. Of specific interest to the audience of the Ocean Optics series of meetings is the dramatic increase in the number of papers in the proceedings of this biennial meeting. This growth is also evident, although not as easily quantifiable, in terms of the diversity of support bases for research in ocean optics now, as

compared with twenty years ago.

3. FUTURE TRENDS

The question at hand, therefore is "Where are we going?" This is best addressed, again, in terms of technology and disciplinary focus.

3.1 Technology

A critical capability for the oceanographic community in general is that of autonomous sampling. The costs and limitations of manned operations demand a supplemental robotic approach. Observational networks, not unlike the mesh of terrestrial meteorological stations are in the offing for the ocean. The message to the optical oceanographic community is that the first sensors to be deployed on such sampling networks will be those with the greatest improvements in power requirements, size, and operational simplicity. Many ocean scientists understand the value of measurements of solar irradiance, beam attenuation and fluorometry. These measurements will soon become standard for inclusion on automatic sampling platforms.

Light sources of the future will always be used by the optical oceanographic community. The question, then, is what does the future bode? Recent discoveries of lasing properties of plastics and organic materials⁹ suggest a whole new generation of very inexpensive, highly monochromatic light sources, with relatively efficient optical outputs, even in the short wavelengths. Some of the current measurements (e.g. 3-D fluorescence spectroscopy) which are limited to bulky and power hungry laboratory instruments may realistically be performed *in situ* within just a few years.

Similarly, very fast pulse (femto-second) lasers are becoming a reality. Given the spatial dimensions of a femto second light pulse (of order 1 micron or less) we can start looking into the spatio-temporal kinetics of light absorption by marine phytoplankton (size of order 10 microns and larger). Research on the kinetics of phytoplankton fluorescence could also be addressed in this way.

The astronomical research community has developed new concepts in "smart optics", especially the applications of phase conjugation for image enhancement. What originally started as mechanically adaptive optical systems has evolved into sophisticated electro-optical methodologies for removing the range dependent noise in an optical signal. Work is just starting in this area, but extrapolation from the atmospheric efforts to date suggests that these techniques might drastically improve the optical depth penetration of underwater imaging systems.

3.2 Disciplinary support

As with the improvements of the past, the trends for the future are driven as much by the disciplinary research requirements as by the technological developments. What, then are the research opportunities and drivers for the next decade in optical oceanography?

This question is part of a larger set of issues regarding the trends for oceanographic research in general. The history of applications to warfighting missions, or to pollution will continue, but the set of societal concerns addressed by research in ocean sciences must broaden and diversify. This need for broadening applications has been the focus of a set of continuing discussions and debates over the last several years. One study¹⁰ has recently identified four focus

areas for ocean research of the next decade: national security, quality of life, economic development and education/communication.

3.2.1 National Security

Where optical oceanography was a linchpin in the development of new concepts for nonacoustic antisubmarine warfare, the focus in the next decade will be on a range of applications, generally specific to littoral warfighting.

- Coastal warfare
 - Strike warfare, in which 'stand-off' weaponry is called to attack specific critical targets (e.g. through the use of cruise missiles) depends critically on accurate definitions of the nature and variability of optical transmission in the marine atmospheric boundary layer. This requirement will translate into needs for improved aerosol characterization and the development of models capable of data assimilation for forecasting targeting parameters (e.g. visibility for optical navigation).
 - Amphibious Assault / Special Operations - the nature of covert operations is such that all potential signals must be characterized. For the underwater optics community this might mean improved understanding of shallow water bioluminescence. The exigencies of this warfare area also call for coupled acoustic and optical samplers capable of characterizing the full set of objects and particles in the water from micron size (as might affect visibility) to meter sized (obstacles).
 - Mine Warfare - with time the variability in types of mines and materials used in their construction will increase. The ever-increasing sensitivity of *in situ* chemical probes suggests that chemical sensors exploiting high resolution spectrometry and spectrofluorometry may be a high priority. Of course continued development of imaging systems such as line-scanners (>20 O.D. object identification) will be an imperative.
 - The needs for submarine detection have not disappeared. Shallow water ASW will persist and active range gated systems, passive detectors of surface properties, and a variety of chemical sensors may continue to be developed.

Much of the present debate on national security focusses on the set of issues, such as counter terrorism and low intensity conflict, which strongly depend on a robust intelligence capability. This also implies direction for developments in optical oceanography:

- Remote sensing - ever increasing resolution in both imaging and non-imaging remote sensing will continue. These capabilities cannot be developed without reliable and accurate sea-truth observations.
- Monitoring and surveillance - observational systems, especially adjacent to coastal harbors and ports will depend on the availability of long term, reliable, low power, non-fouling sensors and simple interpretation methodologies. The concepts embodied in the Navy's fixed sound surveillance system (SOSUS) arrays established in the 1960s for long baseline acoustical surveillance of the world's oceans will be reflected in similar optical systems in shallow water. In a related

fashion, the nature of some covert operations will require new developments in microsensors, deployable from aircraft, and, similarly, robust modeling capabilities derived from studies performed in natural laboratories, serving as surrogate environments.

3.2.2 Quality of life

Developments in optical oceanography will also broaden to include a more active role in support of society's needs in terms of quality of life issues.

- **Pollution** - The control, prevention and remediation of marine pollution will continue to be a central issue for the environment and the agencies associated with its regulation. Policies regarding the specifications within environmental impact statements may require more quantitative optical information such as total suspended load, particle size distribution, and chemical constituency. The recognition that this kind of measurement and monitoring needs to be performed universally also implies portability, ease of use and straightforward interpretation for the measurements. The hand held optical sensors of environmentally-relevant indicators will have to be made robust and easy to apply.
- **Health/Biomedicine** - There is a growing recognition of the role that the oceans play in defining or ameliorating public and individual health. Globally, it is the improvement in ocean observation and long-term forecasting which will help remediate deleterious effects of climate change (e.g. the spread of disease vectors into new global regions). Optical sensors, as described above, will play an important role. In terms of individual health issues the ocean shows great promise as a source of biomedical resources¹¹. Current requirements demand careful search and capture of specific organisms containing key extractable compounds - will ROV-based optical sensors allow improvements for identifying and obtaining these flora and fauna?
- **Recreation** - The decades to come will undoubtedly yield new opportunities for recreational activities in the coastal zone. Ecotourism is just one example. Observationally based measurements of coastal optical properties such as ocean color and bottom nephelometry may support early warning systems for food quality (e.g. is a red tide imminent?) and for sport fishing (e.g. is the water clarity supportive of a high population of visual feeding sport fish such as tuna?).

3.2.3 Economic development

Recently many commercial sectors have recognized the need to develop a better understanding of environmental variability, specifically for the purpose of investment security. Where traditional applications of ocean sciences in the commercial sector have been somewhat limited (e.g. to fisheries, oil and gas, and commercial shipping), there is a burgeoning set of 'non-traditional' industries which will become increasingly dependent on continuous and accurate description and forecasting of ocean environmental variability.

- **Property Development** - All aspects of real estate development, from zoning decisions to building design to market surveys, depend on a good understanding of the nature and quality of the location: what do climatological data suggest about aesthetics of one site over another? Can forecasts be made of the annual cycles in algal blooms along beach property? The simple fact that a blue water lagoon sells more property than a brown swamp suggests optical surveying may be developed as an important component of property development

interests.

- Insurance - In a manner similar to that of property development, there is a clear commercial need for accurate modeling of the environment within the insurance (especially the reinsurance) industry. What optical parameters will improve the forecasting ability for coastal hazards (including hurricanes, and red tides)?
- Sensor development - Central to most of what has already been described above, is that there continue to be healthy progress in the research and development of optical instrumentation for the ocean. What are the market demands for new parameters (e.g. polarimetry). Much of this may be driven by the need to ground truth the next-generation of satellites.

3.2.4 Education/Communication

There is currently a very active movement to strengthen the national science education base at all levels within K-12. Ocean science is barely a part of this, but efforts are underway for improvement. The fundamental concept is the ocean science represents an ideal platform for implementing the new ideas of continuing, interdisciplinary, inquiry-based, hands on learning. In this regard ocean optics holds great potential.

- Formal (i.e. classroom based) education - Optics plays a key role since it is relevant to all disciplines, and its theories lend themselves nicely to all aspects of mathematics. Optical measurements of the simplest nature should be incorporated into the growing set of K-12 based environmental observational programs being used for instructional purposes in classrooms worldwide. It is also incumbent on the community of theoreticians working in ocean optics to strive to have these studies used as models of application of mathematics, including geometry and calculus in high school texts and curricula.
- Informal education - Aquariums and science museums are being constructed at unprecedented rates. These forums for informal education represent wonderful sites for demonstrating the wonder of underwater optics, as long as the measurements and concepts can be kept simple. To this end there is a need for the optical oceanographic community to work with outreach directors of the aquariums and science centers to fold these ideas into the displays and exhibits.

4. CONCLUSIONS

In the decades to come ocean optics will play an increasingly critical role in a wide range of societal applications. These applications will be much more dispersed than those to which the research community has become accustomed in the last half century. As a result, funding sources will have to become more disperse.

We should look to other communities as examples of how this has happened in the past. The researchers working on radio detection and ranging, radar, originally developed their field and its seemingly quirky tools exclusively to find ships and aircraft for battle. This field broadened its horizons after the second World War and now works in support of an astoundingly broad set of societal and commercial interests from weather forecasting (doppler radar), to long-term climate change research (sea ice synthetic aperture radar), to crime detection (police radar), and archaeology (ground penetrating radar).

Ocean optics must also expand. One obvious consequence of this diversification is that the field of ocean optics will continue to be a growth area. We must be prepared to answer the question of where the students and experts are going to come from. Ocean optics centers of excellence were once formally recognized (e.g. The University of Copenhagen and the Scripps Visibility Laboratory). The research community should take steps now to redefine such centers; they should develop by design, not by default.

5. ACKNOWLEDGEMENTS

The author wishes to thank all of the members of the Ocean Optics community for fruitful discussions relevant to this manuscript. Special thanks go to Steve Ackleson for his encouragement to put these thoughts to paper.

6. REFERENCES

1. Secchi, P.A., 1866. Esperimento per determinare la trasparenza del mare. Sul moto ondoso del mare. Cialdi (ed.) Rome, 258-288.
2. Murray, J. And J. Hjort, 1912. Atlanterhavet, fra overflaten til cont. On p. 3 havdypets morke. Pt. 5. M. Aescheloug et Co. (W. Nygaard), Kristiania (now Oslo), p. 197.
3. Bartz, R., J.R.V. Zaneveld and H. Pak, 1978. A transmissometer for profiling and moored observations in water, SPIE Ocean Optics 160:102-108.
4. Spinrad, R.W. And J.R.V. Zaneveld, 1982. An analysis of the optical features of the near bottom and bottom nepheloid layers in the area of the Scotian Rise, J. Geophys. Res. 87:9553-9561.
5. Baker, E.T. And J.W. Lavelle, 1984. The effect of particle size on the light attenuation coefficient of natural suspensions. J. Geophys. Res., 89:8197-8204.
6. Zaneveld, J.R.V., R.W. Spinrad and R. Bartz, 1982. An optical settling tube for the determination of particle size distributions. Marine Geology, 49:357-376.
7. Kirk, J.T.O. 1983. *Light and Photosynthesis in Aquatic Ecosystems*, Cambridge University Press, Cambridge, 401 pp.
8. Gordon, H.R., 1994. Modeling and simulating radiative transfer in the ocean. In *Ocean Optics*, Spinrad, Carder and Perry, eds. Oxford University Press, New York. Pp. 3-39.
9. Service, R., 1996. Plastics may add new colors to lasers' light show. Science 273: 1800-1801.
10. CORE (Consortium for Oceanographic Research and Education), 1996. *Oceans 2000: Bridging the Millennium. Partnerships for Stakeholders in the Ocean*. CORE, Washington, DC. Pp. 51.
11. Fenical, W., 1996. Marine biodiversity and the medicine cabinet: the status of new drugs from marine organisms. Oceanography 9:23-27.

Inverse Radiative Transfer Problems in Environmental Optics

Howard R. Gordon, G. Chris Boynton, and Tianming Zhang

Department of Physics, University of Miami

Coral Gables, FL 33124 USA

ABSTRACT

We present sketches of the solution of several inverse problems in environmental optics. The solutions include all significant orders of multiple scattering and have the attribute that, when the retrieved optical properties are substituted into the radiative transfer equation, they accurately reproduce the given apparent optical properties.

Keywords: radiative transfer, oceanic optics, atmospheric optics, inverse scattering, polarization

1. INTRODUCTION

In the direct problem of radiative transfer the inherent optical properties (IOPs), the absorption coefficient and the volume scattering function, are used with the radiative transfer equation to derive the radiance distribution. In contrast, in the inverse problem the apparent optical properties (AOPs), the radiance distribution or its low-order moments, are combined with the radiative transfer equation to derive the IOPs. In both the ocean and the atmosphere, IOPs derived from solution of the inverse problem have the desirable property that they are not limited by the small sampling volumes typically associated with insitu instrumentation.

We examine two inverse problems in environmental optics: (1) the retrieval of the absorption and backscattering coefficients in an oceanic water column by inversion of vertical profiles of the up- and downwelling irradiances or the upwelling nadir radiance and downwelling irradiance; and (2) the retrieval of IOPs for an optically thick slab, e.g., the atmosphere, from measurement of the boundary radiances. These problems are related by virtue of their importance in the remote sensing of ocean color, and by the fact that very similar methods are employed in effecting a solution.

2. GENERAL METHOD of INVERSION

The method we use for solving the two inverse problems described in the introduction falls under the general category of *implicit* solutions.¹ Briefly, our technique involves solving the radiative transfer equation (RTE) in the scalar (SRTE) or the vector (VRTE) form using a trial set of IOPs. The trial solution (radiances, irradiances, etc.) is then compared to the experimental data and, based on the difference between the trial solution and the data, a "revised" set of IOPs is estimated. These are then inserted into the RTE and a new trial solution is derived. The process continues in an iterative manner until the differences between the trial solution and the data are as small as desired,²⁻⁶ i.e., the resulting IOPs accurately reproduce the given AOPs. Clearly, the key to this process is the manner in which the IOPs are varied prior to the n^{th} iteration based on the results of the $n^{\text{th}} - 1$ iteration. We have found that, for the problems of interest here, this can be effected by simple approximate formulae relating the measured quantities to the IOPs.

3. SPECIFIC PROBLEMS

3.1 Homogeneous Ocean

The ocean problem, the retrieval of the absorption (a) and backscattering (b_b) coefficients in an oceanic water column by inversion of vertical profiles of the up- and downwelling irradiances (E_u and E_d) or the upwelling nadir radiance and downwelling irradiance (L_u and E_d), is central to remote sensing of ocean color, as the diffuse reflectance of the ocean is governed by the ratio b_b/a . In this problem we use the SRTE, i.e., polarization is ignored. Estimation of a at each iteration step in the solution is not difficult because an exact equation is available: Gershun's law.⁷ To estimate b_b we simply assume that the usual relationship between the irradiance reflectance R , just beneath the

surface, and the IOPs,^{8,9} i.e., $R \approx b_b/3a$, is a good approximation at *all* depths. This, and a guess for the scattering phase function of the medium, provides the information necessary to continue the iteration. Fortunately, the results are insensitive to the assumed scattering phase function as long as it is realistic². Embedded in our inversion code is a Monte Carlo SRTE subroutine consisting of an ocean of arbitrary optical properties and a fifty-layer atmosphere including both Rayleigh and aerosol scattering. Thus, the entire radiative transfer process is treated in a realistic manner.

The results of simulations suggest that for a homogeneous medium, a can be estimated with an uncertainty of $\lesssim 1\%$. The error in b_b is similarly small if the assumed phase function is correct; however, with incorrect, but realistic phase functions, errors $\lesssim 10 - 20\%^2$ are typically encountered. We also inverted the experimental data of Tyler¹⁰ in which sufficient measurements were carried out that Gershun's law could be used to obtain an experimental value of a . Approximating the phase function by a Henyey-Greenstein with asymmetry parameter g , the results shown in Table 1 were obtained. The last row provides the experimental value of a . Clearly, the retrieved a is insensitive to the phase function estimate.

Table 1: Test of the irradiance algorithm with Tyler's radiance data from Lake Pend Oreille, ID.

Algorithm	a m^{-1}	$b_b (\times 1000)$ m^{-1}
$g = 0.85$	0.1203	6.18
$g = 0.90$	0.1183	5.98
$g = 0.95$	0.1174	5.70
Gershun's Law	0.116	—

A similar algorithm was developed to utilize the upwelling radiance (L_u) in place of the upwelling radiance (E_u). These quantities are related by the Q -factor:¹¹ $Q = E_u/L_u$. In this case, the algorithm is initiated with $Q = \pi$, which enables estimation of $E_u(z)$ from $L_u(z)$. Then at each step of the iteration the Q -factor from the solution to the SRTE in the previous step is employed to estimate new values of E_u from the measured L_u . The E_u estimates are used to provide revised estimates of the IOPs. Otherwise the algorithm is identical to the irradiance algorithm. Simulations show that the radiance-irradiance algorithm performs as well as the irradiance algorithm; however, the derived b_b is more sensitive to the assumed phase function. Inversion of Tyler's data using the L_u - E_d algorithm provides results similar to those in Table 1. The addition of a lambertian reflecting bottom to the ocean poses no difficulty in the retrieval of a , even in cases for which the bottom strongly influences the upwelling light field; however, in such situations the retrieval of b_b can be very poor.

3.2 Stratified Ocean

We have been studying the extension of the irradiance algorithm to cases in which the IOPs vary with depth. Estimation of a at each step of the algorithm is the same as in the homogeneous case, as Gershun's law can still be used. However, estimation of $b_b(z)$, where z is depth, is now more difficult, because $R(z')$ depends on the variation of the IOPs for $z > z'$. We assume that the Gordon and Clark¹² relationship between $R(0)$ and $b_b(z)/a(z)$, can be extended deeper into the medium. Specifically, we assume

$$R(z) \approx \frac{\langle X(z) \rangle}{3},$$

where

$$\langle X(z) \rangle = \frac{\int_z^\infty X(z')g(z, z') dz'}{\int_z^\infty g(z, z') dz'},$$

$$g(z, z') = [E_d(z')/E_d(z)]^2,$$

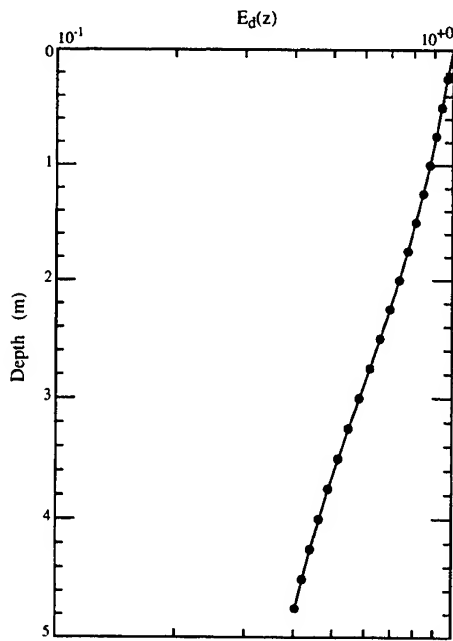


Figure 1a.

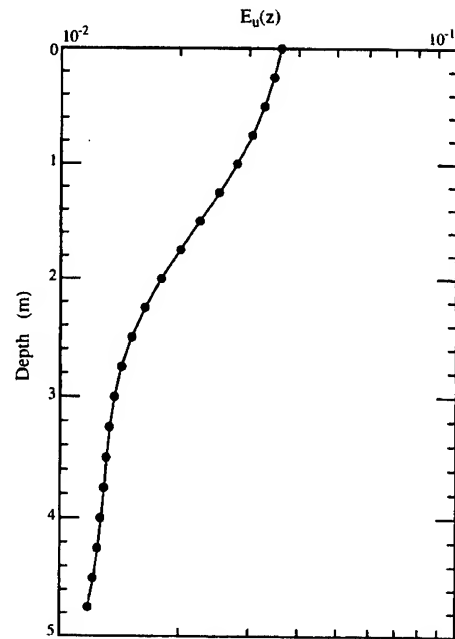


Figure 1b.

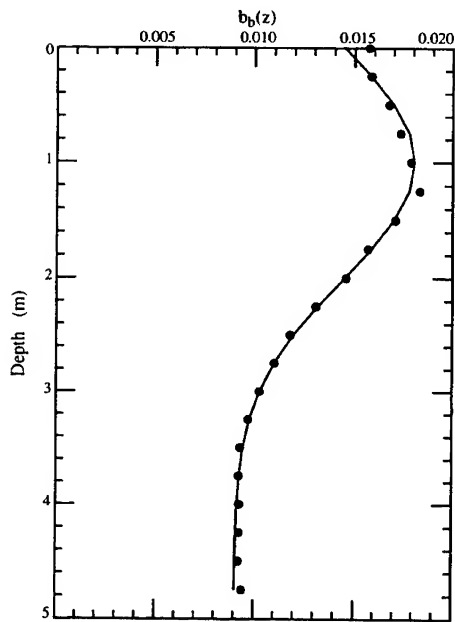


Figure 1c.

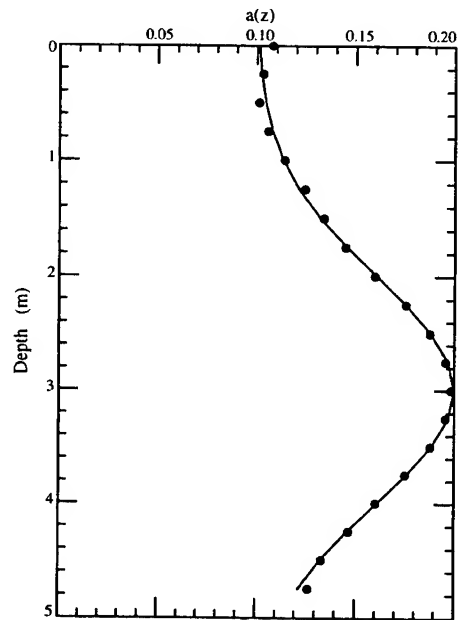


Figure 1d.

Figure 1. Operation of the E_u - E_d algorithm in a vertically stratified ocean: (a) $E_d(z)$; (b) $E_u(z)$; (c) $b_b(z)$; and (d) $a(z)$. $E_d(z)$ and $E_u(z)$ are normalized to $E_d(0)$, and a and b_b are in m^{-1} . Lines are the true values and dots are the retrieved values.

where $z' \geq z$. This enables estimation of $X(z)$ from the $R(z)$ profile; however, since an estimate of $a(z)$ already exists (Gershun's law), $X(z)$ provides an estimate of $b_b(z)$. In practice, the upper limit on the integrals (∞) is taken to be the maximum depth at which data is available. We are in the process of testing this algorithm for its ability to retrieve profiles of a and b_b . Figure 1 provides the results of one sample test in which $a(z)$ and $b_b(z)$ vary independently with depth. Clearly, the approach appears promising.

3.3 Atmospheric Problems

Our application of the inverse problem of radiative transfer to the atmosphere is focused on two needs: (a) estimation of the aerosol optical properties for use in atmospheric correction, remote sensing of aerosols, etc.; and (2) estimation of aerosol properties to predict top-of-atmosphere (TOA) radiances for on-orbit calibration of ocean color sensors. In these problems, measurement of the radiance exiting the bottom of the atmosphere (BOA) I_B , or when polarization is included, the Stokes vector \mathbf{I}_B , and the optical thickness of the atmosphere τ are always assumed to be given. However, space-borne or aircraft-borne sensors may in addition provide TOA radiances in various viewing directions, I_T and \mathbf{I}_T , the scalar and vector radiances, respectively.

Wang and Gordon³ provided an algorithm for estimating the scattering phase function $P_{11}(\Theta)$, where Θ is the scattering angle, and the aerosol single scattering albedo, ω_0 , when only BOA measurements are available. Briefly, ignoring reflection from the sea surface and Rayleigh scattering in the atmosphere, the BOA radiance in the single-scattering (scalar) approximation, is given by

$$I_B \approx \frac{\omega_0 \tau F_0}{4\pi \cos \theta} P_{11}(\Theta) \quad (1)$$

where F_0 is the extraterrestrial solar irradiance, and θ is the viewing angle with respect to the zenith. Θ is the single-scattering angle appropriate to θ . The Wang and Gordon algorithm operates in a manner similar to the ocean algorithms above. Using an assumed form for the product $\omega_0 P_{11}(\Theta)$ and the measured optical thickness, the SRTE is solved, for an atmosphere bounded by a Fresnel-reflecting ocean, to provide an estimate of I_B . This estimate is compared with the measured I_B and an error determined. A portion of this error (25-50%) is then assigned to $\omega_0 P_{11}(\Theta)$ using Eq. (1), providing a new estimate of $\omega_0 P_{11}(\Theta)$. The iteration then proceeds as in the ocean example. Since only single-scattering angles $0 \leq \Theta \lesssim \pi/2 + \theta_0$, where θ_0 is the solar zenith angle, are available from the surface, an assumption regarding the phase function at larger scattering angles must be made, e.g., it is constant.

Gordon and Zhang⁴ provided an extension to the Wang and Gordon algorithm for cases when measurements of I_T are available. This was effected by using an equation similar to Eq. (1), but applicable to the TOA radiance. Examples of the performance of this algorithm, and its sensitivity to errors in the measurements, are provided in Ref. 4 and Ref. 6, respectively, for aerosol optical thicknesses as large as 2, i.e., situations in which multiple scattering totally dominates single scattering.

When the full Stokes vector \mathbf{I} is measured at the BOA, more information can be derived from the sky radiance. In this case, the equation corresponding to Eq. (1) is

$$\mathbf{I}_B = \begin{pmatrix} I_B \\ Q_B \\ U_B \\ V_B \end{pmatrix} \approx \frac{\omega_0 \tau F_0}{4\pi \cos \theta} \begin{pmatrix} P_{11}(\Theta) \\ P_{12}(\Theta) \cos 2\alpha \\ P_{12}(\Theta) \sin 2\alpha \\ 0 \end{pmatrix}, \quad (2)$$

where $P_{11}(\Theta)$ and $P_{12}(\Theta)$ are the 11 and 12 elements of the scattering phase matrix $\mathbf{P}(\Theta)$. The 11 element of $\mathbf{P}(\Theta)$ is usually referred to as the *phase function*. The angle α in Eq. (2) is the angle between the plane formed by the propagation vectors of the incident and scattered photons (the scattering plane) and the plane formed by the propagation direction of the scattered photon and the zenith (the standard reference plane for defining polarization state of photons in the atmosphere). Retrieval of ω_0 , $P_{11}(\Theta)$ and $P_{12}(\Theta)$ from \mathbf{I}_B follows a path similar to the retrieval of ω_0 and $P_{11}(\Theta)$ from I_B , except that the VRTE is used to provide the estimate of \mathbf{I}_B at each stage.¹³ Assumptions must be made regarding the remaining elements of $\mathbf{P}(\Theta)$. If we assume that the aerosol particles are spheres, only $P_{33}(\Theta)$ and $P_{34}(\Theta)$ are required. We use the maritime aerosol model of Shettle and Fenn,¹⁴ with relative

humidity of 0 (which we refer to as M00), to estimate these. Fortunately, the retrieval of $P_{11}(\Theta)$ and $P_{12}(\Theta)$ is not too sensitive to the assumptions regarding $P_{33}(\Theta)$ and $P_{34}(\Theta)$. When TOA measurements of I are available as well, they can be included in the retrieval algorithm in the same manner as in the scalar case. In Figure 2, we provide a simulated example of the retrieval of ω_0 , $P_{11}(\Theta)$ and $P_{12}(\Theta)$ for the Shettle and Fenn¹⁴ tropospheric model with

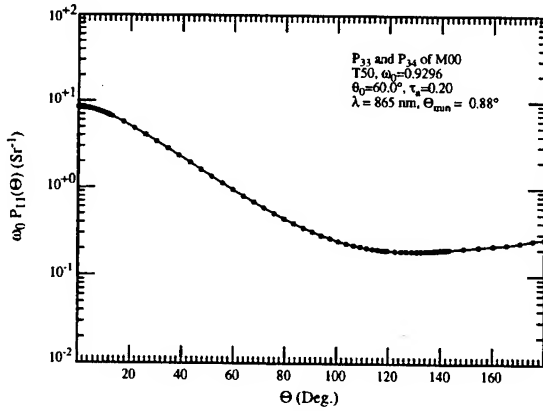


Figure 2a.

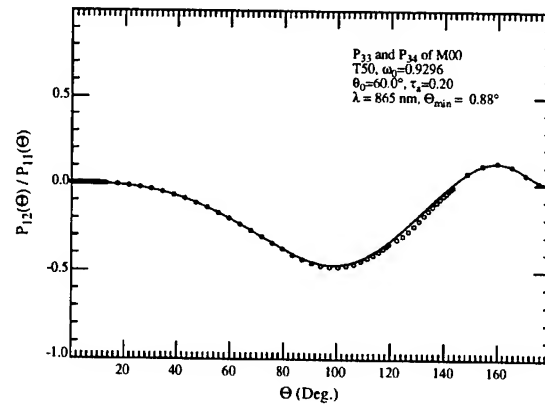


Figure 2b.

Figure 2. Retrieved elements of the scattering Mueller matrix for T50 at 865 nm with an aerosol optical thickness (τ_a) of 0.2. The P_{33} and P_{34} elements were taken from an incorrect aerosol model (M00). Solid curves are the true values and solid circles are the retrieved values. Panel (a): $\omega_0 P_{11}(\Theta)$, Panel (b): $P_{12}(\Theta)/P_{11}(\Theta)$.

50% relative humidity (T50) and an aerosol optical thickness of 0.2. Although this optical thickness may appear small, the multiple scattering effects are still severe enough that if they were neglected, the error in the retrieved $P_{11}(\Theta)$ could be as much as a factor of two over a large range of scattering angles. The small error in the retrieval of $P_{12}(\Theta)$ for $100^\circ \lesssim \Theta \lesssim 145^\circ$, is due to the assumptions regarding $P_{33}(\Theta)$ and $P_{34}(\Theta)$. The pseudodata used in the preparation of Figure 2 consisted of I_B measured in the solar almucantar (with $\theta_0 = 60^\circ$) and then the principal plane (opposite to the sun) down to the horizon, while I_T was measured in the principal plane. We have been able to obtain similar results for aerosol optical thicknesses as large as 2.0, indicating that the algorithm is as effective as in the scalar case. We are in the process of carrying out a complete sensitivity study of the stability of the solutions to errors in the input data.

4. CONCLUDING REMARKS

Iterative algorithms, in which the RTE is solved at each step, can be devised to retrieve IOPs from measured AOPs. The key to the process is the use of simple relationships to "nudge" the solution (the trial IOPs) in the proper direction at each step. In the case of the ocean, the relationship between a and b_b , derived from multiple scattering simulations,^{8,9} was used. In contrast, in the atmospheric problems, appropriate single scattering solutions were employed. It should be stressed, that these relationships are used only to push the solution in the proper direction, the solution itself contains the effects of all orders of multiple scattering.

5. ACKNOWLEDGMENTS

We are grateful to the Office of Naval Research for providing support under Grant Number N00014-89-J-1985, and to the National Aeronautics and Space Administration under Grant NAGW-273 and Contracts NAS5-31363 and NAS5-31743.

6. REFERENCES

- [1] N. J. McCormick, "Inverse Radiative Transfer Problems: A Review," *Nuclear Science and Engineering* **112**, 185-198 (1992).
- [2] H. R. Gordon and G. C. Boynton, 1996, A radiance - irradiance inversion algorithm for estimating the absorption and backscattering coefficients of natural waters: Homogeneous waters, *Applied Optics* (In Press).
- [3] M. Wang and H. R. Gordon, "Retrieval of the Columnar Aerosol Phase Function and Single Scattering Albedo from Sky Radiance over the Ocean: Simulations," *Applied Optics* **32**, 4598-4609 (1993).
- [4] H. R. Gordon and T. Zhang, "Columnar Aerosol Properties Over Oceans by Combining Surface and Aircraft Measurements: Simulations," *Applied Optics* **34**, 5552-5555 (1995).
- [5] H. R. Gordon and T. Zhang, 1996, How well can radiance reflected from the ocean-atmosphere system be predicted from measurements at the sea surface?, *Applied Optics* (In press).
- [6] T. Zhang and H. R. Gordon, 1996, Columnar aerosol properties over oceans by combining surface and aircraft measurements: sensitivity analysis *Applied Optics* (In press).
- [7] C. D. Mobley, *Light and Water; Radiative Transfer in Natural Waters* (Academic Press, New York, 1994), 592 pp.
- [8] H. R. Gordon, O. B. Brown and M. M. Jacobs, "Computed Relationships Between the Inherent and Apparent Optical Properties of a Flat Homogeneous Ocean," *Applied Optics* **14**, 417-427 (1975).
- [9] H. R. Gordon and A. Y. Morel, *Remote Assessment of Ocean Color for Interpretation of Satellite Visible Imagery: A Review* (Springer-Verlag, New York, 1983), 114 pp.
- [10] J. E. Tyler, "Radiance distribution as a function of depth in an underwater environment," *Bull. Scripps Inst. Oceanogr.* **7**, 363-411 (1960).
- [11] R. W. Austin, "The Remote Sensing of Spectral Radiance from below the Ocean Surface," in *Optical Aspects of Oceanography*, edited by N. G. Jerlov and E. S. Nielsen (Academic Press, London, 1974) p. 317-344.
- [12] H. R. Gordon and D. K. Clark, "Remote Sensing Optical Properties of a Stratified Ocean: An Improved Interpretation," *Applied Optics* **19**, 3428-3430 (1980).
- [13] T. Zhang and H. R. Gordon, Passive Remote Sensing of Elements of the Aerosol Scattering Matrix: Simulations. To be presented at the OSA Topical Meeting "Optical Remote Sensing of the Atmosphere, Santa Fe, NM, Feb. 1997.
- [14] E. P. Shettle and R. W. Fenn, *Models for the Aerosols of the Lower Atmosphere and the Effects of Humidity Variations on Their Optical Properties* (Air Force Geophysics Laboratory, Hanscomb AFB, MA 01731, AFGL-TR-79-0214, 1979).

Effects of absorption and boundary conditions on the utility of diffusion theory

Curtis D. Mobley
Robert A. Maffione

Sequoia Scientific, Inc.
9725 S.E. 36th Street, Suite 308
Mercer Island, WA 98040

ABSTRACT

Comparison with exact numerical simulations shows that diffusion theory adequately describes light propagation in sea ice, when optically far from surface or bottom boundaries. More importantly, diffusion theory provides a link between easily measured quantities and other quantities that are crucial to radiative transfer theory, but which cannot be measured directly. In particular, formulas are presented which give the scattering asymmetry parameter and albedo of single scattering as functions of diffuse attenuation and absorption.

Keywords: radiative transfer, diffusion theory, sea ice, optical oceanography, absorption, scattering

1. DIFFUSION THEORY

Classical diffusion theory describes light transport if two conditions are met. First, absorption must be almost negligible compared to scattering and, second, the region of interest must be far from any boundaries. However, there is no simple means to quantify these two conditions or to predict the increasing inaccuracy of diffusion theory as the conditions become less well satisfied. We have therefore used numerical simulations to produce exact radiance distributions for given absorption and scattering properties and for given boundary conditions. These exact solutions are then compared with the predictions of diffusion theory to quantify the errors resulting from the use of diffusion theory.

For later reference, we note that diffusion theory predicts that the radiance (and hence all irradiances) decay with depth at a rate given by

$$\kappa = \sqrt{a/D}, \quad (1)$$

where a is the absorption coefficient of the medium, and D is the diffusion coefficient. The diffusion coefficient is related to the inherent optical properties of the medium by

$$D = \frac{1}{3c(1 - g\omega_o)}. \quad (2)$$

Here $c = a + b$ is the beam attenuation coefficient, b is the scattering coefficient, g is the scattering asymmetry parameter (the average cosine of the scattering angle), and $\omega_o = b/c$ is the albedo of single scattering. Substituting Eq. (2) into Eq. (1) and rewriting gives a useful form for κ :

$$\kappa = c\sqrt{3[1 - \omega_o - g\omega_o(1 - \omega_o)]}. \quad (3)$$

2. NUMERICAL SIMULATIONS

Using the Hydrolight radiative transfer model (Mobley, 1994), numerical simulations were performed for a three-layer system consisting of air, ice, and water. A given sky radiance was incident onto the ice surface, which could be rough or smooth. The ice inherent optical properties were expressed in terms of ω_o and g , which was used in conjunction with a one-term Henyey-Greenstein phase function. The water below the ice was infinitely deep; its optical properties were specified by appropriate values of ω_o and g .

Figure 1 shows an example profile of the diffuse attenuation coefficient for scalar irradiance, K_o . The incident sky radiance was given by a cardioidal distribution, which corresponds to an overcast sky. The ice surface was smooth. The ice was highly scattering, $\omega_o = 0.98$, and had a strongly peaked scattering phase function, $g = 0.9$. The water was more absorbing, $\omega_o = 0.9$, as is appropriate for blue light. Depth is expressed as optical depth; thus K_o is nondimensional. The solid line shows the exact K_o as computed by Hydrolight; the dashed line is the κ predicted by diffusion theory. Diffusion theory clearly gives a good prediction of K_o in the center of the ice layer but is quite inaccurate near the boundaries. However, the notable feature of this profile is that near the air-ice surface, the actual K_o is less than κ , but at the ice-water boundary, the actual value of K_o is greater than κ . This qualitative behavior holds true regardless of the details of the boundary conditions: clear or cloudy sky, rough or smooth surface, different water optical properties.

This observation suggests that the *average* diffuse attenuation throughout the ice layer might be a good approximation to κ . Indeed, detailed analysis reveals that κ can be estimated to within five percent accuracy (for $\omega_o = 0.98$ and $g = 0.9$) by using an average K_d , which can be measured as follows. Place a plane irradiance sensor in the air just above the ice to obtain $E_d(\text{air})$; then make a corresponding measurement in the water just below the ice to obtain $E_d(\text{water})$; then use these two irradiances to compute the average K_d for the ice layer. Such measurements are routinely made by sea ice researchers. Likewise, it is relatively easy to measure the average absorption coefficient a of the ice layer: extract and melt an ice core and then measure the absorption of the meltwater in a spectrophotometer.

Solving Eq. (3) for g and replacing κ by the average K_d yields

$$g = \frac{1}{\omega_o} - \frac{1}{3} \left(\frac{1}{\omega_o} - 1 \right) \left(\frac{K_d}{a} \right)^2. \quad (4)$$

This equation enables us to estimate the scattering asymmetry parameter. We measure the average K_d and a as described above. Observations made in sea ice (Maffione, 1996) indicate that the ω_o for sea ice is in the range of 0.97 to 0.99; we can thus make an educated guess of, say, $\omega_o = 0.98$. Equation (4) then yields an estimate of g . As an example, using $K_d = 2.5 \text{ m}^{-1}$, $a = 0.53 \text{ m}^{-1}$ (appropriate for a wavelength of 670 nm; see Maffione, 1996), and $\omega_o = 0.98$ gives $g = 0.87$. Because the scattering centers in sea ice

– brine pockets, embedded particles, salt crystals, and the like – are much larger than the wavelength of light, we expect that the scattering phase function will be strongly peaked in the forward direction. Thus a value of $g = 0.87$ is physically plausible.

3. A CONNECTION WITH TURBID WATERS

In a series of papers, Kirk (1994, and references therein) found from Monte Carlo simulations that K_d deep in natural water bodies is well approximated by the simple equation

$$K = \sqrt{a^2 + Gab}, \quad (5)$$

where G is a regression parameter determined by the best fit of Eq. (5) to the numerical results of his simulations. Kirk's simulations span the range from $\omega_o = 0$ to 0.995, and he used a highly peaked phase function for which $g = 0.924$. For large ω_o , Kirk finds $G = 0.233$. Since Kirk's simulations extend into the large- ω_o domain where diffusion theory should be useful, it is interesting to compare his results with diffusion theory.

Equation (5) can be rewritten as

$$K = c\sqrt{1 - 2\omega_o + \omega_o^2 + G\omega_o(1 - \omega_o)}. \quad (6)$$

Equating κ and K from Eqs. (3) and (6), respectively, and solving for G gives

$$G = 3(1 - g) + 2\left(\frac{1}{\omega_o} - 1\right). \quad (7)$$

Substituting $g = 0.924$ and $\omega_o = 0.995$, Eq. (7) gives $G = 0.238$, which is only two percent different than the value Kirk determined by regression. Diffusion theory therefore *predicts* the value of Kirk's empirical G parameter. In a similar fashion, all of Kirk's results for the behavior of apparent optical properties at high ω_o values are well described by diffusion theory.

4. RECOVERY OF g AND ω_o

Kirk performed his simulations using a highly peaked phase function, and his results appear to be quite good in the diffusion regime. We have already seen indications that the phase function of sea ice is also highly peaked. It is therefore reasonable to try to apply Kirk's empirical results to sea ice. We can do this by regarding Eq. (4), which rests on diffusion theory, and Eq. (7), which incorporates Kirk's G parameter, as two equations for g and ω_o . Solving for g and ω_o gives

$$g = \frac{\left(1 - \frac{G}{3}\right) \left(\frac{K_d}{a}\right)^2 + G - 1}{\left(\frac{K_d}{a}\right)^2 - 1} \quad (8)$$

and

$$\omega_o = \frac{2}{2 + G - 3(1 - g)} \quad (9)$$

Using Kirk's value of $G = 0.233$ along with $K_d = 2.5 \text{ m}^{-1}$ and $a = 0.53 \text{ m}^{-1}$ as before, we find $g = 0.93$ and $\omega_o = 0.99$. These are both very plausible values for sea ice.

The importance of Eqs. (8) and (9) cannot be overemphasized. *They give us a means of determining both the scattering asymmetry parameter and the albedo of single scattering from easily made measurements of diffuse attenuation and absorption.* Obtaining g is especially important, because it has never been measured *in situ* in sea ice. As was seen in Fig. 1, diffusion theory fails when near boundaries. However, the values of g and ω_o obtained by Eqs. (8) and (9) give us the information that is needed as input to the Hydrolight radiative transfer model, which can then compute light propagation within the ice, including the boundary effects.

We thus see that the value of diffusion theory is that it enables us to connect easily measured quantities with scattering parameters that are crucial to understanding light propagation in sea ice, but which themselves cannot be easily measured.

5. ACKNOWLEDGMENTS

This work was supported by the U.S. Office of Naval Research under the Sea Ice Electromagnetics Accelerated Research Initiative, administered by the ONR Environmental Optics Program.

6. REFERENCES

- Kirk, J. T. O., 1994. Characteristics of the light field in highly turbid waters: A Monte Carlo study. *Limnol. Oceanogr.*, **39**(3), 702-706.
- Maffione, R. A., 1996. Ph.D. Dissertation. Oregon State University, Dept. of Oceanography, Corvallis, Oregon.
- Mobley, C. D., 1994. *Light and Water: Radiative Transfer in Natural Waters*. Academic Press, San Diego, 592 pages.

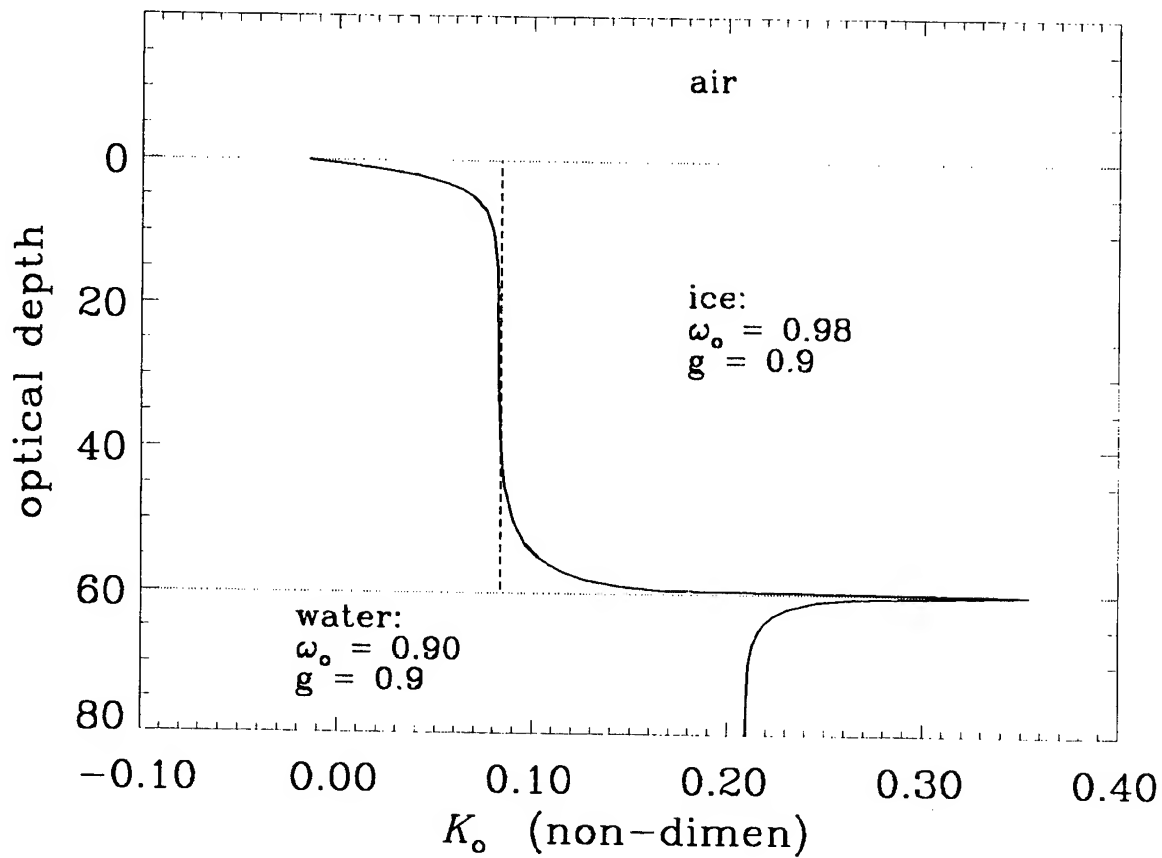


Figure 1. The solid line gives the depth profile of the diffuse attenuation coefficient for scalar irradiance, as computed by Hydrolight for conditions as described in the text. The dashed line is the corresponding value of κ within the sea ice, as given by diffusion theory.

Absorption and scattering coefficient estimation with asymptotic apparent optical properties

R. A. Leathers and N. J. McCormick

University of Washington, Department of Mechanical Engineering
Box 352600, Seattle, Washington 98195-2600 USA

ABSTRACT

In deep, homogeneous waters with no internal sources at a particular wavelength, the vertical profiles of the reflectance $R(z)$ and the downward diffuse attenuation coefficient $K_d(z)$ approach asymptotic values that are inherent optical properties (IOP's) of the water. The apparent optical properties $R(z)$ and $K_d(z)$ are obtained from the upward and downward monospectral irradiance measurements $E_u(z)$ and $E_d(z)$ that are commonly available to optical oceanographers. Given a specific scattering phase function, there are unique correlations between these asymptotic IOP's and the absorption and scattering coefficients a and b that can be derived from the radiative transfer equation. Here we evaluate a method for first determining the asymptotic IOP's from $E_u(z)$ and $E_d(z)$ and then using the correlations to estimate the absorption and scattering coefficients a and b . At depths near the asymptotic radiance regime, both $R(z)$ and $K_d(z)$ can be fitted to a three-parameter model that sometimes helps in the determination of the asymptotic IOP's. A good estimation of a can be obtained from the asymptotic IOP's even when the scattering phase function is unknown; however, estimates of b are highly dependent on the assumed phase function.

Keywords: ocean optics, radiative transfer, optical properties.

1 INTRODUCTION

The absorption and scattering coefficients a and b of natural waters are inherent optical properties (IOP's) that are of primary interest in the field of optical oceanography. They are fundamental inputs to biological and radiative transfer models. In theory, the absorption and scattering coefficients can be determined from the combination of monochromatic irradiance and monochromatic scalar irradiance measurements (e.g. from Gershun's relation¹). Since monochromatic scalar irradiance detectors are not yet readily available, though, we restrict our attention to the use of in-water downward and upward irradiances. The absorption coefficient has been estimated from near-surface irradiance measurements used with simultaneous estimates of the mean cosine of the radiance distribution or with measurements of remote-sensing reflectance. However, such surface methods are complicated by surface waves and ship-shadowing, while above-surface methods require empirical correlations. Thus, there remains a need for a convenient and robust method of *in situ* measurements to determine a and b .

Here we evaluate a method for determining the single-scattering albedo $\omega_0 = b/c$ and $c = (a + b)$ from only monospectral upward and downward irradiance measurements $E_u(z)$ and $E_d(z)$ at several depths z through calculations of the asymptotic values of the reflectance $R(z)$ and downward diffuse attenuation coefficient $K_d(z)$. All IOP's of the water in the euphotic zone are assumed to be constant with depth, and there are assumed to be no light sources at the wavelengths of interest. The homogeneous IOP assumption is valid where either the surface waters are well mixed or light attenuation is high, both of which are more common in coastal waters

than in deep ocean waters. The no-source assumption is valid in waters and at wavelengths where fluorescence, bioluminescence, and Raman scattering are negligible.

The reflectance and the downward diffuse attenuation coefficient are apparent optical properties (AOPs), the vertical profiles of which asymptotically approach IOP's of the water, R_∞ and K_∞ , respectively.^{2,3} At depths near the asymptotic radiance regime, both $R(z)$ and $K_d(z)$ can be fitted to an exponential model^{4,5} that may help in the determination of the asymptotic IOP's because one parameter is the desired asymptotic IOP. The depths at which this model may be helpful depends on the IOP's and the surface illumination.

In this work, we follow the lead of Gordon et al.⁶ in which the scattering phase function is approximated by the Henyey-Greenstein function⁷ parameterized by the scattering asymmetry factor g . Given a specific value of g , there are unique correlations between the asymptotic IOP's and ω_0 and c that can be derived from the radiative transfer equation (RTE). Thus, if the phase function is known, measurements of R_∞ can be used to iteratively solve for ω_0 . Once ω_0 has been estimated, data for K_∞ can be used to determine c .

2 BASIC EQUATIONS

Light propagation at a single wavelength in homogeneous, source-free waters is governed by the integrodifferential RTE,

$$\mu \partial L(z, \mu) / \partial z + c L(z, \mu) = \frac{b}{2} \sum_{n=0}^M (2n+1) f_n P_n(\mu) \int_{-1}^1 P_n(\mu') L(z, \mu') d\mu', \quad (1)$$

where $L(z, \mu)$ is the radiance integrated over the azimuthal angle whose polar angle with respect to the vertical direction z is $\cos^{-1} \mu$. The azimuthally-integrated scattering phase function expanded in $(M+1)$ Legendre polynomials is normalized such that $f_0 = 1$. The $P_n(\mu)$ are the Legendre polynomials, and the expansion coefficients for the Henyey-Greenstein function are $f_n = g^n$. The irradiance reflectance $R(z) = E_u(z)/E_d(z)$, where $E_u(z)$ and $E_d(z)$ are the upward and downward irradiances,

$$E_d(z) = \int_0^1 \mu L(z, \mu) d\mu \quad \text{and} \quad E_u(z) = \int_{-1}^0 |\mu| L(z, \mu) d\mu. \quad (2)$$

The downward irradiance diffuse attenuation coefficient is defined by $K_d(z) = -d \{\ln E_d(z)\} / dz$.

At large depths in homogeneous waters with no internal sources the values of $R(z)$ and $K_d(z)$ approach asymptotic values R_∞ and K_∞ that are IOP's. To evaluate R_∞ and K_∞ in terms of the solution of the RTE, substitute $L(z, \mu) = \phi(\pm \nu_j, \mu) \exp(\mp cz/\nu_j)$ to find the discrete eigenfunctions $\phi(\pm \nu_j, \mu)$ satisfy

$$\phi(\pm \nu_j, \mu) = \frac{\omega_0 \nu_j}{2(\nu_j \mp \mu)} \sum_{n=0}^M (2n+1) f_n g_n(\pm \nu_j) P_n(\mu), \quad \nu_j > 1. \quad (3)$$

The Chandraseaekar polynomials g_n satisfy the recursion formula

$$n g_n(\nu_j) = h_{n-1} \nu_j g_{n-1}(\nu_j) - (n-1) g_{n-2}(\nu_j), \quad (4)$$

where $h_n = (2n+1)(1 - \omega_0 f_n)$, starting with $g_{-1} = 0$ and $g_0 = 1$. From the spherical harmonics (P_N) method,⁸ N odd, the positive eigenvalues ν_j are approximately the solutions to⁸

$$g_{N+1}(\nu) = 0. \quad (5)$$

The value of R_∞ can be determined exactly from the scalars ω_0 and g and is given by⁵

$$R_\infty = \frac{\int_0^1 \phi(-\nu_1, \mu) \mu d\mu}{\int_0^1 \phi(+\nu_1, \mu) \mu d\mu}, \quad (6)$$

and the value of K_∞ is determined exactly from the values of the scalars ω_0 , c and g and is given by

$$K_\infty = c/\nu_1, \quad (7)$$

where ν_1 is the largest positive eigenvalue.

3 ESTIMATION OF THE ASYMPTOTIC IRRADIANCE REFLECTANCE AND DIFFUSE ATTENUATION COEFFICIENT

In the asymptotic regime the profiles of $R(z)$ and $K_d(z)$ are constant with depth, and just above that, in the near-asymptotic regime, the profiles of $R(z)$ and $K_d(z)$ approach R_∞ and K_∞ in an exponential manner. These regimes exist at smallest optical depths when ω_0 is large.⁹ One way to estimate R_∞ and K_∞ is to measure $R(z)$ and $K_d(z)$ in the asymptotic regime and take $R_\infty \approx R(z)$ and $K_\infty \approx K_d(z)$. Alternatively, one can take measurements in the near-asymptotic regime, where^{4,5}

$$R(z) = R_\infty + [R(z_r) - R_\infty] \exp[-\mathcal{P}(z - z_r)], \quad z > z_r, \quad (8)$$

$$K_d(z) = K_\infty + [K_d(z_r) - K_\infty] \exp[-\mathcal{P}(z - z_r)], \quad z > z_r. \quad (9)$$

where z_r is some reference depth, and \mathcal{P} is an IOP that depends on the eigenvalues. Using measurements of $R(z)$ or $K_d(z)$ at three equally-spaced depths z_0 , z_1 , and z_2 ($2z_1 = z_0 + z_2$), R_∞ or K_∞ can be found from, for example,⁵

$$R_\infty = \frac{R(z_0)R(z_2) - R^2(z_1)}{R(z_0) + R(z_2) - 2R(z_1)}, \quad (10)$$

and similarly⁴ for K_∞ . Although the asymptotic values are usually computed from deep-water irradiance measurements, it would be more convenient to be able to obtain these from near-asymptotic measurements if this method is sufficiently accurate. To evaluate the two methods we compared values of R_∞ and K_∞ , obtained from simulated irradiance "data" using each method, to the theoretical values calculated from Eqs. (6) and (7).

It was found that when no simulated noise is added, excellent estimates of R_∞ and K_∞ are obtained from Eq. (10) in both the asymptotic and near-asymptotic regime; when noise is present, Eq. (10) was found to give poor results, even after smoothing of the irradiance data. Better results are obtained by fitting Eqs. (8) and (9); however, whenever noise in $R(z)$ or $K_d(z)$ is severe enough to mask their exponential form, it is better to simply take the average of $R(z)$ or $K_d(z)$ at large depths rather than attempt to extrapolate to the asymptotic values.

4 ESTIMATION OF THE ABSORPTION AND SCATTERING COEFFICIENT

The theoretical value of R_∞ is an exact function of ω_0 and g and is shown in Fig. 1, so given R_∞ and g it is possible to obtain a unique value of ω_0 . We can solve for ω_0 numerically through repetitive calculations of R_∞ while varying ω_0 within a search routine until the calculated R_∞ matches the desired (measured) value within the desired precision. Because the function $R_\infty(\omega_0, g)$ is smooth, such a search is not difficult.

It can be seen from Fig. 1 that the value of g has a significant effect on the value R_∞ , especially for high ω_0 . This is unfortunate because we may not have any *a priori* information about the phase function. Clearly, better results are obtained if one can put narrow limits on the possible values of g . It was found from numerical simulations that the calculated value of ω_0 is relatively insensitive to g when the true value of g is small, but can be very sensitive to g when g is large.

Once ω_0 is obtained, c can be easily calculated from Eq. (7) with $c = \nu_1 K_\infty$. The value of $\nu_1 = \nu_1(\omega_0, g)$ is already available because it is required in order to calculate R_∞ . Any relative error in the measurement of K_∞ results in a relative error in c of the same magnitude. An additional error in c results from any error in ν_1 arising from errors in R_∞ and g .

Figure 1: Asymptotic reflectance versus the single-scattering albedo ω_0 and scattering asymmetry factor g .

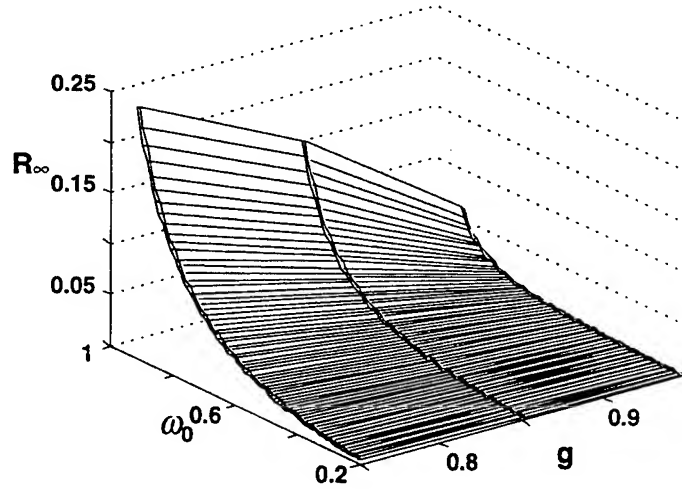


Table 1: Estimates of a and b for $g = 0.85$, $\omega_0 = 0.7$, $c = 1.0$ when R_∞ and K_∞ are known .

g	error in g	a	error in a	b	error in b
0.75	-12%	0.304	1.5%	0.418	-40%
0.95	12%	0.296	-1.3%	2.110	200%

The calculated values of ω_0 and c are easily converted to $a = c(1 - \omega_0)$ and $b = c\omega_0$. An important observation is that when the guess for g is too high, the resulting estimates of ω_0 and c are also both too high and vice versa. Therefore, errors in ω_0 and c due to g are magnified when calculating b , but are significantly reduced when calculating a . Table 1 gives example solutions for a and b when R_∞ and K_∞ are known but g is not. Despite large errors in g , the estimates for a are very good. Conversely, the estimates of b are quite poor.

5 SUMMARY AND CONCLUSIONS

The two IOP's R_∞ and K_∞ of a well-mixed, optically-deep, source-free water column can be obtained from only irradiance profiles $E_u(z)$ and $E_d(z)$. These IOP's can be estimated by taking the average of measured $R(z)$ and $K_d(z)$ values within the asymptotic regime. It was found that under favorable conditions good estimates of R_∞ and K_∞ can alternatively be found by fitting an exponential model of $R(z)$ and $K_d(z)$ in the near-asymptotic regime.

The conversion $\{R_\infty, K_\infty\} \rightarrow \{\omega_0, c\}$ is unique provided that the scattering phase function is known. Because the phase function can not be extracted from $E_u(z)$ and $E_d(z)$ alone, we assume the phase function to be well modeled by the Henyey-Greenstein function. It was found that good estimates of a can be obtained and that precise knowledge of the scattering phase function is not necessary. Conversely, good estimates of b can not be obtained when the scattering phase function is not known. Good estimates of ω_0 and c are possible only for certain ranges of the true IOP's and if the value of g is known to lie within a small range. The normalized sensitivities of a , b , ω_0 , and c to errors in K_∞ are unity, while the sensitivities to errors in R_∞ are significantly less than unity.

These results were obtained under a few important limitations, namely that the waters are deep, spatially homogeneous and source-free. Due to higher concentrations of both organic and non-organic matter in coastal waters, most Case II waters are optically deep despite having smaller geometric depths. Nonetheless, the effects of the bottom on this algorithm will be investigated in future work.

6 ACKNOWLEDGMENTS

This research was supported by the U. S. Office of Naval Research and by the San Diego Supercomputer Center.

7 REFERENCES

1. A. A. Gershun. "The light field," *J.Math.& Phys.*, **18**, 51-151, (1939).
2. N. K. Højerslev and J. R. V. Zaneveld. "A theoretical proof of the existence of the submarine asymptotic daylight field," Univ. Copenhagen Inst. Phys. Oceanogr. Rep. 34, (1977).
3. N. J. McCormick. "Asymptotic optical attenuation," *Limnol. Oceanogr.*, **37**, 1570-1578, (1992).
4. J. R. V. Zaneveld. "An asymptotic closure theory for irradiance in the sea and its inversion to obtain the inherent optical properties," *Limnol. Oceanogr.*, **34**, 1442-1452, (1989).
5. N. J. McCormick. "Analytical transport theory applications in optical oceanography," *Ann. Nucl. Energy*, **23**, 381-395, (1996).
6. H. R. Gordon, K. Ding, and W. Gong. "Radiative transfer in the ocean: computations relating to the asymptotic and near-asymptotic daylight field," *Appl. Opt.*, **32**, 1608-1619, (1993).
7. L. C. Henyey and J. L. Greenstein. "Diffuse radiation in the galaxy," *Astrophys. J.*, **93**, 70-83, (1941).
8. M. Benassi, R. D. M. Garcia, A. H. J. Karp, and C. E. Siewert. "A high-order spherical harmonics solution to the standard problem in radiative transfer," *Astrophys. J.*, **280**, 853-864, (1984).
9. C. D. Mobley. *Light and Water. Radiative Transfer in Natural Waters*. Academic Press, New York, 1994.

Angular structure of under-water light field:
Importance for ocean-colour models

Shubha Sathyendranath^{1,2} and Trevor Platt²

¹ Dept. of Oceanography, Dalhousie University, Halifax, Nova Scotia, Canada B3H 4J1

² Biological Oceanography Division, Bedford Institute of Oceanography, Box 1006, Dartmouth, Nova Scotia, Canada B2Y 4A2.

ABSTRACT

A simple analytical solution for reflectance at the sea surface is presented. The form of this analytical solution is similar to many earlier solutions, in that reflectance depends on the ratio of b_b to $(a + b_b)$. But it brings out explicitly the role of the zenith angular distribution of the underwater light field in modifying reflectance, through the quantities μ_d and μ_u , which determine the mean path lengths of downwelling and upwelling photons, respectively, per unit vertical excursion. The solution also shows that reflectance depends on the shape of the phase function for scattering.

The analytic solution is compared with the results of Monte Carlo simulations to establish its limits of applicability. Limitations of the model when multiple-scattering effects become important, and some possible modifications to the model to deal with such cases, are discussed.

Keywords: ocean colour, remote sensing, sea-surface reflectance, absorption coefficient, back-scattering coefficient, mean cosines.

1. INTRODUCTION

Changes in intrinsic ocean colour are determined by spectral variations in sea surface reflectance R , defined as:

$$R(\lambda, 0) = \frac{E_u(\lambda, 0)}{E_d(\lambda, 0)}, \quad (1)$$

where $E_u(\lambda, 0)$ is the upwelling irradiance at wavelength λ at the surface (depth $z = 0$), and $E_d(\lambda, 0)$ is the corresponding downwelling irradiance. Several existing models of ocean colour express R as a simple function of the absorption coefficient a and the back-scattering coefficient b_b . These models often take the form of either¹

$$R(\lambda, 0) = r \times \frac{b_b(\lambda, 0)}{a(\lambda, 0) + b_b(\lambda, 0)} \quad (2)$$

or^{2,3,4}

$$R(\lambda, 0) = r \times \frac{b_b(\lambda, 0)}{a(\lambda, 0)}. \quad (3)$$

Equations (2) and (3) are equivalent for the condition $b_b \ll a$, which is often satisfied in oceanic regions. In equations (2) and (3), the factor r is a proportionality factor. It has been shown^{2,3} that r often takes the value of 0.33. But it has also been shown that r changes with the zenith angle of incident light^{1,4,5} and with the shape of the phase function^{6,7}. In this paper we develop a simple analytic solution based on quasi-single scattering approximation⁸ for the factor r , which

is consistent with these earlier results. The solution is extended to include Raman scattering, and finally, we examine some consequences of multiple scattering.

2. FIRST-ORDER ANALYTIC SOLUTION

Elastic-scattering case:

The solution is sought for the simple case in which we can assume that all optical properties (inherent *and* apparent) are invariant with depth, and the ocean is optically thick. The approach used is to estimate the contribution from each depth z to the upwelling flux at the surface, and then integrate over depth to obtain the total upwelling irradiance $E_u(\lambda, 0)$. The method has some affinities with those of Gordon *et al.*¹, Gordon and McCluney⁹ and Kirk¹⁰. Since we are assuming no depth dependence in optical properties, the irradiance reaching depth z is simply:

$$E_d(\lambda, z) = E_d(\lambda, 0) \exp[-K(\lambda)z], \quad (4)$$

where K is the diffuse attenuation coefficient for downwelling irradiance. Upward elastic scattering of $E_d(\lambda, z)$ at z over a layer of thickness dz generates an irradiance $dE_u(\lambda, z)$ given by:

$$dE_u(\lambda, z) = \frac{s(\lambda)b_b(\lambda)}{\mu_d(\lambda)} E_d(\lambda, z) dz, \quad (5)$$

where μ_d is the mean cosine for downwelling light, and $s = b_u/b_b$, where b_u is the upward scattering coefficient¹¹. Note that, as defined, s is a shape factor similar to, but not identical to, the shape factor used by Aas¹² and by Stavn and Weidemann¹³. If we now define κ as an attenuation coefficient for upwelling irradiance as it travels from z to the surface¹⁰, then the irradiance $dE_u(z, 0)$ reaching the surface from z would be given by:

$$dE_u(\lambda, z, 0) = dE_u(\lambda, z) \exp[-\kappa(\lambda)z]. \quad (6)$$

The total upwelling flux at the surface, $E_u(\lambda, 0)$, is then obtained by integrating equation (6) from the surface to infinity:

$$E_u(\lambda, 0) = \int_0^\infty \frac{s(\lambda)b_b(\lambda)}{\mu_d(\lambda)} E_d(\lambda, 0) \exp[K(\lambda)z] \exp[-\kappa(\lambda)z] dz. \quad (7)$$

Taking the solution to equation (7) and dividing by $E_d(\lambda, 0)$ we get an expression for R_1 , the first-order solution for reflectance at the sea surface due to elastic scattering:

$$R_1(\lambda, 0) = \frac{E_u(\lambda, 0)}{E_d(\lambda, 0)} = \frac{s(\lambda)b_b(\lambda)}{\mu_d(\lambda)[K(\lambda) + \kappa(\lambda)]}. \quad (8)$$

The development of the solution up to this point is identical to that of Kirk¹⁰, except that Kirk developed his solution for the asymptotic regime. Since inherent and apparent properties are, by definition, independent of depth in the asymptotic regime, the solution is exact in this domain. When applied to shallower depths, as done here, the model becomes an approximation¹⁰. Since our interest is to express the solution in terms of a and b_b , we have to express K and κ as functions of a and b_b . Based on Sathyendranath and Platt¹⁴ and Gordon¹⁵, we can use the approximation:

$$K(\lambda) = \frac{a(\lambda) + b_b(\lambda)}{\mu_d(\lambda)}, \quad (9)$$

and, by analogy, we can use

$$\kappa(\lambda) = \frac{a(\lambda) + b_b(\lambda)}{\mu_u(\lambda)}, \quad (10)$$

where μ_u is the mean cosine of the upwelling flux. However, a note of caution would be in order. Although Gordon¹⁵ has shown that equation (9) is a good approximation for K in near-surface waters using Monte Carlo simulations, no such evidence exists for κ . In equation (9), we are able to use b_b rather than b_u , because the incident light field near the surface is only weakly diffuse. Since this is not true in general of the upwelling light field, equation (10) may not perform as well as equation (9) in high-scattering waters. Substituting for K and κ , equation (8) becomes:

$$R_1(\lambda, 0) = \frac{\mu_u(\lambda) s(\lambda)}{[\mu_u(\lambda) + \mu_d(\lambda)]} \times \frac{b_b(\lambda)}{[a(\lambda) + b_b(\lambda)]}, \quad (11)$$

and by comparison with equation (2) we have:

$$r = \frac{\mu_u(\lambda) s(\lambda)}{[\mu_u(\lambda) + \mu_d(\lambda)]}. \quad (12)$$

The expected dependence of r on the angular structure of the incident light field appears through the mean cosines μ_u and μ_d , and the dependence on the phase function appears through the shape factor s . Comparisons with Monte Carlo simulations have shown¹⁶ that the results are in good numerical agreement with the results of Gordon *et al.*¹ for relatively clear waters, in which molecular scatter apparently dominated upward scatter. In the case of particle-scattering-dominated waters also, the model is able to reproduce many of the features seen in Monte Carlo simulations⁵. However, for the particle-scattering case, the accuracy of the model decreased with increasing scatter, with relative errors in r reaching up to 17% for the cases simulated. Since all the simplifying assumptions made in deriving the solution hold best under low-scattering conditions, these results are not entirely unexpected.

Raman-scattering case:

The result for the elastic-scattering case can be easily extended to include Raman scattering. To obtain the first-order solution, we can follow the same procedure as for the elastic-scattering case, with the following changes: the single upward scattering event now becomes a Raman-scattering event, and, to obtain the Raman upwelling flux at wavelength λ , we have to consider downwelling irradiance at a source wavelength, say λ^S . The reflectance at the sea surface due to first-order Raman scattering, R^R then becomes¹⁷:

$$R^R(\lambda, 0) = \frac{E_d(\lambda^S, 0)}{E_d(\lambda, 0)} \frac{b_b^R(\lambda^S)}{\mu_d(\lambda^S)} \times \frac{1}{[K(\lambda^S) + \kappa^R(\lambda)]}, \quad (13)$$

where the superscript R on b_b^R indicates a Raman-scattering event. Note that the value of κ after a Raman-scattering event (κ^R) may be different from the corresponding value after an elastic-scattering event, since the mean cosines for upwelling associated with the two events need not be the same. Since the phase function for Raman scattering is symmetric, the shape factor for Raman scattering will always be unity and so does not appear explicitly in the solution. The total reflectance at the surface is obtained by adding the contributions due to elastic and Raman scattering.

3. CONSEQUENCES OF HIGHER-ORDER SCATTERING

Multiple, elastic scattering:

Multiple, elastic scattering can affect reflectance through a number of mechanisms:

(1) Multiple forward scattering can progressively modify the angular distribution of the downwelling light field, and hence modify μ_d . This effect is not accounted for here, since we have used the quasi-single-scattering approximation, which assumes that downward-scattered light undergoes no change in direction.

(2) Similarly, the upward-scattered light, as it travels to the surface, can undergo multiple forward scattering, leading to changes in the value of μ_u . This effect is also ignored here.

(3) Upward and downward scattering events occurring in pairs will introduce additional terms to the solution. Only the odd-numbered scattering events will produce a flux in the upward direction. Following a similar procedure to that followed in the previous section, we can obtain a solution to these additional terms, and the equation for reflectance due to elastic scattering will then have the form:

$$R^E = R_1(1 + R_2R_3 + R_2R_3R_4R_5 + \dots) \quad (14)$$

where the subscripts indicate the sequence of scattering. The term R_1 is the same as the first-order solution for reflectance due to elastic scattering presented in equation (11). The higher-order terms differ from the first one only in the mean cosines that are applicable to each of them, which could, in principle, be different from those for the first-order term.

(4) Downward scattering of upwelling light will introduce a negative term into the equation for K , tending to reduce it. In fact, an exact representation for K can be found in Preisendorfer and Mobley¹⁸:

$$K(\lambda) = \frac{a(\lambda) + b_u(\lambda)}{\mu_u} - R(\lambda) \frac{b_d(\lambda)}{\mu_u} \quad (15)$$

where b_d stands for downward scattering of upwelling irradiance. The second term on the right-hand side of equation (15) can be determined by an iterative procedure, with initial estimates of R being used to refine the estimates of K , which could then be used to improve R , and so on.

According to our initial analyses, it appears that, of these four effects, the most important are those due to (1) and (2). The extra terms in equation (14) had only a minor effect on the solution, since, for the simulated cases, R_i ($i = 1, 2, \dots$) were of the order of 10% at the most. The higher-order terms could be potentially important in highly reflective waters. The additional term introduced to the expression for K in equation (15) also had a negligible effect, again because of the small values of R simulated. Thus, the changes in μ_u and μ_d emerged as the most important effects of multiple scattering. Further improvements to the analytic model should therefore focus on refinements to the estimation of these quantities.

Higher-order Raman Scattering

The first-order solution for reflectance due to Raman scattering can be extended by incorporating additional terms due to multiple scattering. Sathyendranath and Platt¹⁷ have considered additional terms that emerge in the solution due to: (a) a downward Raman-scattering event followed by an upward elastic-scattering event; (b) an upward elastic-scattering event followed by an upward Raman-scattering event, and (c) two Raman-scattering events in sequence. Based on order-of-magnitude estimates, they suggested that the term (c) and higher-order scattering

terms could be neglected, compared with the first-order term. The solution obtained can be simplified further for application in relatively clear waters for which we can assume that molecular scattering dominates upward elastic scatter. The simplified solution can be expressed as:

$$R^{Ram}(\lambda, 0) = R^R(\lambda, 0) \left[1 + \frac{b_b(\lambda)}{2\mu_u \kappa^R(\lambda)} + \frac{b_b(\lambda^S)}{\mu_u [K(\lambda^S) + \kappa(\lambda^S)]} \right], \quad (16)$$

where R^R is the first-order scattering solution presented in equation (13). Numerical simulations using a Monte Carlo model incorporating Raman scattering were in good agreement with the analytic solutions for relatively clear waters (oceanic waters, with chlorophyll concentrations less than 1 mg Chl m⁻³).

4. CONCLUSION

The analytic model developed shows features that are consistent with earlier models and results based on numerical simulations. Since the model was developed for low scattering waters, the numerical agreement between the analytic model results and Monte Carlo simulations are better for fairly clear waters than for highly turbid waters. The model is extended to include Raman scattering.

5. ACKNOWLEDGEMENTS

We thank Carla Caverhill for reading and commenting on previous drafts of the manuscript. This work was supported by the Office of Naval Research, the National Aeronautics and Space Administration, the Department of Fisheries and Oceans, and the Natural Sciences and Engineering Research Council. This is a contribution to the Canadian Global Ocean Flux Study.

6. REFERENCES

1. H. R. Gordon, O. B. Brown, and M. M. Jacobs, "Computed relationships between the inherent and apparent optical properties of a flat, homogeneous ocean," *Appl. Optics* **14**, 417-427 (1975).
2. L. Prieur, "Transfert radiatif dans les eaux de la mer. Application à la détermination des paramètres optiques caractérisant leur teneur en substances dissoutes et leur contenu en particules," Ph.D., L'Université Pierre et Marie Curie, Paris, p.243, (1976).
3. A. Morel and L. Prieur, "Analysis of variations in ocean color," *Limnol. Oceanogr.* **22**, 709-722 (1977).
4. J. T. O. Kirk, "Monte Carlo study of the nature of the underwater light field in, and the relationship between optical properties of, turbid yellow waters," *Aust. J. Mar. Freshw. Res.* **32**, 517-532 (1981).
5. J. T. O. Kirk, "Dependence of relationship between inherent and apparent optical properties of water on solar altitude," *Limnol. Oceanogr.* **29**(2), 350-356 (1984).
6. A. Morel and B. Gentili, "Diffuse reflectance of oceanic waters: its dependence on sun angle as influenced by the molecular scattering contribution," *Appl. Optics* **30**(30), 4427-4438 (1991).
7. H. R. Gordon, "Dependence of the diffuse reflectance of natural waters on the sun angle," *Limnol. Oceanogr.* **34**(8), 1484-1489 (1989).

8. H. R. Gordon, "Simple calculation of the diffuse reflectance of the ocean," *Appl. Optics* **12**(12), 2803-2804 (1973).
9. H. R. Gordon and W. R. McCluney, "Estimation of the depth of sunlight penetration in the sea for remote sensing," *Appl. Optics* **14**, 413-416 (1975).
10. J. T. O. Kirk, "The upwelling light stream in natural waters," *Limnol. Oceanogr.* **34**(8), 1410-1425 (1989).
11. S. Sathyendranath and T. Platt, "Angular distribution of the submarine light field: Modification by multiple scattering," *Proc. R. Soc. Lond. Ser. A* **433**, 287-297 (1991).
12. E. Aas, "Two-stream irradiance model for deep waters," *Appl. Optics* **26**(11), 2095-2101 (1987).
13. R. H. Stavn and A. D. Weidemann, "Shape factors, two flow models, and the problem of irradiance inversion in estimating optical parameters," *Limnol. Oceanogr.* **34**(8), 1426-1441 (1989).
14. S. Sathyendranath and T. Platt, "The spectral irradiance field at the surface and in the interior of the ocean: A model for applications in oceanography and remote sensing," *J. Geophys. Res.* **93**(C8), 9270-9280 (1988).
15. H. R. Gordon, "Modeling and simulating radiative transfer in the ocean," in *Ocean Optics*, R. W. Spinrad, K. L. Carder and M. J. Perry, eds., of Oxford Monographs on Geology and Geophysics, Oxford University Press, New York, pp. 3-39, 1994.
16. S. Sathyendranath and T. Platt, "An analytic model of ocean colour," *Appl. Optics*, In press (1996).
17. S. Sathyendranath and T. Platt, "An ocean-colour model incorporating trans-spectral processes," *Appl. Optics*, submitted (1996).
18. R. W. Preisendorfer and C. D. Mobley, "Direct and inverse irradiance models in hydrographic optics," *Limnol. Oceanogr.* **29**(5), 903-929 (1984).

Approximation to beam propagation in ocean water

G.R. Fournier

Defence Research Establishment Valcartier
Courcelette, Quebec, G0A 1R0, Canada

1. ABSTRACT

Using a modified form of the anomalous diffraction approximation we first derived in closed form an analytic expression for the phase function of Mie scatterers integrated over an inverse power law (Junge) size distribution. A simple analysis explained the apparent singularity seen experimentally at the forward scattering angle. Relationships were derived that related the inverse power law as a function of scattering angle in the near forward direction to the power law of the size distribution. The parameters of the formula are the relative index of refraction and the inverse power of the size distribution. Using the formula and path integrals, we have derived approximate analytic expressions that model laser beam propagation in ocean waters. The effect of strong absorption on beam shape and temporal spreading is accounted for. The results are currently being integrated into a comprehensive model of underwater active imaging systems.

Keywords: propagation, multiple scattering, phase function, underwater, path integral

2. INTRODUCTION

In previous work¹ a simple set of approximations involving the anomalous diffraction theory was used to derive from the basic physics an analytic phase function whose parameters can be related to a limited set of physically meaningful quantities. A comprehensive data base of oceanic phase functions² was then fitted to this form. The phase function is given by the following expression:

$$\beta(\theta) = C\pi \left(\frac{2\pi(n-1)}{\lambda} \right)^{\mu-3} \frac{1 + \cos^2 \theta}{8 \sin(-\pi v)} \left[\frac{1}{(1 - \delta^2)\delta^v} \right] \\ \left([v(1 - \delta) - (1 - \delta^v)] + \frac{4}{u^2} [(1 - \delta^{v+1}) - (v+1)(1 - \delta)] \right). \quad (1)$$

Where

$$v = \frac{3 - \mu}{2} \quad (2)$$

$$\delta = \frac{u^2}{3(n-1)^2} \quad (3)$$

$$u = 2 \sin(\theta/2). \quad (4)$$

In these expressions, μ is the exponent of the inverse power law of the particle size distribution, λ is the wavelength and n is the index of refraction of water. From this form

of the phase function it is easy to derive the behaviour at small angles. The constant of proportionality C depends on all the parameters but the inverse power ν of the phase function near $\theta = 0$ only depends on the inverse power μ of the particle size distribution function.

$$\nu = 5 - \mu \quad (5)$$

The slope of the phase function near $\theta = 0$ contains information only about the power law of the particle size distribution. The variation of the total scattering coefficient b is also an inverse power γ of the wavelength.

$$\gamma = \mu - 3 \quad (6)$$

Furthermore, equations 5 and 6 can be used to relate the wavelength dependence of the total scattering coefficient to the logarithm of the slope of the phase function as a function of angle in the near forward direction.

$$\gamma = 2 - \nu \quad (7)$$

The feature of interest in this formulation is the singularity in the forward scattering near $\theta = 0$. This implies that small angle forward scattering should be completely dominant in ocean waters. To verify this hypothesis, equation 1 was fitted to a data base of oceanic phase functions². The distribution of values of the mean square scattering angle $\langle \theta^2 \rangle$ for a large sample of measured phase functions confirmed the overwhelming dominance of forward scatter.

3. PATH INTEGRAL SOLUTION TO BEAM PROPAGATION

Multiple scattering can be viewed as a sophisticated random walk problem and as such is particularly amenable to the path integral method. Feynman and Hibbs⁴ used the path integral approach to solve the neutron scattering problem in the small forward angle regime. Their solution, with an appropriate change in notation, is directly applicable to light scattering in waters where forward scattering dominates. For the time independent one dimensional case, Feynman and Hibbs show that:

$$P(X, \theta_x, l) = C e^{-\frac{1}{2b\langle \theta_i^2 \rangle} \int_0^l (\frac{d^2 x}{dz^2})^2 dz} \quad (8)$$

where P is the probability of finding a photon that started at $z = 0, x = 0, \theta = 0$ at $z = l, x = X, \theta = \theta_x$, b is the total scattering coefficient and $\langle \theta_i^2 \rangle$ is the one dimensional mean square scattering angle

$$\langle \theta_i^2 \rangle = \int_0^\infty f(\theta_i) \theta_i^2 d\theta_i. \quad (9)$$

In equation 8 $x(z)$ is the solution of the differential equation

$$\frac{d^4 x}{dz^4} = 0 \quad (10)$$

with the boundary conditions

$$x(0) = 0, \left(\frac{dx}{dz}\right)_{z=0} = 0, x(l) = X, \left(\frac{dx}{dz}\right)_{z=l} = \theta_x \quad (11)$$

This solution is given by:

$$x(z) = (3X - \theta_x l) \left(\frac{z}{l}\right)^2 + (\theta_x l - 2X) \left(\frac{z}{l}\right)^3 \quad (12)$$

$$\frac{dx(z)}{dz} = \frac{2}{l}(3X - \theta_x l) \left(\frac{z}{l}\right) + \frac{3}{l}(\theta_x l - 2X) \left(\frac{z}{l}\right)^2 \quad (13)$$

$$\frac{d^2x(z)}{dz^2} = \frac{2}{l^2}(3X - \theta_x l) + \frac{6}{l^2}(\theta_x l - 2X) \left(\frac{z}{l}\right) \quad (14)$$

Using equations 8 and 12, and taking into consideration the fact that the scattering in the x and y planes is independent, the two dimensional photon probability distribution is given by:

$$P(X, Y, \theta_x, \theta_y, l) = \frac{3}{\pi^2 u^2} \exp \left\{ \frac{-1}{ul} \left[3(X - \theta_x l/2)^2 + 3(Y - \theta_y l/2)^2 + (\theta_x l)^2 + (\theta_y l)^2 \right] \right\}, \quad (15)$$

where

$$u = b < \theta^2 > l^2 \quad (16)$$

and

$$< \theta^2 > = \frac{1}{2} \int_0^\infty \beta(\theta) \theta^3 d\theta. \quad (17)$$

Note that the factor of 1/2 in front of the integral in equation 17 is there to account for the one dimensional nature of equation (9). Equation 15 is equivalent to the expression found by van de Hulst and Kattawar for the time contracted distribution⁵. The only difference is in the method of derivation. The various contracted distributions can be obtained from equation 15 by simple integration over the desired variables. All the resulting formulas are analytic and will not be quoted here as it would take too much space.

4. CENTRAL PATH APPROXIMATION FOR ABSORPTION

The particular virtue of the path integral approach is the ease with which it allows one to include the effects of strong absorption. Multiplying equation (14) by the following factor accounts for the absorption of the photon along the various paths.

$$P(X, Y, \theta_x, \theta_y, l) = e^{-aS(X, Y, \theta_x, \theta_y, l)} P(X, Y, \theta_x, \theta_y, l) \quad (17)$$

In this expression a is the absorption coefficient and S is the mean path length covered by the photon. This mean path length can be expressed as follows:

$$S(X, Y, \theta_x, \theta_y, l) = \int_0^l \sqrt{1 + \left(\frac{dx}{dz}\right)^2 + \left(\frac{dy}{dz}\right)^2} dz. \quad (18)$$

One can then use equation 13 to obtain an explicit expression for dx/dz and dy/dz . The exact solution of equation 18 leads to a complex set of elliptic integrals. For small values of the path derivatives, which is always the case for small forward angle scattering, the binomial expansion can be used to obtain the expression:

$$S(X, Y, \theta_x, \theta_y, l) = l + s(X, Y, \theta_x, \theta_y, l), \quad (19)$$

where

$$s(X, Y, \theta_x, \theta_y, l) = \left(\frac{1}{2}\right) \int_0^l \left(\frac{dx}{dz}\right)^2 dz + \left(\frac{1}{2}\right) \int_0^l \left(\frac{dy}{dz}\right)^2 dz. \quad (20)$$

5. RESULTS

By substituting equations 19-20 into equation 17 and integrating over the appropriate variables one obtains the following expressions for the contracted distributions:

$$P(\theta^2, l) = \frac{e^{-al}}{u(au/5 + 2)} \exp \left[\frac{(a^2 u^2/8 + 13au/3 + 10)}{2u(au + 10)} l \theta^2 \right] d(l \theta^2), \quad (21)$$

with

$$\theta^2 = \theta_x^2 + \theta_y^2$$

and

$$P(r^2, l) = \frac{3e^{-al}}{u(au/15 + 2)} \exp \left[3 \frac{(a^2 u^2/8 + 13au/3 + 10)}{2u(au + 30)} \left(\frac{r^2}{l}\right) \right] d\left(\frac{r^2}{l}\right), \quad (22)$$

with

$$r^2 = X^2 + Y^2,$$

and

$$P(l) = \frac{10e^{-al}}{(a^2 u^2/8 + 13au/3 + 10)}. \quad (23)$$

Equations 21 and 22 have some significant consequences. If we write the half width of the distributions σ^2 in terms of their half width in the limiting case of no absorption σ_s^2 we obtain

$$\sigma^2 = \sigma_s^2 \left(\frac{au + 10}{a^2 u^2/8 + 13au/3 + 10} \right) \quad (24)$$

for the angular distribution and

$$\sigma^2 = \sigma_s^2 \left(\frac{au + 30}{3(a^2 u^2/8 + 13au/3 + 10)} \right) \quad (25)$$

for the radial distribution. Note that the correction factor for absorption can be entirely expressed in terms of the dimensionless variable

$$au = ab < \theta^2 > l^2 \quad (26)$$

The importance of this parameter has been noted before and the present derivation clarifies its origin. If we take the limit of equation 24 as $l \rightarrow \infty$ we obtain:

$$\sigma^2 \rightarrow \frac{16}{al}. \quad (27)$$

Equation 27 shows that when absorption is significant in the small angle approximation the angular distribution of radiation will narrow indefinitely. This implies that the existence of an asymptotic radiance distribution in the ocean is not a direct consequence of a balance between the beam expansion due to scattering and the narrowing due to absorption. This asymptotic state must instead be reached by a complex feedback between the backward and forward scattered radiances.

In order to verify the accuracy of equations 21 and 22, we used a previously developed Monte-Carlo code. The accuracy of this code was verified against the data of Tyler for Lake Pend Oreille⁶. Since this code gives the radiance distribution, we compared its results with equation 21. Figure 1 shows a comparison of the ratio of the half width with absorption to that without absorption for a uniform scattering function between 0° and 5°. As can be seen the match is excellent and confirms the accuracy of our results.

6. CONCLUSIONS

Using path integrals, we have derived simple formulas for the beam spread function in the case of small forward angle scattering in the presence of the strong absorption typical of ocean waters. We have compared our results with a Monte-Carlo code which itself had been verified against high quality experimental data. We are currently in the process of simplifying the formulas for the time dependent solutions. At this point, the results of van de Hulst and Kattawar⁵ can be used in the case of strong absorption by simply multiplying them by the following factor:

$$\exp\left(\frac{-at}{nc}\right)$$

Where t is the time, n is the index of refraction of water and c is the speed of light. This approach is exact since both the effect of absorption and the delay in the time of arrival are directly proportional to the path length. We are presently implementing these results in a comprehensive model of underwater active imaging systems.

7. REFERENCES

1. G.R. Fournier and J.L. Forand, "Analytic phase function for ocean water", *Proceedings of SPIE*, Vol. 2258, pp. 194-201, Bergen, Norway, 1994.
2. G.R. Fournier and M. Jonasz, "Data base of oceanic optical properties", *Proceedings of SPIE*, Vol. 2258, pp. 576-587, Bergen, Norway, 1994.
3. T.J. Petzold, "Volume Scattering Functions for Selected Ocean Waters," Scripps Institute of Oceanography, SIO Ref. 72-28, 1972.
4. R.P. Feynman and A.R. Hibbs, *Quantum Mechanics and Path Integrals*, pp. 337-339, McGraw-Hill, New York, 1965.

5. H.C. van de Hulst and G.W. Kattawar, "Exact spread function for a pulsed collimated beam in a medium with small-angle scattering", *Applied Optics* **33**(24), pp. 5820-5829 (1994)

6. G.R. Fournier, J.L. Forand, G. Pelletier and P. Pace, "Ground-truthing the oceanic light field using an in-situ tunable transmissometer-nephelometer", 16th Canadian Symposium on Remote Sensing, Sherbrooke, Canada, 1993.

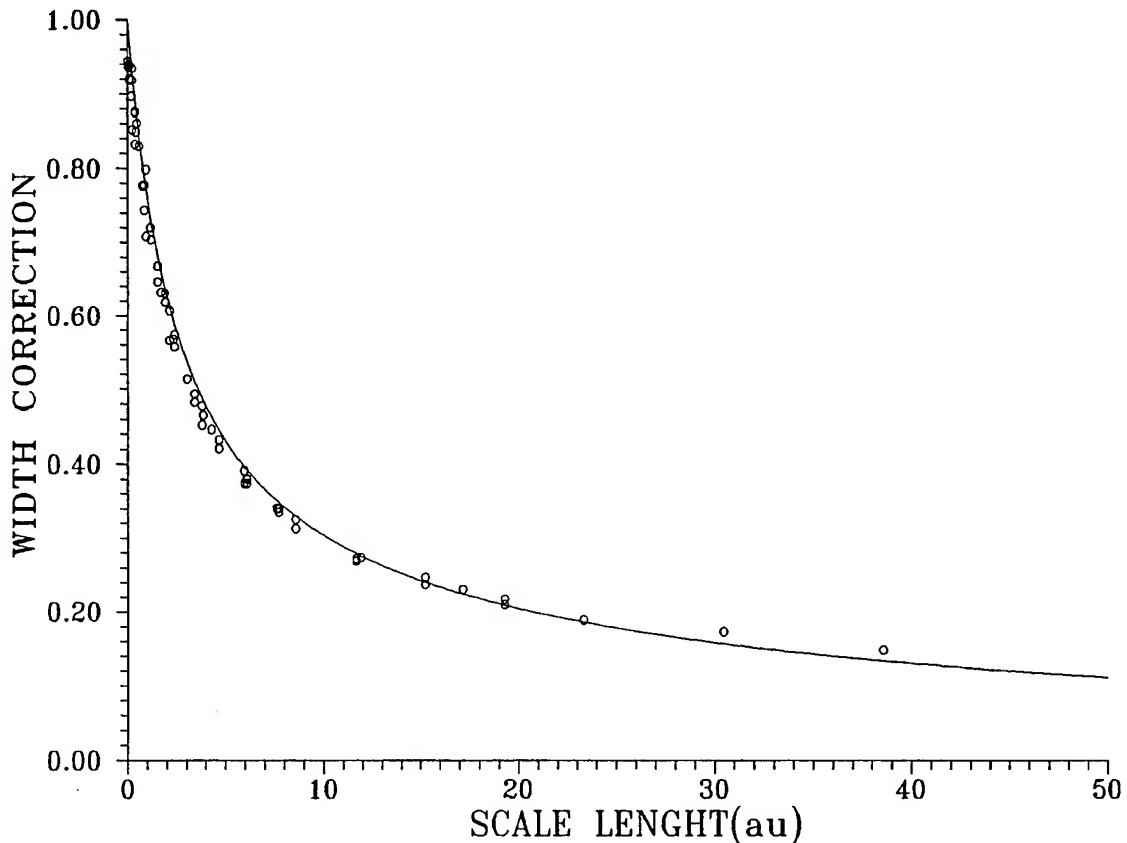


Figure 1. Comparison the analytic formula for the half width ratio with the results of the Monte Carlo code for a uniform phase function between 0° and 5° . The horizontal axis is in units of au .

COASTAL OPTICAL WATER TYPE 2: MODELING AND MINEROGENIC SCATTERING

Robert Hans Stavn

The University of North Carolina at Greensboro
Greensboro, NC, USA, 27412

Alan Dean Weidemann

Naval Research Laboratory
Code 7331
Coupled Dynamic Processes
Stennis Space Center, MS, USA, 39529

ABSTRACT

We are carrying out parameterizations of Type 1 oceanic waters to Type 2 coastal waters and determining the effects of minerogenic matter on attempts to retrieve the backscattering coefficient from radiance and irradiance data. This new parameterization involves the incorporation of suspended minerogenic matter into our ocean optical models. The deeply "lobed" backscattering portion of the volume scattering function for suspended minerogenic matter (clay-like and quartz-like) in coastal Type 2 waters has a profound effect on the upwelling radiance signal and therefore on algorithms that utilize upwelling radiances. Clay-like minerogenic matter can create a 200% overestimate of the backscattering coefficient for Air Mass 1 conditions and a 50% underestimate of the backscattering coefficient under Air Mass 2 conditions in the surface layers of coastal waters. Quartz-like minerogenic matter, range of diameters 60 - 360 μm for size distributions typical of California and Florida, stirred up with and added to suspended clay-like particles, will radically alter further the backscattering shape factor and the error of inversion of the backscattering coefficient. In this case a nearly 30% error of underestimate results in the surface layers that then increases with depth to more than a 15% overestimate of the backscattering coefficient under Air Mass 1 conditions. There is then a 20% overestimate at all depths under Air Mass 2 conditions.

Keywords: scattering, backscatter, remote sensing, coastal ocean modeling

2. INTRODUCTION

As part of the Littoral Optical Environment Program (LOE) of the Naval Research Laboratory, we are interested in predictive optical models of the coastal ocean. This is the type 2 water defined by Morel¹ as being significantly influenced optically by minerogenic matter. Such matter makes a very complex optical environment in contrast to the relatively simpler open ocean water type. Among the difficulties of investigating type 2 waters is the rapidity with which the suspended materials can be changed by advection (such as longshore currents), wave disturbance, internal waves or solitons, and similar processes. We demonstrate some of the rapid changes that occur optically as well as underlying causes of variability and inaccuracy in algorithms developed for the open ocean that have been applied to the coastal ocean. We have shown in the LOE program that some of these algorithms for inverting optical properties are extremely inaccurate.

An optical parameter of importance is the backscattering coefficient $b_p(\lambda, z)$ which is the subject of many inversion algorithms and studies²⁻⁶. This parameter is a useful measure of suspended matter in the oceanic hydrosol and its nature is important not only for passive remote sensing but also in the interpretation of the return signals for active remote sensing and laser bathymetry. The backscattering coefficient, especially in shallow coastal waters, is strongly influenced by the shape of the backscattering lobe of the volume scattering function, $\beta(\gamma, \lambda, z)$, for the marine hydrosol. The upwelling light signal (both active and passive) is essentially generated by single scattering off suspended particulates and thus the relative placement of "peaks" and "troughs" in the backscattering lobe will directly influence the strength of the upwelling optical signal. The suspended mineral matter in the coastal hydrosol will be predominantly clay-like and quartz-like material depending on local coastal conditions. Shifrin⁷ has reported distinct peaks and lobes in the backscattering portion of the volume scattering function for a polydisperse array of clay-like particles of refractive index 1.15. There are distinct peaks in backscattering at 175°-180° and also at 100°-120°, described by Shifrin as rainbow and glory effects. To our knowledge, the effects of these irregularities in the backscattering lobe have been largely ignored⁸. Nearly all algorithms that attempt to retrieve the backscattering coefficient from inverting irradiance data make the assumption that the backscattering function is of uniform shape.

We have been using concepts derived from the Zaneveld's algorithm⁹ on Monte Carlo simulations of the radiative transfer equation to evaluate the effects of variations in the volume scattering function on the efficacy of inversion algorithms for the backscattering coefficient. The Zaneveld algorithm is an accurate derivation from radiative transfer theory that relates the

radiance and irradiances of the marine hydrosol to the inherent optical properties of the hydrosol. Any errors found from applying this algorithm can be considered the "best case" for accuracy of retrieval of the backscattering coefficient from inverted ambient irradiances and the nadir radiance^{8,9}. All of the optical properties for the marine hydrosol and the light field itself are wavelength dependent and this will be considered implicit for the rest of the report. The Zaneveld algorithm utilizes a remotely sensed reflectance defined as $RSR = L(\pi)/E_{od}$, the ratio of the nadir radiance to the downwelling scalar irradiance. In the derivation of this algorithm, a function called the backscattering shape factor, f_b , is produced which has been shown to be a measure of the error in retrieval of the backscattering coefficient from a given hydrosol with given suspended components⁹. Not only is the backscattering shape factor a measure of the error of inversion for the retrieval of the backscattering coefficient but it can also be partitioned. That is, the information available in our Monte Carlo simulations of the solution to the radiative transfer equation can be used to determine the contribution to the shape factor, or error of inversion, of each component of the hydrosol. The shape factor is a function both of the inherent optical properties of the hydrosol and of the radiance distribution of the hydrosol. This makes the backscattering shape factor an apparent optical property. Thus it must be demonstrated that this apparent optical property can, in fact, be partitioned among the components of the hydrosol. We will demonstrate this in the next section and this partitioning will allow us to determine the importance of the suspended minerogenic matter in the accuracy and efficacy of inversion algorithms for the backscattering coefficient.

3. PARTITIONING THE SHAPE FACTOR FUNCTION

Consider the radiative transfer of the nadir radiance $L(\pi)$, no azimuth information needed

$$-\frac{dL(\pi, z)}{dz} = -cL(\pi, z) + L^*(\pi, z), \quad (1)$$

where c is the beam attenuation coefficient, the sum of the absorption coefficient a and the scattering coefficient b while the path function

$$L^*(\pi, z) = \int_0^{2\pi} \int_0^\pi \beta(\pi - \theta', \phi', z) L(\theta', \phi', z) \sin \theta' d\theta' d\phi', \quad (2)$$

or, focusing on the scattering angle, the difference between the nadir angle (π) and the zenith angle (θ') of the trajectory of the radiance contributing a scattering component to the nadir radiance,

$$L^*(\pi, z) = \int_0^{2\pi} \int_0^\pi \beta(\pi - \theta', z) L(\theta', \phi', z) \sin \theta' d\theta' d\phi', \quad (3)$$

where ϕ' is the azimuth angle of the radiance contributing a scattering component to the nadir radiance. It has been shown elsewhere^{5,8} that the contribution of the path function to the nadir radiance implies a backscattering shape factor (f_b) when attempting to invert the RSR, defined as $L(\pi)/E_{od}$, to retrieve the backscattering coefficient b_b

$$f_b(z) = \frac{\int_0^{2\pi} \int_0^\pi \beta(\pi - \theta', z) L(\theta', \phi', z) \sin \theta' d\theta' d\phi'}{\frac{b_b(z)}{2\pi} \cdot E_{od}(z)}. \quad (4)$$

This parameter measures the effect of "lobing" in the backward volume scattering function on the upwelling flux of the nadir radiance. That is, the denominator of Eq. (4) represents an "average" β in the backward direction based on the assumption of uniformity in the backward scattering lobe. The numerator is, of course, the actual contribution to the nadir radiance by the

backward scattering from the volume scattering functions of all the components of the hydrosol. By and large, evaluation and analysis of such a function remains the job of the modeler. We are of course, making great strides in instrument development, who knows what the future holds?

Since the b and β functions are linear and additive, they can be partitioned as follows:

$$b_b(z) = b_{bw}(z) + b_{bql}(z) + b_{bm}(z) + b_{bo}(z) + b_{ba}(z) + b_{bb}(z)$$

$$\beta(\gamma, z) = \beta_w(\gamma, z) + \beta_{ql}(\gamma, z) + \beta_m(\gamma, z) + \beta_o(\gamma, z) + \beta_a(\gamma, z) + \beta_b(\gamma, z)$$

where w represents molecular water, ql represents quartz-like material, m represents suspended minerogenic matter, o represents suspended, particulate organic detritus, a represents algae cells, and b represents bacteria. We can define a shape factor for each of these hydrosol components, molecular water for example:

$$f_{bw}(z) = \frac{\int_0^{2\pi} \int_0^{\pi} \beta_w(\pi - \theta', z) L(\theta', \phi', z) \sin \theta' d\theta' d\phi'}{\frac{b_{bw}(z)}{2\pi} \cdot E_{od}(z)} \quad (5)$$

When we wish to partition f_b into its component f_b s, it is convenient to start with the numerator in Eq. (4). Thus,

$$\begin{aligned} \int_0^{2\pi} \int_0^{\pi} \beta(\pi - \theta', z) L(\theta', \phi', z) \sin \theta' d\theta' d\phi' &= \int_0^{2\pi} \int_0^{\pi} \beta_w(\pi - \theta', z) L(\theta', \phi', z) \sin \theta' d\theta' d\phi' + \\ &\int_0^{2\pi} \int_0^{\pi} \beta_{ql}(\pi - \theta', z) L(\theta', \phi', z) \sin \theta' d\theta' d\phi' + \dots \end{aligned} \quad (6)$$

Each of the individual integrals in the RHS of Eq. (6) can be expressed in the same way as we do here for molecular water by rearranging Eq. (5):

$$\int_0^{2\pi} \int_0^{\pi} \beta_w(\pi - \theta', z) L(\theta', \phi', z) \sin \theta' d\theta' d\phi' = f_{bw}(z) \cdot \frac{b_{bw}(z)}{2\pi} \cdot E_{od}(z) \quad (7)$$

Now by substituting Eq. (7) and similar terms into Eq. (4):

$$f_b(z) = \frac{f_{bw}(z) \cdot \frac{b_{bw}(z)}{2\pi} \cdot E_{od}(z) + f_{bql}(z) \cdot \frac{b_{bql}(z)}{2\pi} \cdot E_{od}(z) + f_{bm}(z) \cdot \frac{b_{bm}(z)}{2\pi} \cdot E_{od}(z) + \dots}{\frac{b_b(z)}{2\pi} \cdot E_{od}(z)} \quad (8)$$

$$f_s(z) = \frac{f_{sw}(z) \cdot \frac{b_{sw}(z)}{2\pi} + f_{wp}(z) \cdot \frac{b_{wp}(z)}{2\pi} + f_{mn}(z) \cdot \frac{b_{mn}(z)}{2\pi} + f_{bo}(z) \cdot \frac{b_{bo}(z)}{2\pi} + f_{ba}(z) \cdot \frac{b_{ba}(z)}{2\pi} + f_{bs}(z) \cdot \frac{b_{bs}(z)}{2\pi}}{\frac{b_s(z)}{2\pi}} \quad (9)$$

And the final collection of terms gives us the partitioning of the total hydrosol shape factor into the shape factors for each hydrosol component

$$f_s(z) = f_{sw}(z) \cdot \frac{b_{sw}(z)}{b_s(z)} + f_{wp}(z) \cdot \frac{b_{wp}(z)}{b_s(z)} + f_{mn}(z) \cdot \frac{b_{mn}(z)}{b_s(z)} + f_{bo}(z) \cdot \frac{b_{bo}(z)}{b_s(z)} + f_{ba}(z) \cdot \frac{b_{ba}(z)}{b_s(z)} + f_{bs}(z) \cdot \frac{b_{bs}(z)}{b_s(z)} \quad (10)$$

We see that the total shape factor is not a simple linear addition of the shape factors for each individual hydrosol component in its interaction with the radiance distribution, but rather a sum weighted by the proportion of the backscattering represented by the particular hydrosol component.

A partitioning of the backscattering shape factors for the observations in Hamlet's Cove, Florida before a storm event is in Table 1.

Table 1. Partitioning of Backscattering Shape Factors: Hamlet's Cove Experiment,
Air Mass 1, 0 m depth, 532 nm, 6 March 1995

$f_{b \text{ Total}}$	$f_{b \text{ water}}$	$f_{b \text{ quartz-like}}$	$f_{b \text{ minerogenic}}$	$f_{b \text{ organic}}$	$f_{b \text{ bacteria}}$	$f_{b \text{ algae}}$
3.175	1.359	2.536	3.582	0.710	0.898	0.866
	(2.19%)	(0.85%)	(84.6%)	(9.91%)	(1.33%)	(1.08%)

With a nearly zenith sun as utilized in the Monte Carlo model and a polydisperse Mie calculation for a clay-like minerogenic suspension, the clay-like suspension contributes about 85% to the total error of inversion of the backscattering coefficient.

4. ANALYSIS OF 2 COASTAL SYSTEMS

4.1 Methods

The NRL Blue Water Model¹⁰, extended previously to cover Type 1 coastal water^{8,9} is now being extended into Type 2 coastal waters. The extension will be complete when more comprehensive coastal surveys will have been incorporated. At present the model has been extended to cover aspects of California shallow coastal situations and aspects of Atlantic and Gulf Coast beaches. We have assumed a distribution of Clay-like particulates, 1 - 60 μm diameter, as shown in Fig. 1 and reported by Robert Arnone and Rick Gould for the nearshore area of Jacksonville, North Carolina during a Naval Research Laboratory (NRL) exercise on 25 April 1996. The distribution of minerogenic particulates (0.75 - 360 μm diameter) we utilized is shown in Fig. 2 as reported by Collin Roesler for the NRL exercise off Oceanside, California, 21 - 25 October 1995 and extrapolated to smaller diameters. The total minerogenic distribution for Hamlet's Cove, Florida is shown in Fig. 3 and represents the data for 5 - 60 μm reported by Collin Roesler, extrapolations to smaller diameters, and the data for 60 - 360 μm diameters was interpolated and incorporated from a size distribution for beach sand near Panama City, Florida collected by Robert Arnone. The beach sand size distribution reported by Arnone had a distinct mode at 220 μm diameter. Data on absorption of all components for the exercises at Oceanside and Hamlet's were available as was chlorophyll concentration. The chlorophyll concentrations were utilized to determine the scattering contribution of algal cells, organic matter, and bacteria. These components were then subtracted from the total hydrosol scattering to determine the scattering coefficient attributable to suspended minerogenic matter⁸. Because of an interest in active remote sensing, the wavelength used in all simulations was 532 nm.

The model simulations were conducted at solar zenith angles of 11° (Air Mass 1) and 60° (Air Mass 2) with 27.4 % and 43.7% respectively of the global radiation due to skylight¹¹. All simulations were homogeneous with a flat water/air interface. The Monte Carlo code has been extensively verified¹². The radiances and irradiances generated by the Monte Carlo model utilizing the input of the inherent optical properties of the extended NRL optical model are combined during the simulation to calculate the backscattering shape factors f_b . If there is not significant interaction between the shape of the backscattering function and the radiance distribution, then the value of f_b is 1.0. Any value below 1.0 represents a percentile underestimate of the backscattering coefficient while any value greater than 1.0 represents a percentile overestimate of the backscattering coefficient⁸. The volume scattering function for the minerogenic matter was determined from Mie calculations on the diameters reported for suspended sediment from the two experimental areas¹³⁻¹⁵. A refractive index of 1.15 was assumed for the clay-like suspension and a refractive index of 1.25 was assumed for the quartz-like suspension. The size distributions were used to combine the Mie calculations of the individual particle diameters into a polydisperse calculation^{7,14}. The volume scattering function for the clay polydispersion is in Fig. 4, while the volume scattering functions for the Clay/Quartz suspensions of Oceanside, California and Hamlet's Cove, Florida are in Figs. 5 and 6. Optical Parameters utilized in the simulations for the two coastal areas are in Table 2.

Table 2. Optical Properties of Field Sites Utilized in Monte Carlo simulations

Hamlet's Cove, Florida	Hamlet's Cove, Florida	Oceanside, California
Before Storm Event, 2-6 March 1995	After Storm Event, 9-14 March 1995	25 October 1995
Chlorophyll: 8 mg/m ³	Chlorophyll: 5 mg/m ³	Chlorophyll: 3 mg/m ³
$a(532) = 0.3033 \text{ m}^{-1}$ $b(532) = 2.86177 \text{ m}^{-1}$	$a(532) = 0.4972 \text{ m}^{-1}$ $b(532) = 4.3172 \text{ m}^{-1}$	$a(532) = 0.5 \text{ m}^{-1}$ $b(532) = 3.5 \text{ m}^{-1}$
$b_a(532) = 0.2712 \text{ m}^{-1}$	$b_a(532) = 0.1695 \text{ m}^{-1}$	$b_a(532) = 0.1017 \text{ m}^{-1}$
$b_{ba}(532) = 0.1033 \text{ m}^{-1}$	$b_{ba}(532) = 0.08087 \text{ m}^{-1}$	$b_{ba}(532) = 0.062008 \text{ m}^{-1}$
$b_o(532) = 0.2692 \text{ m}^{-1}$	$b_o(532) = 0.2374 \text{ m}^{-1}$	$b_o(532) = 0.6220 \text{ m}^{-1}$
$b_m(532) = 2.1876 \text{ m}^{-1}$	$b_m(532) = 3.7989 \text{ m}^{-1}$	$b_m(532) = 2.68377 \text{ m}^{-1}$

4.2 Results

A major event during the observations of Hamlet's Cove, Florida was a heavy storm which occurred during the dates of 6-9 March 1995 (Table 2). We assumed that for the period preliminary to the storm that a predominantly clay-like suspension would hold for the minerogenics while for the period just after the storm there would be significant sand stirred up and mixed with the clay-like suspension. The chlorophyll levels dropped after the storm and the scattering coefficient increased. The backscattering shape factor for the pre-storm period (predominantly clay-like suspension) showed a value of 3.175 at the surface and a decline to 1.09 at 3 meters for Air Mass 1 conditions. For Air Mass 2 conditions the backscattering shape factor was 0.495 at the surface and gradually increased to 0.873 at 3 meters depth. The post-storm event (mixed clay/quartz suspension) had backscattering shape factors of 0.744 at the surface with a gradual increase to 1.186 at 3 meters for Air Mass 1, while the backscattering

shape factor was approximately 1.2 or greater for all depths at Air Mass 2. All the above values are found in Table 3.

Table 3. Backscattering Shape factors, f_b , Hamlet's Cove, Florida

Depth (m)	Before Storm Event Clay-like		After Storm Event Quartz/Clay-like	
	Air Mass 1	Air Mass 2	Air Mass 1	Air Mass 2
0.00	3.175	0.495	0.744	1.234
0.25	2.628	0.582	0.891	1.232
0.50	2.241	0.650	0.985	1.237
0.75	1.956	0.701	1.046	1.236
1.00	1.742	0.740	1.089	1.231
1.25	1.578	0.770	1.118	1.226
1.50	1.449	0.794	1.138	1.221
1.75	1.351	0.813	1.155	1.215
2.00	1.273	0.830	1.164	1.210
2.25	1.211	0.844	1.172	1.208
2.50	1.162	0.856	1.179	1.206
2.75	1.121	0.864	1.182	1.205
3.00	1.090	0.873	1.186	1.203

During the Oceanside exercise the scattering coefficient increased greatly over a very short period and the optical properties for this rapid increase are in Table 2. To effect comparisons between Hamlet's Cove and Oceanside, we maintained the same optical properties for Oceanside but changed the volume scattering function. In Table 4. we have backscattering shape factors recorded for a clay-like minerogenic suspension and a mixed Clay/Quartz suspension under Air Mass 1 and 2 conditions.

Table 4. Backscattering Shape Factors, f_b , Oceanside, California

Depth (m)	Clay-like		Quartz/Clay-like	
	Air Mass 1	Air Mass 2	Air Mass 1	Air Mass 2
0.00	3.039	0.516	0.727	1.130
0.25	2.434	0.614	0.856	1.172
0.50	2.034	0.684	0.942	1.196
0.75	1.758	0.734	1.000	1.205
1.00	1.559	0.770	1.040	1.206
1.25	1.414	0.798	1.070	1.205
1.50	1.306	0.819	1.092	1.202
1.75	1.225	0.837	1.109	1.196
2.00	1.164	0.852	1.121	1.195
2.25	1.118	0.865	1.132	1.189
2.50	1.081	0.875	1.139	1.189
2.75	1.053	0.884	1.145	1.185
3.00	1.032	0.893	1.151	1.182

For the simulation with a clay-like minerogenic suspension the backscattering shape factor is 3.039 at the surface and 1.032 for Air Mass 1 conditions while the shape factor is 0.516 and slowly increasing to 0.893 for Air Mass 2 conditions. For the Clay/Quartz suspension the backscattering shape factor is 0.727 at the surface and increases slowly to 1.151 at 3 meters under Air Mass 1 conditions while the shape factor is 1.13 at the surface and mostly at a value approaching 1.2 for all other depths for Air Mass 2 conditions.

5. DISCUSSION

We illustrate here some of the difficulties in determining a general model for Type 2 coastal ocean waters. We have much work to determine the probable nature of the suspended minerogenic matter and furthermore the effects of this suspended matter on our optical inversion algorithms. The storm event at Hamlet's cove delivered significant amounts of resuspended minerogenic matter to the coastal hydrosol in a matter of a day or so while solitons or internal waves at Oceanside increased scattering by an order of magnitude, presumably by increasing the suspended minerogenic matter, in a space of a few hours. The studies reported here demonstrate by how much the accuracy of open ocean algorithms for retrieving the backscattering coefficient may be degraded. The nature and amount of degradation will depend on the nature of the suspended minerogenic matter.

We assumed that the clay-like suspension (Fig. 1) was representative of a coastal system for which larger and denser materials had settled out. The volume scattering function determined for this suspension type exhibits a very strong backscattering peak at 180° (Fig. 4) which creates significant over estimates (200%) of the backscattering coefficient (Tables 3 and 4), both for Hamlet's Cove and for Oceanside. As the light field penetrates, the backscattering shape factor indicates a decreasing error of inversion for a high sun (Air Mass 1). As the radiance field becomes more diffused, the error situation for the high sun becomes less serious as the potential backscatter into the nadir radiance occurs more and more between the angles of about 140° - 150° off the scatter axis and less energy is returned in the nadir direction for these angles. Thus the "trough" balances off the "peak" in the backscattering function and the error is minimized under these conditions with depth. However, for Air Mass 2, the region of strong interaction of the backscattering function with the radiance distribution is now the region of the "trough" only and there is an underestimate of 50% at the surface that ameliorates to an underestimate of 10 - 15% with depth (Tables 3 and 4).

We utilized the mixed Clay/Quartz distributions for situations that would appear to be affected by vigorous resuspension of a sandy bottom. The storm event provided convenient controls for Hamlet's Cove while we simply utilized the Clay/Quartz distribution for the same optical conditions as the Clay-like distribution for Oceanside. When suspended quartz sand is added to the particle distribution, the volume scattering distribution is radically altered (Figs. 5 and 6). Now the peaks in the backscattering function occur at about 125° and 150° and the region of 180° can be considered a "trough." The sand distributions were different for Hamlet's Cove and Oceanside (Figs. 2 and 3) but this had no effect on the Mie calculations for the volume scattering function (Figs. 5 and 6). Now the error of inversion for the high sun is a significant underestimate of about 25% in the surface. However, as the light field penetrates deeper, the more diffused radiance field interacts with the backscattering peaks in the region of 150° and creates an overestimate error of about 15 - 20% with depth. Here the error increases with depth and doesn't simply approach an "averaged" or "compensated" error situation that would help an inversion algorithm. For a low sun (Air Mass 2) a nearly 20% error of overestimate persists for all depths and for both field sites. The interactions here are with the backscattering peaks at 125° and 150° and the error remains constant with depth as the radiance distribution remains nearly constant with depth.

Thus, the potential errors in inversion are a function of both the nature of the suspended minerogenic matter and the solar angle. We see some encouragement in the fact that the optical interactions of the different types of suspended matter are fairly consistent between the 2 different field sites.

7. SUMMARY

1. The deeply "lobed" backscattering portion of the volume scattering function for suspended minerogenic matter (clay-like and quartz-like) in coastal Type 2 waters has a profound effect on the upwelling radiance signal and therefore on the retrieval of the hydrosol backscattering coefficient. The minerogenic matter makes at least an 85% contribution to the error of retrieval.

2. Clay-like minerogenic matter, range of diameters 1 - $60\text{ }\mu\text{m}$ and of size distribution typical of wave-washed near shore coastal waters, exhibits pronounced backscattering peaks in the regions 100° - 120° and 175° - 180° off the scattering axis. This can result in a 200% overestimate of the backscattering coefficient for Air Mass 1 conditions and a 50% underestimate of the backscattering coefficient under Air Mass 2 conditions in the surface layers of coastal waters.

up with and added to suspended clay-like particles, exhibits peaks in the backscattering function at 122° - 125° and 152° - 156° off the scattering axis. There is a distinct "trough" in the region of 180°. This results in a nearly 30% error of underestimate of the backscattering coefficient in the surface layers that then increases to about a 15% overestimate of the under Air Mass 1 conditions. There is then a 20% overestimate of the backscattering coefficient at all depths under Air Mass 2 conditions.

8. ACKNOWLEDGEMENTS

We wish to acknowledge the continuing support of the Naval Research Laboratory through the Littoral Optical Environment Program. RHS wishes to acknowledge the support of the Naval Research Laboratory through contract # N00014-95-C-6023. Computer simulations are carried out at the North Carolina Supercomputing Center, Research Triangle Park, NC and at the Naval Oceanographic Office, SSC, MS. This article represents NRL contribution NRL/PP/7331-97-0001.

REFERENCES

1. H.R. Gordon and A. Morel, "Remote assessment of ocean color for interpretation of satellite visible imagery," in *Lecture Notes on Coastal and Estuarine Studies*, R.T. Barber, C.K. Mooers, M.J. Bowman, and B. Zeitschel, eds., pp. 1-113, Springer Verlag, New York, 1983.
2. H.R. Gordon, "Dependence of the diffuse reflectance of natural waters on the sun angle," *Limnol. and Oceanogr.*, **34**, 1484-1489 (1989).
3. H.R. Gordon, O.B. Brown, R.H. Evans, J.W. Brown, R.C. Smith, K.S. Baker, and D.K. Clark, "A semianalytic radiance model of ocean color," *J. Geophys. Res.*, **93**, 10909-10924, (1988).
4. A. Morel and B. Gentili, "Diffuse reflectance of oceanic waters: its dependence on sun angle as influenced by the molecular scattering contribution," *Appl. Opt.*, **30**, 4427-4438 (1991).
5. J.R.V. Zaneveld, "Remotely sensed reflectance and its dependence on vertical structure: A theoretical derivation," *Appl. Opt.*, **21**, 4146-4150 (1982).
6. J.R.V. Zaneveld, "A theoretical derivation of the dependence of the remote sensing reflectance on the inherent optical properties," *J. Geophys. Res.*, **100**, 13,135-13,142 (1995).
7. K.S. Shifrin, *Physical Optics of Ocean Water*, pp. 1-285, American Institute of Physics, New York, 1988.
8. A.D. Weidemann, R.H. Stavn, J.R.V. Zaneveld, and M.R. Wilcox, "Error in predicting hydrosol backscattering from remotely sensed reflectance," *J. Geophys. Res.*, **100**, 13,163-13,177 (1995).
9. R.H. Stavn and A.D. Weidemann, "Geometrical light field parameters for improving remote sensing estimates of the backscattering in the marine hydrosol," in *Ocean Optics XII*, Jules S. Jaffe, Editor, Proc. SPIE 2258, 202-209 (1994).
10. R.H. Stavn and A.D. Weidemann, "Optical modeling of ocean light fields: Raman scattering effects," *Appl. Opt.*, **27**, 4002-4010 (1988).
11. D.T. Brine and M. Iqbal, "Diffuse and global solar spectral irradiance under cloudless skies," *Solar Energy*, **30**, 447-453 (1983).
12. C.D. Mobley, B. Gentili, H.R. Gordon, Z. Jin, G.W. Kattawar, A. Morel, P. Reinersman, K. Stamnes, and R.H. Stavn, "Comparison of numerical models for computing underwater light fields," *Appl. Opt.*, **32**, 7484-7504 (1993).
13. C.F. Bohren and D.R. Huffman, *Absorption and Scattering of Light by Small Particles*, John Wiley & Sons, New York, 1983.
14. E.J. McCartney, *Optics of the Atmosphere. Scattering by Molecules and Particles*, John Wiley & Sons, New York, 1976.
15. W.J. Wiscombe, "Mie scattering calculations: advances in technique and fast, vector-speed computer codes," pp. 1-62, NCAR Tech. Note TN-140+STR, (1979).

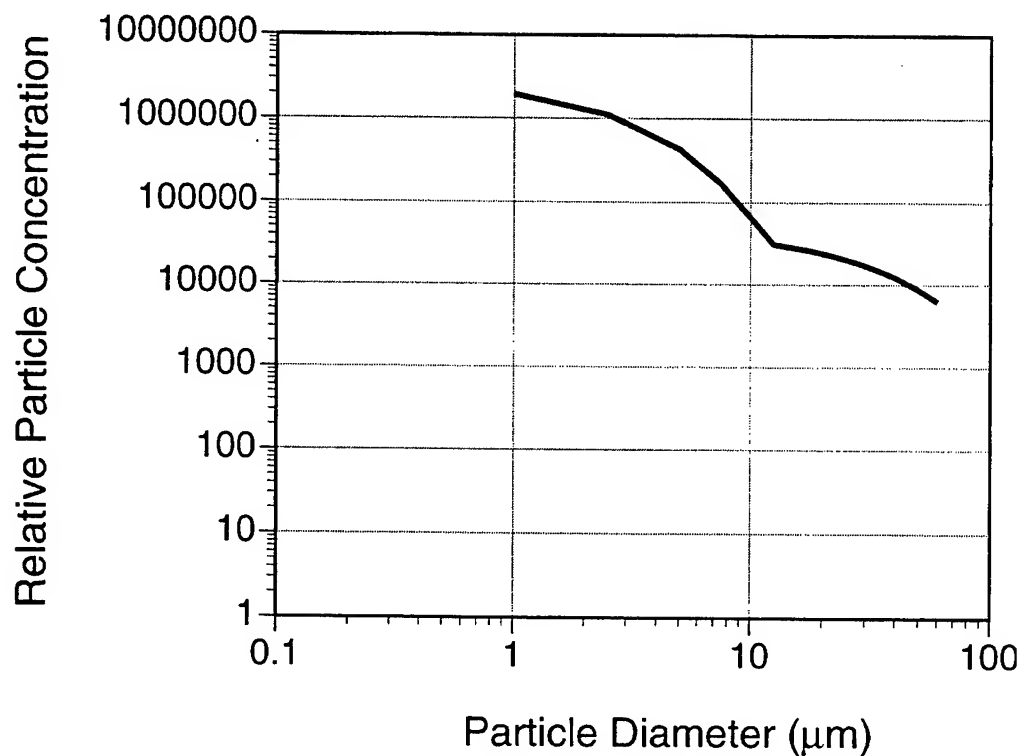


Figure 1. Particle size distribution for near shore wave-agitated region, Jacksonville, NC.

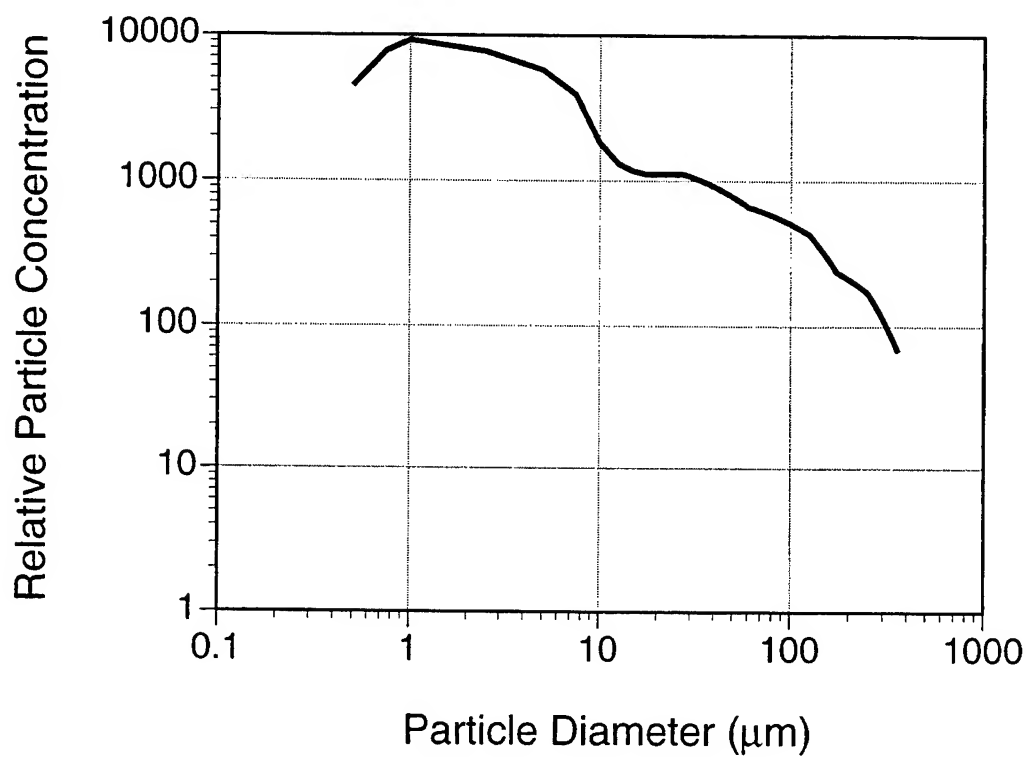


Figure 2. Particle size distribution for near-bottom nepheloid layer, Oceanside, CA.

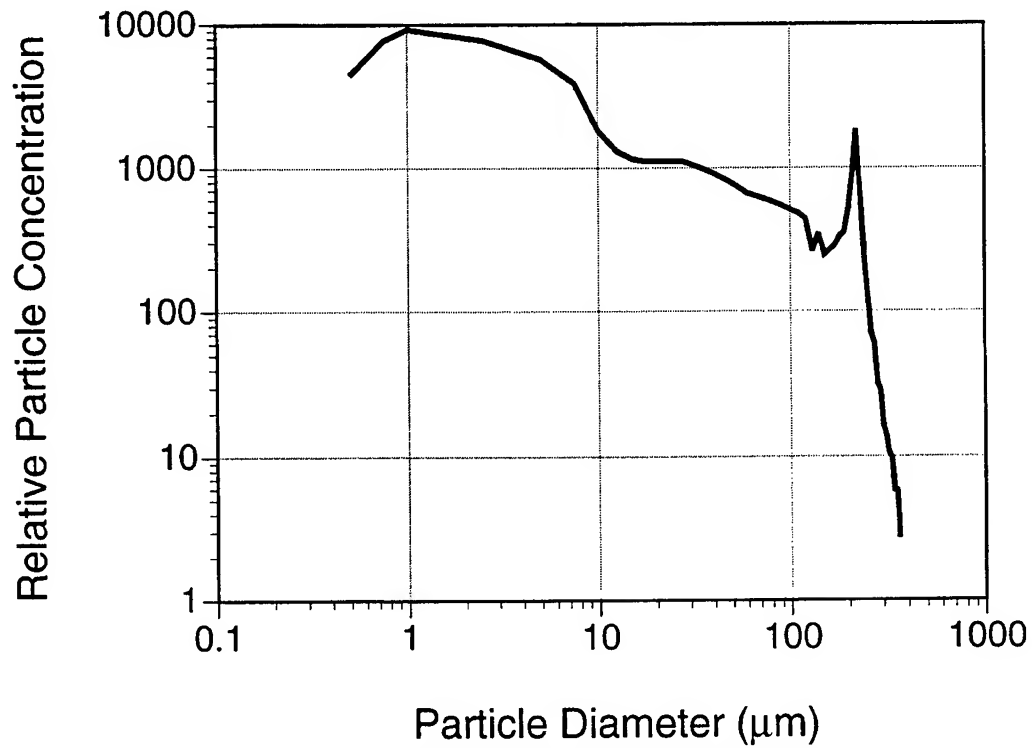


Figure 3. Particle size distribution constructed from Oceanside, CA nepheloid layer and beach sand distribution from Panama City, Florida.

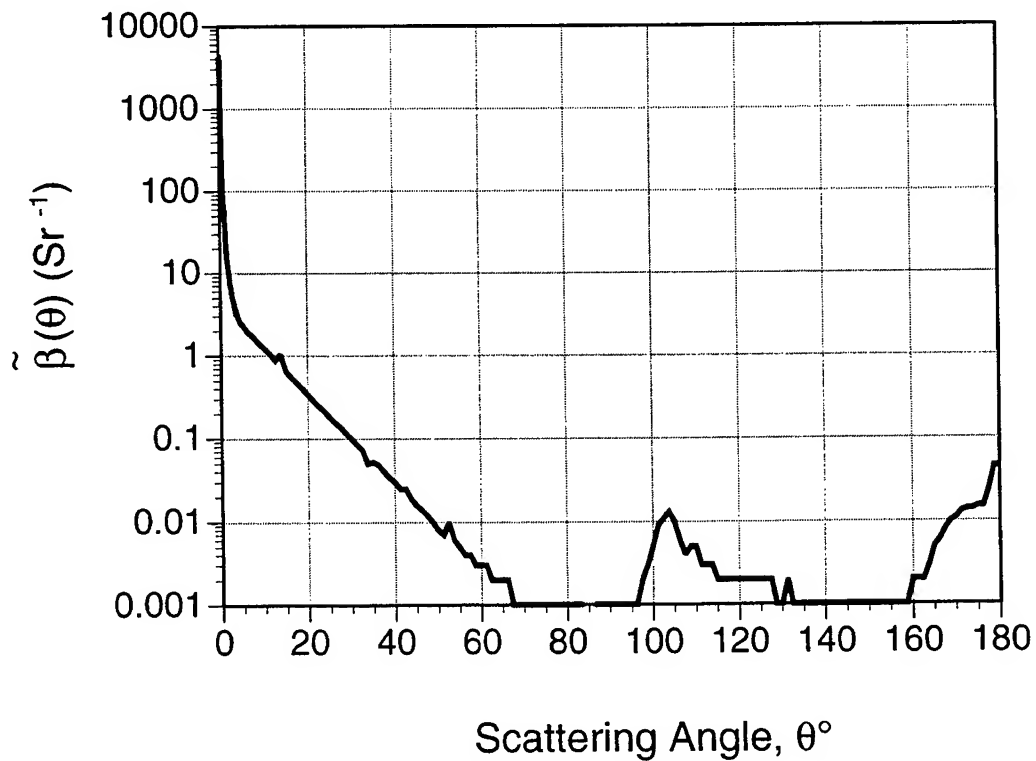


Figure 4. Polydisperse volume scattering function for clay-like suspended particles of near-shore wave agitated area.

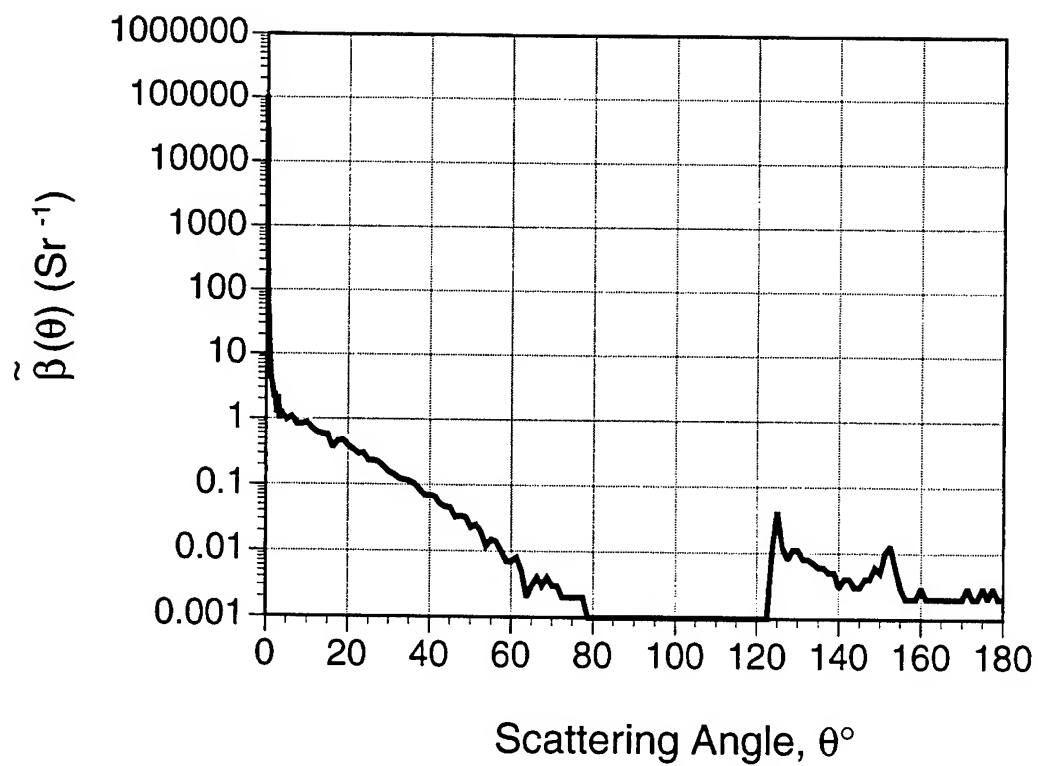
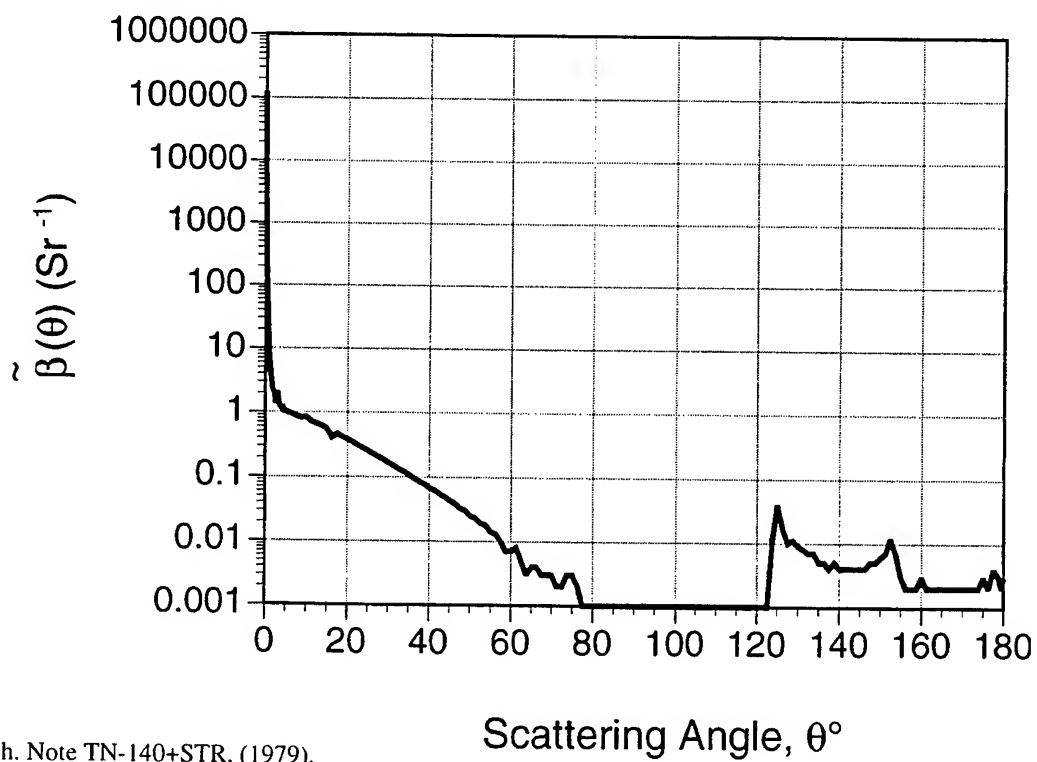


Figure 5. Polydisperse volume scattering function for clay/quartz suspension of nepheloid layer of Oceanside, CA.



NCAR Tech. Note TN-140+STR, (1979).

Figure 6. Polydisperse volume scattering function for clay/quartz suspension for Hamlet's Cove, Florida.

Light scattering on turbulence and on particulates

D. BOGUCKI¹, A. DOMARADZKI¹, D. STRAMSKI² R. ZANEVELD³

¹ *Department of Aerospace Engineering, University of Southern California, Los Angeles*

² *Department of Biological Sciences, University of Southern California, Los Angeles*

³ *College of Oceanic and Atmospheric Sciences, Oregon State University, Corvallis*

ABSTRACT

We have investigated numerically and experimentally the scattering of a light beam by turbulence. We compare the effects of scattering by typical coastal and oceanic particulate distributions with those of turbulence-induced scattering. We find that turbulence can dominate scattering up to 5–10° for the coastal region and for the upper layer of the open ocean. Our preliminary experiment confirms predictions that the frequently observed *in situ* high values of the volume scattering function at small angles are related to scattering on turbulent inhomogeneities in seawater. The ability of turbulent flow to scatter light more than particulates at small angles affects underwater visibility. Current models of underwater visibility account only for the effects of particulates and totally ignore the effects of turbulence. Here we show, with the support of the older experimental data, that turbulence can limit the resolution to an object of size 1 m over a viewing distance of 10m for strong coastal turbulent regimes.

1. INTRODUCTION

It has been proposed that the propagation of light in the ocean is affected by the presence of particulates and by inhomogeneities in seawater density caused by turbulence Yura¹. We refer to any process by which the direction of an individual photon is changed as scattering. In seawater the light beam direction can be changed either by interaction with water inhomogeneities or particulates. The basic quantity describing the scattering ability of the medium is volume scattering function (VSF) $\beta(\theta)$. The goal of this work is to compare the properties of the near-forward scattering on particulates and temperature inhomogeneities in seawater.

2. INTERACTION OF LIGHT WITH TURBULENT INHOMOGENEITIES

Maxwell's equation governs the propagation of a light beam through the turbulent medium. The magnetic permeability of water is negligible while the dielectric constant (refractive index) is assumed to be space variant and the effect of depolarization is negligible. If backscatter is not important, then light propagation is described by the parabolized (diffusion-like) Helmholtz equation Bogucki². For small propagation distances L this equation can be simplified to geometrical optics approximation where the light phase change across the turbulent flow is proportional to the integral $\int_0^L n(x, y, z) dz$, where $n(x, y, z)$ is the index of refraction. The index of refraction must be known in order to describe the interaction of light with turbulence. We obtain $n(x, y, z)$ by numerically simulating temperature in water.

Since most geophysical flows have a large range of scales (dependent on the Reynolds number of the flow) we must first determine which spatial scales of the flow are relevant for light scattering; in the ocean temperature variability ranges between 1 mm and 1 m. It can be shown (see for

example Tatarski³) that the largest contribution to scattering comes from the smallest scales present in the turbulent field. Thus any numerical simulation of the temperature fluctuations used to investigate light propagation in the turbulent flow must reproduce the smallest scales correctly. We chose a model of homogeneous and isotropic turbulent flow to describe the inhomogeneities of the temperature field - Bogucki⁴.

The most important quantity, from a light propagation standpoint, is the rate of dissipation of temperature variance, χ ($\chi = (\partial T'/\partial x)^2 \frac{1}{2}$, where T' is fluctuating temperature), which is routinely measured in the ocean. The physical meaning of χ is the rate at which the temperature fluctuations dissipate to uniformity. The spatial size of the smallest temperature structure, η , is determined by another turbulent parameter, the rate of dissipation of turbulent kinetic energy, ϵ , such that $\eta \simeq (\nu^3/\epsilon)^{1/4}$ where ν is the kinematic viscosity and is approximately equal to $10^{-6} \text{ m}^2/\text{s}$. Typically χ ranges from $10^{-2} \text{ }^\circ \text{C}^2/\text{s}$ a few meters below the surface Farmer⁵ to $10^{-8} \text{ }^\circ \text{C}^2/\text{s}$ in the mid water column. The range for ϵ is from $10^{-4} \text{ m}^2/\text{s}^3$ in a fairly energetic upper layer to $10^{-9} \text{ m}^2/\text{s}^3$ in mid water column Anis⁶.

After scaling the strength of temperature fluctuations in the computational domain given the values of χ and ϵ we calculate the light beam phase distortion on the exit plane of the computational volume. We then calculate VSF for different turbulent flows characterized by different χ and ϵ .

To confirm our calculations, we have carried out a preliminary tank experiment Bogucki². The most important outcome of the experiment is the confirmation that turbulence dominates scattering at small angles, $O(1^\circ)$, for typical concentrations of particulates. Scattering is thus well represented by our numerical DNS database. In spite of large uncertainties in the turbulence quantities of the experiment, the observed scattering was highly consistent with the numerically simulated VSF.

We can estimate the values of χ and ϵ for specific flow regimes using the following dimensional arguments. If we assume that χ is driven by the mean large scale temperature gradient, δT , and the turbulent time scale (u'/L) (where u' is the typical rms current velocity and L is a length scale such as the depth of the water column or the mixed layer, about 10 m in the coastal region), we obtain the relationship $\chi \simeq \delta T^2/(u'/L)$. From this argument, a maximum value for χ is $10^{-2} \text{ }^\circ \text{C}^2/\text{s}$. This is consistent with measurements in the upper few meters of open ocean. The coastal value of ϵ can be given analogously by $\epsilon \simeq u'^3/L$ and can be as high as $10^{-3} \text{ m}^2/\text{s}^3$. Using a range of typical values of ϵ and χ ($10^{-9} - 10^{-2} \text{ }^\circ \text{C}^2/\text{s}$), we have estimated the VSF for conditions which are likely to be encountered in a turbulent patch in the coastal region (Figure 1).

3. SCATTERING ON PARTICULATES

We have used the VSF standard for open ocean water Hodara⁷ and a particle size distribution that is characteristic of coastal waters Brown⁸. The standard small angle VSF form for open ocean waters (with no turbulence) is given by $\beta(\theta) = \theta_0/2\pi(\theta_0^2 + \theta^2)^{3/2}$ with $\theta_0 = 0.03 \text{ rad}$. The slope of the entire (cumulative) coastal particulate size distribution is -3. The VSF corresponding to the particulates of coastal and open ocean sites has been calculated and is also plotted in Figure 1. It is clearly shown that in our simulations of the coastal zone, turbulence scattering can dominate to angles as large as 5° .

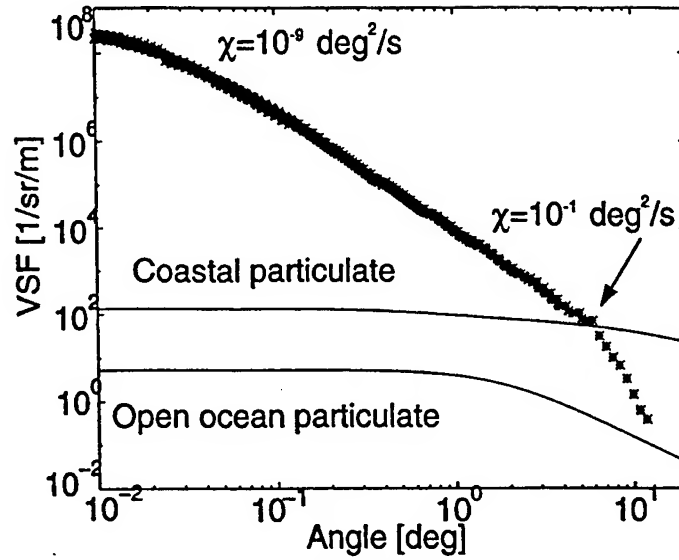


Figure 1: Comparison of VSF due to oceanic turbulence and due to typical open ocean particulates. Turbulence scattering dominates light propagation in the coastal ocean at angles smaller than 5° , and for angles smaller than 10° in the upper layer of the open ocean.

4. LIMIT OF UNDERWATER VISIBILITY IN THE PRESENCE OF TURBULENT FLOW

4.1. Mean scattering angle of a light beam

We use the geometrical optics approximation to quantify the relationship between the root-mean-square spread of the light beam and the χ . We assume that the light beam is traversing a domain filled with discrete eddies consisting of fluid with slightly different temperature than ambient. We will focus on a typical eddy, whose size l is much larger than the wavelength. The considered light beam will undergo refraction on boundaries of the eddy. For a single refraction event we apply Snell's law which relates the incident angle of the light beam θ_1 to the refracted angle θ_2 : $n_1 \sin(\theta_1) = n_2 \sin(\theta_2)$, where n_1 and n_2 are the index of refraction of the eddy and ambient fluid respectively. For small incidence angles: $n_1 \theta_1 \simeq n_2 \theta_2$. We define the change of the refractive index Δn and the beam deflection angle $\Delta \theta$ as: $\Delta \theta = \theta_2 - \theta_1$, $\Delta n = n_2 - n_1$. Substituting them into the previous equation and simplifying we obtain: $\Delta \theta \sim \Delta n$ for the eddy. The beam deflection over a short path-length L (short in a geometrical optics sense), $\Delta \theta_L$, is $\Delta \theta_L \sim L/l \Delta n$. This result tells us that the contribution of a single eddy to the beam scattering angle is proportional to the change in the refractive index across the eddy. Since we are interested in the averaged beam spread over a given path-length, the root-mean-square angle of the beam spread σ is defined as: $\sigma = \overline{\Delta \theta_L^2}^{1/2}$. From above considerations and the definition of χ (given above)

$$\sigma \sim L/l \overline{\Delta \theta^2}^{1/2} \sim L/l \overline{\Delta n^2}^{1/2} \sim L \frac{(\overline{T'^2})^{1/2}}{l} \sim \chi^{1/2}, \quad (1)$$

Thus the root-mean-square angle of the beam spread σ is proportional to the dissipation rate of the temperature fluctuations, χ . It is known (from the MTF approach to visibility) that σ^2

depends on the propagation distance R as: $\sigma^2 = \sigma_0^2 R/R_0$. Combining this relation with previous one, we obtain:

$$\sigma = \sigma_0 \sqrt{R/R_0} \sqrt{\chi/\chi_0} \quad (2)$$

where σ_0 is the root-mean-square angle of the beam spread for the beam traversing a range R_0 where the rate of dissipation of temperature fluctuations is χ_0 . This relationship requires an experimentally known 'standard' σ_0 corresponding to measured R_0 and χ_0 . Presently the only available data are from the thesis of Hodgson⁹ and from Mertens¹⁰. From the experimental data of Hodgson⁹ we find $\sigma_0 = 10^{-4} \text{ rad}$ for distance $R_0 = 1 \text{ m}$ and $\chi_0 = 10^{-8} \text{ }^\circ\text{C}^2/\text{s}$. A similar value of $\sigma_0 = 10^{-4} \text{ rad}$ was estimated by Mertens¹⁰ for "relatively clear and thermally quiet fresh water".

4.2. Underwater visibility limitation due to turbulence

Having estimated σ_0 for a given distance and χ_0 we can find the value of the rms beam scattering angle and estimate the resolution for realistic propagation distances and for typical environmental values of χ . Large values of χ for the coastal zone are associated with thermally-stratified portions of the water column and range typically between $10^{-5} [^\circ\text{C}^2/\text{s}]$ and $10^{-4} [^\circ\text{C}^2/\text{s}]$. In a typical vertical profile for the Southern California shelf in 60 m deep water χ attains a value of $10^{-4} [^\circ\text{C}^2/\text{s}]$ between 40 m and 50 m depth with a background value of $10^{-7} [^\circ\text{C}^2/\text{s}]$. In the vicinity of large scale vertical temperature gradients and of strong currents, χ is likely to be high. Thus the coastal zone is more likely to have a large value of χ than the deep ocean and χ s of order $= 10^{-3} \text{ }^\circ\text{C}^2/\text{s}$ could be observed due to mixing by long internal wave propagating near the bottom.

Using the derived formula for σ and the above estimated values of χ we have calculated the mean beam spread angle and effective resolution, at the distance 10 m from the object (Table 1). Results indicate that resolution may be as low as 1m for strong turbulence.

Table 1. Beam spread and resolution for various coastal environmental conditions at 10 m range from the bottom corresponding to coastal measurements of χ .

Conditions	$\chi [^\circ\text{C}^2/\text{s}]$	$\sigma [\text{deg}]$	Resolution [cm]
Weak turbulence	10^{-7}	0.06	1
Typical turbulence	10^{-4}	1.8	32
Strong turbulence	10^{-3}	5.7	100

5. CONCLUSIONS

- Turbulent scattering may dominate particulate scattering up to 5° in the coastal zone and to 10° in the upper layer of the open ocean.
- Experimental estimates imply that turbulence may limit underwater visibility in coastal conditions.

6. ACKNOWLEDGMENTS

This work was funded by the Ocean Optics Program of the Office of Naval Research under contract number N 00014-94-1-0107. The simulations were carried out at the San Diego Super-computing Center.

References

1. H. T. Yura, 1971: Small-angle scattering of light by ocean water, *Applied Optics*, **10**(1), 114-118.
2. D. Bogucki, J. A. Domaradzki, D. Stramski, and R. Zaneveld, *in prep* : Near-forward scattering on turbulence - comparison with scattering on oceanic particulates, *Applied Optics*.
3. V. I. Tatarski, 1961: *Wave Propagation in Turbulent Media*, McGraw-Hill, New York, 285 pp.
4. D. Bogucki, A. Domaradzki, and P. K. Yeung, Direct numerical simulations of passive scalars with $Pr > 1$ advected by turbulent flow, *Journal of Fluid Mechanics* (submitted).
5. D. M. Farmer, and J. R. Gemmrich, 1996: Measurements of temperature fluctuations in breaking surface waves, *J. Phys. Oceanogr.*, **26**, 816-825.
6. A. Anis, and J. N. Moum, 1995: Surface wave-turbulence interactions: scaling $\epsilon(z)$ near the sea surface, *J. Phys. Oceanogr.*, **25**, 2025-2045.
7. H. Hodara, 1973: *Experimental Results of Small - Angle Scattering*, AGARD Lect. ser. 61, NATO.
8. H. R. Gordon, 1993: Sensitivity of radiative transfer to small-angle scattering in the ocean: quantitative assessment, *Applied Optics*, **32**, 7505-7511.
9. R. T. Hodgson, 1972: Fourier imaging in a hydrological medium; a test of the linear invariant hypothesis, *PhD thesis; Oregon State University, Corvallis, OR*.
10. L. E. Mertens, 1970: *In water photography - theory and practice*, Wiley Interscience.

Polarimetric lidar returns in the ocean:
a Monte Carlo simulation

James T. Adams

George W. Kattawar

Center for Theoretical Physics
Texas A&M University
College Station, Texas 77843-4242

Abstract

Anisotropy in the polarization state of backscattered light from a polarized beam incident on suspensions in water analogous to hydrosols in seawater has been observed experimentally. Viewed through an orientated polarizer, characteristic patterns in the backscattered light are produced. We wish to present the results of Monte Carlo simulations of these physical effects demonstrating excellent agreement with published and unpublished experimental observations. These simulations show that the effects observed are produced by the incoherent scattering of light in the range of volume fractions reported and that this treatment should allow predictions to be made about the application of this technique to ocean probing lidar.

Keywords: lidar, polarimetry, Monte Carlo, incoherent scattering, polarization anisotropy, Mie scattering, Rayleigh scattering, remote sensing, laser light scattering,

1. Introduction

The observation by Pal and Carswell^{1,2} of polarization anisotropy in the backscattered light from a laser beam incident on water droplet clouds and aqueous suspensions of polystyrene spheres has important ramifications to remote sensing in the atmosphere and ocean. Fig.(1a) shows the total light return without the aid of an analysing polarizer compared with the returns observed with polarizers orientated parallel and perpendicular to the incident beam's direction of polarization in the case of an artificially generated cloud of water droplets. Immediately one sees the characteristic polarization cross observed when laser light is focused on a human eye³ and the returned signal is viewed through a polarizer in the perpendicular configuration, strong evidence that it is scattering in the different regions of the eye and not gross geometrical features of the eye which produce these anisotropies in the backscattered light.

Fig. (1b) shows the systematic investigation of these polarization patterns in the backscattered light using suspensions of polystyrene spheres in water. Since it is the size parameter that determines the single scattering characteristics in a Mie calculation, this quantity is used to label the individual observed patterns. Clearly the crossed polarizer configuration shows minimal variation with increasing size parameter. Since exposure times are arbitrary, perceived differences in the crossed orientation examples must be discounted. The qualitative change in the shape of the parallel orientation cases is quite striking. One sees that in the case of the smallest size parameters a horizontal bar is formed with its long axis perpendicular to the incident polarization direction. As the size parameter increases there is the formation of a bar along the incident polarization direction leading the pattern to assume a "+" appearance. This trend is very suggestive as the basis for a means of determining size parameters by polarimetric methods.

Also of interest is the work done by M. Dogariu and T. Asakura^{4,5}. They have recorded the appearance of the patterns produced in the case of a crossed analyser configuration and attempted to explain this appearance using a coherence theory. We believe that such a treatment

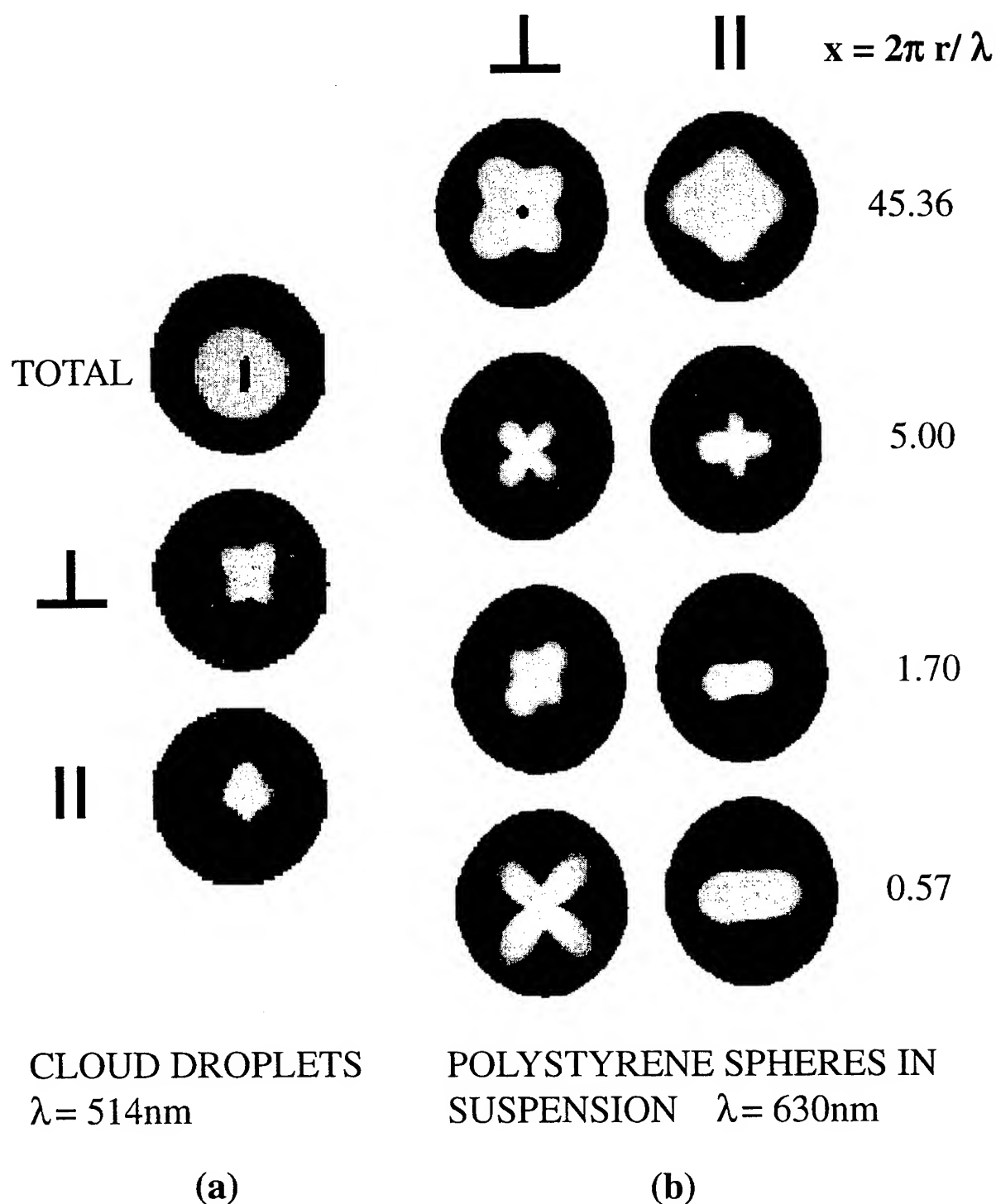


Fig.(1). Observed polarization anisotropy in the backscattered light from water droplets and from polystyrene spheres in suspension as reported by Pal and Carswell.^{1,2}

may be useful when interparticle separations in the suspension become quite small. However, when the turbidity is low as in clear ocean waters we expect that an independent scattering treatment will produce the correct quantitative behavior observed in all analyzer orientations.

2. Double-Scatter Calculation

Since we expect a diminished degree of polarization for multiply scattered photons, it is interesting to examine the case of doubly scattered photons and calculate the patterns produced when only the second scatter contribution is considered. This calculation produces all the qualitative features reported in Pal and Carswell^{1,2} for both analyzer orientations.

Initially we inject the photons with a Stokes Vector referenced to the y-z plane. If the polarization is parallel to the y-axis then the Stokes Vector is,

$$I_{inc} = \begin{pmatrix} 1 \\ 1 \\ 0 \\ 0 \end{pmatrix}. \quad (1)$$

In Fig.(2) one sees that to observe the return at a surface point whose radius vector makes an angle of ϕ with the y-z plane we need to first rotate the initial Stokes vector into the scattering plane. Then one must modify the Stokes vector by two scattering operations whose scattering angles are supplementary. It is then useful to rotate the Stokes vector back into the y-z plane with the result that the final Stokes vector is merely the incident Stokes vector modified by the product of four matrices as,

$$I_{fin} = R(\phi)L(\pi - \Theta)L(\Theta)R(\phi)I_{inc}. \quad (2)$$

The calculation is simplified by the fact that for Rayleigh or Mie scattering the Mueller matrices have the form

$$L(\Theta) = \begin{pmatrix} a & b & 0 & 0 \\ b & a & 0 & 0 \\ 0 & 0 & d & -e \\ 0 & 0 & e & d \end{pmatrix} \quad (3)$$

and $e = 0$ for Rayleigh scattering. The final result may then be expressed in terms of the elements of the two scattering operations and the angle ϕ of the exit point,

$$I_{fin} = \begin{pmatrix} (a_1a_2 + b_1b_2) + (a_1b_2 + a_2b_1)\cos(2\phi) \\ (a_1b_2 + a_2b_1)\cos(2\phi) + (a_1a_2 + b_1b_2)\cos^2(2\phi) - (d_1d_2 - e_1e_2)\sin^2(2\phi) \\ -(a_1b_2 + a_2b_1)\sin(2\phi) - (a_1a_2 + b_1b_2 + d_1d_2 + e_1e_2)\cos(2\phi)\sin(2\phi) \\ (e_1d_2 - d_1e_2)\sin(2\phi) \end{pmatrix}.$$

(4)

Using simple trigonometric relations and the substitutions,

$$\begin{aligned}\alpha &= a_1 a_2 + b_1 b_2 \\ \beta &= a_1 b_2 + a_2 b_1 \\ \gamma &= d_1 d_2 - e_1 e_2\end{aligned}\tag{5}$$

one sees that the first two Stokes vector elements for the backscattered light have the forms

$$\begin{aligned}I &= \alpha + \beta \cos(2\phi) \\ Q &= \beta \cos(2\phi) + \left(\frac{\alpha - \gamma}{2}\right) + \left(\frac{\alpha + \gamma}{2}\right) \cos(4\phi)\end{aligned}\tag{6}$$

The intensities received by the detector with the analyser perpendicular and parallel to the incident polarization direction are proportional to the sum and difference of these first two elements as follows,

$$Perp = I - Q = \left(\frac{\alpha + \gamma}{2}\right)(1 - \cos(4\phi)) \quad , \text{ and} \tag{7}$$

$$Para = I + Q = \left(\frac{3\alpha - \gamma}{2}\right) + 2\beta \cos(2\phi) + \left(\frac{\alpha + \gamma}{2}\right) \cos(4\phi). \tag{8}$$

It is interesting to note in the case of perpendicular orientation that the characteristic "x"-pattern formed is independent of the size parameter. The four-lobed pattern is produced in the case of Rayleigh scattering as well.

3. Monte Carlo Results

The results of a double scatter Monte Carlo calculation using the size parameters from Pal and Carswell are shown in Fig.(3). Clearly the numerical simulation captures all of the qualitative patterns observed in the backscattered light as viewed through the analyzers. Since the volume fractions and scattering coefficients are not reported in the Pal and Carswell articles, it is not possible to exactly simulate these cases. However, such close matching of the images with a second order Monte Carlo simulation suggests that the volume fractions were very low.

4. Conclusions

This Monte Carlo technique produces excellent agreement with the observed polarization anisotropy in backscattered light in the case of laboratory produced suspensions. Since particle separations are smaller here than in the ocean we expect our simulations to be quite accurate in producing similar effects due to both elastic fluctuation and Mie scattering by particulate matter in the water.

We believe that the behavior observed in the parallel returns with increasing size parameters will allow us to remotely determine size distributions of particulate suspended matter. Also, the

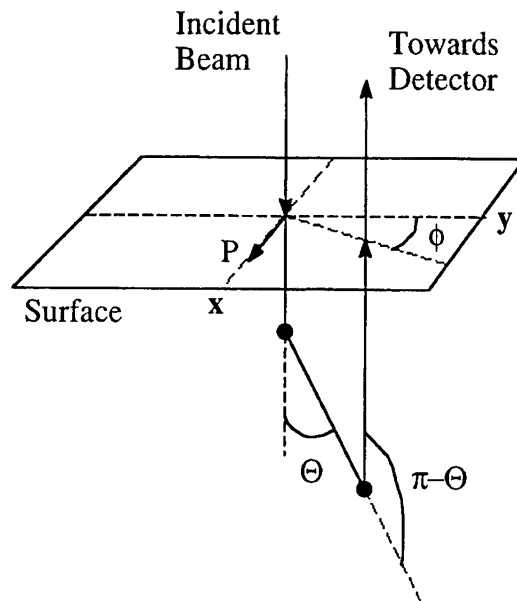


Fig.(2). The geometry of a double scattering event which allows a photon to exit the sample along a radius making an angle of ϕ with the y-z plane.

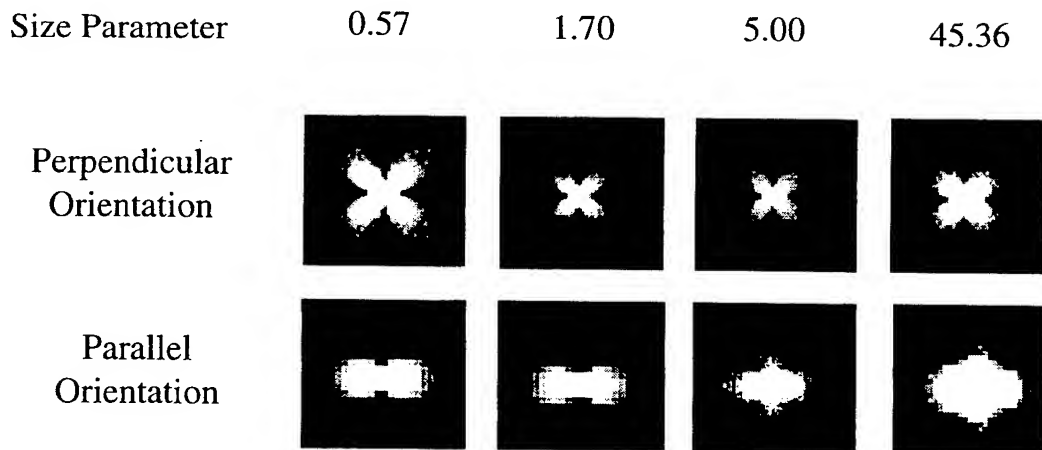


Fig.(3). Results of a Monte Carlo simulation when only second order scattering events contribute to the backscattered light. The characteristic "X" pattern is produced when the analyser orientation is perpendicular to the polarization direction of the incident beam. Note the behavior of the parallel orientation returns with increasing size parameter.

contrast of the crossed polarizer orientation has shown a marked dependence upon the scattering coefficient and thus upon the volume fractions of the suspended particles. This will allow predictions to be made about determining particle concentrations from the perpendicular orientation once the size parameter distribution has been fixed by looking at parallel returns.

5. Acknowledgments

We would like to thank Lihong Wang of Texas A&M for useful discussions and for providing us with experimental results from his own research. This work was supported by the Office of Naval Research under contract number N00014-95-1-0275.

6. References

1. A.I. Carswell and S.R. Pal, "Polarization anisotropy in lidar multiple scattering from clouds", *Appl. Opt.*, **19**, No. 24, 4123-4126 (1980).
2. S.R. Pal and A.I. Carswell, "Polarization anisotropy in lidar multiple scattering from atmospheric clouds", *Appl. Opt.*, **24**, No. 21, 3464-3471 (1985).
3. B.F. Hochheimer and H.A. Kues, "Retinal polarization effects", *Appl. Opt.*, **21**, 3811-3820 (1982).
4. M. Dogariu and T. Asakura, "Polarization-dependent backscattering patterns from weakly scattering media", *J. Optics (Paris)*, **24**, 271-278 (1993).
5. M. Dogariu and T. Asakura, "Photon pathlength distribution from polarized backscattering in random media", *Opt. Eng.*, **35**(8), 2234-2239 (1996).

Models of light pulse propagation in water and determination of inherent optical properties from parameters of the transmitted pulse

Lev S. Dolin

Institute of Applied Physics, Russian Academy of Science, 46, Uljanov Ul., Nizhny Novgorod, 603600, Russia

ABSTRACT

The simple analytical models for the front of laser pulse passed through the water layer, and for decay of the pulsed signal due to diffuse scattering of the pulsed light beam, are derived. It is shown that the whole set of water optical properties may be determined from measurements of temporal and angular distribution of the radiance on the beam axis at the given distance from a light source.

1. INTRODUCTION

The known methods of laser remote determination of water inherent optical properties (IOP) are based on analysis of the backscattering signal. However, a laser pulse passed through a water layer also carries the information on IOP. In particular, the existing theoretical models of light pulse propagation in turbid media with a strong anisotropy of scattering¹⁻³ allow to determine the water scattering coefficient (b) (for the known water phase function) by the difference in durations of emitted and received pulses. It is possible in conditions when a received signal is formed mainly by directed component of underwater light field (ULF), i.e. light unscattered and scattered at small angles. Below is shown that the more complete information about IOP is available from measurements of pulse amplitude depending of receiving direction, and of pulse decay in conditions when received signals are formed by diffuse component of ULF.

2. THE INFORMATIVE PROPERTIES OF THE FRONT OF A SHORT LIGHT PULSE

Monte-Carlo simulations of pulsed light beam parameters in sea water⁴ shows that the front of the pulse with initial duration $\Delta t_0 < 10$ ns passed through the water layer of optical thickness $\tau < 20 \div 30$ is formed mainly by unscattered and single scattered radiation. It allows to determine a rather simple relation between volume scattering function (VSF) of water $\beta(\theta)$ and angle distribution of maximal (peaked) values of radiance $L_m(\theta)$ on the beam axis.

In particular, if the power of the emitted signal is expressed as

$$P(t) = \frac{W}{\Delta t_0} \left(1 - \frac{|t|}{\Delta t_0} \right) 1(\Delta t_0 - |t|), \quad (1)$$

$$1(t) = \begin{cases} 1, & t \geq 0, \\ 0, & t < 0, \end{cases}$$

then above-mentioned relation will be determined by the formulae

$$L_m = \frac{vW \exp(-cr)}{2\pi r^2 (1 - \cos \theta_0)} \Phi(\theta) \beta(\theta), \quad (2)$$

$$\Phi = (1 - \cos \theta)^{-1} \times \begin{cases} 2f - f^2, & f < 1, \\ 1, & f \geq 1, \end{cases}$$

$$f = \frac{N}{2} \left(\frac{\sin \theta + \sin \theta_0}{\sin(\theta + \theta_0)} - 1 \right), \quad N = \frac{r}{v\Delta t_0}, \quad (3)$$

where θ is the angle of the ray deviation from the beam axis direction, W — the emitted pulse energy, Δt_0 — the half-duration of the initial pulse, $2\theta_0$ — the initial beam divergence angle, $v = 2,25 \cdot 10^8$ m/c — velocity of light in

water, c — attenuation coefficient of water, r — the distance between the light source and the receiver. In this case the radiance takes its maximum in the time moment

$$t_m = r/v + \Delta t_m(\theta), \quad \Delta t_m = \begin{cases} \Delta t_0 \cdot f, & f < 1 \\ \Delta t_0, & f \geq 1. \end{cases} \quad (4)$$

The shift of the signal maximum Δt_m in dependence on angle θ is shown on Fig.1. The foregoing formulae were derived on the assumption that $cv\Delta t_0 \ll 1$, $\Delta t_0 \ll r/v$, $\theta \gg \theta_0$. They allow in principle to retrieve the scattering phase function (SPF) of water $p(\theta)$ with angle resolution of the order of $\sim \theta_0$ from the measured dependence $L_m(\theta)$ using the equations:

$$p(\theta) \sim L_m(\theta) / \Phi(\theta). \quad (5)$$

$$\frac{1}{2} \int_0^\pi p(\theta) \sin \theta d\theta = 1. \quad (6)$$

The weight function $\Phi(\theta)$ for several values of θ_0 and N is shown on the Fig.2. Under conditions $N \sin \theta_0 \ll 1$, $\pi - \theta \gg N \sin \theta_0$ for determination of SPF, a very simple equation may be used

$$p(\theta) \sim \sin \theta \cdot L_m(\theta). \quad (7)$$

For testing the considered model of the pulse front forming, we used experimental data obtained by the Gol'din's group from Ocean Optics Laboratory of P.P.Shirshov Institute of Oceanology⁵. Fig.3 demonstrates the results of SPF retrieval (using Eq.7) from peaked values of radiance on the beam axes, measured at the distances $r = 25, 50$ and 75 m in the Indian Ocean. The SPF measured in the same region by standard method is also shown. Taking into account that receiving angle in the experiment was about 10° , the result of SPF retrieval may be considered as satisfactory. Retrieval of SPF for $\theta > 90^\circ$ by the use of Gol'din's experiment turns out impossible since the beam "corn" fell entirely in the receiver's view.

3. THE INFORMATIVE PROPERTIES OF THE DIFFUSION COMPONENT OF A PULSED BEAM

A specified information on water optical properties can be obtained from the measurement of the pulsed radiance in the direction $\vec{\Omega}$, which forms a rather large angle with the beam axis (\vec{z}_0).

This may be achieved owing to the existence of a rather simple relation between the time structure of the diffusion component (L_{dif}) of the pulsed ULF and the space structure of the directed component of the corresponding stationary in time ULF. The mentioned relation emerges when calculating the diffusion component using the quasi-single approximation³.

In this approximation the radiance of the diffusion component of ULF at the time moment t in the point \vec{r} and in the direction $\vec{\Omega}$ is defined by the relation

$$L_{dif}(t, \vec{r}, \vec{\Omega}) = \int_{-\infty}^{\infty} dt' \int_{4\pi} d\Omega' \int_{4\pi} d\Omega'' \int_V L_{sa}(t', \vec{r}', \vec{\Omega}') \times \beta(\vec{\Omega}', \vec{\Omega}'') L_{sa}^{UPS}(t - t', \vec{r} \rightarrow \vec{r}', -\vec{\Omega} \rightarrow -\vec{\Omega}'') d^3\vec{r}', \quad (8)$$

where L_{sa} is the small-angle component of ULF of a pulsed beam, $L_{sa}^{UPS}(t, \vec{r}_1 \rightarrow \vec{r}_2, \vec{\Omega}_1 \rightarrow \vec{\Omega}_2)$ is the small-angle component of ULF in the point \vec{r}_2 and in the direction $\vec{\Omega}_2$ from the unidirectional point source (UPS), radiating at the time moment $t \geq 0$ infinitely short pulse with the unit energy from the point \vec{r}_1 in the direction $\vec{\Omega}_1$. Taking into account the strong anisotropy of the fields L_{sa} , L_{sa}^{UPS} from (8) follows the approximate expression

$$L_{dif}(t, \vec{r}, \vec{\Omega}) = \int_{-\infty}^{\infty} dt' \int_V E_{sa}(t', \vec{r}') \beta(\vec{\Omega}_0, \vec{\Omega}) \times E_{sa}^{UPS}(t - t', \vec{r} \rightarrow \vec{r}', -\vec{\Omega}) d^3\vec{r}', \quad (9)$$

where

$$E_{sa} = \int_{4\pi} L_{sa} d\Omega', \quad E_{sa}^{UPS} = \int_{4\pi} L_{sa}^{UPS} d\Omega'',$$

the unit vector $\vec{\Omega}_0(\vec{r}')$ characterizes the direction of the maximum of the field radiance L_{sa} in the point \vec{r}' .

We limit our problem by the analyses of the dependence L_{dif} on t in the time interval $r/v < t < r/v + \Delta t$, where $\Delta t \ll r/v$. Then the expression for L_{dif} may be reduced to the single integral using the simplest model of the distribution of the scalar irradiance from UPS:

$$E_{sa}^{UPS}(t, \vec{r} \rightarrow \vec{r}', \vec{\Omega}) = \delta(t - l/v) \delta(\vec{\rho}_\perp) \exp(-a_e l) \cdot 1(l), \quad (10)$$

$$a_e = a + b \cdot \tilde{b}_{45} \quad (11)$$

$$\tilde{b}_{45} = \frac{1}{2} \int_{\pi/4}^{\pi} p(\theta) \sin \theta d\theta, \quad (12)$$

$\vec{\rho} = \vec{r}' - \vec{r}$, $l = (\vec{\Omega} \vec{\rho})$, $\vec{\rho}_\perp = \vec{\rho} - l \vec{\Omega}$, a - absorption coefficient. This model ignores the effects of the small-angle scattering. The attenuation of the beam power due to the light scattering by large angles is taken into account by introducing the "effective" absorption coefficient a_e , which as a rule slightly differs from a , because the typical values of the parameter \tilde{b}_{45} (the scattering probability for $\theta > 45^\circ$) lie in the interval $0.03 < \tilde{b}_{45} < 0.1$. The substitution of (10) to (9) leads to the formula

$$L_{dif}(t, \vec{r}, \vec{\Omega}) = \int_0^\infty \beta(\vec{\Omega}_l, \vec{\Omega}) E_{sa}(t - l/v, \vec{r} - l \vec{\Omega}) \exp(-a_e l) dl, \quad (13)$$

in which $\beta(\bullet)$ depends on $\vec{\Omega}_l = \vec{\Omega}_0(\vec{r}' = \vec{r} - l \vec{\Omega})$.

Now we analyse the relation (13) based on the concrete model of distribution $E_{sa}(\bullet)$.

In the small-angle approximation the distribution of irradiance from pulsed collimated source has the form

$$E_{sa}(t, \vec{r}) = W \cdot \bar{E}_{sa}(\vec{r}) \exp(-a_e z) f(t - z/v) 1(z), \quad (14)$$

where $W f(t)$ is the power of pulsed beam, $\bar{E}_{sa} \cdot \exp(-a_e z)$ is the distribution of irradiance from the continuous source with the unit power and with the directivity diagram similar to that of the pulsed source. At $f(t) = \delta(t)$ the substitution of (14) into (13) gives:

$$L_{dif}^s(t, \vec{r}, \vec{\Omega}) = \frac{vW}{1 - \Omega_z} \beta(\vec{\Omega}', \vec{\Omega}) \exp(-a_e v t) \bar{E}_{sa}(\vec{r}') 1(t_1), \quad (15)$$

$t_1 = t - z/v$, $\vec{\Omega}' = \vec{\Omega}_0(\vec{r}')$, $\vec{r}' = \vec{r} - \vec{\Omega} \frac{v t_1}{1 - \Omega_z}$. The calculation of the diffusion component of ULF with taking into account the finite duration of the probing pulse is reduced to smoothing the fine structure of distribution (15):

$$L_{dif}(t, \vec{r}, \vec{\Omega}) = \int_{-\infty}^\infty f(t - t') L_{dif}^s(t', \vec{r}, \vec{\Omega}) dt'. \quad (16)$$

The feasibility of Eqs. 15, 16 is limited by condition

$$3(\Delta r_\perp)^2 (1 - \Omega_z)^3 \gg b < \theta_{45}^2 > (v t_1)^3,$$

as well as by condition $\Delta t_0 \gg \Delta t_1$ or $\Delta t_1 \ll \Delta r_\parallel / v$, where Δr_\parallel and Δr_\perp are the scales of spatial inhomogeneity of distribution \bar{E}_{sa} in the direction $\vec{\Omega}$ and in the perpendicular direction,

$$< \theta_{45}^2 > = \frac{1}{2} \int_0^{\pi/4} \theta^2 p(\theta) \sin \theta d\theta \quad (17)$$

is the variance of the scattering angle for $\theta < 45^\circ$, Δt_1 is the broadening of the signal $E_{sa}(t)$ as it propagates from the source to the receiver.

The formulae (15), (16) relate the space structure of the continuous light beam with the form of the pulsed signal recorded in the fixed point of water medium. They show, in particular, that the results of measuring the radiance of the pulsed light field in two different directions ($\Omega_z = 0, -1$) may be used for defining the parameter a_e and the irradiance distribution $\bar{E}_{sa}(r_\perp, z)$ in the transverse cross-section ($z = \text{const}$) of the narrow light beam. As it follows from (15) (taking into account the weak dependence of β on θ at $\theta \sim 90^\circ$)

$$\begin{aligned} \bar{E}_{sa}(r_\perp, z) &= \left[vW\beta\left(\frac{\pi}{2}\right) \right]^{-1} \cdot \exp(a_e(z + r_\perp)) \\ &\times L_{dif}^\delta(t_1 = r_\perp/v, \vec{r}_\perp = 0, z, \Omega_z = 0), \end{aligned} \quad (18)$$

where r_\perp is the distance between the point \vec{r} and the beam axis, $L_{dif}^\delta(\bullet)$ is the radiance of the pulsed signal at the time moment $t = (z + r_\perp)/v$ on the beam axis ($\vec{r}_\perp = 0$) at the distance z from the source in the direction perpendicular to the beam axis ($\Omega_z = 0$). To get the analogous relation for the case $\Delta t_0 \neq 0$ in the right part of (18) one must substitute $L_{dif}^\delta \rightarrow L_{dif}$, and the function \bar{E}_{sa} should be considered as the distribution of the irradiance from the continuous source having the transmitting angle (beam divergence) $2\bar{\theta} = 2\theta_0 + v\Delta t_0/z$, where $2\theta_0$ is the transmitting angle of the pulsed source.

It is seen from (18) that to define \bar{E}_{sa} together with the function L_{dif} one has to know the parameter a_e . In order to measure it one may use the back-scattering signal ($\Omega_z = -1$) on the beam axis. According to (15)

$$\begin{aligned} L_{dif}(t, \vec{r}_\perp = 0, z, \Omega_z = -1) &= \frac{vW}{2} \beta(\pi) \cdot \exp(-a_e vt) \\ &\times \bar{E}_{sa}\left(0, z + \frac{vt_1}{2}\right) \cdot 1(t_1) \end{aligned} \quad (19)$$

In the small-angle diffusion approximation under the condition that

$$\ln(<\theta_{45}^2> / 3\theta_0^2) + \ln b_e z \ll b_e z < 2\sqrt{\frac{b_e}{a_e <\theta_{45}^2>}} \quad (20)$$

we have

$$\bar{E}_{sa} \sim \frac{1}{S} \exp(-r_\perp^2/S), \quad (21)$$

$$S = \frac{1}{3} b_e <\theta_{45}^2> z^3, \quad (22)$$

$$b_e = (1 - \bar{b}_{45}) b; \quad (23)$$

b_e is the effective scattering coefficient. In this approximation from (19) we obtain:

$$a_e = -\frac{3}{2z} - \frac{1}{v} \frac{d}{dt} \ln L_{dif}(t, \vec{r}_\perp = 0, \Omega_z = -1) \quad (24)$$

at $\Delta t_0 < t_1 \ll 2z/v$.

Thus, the value of a_e and distribution $\bar{E}_{sa}(r_\perp)$ dependent on parameter $d = b_e <\theta_{45}^2>$ are determined by the decay of the signal L_{dif} for $\Omega_z = 0, -1$. Therefore, the order of the retrieval of the entire set of IOP may be the following:

1. $p(\theta)$ is determined by Eq.5.
2. Parameters \bar{b}_{45} and $<\theta_{45}^2>$ are computed by Eqs.12,17.
3. a_e is determined by Eq.24
4. Dependence \bar{E}_{sa} on r_\perp is defined by Eq.18 and on the basis of this dependence parameter b_e is determined.
5. Scattering and absorption coefficients are determined by formulae $b = \frac{d}{<\theta_{45}^2> (1 - \bar{b}_{45})}$, $a = a_e - b \cdot \bar{b}_{45}$.

4.ACKNOWLEDGEMENTS

I am grateful to Drs. V.A.Savel'ev and Yu.A.Gol'din for stimulating discussions. The work was supported by the Russian Foundation of Basic Research (RFBR), Grants No. 95-02-5797 and No. 96-05-64697. I also wish to thanks to ONREUR Visiting Scientist Program and to RFBR for support my participation in the Conference.

5.REFERENCES

1. A.C.Ishimaru, Wave Propagation and Scattering in Random Media (Academic, New York, 1978).
2. H.C.van de Hulst and George W.Kattawar, "Exact spread function for a pulsed collimated beam in a medium with small-angle scattering", Applied Optics, vol.33, No.24, pp.5820-5829, 1994.
3. Lev S.Dolin, Iosif M.Levin, "Optics, Underwater", Encyclopedia of Applied Physics, vol.12, pp.571-601 (1995, VCH Publishers, Inc.).
4. A.K.Zakharov, Yu.A.Gol'din, "The Monte-Carlo calculation of the structure of narrow nonstationary light beams in sea water up to a large optical depth", Izv.Acad.Sci, USSR, Atmos.Oceanic Phys, vol.22, No.5, pp.533-540, 1986 (in Russian).
5. Yu.A.Gol'din, V.N.Pelevin, K.S.Shifrin, "Light field in the sea water from pulsed source", Optics of the ocean and atmosphere, Nauka Publ., Moscow, pp.56-95, 1981 (in Russian).

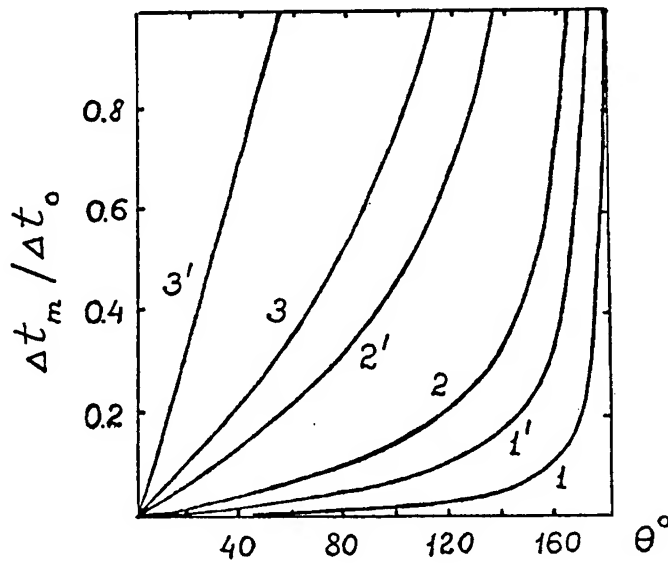


Fig.1. Relative shift of the signal maximum in dependence on the receiving direction for $\theta_0 = 10'$ (curves 1, 1'), 1° (2, 2'), 5° (3, 3'); $N = 15$ (curves 1 - 3), 45 (1' - 3').

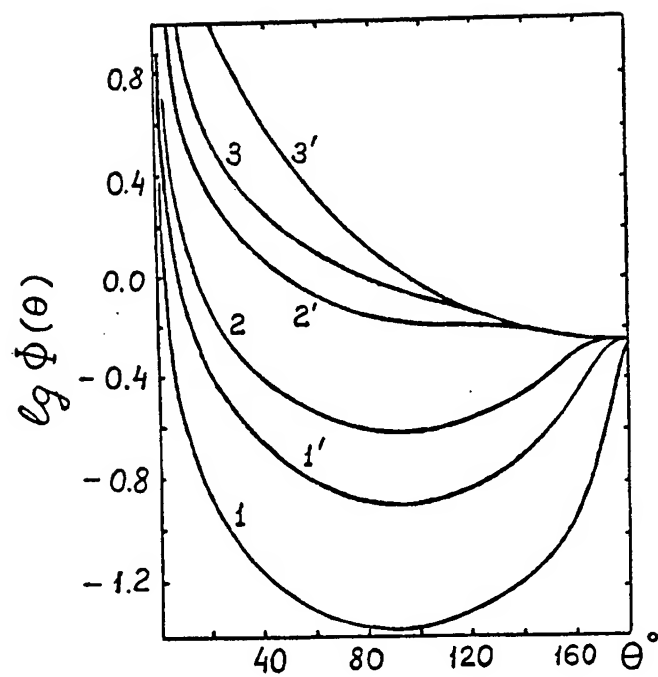


Fig.2. The weight function for $\theta_0 = 10'$ (curves 1, 1'), 1° (2, 2'), 5° (3, 3'); $N = 15$ (curves 1 - 3), 45 (1' - 3')

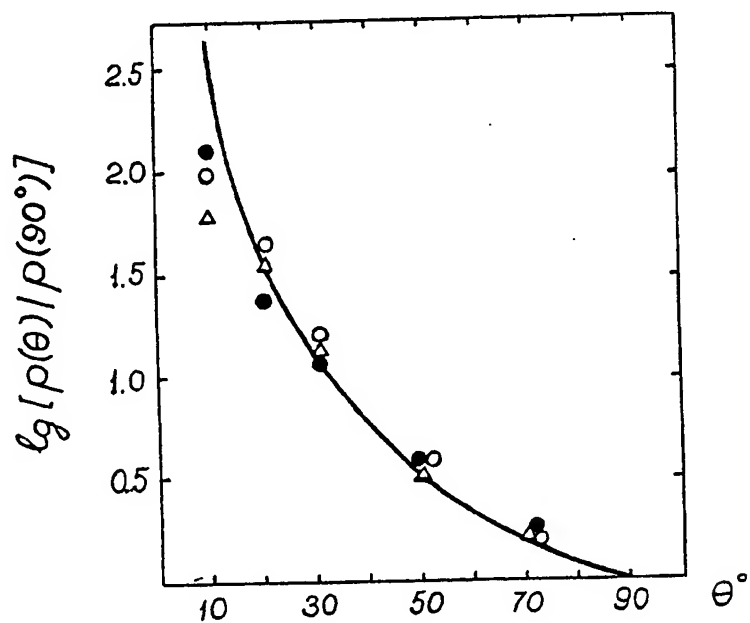


Fig.3. Real SPF (solid curve) and results of SPF retrieval from signals measured at the distances $r = 25m$ (•), $50m$ (Δ), $75m$ (○).

The effect of Raman scattering on the asymptotic average cosine in the ocean.

Juli Berwald
Dariusz Stramski
Dale A. Kiefer

Hancock Institute of Marine Science
University of Southern California
Los Angeles, CA 90089-0371

Curtis D. Mobley

Sequoia International
9725 SE 36th Street, Suite 308
Mercer Island, WA 98040

ABSTRACT

Using the numerical radiative transfer model (Hydrolight 3.0), we investigate vertical changes in the average cosine of the underwater light field throughout the water column and into the asymptotic regime in the presence of Raman scattering. Results from these simulations show that Raman scattering strongly influences the asymptotic average cosine at wavelengths greater than about 500 nm in clear waters and 600 nm in more turbid waters. At these wavelengths both the vertical behavior and the asymptotic value of the average cosine differ drastically in the presence of Raman scattering as compared to source-free waters. In red wavelengths and in clear waters, the effect of Raman scattering on the average cosine is most pronounced and a quasi-asymptotic field may be present. Our radiative transfer simulations confirm that the asymptotic diffuse attenuation coefficients at excitation and emission wavelengths are equivalent in the presence of Raman scattering. Using Gershun's equation with a source, we identify a new parameter P^* which is the ratio of scalar irradiance due to local inelastic scattering to total scalar irradiance. Similar to the asymptotic average cosine, P^*_{∞} , is only dependent on the inherent optical properties of the asymptotic field.

Keywords: average cosine, Raman scattering, radiative transfer modeling, asymptotic regime, underwater light field, inelastic scattering, diffuse attenuation coefficient, Gershun equation

1. INTRODUCTION

Below sufficient depth in a source-free homogeneous ocean, the angular shape of the radiance distribution and the rate of decay of the magnitude of radiance are constant and depend only on the inherent optical properties of the water. This is referred to as the asymptotic field. In the asymptotic field, both the average cosine of the light field, $\bar{\mu}$, and the diffuse attenuation coefficients K for any radiance or irradiance are constant. The existence of the asymptotic regime was discussed by Preisendorfer¹ and subsequently proven rigorously by Højerslev and Zaneveld². However, underwater radiance at a given wavelength can include contributions not only from direct or elastically scattered solar radiation, but also inelastic sources such as Raman scattering. Stavn and Weidemann^{3,4} used Monte Carlo simulations of radiative transfer and showed an increasing effect of Raman scattering on $\bar{\mu}$ as depth increases in the ocean. Gordon et al.⁵ and Gordon and Xu⁶ have provided analyses of the asymptotic field with Raman scattered light. Gordon et al.⁵ focused their study on the asymptotic diffuse attenuation coefficient K_{∞} in particle free seawater in the presence of Raman scattering. They concluded that if the source-free diffuse attenuation coefficient at the excitation wavelength is less than that of the emission wavelength, then in the presence of Raman scattering the asymptotic diffuse attenuation coefficients at excitation and emission wavelengths will be equivalent. Gordon and Xu⁶ developed a method to solve for the asymptotic radiance distribution in the presence of an inelastic source.

However, none of these studies have involved radiative transfer simulations in the presence of Raman scattering to the great optical depths necessary to reach the asymptotic field. In this study we perform such simulations through the water column and into the asymptotic regime and we present complete profiles of both the average cosine and the diffuse attenuation

coefficient. We have also found that Gershun's equation with a source provides a useful basis for understanding changes in the average cosine in the presence of Raman scattering.

2. THEORETICAL CONSIDERATIONS

We can gain insight into the effect of Raman scattering on the asymptotic field by considering Gershun's equation with a Raman source term,

$$\bar{\mu}(z, \lambda) K_E(z, \lambda) = a(z, \lambda) - \frac{\lambda' \int E_o(z, \lambda') b_R(\lambda', \lambda) d\lambda'}{E_o(z, \lambda)}, \quad (1)$$

where K_E is the diffuse attenuation coefficient for net irradiance, a is the absorption coefficient, E_o is scalar irradiance and b_R is the Raman scattering cross section. The wavelength of emission is symbolized by λ , and the Raman excitation wavelength by λ' . We define the term,

$$P^*(\lambda, \lambda') = \frac{\lambda' \int E_o(z, \lambda') b_R(\lambda, \lambda') d\lambda'}{E_o(z, \lambda)}, \quad (2)$$

which represents the ratio of local Raman scattering to total irradiance. If we assume that an asymptotic radiance distribution exists in a vertically homogeneous ocean, the asymptotic diffuse attenuation coefficient and the average cosine are depth independent, and Eq. 2 can be written as,

$$\bar{\mu}_\infty(\lambda) K_\infty(\lambda) = a(\lambda) - P^*_\infty(\lambda', \lambda). \quad (3)$$

Note that the ratio $P^*_\infty(\lambda', \lambda)$ must become independent of depth as $z \rightarrow \infty$. As discussed by Gordon et al.⁵, Raman scattering will be important in the asymptotic field when in source-free conditions, $K_\infty(\lambda') < K_\infty(\lambda)$. In this case, in the asymptotic field $E_o(\lambda)$ will consist entirely of light which has been Raman scattered. Thus, the numerator of $P^*_\infty(\lambda', \lambda)$ becomes proportional to the denominator via the asymptotic diffuse attenuation coefficient. Alternatively, if $K_\infty(\lambda') > K_\infty(\lambda)$, there is negligible inelastic scattering and $P^*_\infty(\lambda', \lambda)$ is zero. In this case, Eqs. 1 and 3 reduce to the well-known Gershun's equation for a source-free medium.

3. APPROACH

Our study is based on radiative transfer modeling. We used Hydrolight 3.0 code which is a numerical model for solving the radiative transfer equation.^{7,8} An important feature of the Hydrolight code is that the accuracy of the solution does not decrease with depth. This feature is important to us because we can exactly solve the radiative transfer equation down to great optical depths including the asymptotic regime.

In order to run the Hydrolight model, one must define the boundary conditions at the sea surface, the inherent optical properties of the water body and bottom boundary conditions. In our simulations the incident spectral distribution of irradiance^{9,10} and the angular distribution of incident radiance¹¹ were modeled realistically. The sun was placed at 45° from the zenith and the sky was 70% overcast. There is a 5 m s⁻¹ wind across the sea surface. To obtain approximately realistic values of the spectral absorption and scattering coefficient, we used bio-optical models based on the concentration of chlorophyll *a*, Chl. Three concentrations of chlorophyll are considered, 0.05, 0.5 and 5 mg m⁻³. The absorption coefficient was calculated according to the model proposed by Prieur and Sathyendranath¹² and later simplified by Morel.¹³ The corresponding model for the spectral scattering coefficient was given by Gordon and Morel¹⁴ and Morel.¹⁵ The phase function $\bar{\beta}(\psi)$ includes both molecular and particulate scattering components (ψ is the scattering angle). A pure water phase function $\beta_w(\psi)$ which is nearly isotropic was used for the water component.⁷ A particle phase function $\beta_p(\psi)$, determined from measurements made by Petzold¹⁶ in San Diego harbor as described by Mobley et al.¹⁷, was chosen for the particle component. We assume a vertically homogeneous ocean where $a(\lambda)$, $b(\lambda)$ and $\bar{\beta}(\psi)$ are independent of depth. The bottom boundary conditions are defined by assuming that the ocean is infinitely deep. Raman scattering was included in the simulations as described in Mobley⁷ (Sect. 5.14 with topographic errors corrected).

All of our calculations were made to at least to 35 optical depths and in some cases to over 100. The asymptotic field was assumed to be reached when $\bar{\mu}$ varied vertically 1% or less between two consecutive discrete output depths. The simulations

were performed spectrally from 355 to 675 nm using 10 nm wide wavebands. Output is given for the nominal wavelengths that correspond to the center of the wavebands.

4. RESULTS AND DISCUSSION

4.1 Average cosine profiles

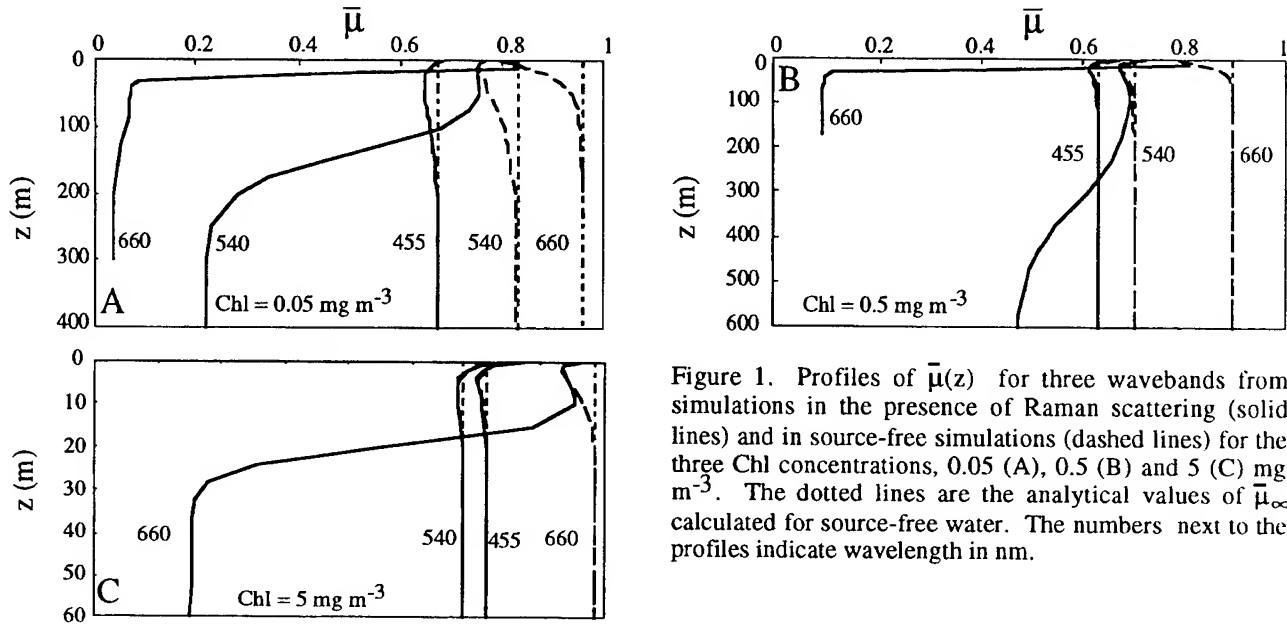


Figure 1. Profiles of $\bar{\mu}(z)$ for three wavebands from simulations in the presence of Raman scattering (solid lines) and in source-free simulations (dashed lines) for the three Chl concentrations, 0.05 (A), 0.5 (B) and 5 (C) mg m^{-3} . The dotted lines are the analytical values of $\bar{\mu}_{\infty}$ calculated for source-free water. The numbers next to the profiles indicate wavelength in nm.

Profiles of the average cosine for source-free simulations and simulations which include Raman scattering are presented in Figure 1. Three major patterns can be observed. First, at the blue wavelength, 455 nm, $\bar{\mu}(z)$ is not affected by Raman scattering regardless of Chl. In simulations which include Raman scattering, the profiles of $\bar{\mu}(z, 455\text{nm})$ are characterized by a small decrease in the surface and then an exponential-like increase with depth to the predicted asymptotic value for source-free waters, $\bar{\mu}_{\infty}$. Second, at the red wavelength, 660 nm, $\bar{\mu}(z)$ is strongly influenced by Raman scattering for all Chl. The profile of $\bar{\mu}(z, 660\text{nm})$ has a complex shape, characterized by a strong vertical gradient and a low asymptotic value. For the low and medium Chl concentrations, there is a quasi-asymptotic field between about 50 and 100 m, below which the deep asymptotic value is reached. Finally, the behavior of $\bar{\mu}(z)$ at the green wavelength, 540 nm, shows the most complicated patterns in the presence of Raman scattering. At low and medium Chl, $\bar{\mu}(z, 540\text{nm})$ profiles are affected by Raman scattering, which is reflected in the presence of a significant vertical gradient and a low asymptotic value. The influence of Raman scattering decreases with increasing Chl, so that at high Chl = 5 mg m^{-3} , $\bar{\mu}(z, 540\text{nm})$ behaves more like $\bar{\mu}(z)$ at blue wavelengths with no discernible effect of Raman scattering.

4.2 Asymptotic average cosine

Figure 2 compares the spectra of the asymptotic average cosine in the presence and absence of Raman scattering. The most remarkable feature in Fig. 2 is that three spectral regions are observed in the curves: 1) at the shorter wavelengths in the visible spectrum, there is a negligible effect of Raman scattering on $\bar{\mu}_{\infty}(\lambda)$ and $\bar{\mu}_{\infty}(\lambda)$ is relatively large; 2) at the longest wavelengths, there is a strong effect of Raman scattering on $\bar{\mu}_{\infty}(\lambda)$ and the $\bar{\mu}_{\infty}(\lambda)$ values are very low; and 3) between these two parts of the spectrum, there is a region where $\bar{\mu}_{\infty}(\lambda)$ decreases significantly with wavelength. The wavelength at which the decrease in $\bar{\mu}_{\infty}(\lambda)$ begins increases from 490 nm at Chl = 0.05 mg m^{-3} to 510 nm at Chl = 0.5 mg m^{-3} to 590 nm at 5 mg m^{-3} .

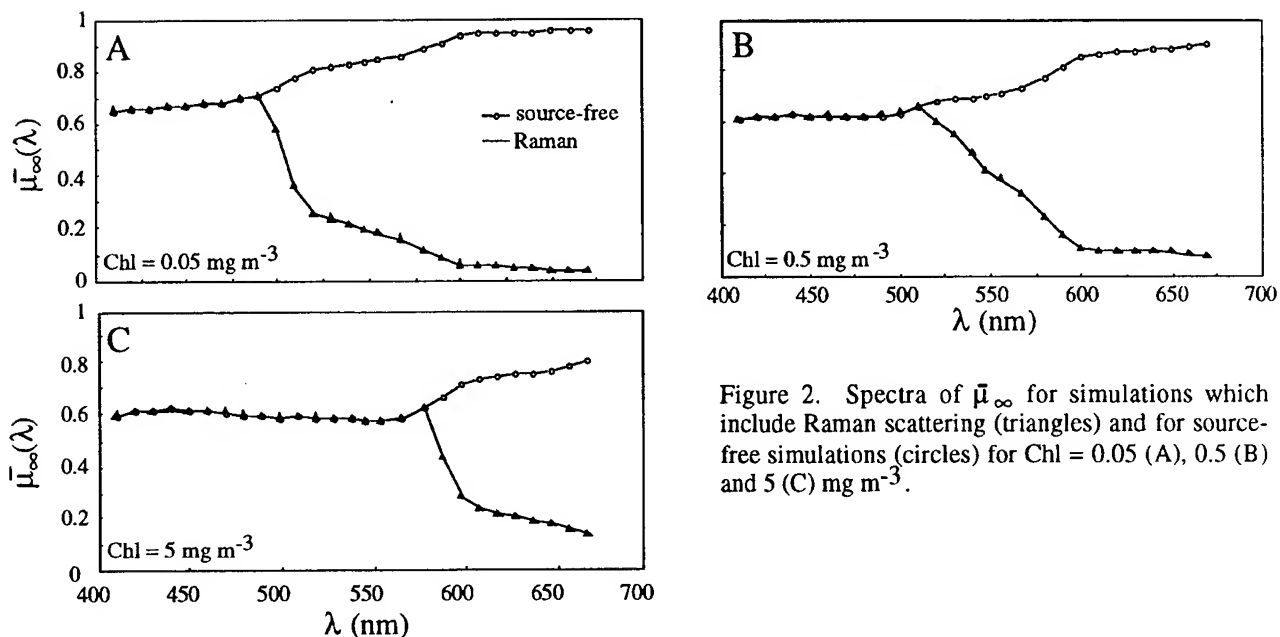


Figure 2. Spectra of $\bar{\mu}_{\infty}$ for simulations which include Raman scattering (triangles) and for source-free simulations (circles) for Chl = 0.05 (A), 0.5 (B) and 5 (C) mg m^{-3} .

For all Chl concentrations at the shorter wavelengths Raman scattering has a negligible effect on $\bar{\mu}_{\infty}$, its spectral behavior is governed by the single scattering albedo and the scattering phase function, just as for source-free waters.¹⁸ This is consistent with the pattern observed in vertical changes of $\bar{\mu}(z, 410)$ in Fig. 1. At longer wavelengths $\bar{\mu}_{\infty}(\lambda)$ is strongly affected by Raman scattering and its value is lower than the source-free values of $\bar{\mu}_{\infty}$. These low values of $\bar{\mu}_{\infty}$ result from the fact that the asymptotic field at longer wavelengths consists of Raman scattered photons and the associated Raman scattering phase function is nearly isotropic. As discussed for $\bar{\mu}(z, 660\text{nm})$ in Fig 1, the vertical behavior of $\bar{\mu}$ at longer wavelengths is characterized by relatively strong vertical gradients and a very low value of $\bar{\mu}_{\infty}$.

The value of $\bar{\mu}_{\infty}$ in the green part of the spectrum is most difficult to characterize because it is located within the region which shifts behavior with variations in inherent optical properties (or Chl concentration). For example, recall the behavior of $\bar{\mu}(z, 540\text{nm})$ for the three different Chl. For Chl is 0.05 and 0.5 mg m^{-3} , 540 nm is greater than the beginning of the decrease in $\bar{\mu}_{\infty}(\lambda)$ (490 nm and 510 nm, respectively) and both $\bar{\mu}(z, 540\text{nm})$ and $\bar{\mu}_{\infty}(540\text{nm})$ are strongly affected by Raman scattering (Figs. 1A and 1B). When Chl = 5 mg m^{-3} , the decrease in $\bar{\mu}_{\infty}(\lambda)$ begins at 590 nm, longer than 540 nm, and $\bar{\mu}(z, 540\text{nm})$ as well as $\bar{\mu}_{\infty}(540\text{nm})$ show a negligible effect of Raman scattering (Fig. 2C).

4.3 Profiles of P^*

Figure 3 shows profiles of P^* for the low Chl concentration. At 440 nm, $P^*(z)$ is zero indicating that the contribution of local Raman scattering is a negligible portion of the total irradiance. This is consistent with the observation that $\bar{\mu}(z, 455\text{nm})$ and $\bar{\mu}_{\infty}(455\text{nm})$ are the same in the presence or absence of Raman scattering (Fig. 1A and 2A). For this blue wavelength, Eqs. 1 and 3 reduce to the well-known Gershun equation for source-free water.

In the upper water column, $P^*(z, 540\text{nm})$ and $P^*(z, 660\text{nm})$ increase vertically as local Raman scattering becomes a greater proportion of the total irradiance. At approximately 150 m and 50 m for $P^*(z, 660\text{nm})$ and $P^*(z, 660\text{nm})$, respectively, the profiles become vertically constant. These depths correspond to the depth where $\bar{\mu}_{\infty}$ occurs in Fig 1A. The profile of $P^*(z, 660\text{nm})$ confirms the presence of a quasi-asymptotic field, similar to that observed in the profile of $\bar{\mu}(z, 660\text{nm})$. As discussed in Section 2, the asymptotic behavior of P^* results from the spectral behavior of K_{∞} .

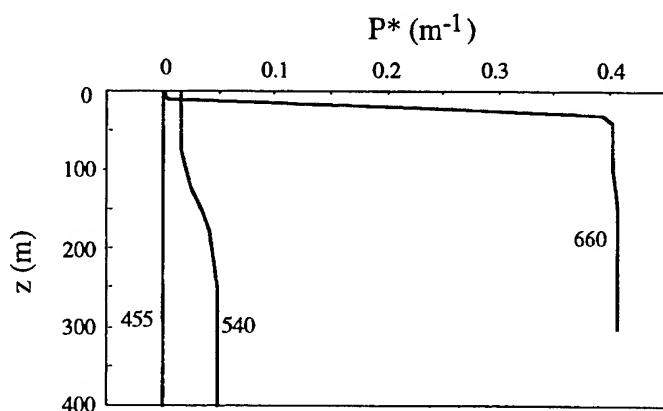


Figure 3. Profiles of P^* for $\text{Chl} = 0.05 \text{ mg m}^{-3}$. The numbers next to the profiles indicate wavelength in nm.

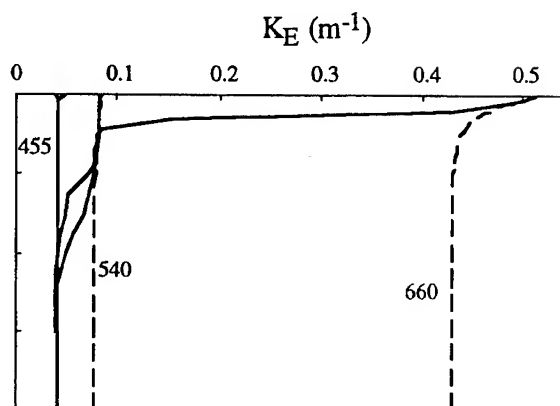


Figure 4. Profiles of K_E for $\text{Chl} = 0.05 \text{ mg m}^{-3}$ from source-free simulations (dashed lines) and from simulations which include Raman scattering (solid lines). The numbers next to the profiles indicate wavelength in nm.

4.4 Profiles of K

The diffuse attenuation coefficient for net irradiance for 455, 540 and 660 nm is shown in Fig. 4. We have chosen to illustrate these three wavelengths because 455 is the center of the Raman excitation band for 540 nm and 540 nm is the center of the Raman excitation band for 660 nm. Note that for the source-free simulations, $K_\infty(455) < K_\infty(540) < K_\infty(660)$. According to our earlier discussion, this indicates that in the presence of Raman scattering we expect $K_\infty(455) = K_\infty(540) = K_\infty(660)$.

For the simulation which includes Raman scattering, $K_E(z, 660)$ is initially very large and solar light is attenuated quickly allowing Raman scattering to make an increasingly greater contribution to the light field with depth (see Fig. 3). This decreases the rate of attenuation of light at 660 nm, until it reaches the same value as that of the excitation band, 540 nm, $K_E(z, 540\text{nm}) = K_E(z, 660\text{nm})$. This occurs between 50 and 100 m and is the region of the quasi-asymptotic field observed in the profiles of $P^*(z, 660\text{nm})$ and $\bar{\mu}(z, 660\text{nm})$ (Figs. 3 and 1A). However, as the solar light at 540 nm continues to decrease with depth, the contribution of Raman scattering at 540 nm makes a greater contribution to the irradiance decreasing the rate of attenuation of light at 540 nm. $K_E(z, 540\text{nm})$ therefore decreases until it reaches the value of its excitation band, 455 nm. $K_E(z, 660\text{nm})$ follows the decreases in $K_E(z, 540\text{nm})$. In the asymptotic field all three values of K_∞ are equivalent.

5. SUMMARY

Our simulations have shown that Raman scattering has an important effect on both vertical changes in and the asymptotic value of the average cosine at wavelengths longer than about 500 nm in clear water and 600 nm in more turbid waters. At these wavelengths, vertical decreases in $\bar{\mu}$ are accompanied by increases in P^* as local Raman scattering accounts for a larger proportion of the scalar irradiance. Finally, the diffuse attenuation coefficient becomes equivalent to the diffuse attenuation coefficient at its Raman excitation wavelength in the asymptotic field. All three of these apparent optical properties become constant in the asymptotic field indicating that they depend only on the inherent optical properties of the water, much as in the case of the source-free asymptotic field. In the future we hope to develop relationships between these various components of Gershun's equation with a source in order to provide a solution method for the average cosine in the presence of Raman scattering which depends only on the inherent optical properties of the water.

6. ACKNOWLEDGMENTS

This research has been supported by a NASA Fellowship in Global Change (JB) and ONR Grant N00014-93-0134 and NASA Grant NAGW3574 (DAK and DS). We thank the Laboratoire de Chimie and Physique Marines, Universite Pierre et Marie Curie and the Food and Agriculture Organization for generously making work space available. We also thank Andre Morel for helpful discussions.

7. REFERENCES

1. R. W. Preisendorfer, "On the existence of characteristic diffuse light in natural waters sea," *J. Mar. Res.* **18**, 1-9 (1959).
2. N. K. Højerslev and J. R. V. Zaneveld, "A theoretical proof of the existence of the submarine asymptotic daylight field," *Rep. 34*, Kobenhavns Universitet Institut for Fysisk Oceanografi, Copenhagen, 1977.
3. R. H. Stavn and A. D. Weidemann, "Optical modeling of clear ocean light fields: Raman scattering effects," *Appl. Opt.* **27**(19), 4002-4011 (1988).
4. R. H. Stavn and A. D. Weidemann, "Raman scattering in ocean optics: quantitative assessment of internal radiant emission," *Appl. Opt.* **31**(9), 1294-1303 (1992).
5. H. R. Gordon, K. Ding and W. Gong, "Radiative transfer in the ocean: computations relating to the asymptotic and near-asymptotic daylight field," *Appl. Optics*, **32**(9), 1606-1619 (1993).
6. H.R. Gordon and X. Xu, "Marine asymptotic daylight field: effects of inelastic processes," *Appl. Optics*, **35**(21), 4194-4205 (1996).
7. C. D. Mobley, *Light and water: radiative transfer in natural waters*. Academic Press, San Diego, 1994.
8. C. D. Mobley, *Hydrolight 3.0 User's Guide*, SRI Project 5632, SRI International, Menlo Park, CA Final Report, 65 pp., 1995.
9. W. W. Gregg and K. L. Carder, "A simple spectral solar irradiance model for cloudless maritime atmospheres," *Limnol. Oceanogr.* **35**(8), 1657-1675 (1990).
10. F. Kasten and G. Czeplak, "Solar and terrestrial radiation dependent on the amount and type of cloud," *Solar Energy*, **24**(2), 177-189 (1980).
11. A. W. Harrison and C. A. Coombes, "An opaque cloud cover model of sky short wavelength radiance" *Solar Energy*, **41**(4), 387-392 (1988).
12. L. Prieur and S. Sathyendranath, "An optical classification of coastal and oceanic waters based on the specific spectral absorption curves of phytoplankton pigments, dissolved organic matter, and other particulate materials," *Limnol. Oceanogr.* **26**(4), 671-689 (1981).
13. A. Morel, "Light and marine photosynthesis: a spectral model with geochemical and climatological implications," *Prog. Oceanogr.*, **26**, 263-306 (1991).
14. H. R. Gordon and A. Morel, "Remote assessment of ocean color for interpretation of satellite visible imagery, a review," *Lecture Notes Coastal Estuarine Studies* Vol. 4, Springer Verlag., 1983.
15. A. Morel, "Optical modeling of the upper ocean in relation to its biogenous matter content (case 1 waters)," *J. Geophys. Res.* **93**(C9), 10749-10768 (1988).
16. T. J. Petzold, "Volume scattering functions for selected ocean waters," *SIO Ref. 72-78*, Scripps Inst. Oceanogr., 1972.
17. C. D. Mobley, B. Gentili, H. R. Gordon, Z. Jin, G. W. Kattawar, A. Morel, P. Reinersman, K. Stamnes, and R. H. Stavn, "Comparison of numerical models for computing underwater light fields," *Appl. Opt.* **32**(36), 7484-7504 (1993).
18. V. A. Timofeeva, "Optics of turbid waters," *Optical aspects of oceanography*, N. G. Jerlov and E. Steemann Nielsen [eds.], Academic, 1974.

Calculation and implementation of 2-flow radiative transfer equations including the effects of fluorescence using MARAS data.

Daniel Buckton and Eon O'Mongain

Seán Danaher

Physics Dept.
University College Dublin
Dublin, Ireland

Leeds Metropolitan University
Calverly Street
Leeds, England

ABSTRACT

Radiative transfer processes in water are often modelled using 2-flow equations. No instrument has been available to date which provides the required observables sufficient to allow an accurate solution of both the absorption and the shape factor modified back-scatter. MARAS, a full spectrum radiometer now fulfils these requirements, measuring both the plane and scalar irradiance. The two flow equations, extended to include fluorescence, have been developed and used to analyse MARAS data. The absorption is shown to be consistent with the direct implementation of the Gershun relation, and the level of back-scatter is found to be non-spectral in the region where we do not expect fluorescence to make a significant contribution to the observed signal. The level of scatter in the non-fluorescent region is used to estimate the level of fluorescence due to photosynthetic processes. This is then related to the chlorophyll concentration.

Keywords: radiative transfer, fluorescence, chlorophyll, ocean optics, absorption

1. INTRODUCTION

Radiative transfer equations (RTE's) are equations that describe how light is propagated through a medium, taking into account absorption and scattering. RTE's usually use radiance as a complete description of the light field.^{1,2} The two flow form however uses irradiances which considerably simplify the mathematical process while allowing the equations to utilise measurements that are acquired by an instrument such as MARAS (Marine Radiometric Spectrometer). The two flow technique that we use here was principally developed by Preisendorfer and Mobley.^{3,4} The methods by which Preisendorfer and Mobley arrived at their solutions is not clear from the literature; we use Laplace transforms as our solution method. This also allows the incorporation of source terms without seriously complicating the equations. Here we show how it is possible to invert irradiance measurements to produce optical properties even in the presence of sources such as fluorescence.

The MARAS system has been shown to be capable of calculating the spectral absorption coefficient of waters of varying optical properties covering water types case I and case II.⁵ This is achieved by calculations based on Gershun's relation which requires measurements of vector and scalar irradiances (E and E_o respectively), at more than one depth. Alternatively two flow equations can be used to provide information pertaining to both the absorption and the backscatter $b_b(\lambda)$. The two flow radiative transfer equations can be put into the form

$$\frac{dE_d}{dz}(z, \lambda) = -(a_d + b_d)E_d(z, \lambda) + b_u E_u(z, \lambda) + \frac{1}{2}E_s(z, \lambda) \quad (1)$$

and

$$-\frac{dE_u}{dz}(z, \lambda) = -(a_u + b_u)E_u(z, \lambda) + b_d E_d(z, \lambda) + \frac{1}{2}E_s(z, \lambda) \quad (2)$$

which describes how the upwelling and downwelling irradiances (denoted by subscripts u and d respectively) are modified with depth in the presence of a source $E_s(z, \lambda)$ $Wm^{-2}nm^{-1}$. a_d , b_d , a_u and b_u are the light field modified absorption and backscatter, given by

$$a_d = \frac{a}{\mu_d}, \quad a_u = \frac{a}{\mu_u}, \quad b_d = \frac{r_d b_b}{\mu_d} \quad \text{and} \quad b_u = \frac{r_u b_b}{\mu_u} \quad (3)$$

Where μ_u and μ_d are the average cosines of the light field, given by the ratio of the vector to scalar irradiance in the upwelling and downwelling directions respectively. r_d and r_u are the downwelling and upwelling shape factors which can be calculated by the equations

$$r_d = \frac{1}{b_b E_{od}} \int_{2\pi_d} \left[\int_{2\pi_u} \beta(\theta, \phi, \theta', \phi') d\omega \right] L(z, \theta', \phi') d\Omega' \quad (4)$$

and

$$r_u = \frac{1}{b_b E_{ou}} \int_{2\pi_u} \left[\int_{2\pi_d} \beta(\theta, \phi, \theta', \phi') d\omega \right] L(z, \theta', \phi') d\Omega' \quad (5)$$

Where θ' and ϕ' represent the angles of the incoming photon and θ and ϕ the angles of the scattered photon with $d\Omega$ representing an infinitesimal solid angle in that direction. With L the radiance and β the scattering phase function. Hence the quantity r_d represents the mean upward scattering coefficient of the downwelling photons and r_u represents the mean downward scattering coefficient of the upwelling photons.

As a method of modeling the light field, two flow equations are limited as they do not allow the calculation of the variations of the angular distribution of the light field, such as variation of the average cosines. This is perhaps a more serious limitation when we are dealing with the case of sources; the ambient light field and the source based field have quite different directional properties. For the MARAS instrument though, we can be quite confident that over the vertical displacement of the sensors (1.2m), the variation of these parameters is not of great significance.

2. 2-flow RTE's with no sources.

Using the upwelling and downwelling irradiances at zero depth as initial conditions, equations (1) and (2) have been solved without the source term, to produce the following equations for the evolution of the light field with depth.

$$E_d(z) = \frac{1}{\alpha} (E_d(0)(K_+ - a_u - b_u) + b_u E_u(0)) e^{K_+ z} - \frac{1}{\alpha} (E_d(0)(K_- - a_u - b_u) + b_u E_u(0)) e^{K_- z} \quad (6)$$

and

$$E_u(z) = \frac{1}{\alpha} (E_u(0)(K_+ + a_d + b_d) - b_d E_d(0)) e^{K_+ z} - \frac{1}{\alpha} (E_u(0)(K_- + a_d + b_d) - b_d E_d(0)) e^{K_- z} \quad (7)$$

where

$$K_{\pm} = \frac{1}{2} ((a_u + b_u - a_d - b_d) \pm ((a_d + b_d + a_u + b_u)^2 - 4b_d b_u)^{\frac{1}{2}}) \quad (8)$$

Based on these equations it is possible to calculate the absorption and shape factor modified backscatter coefficient. To implement this, a function is created in the MATLAB environment that, when presented with an estimate of the absorption and the scatter, calculates the error between the estimated irradiances and the measured irradiance. The MATLAB function minimisation routine *fmins* is then passed the name of this function and initial guesses, *fmins* then returns the absorption and backscatter that produces minimum error.

Based on equations (1) and (2) only two independent solutions can be derived; that of the absorption and the shape factor modified back-scatter. It is impossible based on our equations to separate the shape factors and the back-scatter. Hence we must make assumptions about the magnitude of the shape factors. Considerable work has been undertaken in the calculation of the numerical values of these.⁶⁻⁸ We set $r_d = 1$ and $r_u = 2$ as these are typical values derived in the literature. The values of the back-scatter and shape factors do not affect the estimated value of $a(\lambda)$.

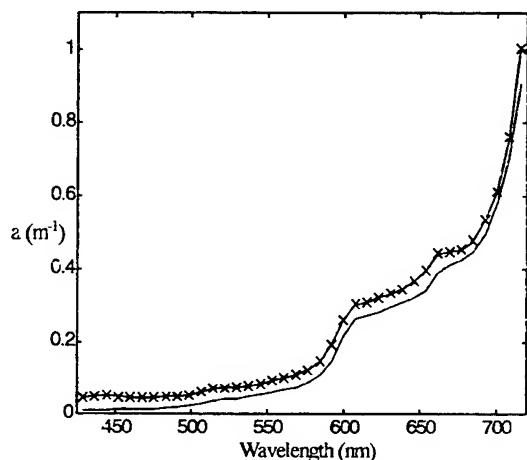


Figure 1: Absorption coefficient for clear water site from the North Sea (secci depth > 20m), calculated using the Gershun relation (solid), and the two flow method, ('x'). The lower curve is the measured absorption of pure water.⁹ Vicarious calibration of the collectors was carried out using the irradiance reflection coefficient and the known water absorption shoulder at 510nm.

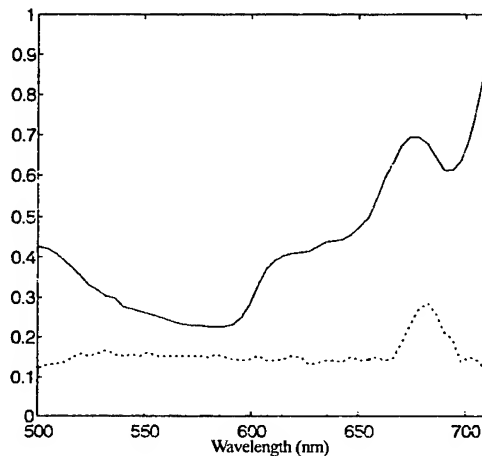


Figure 2: The absorption coefficient $a(\lambda)$ (solid) and $10 \times r_d b_b(\lambda)$ (dashed) calculated from the Baltic cruise data using two flow methods using $r_d = 1$ and $r_u = 2$. Note the increase in the estimated back-scatter centred at 683nm, this is attributed to chlorophyll fluorescence.

This iterative error minimisation procedure results in the calculation of numerically consistent a , $r_d b_b$ and $r_u b_b$ coefficients for the medium. Example solutions implementing these techniques is shown in Figs 1 and 2. Fig. 2 shows the absorption and backscatter for a site with significant chlorophyll. The scatter is non-spectral in the 500-650 nm range. The increase in the calculated scatter centred around 683nm is attributed to chlorophyll fluorescence.

3. Incorporation of sources into the RTE's

It is well documented in the literature, that phytoplankton fluoresce at 683nm with a FWHM of 25nm.^{11,10} The magnitude of fluorescence is a difficult function to calculate accurately as the signal produced by fluorescence and measured by a sensor is affected by both the absorption and back-scatter. To allow calculation of the level of fluorescence, it is desirable to solve the radiative transfer equations in the presence of a source. The source itself will be a function of the exciting radiation at lower wavelengths. The action function for this is difficult to ascertain, but Keifer¹⁰ suggests that it is similar to that of phytoplankton absorption. This may not be strictly applicable to phytoplankton as a number of pigments contribute to its absorption spectra and may not all be associated with the fluorescence mechanism. The two flow RTE equations, in the presence of a source $E_s(z, \lambda)$ can be solved to give

$$E_d(z) = \frac{1}{\alpha} \{ (E_d(0)(K_+ - a_u - b_u) + b_u E_u(0)) e^{K_+ z} + \int_0^z E_s(z-x)(K_+ - a_u - 2b_u) e^{K_+ x} dx \}$$

$$- (E_d(0)(K_- - a_u - b_u) + b_u E_u(0))e^{K_- z} - \int_0^z E_s(z-x)(K_- - a_u - 2b_u)e^{K_- x} dx \quad (9)$$

and for the upwelling irradiance

$$E_u(z) = \frac{1}{\alpha} \{ (E_u(0)(K_+ + a_d + b_d) - b_d E_d(0))e^{K_+ z} - \int_0^z E_s(z-x)(K_+ + a_d + 2b_d)e^{K_+ x} dx \\ - (E_u(0)(K_- + a_d - b_d) - b_d E_d(0))e^{K_- z} + \int_0^z E_s(z-x)(K_- + a_d + 2b_d)e^{K_- x} dx \} \quad (10)$$

3.0.1. Calculation of the level of fluorescence with the MARAS instrument. According to the above equations we should be able to estimate the effects of fluorescence on the calculation of the inherent and apparent optical properties. The fluorescence can be assumed to be formed by the combination of an excitation function and the incident radiation at wavelength ξ , thus the fluorescence at wavelength λ is given by

$$E_s(z, \lambda) = \int_{\lambda_1}^{\lambda_2} f(\xi, \lambda) E_o(z, \xi) d\xi, \quad (11)$$

Due to lack of knowledge of the excitation function, the choice was made between a function which was energy dependent ($E_o(\lambda)$), or photon dependent ($E_o(\lambda)/\lambda$), it was found that this did not produce significantly different levels of accuracies over data investigated. Hence the excitation function can be put in the photon dependent form

$$f(\lambda_i, \lambda_j) = \alpha \frac{\lambda_j}{\lambda_i} \exp(-0.0075(\lambda_j - 683)^2) C_{chl-a} (nm^{-1}) \quad (12)$$

where α is what we shall call the coefficient of fluorescence, and C_{chl-a} the chlorophyll concentration. Here we shall call the product αC_{chl-a} the 'fluorescence product', as this is the factor which determines what proportion of the available photons are re-emitted in the 683 nm region.

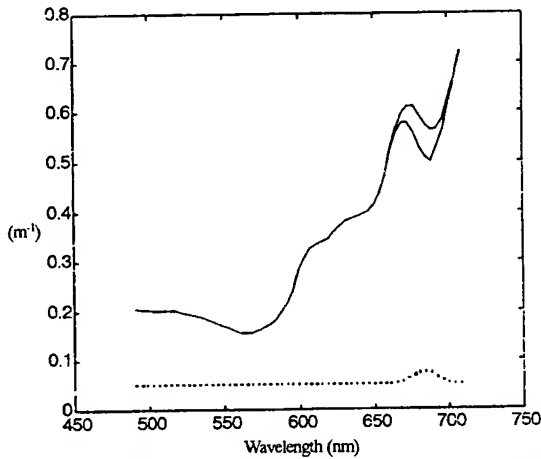


Figure 3: Simulated absorption and the calculated absorption (lower curve) and r_d b_b (dotted) when the presence of fluorescence has not been taken into account.

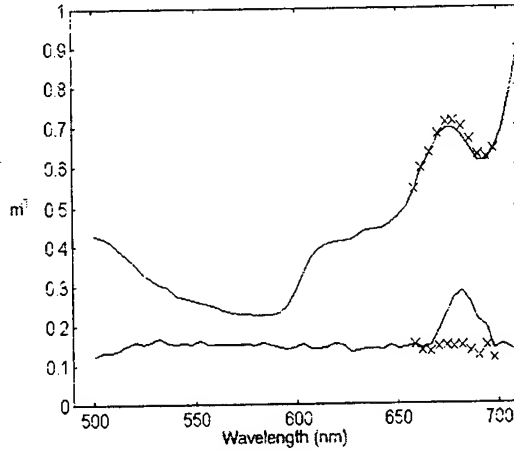


Figure 4: Calculation of a and b_b from MARAS data, 'x' indicates implementation including estimated levels of fluorescence.

In figure 3 typical lighting conditions are simulated using the two flow equations including fluorescence, with waters having a chlorophyll concentration of $10 \mu g/l$. The inversion process is then implemented in its source free

form to ascertain what effects fluorescence will have on the source free solution. As figure 3 shows, fluorescence causes the suppression of the calculated absorption and an increase in the estimated back-scatter, depending on the level of ambient light at the particular wavelength in question. Typically the estimated back-scatter is of a non spectral nature, so we can use this to estimate the level of fluorescence and correct for it.

In June 1994 the MARAS instrument was deployed in the Baltic. Here we show how it is possible from the acquired data to calculate the fluorescence as a function of chlorophyll concentration. In Fig. 4 the 'fluorescence product' is estimated by linearly extrapolating the backscatter of the 600 to 650 nm region to 683nm, and the inversion parameters for the error minimisation algorithm changed from the absorption and the backscatter to the absorption and the 'fluorescence product', as the level of backscatter at this wavelength is now known. With the level of fluorescence thus estimated, the absorption and backscatter are calculated over the 655 to 695nm region. This results in the removal of any spectral variation (within the noise tolerances) in the calculated back-scatter, the corrected absorption coefficient is also produced. This was performed for 10 sites from the cruise and the coefficient α calculated to be $0.00049 \text{ nm}^{-1}(\mu\text{g/l})^{-1}$ for a range of excitation ranging from 500 to 665 nm. The correlation between this chlorophyll indexed fluorescence and the sampled chlorophyll concentration was 0.90 with an RMS error of 20%, this is shown in Fig. 5.

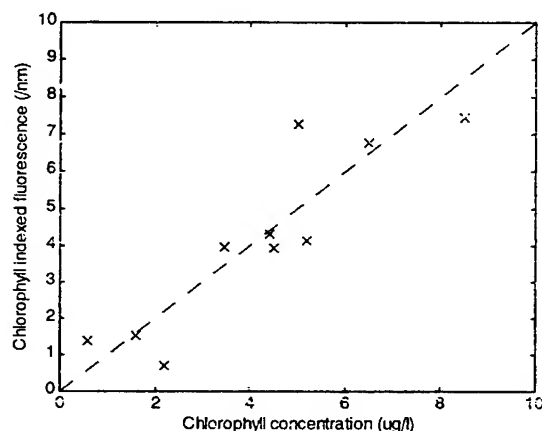


Figure 5: Sampled chlorophyll concentration versus the chlorophyll indexed fluorescence for 10 sites in the southern Baltic, the correlation between the two yielded a value of 0.9 with an RMS error of -13.3 dB, approximately 20%.

The calculations for Fig. 5 do not use the signal below this 500nm as it could not be measured with adequate signal to noise ratio. Improvements to the instrument making measurements possible down to 400nm have now been implemented.

4. CONCLUSION

These results show the calculation of the absorption and backscatter levels from an instrument such as MARAS. It is also shown how it is possible to measure and correct for the effects of fluorescence on irradiance measurements. The action spectrum for photosynthetically related fluorescence is assumed and the fluorescence indexed chlorophyll concentration estimated, the relation between this and the sampled chlorophyll concentration is shown to have an error of less than 20% for ten sites from the Baltic. Further work will concentrate on improving the knowledge of the action spectrum for day light conditions. Also worth examining is the variation of the shape factors as a function of the ratio of ambient to fluorescent light.

5. ACKNOWLEDGEMENTS

The authors acknowledge the support of Leeds Metropolitan University, University College Dublin and the European Commission, Marine Science and Technology (MAST) contract MAS2-CT92-0029 for support of this work at both Universities.

6. REFERENCES

- [1] Mobley, C., 'Light and water: Radiative transfer in natural waters', Academic Press (1994)
- [2] Mobley, C.D., Gentili, B., Gordon, H., Jin, Z., Kattawar, G., Morel, A., Reinersman, P., Stamnes, K., Stavn, R., 'Comparison of numerical models for computing underwater light fields' Appl. Opt., 32(36) 1993
- [3] Preisendorfer, R.W., Hydrologic optics, Vol (1-6) 1976
- [4] Preisendorfer, R.W., Mobley, C.D., Direct and inverse irradiance models in hydrological optics.' Limnol. Oceanogr. Vol 29, No. 5, 903-929, 1984
- [5] O'Mongain, E., Buckton, D., Green, S., Bree, M., Doerffer, R., Danaher, S., Hakvoort, H., Kennedy, J., Fischer, J., Fell, F., Papantoniou, D., McGarrigle, M., Moore, K. 'Spectral Absorption Coefficient Measured in-situ in the North Sea using the MARAS system' Submitted to Applied Optics (1996).
- [6] Aas, Eyvind, Two stream irradiance model for deep waters. Appl. opt. Vol 26, No. 11, pp 2095-2101, 1987
- [7] Stavn, R., Weidemann, A., 'Shape factors, two-flow models, and the problem of irradiance inversion in estimating optical parameters.' Limnol. Oceanogr. 34(8), pp 1426-1441, 1989
- [8] McCormick, N., Francisco, P., 'Radiative transfer two-stream shape factors for ocean optics' Appl. Opt., 34(27), 1995
- [9] Buiteveld, H., 'The optical properties of pure water' SPIE Ocean optics XII 2258, 1994
- [10] Keifer, D.A., Chamberlin, W.S., Booth, C.R., 'Natural Fluorescence of Chlorophyll a: Relationship to photosynthesis and Chlorophyll concentration in the western South Pacific gyre.' Limnol. Oceanogr. Vol 34, No. 5, 868-881, 1989
- [11] Fischer, J., Kronfield, U., 'Sun-stimulated chlorophyll fluorescence 1: influence of oceanic properties' IJRS, 11(12) 2125-2147, 1990

Effects of the wind direction on the light field reflected from a wind roughened sea surface

Frank Fell and René Preusker

Freie Universität Berlin, Institut für Weltraumwissenschaften
Fabeckstraße 69, D-14195 Berlin, Germany

ABSTRACT

A method is presented which allows for an approximate treatment of the radiative transfer above an asymmetrically reflecting wind roughened sea surface. The radiative transfer model used for this purpose is based on the matrix operator method. The efficiency of this method is mainly due to the separation of zenith and azimuth dependence, expanding the latter into a Fourier series. In the case of light fields symmetric with respect to the principal plane, the Fourier expansion of all relevant parameters consists of cosine terms only and the radiative transfer is calculated independently for each Fourier coefficient. However, when taking the effects of the wind direction into account, the light field produced at the rough sea surface is asymmetric. As a result, cosine and sine coefficients of all spectral frequencies are coupled in the layer representing the sea surface. The problem is considerably simplified, when the asymmetric reflection at the sea surface is only applied to the direct solar radiation, and symmetric reflection is assumed for the diffuse radiation incident on the sea surface. Using this simplified treatment, the Fourier coefficients again decouple, and the asymmetrically reflecting rough sea surface can easily be incorporated into the matrix operator method. The effect of the wind direction on the light field at the sea surface and at the top of the atmosphere is shown for a few examples. The calculations show that the radiances at the top of the atmosphere are altered up to 10% - 30 % in the sunglint affected angular domains, depending on wind speed and direction. In contrast to that, the fluxes remain fairly independent on the wind direction.

Keywords: asymmetric reflection, matrix operator method, radiative transfer, rough sea surface, wind direction

1. INTRODUCTION

The light field above the ocean depends strongly on the state of the sea surface whose reflective properties vary with both wind speed and direction. In order to determine quantitatively the interaction of the rough sea surface with the atmospheric light field, appropriate radiative transfer models able to deal with the asymmetric light fields produced at the rough sea surface are required. Radiative transfer models based on the Monte Carlo method have extensively been used for such purpose.¹ Unfortunately, these models are computationally expensive and therefore not perfectly suited for the development of inverse modelling schemes or evaluation algorithms based on a large number of simulations. On the other hand, computationally more efficient methods such as the matrix operator method² are usually based on the assumption that the volume scattering function depends on the scattering angle only. This assumption results in light fields symmetric with respect to the principal plane. As a consequence, the azimuth dependence of the reflection and transmission functions describing the redistribution of radiation inside the medium may be expanded into Fourier series consisting of cosine terms only. Since the cosine coefficients of the different spectral frequencies do not interact, the radiative transfer can be calculated independently for each frequency. The Fourier expansion significantly reduces the size of the operators describing the reflection, transmission and sources of radiation. This is the main reason for the efficiency of the matrix operator method. To allow for a straight-forward incorporation of the wind roughened sea surface into the matrix operator method, it is mostly assumed that the reflection and transmission functions of the sea surface are azimuthally symmetric with respect to the direction of the incident light and therefore can also be expanded into Fourier series consisting

of cosine terms only. The drawback of this assumption is, that it does not allow for the treatment of the effects of the wind direction on the light field. On the other hand, when taking the wind direction into account, the Fourier expansions of both the atmospheric light field and of the sea surface reflectance consist of cosine and sine terms, which are coupled for all spectral frequencies.³ This coupling makes it rather difficult to include the general description of the rough sea surface into the matrix operator method. We therefore suggest a simplified approach which allows for an approximate treatment of the effects of the rough sea surface on the atmospheric light field: the asymmetric reflection at the sea surface is only applied to the direct solar radiation, whereas symmetric reflection is assumed for the diffuse radiation incident on the sea surface. Under this assumption, existing radiative transfer codes of the matrix operator method can easily be extended towards the inclusion of the asymmetrically reflecting and transmitting rough sea surface.

2. THE WIND ROUGHENED SEA SURFACE

The rough sea surface can be approximated by a large number of small planar facets which reflect and transmit light according to the Fresnel laws. The contributions of all planar facets are summed up in order to obtain the reflection and transmission functions of the sea surface. Statistically, the rough sea surface is described by a two-dimensional Gaussian distribution of its (independent) surface slopes ζ_u , ζ_c in upwind and crosswind direction⁴:

$$p(\zeta_u, \zeta_c) = \frac{1}{2\pi\sigma_u\sigma_c} \times \exp \left\{ -\frac{1}{2} \left[\frac{\zeta_u^2}{\sigma_u^2} + \frac{\zeta_c^2}{\sigma_c^2} \right] \right\}, \quad (1)$$

where the variances depend linearly on the windspeed in 10 m height:

$$\begin{aligned} \sigma_u^2 &= 3.16 \times 10^{-3} v_{10} + 0.003, \\ \sigma_c^2 &= 1.92 \times 10^{-3} v_{10}. \end{aligned} \quad (2)$$

The above statistical description of the rough sea surface is commonly used in the literature and is so in this work. More sophisticated descriptions of the rough sea surface exist, which relate the variances σ_u^2 and σ_c^2 not only to the wind speed but also to a number of other parameters such as wind fetch, surface pressure, etc.⁵ If desired, these descriptions can be introduced into the method outlined below. In order to incorporate the rough sea surface into the matrix operator method, a coordinate transformation from the wind based coordinates ζ_u , ζ_c to the angular coordinates μ_n , ϕ_n is required:

$$p(\mu_n, \phi_n) = \frac{1}{2\pi\sigma_u\sigma_c\mu_n^3} \times \exp \{ -f(\sigma_u^2, \sigma_c^2, \mu_n, \phi_n - \gamma) \}, \quad (3)$$

where μ_n is the angle between the normal on a sea surface facet and the z-axis, ϕ_n is the azimuth difference between the normal on a surface facet and the solar azimuth, and γ is the angle between the solar azimuth and the wind direction. For simplicity reasons, the solar azimuth is set to 0°. The function $f(\sigma_u^2, \sigma_c^2, \mu_n, \phi_n - \gamma)$ is given by the following formula:

$$f(\sigma_u^2, \sigma_c^2, \mu_n, \phi_n - \gamma) = \frac{1 - \mu_n^2}{4\sigma_u^2\sigma_c^2\mu_n^2} [\sigma_u^2 + \sigma_c^2 - (\sigma_u^2 - \sigma_c^2) \times \cos 2(\phi_n - \gamma)]. \quad (4)$$

The statistical description of the sea surface is combined with the Fresnel laws in order to obtain the reflectance of the rough sea surface⁶:

$$r_{RS}(\mu', \phi'; -\mu, \phi) = \frac{1}{4\mu\mu_n} r_F(\cos \omega', \tilde{n}) p(\mu_n, \phi_n). \quad (5)$$

In this formula, $p(\mu_n, \phi_n)$ is the probability of the occurrence of such sea surface facet orientations which allow specular reflection from the direction (μ', ϕ') into the direction $(-\mu, \phi)$, $r_F(\cos \omega', \tilde{n})$ is the Fresnel reflection for the angle ω' between the facet normal and the incident light, and \tilde{n} is the refractive index of water. In most radiative

transfer models based on the matrix operator method, a simplified statistical description of the rough sea surface is used which is independent on the azimuth of the surface facet normal and the wind direction:

$$p(\mu_n) = \frac{1}{\pi \sigma^2 \mu_n^3} \times \exp \left\{ -\frac{1 - \mu_n^2}{\sigma^2 \mu_n^2} \right\}, \quad (6)$$

where

$$\sigma^2 = 5.12 \times 10^{-3} v_{10} + 0.003. \quad (7)$$

This simplified statistical description of the rough sea surface will be used to account for the reflection of diffuse radiation.

3. THE MATRIX OPERATOR METHOD

In matrix operator theory, the vertical structure of the medium under consideration is approximated by an appropriate number of plane parallel layers. The optical properties of the layers are formally expressed by operators, which describe the redistribution and the sources of radiation within each layer. An algorithm is used to combine identical (doubling) or different (adding) layers, and to calculate the light fields at the internal boundaries.² When the angular dependence of the light field is discretized, the operators are represented by matrices, where each element accounts for the redistribution of light between two discrete directions, resp. for the sources of radiation into the considered direction for the considered solar zenith angle. In order to allow for an accurate quadrature, only diffuse radiation is considered. The direct solar radiation is treated separately and added to the calculated diffuse light field. The efficiency of the matrix operator method is to a large extent due to the separation of zenith and azimuth dependence, which significantly reduces the size of the matrices.

4. INCORPORATION OF THE ROUGH SEA SURFACE INTO THE MATRIX OPERATOR METHOD

The incorporation of the rough sea surface is shown for both the symmetrically and the asymmetrically reflecting sea surface. For simplicity reasons, the water leaving radiance is assumed to be zero; besides, multiple scattering inside the sea surface, as well as effects due to internal shielding of the surface facets and foam cover are not considered. The reflection at the rough sea surface is given by

$$L(-\mu, \phi) = \int_0^1 \int_0^{2\pi} r_{RS}(\mu', \phi'; -\mu, \phi) L'(\mu', \phi') d\phi' d\mu', \quad (8)$$

where L is the reflected radiance, L' is the radiance incident on the surface, and r_{RS} is the radiance reflectance given by (5). In matrix operator theory, this equation is symbolically expressed by:

$$\mathcal{L}^- = \mathcal{R}_{RS} \mathcal{L}'^+, \quad (9)$$

where the minus sign stands for upward directed and the plus sign for downward directed radiation. When the Fourier expansion of the azimuth dependence is applied to this equation, four processes can be considered:

1. an asymmetric diffuse light field is reflected at an asymmetrically reflecting surface.
2. direct solar radiation is reflected at an asymmetrically reflecting surface.
3. an asymmetric diffuse light field is reflected at a symmetrically reflecting surface.
4. an asymmetric light field is propagated through an atmosphere characterized by a volume scattering function which depends on the scattering angle only.

4.1. Processes at the asymmetrically reflecting rough sea surface

The asymmetric reflection at the sea surface results in an asymmetric light field above the sea surface. Therefore, the Fourier expansion of the light field consists of both cosine and sine terms:

$$L(\mu, \phi) = \sum_{m=0}^M \left\{ L_m^{(1)}(\mu) \cos m\phi + L_m^{(2)}(\mu) \sin m\phi \right\}. \quad (10)$$

The reflective properties of an asymmetrically reflecting surface depend on the azimuth angles of both the incident and the reflected radiation. The Fourier expansion of the sea surface reflectance therefore consists of a multiple series:

$$\begin{aligned} r_{RS}(\mu', \phi'; -\mu, \phi) = & \sum_{k,l=0}^M \left\{ r_{k,l}^{(1)}(\mu'; -\mu) \cos k\phi' \cos l\phi + r_{k,l}^{(2)}(\mu'; -\mu) \cos k\phi' \sin l\phi + \right. \\ & \left. r_{k,l}^{(3)}(\mu'; -\mu) \sin k\phi' \cos l\phi + r_{k,l}^{(4)}(\mu'; -\mu) \sin k\phi' \sin l\phi \right\}. \end{aligned} \quad (11)$$

Introducing the expansions (10) and (11) into equation (8) results in a set of equations, where the Fourier coefficients of all spectral frequencies are coupled.³ This does not allow for a simple incorporation of the reflection of diffuse radiation at the rough sea surface into the matrix operator method. Things are easier for the direct solar radiation. In the chosen coordinate system, the direct solar radiation $S(\tau) = S_0 e^{-\tau/\mu_0}$ incident on the sea surface is by definition assigned an azimuth angle of $\phi'_0 = 0^\circ$. The Fourier expansion (11) for the asymmetrical reflection of direct solar radiation reduces to

$$r_{RS}(\mu', \phi' = 0^\circ; -\mu, \phi) = \sum_{l=0}^M \left\{ r_l^{(1)}(\mu'; -\mu) \cos l\phi + r_l^{(2)}(\mu'; -\mu) \sin l\phi \right\}. \quad (12)$$

The sources of diffuse radiation generated by reflection of direct solar radiation at the rough sea surface are expressed by the following set of independent equations:

$$J_m^{(1)}(-\mu) = r_m^{(1)}(\mu_0; -\mu) S_0 e^{-\tau/\mu_0} \equiv \mathcal{J}_{RS,m}^{(1)-}, \quad (13)$$

$$J_m^{(2)}(-\mu) = r_m^{(2)}(\mu_0; -\mu) S_0 e^{-\tau/\mu_0} \equiv \mathcal{J}_{RS,m}^{(2)-}, \quad (14)$$

where τ is the total optical thickness of the atmosphere, μ_0 is the cosine of the solar zenith angle and S_0 is the solar constant. In matrix operator theory, the upward directed diffuse radiation generated at the sea surface is represented by the source operators $\mathcal{J}_{RS,m}^{(1)-}$ and $\mathcal{J}_{RS,m}^{(2)-}$.

4.2. Processes at a symmetrically reflecting surface or inside a symmetrically scattering medium

The asymmetric diffuse light field which is produced by the reflection of direct solar radiation at the rough sea surface interacts with the atmosphere and therefore is partly reflected back to the sea surface. In this work, the propagation of diffuse radiation through the atmosphere and the reflection of diffuse radiation at the rough sea surface are principally treated in the same way: it is assumed that both reflection at the sea surface and scattering in the atmosphere are symmetric with respect to the direction of the incident light. In this case, the Fourier expansion of the relevant functions consist of cosine terms only (shown here is the reflection at the rough sea surface):

$$r_{RS}(\mu', \mu, \phi' - \phi) = \sum_{m=0}^M r_m^{(1)}(\mu'; \mu) \cos m(\phi' - \phi). \quad (15)$$

Introducing the expansions (10) and (15) into equation (8), one obtains two sets of independent equations which, in matrix form, are represented by:

$$\mathcal{L}_m^{(1)-} = \mathcal{R}_{RS,m}^{(1)} \mathcal{L}_m'^{(1)+}, \quad (16)$$

$$\mathcal{L}_m^{(2)-} = \mathcal{R}_{RS,m}^{(2)} \mathcal{L}_m'^{(2)+}. \quad (17)$$

Two similar sets of equations are obtained for the reflection of light back from the atmosphere to the sea surface:

$$\mathcal{L}_m^{(1)+} = \mathcal{R}_{A,m}^{(1)} \mathcal{L}_m'^{(1)-}, \quad (18)$$

$$\mathcal{L}_m^{(2)+} = \mathcal{R}_{A,m}^{(2)} \mathcal{L}_m'^{(2)-}. \quad (19)$$

Here, \mathcal{R}_A represents the reflective properties of the atmosphere for the upward directed light field.

4.3. Interaction processes between the sea surface and the atmosphere

The interaction processes between atmosphere and sea surface are in matrix operator theory expressed by the following equations²:

$$\mathcal{L}^- = (\mathcal{E} - \mathcal{R}_{RS}\mathcal{R}_A)^{-1} \{ \mathcal{R}_{RS}\mathcal{J}_A^+ + \mathcal{J}_{RS}^- \}, \quad (20)$$

$$\mathcal{L}^+ = (\mathcal{E} - \mathcal{R}_A\mathcal{R}_{RS})^{-1} \{ \mathcal{R}_A\mathcal{J}_{RS}^- + \mathcal{J}_A^+ \}, \quad (21)$$

where it is assumed that the ocean is black, and that no diffuse radiation is incident at the top of the atmosphere. \mathcal{E} is the unity operator and \mathcal{J}_A^+ is the diffuse downward directed radiation produced in the atmosphere by scattering of direct solar radiation. When expanding the azimuth dependence into a Fourier series, equation (20) describing the upward directed radiation above the sea surface splits up into two sets of independent equations for the cosine and sine coefficients:

$$\mathcal{L}_m^{(1)-} = (\mathcal{E} - \mathcal{R}_{RS,m}^{(1)}\mathcal{R}_{A,m}^{(1)})^{-1} \{ \mathcal{R}_{RS,m}\mathcal{J}_{A,m}^{(1)+} + \mathcal{J}_{RS,m}^{(1)-} \}, \quad (22)$$

$$\mathcal{L}_m^{(2)-} = (\mathcal{E} - \mathcal{R}_{RS,m}^{(2)}\mathcal{R}_{A,m}^{(2)})^{-1} \{ \mathcal{J}_{RS,m}^{(2)-} \}. \quad (23)$$

The equations for the sine coefficients are simpler, since there is no asymmetric scattering in the atmosphere, and therefore no asymmetric diffuse radiation due to scattering of direct solar radiation is generated in the atmosphere. Equation (21) describing the downward directed radiation above the sea surface is treated analogously.

4.4. Limitations of the method

The method outlined above accounts for the asymmetric reflection of direct solar radiation at the rough sea surface, whereas diffuse radiation is considered symmetrically reflected with respect to the direction of the incident light. The method does therefore not improve the accuracy of the calculated light fields outside the sunglint affected angular domains. Inside the sunglint affected angular domains, the improvements are significant as compared to the standard matrix operator method.

5. RESULTS

The asymmetric reflection of direct solar radiation at the wind roughened sea surface was incorporated into a radiative transfer model based on the matrix operator method. A number of calculations were then performed to assess the effects of the wind direction on the atmospheric light field. The results of the calculations show, that the wind direction exhibits a major influence on the structure of the light field in the sunglint affected angular domains. Due to the limited space, only a few results can briefly be presented.

For a wind speed of 2 m/s and an atmosphere characterized by a Rayleigh optical depth of 0.095 and an aerosol optical depth of 0.20, radiance differences up to about 30% were observed at the top of the atmosphere for wind directions parallel and perpendicular to the principal plane. The differences were confined to an azimuth angular

range of $\pm 30^\circ$ off the principal plane for solar zenith distances of about 50° . For azimuth angles larger than about 30° off the principal plane, the main contribution of the light field is from the atmosphere, and the radiance differences of for the two wind directions become smaller than 1%.

For a wind speed of 10 m/s, the maximal influence of the wind direction on the light field at the top of the atmosphere is on the order of 10% for a broad range of solar zenith angles. The azimuth angular range affected by the changes is generally larger than it is the case for a windspeed of 2 m/s; its extension depends strongly on the solar zenith angle. The effect of the wind direction on the albedo is less prominent. At the sea surface, a slight increase of the albedo is observed with increasing angles between the solar azimuth and the wind direction for solar zenith angles larger than about 45° . The wind direction has only a minor effect on the albedo at the top of the atmosphere.

6. CONCLUSION AND OUTLOOK

A method was presented which allows for a simplified incorporation of the asymmetric reflection at the rough sea surface into the matrix operator method. Radiance differences of up to 30 % for different wind directions were observed at the top of the atmosphere in the sunglint affected angular domains. The effect of the wind direction on the albedo was found to be small. Calculations of the light field at the top of the atmosphere for different wind speeds, directions and atmospheric states may be used to derive methods to correct ocean color satellite data for sunglint effects, if the necessary information on wind speed, wind direction, and the atmospheric aerosol load can be obtained from other sources (such as wind speed and direction from SSM/I data).

7. ACKNOWLEDGEMENTS

This work was partly carried out with assistance of funding under the E.U. Marine Science and Technology, MAST II programme, under contract MAS2-CT-92-0020. This contract, the MARAS-System Deployment and Application Development Programme, was co-ordinated by the Physics Department, University College Dublin.

8. REFERENCES

- [1] R. W. Preisendorfer and C. D. Mobley, "Albedo and glitter patterns of a wind-roughened sea surface", *J. Phys. Oceanogr.*, **16**, 1293-1316 (1986).
- [2] G. N. Plass, G. W. Kattawar, and F. E. Catchings, "Matrix operator theory of radiative transfer. 1: Rayleigh scattering", *Appl. Opt.*, **12**(2), 314-329 (1973).
- [3] C. D. Mobley, *Light and water*, pp. 388-409, Academic Press, San Diego, 1994.
- [4] C. Cox and W. Munk, "The measurement of the roughness of the sea surface from photographs of the sun's glitter", *J. Opt. Soc. Amer.*, **44**, 838-850 (1954).
- [5] K. Yoshimori, K. Itoh, and Y. Ichioka, "Optical characteristics of a wind-roughened water surface: a two-dimensional theory", *Appl. Opt.*, **34**(27), 6236-6247 (1995).
- [6] T. Nakajima and M. Tanaka, "Effect of wind-generated waves on the transfer of solar radiation in the atmosphere-ocean system", *J. Quant. Spectros. Radiat. Transfer*, **29**(6), 521-537 (1983).

Modelling of the environmental factors influence on solar irradiance reflectance and transmittance through the wind-ruffled sea surface

Sławomir B. Woźniak

Institute of Oceanology Polish Academy of Sciences
Powstańców Warszawy 55, 81-712 Sopot, P.O.Box 68

ABSTRACT

The spectral model of solar irradiance transmittance through the wind - ruffled sea surface was developed. Modified dependencies for both wind - ruffled sea surface slope distribution based on Cox and Munk¹ and foam coverage of the sea surface based on Gordon and Jacobs² were used, with incorporation of effects of hydrometeorological factors and basin geometry. Snell and Fresnel laws were applied for light transmission through the surface. Spectral dependencies of light refraction in the range 350 - 18000 nm were taken into account. Polarisation effects were neglected. This approach seems to be much more accurate than presented in known monographs, such as Mullamaa.³ This model is a part of the model of radiation inflow to the Baltic developed by the team from the Institute of Oceanology PAS Sopot.

Keywords: surface reflectance, surface transmittance, wind waves, slope distribution, foam coverage, mean wave height, modified Cox and Munk expression, modified Gordon and Jacobs expression.

1. ASSUMPTIONS

1. Light reflection and transmission have an especially complicated nature due to surface ruffling and partial cover with foam.
2. Existing formulae for slope distribution and foam coverage as functions of wind speed are not of general nature.
3. Problem related to reckoning reflectance and transmittance of irradiance through a ruffled surface with determined distributions of wave slopes has not fully been solved up till now. The issue needs arduous numerical calculations and was undertaken by few authors only.^{3,4,5} Existing solutions are for specific cases only and they are not sufficient.

2. MAIN AIMS

1. Determination of the dependence of ruffled sea surface slope distribution and foam coverage on environmental factors.
2. Formulation of mathematical spectral model of solar irradiance reflectance and transmittance through the wind-ruffled sea surface.

3. APPARATUS

Fig. 1. gives simplified model block diagram, and more precisely, the algorithm of determining characteristics of radiation fluxes reflected and transmitted through the sea surface.

Basic value of input data class in the model is angular and spectral distribution of the radiance at the sea surface $L(\Theta, \varphi, \lambda)$ (block 2). The rest of model input parameters are hydrometeorological and geometrical factors (block 1) (i.e. the wind speed v also signed as u_{10} and wind direction φ , (azimuth angle), the wind fetch D , the sea area depth h and the coast line geometry as well, etc.). They determine the wave state of sea surface and its foam coverage and then can be approximately replaced with one parameter, namely the mean height of wind waves \bar{H} (block 1').

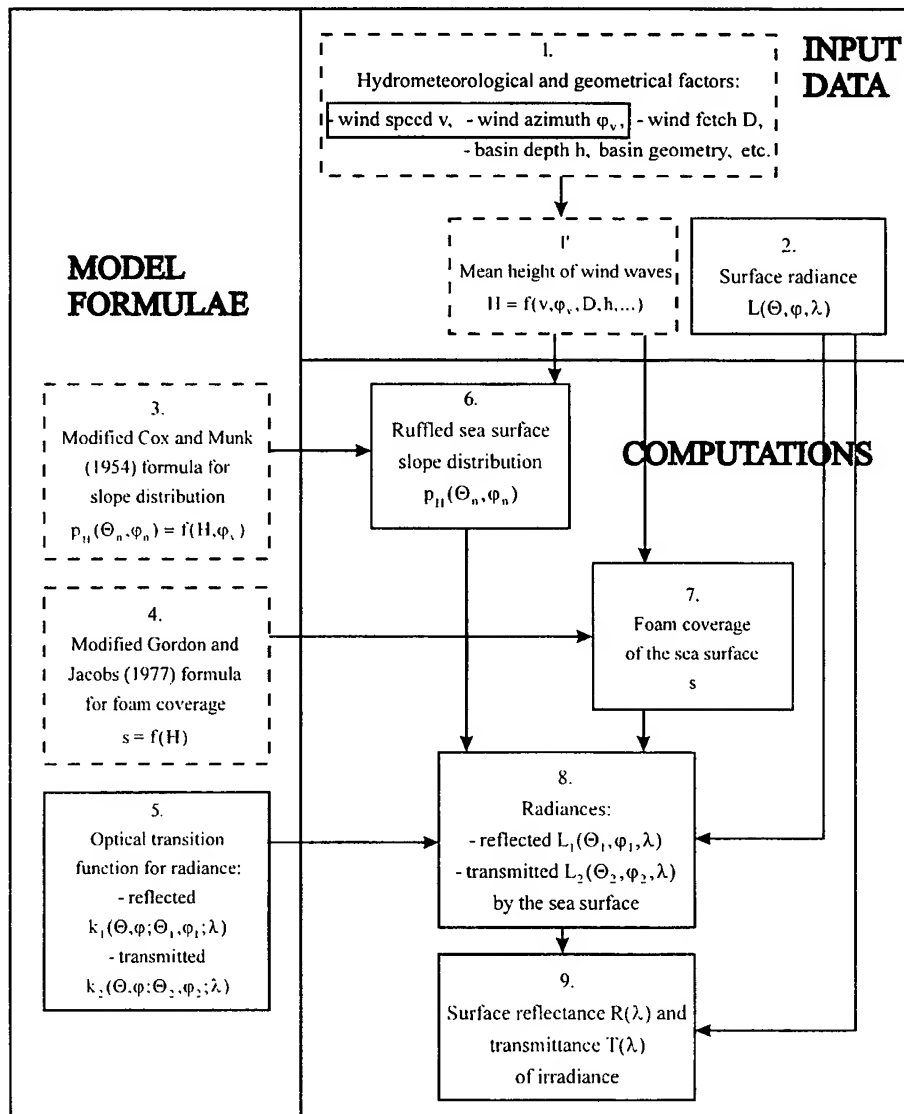


Fig. 1. Block diagram of the model.

Dashed line blocks signify the innovation applied by the author, on the contrary to previous model, it means considering all the set of environmental factors (hydrometeorological and geometrical) influencing the state of ruffled surface. Up till now, the only parameter to be considered was the wind speed over basin v . This parameter is not sufficient for describing the state of the sea surface, especially for basins like the Baltic Sea. The author proposes to adopt a different parameter namely the mean height of wind waves H . Mean height of wind waves is functionally connected with all the set of environmental factors throughout hydrodynamic models in the form of more or less complicated functions:

$$\bar{H} = f(v, D, h, \dots). \quad (1)$$

An example of such a function for simple case of wind blowing from straight coast line is formula given by Krylov⁶ (where g - acceleration due to gravity):

$$\frac{g\bar{H}}{v^2} = 0.16 \left[1 - \left[\frac{1}{1 + 6.0 \cdot 10^{-3} \left(\frac{gD}{v^2} \right)^{1/2}} \right]^2 \right] \times \text{th} \left[\frac{0.625 \left(\frac{gh}{v^2} \right)^{0.8}}{1 - \left[1 + 6.0 \cdot 10^{-3} \left(\frac{gD}{v^2} \right)^{1/2} \right]^{-2}} \right]. \quad (2)$$

This parameter can equivalently describe the state of ruffled sea surface with steady wind waves in the first approximation.

And so, the author modified the existing dependencies for surface slope distribution as well as foam coverage of the surface as functions of wind speed, and then he gave them in the shape of hydrodynamic parameter function, i.e. mean height of wind waves \bar{H} .

This modification made, among others, that the differences between empirical dependencies of surface slope distribution dispersions σ_x^2, σ_y^2 , given by different authors, was getting smaller (comp Fig. 2.). It was confirmed by analysis of the correlation coefficients (for example for empirical data given by Pelevin and Burtsev⁷ correlation coefficients are equal: $r(\sigma_x^2 \text{ vs } v) = 0.60$, $r(\sigma_x^2 \text{ vs } \sqrt{\bar{H}}) = 0.76$ and $r(\sigma_y^2 \text{ vs } v) = 0.58$, $r(\sigma_y^2 \text{ vs } \sqrt{\bar{H}}) = 0.77$).

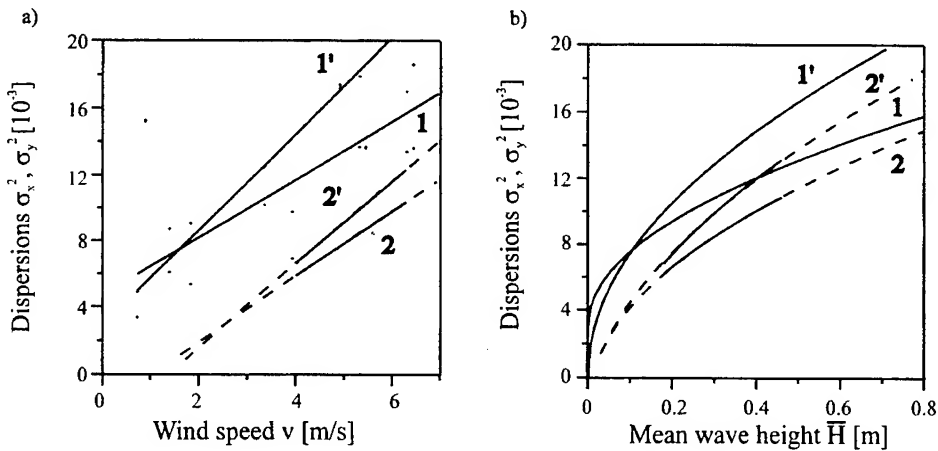


Fig. 2. Variability of ruffled sea surface slope distribution dispersions σ_x^2 and σ_y^2 : (a) on the wind speed v , (b) on the mean height of wind waves \bar{H} (from Cox and Munk¹ data - curves 1 and 1', and from Pelevin and Burtsev⁷ data - curves 2 and 2').

A full theoretical basis for applying new parameter mean height of wind waves \bar{H} and for mentioned modifications and also initial verification of that idea was published by the author of this paper.⁸

Proposed model formulae are:

- the ruffled surface slope (Θ_n, φ_n) probability distribution $p_{\bar{H}}$ (block 6), which is determined basing on Cox and Munk¹ distribution, modified by the author (block 3);

$$p_{\bar{H}}(\Theta_n, \varphi_n) = \frac{\sec^3 \Theta_n}{2\pi\sigma_x\sigma_y} \exp \left\{ -\frac{1}{2}(\zeta^2 + \eta^2) \right\} \cdot \left[1 - \frac{1}{2}c_{21}(\zeta^2 - 1)\eta + \frac{1}{6}c_{03}(\eta^2 - 3\eta) + \frac{1}{24}c_{40}(\zeta^4 - 6\zeta^2 + 3) + \frac{1}{4}c_{22}(\zeta^2 - 1)(\eta^2 - 1) + \frac{1}{24}c_{04}(\eta^4 - 6\eta^2 + 3) + \dots \right], \quad (3)$$

where:

$$\zeta = \frac{\sin(\varphi_n - \varphi_v) \text{tg} \Theta_n}{\sigma_x}, \quad \eta = \frac{\cos(\varphi_n - \varphi_v) \text{tg} \Theta_n}{\sigma_y}; \quad (4)$$

and modified parameters:

$$\begin{aligned}
 \sigma_x^2 &= f(\bar{H}) = 0.003 + 0.0143\sqrt{\bar{H}} \pm 0.002, \\
 \sigma_y^2 &= f(\bar{H}) = 0.0235\sqrt{\bar{H}} \pm 0.004, \\
 c_{21} &= f(\bar{H}) = 0.01 - 0.0640\sqrt{\bar{H}} \pm 0.03, \\
 c_{03} &= f(\bar{H}) = 0.04 - 0.2458\sqrt{\bar{H}} \pm 0.12, \\
 c_{40} &= 0.4 \pm 0.23, \quad c_{22} = 0.12 \pm 0.06, \quad c_{04} = 0.23 \pm 0.41;
 \end{aligned} \tag{5}$$

- the sea surface foam coverage (block 7), which is determined by Gordon and Jacobs² formula, modified by the author (block 4).

$$\begin{aligned}
 s &= f(\bar{H}) = 9.05 \cdot 10^{-3} \cdot (\sqrt{\bar{H}})^{3.3} \quad (\text{for } \bar{H} \leq 1.46\text{m}), \\
 s &= f(\bar{H}) = 9.05 \cdot 10^{-3} \cdot (\sqrt{\bar{H}})^{3.3} (1.676\sqrt{\bar{H}} - 0.99) \quad (\text{for } \bar{H} \geq 1.46\text{m}).
 \end{aligned} \tag{6}$$

In practice, the application of those formulae is reduced to the measurements of the wind speed v and wind azimuth φ , and, in addition, of other environmental factors enabling the mean wave height to be predicted.

The last two values, i.e. surface slope distribution $p_{\bar{H}}(\Theta_n, \varphi_n)$ and foam coverage s , in connection with geometrical optics rules (Snell and Fresnel laws) and also basing on the so called optical transition functions k_1 and k_2 (block 5), give possibility to calculate the angular distribution of radiance reflected from the surface $L_1(\Theta_1, \varphi_1, \lambda)$ and transmitted through the surface $L_2(\Theta_2, \varphi_2, \lambda)$ (block 8):

$$L_1(\Theta_1, \varphi_1, \lambda) = \int_{\Omega_-} k_1(\Theta_1, \varphi_1; \Theta, \varphi; \lambda) \cdot L(\Theta, \varphi, \lambda) d\omega, \tag{7}$$

$$L_2(\Theta_2, \varphi_2, \lambda) = \int_{\Omega_-} k_2(\Theta_2, \varphi_2; \Theta, \varphi; \lambda) \cdot L(\Theta, \varphi, \lambda) d\omega, \tag{8}$$

where:

$$k_1(\Theta_1, \varphi_1; \Theta, \varphi; \lambda) = (1-s) \frac{1}{4 \cos \Theta_1 \cos \Theta_n} \rho(\alpha, \beta) p_{\bar{H}}(\Theta_n, \varphi_n) + s \frac{A_f(\lambda)}{\pi} \cos \Theta, \tag{9}$$

$$k_2(\Theta_2, \varphi_2; \Theta, \varphi; \lambda) = (1-s) \frac{n^2 \cos \alpha \cos \beta}{(n \cos \beta - \cos \alpha)^2 \cos \Theta_2 \cos \Theta_n} \tau(\alpha, \beta) \cdot p_{\bar{H}}(\Theta_n, \varphi_n) + s \frac{T_f(\lambda)}{\pi} \cos \Theta, \tag{10}$$

integration is made over solid angle top hemisphere (i.e. Ω_-), $d\omega = \sin \Theta d\Theta d\varphi$, $\rho(\alpha, \beta)$ and $\tau(\alpha, \beta)$ are respectively reflectance and transmittance for the flat surface, $A_f(\lambda)$ and $T_f(\lambda)$ are respectively albedo and transmittance of the foam.

Based on angular distribution of radiance reflected and transmitted through the surface it is possible to calculate surface reflectance and transmittance of solar irradiance:

$$R = \frac{\int_{\Omega_-} \left[\int_{\Omega_-} k_1(\Theta_1, \varphi_1; \Theta, \varphi; \lambda) L(\Theta, \varphi, \lambda) d\omega \right] \cos \Theta_1 d\omega_1}{\int_{\Omega} L(\Theta, \varphi, \lambda) \cos \Theta d\omega}. \tag{11}$$

The essential simplification of the problem can be obtained by an approximation of real angular incident light radiation distribution with the sum of two components: direct radiance and diffuse radiance with cardioidal distribution $L_D(\Theta) = L_D(\Theta = 90^\circ) \cdot (1 + B \cdot \cos \Theta)$. Simplified formula for surface reflectance and transmittance is as follows:

$$R = (1-s)[(1-d_E)R_S + d_ER_D] + s \cdot A_f \text{ and } T = 1 - R, \quad (12)$$

where: d_E - diffuseness of irradiance, A_f - foam albedo, R_S - reflectance of direct irradiance, R_D - reflectance of diffuse irradiance.

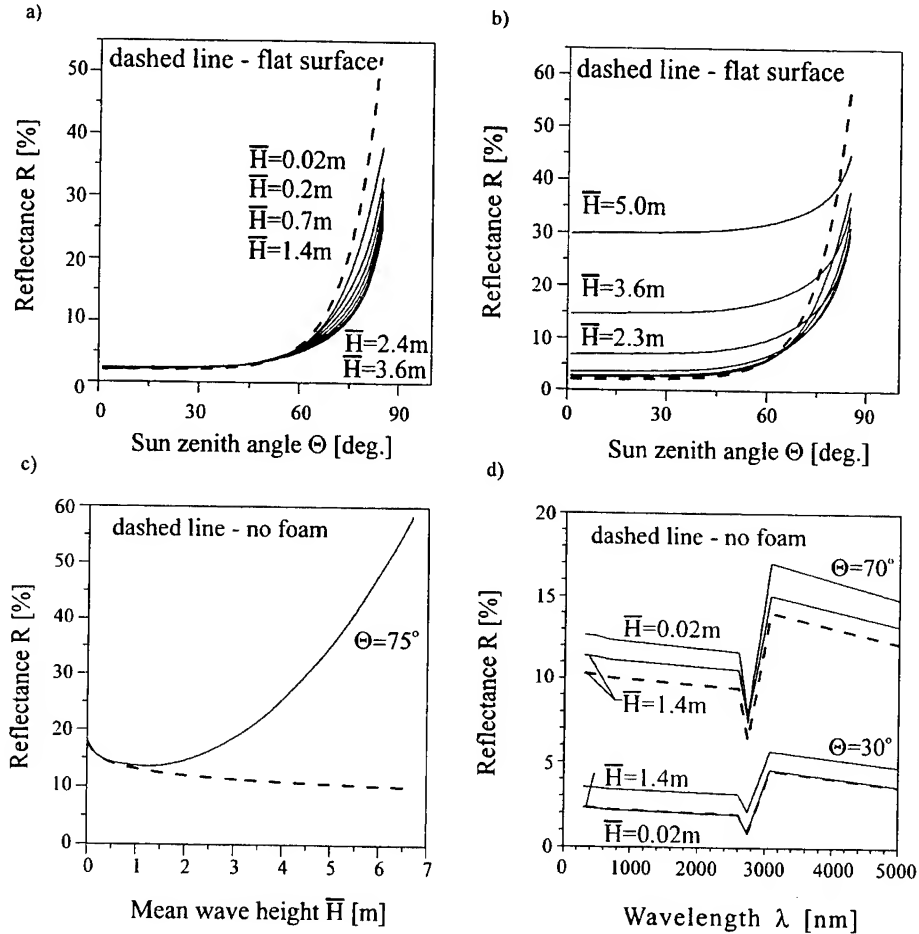


Fig. 3. Variability of surface reflectances of solar irradiance: (a) on Sun zenith angle Θ without foam coverage effect, (b) on Sun zenith angle Θ with foam coverage effect, (c) on mean height of wind waves \bar{H} (for wavelength $\lambda = 680nm$, diffuseness of irradiance $d_E = 0.2$, cardioid distribution parameter of diffuse irradiance $B=3$, wind azimuth equal Sun azimuth $\varphi_s = \varphi$) and (d) spectral dependence.

4. RESULTS

Basing on the worked out theoretical model the author created a program which finds by using numerical methods values of the reflectance R_S and transmittance T_S of direct light irradiance, and also diffuse ones R_D and T_D as well through the non-foamed part of the sea surface, and on their basis calculated values of the reflectance R and transmittance T of the total irradiance (according to simplified formula (12)). A complete modelling results and its application was presented in author's publications.^{9,10}

Exemplary results are shown in Fig. 3. Figures (a), (b) and (c) shows dependence of surface reflectance for the wavelength $\lambda = 680nm$ and for the exemplary conditions with diffuseness of irradiance $d_E = 0.2$ and cardioidal

parameter $B=3$ at nearly cloudless sky. Fig. 3. (d) presents spectral dependencies of surface reflectance R as the wavelength function.

5. CONCLUSIONS

1) Surface slope distribution, through dispersions σ_x^2, σ_y^2 , seems to be a function of a dynamic parameter mean height of wind waves \bar{H} , and thus a function of environmental factors.

$$p_{\bar{H}}(\Theta_n, \varphi_n) = f(\bar{H}, \varphi_v) = f(v, \varphi_v, D, h, \dots) \quad (13)$$

2) Foam coverage seems to be a function of mean height of wind waves \bar{H} , and thus a function of environmental factors.

$$s = f(\bar{H}) = f(v, D, h, \dots) \quad (14)$$

3) The fact of taking those formulae into account gives more precise results in modelling surface reflectance and transmittance of irradiance for any sea basin.

6. REFERENCES

1. C. Cox and W. H. Munk, „Measurement of the Sea Surface from Photographs of the Sun's Glitter," *J. Opt. Soc. Amer.*, Vol. 44(11), 838-850 (1954).
2. H. R. Gordon and M. M. Jacobs, „Albedo of the ocean - atmosphere system, influence of the foam," *Appl. Phys.*, Vol. 16(8), 2257-2263 (1977).
3. J. A. P. Mullamaa, *Atlas of the optical characteristics of a wave-roughened sea surface*, pp. 494, Acad. Sci. of Estonian SSR, Inst. of Physics and Astronomy, Tartu, 1964 (in Russian).
4. E. Raschke, *Berechnung des durch Mehrfachstreuung entstehenden Felds solarer Strahlung in einem System Ocean-Atmosphäre*, Bundesministerium für Bildung und Wissenschaft Forschungsbericht, Vol. 71(20), 1971.
5. J. Olszewski, „Time course of natural light reflection from an undulated sea surface," *Stud. i Mater. Oceanolog. KBN-PAN*, Vol. 26, 179-202, (1979) (in Polish).
6. J. M. Krylov, S. S. Strikalov and V. F. Cyplukhin, *Wind waves and its effect on marine constructions*, pp. 256. Gidrometeoizdat, Leningrad, 1976 (in Russian).
7. V. N. Pelevin and J. G. Burtsev, „The measurements of the sea surface slope distribution under the wind roughness," *Optical investigations in the ocean and in the atmosphere above the ocean*, K. S. Shifrin, B. F. Kelbalikhanov and M. V. Kozlyaninov, Inst. Okean. AN SSSR, Moskva, pp. 202-218, 1975 (in Russian).
8. S. B. Woźniak, „Sea surface slope distribution and foam coverage as functions of the mean height of wind waves," *Oceanologia*, 38 (3), 317-332 (1996).
9. S. B. Woźniak, „Mathematical preliminary spectral model of solar irradiance reflectance and transmittance by the wind ruffled sea surface. Part I : Physical problem and mathematical apparatus," *Oceanologia*, (in press).
10. S. B. Woźniak, „Mathematical preliminary spectral model of solar irradiance reflectance and transmittance by the wind ruffled sea surface. Part II : Modelling results and applications," *Oceanologia*, (in submit).

Method of the retrieval of the aerosol particle size distribution (APSD) in the marine atmosphere boundary layer (MABL)
from optical measurement data

Kusiel Shifrin and Ilia Zolotov

Oregon State University, College of Oceanic and Atmospheric Sciences
104 Ocean Admin Bldg, Corvallis, OR 97331-5503

ABSTRACT

The retrieval of the aerosol particle distribution function in the marine atmosphere boundary layer for the radius interval up to $30\mu\text{m}$ is considered with the use of simultaneous data on the spectral attenuation (in the spectral range $0.4\text{--}5\mu\text{m}$) and small-angle phase function (in the angle interval $0^\circ\text{--}6^\circ$). An iterative procedure is constructed combining inversion algorithms for the spectral attenuation and phase function, each of them being efficient for a specific particle size interval. Numerical experiments with two aerosol models are performed. It is shown that the inversion methodology under discussion makes it possible to retrieve the particle size distribution function for the radius interval $0.2\text{--}30\mu\text{m}$ with a mean relative error less than 10%.

Keywords: aerosol particle size distribution, marine atmosphere boundary layer, inversion algorithm, spectral attenuation, small-angle phase function.

1. INTRODUCTION

The objective of the present work is the investigation of the possibility of obtaining the size distribution function for aerosol particles of every size in the marine atmospheric boundary layer (MABL) using data for commonly measured optical characteristics: the spectral attenuation and small-angle phase function. In [1], we showed that the inversion of the spectral attenuation in the visible and near IR range ($0.4\text{--}5\mu\text{m}$) cannot yield a reliable size distribution for large particles.

The common way of retrieving information on large particles is the inversion of the small-angle phase function (SAPF) into the particle size distribution function (PSDF). This method is specifically intended for large particles [2]. However, when using this method in MABL, one faces a fundamental difficulty caused by the effect of a great number of small particles on the diffraction pattern. This suggests that a prospective way of determining the entire aerosol particle size distribution in MABL is the simultaneous use of the spectral transmittance and small-angle phase function. In doing so, one can take advantage of both inversion methods, and at the same time improve their drawbacks.

Let us represent the sought-for PSDF as

$$f(r) = \begin{cases} f_o(r), & r \leq r_o \\ f_t(r), & r > r_o \end{cases}$$

We will derive the function $f_o(r)$ by inverting the spectral attenuation (Algorithm I), and the function $f_t(r)$ by inverting the small-angle phase function (Algorithm II).

2. THE INVERSION OF THE SPECTRAL ATTENUATION (ALGORITHM I)

The beginning part of PSDF (the function $f_o(r)$) can be obtained by the numerical inversion of the integral equation for the spectral attenuation. In order to regularize the incorrect inverse problem, we used the assumption that the function $f_o(r)$ was smooth. For this, we minimized the third derivative of $f_o(r)$.

Fig. 1 shows two types of the aerosol PSDF in MABL and the results of inverting the spectral attenuation using the above-mentioned algorithm. Hereafter we shall experiment with the same distributions. The first one is the distribution function for typical aerosols in MABL [3] at RH=90% (Model I); the shape of the second one is close to the distribution obtained from direct observations and the NOVAM model for aerosols in MABL [4] (Model II).

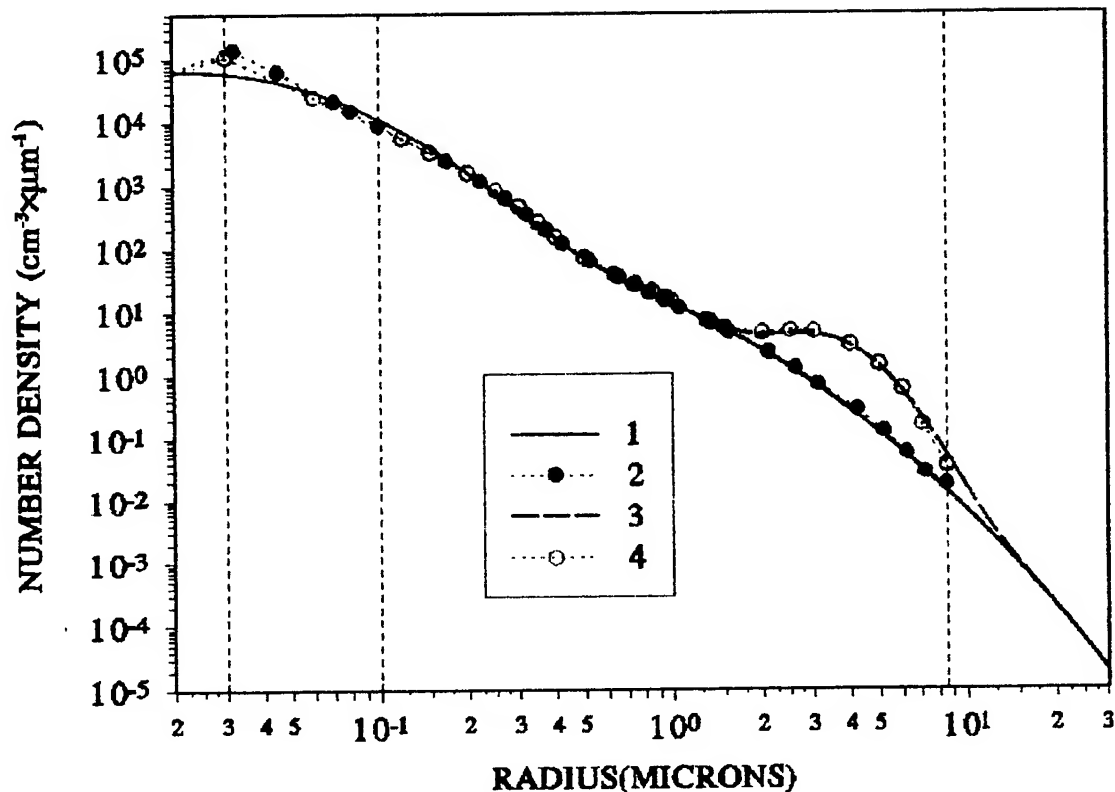


Fig. 1. Models of particle size distribution functions for aerosols in the marine atmospheric boundary layer. 1, 3 - initial curves for the Models I and II respectively, 2, 4 - inversion results using the Algorithm I for the Models I and II respectively.

It is seen from Fig. 1 that the inversion method for the spectral attenuation in the range 0.4-5 μ m presented in [1] yields the satisfactory results (the mean deviation is 7.4% and 9.2% respectively) for the particle radius interval from $r_{\min}=0.1\mu$ m to $r_0=8.5\mu$ m.

The limiting value of r_0 up to which it is possible to invert the spectral attenuation in the range 0.4-5 μ m is $r_0=8.5\mu$ m. For larger radii, the kernel of the integral equation is practically radius-independent. In order to find $f_t(r)$, it is necessary to invoke the small-angle phase function.

3. THE INVERSION OF THE SMALL-ANGLE PHASE FUNCTION (ALGORITHM II)

The analytical formula derived from the Kirchhoff's formula is used for inverting SAPF. Because of this, the regularization is not needed. Moreover, one does not need to know the refractive indices of aerosol particles when using this formula [2, 5].

However, in the process of numerical realization of the analytical inversion formula, the obtained values of $f_t(r)$ oscillate about the initial PSDF and deviate from it significantly in the beginning part of the curve (see Fig. 2). Our numerical experiments show that the efficient way of getting rid of this drawback is the polynomial filtration and cutting off the beginning part of the curve from r_0 to $r_0+1\mu$ m.

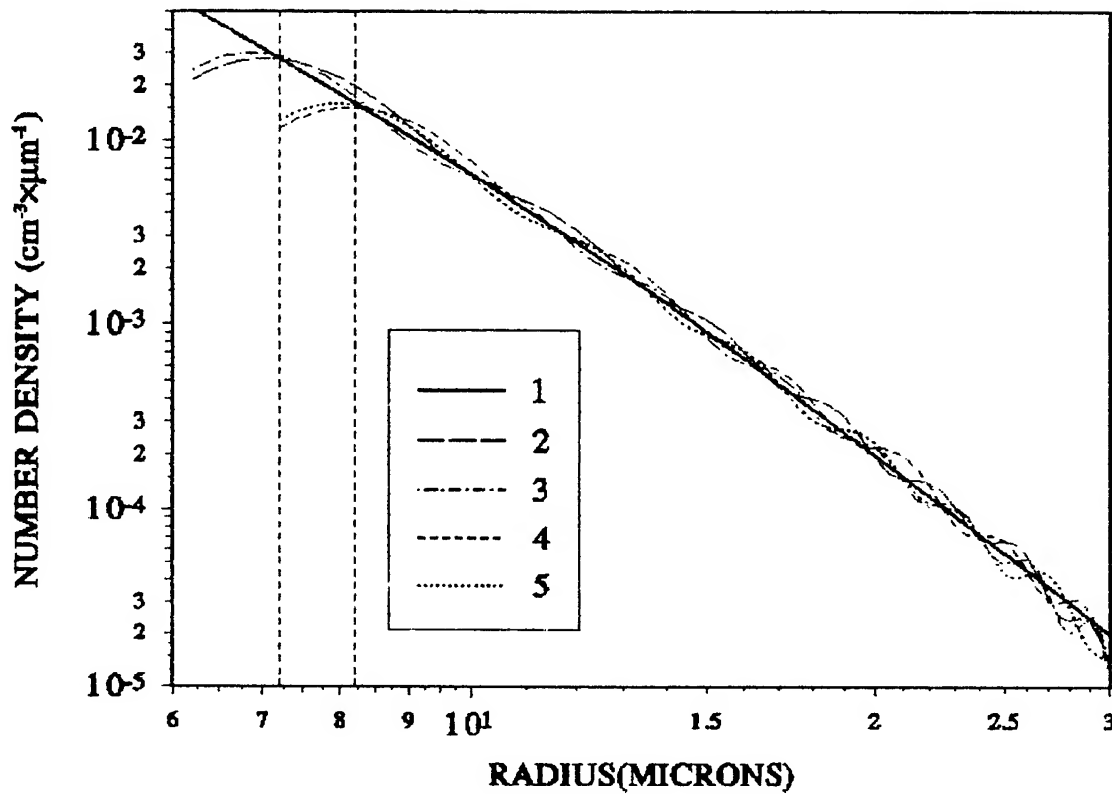


Fig. 2. The comparison of the retrieved tail of PSDF $f_t(r)$ with the initial one. 1-initial $f_t(r)$; 2,4- $f_t(r)$ calculated by the Mie formulas for $r_0=6.2$ and $7.2\mu\text{m}$ respectively; 3,4- $f_t(r)$ calculated by the Kirchhoff's formula for $r_0=6.2$ and 7.2 respectively.

After the polynomial filtration, the inversion results using the Mie and Kirchhoff's formulas become quite close to each other.

4. THE PROCEDURE FOR THE DETERMINATION OF THE ENTIRE PSDF

In order to obtain the entire PSDF, we performed numerical experiments on the simultaneous use of the Algorithms I and II. The first step of the calculation procedure is the numerical inversion of the spectral attenuation into PSDF for the radius interval $r_0 \leq 8.5\mu\text{m}$ using the Algorithm I. The next step is the calculation of the part of SAPF created by this small-particle fraction. By subtracting it from the total SAPF, we obtain SAPF created by large particles. This is the end of the zeroth iteration of the procedure.

Then we retrieve PSDF for $r > r_0$ using the small-angle method. From this PSDF, we calculate the spectral attenuation due to large particles and subtract it from the initial attenuation. The result is the attenuation due to small particles. After the inversion, we get PSDF for $r < r_0$. This is the end of the first iteration. As a result, we have the first approximation for PSDF for the entire radius interval from $r_{\min}=0.03\mu\text{m}$ to $r_{\max}=30\mu\text{m}$. The process is repeated for the next iteration, and so on. In our numerical experiments, we could stop the iterative process after the third iteration.

5. ESTIMATES OF ERRORS OF THE PROCEDURE

Let us evaluate the accuracy of the retrieval of the entire PSDF and of its parts. Fig 3 shows the relative difference between the retrieved PSDF and initial one as a function of the particle radius for successive iterations for the Model I.

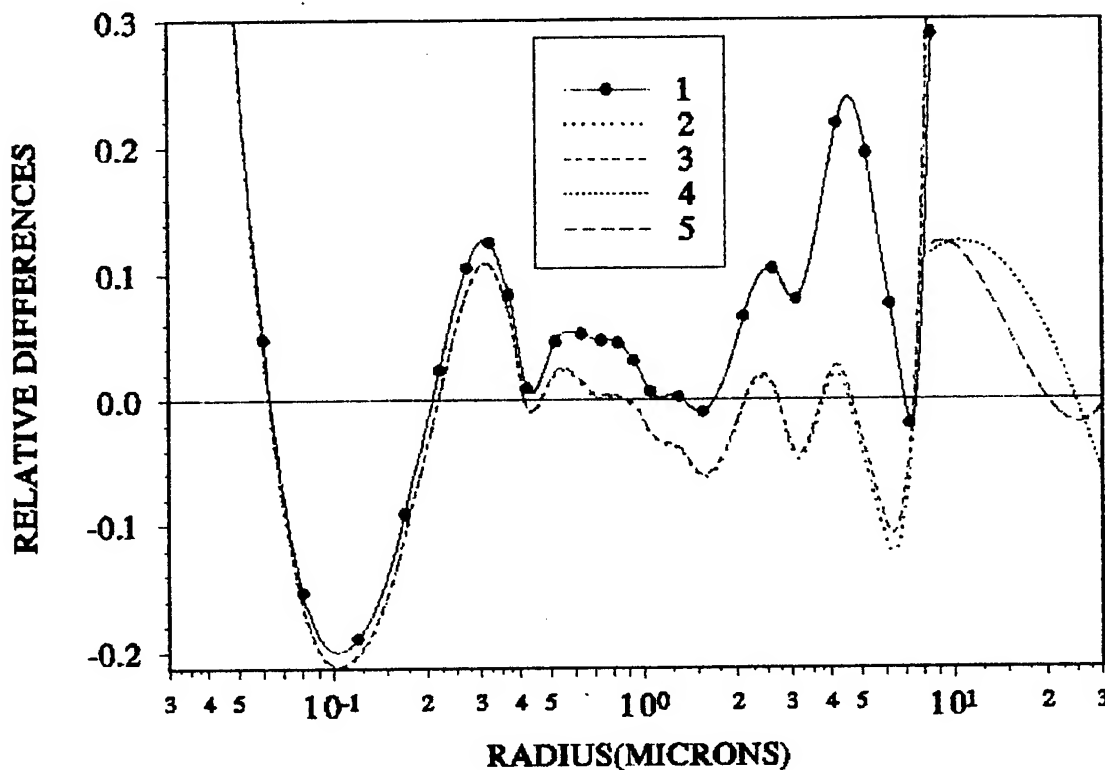


Fig. 3. Relative differences between PSDF retrieved after successive iterations using the Algorithms I and II and the initial PSDF (Model I; $r_0=8.5\mu\text{m}$). 1- $[f_0(r)-f(r)]/f(r)$ for the zeroth iteration; 2,3-the same for the first and third iterations respectively; 4,5- $[f_1(r)-f(r)]/f(r)$ for the first and third iterations respectively.

It is seen that the best approximation is obtained within the radius interval $0.2-7\mu\text{m}$ where the maximum deviation does not exceed 25%. Beyond this interval, the deviation grows reaching 30% at $r>7\mu\text{m}$ and 70% at $r<0.1\mu\text{m}$. This is caused by the peculiarities of the kernel of the integral equation for the spectral attenuation which means that these errors cannot be decreased radically when using the Algorithm I.

The important feature of the curve 1 is that it is situated almost entirely above the abscissa axis, in other words, it gives too high values of PSDF. This follows from the fact that at the zeroth iteration of the Algorithm I, the tail of PSDF is not considered, though it is responsible for approximately 8% of attenuation.

As the iterative process moves on, this shift decreases within the radius interval $0.2-7\mu\text{m}$, with the oscillation amplitude diminishing. At the same time, we obtain the tail of PSDF $f_1(r)$ for the radius interval $8.5-30\mu\text{m}$, with the maximum deviation not exceeding 12%.

6. CONCLUSIONS

We examined the possibilities of retrieving PSDF up to $r_{\text{max}}=30\mu\text{m}$ for aerosols in MABL using simultaneous data for two optical characteristics: the spectral attenuation ($0.4-5\mu\text{m}$) and small-angle phase function ($\vartheta_{\text{max}}=6^\circ$). The mean relative error of the retrieval of the entire PSDF is less than 5% for the Model I and is approximately equal to 10% for the Model II. Both the spectral attenuation and SAPF calculated from the retrieved PSDF have an error of about 1%.

The performed analysis shows that the inversion of SAPF combined with the polynomial filtration makes it possible not only to determine the tail of PSDF for $r > r_0$, but also to refine PSDF values in the vicinity of $r = r_0$ where the Algorithm I introduces large errors.

7. ACKNOWLEDGMENTS

This work was supported by the Office of Naval Research (ONR) under Grant No. 9410064. We thank ONR for this support.

8. REFERENCES

1. K. S. Shifrin and I. G. Zolotov, "Spectral attenuation and aerosol particle size distribution." *Appl. Opt.*, **35**(12), 2114-2144, (1996).
2. K. S. Shifrin and G. Tonna, "Inverse problems related to light scattering in the atmosphere and ocean", in Vol. 34 of *Advances in Geophysics*, pp. 175-252, Academic, New York, 1993.
3. E. P. Shettle and R. W. Fenn, "*Models for aerosols in the lower atmosphere and the effects of humidity variations on their optical properties*", p. 94, AFGL-TR-79-0214, U.S. Air Force Geophysics Laboratory, Hanscomb Air Force Base, Mass., 1979.
4. S. G. Gathman, D. R. Jensen et al., *NOVAM Evaluation Utilizing Electro-Optics and Meteorological Data from KEY-90*, NCCOSC Tech. Report No. 1608, US Navy, San Diego, Sept. 1993.
5. J. Koo, and E. Hirleman, "A synthesis of integral transform technique for reconstruction of particle size distribution from the forward scattered light", *Appl. Opt.*, **31**(12), 2130-2140, 1992.

James E. Davies and Mervyn J. Lynch

School of Physical Sciences, Curtin University of Technology,
GPO Box U1987, Perth, Western Australia, 6001

ABSTRACT

Passive remote sensing of ocean colour relies on the sunlight backscattered from the ocean, the water-leaving radiance, to convey information on the concentrations of optically active marine constituents. Observations of ocean colour from space also contain light scattered by the overlying atmosphere. The determination and removal of the atmospheric contribution to the satellite detected radiance, in order to accurately determine the water-leaving radiance, is known as atmospheric correction. The atmospheric correction must be applied carefully since the ocean colour community requires water-leaving radiance estimates to better than 5% from beneath an atmosphere that can, in some spectral regions of interest, account for 90% of the total satellite signal. Aerosols play an important role in determining the atmospheric scattered radiance to the extent that the principal difficulty that remains in atmospheric correction is accounting for the variability in space and time of aerosol optical properties. We are developing an atmospheric correction algorithm based on a tri-modal maritime aerosol model. Results are presented within the context of present and future ocean colour sensors.

Keywords: ocean colour, atmospheric correction, SeaWiFS, marine aerosol

1. INTRODUCTION

A number of ocean colour satellite sensors have recently been, or are about to be, launched. These include the Sea-viewing Wide Field-of-view Sensor (SeaWiFS), the Ocean Colour and Temperature Sensor (OCTS), the Medium Range Imaging Spectrometer (MERIS) and the Moderate Resolution Imaging Spectrometer (MODIS). SeaWiFS was to have been launched in August of 1993, but a variety of problems have seen the launch slip to 1997. This work is chiefly concerned with the development of an ocean colour atmospheric correction algorithm for use with SeaWiFS observations in the reception area of the Western Australian Satellite Technology and Applications Consortium (WASTAC) HRPT station located in Perth, Western Australia. Fig. 1 is a simulated SeaWiFS pass over the Western Australian region.

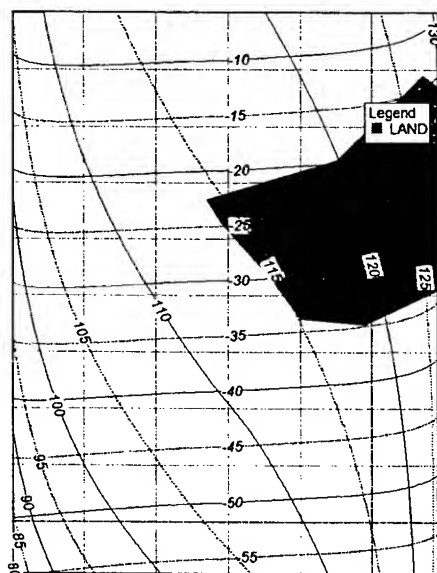


Fig.1. Simulated SeaWiFS pass over Western Australia. The simulated image space is represented by 6,000 pixels (100 lines \times 60 columns).

The first instrument to acquire ocean colour data from space was the Coastal Zone Colour Scanner (CZCS). Launched in 1978 and carried aboard NASA's Nimbus-7 satellite, the CZCS provided visible radiance data over most of the world's oceans until it ceased operations in June, 1986. This instrument demonstrated the feasibility of determining phytoplankton concentrations from space¹. However, processing CZCS measurements to obtain phytoplankton concentration is far from straightforward. Over the lifetime of the CZCS (and beyond) algorithms have been developed and refined to recover ocean data products from CZCS observations which comprise the water-leaving radiance and a host of ocean surface, atmosphere and instrument effects². L_t is the total radiance exiting the top of atmosphere in a specified direction at any wavelength λ and can be written as³

$$L_t(\lambda) = L_R(\lambda) + L_a(\lambda) + L_{Ra}(\lambda) + T(\lambda)L_w(\lambda) \quad (1)$$

where

- L_R radiance due to Rayleigh scattering by molecules;
- L_a radiance due to scattering by atmospheric aerosol;
- L_{Ra} interaction term between aerosol and molecular scattering;
- L_w water leaving radiance;
- T atmospheric total (direct plus diffuse) transmittance⁴.

In this form of CZCS constraint equation the specular reflection of the solar beam from the ocean surface is ignored as the scan plane of most ocean

colour sensors can be tilted to avoid this effect³. In most circumstances that arise in ocean colour remote sensing, the atmospheric contribution to the total radiance is dominated by atmospheric backscattering. In the single scattering approximation, solar radiation at the top of the atmosphere is considered as the only intensity source and the radiance backscattered from a plane parallel atmosphere is given by⁵

$$L = \frac{\omega_0 \mu_0 \pi F_0}{\mu + \mu_0} \frac{p(\psi)}{4\pi} \left\{ 1 - \exp \left[-\tau \left(\frac{1}{\mu} + \frac{1}{\mu_0} \right) \right] \right\} \quad (2)$$

where

- L upwelling radiance due to scattering;
- τ optical depth;
- ω_0 single-scattering albedo;
- μ_0, μ cosine of solar zenith angle, cosine of satellite zenith angle;
- $p(\psi)$ scattering phase function evaluated at scattering angle ψ ;
- πF_0 extra-terrestrial solar irradiance.

Atmospheric radiance contributions, in the single scattering approximation, can also be attributed to photons which have been forward scattered and reflected by the ocean surface. However, Eqn. 2 is adequate for the present purpose of establishing a nomenclature for summarising the approximations employed in the CZCS atmospheric correction algorithms.

2. APPROXIMATIONS IN CZCS APPROACHES

The CZCS atmospheric correction algorithms are replete with approximations and assumptions and with good reason. Firstly, the limited accuracy and precision of the CZCS instrument permits approximations at a certain level without loss of information. Secondly, in Eqn. 1 L_t is measured and L_R can be computed to good accuracy but there remains unknown not only the required L_W but also L_a and L_{Ra} (and T to the extent that it is correlated to L_a). A spectral approach to closure can only assist if some quantities take on fixed values at certain wavelengths or if quantities vary with wavelength in a known manner. Approximations and assumptions made in the various CZCS atmospheric correction algorithms include: Eqn. 2 approximated by its Taylor series expansion to first order^{6,7,8}; L_W assumed known for clear, open ocean water in some spectral regions⁹; radiances approximated by single scattering theory^{6,7,10}; aerosol optical depth assumed to be proportional to $\lambda^{-\alpha}$, where α is either assigned⁸ or is calculated for power law aerosol size distribution⁹; total atmospheric radiance approximated by the separate calculation of molecular and aerosol contributions^{7,8} (rather than employing a phase function weighted by scattering optical depth^{12,13}); aerosol phase function assumed^{14,15}; scattering atmosphere assumed vertically homogeneous; polarisation neglected.

With the arrival of the new ocean colour sensors, many of the approximations and assumptions listed above have come under renewed scrutiny^{1,21}. The SeaWiFS instrument, for example, has more channels than CZCS, more bits per sample, higher signal to noise ratio and a radiometric accuracy assured by on-board calibration¹⁶. Rejecting of even some of the above simplifications can lead to systems of equations which cannot be inverted to provide L_W . It is, however, possible to construct forward models of radiative transfer in the atmosphere/ocean system to provide estimates of L_t ^{17,18,19,20}. Such models can be used to evaluate the sensitivity of top of atmosphere radiances to perturbations in atmospheric state parameters. Presented with observations of the spectral radiance exiting the ocean/atmosphere system, and provided that an initial estimate of the state of the system can be made, the sensitivities can be used to revise the initial estimate in a manner that drives Eqn. 1 towards closure²⁰. If the least well known state parameter is the amount and type of atmospheric aerosol, it makes sense to investigate the sensitivity of top of atmosphere spectral radiances to changes in this parameter.

3. MARINE ATMOSPHERIC BOUNDARY LAYER AEROSOL MODEL

The particle size distribution function for aerosols in the marine atmospheric boundary layer can be represented as a sum of components of different composition, each having a log-normal distribution²². Based upon hundreds of observations of

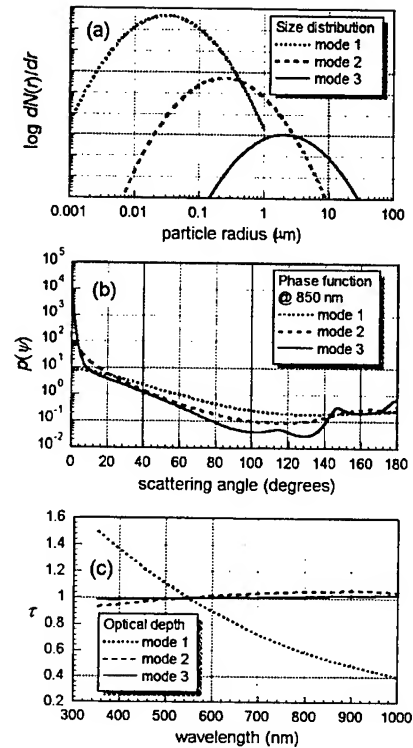


Fig. 2. Properties of the Navy aerosol: (a) size distribution; (b) phase function at 850 nm; (c) optical depth normalised to unity at 550 nm; of each mode.

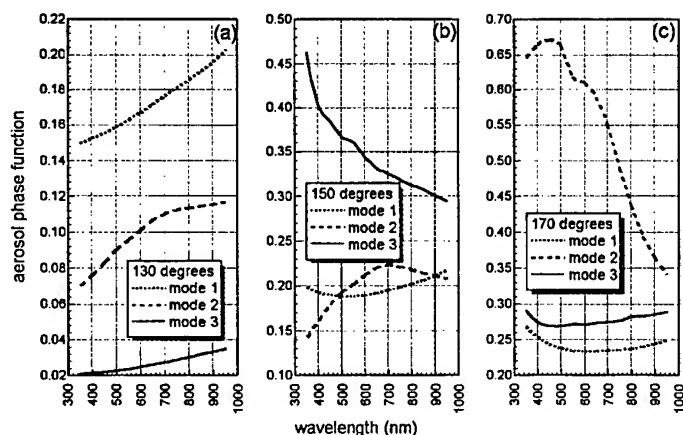


Fig. 3. Wavelength dependence of the phase function for each aerosol mode: (a) at 130° scattering angle; (b) at 150°; (c) at 170°.

The advantage of using the Navy aerosol model is that it provides a basis for allocating the physical properties of the various modes and for inferring their spatial variability. The mode 1 aerosol population we expect to remain nearly constant on scales of many hundreds of kilometres, at least in regions far from shore. Based on mean wind speed data over the global oceans¹¹, the mode 2 aerosol population is predicted to have a spatial scale of circa 500 km. We assume mode 3 to have a similar spatial scale as mode 2 in open ocean regions. We have used the Navy aerosol model in the work presented here with the following adjustments: the relative humidity is assumed fixed at 80%; mode 1 has refractive index of “dust-like” aerosols²⁴; mode 2 has refractive index of “water-soluble” aerosols²⁴; mode 3 has refractive index of “oceanic” aerosols²⁴; optical properties are computed from Mie theory.

Fig. 2(b) gives the phase function of each mode at 850 nm and Fig. 2(c) shows how the aerosol optical depth of each mode varies with wavelength. If the Navy aerosol model is a good approximation to the marine and coastal aerosol, it becomes clear that there are good reasons for wishing to know the mixing ratio of its components as well as the total aerosol optical depth. This is further underlined by Fig. 3 which shows, for three scattering angles, how the phase function of each mode varies with wavelength.

4. RETRIEVALS FROM SYNTHETIC DATA

A layered atmosphere radiative transfer model (LARTM) computer code was developed at Curtin University for use in sensitivity studies²⁵. The model is a plane-parallel, successive orders of approximation²⁶ code. It employs the scalar radiative transfer approximation in which radiative transfer is framed in terms of phase function and scalar intensities rather than the phase matrix and Stokes vector representation of the exact radiative transfer equation²⁷. The radiance errors arising from neglecting polarisation are estimated to be at about the 1% level at the wavelengths used to determine aerosol mode optical depths. At shorter wavelengths, where the atmospheric correction is to be applied, neglect of polarisation can lead to errors of more than 3%.

LARTM, in single-scattering mode, computes single-scattered radiances for geometry vector Ω (θ_0 , θ_s , $\Delta\phi$) where θ_0 is the solar zenith angle, θ_s the satellite zenith angle and $\Delta\phi$ the relative azimuth angle. In multiple scattering mode LARTM delivers single-scattered and total radiances at grid points Ω'' (θ_0'' , θ_s'' , $\Delta\phi''$). LARTM is used to pre-compute the additional radiance due to multiple scattering about some base model (first guess) optical depth $\tau^B[\tau_1, \tau_2, \tau_3]$. From these, the partial derivatives of multiple scattering reflectance with respect to τ are approximated for use in a linear least squares matrix inversion. It is important that these sensitivities are spatially smooth to allow meaningful interpolation between grid points. The retrieval proceeds as follows:

1. compute base model single scattered radiance for pixel geometry Ω and for perturbations to base model optical depth τ^B and convert to single scattered reflectance R_S ;
2. estimate the partial derivatives of R_S with respect to τ ;
3. compute matrix A from pre-computed partials $\partial R_M / \partial \tau$ (interpolated to pixel geometry; R_M is additional reflectance due to multiple scattering) and from $\partial R_S / \partial \tau$ at the pixel;

aerosol size distributions, made predominantly over the North Pacific and North Atlantic oceans, Gathman²³ proposed the Navy aerosol model which is comprised of three modes, each of fixed width parameter. Fig. 2(a) shows the amplitudes of the three aerosol mode size distributions at 80% relative humidity where the mode radii are 0.03 μm (mode 1), 0.24 μm (mode 2) and 2.0 μm (mode 3). Mode 1 is identified as a background aerosol of continental origin whose number density is correlated to the air mass travel time from the continental land mass. Mode 2 is populated by marine aerosols which have been produced by earlier high wind conditions with a number density correlated to the mean wind speed of the previous 24 hour period. Mode 3 aerosols are salt spray particles with number density correlated to the current wind speed.

4. convert radiance data L^D to reflectance data R^D ;
5. assign to first guess τ^G the base model optical depth τ^B ;
6. repeat until convergence criterion is met (presently we just iterate 5 times);
 - compute single scatter and total radiances at model grid points Ω'' for τ^G ;
 - convert additional radiance due to multiple scattering to reflectance R_M ;
 - compute single scatter radiance at each pixel for τ^G and convert to reflectance R_S ;
 - estimate total reflectance R^G for pixels from R_S , and from R_M that is spatially interpolated about the nearest model grid point Ω' ;
 - compute optical depth difference $\Delta\tau$ from the inverted sensitivity matrix A and from $R^D - R^G$;
 - update the guess τ^G with the difference $\Delta\tau$;
7. take τ^G as the retrieval solution and evaluate radiance residual ΔL in the 443 nm channel.

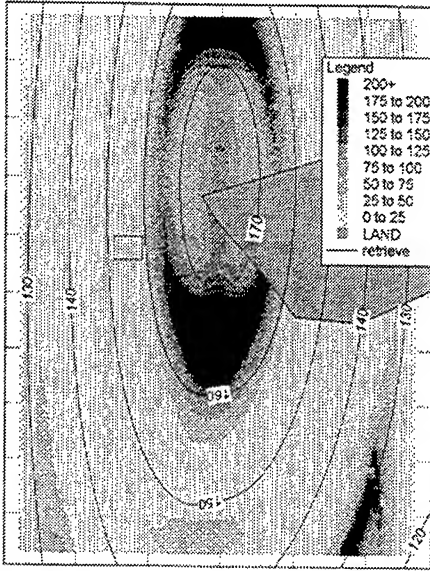


Fig 4. Square root of the condition number of $A^T A$ (Euclidean norm) for a 5×5 pixel retrieval employing the 765 and 865 nm channels of SeaWiFS. The model atmosphere is *oceanE* and it overlies a flat, black, Fresnel reflecting ocean. Overlain are contours of the backscattering angle. The retrieval area is shown at 26.9°S , 110.5°E .

designated *oceanE*, is the Lenoble profile 3 atmosphere²⁴ with boundary layer aerosol as the Navy model with optical depth $\tau[0.01, 0.06, 0.04]$. Values of less than 50 in Fig. 4 can be considered as relatively stable. Where the value exceeds 100, an unconstrained inversion of this type may be quite unstable. The contour lines on Fig. 4 show the atmospheric backscattering angle, which is clearly highly correlated to the condition number.

An area of 5×5 pixels centred on location 26.9°S , 110.5°E was selected for testing the retrieval algorithm. Two retrievals are shown in Fig. 5. They used as first guess, respectively, the *oceanE* model and the *coastB* model, where the latter has Navy model optical depth $\tau[0.2, 0.006, 0.004]$. In both cases 3% noise (uniform random deviate) was added to the synthetic radiance data and in each case the synthetic data optical depth was $\tau[0.03, 0.01, 0.02]$. The first guess optical depths $[\tau_1, \tau_2, \tau_3]$ for each of the three modes are shown on the LHS of Figs. 5(a) and 5(b) with the convergence after five iterations compared to the correct value on the RHS. It is clear that, for the retrievals attempted, it is not essential for the first guess optical depth to be very close to the data value sought. On convergence, the retrieval yields the optical depths for the three modes and provides a composite optical depth over the size range 0.001 to 50 μm . These optical depths are used

The scheme outlined above relies upon the stable inversion of the sensitivity matrix A which relates aerosol optical depth perturbations to differences in observed spectral reflectance,

$$\begin{bmatrix} R_1^D - R_1^G \\ R_2^D - R_2^G \\ \vdots \\ R_n^D - R_n^G \end{bmatrix} = \begin{bmatrix} \frac{\partial R_1}{\partial \tau_1^G} & \frac{\partial R_1}{\partial \tau_2^G} & \frac{\partial R_1}{\partial \tau_3^G} \\ \frac{\partial R_2}{\partial \tau_1^G} & \frac{\partial R_2}{\partial \tau_2^G} & \frac{\partial R_2}{\partial \tau_3^G} \\ \vdots & \vdots & \vdots \\ \frac{\partial R_n}{\partial \tau_1^G} & \frac{\partial R_n}{\partial \tau_2^G} & \frac{\partial R_n}{\partial \tau_3^G} \end{bmatrix} \begin{bmatrix} \tau_1^D - \tau_1^G \\ \tau_2^D - \tau_2^G \\ \tau_3^D - \tau_3^G \end{bmatrix} \quad (3a)$$

$$\Delta R = A \Delta \tau \quad (3b)$$

To arrive at $\Delta\tau$, the unconstrained linear least squares inversion is,

$$\Delta \tau = (A^T A)^{-1} A^T \Delta R \quad (4)$$

It is instructive to evaluate the condition number of $A^T A$ in order to assess the stability of the system. Provided that $A^T A$ is not so ill-conditioned as to make its inversion numerically unstable, the square root of its condition is the more useful measure of system robustness. Fig. 4 is a greyscale image of this measure computed for SeaWiFS 765 nm and 865 nm channels for all pixels in a 5×5 pixel box moved over the entire simulated image space. Note that SeaWiFS local area coverage (LAC) pixels are about 1 km^2 at nadir but in this simulated SeaWiFS data we have treated the overpass as a 100×60 pixel image space with 1 pixel representing approximately $50 \times 50 \text{ km}$ on the earth's surface at nadir. The base model atmosphere in this example,

in the calculation of the radiance for a short wavelength channel (443 nm) in order to assess the radiance differences arising from the error levels in the retrieval. The maximum radiance residual at 443 nm is found to be less than 0.3%. This can be considered as encouraging but it must be remembered that in this synthetic study the assumption of aerosol spatial invariance over the retrieval region holds true and the atmospheric profile (apart from the boundary layer aerosol optical depth) is known with absolute precision.

5. VALIDATION

With the delay of SeaWiFS it has been necessary to seek validation phase data from other sources. MODIS Airborne Simulator (MAS) data from the SCAR-A experiment is the only calibrated, over ocean data source located to date. Fig. 6 shows MAS 664 nm and 875 nm channels from flight line 23 collected offshore from Atlantic City on 16th July, 1993. The flight line runs approximately parallel to the coastline with Atlantic City about 20 kms to the right and open ocean to the left in Fig. 6. The 12 μm channel was used to clear cloud contaminated pixels. Contours of backscattering angle and forward scattering angle are overlain on Figs. 6(a) and 6(b), respectively. Aerosols on the coastal side of the MAS image are probably of urban origin and are not adequately approximated by the Navy aerosol model. Also, in nearshore waters, the assumption of zero water-leaving radiance at 664 nm is probably poor. Fig. 6(c) shows the quantisation of radiance levels for a single scan line. The 875 nm channel is quantised into only 4 levels. This means that any structure in the open ocean side of the MAS image cannot be seen. The same image sampled by SeaWiFS would have approximately 250 levels ($\frac{1}{4}$ of the SeaWiFS 865 nm dynamic range, 10 bit digitisation). The location of the SCAR-A experiment and the precision of the MAS 664 nm and 875 nm channel measurements makes this data set unsuitable for our purposes.

6. CONCLUSIONS AND FURTHER WORK

At present we seek calibrated top of atmosphere radiances before we can proceed with the validation of our work. We acknowledge that in practice an unconstrained inversion scheme, Eqn. 4, may not always be satisfactory and an extension with a constraint may be required.

7. ACKNOWLEDGMENTS

MAS data was obtained from the data archive managed by the Langley Research Center. Financial contributions from Curtin University of Technology, WASTAC and the Ocean Optics XIII conference secretariat have made conference attendance possible and are gratefully acknowledged. Our thanks also to Liam Gumley of SSEC, Madison, for computer code to manipulate MAS data sets and to Associate Professor Brian White of the Department of Mathematics and Statistics, Curtin University, for many helpful discussions.

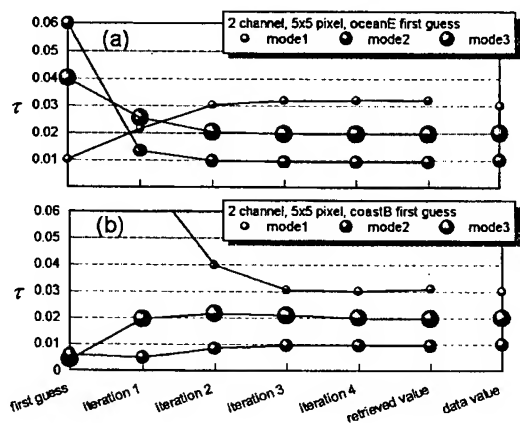


Fig 5. Retrievals of aerosol mode optical depths. On the LHS of each graph are shown the initial guess optical depths for each of the three modes. On the RHS are the optical depths retrieved after 5 iterations ("retrieved value") and the correct optical depths ("data value").

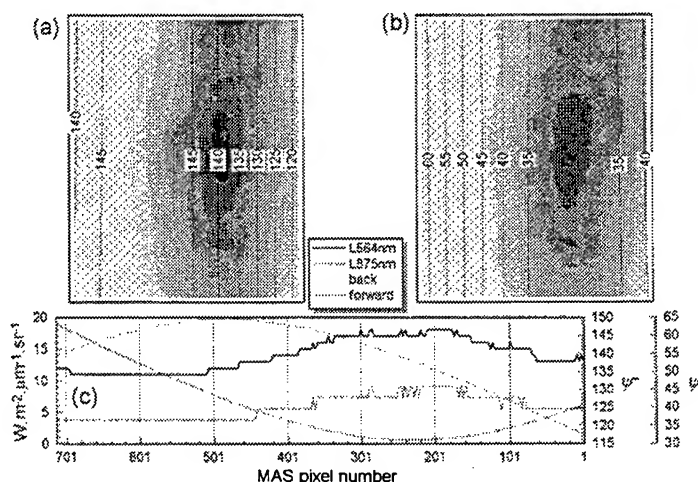


Fig. 6. SCAR-A experiment MAS flight line 23 on 16th July, 1993: (a) 664 nm channel; (b) 875 nm channel; (c) quantisation in radiance data. The greyscale images (a) and (b) are cloud cleared using the 12 μm channel and are spatially binned. The single scan line of radiance data in (c) shows the few digital levels in the 664 nm and 875 nm channels in this scene.

8. REFERENCES

1. S.B. Hooker, W.E. Esaias, G.C. Feldman, W.W. Gregg and C.R. McClain, "An overview of SeaWiFS and ocean color," *NASA Tech. Memo. 104566, Vol. 1*, S.B. Hooker and E.R. Firestone (Eds.), pp. 1-16, NASA, Maryland, July 1992.
2. J.J. Simpson, "The Coastal Zone Colour Scanner (CZCS) algorithm. A critical review of residual problems," in *Ocean colour: Theory and applications in a decade of CZCS experience*, V. Barale and P.M. Schlittenhardt (Eds.), pp. 117-166, Kluwer Academic, Dordrecht, 1984.
3. H.R. Gordon, "Remote sensing of ocean color: a methodology for dealing with broad spectral bands and significant out-of-band response," *Appl. Opt.* **34**(36), 8363-8374 (1995).
4. P.Y. Deschamps, M. Herman and D. Tanre, "Definitions of atmospheric radiance and transmittance in remote sensing," *Rem. Sens Environ.* **13**, 89-92 (1983).
5. K-N. Liou, *An introduction to atmospheric radiation*, chapter 6, Academic Press, New York, 1980.
6. B. Sturm, "The atmospheric correction of remotely sensed data and the quantitative determination of suspended matter in marine water surface layers," in *Remote sensing in meteorology, oceanography and hydrology*, A.P. Cracknell (Ed.), pp. 163-197, Ellis Horwood, Chichester, 1981.
7. H.R. Gordon, D.K. Clark, J.W. Brown, O.B. Brown, R.H. Evans and W.W. Broenkow, "Phytoplankton pigment concentrations in the Middle Atlantic Bight: comparison of ship determinations and CZCS estimates," *Appl. Opt.* **22**(1), 20-36 (1983).
8. S.M. Singh, "Ocean colour from space: radiative transfer," in *Space oceanography*, A.P. Cracknell (Ed.), pp. 139-161, World Scientific, Singapore, 1990.
9. H.R. Gordon and D.K. Clark, "Clear water radiances for atmospheric correction of coastal zone color scanner imagery," *Appl. Opt.* **20**(24), 4175-4180 (1981).
10. S.P. Williams, E.F. Szajna and W.A. Hovis, "Nimbus-7 Coastal Zone Color Scanner: Level 2 data product users' guide," *NASA Tech. Memo. 86202*, 1985.
11. W.W. Gregg and K.L. Carder, "A simple spectral irradiance model for cloudless maritime atmospheres," *Limnol. and Oceanogr.* **35**(8), 1657-1675 (1990).
12. Y.J. Kaufman and J.H. Joseph, "Determination of surface albedos and aerosol extinction characteristics from satellite imagery," *J. Geophys. Res.* **87**(C2), 1287-1299 (1982).
13. A. Jayaraman and P. Koepke, "Accounting for the multiple-scattering effect in radiation intensities at the top of the atmosphere," *Appl. Opt.* **31**(18), 3473-3480 (1992).
14. R. Guzzi, R. Rizzi and G. Ziborbi, "Atmospheric correction of data measured by a flying platform over the sea: elements of a model and its experimental validation," *Appl. Opt.* **26**(15) 3043-3051 (1987).
15. H.R. Gordon and D.J. Castano, "Aerosol analysis with the Coastal Zone Color Scanner: a simple method to include multiple scattering effects," *Appl. Opt.* **28**(7), 1320-1326 (1989).
16. C.R. McClain, W.E. Esaias, W. Barnes, B. Guenther, D. Endres, S.B. Hooker, B.G. Mitchell and R. Barnes, "Volume 3, SeaWiFS calibration and validation plan," *NASA Tech. Memo. 104566, Vol. 3*, S.B. Hooker and E.R. Firestone (Eds.), pp. 1-13, NASA, Maryland, September 1992.
17. A. Berk, L.S. Bernstein and D.C. Robertson, *MODTRAN: A moderate resolution model for LOWTRAN 7*, final report, GL-TR-0122, AFGL, Hanscomb AFB, MA, 1989.
18. F.X. Kneizys, E.P. Shettle, L.W. Abreu, G.P. Anderson, J.K. Chetwynd, J.E.A. Selby. and S.A. Clough, *LOWTRAN7 computer code: Users manual*, 1988.
19. E. Vermote, D. Tanre, J.L. Deuze, M. Herman and J.J. Morcrette, *6S user guide version 1*, May 1996.
20. F.M. Breon, "An analytical model for the cloud-free atmosphere/ocean system reflectance," *Rem. Sens. Environ.* **43**, 179-192 (1993).
21. H.R. Gordon and M. Wang, "Retrieval of water-leaving radiance and aerosol optical thickness over the oceans with SeaWiFS: a preliminary algorithm," *Appl. Opt.* **33**(3), 443-452 (1994).
22. K.S. Shifrin and I.G. Zolotov, "Spectral attenuation and aerosol particle size distribution," *Appl. Opt.* **35**(12), 2114-2124 (1996).
23. S.G. Gathman, "Optical properties of the marine aerosol as predicted by the Navy aerosol model," *Opt. Eng.* **22**(1), 57-62 (1983).
24. J. Lenoble (Ed.), *Radiative transfer in scattering and absorbing atmospheres: Standard computational procedures*, chapter 7, A. Deepak Publishing, Hampton, Virginia, 1985.
25. J.E. Davies and M.J. Lynch, "Modelling sky radiances for SeaWiFS," Joint APOC/AMOS Conference, Lorne, Victoria, Australia, March 1995.
26. J.E. Hansen and L.D. Travis, "Light scattering in planetary atmospheres," *Space Sci. Rev.* **16**, 527-610 (1974).
27. H.R. Gordon, J.W. Brown and R.H. Evans, "Exact Rayleigh scattering calculations for use with the Nimbus-7 Coastal Zone Color Scanner," *Appl. Opt.* **27**(5), 862-871 (1988).

David Antoine¹ and André Morel¹

¹ Laboratoire de Physique et Chimie Marines, Université Pierre et Marie Curie et INSU/CNRS, B.P. 08 06230
Villefranche-sur-mer, France.

ABSTRACT

An algorithm is proposed for the atmospheric correction of the ocean color observations by the MERIS instrument. The principle of the algorithm, which accounts for all multiple scattering effects, is presented. The algorithm is then tested, and its accuracy assessed in terms of errors in the retrieved marine reflectances.

Keywords: ocean color, aerosols, radiative transfer, atmospheric correction, MERIS, water-leaving radiance

1. INTRODUCTION

When an ocean-color sensor aboard a satellite measures the radiance backscattered by the ocean-atmosphere system, it receives in the visible part of the spectrum a signal which is largely dominated by the "atmospheric path radiance". This radiance originates from photons scattered by air molecules and aerosols, which can also have been reflected at the sea surface, but have never penetrated the ocean. In the most favourable conditions of observation, the water-leaving radiance in the visible domain is always weak and hardly reaches 10% of the total radiance, and have then to be properly extracted. Over oceanic Case 1 waters, the radiances measured in the near infrared exclusively originate from scattering within the atmosphere and reflection at the sea surface.

Up to now, experience comes only from the Coastal Zone Color Scanner (CZCS) instrument^{1,2}, which was aboard the Nimbus 7 satellite from 1978 to 1986. The various algorithms developed for atmospheric correction of CZCS observations^{3, 4, 5, 6} had to cope with the limited radiometric sensitivity of the instrument, and the absence of channels to measure the backscattered radiation in the near infrared part of the spectrum, so that the estimation of the aerosol contribution was a difficult task.

Several ocean color sensors are now either launched or planned to be aboard future satellite platforms, like the European MEdium Resolution Imaging Spectrometer (MERIS)⁷. These new generation instruments circumvent the two limitations or difficulties evoked above, thanks to improved radiometric characteristics and to channels in the near infrared, precisely dedicated to atmospheric correction. Several algorithms have been developed for atmospheric correction of the ocean color observations by these sensors^{8, 9}.

The central problem of atmospheric correction lies in the estimation of the radiances due to aerosol scattering. Indeed, the aerosol distribution and the aerosol optical properties are not a priori known. In principle, and thanks to the 2 channels in the near infrared where the ocean is black, the retrieval of the aerosol type and optical thickness is possible in this region of the spectrum. Hypotheses, however, are needed to extrapolate the information gained in the near infrared toward the visible domain. Without using external knowledge on the actual aerosol, the only way would be to adopt an a priori spectral dependence of aerosol scattering. A technique based on this assumption cannot meet the desired accuracy, so that external knowledge about the aerosol is needed. These additional information can be conveniently represented by pre-computed data and relationships, generated from the radiative transfer simulations, and making use of aerosol models.

In the present paper, an atmospheric correction algorithm is proposed for the MERIS instrument, and its principle is derived from the results of a previous study¹⁰ about the change of the atmospheric path radiance with increasing aerosol optical thickness. This algorithm accounts for all multiple scattering effects, and allows the visible observations to be corrected for the effect of several kinds of aerosols, including absorbing ones, once their identification in the near infrared has been achieved.

2. PHYSICAL BASIS AND PRINCIPLE OF THE ALGORITHM

The signals at the TOA level will be here expressed as dimensionless bidirectional reflectances, ρ , which are related to radiances, L , through

$$\rho(\lambda, \theta_s, \theta_v, \Delta\phi) = \pi L(\lambda, \theta_s, \theta_v, \Delta\phi) / F_0(\lambda) \cos(\theta_s) \quad (1)$$

where F_0 is the extraterrestrial irradiance, λ is wavelength, θ_s is the sun zenith angle, θ_v is the satellite viewing angle, and $\Delta\phi$ the azimuth difference between the pixel-sensor and pixel-sun half vertical planes. The MERIS instrument has

been designed to meet the requirement that the discrimination of 30 classes of chlorophyll concentration, (10 classes within each orders of magnitude from 0.03 to 30 mg Chl m⁻³) should be possible. To meet this requirement, errors of about 5 10⁻⁴ to 1 10⁻³ in the water-leaving reflectance are tolerable, and can even reach $\pm 2 \cdot 10^{-3}$. It has been shown elsewhere⁹ that an algorithm based on the assumption of single scattering was not able to meet this accuracy. The principle of the multiple scattering algorithm developed here is as follows.

In a situation where white caps are absent, and θ_v is such that the specular reflection of direct sun rays (sun glint) is excluded, the total reflectance at the top of atmosphere level, ρ_t , is

$$\rho_t = \rho_{\text{path}} + t \rho_w \quad (2)$$

where ρ_w is the water-leaving reflectance, t is the diffuse transmittance along the pixel-to-sensor path, and ρ_{path} is the atmospheric path reflectance. The reflectance ρ_{path} accounts for all kinds of photon histories (except sun glint). The path reflectance can be expressed as a function of the type of scattering events, either of molecular or of aerosol type, with the following decomposition (the notations are those used in Ref¹⁰)

$$\rho_{\text{path}} = \rho_r^* + \rho_a^* + \rho_{ra}^* \quad (3)$$

where ρ_r^* is the reflectance which originates from scattering (single and multiple) by molecules only, but *in presence of aerosols*, ρ_a^* is the equivalent term for aerosols, also *in presence of molecules*, and ρ_{ra}^* stands for that part of ρ_{path} which strictly results from heterogeneous multiple scattering. In Ref¹⁰, the behavior of the 3 terms in Eq. (3) has been examined as a function of increasing aerosol load (in absence of aerosol absorption), and it has been shown that, whatever the specific geometry (θ_s , θ_v , $\Delta\phi$) envisaged, the change in ρ_{path} resulting from the simultaneous changes of its three constitutive terms is nearly linear.

In the context of atmospheric correction, the three terms of Eq. (3) are not separately known or calculable, because aerosols are unknown. The only quantities at disposal are ρ_{path} , as measured in the near infrared (where it is equal to ρ_t because $t \rho_w = 0$), and ρ_r , as calculated for any wavelength (depending only on the actual atmospheric pressure). The ratio $[\rho_{\text{path}} / \rho_r]$, was also examined¹⁰ as a function of increasing aerosols loads. Its increase is, as for ρ_{path} , nearly linear with increasing τ_a . Examples of the change in the ratio $[\rho_{\text{path}} / \rho_r]$ at 865 and 775 nm are displayed in Fig. 1 as a function of τ_a and for several aerosol models.

The scheme for atmospheric correction is based on the above results concerning the variations of the ratio $[\rho_{\text{path}} / \rho_r]$ with τ_a , and on the computation of ρ_r at all wavelengths. The successive steps of the correction are as follows : to the measured value of $\rho_{\text{path}}(865)$, it is possible to associate several guess values for τ_a , each one corresponding to a given aerosol model (steps 1 and 2 in Fig. 1). Several $\tau_a(775)$ are then obtained from the spectral optical thickness of each aerosol (step 3). To these $\tau_a(775)$ values correspond several values of the ratio $[\rho_{\text{path}} / \rho_r]$ at 775 nm, differing according to the aerosol type (steps 4 and 5). The last step consists in comparing this set of values to the actual ratio $[\rho_{\text{path}} / \rho_r]$ at 775 nm, and by this way in selecting the two aerosol models which most closely bracket the actual $[\rho_{\text{path}} / \rho_r]$ ratio (step 6). The following rests on the assumption⁸ that the proportion defined in the near infrared by the actual $[\rho_{\text{path}} / \rho_r]$ ratio and those of the two bracketing aerosols remains unchanged in the visible. A "mixing ratio" can therefore be computed, from the actual and the two bracketing values of $[\rho_{\text{path}} / \rho_r]$. It is then possible to transfer the estimate of $[\rho_{\text{path}} / \rho_r]$ at any other wavelength, in particular toward the visible spectrum, provided that the relationships with τ_a have been previously established for all wavelengths. The ratios $[\rho_{\text{path}} / \rho_r]$ in the visible are re-multiplied by the corresponding values of ρ_r , and therefore lead to ρ_{path} , and to the desired marine reflectances. These reflectances, converted into radiances (Eq. 1), are divided by the diffuse transmittance to obtain the water-leaving radiances.

The retrieval of the aerosol optical thickness becomes straightforward, as a by-product of the algorithm, since a couple of aerosol models has been selected : the two values of $\tau_a(865)$ associated with these two aerosol models are simply averaged. The mean of these two values provides the best estimate⁹ of the actual aerosol optical thickness at 865 nm.

3. IMPLEMENTATION AND TEST OF THE ALGORITHM

To implement the above algorithm, aerosol models have to be selected, which have to be as representative as possible of actual aerosols over the ocean. From the outputs of radiative transfer simulations (Monte Carlo), making use of the optical properties of these aerosols, the relationship between $[\rho_{\text{path}} / \rho_r]$ and τ_a can be stored for various wavelengths and geometries. Aerosols are variable in nature and vertical distribution, so that a lot of situations can be encountered. Assumptions are therefore mandatory to define more or less generic cases to be used when generating lookup tables. In the present work, it has been decided to consider the boundary layer (from the sea surface up to 2 km),

the free troposphere (2-12 km), and the stratosphere (12-50 km), within which aerosols and molecules are uniformly mixed.

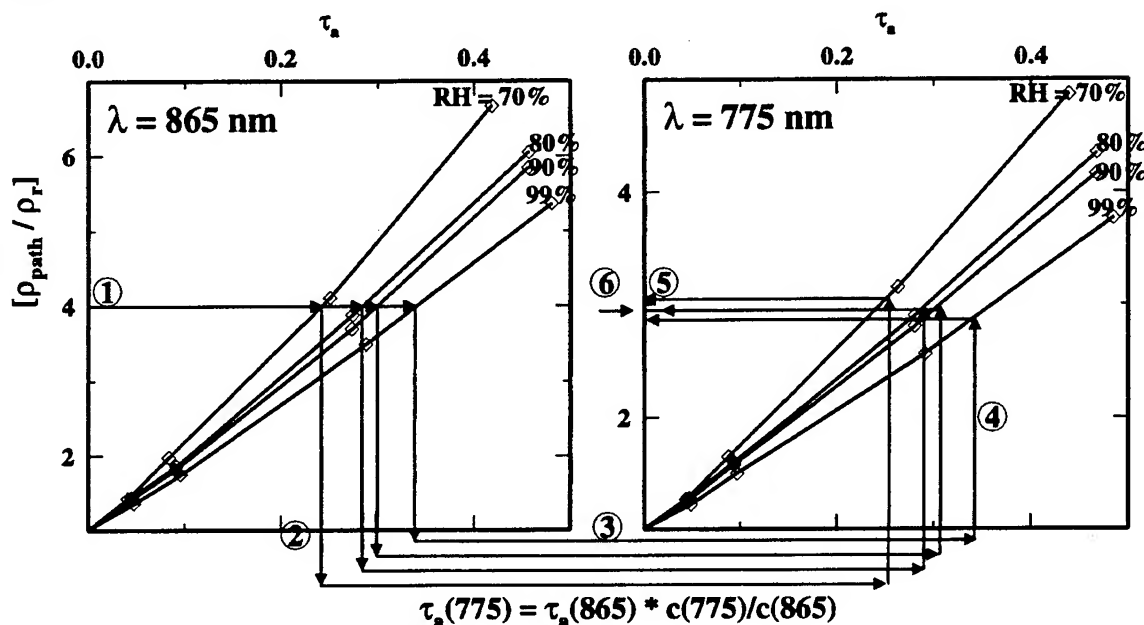


Fig. 1. Variation of the path reflectance at 865 and 775 nm as a function of the aerosol optical thickness τ_a , and expressed as the ratio $[\rho_{\text{path}} / \rho_r]$, when $\theta_s = 40^\circ$, $\theta_v = 30^\circ$, and $\Delta\phi = \pi/2$. The maritime aerosol model is used, for 4 values of the relative humidity, as indicated. Arrows symbolize a possible way for identifying a couple of aerosol models enclosing the actual aerosol. The circled numbers identify the successive steps of this scheme (see text).

The aerosol vertical structure as recommended by the experts working group on aerosols¹¹, is presently adopted to represent clear maritime atmospheres. The aerosol models for each layer are constructed from the basic aerosol components defined in Refs^{11, 12}. Five aerosols assemblages are defined (the word "assemblage" is used to describe the whole ensemble made up of the 3 aerosols located in the boundary layer, the free troposphere, and the stratosphere) by the relative humidity of the maritime boundary layer aerosol (i.e. 50, 70, 80, 90, or 99%). A constant aerosol background is present in the free troposphere (continental aerosol, with $\tau_a(550) = 0.025$) and in the stratosphere (H_2SO_4 aerosol, with $\tau_a(550) = 0.005$). The algorithm has been tested by using "pseudo data" obtained from the radiative transfer simulations (ρ_t and ρ_r) and the lookup tables. An histogram of the errors in the retrieved marine reflectances (t_{pw}) at 443 nm is displayed in Fig. 2, where results have been pooled together for several values of the optical thickness and geometry. Eighty percent of the errors are within $\pm 5 \cdot 10^{-4}$, and the larger errors are about $\pm 1 \cdot 10^{-3}$.

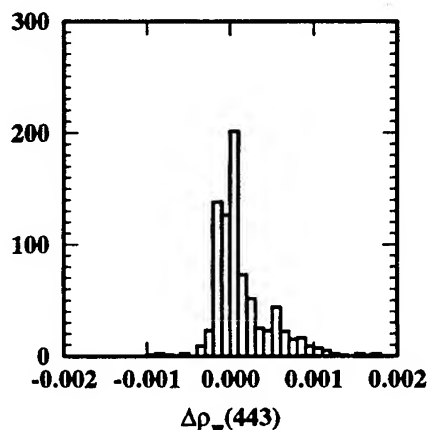


Fig. 2. Histogram of the error in the retrieved marine reflectance at 443 nm. The results for the five "standard" aerosol assemblages, four aerosol optical thicknesses, and various geometries, are here pooled together (800 cases).

The presence over the ocean of absorbing aerosols of continental origin is not anecdotal^{13, 14}, and Fig. 3 shows how large the error in the retrieved marine reflectances at 443 nm might be, when the atmospheric correction is carried out by using the "standard" maritime aerosol models while the actual aerosol is absorbing. It is assumed here that absorbing aerosols over the ocean are of three main types, namely the continental aerosol, the desert dust aerosol, and the urban aerosol. The continental and desert dust aerosols are assumed to be located within the free-troposphere (2-12 km), and the urban aerosol within the boundary layer (0-2 km). The stratosphere remains unchanged in all cases. Several additional aerosol assemblages have been therefore defined, with fixed proportions between the aerosols within the boundary layer and the free troposphere.

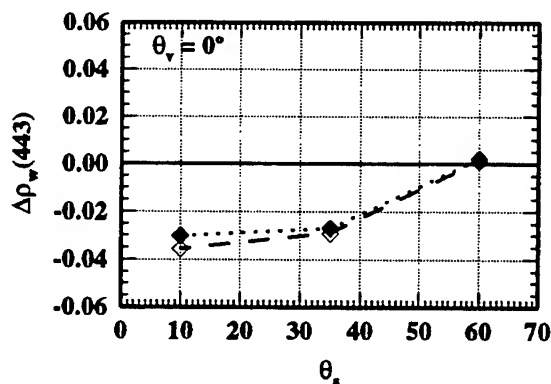


Fig. 3. Error $\Delta\rho_w(443)$, for the urban aerosol with RH = 98%, and when the standard set of aerosol models (clear maritime atmospheres) is used to carry out the correction.

To identify the presence of absorbing aerosols, a tentative correction is carried out by using the standard set of aerosol models, and then the error that is made at 705 and 510 nm is examined. At 705 nm the error in the atmospheric correction is straightforwardly obtained ($\rho_w = 0$). The band at 705 nm is however close to the two bands used in the correction process (775 and 865 nm), and the error that is made when extrapolating to 705 nm is usually too low to detect any failure of the algorithm, except for the strongly absorbing urban aerosol. The converse problem is faced at 510 nm, with possibly large errors in the atmospheric correction, added or subtracted however to significant water-leaving reflectances. The clue lies here in the relatively constant value of the water-leaving reflectance at 510 nm. Measured values^{15, 16, 17, 18} of the diffuse reflectance of oceanic Case 1 waters at 510 nm, $R(0^-)_{510}$, are displayed in Fig. 4 as a function of chlorophyll concentration, along with the values calculated from a reflectance model^{19, 20}, and for two values of the sun zenith angle. Considering the scatter of the points, it seems wise to assign a mean value of 2% to $R(0^-)_{510}$, which leads to a mean value of the bidirectional marine reflectance ($t\rho_w$) of about 0.007, with an attached uncertainty of about ± 0.001 . Thresholds on $\Delta\rho(510)$ have been defined : absorbing aerosols are revealed if $|\Delta\rho(510)|$ is greater than 0.002, or if it is included between 0.001 and 0.002 and the aerosol optical thickness is lower than 0.1. To ensure that the indication of the presence of absorbing aerosols is not due to an incorrect assumption on the value of $t\rho_w(510)$, rather than to an incorrect atmospheric correction, the test is carried out twice, first with the mean value of $t\rho_w(510)$, and second by introducing the typical error of $t\rho_w(510)$.

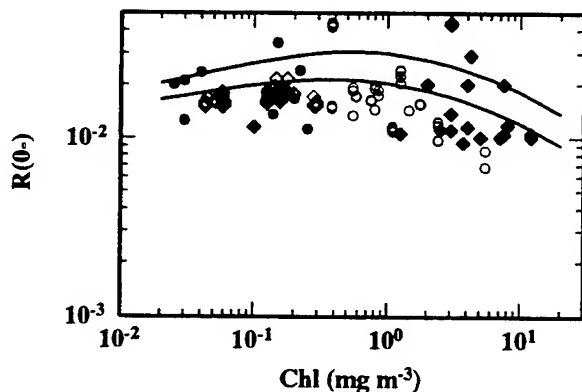


Fig. 4. Diffuse reflectance of the ocean at 510 nm, for Case 1 waters with variable chlorophyll concentration. The two curves have been obtained from a reflectance model^{19, 20}, either for a sun at zenith (bottom), or with a sun zenith angle of 60° (top). Reflectance values extracted from reflectance spectra measured at sea are also shown (Black diamonds : northeast Atlantic ocean, off Mauritania¹⁵; Black circles : Galapagos islands, Caribbean sea, sargasso sea¹⁶; open circles and open diamonds : Pacific ocean^{17, 18}).

The implementation of the above algorithm for identification of absorbing aerosols and for the estimation of their contribution to the path reflectance has been tested, following the same principle than for the clear maritime atmospheres. The ability of the tests at 510 and 705 nm to detect the presence of absorbing aerosols is increasing with increasing optical thickness, and most of the absorbing aerosols are detected (not shown).

Histograms of the errors in the retrieved marine reflectance at 443 nm are shown in Fig. 5. For each kind of absorbing aerosol, 1920 values of $\Delta\rho_w(443)$ are pooled together, and correspond to 4 values of the aerosol optical thickness, 40 geometries and 12 aerosol assemblages, each one corresponding to 4 values of the relative humidity for the maritime aerosol within the boundary layer, and to 3 values of the sharing of optical thickness between the boundary layer and the free troposphere. The atmospheric correction is not so accurate as for clear maritime atmospheres (Fig. 2), yet a significant percentage of the $\Delta\rho_w(443)$ values remain within $\pm 2 \cdot 10^{-3}$, namely 97, 72, and 77%, for the aerosol assemblages containing respectively the continental aerosol, the desert dust, or the urban aerosol. The above results, even if not perfect, clearly improve the quality of the atmospheric correction in situations where a classical algorithm, without the ability to address separately different kind of aerosols, would totally fail (see Fig. 3).

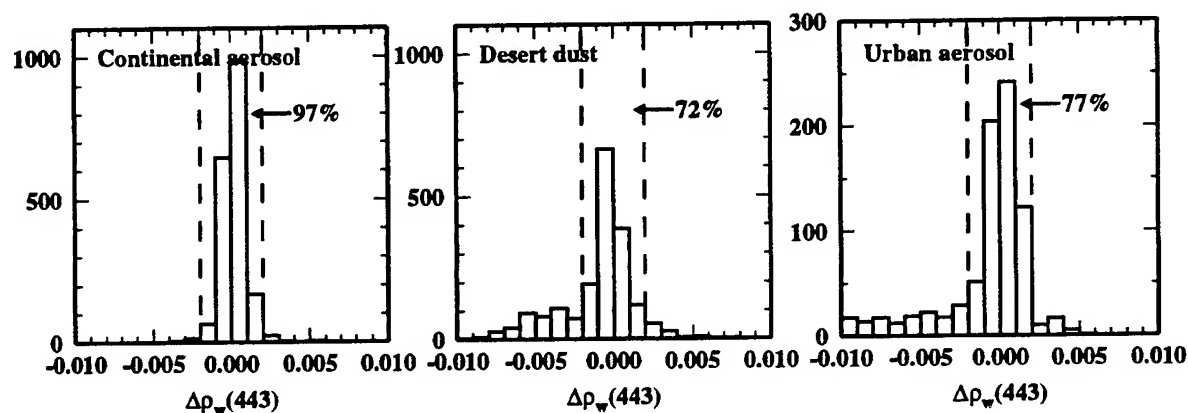


Fig. 5. Histogram of the error in the retrieved marine reflectance at 443 nm, and for the three "non-standard" aerosol assemblages, as indicated. The results for the four aerosol optical thicknesses, the three "mixing ratios" (the proportion of aerosols within the boundary layer and the free troposphere), and various geometries, are here pooled together (1920 cases for each aerosol assemblage). The percentages indicated correspond to the errors within ± 0.002 in reflectance.

4. CONCLUSION

The algorithm proposed here for atmospheric correction of ocean color observations seems to work well, and the accuracy required for the new generation ocean color sensors is met in most situations, regarding the aerosol types and their vertical distribution.

A critical aspect concerns however the use of aerosol models, which, even if constructed from measurements and modeling studies, and also partly validated against measurements²¹, could reveal insufficiently representative of real aerosols in some situations. The aerosol assemblages defined here seem however to capture the essential features of possible spectral dependencies of aerosol scattering. As a consequence, when the actual aerosol type or vertical distribution are not represented within the database, the correction remains possible, and its accuracy is preserved. A weakness could appear if the water-leaving reflectance at 510 nm actually was more variable in the real ocean than in the data shown here (Fig. 4). The examination of additional and recent measurements, and above all the operational use of the algorithm, will confirm or invalidate the present approach.

Several aspects of the radiative transfer in the ocean-atmosphere system have been neglected in the present work, since they do not intervene when defining the principle of the algorithm and its implementation. They could have however an impact on the accuracy of the atmospheric correction, and remain to be studied. These points concern, not exhaustively, the effect of white caps, the calculation of the diffuse transmittance, polarization, and instrumental errors.

5. ACKNOWLEDGMENTS

This work was jointly supported by the Centre National de la Recherche Scientifique (UA 2076, INSU/CNRS) and by the Agence Spatiale Européenne (contract ESTEC 11878/96/NL/GS).

6. REFERENCES

1. W. A. Hovis, D. K. Clark, F. Anderson, R. W. Austin, W. H. Wilson, E. T. Baker, D. Ball, H. R. Gordon, J. L. Mueller, S. Z. ElSayed, B. Sturm, R. C. Wrigley and C. S. Yentsch, "Nimbus-7 Coastal Zone Color Scanner : system description and initial imagery," *Science* **210**, 60-63 (1980).
2. H. R. Gordon, D. K. Clark, J. L. Mueller and W. A. Hovis, "Phytoplankton pigments from the Nimbus-7 Coastal Zone Color Scanner : comparisons with surface measurements," *Science* **210**, 63-66 (1980).
3. H. R. Gordon, "Removal of atmospheric effects from satellite imagery of the oceans," *Appl. Opt.* **17**, 1631-1636 (1978).
4. M. Viollier, D. Tanré, and P. Y. Deschamps, "An algorithm for remote sensing of water color from space," *Boundary Layer Meteorol.* **18**, 247-267 (1980).
5. A. Bricaud and A. Morel, "Atmospheric corrections and interpretation of marine radiances in CZCS imagery : use of a reflectance model," *Oceanol. Acta* **7**, 33-50 (1987).
6. J. M. André and A. Morel, "Atmospheric corrections and interpretation of marine radiances in CZCS imagery, revisited," *Oceanol. Acta* **14**, 3-22 (1991).
7. M. Rast and J. L. Bézy, "The ESA medium resolution imaging spectrometer (MERIS) : requirements to its mission and performance of its system," in RSS95, Remote Sensing in Action, Proc. 21st Annual Conf. Remote Sensing Soc., 11-14 September, 1995, University of Southampton, 125-132 (1995).
8. H. R. Gordon and M. Wang, "Retrieval of water-leaving reflectance and aerosol optical thickness over the oceans with SeaWiFS : a preliminary algorithm," *Appl. Opt.* **33**, 443-452 (1994).
9. H. R. Gordon, "Atmospheric correction of ocean color imagery in the Earth observing system era," Accepted in *J. Geophys. Res.* (1997).
10. D. Antoine and A. Morel, "Relative importances of homogeneous and heterogeneous multiple scattering by air molecules and aerosols in forming the atmospheric path radiance in the visible and near infrared parts of the spectrum," Accepted in *J. Geophys. Res.* (1997).
11. World Climate Research Program, "A preliminary cloudless standard atmosphere for radiation computation," Int. Ass. Meteorol. Atm. Phys., Radiation Commission, March 1986, WCP-112, WMO/TD-N° 24, 60 pp (1986)
12. E. P. Shettle and R. W. Fenn, "Models for the aerosols of the lower atmosphere and the effects of humidity variations on their optical properties," Environmental Research Papers, AFGL-TR-79-0214, Air Force Geophysics Laboratory, 20 September 1979 (1979).
13. X. Li, H. Maring, D. Savoie, K. Voss, and J. M. Prospero, "Dominance of mineral dust in aerosol light-scattering in the north Atlantic trade winds," *Nature* **380**, 416-419 (1996).
14. M. O. Andreae, "Raising dust in the greenhouse," *Nature* **380**, 389-390 (1996).
15. MEDIPROD group, "Résultats de la campagne CINECA 5 - J. Charcot - Capricorne 7403 (1^{er} Mars au 20 Avril 1974)," Publications du CNEXO, N°10 (1976).
16. J. E. Tyler, "Measurements of photosynthesis, available radiant flux, and supporting oceanographic data, Data report, SOCR Discoverer expedition, May 1970," S.I.O. Ref. 73-16, Univ. California (1973).
17. PACIPROD campaign, data unpublished.
18. OLIPAC (JGOFS) campaign, data unpublished.
19. A. Morel, "Optical modeling of the upper ocean in relation to its biogenous matter content (case 1 waters)," *J. Geophys. Res.* **93**, 10749-10768 (1988).
20. A. Morel and B. Gentili, "Diffuse reflectance of oceanic waters : its dependence on sun angle as influenced by the molecular scattering contribution," *Appl. Opt.* **30**, 4427-4438 (1991).
21. M. Schwindling, "Modèles et mesures pour l'observation spatiale de la couleur de l'océan : diffusion atmosphérique par les aérosols et réflexion de surface par l'écume," Thèse de Doctorat de l'Université de Lille, Villeneuve d'Ascq, France, 245 pp. (1995).

Optical Properties

Optical properties of oceanic Case 1 waters, revisited

André Morel

Laboratoire de Physique et Chimie Marines, Université Pierre et Marie Curie et CNRS
BP 08, 06238 Villefranche-sur-mer CEDEX, France.

ABSTRACT

Since the Case 1 waters have been defined and their optical properties described as a function of the chlorophyll *a* concentration, continuing observations and laboratory experiment have brought new insight into the specific effects of some of the various components of the biological compartment. These results are examined, as well as their impact on models, used as diagnostic tools for understanding, or as prognostic tools for predicting, the bulk optical properties of these waters, with a special reference to reflectance and the remote sensing of ocean color.

Keywords : Case 1 waters, modeling, reflectance, ocean color.

INTRODUCTION

In Case 1 waters, which, by definition, are outside of any notable terrigenous influence, the optical properties depend only on the varying absorption and scattering properties of the material which is locally formed. These waters are generally seen as a simple two-component system. The first, and constant, component is the optically pure sea water. The second and varying component, related to the biological activity, comprises the phytoplanktonic cells resulting from photosynthesis, all the commensal heterotrophic planktonic community (including free living bacteria and viruses), generated debris of all kinds and sizes, and also released dissolved organic compounds. Considering such a complex assemblage as a single "biological" component is obviously an oversimplifying vision.

To the extent that these various materials are not in constant proportions to each other, and in particular in constant ratio with the chlorophyll *a* concentration (denoted Chl), the changes in optical properties of case 1 waters with changing Chl are neither linear, nor as simple as it could be expected for a two-component system. This complexity has been acknowledged for a long time. The first empirical approaches which have consisted in relating the bulk apparent optical properties (AOP), such as reflectance or diffuse attenuation, to Chl, actually have led to non-linear, spectrally dependent, relationships (see e.g. Gordon and Morel'). Also soon recognized, was the existence of a natural "noise" affecting these relationships. It originates from the fluctuations in the relative proportions between the diverse constituents inside the biological compartment, as well as from the variability in the specific effect of each of these constituents. The extent to which such a noise is predictable remains an open question.

In revising the optical properties of Case 1 waters, several questions can be raised, such as: Are we able to go beyond the previously established empirical relationships? In other words, could an analytical approach be presently attempted, by which the role of each constituent would be separately assessed and its variability quantified, as a source of noise ?

In reference to the particular problem of the remote sensing of ocean color, is it now possible to accurately model the relationships between the spectral reflectance, $R(\lambda)$, (an AOP) and Chl, the chlorophyll concentration in the upper oceanic layer ?

Such a model, as well as the analytical approach suggested above, require the determination of the inherent optical properties (IOP) of each (if possible) of the various constituents, in so far as they can be identified and separately studied. Extremely accurate and numerically efficient methods and codes are presently available² for solving the radiative transfer equation (RTE) and thus to derive the AOP, once the IOP are prescribed and the boundary conditions are imposed. The on-going (and likely next future) efforts aim at determining the IOP for the diverse components, before summing them to obtain the global IOP of the water bodies. The present state of knowledge and remnant deficiencies are succinctly examined below, by starting with the water itself and then continuing with the biological component.

OPTICAL PROPERTIES OF OPTICALLY PURE SEA WATER

The density fluctuation theory (Einstein-Schmoluchowski) and the measurements³ of the scattering properties of water molecules agree very well, namely for the shape of the volume scattering function, the total scattering coefficient, b_w , and its spectral dependency. The agreement⁴ is even better if revised values for the physical constants involved in the theoretical expression of $b_w(\lambda)$ are used⁵. The slightly modified set (by about -10%) of $b_w(\lambda)$ values could be adopted without leading to important consequences. Further investigations seem to be appropriate with regards to the depolarization ratio (0.09 as measured by Morel³ vs 0.05 adopted by Buiteveld et al.⁵), which limits the accuracy of the theoretical prediction. For optically pure sea water, the increase in scattering, which results from the presence of ions and therefore from concentration fluctuations and would reach about 30% (as previously estimated³) has apparently never been confirmed, even though it appears reasonable according to the Debye theory for electrolyte solutions.

More important are the recent findings^{6,7} concerning the absorption of pure water in the spectral region of its greatest transparency. According to these new determinations, $a_w(\lambda)$, the absorption coefficient of pure (and fresh) water would be notably below the consensus values (as previously selected by Smith and Baker⁸) in the wavelength domain $\lambda = 380-500$ nm, with a minimum occurring at about 420nm, 3 times lower (0.005 vs 0.015 m^{-1}) than the old value. Such a drastic revision is of considerable impact, in particular on the understanding of the optical properties of extremely pure, oligotrophic, waters, which form a wide part of the world ocean. These new values, in the violet part of the spectrum, strongly suggest that the currently admitted absorption coefficients in the near-UV (400-300nm) domain are likely to be also revised.

ABSORPTION BY PLANKTONIC ALGAE AND OTHER PARTICLES

During the last decade various phytoplankters grown in monospecific culture have been studied in a rather systematic manner. These studies^{9,10,11,12} have demonstrated the large variability in the spectral absorption capabilities of algal cells, particularly when they are normalized with respect to Chl. The shape of the absorption spectra, beside common features due to chlorophyll *a*, is changing in response to varying (accessory) pigment composition¹³. Meanwhile, the amplitudes of the major absorption peaks are also changing, as a consequence of the package effect¹⁴. Natural assemblages have also been studied in the field^{15,16,17} by using the filter pad technique¹⁸, often followed by the extractive depigmentation method developed by Kishino¹⁹. Thus the absorption by the sole algal cells (a_p) has been separately measured, and subtracted from the total (algal and non-algal) particle absorption, a_p , to obtain the absorption by detritus, a_d , (actually by all the non-algal, suspended materials rather than by detritus, *sensu stricto*).

Recent measurements^{20,21,22}, systematically carried out in various parts of the world ocean, have revealed important features. After normalizing with respect to Chl, the Chl-specific absorption coefficients of phytoplankton ($a_p^*(\lambda) = a_p(\lambda) / \text{Chl}$) exhibit a rather regular trend, with lower values in eutrophic waters, and the highest ones in oligotrophic, low-Chl, waters. Roughly speaking, there is an increase by a factor of 10 in a_p when Chl spans 3 orders of magnitude (from 30 to 0.03 $mg\ m^{-3}$). The spectral shape of $a_p(\lambda)$ is also slightly varying with Chl²². The factor 10 is attributable (half and half, approximately) to a reduction in the package effect for the tiny algal cells which predominate in oligotrophic waters, and to an increase in accessory (photosynthetic and non-photosynthetic) carotenoids in these cells.

When dealing with the whole particle assemblage and considering $a_p^*(\lambda)$, the general ascending slope, from eutrophic to oligotrophic waters, is maintained. Compared to those for the sole phytoplankton, the absorption values for all particles are higher by about 50%. This increase seems to originate essentially from detritus, inasmuch as heterotrophic bacteria and other heterotrophic organisms have an extremely reduced impact on absorption, except perhaps in the vicinity of 415 nm, as a result of the main cytochrome absorption band^{27,28}. These new results for $a_p^*(\lambda)$, with their intrinsic non-linear character inside the Chl range, bring for the first time a good explanation to the empirical, also non-linear, relationships previously observed between $K(\lambda)$, the diffuse attenuation coefficient, and Chl^{23,24}. The exponents in these relationships can be quantitatively interpreted, as well as the variability around the average laws, which already exists in the absorption-Chl relationships, and therefore must persist in the $K(\lambda)$ -Chl relationships.

SCATTERING BY PLANKTONIC ALGAE AND OTHER PARTICLES

Again, *in vitro* measurements using organisms grown in culture¹², as well as theoretical studies^{25,26}, have greatly improved our knowledge about scattering and backscattering properties of living particles. Algal cells, including picoplankton, heterotrophic organisms and free living bacteria were studied^{12,27,28,29}. For natural heterogeneous assemblages

(algal and non-algal particles) observed in the field, the Chl-specific scattering coefficient for particles, b_p^* , has proven to be also a power function of the chlorophyll concentration^{1,30}, with an exponent (= -0.38) quite similar to those appearing for the Chl-specific absorption coefficients.

New results based on strictly coincident measurements of the pigment concentration (rosette sampling followed by HPLC determination) and of the beam attenuation coefficient (Seatech instrument attached to the rosette), once corrected for absorption, fully confirm the previous results. Because of the non-simultaneity in the measurements of the two quantities, these previous results (summarized by Fig. 5a in Gordon and Morel¹), could have been suspected of being noisy. It is not the case, and surprisingly the variability in the b-Chl relationship is not reduced in the new set of determinations. Therefore the "band" used in Gordon and Morel to demarcate the Case 1 waters remains unchanged and is not found narrower. The spectral dependency of b_p (an inverse proportionality to wavelength is usually adopted) actually lacks of systematic determinations and confirmation.

The spectrum of the backscattering coefficient is influenced in a complex manner by the absorption bands of the pigments present in algae. This has been experimentally verified¹², as well as the extremely low values of the backscattering ratio \tilde{b}_b ($= b_b/b$). Apart from the smallest species (as prochlorophytes and cyanobacteria²⁹), for which $\tilde{b}_b(\lambda)$ may slightly exceed 10^{-3} , the most common values for phytoplankters are in the 10^{-4} - 10^{-5} range. Such low values raise the question of what can be responsible for the formation of the backscattering coefficient of oceanic waters.

It has been shown²⁸ that the formation of the scattering coefficient of oceanic waters, and its variations with Chl are well understood. The algal cells are the major contributors, followed, in order of importance, by heterotrophic organisms among which the free living bacteria have an almost negligible influence; debris of all kinds contribute to the remnant and varying part. The contrary holds true for the constitution of the backscattering coefficient; algae would play a minor or even negligible role and only small sized free bacteria hardly contribute to the actual coefficient. The main part of this coefficient remains unexplained^{26,29}, and is hypothetically attributed to virtually non identified particles, such as colloids, viruses and other minute debris, the importance of which has been recently emphasized³¹.

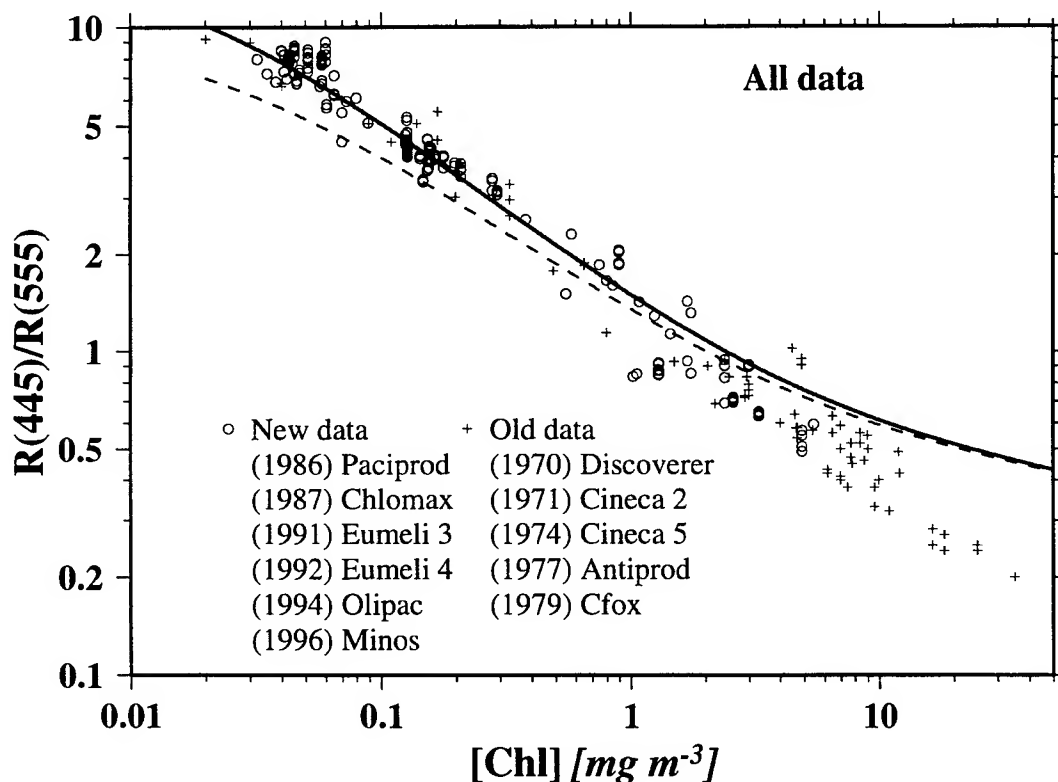
It must be recalled that $b_b(\lambda)$ for oceanic waters is only indirectly known; it is actually inferred from reflectance measurements combined with absorption measurements or assumptions about absorption. The systematic effort during the sixties and seventies aiming at studying the volume scattering function (VSF) of suspended matter in oceanic waters has not been pursued, so that reliable information about $\tilde{b}_b(\lambda)$ is still lacking, even if inverse modeling has provided some information³³. The relationships between $\tilde{b}_b(\lambda)$ and the chlorophyll concentration, as presently proposed for case 1 waters, are educated guess, used in absence of true determinations. In addition, these relationships, as those proposed by Gordon et al³³, by Morel²⁴, and by Haltrin and Kattawar (quoted in Mobley³⁴), differ in a notable fashion. These uncertainties, and also the ignorance of the variations with Chl of the actual VSF, and of its backward portion in particular, are the main weaknesses in the attempts for developing predictive models.

MODELING CASE 1 WATERS

A fully analytical model of the IOP for Case 1 waters is not yet available. Even if databases of single-particle optical properties are under development³⁵, and tentatively used³⁶, a realistic representation of natural populations of marine particulates would require a detailed knowledge of all the components (microbial, detrital and minerogenic), which is almost unreachable. It can be reasonably expected, however, that a sufficient knowledge of the major components, and of their variations with Chl, can be attained in a near future. The first step in this direction is already represented by the Chl-specific absorption of the whole particulate compartment ($a_p(\lambda)$), which has been found varying with Chl, in a rather regular way. Such a parameterization can be introduced in models, together with a similar expression for the Chl-specific scattering coefficient. As underlined above, the main limitation for a meaningful use of any RTE model originates from the imperfect representation of the VSF, and its change with varying chlorophyll concentration and with wavelength. This limitation has already been encountered (and discussed³⁷) when dealing with the bi-directional character of the ocean reflectance, heavily depending on the shape of the VSF particularly in the backward directions.

Another difficulty which deserves attention is related to the absorption by colored dissolved organic matter (CDOM). If the spectral effect of CDOM is already well known and regularly documented³⁸, the magnitude of this absorption in relation to Chl (a direct proportionality is often assumed³⁹) remains an open question⁴⁰.

Semi-empirical models for AOP, in particular models aiming at interpreting and predicting the spectral reflectance of oceanic waters as a function of Chl, in the perspective of remote sensing of ocean color, have been developed^{24,32}. Rather than being based on absorption, they made use of $K(\lambda)$ as a proxy for $a(\lambda)$. Interestingly, if the new results concerning $a_p(\lambda)$ are used instead of $K(\lambda)$, the previously modeled²⁴ $R(\lambda)$ - Chl relationships are left practically unchanged, and are thus confirmed with a completely independent data set. Combined with a parameterization of $b(\lambda)$ as a function of Chl (generally taken in ref 1), an expression describing the backscattering ratio is also needed. The main weakness of present models originates from the somewhat arbitrary choice of such an expression; it is particularly crucial when the backscattering coefficient of the water body becomes dominated by that of particles (high Chl), while at low Chl, when the molecular scattering is dominating, the uncertainty is vanishingly low.



Ratio of the reflectances of oceanic Case 1 waters at two wavelengths 445 and 555 nm, plotted as a function of the chlorophyll concentration within the upper layers. Symbols are for old and recent determinations, as indicated, and curves for modeled values (see text). These data have been obtained in Pacific Ocean (Paciprod, Olipac, Cfox and partly Discoverer cruises), Atlantic Ocean (Chlomap, Eumeli 3 and 4, Cineca 2 and 5, and partly Discoverer), Indian Ocean - Antarctic sector (Antiprod), and Eastern Mediterranean Sea (Minos).

The modeled and experimental values can be compared in a condensed manner (Fig. 1) by plotting as a function of Chl the "blue-to-green ratio", i.e. the ratio of reflectances at 445 and 555nm. The old and more recent data are pooled together, the dashed curve is redrawn from ref 24 (Fig. 14), except for the slight change in wavelengths, and the solid curve differs from the dashed one only by replacing the previous absorption for pure water by the new values^{6,7}. Between these

two curves, the main divergence occurs, as expected, for oligotrophic waters, and the solid curve leads to a better agreement with the experimental determinations and to higher $R(443)/R(555)$ values in this Chl range. For chlorophyll concentration larger than 1 or 2 mg/m^3 , the models (insensitive to pure water absorption) do not account for the observed blue-to-green ratios, progressively departing from, i.e. below, the predicted values. To the extent that the variations in the ratio of absorption by algae [the ratio $a(555)/a(443)$] are limited, the backscattering coefficient with its spectral dependency is the only free parameter; its parameterization can be modified, and thus the model constrained to reach a better agreement. There is, however, no external and independent information to justify such a modification. From a practical viewpoint (that of using a ratio of reflectances measured at two wavelengths to infer Chl), this drawback which affects the high concentration domain is evitable, provided that confidence is given to actual data, regardless of their present predictability.

In summary, the case 1 waters constitute a rather complex system, far from being entirely analyzed and therefore from being accurately predictable. Even if recent progress allows the somewhat enigmatic, non-linear, empirical relationships to be understood, some important characteristics (VSF, backscattering ratio, sub-micrometer particles abundance) remain poorly documented. The natural variability in $a_p^*(\lambda)$ and in $b_p^*(\lambda)$, which seems confirmed, will limit the predictive skill of any model, including reflectance models. Some rules governing this variability likely exist inside the biological compartment under the control of the physical and chemical environment; they are not yet discovered. When reminding the importance of Case 1 waters in the world ocean, in terms of area or of biogeochemical impact⁴¹, improvements in the understanding of their optical behavior are certainly urgently needed. There are many good reasons for studying also the more complicated Case 2 waters; postulating that the "simple" Case 1 waters are presently well known, so that additional studies are not required, is just a bad reason, if not the worst one.

REFERENCES

1. H.R. Gordon and A. Morel, "Remote assessment of ocean color for interpretation of satellite visible imagery; a review". Lecture notes on coastal and estuarine studies, edited by R.T. Barber, C.N.K. Mooers, M.J. Bowman, and B. Zeitzschel, 114 pp., Springer-Verlag, New York (1983).
2. C. D. Mobley and others, "Comparison of numerical models for computing underwater light fields". *Appl. Opt.*, 32, 7484-7503 (1993).
3. A. Morel, "Etude expérimentale de la diffusion de la lumière par l'eau, les solutions de chlorure de sodium et l'eau de mer optiquement pures". *J. Chim. Phys.*, 10, 1359-1366 (1966).
4. A. Morel. "Optical properties of pure water and pure sea water" in *Optical Aspects of Oceanography*, edited by N.G. Jerlov and E.S. Nielsen, pp 1-24, Academic, San Diego, Cal., (1974).
5. H. Buiteveld, J.H.M. Hakvoort and M. Donze. "The optical properties of pure water". *SPIE vol 2258, Ocean Optics XII*, 174-183, (1994).
6. F.M. Sogandares. "The spectral absorption of pure water", Dissertation, Texas A&M University, College Station, Texas, (1991).
7. R.M. Pope. "Optical absorption of pure water and sea water using the integrating cavity absorptionmeter". Dissertation, Texas A&M University, College Station, Texas. (1993).
8. R.C. Smith and K.S. Baker. "Optical properties of the clearest natural waters". *Appl. Opt.*, 20, 177-184, (1981).
9. A. Morel and A. Bricaud. "Inherent optical properties of algal cells, including picoplankton: theoretical and experimental results". in T. Platt and W.K.W. Li (eds); *Photosynthetic Picoplankton*, Can. Bull. Fish. Aquat. Sci., 521-559, (1986).
10. S. Sathyendranath, L. Lazzara and L. Prieur. "Variations in the spectral values of specific absorption by phytoplankton". *Limnol. Oceanogr.* 32, 403-415, (1987).
11. A. Bricaud, A.-L. Bedhomme and A. Morel. "Optical properties of diverse phytoplanktonic species: experimental results and theoretical interpretation". *J. Plankton Res.* 10, 851-873, (1988).
12. Y.-H. Ahn, A. Bricaud and A. Morel. "Light backscattering efficiency and related properties of some phytoplankters". *Deep-sea Res.* 39, 1835-1855, (1992).
13. R.R. Bidigare, M.E. Ondrusek, J.H. Morrow and D.A. Kiefer. "In vivo absorption of algal pigments" *SPIE vol 1302, Ocean Optics X*, 290-302, (1990).

14. J.T.O. Kirk. "A theoretical analysis of the contribution of algal cells to the attenuation of light within waters, II, Spherical cells; New Phytol., 75, 21-36, (1975).
15. C.S. Yentsch and D.A. Phinney. "A bridge between ocean optics and microbial ecology". Limnol. Oceanogr., 34, 1694-1705, (1989).
16. B.G. Mitchell and D.A. Kiefer. "Variability in pigment specific particulate fluorescence and absorption spectra for light limited phytoplankton". Deep-Sea Res., Part A, 38, 639-663, (1988).
17. A. Bricaud and D. Stramski. "Spectral absorption coefficients of living phytoplankton and nonalgal biogenous matter: A comparison between the Peru upwelling area and Sargasso Sea" Limnol. Oceanogr., 35, 562-582, (1990).
18. H.G. Trüper and C.S. Yentsch. "Use of glass fiber filters for the rapid preparation of in vivo absorption spectra of photosynthetic bacteria". J. Bacteriol., 94, 1255-1256, (1967).
19. M. Kishino, M. Takahashi, N. Okami and S. Ichimura. "Estimation of the spectral absorption coefficients of phytoplankton in the sea". Bull. Mar. Sci., 37, 634-642, (1985).
20. S.A. Garver, D.A. Siegel and B.G. Mitchell. "Variability in near-surface particulate absorption spectra: What can a satellite ocean color imager see?". Limnol. Oceanogr., 39, 1349-1367, (1994).
21. J.S. Cleveland. "Regional models for phytoplankton absorption as a function of chlorophyll a concentration". J. Geophys. Res., 100, C7, 13 333-13 344, (1995).
22. A. Bricaud, M. Babin, A. Morel and H. Claustre. "Variability in the chlorophyll-specific absorption coefficients of natural phytoplankton: Analysis and parameterization". J. Geophys. Res., 100, C7, 13 321-1332, (1995).
23. K.S. Baker and R.C. Smith. "Bio-optical classification and model of natural waters II" Limnol. Oceanogr., 27, 500-509, (1982).
24. A. Morel. "Optical modeling of the upper ocean in relation to its biogenous matter content (Case 1 waters)". J. Geophys. Res., 93, C9, 10 749-10 768, (1988).
25. A. Morel and A. Bricaud. "Theoretical results concerning the optics of phytoplankton, with special reference to remote sensing applications". COSPAR/SCOR/IURCM Symposium "Oceanography from Space", Venice, Plenum Press, New York, pp313-327, (1980).
26. D. Stramski and D.A. Kiefer. "Light scattering by microorganisms in the open ocean". Prog. Oceanogr., 28, 343-383, (1991).
27. A. Morel and Y.-H. Ahn. "Optical efficiency factors of free living bacteria: Influence of bacterioplankton upon the optical properties and particulate organic carbon in oceanic waters". J. Mar. Res., 48, 145-175, (1990).
28. A. Morel and Y.-H. Ahn. "Optics of heterotrophic nanoflagellates and ciliates: A tentative assessment of their scattering role in oceanic waters compared to those of bacterial and algal cells". J. Mar. Res., 49, 177-202, (1991).
29. A. Morel, Y.-H. Ahn, F. Partensky, D. Vaultot and H. Claustre. "Prochlorococcus and Synechococcus: A comparative study of their optical properties in relation to their size and pigmentation". J. Mar. Res., 51, 617-649, (1993).
30. A. Morel. "Chlorophyll-specific scattering coefficient of phytoplankton; a simplified theoretical approach". Deep-Sea Res., 34, 1095-1105, (1987).
31. I. Koike, S. Hara, K. Terauchi and K. Kogure. "Role of sub-micrometer particles in the ocean". Nature, 345, 242-244, (1990).
32. C.S. Roesler and M.J. Perry. "In situ phytoplankton absorption, fluorescence emission, and particulate backscattering spectra determined from reflectance". J. Geophys. Res., 100, C7, 13 279-13 294, (1995).
33. H. R. Gordon and others, "A semianalytic model of ocean color". J. Geophys. Res. 93, D9, 10 909-10 924, (1988).
34. C.D. Mobley. "Light and Water, radiative transfer in natural waters" Academic Press, pp 592, (1994).
35. D. Stramski and C.D. Mobley. "Effects of microbial particles on oceanic optics: A database of single-particle optical properties". Limnol. Oceanogr., in press (1997).
36. C.D. Mobley and D. Stramski. "Effects of microbial particles on ocean optics: Methodology for radiative transfer modeling and example simulations". Limnol. Oceanogr., in press, (1997).
37. A. Morel and B. Gentili. "Diffuse reflectance of oceanic waters: its dependence on Sun angle as influenced by the molecular scattering contribution". Appl. Opt., 30, 4427-4438, (1991).
38. C.S. Roesler, M.J. Perry and K.L. Carder. "Modeling in situ phytoplankton absorption from total absorption spectra in productive inland waters". Limnol. Oceanogr., 34, 1510-1523, (1989).
39. L. Prieur and S. Sathyendranath. "An optical classification of coastal and oceanic waters based on the specific absorption of phytoplankton pigments, dissolved organic matter and other particulate materials". Limnol. Oceanogr., 26, 671-689, (1981).
40. D.A. Siegel and A.F. Michaels. "Quantification of non-algal light attenuation in the Sargasso Sea: Implications for biogeochemistry and remote sensing". Deep-Sea Res. II, 43, 321-345, (1996).

41. D. Antoine, J.M. André and A. Morel. "Oceanic primary production 2. Estimation at global scale from satellite (coastal zone color scanner) chlorophyll". *Global Biogeochem. Cycles*, 10, 57-69, (1996).

PHOTOBIOLOGY OF THE DEEP TWILIGHT ZONE AND BEYOND (A Review)

Talbot H. Waterman, Biology Department, Yale University, P.O. Box 208103, New Haven, CT, USA, 06520-8103

Keywords: optic adaptations, twilight zone, sunlight, bioluminescence, aphotic zone glow?, eyes, light organs, visual pigments, symbiotic bacteria, hydrothermal vents

Photobiology in the twilight zone of the deep sea depends on faint light of two, or possibly three, origins: sunlight, bioluminescence and some visible radiation near the bottom associated with hydrothermal vents. The deep twilight zone also contains two quite distinct ecosystems: the vast open ocean *pelagic* regime far from the shore and the bottom as well as the far less expansive benthic regime with quite different characteristic animals that live on, in or near the sea bottom.¹⁰ Most of the whole ocean's benthic regime with a mean depth over 3000m is well below the twilight zone, which eliminates sunlight as a light source there. Many of the most familiar deepsea animals with their spectacular arrays of dermal light organs and remarkable eyes are from the pelagic regime.^{19, 25} The less familiar benthic fishes and crustaceans sometimes have curious internal light organs powered by bacteria¹³ and occasional incredibly modified eyes.³⁰ With the exception of those on the fishing rods of most female deepsea anglerfish, where the light is produced by symbiotic bacteria, all the numerous light organs of pelagic deepsea fishes are generally believed to manage their own chemiluminescence independent of luminous bacteria.¹⁷

The benthic fauna is apparently unique in including scattered and rather ephemeral communities which do not depend on sunlight and photosynthesis as a source of their organic carbon and metabolic energy. Instead a number of invertebrates inhabiting hydrothermal vents and cold mineral seeps obtain these necessities from the chemosynthesis of autotrophic bacteria.²⁹ The microorganisms, such as sulfur bacteria, are either eaten by the animals concerned or live as symbionts within them. The faunas of the two subhabitats show only minor overlap in species makeup and seem to reflect quite distinct evolutionary histories. For instance brotulid and macrourid fishes, common near and on the bottom are only remotely related to lantern fishes and stomiids typical of the pelagic deepsea regime.

With regard to the two or three kinds of light in deep water, *sunlight* in the twilight zone is dim, on the verge of extinction; diffuse, but still ellipsoidal in distribution with the major axis close to vertical; nearly monochromatic, with a lambda max near 465 nm, and partially linearly polarized. *Bioluminescence*, the second light source, is, of course far dimmer than daylight in air or in the upper water levels. Evidence for a third source of deepsea light has been sought to explain highly modified compound eyes in deepwater shrimp (*Rimicaris*) swarming around hydrothermal vents well below the twilight zone at 3500m depth on the Midatlantic Ridge.³² Without the usual cornea, crystalline cones and eyestalks, these receptors have thousands of hyper-developed reticular cells with large rhabdoms and dense visual pigment.³⁰ Instrumental evidence for luminous glows from the outflow of black smoker hydrothermal vents suggests that the shrimp photoreceptors have some light to see at depths usually considered far below the photic zone.³³ Whether black body radiation from high temperature hydrothermal plumes or some other source of light is involved remains to be seen. Can the somewhat comparable cephalic eyes of the benthic fish *Ipnops* serve a similar function?

Animal light equals or exceeds the ambient sunlight intensity in clearest ocean water at depths of about 500m and greater. At 1000m bioluminescence could be six or seven log units more intense than the ambient daylight. Usually, animal light is a point or small angle source.¹⁶ Peak wavelengths may range widely from violet to deep red, but typically lie between 450 and 525nm¹⁵. Instead of being mainly unidirectional like downwelling sunlight, bioluminescence may come from any spatial angle relative to the observer. Light from complex light organs of crustaceans, squids and fishes typically matches rather closely both the spectral sensitivity of the animal's retina as well as the spectral distribution of the deepwater sunlight. This would maximize the range at which luminous flashes could be seen, perhaps to 100 to 150m.³

Bioluminescence, unlike sunlight, may be present 24h a day in deep water and luminous species range, specially among benthic and benthopelagic types, down into the deepest trenches.¹⁷ Observations and experiments on shallow water animals have shown that bioluminescence has many functions²⁷: species and sex recognition, schooling behavior, mating behavior, prey attraction, prey detection, predator startling, escape cover or decoy (for externally secreted luminescent clouds or blobs) and the so-called burglar alarm effect. This last function is served

when the luminescence of dinoflagellates or some passive animal like a jellyfish evoked by the attack of a predator, attracts another predator which harasses or eliminates the original aggressor.⁹

One of the most astonishing uses of bioluminescence in counterillumination or *camouflage* is an exception for which direct observations and experiments have been carried out on a few pelagic deepwater animals (hatchet fishes, lantern fishes and squids such as *Abralia*). Deepwater animals using ambient sunlight to locate prey or avoid predators, would get little signal from most nearby animal's reflected daylight. The common black, brown or deep red pigment of twilight zone animals would render them largely invisible looking horizontally or downward in the weak blue light present.²⁵ Yet when looking upward, the silhouetted shadows of animals above the potential prey or predator might indeed provide good visual images. This poses a double challenge: how best to see such silhouettes of potential prey or predators and how best to avoid casting shadows for the benefit of potential prey or predators?

Correlated adaptations of eyes and light organs have provided remarkable responses to this dilemma. Briefly, a large array of photophores is used by squids and many fishes, and a more modest one, by crustaceans, to match closely the intensity, wavelength and directionality of downwelling sunlight. The research of Denton and others⁴ on fish and Young's data³⁵ for squids show that their counterillumination provides extraordinary camouflage to weaken or block contrast for other animals' overhead lines of sight. There is evidence that dedicated visual circuits are present constantly to monitor sunlight intensity and perhaps wavelength so as to provide continuous regulation of light organs' emission to match the ambient daylight. Special retinal pockets in fishes may serve this purpose while squids use extra ocular light sensors. In this connection, the rather surprising presence of more than one visual pigment in eyes of deepsea squids and fishes may provide fine-tuning to break the luminous camouflage. The puzzling widespread occurrence of yellow pigments in the lenses of upper twilight zone fishes may act as a similar spoiler by weakening or blocking any residual sunlight from reaching the retina.^{8, 26}

The dragon fish, *Malacosteus*, and two related genera, are notable for producing deep red light, thanks to a red filter over their large subocular light organs.^{4, 31} They also possess red-sensitive cones in their retinas as well as deep red reflecting layers back of their retinas. This whole exceptional long wavelength system may function in hunting red shrimps and fishes as well as in a private communication system undetectable by other animals.

Strangely, despite numerous recent deepsea dives by crewed research submarines and the like, almost no direct data, except those on counterillumination and the burglar alarm effect, are available on *in situ* luminescence of deep sea animals. The vivid luminescence of various deep pelagic types described in the 1930's by William Beebe from the bathysphere at depths off Bermuda is quite exceptional. Hence most of bioluminescence's numerous proposed functions in deep water remain untested and unproved. In contrast, the complex structure and patterns of the dermal photophores which produce light in deepwater pelagic types have been widely studied in crustaceans, cephalopods and fishes since the pioneer cruises of "Challenger" and "Valdivia." The lenses, reflectors, pigment screens and color filters often process the light produced by the oxidative chemiluminescence of the light emitting cells. The biochemistry of self luminescence has been detailed mainly in shallow water species although some recent research has illuminated the symbiotic interactions between hosts, such as cephalopods⁷ and deepsea anglerfish,¹⁴ and the luminous bacteria which they "cultivate" in their light organs.

The quite different optical properties of sunlight and animal light in the twilight zone, as well as their distinct potential uses are reflected in specializations of both the compound and the camera eyes of its various inhabitants. Optical parts of their eyes or their retinas seem particularly receptive to one or the other light stimulus. Their prominence shifts in related species which live at different depths where the ratios of the two light sources change.²² Thus in twilight zone sunlight vision depends on detecting and recognizing light reflected by animal surfaces or shadows they cast in downwelling light. Contrast of intensity or wavelength is essential for discriminating object and background. Deepwater sunlight no doubt also helps synchronize biological clocks and through its verticality below the critical depth provides a reference for spatial orientation.

Vision at threshold light intensities depends optically on collecting and focusing as much light as possible on an optimally sensitive photoreceptive membrane surface.^{20,23,24} Also efficiencies of photon capture and transduction to threshold neural excitation as well as a low noise level in the membrane itself may all be critical. For camera eyes increasing the size of the lens is important in dim light. Yet there are practical limits to lens and eye sizes. Fishes and cephalopods even in shallow water, already have large spherical lenses to counteract the near lack of corneal surface refraction underwater. In some deepsea fishes with eyes of normal hemispherical shape, the lens nearly fills the eye cup and protrudes about half its volume through the pupil which has a diameter nearly as

large as the eye.²⁵ In such cases only part, or none, of the image can be sharply focused on the retina. Often in deepsea fish eyes there are aphakic spaces around the lens. These might be intolerable for imaging at moderate to high light intensities, but around threshold any light may help provide some signal.

Alternatively, a number of fishes and some squids with tubular eyes have combined a large lens with a good focus for a much reduced visual field. Such elongate eyes, which are also present in some owls and a nocturnal primate, accomplish this with a lens which completely fills one end of a cylinder and a small retina the other.²⁴ Because these eyes in deepsea fishes cannot be swiveled around like those of a chameleon, there is a substantial reduction in the visual field surveyed. This may be supplemented by a secondary retina. A comparable increase in light collecting power at the expense of a wide angle of view also occurs in a variety of crustacean compound eyes. Remarkable F numbers of 0.5 or less are known to be present. Certain deepwater shrimps, krill and pelagic amphipods have upward looking areas of their eyes with unusually large ommatidia, which are the building blocks beneath each facet.²³ These large aperture units collect more light than ordinary ones and their optical axes diverge only slightly. Hence their visual fields are close together or overlap so that a large number of units receive light from the same point in the reduced visual field. Narrow waveguide-like channels transmit light to deep-lying photoreceptor elements. The second part of the double eye has a much wider visual field sampled by less sensitive units providing less detailed definition.

Another way to lower an eye's threshold is to place a reflector behind the retina so that the receptor cells have a second chance to intercept incoming photons. Like many terrestrial and aquatic nocturnal animals, twilight zone fishes and crustaceans often have such ocular reflectors. Most of these are white, but in certain fishes they may be rather brightly blue or red.³ Some of them are specular, others diffuse reflectors.¹⁸ Curiously squid and octopus, highly visual animals common in the deep sea, have not been found to have tapeta in their eyes even though they have excellent reflectors in their complex light organs.

In the absence of experimental and field data, estimates suggest that some deepsea compound eyes are extraordinarily sensitive.²³ In decapod crustaceans these are so-called superposition eyes. Their optical pattern is such that many facets collect light from a point in object space and by means of multiple mirrors direct it onto a corresponding point in image space. Such mechanisms are present in dim light adapted forms like crayfish and lobsters. They are particularly well developed in certain deep water species.¹¹ The bathypelagic shrimp *Oplophorus*, for example, may be about 80 times more sensitive to low light intensities than its shallow water relative *Palaemonetes*.²¹ Even the latter's threshold is about the same as that of the very sensitive dark adapted human eye.³ Considerably more sensitive even than *Oplophorus*, the deepwater isopod *Cirolana* appears to have a light collecting capacity 1000 times greater than that of the honey bee. Physiological and behavioral support for such bold extrapolations is much needed.

In addition to the dioptric aspects of vision at marginal light intensities, the retinas and visual pigments of deepwater eyes have been extensively studied. Compared with shallow water relatives, receptor units in the retinas of twilight zone species tend to be axially longer, and sometimes larger in diameter. Both changes could increase the chances of photon capture by a receptor unit. Although the dim and nearly monochromatic nature of twilight zone sunlight should generally favor uniform all rod retinas in fishes living there, retinal areas of pure cones and even pure rod foveas have been reported in various pelagic twilight zone species. Even a retina made up mostly of cones, usually functional for color vision at much higher light intensities, is known for the deepsea fish *Omosudis*.²⁴ This species also has unusually large eyes for a deep pelagic species.

Presumably to increase their threshold sensitivity, a number of deepsea fishes have banked retinas with several to many layers of receptor outer segments. One species is known to have more than 25 such in-depth layers in its fovea. A banked retina has recently been reported also in the luminous deepwater squid *Watasenia*.²⁸ Such sequential receptors could act as more efficient photon catchers without increasing visual pigment density (and thus potentially decreasing the signal to noise ratio). Calculated absorption curves for a banked retina with only a single visual pigment suggest that at least the first five layers should all be catching photons in the peak wavelengths around 480nm.⁶ Similarly the 10th and 25th layers would be still be absorbing photons but at wavelengths remote from the pigment's lambda max. This shift, of course, depends on the outer layers' screening effect on deeper units.

Among other things the optical density of visual pigment in deepsea eyes usually is significantly greater than in shallow water species. Yet pigment density, in addition to increasing photon catches, also determines the

level of membrane noise, "dark light," induced by spontaneous pigment isomerization. In fishes, squids and crustaceans in deep water, the peak absorption has shifted from around 500nm or higher in shallow water marine species towards 475 to 490 nm. For a long time this blue shift with increasing depth has been interpreted as a molecular adaptation to maximize absorption of the deepest penetrating wavelengths in the clearest ocean water. Yet in fishes the absorption curves of visual pigments in the receptor outer segments are sufficiently flat around their maxima to question the functional gain of the observed shift.¹² Recent research on a large number of closely related cottoid fish species at various depths down to the bottom at 1600m in Lake Baikal does show a blue shift in the peak absorption of visual pigments with increasing depth.¹ Yet in this freshwater case the shift is away from the maximum penetrating wavelength. In Lake Baikal yellowish water in the top 100m or so filters the light reaching the much clearer deeper water so that its peak wavelength is in the greenish-blue above 500nm.

An extraordinary pair of deepsea eyes, each operating like a reflecting telescope, is present in the common twilight zone pelagic ostracod *Gigantocypris*.²⁰ This nearly spherical planktonic form, despite its name, is only about a centimeter in diameter, but large for an ostracod. Two large cup-shaped eyes are prominent because of their silvery reflection which shines through a clear window in an otherwise opaque orange carapace. The reflectors are curiously shaped (spherical in the vertical plane and parabolic horizontally). They collect light and focus it on sausage-shaped many-layered retinas suspended in front of them where the secondary mirror would be in a reflecting telescope. Although image quality is no doubt quite poor, the eye's F number may reach a remarkable 0.25 and their light collecting ability could be about 25 times that of a fish eye lens. Interestingly, most of the light organs in lantern fishes, the myctophids, that are numerous in both individuals and species world wide in the upper twilight zone, use an optical system somewhat similar to that in *Gigantocypris* eyes but in reverse.⁵ The light producing cells in these myctophid photophores lie inside a bar that crosses the aperture, as in a common type of dentists' light. The emitted light radiates inward into a shallow concave silvery reflector so shaped that it forms an emergent beam directed ventrolaterally.

In the pelagic regime below the twilight a general decrease in dependence on light seems to occur. Some types of luminescence are common all the way down to the bottom of the trenches, but the dermal photophores of most shrimps, squids and fishes become reduced or absent at increasing depths in the deep aphotic zone. For instance, a bathy pelagic species of *Gonostoma* has smaller eyes and smaller light organs than a closely-related meso pelagic species. The deeper living one also has smaller optic lobes of the brain as well as reduced gill filaments.²⁵ This suggests that at lower light intensities the animals are overall less active than in well-lit environments. It has been known for some time that the metabolic rates of certain pelagic deepwater animals decrease significantly with increasing habitat depth. Yet in other kinds of animals, this correlation is absent. Decreasing availability of food or increasingly high ambient pressure seem inadequate to account for such differences. A recent detailed survey of the facts already known for different kinds of animals caught in different locations at various depths indicates that light and vision may be involved.² Those animals with diminishing metabolic rates with depth are squids, pelagic crustaceans and fishes that have well developed image-forming eyes. Jelly fish, comb jellies, arrow worms and other pelagic types that lack image-forming eyes, do not have lower metabolic rates when they live at greater depths. How image forming eyes affect metabolic rates remains an intriguing question.

REFERENCES

1. Bowmaker, J. K., V. I. Govardovskii, S. A. Shukalyukov, L. V. Zueva, D. M. Hunt, V. G. Sideleva and O. G. Smirnova, Visual pigments and the photic environment: the cottoid fish of Lake Baikal. *Vision Res.* 34: 591-605, 1995.
2. Childress, J. J., Are there physiological and biochemical adaptations of metabolism in deep-sea animals? *Trends in Ecol. Evolution* 10:30-36, 1995.
3. Denton, E. J., Light and Vision at depths greater than 200 meters. pp. 127-148 in ref. 19, 1990.
4. Denton, E. J., J. B. Gilpin-Brown and P. G. Wright, The angular distribution of the light produced by some mesopelagic fish in relation to their camouflage. *Proc. R. Soc. London*, B182: 145-158, 1972.
5. Denton, E. J., P. J. Herring, E. A. Widder, M. F. Latz and J. F. Case, The roles of filters in the photophores of oceanic animals and their relation to vision in the oceanic environment. *Proc. R. Soc. London*; B225: 63-97, 1985.
6. Denton, E. J. and N. A. Locket, Possible wavelength discrimination by multibank retina in deep-sea fishes, *J. Mar. Biol. Assoc. U.K.*, 69: 409-435, 1989.
7. Doi no, J. A., and M. J. McFall-Ngai, A transient exposure to symbiosis-competent bacteria induces light organ morphogenesis in the host squid. *Biol. Bull. (Woods Hole)*, 189: 347-355, 1995.

8. Douglas, R. H., J. C. Partridge and A. J. Hope, Visual and lenticular pigments in the eyes of demersal deep-sea fishes. *J. Comp. Physiol. A*, 177: 111-122, 1995.
9. Fleischer, K. J. and J. F. Case, Cephalopod predation facilitated by dinoflagellate luminescence. *Biol. Bull. (Woods Hole)*, 189: 263-271, 1995.
10. Gage, J. D. and P. A. Tyler, *Deep-sea Biology*. 504pp. Cambridge University Press, Cambridge, 1991.
11. Gaten, E., P. M. J. Shelton and P. J. Herring, Regional morphological variations in the compound eye of certain mesopelagic shrimps in relation to their habitat. *J. Mar. Biol. Assoc. U.K.*, 72: 61-75, 1992.
12. Goldsmith, T. H., Optimization, constraint, and history in the evolution of eyes. *Quart. Rev. Biol.*, 65: 281-322, 1990.
13. Hastings, J. W., Bioluminescence pp. 665-681 in N. Sperelakis (ed.) *Cell Physiology Source Book*. 738pp. Academic Press, San Diego, 1995.
14. Haygood, M. G., Light organ symbiosis in fishes. *Crit. Revs. Microbiol.*, 19: 191-216, 1993.
15. Herring, P. J., The spectral characteristics of luminous marine organisms. *Proc. R. Soc. London*, B220: 183-217, 1983.
16. Herring, P. J., How to survive in the dark: bioluminescence in the deep sea. pp. 323-350 in M. S. Laverack, *Physiological Adaptations of Marine Animals*, Soc. Exp. Biol. Symp. 39, Cambridge, 1985.
17. Herring, P. J., Systematic distribution of bioluminescence in living organisms. *J. Biolum. Chemilum.*, 1:147-163, 1987
18. Herring, P. J., Reflective systems in aquatic animals. *Comp. Biochem. Physiol.*, 109A: 513-546, 1994
19. Herring, P. J., A. K. Campbell, M. Whitefield and L. Maddock (eds.), *Light and Life in the Sea*. 357pp. Cambridge University Press, Cambridge, 1990.
20. Land, M. F., Optics and vision in invertebrates. pp. 471-592 in H. Autrum (ed.) *Handbk of Sensory Physiology*, Vol. VII/6B, 629pp., Springer-Verlag, Berlin, 1981.
21. Land, M. F., Crustacea. pp. 401-438 in M. A. Ali (ed.) *Photoreception and Vision in Invertebrates*, 858pp. Plenum Press, New York, 1984.
22. Land, M. F., The eyes of hyperiid amphipods: relations of optical structure to depth. *J. Comp. Physiol.*, A, 164: 751-762, 1989.
23. Land, M. F., Optics of the eyes of marine animals. pp. 149-166 in ref. 19, 1990.
24. Locket, N. A., Adaptations to the deep-sea environment. pp. 68-192 in F. Crescitelli (ed.) *Handbk of Sensory Physiology*, Vol. VII/5, 813pp., Springer-Verlag, Berlin, 1977.
25. Marshall, N. B., *Deep-Sea Biology*. 566pp. Garland STPM Press, New York, 1979.
26. Matsui, S., M. Seidou, K. Narita and M. Michinomae, Adaptations of a deep-sea cephalopod to the photic environment. *J. Gen. Physiol.*, 92: 55-66, 1988.
27. McFall-Ngai, M. J. and P. V. Dunlap, Three new modes of luminescence in the leionathid fish, *Gazza minuta*: discrete projected luminescence, ventral body flash and buccal luminescence. *Mar. Biol.*, 73: 227-237, 1983.
28. Michinomae, M., H. Masuda, M. Seidou and Y. Kito, Structural basis for wavelength discrimination in the banked retina of the firefly squid *Watasenia scintillans*. *J. Exp. Biol.*, 193:1-12, 1994
29. Nelson, D. C., and C. R. Fisher, Chemoautotrophic and methanotrophic endosymbiotic bacteria at deep-sea vents and seeps. pp. 125-167 in D. M. Karl (ed.) *The Microbiology of Deep-sea Hydrothermal Vents*. CRC Press, Boca Raton, 1995.
30. O'Neil, P. J., R. N. Jinks, E. D. Herzog, B. Battelle, L. Kass, G. H. Renninger and S. C. Chamberlain, The morphology of the dorsal eye of the hydrothermal vent shrimp, *Rimicaris exoculata*. *Visual Neuroscience*, 12, 861-875, 1995.
31. Partridge, J. C. and R. H. Douglas, Far-red sensitivity of dragon fish. *Nature*, 375:21-22, 1995.
32. Van Dover, C. L., E. Z. Szuts, S. C. Chamberlain and J. R. Cann, A novel eye in "eyeless" shrimp from hydrothermal vents of the Mid-Atlantic Ridge. *Nature* 337: 458-460, 1989.
33. Van Dover, C. L., J. R. Cann, C. Cavanaugh, S. Chamberlain, J. R. Delany, D. Janecky, J. Imhoff, J. A. Tyson, et al., Light at deep sea hydrothermal vents. *EOS, Trans., Am. Geophys. U.*, 75:41-2, 1994
34. Warren, E. J., and P. D. McIntyre, Strategies for retinal design in arthropod eyes of low F-number. *J. Comp. Physiol. A*, 168: 499-512, 1991.
35. Young, R. E., and C. F. E. Roper, Intensity regulation of bioluminescence during countershading in living midwater animals. *Fishery Bull.*, 75: 239-252, 1977.

Yellow substances in the coastal waters of the Gulf of Maine: implications for ocean color algorithms.

Charles S. Yentsch and David A. Phinney

Bigelow Laboratory for Ocean Sciences, McKown Point, W. Boothbay Harbor, ME, USA, 04575.

ABSTRACT

We believe that the coastal estuaries of the Gulf of Maine during spring runoff are among the worst possible cases for the measurement of phytoplankton chlorophyll by satellite colorimetry. Five coastal sections were sampled during May, 1996, extending from the 100m isobath shoreward to the mouths of major rivers in the southern Gulf of Maine. Water columns were dominated by short wavelength absorbing materials of terrestrial origin (yellow substances) which, like many coastal areas, are inversely correlated with salinity. Excluding water absorption which is negligible at short visible wavelengths, we have modeled the system using two major absorbers: dissolved yellow substances and particulates. In Gulf of Maine coastal waters during spring, 80-90% of the total absorption coefficient at short visible wavelengths is due to yellow substances. At salinities greater than 30 parts per thousand and at wavelengths longer than 450nm, the dominance of dissolved yellow substances decreases.

In terms of remote sensing reflectance, the use of two wavelength ratio algorithms leads to disastrous overestimates of phytoplankton chlorophyll concentrations. On the positive side, this dataset will be useful for testing algorithms designed to retrieve phytoplankton chlorophyll from water leaving radiances measured at stations with high concentrations of colored dissolved organic matter.

2. INTRODUCTION

European oceanographers have long recognized the importance of dissolved yellow substances in determining ocean color. It has been shown that, for many areas, there exists a close correspondence between salinity and the concentration of short wavelength absorbing yellow substances (Hojerslev et al., 1996). During the development of chlorophyll algorithms for the Coastal Zone Color Scanner (CZCS), it was recognized that the presence of these colored dissolved organic materials in high concentrations would confound estimates of phytoplankton pigments. In an attempt to avoid these errors, the CZCS NET Team elected to image areas of the ocean where surface salinities were known to be greater than 32 parts per thousand (Yentsch, 1983). With the impending availability of new ocean color products from sensors such as OCTS and SeaWiFS, serious consideration must be given to the problem of correcting phytoplankton chlorophyll estimates for the presence of yellow substances if reliable measurements of pigments are to be made from space.

In the Gulf of Maine, we have attempted to assess the worst case scenario for the competitive influence of yellow substances in coastal waters which is primarily transported to the open ocean by freshwater inflow from riverine sources (Figure 1). We have measured the distribution of the absorption coefficients of yellow substances (a_y) and particulates (a_p) in the nearshore waters of five rivers along the southern coast of the Gulf of Maine. In this report, we have focussed on the

Kennebec River estuary in order to assess the dominance of yellow substance absorption over phytoplankton chlorophyll

3. METHODS

Stations were spaced 4-5km apart along straight line transects from the head of the Merrimack, Piscataqua, Saco, Kennebec and Sheepscot River estuaries to the 100m isobath. Temperature, salinity and *in-situ* fluorescence were profiled using a SeaCat 19 CTD/WetStar mini-fluorometer package. Discrete water samples were obtained using 5 liter Niskin bottles from three depths at stations shallower than 15m, five depths at deeper stations. Aliquots of sample were filtered through Millipore HA 0.45 μ m filters and analysed for chlorophyll fluorimetrically by the method of Yentsch and Menzel (1963). Total suspended solids (TSS) samples were collected on preweighed Watman GFF filters, dried and reweighed by the method of Strickland and Parsons (1972). Spectral particulate absorption (a_p 350-750nm) samples were filtered through Whatman GFF filters and analysed using a Bausch and Lomb dual beam spectrophotometer by the method of Yentsch and Phinney (1989). Dissolved yellow substance absorption (a_y 200-750nm) samples were filtered using 0.22 μ m Millipore Sterivex-GS cartridges and stored in amber glass bottles. Spectral measurements were obtained using 10cm quartz cuvettes in a dual beam spectrophotometer with 0.22 μ m filtered Nannopure water in the reference cell (Phinney and Yentsch, 1991). Finally, a Satlantic TSRB II reflectance buoy was deployed for 15 minutes at each station to obtain measurements of surface incident solar irradiance (E_{da}) and upwelling radiance (L_{uw}) in seven wavelength bands (406, 412, 443, 490, 510, 555 and 665nm). One minute averaged data were post-processed by propagating E_{da} across the surface interface to the depth of the upwelling sensor (0.7m) before calculating remote sensing reflectance R_{rs} as the ratio E_{dw}/L_{uw} (Phinney, et al., this volume).

4. RESULTS

In the Kennebec River estuary, the discharge of dissolved yellow substances (Figure 2) mirrors the strong frontal pattern set up by a combination of steep temperature and salinity gradients observed on the shoreward side of the section (Figure 3). The combination of warm freshwater flowing seaward over cool salty water produces a strong density gradient with depth seaward of the main discharge of freshwater (Figure 4a). This is in contrast to the shallower region which appears to be vertically mixed by tidal flow or current velocity, or a combination of both. High levels of yellow substance absorption can be seen across the surface of the section with extremely high levels associated with the low salinity surface waters extending from the vertically mixed region to 10km offshore. The highest concentrations of chlorophyll are observed in the stratified offshore region where the subsurface chlorophyll maximum occurs between 10-20m with values greater than 10 μ g/L. Surface chlorophyll concentrations range from 2-4 μ g/L.

The surface values for the absorption coefficients of yellow substances, particulates and % total absorption as a function of salinity (Sal) at three visible wavelengths are shown in Figures 5-7. An inverse relationship was observed in the surface waters of the Kennebec River for a_y 400 (m^{-1}) with values slightly less than 6.0 at Sal<10ppt to 0.5 at Sal>30ppt (Figure 5a). Particulate absorption, a_p 400 (m^{-1}) was related to chlorophyll concentration with values less than 1.0 at all stations. Ignoring the absorption due to water, yellow substances accounted for 80-90% of the total absorption at all observed salinities (Figure 5b). The same was true at 450nm with low salinity values

of $a_{\lambda 450}$ (m^{-1}) approaching 3.0 (Figures 6a,b). At 500nm, the contribution of yellow substances was lower and more variable (Figures 7a,b). Values for $a_{\lambda 500}$ (m^{-1}) were less than 0.1 at all observed salinities and account for only 20-60% of the total absorption.

5. DISCUSSION

We have used a coastal oceanographic section extending from the mouth of the Kennebec River in the Gulf of Maine to demonstrate that the attenuation of short visible wavelengths of light in waters with high concentrations of dissolved yellow substances is pronounced; the percentage of light leaving the surface is very low. However, between 400 and 500nm, water leaving radiances increase with increasing salinity (Figure 8). The curves exhibit a hinge point at 555nm with surprising result at the red end of the spectrum. Waters with high concentrations of yellow substances show high reflectance at wavelengths greater than 650nm. Both of the chromophores a_{λ} and a_p are strong absorbers at these wavelengths at high concentrations which leads us to conclude that this phenomenon is the result of elastic scattering by refractory and non-refractory compounds in the water column. It may also be an instrumental artifact such as self-shading by the Satlantic buoy which becomes important at long wavelengths when total absorption is high (D. Clark, pers. comm.).

During the spring runoff, the amounts of dissolved yellow substances increases markedly in the estuaries of the Gulf of Maine. The magnitude of the absorption coefficient, a_{λ} , is in close agreement with those observed in the North Sea-Baltic region (Hojerslev et al., 1996). At 400 nm, the highest values exceed 5.0 (m^{-1}) but are generally confined to waters where salinity is less than 10 parts per thousand. In the open basins of the Gulf of Maine where salinities are generally greater than 30 parts per thousand, $a_{\lambda 400}$ is less than 0.1 (m^{-1}).

In the future, we will attempt to determine the seasonal cycle of primary production of these coastal waters using the next generation ocean color sensors. Accurate determinations of phytoplankton chlorophyll during the spring runoff will be crucial to this effort. It is obvious that the application of a simple two band ratio algorithm on the short wavelength side of the hinge point will produce erroneously high pigment values. We originally hypothesized that the competition by yellow substances might be minimized by using ratios at longer wavelengths, however, in waters where $a_{\lambda 400}$ is greater than 6 (m^{-1}), $a_{\lambda 650}$ is greater than the absorption due to water, such that retrieval of chlorophyll concentrations seems highly impractical. Given the spatial scales measured in the present study, 1km pixels and coastal ringing of 2-3 pixels will not be able to resolve the mouth of the Kennebec River. This will preclude the worst case scenario, however, the coastal waters of the Gulf of Maine will provide an excellent laboratory for the study of these ocean color problems.

6. ACKNOWLEDGEMENTS

The authors wish to express their thanks to J. Brown, D. I. Phinney and S. Woodman for excellent technical assistance at sea and in the preparation of this manuscript. This work was supported by grants from the Regional Marine Research Program for the Gulf of Maine (UM-S262) and by NASA (NAGW-4672).

7. BIBLIOGRAPHY

Hojerslev, N.K., N. Holt and T. Aarup. (1996) "Optical measurements in the North Sea-Baltic Sea transition zone. 1. On the origin of the deep waters in the Kattegat." *Cont.Shelf Res.*, 16:1329-1342.

Phinney, D.A. and C.S. Yentsch. (1991) "On the contribution of particles to blue light attenuation in the sea." *Jour. Plank. Res.*, 13 (Supp.): 143-152.

Strickland, J.D.H. and T.R. Parsons. (1972) "The determination of the weight of microscopic particles in sea water." In: A Pratical Handbook for the Analysis of Seawater. Fisheries Research Board of Canada, Ottawa, pp. 181-184.

Yentsch, C.S. (1983) "Remote sensing of biological substances." In: Remote Sensing Applications in Marine Science and Technology, A.P. Cracknell (ed.), D. Reidel Co., pp.263-297.

Yentsch, C.S. and D.W. Menzel. (1963) "A method for the determination of phytoplankton chlorophyll and phaeophytin by fluorescence." *Deep Sea Res.*, 10: 221-231.

Yentsch, C.S. and D.A. Phinney. (1989) "A bridge between ocean optics and microbial ecology." *Limnol. Oceanogr.*, 34: 1698-1709.

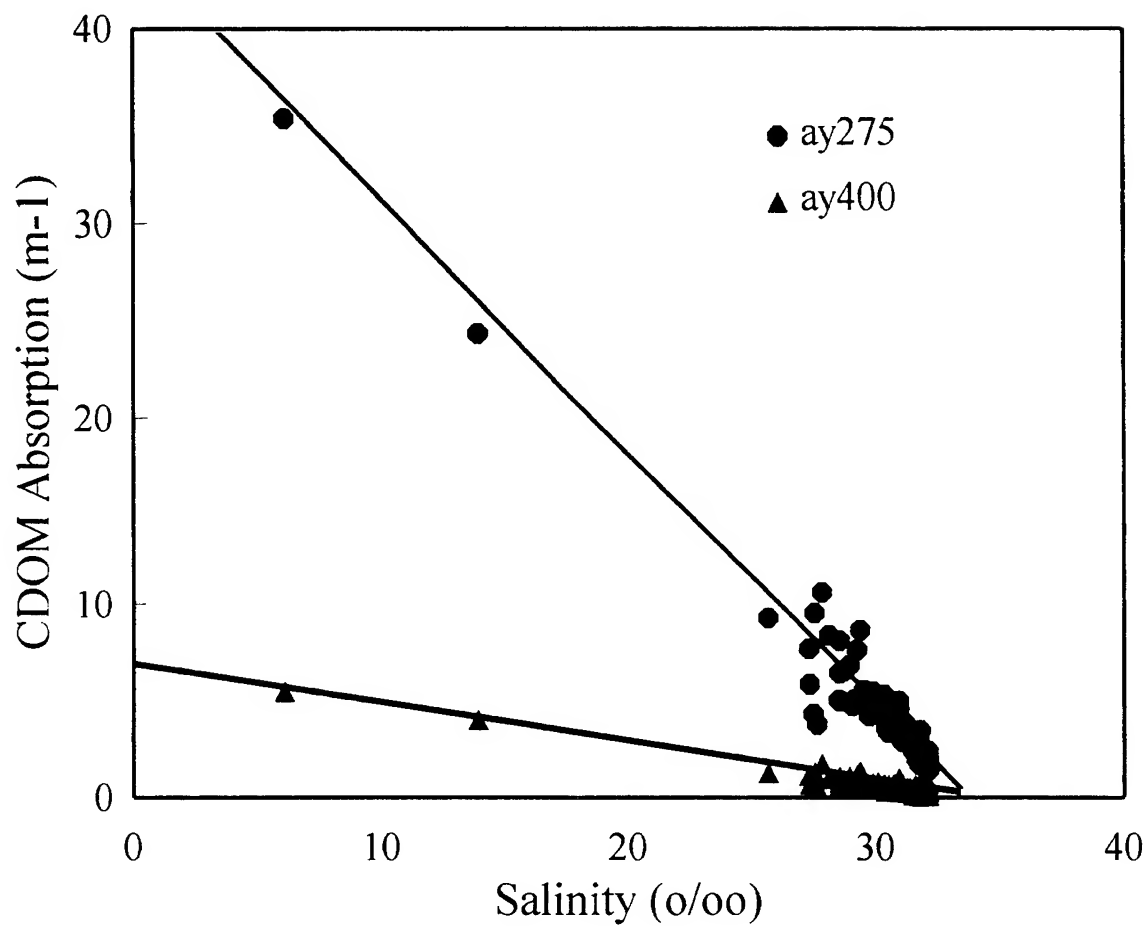


Figure 1. Light absorbed by CDOM at 400nm and 275nm in the water columns of five estuaries. Gulf of Maine, May, 1996.

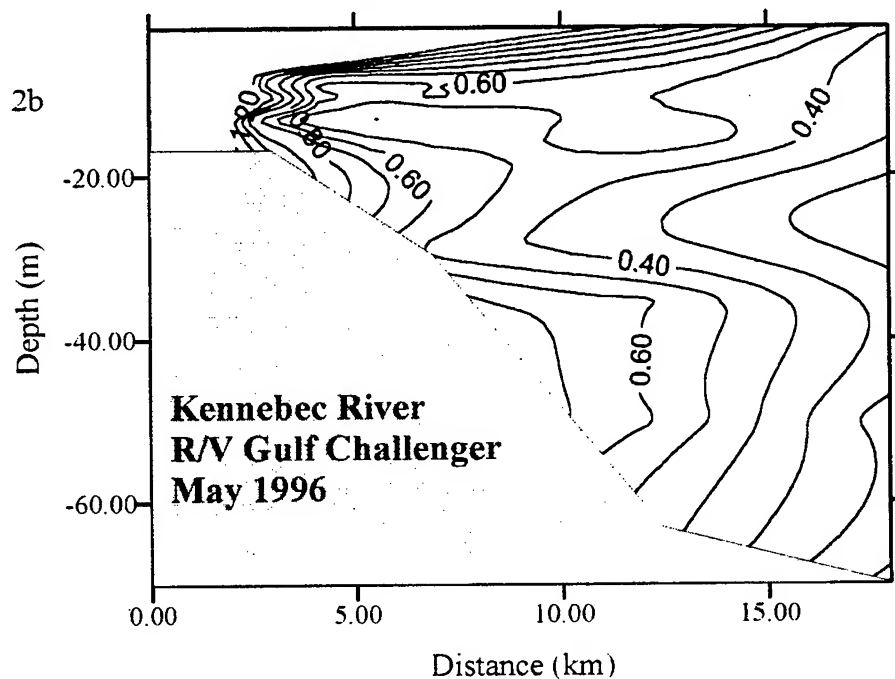
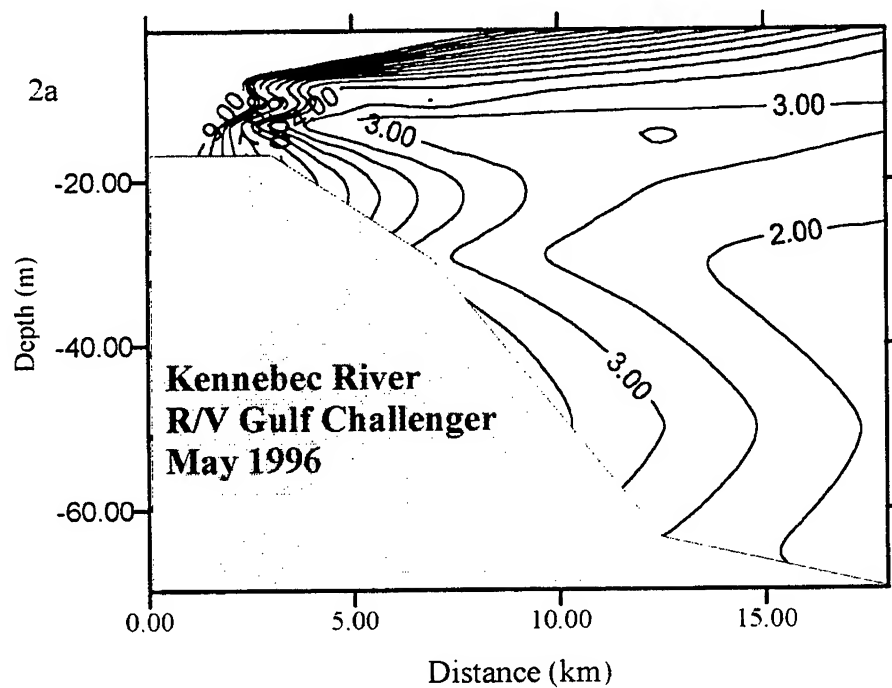


Figure 2. a.) Absorption coefficients of CDOM at 275 nm.
b.) Absorption coefficients of CDOM at 400 nm. Kennebec River, May, 1996.

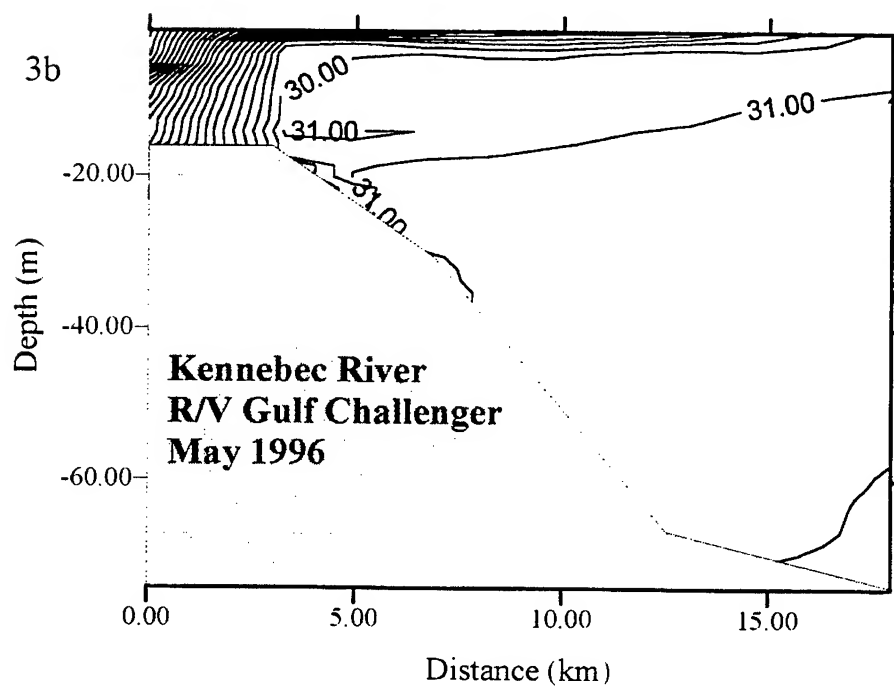
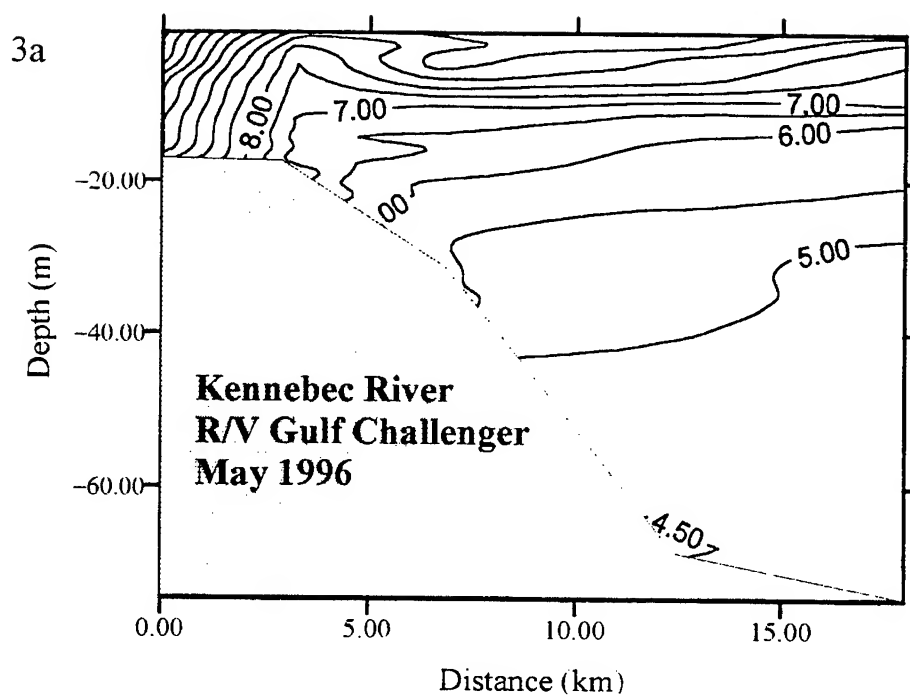


Figure 3. a.) Water temperature in degrees centigrade.
b.) Water salinity in o/oo. Kennebec River, May, 1996.

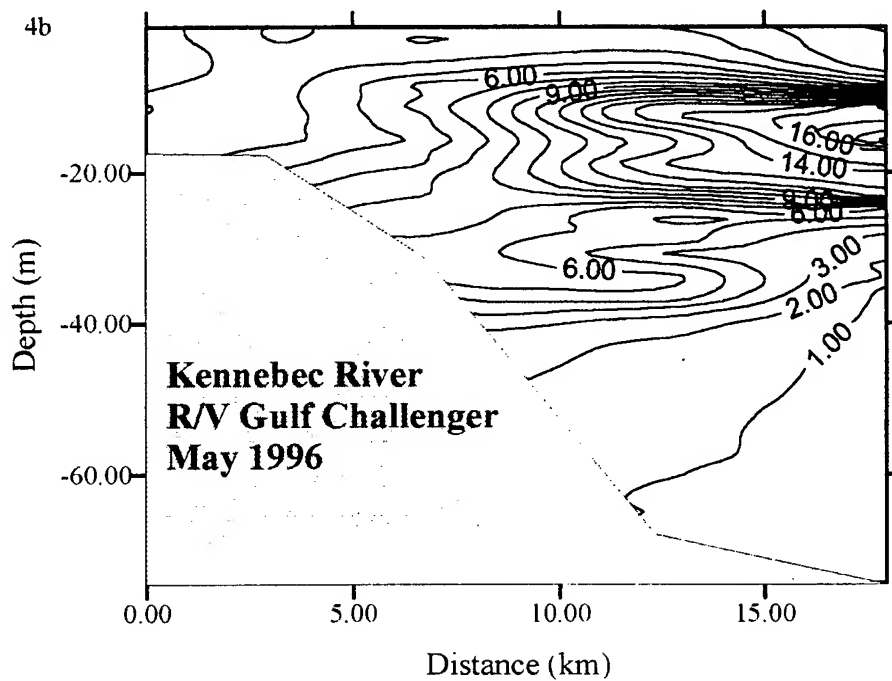
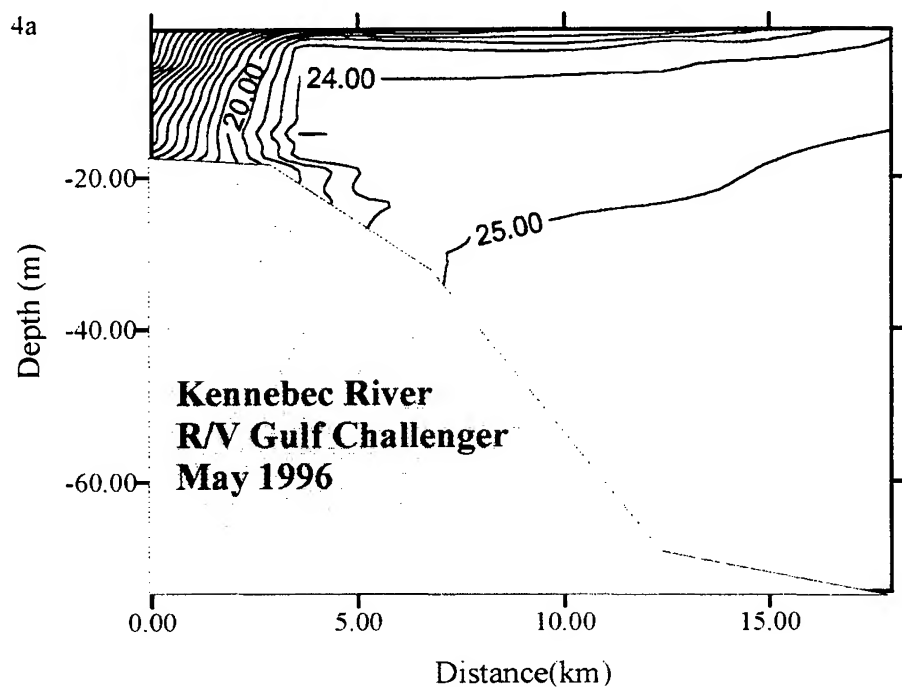


Figure 4. a.) Water density as sigma-t.
b.) Phytoplankton chlorophyll in ug/l. Kennebec River, May, 1996.

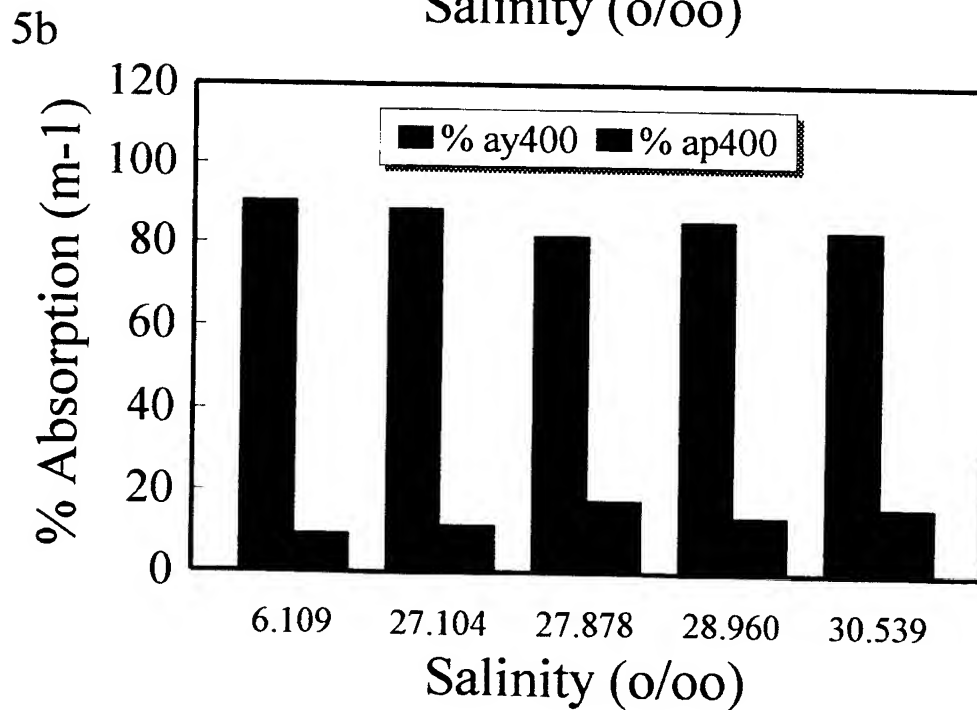
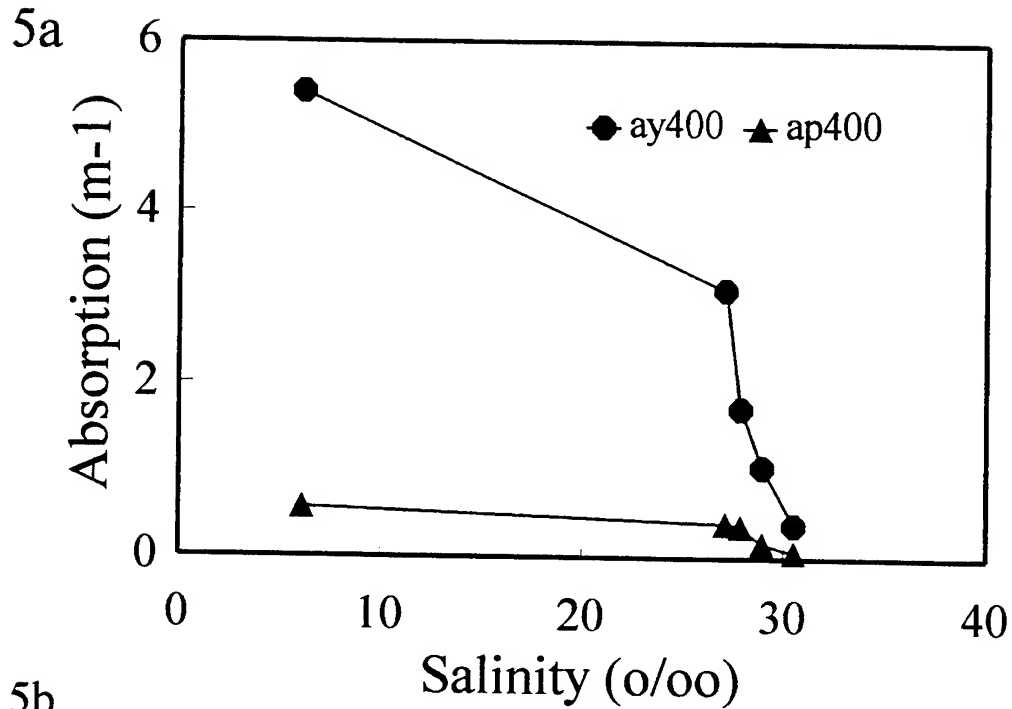


Figure 5a. Absorption coefficients of ay and ap at 400nm. Figure 5b. Percentage of absorption excluding water. Kennebec River, May, 1996.

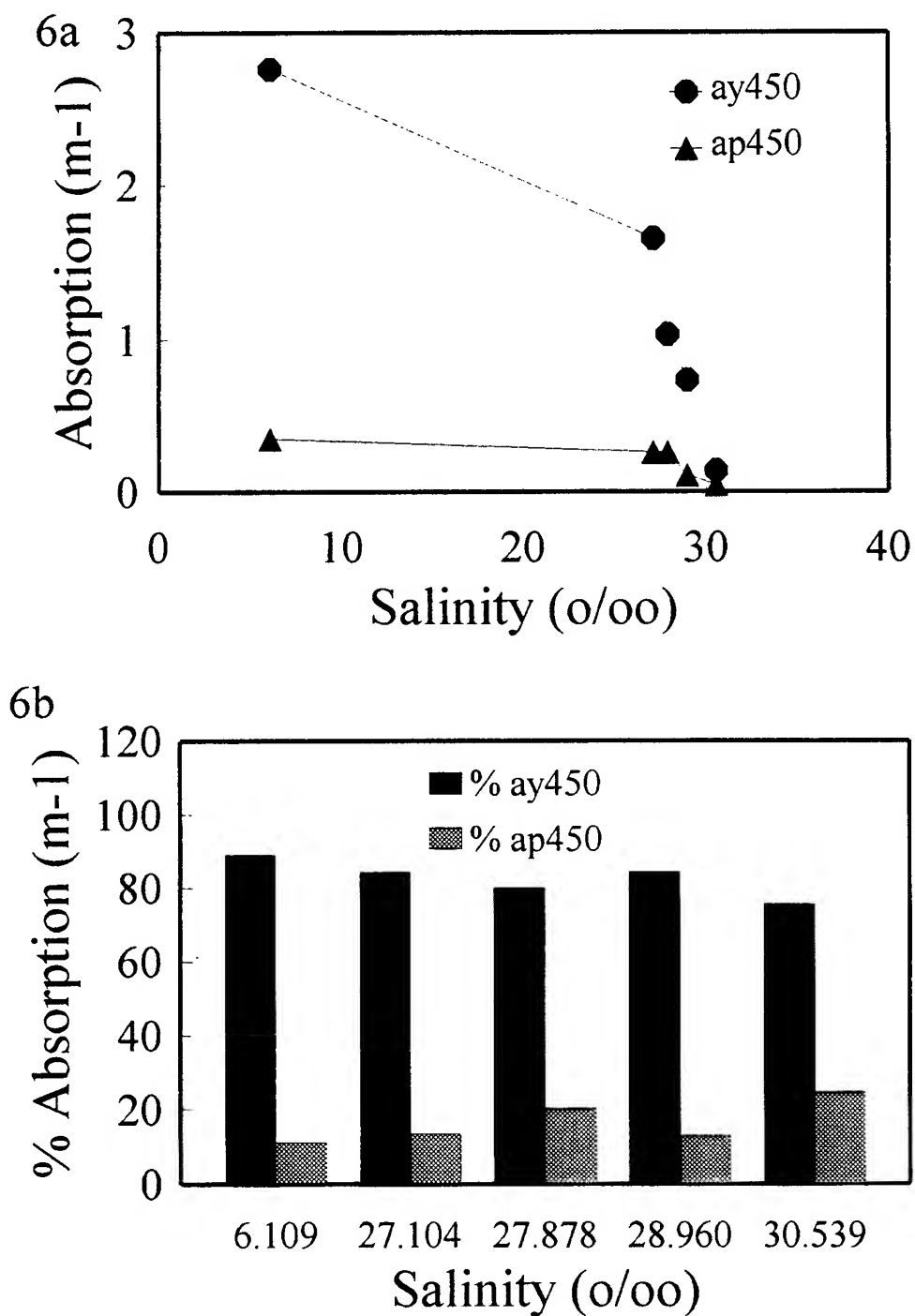
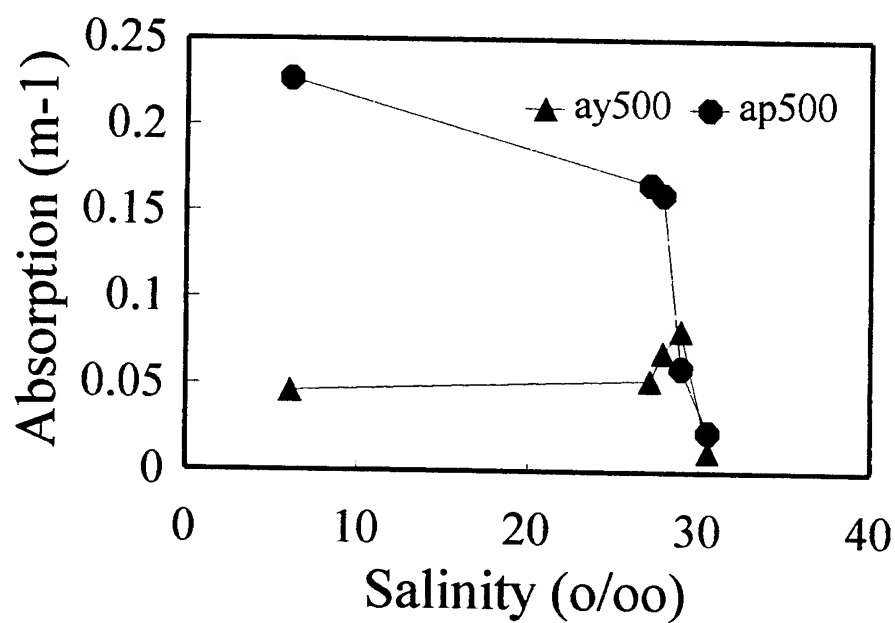


Figure 6. a.) Absorption coefficients of ay and ap at 450 nm. b.) Percentage of absorption excluding water. Kennebec River, May, 1996.

7a



7b

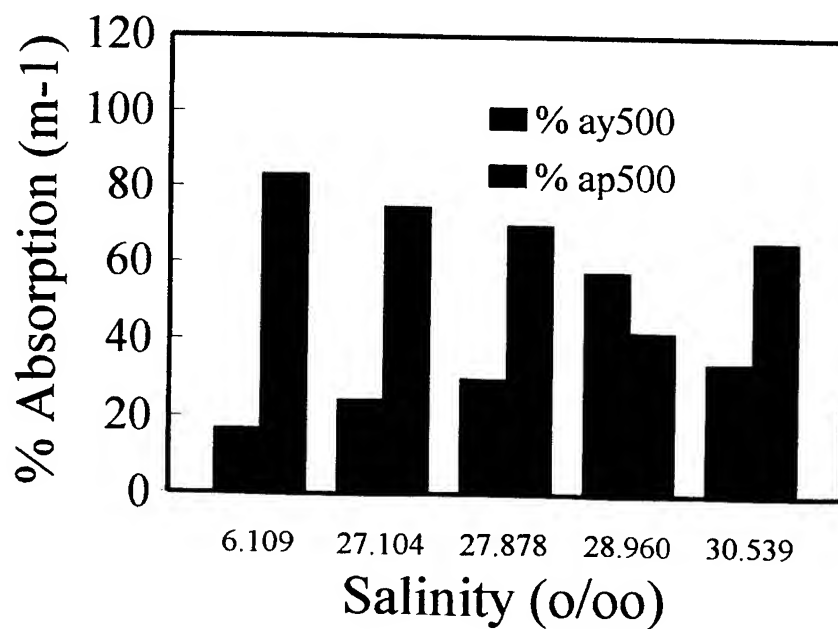


Figure 7. a.) Absorption coefficients of ay and ap at 500 nm. b.) Percentage of absorption excluding water. Kennebec River, May 1996.

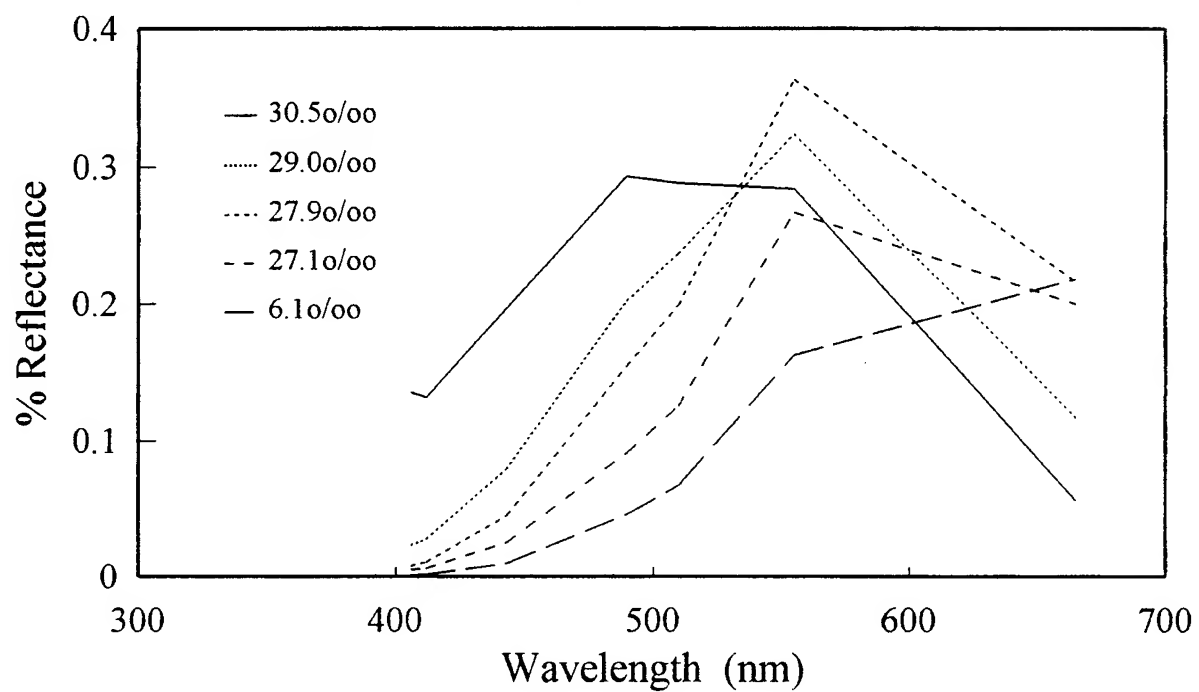


Figure 8. Spectral reflectance of Kennebec River stations May, 1996, with surface salinity. Salinity increases with distance from shore.

Seasonal variation of CDOM in the Middle Atlantic Bight: Terrestrial inputs and photooxidation

Anthony Vodacek and Neil V. Blough

University of Maryland, Department of Chemistry and Biochemistry, College Park, Maryland 20742

ABSTRACT

Surveys of the fluorescence and absorption of chromophore-containing dissolved organic matter (CDOM) were made along a cruise line extending from the mouth of Delaware Bay southeast to the Sargasso Sea. With shallow stratification in August, photobleaching dramatically altered the optical properties of the surface waters, with ~70% of the CDOM absorption and fluorescence lost through photooxidation in the waters at the outer shelf. S , the slope of the log-linearized absorption spectrum of CDOM, increased offshore and appeared to increase with photodegradation. The increase in S underscores the difficulty in developing ocean color algorithms to predict Chl concentrations in highly absorbing coastal waters. The seasonal variation in the CDOM fluorescence-absorption relationship and fluorescence quantum yields was less than 15%, making the airborne lidar approach for remote determination of CDOM absorption coefficients a robust technique. The photooxidation of CDOM in August also affected the relationship between CDOM and DOC, which can be described by a simple model.

Keywords: CDOM, photochemical bleaching, absorption coefficient, lidar, remote sensing, fluorescence

1. THE ROLE OF CDOM IN OCEAN OPTICS AND BIOGEOCHEMISTRY

At the levels observed in many coastal waters^{1,2} and in oceanic regions experiencing major freshwater inputs³, CDOM can substantially interfere with satellite determinations of phytoplankton biomass^{4,5}. Further, the absorption of sunlight by CDOM leads to the deposition of heat and the production of a variety of photochemical intermediates and products^{6,7}. The products of these reactions include the atmospherically-important trace gases COS⁸, CO⁹ and CO₂¹⁰, as well as biologically labile low molecular weight organic compounds¹¹. The photooxidative reactions giving rise to these products lead to the degradation of the CDOM and the bleaching of its absorption and fluorescence emission bands^{10,12}, thus acting as a feedback to the aquatic light field.

CDOM plays an essential role in a variety of biogeochemical processes in surface waters. Because it absorbs light strongly in the UV, CDOM can limit the penetration of biologically damaging UV radiation into surface waters and thus act to protect phytoplankton and other biota. Alternatively, under some conditions aquatic organisms may be harmed by reactive oxygen species produced photochemically from the CDOM¹³. At high CDOM levels, light absorption by CDOM can extend well into the visible wavelength regime and reduce the photosynthetically active radiation available to phytoplankton, thus decreasing primary productivity and affecting ecosystem structure¹⁴. Despite the importance of CDOM to upper ocean biogeochemical processes and optics, our present understanding of its spatial and temporal distributions and the factors controlling these distributions is very limited.

2. METHODS

CDOM fluorescence was determined at 10 or 30 s intervals during each cruise using an HPLC-type fluorescence detector and the method described by Vodacek et al.¹⁵. Emission data are in fluorescence units, $F_n(\lambda_{ex})$, where λ_{ex} is the excitation wavelength, relative to a solution of quinine sulfate in 0.1 N H₂SO₄. The emission intensity of a 1 μ g liter⁻¹ solution of quinine sulfate is defined to be 1 $F_n(\lambda_{ex})$. Bucket and Niskin bottle samples were filtered immediately after collection using GF/F filters. Samples for optical measurements were stored refrigerated in glass bottles with teflon-lined caps while DOC samples were stored frozen in glass vials with teflon-lined septa. DOC concentration was determined by high temperature combustion¹⁶. CDOM absorbance was determined with an HP 8451A or 8452A diode array spectrophotometer following a second filtration of samples with 0.2 μ m pore nylon filters³. Milli-Q water was the blank and the spectra were baseline corrected using the average absorbance from 700-800 nm and then converted to absorption coefficients, $a_{CM}(\lambda)$ ¹⁷. The spectral slopes, S , obtained from the

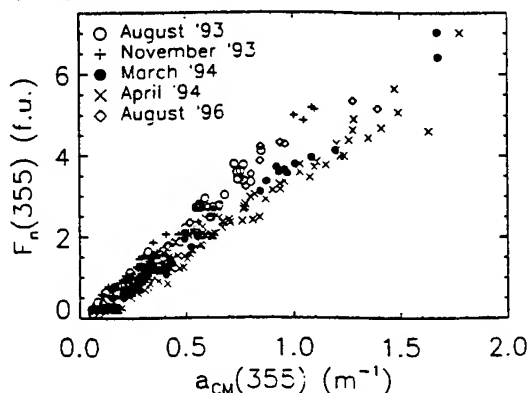
natural log of the absorption coefficient versus wavelength (nm^{-1}), were determined from linear least-squares regression over the data from 290 nm up to the wavelength at which the absorbance decreased to 0.002 absorbance units. CDOM fluorescence spectra (355 nm excitation) were determined with an SLM SPF 500C or AB2 spectrofluorometer. The spectra were corrected for the emission response of the instrument and analyzed according to the method of Hoge et al.¹⁸, where fluorescence is normalized to the water Raman signal (F/R). The F/R values were transformed to $F_n(355)$ by standardizing to the F/R value of a quinine sulfate solution analyzed using identical procedures^{18,15}. The quinine sulfate solutions used were the same as those employed to standardize the shipboard fluorescence measurements. Fluorescence quantum yields were calculated relative to quinine sulfate, which has a quantum yield of 0.51 in 0.1 N H_2SO_4 ¹⁷.

3. RESULTS AND DISCUSSION

3.1 Fluorescence/absorption relationship and quantum yields

The dependence of CDOM fluorescence on its absorption was linear for all cruises and similar to previous results³. The ratio of fluorescence to absorption and the fluorescence quantum yields were slightly higher in the summer and fall than in the spring (Fig. 1).

Fig. 1. A. The dependence of CDOM fluorescence, $F_n(355)$, excited at 355 nm on the CDOM absorption coefficient at 355 nm, $a_{CM}(355)$, for stations sampled in August and November 1993, March and April 1994, and August 1996 between the mouth of the Delaware Bay and the Sargasso Sea.



For surface waters with $a_{CM}(355) < 2 \text{ m}^{-1}$, the linear equation for predicting absorption from fluorescence is

$$a_{CM}(355) = 0.243 \cdot F_n(355) + 0.055; r^2 = 0.94. \quad (1)$$

We have used the in situ samples to provide a vicarious calibration of the CDOM fluorescence determined by the Airborne Oceanographic Lidar and then applied Eq. 1 to produce tracklines of CDOM absorption coefficients from the lidar data (Fig. 2).

3.2 Absorption spectra

CDOM absorption spectra, plotted as the natural log of the absorption coefficient versus wavelength, were approximately linear for all samples. Offshore waters had consistently higher values of the spectral slope, S , as observed previously for other waters^{2,3,17} except in April, when S did not rise above 0.020 nm^{-1} except in Gulf Stream or Sargasso waters (Fig. 3). The increase in S from coastal to offshore waters is thought to arise from the transformation of terrestrial CDOM and/or its replacement by CDOM generated in situ^{3,19}. The lower values of S in April may be explained by the greater freshwater input during spring runoff and the absence of strong thermal stratification. In contrast, in August 1993, with low flow and strong thermal stratification, the values of S in the mixed layer increased away from the bay mouth even when there was very little change in salinity, providing strong evidence for a photochemical transformation of the CDOM.

3.3 Photochemical degradation of CDOM

Further evidence for a substantial photochemical loss of CDOM from the mixed layer in August 1993 and 1996 was acquired from hydrocast data (Fig. 4). Both in and below the surface mixed layer the fluorescence and absorption decrease and the salinity increases as distance from the bay mouth increases.

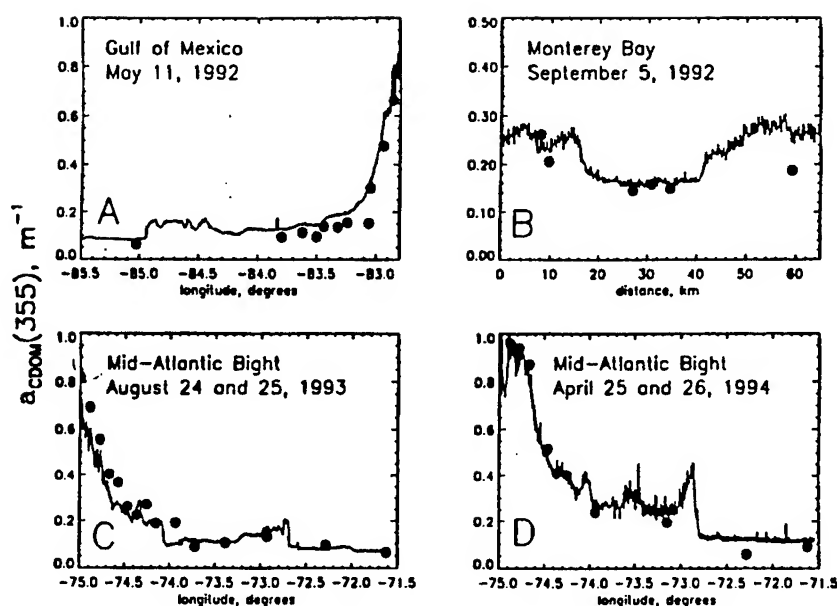
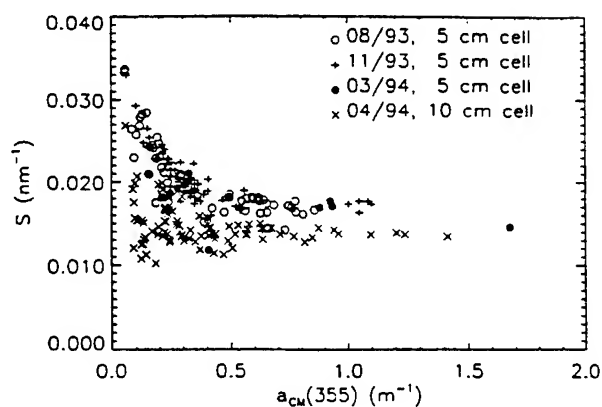


Fig. 2. $a_{CDM}(355)$ determined with a laboratory spectrophotometer (\bullet), and with the Airborne Oceanographic Lidar (lines).

Fig. 3. The relationship between S and the absorption coefficient at 355 nm in all four seasons.



The decreases in fluorescence and absorption are largest in the mixed layer while the salinity increase is greatest below the mixed layer. At the outer shelf stations a situation ensues where the surface waters are both less saline and clearer than the waters below the mixed layer. This situation is not at all anticipated in coastal waters strongly impacted by freshwater inputs and is further evidence for photochemical bleaching of CDOM in the surface waters.

The dependence of fluorescence on salinity exhibited distinct behavior among the seasons. This variability was most evident on the shelf. In March and April conservative mixing of CDOM fluorescence extended across the shelf over a range of salinity from about 27.6 to 33. In November, the mixing curve on the continental slope was very similar to those observed in March and April, but on the shelf there was significantly higher fluorescence at a given salinity than in the spring. In contrast, the mixing curve for surface waters in August 1993 and 1996 were very different from those of the other seasons (Fig. 5). A marked decrease in fluorescence and absorption was observed over a very small salinity gradient from the bay mouth to the shelf break, while over the continental slope there was less fluorescence at any given salinity than in any other season. These results are consistent with a strong photochemical sink of CDOM in the surface waters of the shelf and slope. Because the data suggest that the CDOM below the mixed layer was protected from photobleaching, the absorption-salinity relationship at these depths can provide

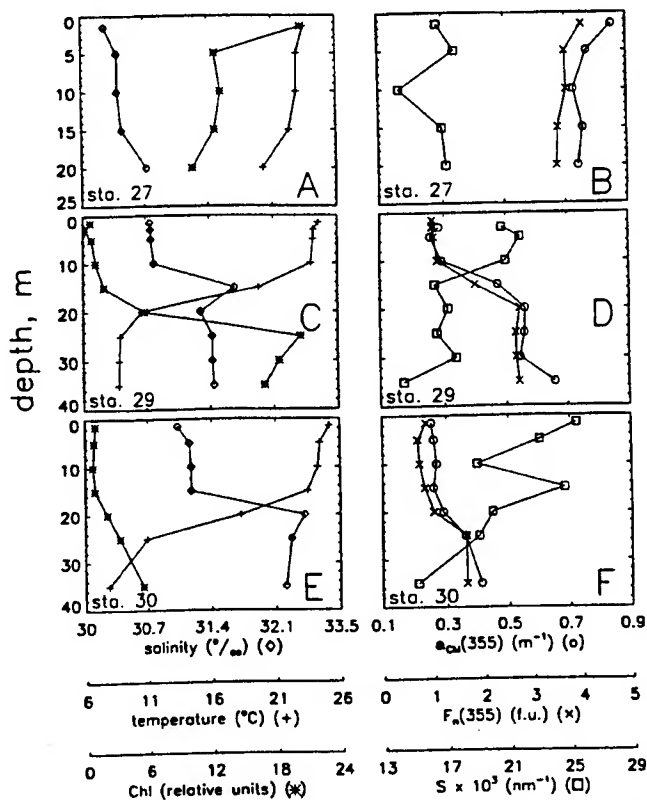


Fig. 4. August 1993 hydrocast data for three stations on the shelf. A., C., E. Vertical profiles of temperature, salinity, and Chl fluorescence. B., D., F. Vertical profiles of fluorescence, absorption, and S.

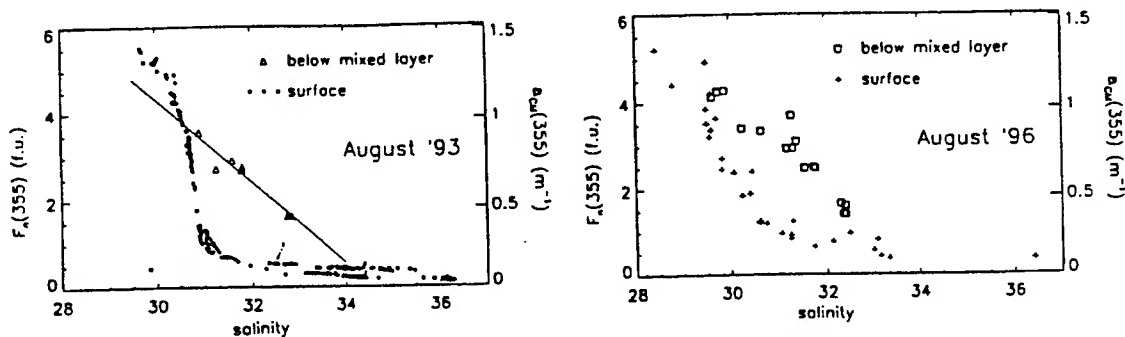


Fig. 5. A. Relationship between CDOM fluorescence or absorption and salinity along the trackline in August 1993 and 1996.

the means to estimate the absorption expected in the mixed layer in the absence of photobleaching.

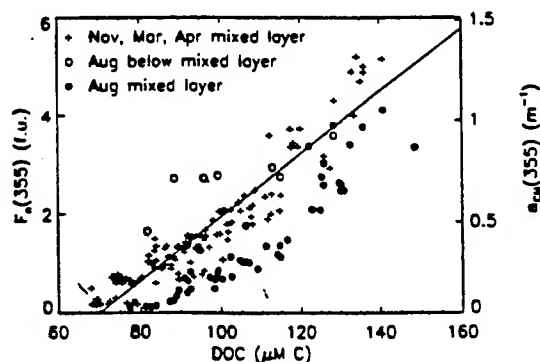
$$a_{CM}(355) = -0.186 \cdot \text{salinity} + 6.48; r^2 = 0.84; n = 8. \quad (2)$$

Equation 2, a similar equation developed with the fluorescence data, and the average salinity, fluorescence, and absorption values from above and below the thermocline were employed to estimate the loss in mixed layer absorption and fluorescence due to dilution. The difference between the predicted and measured absorption (fluorescence) values was then divided by the predicted value, to yield the fraction of absorption (fluorescence) lost due to photobleaching. These calculations show that the percent photobleaching of

absorption and fluorescence increased across the shelf and that at the two outer shelf stations, 65 to 70% of the absorption and fluorescence in the surface mixed layer had been eliminated.

Additional evidence for a strong photochemical sink of CDOM in surface waters during the summer months is evident in the plot of the dependence of fluorescence (absorption) on DOC for the August 1993 mixed layer samples (Fig. 6).

Fig. 6. Relationship between fluorescence and DOC in all four seasons. The absorption coefficient (right axis) is scaled from the fluorescence using Eq. 1.



These samples had lower fluorescence at a given DOC concentration than those from the spring or fall. A two pool model consisting of a colored terrestrial end member and an uncolored oceanic end member can be used to describe the behavior of the CDOM with respect to the DOC and delineate the light-mediated conversion of CDOC (colored dissolved organic C) to UDOC (uncolored dissolved organic C) and DIC (dissolved inorganic C). The detailed model can be found in a manuscript accepted for publication (Vodacek et al. *Limnology and Oceanography*). This two pool model relies on several assumptions. One is that the primary end member for shelf waters was the Delaware Bay or that other sources had very similar end members. Another assumption is that the fluorescence (absorption) end member at the bay mouth did not vary greatly from the time the CDOM at the shelf break first exited the bay to the time of offshore sampling. Both of these assumptions are supported by the apparently conservative dilution of CDOM observed for the water below the mixed layer. The influence of other sources or sinks, such as bacterial utilization of the CDOM, would have been likely to create non-linearity in the dilution curve.

The model approach is similar to that used to estimate the loss of absorption due to photobleaching. The DOC in the surface mixed layer in the absence of photobleaching is estimated from the specific absorption and the estimated value for the absorption coefficient. If the estimated value for the DOC concentration is the same as the measured value, but the absorption is much lower, then UDOC has been formed. If the estimated value for the DOC concentration is less than the measured value, then both UDOC and DIC have been formed. We observed the production of both UDOC and DIC and that there is an increase in DIC production relative to UDOC production as CDOM is bleached more extensively. Since the derivations rely only on the initial and final values of DOC concentration and absorption, the analysis does not provide information on the pathways to the products. However, we can compare our results to estimates of the photochemical remineralization of DOC to DIC using the relationship provided by Miller and Zepp¹⁰, where the fractional DIC production is proportional to the fraction of material undergoing photochemical reaction. The fractional DIC production calculated from our model is close to the values calculated using our fading estimates and Miller and Zepp's relation, suggesting both that our procedure for estimating the loss of absorption was valid and that the direct production of DIC was dominant.

3.4 The effects of photodegradation on the remote sensing of CDOM and DOC

CDOM has a strong impact on the aquatic environment through its absorption of UV and visible light. Photobleaching of CDOM absorption and fluorescence can reduce the surface water optical signals by up to 70% and to increase the value of S . Photobleaching does not, however, affect significantly the accuracy of remote estimates of CDOM absorption based on fluorescence measurements, since the fluorescence per unit absorption and the fluorescence quantum yields are relatively constant. The results of algorithms for analyzing passive ocean color measurements may however, be strongly influenced by the choice of the CDOM slope parameter, S .

4. ACKNOWLEDGMENTS

We thank the captain and crew of the RV *Cape Henlopen*, Steve Andrews, Liz Bruce, Sigi Caron, Mike Giancola, Nancy Hayward, Sarah Herbelin, Frank Hoge, Joyce Irvine, and Tim Pfeiffer for their contributions to this work. Support was provided by the Office of Naval Research (N. V. B.), the NASA EOS Interdisciplinary Program (N. V. B.), and a NRC-NASA resident research associateship (A.V.)

5. REFERENCES

1. M. D. DeGrandpre, A. Vodacek, R. K. Nelson, E. J. Bruce, and N. V. Blough, "Seasonal seawater optical properties of the U.S. Middle Atlantic Bight," *J. Geophys. Res.* **101**, (1996)
2. J. R. Nelson and S. Guarda, "Particulate and dissolved spectral absorption on the continental shelf of the southeastern United States," *J. Geophys. Res.* **100**, 8715-8732 (1995).
3. N. V. Blough, O. C. Zafiriou, and J. Bonilla, "Optical absorption spectra of waters from the Orinoco river outflow: Terrestrial input of colored organic matter to the Caribbean," *J. Geophys. Res.* **98**, 2271-2278 (1993).
4. K. L. Carder, S.K. Hawes, K.A. Baker, R.C. Smith, R. G. Steward, and B.G. Mitchell, "Reflectance model for quantifying chlorophyll *a* in the presence of productivity degradation products," *J. Geophys. Res.* **96**, 20599-20611 (1991).
5. H. Hochman, F. E. Muller-Karger, and J. J. Walsh, "Interpretation of the color signature of the Orinoco River plume," *J. Geophys. Res.* **99** 7443-7455 (1994).
6. J. T. O. Kirk, "Solar heating of water bodies as influenced by their inherent optical properties," *J. Geophys. Res.* **93**: 10,987-10,908 (1988).
7. N. V. Blough, "Photochemistry in the sea-surface microlayer," *P. S. Liss and R. Duce [eds.], The sea surface and global change*. in press, Cambridge University Press, 1996.
8. P. S. Weiss, S. S. Andrews, J. E. Johnson, and O. C. Zafiriou, "Photoproduction of carbonyl sulfide in South Pacific Ocean waters as a function of irradiation wavelength," *Geophys. Res. Lett.* **22**, 215-218 (1995)
9. R. L. Valentine and R. G. Zepp, "Formation of carbon monoxide from the photodegradation of terrestrial dissolved organic carbon in natural waters," *Environ. Sci. Technol.* **27**, 409-412 (1993).
10. W. L. Miller and R. G. Zepp, "Photochemical production of dissolved inorganic carbon from terrestrial organic matter: Significance to the oceanic organic carbon cycle," *Geophys. Res. Lett.* **22**, 417-420 (1995).
11. D. J. Kieber, J. A. McDaniel, and K. Mopper, "Photochemical source of biological substrates in seawater: Implications for geochemical carbon cycling," *Nature* **341**, 637-639 (1989).
12. A. M. Kouassi and R. G. Zika, "Light-induced alteration of the photophysical properties of dissolved organic matter in seawater. Part I. Photoreversible properties of natural water fluorescence," *Neth. J. Sea Res.* **27**, 25-32 (1990).
13. N. V. Blough and R.G. Zepp, "Reactive oxygen species in natural waters," *C.S. Foote et al. [eds.], Active oxygen in chemistry*, pp. 280-333, Chapman and Hall, 1995.
14. R. R. Bidigare, M. E. Ondrusek, and J. M. Brooks, "Influence of the Orinoco River outflow on distributions of algal pigments in the Caribbean Sea," *J. Geophys. Res.* **98**, 2259-2269 (1993).
15. A. Vodacek, F. E. Hoge, R. N. Swift, J. K. Yungel, E. T. Peltzer, and N. V. Blough, "The use of in situ and airborne fluorescence measurements to determine UV absorption coefficients and DOC concentrations in surface waters," *Limnol. Oceanogr.* **40**, 411-415 (1995).
16. E. T. Peltzer and P. G. Brewer, "Some practical aspects of measuring DOC—sampling artifacts and analytical problems with marine samples," *Mar. Chem.* **41**, 243-252 (1993).
17. S. A. Green, and N. V. Blough, "Optical absorption and fluorescence properties of chromophoric dissolved organic matter in natural waters," *Limnol. Oceanogr.* **39**, 1903-1916 (1994).
18. F. E. Hoge, A. Vodacek, and N. V. Blough, "Inherent optical properties of the ocean: Retrieval of the absorption coefficient of chromophoric dissolved organic matter from fluorescence measurements," *Limnol. Oceanogr.* **39**, 1394-1402 (1993)
19. N. V. Blough and S. A. Green, "Spectroscopic characterization and remote sensing of non-living organic matter," *R. G. Zepp and C. Sonntag [eds.], The role of non-living organic matter in the earth's carbon cycle*. pp. 23-45, John Wiley & Sons, 1995.

Spectral irradiance, radiance and polarization in
blue Western Mediterranean waters

Niels K. Højerslev

Niels Bohr Institute of Astronomy, Physics and Geophysics
Department of Geophysics, Juliane Maries Vej 30,
DK-2100 Copenhagen Ø, Denmark

Eyvind Aas

University of Oslo, Department of Geophysics, PO Box 1022 Blindern
N-0315 Oslo, Norway

ABSTRACT

Spectral downward and upward irradiance, radiance and polarization have been measured in the visible part of the spectrum down to 275 m in blue Western Mediterranean waters. The irradiance reflectance varied by a factor of 10 in the spectral mode and around a factor of 4 with depth.

Spectral radiance and polarization were measured at discrete depths where the radiance meter was rotated around the vertical cable for selected zenith angles in order to give the azimuthal radiance distribution, which can be represented by a simple function of elliptic shape. Irradiance calculated from the radiance data sets compares favourably with directly measured irradiance, except for the near-surface measurements where ship shadows and sun glints are problematic. Inspection of the radiance data indicates that self-shading effects from the instrument are small for the upward radiance.

Various distribution functions have been calculated. The average cosine varies around 0.8, the average cosine for the upward radiance around 0.4, and the ratio of the upward irradiance and the nadir radiance is about 4. The latter parameter displays the highest variation in the present data set.

The upward radiances in the zenith angle interval 150-180 degrees in the anti-sun direction were about the same at all depths and wavelengths. The vertical attenuation coefficients for these upward radiances approach the asymptotic k -value. This implies that a flat sea surface acts like a Lambert diffusor for water-leaving radiances in the (upward) nadir angle interval 0-40 degrees in the anti-sun direction. The degree of polarization varied between 0 and 50%, which is somewhat lower than earlier reported in the literature.

An analytic expression for the angular distribution of upward radiance is proposed.

Keywords: radiance, remote sensing light, irradiance, polarization

1. INTRODUCTION

Underwater radiance *and* polarization measurements are very scarce. A few such examples can however be given^{1,2}, but it is noteworthy that one has to go 25 years back in time. The situation with respect to (spectral) radiance is about the same for the last 25 years. Only rather few radiance data and results from coastal and blue ocean waters have been presented^{3,4,5}. Prior to 1971 (and beginning in the mid 1930-ies with the pioneer work on underwater radiance made by Johnsen (Jerlov) and Liljequist⁶) there was a relatively high measuring activity in this field in France, Japan, Sweden, USA and USSR.

Radiance is the single most important quantity from which various irradiances and vertical attenuation coefficients can be derived. In addition irradiance distribution functions, the light absorption coefficient, and in principle by inverse methods the light scattering function can be determined for a completely specified radiance field. The total radiance field combined with the physical laws by Snell and Fresnel give us all the pertinent inherent and apparent parameters describing the optical characteristics of a hydrosol.

In remote sensing studies involving water-leaving radiances it is evident that radiance is the appropriate parameter to study rather than irradiance which however seems to be the preferred method generally speaking.

Here we present excerpts from the remaining part of a fairly large and complete marine optical data set obtained at the

Nordic optical expedition with *r/v Helland-Hansen* in the Western Mediterranean during May-August, 1971, from west of Sicily to south of Malaga. Observations of the absorption coefficient, the scattering coefficient, the scattering function, the attenuation coefficient, the size distribution function, the scalar irradiance, the downward and upward irradiances, and the radiance, have already been published^{4,7,8,9}.

2. DEFINITIONS AND NOMENCLATURE

The usual definitions and the nomenclature applied here is the one approved by IAPSO¹⁰. A few parameters will however be defined and briefly discussed below:

$L(z, \theta, \phi)$ is the radiance at the depth z from the direction θ, ϕ , defined by the zenith angle θ and the azimuth angle ϕ . $L(\theta+) \equiv L(z, \theta, \phi=0)$ is radiance in the solar plane with the same azimuth as the sun. $L(\theta-) \equiv L(z, \theta, \phi=180^\circ)$ is radiance in the solar plane opposite to the sun. The vertical attenuation coefficients for radiance are termed as $K_L(z, \theta, \phi)$, $K_L(\theta+)$ and $K_L(\theta-)$ in an analogue manner as for the radiance.

$$\epsilon(z, \theta) \equiv \epsilon \equiv \frac{L(\theta+) - L(\theta-)}{L(\theta+) + L(\theta-)} \quad (1)$$

is termed the azimuth ellipticity since an early radiance data set³ has revealed that

$$L(z, \theta, \phi) = L(\theta-) \frac{1 + \epsilon}{1 - \epsilon \cos \phi} \quad (2)$$

Eq. (1) gives directly

$$L(\theta+) = L(\theta-) \frac{1 + \epsilon}{1 - \epsilon} \quad (3)$$

and eq. (2) gives, after some calculations, the azimuthal average as

$$\overline{L(\theta)} \equiv \frac{1}{2\pi} \int_0^{2\pi} L(z, \theta, \phi) d\phi = \sqrt{L(\theta+)L(\theta-)} = L(\theta-) \sqrt{\frac{1 + \epsilon}{1 - \epsilon}} \quad (4)$$

By applying eq. (4) the downward irradiance E_d can be calculated from the observed values of $L(\theta+)$ and $L(\theta-)$ as

$$E_d = 2\pi \int_0^{\pi/2} \sqrt{L(\theta+)L(\theta-)} \cos \theta \sin \theta d\theta \quad (5)$$

and similarly the upward irradiance E_u is obtained from

$$E_u = 2\pi \int_{\pi/2}^{\pi} \sqrt{L(\theta+)L(\theta-)} |\cos \theta| \sin \theta d\theta \quad (6)$$

The irradiance ratio R is defined by

$$R = \frac{E_u}{E_d} \quad (7)$$

The radiance distribution function Q is expressed as

$$Q = \frac{E_u}{L(180^\circ)} \quad (8)$$

A so-called remote sensing reflectance RSR introduced by Zaneveld¹¹ is defined as

$$RSR = \frac{L(180^\circ)}{E_{od}} \quad (9)$$

where E_{od} is the downward scalar irradiance. Note that Q , R and RSR vary with depth (and wavelength). The definitions (7), (8) and (9) combine into

$$RSR = \mu_d \frac{R}{Q} \quad (10)$$

where

$$\mu_d = \frac{E_d}{E_{od}} \quad (11)$$

is the average cosine for the downward radiance.

3. MODELS AND THEORY

It is generally taken for granted that $L(\theta+) \geq L(\theta-)$ at all depths. It is further known that $L(\theta+) = L(\theta-)$ in the asymptotic region¹². This implies that for ϵ in eq. (1), $0 \leq \epsilon \leq 1$, and $\lim \epsilon = 0$ for $z \rightarrow \infty$. It can also be argued that the inequality $K_L(\theta+) \geq K_L(\theta-)$ is valid from a certain depth z_0 and below since $L(\theta+)$ eventually becomes equal to $L(\theta-)$ at great depths.

From the definition of K_L

$$K_L(z, \theta, \phi) = - \frac{1}{L(z, \theta, \phi)} \frac{\partial L(z, \theta, \phi)}{\partial z} \quad (12)$$

and from eq. (2) it can after some calculations be shown that

$$K_L(z, \theta, \phi) = K_L(\theta-) + \frac{1 + \cos \phi}{(\epsilon + 1)(\epsilon - \cos \phi)} \frac{d\epsilon}{dz} \quad (13)$$

and

$$K_L(\theta+) - K_L(\theta-) = \frac{2}{(\epsilon^2 - 1)} \frac{d\epsilon}{dz} \quad (14)$$

Eqs. (13) and (14) lead to

$$K_L(\theta-) = K_L(\min) \leq K_L(z, \theta, \phi) \leq K_L(\max) = K_L(\theta+) \quad (15)$$

provided that $d\epsilon/dz < 0$ from z_0 and below. We consider ϵ to be one of the key parameters in modelling efforts.

We now introduce a new parameter α which has useful properties for modelling the upward radiance¹³:

$$\alpha = \frac{L(90^\circ)}{L(180^\circ)} - 1 = \frac{L(90^\circ)}{L(180^\circ)} \sqrt{\frac{1 + \epsilon(90^\circ)}{1 - \epsilon(90^\circ)}} - 1 \quad (16)$$

According to Aas¹³ the azimuthal averages of the upward radiance can be modelled as

$$\overline{L_u(z, \theta)} = L(180^\circ) \frac{1 + \alpha}{1 - \alpha \cos \theta} \quad (17)$$

This model compares extremely well with the excellent set of radiance data provided by Tyler¹⁴. Combining eqs. (2) and (17) we get directly the complete angular distribution function of L_u . Thus

$$L_u(z, \theta, \phi) = L(180^\circ) \frac{\sqrt{1 - \epsilon(\theta)^2}}{1 - \epsilon(\theta) \cos \phi} \frac{1 + \alpha}{1 - \alpha \cos \theta} \quad (18)$$

The α -model for $L_u(z, \theta, \phi)$ (or for $\overline{L_u(z, \theta)}$) allows Q to be expressed analytically by α :

$$Q = 2\pi \frac{1 + \alpha}{\alpha} \left[1 - \frac{1}{\alpha} \ln(1 + \alpha) \right] \quad (19)$$

Inspection of eqs. (16) and (17) reveals that a straightforward and highly reasonable constraint on α is $0 \leq \alpha \leq \infty$. When the upward radiance $L_u(z, \theta, \phi)$ is isotropic ($L_u = \text{constant}$) α becomes zero, and Q obtains the value π . If however the horizontal radiances become much larger than the nadir radiance so that $\alpha \rightarrow \infty$, then $Q \rightarrow 2\pi$. This implies that $\pi \leq Q \leq 2\pi$ for all natural radiance distributions in the sea.

Likewise the α -model gives for μ_u :

$$\mu_u = \frac{1 - \frac{1}{\alpha} \ln(1 + \alpha)}{\ln(1 + \alpha)} \quad (20)$$

and we find that $0 \leq \mu_u \leq 1/2$.

According to eqs. (4) and (16) it apparently takes three parameters in order to specify the azimuthal average $\overline{L_u(z, \theta)}$, namely $L(90^\circ +)$, $L(90^\circ -)$ and $L(180^\circ)$. Strictly but not necessarily practically speaking two parameters are sufficient. Any two of the four parameters $L_u(90^\circ)$, $L(180^\circ)$, $E_u (= L(180^\circ) Q)$ and $E_{ou} (= E_u / \mu_u)$ will do.

4. INSTRUMENTATION

The radiance meter consists of 4 parallel radiance tubes mounted on gimbals. Each tube is equipped with polarization filters, double interference filters, grey (neutral) filters and a lense $f/2.8$, 85 mm, which accepts light from within a half opening angle in water of 0.7° . The tubes can be set at different zenith angles θ in steps by 2° , ranging from 0 to 180° . For each fixed θ , the radiance is rotated around the (vertical) cable, giving the azimuthal dependence of L . In this way the total radiance field is obtained together with a combined measurement of the 4 Stokes parameters, leading to a determination of the degree of polarization¹.

The irradiance meter is equipped with a cosine collector, 8 double interference filters, and 3 grey filter combinations (0, 1 and 2 grey filters). It measures the downward and upward irradiances³ (the latter quantity in the upside down position).

5. RESULTS

5.1. Irradiance

The Western Mediterranean waters belong to the optical water types *IB-II*, according to Jerlov's optical classification for the upper 10 meters of the surface layer² (Fig. 1). A later attempt by Jerlov¹⁴ to extend his original classification to greater water depths cannot be characterized as being successful, judged from the present data set (note the deviation for 371 nm at 50 m depth in Fig. 1). This can be attributed to the fact that the waters in question were optically stratified with subsurface maxima of suspended matter^{7,8}. It is also reflected in the vertical variation of R by a factor of 4 (Table 1).

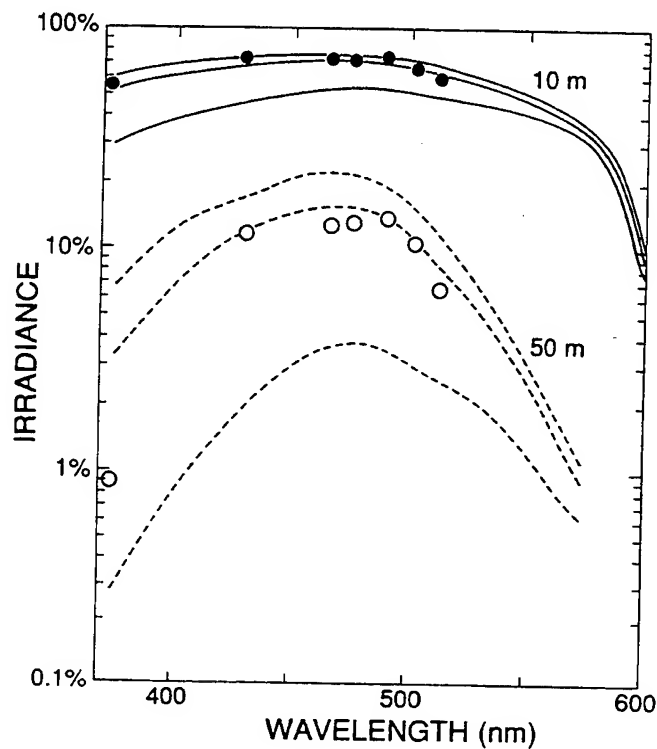


Fig. 1 (above). Spectral irradiance observed at Station E2, 6 July 1971, $h_s=68^\circ$, at 10 m (●) and 50 m (○), as compared with Jerlov's optical ocean water types IA, IB, and II at 10 m (solid lines) and 50 m (dashed lines).

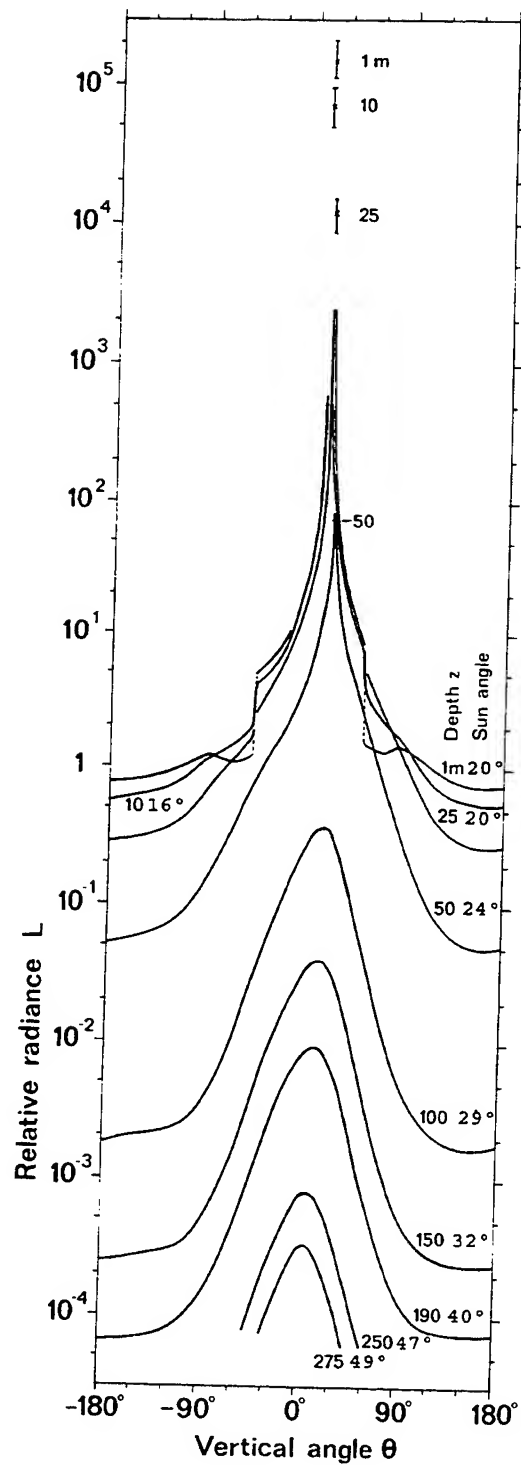


Fig. 2 (right). Angular radiance distribution $L(\theta)$ in the solar plane at Station D2, 8 July 1971, $\lambda=474$ nm, for different depths and solar zenith angles in air (Lundgren, pers. comm.).

Table 1. Irradiance ratio at Station J1 (°: 24 June 1971, $h_s=68^\circ$; °: 26 June 1971, $h_s=42^\circ$)

λ (nm)	371°	429°	454°	465°	474°	502°	528°	548°	574°	601°	630°	649°	693°
Depth (m)	R (%)												
0	4.8	3.8	3.7	3.6	3.2	2.2	1.0	1.1	.63	.13	.083	.064	.049
1	4.5	3.7	3.6	3.5	3.2	2.1	.99	1.1	.64	.16	.094	.072	.061
5	3.5	3.5	3.5	3.3	2.8	2.0	1.1	1.0	.60	.24	.16	.14	.19
10	3.1	3.3	3.2	3.3	3.0	1.9	1.0	.95	.54	.36	.33		
25	1.5	2.8	2.6	2.6	2.5	1.6	1.0	.82	.57				
50	1.2	2.1	2.1	2.0	2.0	1.8	1.4						
75	1.1	1.7	1.8	2.0	1.8	1.6	1.5						
100		2.3	2.2	2.1	2.1								

5.2. Radiance

The radiance field is depicted in two various ways in Figs. 2 and 3. We note that the maximum value for L is found in the sun's direction in the surface layers. Deeper down this maximum moves towards smaller zenith angles, thus approaching the asymptotic state¹². It should also be emphasized that Figs. 2 and 3 suggest that $L(\theta+) \geq L(\theta-)$ for all θ and depths. Fig. 4 reveals that $L(180^\circ) \approx L(150^\circ-)$, which means that the water-leaving radiances in the zenith angle interval 150° - 180° away from the sun are approximately the same. This implies that a remote sensing color scanner will "see" the radiances transmitted through a flat sea surface in the anti-sun direction as emanating from a Lambert diffusor. It also follows from Fig. 4 that $K_L(180^\circ) \approx K_L(150^\circ-) \approx K_L(150^\circ+)$.

The values of the ratios between azimuthally averaged upward radiance and nadir radiance (blue light: 465 and 474 nm, 45 observations at all stations and depths) deviate significantly from the isotropic case:

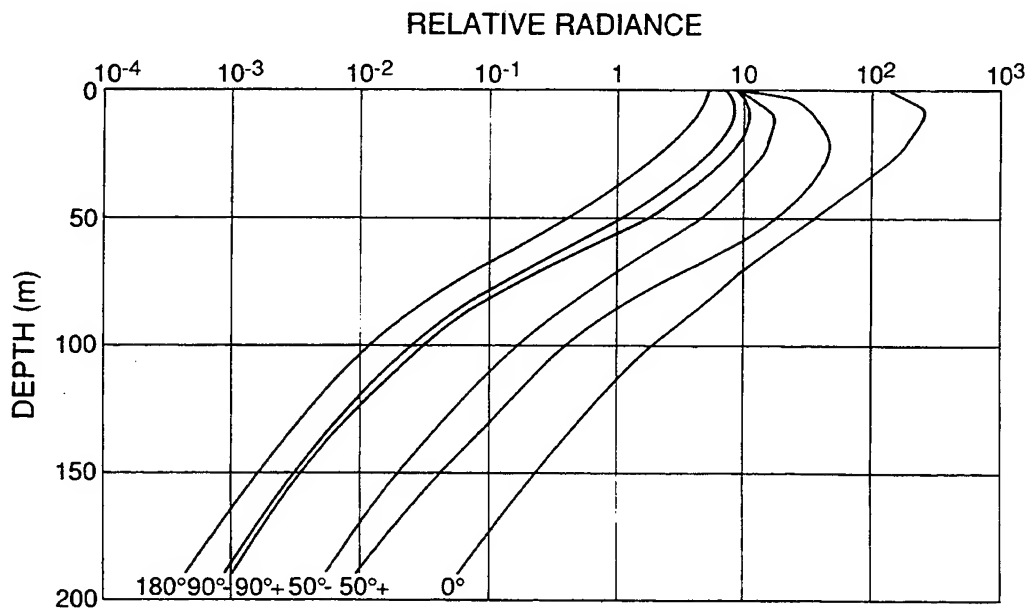


Fig. 3. Vertical profiles of $L(\theta)$ at Station D2, 8 July 1971, $\lambda=474$ nm, based on Fig. 2.

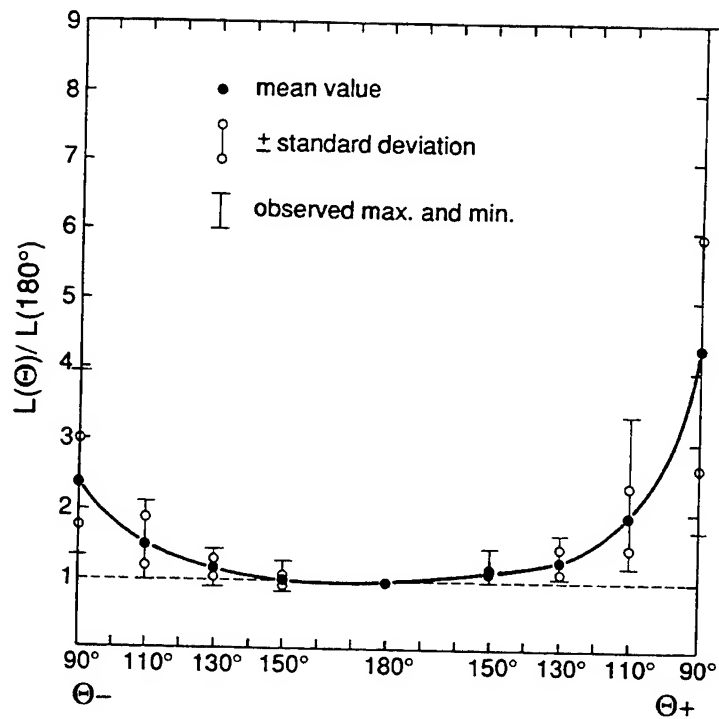


Fig. 4. The mean values and variations of the ratio $L(\theta)/L(180^\circ)$ at 465 and 474 nm, for all stations and depths (45 data sets).

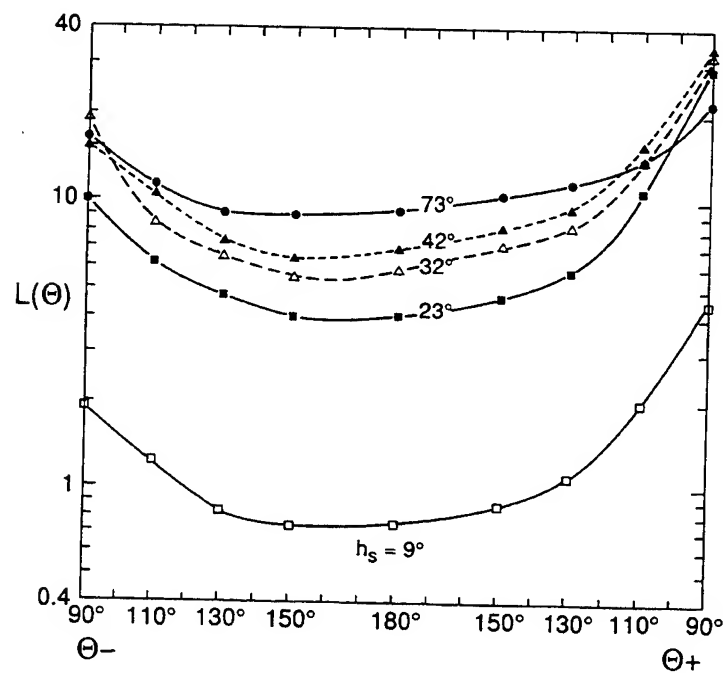


Fig. 5. Upward radiance $L(\theta)$ at Station J2A, 2 July 1971, $\lambda=465$ nm, for different solar elevations h_s at 5 m depth.

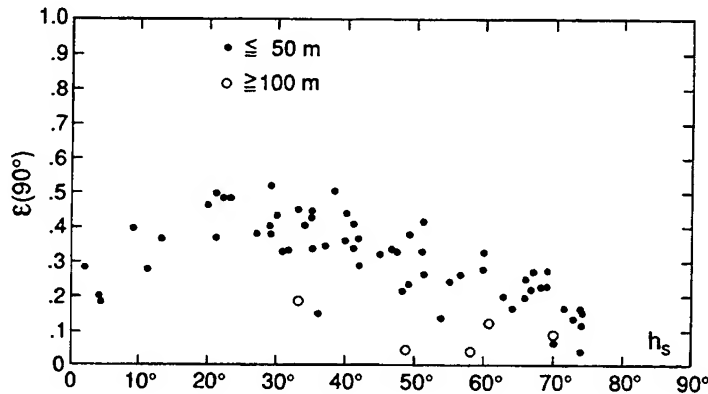


Fig. 6. The ellipticity $\epsilon(90^\circ)$ at 465 and 474 nm, as a function of the solar elevation h_s , for the depth ranges 0-50 m and 100-190 m.

$$\begin{aligned}\bar{L}(90^\circ)/L(180^\circ) &= 3.0 \pm 0.9 \\ \bar{L}(110^\circ)/L(180^\circ) &= 1.7 \pm 0.3 \\ \bar{L}(130^\circ)/L(180^\circ) &= 1.2 \pm 0.1 \\ \bar{L}(150^\circ)/L(180^\circ) &= 1.1 \pm 0.1\end{aligned}$$

The upward radiance measured for $90^\circ \leq \theta \leq 180^\circ$ and $\phi = 0, 180^\circ$ at 5 m depth varies with the solar elevation h_s in a systematic manner as shown by Fig. 5. Note that at grazing angles this variation is appreciable. If we introduce a concept termed the "remote sensing light" and define it as the underwater radiance in the ranges $150^\circ \leq \theta \leq 180^\circ$ and $150^\circ + \leq \theta + \leq 180^\circ$, respectively, it is straightforward to model $L(\theta+)$ and $L(\theta-)$ for the aforementioned θ -values by eq. (18).

In Fig. 6 the values of $\epsilon(90^\circ, h_s)$ versus solar elevation for the depth ranges 0-50 m and 100-190 m have been chosen as informative examples. It is known that for $h_s = 90^\circ$, $\epsilon(90^\circ, 90^\circ) = 0$ exactly, but the observations showing $\epsilon(90^\circ, 0^\circ) \sim 0.2$ and $\epsilon(90^\circ, 25^\circ) \sim \epsilon_{\max}$ are not self-evident results.

Finally it can be stated that from our total data set

$$\begin{aligned}\mu_d &\sim 0.75 \pm 10\% \\ \mu_u &\sim 0.40 \pm 10\% \\ \mu_d/\mu_u &\sim 1.9 \sim \text{constant}\end{aligned}$$

where μ_d and μ_u are the average cosines for the downward and upward radiances, respectively, and that

$$Q \sim 4 \pm 20\% \text{ for all our cases.}$$

Because the present observations show that R varies 10 times more than μ_u and Q , the variation of the remote sensing reflectance RSR is most probably dominated by R , according to eq. (10).

5.3. Polarization

The degrees of polarization are low to intermediate *i.e.* ranging from a few percent up to 25% just below the sea surface. The corresponding upward radiances in the sun's direction attain their minimum degrees of polarization ranging from ~ 0 to a few percent. The maximum degree of polarization, $\sim 50\%$, occurs when $\theta \sim 80^\circ$ - 110° towards and away from the sun. Finally, the degree of polarization is rather constant with depth.

6. DISCUSSION AND CONCLUSIONS

Downward irradiance calculated from the observed radiance at 465 nm by eq. (5) compares favourably with earlier published irradiance observations at this wavelength⁹, so we are assured that the accuracy of the radiance data is high, except for the near surface measurements where ship shadows and wave effects (like for instance sun glints) are problematic, especially for radiance measured in the ship's direction and in directions close to the solar rays. Inspection of the upward

radiance data reveals no evidence of self-shading effects from the meter itself.

In Chapter 3 we have assumed *a priori* that $L(\theta+) \geq L(\theta-)$ and $d\epsilon/dz < 0$ for all depths below a certain depth z_o in the surface layer. These assumptions have not been justified in a strict analytical sense, solely based on the equation of radiative transfer, plausible light scattering functions and surface light conditions, respectively, but are purely based on the existing experimental knowledge^{2,4,6,14}.

The approximation stated in eq. (2) is of paramount importance. It has for this reason been tested with a highly satisfactory result (note that in the surface layers in the vicinity of the ship or in the sun's direction there might occur deviations due to shadows and sun glints, respectively). Fitting radiance data from clear sky conditions with the approximation leads to errors in the azimuthal mean values of the order of 5%^{3,14}, while an overcast sky reduces the errors to $\sim 1\%$ ¹⁴.

The azimuthal mean value $\overline{L(z, \theta)}$, modelled by eq. (17), was compared with the observed values based on $L(\theta+)$, $L(\theta-)$ and eq. (4), with the following results:

$$\overline{L(110^\circ)}_{\text{modelled}} = (1.06 \pm 0.10) \overline{L(110^\circ)}_{\text{observed}}$$

$$\overline{L(130^\circ)}_{\text{modelled}} = (1.07 \pm 0.07) \overline{L(130^\circ)}_{\text{observed}}$$

$$\overline{L(150^\circ)}_{\text{modelled}} = (1.02 \pm 0.06) \overline{L(150^\circ)}_{\text{observed}}$$

This implies that the α -model on average will overestimate the radiance by 2% up to 7%, which are rather small errors.

Comparison of the distribution functions Q and μ_u calculated from the α -model (eqs. (19) and (20)) with the corresponding values based on numerical integrals of the radiance field gives that

$$Q_{\text{modelled}} = (1.06 \pm 0.10) Q_{\text{observed}}$$

$$\mu_{u, \text{modelled}} = (1.01 \pm 0.02) \mu_{u, \text{observed}}$$

Similarly we find that

$$E_{u, \text{modelled}} = (1.04 \pm 0.06) E_{u, \text{observed}}$$

$$E_{ou, \text{modelled}} = (1.03 \pm 0.06) E_{ou, \text{observed}}$$

A satisfactory agreement between model and observations can again be noted.

Radiance is the key parameter in marine optics and modelling. Accordingly there should be a much stronger focus on a development towards modern and speedy radiance instrumentation. This holds true in particular with the perspectives of new-coming satellite color scanning sensors having highly improved measuring capabilities. We see no great potential for the combination of irradiance data with algorithms and/or computational schemes like Monte Carlo techniques, because validation of the end results is hampered by the limited information contained in the irradiance data.

7. ACKNOWLEDGEMENTS

The Nordic cruise to the Mediterranean was made possible through grants from the Danish Scientific Council and the Norwegian Council for Natural Science and the Humanities. The Nordic Council for Physical Oceanography has on several occasions supported this project. We are also due thanks to Jørgen Holck and Niels Berg Olsen for their contributions to the field work and the analysis of the recordings. Especially we want to thank Bo Lundgren, who not only constructed the radiance meter and lead the field work in 1971, but who also has given his permission to present these results.

8. REFERENCES

1. B. Lundgren, "On the polarization of the daylight in the sea", Rep. Dept. Phys. Oceanogr., Univ. Copenhagen, **17**, 34 pp. (1971).
2. N. G. Jerlov, *Marine Optics*, p. 119 and 154, Elsevier, Amsterdam, 1976.
3. B. Lundgren and N. K. Højerslev, "Daylight measurements in the Sargasso Sea. Results from the "Dana" Expedition January-April 1966", Rep. Dept. Phys. Oceanogr., Univ. Copenhagen, **14**, 44 pp. (1971).
4. R. C. Smith, "Structure of solar radiation in the upper layers of the sea", in *Optical Aspects of Oceanography*, Eds. N. G. Jerlov and E. Steemann Nielsen, 95-119, Academic Press, London, 1974.
5. K. J. Voss, "Radiance distribution measurements in coastal water", in *Ocean Optics IX*, ed. M. A. Blizard, SPIE **925**, 56-66, Proc. 4-6 April, Orlando, 1988.
6. N. G. Johnson and G. Liljequist, "On the angular distribution of submarine daylight and on the total submarine illumination", *Sven. Hydrogr.-Biol. Komm. Skr., Ny Ser. Hydrogr.*, **14**, 15 pp. (1938).
7. G. Kullenberg and N. Berg Olsen, "A comparison between observed and computed light scattering functions - II", Rep. Dept. Phys. Oceanogr., Univ. Copenhagen, **19**, 27 pp. (1972).
8. N. K. Højerslev, "Inherent and apparent optical properties of the Western Mediterranean and the Hardangerfjord", Rep. Dept. Phys. Oceanogr., Univ. Copenhagen, **21**, 72 pp. (1973).
9. N. K. Højerslev, "Daylight measurements for photosynthetic studies in the Western Mediterranean", Rep. Dept. Phys. Oceanogr., Univ. Copenhagen, **26**, 38 pp. (1974).
10. N. K. Højerslev, "Optical properties of sea water", in *Landolt-Börnstein Numerical Data and Functional Relationships in Science and Technology, New Series, Vol. 3a*, Ed. J. Sündermann, 383-462, Springer-Verlag, Berlin, 1986.
11. J. R. V. Zaneveld, "Remotely sensed reflectance and its dependence on vertical structure: a theoretical derivation", *Appl. Opt.*, **21**(22), 4146-4150 (1982).
12. N. K. Højerslev and J. R. V. Zaneveld, "A theoretical proof of the existence of the submarine asymptotic light field", Rep. Dept. Phys. Oceanogr., Univ. Copenhagen, **34**, 16 pp. (1977).
13. E. Aas, "The absorption coefficient of clear ocean water", Rep. Dept. Geophys., Univ. Oslo, **67**, 17 pp. (1987).
14. J. E. Tyler, "Radiance distribution as a function of depth in an underwater environment", *Bull. Scripps Inst. Oceanogr., Univ. Calif., La Jolla, Calif.*, **7**(5), 363-412 (1960). The radiance data are also published in: J. E. Tyler and R. W. Preisendorfer, "Light", in *The Sea, Vol. 1*, Ed. M. N. Hill, 397-451, Interscience, London, 1962.
15. N. G. Jerlov, "The optical classification of sea water in the euphotic zone", Rep. Dept. Phys. Oceanogr., Univ. Copenhagen, **36**, 46 pp. (1978).

ABSTRACT

Spectral irradiance of incident light was measured throughout the day during 6 days from December 1995 to March 1996. Variations in incident light with zenith angle were recorded by shading the cosine collector, allowing light from only a 10° zenith angle band to reach the sensor. On bright days total irradiance showed an asymmetrical pattern with high mean levels in the afternoon for equivalent zenith angles of the sun. This may be attributed to morning haze and low cloud which gradually cleared. Spectra contained a higher proportion of blue light in the morning and late afternoon, and during overcast periods. For periods of changeable cloud cover, good correlation was found between the natural log of blue to red spectral ratios and total irradiance adjusted for sun zenith angle. Lower blue to red ratios were found in the $60\text{--}90^\circ$ bands, and higher ratios in the $0\text{--}50^\circ$ bands, reflecting the high zenith angle of the sun and the presence of haze and cloud near the horizon. Comparison with model output show reasonable agreement at medium sun zenith angles in March, but more variable fit at high zenith angles in December and January.

Keywords: spectral irradiance, incident light, spectral ratios, remote sensing, photosynthetically available radiation

2. INTRODUCTION

Determination of incident irradiance is necessary for calculations of reflectance. It is difficult to obtain simultaneous spectral measurements of incident and reflected light and allowance must be made for errors arising from short term differences in irradiance between reference and target measurements. When the sky is partially overcast fluctuations may be quite rapid. Intermittent shadowing leads to changes, not only in total irradiance, but also in the balance between direct and diffuse light. As these two contributions are spectrally different, the result is an overall change in spectral ratios. A method which allows the estimate of spectral shape from a combination of regular spectral reference measurements and continuous records of total light intensity, would therefore be of value, both for near surface measurements used for development of algorithms and for airborne remote sensing where the aircraft may be in sunlight when the target is not, or vice versa.

In situ measurements of spectral irradiance during different meteorological conditions and at different locations is also important for the testing of radiative transfer models. A clarification of the relationship between solar zenith angle, cloud cover and atmospheric aerosols on the one hand and the intensity, spectral composition and angular distribution of incident light on the other has implications not only for atmospheric corrections in remote sensing, but also for studies of photosynthetic processes.

This study aims to 1) link changes in total irradiance and spectral ratios to changes in cloud-cover and sun zenith angle, 2) ascertain whether the relationship between spectral ratios and overall light intensity may be assumed relatively constant in the short term, 3) measure the zenith angle distribution of incident light, relating this to meteorological information and sun zenith angle and 4) compare in situ measurements to spectral irradiance as calculated by the Hydrolight 3.0 model developed by Mobley.¹

3. METHODS

3.1 Field measurements

Hurst Spit is a low shingle spit extending into the Solent towards the Isle of Wight at $50^\circ 42'$ North and $1^\circ 34'$ West. It is likely to have atmospheric conditions somewhere between continental and marine, and typical of coastal regions. Irradiance was measured at this site at approximately 1-2 minutes intervals using the cosine collector of a Spectron SE-590 spectrometer mounted on a tripod. There were occasional short breaks in data for a variety of reasons. A few times during the day the cosine collector was shaded with hemispherical 'hats' of matt, black plastic with a 10° zenith angle band cut out to

allow light to reach the sensor. The radius of the hats was chosen so as to be more than 10 times the radius of the cosine diffuser, thereby minimising the error arising from internal shading. The accuracy of the band edges has been determined through measuring the hats to $\pm 0.5^\circ$. The 9 hats were applied consecutively, immediately preceeded and followed by a measurement of the unshaded sensor. A typical series of measurements would last 5-6 minutes. To account for changes in overall light-levels during this period, simultaneous measurements were taken of the light reflected from a white, Lambertian reference panel using a Spectrascan PR-650 spectrometer at a nadir viewing angle of about 10° , from the anti-solar direction. Both cosine collector and reference panel were carefully levelled and horizontal.

3.2 Instrument specifications and calibration

The Spectron SE-590 has a sampling interval ranging from 2.5nm (at 350nm) to 3.6nm (at 1100nm) and a nominal bandwidth of 10nm, although the true bandwidth has been found by Starks *et al.* to be somewhat larger.² The recorded measurements were automatically channel shifted to ensure accurate positioning of the minimum from atmospheric absorption at 762nm, and spectral irradiance in $\text{mWm}^{-2}\text{nm}^{-1}$ calculated using the calibration and algorithm provided by the Natural Environment Research Council's Field Spectroscopy Unit. The Spectrascan measures radiance in a 1° solid angle, and has a nominal bandwidth of 8nm and a sampling interval of 4nm with a spectral accuracy of 2nm in the region 380-780nm. For this instrument the manufacturer's calibration was used, and checked for the position of the 762nm atmospheric absorption band, which in all cases fell between 760 and 764nm. Measurements were adjusted to allow for the incomplete reflectance of the reference panel and converted to units of irradiance.

Differences between the two instruments were found in wave-bands of high atmospheric absorption, with the Spectrascan recording lower light levels, consistent with its lower nominal bandwidth. The Spectrascan also showed light levels over twice those of the Spectron at 400nm. The ratio between the two sets of measurements declined exponentially to level out at about 540nm. The percent difference in the 540-700nm region varied with zenith angles of the sun, visibility and cloud cover as may be seen in Table 1. Closer examination of the raw Spectron data revealed a displacement of the 762nm absorption band to 753.1nm, which had been automatically moved to its correct position on calibration. As a result the steep rise in irradiance towards 450nm due to increasing extraterrestrial solar irradiance³, was shifted by 10-12nm towards higher wavelengths, and the calibrated data under-estimated irradiance in the blue. Recalibration under temperature conditions like those found in the field were not a practical possibility. Nor could the error be corrected for by stretching the calibrated spectra to position wavebands correctly, because clearly defined features such as the 762 absorption band are absent in the blue. Instead a correction factor was developed on the basis of the average of 144 reference panel measurements (rms error 7%) taken at intervals through all 6 days at sun zenith angles of 51° - 80° (mean 61.5°), and assuming a percent panel error in the blue similar to that in the region 540-700nm, where the Spectron calibration seemed reliable. This factor was used to adjust the 400-560nm waveband of the cosine collector measurements, and to compensate for the lower spectral sensitivity to the water absorption peaks around 590 and 651nm.

Table 1. Reference panel measurements as % of cosine collector measurements in the 540-700nm waveband.

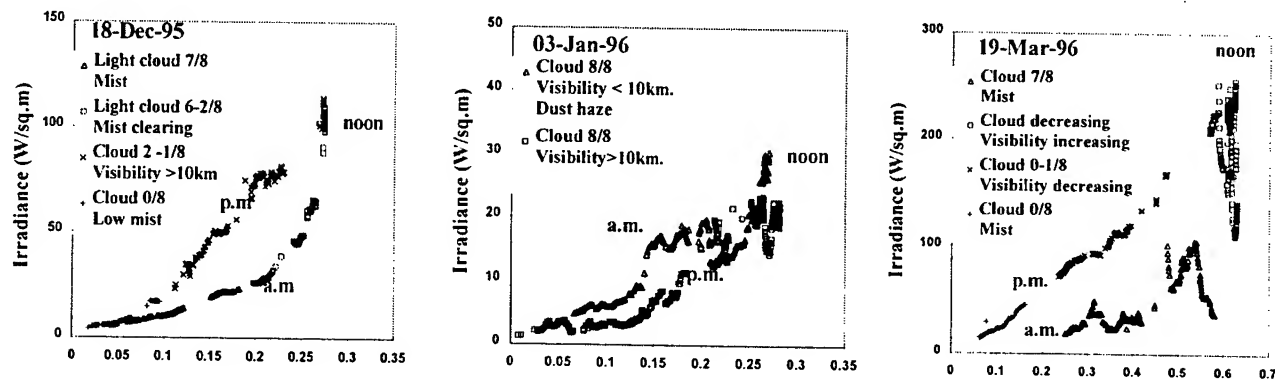
Date	Dec. 13		Dec. 18		Jan. 01		Jan. 10		Mar. 18		Mar. 19	
Cloud cover	8/8	8/8	7/8	2/8	8/8	8/8	7/8	3/8	4/8	2/8	0/8	0/8
Visibility	15km	15km	Haze	10km	10km	10km	Haze	10km	15km	15km	10km	Haze
Sun Zenith Angle	88°	78°	89°	75°	89°	74°	88°	75°	51°	79°	51°	84°
% Irradiance Recorded	60%	85%	81%	92%	76%	95%	89%	90%	96%	102%	105%	101%

3.3 Data analysis

Where low light levels led to noisy spectra these were smoothed using a moving 9 point polynomial smoothing algorithm;⁴ this was generally necessary where the cosine collector was measuring light from the 0 - 10° and 80 - 90° zenith angle bands. Total irradiance was calculated for the 400-700nm band, and cosine adjusted irradiances obtained by dividing these by the cosine of the sun zenith angle. Blue to red spectral ratios were derived from the summed irradiances in the 452-472 and 660-680nm bands. For periods of high short term variability, correlation coefficients and regression lines were calculated for the relationship between cosine adjusted irradiances and the natural log of blue to red spectral ratios. Sun zenith angles were derived from automatically recorded measurements of time, latitude, longitude, declination at noon and the meridian pass. Allowing for errors in timing of up to 5 minutes, and for assuming a constant declination through the day, calculations should be accurate to $\pm 0.5^\circ$ or better for angles less than 89° . On-site records of cloud-cover in octas, approximate wind-speed and degree of haziness was supplemented with data provided by the Met Office from Hurn Airport

near the coast 20km away. This included vapour pressure, relative humidity, visibility and cloud cover at 9 a.m each day. Precipitable water was calculated both from the vapour pressure, and from temperature and relative humidity according to the method described by Garrison and Adler.⁵ The two figures were then averaged. Together with sun zenith angle, these parameters were used as input into the "qrealsky" sub-routine of Mobley's Hydrolight 3.0 model.¹

a)



b)

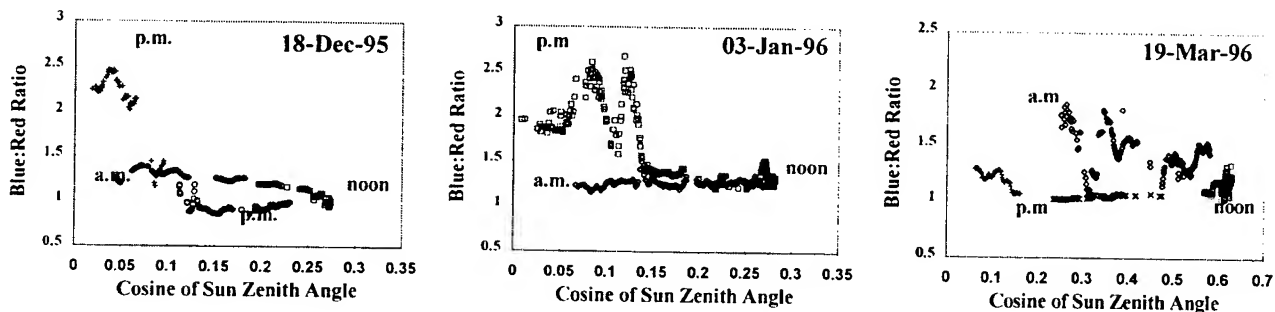


Figure 1. a) Total irradiance (400-700nm) plotted against the cosine of the sun's zenith angle for 2 bright and one overcast day. Note the difference in scales. b) Blue: to red ratios (452-472nm : 660-680nm) for the same three days.

4. RESULTS

4.1 Total irradiance and spectral ratios

Figure 1a shows asymmetry between morning and afternoon for the bright days (18/12 and 19/3). Initial slopes of total irradiance against cosine of sun zenith angle are similar to those of the overcast day (3/1) followed by an exponential increase as skies clear. Short term variability was greater on the windier March morning. During the relatively cloud-free afternoons irradiance decline is almost linear. This pattern was evident also on the other bright days, with asymmetry caused by morning haze and cloud, clearing towards the early afternoon. In the partially cloud-covered periods there was good negative correlation between the natural log of the spectral ratios and irradiance adjusted for sun zenith angle, even when light levels varied considerably (table 2). A given relationship would hold for about 1 hour, sometimes longer, depending on how rapidly overall cloud-cover changed. For fully overcast days correlation was lower or did not exist.

4.3 Spectral variations with zenith angles.

As may be seen from Figure 2 the spectral variation with zenith angle was greater during the clear afternoons than during the cloudy mornings. In the afternoon bands 1-7 (0-70°) are increasingly dominated by shorter wavelengths towards zenith. Band 8 (70-80°) contains the contribution of direct sunlight and has a lower blue to red ratio than the others. Band 9 (80-90°), which contains most of the cloud and banks of haze, is intermediate between band 8 and the rest, as is total hemispherical light. This pattern, with the band dominated by direct sun-light markedly different from the rest, is seen also on other bright days. For bands where diffuse light makes the only contribution, the increasing dominance of shorter wavelengths towards low zenith angles is evident. Fully overcast days have spectral distributions broadly similar to those seen on the cloudy December morning. The column charts show that during the hazy, cloudy early morning, the majority

Table 2. Correlation Blue:Red Ratio v. Adjusted Irradiance

Date	Time	Cloud	No. 1	CV ²	r	Slope
13/12	10-11	8/8	53	85%	0.23	
	12-14	8/8	100	80%	-0.80	-0.001
3/1	10-11	8/8	148	97%	-0.2	
	12-14	8/8	189	47%	-0.88	-0.005
18/12	09-11	5-6/8	140	122%	-0.95	-0.0012
	11-12	3-4/8	52	21%	-0.87	-0.0013
10/1	10-11	5/8	22	62%	-0.96	-0.0020
	11-12	4/8	44	61%	-0.98	-0.0011
	12-13	3/8	48	79%	-0.96	-0.0014
18/3	09-10	6/8	81	140%	-0.93	-0.0010
	10-11	5/8	81	134%	-0.91	-0.0003
	11-13	3-4/8	137	72%	-0.96	-0.0003
19/3	09-10	6-7/8	48	80%	-0.71	-0.0016
	10-11	5/8	98	94%	-0.98	-0.0013
	11-12	4/8	48	122%	-0.84	-0.0012
	12-13	2-3/8	72	39%	-0.94	-0.0011

¹ Number of measurements made in the period

² Variability: Range as percentage of mean irradiance

the model input. Means are still somewhat higher than model results for 18/12 and 18/3, although the model spectra fall within the range of the observations.

5. DISCUSSION

5.1. Calibration

To use the reference panel measurement as a basis for cosine collector calibration may seem questionable, given that errors due to non-Lambertian properties of the panel are known to increase when the incident light comes from high zenith angles,⁶ as would be the case in most of this study. However, if a constant calibration is applied, measurements should be

of the contribution to irradiance came from the 40-70° zenith angle bands. Once the sun was out, direct light far outweighed the contribution of skylight, as may be seen from the peak in the 70-80° band.

4.4 Comparison with model output

Figure 3 shows model runs for the hazy morning of 18/12, the clear, partially overcast mid-morning of 18/3 and the cloud-free but hazy mid afternoon of 19/3. The overall spectral slope, the blue peak around 460nm and the red peak around 670nm are in good agreement between model and observations. The water absorption bands at 590 and 652nm, on the other hand, are less clearly defined in the observed data. These are narrow features, and the bandwidth of the Spectron, 10nm or more, would make them wider and shallower. To diminish the effect of short-term irradiance fluctuations, the mean has been calculated from spectra of $\pm 1^\circ$ sun zenith angle from that used in

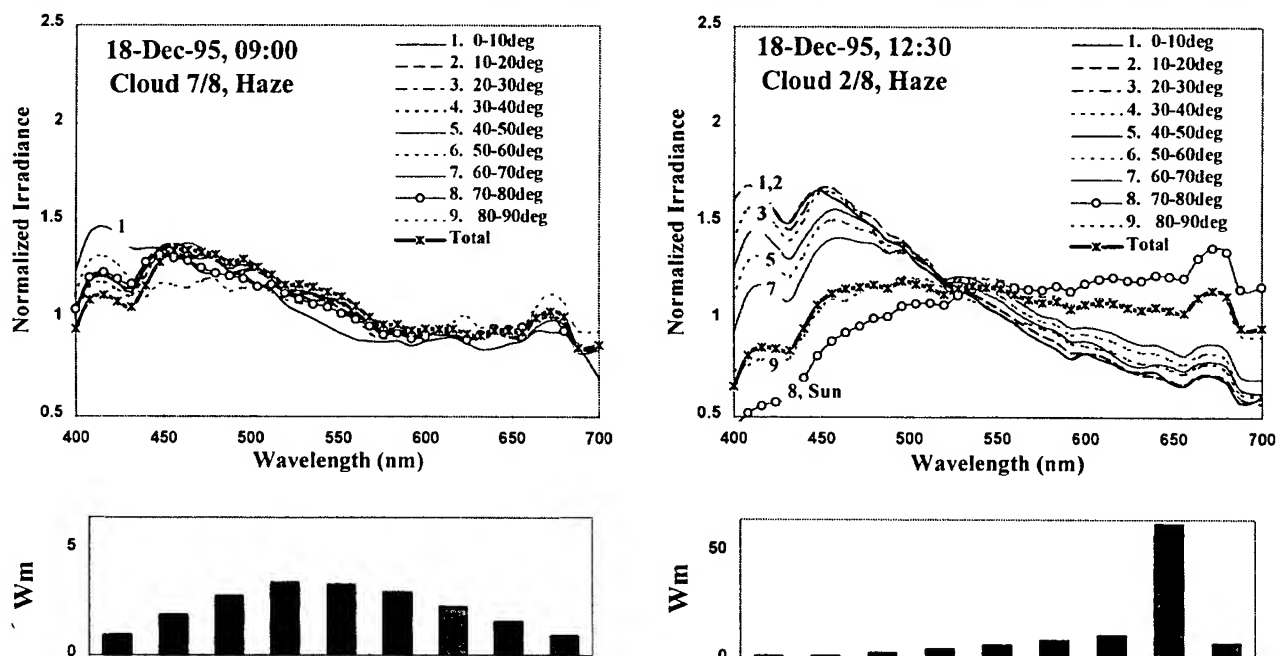


Figure 2. Irradiance normalised to spectral mean for 9 zenith angle bands on December 18th. Total irradiance from different zenith angle bands are shown underneath. Note the order of magnitude difference in scale..

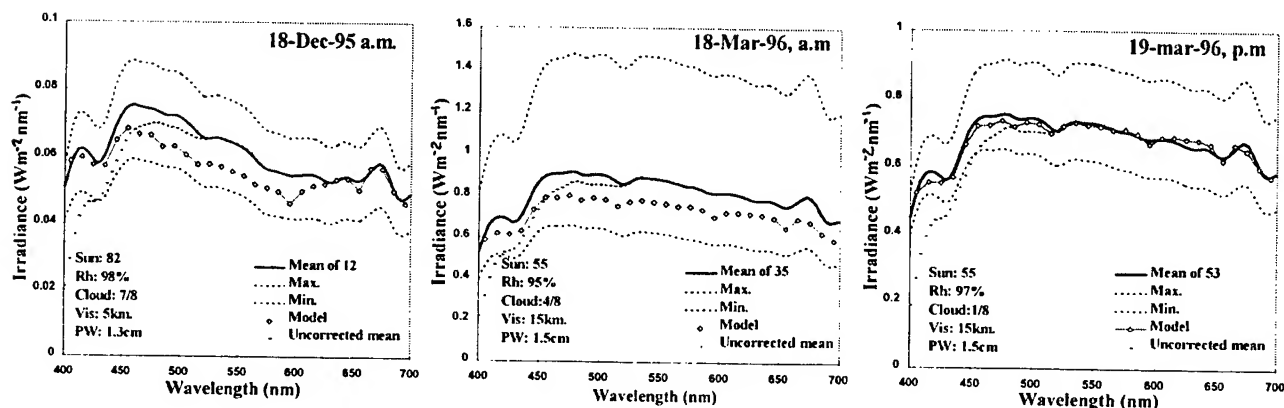


Figure 3. Recorded irradiance spectra compared to model output from the Hydrolight 3.0 model. Input parameters for each run are listed within the frame Rh : relative humidity, Vis: visibility, PW: Precipitable water.

comparable with each other, even if absolute values are more uncertain. The assumption that panel errors are of the same order across the spectrum forms the basis for the calculations and needs some consideration. Diffuse and direct light are different both spectrally and in angular distribution. In Kimes and Kirchner's data, the error curves for the two types cross at 60° for hazy skies and about 65° for clear skies, with the errors in diffuse light being greater at lower zenith angles of the sun and less at higher angles. As reference panel measurements forming the basis for the correction factor were taken during a wide variety of sky conditions at sun zenith angles ranging from 51° to 80° , any bias in favour of one irradiance component over the other is unlikely. The obvious improvement in comparison with model output would seem to vindicate the method at least to some extent. The correction also brought overall slope of observed spectra more into line with expectations based on measurements by other authors and estimates from literature.^{3, 7}

5.2 Total irradiance and spectral ratios.

The asymmetry between morning and afternoon evident on the bright days is likely to be a common phenomenon in coastal areas of temperate latitude in autumn, winter and early spring, as the weak sun takes time to burn off mist and clouds. Because of its effect both on total irradiance and spectral ratios, it may be necessary to take it into consideration when calculating irradiance budgets. The short periods of high irradiance seen on 18/3 (fig.4), may also be noteworthy. They are probably caused by a combination of focusing and reflection by clouds. Changes in angular radiance distribution caused by such reflection may well have some effect also on mean irradiance. Unfortunately this cannot be checked from the present data as no measurements of distribution with zenith angle band were carried out during this period. The effect could, however, explain the discrepancy between model output and observations on 18/3 (fig.3), where the mean may have been raised above expected levels by a number of very bright periods such as the maximum shown.

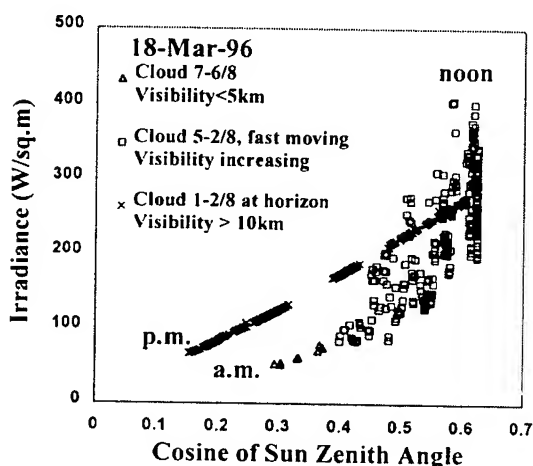


Figure 4. Irradiance with cosine of sun zenith angle.

The close link between spectral ratios and total irradiance during partially overcast periods is encouraging. Provided the degree of cloud cover does not change too much within a given period, it is possible to calculate the spectral shape of the light on the basis of total irradiance and a reasonable number of reference spectra. The high correlation coefficient between blue to red ratios and overall irradiance seen on 18th of March is of particular importance, as the rapid fluctuations of this day are of a kind known to create problems for reflectance measurements.

5.3. Spectral variations with zenith angles

The spectra obtained from different zenith angle bands agree with more subjective visual observations that the sky is bluer straight overhead than near the horizon. The shift in distribution of total irradiance towards a brighter horizon once the sun is out, is a feature also observed by other authors.⁵

5.4 Comparison with model output.

As mentioned above, bright clouds may have been the cause of mean irradiance being higher than expected on 18/3. On 19/3, when skies were cloud-free but hazy, spectral shape and irradiance level show almost perfect fit with model calculations. The greater discrepancy on 13/12 may be due partly to difficulties in establishing values for model input. Some of the parameters were based on observations some distance away at an earlier time, while others such as visibility were only broad estimates based on the clarity of landscape features. Visibility is known to affect model output particularly at shorter wavelengths^{1,3}. Another important parameter, precipitable water, was estimated by a method which strictly speaking holds only for mean daily values.^{3,5} A failure to determine this correctly would particularly affect the water absorption bands at 590 and 651nm. To what extent this and not the sensor bandwidth is the reason for the discrepancy seen, is hard to determine. Short term fluctuations may also create problems in matching model and observation, although this can be minimised by averaging several spectra. On 18/12 the model output is close to the spectrum of the minimum observation, both in shape and level. This may mean that the contribution of direct light was greater than anticipated. Although cloudiness was 7/8, much of this cloud was light and wispy, and their effect may have been over-estimated. Variations in thickness and type of cloud, not covered in the octa descriptions may also have caused discrepancies between model and results on 3/1 (not shown) when the model was close to the bottom of the range in the morning and near the top in the afternoon. In general, however, the agreement between model and observations must be classed as good.

5.5. Summary

Changes in light level and spectral ratios are clearly linked to changes in cloud cover and sun zenith angle, with high blue-red ratios at low elevations of the sun and during cloudy conditions. The link between spectral ratio and total irradiance has been established for periods of highly variable total irradiance. Correlation is best when skies are partially overcast, and hold for short periods, but are more questionable in fully overcast conditions. Despite this, a degree of correlation may be found also in these circumstances, as in case of the two overcast afternoons. The contribution to hemispherical irradiance from different zenith angle bands varies more in clear than in overcast conditions, reflecting the position of the sun, with the horizon brighter on clearer days. Agreement with model spectra was generally good, particularly for periods where short term fluctuations were of a limited magnitude. It is clear that some error must exist, both due to uncertainty about the input parameters of the model and due to variability in atmospheric conditions and cloud cover which cannot be adequately determined by the methods used.

6. ACKNOWLEDGEMENTS

Particular thanks are due to Dr. Curtis D. Mobley for the use of the Hydrolight 3.0 model, and to Dr. Toby Tyrrell for carrying out the model runs. The research was carried out with on a grant from the Natural Environment Research Council, England, which also provided some of the equipment.

7. REFERENCES

- ¹ C.D. Mobley, "Hydrolight 3.0 Users Guide," Section 4.1.2, SRI International, Menlo Park, CA, (1995).
- ² P.J. Starks, F.R. Schiebe and J.F. Schalles, "Characterization of the accuracy and precision of spectral measurements by a portable, silicon diode array spectrometer," *Photogrammetric Engineering & Remote Sensing*, **61**(10), 1239-1246 (1995).
- ³ W.W. Gregg and K.L. Carder, "A simple spectral solar irradiance model for cloudless maritime atmospheres," *Limnology and Oceanography*, **35**(8), 1657-1675, (1990).
- ⁴ A. Savitzky and M.J.E. Golay, "Smoothing and differentiation of data by least squares procedures," *Analytical Chemistry*, **36**, 1627-1639 (1964).
- ⁵ J.D. Garrison and G.P. Adler, "Estimation of precipitable water over the United States for application to the division of solar radiation into its direct and diffuse components," *Solar Energy*, **44**(4), 225-241 (1990).
- ⁶ D.S. Kimes and J.A. Kirchner, "Irradiance measurement errors due to the assumption of a Lambertian reference panel," *Remote Sensing of Environment*, **12**(4), 141-149, (1982).
- ⁷ Morel A., "Light and marine photosynthesis: a spectral model with geochemical and climatological implications," *Prog. Oceanogr.*, **26**, 263-306, (1991).

Recent measurements of the spectral backward-scattering coefficient in coastal waters

Robert A. Maffione and David R. Dana

Sequoia Scientific, Inc., Mercer Island, Washington 98040

ABSTRACT

The backward scattering coefficient, b_b , was measured in various coastal waters with fixed-angle backscattering sensors developed by the authors. Measurements were made at four discrete wavelengths covering the spectral range 440 to 675 nm. A power law spectral dependence of b_b due to scattering by particles was investigated of the form $b_b^p(\lambda) = b_b^p(\lambda_0)(\lambda_0/\lambda)^\gamma$, where the superscript p denotes particle scattering and λ is the wavelength. The exponent γ depends on the particle size distribution and composition of particles. Extensive measurements in Monterey Bay, California, showed that $0.1 \leq \gamma \leq 1.1$, where the lower values were in the clear, interior waters generally below 10 m. For the upper 10 m, $0.7 \leq \gamma \leq 1.0$, and $\bar{\gamma} \approx 0.8$. In the relatively clear Gulf of Mexico waters near Panama City, Florida, γ for the upper 10 m was found to be in the range, $0.9 \leq \gamma \leq 1.1$, with $\bar{\gamma} \approx 1.0$. At Dry Tortugas, which consists of clear coral reef water, $0.9 \leq \gamma \leq 1.1$, and $\bar{\gamma} \approx 1.0$. In the thick, green-brown waters of East Sound, Washington, $0 \leq \gamma \leq 0.1$, which thus were the most spectrally "flat" waters measured.

Key words: ocean optics, optical backscattering, backscattering sensors

1. INTRODUCTION

The backward scattering coefficient, b_b , is an inherent optical property (IOP) that is of central importance to ocean-color remote-sensing models. For example, it is well known that, to first order, the remotely-sensed reflectance is proportional to $b_b/(a + b_b)$, where a is the absorption coefficient. Although a has been measured for many years using a variety of techniques¹, surprisingly little attention has been given to measuring b_b , although modeling it has been a focus of considerable research. The authors have developed several types of fixed-angle backscattering sensors for measuring b_b *in situ*. These sensors, and the calibration technique developed specifically for them, are described in detail elsewhere^{2,3}.

Measurements of b_b were made at four discrete wavelengths, covering the spectral range 440 to 675 nm, at a variety of locations for the purpose of investigating the spectral dependence of backscattering by coastal waters. It was assumed that the spectral dependence of b_b is described by the power-law model:

$$b_b(\lambda) = b_b^w(\lambda_0) \left(\frac{\lambda_0}{\lambda} \right)^{4.32} + b_b^p(\lambda_0) \left(\frac{\lambda_0}{\lambda} \right)^\gamma, \quad (1)$$

where the superscript w refers to pure sea-water scattering and p refers to particle scattering; λ denotes the wavelength and λ_0 is a reference wavelength. The exponent 4.32 for pure sea-water scattering comes from Morel⁴. The exponent γ depends on the particle size distribution and composition of particles. After subtracting off $b_b^w(\lambda)$ from the total $b_b(\lambda)$ measurements, a linear regression to

$$\ln[b_b^p(\lambda)] = \ln[b_b^p(\lambda_0)] + \gamma \ln(\lambda_0/\lambda) \quad (2)$$

was performed, where the slope yields γ .

2. RESULTS

Figure 1 shows a profile of b_b from Monterey Bay, California. This profile is typical for the shallow regions around the Bay where bottom depth is less than 50 m. The upper 10 m are generally productive and often show strong layering during blooms. The interior waters are usually much clearer than the surface waters, which is also revealed in this b_b profile. As the bottom is approached, resuspended sediments causes the backscattering to increase. The computed profile of γ from the b_b data, using Eq. 2, reveals a strong positive correlation with b_b . Mie theory predicts that, for particles with a constant and real index of refraction, γ increases as particle size decreases. The γ profile thus suggests that relatively larger particles make a greater contribution to backscattering in the clearer interior waters compared with the surface and bottom waters. The data are also consistent with the assumption of a hyperbolic particle size distribution (PSD). If the slope of the PSD is higher for the surface and bottom waters, there will be a much larger contribution to backscattering by the smaller particles, which also increases the absolute value of b_b .

The clearest waters and thus lowest values of b_b that were measured was of coral reef waters at Dry Tortugas. Figure 2 shows a typical profile of b_b and γ from a two-week measurement period in July, 1996. Although the average of all the data gave $\bar{\gamma} = 0.99 \pm 0.05$, the standard error in the regression was more like 0.2, or about four times higher than the standard deviation in the average of γ . The larger standard error in the regression suggests that the spectral dependence of backscattering by these particles is not perfectly described by the power law model, Eq. 1, as opposed to the interpretation that this is due to measurement error. It is interesting to note that the power law model worked well over the shorter wavelengths, but at longer wavelengths it seems to break down, at least for the Dry Tortugas data.

Measurements of b_b were made about seven miles off the shores of Panama City, Florida over a two month period in the summer of 1994. During this entire period, the water optical properties showed very little temporal variability. The profile shown in Figure 3 was quite typical. Interestingly, especially compared with the Monterey Bay data, γ decreased as b_b increased due to resuspended sediment near the bottom. This might be explained by different nature of the Florida coast sediment, which in this region tend to be composed of fine "white" sand particles. These particles might therefore be expected to have spectrally "flat" reflectance, or backscattering, properties, resulting in low values for γ . This is purely conjecture, however, and much research remains to be done on the spectral variability of b_b , which is now possible with these new multi-spectral backscattering sensors.

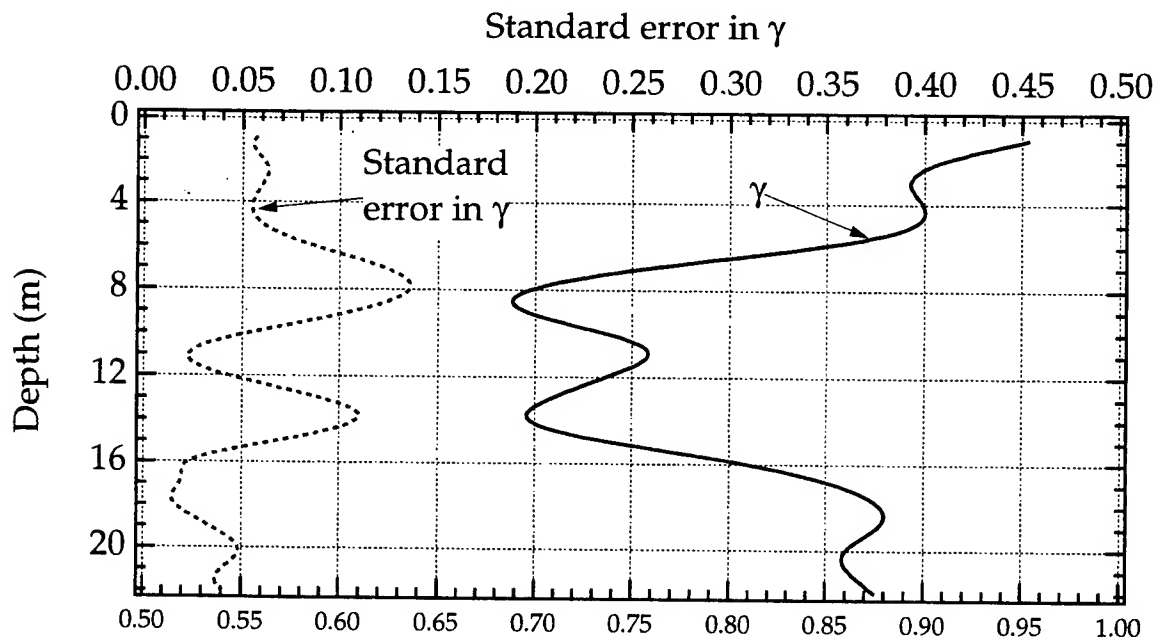
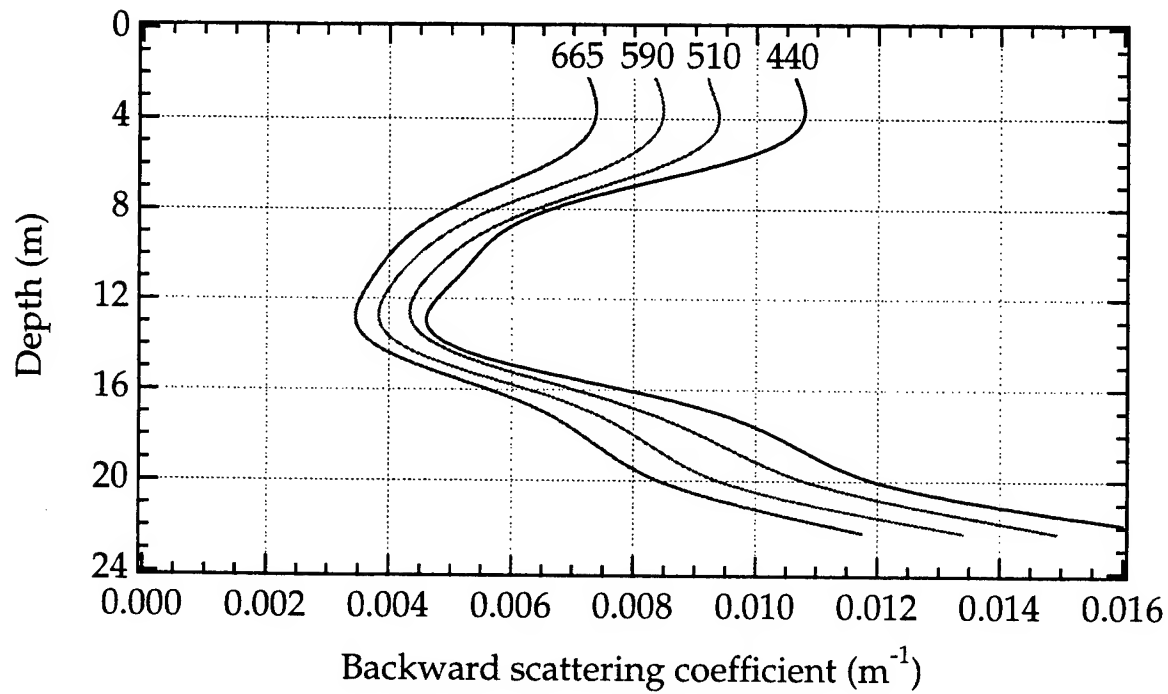


Figure 1. Top) Profile of b_b in Monterey Bay on 7/2/96. Bottom) Computed profile of γ and the standard error in γ (top axis) from the linear regression using Eq. 2.

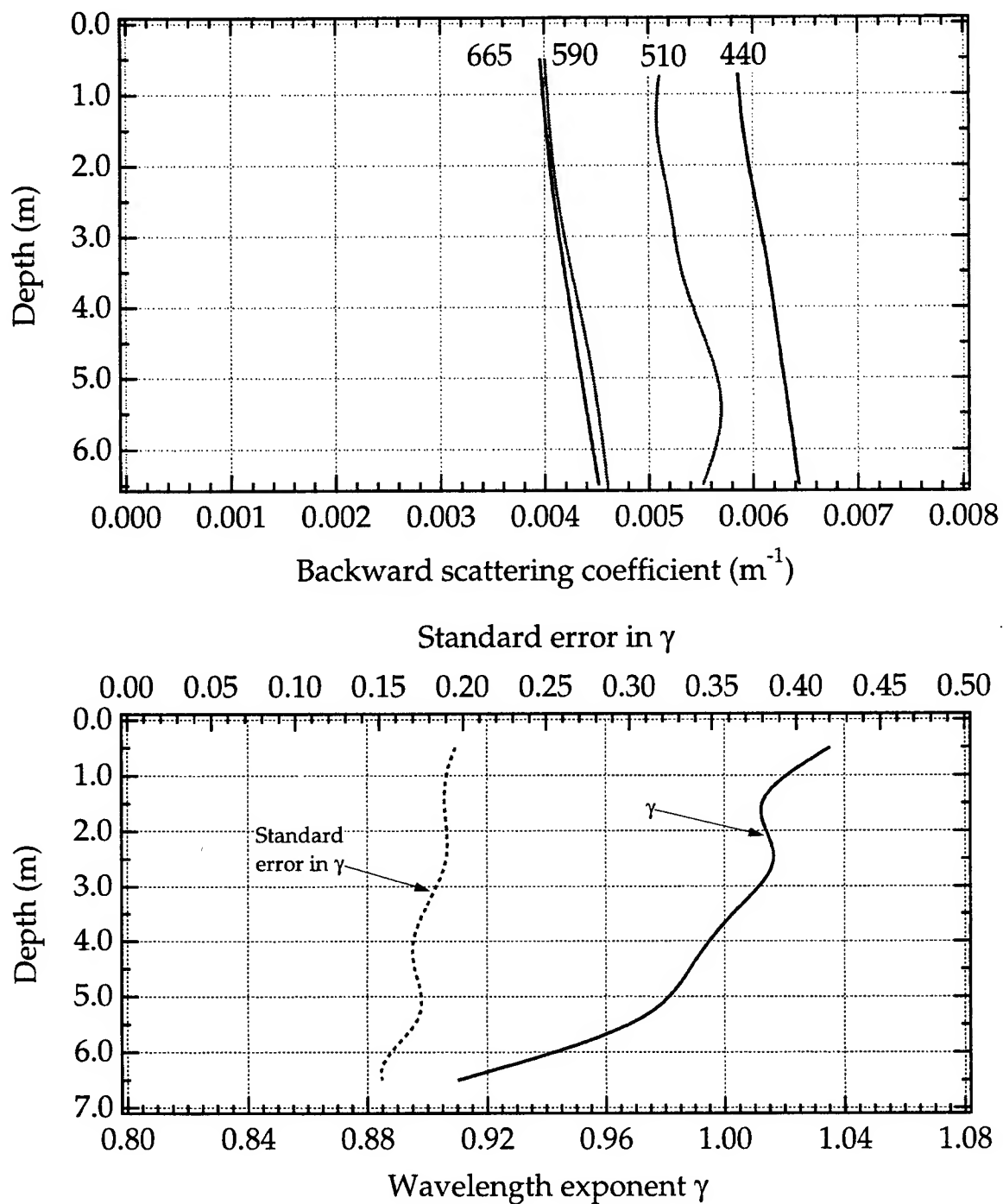


Figure 2. Top) Profile of b_b in clear coral reef water at Dry Tortugas on 7/12/96. Bottom) Computed profile of γ and the standard error in γ (top axis) from the linear regression using Eq. 2.

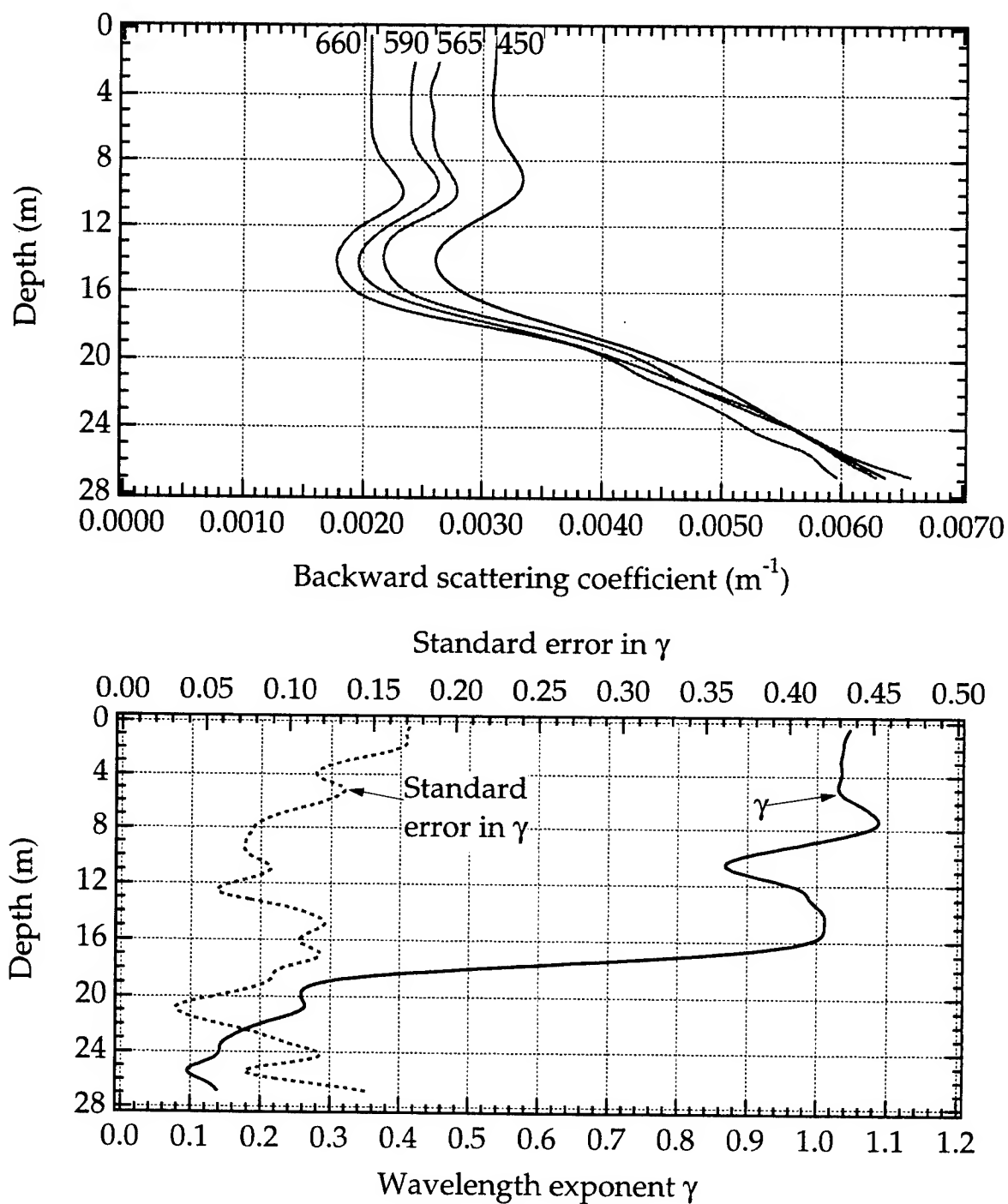


Figure 3. Top) Profile of b_b in the Gulf of Mexico about 7 miles south of Panama City, Florida, on 8/3/94. Bottom) Computed profile of γ and the standard error in γ (top axis) from the linear regression using Eq. 2.

3. ACKNOWLEDGEMENTS

The authors thank Jeff Voss at SRI International for his assistance in making many of these measurements. This work was supported by the Environmental Optics Program at the Office of Naval Research, Naval Research Laboratory at Stennis, Mississippi, and Coastal Systems Station at Panama City, Florida.

4. REFERENCES

1. Pegau, W. S., J. S. Cleveland, W. Doss, C. D. Kennedy, R. A. Maffione, J. L. Mueller, R. Stone, C. C. Trees, A. D. Weidemann, W. H. Wells, and J. R. V. Zaneveld, "A comparison of methods for the measurement of the absorption coefficient in natural waters," *J. Geophys. Res.*, **100**, 13201-13220, 1995.
2. Maffione, R.A., D.R. Dana, and R.C. Honey, "Instrument for underwater measurement of optical backscatter," *Underwater Imaging, Photography, and Visibility*, R.W. Spinrad, Editor, Proc. SPIE, **1537**, 173-184, 1991.
3. Maffione, R.A., and D.R. Dana, "Instruments and methods for measuring the backward-scattering coefficient of ocean waters," *Appl. Opt.* (submitted), 1996.
4. Morel, A., "Optical properties of pure water and pure sea water," *Optical Aspects of Oceanography*, N.G. Jerlov and E. S. Nielsen, Editors, Academic Press, New York, 1-23, 1974.

REMOTE-SENSING REFLECTANCE AND INHERENT OPTICAL PROPERTIES OF OCEANIC WATERS DERIVED FROM ABOVE-WATER MEASUREMENTS

Z. P. Lee¹, K. L. Carder¹, R. G. Steward¹, T. G. Peacock¹, C. O. Davis² and J. L. Mueller³

¹Department of Marine Science
University of South Florida
St. Petersburg, FL 33701

²Naval Research Laboratory
Washington, D.C. 20375

³Center of Hydro-Optics and Remote Sensing
San Diego State University
San Diego, CA 92120

ABSTRACT

Remote-sensing reflectance (R_{rs} , ratio of the water-leaving radiance to downwelling irradiance just above the surface) and inherent optical properties of oceanic waters are important parameters for ocean optics. Due to surface reflectance, R_s , or water-leaving radiance is difficult to measure from above the surface. It usually is derived by correcting for the reflected skylight in the measured above-water upwelling radiance using a theoretical Fresnel reflectance value (Quick-and-Easy method). As it is difficult to determine the reflected skylight, there are errors in the Q&E derived R_{rs} , and the errors may get bigger for high chl_a coastal waters. For better correction of the reflected skylight, we propose the following derivation procedure: partition the skylight into Rayleigh and aerosol contributions, remove the Rayleigh contribution using the Fresnel reflectance, and correct the aerosol contribution using an optimization algorithm. During the process, R_{rs} and in-water inherent optical properties are derived at the same time. For measurements of 45 sites made in the Gulf of Mexico and Arabian Sea with chl_a concentrations ranging from 0.07 to 49 mg/m³, the derived R_{rs} and inherent optical property values were compared with those from in-water measurements. It was found that the ratios of $R_{rs}(440)/R_{rs}(550)$ were very consistent with those from in-water measurements (9.7 % Root-Mean-Square-Difference for chl_a < 1.0 mg/m³). For the derived inherent optical properties, the total absorption coefficients and particle absorption coefficients agreed well with the values from in-water measurements (16.2% and 19.0% RMSD, respectively). These results indicate that for the waters studied, the proposed algorithm performs quite well in deriving R_{rs} and in-water inherent optical properties from above-surface measurements for clear and turbid waters.

Keywords: remote-sensing reflectance, optimization, apparent and inherent optical properties

1. INTRODUCTION

For field measurements of water color, remote-sensing reflectance of the water (R_{rs} , ratio of the water-leaving radiance $L_w(0^+)$ to downwelling irradiance $E_d(0^+)$ just above the surface) is an important parameter to be measured. Traditionally this has been done using in-water profiles of radiance and irradiance¹. For turbid and/or shallow coastal waters, those profiles are hard to measure using in-water instruments due to for example instrument-self-shading. This provides our motivation to make the measurements from above the surface.

What can be directly measured by viewing the water from above the surface, however, is the above-water upwelling radiance ($L_u(0^+)$); water-leaving radiance (L_w) can only be mathematically derived from this measurement. Most of the $L_u(0^+)$ comes from the water, while part of it comes from unavoidable reflected skylight and solar glint introduced by surface roughness (waves) or foam. So $L_u(0^+)$ is a mixture of the water-leaving radiance and other unwanted "contaminations". In the reflectance mode, there is (wavelength dependence is dropped for brevity unless it is necessary)

$$T_{rs} = R_{rs} + r(i)S_{rs}(i) + \Delta \quad (1)$$

where T_{rs} , R_{rs} and $S_{rs}(i)$ are the *total-remote-sensing reflectance*, *remote-sensing reflectance of the water*, and *sky input*, respectively, and are defined as

$$T_{rs} = \frac{L_u(0^+)}{E_d(0^+)}, \quad R_{rs} = \frac{L_w(0^+)}{E_d(0^+)}, \quad \text{and} \quad S_{rs}(i) = \frac{L_{sky}(i)}{E_d(0^+)} \quad (2)$$

In Eq. 1, both T_{rs} and S_{rs} can be easily calculated from direct measurements. In order to derive R_{rs} from Eq. 1, the values for $r(i)$ and Δ have to be determined. In the traditional Quick-and-Easy method², R_{rs} is derived by

$$R_{rs} = T_{rs} - r S_{rs} - \Delta \quad (3)$$

with r calculated based on the measurement geometry, and Δ derived by assuming $R_{rs}(750)$ approximates 0.

Due to the uneven sea surface, it is often hard to determine the actual direction of the skylight which is reflected into the sensor, as the skylight entering the sensor may come from a big effective solid angle. In that angle, the sky radiance is not in uniform distribution, especially for cloudy skies. So errors will be introduced in the Q&E derived R_{rs} spectra. This error will be bigger for coastal waters where water-leaving radiance in the blue is low. A small error in r or S_{rs} may cause big error in the derived R_{rs} in the blue channels. Also, for turbid coastal waters, $R_{rs}(750)$ may no longer be close to 0.

For the derivation of R_{rs} under general situations such as open ocean to coastal waters, and clear to cloudy skies, we propose the following protocol for the measurement and derivation (OPTIMIZATION method). In the derivation procedure, we partition the skylight into Rayleigh- and aerosol-like contributions, remove the Rayleigh contributions first, and do not assume values regarding $R_{rs}(750)$. For the removal of aerosol contributions, the full spectral information from 400 - 830 nm were used. To support the protocol, the derived values for R_{rs} and absorption coefficients were compared with those from in-water measurements.

2. DERIVING R_{rs} FROM ABOVE-SURFACE MEASUREMENTS

2.1 Partition S_{rs}

The reflected skylight consists of two components: Rayleigh- and aerosol-like contributions. Here the cloud effects are included in the aerosol-like component. Then Eq. 1 can be written as

$$T_{rs} = R_{rs} + r_R S_{rsR} + r_a S_{rsa} + \Delta \quad (4)$$

where S_{rsR} and S_{rsa} represent Rayleigh and aerosol contributions, respectively. Eq. 4 indicates that both Rayleigh and aerosol contributions have to be removed in order to properly derive R_{rs} . Unlike the CZCS algorithm³, which calculates the Rayleigh contribution, we derive the Rayleigh contribution from measured S_{rs} .

S_{rs} can be partitioned as two parts⁴: one for Rayleigh scattering and one for aerosol scattering:

$$S_{rs} = S_{rsR} + S_{rsa} = S_R \left(\frac{400}{\lambda} \right)^{4.1} + S_a \left(\frac{400}{\lambda} \right)^{\eta} \quad (5)$$

with $0 \leq \eta \leq 1.5$ for λ from 400 to 700 nm. S_R and S_a are the multiple-scattering values at 400 nm, respectively. Rayleigh-aerosol multiple-scattering interactions are spectrally similar to Rayleigh scattering⁵ and are included in S_R . For each measurement of S_{rs} , S_R , S_a and η can be derived.

2.2 Removal of the Rayleigh component

From field studies, we found that for clear and cloudy sky conditions, the S_R values varied about 15% for measurement angles at 30° and 45° from zenith, while the S_a values varied by a factor of 4. This suggests that the S_R component is quite representative of the Rayleigh component in the effective solid angle. We know the spectral dependence for the Rayleigh component, so we may assume the Rayleigh component in the effective solid angle is close to constant. This provides an adequate removal of the Rayleigh contribution from T_{rs} using a Fresnel reflectance value calculated from the angles involved, as in the CZCS algorithm³.

We use 0.022 as an effective average for r_R at 30° from zenith, and the Rayleigh-corrected T_{rs} is

$$TR_{rs} = T_{rs} - r_R S_{rsR} = T_{rs} - 0.022 S_R \left(\frac{400}{\lambda} \right)^{4.1} = R_{rs} + r_a S_a \left(\frac{400}{\lambda} \right)^{\eta} + \Delta \quad (6)$$

Now, to derive R_{rs} we must find the proper r_a and Δ values. As the measured signal (TR_{rs}) is a lump sum of contributions

from water and sky, we have to somehow know R_{rs} at certain wavelengths for the removal of the aerosol/glnt effects. For coastal waters, $R_{rs}(550)$ is no longer a constant, a variable R_{rs} has to be taken into account.

2.3 Modeling of R_{rs}

R_{rs} is an apparent optical property⁷, controlled primarily by the absorption and scattering properties of the constituents in the water, influenced by fluorescence and Raman emission⁸, and is a function of solar altitude and sensor view geometry⁹. In general, for optically deep waters, and ignoring inelastic scattering, there is

$$R_{rs} = f(a, \beta, \theta_0, \theta, \delta\phi) \quad (7)$$

where a is the absorption coefficient, β is the volume scattering function, θ_0 is solar zenith angle, θ is the viewing angle from nadir, and $\delta\phi$ is the azimuth angle from solar plane.

For field measurements of R_{rs} , we have¹⁰

$$R_{rs} \approx \frac{0.17}{a_w + a_p + a_g} \left[\frac{b_{bw}}{3.4} + X \left(\frac{640}{\lambda} \right)^Y \right] \quad (8)$$

where a_w and b_{bw} are the absorption and backscattering coefficients of pure sea water (here we use the values from Smith and Baker¹¹), a_p is the particle absorption coefficient, and a_g is the gelbstoff absorption coefficient. X includes the particle scattering and geometry functionality, and Y provides the wavelength dependence of particle scattering.

a_g can be expressed as

$$a_g = g \text{ EXP}(-0.015(\lambda - 440)) \quad (9)$$

with $g = a_g(440)$. A 0.015 nm⁻¹ spectral slope is used here, as numerous field measurements found this number a reasonable average¹², although it may vary from coastal to open ocean waters¹³.

In order to reduce the number of mathematical unknowns in Eq. 8, we used the measured a_p curvature, and an empirical Y relationship,

$$Y = 3.44(1 - 3.17 \text{ EXP}(-2.01\chi)) \quad (10)$$

with $\chi = R_{rs}^{ini}(440)/R_{rs}^{ini}(490)$. $R_{rs}^{ini}(\lambda)$ is the initial R_{rs} derived by the Q&E method. We keep $0 \leq Y \leq 2.5$. Thus,

$$R_{rs} \approx \frac{0.17}{a_w + p a_p^{mea} + g e^{-0.015(\lambda - 440)}} \left[\frac{b_{bw}}{3.4} + X \left(\frac{640}{\lambda} \right)^Y \right] \quad (11)$$

and this leads Eq. 6 to (bold letters indicate the unknowns)

$$TR_{rs} \approx \frac{0.17}{a_w + p a_p^{mea} + g e^{-0.015(\lambda - 440)}} \left[\frac{b_{bw}}{3.4} + X \left(\frac{640}{\lambda} \right)^Y \right] + r_a S_a \left(\frac{400}{\lambda} \right)^\eta + \Delta \quad (12)$$

2.4 Removal of aerosol and glint "contaminations"

As strong signals for both aerosols and waters are in the shorter wavelengths, here we use the full spectral information from measurements for the correction of the aerosol effect. With the considerations in section 2.3, there are only 5 unknowns for Eq. 12: p , g , X , r_a and Δ . For sensors with 5 or more channels, the 5 unknowns could then be solved.

Optimization

We use the optimization process described in Lee et al.¹⁰ for the derivation of the 5 unknowns, which is to minimize the "error-of-fit", defined as

$$err = \frac{\left[AVG_{400}^{670} (R_{rs} - \check{R}_{rs})^2 + AVG_{750}^{830} (R_{rs} - \check{R}_{rs})^2 \right]^{0.5}}{AVG_{400}^{670} (R_{rs}) + AVG_{750}^{830} (R_{rs})} \quad (13)$$

where $AVG_{\lambda_1}^{\lambda_2}$ is the average value in the wavelength range λ_1 to λ_2 . In Eq. 13, \hat{R}_{rs} is Eq. 11, and R_{rs} is from Eq. 6.

For non-linear optimization process, choosing initial values for the variables is an important step. We select the initial values for the 5 unknowns as follows:

$$\begin{aligned} r_a^{in} &= 0.022; \\ \Delta^{in} &= TR_{rs}(750) - 0.022 S_a \cdot (400/750)^n; \\ X^{in} &= R_{rs}^{in}(640) \cdot a_w(640)/0.17 - b_{hw}(640)/3.4; \\ p^{in} &= 1; \\ g^{in} &= p^{in} \cdot a_p^{mea}(440). \end{aligned}$$

For each optimization process, the variable ranges are set as follows: p , g , X and $r_a \geq 0$, while Δ could be positive or negative. Thus, for each station, a set of p , g , X , r_a and Δ will be derived by minimizing err . From the derived p and g , a can be calculated with known values for a_w ; and with derived r_a and Δ , R_{rs} can be calculated.

3. MEASUREMENTS

For sites in the Gulf of Mexico in April and June 1993, and in the Arabian Sea in December 1994, measurements were made regarding $L_u(0^+)$, L_{sky} , $E_d(0^+)$, a_p , $E_d(z)$ and $L_u(z)$. These sites covered coastal to open ocean waters, including regions of the Mississippi River plume. Both clear sky and variable cloudy sky situations were encountered. $L_u(0^+)$, L_{sky} and $E_d(0^+)$ were measured using a Spectron Engineering spectroradiometer (Spectron Model SE-590). For the calculation of measured a_p , the "beta factor" of Bricaud and Stramski¹⁴ was used. A 0.54 (Ref. 15) sea-air divergence factor was used to transfer MER derived $R_{rs}(0^-)$ to $R_{rs}(0^+)$. In-water total absorption coefficients at 440 nm were derived using the Eq. 16 in Lee et al.¹⁰.

4. RESULTS AND DISCUSSION

R_{rs} is an apparent optical property, and its value is dependent on the viewing geometry of the sensor. Due to waves and currents, the above- and in-water sensors may not be in the same orientation, thus we may not expect to see the same values in R_{rs} , as the subsurface radiance field is not in completely diffuse distribution.

For $R_{rs}(440)$ and $R_{rs}(550)$ values in this study, the MER derived values follow the OPTIMIZATION derived values well (R^2 is 0.89 for $R_{rs}(440)$, and 0.73 for $R_{rs}(550)$), but do not match perfectly with each other (when the water was very dark, such as sites in the river plume, more uncertainties in MER derived $R_{rs}(410)$ and $R_{rs}(440)$ values due to the low $L_u(z)$ signals). More important, as remote-sensing algorithms are driven by the curvature of R_{rs} , we compared the R_{rs} ratios from the above- and in-water measurements. What we found is that the ratios of $R_{rs}(440)/R_{rs}(550)$ match each other much better than the individual parameters, with R^2 of 0.98 and 9.7% Root-Mean-Square-Difference (RMSD) for the ratios greater than 1.0 (chl_a equivalent is less than ~ 1.0 mg/m³) (see Fig. 1b). RMSD is calculated by the following formula:

$$RMSD = \left(AVG \left(1 - \frac{OPTIMIZATION}{MER} \right)^2 \right)^{0.5} \quad (14)$$

Unlike R_{rs} , absorption coefficients belong to the category of inherent optical properties⁷. For well mixed waters, we should expect to see the above- and in-water derived absorption values match each other closely.

For $a(440)$ values ranging from 0.028 to 2.6 m⁻¹ (OPTIMIZATION derived), the above- and in-water derived values match each other very closely, with a 16.2% RMSD (Fig. 2a). And, for $a_p(440)$ values ranging from 0.008 to 2.1 m⁻¹ (pad measurements, chlorophyll range is 0.07 to 49 mg/m³), the average difference is 19.0% RMSD (see Fig. 2b). The differences of $a_p(440)$ reduce to 13.9% if we exclude stations with chl_a ≥ 5.0 mg/m³, where small-scale patchiness are more possible.

In comparing the derived values from above- and in-water measurements, we must remember the inherent difficulties with regard to both methodologies: instrument-self shading of the in-water measurements, skylight correction of the above-water measurements. Other possible sources of errors include the extrapolation of the in-water $L_u(z)$ and $E_d(z)$ profiles to the surface, variations of the reflectivity of the grey card, and ship perturbation in the field. With the consideration of these possible error sources in the measurements, a $\sim 10\%$ RMSD in R_{rs} ratio is quite small, which suggests that the OPTIMIZATION procedure works very well in correcting the unwanted "contaminations", especially for waters with very low signals in the blue. Also, the result suggests that the ratio-dependent application algorithms (such as CZCS) will work well for either above- or in-water measurements, as long as proper corrections can be made for each method.

Notice that values from remote sensing measurements represent the average of the upper water column, while those from pad are for discrete depths. And, for the calculation of pad measured a_p , a "beta factor" must be applied. However, this

"beta factor" is not a constant in any sense, which makes it difficult to distinguish if the 19% RMSD is due to pad measurement corrections, or water patchiness or the algorithm errors. If we accept a 10% random variation in the "beta factor", a 14 or 19% RMSD is quite small in comparing $a_p(440)$ values, which suggests the three parameter remote-sensing reflectance model (Eq. 11) and the optimization algorithm (Eq. 13) works very well in deriving in-water absorption coefficients.

The above results suggest that for the calibration of an ocean color satellite sensor/algorithm, not only should we compare the R_{rs} values, more important we might compare the R_{rs} derived absorption coefficients.

5. ACKNOWLEDGMENTS

Financial support was provided by NASA through grant NAGW-465 and GSFC contract NAS5-30779, and by ONR through grants N00014-89-J-1091, N00014-95-1-0578. Ship support was provided by the *R/V Suncoaster*, the *R/V Bartlett*, and the *R/V Thomas G. Thompson*.

6. REFERENCES

1. H. R. Gordon and A. Morel, *Remote assessment of ocean color for interpretation of satellite visible imagery: A review*, Springer-Verlag, New York, 1983.
2. K. L. Carder and R. G. Steward, "A remote-sensing reflectance model of a red tide dinoflagellate off West Florida. *Limnol. Oceanogr.* **30**, 286-98 (1985).
3. H. R. Gordon, D. K. Clark, J. W. Brown, O. B. Brown, R. H. Evans, and W. W. Broenkow, "Phytoplankton pigment concentrations in the Middle Atlantic Bight: Comparison of ship determinations and CZCS estimates", *Appl. Opt.* **22**, 20-36 (1983).
4. W.E.K. Middleton, "The color of the overcast sky", *J. of the Opt. Soc. of Am.* **44**, 793 (1954).
5. P. N. Reinersman and K. L. Carder, "Monte Carlo simulation of the atmospheric point-spread function with an application to correction for the adjacency effect", *Appl. Opt.* **34**, 4453-4471 (1995).
6. H. R. Gordon and D. K. Clark, "Clear water radiances for atmospheric correction of coastal zone color scanner imagery", *Appl. Opt.* **20**, 4175-4180 (1981).
7. R. W. Preisendorfer, *Hydrologic optics vol. 1: introduction*. NTIS PB-259 793/8ST. National Technical Information Service, Springfield, Ill. 1976.
8. B. R. Marshall and R. C. Smith, "Raman scattering and in-water ocean properties", *Appl. Opt.* **29**, 71-84 (1990).
9. A. Morel and B. Gentili, "Diffuse reflectance of oceanic waters (2): Bi-directional aspects. *Appl. Opt.* **32**, 6864-879 (1993).
10. Z. P. Lee, K. L. Carder, S. K. Hawes, R. G. Steward, T. G. Peacock, and C. O. Davis, "Method to derive ocean absorption coefficients from remote-sensing reflectance", *Appl. Opt.* **35**, 453-462 (1996).
11. R. C. Smith, and K. S. Baker, "Optical properties of the clearest natural waters", *Appl. Opt.* **20**, 177-84 (1981).
12. A. Bricaud, A. Morel, and L. Prieur, "Absorption by dissolved organic matter of the sea (yellow substance) in the UV and visible domains", *Limnol. Oceanogr.* **26**, 43-53 (1981).
13. K. L. Carder, R. G. Steward, G. R. Harvey, and P. B. Ortner, "Marine humic and fulvic acids: their effects on remote sensing of ocean chlorophyll", *Limnol. Oceanogr.* **34**, 68-81 (1989).
14. A. Bricaud and D. Stramski, "Spectral absorption coefficients of living phytoplankton and nonalgal biogenous matter: A comparison between the Peru upwelling area and the Sargasso Sea", *Limnol. Oceanogr.* **35**, 562-82 (1990).
15. R. W. Austin, "Inherent spectral radiance signatures of the ocean surface", *Ocean Color Analysis. SIO Ref. 7410* (1974).

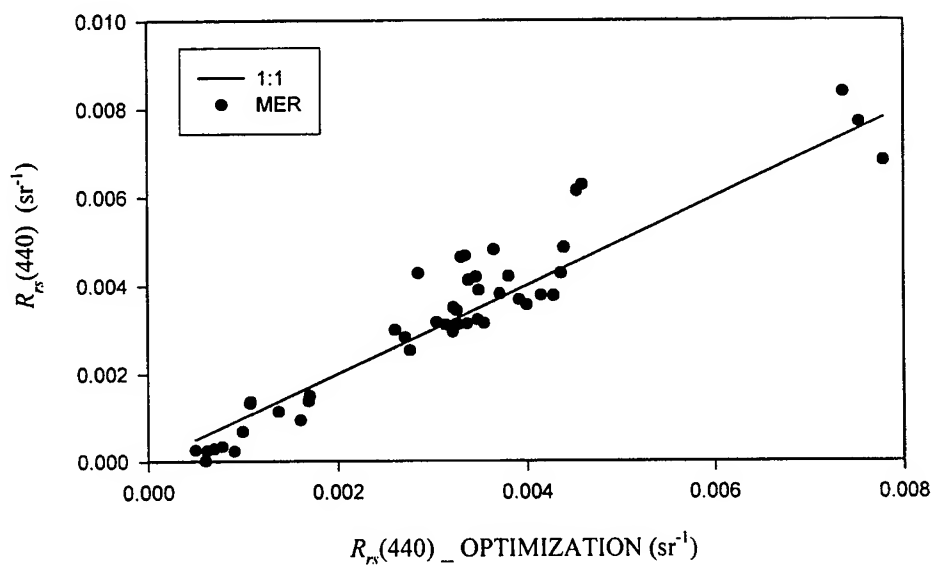


Figure 1a. Comparison of $R_{rs}(440)$ (OPTIMIZATION vs. MER).

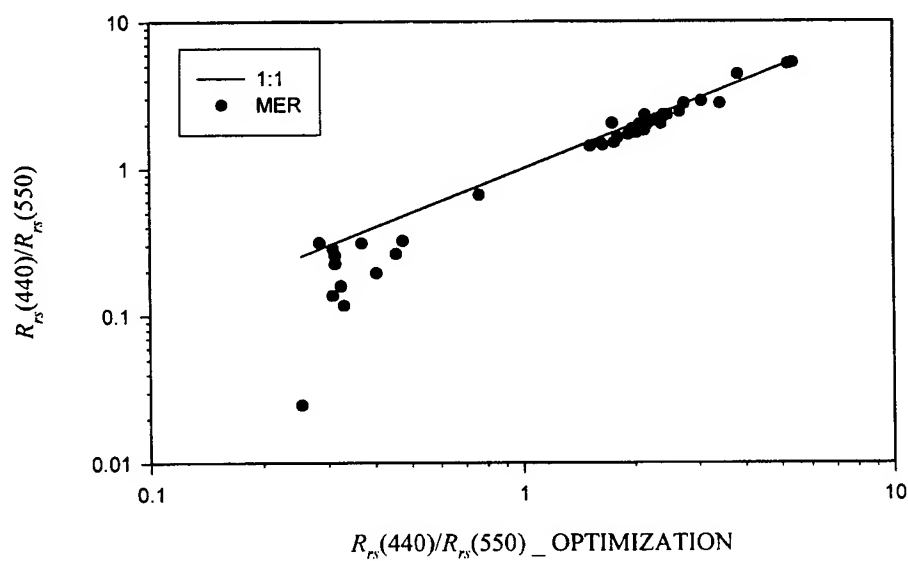


Figure 1b. Comparison of $R_{rs}(440)/R_{rs}(550)$ (OPTIMIZATION vs. MER).

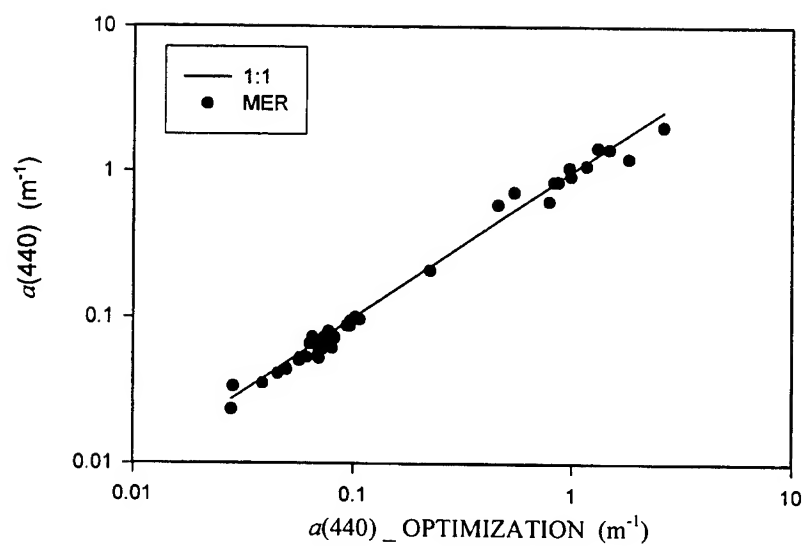


Figure 2a. Comparison of total absorption coefficients at 440 nm.

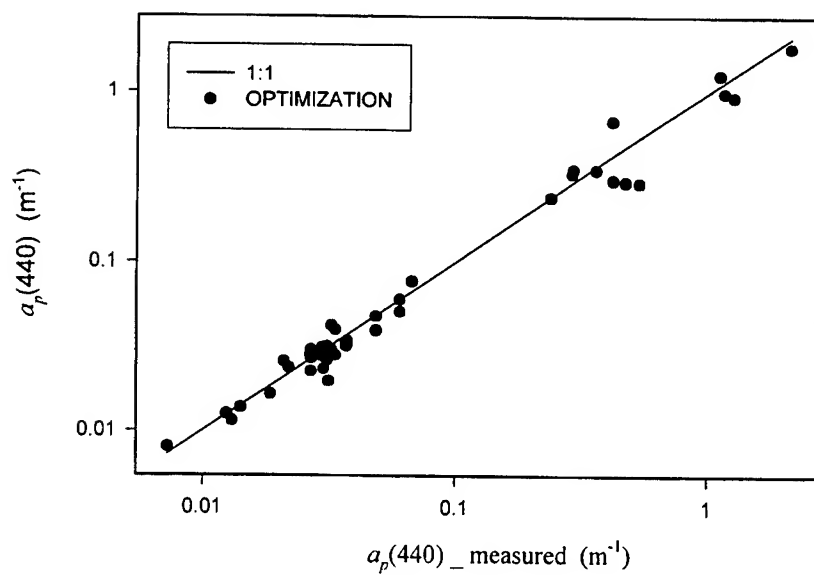


Figure 2b. Comparison of particulate absorption coefficients at 440 nm.

Model for seawater optical characteristics at UV spectral region

Oleg V. Kopelevich

P.P. Shirshov Institute of Oceanology,
Laboratory of Ocean Optics, Moscow, Russia 117218

Svetlana V. Ershova

Moscow Institute of Physics and Technology,
graduate student, Dolgoprudny, Moscow Region, Russia 141700

ABSTRACT

The goal of this work is development of a model for calculation of seawater optical characteristics at UV spectral range by using their values at visible region. Modified model based on physical factors caused optical properties of seawater is considered. Different models of spectral absorption have been compared at visible spectral region, and simple additive model is proposed. Contributions arising from different factors are calculated and analyzed.

Keywords: light, ultraviolet, seawater, absorption, model, phytoplankton pigments, yellow substance

1. INTRODUCTION

The stratospheric ozone depletion observed in the past decade over the different regions of the earth raises the question of assessment of effects of potential increase of harmful UV-B radiation (290-320 nm) on human health, terrestrial plants and marine ecosystems. Such an assessment for the latter implies a calculation of the levels of UV-radiation at different depths in water body depending on the ozone content, meteorological conditions, seawater optical characteristics. Unfortunately, seawater optical properties at UV spectral region are still not clearly understood now: there is a lack of reliable data measurements, and they do not encompass all optical characteristics. So it is appropriate to consider a possibility of the model development for calculation of seawater optical characteristics at UV region by their values at visible region. Successful solving of this problem would give an opportunity to use for prediction of UV-penetration in different waterbodies satellite ocean color data which allow to make global estimates of seawater optical characteristics in surface layer at visible spectral region.

2. SPECTRAL ABSORPTION MODEL AT VISIBLE REGION

Up-to-date models of seawater light absorption at visible region based on physical governing factors consider, other than the water itself, as many as four absorbing components: phytoplankton pigments; nonchlorophyllous particles; humic and fulvic acids which constitute "yellow substance" - colored part of seawater organic matter¹⁻⁴. Of course, the greater is a number of input parameters, the more adequately is possible to bring the model spectra to the measured ones, but only when the values of these parameters can be reliably determined. In practice, we need to solve an incorrect inverse problem when small errors in the initial data can result to the solution instability. Potential instability is the more than the greater is a number of unknowns, so in general a number of the unknown input parameters should be decreased. This is especially important when the satellite data are treated because in this case the spectral values of optical thickness of atmospheric aerosol and of seawater backscattering must be found along with the spectral absorption.

Simple two-parametric model of seawater light absorption has been developed before⁵⁻⁷; it takes into account an absorption of yellow substance, phytoplankton pigments and pure seawater:

$$a(\lambda) = a_y(\lambda) c_y + a_{ph}(\lambda) c_a + a_w(\lambda), \quad (1)$$

where c_y is a concentration of yellow substance expressed as the absorption coefficient of yellow substance at 390 nm, $a_y(390)$, m^{-1} ; c_a is a concentration of chlorophyll *a*, $mg \cdot m^{-3}$; $a_y(\lambda)$, $a_{ph}(\lambda)$ are spectral specific absorption

coefficients of yellow substance and phytoplankton pigments; $a_w(\lambda)$ is spectral absorption coefficient of pure water. It should be noted that this model does not include the term related to absorption by nonchlorophyllous particles (detritus). Its spectral absorption curve is similar to the one of yellow substance^{8,9}; so the detritus absorption can be integrated with the yellow substance absorption³. It can be interpreted as if the detritus absorption is an absorption of yellow substance particulated or sorbed by suspended particles, and $c_y = a_y(390)$ is a total concentration of seawater yellow substance both dissolved and particulated or sorbed by particles.

2.1 Absorption of yellow substance

The advanced model of yellow substance absorption makes use of two exponential curves^{7,10}:

$$a_y'(\lambda) = \begin{cases} \exp[-0.017(\lambda-390)], & \lambda < 500 \text{ nm} \\ 0.0154 \exp[-0.011(\lambda-500)], & \lambda \geq 500 \text{ nm} \end{cases} \quad (2)$$

Physical interpretation of this model can be given with the results of the work of Carder et al.⁴ In accordance with it, the yellow substance absorption can be expressed as a sum of two exponential terms: the first is caused by marine fulvic acid with the exponent 0.0189 nm^{-1} , the second - by marine humic acid with the exponent 0.01105 nm^{-1} . The model (2) assumes that these terms are such that the fulvic acid absorption is dominant at $\lambda < 500 \text{ nm}$, and the humic acid absorption is dominant at $\lambda \geq 500 \text{ nm}$. The value of the former exponent is not in fact constant, and best choice of it for the model should be discussed. Our value (0.017 nm^{-1}) is the same as in more recent work of Carder et al.³

2.2 Absorption of phytoplankton pigments

The second term of model (1) is taken as $a_{ph}''(\lambda)a_{ph}(440)$, where $a_{ph}''(\lambda)$ is according to Prieur, Sathyendranath¹; $a_{ph}(440)$ is a new input parameter (instead c_a). Nonlinear models for calculation of $a_{ph}(\lambda)$ through c_a have been developed recently by Bricaud et al.¹¹, Carder et al.³ To compare different models, calculations of seawater absorption spectra have been performed by using model (1) with the second term as from Prieur, Sathyendranath¹ - PS, or Bricaud et al.¹¹ - B, or by model of Carder et al.³ As measured, spectral absorption coefficients from Morel, Prieur¹² are taken; they vary widely, and the values of $a(410)$ ranges from the same ones as of pure water to more than 0.6 m^{-1} . For the sake of comparison of the results, the measured data set (48 spectra) is subdivided into four groups by the values of $a(410)$: 1 - $\leq 0.06 \text{ m}^{-1}$ (11 spectra); 2 - $0.06-0.18$ (19 spectra); 3 - $0.18-0.37$ (22 spectra); 4 - >0.37 (3 spectra); the mean values of $a(410)$, m^{-1} with their standard deviations for the groups are: 1 - 0.033 ± 0.009 ; 2 - 0.128 ± 0.042 ; 3 - 0.258 ± 0.043 ; 4 - 0.531 ± 0.100 .

The inverse problem of determining two unknown parameters of the model is solved by method of least squares at 10-nm intervals from 410 to 570 nm (17 wavelengths). For C-model only five wavelengths corresponding to SeaWiFS wavebands (412; 443; 490; 510; 555 nm) have been taken. In Table 1 are listed for each

Table 1. Comparison of results of modelling with different models of $a_{ph}'(\lambda)$.

Groups	PS				B				C			
	\bar{a}_y, m^{-1}	s_y, m^{-1}	\bar{s}, m^{-1}	$\bar{\delta}, \%$	\bar{a}_y, m^{-1}	s_y, m^{-1}	\bar{s}, m^{-1}	$\bar{\delta}, \%$	\bar{a}_y, m^{-1}	s_y, m^{-1}	\bar{s}, m^{-1}	$\bar{\delta}, \%$
1	0.0099	0.0334	0.0043	6.1	-0.0026	0.0294	0.0064	9.2	0.0115	0.0096	0.0039	5.9
2	0.0493	0.0684	0.0075	7.4	0.0153	0.0527	0.0075	7.6	0.0737	0.0223	0.0040	3.5
3	0.115	0.057	0.010	5.8	0.053	0.041	0.010	5.5	0.128	0.046	0.012	6.1
4	0.294	0.153	0.026	7.7	0.264	0.057	0.028	6.5	0.269	0.135	0.027	7.8

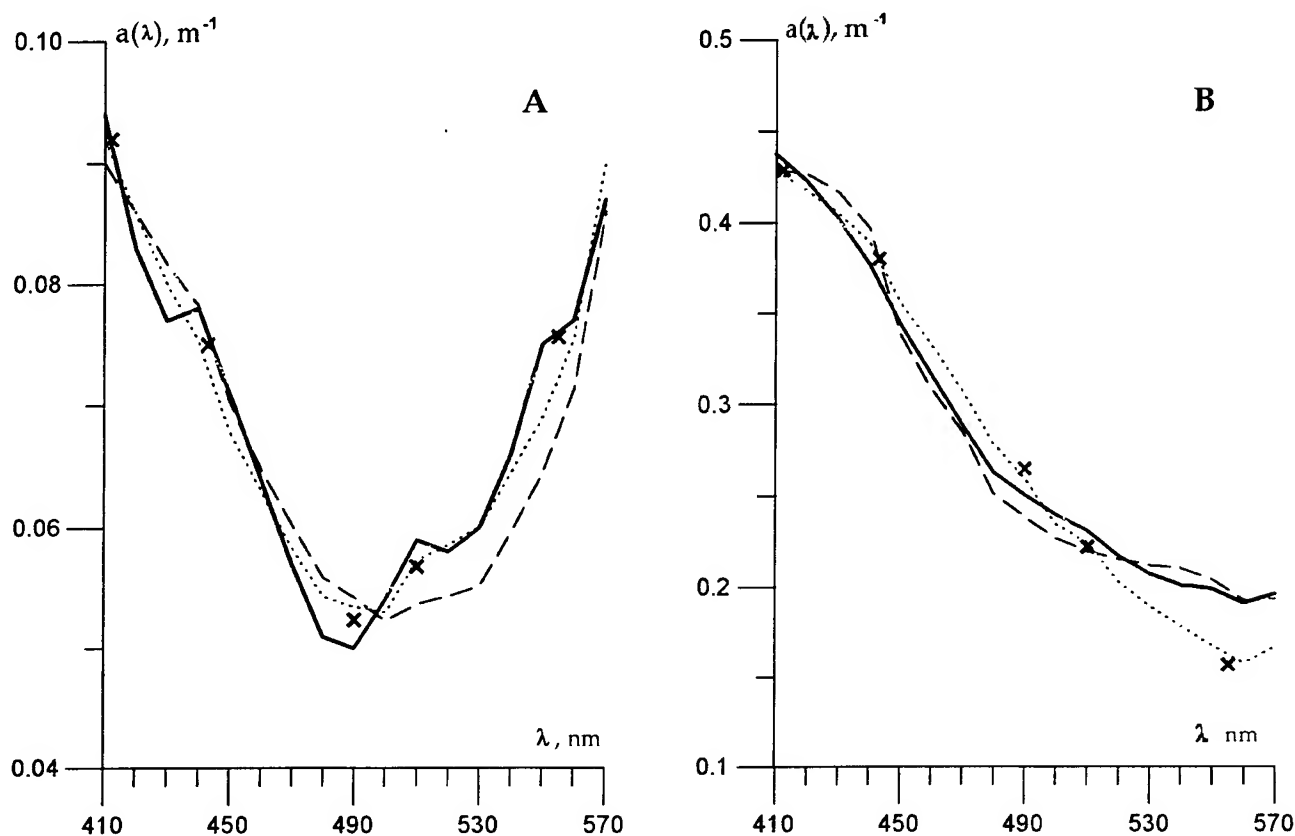


Fig 1. Comparison between measured spectra, $a(\lambda)$ (solid lines) and calculated by model (1) with different $a_{ph}(\lambda)$ - Prieur, Sathyendranath¹ (dotted lines) and Bricaud et al.¹¹ (dashed lines), as well as by model³ (x). A - clear water (20°20'N, 70°50'W); B - turbid coastal water (21°42'N, 17°02'W).

of groups the mean values of a_y , \bar{a}_y , m^{-1} ; their standard deviations, s_y , m^{-1} ; standard errors of the modelled spectra averaged over the considered spectral range, \bar{s} , m^{-1} , and the relative errors, $\bar{\delta}$, %. The presented results demonstrate that the more complicated nonlinear models for the phytoplankton pigment absorption do not improve significantly an accuracy as compared with the simple linear model (1). For the latter, standard errors of the modelled spectra for different groups are in the range 0.0043 ± 0.026 and 5.8 ± 7.7 %; that is quite reasonable. The close values of a_y with models (1) and Carder et al.³ are noteworthy (B - model gives lower values for each group except the fourth); they testify that both models are adequate. Examples of comparison of calculated and measured spectra are shown in Fig. 1 a,b.

3. SPECTRAL ABSORPTION MODEL AT UV REGION

Development of model of seawater spectral absorption at UV region presents a considerable difficulty. Of three terms of model (1) only the first one has been studied with some degree of certainty. Regarding two others, reliable knowledge about them is lacking.

3.1 Absorption of pure seawater

A convention uses the values of $a_w(\lambda)$ from Smith, Baker¹³ as a values of spectral absorption coefficients of pure seawater, a_{sw} at UV region. But the authors themselves recognize a poor accuracy of their values at UV

region. In the 300-380 nm region they have chosen the lower limit of available data; by their words they could have selected a curve ~ 30% higher. In the wavelength region below 300 nm they have extrapolated available data following the shape of curve for pure fresh water; in the authors' opinion there is merely an educated estimate.

In our opinion, the values of $a_w(\lambda)$ from Smith, Baker¹³ underestimate absorption of inorganic salts, and they should be corrected for their increase. Such a question has been arisen before.¹⁴ The corrected values have been refined here with the same procedure as before. Refined values of spectral absorption coefficients of pure seawater, $a_{sw}(\lambda)$, m^{-1} are given in Table 2.

Table 2. Spectral absorption coefficients of pure seawater.

λ, nm	290	300	310	320	330	340	350	360	370	380	390
$a_{sw}(\lambda)$	0.365	0.237	0.180	0.144	0.121	0.101	0.081	0.063	0.045	0.027	0.019

It should be noted that the inorganic salts absorption can provide an explanation for sharp increasing of slope in the spectral absorption curves on a half-logarithmic scale in the 290-320 nm region: according to data of Blough et al.¹⁵, from ~ 0.015 nm^{-1} to 0.053 nm^{-1} in "blue water". In their work the spectral absorption coefficients of filtered seawater were measured in reference to distilled water so their values can be considered as a sum of absorption by yellow substance and inorganic salts. According to our data, the latter in the 270-300 nm region can also be approximated by exponential curve with much larger value of the exponent (~ 0.06 nm^{-1}) compared with yellow substance. When yellow substance concentration is great a contribution of inorganic salts is negligible but in clear waters this contribution is significant. The same explanation is adaptable to data of Green, Blough¹⁶: there are lower values of the slope in coastal waters with high absorption (0.018-0.020 nm^{-1}), and its values increase in clear water with low absorption (0.03-0.06 nm^{-1}). If absorption of inorganic salts is taken into account, the approximation of the measured spectra by modelled ones is better for all samples than without the account.

3.2 Absorption of phytoplankton pigments

The another group of pigments absorbs at UV region as compared with visible, - not photosynthetic but photoprotective; relation between these different forms of pigments is poorly known. There is also a lack of representative data for spectral dependency of pigment absorption at UV region; available data show that these dependencies vary widely. In vivo pigment-specific spectral absorption coefficients of Antarctic marine particles are given by Vernet et al.¹⁷; average absorption spectra for surface waters in Antarctica and off southern California are presented by Sosik et al.¹⁸ We have normalized the specific phytoplankton absorption spectra given in the second work, $a_{ph}(\lambda)$, to $a_{ph}(440)$; the mean of derived spectra, $a_{ph}''(\lambda)$ has been butted together with the spectrum $a_{ph}''(\lambda)$ from Prieur, Sathyendranath¹. This mean spectrum is from data of CalCOFI cruise 9110 to the waters off southern California (Sept.-Oct. 1991, 63 stations). The buttered spectrum, $a_{ph}''(\lambda)$ is given in Table 3.

Table 3. Spectral values of normalized phytoplankton pigment absorption, $a_{ph}''(\lambda) = a_{ph}(\lambda) / a_{ph}(440)$.

λ, nm	290	300	310	320	330	340	350	360	370	380	390	400
$a_{ph}''(\lambda)$	0.67	0.68	0.69	0.69	0.68	0.61	0.48	0.42	0.44	0.49	0.55	0.69

In the same manner as for visible region, the phytoplankton pigment absorption will be calculated as $a_{ph}''(\lambda) \cdot a_{ph}(440)$, where $a_{ph}(440)$ is input parameter to be determined by data in visible region. This approach assumes that the photoprotective pigments responsible for absorption at UV region, and the photosynthetic

pigments causing absorption at visible region correlate rigidly. This assumption can be justified by that both of them depend on total content of phytoplankton.

4. CONTRIBUTIONS ARISING FROM DIFFERENT FACTORS

In Table 4 are given contributions into UV-absorption arising from different factors; examples of calculations for each of four groups mentioned above are presented. It is seen that pure seawater is a dominant factor in clear waters; yellow substance become dominant in turbid coastal waters. Contributions from phytoplankton pigments do not exceed 20% at UV-B spectral range.

The important parameter for calculation of UV-penetration into water body is a sum of absorption and backscattering coefficients, $[a(\lambda)+b_b(\lambda)]$. This parameter is closely related to diffuse attenuation coefficient,¹⁹ and has been used with profit for calculation of underwater UV-irradiation with quasi-single approximation.²⁰

To make estimates of $[a(\lambda)+b_b(\lambda)]$, a correlation between $b_b(550)$ and $a(\lambda)$ at different λ has been calculated with available data of measurements.¹⁴ Spectral dependency of $b_b(\lambda)$ is assumed as

$$b_b(\lambda) = (550/\lambda) \cdot b_{bp}(550) + b_{bw}(\lambda), \quad (3)$$

where b_{bp} , b_{bw} are backscattering coefficients of particulate matter and pure seawater. Computations of $[a(\lambda)+b_b(\lambda)]$ demonstrate that in all cases absorption is dominant at UV region: 92-98% at UV-B, 81-97% at UV-A; contribution arising from particulate matter do not exceed 3% at UV-B, and 10% at UV-A.

Table 4. Contributions into UV-absorption arising from different factors.

location ¹²	0°; 1°35' W			21°04' N; 17°44' W			21°04' N, 17°32' W			21°42' N, 17°02' W		
λ , nm	290	320	400	290	320	400	290	320	400	290	320	400
$a(\lambda)$, m ⁻¹	0.42	0.18	0.034	0.83	0.46	0.168	1.13	0.65	0.23	2.09	1.25	0.43
a_{sw} , %	87.1	79.8	52.3	43.9	31.2	10.7	32.2	22.1	7.7	17.4	11.5	4.2
a_y , %	10.7	14.9	20.1	45.3	48.8	34.5	58.0	60.4	43.3	74.4	74.6	55.6
a_{phv} , %	2.2	5.3	27.6	10.8	19.9	54.8	9.8	17.6	49.0	8.1	13.9	40.2

5. CONCLUSION

Proposed model is really only a skeleton for development of workable model for calculation of seawater optical characteristics at UV region. The results presented in the latter paragraph point up what factors should receive the bulk of attention. First, more exact information is required about absorption of pure seawater at UV region. Also regional variations of yellow substance absorption should be studied better. And of course, a data set of optical characteristics measured at UV region must be extended widely to validate the models developed.

6. ACKNOWLEDGMENTS

Financial support for this research was provided by grant 96-05-65532 from Russian Science Foundation. The authors also wish to express their gratitude to ONREUR Visiting Scientist Program for support of participation in the Conference.

7. REFERENCES

1. L.Prieur, S.Sathyendranath, "An optical classification of coastal and oceanic waters based on the specific spectral absorption curves of phytoplankton pigments, dissolved organic matter, and other particulate materials", *Limnol. Oceanogr.* 26(4), 671-689(1981).

2. S.A.Garver, D.A.Siegel, B.G.Mitchell, "Variability in near-surface absorption spectra: What can a satellite ocean color imager see?", *Limnol. Oceanogr.* **39**(6), 1349-1367(1994).
3. K.L.Carder, Z.Lee, S.Hawes, F.R.Chen, "Optical model of ocean remote sensing: Application to ocean color algorithm development", *COSPAR Colloquium Space Remote Sensing of Subtropical Oceans*, 15A3-1-13A3-6 (1995).
4. K.L.Carder, R.G.Steward, G.R.Harvey, P.B.Ortner, "Marine humic and fulvic acids: Their affects on remote sensing of ocean chlorophyll", *Limnol. Oceanogr.* **34**(1), 68-81(1989).
5. O.V.Kopelevich, "Optical properties of ocean waters", Dr.Sci. thesis, IO RAS, Moscow, 1981.
6. O.V.Kopelevich, "Low-parametric model of seawater optical properties", *Optika okeana*, Vol. 1, pp 208- 234, Nauka, Moskow, 1983.
7. O.V.Kopelevich, "Optical properties of ocean waters", *Light scattering and absorption in natural and artificial dispersive media*, pp 289-309, Inst. Physics AN BSSR, Minsk, 1991.
8. C.S.Roesler, M.J.Perry, K.L.Carder, "Modelling in situ phytoplankton absorption from total absorption spectra in productive inland marine waters", *Limnol. Oceanogr.* **34**, 1510-1523(1989).
9. K.L.Carder, S.K.Hawes, K.S.Baker, R.C.Smith, R.G.Steward and B.G.Mitchell, "Reflectance model for quantifying chlorophyll a in the presence of productivity degradation products", *J. Geophys. Res.* **96**(C11), 20599-20611(1989).
10. O.V.Kopelevich, S.V.Lutsarev, V.V.Rodionov, "Spectral absorption by "yellow substance" of ocean waters", *Oceanologia* **29**(3), 409-414(1989).
11. A.Bricaud, M.Babin, A.Morel, H.Claustre, "Variability in the chlorophyll-specific absorption coefficients of natural phytoplankton: Analysis and parametrization", *J. Geophys. Res.* **100**(C7), 13,321-13,332(1995).
12. A.Morel and L.Prieur, "Analyse spectrale des coefficients d'attenuation diffuse, de reflexion diffuse, d'absorption et de retrodiffusion pour diverses regions marines", *Laboratoire d'Océanographie Physique, Rapport* 17, 1975.
13. R.C.Smith and K.S.Baker, "Optical properties of the clearest natural waters (200-800 nm)", *Applied Optics* **20**(2), 177-184(1981).
14. O.V.Kopelevich, Y.V.Filippov, "Comparison between different spectral models of the diffuse attenuation and absorption coefficients of sea water", *Ocean Optics* **12** 2258, 210-221(1994).
15. N.V.Blough, O.C.Zafiriou, J.Bonilla, "Optical absorption spectra of waters from the Orinoco river Outflow: terrestrial input of colored organic matter to the Caribbean", *J. Geophys. Res.* **98**(2), 2271-2278(1993).
16. S.A.Green, N.V.Blough, "Optical absorption and fluorescence properties of chromophoric dissolved organic matter in natural waters", *Limnol. Oceanogr.* **39**(8), 1903-1916(1994).
17. M.Vernet, E.A.Brody, O. Holm-Hansen, B.G.Mitchell, "The response of Antarctic phytoplankton to ultraviolet radiation: absorption, photosynthesis, and taxonomic composition. - Ultraviolet radiation in Antarctica: measurements and biological effects", *Antarctic research series*, edited by C.S.Weiler and P.A. Penhale, vol. 62, pp 143-158, 1994.
18. H.M.Sosik, M.Vernet, B.G.Mitchell, "A comparison of particulate absorption properties between high- and mid-latitude surface waters", *Antarctic Journal* **27**(5), 162-164(1992).
19. H.R.Gordon, "Can the Lambert - Beer law be applied to the diffuse attenuation coefficient of ocean water?", *Limnol. Oceanogr.* **34**(8), 1389-1409(1989).
20. N.A.Krotkov, A.P.Vasilkov, "Ultraviolet radiation in the atmosphere - ocean system: a model study", *SPIE* **2049**, 244-255(1993).

Optical characteristics of seawater in the North Pacific Ocean

M. Kishino

Photosynthesis Research Laboratory, Solar Energy Research Group
The Institute of Physical and Chemical Research, Wako, Saitama 351-01, Japan

J. Ishizaka

National Institute for Resources and Environment, Onogawa, Tsukuba, Ibaraki 305, Japan

H. Satoh and K. Kusaka

Tokyo University of Fisheries, Koumann, Minato, Tokyo 108, Japan

S. Saitoh and T. Miyoi

Hokkaido University, Minato, Hakodate, Hokkaido 041, Japan

K. Kawasaki

National Research Institute of Fisheries Science, Kanazawa, Yokohama, Kanagawa 236, Japan

ABSTRACT

The downward spectral irradiance and upward spectral radiance, and chlorophyll *a* concentration of surface water were determined in the North Pacific Ocean: Bering Sea, Gulf of Alaska, Central and Equatorial Pacific, Kuroshio region, Yellow Sea, Japan Sea, Tokyo Bay, and Ise Bay. These areas included Case I and Case II water.

The optical characteristics in the study area were based on measurements of underwater spectral irradiance. The strong correlation between the attenuation coefficient at 490 nm, *K*₄₉₀, and other at wavelengths were observed. The relation between chlorophyll concentration and *K*₄₉₀ showed a good correlation at the coastal and bay areas except at the stations near river mouths. These relation suggested that suspended and dissolved matter were largely of biogenous origin such as fragmented and decomposed phytoplankton. In the clear ocean, at low chlorophyll concentrations, the data points were widely scattered, implying that *K*₄₉₀ is sensitive to changes in suspended particles.

Key Words: attenuation coefficient, *K*₄₉₀, chlorophyll *a*, spectral irradiance, North Pacific Ocean

1. INTRODUCTION

Light is one of the key environmental factors for phytoplankton life in the sea. Light energy penetrating into the sea is diminished almost exponentially with depth with an accompanying drastic change in the energy spectrum as the result of absorption by various components in the seawater. Such a change in the light environment could affect phytoplankton life. In the study of primary production, it is essential to have a complete understanding of the optical characteristics in the sea as previously pointed out¹.

Light absorption components in the seawater are those such as phytoplankton, other living and non-living particles, dissolved organic matter and water itself. Several authors have attempted to estimate the spectral absorption of individual components in the seawater^{2,3,4,5,6,7}. However, model estimation of the spectral irradiance requires many input parameters to calculate the absorption coefficient. Therefore, it is very useful that the spectral irradiance can be simply empirically related to parameters such as chlorophyll *a* concentration or attenuation coefficient at 490 nm. Various investigators have found a strong correlation between chlorophyll concentration and attenuation^{8,9,10}, although these relations might be highly location specific.

Recently, the measurements of downward spectral irradiance and concentration of chlorophyll pigments were carried out at various stations and various seasons in the North Pacific Ocean. In this paper, the relation between attenuation coefficient at 490 nm, *K*₄₉₀, and the attenuation coefficient at other wavelengths, *K*(λ), and the relation between *K*₄₉₀ and chlorophyll *a* concentration were examined by means of a regression analysis. Similarly the spectral attenuation coefficient could be determined from *K*₄₉₀ or chlorophyll *a* concentration using ocean color data obtained by satellite, such as ADEOS/OCTS and Seastar/SeaWiFS.

2 Methods

Field observations were carried out at various stations covering a wide range of optical water types in Bering Sea, Gulf of Alaska, Central and Equatorial Pacific, Kuroshio region, Yellow Sea, Japan Sea, Tokyo Bay, and Ise Bay (Fig. 1). At all stations, spectral irradiance was measured with the underwater spectral irradiance meter (MER-2040, MER-2020, and PRR-600, Biospherical Inc.). Seawater was collected with a Niskin Bottle or bucket at the surface for the determination of chlorophyll concentration. Chlorophyll *a* concentration was determined by the fluorometric method¹¹, or spectrophotometric method¹¹.

The vertical distribution data of spectral irradiance were examined to identify any ship shadow effects and such data were omitted. The attenuation coefficient, $K(\lambda)$, was calculated at the surface layer as follows,

$$K(\lambda) = - \frac{\ln \{E_d(\lambda, z_1)/E_d(\lambda, z_2)\}}{z_2 - z_1} \quad (1)$$

where $E_d(\lambda, z)$ is downward irradiance at wavelength λ , at depth z . The depth z_1 was selected at the upper layer close the surface and depth z_2 was selected from 2 m to 20 m depending on the turbidity.

The regression analysis was carried out between the attenuation coefficient at 490 nm, K_{490} , and other wavelengths, $K(\lambda)$, and between the chlorophyll *a* concentration at the surface and K_{490} .

3. RESULTS

3.1 The correlation between K_{490} and $K(\lambda)$

In the study areas, K_{490} in the surface layer ranged between 0.0217 m^{-1} at the Central Pacific Ocean and 2.42 m^{-1} at Ise Bay. The correlation between K_{490} and $K(\lambda)$ is examined and is shown in Fig. 2. The total number of stations is 151. There is a high correlation between K_{490} and $K(\lambda)$. The correlation for K_{490} versus $K(665)$ is a little lower. The regression lines and the correlation coefficients, r , are as follows.

$$K(412) = 1.441 K_{490} + 0.022 \quad r^2 = 0.991 \quad (2)$$

$$K(443) = 1.364 K_{490} + 0.0007 \quad r^2 = 0.997 \quad (3)$$

$$K(510) = 0.897 K_{490} + 0.011 \quad r^2 = 0.999 \quad (4)$$

$$K(555) = 0.629 K_{490} + 0.046 \quad r^2 = 0.985 \quad (5)$$

$$K(665) = 0.627 K_{490} + 0.404 \quad r^2 = 0.956 \quad (6)$$

The minimum $K(\lambda)$ is occurred between the wavelengths 443 nm and 490 nm with values under 0.05 m^{-1} , which corresponds to very clear water. The wavelength of minimum $K(\lambda)$ is shifted to longer wavelengths with increases in K_{490} . When K_{490} increased to values over 0.2 m^{-1} , the wavelength of minimum K is greater than 555 nm.

3.2 The correlation between chlorophyll *a* and K_{490}

In the study area, chlorophyll *a* concentration in the surface water ranged between $0.01 \mu\text{g l}^{-1}$ at the Kuroshio Region and $68.31 \mu\text{g l}^{-1}$ at the Tokyo Bay.

The relation between the chlorophyll *a* and K_{490} is shown in Fig. 3. A good correlation occurred in the coastal and bay regions except for stations near the mouth of the river at Ise Bay. K_{490} is linearly related to *Chl. a* with a correlation coefficient of 0.978, according to:

$$K_{490} = 0.0292 (\text{Chl}) + 0.0365 \quad (7)$$

where *Chl* is chlorophyll *a* concentration.

The data points in the low chlorophyll *a* concentration shown in Fig. 3B, are scattered over a wide range. It seems that there are two relations; one follows the same tendency as for the coastal and bay water, and the other follows more turbid water trends, although with a low chlorophyll *a* concentration. This poses difficulty in determination of a suitable regression line.

4. DISCUSSION

The relation between attenuation coefficient at 490 nm and the other wavelengths is excellent but with some weakening at 665 nm. Some reasons can be postulated for the scattered data points at $K(665)$. One is due to the calculated error $K(665)$, since the downward irradiance at wavelength of 665 nm decreases rapidly with increase of depth and accuracy of the irradiance in the deeper layer is low. The other is due to the effect of the natural chlorophyll fluorescence, which depends on the concentration of chlorophyll *a* and downward irradiance at the blue-green region^{12, 13}.

The second terms of right hand side of equations (2) - (6), which are the intercepts at the $Chl = 0$, are compared with the seawater attenuation, K_{sw} ¹⁴. The values at wavelengths 412 and 443 nm are larger than K_{sw} , whereas the values over 510 nm are nearly same or only a little larger. It is considered that the attenuation coefficient at shorter wavelengths is influenced by the absorption of dissolved organic matter.

The relation between chlorophyll *a* and $K490$ is good at the coastal and bay areas except the stations near the mouth of the river. It is considered that the suspended and dissolved matters in the almost coastal and bay are related to phytoplankton except the areas affected the river water. The values of $K490$ in some stations in the Yellow Sea, which are located near Yangtze River, are larger than the values calculated from equation (7), due the large amount of suspended particles from the Yangtze River. It seems that the value of $K490$ changes with changes in suspended particles. Otherwise the values at far stations follow nearly same tendency as at the coastal and bay stations.

The data points scattered widely in the stations of low chlorophyll concentration, which corresponded to the clear water. It is considered that the strong effect of suspended particles other than phytoplankton is present since the chlorophyll *a* concentration is low and the value of $K490$ is also small. Then, the value of K is sensitive to the change of the suspended particles concentration.

The attenuation coefficients are calculated from the equations from 2 to 6 with the function $K490$ and is shown in Fig 4. The minimum K value occurs at the wavelength between 443 and 490 when $K490$ equals 0.02 m^{-1} which is nearly equal K_{sw} . The value of K over the wavelength of 510 nm is also nearly the value of attenuation coefficient of seawater. However, the values of K at wavelength of 443 and 412 nm is larger than K_{sw} . This suggests the effect of the absorption of the dissolved matter. It is clear that the wavelength of minimum K value increases with $K490$.

5. CONCLUSIONS

The optical characteristics of seawater in the North Pacific Ocean were investigated. Strong correlation was observed between the attenuation coefficient at wavelength of 490 nm and other wavelength. Then, the spectral attenuation in the surface layer is estimated from the regression with $K490$, presented as equations (2) - (6). The relation between chlorophyll *a* and $K490$ shows a good correlation at the coastal and bay areas except at stations near the mouth of river. These relations suggested that suspended and dissolved matter were largely of biogenous origin such as fragmented and decomposed phytoplankton. In the open ocean, however, the data points were scattered widely. It is considered that the values of $K490$ are sensitive to the changes of suspended particle concentration. It is necessary to continue study the relation between the attenuation coefficient and chlorophyll concentration in the sea, especially, in clear regions.

6. REFERENCES

1. S. Sathyendranath, T. Platt, C.M. Caverhill, R.E. Warnock and M.R. Lewis, "Remote sensing of oceanic primary production: computations using a spectral model," *Deep-Sea Res.*, **36**, 431-453 (1989).
2. A. Morel, and L. Prieur, "Analysis of variations in ocean color," *Limnol. Oceanogr.*, **22**, 709-722 (1977).
3. R.C. Smith, and K.S. Baker, "The bio-optical state of ocean waters and remote sensing," *Limnol. Oceanogr.*, **23**, 247-259 (1978).
4. N. Okami, M. Kishino, S. Sugihara, N. Takematsu and S. Unoki, "Analysis of ocean color spectra (III). Measurements of optical properties of sea water," *J. Oceanogr. Soc. Japan*, **38**, 362-372 (1982).
5. A.D. Weidemann, T.T. Bannister, S. Effler and D. Johnson, "Particulate and optical properties during CaCO_3 precipitation in Otisco Lake," *Limnol. Oceanogr.*, **30**, 1078-1083 (1985).
6. C.S. Roesler, M.J. Perry and K.L. Carder, "Modeling in situ phytoplankton absorption from total absorption spectra in productive inland marine waters," *Limnol. Oceanogr.*, **34**, 1510-1523 (1989).
7. A. Bricaud, and D. Stramski, "Spectral absorption coefficients of living phytoplankton and nonalgal biogenous matter: A comparison between the Peru upwelling and the Sargasso Sea," *Limnol. Oceanogr.*, **35**, 562-582 (1990).
8. D.A. Siegel and T.D. Dickey, "On the parameterization of irradiance for open ocean photoprocesses," *J. Geophys. Res.*, **92**, 14,648-14,662 (1987).

9. A. Morel, "Optical modeling of the upper ocean in relation to its biogenous matter content (case I water)," J. Geophys. Res., **93**, 10,749-10,768 (1988).
10. R.C. Smith, K.J. Waters and K.S. Baker, "Optical variability and pigment biomass in the Sargasso Sea as determined using deep sea optical mooring data," J. Geophys. Res., **96**, 8665-8686 (1991).
11. J.D. Strickland, and T.R. Parsons, "A Practical Handbook of Seawater Analysis," Bull. Fish. Res. Bd. Canada, **167**, pp. 310 (1972).
12. R.C. Smith and K.S. Baker, "Optical classification of natural waters," Limnol. Oceanogr., **23**, 260-267 (1978).
13. M. Kishino, S. Sugihara and N. Okami, "Influence of fluorescence of chlorophyll a on underwater upward irradiance spectrum," La mer, **22**: 224-232 (1984).
14. R.C. Smith, and K. S. Baker, "Optical properties of the clearest natural water (200-800nm)," Appl. Opt., **20**, 177-184 (1984).

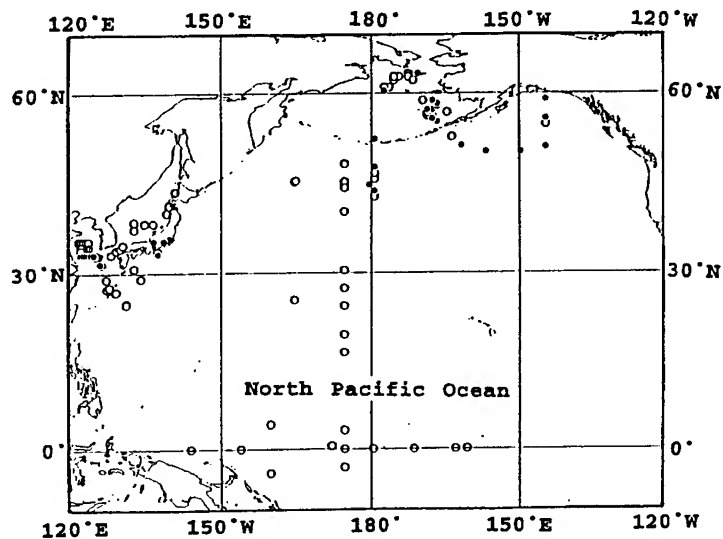


Fig. 1. Location of the stations in the North Pacific Ocean.

Open circle: chlorophyll a < 0.5 µg l⁻¹,
Solid circle: chlorophyll a > 0.5 µg l⁻¹.

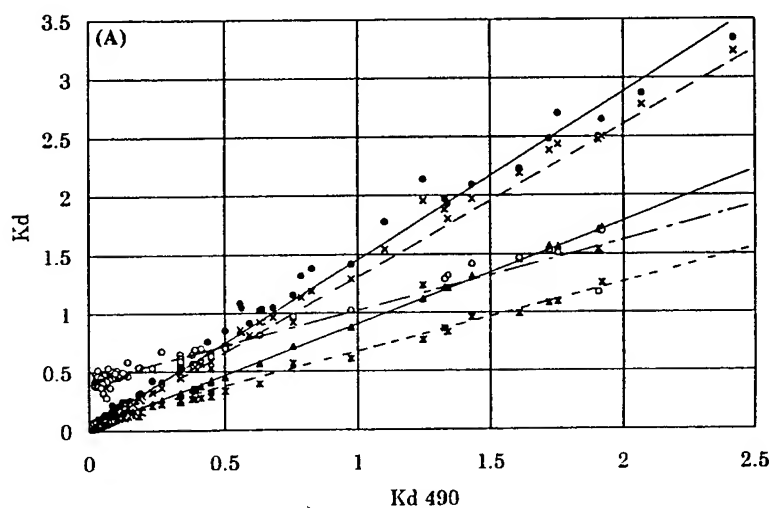
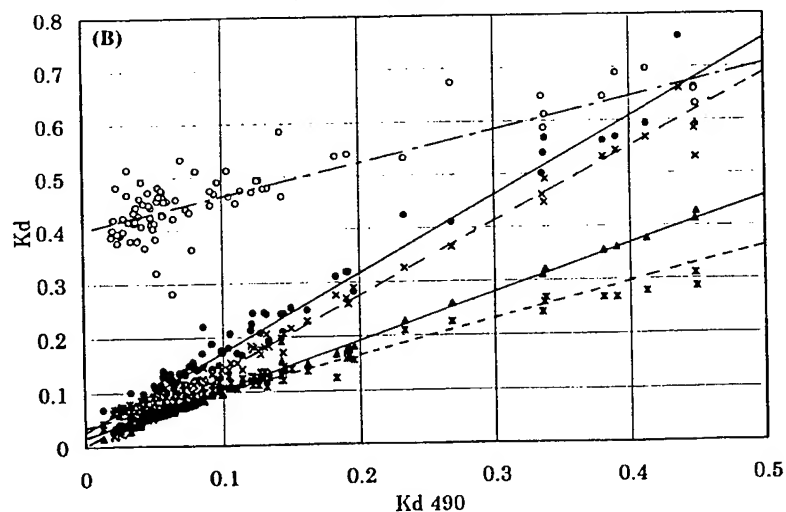


Fig. 2. The attenuation coefficient, $K(\lambda)$ versus attenuation coefficient at 490 nm, K_{490} . The regression lines shown are expressed by equations (2) - (6).

(A) All stations.

The lines, from top to bottom, represent wavelength = 412 nm, 443 nm, 510 nm, 665 nm and 555 nm.



(B): The clear water areas ($K_{490} < 0.5 \text{ m}^{-1}$).

The lines, from top to bottom, represent wavelength = 665 nm, 412 nm, 443 nm, 510 nm and 555 nm.

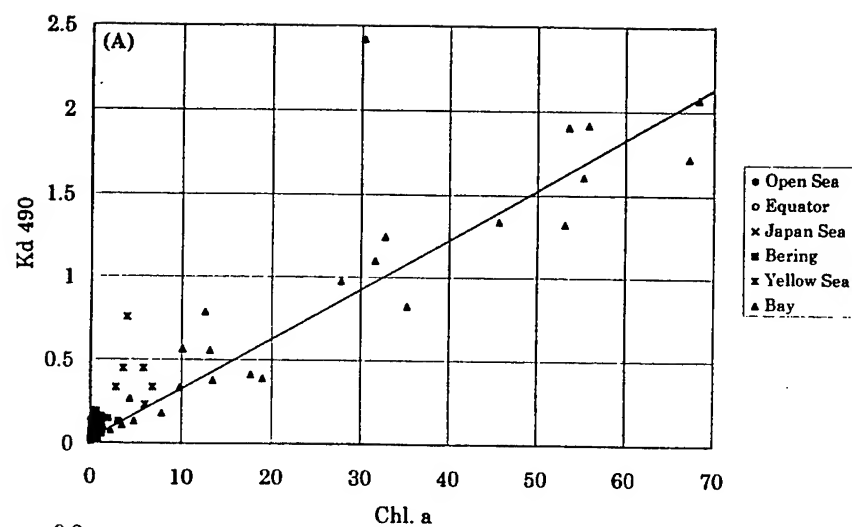
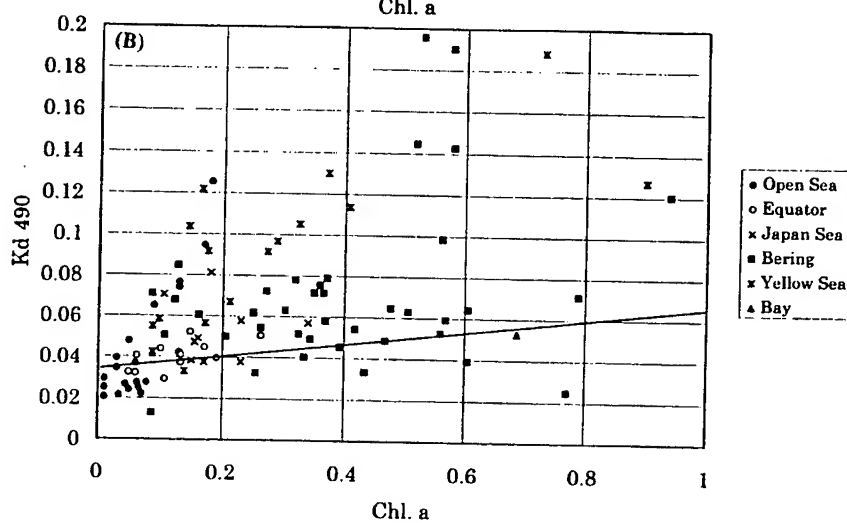


Fig. 3. The attenuation coefficient at 490 nm, K_{490} , versus chlorophyll concentration. The regression line shown is expressed by equation (7).

(A) All stations.



(B) The clear water areas
($\text{Chl} < 1.0 \mu\text{g l}^{-1}$).

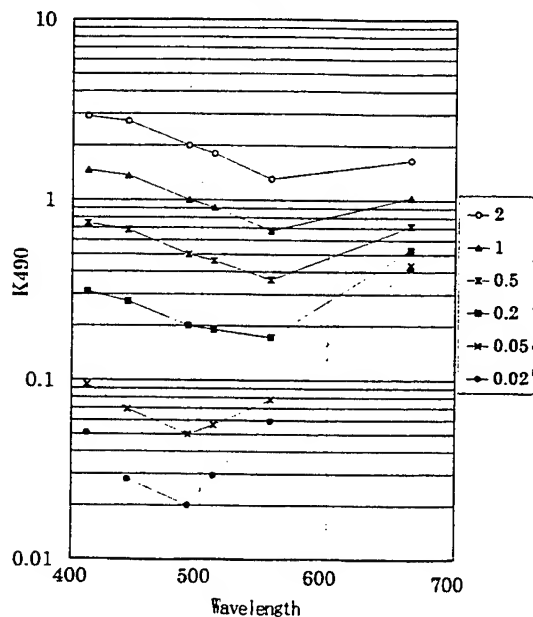


Fig. 4. The estimated attenuation coefficient from the regression equations (2) - (6).

The curves, from top to bottom, represent $K_{490} = 2.0 \text{ m}^{-1}$, 1.0 m^{-1} , 0.5 m^{-1} , 0.2 m^{-1} , 0.05 m^{-1} and 0.02 m^{-1} .

Spatial variability in the chlorophyll-specific absorption coefficients of phytoplankton and photosynthetic pigments in the Equatorial Pacific

Karima Allali¹, Annick Bricaud¹ and Hervé Claustre¹

¹Laboratoire de Physique et Chimie Marines, CNRS and Université Pierre et Marie Curie,
B.P. 8, 06230 Villefranche-sur-Mer, France

ABSTRACT

Chlorophyll-specific absorption coefficients of phytoplankton (a_{ph}^*) were determined in the upper 200 m along 150°W in the equatorial and subequatorial Pacific (13°S-1°N), during the OLIPAC-JGOFS FRANCE cruise (November 1994). A spectral reconstruction technique using the HPLC pigment information was used to partition a_{ph}^* into the contributions of photosynthetic pigments (a_{ps}^*) and non-photosynthetic pigments (a_{nps}^*). The values of a_{ph}^* were observed to decrease from the oligotrophic waters of the sub-equatorial area to the mesotrophic waters of the equatorial area, and from the surface to deep waters. These variations were primarily, but not exclusively, caused by changes in the concentrations of non-photosynthetic pigments. The level of pigment packaging was also variable, both horizontally as a result of changes in populations, and vertically as a result of photoacclimation.

In comparison with a_{ph}^* , the chl-specific absorption coefficients of photosynthetic pigments (a_{ps}^*) exhibited a reduced range of variation with depth and from site to site. The variations in a_{ps}^* originating from the package effect were partly compensated by variations in the concentrations of photosynthetic pigments.

In agreement with a previous study¹, we conclude that a_{ps}^* is less dependent on environmental parameters than a_{ph}^* . In addition, our results provide evidence that the variability in a_{ps}^* cannot be neglected. The use of a_{ps}^* instead of a_{ph}^* in light-photosynthesis models might present the advantage of eliminating the variability associated with non-photosynthetic pigments.

Keywords: Equatorial Pacific, phytoplankton, absorption, photosynthetic pigments, non-photosynthetic pigments, package effect.

1. INTRODUCTION

Specific absorption coefficients are key input parameters when modelling various phenomena such as light propagation within the ocean^{2,3}, carbon fixation by phytoplankton⁴, and the heating rate of the upper ocean⁵. The variability of these coefficients has been extensively documented for cultures in the laboratory⁶⁻¹¹ and natural populations¹²⁻¹⁷. These various studies have shown that the variability in the chl-specific absorption coefficients of phytoplankton ($a_{ph}^*(\lambda)$) is driven by both the packaging effect and the pigment composition, in varying proportions. In return, only few studies have investigated the respective roles of absorption attributable to photosynthetic ($a_{ps}^*(\lambda)$) and non-photosynthetic ($a_{nps}^*(\lambda)$) pigments in the variability of $a_{ph}^*(\lambda)$. Such a distinction is particularly relevant when absorption coefficients are used as input parameters in light-photosynthesis models¹.

A reconstruction technique using the HPLC pigment information, and taking into account the package effect¹⁸ was used to estimate a_{ps}^* and a_{nps}^* for waters of the Equatorial Pacific. This oceanic region offered the opportunity to observe various situations along a meridian transect, from the oligotrophic waters near the South-Pacific gyre to the mesotrophic waters of the Equatorial upwelling. The aims of this study are to determine the spatial (vertical and horizontal) patterns of variability in a_{ph}^* , a_{ps}^* and a_{nps}^* , so as to quantify the part of variability in a_{ph}^* attributable to non-photosynthetic pigments, and to estimate the importance of the packaging effect in oligotrophic and mesotrophic waters.

2. MATERIALS AND METHODS

Spectral absorption coefficients of marine particles were measured with the glass-fiber filter technique¹⁹. The procedure was identical to that described in¹³, except that a Perkin-Elmer Lambda 19 dual-beam spectrophotometer, equipped with an integrating sphere, was used.

A β -correction algorithm was derived from our field data by using simultaneously, for some samples, the glass-fiber filter technique¹⁹ and the "slide technique"²⁰. As the pathlength amplification is avoided in this latter procedure, the measured optical densities are equal to the optical densities measured on suspensions (OD_s). The empirical relationship between the spectral values of $OD_s(\lambda)$ and those obtained on the filter ($OD_f(\lambda)$) fits a second-order polynomial:

$$OD_s(\lambda) = 0.293 OD_f(\lambda) + 0.302 OD_f(\lambda)^2$$

This relationship, which is to our knowledge the first algorithm for the correction of the β factor established from field data, appears to confirm the results of Moore et al.²¹ obtained on cultures. Although Eq.1 was obtained on only a few samples, it was confirmed by a more systematic study performed also in the Equatorial Pacific, along a meridian transect at 165°E and a transect along the Equator from 167°E to 150°W (FLUPAC-ORSTOM cruise²²).

The measured optical densities $OD_f(\lambda)$ were converted into $OD_s(\lambda)$ using the above equation, and the absorption coefficients $a_p(\lambda)$ (m^{-1}) were computed as follows:

$$a_p(\lambda) = 2.3 OD_s(\lambda) S/V$$

where S is the clearance area of the filter (m^2) and V is the filtered volume (m^3). Each $a_p(\lambda)$ spectrum was then decomposed into phytoplankton ($a_{ph}(\lambda)$) and non-algal components ($a_d(\lambda)$) using the numerical approach of Bricaud and Stramski¹³. The absorption coefficients of living phytoplankton ($a_{ph}(\lambda)$) were then converted into chl a -specific absorption coefficients ($a_{ph}^*(\lambda)$), by normalizing to the sum of chlorophyll a and divinyl-chl a (DV-chl a) concentrations, denoted Tchl a . Algal pigments were separated and quantified using high-performance liquid chromatography (HPLC)²³. Finally, the chl a -specific absorption spectrum of phytoplankton ($a_{ph}^*(\lambda)$) was partitioned into its photosynthetic and non-photosynthetic components, $a_{ps}^*(\lambda)$ and $a_{nps}^*(\lambda)$, following the method proposed by Babin et al.¹⁸.

3. RESULTS AND DISCUSSION

The areal Tchl a content (integrated over the water column) increases from 26 to 42 $mg\ m^{-3}$ along the transect, with a steep gradient around 1°S. This gradient was used to delimit two areas differing with respect to their trophic state: the oligotrophic subequatorial area (13°S-2°S) and the mesotrophic Equatorial area (1°S-1°N).

Mean and standard deviation values of specific absorption coefficients of particulate matter (a_p^*), phytoplankton (a_{ph}^*), photosynthetic (a_{ps}^*) and non-photosynthetic pigments (a_{nps}^*) (at 440 nm) were computed as functions of the optical depth, ζ ($=4.6 Z/Z_e$, where Z_e represents the euphotic depth and Z the depth), for the subequatorial and equatorial areas (Fig. 1).

In the subequatorial area, $a_p^*(440)$ and $a_{ph}^*(440)$ are high in the upper layer and gradually decrease with increasing depth (Fig. 1a, b). The major part of variability (about 80%) of the $a_{ph}^*(440)$ vertical variations is related to changes in $a_{nps}^*(440)$, which decreases by one order of magnitude along the vertical (Fig. 1c). In contrast to $a_{nps}^*(440)$, $a_{ps}^*(440)$ shows a weak decrease with depth. A small part (about 20%) of the variations in $a_{ph}^*(440)$ can be ascribed to this decrease.

In the equatorial area, $a_p^*(440)$ and $a_{ph}^*(440)$ are lower in the upper layer than in the subequatorial area (Fig. 1e, f). They also show a gradual decrease downward, although less pronounced than in subequatorial waters, and converge toward similar values at 6-8 optical depths. The $a_{nps}^*(440)$ coefficient is about twice lower than in the subequatorial area and decreases down to a similar value at depth (Fig. 1g). As in the subequatorial area, $a_{ps}^*(440)$ shows low variability throughout the water column, with also a slight decrease with depth (Fig. 1h).

The decrease in $a_{ph}^*(440)$ along the vertical observed in both areas is consistent with previous observations made in other parts of the world's ocean^{1,18,24}. The decrease in a_{ph}^* surface values from oligotrophic to mesotrophic areas was also observed and related to the nutrient availability^{1,16,25}.

The vertical and intersite variations in a_{ph}^* are, for the major part, accounted for by changes in absorption by non-photosynthetic pigments, and especially by zeaxanthin. The zeaxanthin concentration (relatively to Tchl a) decreases with depth by one order of magnitude in subequatorial waters (Fig. 2a), and still by a factor of 5 in the equatorial area (Fig. 2e). Diadinoxanthin and diatoxanthin, with much lower concentrations along the vertical, have only a minor influence upon the a_{ph}^* variations.

The residual variations observed in a_{ps}^* suggest that non-photosynthetic pigments are not the sole factor influencing the a_{ph}^* variations. Furthermore, the a_{ps}^* variations with depth cannot be related to the dominating photosynthetic pigments (Tchl $b = chl\ b + DV-chl\ b$, T19°=19°-HF+19°-BF), which vary in an opposite way (Figs. 2b, f). Therefore, it must be pointed out that the vertical distributions of a_{ph}^* , a_{ps}^* and a_{nps}^* are also influenced by the packaging effect. This effect is closely related to the average cell size (d) and the absorption coefficient of the cellular material ($a_{cm}(\lambda)$)²⁶. To account for this effect, the mean values of the "package effect index", Qa^* , were computed at 675 nm as functions of the optical depth for both subequatorial and Equatorial areas. This index was calculated as in¹⁶.

$Qa^*(675)$ decreases gradually with depth, in both subequatorial and Equatorial areas (Figs. 2c, g). The package effect is practically negligible near the surface in the subequatorial area but becomes more significant in equatorial waters, and progressively increases with depth in both areas. As previously stated, the vertical variations in $Qa^*(675)$ originate from vertical variations in the average cell size and/or from those in $a_{cm}(675)$, which in turn follow those of the intracellular Tchl a concentration (c_i). These c_i can be evaluated for the population of *Prochlorococcus* cells, from DV-chl a concentrations and

flow cytometric enumerations, and assuming an average cell size of $0.6 \mu\text{m}^2$. In accordance to what was observed in other oligotrophic areas^{27,28}, they reveal a strong increase, by about one order of magnitude, from the surface to the deeper layers (Fig. 2d, h) in response to decreasing irradiances with depth. Vertical variations in cell size, although not documented here, may also contribute to increase the package effect with depth²⁴. Although the c_1 values for *Prochlorococcus* are on average higher in the Equatorial area than in the subequatorial area (Fig. 2d, h), variations in cell size are probably the dominant factor. This is evidenced by the fucoxanthin/Tchl *a* ratio, which is enhanced by more than a factor of 2 from 2°S to 1°N, indicating an increasing presence of large cells (diatoms) close to the equator.

4. CONCLUSIONS

$a_{ph}^*(440)$ exhibits important vertical and site-to site variations, driven by changes in pigment composition, species composition and photoacclimation to the light regime. The natural variability in $a_{ps}^*(440)$ is significantly lower, evidencing that non-photosynthetic pigments are actually the major source of variation in a_{ph}^* . However, the package effect was found to be not negligible as often claimed, particularly below the mixed layer. The use of a_{ps}^* instead of a_{ph}^* in primary production models may therefore reduce the natural variability of the absorption capacity of phytoplankton, by removing the "artifactual" source of variability related to non-photosynthetic pigments.

5. ACKNOWLEDGMENTS

This study is a contribution to the EPOPE (JGOFS-FRANCE) program. We wish to thank the chief scientist and crew of the OLIPAC cruise, P. Raimbault for making available nutrient data, D. Vaultot and D. Marie for flow-cytometric data, A. Morel and S. Maritorena for *in situ* optical data, D. Tailliez and C. Bournot for CTD data, and C. Cailliau and J.C. Marty for their contribution to HPLC measurements. We are also grateful to A. Morel and D. Stramski for comments.

6. REFERENCES

1. Sosik H. M., and B. G. Mitchell, "Light absorption by phytoplankton, photosynthetic pigments, and detritus in the California Current System," *Deep-Sea Res.*, **42**, 1717-1748 (1995).
2. Gordon, H. R., O. B. Brown, R. H. Evans, J. W. Brown, R. C. Smith, K. S. Baker and D. K. Clark, "A semianalytic radiance model of ocean color," *J. Geophys. Res.*, **93**, 10909-10924 (1988).
3. Morel, A., "Optical modelling of the upper ocean in relation to its biogenous matter content (Case 1 waters)," *J. Geophys. Res.*, **93**, 10749-10768 (1988).
4. Kiefer, D. A. and B. G. Mitchell, "A simple, steady-state description of phytoplankton growth based on absorption cross section and quantum efficiency," *Limnol. Oceanogr.*, **28**, 770-776 (1983).
5. Morel, A. and D. Antoine, "Heating Rate within the Upper Ocean in relation to its Bio-Optical State," *J. Phys. Oceanogr.*, **24**, 1652-1665 (1994).
6. Bricaud, A., A. Morel and L. Prieur, "Optical efficiency factors of some phytoplankters," *Limnol. Oceanogr.*, **28**, 816-832 (1983).
7. Bricaud, A., A. L. Bédhomme and A. Morel, "Optical properties of diverse phytoplanktonic species: experimental results and theoretical interpretation," *J. Plankt. Res.*, **10**, 851-873 (1988).
8. Mitchell, B. G. and D. A. Kiefer, "Chlorophyll *a*-specific absorption and fluorescence excitation spectra for light-limited phytoplankton," *Deep-Sea Res.*, **35**, 639-663 (1988a).
9. Berner, T., K. Wyman and P. G. Falkowski, "Photoadaptation and the "package" effect in *Dunaliella tertiolecta* (Chlorophyceae)," *J. Phycol.*, **25**, 70-78 (1989).
10. Stramski, D. and A. Morel, "Optical properties of photosynthetic picoplankton in different physiological states as affected by growth irradiance," *Deep-Sea Res.*, **37**, 245-266 (1990).
11. Ahn, Y. H., A. Bricaud and A. Morel, "Light backscattering efficiency and related properties of some phytoplankters," *Deep-Sea Res.*, **39**, 1835-1855 (1992).
12. Mitchell, B. G. and D. A. Kiefer, "Variability in pigment specific particulate fluorescence and absorption spectra in the northeastern Pacific Ocean," *Deep-Sea Res.*, **35**, 665-689 (1988b).
13. Bricaud, A., and D. Stramski, "Spectral absorption coefficients of living phytoplankton and nonalgal biogenous matter: A comparison between the Peru upwelling area and Sargasso Sea," *Limnol. Oceanogr.*, **35**, 562-582 (1990).
14. Hoepffner, N. and S. Sathyendranath, "Bio-optical characteristics of coastal waters: Absorption spectra of phytoplankton and pigment distribution in the Western North Atlantic," *Limnol. Oceanogr.*, **37**, 1660-1679 (1992).

15. Babin, M., J. -C. Therriault, L. Legendre and A. Condal, "Variations in the specific absorption coefficient for natural phytoplankton assemblages: Impact on estimates of primary production," *Limnol. Oceanogr.*, **38**, 154-177 (1993).
16. Bricaud, A., M. Babin, A. Morel and H. Claustre, "Variability in the chlorophyll-specific absorption coefficients of natural phytoplankton: Analysis and parameterization," *J. Geophys. Res.*, **100**, 13,331-13,332 (1995).
17. Cleveland, J. S., "Regional models for phytoplankton absorption as a function of chlorophyll *a* concentration," *J. Geophys. Res.*, **100**, 13333-13344 (1995).
18. Babin, M., A. Morel, H. Claustre, A. Bricaud, Z. Kolber and P. G. Falkowski, "Nitrogen- and irradiance-dependent variations of the maximum quantum yield of carbon fixation in eutrophic, mesotrophic and oligotrophic marine systems," *Deep-Sea Res.*, in press.
19. Trüper, H. and C. S. Yentsch, "Use of glass-fiber filters for the rapid preparation of *in vivo* absorption spectra of photosynthetic bacteria" *J. Bacteriol.*, **94**, 1255-1256 (1967).
20. Allali, K., A. Bricaud, M. Babin, A. Morel and P. Chang, "A new method for measuring spectral absorption coefficients of marine particles," *Limnol. Oceanogr.*, **40**, 1526-1532 (1995).
21. Moore, L. R., R. Goericke and S. Chisholm, "Comparative physiology of *Synechococcus* and *Prochlorococcus*: influence of light and temperature on growth, pigments, fluorescence and absorptive properties," *Mar. Ecol. Prog. Ser.*, **116**, 259-275 (1995).
22. Le Borgne, R. and H. Gesbert (eds.), "Campagne océanographique FLUPAC à bord du N.O. l'ATALANTE, 23 septembre au 29 octobre 1994, Recueil de données". ORSTOM, Archives Sciences de la Mer, Océanographie, N°2, 330 pp. (1995).
23. Vidussi, F., H. Claustre, J. Bustillos-Guzman, C. Cailliau and J. C. Marty, "Determination of chlorophylls and carotenoids of marine phytoplankton: separation of chlorophyll *a* from Divinyl-chlorophyll *a*, and zeaxanthin from lutein," *J. Plankton Res.*, in press.
24. Lazzara, L., A. Bricaud and H. Claustre, "Spectral absorption and fluorescence excitation properties of phytoplanktonic populations at a mesotrophic and an oligotrophic site in the Tropical North Atlantic (Eumeli program)," *Deep-Sea Res.*, in press.
25. Yentsch, C. S., and D. A. Phinney, "A bridge between ocean optics and microbial ecology," *Limnol. Oceanogr.*, **34**, 1694-1705 (1989).
26. Morel, A. and A. Bricaud, "Theoretical results concerning light absorption in a discrete medium, and application to specific absorption of phytoplankton," *Deep-Sea Res.*, **28**, 1375-1393 (1981).
27. Morel, A., Y. Ahn, F. Partensky, D. Vaultot and H. Claustre, "*Prochlorococcus* and *Synechococcus*: a comparative study of their optical properties in relation to their size and pigmentation," *J. Mar. Res.*, **51**, 617-649 (1993).
28. Campbell, L., and D. Vaultot, "Photosynthetic picoplankton community structure in the subtropical North Pacific Ocean near Hawaii (station ALOHA)," *Deep-Sea Res.*, **40**, 2043-2060 (1993).

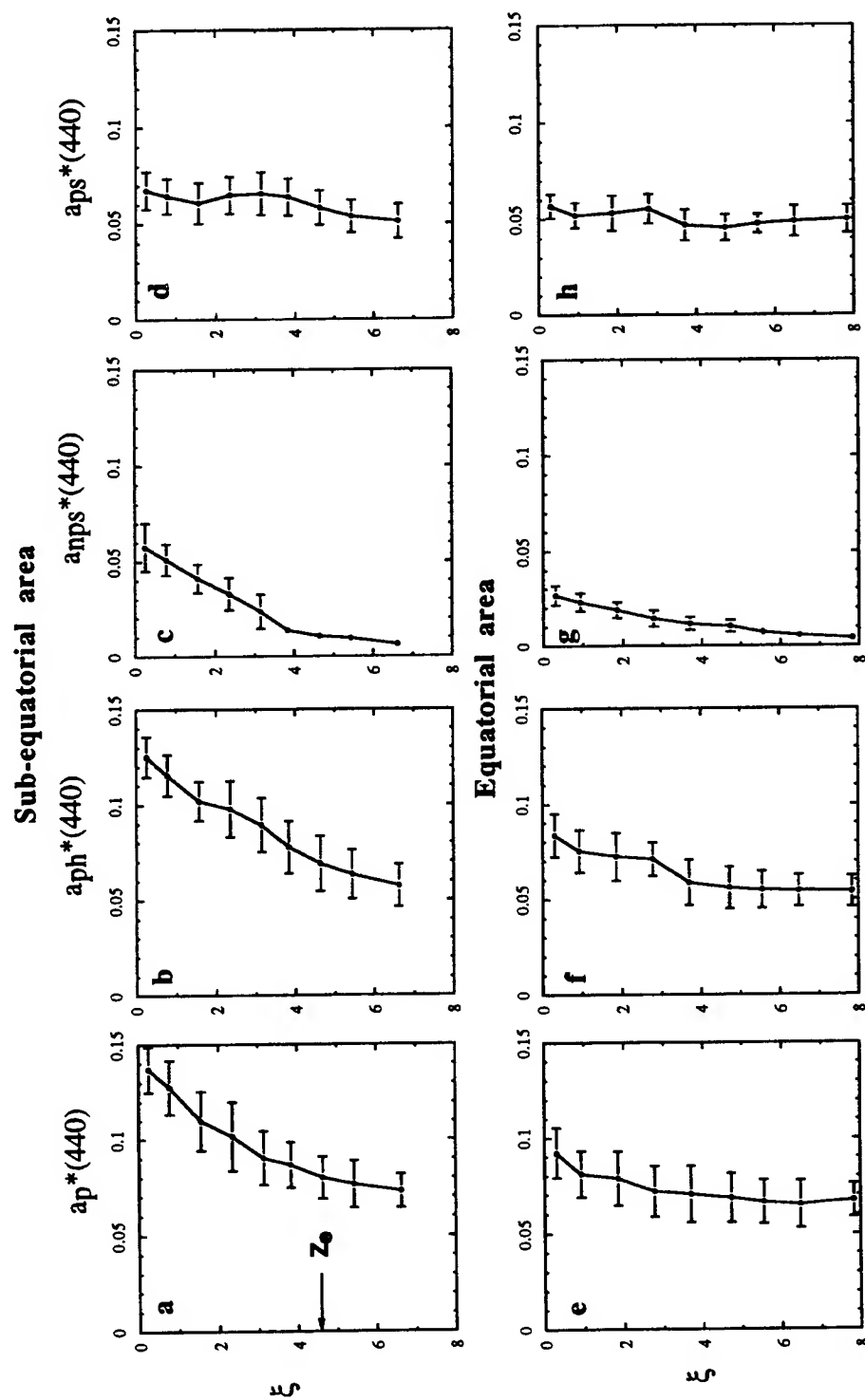


Fig. 1. Mean variations of the absorption coefficient at 440 nm of particles, $a_p^*(440)$, phytoplankton, $a_{ph}^*(440)$, non-photosynthetic pigments, $a_{nps}^*(440)$ and photosynthetic pigments, $a_{ps}^*(440)$, vs. the optical depth ζ , in the subequatorial area (13°S - 1°S , upper panels) and in the Equatorial area (1°S - 1°N , lower panels). Units are m^2mg^{-1} . Averages correspond to 16 profiles (8 stations) for the subequatorial area and 6 profiles (3 stations) for the Equatorial area. Horizontal bars indicate the standard deviations.

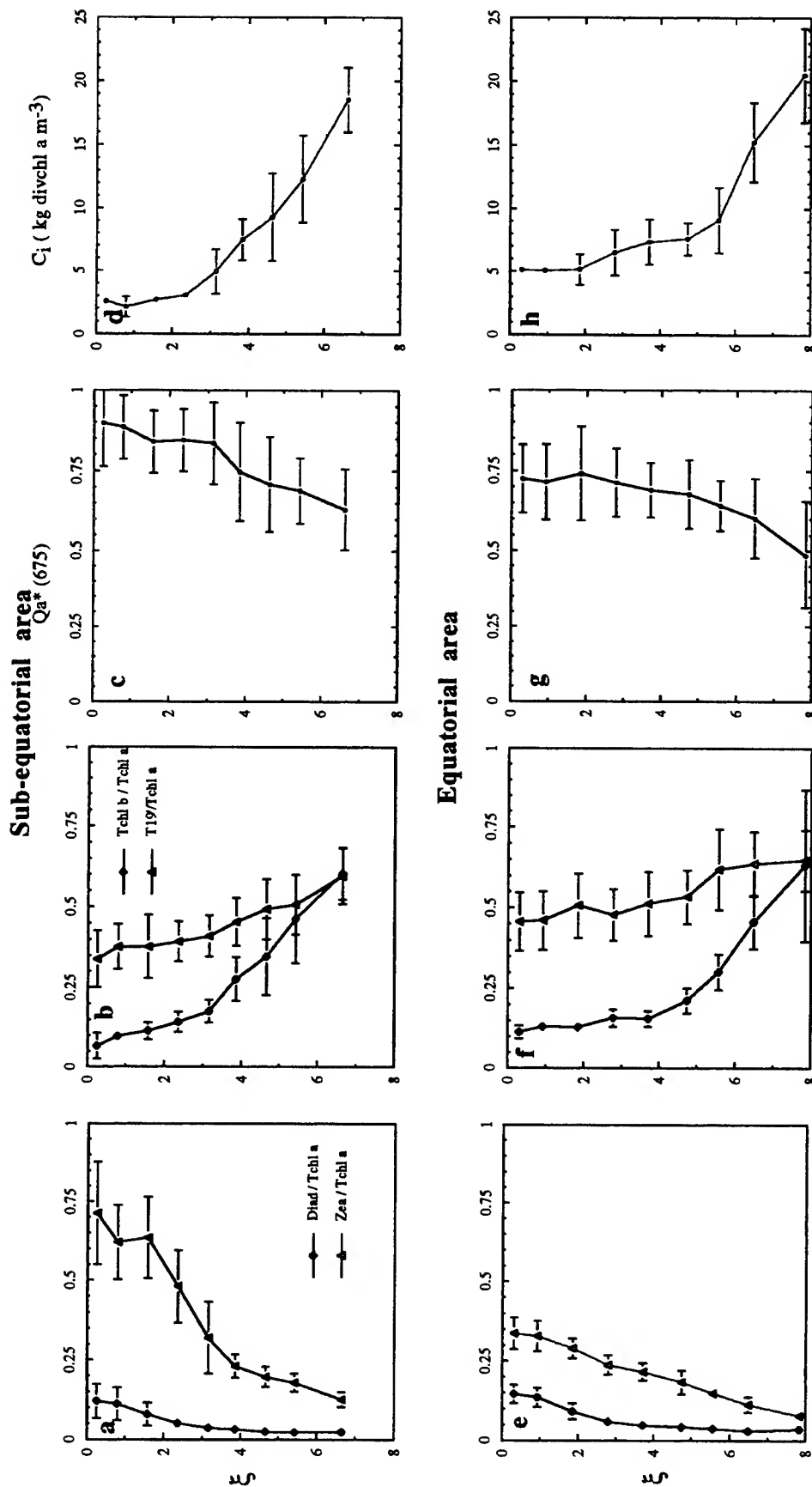


Fig. 2: Mean vertical variations, vs. the optical depth ξ , of (a) the concentrations of non-photosynthetic pigments (zeaxanthin and diadinoxanthin) relatively to Tchl a (chl a+DV-chl a), (b) the concentrations of the main photosynthetic pigments, (chl b + DV-chl b) and (19'-HF + 19'-BF), relatively to Tchl a, (c) the package effect index $Q_a^*(675)$ and (d) the intracellular concentration of DV-chl a (C_i) for *Prochlorococcus* cells. Upper and lower panels correspond to averages for the subequatorial area and the Equatorial area, respectively, as in Fig. 1. Horizontal bars indicate the standard deviations. Note that in Figures 2b and f, the vertical profiles of chl c, α -carotene, peridinin and fucoxanthin were omitted as their ratio to the Tchl a concentration was < 0.2 throughout the water column.

Optical spectral signatures of marine sediments

Walton E. McBride III
Planning Systems Inc., 115 Christian Lane, Slidell, LA 70458, USA
e-mail: <walt_mcbride@psislidell.com>

Vladimir I. Haltrin, Clark D. Kennedy, and Alan D. Weidemann
Naval Research Laboratory, Ocean Sciences Branch, Code 7331
Stennis Space Center, MS 39529-5004, USA. e-mail: <haltrin@nrlssc.navy.mil>

ABSTRACT

In studying light and image transfer in coastal waters the influence of bottom reflection is as significant as scattering and absorption phenomena. In these cases a knowledge of the reflective properties of different types of bottoms is very important. At present, little is known about these properties. We present results of experimental spectral measurements of different kinds of sedimental material such as sands and clays, both major components of coastal water bottoms.

We have determined the spectral index of refraction from measurements of the optical spectral signatures of various clays and sands, as they represent the most common bottom components found in coastal waters. The measured optical spectral signatures and the associated complex indexes of refraction are presented. This preliminary study should provide insight on improving the inverse problem algorithm for extracting the spectral index of refraction. This spectral information can then be used as input into radiative transfer models which include the ocean bottom.

Keywords: reflectance, refraction index, optical constants, optical signatures, ocean sediments.

1. INTRODUCTION

Our overall motivation is to be able to characterize bottom properties with a wavelength- dependent spectrum of dielectric permittivities to be used as input into an underwater propagation model. Equivalently, we would like to obtain a rough estimate for the complex index of refraction of particular samples as a function of wavelength from the simplest possible assumptions and measurements about the reflective properties of typical bottom sediments. From these acquired spectral values for the real and imaginary parts of the index of refraction, the reflective properties of a sample can be calculated as a function of the angle of incidence for a particular wavelength, a characterization which can easily be input into the numerical simulation of a theoretical model. Because of the simple experimental design our initial goal is to obtain reflectances within 20% of their measured values over a range of incidence angles varying from normal to 30 degrees.

For each wavelength in the spectrum, there are two unknowns, *i.e.*, the real and imaginary part of the index of refraction, often referred to as the optical constants. Methods exist [1] to deal with the inverse problem of determining these quantities for flat surfaces, such as reflectometry and ellipsometry. Specular reflectance measurements were performed in order to try to infer the complex index of refraction as a function of wavelength. In the next section, we describe the algorithm which we used to address this inverse problem.

2. INVERSION ALGORITHM

In order to quantify the real and imaginary parts of the complex index of refraction, two different measurements must be made. For specular reflectance measurements, there are two variables which can be used in tandem: the source polarization (perpendicular or transverse to the plane of incidence) and the angle of incidence (from 0 to 90 degrees).

In an effort to obtain an estimate of the complex index of refraction as a function of wavelength, the following simplifying assumption was made: only single reflections from the air/sample interface contribute to the intensity at the spectral radiometer. In effect, for a particular angle of incidence, only those facets at the sample surface which specularly reflect light into the spectral radiometer aperture are assumed to contribute. Multiple reflections from facets at different orientations to each other are not considered. For rough surfaces such as clays and sands, it is expected that some modification of the simple theory involving the Fresnel intensity reflection coefficients for flat surfaces will be needed.

2.1. Fresnel intensity reflection coefficients

Given the angle of incidence θ_i with respect to the boundary normal between two dielectrics, the Fresnel intensity coefficients for the parallel and transverse polarizations at the specular reflection angle are respectively given by [2]:

$$R_p = \left| \frac{\sqrt{m^2 - \sin^2 \theta_i} - m^2 \cos \theta_i}{\sqrt{m^2 - \sin^2 \theta_i} + m^2 \cos \theta_i} \right|^2 \quad \text{and} \quad R_t = \left| \frac{\sqrt{m^2 - \sin^2 \theta_i} - \cos \theta_i}{\sqrt{m^2 - \sin^2 \theta_i} + \cos \theta_i} \right|^2 \quad (1)$$

where the complex index of refraction $m = n_r + in_i$. For normal incidence the reflectance is the same for both polarizations, effectively resulting in only one measurement. An incidence angle of 30 degrees was also chosen, giving two more measurements depending on the source polarization.

2.2. Algorithm description

Our simple algorithm makes use of all three measurements in a search for the minimum of a sum of absolute differences for each wavelength. The differences in this sum are between the corresponding measured and theoretically-predicted reflectances. Let R_{00}^{data} be the reflectance value at normal incidence (same for both polarizations) and R_{30p}^{data} and R_{30t}^{data} be the reflectance values for parallel and transverse polarizations at 30 degrees. Then, for each wavelength in the measured reflectance spectra, the inversion algorithm proceeds as follows.

Loops are performed over a user-given range of values for n_r and n_i . For each (n_r, n_i) pair, the Fresnel intensity reflection coefficients R_{00}^{theory} , R_{30p}^{theory} and R_{30t}^{theory} are calculated and differenced with their measured counterparts. The sum of the three absolute differences, $abs(R_{00}^{theory} - R_{00}^{data}) + abs(R_{30p}^{theory} - R_{30p}^{data}) + abs(R_{30t}^{theory} - R_{30t}^{data})$, is then minimized while keeping track of the (n_r, n_i) pair which resulted in the minimum for each wavelength.

The range over which both n_r and n_i are searched is determined by the user, as well as the discretization of these variables. Discretization was chosen to be a grid of 1000 by 1000 possible values for n_r and n_i . For the first pass, values of n_r and n_i between 0.0 and 3.0 are allowed since we have no initial idea of the range of these variables. The grid described above enables the algorithm to find the values to at least the second decimal place while narrowing the ranges in n_r and n_i . In order to further zoom in on the minimum, two additional passes are performed with a 100 by 100 grid of total width equal to twice the previous increments in n_r and n_i and centered on the inferred values of n_r and n_i from the previous pass.

Problems were anticipated when $n_i \ll n_r$ due to the statistical nature of the reflectance measurements. Realistically, only when n_i is comparable in size to n_r can the inversion algorithm be expected to predict n_i with any confidence. In order to get an idea of the inversion capabilities of the algorithm when the reflectance data is known exactly, synthetic data was generated.

2.3. Synthetic data for algorithm test

Before the algorithm was applied to experimental data, its performance was tested against synthetic reflectance data generated over a wavelength spectrum between 450 and 800 nm. The data was generated from assumed Gaussian functional forms for both the real and imaginary parts of the index of refraction:

$$n_r(\lambda) = 2.0 - e^{-\left(\frac{\lambda - 450.0}{150.0}\right)^2} \quad \text{and} \quad n_i(\lambda) = .5e^{-\left(\frac{\lambda - 450.0}{150.0}\right)^2} \quad (2)$$

The functional form for n_i was chosen so as to span a wide range of values, from .5 at 450 nm to about 2.2×10^{-3} at 800 nm, as small values for that parameter were expected.

The Fresnel intensity reflection coefficients were then calculated for each wavelength to obtain the theoretically-predicted reflectance spectra for normal incidence as well as for the two polarizations at 30 degrees. These reflectance spectra were used as "experimental" data input to the inversion algorithm which then finds the (n_r, n_i) pair that best matches.

Figure 1 below is an illustration of the assumed functional shapes for n_r and n_i and the inferred values (asterisks) for both parameters. Figure 2 shows the original synthetic reflectances (R_{30t} , R_{00} and R_{30p} from top to bottom) computed directly from the assumed Gaussian functional forms for n_r and n_i and the reflectances at 11 equally spaced points computed from the inferred values of n_r and n_i . The percentage difference between the two reflectances is under 1% for all points on each of the three curves.

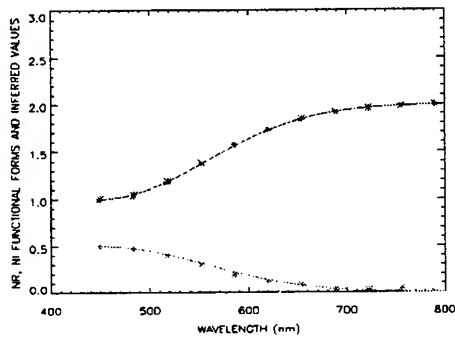


Figure 1: Inferred and synthetic values of index of refraction.

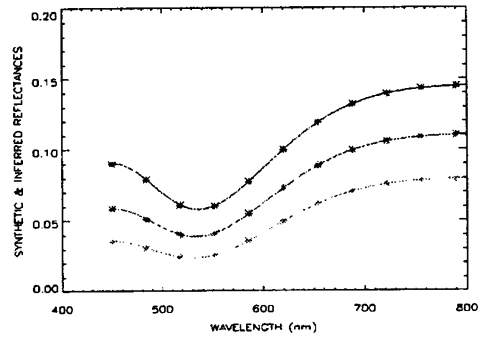


Figure 2: Comparison between inferred and synthetic reflectances

Satisfied with the ability of the algorithm to reliably predict the (n_r, n_i) spectra which generated the synthetic data, we applied the algorithm to the experimental data we collected.

3. EXPERIMENTAL REFLECTANCE MEASUREMENTS

Experimental data was gathered in air with a xenon arc lamp as the light source. The output of the lamp was defocused at a 2.5 cm aperture. The image of the aperture was projected through a second lens to form a 10 cm circular spot (at normal incidence) at 34 cm from the lens. This produced a diffuse image of the aperture which would be the same as that produced from a point source at 45 cm from the surface which has been stopped down to 12.2 degrees. The polarizer was mounted between the projecting lens and the target surface. The detector was a CCD-based spectral radiometer (ASD). The foreoptic of the radiometer had a 1 degree acceptance angle and is mounted at 53 cm from the target. The detected spot diameter was about 1 cm near the center of the projected aperture image.

Three different samples were used for measurement purposes: a backyard orange-brown clay affectionately coined "Waltonian" clay by our group and two types of sand collected from coastal areas, referred to simply as gray sand and brown sand. Calibration of the measured reflectance spectra was performed with the help of a gray reflector with known reflective properties. All inferred values for n_r and n_i are with respect to air.

4. INVERSION ALGORITHM APPLIED TO EXPERIMENTAL DATA

As with the synthetic data, 11 points were picked from the three experimental reflectance curves in order to save computing time. Because each reflectance curve represents an average over only 10 spectrometer samples, enough "noise" in these curves is present to adversely effect the inversion algorithm.

Figure 3a below shows the values of n_r and n_i inferred from the experimental reflectance curves in Figure 3b for Waltonian clay (top is R_{30r} , middle is R_{00} and (almost overlapping) bottom is R_{30p}). As can be seen, the inversion algorithm predicts values for n_r only below 500 nm. Predictions for n_i over the rest of the wavelength band appear to be meaningless when compared to the more gradual falloff in Figure 1. Interestingly enough, the inferred values for n_r below 500 nm are comparable in size to n_r , a criterion we needed for the inversion algorithm to predict values of n_i with any confidence. The thin lines in Figure 3b connect the 11 reflectance points corresponding to the inferred (n_r, n_i) pairs. Error percentages between corresponding reflectances are presented later in Section 5.

For materials such as sands, however, simple Fresnel theory had to be modified. As can be seen from the experimental data in Figures 4b and 5b, two trends occur which Fresnel theory is incapable of explaining: the top curve is now R_{00} followed by R_{30r} and R_{30p} while the gap between the latter two is much narrower than the gap predicted by Fresnel theory for the inferred (n_r, n_i) values. We have therefore applied two modifications to the inversion algorithm in the case of sands.

The first modification involves the fall-off of the unpolarized reflected intensity at 30 degrees for both polarizations as compared to simple Fresnel theory. As shown in Ref. [3], the unpolarized reflectance is almost constant from normal to 30 degrees incidence over the n_r and n_i ranges of interest here. The inversion algorithm candidate reflectances at 30 degrees were therefore divided by the ratio of the unpolarized reflectances at normal and 30 degrees incidence, $2R_{00}^{data} / (R_{30p}^{data} + R_{30r}^{data})$, before performing the sum of the three absolute differences, as explained in Section 2.2. The second modification is discussed in Section 5.

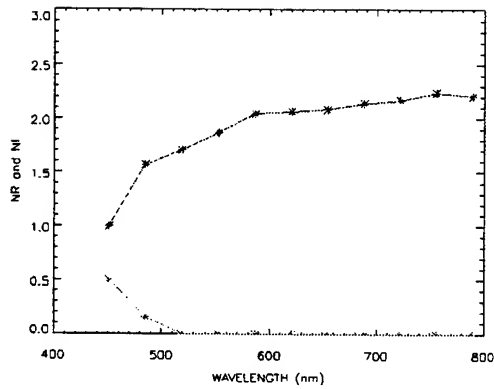


Figure 3a. Inferred values of n_r and n_i for Waltonian clay

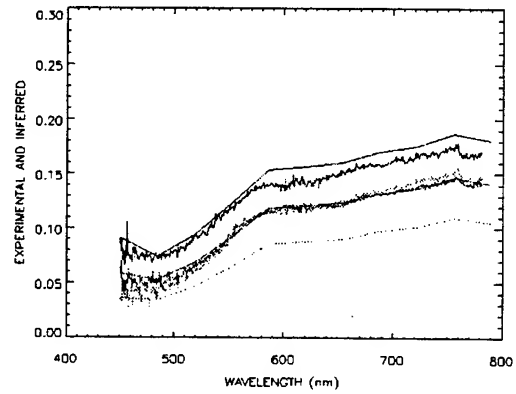


Figure 3b. Experimental and inferred reflectances for Waltonian clay

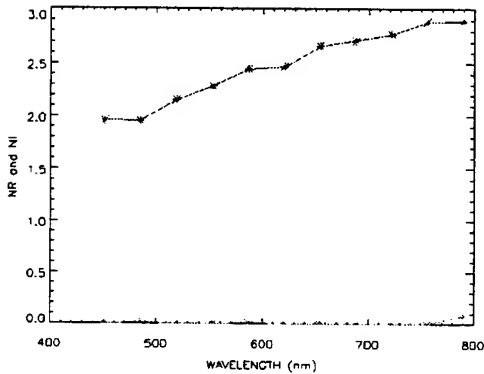


Figure 4a. Inferred values of n_r and n_i for brown sand

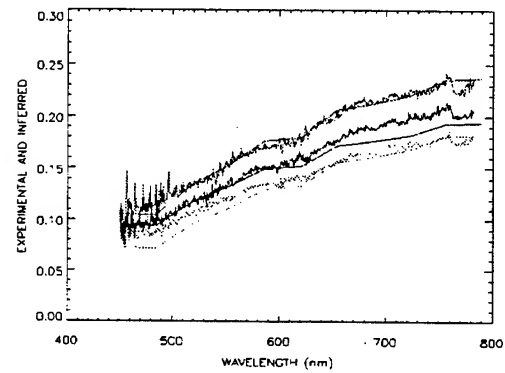


Figure 4b. Experimental and inferred reflectances for brown sand

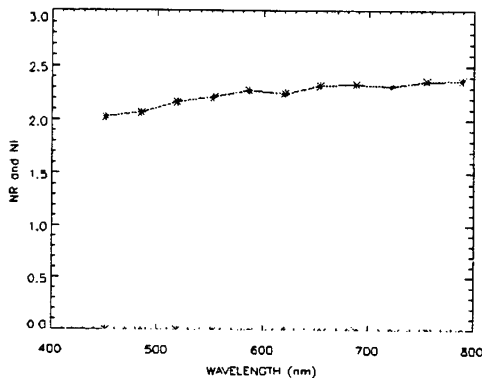


Figure 5a. Inferred values of n_r and n_i for gray sand

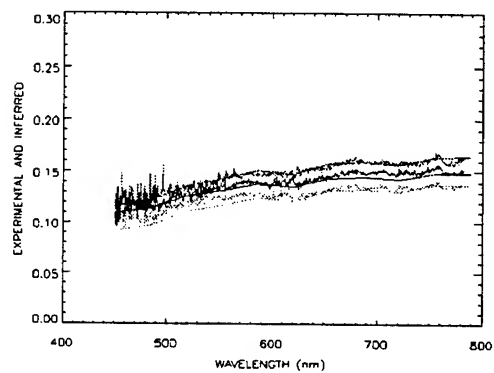


Figure 5b. Experimental and inferred reflectances for gray sand

Although values for n_r were predicted for a few wavelengths in the Waltonian clay case, disappointing results can be seen for both types of sand, as shown in Figures 4a and 5a. Nevertheless, values for n_r were obtained. Whether the absence of any predictions for n_i is due to the noise in the reflectance curves, the smallness of n_i , or the inapplicability of Fresnel theory altogether needs to be investigated.

5. REFLECTANCE PLOTS AS A FUNCTION OF INCIDENCE ANGLE

Once the optical constants of each sample were obtained as a function of wavelength, reflectance plots as a function of incidence angle were produced over the visible spectrum. Figures 6a, 7a and 8a show such predictions at a wavelength of 600 nm for the three samples in our experiment (top for perpendicular, middle for unpolarized and bottom for parallel), while figures 6b, 7b, and 8b show the percentage error between experimental and inferred reflectances discussed in Section 4 (light for R_{30p} , medium for R_{00} , and dark for R_{30i}). In all cases there is excellent agreement for R_{00} . Overall, our original goal of obtaining reflectances within 20% of their experimental values seems to be achievable.

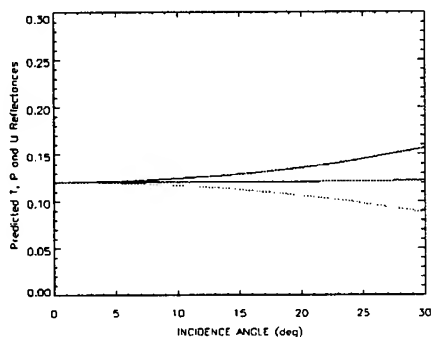


Figure 6a. Reflectances at 600 nm for Waltonian clay

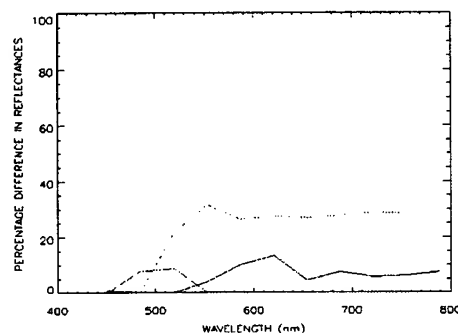


Figure 6b. Percentage error between reflectances for Waltonian clay

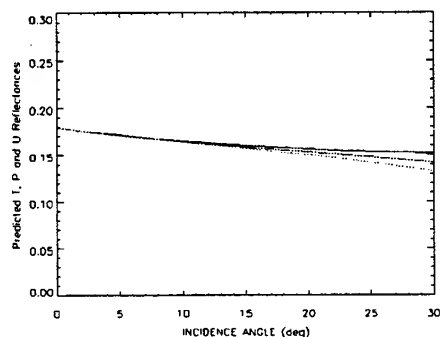


Figure 7a. Reflectances at 600 nm for brown sand

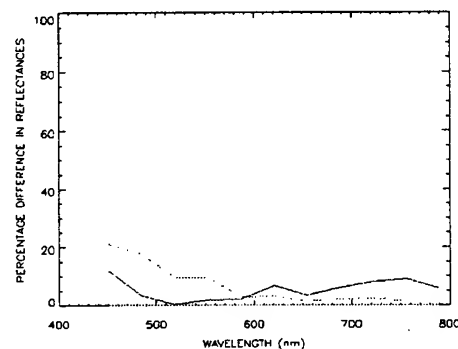


Figure 7b. Percentage error between reflectances for brown sand

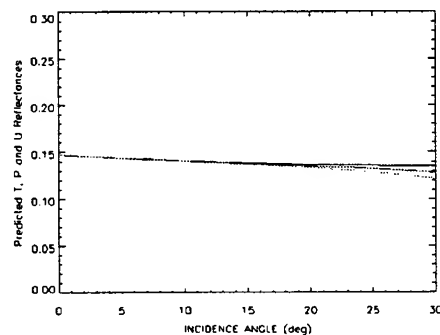


Figure 8a. Reflectances at 600 nm for gray sand

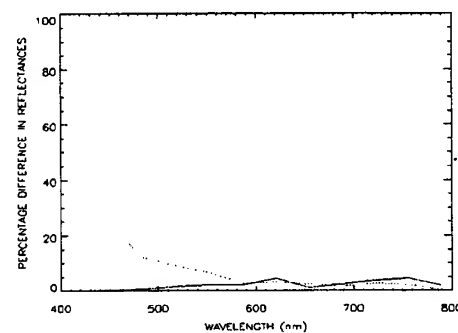


Figure 8b. Percentage error between reflectances for gray sand

Except for Waltonian clay where the inversion algorithm was run without modifications, the percentage error between experimental and inferred reflectances at 30 degrees was calculated by adjusting the gap between the curves corresponding to different polarizations. Because of the large inferred values for n_i in sands, the gap predicted by Fresnel

theory is much wider than the one gathered from experimental data. A second modification to simple Fresnel theory was therefore necessary.

Because of its constancy over the incidence angles of interest to our study, the unpolarized reflectance at 30 degrees was used as a reference point from which the modification was made. Let *gapdata* be the ratio of the transverse to unpolarized reflectances from experimental data at 30 degrees for the middle wavelength of 600 nm, while *gaptheory* is the corresponding quantity derived from Fresnel theory. Then the theoretical transverse and parallel reflectances were modified as follows:

$$R_{30t}^{modified} = \frac{R_{30t}}{falloff} \left(\frac{gapdata}{gaptheory} \right) \quad \text{and} \quad R_{30p}^{modified} = \frac{R_{30p}}{falloff} \left(\frac{2 - gapdata}{2 - gaptheory} \right) \quad (3)$$

where *falloff* represents the first modification discussed previously involving the fall-off of reflected intensity as the incidence angle increases, $2R_{00}^{data} / (R_{30p}^{data} + R_{30t}^{data})$. In order to produce Figures 7a and 7b for sands, the following interpolations were performed:

$$R_t = R_t^{theory} \frac{R_t^{fact}(\theta)}{fall(\theta)} \quad \text{and} \quad R_p = R_p^{theory} \frac{R_p^{fact}(\theta)}{fall(\theta)} \quad (4)$$

where

$$fall(\theta) = 1.0 + (falloff - 1.0)F(\theta), \quad (5)$$

$$R_t^{fact} = 1.0 + \left(\frac{gapdata}{gaptheory} - 1.0 \right) F^2(\theta) \quad \text{and} \quad R_p^{fact} = 1.0 + \left(\frac{2 - gapdata}{2 - gaptheory} - 1.0 \right) F^2(\theta) \quad (6)$$

and

$$F(\theta) = \frac{\sin \theta}{\sin 30^\circ}. \quad (7)$$

The result of the two modifications can be seen in figures 7a and 8a for brown and gray sands, respectively. Notice how the unpolarized reflectance shows a fall-off as the angle of incidence increases from normal to 30 degrees. The second modification is also apparent as the gap between the two polarizations is much narrower than predicted by simple Fresnel theory for the range of values of n_t encountered in our study.

6. CONCLUSIONS

We have used an inversion algorithm involving simple Fresnel reflection theory to determine the spectral index of refraction from specular reflectance measurements of clay. It was found that two modifications to simple theory were necessary for sands in order to reproduce the experimental reflectance curves from the inferred optical constants.

Because our interest in the complex index of refraction stems from our theoretical modeling requirements, our next priority is to build a small database of the optical constants for the most common types of marine sediment. In that regard, more automated instrumentation would be preferred and a more thorough investigation of the reason behind the disappointing results for n_t will be undertaken. As work progresses, a search for more efficient and accurate methods to find n_t and n_i such as neural network and simulated annealing will be undertaken.

Water tank experiments are also needed so that the marine sediments are in their natural environments. Some simple way will be found to illuminate a submerged surface and to obtain n_t and n_i relative to the index of refraction of water.

7. ACKNOWLEDGMENTS

The authors wish to thank continuing support at the Naval Research Laboratory through the Littoral Optical Environment (LOE 6640-06) and Optical Oceanography (OO 73-5051-05) programs. This article represents NRL contribution NRL/PP/7331-96-0010. The authors would like to take this opportunity to thank Richard Ray for his assistance.

8. REFERENCES

1. L. Ward, Ed., *The Optical Constants of Bulk Materials and Films*, Institute of Physics Publishing, Bristol and Philadelphia, PA, p. 350, 1994.
2. D. V. Sivukhin, *General Course in Physics, Vol. 4: Optics* (in Russian), Moscow, Nauka, p. 406, 1985.
3. E. Palick, *Handbook of Optical Constants of Solids*, Academic Press, New York, N.Y., p.72, Figure 1, 1985.

In-Situ and Remote Sensing Sensors and Systems

Invited Paper

Absorption coefficients of the ocean: their measurement, and implications for remote sensing

John T.O. Kirk

CSIRO Plant Industry, GPO Box 1600, Canberra 2601, Australia

ABSTRACT

The spectral energy distribution of the emergent radiant flux from the ocean is determined by the inherent optical properties of the water, especially the absorption coefficients. To interpret the remotely sensed spectral distribution in terms of ocean composition we need a data base relating seawater absorption spectra to composition, especially in terms of phytoplankton concentration and type, and soluble and detrital colour. Measurement of seawater absorption spectra is difficult because absorption is so low, and because of the confounding effects of scattering. The use of the integrating cavity absorption meter to overcome these problems is discussed, and an account is also given of the potential and limitations of seeking to estimate absorption coefficient values from in-water spectral irradiance data.

(*Keywords:* absorption coefficients, absorption meter, inherent optical properties, remote sensing)

1. INTRODUCTION

Consider the ocean - and the continual stream of solar radiation falling upon it. A small fraction - typically two or three percent - is reflected at the surface, but the rest passes through into the sea, where it gives rise to the underwater light field. A small part of the energy in this underwater light field escapes up through the surface again. This emergent flux is not only much less intense than the incident solar flux - being proportionately no more than a few percent - but is drastically changed in its energy distribution across the spectrum. The change is brought about by the operation of the inherent optical properties of the water upon the incident solar light stream which passes down through the surface. We may therefore reasonably hope that by close examination of this emergent flux we can learn something about the inherent optical properties of the water, and thus by inference learn something about those constituents of the sea which determine these optical properties, and it is upon this hope that the whole oceanic remote sensing enterprise in the visible region is based.

It is only certain constituents of the sea that need concern us: specifically water itself, the phytoplankton, the particulate organic detritus derived mainly from phytoplankton, the dissolved yellow substances derived from land drainage and from breakdown of marine organic matter, sedimentary particles carried in by rivers or resuspended from the bottom, and marine bacteria. All six of these constituents absorb and scatter light, and by doing so make their individual additive contributions to the two inherent optical properties of most interest to us, namely the spectrally varying absorption and scattering coefficients, $a(\lambda)$ and $b(\lambda)$. It is the scattering of the light within the water that in the first instance converts some of the downwelling light flux to an upwelling light flux, some of which escapes through the surface as the emergent flux. And it is the differential absorption at different wavelengths, with some contribution from the spectral variation in scattering, which gives the emergent flux its characteristic spectral energy distribution.

If we are to understand and therefore predict how the absorption properties of marine waters will vary with water composition, there is no escaping the need to actually collect data; to create a data base of spectral absorption measurements for a range of seawater types, over a wide range of composition from around the world's oceans. Furthermore, as the new generation of satellite-borne ocean colour scanners are put into orbit over the next few years, there will need to be validation work, relating sea truth values of absorption coefficients to those that particular algorithms calculate from the remotely sensed data. Accurate calculations of oceanic primary production - directly relevant of course to the role of the ocean in the global carbon cycle and therefore the greenhouse effect - also require information not only on the absorption spectra of the phytoplankton, but also on the competing absorption by other components of the system. For these kinds of reason there is general recognition, in the remote sensing, and marine productivity communities, of the need for good spectral absorption data for the oceans. That is easily said, but not so easily achieved. The essential problem is that absorption by most seawaters is too low to measure accurately with normal laboratory spectrophotometers. Furthermore, scattering is invariably

also present, and if we seek to overcome the problem of low absorption by simply increasing the pathlength of our instrument, then the scattering also increases and we are still left with the problem of deciding how much of our apparent absorption is really absorption, and how much is due to scattering.

I shall not review here all the different approaches that have been used in attempts to overcome these problems, but will concentrate rather on one recent instrumental approach that seems to me to be very promising. I shall also consider the completely different approach of not measuring absorption coefficients directly, but calculating them from underwater spectral irradiance data measured in the field.

2. THE INTEGRATING CAVITY ABSORPTION METER

The instrumental approach involves what is known as the integrating cavity absorption meter (or ICAM). This has been developed by Fry, Kattawar & Pope,¹ and the essential principle is that if a sample is placed within an isotropic homogeneous field then the absorbed radiant power is unaffected by scattering. Putting it another way, if the light field is already completely diffuse, then scattering cannot make it any more diffuse. The isotropic field is created by introducing light into a cavity with a diffusely reflecting surface, and the absorbing sample is placed within the cavity. A second advantage that the integrating cavity has, in addition to its immunity to scattering, is that because of multiple reflection from the wall the effective pathlength through the sample is much greater than the diameter of the cavity and so the sensitivity for weakly absorbing samples is correspondingly increased. Fry et al. have built a prototype instrument for liquid samples. This has a cylindrical cavity made of the highly reflective, but also slightly translucent plastic, Spectralon, the cavity being lined with quartz. To create a homogeneous isotropic light field, this inner cavity is placed within an outer cavity also made of Spectralon. Light is introduced into the annular space between the two cavities by means of optical fibres, and as a result of multiple reflection between the two surfaces a diffuse light field is set up. Some of this light penetrates through the Spectralon wall of the inner cavity and, we may reasonably assume, thus gives rise to a highly diffuse light field within the sample. The outward irradiance on the inside of the cavity, F_o , is measured as is also irradiance F_i at a point within the Spectralon wall of the inner cavity. Fry et al. showed that if the simplifying assumption is made that the radiance distribution is homogeneous and isotropic throughout the cavity, as will approximately be the case for weakly absorbing samples, then the absorbed power is a linear function of the absorption coefficient, in accordance with

$$P = 4aVF_o \quad (1)$$

where V is the volume of the cavity and F_o is the outward irradiance on the surface. From this they arrived at an expression for absorption coefficient in terms of measurable quantities

$$a = K_1 \frac{S_1}{S_0} - K_2 \quad (2)$$

S_1 and S_0 being measured signal voltages proportional to the irradiances F_i and F_o , and K_1 and K_2 are instrument-calibration factors whose values can be determined by the use of samples of known absorption coefficients. Fry et al. tried out their prototype instrument on various made-up samples, and it performed as anticipated, showing both a high sensitivity to weakly absorbing samples, and a very satisfactory insensitivity to high levels of scattering.

The assumption of weak absorption and therefore a homogeneous energy distribution within the cavity (the HED assumption) does indeed apply to most seawaters, but does not apply to some estuarine waters, and many inland waters, with high levels of soluble and/or particulate colour. I decided to look more closely at the light field in the cavity at high absorption coefficient values. Clearly, to achieve this we need a theoretical treatment which makes no assumption about the

energy distribution within the cavity. It turns out that for a spherical integrating cavity it is possible to arrive at some quite simple mathematical relationships which describe the behaviour of the photons emitted into the cavity.² For a cavity of radius r and reflectivity ρ filled with medium of absorption coefficient a , the average number of collisions with the cavity per photon is

$$C_F = \frac{P_s}{1 - \rho P_s} \quad (3)$$

and the average pathlength per photon is

$$l_F = \frac{1}{a} \left(\frac{1 - P_s}{1 - \rho P_s} \right) \quad (4)$$

where P_s is the probability of survival of a single emitted photon in its trajectory across the cavity. P_s as a function of the absorption coefficient and the radius is given by

$$P_s = \frac{1}{2a^2r^2} [1 - e^{-2ar}(2ar + 1)] \quad (5)$$

In the derivation of these equations no assumption is made about energy density distribution within the cavity, and so they apply to any values of absorption coefficient or sphere diameter regardless of how far the field within the cavity departs from homogeneity. For a given rate of emission of photons into the cavity the irradiance produced on the wall is proportional to the average number of collisions per photon with the wall. Thus with the help of the equations for C_F and P_s we can calculate how the measured irradiance will vary as a function of the absorption coefficient of the medium and the diameter of the cavity. With these equations it was possible to carry out² a detailed exploration of the performance of the ICAM as a function of cavity size, cavity reflectivity, and absorption coefficient of the water.

As anticipated, the assumption of a homogeneous energy distribution departs increasingly from reality as the absorption coefficient increases to high values, and this causes the instrument to overestimate the value of a . However, for a values up to 1.0 m^{-1} , and that certainly covers most marine waters, the error does not exceed 3%. For higher values of a there is a simple iterative calculation procedure which, starting from the measured value will yield the correct value.

In all the calculations I have described so far it has been assumed that the medium absorbs, but does not scatter, light. However, the field within a scattering sample can be simulated with considerable accuracy by the Monte Carlo procedure, and such modelling shows, in agreement with the experimental observations of Fry et al., that the irradiance on the cavity wall is completely unaffected by scattering, even at very high levels. Furthermore, the performance characteristics of the instrument as predicted by the equations, that we have just surveyed, are confirmed. This means that the equations for the field apply equally well whether the medium scatters or not.

On the basis of what we now know, how should we best proceed towards a practical instrument to be used by oceanographers, limnologists, environment protection agencies, industries discharging wastewater, and anyone else who needs to characterize the absorption spectra of waters occurring in, or to be discharged to, the environment? As a step in this direction I propose that as a simpler, and less expensive way of creating a uniform light field, we emit the photons not from all around the cavity wall, but from a point source located at the centre of the cavity.

The average number of collisions with the wall per emitted photon, in its lifetime is now given by

$$C_F = \frac{e^{-ar}}{1 - \rho P_s} \quad (6)$$

similar to the previous expression except that P_s in the numerator is now replaced by $e^{-a_w r}$. The transmittance (ratio of the F_0 irradiance values) of the cavity filled with sample relative to that of a cavity filled with pure water is given by

$$T = \frac{e^{-ar}(1 - \rho P_s^w)}{e^{-a_w r}(1 - \rho P_s)} \quad (7)$$

where a_w is the absorption coefficient of pure water, and P_s^w is the analogue of P_s for a cavity containing pure water. In order to obtain an expression for a in terms of the measurable quantity, T , we must invoke the HED assumption, and this gives us the equation

$$a = \left[\frac{4/3 a_w r + (1 - \rho)}{4/3 r} \right] \frac{1}{T} - \frac{3(1 - \rho)}{4r} \quad (8)$$

I have carried out the same series of calculations with this point source integrating cavity absorption meter, (PSICAM) as with the other absorption meter.³ The results are broadly similar, although not identical. Where the difference becomes interesting is in the calculation of the size of the error that emerges at high values of absorption coefficient. The figure shows the measured absorption coefficient, i.e. as calculated from transmittance with the HED equation, as a function of the true absorption coefficient, for an integrating cavity in which the photons are emitted from the wall (the upper curve) or from a central point source (the middle curve). In both cases the instruments give good values at the lower end of the scale, but as we proceed to high values of a , error begins to appear, but is significantly less in the PSICAM than in the other instrument configuration. Perhaps emission of the photons from the centre of the cavity rather than the wall gives rise to a more uniform light field, and therefore a lesser departure from the HED assumption. A simple laboratory prototype of the PSICAM has been constructed and is giving encouraging results.

All this leads to the conclusion that in the form of the integrating cavity absorption meter we now have, in principle if not yet commercially available, a satisfactory method of measuring the absorption coefficients of marine and other natural waters, which solves the problems both of low absorption and the interfering effects of scattering. The task that remains is to develop a simple, robust, user-friendly version of this instrument, for shipboard as well as laboratory use, for the benefit of the potential user community.

3. DERIVING ABSORPTION COEFFICIENTS FROM IN-WATER IRRADIANCE DATA

As well as those approaches to the measurement of absorption coefficient which involve some kind of spectrophotometry on samples of the water, there is a quite different approach which seeks to infer the values of absorption coefficient from the measured properties of the light field established within the sea. The principle upon which this is based is that for a given incident light flux at the surface the characteristics of the light field at any specified optical depth are entirely a function of the inherent optical properties of the water. This raises the possibility, therefore, of working backwards from the the properties of the light field to the particular values of the inherent optical properties which determine that light field, and over the years there have been a number of papers describing ways of doing this. A particular method I developed about 16 years ago⁴ involved the use of a nomogram from which, using the measured value of reflectance at a certain optical

depth (z_m , the 10% irradiance depth), the values of the average cosine and the scattering/absorption coefficient ratio could be read off. From these, together with the measured value of vertical attenuation coefficient for net downward irradiance, the values of a and b could be determined. The nomogram was constructed with data from Monte Carlo modelling of the light field in waters over a range of optical type. More recently,⁵ by curve-fitting to the same Monte Carlo-derived relationships I have replaced the graphical relationships in the nomogram by equations. For the absorption coefficient we have

$$a = \mu_0 K_E(z_m) \left(\frac{1 - R(z_m)}{1 + R(z_m)[103 G_E(\mu_0) - 1]} \right)^{1/2} \quad (9)$$

where μ_0 is the cosine of the refracted solar beam beneath the surface, K_E is the vertical attenuation coefficient for net downward irradiance, $R(z_m)$ is the irradiance reflectance at depth z_m , and G_E is a numerical coefficient whose value depends on μ_0 . The scattering/absorption ratio is given by

$$\frac{b}{a} = \frac{103 R(z_m)}{1 - R(z_m)} \quad (10)$$

and with this we obtain the scattering as well as the absorption coefficient.

The nomogram has been used to determine inherent optical properties by a number of workers on a variety of water bodies around the world, but generally on inland or estuarine waters with much stronger absorption in the blue and green than in typical marine waters, and therefore with negligible contribution of Raman emission to the light field. The question we need to address, therefore, is - how well does this approach work in the clear, relatively colourless waters of the ocean? An opportunity to put it to the test arose on a recent cruise with New Zealand colleagues⁶ in the South Pacific Ocean.

The region of ocean studied was East of the South Island of New Zealand in the Sub-tropical Convergence zone. We used a Licor spectroradiometer to measure upwelling and downwelling spectral irradiance at numerous stations, as well as carrying out a range of other measurements. The algorithm embodied in equations (9) and (10) was then applied to the spectral data for reflectance, and vertical attenuation coefficient, to calculate absorption coefficient values across the spectrum. What we typically observed, both here and at other stations, was that the calculated absorption coefficient was lower than K_d , as expected, and paralleled K_d from 350 nm up to about 590-600 nm. Above ~ 600 nm the calculated values of absorption coefficient fell away quite sharply, while the K_d values continued to increase. The reason for this was clearly revealed in the spectral curve for reflectance in the mid-region of the euphotic zone. Above 600 nm it began to rise very steeply, and in some cases increased to about 100% further into the red.

Reflectance of course is one of the key parameters in the algorithm, but refers to true reflectance, i.e. upward redirection of downwelling light by elastic scattering. It seems very likely that in the present case, superimposed upon true reflectance above 600 nm we were seeing Raman emission, to which was added chlorophyll fluorescence above 650 nm. The calculated a values above 600 nm thus bear no relation to reality. Nevertheless, setting aside any possible systematic errors embedded within the nature of the algorithm, these observations encourage some confidence in the validity of this and similar algorithms for estimating values of absorption (and scattering) coefficients from underwater irradiance data in the ocean at wavelengths from the near-UV to about 600 nm. In the orange-red region of the spectrum where such methods clearly do not work, most of the absorption is due to water anyway, the absorption coefficients of which are well known.

4. ACKNOWLEDGEMENTS

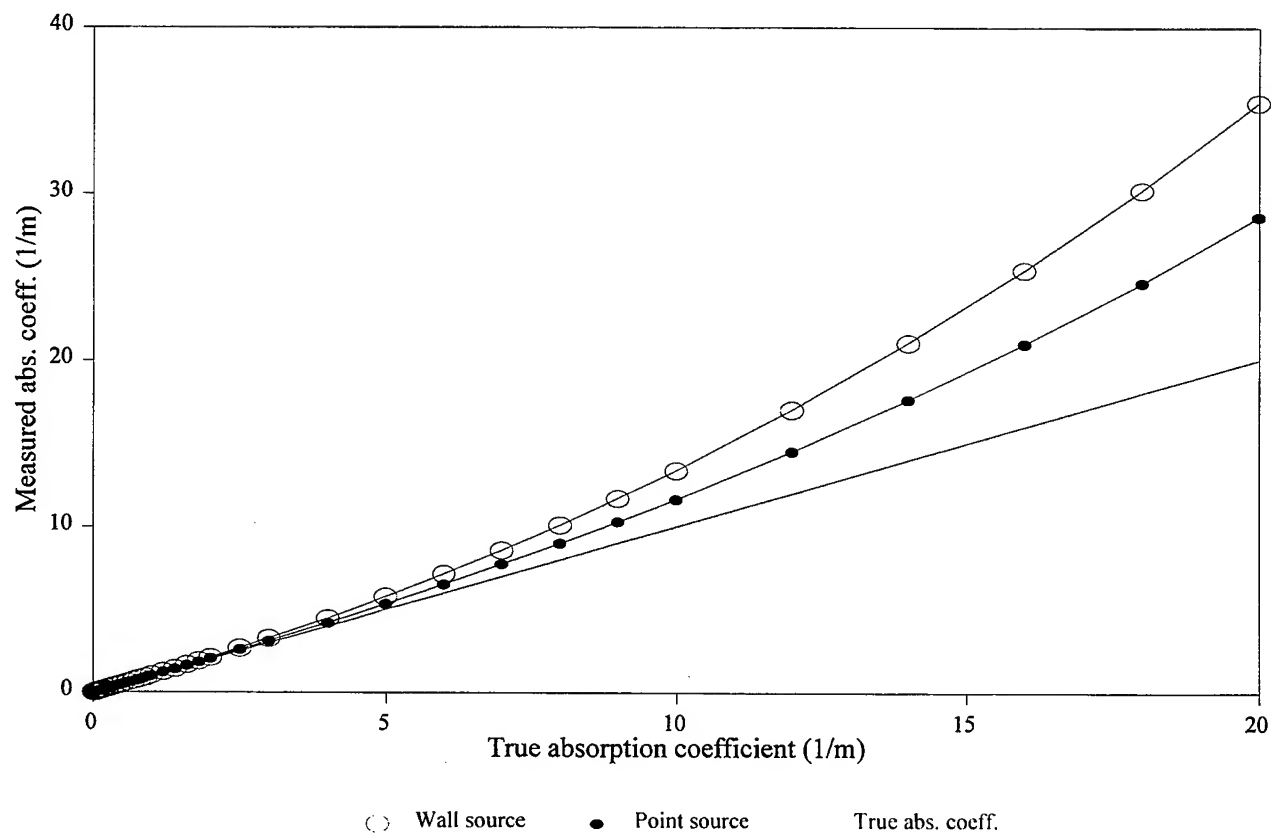
This research received support from the Ocean Optics Program of the U.S. Office of Naval Research under grant N00014-91-J-1366

5. REFERENCES

1. E.S. Fry, G.W. Kattawar and R.M. Pope, "Integrating cavity absorption meter," *Appl. Opt.* **31**, 2055-2065 (1992).
2. J.T.O. Kirk, "Modeling the performance of an integrating-cavity absorption meter: theory and calculations for a spherical cavity," *Appl. Opt.* **34**, 4397-4408 (1995).
3. J.T.O. Kirk, "Point source integrating cavity absorption meter: theoretical principles and numerical modeling," *Appl. Opt.* (submitted).
4. J.T.O. Kirk, "Estimation of the scattering coefficient of natural waters using underwater irradiance measurements," *Aust. J. Mar. Freshwater Res.* **32**, 533-539 (1981).
5. J.T.O. Kirk, "Estimation of the absorption and scattering coefficients of natural waters by use of underwater irradiance measurements," *Appl. Opt.* **33**, 3276-3278 (1994).
6. J.T.O. Kirk, R.J. Davies-Colley, D. Shooter, and A.-M. Schwarz, "Optical properties of ocean waters in the vicinity of the Chatham Rise, South Pacific Ocean," (in preparation).

ICAM point source and wall source

Apparent abs. coeff. versus true



Three-parameter optical studies in Scottish coastal waters

David McKee, Alex Cunningham and Ken Jones*

University of Strathclyde, Department of Physics and Applied Physics
107 Rottenrow, Glasgow, G4 0NG, Scotland, UK

*Dunstaffnage Marine Laboratory, P.O. Box 3, Oban, Argyll
PA34 4AD, Scotland, UK

ABSTRACT

A new submersible optical instrument has been constructed which allows chlorophyll fluorescence, attenuation and wide-angle scattering measurements to be made simultaneously at the same point in a body of water. The instrument uses a single xenon flashlamp as the light source, and incorporates its own power supply and microprocessor based data logging system. It has been cross-calibrated against commercial single-parameter instruments using a range of non-algal particles and phytoplankton cultures. The equipment has been deployed at sea in the Firth of Clyde and Loch Linnhe, where it has been used to study seasonal variability in optical water column structure. Results will be presented to illustrate how ambiguity in the interpretation of measurements of a single optical parameter can be alleviated by measuring several parameters simultaneously. Comparative studies of differences in winter and spring relationships between optical variables have also been carried out.

Keywords: fluorometry, nephelometry, transmissometry, integrated optics, depth profiling

1. INTRODUCTION

Over the last twenty years or so the deployment of in-situ optical instrumentation of various types has become a widely used method of generating information regarding water column structure and time-series variations¹. Unfortunately relationships between environmentally significant parameters such as phytoplankton biomass and mass of suspended particulate material, and easily measured optical variables such as fluorescence and attenuation are often ambiguous. Attenuation, for example, can be caused by absorption and scattering by algae, scattering by non-algal particulates, absorption by gelbstoff or any combination of the above. Much of this ambiguity can be eliminated by measuring several optical parameters simultaneously². ISOPOD (Integrated Submersible Optical Package for Ocean Deployment) has been developed to measure three bulk optical properties simultaneously using only a single light source³. This efficient use of light is designed to make the device particularly suitable for moored deployments and for possible incorporation on-board autonomous vehicles such as AUTOSUB.

2. INSTRUMENT DESIGN

The general layout of the instrument is illustrated in Figure 1, while more detailed views of the optics are shown in Figure 2.

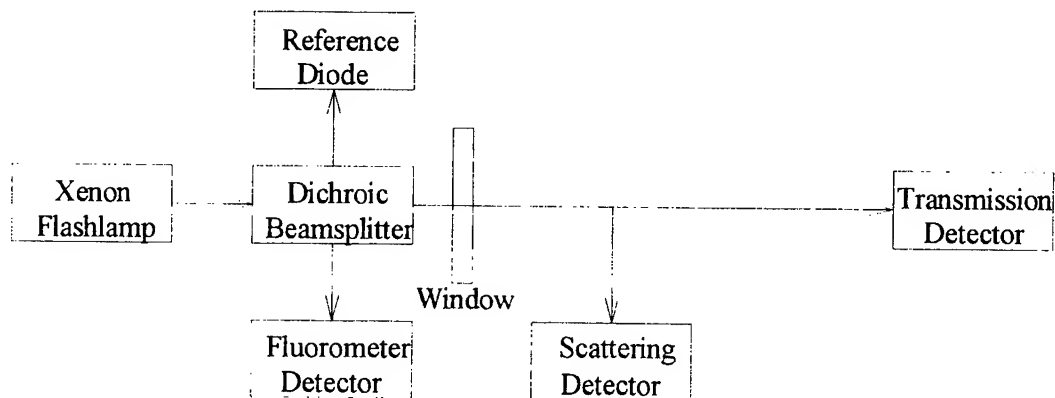


Figure 1. Schematic diagram of ISOPOD signal generation.

Light from a xenon flashlamp is collimated and filtered to remove all but the blue (400–490nm) portion of its emission spectrum. Approximately 10% of this blue light is reflected by the dichroic beamsplitter and used as reference beam to monitor the intensity of the lamp output. The remaining blue light is brought to a focus in the seawater just outside the optical window. Red fluorescence returning from the sample volume is collected by the focusing lens and reflected by the dichroic beamsplitter through a secondary red filter (645nm longpass) into the fluorescence detector. A generalised wide angle light scattering measurement through a range of angles centred on 90° is made by a simple nephelometer consisting of a photodiode with a 40mm² sensitive area located at the base of a 20mm diameter, 45mm deep collecting tube. The

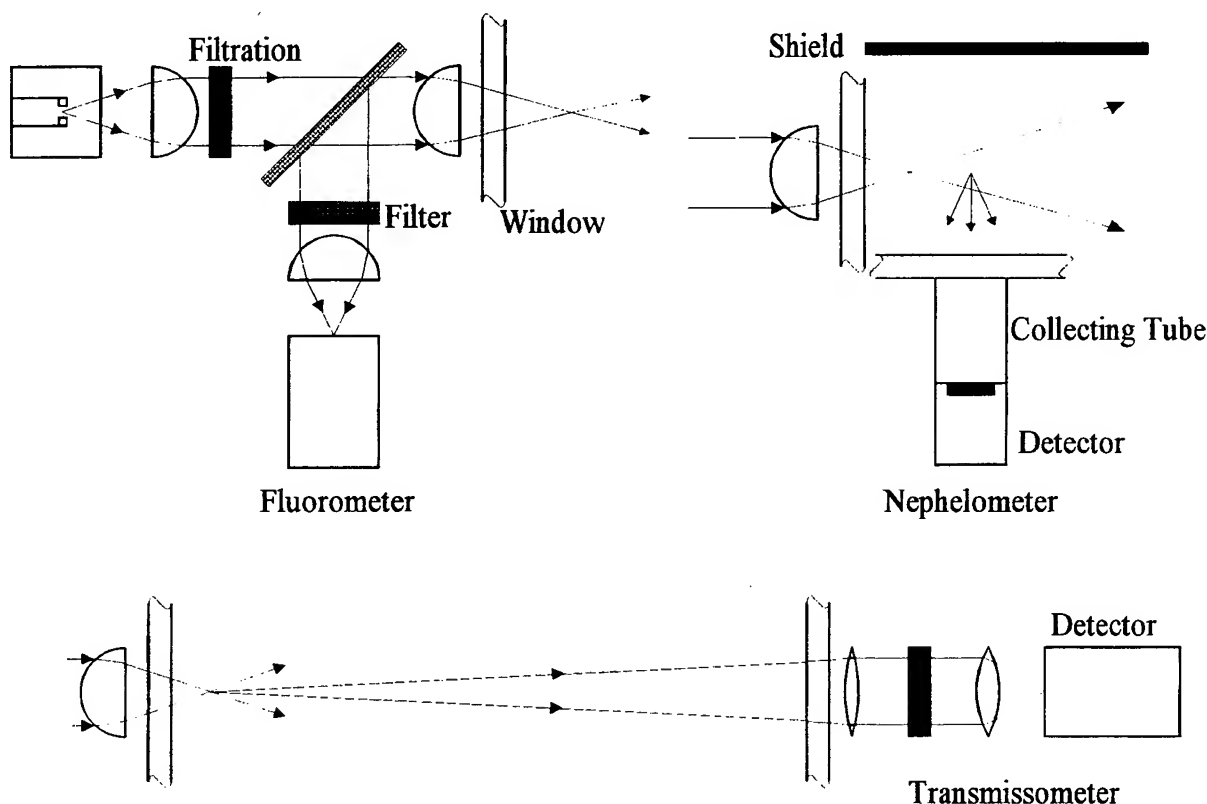


Figure 2. Optical layout of ISOPOD sensors.

nephelometer sensor is shielded from ambient light by a hood with a blackened inner surface. The highly diverging nature of the light leaving the fluorescence sensing zone means that the normal collimated beam configuration cannot be adopted for the transmissometer. Instead, the image of the arc lamp is reformed on a pinhole in the transmission sensing head. This is achieved by a combination of two lenses, which allows a wavelength selection filter (450±20nm) to be inserted in the zone of collimation between them. The transmissometer therefore measures the loss of light from rectilinear propagation either by absorption or scattering: it produces a signal which correlates linearly with that obtained from a collimated beam transmissometer, but which differs in numerical value by an instrument-specific factor determined by the beam geometry. Recovery of the attenuation coefficient, an inherent property of the water body, is therefore only possible by in-situ calibration against a collimated beam instrument operating at the same wavelength. However from the point of view of bio-optical profiling, an instrument-specific attenuation measurement is a useful parameter in its own right.

3. CALIBRATIONS

All calibrations were carried out in a tank containing 150L of seawater. As well as the multiparameter device, a SeaTech fluorometer and a SeaTech transmissometer were connected to a data logging system and placed in the same tank. Calibrations were carried out with four algal species representing various different taxonomic groups and three types of suspended particulate material. The results of these experiments are presented below.

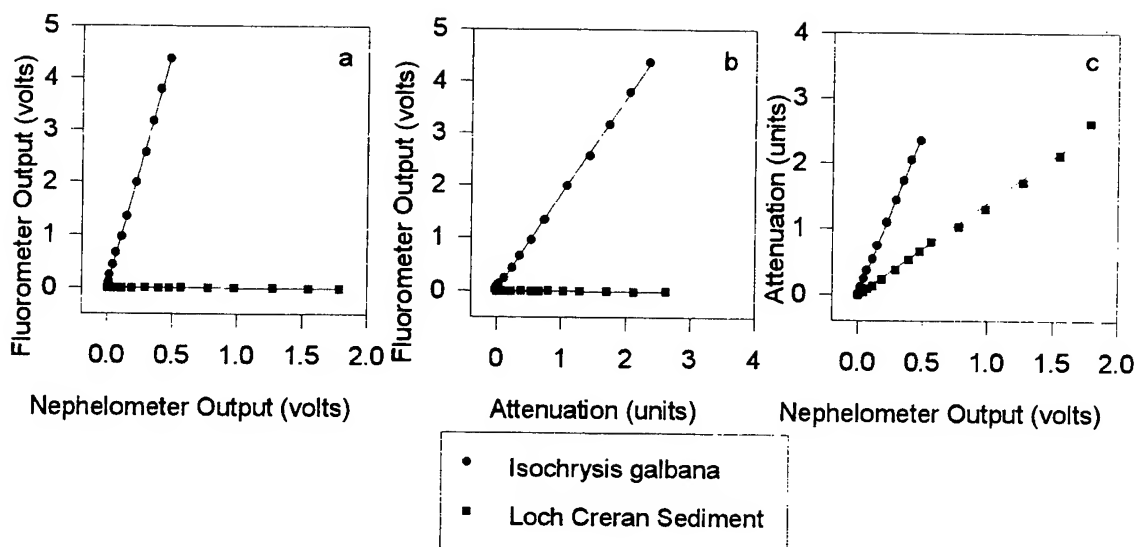


Figure 3. Calibration with one algal species and one non-algal particulate.

The effect of addition of different types of material on the three sensor outputs is demonstrated in Figure 3. The addition of phytoplankton generates signals in all three sensors, whereas non-algal particulates only influence the nephelometer and the transmissometer. Despite reaching relatively high scattering levels (Figure 3a) there is no breakthrough in the fluorometer when Loch Creran sediment is added, suggesting that the fluorometer filtration adequately blocks backscattered light. Figure 3c demonstrates the relatively high attenuation to scattering ratio of phytoplankton compared to non-algal particulates.

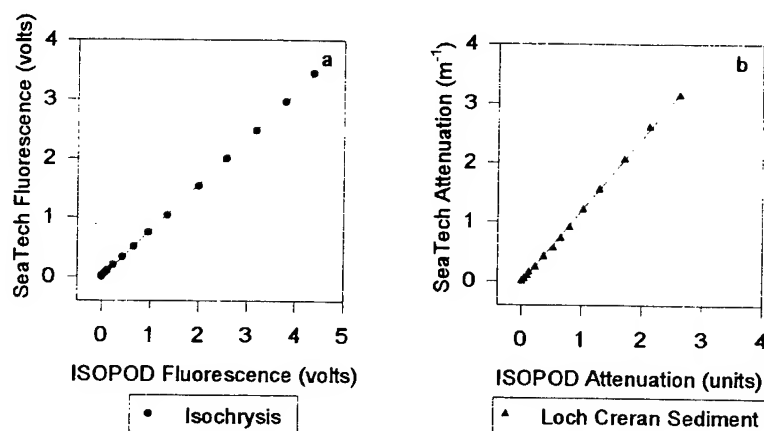


Figure 4. Cross-calibration of ISOPOD sensors with SeaTech instruments.

Cross-calibrations of the ISOPOD sensors with the SeaTech fluorometer and transmissometer exhibit excellent linearity and similar levels of sensitivity and dynamic range.

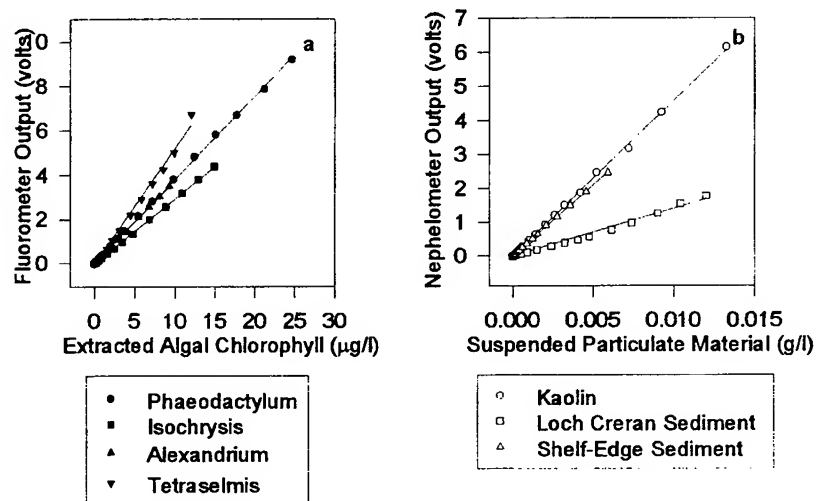
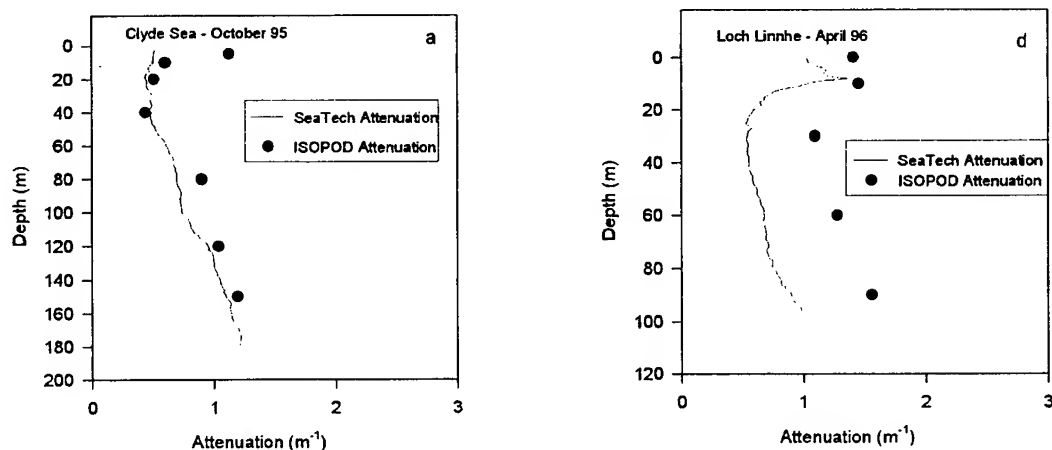


Figure 5. ISOPOD optical signals plotted against chemical parameters.

The yield of fluorescence per unit chlorophyll varies between species, as is demonstrated in Figure 5a. Similarly, wide-angle scattering per unit weight of suspended particulate material shows a wide range of values depending upon the material in question. These results indicate some of the difficulties in attempting to quantitatively interpret field measurements of optical parameters in terms of the concentrations of constituents in seawater⁴.

4. FIELD RESULTS

Results from two sets of deployments are presented below. The first cruise took place in October 1995 in the Clyde Sea, while the second occurred in April of 1996 in Loch Linnhe. Both of these water bodies are fjordic sea-lochs off the west coast of Scotland. At present ISOPOD does not have a pressure sensor on-board, which restricts the number of points sampled per depth profile. To compensate for this, profiles are presented with associated SeaTech fluorometer and transmissometer data obtained from CTD casts at the same stations.



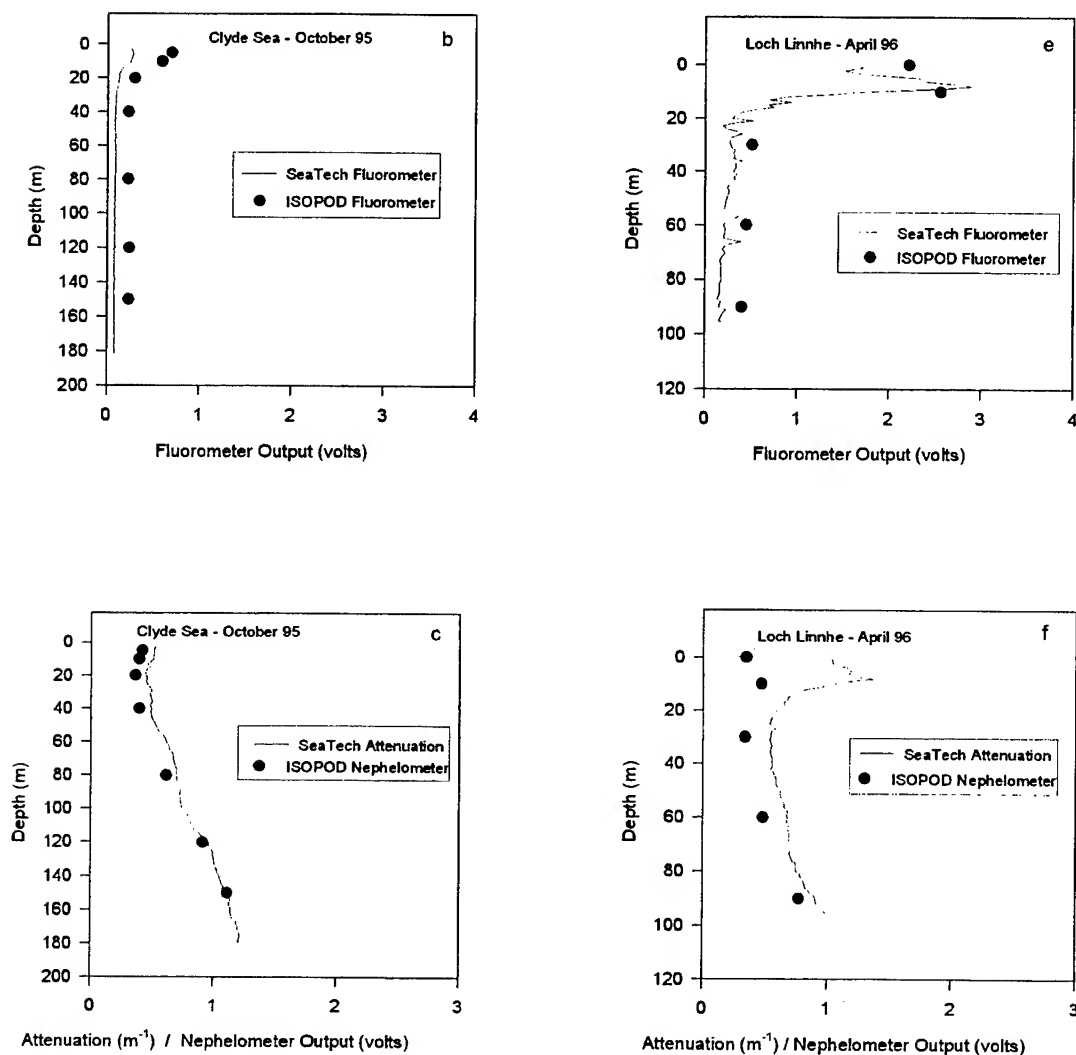


Figure 6. Depth profiles from the Clyde in autumn (a,b,c) and Loch Linnhe in spring (d,e,f).

The first point to note from this set of profiles is the deviation between the SeaTech and ISOPOD attenuation measurements in the surface layer (Figure 6a) due to the higher sensitivity of the blue ISOPOD sensor to absorption by gelbstoff. Secondly, Figure 6b shows that both fluorometers record similar signals at low ($1 \mu\text{g l}^{-1}$) chlorophyll concentrations. Lastly note the close correlation between SeaTech attenuation and ISOPOD nephelometer signals (Figure 6c), indicating that at this station the SeaTech instrument is measuring losses mainly due to scattering. A second set of profiles taken in the spring provides an interesting comparison with the autumn set of data. Here both the SeaTech and ISOPOD attenuation sensors give profiles of similar shape (Figure 6d), but the ISOPOD attenuation (measured in the blue) is generally higher than that of the SeaTech device (which uses a red beam). The source of this difference is found by examining the fluorometer profiles (Figure 6e), which not only show a close correlation between the SeaTech and ISOPOD fluorescence signals, but also exhibit generally higher levels of fluorescence throughout the water column than were observed in autumn. During spring bloom conditions there is a significant increase in the blue to red attenuation ratio caused by the presence of substantial quantities of phytoplankton. The sub-surface fluorescence maximum corresponds to a chlorophyll *a* concentration of $11 \mu\text{g l}^{-1}$. This chlorophyll maximum is also the source of the SeaTech attenuation peak.

Since algae have a much greater attenuation to scattering ratio than non-algal particulates (Figure 3c), it is no surprise that this SeaTech attenuation peak is significantly greater than the corresponding ISOPOD nephelometer signal (Figure 6f). At depths greater than 20m the attenuation is dominated by scattering from non-algal particulates and both the SeaTech transmissometer and the ISOPOD nephelometer signals are of similar magnitude once more. Note, however, that the raised background level of phytoplankton found at these depths in spring results in a slightly increased SeaTech attenuation to ISOPOD nephelometer signal ratio relative to that observed in autumn.

5. CONCLUSIONS

A novel submersible device has been designed and constructed which measures fluorescence, attenuation and wide-angle scattering using only a single light source. Single-component laboratory calibrations demonstrate excellent linearity both between optical parameters, and between optical and chemical measurements. ISOPOD sensors and corresponding single-parameter commercial instruments have been shown to have similar levels of sensitivity and dynamic range. The instrument has been successfully deployed in Scottish coastal waters, where it has been used for depth profiling purposes. By measuring three optical parameters simultaneously it is possible to investigate water column structure in terms of the phytoplankton, other suspended particulate, and gelbstoff constituents. Work on the acquisition and interpretation of 3-parameter optical time-series in coastal waters is currently in progress.

6. REFERENCES

1. T.Dickey, T.Granata, M.Hamilton, J.Wiggert, J.Marra, C.Langdon and D.Siegel, "Time series observations of bio-optical properties", *Ocean Optics X*, SPIE Vol. 1302, pp. 202-213, 1990.
2. A.Bricaud, C.Roesler and J.R.V. Zaneveld, "In situ methods for measuring the inherent optical properties of ocean waters", *Limnol. Oceanogr.* **40**(2), 393-410 (1995).
3. D.McKee, A.Cunningham and K.Jones, "An integrated submersible fluorometer / nephelometer / transmissometer: design and testing at sea", *Optics and Laser Tech.*, in press.
4. A.Cunningham, "Variability of in-vivo chlorophyll fluorescence and its implications for instrument development in bio-optical oceanography", *Sci. Mar.*, **60**(Supl. 1), 309-315, 1996.

Estimation of irradiance just below the air-water interface

Heidi M. Dierssen and Raymond C. Smith

Institute for Computational Earth System Science and Department of Geography
University of California Santa Barbara
Santa Barbara, California 93106

ABSTRACT

Measuring irradiance just beneath the air-water interface, $E_d(0^-)$, is challenging because of environmental variability of the incident radiation field, such as effects of waves, perturbation by the instrument platform (ship shadow) and instrument limitations (i.e., size, orientation). Accurate measurements of subsurface irradiance and radiance, however, are critical in the estimation of remote-sensing reflectance values and the development of ocean color algorithms. Subsurface irradiance is typically estimated by extrapolating measured near-surface underwater spectra back to just beneath the surface. Such an approach, assumes that the water's optical properties are consistent within the extrapolation interval. However, the diffuse attenuation coefficients can vary widely in the surface layer due to selective absorption of the short and long wavelengths, pigment concentrations, and ship shadow effects and are strongly dependent on the sampling depth used in the calculation. Another independent estimate of $E_d(0^-)$ is derived by propagating irradiance measured above the sea surface to just beneath the air-water interface. Here, we compare these two independent estimates of $E_d(0^-)$ to examine the accuracy of our methods and instrumentation. We use measurements of downwelling spectral irradiance collected over two seasons at Palmer Station, Antarctica using a Profiling Reflectance Radiometer (PRR) deployed in freefall mode from a small zodiac, so as to minimize ship shadow effects. While estimates of $E_d(0^-)$ made from above and below the sea surface data were highly correlated for overcast days, clear days showed much more scatter between the two estimates. This was attributed to wave effects and the lack of completely clear skies without haze or high clouds. Comparison of above and below water observations with theoretical computations suggest systematic error in immersion coefficients used to calibrate the instrument. Further, very shallow (1-2m) density structure introduces layers of water with differing optical properties and causes error in the estimation of $E_d(0^-)$.

Keywords: ocean optics, irradiance, air-water interface, immersion coefficient, transmittance, diffuse attenuation coefficient

1. INTRODUCTION

Estimates of irradiance and radiance just beneath the air-water interface ($E_d(0^-)$ and $L_u(0^-)$) are used to develop and validate algorithms for remotely sensed ocean color observations. When propagated through the sea surface, $L_u(0^-, \lambda)$ is equivalent to the water-leaving radiance $L_w(0^-, \lambda)$ which, neglecting atmospheric effects, is the signal measured from a remote platform (e.g., satellites, planes). Further, $E_d(0^-, \lambda)$ can be used to normalize estimates of $L_w(0^-, \lambda)$ to account for the variability in solar zenith angle and atmospheric conditions. Measuring these quantities at an infinitesimal depth below the sea surface, however, is difficult due to instrument limitations (i.e., size, orientation, shadowing), perturbation by the instrument platform, fluctuations in cloud cover, and waves. In lieu of direct measurement, one technique has been to extrapolate from a measured profile of irradiance/radiance versus depth to estimate a value just beneath the sea surface. This approach assumes that the diffuse attenuation coefficients of upwelled and downwelled light, K_d and K_L , do not vary over the depth interval used in the extrapolation. However, estimates of K_d and K_L can vary widely within the surface layer due to selective absorption of the short and long wavelengths, pigment concentrations, and ship shadow effects. Consequently, extrapolation results can be strongly dependent on the sampling depth used in the regression calculation.

Another method of obtaining $E_d(0^-)$ is to propagate estimates of irradiance made above the sea surface, $E_d(0^+)$, through the air-water interface. These estimates of $E_d(0^-)$, hereafter referred to as $+E_d(0^-)$, should be comparable to the estimates made from below the sea-surface, hereafter referred to as $-E_d(0^-)$. Additionally, such estimates can be used to correct data for shadowing due to the ship's presence¹. Ship shadow can be especially significant during overcast conditions¹ and when optical instruments are deployed less than 1 m off the stern of a ship². This paper attempts to reconcile values of $+E_d(0^-)$ and $-E_d(0^-)$ which have been estimated from data which is not perturbed by ship and shadowing problems.

The polar environment can provide additional difficulty in obtaining accurate near-surface radiation estimates. The presence of ice near the instrumentation can contaminate irradiance measurements and lead to a sampling bias of just the open water. Further, melting of ice from glaciers and pack ice can lead to a surface lens of fresh water that can cause relatively

large changes in the diffuse attenuation over just a few meters in water depth. At Palmer Station, extensive cloud cover serves to reduce the theoretical clear sky daily photosynthetically available radiation (PAR) on average by 40% in the spring time and 50% during the remainder of the year³. The extreme southern latitude of this site also means that the solar angle is always greater than 40 degrees and estimating the transmittance through the air-water interface more difficult.

2. METHODS

2.1 Data Collection

This paper utilizes two datasets collected in the 94/95 and 95/96 field seasons at Palmer Station (64°46S, 64°03W). Weather and ice permitting, data was collected weekly from a series of coastal stations during the season of maximum production (November to March). A Profiling Reflectance Radiometer (manufactured by Biospherical Inc. (BSI)) with wavebands centered at 412, 443, 490, 510, 555, and 665 (or 656) nm was deployed in freefall mode at a distance from the zodiac so as to minimize ship shadow effects⁴. Different PRR units with nearly identical instrument configuration were used in the 94/95 and 95/96 field seasons: the 94/95 PRR contained a channel centered at 656 nm and the 95/96 PRR contained a channel centered at 665 nm. Simultaneous measurements of downwelling irradiance were taken for these same wavebands from the deck of the zodiac. In order to completely avoid ship shadow perturbations of the light-field, SeaWiFS Ocean Optics Protocol⁵ provide estimates of the minimum distance to deploy optical instrumentation away from the ship, expressed in terms of attenuation lengths in the water column. Based on the mean upwelling and downwelling attenuation coefficients measured during the 94/95 field season, the recommended average distance for deployment of the PRR for measuring downwelling irradiance is approximately 4 m and for upwelling radiance is 9 m. The PRR was typically deployed 15-20m from the zodiac.

2.1 Estimating $E_d(0^-)$ from above sea surface ($+E_d(0^+)$)

Smith and Baker (1986)¹ show that to within a few percent, the downward irradiance just beneath the sea surface, $E_d(0^-)$, can be calculated from the irradiance measured just above the sea surface, $E_d(0^+)$ as follows:

$$E_d(0^-) \approx 1.03 t(\lambda, \theta) E_d(0^+) \quad (1)$$

The global transmittance, $t(\lambda, \theta)$ includes reflectance of both direct (ρ_{sun}) and diffuse (ρ_{sky}) irradiance, such that:

$$t(\lambda, \theta) = (1 - \rho_{sun}(\theta)) (1 - y(\lambda, \theta)) + (1 - \rho_{sky}(\theta)) y(\lambda, \theta) \quad (2)$$

In this formulation, the parameter y (or y -ratio) is the ratio of diffuse to total irradiance; ρ_{sun} is the Fresnel reflectance of direct radiation; and ρ_{sky} is assumed to be approximately 0.066. On a cloudy day, the y ratio approaches 1.0 and the above equation, assuming ρ_{sky} is 0.066^{1, 6}, reduces to:

$$E_d(0^-) = 0.96 E_d(0^+) \quad (3)$$

For sunny days, the Fresnel reflectance was used to estimate ρ_{sun} in Equation 2. The y -ratio was assumed to be 0 for sunny days and the possible consequences of this decision are discussed in the results section.

2.2 Estimating $E_d(0^-)$ from below sea surface ($-E_d(0^-)$)

Profiles of $E_d(z, \lambda)$ were measured over the upper few optical depths and estimates of $E_d(0^-)$ were obtained by propagating $E_d(z, \lambda)$ back to the surface using a least squares regression technique^{7, 8}. Mathematically:

$$K_d = \frac{-d \ln E_d}{dz} \quad (4)$$

$$\ln E_d(0^-) = \ln E_d(z) + K_d z \quad (5)$$

For clear waters, using the same depth interval to obtain estimates of $E_d(0^-)$ is appropriate⁸. Choosing an appropriate averaging depth for the red region of the spectrum, which attenuates rapidly in the water column, can be problematic. For coastal waters with considerable vertical structure in the water column, moreover, difficulties can arise in choosing an averaging depth that is representative of the near-surface waters. We found that extrapolating irradiance over a specified optical depth was more appropriate both conceptually and experimentally.

3. RESULTS

Figures 1a and 1b are comparisons of $+E_d(0^-)$ and $-E_d(0^-)$ for overcast days from the 94/95 and 95/96 field seasons, respectively. The vertical axis contains estimates of $+E_d(0^-)$ from the deck unit (Eq. 3) and the horizontal axis contains $-E_d(0^-)$ estimated by extrapolating the measured in-water irradiance to just beneath the surface (Eqs. 4 and 5). An extrapolation depth corresponding to 1 optical depth was used. While there is a good correlation between these two methods ($r^2=0.97-0.99$), the 94/95 data do not have a 1:1 data. The estimates of $E_d(0^-)$ from measured in-water irradiance are higher for all channels than those derived from $E_d(0^+)$ and frequently from the measured $E_d(0^+)$ itself. While this could be possible for a few stations with high near-surface reflectance, this is highly unlikely for all sampling stations. The 95/96 data, however, is very close to a 1:1 correspondence for all channels. As expected, the lowest correlation (0.95) occurs for the red channel (656/665 nm) due to the rapid attenuation of these wavelengths by water itself. As noted earlier, two different PRR instruments were used for these two field seasons.

Figures 2a and 2b are clear sky comparisons of $+E_d(0^-)$ and $-E_d(0^-)$ for the 94/95 and 95/96 seasons. Reflectance has been calculated using Fresnel reflectance and the assumption of no cloud influences (y -ratio=0). Fewer datapoints are in this analysis as clear skies occur infrequently. As shown, both seasons show greater scatter in the data, with r^2 values as low as 0.6. Moreover, the 94/95 field season shows an even more exaggerated trend of higher $-E_d(0^-)$ to $+E_d(0^-)$ ratio than was found for cloudy skies and the 95/96 data no longer exhibits a 1:1 correspondence. One reason for the large amount of scatter in this data is due to the assumption that the y -ratio is 0 for clear skies. Figure 3 presents the results of modeling the direct and diffuse portions of the clear sky irradiance for different sampling days and times at Palmer Station using SBDart⁹. Because of the large atmospheric pathlength that photons travel in polar regions, the diffuse portion of the skylight, especially for the blue wavelengths, can be as high as 50% of the total irradiance. Depending on the day and time (i.e., p_{sun} varying from 0.02 to 0.07) and the wavelength, this would cause a few percent difference in the transmittance. If this were the only factor, however, the data from the blue wavelengths would be much more scattered than from the red wavelengths, which is not observed. Another reason for the observed scatter is the high variability in incoming irradiance during the casts. While the solar disc may be visible on these days, and hence by "Antarctic standards" are judged to be clear, they are, in fact, often hazy or contain high clouds that cause large variability in incoming insolation. Such atmospheric variability, especially given the larger solar angles in this region, make estimating $-E_d(0^-)$ relatively difficult. Variations in incoming insolation on clear days also indicate that the y -ratio should be greater than under clear skies. Because global transmittance is relatively insensitive to changes in the y -ratio for solar angles less than 70° ¹, however, this would only change the value of $+E_d(0^-)$ by a few percent. Finally, wave slopes on the ocean surface can increase transmittance through the air-water interface, especially at high solar angles. At the solar angles corresponding to our sampling, this could cause a few percent difference in transmittance. There are too few days with completely clear skies and calm seas to statistically evaluate the impact of waves on the estimates of $+E_d(0^-)$. The cumulative impact of all of these factors contributed to the high scatter in the clear sky data.

The $-E_d(0^-)$ from above were calculated using an optical depth of 1. However, we also evaluated the impact of using various other optical depths to estimate $-E_d(0^-)$ in relation to estimates of $+E_d(0^-)$. Figure 4 presents the mean values of $-E_d(0^-)/+E_d(0^-)$ and one standard deviation from the mean for the 94/95 and 95/96 data. The wavebands centered at 412 nm and 656/665 nm are representative of the remaining bands. For 94/95, $-E_d(0^-)$ is about 8-10% higher than $+E_d(0^-)$ regardless of the optical depth used in the extrapolation. The 95/96 field data show less than 4% difference between $-E_d(0^-)$ and $+E_d(0^-)$ regardless of the optical depth used in the extrapolation. Further, the 94/95 errorbars are generally larger, especially with depth, than the 95/96 errorbars. This difference is primarily because several stations in 94/95 contained a surface lens of fresh water with different optical properties from the underlying water column. Figure 5a illustrates the physical and optical water column properties for one of these stations. As shown, the first few meters of water are fresher and less dense than the underlying water column, and the diffuse attenuation coefficient for PAR (K_{par}) drops off dramatically within this surface layer. Figure 5b shows a very strong bias in the depth interval chosen to estimate $-E_d(0^-)$ also for this station. The estimate of $-E_d(0^-)$ using 10 m was 50% of that estimated using 2 m. Water structure of this type is not as readily observed in data obtained from larger ships because of the mixing of surface waters caused by movement of the vessel.

4. DISCUSSION

Estimates of $E_d(0^-)$ making use of above-water and in-water profiles can be made independently of each other. Comparisons should be made of these independent estimates to provide a check of both the methodology and instrumentation used in sampling programs. We find that estimates of $E_d(0^-)$ from below and above the sea surface were highly correlated for both field seasons for the overcast days. For the 94/95 PRR, however, $-E_d(0^-)$ was consistently 8-10% higher than estimates of $+E_d(0^-)$. One reason for such a bias, could involve the methods used to estimate $E_d(0^-)$. As shown in Figure 3, no systematic bias was found by using different depth intervals in estimating $-E_d(0^-)$. Such a bias could occur if the transmittance through the air-water interface on overcast days was greater than the 0.96 used above. However, this

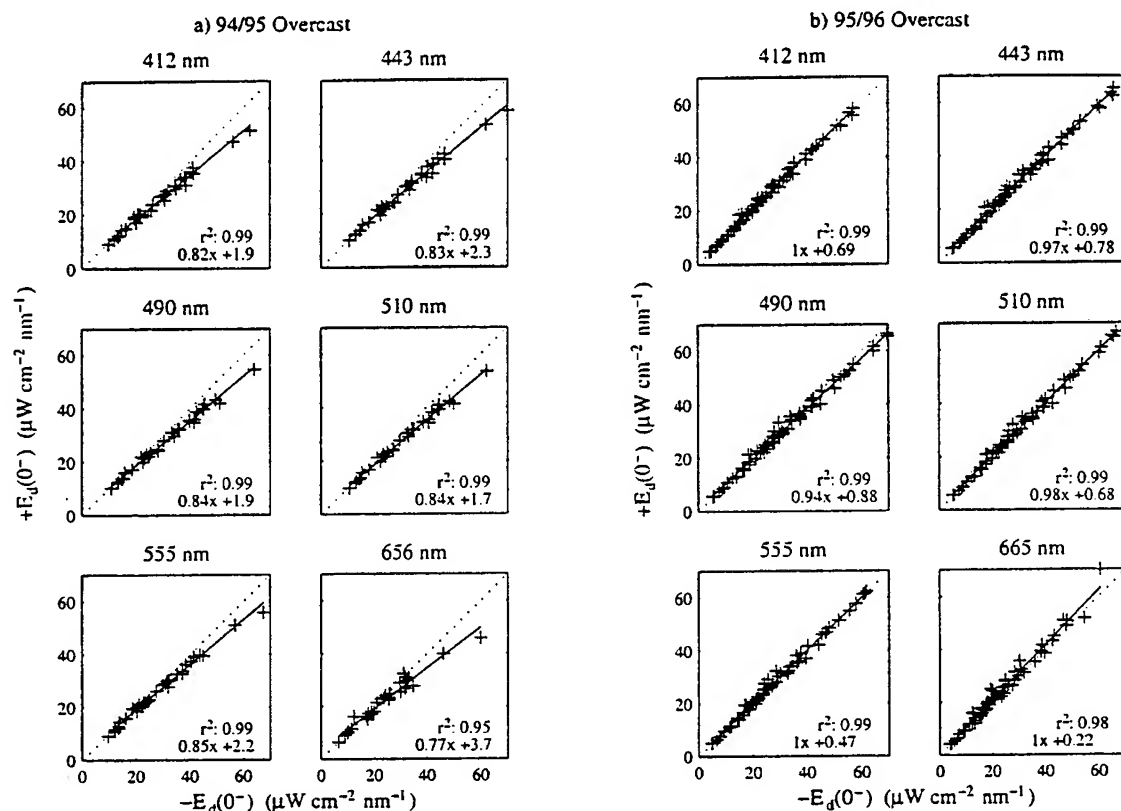


Fig. 1 Estimates of spectral irradiance just beneath the air-water interface made from above-water, $+E_d(0^-)$, and in-water, $-E_d(0^-)$, measurements. Data is from overcast days sampled around Palmer Station, Antarctica.

(a) 94/95 field season. (b) 95/96 season, using a different PRR.

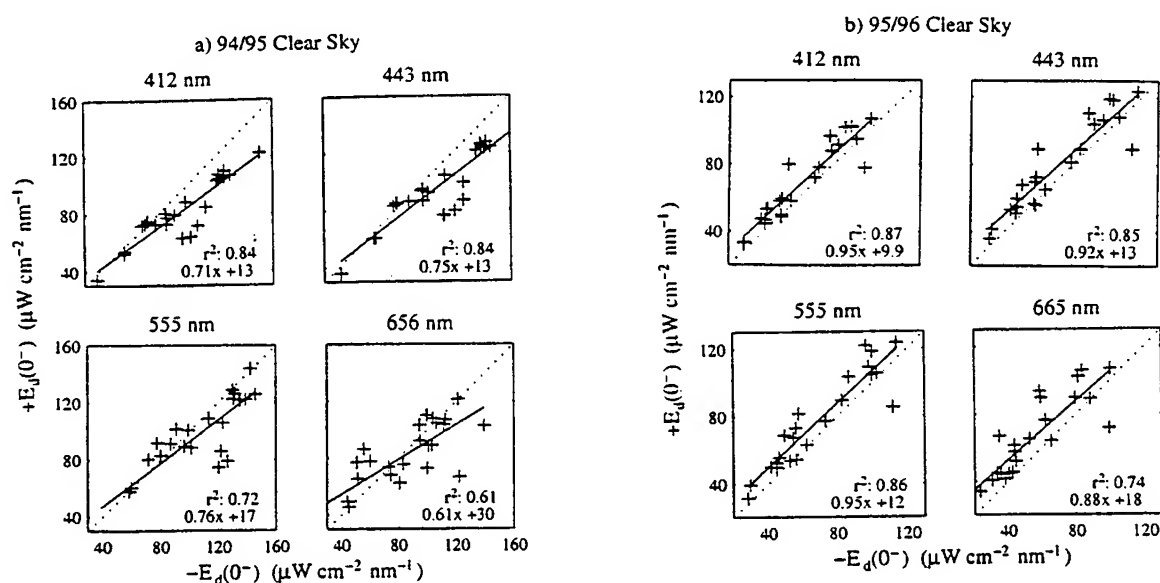


Fig. 2 Estimates of spectral irradiance just beneath the air-water interface made from above-water, $+E_d(0^-)$, and in-water, $-E_d(0^-)$, measurements. Data is from mostly clear days sampled around Palmer Station, Antarctica.

(a) 94/95 field season. (b) 95/96 season, using a different PRR.

assumption appeared to be correct for the 95/96 data and even if transmittance is assumed to be 1.00 (highly unlikely), $-E_d(0^-)$ is still found to be 4-6% higher than estimates of $+E_d(0^-)$ for the 94/95 data. In addition, one would not expect to find systematic biases due to improper tilting of the instrumentation. While these factors could account for some scatter in the data, they generally do not create a consistent bias.

The most probable explanation for the systematic differences between the 94/95 instruments involves problems with the instrument calibration, particularly the immersion coefficients. Both the deck unit and the PRR unit are calibrated in air, but an immersion coefficient is applied to the PRR to account for differences in reflectance between the collector in air and in water¹⁰. Some transmission is lost when the collector is submerged in water. The same immersion factors (supplied by BSI) were applied to the calibrations of both the 94/95 and 95/96 PRR instruments. However, individual collectors, even with the same materials and design specifications, can have widely varying immersion coefficients. Mueller (1995)¹¹ measured the total range between immersion coefficients of 12 collectors to be as high as 15% at some wavelengths. If immersion coefficients are decreased by 8-10% for the 94/95 PRR, the two estimates of $E_d(0^-)$ correspond to within a few percent. As estimates of $-E_d(0^-)$ and $+E_d(0^-)$ are on average within a few percent of each other for the 95/96 data, the immersion coefficients for the 95/96 PRR appear to be nearly correct. An analysis of the immersion coefficient for both instruments is in progress.

In conclusion, comparisons of the two independent estimates of $E_d(0^-)$, one from above and one from below the sea surface, can provide useful information about the water properties, air-sea interactions, and the instrumentation and methods used to obtain the data. The very high correlation between $-E_d(0^-)$ and $+E_d(0^-)$ for overcast days suggests that the methods used to make these estimates are consistent. However, the systematic offsets between these estimates of $E_d(0^-)$ for the 94/95 data suggest systematic error in the immersion coefficients used in the calibration of the PRR. For clear skies, the lower correlation between these two estimates of $E_d(0^-)$ is likely due to a combination of physical effects: the high fraction of diffuse sky in polar regions on clear days, the presence of fog, haze, and clouds during "clear" days that cause a high level of variability in incoming radiation during each cast; and the presence of waves which change the reflectance of the direct solar beam used to estimate $+E_d(0^-)$. As remotely sensed ocean color observations will only be possible on clear days, developing algorithms and interpreting remotely sensed data from this region will be challenging. In addition, large biases in estimates

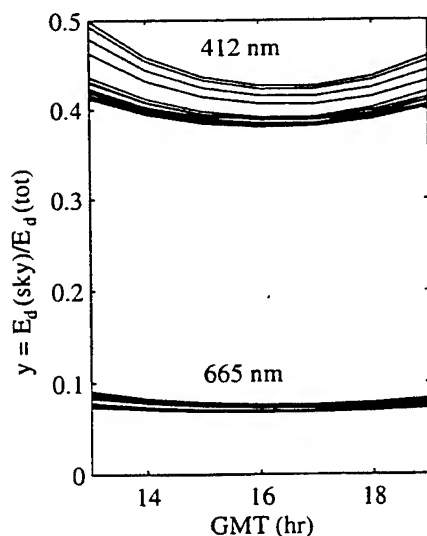


Fig. 3 Estimates of the y-ratio for clear skies at Palmer Station for different sampling days and times. Estimates made using SBDart with a 10 nm spectral band-width centered at both 412 nm and 665 nm.

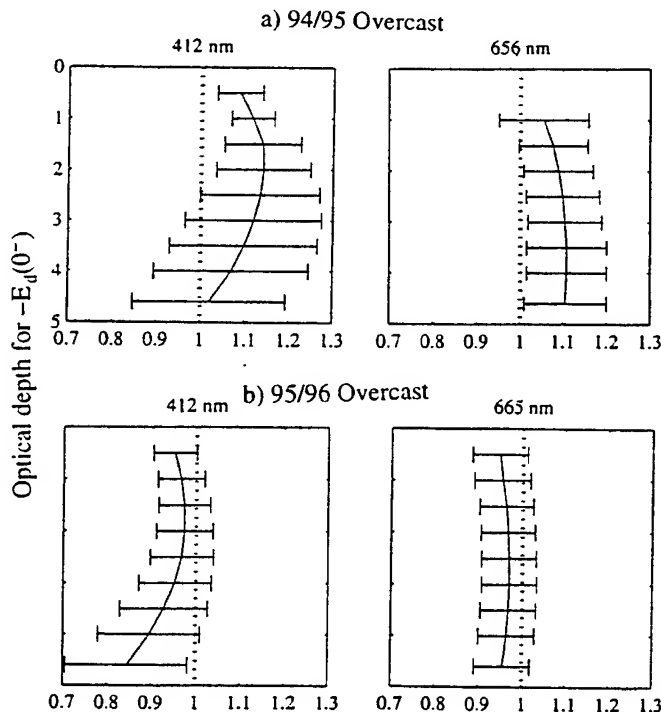


Fig. 4 Mean $+E_d(0^-)/-E_d(0^-)$ for all stations. Errorbars are one standard deviation from the mean. The vertical axis is the depth interval, in optical depth, used to estimate $-E_d(0^-)$. (a) 94/95 season. (b) 95/96 season.

of $-E_d(0^-)$ can arise when ice melt, unique to polar regions, produces a shallow (1-2 m) surface layer of fresh water with differing optical properties from the underlying water column. Such conditions are not typically encountered with sampling from larger ships that cause mixing of the surface layer of water and are better dealt with using optical depths, rather than discrete depths, to estimate $-E_d(0^-)$. Future refinement of this analysis would involve using a radiative transfer model to estimate $E_d(0^-)$ and comparing the modeled estimates to those calculated here.

5. ACKNOWLEDGMENTS

This research was funded by the Palmer LTER, National Science Foundation Office of Polar Programs (DPP90-11927, to RCS), the National Aeronautics and Space Administration (NAGW 290-3, to RCS), and a California Space Grant Fellowship (to HMD). The authors would like to acknowledge David Menzies for sharing his time and expertise.

6. REFERENCES

1. Smith, R.C. & Baker, K.S., "Analysis of ocean optical data II," *SPIE - Ocean Optics VIII* 637,95-107 (1986).
2. Weir, C.T., Siegle, D.A., Michaels, A.F. & Menzies, D.W., "In situ evaluation of a ship's shadow," *SPIE - Ocean Optics XII* 2258,815-821 (1994).
3. Dierssen, H.M., Smith, R.C. & Vernet, M. in *AGU/ASLO, Ocean Sciences Meeting 12-16 Feb* San Diego, 1996).
4. Waters, K.J., Smith, R.C. & Lewis, M.R., "Avoiding ship-induced light-field perturbation in the determination of oceanic optical properties," *Oceanography November*, 18-21 (1990).
5. Mueller, J.L. & Austin, R.W., *Volume 5, Ocean Optics Protocols for SeaWiFS Validation* NASA Technical Memorandum 104566: Sea WiFS Technical Report Series, Goddard Space Flight Center, 1992.
6. Preisendorfer, R.W., *Hydrologic Optics*, U.S. Dept. of Commerce, National Oceanic and Atmospheric Administration, Honolulu, Hawaii, 1976.
7. Smith, R.C. & Baker, K.S., "The analysis of ocean optical data," *SPIE - Ocean Optics VII* 489,119-126 (1984).
8. Siegel, D.A., O'Brien, M.C., Sorensen, J., Konnoff, D.A. & Fields, E., *BBOP data processing and sampling procedures* Institute for Computational Earth System Science, Santa Barbara, CA, 1995.
9. Ricchiazzi, P., Gautier, C. & Lubin, D., "Cloud scattering optical depth and local surface albedo in the Antarctic: Simultaneous retrieval using ground-based radiometry," *Journal of Geophysical Research* 100(D10), 21091-21104 (1995).
10. Smith, R.C., "An underwater spectral irradiance collector," *Journal of Marine Research* 27(3), 341-351 (1969).
11. Mueller, J.L. in *Volume 27, Case Studies for SeaWiFS Calibration and Validation, Part 3.* (eds. Hooker, S.B., Firestone, E.R. & Acker, J.G.) (NASA Technical Memorandum 104566: Sea WiFS Technical Report Series, 1995).

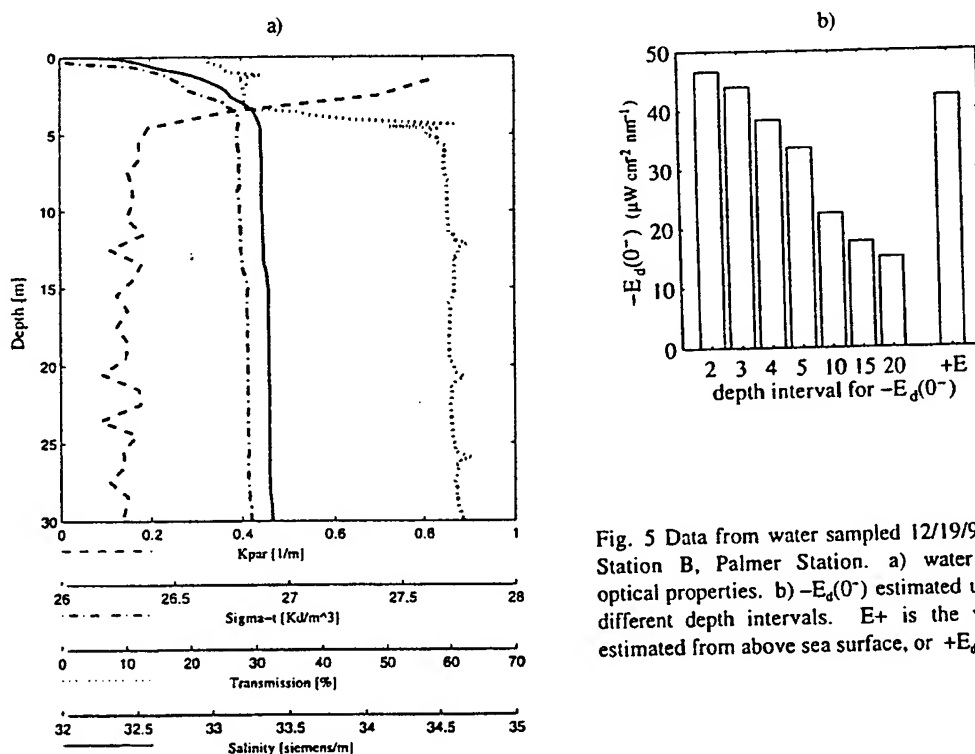


Fig. 5 Data from water sampled 12/19/94 at Station B, Palmer Station. a) water and optical properties. b) $-E_d(0^-)$ estimated using different depth intervals. E+ is the value estimated from above sea surface, or $+E_d(0^-)$.

Laboratory development of a LIDAR for measurement of sound velocity in the ocean using Brillouin scattering

Yves Emery and Edward S. Fry

Physics department, Texas A&M University, College Station, TX, USA, 77843-4242

Tel. (409) 845-1910, Fax (409) 845-2590, Email fry@phys.tamu.edu.

ABSTRACT

There have been several studies of the potential accuracy of LIDAR measurements of sound velocity in the ocean by measuring the spectral shift of the backscattered Brillouin lines. However, due to technical limitations, such systems have not previously been experimentally demonstrated. Measurement of the Brillouin shift as a function of depth in the ocean requires a stabilized, narrow linewidth, pulsed laser, and a high-resolution spectroscopic technique. We have used a scanning Fabry-Perot to obtain the first frequency resolved measurements of Brillouin scattering in water using a pulsed laser; these results will be presented here. But for the practical application of measuring Brillouin shifts as a function of depth in the ocean a non-scanning spectroscopic technique is required to measure the small frequency shifts; the edge technique meets this requirement. Using it in conjunction with the edges of absorption lines in the molecular spectra of I_2 and/or Br_2 , avoids the limitations associated with use of a Fabry-Perot etalon; specifically, its small solid angle of acceptance and its vulnerability in noisy environments. This new approach will be briefly described.

Keywords: Brillouin LIDAR remote sensing, sound velocity, ocean, edge technique, molecular absorption lines.

1. INTRODUCTION

Several studies have discussed the importance of remote measurements of sound velocity in the upper-ocean mixed layer.¹⁻⁵ Real-time range-resolved monitoring provides a crucial input to the understanding of the physical behavior of the ocean. A Brillouin LIDAR is a promising tool for such remote measurements of the sound velocity as a function of depth. Brillouin scattering produces two inelastically scattered Lorentzians centered symmetrically with respect to the laser line; they have a FWHM of about 0.5 GHz. The so-called Brillouin shift ν_B , that is to say the frequency shift between the laser line and each of the Brillouin lines, is typically between 7 and 8 GHz, and is proportional to the sound velocity. In pure water, the scattering spectrum is almost solely composed this doublet. An elastically scattered central line (also called the unshifted line, or improperly the Rayleigh line)⁶ appears when the water is contaminated by hydrosols.

The limits in the accuracy of sound velocity and temperature profiles in the ocean from LIDAR Brillouin shift measurements have been discussed in detail by Fry, *et al.*⁷ Briefly, for a given incident laser wavelength λ the Brillouin shift ν_B is proportional to the refractive index of water n and the sound velocity v_s . The refractive index itself is function of the salinity S and temperature T . In addition to these two variables, the sound velocity also has a weak dependence on pressure, but for present purposes, this dependence will be neglected; the generalization to include pressure dependence is straightforward. The Brillouin shift is then expressed as:

$$\nu_B(S, T) = \frac{2n(S, T)}{\lambda} v_s(S, T) \sin(\theta/2), \quad (1)$$

where θ is the scattering angle ($\sin(\theta/2)=1$ for 180° backscattering). Clearly, there are five parameters (ν_B , v_s , n , S , and T), but there are only three relations between them and only one measurement (ν_B). The three relations are Eq. 1 and empirical equations for $n(S, T)$ and $v_s(S, T)$. Thus one additional piece of information is required. For present purposes, it is provided by the means and standard deviations of the extensive set of salinity measurements (from 1900 to 1990) compiled by the National Oceanic and Atmospheric Administration.⁸ With these salinity estimates based on historical data, i.e. without actual measurements of salinity, the limits on the sound velocity accuracy can be better than 0.3 m/s.

Our primary interest is in developing a LIDAR for range-resolved measurements of sound velocity in the ocean via the measurement of the Brillouin shift. Although the idea of a Brillouin LIDAR is not new,¹⁻³ such systems have not yet been experimentally demonstrated due to technical limitations. Measurements of the Brillouin shift as a function of depth in the ocean requires both a stabilized narrow linewidth pulsed laser, and a high-resolution non-scanning spectroscopic technique.

Sound velocity measurements with depth resolution δz of 1 meter require a Brillouin frequency shift measurement for each successive 10 ns ($=2n\delta z/c$) interval of the LIDAR return. In addition, a precision of 1 m/s for the sound velocity requires the measurement of Brillouin shifts with an accuracy better than about 4 MHz.⁷ This small value compared to the linewidth of the Brillouin line (500 MHz) does not allow the use of a conventional spectrometer. In this paper we discuss our recent progress in development of a Brillouin LIDAR.

The first laboratory measurements of frequency resolved Brillouin lines using a pulsed laser and a scanning Fabry-Perot technique for frequency discrimination are presented in Sect. 2. Previous pulsed laser measurements² were not completely resolved, but our results clearly demonstrate this resolution with pulsed lasers. However, the scanning Fabry-Perot measurement technique used to obtain this data is not accurate and fast enough to be used directly for LIDAR measurements of the Brillouin shift. Nevertheless, these results and the measurement apparatus will provide a valuable reference for the initial data obtained with our new non-scanning spectroscopic technique.

This new technique is a version of the edge technique, and is a powerful non-scanning spectroscopic technique for the measurement of small frequency shifts.⁹ It has numerous applications, and has been successfully used in a Doppler LIDAR for atmospheric wind velocity measurements.¹⁰ From the standpoint of an oceanic Brillouin LIDAR, the main limitations of previous implementations of this method are the small acceptance angle of the Fabry-Perot etalons used for the frequency discrimination, and the difficulties associated with operating these interferometers in noisy vibrational and acoustic environments. We are implementing a version of the edge technique in which the frequency discriminants are the edges of absorption lines in the molecular spectra of I_2 and/or Br_2 . Explicitly, the frequency of the laser transmitter is chosen so that the edges of two different molecular absorption lines (with opposite slopes) are located at the centers of the Brillouin lines. Because of the steep slope of the absorption edges, small changes in the Brillouin shift produce large changes in transmission. The details of the experimental set up are described in Sect. 3.

2. FREQUENCY RESOLVED MEASUREMENTS OF BRILLOUIN LINES

The theoretical model for Brillouin scattering in a liquid was developed by Mountain⁴ and Fabelinskii.¹¹ Early attempts to examine the use of Brillouin scattering for the determination of sound velocity in pure water were by Chiao, *et al.*¹² and by Benedek, *et al.*¹³ Since then, considerable effort with CW lasers has been reported,⁵ but no definitive results have previously been performed using a pulsed laser. To our knowledge, the only such published results show a FWHM of the Brillouin lines of about 3 GHz; this indicates that the stability and linewidth of the laser transmitter were not sufficient.²

Our experimental set up for the Brillouin spectrum measurements is shown in Fig. 1. A frequency doubled, injection seeded, Q-switched, pulsed Nd:YAG laser provides 75 mJ at 532 nm, with a repetition rate of 10Hz. Using an injection locking technique developed in our laboratory,¹⁴ it operates at a single frequency and has stable Fourier transform limited pulses of 10 ns, i.e. a frequency bandwidth of about 50 MHz. A horn shaped water cell is used to avoid backreflections. An additional light baffle consisting of two pierced parallel plates was added in the bottom of the water cell to further suppress parasitic backreflections. Noise due to the reflection from the surface of the water is avoided by using another thin baffle plate. The backscattered light is collected at an angle of 175° relative to the laser beam direction. The acceptance angle of the optical system is $\approx 1^\circ$ and is determined by the focal length and the size of lens L1; this acceptance angle does not significantly increase the FWHM of the Brillouin lines. The most critical point in order to obtain good frequency discrimination is to provide a very well collimated beam to the input of the Fabry-Perot (FP) etalon. A spatial filter consisting of 2 lenses (L1 and L2), a pinhole (P1) of 10 μ m diameter, and one iris (I) is used for this purpose. To avoid background radiation, the output of the etalon is focused through pinhole P2 onto a photomultiplier, PM, and the overall receiver system is enclosed in a black box.

The Fabry-Perot has a resolution of 0.25 GHz ($R=96\%$) and a Free Spectral Range (FSR) of 18 GHz. The etalon piezoelectric transducers are driven by a Burleigh RC-42 ramp generator. The measurements are performed with a scanning ramp duration of 2 minutes per FSR. The detector is a Hamamatsu R446 photomultiplier tube operating in the analog mode. The signal is integrated and averaged over 10 laser shots by a gated integrator and boxcar averager. It is digitized and stored using a Labview program on a MacII computer.

Fig. 2 shows a measured frequency spectrum, superposed on the theoretical one for a water temperature of 29°C (corresponding to a Brillouin shift of 7.55 GHz). Only one free spectral range of the Fabry-Perot is presented in the figure. The experimental points are raw data from a single scan; no further processing has been performed. There is very good

agreement with theory. The strong central peak is due to particulate contamination of the water, which is apparently due mostly to oxidation of the metal light baffle submerged in the horn shaped water cell.

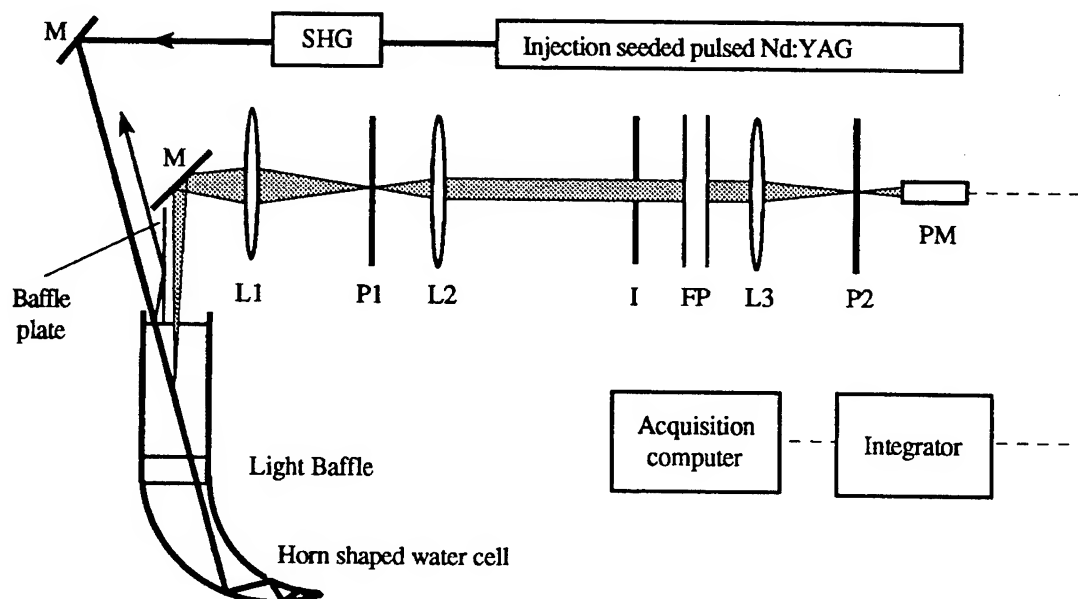


Fig. 1. Brillouin spectrum measurement set up. L1, L2, and L3 are biconvex lenses of focal length 50 cm, 20 cm and 8 cm, P1 is a 10 μ m diameter pinhole, I is an iris used to select the lower interference order, P2 is a 1 mm diameter pinhole, SHG is second harmonic generator, M are mirrors, and PM is the photomultiplier.

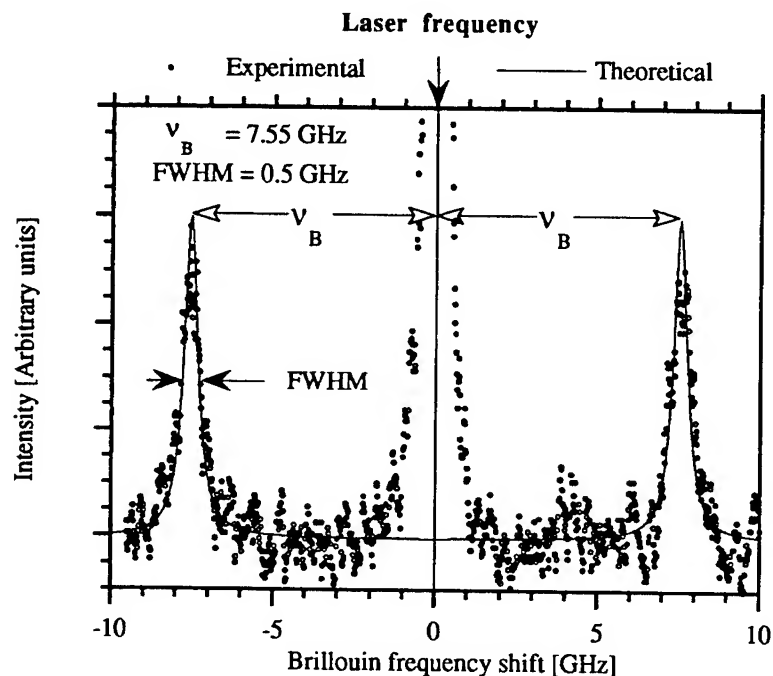


Fig. 2. Experimental (dots) and theoretical Brillouin spectrum of water at 29°C using the second harmonic of a pulsed injection seeded Nd:YAG laser (532 nm).

3. BRILLOUIN SHIFT MEASUREMENT

As discussed in the introduction, a Brillouin LIDAR based on a version of the edge technique is under development. Using the edge technique, atmospheric measurements at 1064 nm have shown wind velocity accuracies of 0.25 m/s, corresponding to frequency changes smaller than 470 kHz.¹⁰ This is the most sensitive method yet demonstrated for small frequency shift LIDAR measurements.¹⁵ Versions of the edge technique had already been considered by Hirschberg, *et al.*³ and by Hickman, *et al.*¹ for oceanic Brillouin shifts measurements using a laser wavelength of 532 nm. In the latter study the statistical uncertainty δv_B in the measurement of the Brillouin shift is calculated assuming a single laser shot with an energy of 500 mJ and a depth resolution of 1.1 meter. For $\gamma < 0.04 \text{ m}^{-1}$, shot noise limited uncertainties in δv_B of less than 1 MHz can be expected for depths down to 75 meters, and of less than 4 MHz down to 100 meters. These correspond to sound velocity measurement accuracies that can be better than 0.3 m/s and 1 m/s,⁷ respectively.

We are developing a version of the edge technique that makes use of the edges of absorption lines in the molecular spectra of I_2 and/or Br_2 , as opposed to the Fabry-Perot interferometers used in other applications^{1-3, 9} of the edge technique. The schematic of such a LIDAR receiver is shown in Fig. 3. The second harmonic of an injection-seeded pulsed Nd:YAG laser is used as the transmitter. The laser signal backscattered by the ocean water is collected by a telescope, and is first directed through an atomic cell (used as a blocking-filter) where the central line of the backscattered frequency spectrum is absorbed. The backscattered signal transmitted by the blocking filter is then split into two equal parts: one part is detected to produce a normalization signal (S2). The other part passes through the edge filter and is detected to produce the signal (S1). The Nd:YAG laser frequency stabilization is performed by picking off a small part of the cw seed laser beam, frequency doubling it in an external ring build-up cavity, and locking the seed laser to the absorption line of the blocking-filter. The return signals S1 and S2 are sampled every 2-3 ns to produce a range-resolved measurement (of course, the temporal resolution is limited by the 10 nanosecond laser pulse).

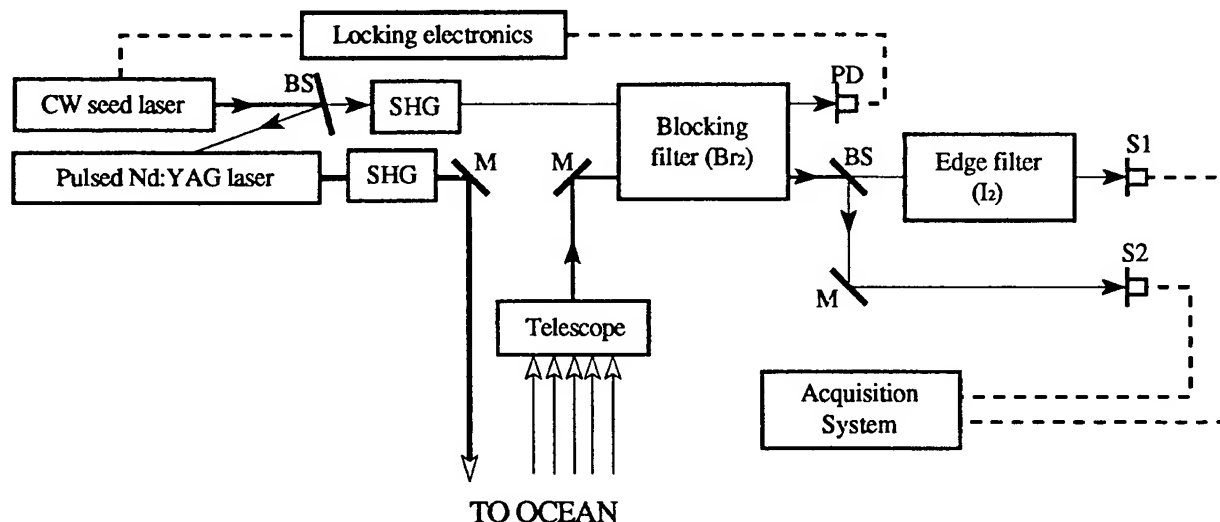


Fig. 3. Brillouin LIDAR receiver schematic. The Brillouin shift is determined from the ratio $S1/S2$. BS are beam splitters, M are mirrors, SHG is second harmonic generators, M are mirrors, and PD are photo detectors. Solid lines correspond to light paths, and dotted lines to electrical connections.

As an example of an edge filter, consider a $^{127}\text{I}_2$ absorption cell. For a laser wavelength of 532.573806 nm, it provides two appropriately positioned absorption edges (see Fig. 4). Because of the steep average slope of the absorption edges, small changes in the Brillouin shift produce large changes in the transmission of the edge filter. The temperature of the gas and/or the vapor pressure in the cells can be changed for a fine adjustment of the absorption line slopes and frequencies.

An important advantage of this edge filter version is that a change in the incident laser frequency or any Doppler shifts due to movements will increase the edge filter signal corresponding to one Brillouin line and decrease the signal corresponding to the other; thus such systematic effects are canceled to first order. The ratio $S1/S2$ provides a

normalization which makes the frequency discrimination independent of the intensity of the light backscattered by the ocean water, i.e. independent of the attenuation due to water absorption or hydrosols scattering.

An ideal blocking filter should exhibit total absorption for the central line of the backscattered spectrum, and good transmission for the Brillouin peaks. The FWHM of the central line is mainly the linewidth of the laser transmitter, and is ≈ 50 MHz. Fig. 5 shows the absorption spectrum of Br_2 superposed on theoretical Brillouin lines with a shift of 7.5 GHz, and for the same incident laser wavelength as for the I_2 data in Fig. 4. This absorption line provides a satisfactory, although not perfect blocking filter. Of course, the convolution of the Brillouin lines and of the transmission spectrum of Br_2 has to be considered as the input to the edge filter.

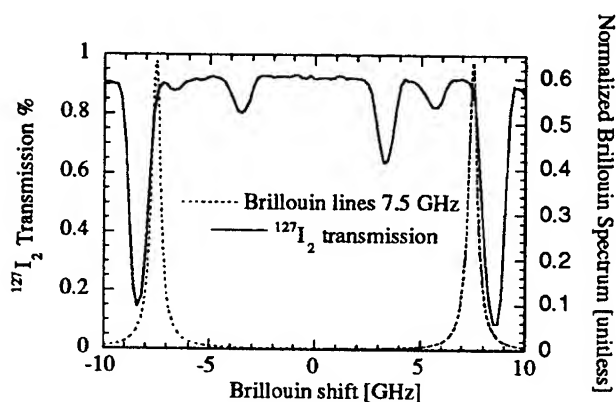


Fig. 4. Edge filter: theoretical Brillouin lines for a frequency shift of 7.5 GHz superposed on the absorption spectrum of $^{127}\text{I}_2$. Small changes of the Brillouin shift make large changes in the transmitted signal. The incident wavelength for the Brillouin spectrum is 532.573806 nm.

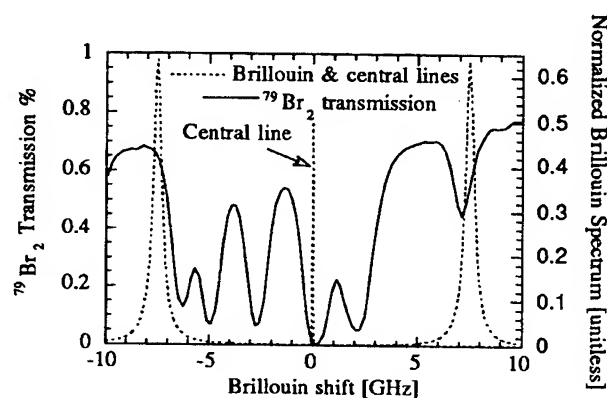


Fig. 5. Blocking filter : The ideal blocking filter should have a good transmission for the Brillouin lines and a total absorption for the central line of the backscattered spectrum. The absorption lines of $^{79}\text{Br}_2$ provide a satisfactory blocking filter for an incident laser wavelength of 532.573806 nm.

4. PROSPECTS AND CONCLUSION

We have shown that an injection seeded pulsed laser can be used to obtain completely resolved measurements of Brillouin lines. This verifies that Brillouin shift data can be used to measure sound velocity as a function of depth in the ocean. A version of the edge technique for the measurement of the Brillouin shift has been outlined.

In comparison to other LIDAR receiver designs (using, for example, a Fabry-Perot) the I_2 and/or Br_2 absorption cells provide a simpler and more robust approach that requires no critical alignments. The optical efficiency of a receiver using the absorption lines discussed here, would be as good as that using a Fabry-Perot based receiver. A systematic search for other combinations of transmitter wavelength and absorption lines is underway. This includes direct experimental examination and comparison of the absorption lines of $^{127}\text{I}_2$, $^{129}\text{I}_2$, $^{79}\text{Br}_2$, and $^{81}\text{Br}_2$.

5. ACKNOWLEDGMENTS

The authors would like to thank George Kattawar, Thomas Walther, Jeffery Katz, and Jason Pan for many useful discussions. The work is supported by the Robert A. Welch Foundation Grant No. A-1218, the Texas Advanced Technology Program Grant 010366-16, the Office of Naval Research Grant No N00014-96-1-0410, and the Swiss National Foundation of Sciences.

6. REFERENCES

1. G. D. Hickman, J. M. Harding, M. Carnes, A. Pressman, G. W. Kattawar, and E. S. Fry, "Aircraft Laser Sensing of Sound Velocity in Water: Brillouin Scattering", *Remote Sens. Environ.*, **36**, 165-178 (1991).
2. J. L. Guagliardo and H. L. Dufilho, "Range Resolved Brillouin Scattering Using a Pulsed Laser", *Rev. Sci. Instrum.*, **51**, 79-81 (1980).
3. J. G. Hirschberg, J. D. Byrne, A. W. Wouters, and G. C. Boynton, "Speed of Sound and Temperature in the Ocean by Brillouin Scattering", *Appl. Opt.*, **23**, 15, 2624-2628 (1984).
4. D. A. Leonard and B. Caputo, "Remote sensing of the ocean mixed-layer depth", *Optical Engineering*, **22**, 3, 288-91 (1983).
5. D. J. Collins, J. A. Bell, R. Zaoni, I. S. McDermid, J. B. Breckinridge, and C. A. Sepulveda, "Recent Progress in the Measurement of Temperature and Salinity by Optical Scattering", M. A. Blizards, Ocean Optics VII, vol. 489, pp. 247-263, (Proc. SPIE, 1984).
6. A. T. Young, "Rayleigh Scattering", *Physics Today*, **35**, 1, 42-48 (1982).
7. E. S. Fry, Y. Emery, X. Quan, and J. Katz, "On Brillouin LIDAR Measurements of Oceanic Temperature and Sound velocity", *Submitted to Applied Optics*, (1996).
8. National Oceanographic Data Center (NODC), User Services Branch, NOAA/NESDIS E/OC21, Washington, D. C., (1993),
9. C. L. Korb, B. M. Gentry, and C. Y. Weng, "Edge Technique; Theory and Application to the Lidar Measurement of Atmospheric Wind", *Applied Optics*, **31**, 21, 4202-4213 (1992).
10. C. L. Korb, B. M. Gentry, and C. Y. Weng, "Spaceborne Lidar Wind Measurements with the Edge Technique", Satellite Remote Sensing, Rome, (1994)
11. I. L. Fabelinskii, *Molecular Scattering of Light*. (Plenum Press, New York, 1968).
12. R. Y. Chiao and B. P. Stoicheff, "Brillouin scattering in liquids excited by the He-Ne maser", *Journal of the Optical Society of America*, **54**, 1286-87 (1964).
13. G. B. Bendek, J. B. Lastovka, K. Fritsch, and T. Greytak, "Brillouin scattering in liquids and solids using low-power lasers", *Journal of the Optical Society of America*, **54**, 1284-85 (1964).
14. E. S. Fry, Q. Hu, and X. Li, "Single-Frequency Operation of an Injection-Seeded Nd:YAG Laser in High Noise and Vibration Environments", *Appl. Opt.*, **30**, 9, 1015-1017 (1990).
15. L. Bertotti, Y. Emery, C. Flesia, R. Miles, G. Galletti, and E. Zanzotera, "Incoherent Doppler wind Lidar Technologies", ESA/ESTEC 12789/94/NL/SB, (1995).

Bio-optical drifters - Scales of variability of chlorophyll and fluorescence

Mark R. Abbott and Ricardo M. Letelier

College of Oceanic and Atmospheric Sciences
Oregon State University
Corvallis, OR 97331-5503

ABSTRACT

Both the California Current System and the Antarctic Polar Front are characterized by mesoscale variability and meandering jets. These meanders lead to regions of strong vertical motion, on the order of several tens of meters per day. To study physical and biological scales of variability in these two systems, near-surface drifters were released in these two environments; twenty-six in the California Current and five in the Polar Front. Each drifter was equipped with a spectroradiometer to measure upwelled radiance at the SeaWiFS wavelengths as well as at 683 nm. A temperature system was also included. Data were relayed to shore via satellite. These data were converted into biological quantities, including chlorophyll and an apparent quantum yield of fluorescence. Decorrelation time scales were calculated and compared with corresponding statistics of the physical environment. Time scales for all variables increased as the drifters moved from nearshore to offshore. The scales associated with temperature and chlorophyll were similar nearshore, but increased more rapidly offshore for temperature. This suggests that the processes regulating the distribution of temperature and chlorophyll are similar in the nearshore region and significantly differ offshore.

Keywords: California Current, upwelling, time scales, phytoplankton, drifters, chlorophyll, fluorescence

1. INTRODUCTION

Over the past decade, developments in smaller and less expensive instrumentation have allowed oceanographers to collect data sets at time and space scales that are difficult to observe from conventional platforms.¹ For example, time series from a fixed point mooring are a combination of both temporal changes and spatial changes as new water masses are swept past the mooring. Free-drifting buoys that can be drogued to follow upper ocean circulation help separate temporal variations in a water mass from those that occur spatially. Bio-optical drifters deployed in the California Current were initially used to examine physical and biological processes within a specific physical feature.^{2,3} The advent of lower cost sensors as well as the use of satellite data relay now allows the deployment of large numbers of drifters to conduct systematic studies of the statistical properties of the upper ocean bio-optical field. In this paper, we restrict our discussion to results of drifter studies in the California Current although some bio-optical drifters were also deployed in the Southern Ocean. Our analyses followed two paths. First, we calculated large-scale statistics of the biological and physical fields. Second, we analyzed the impact of specific physical features on upper ocean biology.

2. METHODS

The standard World Ocean Circulation Experiment (WOCE) surface drifters have been modified by METOCEAN Data Systems to include a Satlantic spectroradiometer (OCR-100) in the bottom of the surface float. This sensor measures upwelled radiance at 412, 443, 490, 510, 555, 670, and 683 nm. The surface float also includes pressure and temperature sensors. A Satlantic narrow band irradiance sensor (ED-100), centered at 490 nm, is mounted in the top of the surface float. A 40 m long drogue is attached below the surface float such that the drifter responds primarily to currents at 15 m depth. Data are averaged over 60 minutes and then transmitted. If a NOAA polar-orbiting satellite is in range, then the message is relayed to shore. Otherwise the message is updated the next hour and the new message transmitted. On average, approximately eight messages were received per day in the California Current and fifteen in the Southern Ocean. The data set also includes "housekeeping" information from the drifter such as battery voltage, number of samples, average time that the surface float was submerged, etc.

Twenty-six drifters were released over a three-year period in the California Current. Three drifters failed soon after deployment (presumably due to high seas); the remainder had an average lifetime of six months with the maximum being nearly ten months. Figure 1 shows all of the drifter tracks collected between 1993 and 1995. Most of the drifters were deployed along a line at 39.5°N between 125° and 128°W. As expected, the general trend is for the drifters to move south and west with the prevailing summertime currents (when most of the drifters were deployed). To date, only five drifters have

been released in the Southern Ocean: two in Drake Passage and three in the Polar Front at 170°W. These last three drifters are equipped with a Global Positioning System (GPS) transmitter to provide more accurate location information.

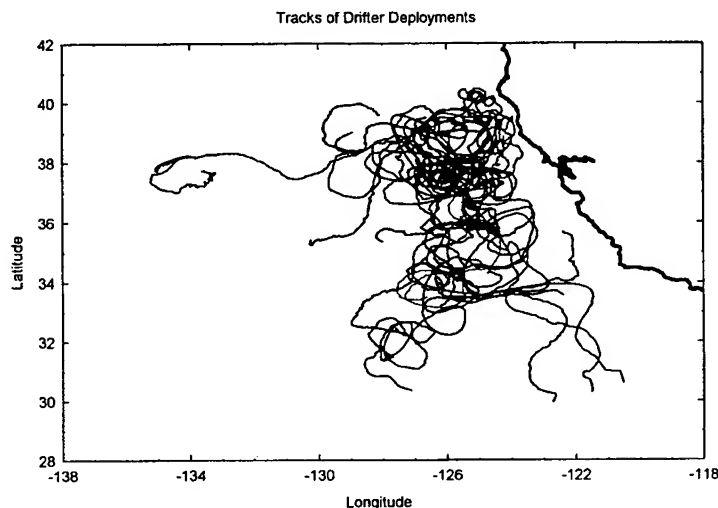


Figure 1. Composite view of drifter deployments in the California Current System in 1993-1994.

Once the data are received, several screening tests are applied to eliminate low quality data points. Occasionally bits are dropped from the Service Argos transmissions, resulting in unrealistic values in many of the drifter variables such as battery voltage, downwelling irradiance, etc. Argos data files also include the position of the drifter. Sometimes these positions are either missing or are obviously in error (sudden, large jumps in position, etc.) The Argos files also include the number of messages received during a given transmission from the drifter. If this number is small, then the probability of erroneous or corrupted data increases. We also screen for bio-fouling (through examination of the level and variability of the 683/555 radiance ratio) and test faulty bio-optical measurements through examination of band ratios. However, the largest amounts of data removed through screening occur when we eliminate those records that were obtained when the absolute solar angle (elevation) is less than 20°. This constrains the study data set to observations collected with a few hours of local solar noon.

After screening, chlorophyll is calculated using the following equation:

$$chl = 0.56353 * \left(\frac{L_u 443}{L_u 555} \right)^{-0.595} \quad (1)$$

where L_u is upwelling radiance at a specific wavelength. This form is derived from earlier bio-optical models,⁴ and the coefficients are based on comparisons with chlorophyll samples collected near one of the drifters in 1994.

Once the data files were cleaned and the various derived quantities were calculated, we then estimated decorrelation scales from the drifter data set. We calculated a "daily average" for the variables of interest: SST, chlorophyll, fluorescence/chlorophyll, and drifter speed. Some of the data records were too short or too gappy for further statistical analyses. However, the majority of the drifters were nearly complete with only occasional missing data points. These gaps were filled using linear interpolation between adjacent days. A linear trend was removed from each time series, and the autocorrelation function was calculated. The decorrelation scale was estimated as the point at which this function first became insignificantly different from zero. Figure 2 shows a typical pair of autocorrelation functions for SST and chlorophyll from one drifter in the California Current. Cross-correlation functions were calculated in a similar manner between detrended time series of SST and chlorophyll.

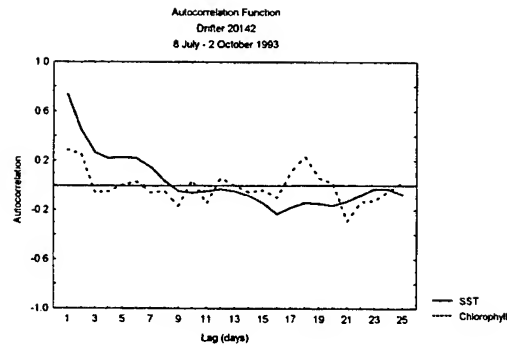


Figure 2. Autocorrelation functions of SST and chlorophyll from drifter 20142. The decorrelation scale is approximately 6.5 days for SST and 2.5 days for chlorophyll.

3. RESULTS AND DISCUSSION

The average length of the bio-optical time series was 73 days before fouling became evident, although some drifters lasted well over 90 days before there was any evidence in the bio-optical signals that fouling had occurred. For these long time series, it was possible to divide the record into two parts, each one covering a different season. As part of our analysis, we also calculated the average distance from the coast for each drifter.

The average decorrelation time scale was longest for SST at 6.3 days. The decorrelation scale for chlorophyll was 3.7 days, 2.3 days for fluorescence/chlorophyll, and 3.3 days for drifter speed. These results are within the range for the same region off northern California from a study using time series of satellite imagery of chlorophyll and SST.⁵ In that study, it was found that the time scales were between one and seven days, depending on length scale.

Figure 3 shows the decorrelation scale for SST, chlorophyll, fluorescence/chlorophyll, and drifter speed as a function of average offshore distance of the drifter. We have divided the distance offshore into three categories: <200 km (nearshore), >200 km but less than 400 km (transition), and >400 km (offshore). There is a general trend for SST and chlorophyll scales to increase as one moves offshore, but this is by no means consistent. However, the more interesting result is that the time scales associated with SST and chlorophyll are relatively similar in the nearshore and diverge as one moves offshore. This suggests that the processes governing SST and chlorophyll are similar in the nearshore region whereas they are controlled by different processes offshore. This is in contrast to earlier results⁵ where no significant differences could be detected between the SST and chlorophyll fields. Coastal upwelling should control both SST and chlorophyll in the nearshore, whereas different physical processes or perhaps changes in the biological community lead to different statistical properties of the fields offshore. Another feature of Fig. 3 is that fluorescence/chlorophyll shows more variability nearshore (shorter time scales) whereas it is nearly equal to the chlorophyll time scale offshore. Rapid changes in fluorescence relative to chlorophyll concentration are indicative of variability in the distribution of energy in the photochemical apparatus of the phytoplankton. This observation suggests that in the nearshore region, the time scales of physiological adaptation are significantly shorter than the time scales of changes in phytoplankton biomass.

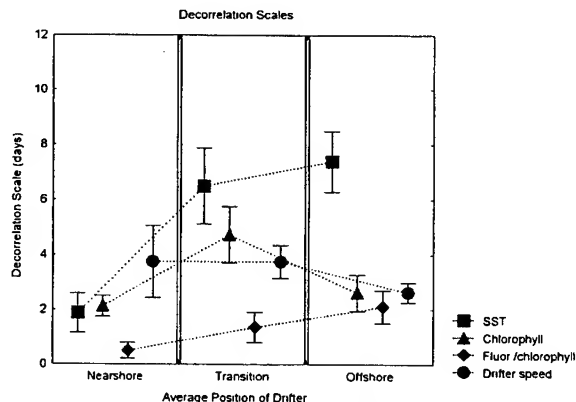


Figure 3. Average decorrelation scales for SST, chlorophyll, fluorescence per unit chlorophyll, and drifter speed as a function of distance offshore. The boxes represent ± 1 standard deviation and the whiskers represent ± 1 standard error.

Figure 4 shows the track and cross-correlation function for drifter 22622. The drifter made nearly two complete circuits around a large anticyclonic eddy. Note that changes in SST led changes in chlorophyll by one day. Figure 5 shows the same information for drifter 20139 which made two circuits around a much smaller, cyclonic eddy. Although it is not possible to draw robust conclusions from results from two eddies, it is worth noting that the negative correlation (at near zero lag) is much larger in the anticyclonic eddy than in the cyclonic eddy, whereas the cyclonic eddy has large, negative lobes at ± 12 days. The time scale of the positive correlations (twelve days for 22622 and six days for 20139) corresponds to the travel time around the eddy (cold water, high chlorophyll on the south side of the eddy and warm water, low chlorophyll on the north). Earlier evidence of a lag between SST and chlorophyll was found in only one region off northern California.⁵ It was inferred that this region was near an upwelling center, and that the lag was the result of the delay in biological processes responding to high nutrients in the surface water. In comparison, many of the drifter deployments revealed that changes in SST led changes in chlorophyll by roughly 1-2 days. However, most of the drifters were released in active upwelling regions, and we suspect that the satellite imagery⁵ was simply not adequate to evaluate these small time scale patterns.

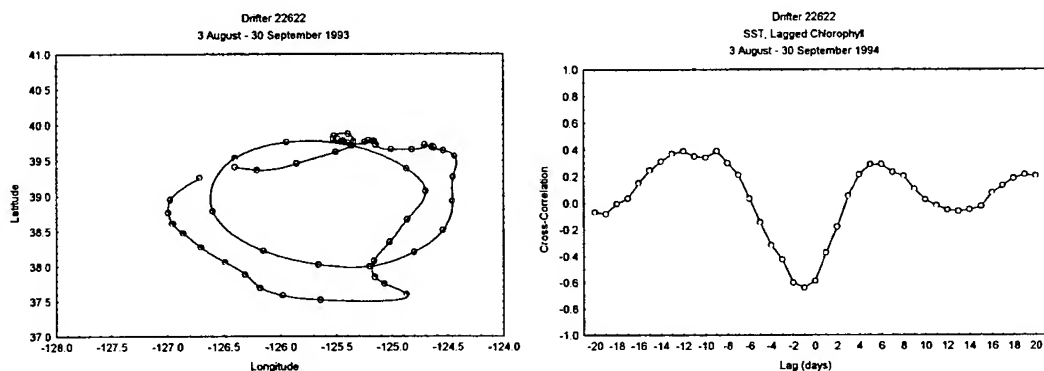


Figure 4. (Left) Track of drifter 22622. (Right) Cross-correlation function of SST and chlorophyll. Negative lags indicate that SST leads chlorophyll.

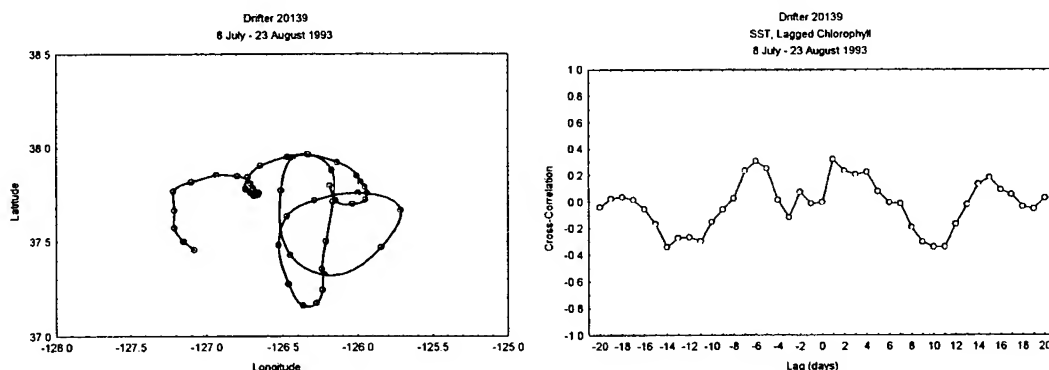


Figure 5. (Left) Track of drifter 20139. (Right) Cross-correlation function for SST and chlorophyll.

Although the optical sensors are calibrated by Satlantic, there are few opportunities to compare readings between sensors in the field unless two or more drifters are found simultaneously sampling the same water mass. Drifter 20140 (not shown) also traversed the same eddy as 22622 (Fig. 4) several days later. Drifters 20140 and 22622 were deployed at $39^{\circ}33'N$, $124^{\circ}55'W$ and $39^{\circ}25'$, $126^{\circ}27'W$ respectively. Although these drifters were released approximately 130 km apart, they followed the same circulation path over a period of 50 days with an average lag time of 18 hours and average distance of 62 km between drifters (Fig. 6, top).

When comparing the temperature records between sensors mounted in these two drifters we observe that both instrument packages appear to be sampling different water masses over the first 30 days (Fig. 6, middle). However, following day 245, the temperature records display strong similarities in the magnitude and trend of the readings, suggesting that both drifters are located in the same water mass. It is also during this period that the distance between both drifters is reduced to an average of 18 km (Fig. 6, top). Furthermore, estimates of algal pigment concentration (chlorophyll a + phaeopigments) also display strong similarities during this period. This observation suggests that, at least in this particular case, the principal physical and biological processes controlling phytoplankton biomass over temporal scales of days appear to be acting over large spatial scales (1-100 km).

Similar trends over the same time period are observed when normalizing the upwelling irradiance at 683 nm (L_u683) and 670 nm (L_u670) to the downwelling radiance measured at 490 nm (E_d490). However, because the absolute value of these measurements differs by a factor of 1.7 between drifters, it is not possible to convert our records into absolute fluorescence quantum efficiency of chlorophyll *a*. Nevertheless, it is still possible to compare the variance in algal pigment concentration to the variance in relative chlorophyll natural fluorescence. Multiple regression analyses, using model II geometric linear regressions, suggests that the variance in chlorophyll fluorescence is correlated with changes in chlorophyll concentration. However, the correlation coefficient of the regression low ($r=0.45$, $p < 0.05$) suggesting that the variance in chlorophyll concentration and E_d490 contribute only partially to the variability in absolute chlorophyll natural fluorescence in these water masses.

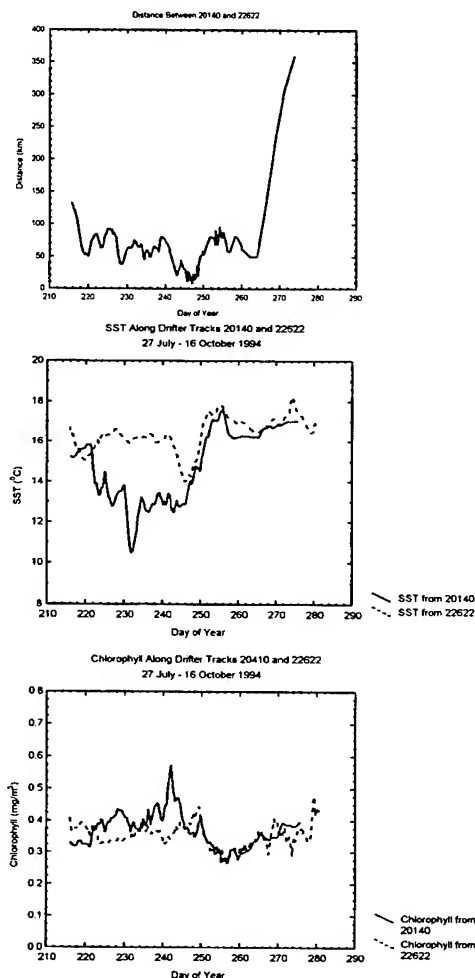


Figure 6. (Top) Distance between drifters 20140 and 22622. (Middle) SST from drifters 20140 and 22622. (Bottom) Same except for chlorophyll.

4. CONCLUSIONS

Time scales of SST, chlorophyll, and fluorescence/chlorophyll increase as one moves offshore. This is to be expected, given the higher levels of mesoscale variability near the coast.⁵ Complex interactions of local wind forcing and ocean circulation should result in intense heterogeneity of vertical motions in the upper ocean, thus affecting SST and nutrient availability, which in turn will affect phytoplankton abundance. This leads to a separation in the statistics of the two data sets, with SST having in general longer time scales than chlorophyll. Although coastal upwelling and presumably rapidly growing phytoplankton dominate the nearshore environment,⁶ both biological and physical processes in the offshore environment may be quite different. Historical evidence suggests that the offshore phytoplankton community is dominated by small, slow-

growing forms⁶ which may lead to a decoupling between the physical processes governing SST and those governing chlorophyll. Given the time scales of phytoplankton growth, we expect to see a lag between changes in the physical environment and the biological response. As most of the drifters covered the summer season, we cannot determine if there is any seasonal modulation in these patterns. Of note is that the decorrelation scales are relatively small, implying that these mesoscale processes will continue to be difficult to resolve with conventional ship sampling.

These interpretations can be further complicated by temporal and spatial changes in the bio-optical models themselves.³ That is, changes in fluorescence efficiency, particulate backscattering, chlorophyll package effect, etc., will be manifested as changes in chlorophyll abundance and other derived properties. We expect that such changes will act to decrease the decorrelation scales, so that the estimates provided here are likely to be an upper bound on these scales.

5. ACKNOWLEDGMENTS

We thank the many people who assisted with deployment of the drifters in the California Current and the Polar Front. We especially thank Dick Limeburner, Bob Beardsley, and Ken Brink of Woods Hole Oceanographic Institution, Mike Kosro, Jane Huyer, Jack Barth, and Tim Cowles of Oregon State University, Jeff Paduan of the Naval Postgraduate School, and Bob Anderson of Lamont-Doherty Earth Observatory. Brett Barksdale and Curt Vandetta assisted with programming and data base management. This research was supported by the Office of Naval Research (Grant N00014-92-J-1536), and the National Aeronautics and Space Administration (Contract NAS5-31360 and Grant NAGW-4596).

6. REFERENCES

1. T.D. Dickey, "The emergence of concurrent high-resolution physical and bio-optical measurements in the upper ocean and their applications," *Rev. Geophys.* **29** (3), 383-413 (1991).
2. M.R. Abbott, K.H. Brink, C.R. Booth, D. Blasco, L.A. Codispoti, P.P. Niiler, and S.R. Ramp, "Observations of phytoplankton and nutrients from a Lagrangian drifter off northern California," *J. Geophys. Res.* **95** (6), 9393-9409 (1990).
3. M.R. Abbott, K.H. Brink, C.R. Booth, D. Blasco, M.S. Swenson, C.O. Davis, and L.A. Codispoti, "Scales of variability of bio-optical properties as observed from near-surface drifters," *J. Geophys. Res.* **100** (7), 13,345-13,367 (1995).
4. D.K. Clark, "Phytoplankton pigment algorithms for the Nimbus-7 CZCS," *Oceanography from Space*, J.F.R. Gower (ed.), 227-238, Plenum Press, New York, 1981.
5. K.L. Denman and M.R. Abbott, "Time scales of pattern evolution from cross-spectrum analysis of advanced very high resolution radiometer and coastal zone color scanner imagery," *J. Geophys. Res.* **99** (4), 7433-7442 (1994).
6. R. Hood, M.R. Abbott, P.M. Kosro, and A.E. Huyer, "Relationships between physical structure and biological pattern in the surface layer of a northern California upwelling system," *J. Geophys. Res.* **95** (10), 18,081-18,094 (1990).

Remote Sensing Reflectance of Case 2 Waters

Rober A. Arnone

Naval Research Laboratory, Code 7243, Stennis Space Center, MS, USA 39529

Michael Sydor

U of Minnesota, Duluth, Duluth, MN, USA 55812

Richard A. Gould

Planning Systems Inc. 115 Christian Lane, Slidell, LA, USA 70458

ABSTRACT

We consider the variability of spectra in case 2 waters with different scattering and absorption coefficients in order to examine the limits on the validity of $RSR = C b_{bt}/a_t$. The spectral scattering coefficient is shown to be strongly correlated with sediment cross sectional area. In high scattering environments the remote sensing reflectance can be linearly related to the particle cross sectional area. RSR spectra show a decrease with the absorption by Dissolved Organic Matter (DOM) for $\lambda < 600$ nm. However, at extremely high scattering levels, absorption by DOM and even pure water become less important in this region. The transition from case 2 to case 1 waters appears to occur when the scattering to absorption ratio is less than 0.6.

In situ a_{c9} and RSR data were collected in the northern coastal Gulf of Mexico and off North Carolina. The RSR spectra are shown to be related to the in situ absorption and scattering coefficients, and the cross sectional area of the particles. We explore methods of characterizing waters based on the dimensionless ratio of the scattering and absorption coefficients.

1. INTRODUCTION

In remote sensing of case 2 waters we are primarily interested in the suspended particulate load and the dissolved organic material (DOM). Since both parameters affect the remote sensing signal (RSR) in a complex way, there has been a concerted effort to devise remote sensing algorithms that can separate the two constituents. Most efforts have concentrated on empirical techniques based on correlation of suspended solids and DOM with ratios of RSR in various spectral bands. Usually, the algorithms meet only with limited success because they attempt to exploit subtle differences in light absorption by the two components. Furthermore, in using RSR ratios we tacitly assume that $RSR = C b_b/a$, where b_b is the backscattering coefficient, a is the absorption coefficient, and C is a constant independent of wavelength. However, there is evidence that C varies with water turbidity and spectrally as well as the observational conditions.¹ These difficulties aside, the simplicity of algorithms based on RSR ratios warrants further investigation of the behavior of RSR with particulates and DOM to determine the best possible choices for RSR ratios used in remote analysis of turbid waters.² With this in mind, we set out to perform a systematic set of on-board RSR and cross-checked optical measurements on case 2 waters. We applied these measurements to examine the variability of RSR with λ , and test the range of C as a function of suspended load and DOM concentration.

2. DATA SET

The Mississippi sound in the Northern Gulf of Mexico represent a wide variety of case 2 waters. The sound is strongly influenced by discharge of several river systems, including the Mississippi River to the west. The Jordon River Basin drains the Pearl River Honey Island swamp which contributes high DOM levels to the sound. In addition to the DOM variability, elevated suspended sediments concentrations with a variety of particle size distributions result from bottom resuspension and river discharge. The wide variety of DOM and particle concentration provided an opportunity to characterize the optical properties and the behavior of Case 2 RSR spectra.

We collected data from several time periods covering a range of both absorption and scattering environments to define the temporal and spatial variability of optical signatures. Two transects of standard stations were established; 1) across Bay Saint Louis into the Jordon River (labeled B1-B7) and 2) transect

across the Mississippi sound from Gulfport, MS past the barrier island into the Northern Gulf of Mexico (labeled G1-G7). Data presented are from June and July 1995 and July, 1996. An additional data set was collected in Camp Lejeune, North Carolina in April, 1996 in which identical optical measurements were made.

Spectral absorption and scattering measurements were made with the WetLabs ac9 instrument with single scattering corrections applied. RSR measurements were made using a Dual Spec Analytical Spectral Devices spectrometer using above water techniques outlined in the SeaWiFS protocol (12% spectron grey card). In addition, measurements of particle absorption, a_p , and phytoplankton absorption, a_{phy} , were made using the filter pad technique and hot methanol. We also measured the a_{DOM} from the filtrate of the filter pad technique. Inter-comparisons of these measurements were robust and reliable. Lastly, we determined the particle size distribution from 1 to 100 μm in 32 bin sizes using a Spectrix laser particle counter. This measurement included both the size and total suspended particulate concentrations

3.RELATION OF RSR TO OPTICAL PARAMETERS

Generally, RSR is related to b_b which is difficult to measure. Furthermore, b_b can have a spectral dependence that need not mimic b . However, we see that for case 2 waters, b_b/b appears constant. Thus, a measure of b might suffice in unraveling the dependence of RSR on suspended solids concentration which predominates in case 2 waters. Unfortunately, b is measured indirectly (ac9 instrument) as the difference in extinction coefficient, c and absorption coefficient, a . To ensure the accuracy of b , we needed a direct measure of light scattering from particulates as a cross-check on the difference measurement of b . We

found a good cross-check on b in the optical measurement of particle size distributions. In examining particle size distributions for case 2 waters, we found that the effective cross sectional area of suspended particulate per unit volume, x_g , correlated surprisingly well with b , even for different geographical areas (Mississippi Sound and North Carolina, Fig. 1). The reason for the generally good correlation of b and x_g for case 2 waters is attributed to the remarkably similar particle size distributions in the 1 - 10 μm size range for different locations. Furthermore, the main contribution to scattering for case 2 waters appeared to come from the 1 - 4 μm particles. Since b and b_b are related to x_g through the average scattering efficiency per particle and the average front-to-back scattering ratio per particle,³ we can safely assume that for similar particle size distributions b_b and x_g should correlate.

We can relate the magnitude of x_g to b_b , and find b_b/b experimentally by examining the data for RSR at constant λ and a . Fig.2 shows that $RSR(660) = 0.0125 x_g$. Using the relationship $RSR = C b_b/a$, and substituting for the measured value of $a = 0.62 m^{-1}$ in Fig. 2 and the accepted value of $C = 0.051$,¹ we obtain $b_b = 0.15x_g$. Fig. 1 shows that $b = 12x_g$ at 660 nm, thus we have $b_b/b = 0.0126$, in good agreement with previously reported b_b/b for the Mississippi Sound⁴ and with the ratio computed from Petzold's volume scattering function (0.0187).

Figure 2. $RSR \propto x_g$ for $\lambda > 650 nm$ since absorption is only from pure water not from particle or DOM. Stations from B1-B7 from the Jordon River to Bay St. Louis.

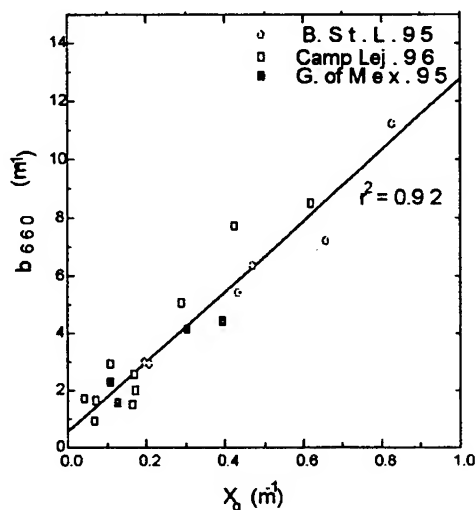
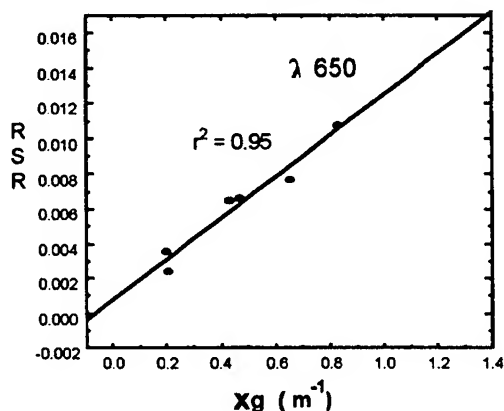


Figure 1 Global correlation of b with x_g . Bay St. Louis, MS; Gulf of Mexico, Camp Lejeune NC.

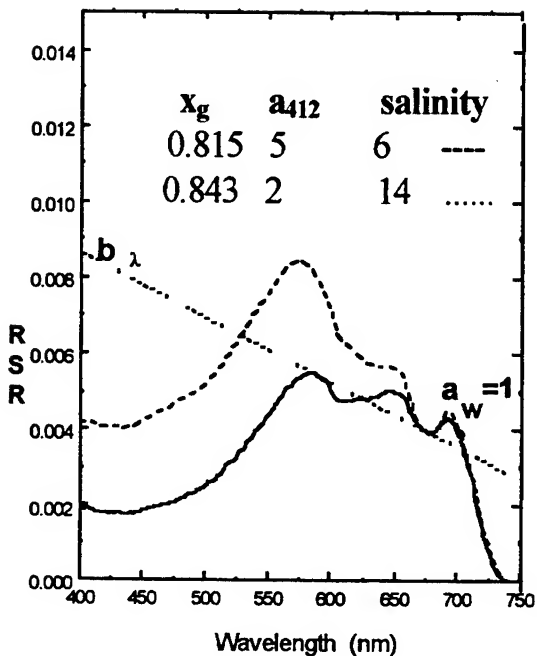
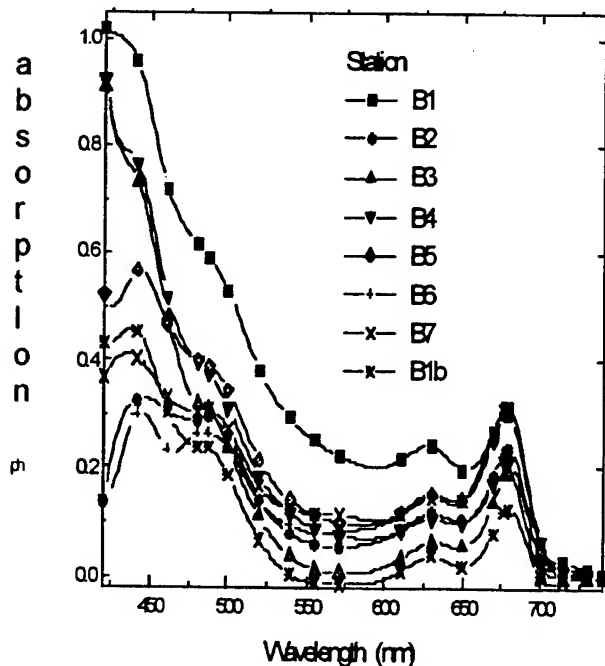


4.EFFECTS OF DOM AND PARTICLE CONCENTRATION

Fig. 3 shows how RSR changes with DOM for two stations with equivalent x_g or scattering efficiencies but with different absorption coefficients. DOM absorption affects mainly the region of RSR below 660 nm. The RSR spectra overlap for $\lambda > 670$ nm in Fig. 3 and demonstrates that suspended solids concentration determine the magnitude of RSR for $\lambda > 650$, provided chlorophyll absorption at 676 nm is small. If $a(\lambda)$ in Fig. 3 were constant, one would expect RSR to follow a line parallel to $b(\lambda)$.

Figure 3. RSR spectra for two stations with nearly same x_g but different concentrations of DOM. The station represented by the solid line is further up the Jordan River. Notice that the RSR spectra overlap for $\lambda > 670$ nm.

The small dip at 676 nm in Fig. 3 is due to chlorophyll, see Fig. 4. Light scatterers in case 2 waters are mainly silt, clay, and detrital particles. Typical absorption by phytoplankton in case 2



waters is shown in Fig. 4. Absorption by DOM is exponential and in general a factor of 10 higher in Mississippi Sound waters.

Figure 4. Absorption by phytoplankton in case 2 waters ranges from $0.2 - 1 \text{ m}^{-1}$. The a_{ph} shape varies dependent on pigment content. a_{DOM} has an exponential behavior with significantly higher ranges from 2 to 18 m^{-1} . The lower curves in Figure 4 represent riverine stations. The highest curve represents the relatively clearer coastal Gulf of Mexico water.

In Fig. 3, the large drop in RSR in the 400 - 450 nm range comes as a result of light absorption by DOM assuming low phytoplankton concentration. We show this in Fig. 5 through correlation of light absorption by sample water filtered through $0.2 \mu\text{m}$ filters versus the average slope of RSR in the 400 - 450 nm region.

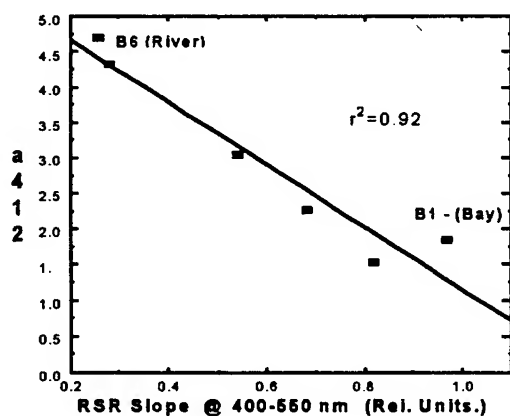
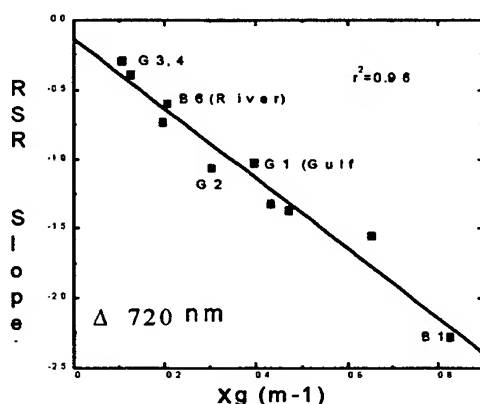


Figure 5. Light absorption at 412 nm by sample water filtered through 0.2 μ m filter represents an estimate of DOM concentration. a_{412} Icorrelates well with the average slope of RSR in the 400 - 450 nm region.

Although we see a good correlation in Fig. 5, we note that the correlation holds only for samples filtered through the 0.2 μ m filter. Samples filtered through 0.5 μ m filter show much poorer correlation than Fig. 5 and suggests the influence of the small particle scattering have on absorption measurements.

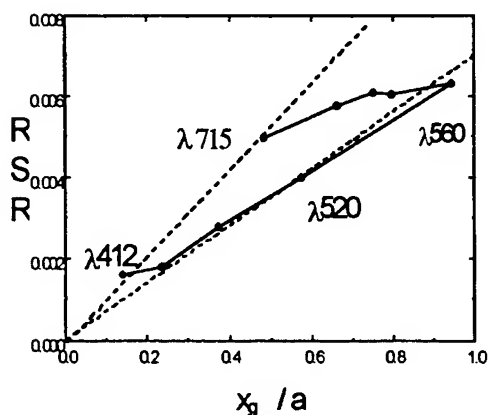


Returning to Fig. 3, we also pointed out that RSR for $\lambda > 700$ nm depends only on x_g and a_{water} . Thus, the slope of RSR at 720 nm should correlate with x_g (and b_{720}). This is demonstrated in Fig. 6. Since water dominates the absorption at 720 nm, we view at 720 nm a constant attenuation depth due to pure water independent of DOM and particle concentration. The particulate absorption at 720 is presumed negligible.

Figure 6. A measure of suspended solids as determined by the relative magnitude of x_g correlates well with the average slope of RSR at 720 nm. The stations marked B represent St. Louis Bay and Jordan River (B6). The stations marked G are Gulf of Mexico stations. G3 and 4 represent clearer water stations.

5. BEHAVIOR OF $\text{RSR} = C \cdot b_p/a$ WITH DOM AND PARTICULATE CONCENTRATION

In discussion of RSR for case 2 waters, we are interested in the dependence of RSR on particulate concentrations and DOM. We can replace $\text{RSR} = C \cdot b_p/a$ with $\text{RSR} = G \cdot x_g/a$ where G is related to C through the dimensionless ratio b_p/x_g . The advantage of considering $\text{RSR} = G \cdot x_g/a$ in place of $\text{RSR} = C \cdot b_p/a$ comes from the fact that x_g is a geometric parameter based on the cross sectional area of suspended particulate. In optical instruments calibrated using latex spheres, x_g is measured in terms of the physical size of spheres that provide forward scattering equivalent to the scattering by the particulate in case 2 water samples. Thus, by plotting RSR versus x_g/a we can investigate the behavior of RSR as a function of



λ , for constant DOM, and constant particle concentrations. A plot of RSR versus x_g/a is shown in Fig. 7 by averaging the RSR in all stations in Bay Saint Louis (B1-B7) for each of the SeaWiFS wavelengths. Here the average $a_{\text{DOM}} = 5 \text{ m}^{-1}$ and the average suspended load is $\sim 4 \text{ g/m}^3$. The spectral spread is delineated by the two dotted lines which shows the spectral variation in the constant G .

Figure 7. RSR for an average suspended load of 4 g/m^3 and $a_{\text{DOM}} = 5 \text{ m}^{-1}$ versus x_g/a shows a characteristic wavelength dependence of the coefficient G , or C . The loop-like pattern of the spectral distribution is evident for these high DOM case 2 stations. The location of the

715 nm point in Fig. 7 depends only on x_g and the absorption by water. On the other hand, the 412 nm point depends on x_g and the concentration of DOM (neglecting chlorophyll). For a fixed suspended load but higher DOM concentrations, the lower end of the loop in Fig 7 moves down toward the origin between the two dotted lines, but the 715 nm point remains fixed. For constant DOM, but increased suspended load, the whole loop in Fig. 7 moves up between the dashed lines and bends over at the higher values of x_g/a .

Figure 8 shows the behavior of the loop for two stations with different values of x_g and DOM concentrations. Here we explore the basic RSR behavior with the ratio of b/a and the variability of the constant slope, C . Note the increase in the 715 values between the two stations which varies because of the particle scattering only. These values align with the 412 values and form the dotted line boundary. The other spectral values have different slopes in response to the scattering to absorption ratio. Notice that in aligning the spectral values, there is tendency that the slope bends over and flattens at higher x_g/a .

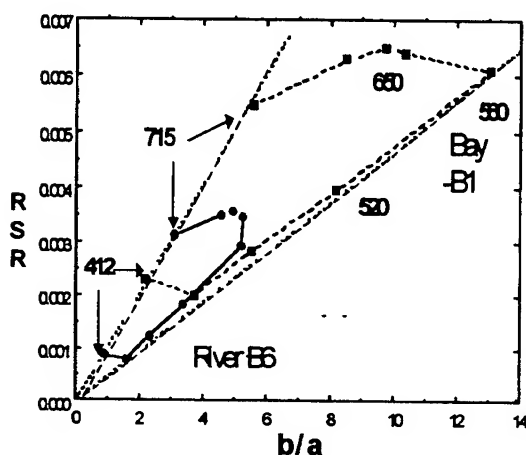


Figure 8. RSR versus b/a at a Jordan River station (solid line) with high DOM and $\sim 2 \text{ g/m}^3$ suspended solids. The clearer St. Louis Bay station at the mouth of Jourdan River (dashed line) shows an expanded and slightly bent over loop. Notice that 412 and 715 nm points still lie along a straight line.

We can examine the dependence of RSR on the ratio of x_g/a independent of λ , by averaging RSR for equal intervals of x_g/a over all wavelengths, as shown in Fig. 9. We see from Fig. 9 that the relationship between the average RSR and x_g/a becomes non linear for $x_g/a > 0.6$. We note that x_g/a provides a measure of the probability that a photon encounters a particle and is scattered versus the probability that a photon becomes

absorbed. Therefore, x_g/a is a measure of the multiple scattering process. As x_g/a increases because of low absorption or high particulate concentration, RSR spectra flatten out by shifting up the curve in Fig. 9 to the non linear region.

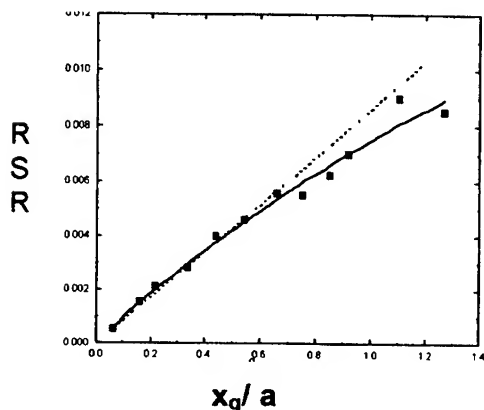


Figure 9. Shows the dependence of RSR on x_g/a independent of λ . The dotted line represents the linear region. The solid line gives a second order polynomial fit to the experimental points according to: $RSR = 0.0093(x_g/a) - 0.2(x_g/a)^2$

A polynomial fit for points in Figure 7 would look much the same as the polynomial fit shown in Fig. 9.

The general characteristic of multiple scattering is a flattening of the RSR spectrum accompanied by a rise of RSR above zero at the short wavelengths and, depending on x_g , a rise in RSR at the long wavelengths. In case 1 waters, the absorption by water at long wavelengths remains important thus, RSR in case 1

waters increases at the short wavelengths and remains low at the long wavelengths. Of course the scattering in case 1 waters changes, thus x_g loses its original meaning. For case 3 waters, the absorption by particulate becomes important at the shorter wavelengths, but multiple scattering dominates RSR in case 3 waters over the entire 400 - 750 nm spectral range. Thus, in case 3 waters, RSR becomes elevated at the short and the long wavelengths. An example of RSR for various types of water are shown in Fig. 10.

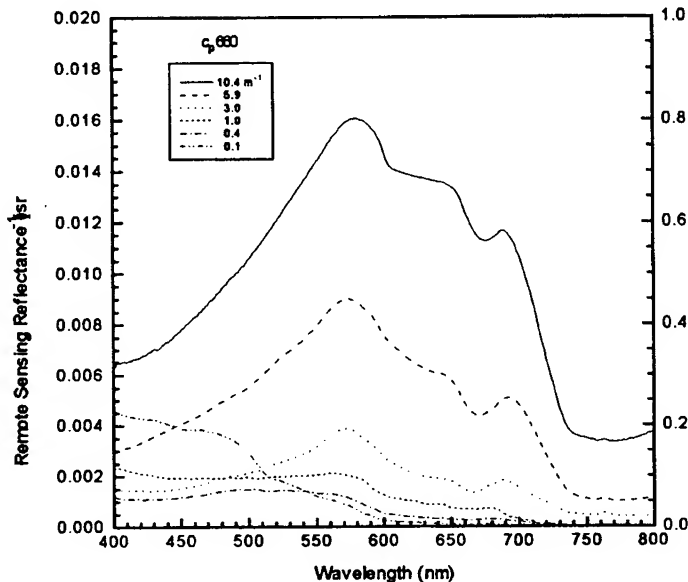


Figure 10. RSR for various values of the extinction coefficient, c_{660} , show characteristic types of spectra for case 1 and case 2 waters. The highest RSR represents borderline case 3 water. The borderline case 3 waters (top curve) shows elevated RSR at longer wavelength. In case 3 waters, RSR also increases at the short wavelengths, but absorption by particulate and DOM limits its rise in this region.

6. CONCLUSION

Figs. 8 and 9 have important implication in remote sensing algorithms based on RSR ratios. The data in Fig. 8 was averaged from stations collected over a 1 km^2 area. It suggests that for any given satellite pixel, the ratios of RSR are constant for the $440 < \lambda < 560 \text{ nm}$ range. However, outside the $440 - 560 \text{ nm}$ range, RSR includes the variability of C_{b_b} as a function of λ , as indicated by the lateral extent of the loops in Figs. 8 and 9. The variability of C_{b_b} is quite large for the $\text{RSR}_{412}/\text{RSR}_{440}$ ratio which is often used in DOM algorithms. Fig. 8 suggests for any given pixel in case 2 waters $\text{RSR}_{720}/\text{RSR}_{412} \propto a_{720}(\text{water})/a_{412}(\text{mainly DOM})$. The use of spectral RSR slope can be used for characterizing the absorption and scattering processes in case 2 waters. Specifically, the use of red spectral area ($>600 \text{ nm}$) is important in Case 2 waters for understanding the role of scattering resulting from suspended sediments. Satellite algorithms can exploit the red spectral shape for separating DOM and sediment concentrations in Case 2 waters.

7. ACKNOWLEDGEMENTS

The authors would like to thank S. Ladner and G. Terrie for data collected in North Carolina. Appreciation is extended to C. Wood for data analyses. This research was supported by the NRL/ONR 6.2 research program MCM Coastal Optics program, Dan Ramsdale manager.

8. REFERENCES

1. Morel A., B. Gentili "Diffuse reflectance of oceanic waters. III. Implication of bidirectionality for the remote-sensing problem. Appl. Opt. 35, 4850-4862, (1996).
2. Tassan S. "Local algorithms using SeaWiFS data for the retrieval of phytoplankton, suspended sediment, pigments and yellow substance in coastal waters. Appl. Opt. 33, 2369-2378 (1994).
3. Kortum, G. (page 88-92) *Reflectance Spectroscopy*, Springer-Verlag, New York (1969).
4. Carder, K. L., S. K. Hawes, and Z.P. Lee "SeaWiFS Algorithm for chlorophyll *a* and dissolved organic matter in a subtropical environment" pending J. Geophys. Res. (1996)

Optimal selection of spectral channels for remote sensing of optically active matters
in the ocean: application of the experimental design theory

Iosif M. Levin and Igor V. Zolotukhin

P.P. Shirshov Institute of Oceanology RAS, St. Petersburg Branch, Laboratory
of Ocean and Atmospheric Optics, 11, Tavricheskaya Ul., St. Petersburg, 193015, Russia

ABSTRACT

The mathematical theory of the experiment optimal design is applied for the problem of remote sensing of optically active matters, such as phytoplankton, dissolved organic matter, or suspended particles. An optimal design (OD) determines the number of spectral channels, the position in spectrum and the width of spectral "windows" in each channel, and distribution of measurement time between the channels, with account of shot (photon) receiver noises. The optimal designs for shipboard and satellite measurements of chlorophyll concentration for the case of pure atmosphere were computed on the basis of the previously published algorithm. For computing OD, arrays of 1000 random radiation spectra above sea surface and on the upper atmosphere boundary were simulated using improved model of upwelling radiance. These spectra were also used for retrieval of the chlorophyll concentration from shipboard "measurements" of color indexes and of ocean radiance in five wavelengths recommended in literature on the basis of principal component analysis. The comparison shows that OD provides the highest retrieval accuracy among methods considered. The stability of computed OD was tested by varying the sensor parameters, observation conditions, and water property models.

Keywords: remote sensing, optically active matters, experimental design theory.

1. INTRODUCTION

At present, measurements of ocean color (water-leaving spectral radiance) are widely used for remote determination of optically active matters (OAM) such as phytoplankton pigments, suspended sediment particles, and dissolved organic matter. Color ratio algorithms proved to be too rough for retrieval of OAM concentrations, especially in coastal waters. Recently the principal component analysis (PCA) was used for a more accurate solution of this problem. A paper by Sathyendranath et al.¹ seems to be one of the most typical and consistent. The authors have simulated a large array of diffuse reflectance spectra $R(\lambda)$ for various concentrations of chlorophyll C , sediment particles X and organic matter (yellow substance) Y . Using these spectra, they computed the eigenvectors and the weighting factors of the covariance matrices for several sets of wavelength, and found multiple regressions between the weighting factors and the concentrations. Those sets of wavelengths for which the correlation coefficients in the regressions were the highest, were recommended to use. In particular, it was shown that measurements of R in five wavelengths (400, 445, 520, 565 and 640 nm) allow to retrieve the concentrations X , Y , and C with accuracy not less than measurements in 27 wavelengths.

Certainly, the PCA-algorithm is a step forward in comparison with the color ratio method. However, this algorithm has not exhausted the potentialities of improving retrieval accuracy. Indeed, the wavelengths for the analysis are selected on the basis of some empirical considerations, so the search of the best wavelength set is not exhaustive. Besides, the width of spectral windows for all wavelengths are taken to be the same (e.g., 5 nm)¹, and the problem of the optimum spectral width for each window is not considered. At

last, shot noises of a receiver, playing an important role in measurements in visual spectrum are not taken into account, as well as the problem of the optimum distribution of the allotted time between the spectral channels.

We believe that the next natural step in this problem is to employ the modern theory of optimal design of experiment (OD). The mathematical basis of this theory as applied to optical experiment was developed by Victor P. Kozlov². The optimization method proposed by Kozlov demonstrated that the accuracy of retrieval of a nonobservable parameter statistically connected with measured spectra may be significantly increased by optimum selection of the spectral channels, namely, their number, arrangement in spectrum and widths. As shown, use of a large number of independent channels would not be the most effective way because of the high spectral resolution required and, as a consequence, decrease of signal energy in each channel. It turned out that it is worthwhile not to throw out the unnecessary channels but to join the radiant energy in the "dependent" channels on the same detector. In this case the measurement accuracy will be greater than in high-resolution spectrometers. The method was applied by V.P. Kozlov in the problem of remote measurements of the water surface radiative temperature³. It is proved that an optimum channel system makes it possible to increase the accuracy of the temperature retrieval (from satellite measured IR spectra) from 1.6 to 0.2-0.3 °C.

In such measurements the main type of detector noises is the thermal noise which does not depend on received radiant power. In visual spectrum, where OAM are measured, the photon (shot) noise dominates over the thermal one. The variance of shot noise, which obeys Poisson's distribution, is proportional to the receiver signal. In this case the definition and the solution of the OD-problem differ essentially from ones where the noises don't depend on the signal. The general solution of the OD-problem with account of shot noise was given by Kozlov and Zolotukhin⁴. Then, the algorithms for searching the optimal spectral channels for OAM remote sensing, and for OAM-concentration retrieval were developed⁵⁻⁷, and preliminary results of applying these algorithms in the problem of shipboard measurements of chlorophyll concentration C were published⁵⁻⁶. Here we present results of applying the OD-theory in the problem of remote measurement of C from ship, and from satellite for the case of pure atmosphere. In the next section we briefly repeat the definition of the problem and several basic equations published earlier⁵⁻⁷.

2. DEFINITION OF THE PROBLEM AND SOME RESULTS OF OD-THEORY

Let Θ be a scalar sea parameter (the concentration of OAM), which is not accessible to direct measurement, but is statistically connected with radiance spectra of the ocean.

Let $u(\lambda)$ be the registered by a sensor spectrum, expressed by a number of "effective" photons (primary electrons for an electronic detector) per unit wavelength and per unit time. The sensor consists of N independent channels, each of which has an apparatus function $x_i(\lambda)$, $0 \leq x_i(\lambda) \leq 1$, determined by transmittance of optical filter or some other spectral device. Each channel can include several spectral "windows". A signal (the number of primary electrons in the i -th channel registered in the time period t_i) will obey the Poisson distribution with conditional expectation

$$\langle y \rangle = t_i \left(\int u(\lambda) x_i(\lambda) d\lambda + \nu \right), \quad (1)$$

where ν is the thermal noise. The integral is taken over the entire spectral region used in the measurements. The total allotted time of measurements $\sum t_i = t$ is limited. The number of channels N , their apparatus functions $x_i(\lambda)$, and distribution of the time resource between channels t_i/t will be called the experimental design ξ for estimation of the

unknown parameter Θ . Our goal is to find the optimal design ξ^* and the algorithm of the retrieval of Θ from measured signals y_1, \dots, y_N . As a criterion of the design ξ optimality, it is natural to consider the residual variance $\sigma^2(\xi)$ of the best linear estimate $\hat{\Theta}$ of the parameter Θ from the results of measurements.

In order to compute the OD it is necessary to know the first two moments of the joint distribution $(u(\lambda), \Theta)$, namely: $\langle \Theta \rangle$, mean of Θ ; s^2 , variance of Θ ; $f(\lambda) = \langle u(\lambda) \rangle$, mean of $u(\lambda)$; $K(\lambda, \lambda) = \text{cov}(u(\lambda), u(\lambda))$, covariance function of $u(\lambda)$, and $q(\lambda) = \text{cov}(u(\lambda), \Theta)$, covariance between $u(\lambda)$ and Θ . It is assumed that these moments are known. Earlier it was proven^{4,7}, that

$$\hat{\Theta} = \langle \Theta \rangle + q^T D^{-1} T^{-1} y, \quad (2)$$

$$\sigma^2(\xi) = s^2 - q^T D^{-1} q, \quad (3)$$

where $q = (q_1 \dots q_r)^T$, $q_i = \int q(\lambda) x_i(\lambda) d\lambda$; $D = K + \text{diag}(f_i + \nu) T^{-1}$; $K = \|K_{ij}\|_{i,j=1}^r$;

$$K_{ij} = \iint K(\lambda, \lambda') x_i(\lambda) x_j(\lambda') d\lambda d\lambda'; \quad f_i = \int f(\lambda) x_i(\lambda) d\lambda; \quad T = \text{diag}(t_i); \quad y = (y_1 \dots y_r)^T.$$

Several properties of OD were proven^{4,7}, and a recurrent algorithm for optimum channel selection was suggested^{5,7}. An input of the algorithm is the set of the statistical moments just listed. However, statistics of the system $(u(\lambda), \Theta)$ known from literature is highly insufficient. So, we performed the Monte-Carlo simulation of this system.

3. MODELS OF UPWELLING RADIANCE AND WATER PROPERTIES USED IN SIMULATIONS

The spectrum registered by a sensor located directly over the sea surface, can be written as

$$u(\lambda) = E(\lambda) [0.53\rho(\lambda) + \rho_s(\lambda)] A \gamma^2 \eta(\lambda) / e, \quad (4)$$

where $E(\lambda)$ is the surface irradiance, $\rho(\lambda) = \pi L / E_d$ the sea radiance coefficient (L and E_d are the upwelling radiance and downwelling irradiance just beneath the surface); $\rho_s(\lambda) = \pi L_s / E(\lambda)$ is the rough sea surface radiance coefficient (L_s the reflected radiance); A , 2γ , and η are the sensor parameters, namely, the aperture (the entrance pupil area, multiplied by its transmittance), the receiving angle, and the spectral sensitivity of the detector's photocathode; e is the elementary charge. The coefficient 0.53 takes into account the radiance change on the water/air interface due to reflection and refraction. The radiance coefficients have different values for direct sunlight (ρ^{dir} , ρ_s^{dir}) and for diffuse light of the sky (ρ^{dif} , ρ_s^{dif}):

$$\rho = \alpha \rho^{\text{dir}} + (1 - \alpha) \rho^{\text{dif}}, \quad \rho_s = \alpha \rho_s^{\text{dir}} + (1 - \alpha) \rho_s^{\text{dif}}. \quad (5)$$

where α is the ratio of direct sunlight to the total irradiance $E(\lambda)$, which was taken from experimental data.

The coefficients ρ_s^{dir} and ρ_s^{dif} may be computed using Mullamaa's formulas⁹. They depend on solar zenith angle ϑ , wind velocity v and azimuth φ_v . We have derived expressions for ρ^{dir} and ρ^{dif} with account of particle and molecular scattering in quasi-single approximation. For nadir viewing direction they are:

$$\rho^{\text{dir}} = \frac{A (180^\circ - \vartheta') (1 - \eta_b) + 0.8(1 + 0.8 \mu_0^2) \eta_b}{2 (1 + \mu_0)} \frac{b_b}{a + b_b} \quad (6)$$

$$\rho^{\text{dif}} = [0.25 (1 - \eta_b) + 0.34 \eta_b] b_b / (a + b_b), \quad (7)$$

where $A(\theta) = 2\pi b P(\theta) / b_b$; a , b and b_b are the absorption, scattering and backscattering coefficients; $P(\theta)$ the phase function for particles; $\eta_b = b_{bw} / b_b$; b_{bw} the backscattering coefficient of optically pure water; $\mu_0 = \cos \vartheta'$; ϑ' is the solar refraction angle.

Computation of Eqs.(6),(7) shows that for the range of $\vartheta = 0^\circ \dots 80^\circ$ ($\mu_0 = 1 \dots 0.68$), for Kopelevich's model of particle scattering¹⁰ all values of $\rho' = \rho (a + b_b) / b_b$ fall within the range (0.242...0.36), i.e. radiance coefficient may be considered as a constant with mean $\langle \rho' \rangle = 0.301$ and dispersion $\pm 20\%$. This is in excellent agreement with the results of Monte-Carlo simulations of Gordon et al.¹¹. According to them, $R / Q = \rho' / \pi = 0.0949$ with dispersion 16%, i.e. $\rho' = \pi R / Q = 0.298$, and the range of ρ' is (0.25...0.346). Radiance coefficients for diffuse light computed by Eq.(7) also agree very well with Monte-Carlo simulation data¹², if single scattering albedo less than 0.8.

For calculation of the radiance coefficients ρ^{dir} and ρ^{dif} , as follows from Eqs.(6),(7), it is necessary to know $a(\lambda)$ and $b_b(\lambda)$. We used the model¹, which relates these coefficients to concentrations C , X and Y . In this model, both absorption and scattering are determined by pure water (a_w , b_w), chlorophyll (a_c , b_c) and sediment particles (a_x , b_x), with addition of yellow substance for absorption (a_y), C being expressed in mg/m^3 , $X = b_x(550)$ and $Y = a_y(440)$ in m^{-1} .

The spectrum registered by a sensor located on the upper atmosphere boundary is expressed by

$$u_A(\lambda) = \{ E(\lambda) [0.53 \rho(\lambda) + \rho_s(\lambda)] \exp(-\tau(\lambda)) + E_0(\lambda) \rho_A \} A \gamma^2 \eta(\lambda) / e, \quad (8)$$

where $\tau = \tau_r + \tau_a$ is the sum of Rayleigh and aerosol optical thicknesses, $E_0(\lambda)$ the extraterrestrial solar irradiance, ρ_A the atmosphere radiance coefficient. We set $\tau_a(\lambda) = (550/\lambda)^m \tau_a(550)$, $m = 0.4$,¹³ $\tau_a(550) = 0.07$. The coefficient ρ_A was calculated in single scattering approximation for marine atmosphere phase function¹³.

4. SIMULATION

An array of 1000 spectra $u(\lambda)$ and 1000 spectra $u_A(\lambda)$ with a step of 5 nm has been simulated. Following Sathyendranath et al.¹, we have chosen the ranges of C , X and Y : $0.01 \leq C \leq 100 \text{ mg}/\text{m}^3$, $0.01 \leq X \leq 10 \text{ m}^{-1}$, $0.01 \leq Y \leq 1 \text{ m}^{-1}$. C , X and Y were simulated by a Monte-Carlo method independently, on the assumption that the logarithm of each concentration is distributed uniformly in the range indicated. The solar angle ϑ , velocity of wind v and its azimuth φ_v were simulated on the assumption that ϑ is distributed uniformly within the limits of $40^\circ \dots 60^\circ$, v having the Rayleigh distribution with mean $\langle v \rangle = 10 \text{ m/s}$, φ_v is uniform within the limits of $0^\circ \dots 180^\circ$. It was assumed that spectral sensitivity of the receiver $\eta(\lambda) \equiv \eta(550)$, and value of $[A \gamma^2 \eta(550)] = 10^{-6} \text{ m}^2 \text{ A/W}$. The last number corresponds, for example, to $A = 5 \cdot 10^{-3} \text{ m}^2$ (the entrance pupil diameter about 8 cm), $\gamma^2 = 0.005 \text{ rad}^2$ (the viewing angle of a receiver $2\gamma \approx 8^\circ$), $\eta(550) = 0.04 \text{ A/W}$.

5. OPTIMAL DESIGN

Based on the array of the simulated spectra, the moments of the system (C , $u(\lambda)$) and then the optimal designs were computed by the algorithm given above for the total time of the measurement $t = 0,01$ s and the thermal noise $v = 10^7$. For the shipboard case, the first channel consists of the following spectral windows: 400-405, 526-535, 553-571, 593-616, 687-700 nm, the second one: 444-462, 535-553, 571-593, 670-685 nm. The signals formed by radiation passed through all windows of each channel should be summed on one detector. The optimal time of measurement $t_1 = 0,44$ t and $t_2 = 0,56$ t. Note, that if the both channels receive radiation during the total time t , the variance of estimate C will not be higher than for the receiver with divided t .

For the given value of system resource $M = A\gamma^2\eta(550)t = 10^{-8}$ m² C/W, Eq.(2) transforms into:

$$\hat{\log C} = -0.02 + 2.09 \cdot 10^{-7} y_1 - 3.7 \cdot 10^{-7} y_2. \quad (9)$$

The variance of $\log C$ estimate computed by Eq.(2) $\sigma^2 = 0,0073$ (the retrieval accuracy $\sigma = 8.5$ %). For comparison we have computed the color ratio $I_1 = L(443) / L(550)$ and $I_2 = L(520) / L(550)$ for the whole array of simulated spectra. Regression coefficients between $\log C$ and I_1 and I_2 were computed by the method of least squares. The variances $\sigma^2(\xi)$ are 0,131 ($\sigma = 36\%$) and 0,067 ($\sigma = 26\%$) respectively. Besides, the coefficients of multiple regression between $\log C$ and the signals y_i in five wavelengths (400, 445, 520, 565 and 640 nm), with 5 nm half-width of each window¹ were computed. In this case the variance $\sigma^2(\xi) = 0.039$ ($\sigma = 20\%$). We can conclude that among all considered methods the OD-method provides the higher retrieval accuracy.

For the satellite measurements (case of very pure atmosphere) the first channel consist of the windows: 524-564, 600-610, 689-700 nm, the second one: 431-457, 564-600, 672-680 nm. In this case the variance $\sigma^2(\xi) = 0.016$ ($\sigma = 13\%$).

6. ANALYSIS OF THE OPTIMAL DESIGN STABILITY

We tested the computed (for shipboard measurements) OD stability to changes of experiment conditions.

1. Stability to sensor parameters. We repeated the computations for the 10^6 times smaller value of resource $M = 10^{-14}$ (m²A/W). The new OD consist of 7 spectral windows instead of 9, the variance of estimate $\sigma^2(\xi) = 0.0010$ is about 35 % greater.

2. Stability to observation conditions. We computed OD for the another range of solar zenith angle $\vartheta = 30^\circ \dots 70^\circ$. The new OD also consists of 7 windows, the variance $\sigma^2 = 0.009$.

3. Stability to the range of OAM-concentrations. Computations were repeated for a narrower range of values $C = 0.02 \dots 20$ mg/m³, $X = 0.02 \dots 3$ m⁻¹, $Y = 0.01$ m⁻¹...1 m⁻¹. In addition, correlation¹⁴ between C and Y was introduced. The OD and the variance $\sigma^2(\xi) = 0.007$ in this case changed insignificantly.

4. Stability to water property model used. For simulations, the Kopelevich model of sea water properties^{10,14} was used. This model differs from initial one in determination of coefficients $a_y(\lambda)$, $b_c(\lambda)$. Besides, it is assumed that $a_x(\lambda) = 0$. The location of windows in the spectrum was slightly different, the variance $\sigma^2(\xi) = 0.008$.

Besides, we tested the robustness of OD, i.e. we used initial OD for retrieval of C under changed experiment conditions just listed, and found the increase of mean squared error σ^2 for all four cases as compared with initial $\sigma^2(\xi) = 0.0073$. Computations show that $\sigma^2 = 0.013$ for the changed sensor resource, $\sigma^2 = 0.014$ for the changed solar angle range, $\sigma^2 = 0.011$ for the new range of OAM concentrations, and $\sigma^2 = 0.017$ for Kopelevich's model.

7. CONCLUSIONS

Of course, the computed optimal design has its own drawbacks. It is based on the approximate model of water properties, in particular, the fluorescence and the sea bottom were not be taken into account. Before being recommended for practical use, our OD should be corroborated by the field experiments. However, our computation shows that OD-method provides higher retrieval accuracy than other known methods. Besides, the computed OD is rather stable for changes of measurement conditions. Our next goal is to find the OD for satellite measurements for any atmosphere turbidity. We also hope to find the experimental data on ocean radiance spectra together with OAM concentration and compute the OD on the basis of these data instead of statistical simulation.

8. REFERENCES

1. S. Sathyendranath, L. Prieur and A. Morel, "A three-component model of ocean colour and its application to remote sensing of phytoplankton pigments in coastal waters", *Int. J. Remote Sensing*, Vol. 10, No. 8, pp. 1373-1394, 1989.
2. V.P. Kozlov, "Problem of the experimental design with range in functional space", *Mathematical theory of experimental design*, S. M. Ermakov (Ed.), Nauka Publ., Moskva, pp. 189-208, 1983 (in Russian).
3. V.P. Kozlov. "About removal of atmospheric effect when remote sensing of radiative temperature of a water surface", *Izv. AN SSSR. Fizika atm. i okeana (Izv. Atm. Ocean. Phys.)*, Vol. 14, No 9, pp. 974-982, 1988 (in Russian).
4. V.P. Kozlov and I.V. Zolotukhin, "A structure of the optimum experimental design in a problem of estimate of non-observable parameter, correlated with the observable Poisson random field", *Optimum design and planning of experiments and simulation of multifactor objects*, NETI Publ., Novosibirsk, pp. 126-131, 1989. (in Russian).
5. I.M. Levin and I.V. Zolotukhin "Method of experimental design for optical remote sensing of chlorophyll concentration in ocean waters", *Proc. SPIE, Ocean Optics XII*, Vol. 2258, pp. 861-888, 1994.
6. I.V. Zolotukhin and I.M. Levin. Optimal design of experiment in the problem of remote determination of optically active matters in the ocean, Submitted to *Doklady RAN (Proc. Russian Academy of Sci.)*, (in Russian).
7. I.M. Levin and I.V. Zolotukhin. "Application of theory of optimization of optical experiment to the problem of ocean remote sensing in visual spectrum", Submitted to *Opticheskiy Zhurnal (Optical Journal)*, (in Russian).
8. R.W. Austin, "Coastal zone color scanner radiometry", *Proc. SPIE, Ocean Optics VI*, Vol. 208, pp. 170-177, 1979.
9. Y.A.R. Mullamaa, *Atlas of rough sea surface optical properties*, Estonian Acad. of Sciences, Tartu, 1964 (in Russian).
10. O.V. Kopelevich "Optical properties of sea water", *Ocean Optics*, Vol. I, A.S. Monin (Ed.), Nauka Publ., Moscow, pp. 150-234, 1983 (in Russian).
11. H.R. Gordon, O.B. Brown, R.H. Evans, J.W. Brown, R.C. Smith, K.S. Baker, D.K. Clark "A semianalytic radiance model of ocean color", *J. Geophys. Res.*, Vol. 93. pp. 10,909 - 10,924. 1988.
12. A. Morel and B. Gentili "Diffuse reflectance of oceanic waters. II. Bidirectional aspects", *Appl. Optics*, Vol. 32. pp. 6864-6879, 1993.
13. L.S. Dolin and I.M. Levin. *Theory of underwater imaging. Reference book*, Gidrometeoizdat Publ., Leningrad, 1991 (in Russian).
14. O.V. Kopelevich, Y.V. Filippov "Comparison between different spectral models of the diffuse attenuation and absorption coefficients of sea water", *Proc. SPIE. Ocean Optics XII*, Vol. 2258. pp. 210-221, 1994.

APPLICATION OF A MULTISPECTRAL INTERPRETATION ALGORITHM TO REMOTE SENSING DATA OVER THE BALTIC SEA

Krawczyk H., Neumann A., Walzel Th., Hetscher M.

German Aerospace Research Establishment
Institute for Space Sensor Technology
Rudower Chaussee 5, 12484 Berlin, Germany
Siegel H.

Baltic Sea Research Institute Warnemuende
Seestr. 15., 18199 Rostock Germany

1. ABSTRACT

In the Institute for Space Sensor Technology a new generation of remote sensing imaging spectrometers was developed, measuring the reflected from the ocean atmosphere system radiance in the visible to near-infrared spectral range. This Modular Optical Scanner (MOS) was successfully launched on 21 March 1996 with an Indian satellite (IRS-P3) to a polar sunsynchronous orbit, and on 23 April 1996 with the Russian Priroda Module on the MIR station. For the purpose of interpretation of these measurements over oceans and coastal zones has been developed a special algorithm based on Principal Component Analysis, using a special inversion technique for a given ocean-atmosphere physical model. An important question in the description of such models are the inherent optical properties of the water. In the paper will be given a description of the derivation of the interpretation algorithm for different water constituents, with an inherent atmospheric correction. It will be shown how specific optical properties are influencing the interpretation results. This work was performed in cooperation with the Baltic Sea Research Institute Warnemuende.

Keywords: MOS, remote sensing, ocean color, coastal zones, pigment, principal component analysis

2. INTRODUCTION

Investigating marine ecosystems, the knowledge of the waterquality is of high interest. The oceans play an important role in climatological processes, with phytoplankton being the main factor in bioproductivity. Many questions are also related to the influence of human activities, especially in coastal zones. From 1978 to 1986 the Coastal Zone Color Scanner (CZCS) worked on the Nimbus-7 satellite, a sensor especially designed for determining phytoplankton pigment concentration in open oceans. Because of a lack of remote sensing data since 1986 there are now under development a number of new instruments, to continue the successful investigations since CZCS, from NASA the SeaWiFS, from the Institute of Space Sensor Technology the Modular Optical Scanner (MOS), from NASDA the OCTS.

In principle the opportunity to obtain information about the water body using remote sensing data results from the effect, that different states of the water body (different concentrations of inherent constituents) lead to different reflectance spectra in the water. A description of such relations can be given by physical models, which are found empirically together with theoretical considerations. Because of the great variety of constituents, which could be found in different ocean and coastal water areas, a universal model description is nearly impossible and very difficult. For the description of the more complicated case 2 waters in coastal areas, often are used models containing beside the pigment concentration an anorganic part (sediments) and dissolved organic matter (Gelbstoff). The interpretation of remote sensing measurements is complicated by the influence of the atmosphere. An important factor in the mapping properties from the geophysical parameter set to the measured spectral radiances are the instruments characteristics, especially central wavelengths, bandwidths, radiometric resolution (quantisation), measurement accuracy (signal to noise ratios).

In this paper will be investigated the question, how the multispectral remote sensing measurements from the MOS instrument can be interpreted with the above mentioned linear estimation algorithm and what is the influence of the appropriate choice of the model describing the optical properties of the water body. Results are shown and discussed with an example of Baltic Sea satellite data.

3. THE MOS-INSTRUMENT

MOS is the worldwide first spaceborn imaging spectrometer for space use and was especially designed for remote sensing of the ocean-atmosphere system. It will be used in two versions on different missions: one on the multisensor-remote sensing module PRIRODA of the Russian space station MIR and one on the Indian remote sensing satellite IRS-P3. In table 1 are listed the basic parameters of the MOS-IRS device^{1,2}.

The mission IRS-P3 is a common Indian-German experimental mission in the field of earth remote sensing. The mission serves for scientific-technological and methodological experiments. Because of the pre-operational character of the mission there does not exist an on-board storage for the data. The reception is only possible real time over areas in the radio view of the ground stations. The control of the payload will be performed through a timer, programmable by the control station in Hyderabad. The German Space Operations Center GSOC of the DLR works as a backup station and control center for the European receiving area, the data reception at DLR is realized the ground station Neustrelitz.

table 1 Modular Optical Scanner MOS-IRS

Parameter	MOS-A	MOS-B	MOS-C
Spectral Range [nm]	755 - 768	408 - 1010	SWIR
No. of Channels	4	13	1
Wavelengths [nm]	756.7; 760.6; 763.5; 766.4 O ₂ A-band	408; 443; 485; 520; 570; 615; 650; 685; 750; 870; 1010 815; 945 (H ₂ O-vapor)	1600
spectral halfwidth [nm]	1.4	10	100
FOV along track x [deg]	0.344	0.094	0.14
across track [deg]	13.6	14.0	13.4
Swath Width [km]	195	200	192
No. of Pixels	140	384	299
Pixel Size x*y [km ²]	1.57x1.4	0.52x0.52	0.52x0.64

4. THE INTERPRETATION METHOD

Different approaches can be used to solve the problem of developing inverse algorithms for remote sensing , as for example:

- Selecting a subset of wavelength bands based on a priori knowledge (laboratory or field measurements) for linear combination: while this gives good results for dedicated case studies focused on specified regions, the disadvantage is that the algorithms have to be redefined or modified for each special case. This has to be done using new field data sets and trying to find suitable correlation results what is usually done in a "trial and error" manner.
- Complete inverse modeling using as much spectral information as possible: this theoretically should give the best results, if the used models properly reflect the physical reality. But in practice serious problems occur regarding time consumption of the calculations as well as unambiguity and convergence. Although special calculation schemes (Doerffer, 1993) allow a significant step forward, the inversion still needs careful supervision and is not easy to handle. A main disadvantage is that inverse modeling therefore is hard to be applied for operational processing and product generation from remote sensing missions.

Both approaches have their advantages and disadvantages: fast and stable computation but possibly poor accuracy for the first, high accuracy but consumptive and instable computations for the second way. The idea here used, was to derive a linear estimation scheme that is applicable to the measured spectral value sets: this makes a combination of ideas used in the mentioned above algorithms by using radiative transfer modeling and adding information theory criteria to derive and optimize the algorithms. The necessary modeling and generation of look-up-tables then can be done in the forefield of the mission, the generation of derived parameter maps is realized by simple linear calculations.

The main goal of the derivation of such a algorithm was to develop an estimator for the determination of the atmosphere-ocean-system state

- with a simple to implement algorithm
- fast in use for processing of large data sets
- estimation of a multiple parameter set \vec{p}
 - C, S, Y -water constituents (pigment sediments, gelbstoff)
 - $\tau(750\text{nm})$ - aerosol optical thickness

Therefore it was chosen a linear statement from L_{sat} (satellite radiances) to \vec{p}

$$p_i = \sum_{k \in \text{MOS}} L_{\text{sat}}^k * f_{ik} + b_i$$

The main advantages of this view are the linearity which allows a simple implementation in image processing systems and a short processing time even for large data sets. The main problems are that the original relation $L_{\text{sat}} \Leftrightarrow \vec{p}$ is nonlinear and therefore the estimation is valid only approximately.

For different Atmosphere-Ocean-types it is necessary to use different coefficient sets which must be than precalculated. The coefficient sets are model-dependent and a nonadequateness of the model with the real geophysical situation can cause systematic misinterpretation errors

Short outline of the Method

A detailed description can be found in ³

Initial point is the direct description of the atmosphere-ocean model with its inherent properties:

$$\vec{p} \rightarrow L_{\text{sat}}$$

which allows from the knowledge of geophysical parameters estimate the satellite radiances.
that means:

- solutions of radiative transfer equations
- simplifications of exact solutions (for example two stream approximations)
- Computer simulation programs
- numerical algorithms for the calculation of L_{sat} from known values of \vec{p}
- under considerations of the MOS-properties

1. Step: Simulation

Simulation of a test data set for the expected geophysical situation, characterized by the order of magnitude of parameters and possible correlations with a concrete (adapted) model.

2. Step: Principal Component Analysis

Analysis of information content of the test data set

- a) definition of a subset of MOS-channels to be used for interpretation
- b) calculation of the intrinsic dimensionality of the data set
- c) calculation of the principal components and eigenvectors

3. Step: Correlation

correlation of the geophysical parameters with the informative principal components

Linear regression of \vec{p} and PC There follows a scenespecific interpretation formula dependent from the principal component values

4. Step: Backtransformation to L_{sat}

Back transformation of the principal components PC via the eigenvectors to the satellite radiances and so obtaining a global interpretation formula for L_{sat}

5. The Ocean Atmosphere Model

The atmospheric model

The spectral response functions of the MOS channels are known from laboratory measurements and were used to calculate for each channel the extraterrestrial sun irradiance after Neckel and Labs 1984 [2] as well as the rayleigh optical thicknesses. The here used atmospheric model is based on the atmospheric corrections models for CZCS, developed and successfully used by H. Gordon ⁴ and B. Sturm ⁵. The basic equation for the radiance at the top of atmosphere (TOA) is:

$$L_{\text{sat}} = L_{\text{path}} + L_{\text{sky}} + L_{\text{sun}} + L_{\text{w}}$$

The TOA radiance is divided into 4 parts:

- L_{path} - the path radiance is the scattered sun light in the atmosphere never reaching the ocean surface
- L_{sky} - the surface reflected sky light is scattered in the atmosphere, Fresnel reflected at the water surface and passed through the atmosphere to the sensor
- L_{sun} - the direct transmitted sun light, Fresnel reflected at the surface and diffusely transmitted to the sensor

- L_w - the light portion penetrating the sea surface, scattered in the water, back transmitted through the sea air interface and transmitted to the sensor

Regarding the water constituents L_w is the only informative part. The other parts are strongly affected by atmospheric properties, especially molecular and aerosol scattering. The gaseous absorbers ozone and water vapor were accounted for as two thin absorbing layers at the top of atmosphere. The path radiance was calculated by the linear single scattering approximation. The skylight and the sunlight are calculated using two stream like approximations []

Another question in the model is the wavelength dependence of the optical thicknesses. The rayleigh scattering due to molecules only can be exactly calculated using MIE-theorie and then summed with the spectral response functions. For the aerosol optical thickness here was assumed an Angstroem law:

$$\tau_A(\lambda) = \tau_A(750\text{nm}) * \left[\frac{\lambda[\text{nm}]}{750} \right]^{-\alpha_A}$$

with α_A being the Angstroem coefficient for the atmosphere.

The ocean model

The main ideas for the 3 component ocean model were taken from ⁶, that was adapted to the characteristics of the MOS instrument. The parameters characterizing the in-water properties are the chlorophyll concentration C , the sediment concentration S , described by the scattering coefficient at 550 nm and the yellow substance concentration Y , described by their absorbtion coefficient at 440nm. The volume reflectance coefficient can be calculated by $R_- = 0.33 \frac{b_B}{a}$, where b_B is

the total backscattering and a the total absorption coefficient in the water. They are calculated using specific absorbtion and scattering coefficients for the water and their constituents ⁷. For the spectral dependence of the sediment scattering

coefficient also was assumed an Angstroem law $b_p(\lambda) = S * \left[\frac{\lambda[\text{nm}]}{550} \right]^{-\alpha_S}$. The Angstroem coefficient α_S can be selected in

the program. There were used fixed backscattering coefficients for the sediment of 2% and for the chlorophyll of 0.5 %. The described model is implemented in FORTRAN 77 and calculates the TOA radiances in the 13 MOS-B channels.

5. RESULTS AND DISCUSSION

The principal possibility of application of the linear estimation algorithm was shown in ⁸. The next step is the application to real measurement data, what was possible with the availability of MOS-IRS data. For the first attempt of derivating interpretation formulas was used a universal model mainly basing on ⁶ with a wide range of parameter variation: C from 0 to 100 $\mu\text{g/l}$, S from 0 to 10 ($b_p(550\text{nm})$ 1/m), Y from 0 to 1 ($a_y(440\text{nm})$ 1/m). Also was assumed that all parameters were uncorrelated. This was applied to scenes over the Mediterranean Sea (Adriatic Sea) and the Baltic Sea (near island Ruegen). The results showed reasonable pattern in the concentrations of the constituents, but for the water constituents the absolute values of Pigment and Gelbstoff were out of physical plausibility, so the range could only be relatively scaled (i.e. high - low). Another reproducible effect was, that C and Y were estimated in an anticorrelated matter, i.e. in areas where the concentrations are higher expected, especially in river mouths, one got increased gelbstoff concentration together with decreased pigment concentrations. The sediment concentration were increased and also had expected order of magnitude. Together with the nonphysical ranges of C and Y this lead to the conclusion, drastically reduce the parameter variety in the simulations and make use of known correlations between the parameters. By private communication we had the opportunity to compare the results with calculations made by B. Sturm with the same data set. After the application of a suggested by B. Sturm modification of the model - the introduction of a strong correlation between the water constituents in a form of power law and the reduction of chlorophyll range to suggested from long term measurements in this region values from 0-to 20 the linear estimator gave very similar results to compared to his calculations.

From the Baltic Sea it is known that is also a special water case often dominated by high Gelbstoff concentrations. The Institute of Space Sensor technology has a close cooperation with the Baltic Sea Research Institute. Within this cooperation in 1996 was organized a common ship campaign for the investigation of Baltic Sea with a goal to validate a Baltic Sea water model usable for the interpretation of remote sensing measurements. Because of organizational reasons the expedition took part only in end of September, that's why we up to now could use only a preliminary model. In this model the water state is described by 5 parameters: Pigment concentration, Gelbstoff, Detritus, total suspended matter - characterized by their specific spectral absorbtion properties and the total backscattering coefficient of water at 633nm with its specific spectral scattering coefficient. Additionally were given expected parameter ranges of the constituents. Beside biological measurements, during the ship campaign were made radiometric measurements with a ground field spectrometer

HiRES, covering the spectral range from 400nm to 800nm with a bandwidth of about 1.5 nm. It was measured the global upwelling irradiance, the diffuse sky irradiance and the downwelling radiance - all above water. This gave the opportunity to compare, how the models fit to regional specifics of this local area. In figure 1 are shown the results of comparison of the spectrometer measurements and the model after Sathyendranath, Morel, Prieur and the Baltic Sea model. The estimated parameter values are fitted manually, because the final results from the biological measurements are not available yet. The result shows that the models are delivering reasonable values for the measured spectra for given parameters and it makes sense to use them for interpretation purposes. First calculations with the Baltic Sea model showed that there is absolutely needed additional information about correlations between the parameters, because the intrinsic dimensionality of the 6 parameter model (5 water parameters, 1 atmospheric parameter) is three. It is only possible to estimate the atm. optical thickness and the $b_B(633\text{nm})$ as scattering parameters and one absorbing parameter. Because all water parameters except the gelbstoff are contributing to the total scattering it was assumed a correlation of about 50% between C, S and the $b_B(633\text{nm})$. Because of a very similar absorption behavior of the gelbstoff and detritus, both are following an exponential law, the algorithm was not able to distinguish between them. Therefore the detritus in the simulations was neglected. So the estimated gelbstoff must be interpreted as a sum of absorption effects both from gelbstoff and detritus. A solution of this problem can be to give a strong correlation formula between these constituents similar to the Adria model. This can be done only after the detailed evaluation of the ship cruise measurements. On 23 September took part a simultaneous with the ship experiment overflight of MOS-IRS near the island of Ruegen. The described models (Sathyendranath, Morel, Prieur; Adria and Baltic Sea) were used in the linear estimator and applied to the remote sensing measurements. Results are demonstrated in figure 2. In the Sathyendranath Morel Prieur model with no correlated parameters we have again the effect of anticorrelation between pigment and gelbstoff. The area of increased sediment concentration is the mouth of the river Peene. The application of the Adria model gives reasonable values and pattern of the parameter behavior. About the absolute values of water parameters there is a question, because the applied correlation formulas between C, S and Y have not to be valid for the case of Baltic Sea. After the reduction of the Baltic Sea model the results are reasonable and comparable to them of the other models. The total backscatter coefficient is very similar to the C and S concentrations in the Adria model and the gelbstoff concentration is comparable to that of the Sathyendranath Morel Prieur model. The atmospheric optical thickness in all cases was estimated very similar.

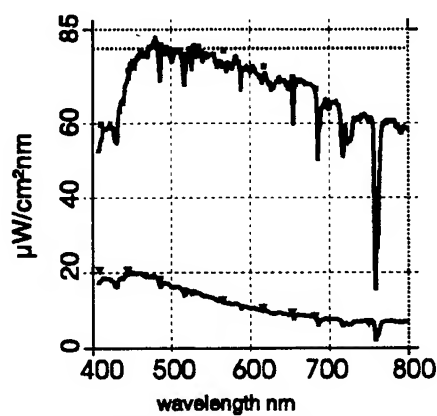
The investigations show that the proposed algorithm is applicable to MOS-IRS data, but also strictly underline the necessity of an appropriate choice of the ocean model. For questions of absolute interpretation accuracy their must be included in situ measurements (which were not available because of the late date of the ship cruise).

Many thanks to Mr. Boris Sturm from Ispra for his helpful discussions and useful hints regarding the model for interpretation of Adria-scenes.

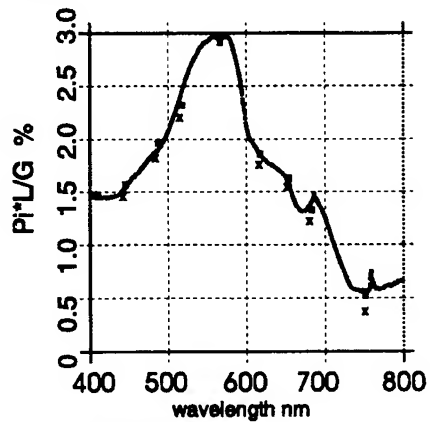
6. REFERENCES

1. Zimmermann G. et. al.: "MOS/PRIRODA: An Imaging VIS/NIR Spectrometer for Ocean Remote Sensing", SPIE Proceedings, Vol. 1937, pp. 201-206, 1993
2. Neumann, A.: "Spaceborne Imaging Spectrometers for Ocean Color Remote Sensing: MOS-PRIRODA and MOS-IRS"; NASA Multisensor Ocean Color Workshop, Miami 1995
3. Krawczyk H. et. al.: "Investigation of interpretation possibilities of spectral high dimensional measurements by means of principal component analysis - A concept for physical interpretation of those measurements", SPIE Proceedings, Vol. 1938, pp. 401-411, 1993
4. Gordon H.R.: "Removal of atmospheric effects from satellite imagery of the oceans", Applied Optics, Vol. 17, pp. 1631-1635, May 1978
5. Sturm B.: "Ocean color remote sensing and quantitative retrieval of surface chlorophyll in coastal waters using NIMBUS CZCS data" in "Oceanography from Space", Plenum Press N. Y. (1981)
6. Sathyendranath S., Morel A., Prieur M.: "A three component model of ocean color and its application to remote sensing of phytoplankton pigments in coastal waters", Int. J. of Remote Sensing, Vol. 10, pp. 1373-1394 (1989)
7. Prieur L., Sathyendranath S.: Limnol. and Oceanogr. 26 (1981) 4, pp. 671ff.
8. Neumann A. et. al.: A complex approach to quantitative Interpretation of spectral high resolution imagery, Proceedings of the Third Thematic Conference Remote Sensing for Marine and Coastal Environments, Technology and Applications, Vol. II, pp. 641-649

Baltic Sea September 1996



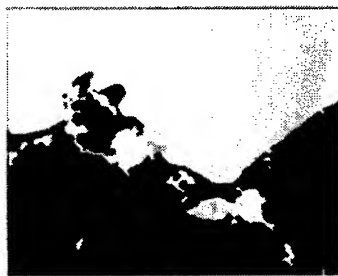
Global Irradiance HIRES
Diffuse Skylight HIRES
• Model with $\theta_s=55^\circ$ Angstr. =0



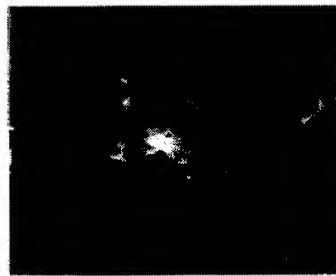
Reflectance HIRES
• Model Sath. Morel Prieur
 $C=2\mu\text{g/l}$ $b_s(550\text{nm})=1.2$ $a_s(440\text{nm})=0.7$
x Model Baltic Sea
 $C=2\mu\text{g/l}$ $b_s(550\text{nm})=1.2$ $a_s(440\text{nm})=0.6/\text{m}$
 $\text{detritus}=0.01/\text{m}$ $b_s(633\text{nm})=0.033/\text{m}$

Fig.1 Comparison of models and in situ measurements

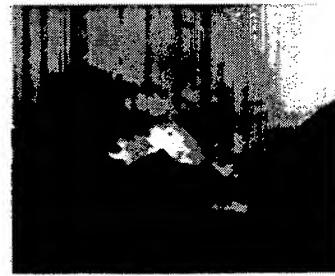
Model Sathyendranath Morel Prieur



0 4
pigment

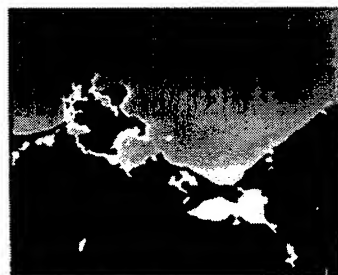


0 4
sediment

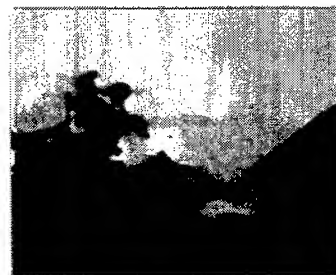


0 1.2
gelbstoff

Model Baltic Sea



0 0.25
aer. opt. thickness



0 0.07
total backscatter coeff.



0 1.2
gelbstoff

Fig.2 Application of different models

Coral fluorescence characteristics: excitation - emission spectra,
fluorescence efficiencies, and contribution to apparent reflectance

Charles H. Mazel

Massachusetts Institute of Technology, Department of Ocean Engineering
Rm. 4-406, 77 Massachusetts Ave., Cambridge, MA 02139

ABSTRACT

The fluorescence characteristics of Caribbean corals have been investigated through in situ and laboratory spectral measurements. Four pigments (as defined by spectral characteristics) are the source of most of the observed emissions. In vivo excitation/emission spectra were measured to determine Stokes shift and bandwidth (FWHM) of each of the types. Fluorescence efficiencies for natural fluorescence of the chlorophyll in the zooxanthellae were estimated from 18 in situ measurements, yielding values from 0.15 - 0.91%. Fluorescence efficiencies of the host pigments in 3 strongly fluorescent coral specimens were estimated from shipboard measurements and ranged from 4 - 6%. The quantitative data are being used in a computational model to investigate the contribution of fluorescence to apparent reflectance signatures.

Keywords: fluorescence, reflectance, corals, spectroscopy, fluorescence efficiency

1. INTRODUCTION

Reef-building corals are invertebrate animals that contain photosynthetic algae (zooxanthellae). The optical characteristics of corals are determined by the pigments that they contain¹, both photosynthetic and non-photosynthetic. In addition to the red-fluorescent chlorophyll in the zooxanthellae, many corals contain autofluorescent pigments in the host tissues^{2,3} that can make a significant, and sometimes dominant, contribution to the appearance of the organism either under ambient daylight illumination⁴ or when stimulated by an active sensing system^{5,6,7}. It is possible in at least some cases that fluorescence from pigments in host tissues may contribute to photosynthesis⁸. Despite the striking nature of the phenomenon, there has been only sporadic attention to the topic and limited qualitative^{4,5,6,9} or quantitative^{10,11} data on the spectral characteristics of the fluorescence effects in corals.

Coral fluorescence has been investigated through in situ and shipboard measurement of excitation and emission properties. The predominant spectral types have been characterized. Estimates have been made of the fluorescence efficiency (ratio of photons fluoresced to photons incident) for several cases, including the natural fluorescence of chlorophyll under daylight illumination. Measurements have been made to document the contribution of fluorescence to apparent reflectance for some corals, and a mathematical approach to predicting that contribution has been implemented.

2. METHODS

2.1 In situ fluorescence and reflectance

Spectral reflectance and fluorescence emission data were collected with a prototype diver-operated instrument designated the Benthic SpectroFluorometer (BSF). The 1024-pixel CCD array in the instrument measures optical radiation over the spectral range of 300 to 800 nm with a spectral resolution of 5 nm. A one meter long, 600 μ diameter optical fiber for light collection extends from the instrument housing to a hand-held probe. A separate fiber bundle carries excitation light from a halogen bulb to the measuring area. A four-position filter wheel provides the capability to select excitation wavelength. Data are stored on a hard disk in the instrument for post-processing, which consists of removal of electrical and dark current offsets and application of a correction factor to produce radiometrically correct values. A Savitzky-Golay smoothing function^{12,13} may be applied to reduce residual pixel-to-pixel variation.

More than 300 in situ measurements of fluorescence and reflectance spectra have been made at sites at Lee Stocking Island, Bahamas; Key Largo, Florida Keys National Marine Sanctuary; and Dry Tortugas, Florida.

2.2 Shipboard measurements of fluorescence excitation and emission

Shipboard measurements of in vivo fluorescence excitation and emission spectra were made in July 1996 at a site in the Dry Tortugas, Florida. 25 live coral specimens, representing 10 species, were collected from a depth of approximately 18 meters. Spectra were measured with a FluoroMax 2 spectrofluorometer (Spex Industries) fitted with a 2 meter fiber optic probe. The corals were maintained in flowing seawater between collection and measurement. For all specimens, emission spectra were measured with excitation wavelengths of 365, 450, and 488 nm (2 nm slit, 0.2 sec integration). Excitation spectra were measured with emission wavelength settings of 490, 530 and 690 nm (2 nm slit, 0.5 sec integration). For some specimens an additional excitation scan was made with an emission wavelength setting of 590 nm. Synchronous scans with a wavelength offset of 5 nm were made to determine the presence or absence of particular pigment types.

2.3 Fluorescence efficiency

Fluorescence efficiencies were determined for the host pigments in three coral specimens. The selected specimens each contained only one of either pigment 486 or 515. These measurements were made in a darkened laboratory on board ship, using a filtered light source for excitation. In addition, fluorescence efficiencies were determined for the in situ chlorophyll emission in 18 specimens representing 7 coral species, at a depth of 15 - 18 meters. The filtering effect of the water column effectively removed incident radiation at the wavelengths of chlorophyll emission.

Fluorescence efficiency was determined as the ratio of photons fluoresced to photons incident. The incident irradiance ($\mu\text{W}\cdot\text{cm}^{-2}\cdot\text{nm}^{-1}$) was measured by directing the fiber optic probe of the BSF at a reference surface (Spectralon®, 20% reflectance) at an angle of 45°. The data were then converted to units of photon flux ($\text{photons}\cdot\text{sec}^{-1}\cdot\text{cm}^{-2}\cdot\text{nm}^{-1}$) by dividing by hc/λ , the energy per photon at each wavelength λ (h = Planck's constant = 6.63×10^{-34} J-sec, c = velocity of light = 3×10^8 m/sec). At each wavelength the intensity value was multiplied by the normalized value of the excitation spectrum at that wavelength. This was done to adjust for the fact that not all incident photons are equally likely to stimulate fluorescence. The data were then integrated over all excitation wavelengths to calculate the total number of incident photons, N_i , available to stimulate fluorescence.

The surface emittance was measured in the same manner as the incident irradiance. The emission spectrum was post-processed in a similar way to calculate the number of fluoresced photons, N_f . In this case, however, the integration was restricted to the portion of the spectrum in which the fluorescence occurs. Fluorescence efficiency was then calculated as the dividend N_f/N_i , the ratio of fluoresced photons to incident photons.

2.4 Fluorescence contribution to reflectance

In situ reflectance and fluorescence measurements were made to confirm the contribution of fluorescence to the appearance of corals under daylight illumination. In some cases the influence of fluorescence was obvious, as when a coral appeared orange or red at a depth of 15-20 meters, where photons of those wavelengths do not penetrate. In other cases the intensity of green coloration suggested a fluorescence contribution.

A mathematical treatment was formulated for the contribution of fluorescence to reflectance. The total apparent surface spectral emittance ($E_T(\lambda)$, $\mu\text{W}\cdot\text{cm}^{-2}\cdot\text{nm}^{-1}$) is:

$$E_T(\lambda) = E_D(\lambda)R(\lambda) + \sum F_i(\lambda), \quad [1]$$

where $E_D(\lambda)$ is the incident irradiance, $R(\lambda)$ is the true (non-fluorescent) reflectance factor, and $F_i(\lambda)$ is the emittance at λ due to the fluorescence of pigment i . The emittance contributed by fluorescence for each pigment can be written as:

$$F_i(\lambda) = \frac{\epsilon_i \phi_i}{\lambda} \int_{\lambda_{ex}} E_D(\lambda_{ex}) \lambda_{ex} X_i(\lambda_{ex}) d\lambda_{ex}, \quad [2]$$

where ϵ_i is the fluorescence efficiency, ϕ_i is the fraction of the total fluoresced photons emitted in the wavelength band around λ , and $X_i(\lambda_{ex})$ is the normalized (peak value = 1) value of the excitation spectrum for pigment i at excitation wavelength λ_{ex} . The integral, carried out over the full range of excitation wavelengths, represents the total number of potentially useful

incident photons, as defined above. Multiplying this quantity by ϵ_i yields the total photons emitted. Multiplication by ϕ_i yields the number of those photons that are fluoresced at wavelength λ , and division by λ converts the result from units of photon flux to units of energy flux.

3. RESULTS AND DISCUSSION

3.1 Excitation and emission characteristics

The in situ and shipboard data sets indicate that there are four pigments (as defined by spectral characteristics) that are the source of most of the observed emissions. For purposes of simplicity I have designated these as 486, 515, 575, and 685, naming them for the approximate location of the emission peak, although the actual location of the peak may vary by up to approximately 10 nm. One of these pigments (685) is chlorophyll contained in the zooxanthellae, while the other three are located in host tissues¹¹. Excitation and emission spectra for representative samples of each type are shown in Figure 1, and the spectral characteristics are summarized in Table 1. Only chlorophyll is found in all symbiotic corals: the other pigments may occur singly or in mixtures within a given specimen (Figure 2).

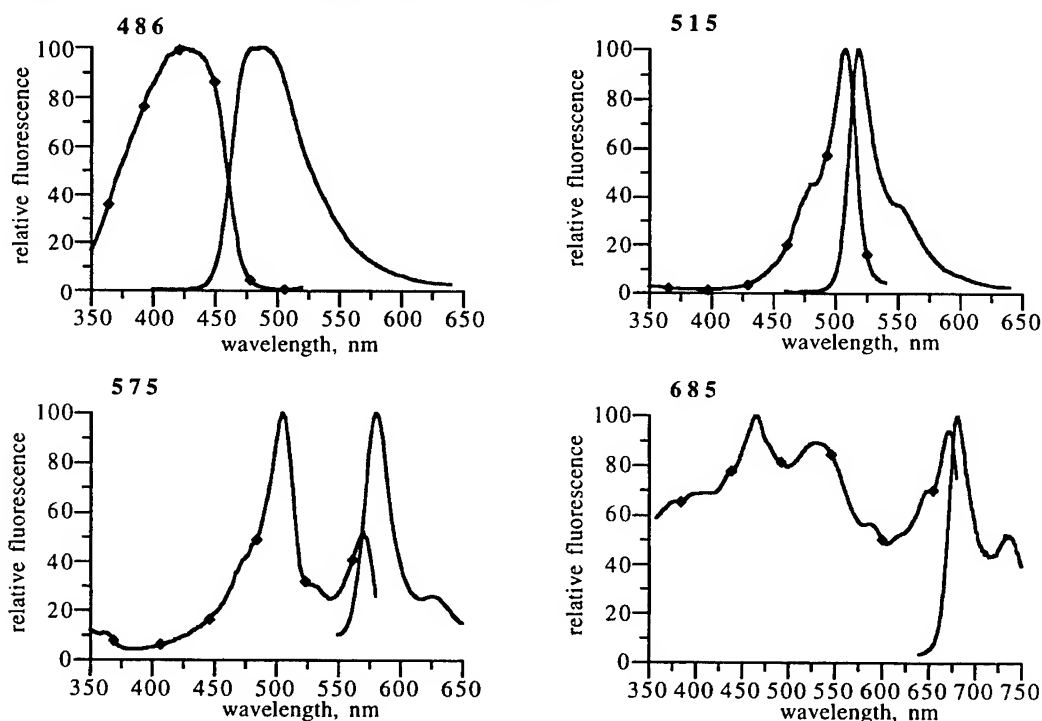


Figure 1. Excitation (—◆—) and emission (—) spectra for the four pigment types commonly found in corals. Species: 486 - *Agaricia* sp.; 515 - *Mycetophyllia lamarckiana*; 575 - *Montastrea cavernosa*; 685 - *Montastrea annularis*.

peak, nm	bandwidth, nm	
	FWHM	Stokes shift, nm
486	65	60
515	25	10-15
575	30	10/75
685	[chlorophyll]	

Table 1. Fluorescence characteristics of the four most common pigment types.

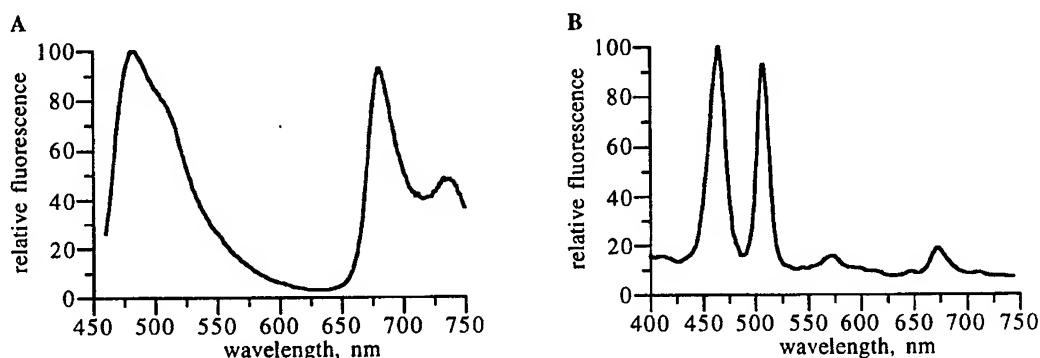


Figure 2. Fluorescence emission scan (excitation at 450 nm) (A) and synchronous scan (B) for a specimen of *Montastrea annularis*. The synchronous scan data show that the broad peak on the left is actually formed from the emissions of two separate pigments (486 and 515). The 685 pigment (chlorophyll) is clear in both graphs, and there is also some 575 pigment present, although it is not evident in A.

The four fluorescent pigments described above are the ones most commonly found. A fifth spectral type (yellow-fluorescent, emission peak at about 557 nm, bandwidth 55 nm FWHM, Stokes shift 50 nm) has been found in one species of *Agaricia* at several locations, and it is likely that continued investigation will reveal additional pigments. While most observations have been made of Caribbean species, limited measurements from Indo-Pacific species indicate the presence of the same general pigment types.

With the exception of the 685 pigment (chlorophyll), the pigments have not yet been identified biochemically. It has been suggested^{2,14} that one or both of the shorter-wavelength pigments (486, 515) may be biliproteins. There is evidence^{11,15} suggesting that the 575 pigment is phycoerythrin, a photosynthetic accessory pigment normally found in red algae and cyanobacteria. There is also evidence to suggest¹⁵ that the 515 and 575 pigments are biochemically related. Note the two distinct peaks in the excitation spectrum, and the similarity of the shorter-wavelength of those two peaks to the excitation spectrum for the 515 emission.

3.2 Fluorescence efficiencies

Figures 3 and 4 illustrate representative data for incident and emitted radiation used in the computation of fluorescence efficiencies for coral pigments and for chlorophyll in zooxanthellae, respectively.

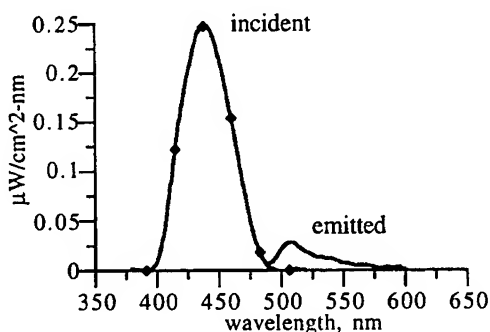


Figure 3. Incident (—♦—) and emitted (—) light for a brightly fluorescent specimen of *Scolymia* sp. containing only the 515 pigment. Shipboard measurement.

Computed fluorescence efficiencies for the coral host pigments were in the range of 4 - 6% for the three samples. One of the specimens contained only the 486 pigment, while the other two contained only the 515 pigment. All three specimens were chosen for their particularly strong fluorescence response under longwave ultraviolet illumination, and these values are liable to represent the high range of values for all corals.

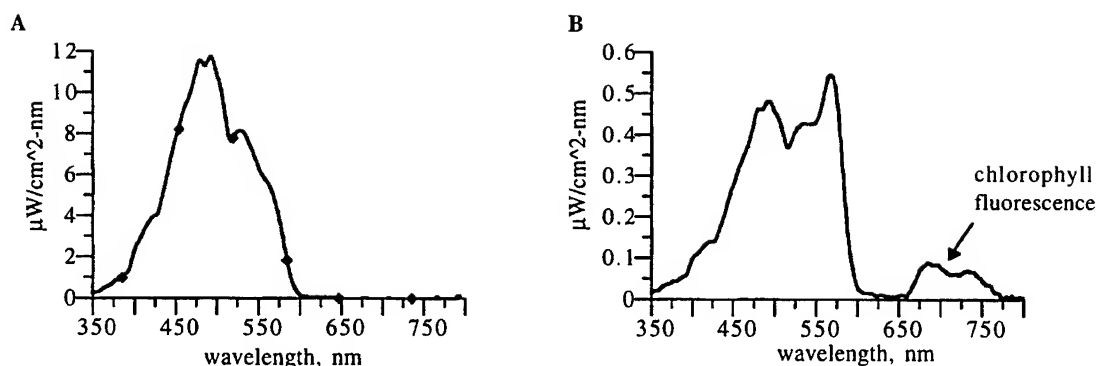


Figure 4. Spectra of downwelling (A) and reflected (B) light used for determination of natural fluorescence efficiency of chlorophyll in symbiotic algae. Specimen of *Montastrea annularis*, depth 18 meters.

Computed efficiencies for natural (daylight stimulated) chlorophyll fluorescence in 18 corals specimens ranged from 0.15 - 0.91% (mean 0.43%, standard deviation 0.21%). The 18 specimens were located at two sites that had significantly different ambient illumination levels due to differences in water clarity, and the measurements were not made at the same time of day. The sample size is as yet too small to determine if the variation between the values at the two sites is significant, and what might be causing the difference.

The definition of fluorescence efficiency (photons fluoresced/photons incident) differs from the traditional definition of fluorescence quantum yield, $\Phi_F = N_F/N_A$ ¹⁶, where N_F is the number of photons fluoresced and the divisor N_A is the number of photons absorbed rather than the number of photons incident. The measurement method used here views the undisturbed coral surface and is thus viewing a complex mixture of pigments, with no way of knowing what percentage of the incident photons were absorbed by the pigments producing the fluorescence. Since the absorbance by the fluorescing pigment must be <1, the quantum yield values for all cases would be larger than the fluorescence efficiency values reported here. The sense of fluorescence efficiency defined here is suitable for model computations related to optical closure or to the performance of active remote sensing systems.

3.3 Fluorescence contribution to apparent reflectance

Figure 5 shows the contribution of fluorescence to the in situ spectrum of light reflected from a coral at a depth of 18 meters under daylight illumination. The coral appeared orange to the eye. The peaks at 515, 575 and 685 nm are due to the fluorescent pigments in the host and the zooxanthellae. (The apparent peak at about 475 nm may be due to 486 pigment, or to the distribution of downwelling light.)

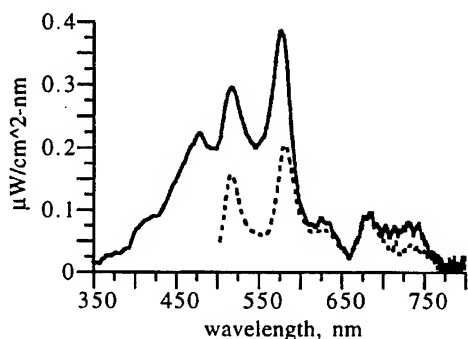


Figure 5. Reflected light spectrum (—) under daylight illumination and induced fluorescence (---) (excitation wavelength = 488 nm) for a specimen of *Montastrea cavernosa*, depth 18 meters. The scaling of the induced fluorescence is for comparison purposes only and is not the absolute magnitude of the fluorescence contribution.

The computational approach to fluorescence-enhanced reflectance was used to produce the model curves for natural chlorophyll fluorescence in Figure 6. Using a prototype spectrum for the chlorophyll fluorescence and the measured downwelling light spectrum as excitation source, a series of emission curves were generated for efficiencies from 0.4 - 1.0%.

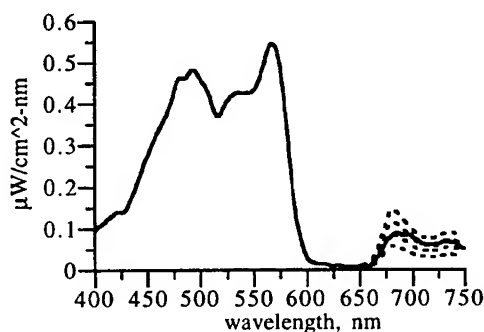


Figure 6. Measured (—) and modeled (---) spectra of light reflected from a coral surface (*Montastrea annularis*, depth 18 meters). The four model curves represent chlorophyll fluorescence efficiencies of 0.4 to 1.0%, in steps of 0.2%.

3.4 Future directions

While advances have been made in quantifying the spectral properties related to fluorescence effects in corals, there is much that remains to be done. The biochemical nature and role of the pigments in the host tissues are not known. The intensity and/or peak wavelength of fluorescence emission may vary within a species, and at times within a single specimen, but the causes and possible interpretive value of these variations are not understood. Additional measurements of fluorescence efficiency are needed to supplement the initial set reported here, with an effort to determine the cause of variations.

4. ACKNOWLEDGMENTS

This research was supported by the Office of Naval Research, Environmental Optics Program, grant numbers N00014-95-1-0837 and N00014-96-1-0221.

5. REFERENCES

1. G. Y. Kennedy, "Pigments of marine invertebrates," *Adv. Mar. Biol.*, 16, 309-381 (1979).
2. S. Kawaguti, "On the physiology of reef corals VI. Study on the pigments," *Palao Trop. Biol. Stn. Stud.*, 2, 617-674 (1944).
3. S. Kawaguti, "Electron microscopy on the fluorescent green of reef corals with a note on mucous cells," *Biol. J. Okayama University*, 2, 11-21 (1966).
4. C. Limbaugh and W. J. North, "Fluorescent, benthic, Pacific Coast coelenterates," *Nature* 178, 497-498 (1956).
5. R. Catala, "Fluorescence effects from corals irradiated with ultra-violet rays," *Nature*, 183, 949 (1959).
6. R. Catala, "Nouveaux organismes marins présentant des effets de fluorescence par l'action des rayons ultra-violet," *C. R. Acad. des Sciences*, 250, 1128 (1960).
7. J. T. Hardy, F. E. Hoge, J. K. Yungel and R. E. Dodge, "Remote detection of coral 'bleaching' using pulsed-laser fluorescence spectroscopy," *Mar. Ecol. Prog. Ser.*, 88, 247-256 (1992).
8. D. Schlichter, H. W. Fricke, and W. Weber, "Light harvesting by wavelength transformation in a symbiotic coral of the Red Sea twilight zone," *Mar. Biol.*, 91, 403-407 (1986).
9. A. Logan, K. Halcrow, T. Tomascik, "UV excitation-fluorescence in polyp tissue of certain scleractinian corals from Barbados and Bermuda," *Bull. Mar. Sci.*, 46, 807-813 (1990).
10. C. H. Mazel, "Spectral transformation of downwelling radiation by autofluorescent organisms in the sea," *SPIE Vol. 1302 -- Ocean Optics X*, 320-327 (1990).
11. C. H. Mazel, "Spectral measurements of fluorescence emission in Caribbean cnidarians," *Mar. Ecol. Prog. Ser.*, 120, 185-191 (1995).
12. A. Savitzky, and M. J. E. Golay, "Smoothing and differentiation of data by simplified least squares procedure," *Anal. Chem.*, 36, 1627-1639 (1964).
13. J. Steinier, Y. Temonia and J. Deltour, "Comments on smoothing and differentiation of data by simplified least squares procedure," *Anal. Chem.*, 44, 1906-1909 (1972).
14. V. M. Buchsbaum, "Behavioral and physiological responses to light by the sea anemone *Anthopleura elegantissima* as related to its algal endosymbionts," Ph. D. Thesis, Stanford University (1968).
15. C. H. Mazel, "Fluorescence in Caribbean coral reef cnidarians," Ph. D. Thesis, Boston University (1993).
16. I. D. Campbell and R. A. Dwek, "Biological Spectroscopy," Benjamin/Cummings Publishing, Menlo Park (1984).

Whitecaps: Spectral reflectance in the open ocean and their contribution to water leaving radiance

Karl D. Moore, Kenneth J. Voss, Howard R. Gordon

University of Miami, Physics Dept., Coral Gables, FL 33124

ABSTRACT

The reflectance of whitecaps (foam) in the open ocean is obtained with a 6-channel spectral radiometer, extended from the bow of a ship, at wavelengths: 410, 440, 510, 550, 670 and 860 nm. In addition to reflectance data, air / water temperature, wind speed and direction are obtained as well as GPS (global positioning system) information in order to characterize ocean surface conditions. A visual reference for sea surface conditions measured by the radiometer is recorded using a video camera mounted beside the radiometer. By measuring a small area of the water surface over time, the presence and spectral influence of whitecaps can be quantified. Using this technique the spectral reflectance of individual whitecaps can be measured and tracked through their complete life cycle. Also, integration over a larger time series of ocean surface reflectance data provides a measurement of the augmented or extra contribution from white water reflectance to the water leaving radiance observed by ocean color satellites. Estimates of the augmented reflectance are subsequently correlated to sea surface state, and include the frequency of occurrence and spectral contribution from various levels of white water reflectance as whitecaps grow and decay.

Keywords: whitecaps, spectral reflectance, augmented reflectance contribution.

1. INTRODUCTION

To assess the contribution of whitecaps to the upwelling radiance from the ocean surface, instrumentation operated from a ship has been developed to measure the spectral characteristics of both individual foam types and their appearance as a collective whole as observed by a satellite image pixel. For given environmental parameters, such as wind speed, air and water temperature, the augmented spectral contribution of whitecap foam must be investigated to quantify atmospheric correction and ocean color accuracy.

Previous researchers have assumed a wavelength independent reflectance of whitecaps and have used reflectances of 50%- 100%^{1,2,3}. Koepke⁴ reduced this reflectance estimate to ~22% by taking into account the decrease in reflectance and increase in area of a whitecap as it ages. Whitlock, Bartlett and Gurganus⁵ reported spectral variation from laboratory measurements of foam with a decrease in reflectance beyond ~0.8 μm . Smaller reflectances beyond ~0.8 μm were reported by Frouin, Schwindling and Deschamps⁶ in their observations of real breaking waves in the surf zone. The smaller reflectance at longer wavelengths found in real breaking waves is thought to be due to the presence of submerged bubbles reflecting light through a small layer of water where water absorption is much greater than in the shorter wavelengths. This dependence of the spectral reflectance of whitecaps on wave breaking characteristics and distribution of different foam types (thick, thin, streaky and submerged), may complicate any expectation of a single whitecap spectral profile solution.

Whitecap fractional coverage and the distribution of foam types is primarily dependent on wind speed but can be dependent on many factors such as air temperature, water temperature⁷, stability of the lower atmosphere⁸, fetch and duration⁹, salinity¹⁰ and even the presence of thin organic films which can effect surface tension¹¹. Estimates of fractional coverage related primarily to wind speed and air / water temperature have been established^{12,13,14,15,16} but are found to be quite noisy. Certainly the threshold point where foam is distinguished from foam free water is difficult to objectively define and correlation is further complicated by the dynamic nature and interdependence of the many parameters involved in whitecap formation.

In the past, independently determined estimates of fractional coverage, reflectance and spectral characteristics have been combined to quantify the augmented reflectance contribution of whitecaps. In this paper, instrumentation has been developed and utilized to acquire data so that the augmented spectral reflectance contribution can be measured directly, and the spectral reflectance of individual whitecaps, foam types and their distribution can also be assessed for different sea states.

2. INSTRUMENT DESCRIPTION

The whitecap measurement system has been developed for operation from a surface vessel such as a ship or other overwater surface platform¹⁷. The radiometric part of the system consists of a 6-channel radiometer aimed at the water surface to measure upwelling radiance and a deck cell (cosine collector) with matching wavebands measuring downwelling irradiance. Ancillary parameters are measured by an anemometer to determine wind speed and direction, air / water temperature sensors and a global positioning system (GPS) to provide position and UTC time. Equipment providing a visual reference of the water surface consists of a color TV camera, video recorder and monitor. Processing equipment is supplied by a Power Macintosh computer PC with a 16-channel acquisition board (National Instruments, NB-MIO-16XL) controlled by LabVIEW software. The TV camera is mounted beside the radiometer and both are extended from the bow of the ship by means of a boom (~1-10 m). This boom is made of individual segments so that extension can easily be adjusted to avoid ship shadow and shortened during rough seas.

The 6-channel radiometer has a narrow field of view ($\sim 1^\circ$) with channels at 410, 440, 510, 550, 670 and 860 nm. Each channel consists of an optical tube aligned parallel to one another. Light entering each channel passes through a BK-7 window and is focused by a 25 mm diameter, 100 mm focal length achromat onto a 1.8 mm pinhole aperture. Before the pinhole aperture, light first passes through a 10 nm interference filter and broadband blocking filters to enhance out-of-band blocking of unwanted light. The active area of a photodiode is positioned 1.5 mm behind the pinhole aperture. Each photodiode has its own integrated operational amplifier whose output is fed to a low noise precision opamp with the gain set appropriately to offset variation in photodiode spectral response. Each signal is sent back over ~80 m cable to its own differential opamp resident in an electronics console which also supplies the appropriate power requirements and cable interfaces for all equipment. The channels are arranged in a concentric fashion about the long axis of the radiometer housing with the exception of the 410 nm channel which takes up the central position. The radiometer is housed in a black anodized aluminum cylinder 24 cm in length and 11 cm in diameter. The radiometer also has a 5 cm hood extension to prevent rain falling on the window and to reduce unwanted light that may be reflected and refracted by sea spray and salt deposits that inevitably collect on the window.

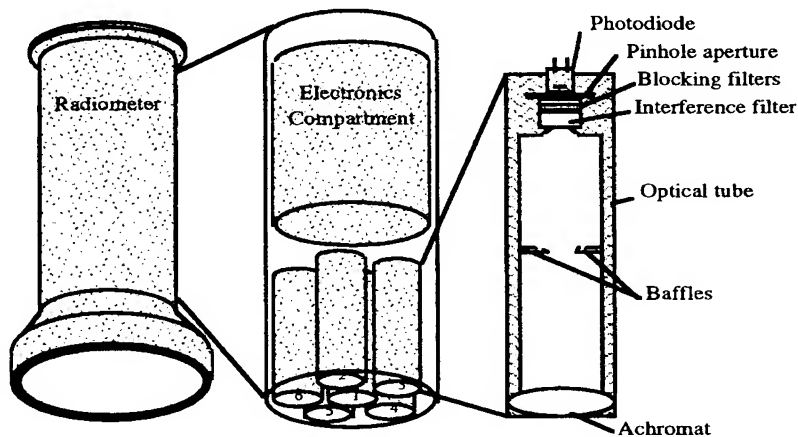


Fig. 1. Radiometer and position of six spectral channels

The deck cell is similar to the radiometer with the exception of the collection optics. The deck cell is a cosine collector positioned in an unobstructed part of the deck. It utilizes a ~5 cm white diffusive acrylic disk, that protrudes ~1 cm above a dark rigid PVC base. The base is terraced to reduce unwanted reflections and increases in height becoming flush with the top of the acrylic disk at a radius of 62 mm. This combination of terraced base and protruding acrylic disk defines a 2π field of view and ensures cosine response at larger zenith angles. Each waveband channel is positioned to view the center of the backside of the diffusive acrylic disk. Since each channel with its filter / photodiode assembly is arranged in a concentric fashion with exception of the 440 nm channel, five of the channels are angled to view the center of the acrylic disk. The deck cell housing is made from rigid PVC and held in a two axis gimbal. The bottom base plate of the deck cell is made from lead and in combination with the gimbal mount helps the deck cell maintain a horizontal attitude.

The anemometer is positioned to prevent wind sheltering by the ship with power and signal received by the electronics console via ~50 m cable. The water temperature sensor utilizes a thermistor with signal conditioning circuitry to provide a linear output. The thermistor and its cable have been fed down the center of a polypropylene rope with the thermistor exposed ~0.2 m from the end. The polypropylene rope provides buoyancy and keeps the thermistor in the water and close to the surface. The remaining ~0.2 m of rope beyond the thermistor is flayed to ensure the thermistor stays in the water.

The air sensor uses an identical thermistor and its cable is also fed down the center of a polypropylene rope for strength and protection. The thermistor is mounted in the center of a white louvered housing. The air sensor is typically suspended close to the water surface but at a sufficient height to avoid excessive sea spray.

Radiometric data, wind speed / direction, air / water temperature are acquired at the rate of ~ 7 Hz until 200 contiguous samples have been obtained. This takes ~30 seconds where upon GPS data is read and appended to file and the cycle is repeated until a time determined by the operator. In addition, the TV camera simultaneously displays and records images of the water surface in order to identify and correlate white water events with radiometric data. To assist identification, individual TV frames are time and date stamped when the radiometer acquires data. The radiometric integration time has been set to ~30 ms which is just less than the integration time of a TV frame.

Taking many measurements of the water surface over time is equivalent to covering a large area of water surface at any instant. Using a 6-channel radiometer, the frequency and spectral information of white water events and different foam types are obtained. By integrating over a large number of samples provides an estimate of fractional coverage and the augmented spectral reflectance contribution.

3. RADIOMETRIC CALIBRATION

The whitecap radiometer and deck cell have been calibrated to produce water surface reflectance measurements under a variety of sky conditions and solar zenith angles. This was necessary in order to provide confident reflectance measurements whenever whitecaps occurred during a ship cruise. Calibration was determined (i) to establish reflectance calibration factors between the radiometer and deck cell, (ii) to correct for solid angle response deviation of the deck cell from true cosine, and (iii) to correct bandwidth mismatch between each channel of the deck cell and radiometer¹⁷.

(i) Laboratory radiometric calibration of the deck cell and radiometer was carried out using a 1000 W (FEL) quartz halogen lamp referenced to a NIST standard. The deck cell was positioned 50 cm from the lamp and normally illuminated. For the radiometer, a Spectralon reflectance plaque was normally illuminated by the lamp 50 cm away and viewed by the radiometer at an angle of 45°.

(ii) The deck cell was corrected for solid angle response by first determining its angular response. The angular response of the deck cell was determined by normally illuminating its cosine collector with the lamp and rotating the deck cell from 0° to 90°, in both directions, with measurements taken in 5° increments. The solid angle response was then calculated by weighting with $2\pi \sin \theta d\theta$, where θ is the angle of incidence. Solid angle deviation from true cosine response could then be calculated. A set of correction factors for each waveband channel were then established for different downwelling angular sky distributions such as, overcast, uniform (constant radiance with zenith angle) and clear sky with solar zenith angles at 0°, 10°, 20°, 30°, 40°, 50°, 60°, 70° and 80°.

(iii) A correction factor for each waveband channel was determined to offset filter mismatch between the deck cell and radiometer. This factor includes correction in going from the laboratory calibration to outside under the differently weighted solar spectrum.

4. DATA DESCRIPTION AND ANALYSIS

Examples of both whitecap data and foam data generated by the bow wake of a moving ship have been described in detail elsewhere^{17,18}. The data presented here is from whitecaps acquired in the Gulf of Mexico, taken in April 1996 during a 21-day ship cruise on board the RV Malcolm Baldrige. The location was approximately 70 miles offshore from Cedar Key in the Apalachicola Bay (Florida). Water temperature was relatively warm (~16 - 17° C) with a number of cold fronts moving down off the continental mainland. This provided an unstable atmosphere with lower air temperatures (~12° C) and good winds (~12 m/s).

In Fig. 3(a) an example of a whitecap captured by the whitecap measurement system is shown as the whitecap comes into view of the radiometer and decays into thin foam. In fig. 3(b) the spectral profile of each sample point is shown.

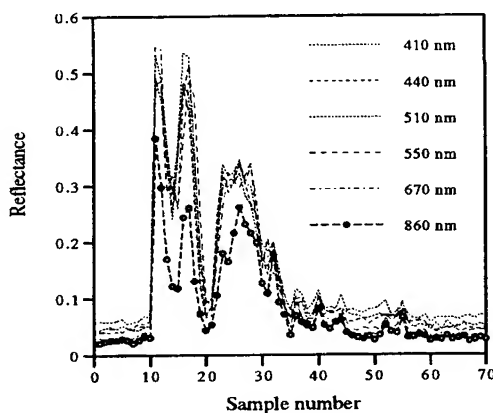


Fig. 3(a)

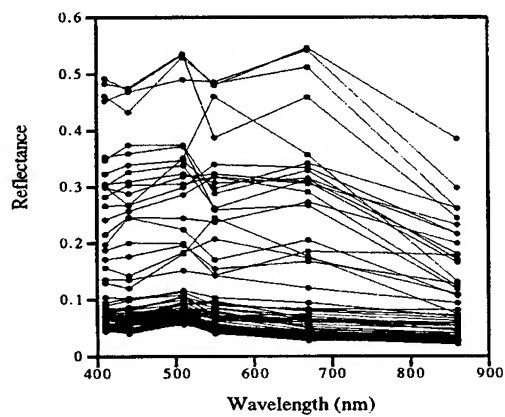


Fig. 3(b)

From Fig. 3(b) it is difficult to distinguish individual spectral profiles for foam types that correspond to different levels of reflectance. The situation is further complicated when large data sets are used in providing a good statistical base. To overcome this, the reflectance values of each sample point are grouped into reflectance intervals. The reflectance range (0 - 1.0) has been divided into 48 intervals; starting from 0 to 0.005 for the first level, and incrementing in 0.0025 reflectance steps up to 0.1. Between 0.1 and 1.0 the interval is incremented in 0.1 steps. The higher resolution step intervals between 0 and 0.1 have been implemented to provide information on the threshold between white water and foam free reflectance contributions. Any sample whose mean spectral value (mean value of the 6 wavebands) falls into a particular interval is added to any previous value. The number of spectra that fall into a particular interval is recorded and provides a record of the frequency of foam types (defined by reflectance value). The fractional coverage of a particular reflectance interval can be calculated by dividing the number of samples in an interval by the total number of samples taken.

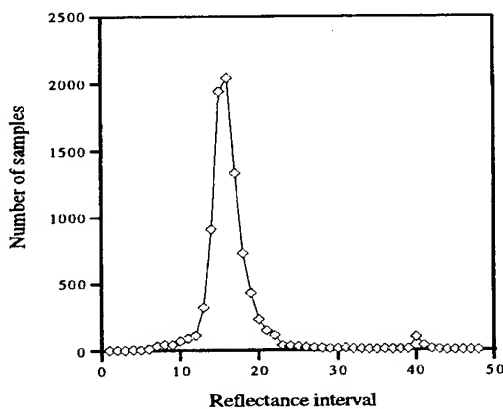


Fig. 4(a)

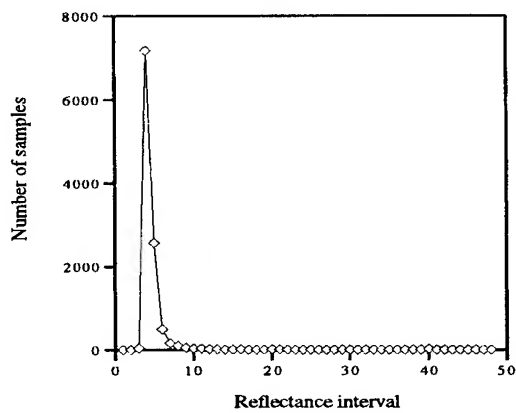


Fig. 4(b)

Fig. 4. (a) Distribution of reflectance samples for overcast sky conditions, and (b) distribution of reflectance samples for clear sky with 60° solar zenith angle.

In Fig. 4(a) and 4(b) the number of samples that contribute to different reflectance intervals is shown for large data sets (~10,000 samples). The histogram of number of samples vs. reflectance interval in Fig. 4(a) was taken during overcast sky conditions and in Fig. 4(b) for data acquired during clear sky conditions with solar zenith angle of 60°. The overcast condition produces a broader distribution with most samples occurring at a higher reflectance due to the greater contribution of Fresnel reflection of the diffuse sky from the water surface. In the clear sky case, the distribution about the peak is tighter and occurs at a lower reflectance interval.

As might be expected, the peak number of samples occurs from (predominantly) foam free water contributions. The white water contributions having a greater reflectance than the water, must occur at some

higher reflectance interval, but it is not immediately obvious. Also, a thin foam reflectance contribution can fall into a lower reflectance interval than a foam free contribution if it is shadowed by an adjacent wave. Likewise, a foam free facet of the water surface can reflect bright or dark patches of the sky. In both Figs. 4(a) and 4(b), the distributions represent a region where white water and foam free contributions overlap. As the choice of threshold is moved into higher reflectance intervals, the proportion of white water to non-white water contribution increases, but in doing so, the white water contribution may be underestimated by omitting the thinner foam reflectance contributions. Thin foam contributions, although having a very small augmented reflectance than thick dense foam from a freshly breaking wave, endure for a much longer period of time and as such are of great statistical importance. This inability to accurately define the threshold, inherently leaves estimates of fractional coverage and the augmented reflectance contribution prone to an error of a few percent¹⁸ (see below).

To calculate the augmented spectral reflectance contribution of a particular data set, a threshold reflectance interval must be chosen. The spectral reflectance values of the threshold interval are subtracted from the spectral reflectance values of every reflectance interval above the threshold. The resulting spectral profile from each interval is multiplied by its fractional coverage. This yields the individual augmented spectral reflectance contribution of each reflectance interval. By summing the individual augmented spectral reflectance contributions, the augmented spectral reflectance contribution is obtained.

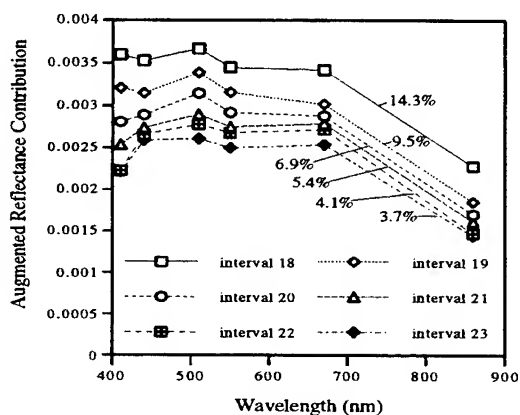


Fig. 5(a)

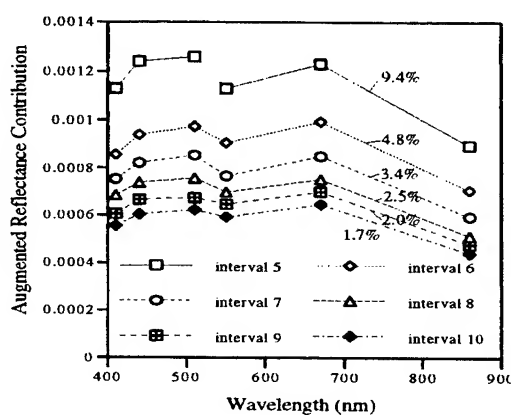


Fig. 5(b)

In Figs 5(a) and 5(b) the augmented spectral reflectance contribution fractional coverage is shown for the data acquired under overcast and clear sky (solar zenith angle 60°) conditions using different reflectance intervals as the threshold.

Figs. 5(a) and 5(b) were acquired under similar wind speeds (~11.86 m/s and 11.7 m/s respectively) although the sea state had become more fully developed in 5(b). The wind speed in 5(a) was gusting and variable and in 5(b) it was more constant. Air temperature had dropped from 16.2°C in 5(a) to 12°C in 5(b) with water temperature roughly 17°C -16.5°C respectively. Fig. 5(a) has a higher augmented reflectance contribution due to many small whitecaps whereas Fig. 5(b) has a lower augmented reflectance due to predominantly greater proportion of foam patches and less frequent but larger whitecaps.

As a higher reflectance threshold is chosen, the shape of augmented profile becomes more consistent. This is due to higher proportion of thicker foam types with higher reflectance and the estimate is more likely to exclude foam free reflectance contributions. In the overcast case, the spectral profile continues to change until it becomes relatively consistent, particularly threshold intervals 22 and 23. However, augmented spectral reflectance for threshold interval 21 and 20 may also contain a large proportion of thin foam types (and possibly a few foam free contributions) which have a less acute spectral profile than thick dense foam.

In 5(b) a similar spectral shape occurs with a relatively flat region over much of the visible with decreased reflectance at 410 and 860 nm. The drop off between 440 nm and 860 nm is not as great as in the overcast sky case due to a different sea state and type of wave breaking. There is also less augmented reflectance contribution for similar wind speed. For Fig. 5(a) many more whitecaps were visually observed than in the Fig. 5(b) data. In addition, the 670 nm and 860 nm values are relatively higher in the clear sky data due to a high solar zenith angle and the ability of the whitecap foam protruding above the water surface (and to a certain extent foam free waves) to reflect the yellow red glow of a low sun.

5. CONCLUSION

The whitecap measurement system has demonstrated its ability to measure the spectral reflectance of individual whitecaps as well as provide estimates of fractional coverage and the augmented spectral reflectance contribution. The accuracy of these estimates are limited by the choice of threshold between white water and non-white water events. In the presence of waves, the reflectances of a white water event and a non-white water event can overlap due to shadowing of an adjacent wave and can be further complicated by Fresnel reflection from the foam free water of a brighter or darker region of the sky. Even with a small incremental change in reflectance (0.0025), the choice of threshold can effect the estimate of fractional coverage and the augmented spectral reflectance by a few percent. However, even with a loose definition of threshold, the spectral profile appears consistent above a certain point but its shape can be influenced by sky conditions, solar zenith angle, sea state and direction of wave breaking with respect to the sun particularly at low sun angles. At the same time, since the choice of threshold can cover a range of possible candidates, any subtle spectral characteristics in the augmented spectral reflectance profile may have negligible impact in comparison to the greater inaccuracy in threshold choice.

6. ACKNOWLEDGMENTS

This research was funded by NASA / EOS - MODIS, Goddard Space Flight Center under contract #NAS5-31363. We would also like to thank Al Chapin for his help in the construction of the equipment. Also we would like to thank Dr. Rik Wanninkhof (NOAA/AOML), Dr. Gary Hitchcock (RSMAS / University of Miami) and the Captain and crew of the R/V Malcolm Baldrige for allowing us to participate in their oceanographic excursion.

7. REFERENCES

1. R.E. Payne., "Albedo of the Sea Surface," *Journal of Atmospheric Physics*. Vol. 29, pp. 959-970, 1972.
2. H.R. Gordon and M.M. Jacobs, "Albedo of the Ocean-Atmosphere System: Influence of Sea Foam," *Applied Optics*, Vol. 16, pp. 2257-2260, 1977.
3. G.A. Maul and H.R. Gordon, "On the Use of Earth Resources Technology Satellite (LANDSAT-1) in Optical Oceanography," *Remote Sensing Environment*, 4, 95 (1975).
4. P. Koepke, "Effective Reflectance of Oceanic Whitecaps," *Applied Optics*, Vol. 23, 1816-1824.
5. C.H. Whitlock, D.S. Bartlett, and E.A. Gurganus, "Sea Foam Reflectance and Influence on Optimum Wavelength for Remote Sensing of Ocean Aerosols," *Geophys. Res. Letters*, Vol. 9, pp 719-722, 1982.
6. R. Frouin, M. Schwindling and P. Deschamps, "Spectral Reflectance of Sea Foam in the Visible and Near Infrared: In Situ Measurements and Remote Sensing Implications," *J. of Geophys. Res.*, 1996.
7. Y. Miyake and T. Abe, "A study of the foaming of sea water," *J. Marine Res.*, 7, 67-73, 1948
8. E.C. Monahan and I.G. O'Muirceartaigh, "Whitecaps and the Passive Remote Sensing of the Ocean Surface", *Int. J. Remote Sensing* 7, 627-642, 1986.
9. V.J. Cardonne, "Specification of the wind field distribution in the marine boundary layer for wave forecasting," *Tech. Rep. GSL 69-1*, pp. 1-131, New York Univ, 1969.
10. E.C. Monahan and C.R. Zietlow, "Laboratory Comparisons of Freshwater and Salt-water Whitecaps", *J. Geophys. Res.*, 74, 6961-6966, 1969.
11. W.D. Garrett, "The Influence of surface-active material on the properties of air bubbles at the air / sea interface. Naval Research Lab., Rept. 6545, Washington, D.C., pp 14, 1967.
12. E.C. Monahan, "Oceanic whitecaps," *J. Phys. Oceanogr.*, Vol. 1, pp 139-144, 1971.
13. Y. Toba and M. Chaen, "Quantitative expression of the breaking of wind waves on the sea surface," *Rec. Oceanogr. Works Japan*, 12, pp. 1-11., 1973.
14. D.B. Ross and V.J. Cardonne, "Observations of oceanic whitecaps and their relation to remote measurements of surface wind speed," *J. Geophys. Res.*, Vol. 79, pp. 444-452. 1974.
15. J. Wu, "Oceanic whitecaps and sea state," *J. Phys. Oceanography*, Vol. 9, pp. 1064-1068, 1979.
16. E.C. Monahan and I.O'Muirceartaigh, "Optimal power-law description of oceanic whitecap coverage dependence on wind speed," *J. Phys. Oceanogr.*, Vol. 10, pp. 2094-2099, 1981.
17. K.D. Moore, K.J. Voss and H.R. Gordon, "Spectral reflectance of whitecaps: instrumentation, calibration and performance in coastal waters," To be submitted to *J. Marine and Atmos. Tech.*, Nov. 1996.
18. K.D. Moore, K.J. Voss and H.R. Gordon, "Spectral reflectance of whitecaps: fractional coverage and the augmented spectral reflectance contribution to water leaving radiance," To be submitted *J. of Geophys. Res.*, Nov. 1996.

Process Studies

A Decade of Interdisciplinary Process Studies

T. D. Dickey
Institute for Computational Earth System Science
University of California, Santa Barbara
Santa Barbara, CA 93106-3060

B.H. Jones
Department of Earth Sciences
University of Southern California
Los Angeles, CA 90089-0740

ABSTRACT

During the past decade, interdisciplinary process studies have been conducted in many regions of the world oceans. The focus of this review is on studies which have utilized new and emerging optical sensors and systems which have been deployed from multiple sampling platforms. These studies have led to increased understanding of ocean processes which are of interest for problems concerning 1) fundamental ocean optics, 2) remote sensing of the ocean, 3) the ocean's ecology and renewable resources, 4) the ocean's role in global climate change, and 5) pollution and its effects. Here we describe some of the methodologies which have enabled advances and provide brief summaries of a few studies in diverse geographical regions.

KEYWORDS: oceanography, interdisciplinary, regional, processes, technologies, optics, acoustics

1. INTRODUCTION

Interdisciplinary process studies have been conducted in several regions of the world oceans during the past decade. Regional studies allow oceanographers to focus on processes which are either unique to or more dominant in a given oceanic domain (e.g., equatorial waves, monsoons, coastally trapped waves, etc.). These studies have been motivated by interest in a host of ocean problems which can only be studied by combining the collective expertise of oceanographers from subdisciplines including physics, chemistry, and biology. The problems of interest involve a multiplicity of variables and span ten orders of magnitude in temporal and spatial scale.¹⁻³ Progress in understanding how the ocean functions as a dynamic system has been limited to a large degree by sampling capabilities. While many of the basic and larger scale physical and chemical processes are reasonably well understood, the physics and chemistry relevant to the smaller scales and individual organisms remain a challenge. It has become a well accepted notion that advancement of understanding of biological and optical processes requires concurrent, interdisciplinary sampling from a suite of platforms.³⁻⁵ Fortunately, major technological advances have been made in the areas of applied optics and acoustics along with data acquisition, storage, and telemetry.^{4,6} The various studies described herein have all benefited from emerging technologies. Problems of interest concern 1) fundamental ocean optics, 2) remote sensing of the ocean, 3) the ocean's ecology and renewable resources, 4) the ocean's role in global climate change, and 5) pollution and its effects. Some of the methodologies which have enabled advances are described herein and are illustrated through examples of a few studies in different geographical regions. Because of limited space, our review is by no means comprehensive; thus several important studies could not be treated. The reader is directed to other review papers and reports for further information.¹⁻¹²

2. METHODOLOGIES

Optical and acoustical sensors and systems have been developed for a variety of oceanographic applications over more than a decade. One of the more important motivations has been to develop *in situ* optical sensors which can be used to relate *in situ* water properties such as chlorophyll pigment concentration to upwelled water-leaving radiance measured by satellite- or airplane-based ocean color sensors.^{8,13,14} Another need is to determine light available for photosynthesis by phytoplankton, which is important for the ecology of and the carbon uptake by the ocean as well as heating effects.⁸ There is also increasing use of optical and acoustical measurements for pollution studies and monitoring.^{6,15,16} Presently available optical and

acoustical instruments can be used to sample organisms ranging in size from a few microns to meters virtually continuously.¹⁻³ Many of these are small enough to be deployed from shipboard profiling and towed packages, moorings, drifters, remotely operated vehicles (ROVs), and autonomous underwater vehicles (AUVs). The beam transmissometer (beam c at 660nm) and stimulated fluorometer have been used on CTD profilers, drifters, and moorings. Within the past few years, a new generation of spectral optical sensors and systems have been developed to measure both inherent and apparent optical properties spectrally.^{5,8} Several of these are designed to measure the same wavelengths as those of satellite color imagers (e.g., SeaWiFS). In addition, it may be possible to differentiate major taxa of phytoplankton using spectral signatures. One of the exciting aspects of these measurements is the potential for attaining optical closure.¹⁷ Spectral fluorometers with multiple excitation and emission wavelengths are now being used to attempt to characterize water constituents such as colored dissolved organic material.^{18,19} Other optical devices are designed to measure distributions of zooplankton. These include optical plankton counters which pass a sheet of light through a test volume to a detector and video plankton recorders which utilize video cameras.¹¹ Multi-frequency acoustical devices are being used to measure zooplankton and fish in size classes from about 100µm to a meter.^{21,22} Acoustic Doppler current profilers (ADCPs) can provide backscatter data relevant to limited size classes of zooplankton.^{20,22,23}

3. REGIONAL STUDIES

The study of Gulf Stream warm core rings was significant not only because of the importance of mesoscale dynamics, but also because some of the first profile measurements of apparent spectral radiation were made.^{24,25} Satellite measurements of sea surface temperature and color (Coastal Zone Color Scanner, CZCS) were obtained as well and thus enabled synoptic observations relevant to phytoplankton and optical properties of the upper ocean. The Biowatt program was conducted in the Sargasso Sea (34°N, 70°W) in 1985 and 1987 and dealt with variability of phytoplankton and optical properties including bioluminescence on time scales ranging from minutes to the seasonal cycle.^{13,25-28} Mooring time series measurements included several optical variables (e.g., chlorophyll fluorescence, beam attenuation, PAR, spectral radiation, etc.). Episodic phytoplankton blooms and busts were observed. The downward propagation of an inertial wave along a front resulted in an apparent increase in productivity as nutrients were entrained into the euphotic layer.²⁹ Smith et al.¹³ demonstrated the utility of moored measurements for developing color satellite algorithms. Using mooring data, Marra et al.²⁷ and Waters et al.²⁸ estimated virtually continuous primary productivity and Wiggert et al.³⁰ quantified the effect of temporal undersampling on primary productivity determinations. Although no color satellite imager was in orbit, Geosat altimetry data were valuable for interpretation of mooring data at the site which was subject to warm outbreaks and mesoscale features associated with the Gulf Stream.²⁶ The British have conducted several studies devoted to open ocean mesoscale features and associated local upwelling on the eastern side of the North Atlantic using towed systems (Sea Rover and SeaSoar) simultaneously with ADCP measurements.^{22,31} These studies have allowed quantification of scales of patchiness (primary at 100-300km and secondary between 10-20km) and associations between eddies and fronts with high concentrations of chlorophyll fluorescence. Other similar studies, but with even more optical sensors, have been conducted in this region with the Undulating Oceanographic Recorder.³² The U.S. JGOFS Bermuda Atlantic Time-series Study (BATS) was not specifically planned as a process studies program.³³ However, it has been effectively used to study a variety of phenomena including the seasonal evolution of the diffuse attenuation coefficient spectrum and colored dissolved material^{34,35} and the effects of the passage of Hurricane Felix.³⁶ The Marine Light in the Mixed Layer (MLML) program had many of the same objectives as the Biowatt program³⁷; however the setting was at a high latitude (south of Iceland: 59°N 21°W) in 1989 and 1991. The JGOFS North Atlantic Bloom Experiment (NABE) was conducted in 1989 with its most northern stations near the MLML site. This high latitude, dynamic location presented a major challenge for moored observations, but excellent bio-optical and physical time series were obtained along with shipboard profile and tow-yo data and P-3 aircraft overflight observations. The spring shoaling of the mixed layer was dramatic³⁸ (from ~550m to ~50m within 5 days). One of the interesting processes revealed from the mooring observations was the onset of a phytoplankton bloom (apparently associated with modest near surface stratification) prior to the major springtime shoaling of the mixed layer and the seasonal spring bloom. Furthermore, an increase of near surface temperature of 0.2°C was associated with the phytoplankton increase.³⁹ Spatial maps of physical and bio-optical variables were obtained using SeaSoar, tow-yo, and Paravane systems. The SeaSoar and Paravane were able to

map over hundreds of kilometers and demonstrated the importance of water mass variability and mesoscale eddies on bio-optical characteristics⁴⁰ (e.g., Washburn et al., in prep.). In addition, the Paravane obtained bioluminescence data throughout the upper 150m and showed that bioluminescence was quite patchy. The tow-yo results show much smaller scale features. During these observations, bio-optical characteristics were uniformly distributed within the mixed layer, but showed significant horizontal variability at scales less than 10km due to the interleaving of water masses within the region (Jones et al., in prep.). The Iceland-Faeroes front was studied in 1990 using simultaneous SeaSoar and ADCP observations by Roe and Griffiths²² and Roe et al.²³ These observations provided quantitative evidence of enhanced biomass near the front and its associated eddies along with associated large vertical water velocities and vertical migration of organisms.

The equatorial Pacific has been the subject of several international studies (e.g., JGOFS) in recent years. The region is especially interesting because of the high degree of variability associated with equatorial waves (Kelvin waves, Tropical Instability Waves or TIWs, etc.) and the global impact of the El Nino-Southern Oscillation (ENSO) phenomenon. The establishment of the Tropical Ocean-Global Atmosphere (TOGA) array of moorings in the equatorial waveguide has led to major advances in predicting El Ninos. One of the earliest mooring sites (0°, 140°W) was used for JGOFS and NOAA studies for an 18-month period (1992-1993) during which both El Nino and non-El Nino conditions prevailed.^{41,42} Moored optical measurements were used to produce high resolution (few minutes) time series of PAR, chlorophyll fluorescence, and primary productivity³⁰ (Foley et al., in prep.). These measurements revealed large variations in bio-optical properties and primary productivity which were likely associated with Kelvin waves and TIWs. In addition, drifters with radiometers were released at the mooring site and provided a Lagrangian view of increasing biomass with increasing distance from the equator as TIWs moved through the site. A dramatic "line in the sea" resulted in part from high concentrations of phytoplankton (*Rhizosolenia* sp., a buoyant diatom) north of the equator.⁴³ The line traced the northern edge of a TIW and was evident in measurements made from ship, aircraft, satellite, and Space Shuttle Atlantis. The biologically rich front was located between the colder, upwelled waters to the south and warmer less productive waters to the north.

One of the most recent process studies was conducted in the Arabian Sea as part of an international program (i.e., U.S. JGOFS and ONR, several other nations). An array of five moorings (50km square) was used to collect data spanning a year-long period, thus sampling both the northeast and southwest monsoons. The central mooring (15° 30'N, 61° 30'E), which included bio-optical moored sensors, was located under the climatological axis of the atmospheric Findlater Jet. Bi-annual mixed layer shoaling and deepening of the mixed layer was observed with associated phytoplankton bloom cycles.⁴⁴ One of the interesting results of this study was the observance of mesoscale features (e.g., filaments, eddies) of apparent coastal origin which influenced the mooring site roughly 550km away.^{45,46} SeaSoar surveys (Brink et al. and Jones et al., in prep.) were able to characterize these features with variability in physical and bio-optical properties on horizontal scales from 10km to a few hundred km. TOPEX Poseidon altimetry data and underway shipboard ADCP data also provided important information concerning mesoscale features for this energetic and biologically rich region. Finally, Roe et al.²³ have reported extreme biological layering (16 distinct layers in upper 350m) off of Oman based upon backscattering acoustic data, further illustrating the complexity of the Arabian Sea.

A comprehensive interdisciplinary ocean survey was conducted in the Bellingshausen Sea as part of the British Ocean Flux Study (BOFS) in the austral spring of 1992 by Weeks et al.⁴⁷ A SeaSoar equipped with bio-optical as well as physical sensors and a ship-mounted ADCP were used to quantify scales of variability and correlations among physical properties and currents and phytoplankton and zooplankton distributions. The study focused on a major frontal feature (67-68° 30'S and 84-88°W). Elevated phytoplankton and zooplankton concentrations were well correlated in the surface waters, a result which is not always found. The light field and chlorophyll distributions were important factors affecting zooplankton at greater depth. This study reinforced the need for concurrent sampling of physics and biology and the utility of ship-mounted ADCPs. Upcoming international studies in the Southern Ocean are to be conducted as contributions of JGOFS and GLOBEC.

The coastal ocean presents optical oceanographers with several interesting, though challenging, problems. For example, particulate and dissolved organic matter of terrestrial origin are important and biomass is typically more diverse and abundant. In addition, the physical scales of the coastal ocean are shorter, response to wind forcing is more rapid, and tides and surface waves are quite important. The west coast of the U.S. has been a region of many important interdisciplinary studies over the past decade. For example, the Coastal Transition Zone (CTZ) experiment examined the development of

filaments and eddies off of central California using satellite sensing, shipboard profiling, and towed systems.⁴⁸ In addition a drifter, equipped with bio-optical sensors, was deployed and recorded the evolution of biomass and optical properties as it drifted seaward.⁴⁹ Bio-optical observations provided some of the first hints of subduction processes that are associated with upwelling filaments.⁵⁰ Beam attenuation coefficient and chlorophyll maxima appeared well below the euphotic zone indicating that upper layer water was being transported downward as well as horizontally.⁵¹ Another major interdisciplinary sampling program, which employs new technologies, is underway in coastal waters off Monterey, California (Chavez et al). Optical methods have also been applied to pollution studies in the coastal zone. Off the coast of Los Angeles, one of the most severely impacted coastal regions in the U.S, optical sensors have been deployed from towed systems, moorings with telemetry, bottom tripods, airplane color scanners, and satellite imagers. These various platforms have been used to study how sewage outfall plumes disperse^{15,16} and how sediments are resuspended.⁵² The use of bio-optical data has allowed partitioning of water masses using beam attenuation and chlorophyll fluorescence as well as salinity and temperature relationships.^{15,16} The discovery of sediment resuspension resulting from near bottom internal solitary waves was possible because of high frequency optical sampling.⁵² An extension of the work off the Los Angeles coast has been conducted off Honolulu. In this study, a spectral absorption and attenuation meter, a stimulated spectral fluorometer (6 wavelengths of excitation and 16 wavelengths of emission), and a particle sizing instrument were used to study an outfall plume and to characterize the particle fields associated with both plume and ambient waters.¹⁹ The fate of continental shelf particulate matter (e.g., carbon) has been the subject of two major interdisciplinary experiments in the Middle Atlantic Bight off the east coast of the U.S.⁵³ The second of these, Shelf Edge Exchange Processes-II, was conducted in 1988 and 1989 and utilized moored ADCP and bio-optical systems (e.g., transmissometers and fluorometers). The general finding was that the major portion of primary production landward of the 90-m isobath was not transported seaward, negating the experiment's working hypothesis (at least for this study area⁵⁴). The time series data indicated that the phytoplankton and zooplankton concentrations were highly variable with a continuum of energy at all frequencies and generally low coherences between these variables and local physics.⁵⁵ The ONR Coastal Mixing and Optics (CMO) program is presently being conducted south of Martha's Vineyard, Massachusetts and should provide another important data set as a comprehensive suite of optical and physical measurements are being collected from several platforms. Interestingly, Hurricane Edouard passed over the site in September, 1996 and preliminary results show a major sediment resuspension event and large variations in optical properties. Other relevant east coast studies presently underway include the George's Bank GLOBEC experiment and the Ocean Margins Program off Cape Hatteras.

4. ACKNOWLEDGMENTS

Support for this work was provided to TD under ONR Grants N00014-96-1-0669 and N00014-96-1-0505, NSF Grant OCE-9627281, and NASA Grant NAGW-3949, and to BJ under ONR Grant N00014-94-0362 and NOAA Grant CE-2.

5. REFERENCES

1. T. Dickey, "Recent advances and future directions in multidisciplinary *in situ* oceanographic measurement systems," in *Toward a Theory on Biological and Physical Interactions in the World Ocean*, B. Rothschild (ed.), Kluwer Academic, Dordrecht, The Netherlands, 555-598 (1988).
2. T.D. Dickey, "Physical-optical-biological scales relevant to recruitment in large marine ecosystems," in *Large Marine Ecosystems: Patterns, Processes, and Yields*, K. Sherman, L.M. Alexander, and B.D. Gold (eds.), AAAS, Washington, DC, 82-98 (1990).
3. T. Dickey, "The emergence of concurrent high-resolution physical and bio-optical measurements in the upper ocean," *Rev. of Geophys.*, **29**, 383-413 (1991).
4. T. Dickey, T.C. Granata, and I. Taupier-Letage, "Automated *in situ* observations of upper ocean biogeochemistry, bio-optics, and physics and their potential use for global studies," in *Proc. of the Ocean Climate Data Workshop*, Goddard Space Flight Center, Greenbelt, MD, 317-353 (1993).
5. T. Dickey, A. Plueddemann, and R.A. Weller, "Current and water property measurements in the coastal ocean," *The Sea*, A. Robinson and K. Brink (eds.), in press (1996).
6. T. Dickey, R.H. Douglass, D. Manov, D. Bogucki, P.C. Walker, and P. Petrelis, "An experiment in duplex communication with a multivariable moored system in coastal waters," *J. Atmos. Ocean. Tech.*, **10**, 637-644 (1993).

7. K.L. Denman and T.M. Powell, "Effects of physical processes on planktonic ecosystems in the coastal ocean," *Ocean Mar. Biol. Ann. Rev.*, **22**, 125-168 (1984).
8. U.S. JGOFS Planning Report Number 18, "Bio-optics in U.S. JGOFS," T. Dickey and D. Siegel (eds.), 180pp. (1993).
9. U.S. GLOBEC Report Number 4, Workshop on Acoustical Technology and the Integration of Acoustical and Optical Sampling Methods," C. Greene, C. Greenlaw, V. Holliday, P. Ortner, R. Pieper, T. Stanton, and J. Traynor (eds.), 58pp. (1991).
10. U.S. GLOBEC Report Number 8, U.S. GLOBEC Workshop on Optics Technology," G. Paffenhofer and T.R. Osborn (eds.), 18pp. (1993).
11. SCOR, "Sampling and Observing Systems," *GLOBEC Report Number 3*, GLOBEC-International, T. Dickey (ed.), 99pp (1993).
12. SCOR, "An Advanced Modeling/Observational System (AMOS) for Physical-Biological-Chemical Ecosystem Research and Monitoring, a working paper/technical report prepared by GLOBEC.INT Working Groups on Numerical Modeling and Sampling and Observing Systems," *GLOBEC Report Number 3*, GLOBEC-International, A. Robinson and T. Dickey (eds.), (1996).
13. R.C. Smith, K.J. Waters, and K.S. Baker, "Optical variability and pigment biomass in the Sargasso Sea as determined using deep-sea optical mooring data," *J. Geophys. Res.*, **96**, 8665-8686 (1991).
14. J.L. Mueller and R.W. Austin, "Ocean optics protocols for SeaWiFS validation, *SeaWiFS Tech. Report Series*, NASA Tech. Mem. 104566, Goddard Space Flight Center, Greenbelt, MD, 43pp (1992).
15. B.H. Jones, A. Bratkovich, T. Dickey, G. Kleppel, A. Steele, R. Iturriaga, and I. Haydock, "Variability of physical, chemical, and biological parameters in the vicinity of an ocean outfall plume," in *Stratified Flows: Proc. Third Int. Symp. on Stratified Flows*, E.J. List and H.H. Jirka (eds.), ASCE, New York, 877-890 (1990).
16. L. Washburn, B.H. Jones, A. Bratkovich, T.D. Dickey, and M.-S. Chen, "Mixing, dispersion, and resuspension in vicinity of ocean wastewater plume," *J. Hydraul. Eng.*, **118**, 38-58 (1992).
17. W.S. Pegau, R.V. Zaneveld, and K.J. Voss, "Toward closure of the inherent optical properties of natural waters," *J. Geophys. Res.*, **100**, 13,193-13,221 (1995).
18. Coble, P.G., "Characterization of marine and terrestrial DOM in seawater using excitation-emission matrix spectroscopy, *Mar. Chem.*, **51**, 325-346 (1996).
19. A.A. Petrenko, B.H. Jones, T.D. Dickey, M. LeHaitre, and C. Moore, "Bio-optical characterization of the particle field in Mamala Bay, HI: effluent and naturally occurring particles, submitted to *J. Geophys. Res.*
20. S.L. Smith, R.E. Pieper, M.V. Moore, L.G. Rudstram, C.H. Greene, J.E. Zanon, C.M. Flagg, and C.E. Williamson, "Acoustic techniques for the *in situ* observations of zooplankton," *Archiv. fur Hydro-biologie Ergebnisse der Limnologie*, **36**, 23-43 (1992).
21. D.V. Holliday and R.E. Pieper, "Bioacoustical oceanography at high frequencies," in *Zooplankton Production*, Proc. of a Symp. held in Plymouth, England, R. Harris (ed.), *ICES J. of Mar. Sci.*, **52**, 279-296 (1995).
22. H.S.J. Roe and G. Griffiths, "Biological information from an acoustic Doppler current profiler," *Mar. Biol.*, **115**, 339-346 (1993).
23. H.S.J. Roe, G. Griffiths, M. Hartman, and N. Crisp, "Variability in biological distributions and hydrography from concurrent acoustic Doppler current profiler and SeaSoar surveys," *ICES J. of Mar. Sci.*, **53**, 131-138 (1996).
24. R.C. Smith and K.S. Baker, "Spatial and temporal patterns in pigment biomass in Gulf Stream warm-core ring 82B and its environs," *J. Geophys. Res.*, **90**, 8859-8870 (1985).
25. T. Dickey, J. Marra, T. Granata, C. Langdon, M. Hamilton, J. Wiggert, D. Siegel, and A. Bratkovich, "Concurrent high resolution bio-optical and physical time series observations in the Sargasso Sea during the spring of 1987," *J. Geophys. Res.*, **96**, 8643-8663 (1991).
26. T. Dickey, T. Granata, J. Marra, C. Langdon, J. Wiggert, Z. Chai-Jochner, M. Hamilton, J. Vazquez, M. Stramska, R. Bidigare, and D. Siegel, "Seasonal variability of bio-optical and physical properties in the Sargasso Sea," *J. Geophys. Res.*, **98**, 865-898 (1993).
27. J. Marra, T. Dickey, W.S. Chamberlin, C. Ho, T. Granata, D.A. Kiefer, C. Langdon, R. Smith, K. Baker, R. Bidigare, and M. Hamilton, "The estimation of seasonal primary production from moored optical sensors in the Sargasso Sea," *J. Geophys. Res.*, **97**, 7399-7412 (1992).
28. K.J. Waters, R.C. Smith, and J. Marra, "Phytoplankton production in the Sargasso Sea as determined using optical mooring data, *J. Geophys. Res.*, **99**, 18,385-18,402 (1994).
29. T.C. Granata, J. Wiggert, and T. Dickey, "Trapped, near-inertial waves and enhanced chlorophyll distributions," *J. Geophys. Res.*, **100**, 20,793-20,804 (1995).

30. J. Wiggert, T. Dickey, and T. Granata, "The effect of temporal undersampling on primary production estimates," *J. Geophys. Res.*, **99**, 3361-3371 (1994).
31. V.H. Strass, "Chlorophyll patchiness caused by mesoscale upwelling at fronts," *Deep-Sea Res.*, **39**, 23-43 (1992).
32. J. Aiken and I. Bellan, "Synoptic optical oceanography with the undulating oceanographic recorder," *Proc. SPIE-Int. Soc. Opt. Eng.*, **637**, 221-230 (1986).
33. A.F. Michaels and A.H. Knap, "Overview of the U.S. JGOFS Bermuda Atlantic Time-series Study," *Deep-Sea Res. II*, **43**, 157-198 (1996).
34. D.A. Siegel, A.F. Michaels, J.C. Sorensen, M. O'Brien, and M.A. Hammer, "Seasonal variability of light availability and utilization in the Sargasso Sea," *J. Geophys. Res.*, **100**, 8675-8713 (1995).
35. D.A. Siegel and A.F. Michaels, "Quantification of non-algal light attenuation in the Sargasso Sea: implications for biogeochemistry and remote sensing," *Deep-Sea Res. II*, **43**, 321-345 (1996).
36. T. Dickey, D. Frye, J. McNeil, D. Manov, N. Nelson, D. Sigurdson, H. Jannasch, D. Siegel, T. Michaels, and R. Johnson, "Upper ocean temperature response to Hurricane Felix as measured by the Bermuda Testbed Mooring, submitted to *Mon. Wea. Rev.* (1996).
37. J. Marra, "Marine bioluminescence and upper ocean physics: seasonal changes in the northeast Atlantic," *Oceanography*, **2**, 36-38 (1989).
38. T. Dickey, J. Marra, M. Stramska, C. Langdon, T. Granata, A. Plueddemann, R. Weller, and J. Yoder, "Bio-optical and physical variability in the subarctic North Atlantic Ocean during the spring of 1989," *J. Geophys. Res.*, **99**, 22,541-22,556 (1994).
39. M. Stramska and T.D. Dickey, "Phytoplankton bloom and the vertical thermal structure of the upper ocean," *J. Mar. Res.*, **51**, 819-842 (1993).
40. D.G. Ondercin, C.A. Atkinson, and D.A. Kiefer, "The distribution of bioluminescence and chlorophyll during the late summer in the North Atlantic: maps and a predictive model," *J. Geophys. Res.*, **100**, 6575-6590 (1995).
41. J.W. Murray, E. Johnson, and C. Garside, "A U.S. JGOFS Process Study in the equatorial Pacific (EqPac): introduction," *Deep-Sea Res. II*, **42**, 275-293 (1995).
42. W.S. Kessler and M.J. McPhaden, "The 1991-1993 El Nino in the central Pacific," *Deep-Sea Res. II*, **42**, 295-333 (1995).
43. J.A. Yoder, S.G. Ackleson, R.T. Barber, P. Flament, and W.M. Balch, "A line in the sea," *Nature*, **371**, 689-392 (1994).
44. D.L. Rudnick, R.A. Weller, C.C. Eriksen, T.D. Dickey, J. Marra, and C. Langdon, "One-year moored observations of the Arabian Sea monsoons," submitted to *EOS* (1996).
45. D.E. Sigurdson, T.D. Dickey, and D. Manov, "Arabian Sea Mooring Data Report," *Univ. of Calif., Santa Barbara Ocean Physics Laboratory Tech. Rep. OPL-2-95*, 26pp (1995).
46. D.E. Sigurdson, T.D. Dickey, and D. Manov, "Arabian Sea Mooring Data Report," *Univ. of Calif., Santa Barbara Ocean Physics Laboratory Tech. Rep. OPL-2-96*, 26pp (1996).
47. A.J. Weeks, G. Griffiths, H. Roe, G. Moore, I.S. Robinson, A. Atkinson, and R. Schreeve, "The distribution of acoustic backscatter from zooplankton compared with physical structure, phytoplankton, and radiance during the spring bloom in the Bellingshausen Sea," *Deep-Sea Res.*, **42**, 997-1019 (1995).
48. K.H. Brink and T.J. Cowles, "The Coastal Transition Zone Program," *J. Geophys. Res.*, **96**, 14,637-14,648.
49. M.R. Abbott, K.H. Brink, C.R. Booth, D. Blasco, L.A. Codispoti, P.P. Niiler, and S.R. Ramp, "Observations of phytoplankton and nutrients from a Lagrangian drifter off northern California," *J. Geophys. Res.*, **95**, 9393-9409 (1990).
50. B.H. Jones, C.N.K. Mooers, M. Reinecker, T. Stanton, and L. Washburn, "Chemical and biological structure of a cool filament observed off northern California in July 1986 (OPTOMA21)," *J. Geophys. Res.*, **96**, 22,207-22,225 (1991).
51. L. Washburn, D.C. Kadko, B.H. Jones, T. Hayward, P.M. Kosro, T.P. Stanton, S. Ramp, and T. Cowles, "Water mass subduction and the transport of phytoplankton in a coastal upwelling system," *J. Geophys. Res.*, **96**, 14,927-14,946 (1991).
52. D. Bogucki, T. Dickey, and L.G. Redekopp, "Sediment resuspension and mixing by resonantly-generated internal solitary waves," *J. Phys. Oceanogr.*, in press (1996).
53. P.E. Biscaye, C.N. Flagg, and P.G. Falkowski, "The Shelf Edge Exchange Processes experiment, SEEP-II: an introduction to hypotheses, results, and conclusions," *Deep-Sea Res. II*, **41**, 231-252 (1994).
54. C.D. Wirick, "Exchange of phytoplankton across the continental shelf-slope boundary of the Middle Atlantic Bight during spring 1988," *Deep-Sea Res. II*, **41**, 391-410 (1994).
55. C.N. Flagg, C.D. Wirick, and S.L. Smith, "The interaction of phytoplankton, zooplankton, and currents from 15 months of continuous data in the Mid-Atlantic Bight," *Deep-Sea Res. II*, **41**, 411-435 (1994).

Observations of a *Synechococcus*-dominated cyclonic eddy in open-oceanic waters of the Arabian Sea

Robert R. Bidigare and Mikel Latasa

Department of Oceanography, University of Hawai'i, Honolulu, HI 96822

Zachary Johnson and Richard T. Barber

Marine Laboratory, Duke University, 135 Duke Marine Lab Road, Beaufort, NC 28516-9721

Charles C. Trees

Center for Hydro-Optics & Remote Sensing, San Diego State University, San Diego, CA 92120-5005

William M. Balch

Bigelow Laboratory for Ocean Sciences, PO Box 475, McKown Point, W. Boothbay Harbor, ME 04575

ABSTRACT

The optical, chemical and biological characteristics of a cyclonic eddy were investigated in the Arabian Sea during November 1995. This eddy was 3,000 km² in area and located 350 km offshore of the coast of Oman. The mixed layer of this feature extended to a depth of 17 m, below which oxygen concentrations were depleted to 10% of surface values. Chlorophyll *a* concentrations within the mixed layer averaged 1.7 mg m⁻³. Microscopic observations and flow cytometric measurements revealed that the algal community was dominated by the coccoid cyanobacterium *Synechococcus*. Detailed pigment analyses documented additional phytoplankton biomass contributions by *Prochlorococcus*, diatoms, dinoflagellates, prymnesiophytes, cryptophytes, chlorophytes and pelagophytes. This algal community caused a marked attenuation of the blue to bluegreen wavelengths of light, resulting in a preferential transmittance of green light with increasing depth. Measurements of photosynthetic performance and the spectral absorption coefficient document that the phytoplankton community was photo- and chromatically-adapted to the light environment within the eddy. The results of this field work support a previous laboratory study which found that the nonphotosynthetic carotenoid zeaxanthin produces significant decreases in the maximum quantum yield of photosynthesis of the marine cyanobacterium *Synechococcus*.

Keywords: Arabian Sea, cyclonic eddy, *Synechococcus*, chlorophylls, carotenoids, zeaxanthin, phycoerythrin, quantum yield, photosynthesis, spectral irradiance

1. INTRODUCTION

Process cruise 6 of the U.S. Joint Global Ocean Flux Study (JGOFS) Arabian Sea project was designed to characterize the biological and optical variability associated with hydrographic features of the northern Indian Ocean. The specific goals of the cruise were to (i) sample unique phytoplankton communities associated with hydrographic anomalies; (ii) characterize the optical properties of these phytoplankton; and (iii) assess how these optical properties would affect remotely-sensed ocean color. As a primary tool, we used real-time Advanced Very High Resolution Radiometer (AVHRR) imagery to locate fronts and eddies for direct observation aboard the R/V *Thomas G. Thompson*. This cruise was performed during November 1995, a period which followed the southwest monsoon. A cold core eddy located in the western Arabian Sea was present in the AVHRR imagery throughout the duration of the cruise. This feature was also detected using a towed Undulating Oceanographic Recorder (UOR) and shipboard multivariable along-track sensing system. This report highlights the bio-optical and photo-physiological observations performed within this cyclonic eddy feature.

2. METHODOLOGY

An extensive set of bio-optical measurements were made within a cold core eddy sampled on 23 November 1995 during cruise TTN-053 of the R/V *Thomas G. Thompson*. *In situ* spectral irradiance measurements (405, 410, 442, 489, 508, 555 and 666 nm) were performed using a Biospherical Instruments MER 2040 spectroradiometer. Chlorophyll and carotenoid concentrations were determined by high-performance liquid chromatography (HPLC).¹ Spectral phytoplankton absorption coefficients were measured using the filter pad method.² Resulting spectra were corrected for pathlength amplification using the coefficients published for *Synechococcus*.³ Absorption contributions by nonphotosynthetic carotenoids were determined by spectral reconstruction.⁴ Photosynthesis vs. irradiance (P vs. E) responses were measured using a photosynthetron.⁵

3. RESULTS

The cyclonic eddy was located near 18.3°N, 60.3°E, approximately 350 km off the coast of Oman. This study site was designated as Station 25. The eddy was 3,000 km² in area and had a mixed layer depth

Table 1. Photosynthetic parameters of phytoplankton sampled at Station 25 (α = mg C mg Chl⁻¹ hr⁻¹ (μ Ein m⁻² s⁻¹)⁻¹; P_{\max} = mg C mg Chl⁻¹ hr⁻¹; E_k = μ Ein m⁻² s⁻¹; and a_{ph} *, a_{ph-npc} * = m² mg Chl⁻¹).

Depth (%E ₀)	α	P_{\max}	E_k	a_{ph} *	a_{ph-npc} *
3 m (75%)	0.040	13.6	340	0.022	0.018
11 m (15%)	0.040	10.8	275	0.019	0.015
17 m (1%)	0.087	6.9	80	0.048	0.037

Table 2. Maximum quantum yield of photosynthesis (Φ_{\max} , mol C Ein⁻¹) calculated for phytoplankton with (Φ_{+npc}) and without (Φ_{-npc}) absorption contributions by nonphotosynthetic carotenoids.

Depth (%E ₀)	Φ_{+npc}	Φ_{-npc}	$\Phi_{-npc} / \Phi_{+npc}$
3 m (75%)	0.041	0.052	1.25
11 m (15%)	0.049	0.060	1.22
17 m (1%)	0.042	0.054	1.29
Mean (n = 3)	0.044	0.055	1.25

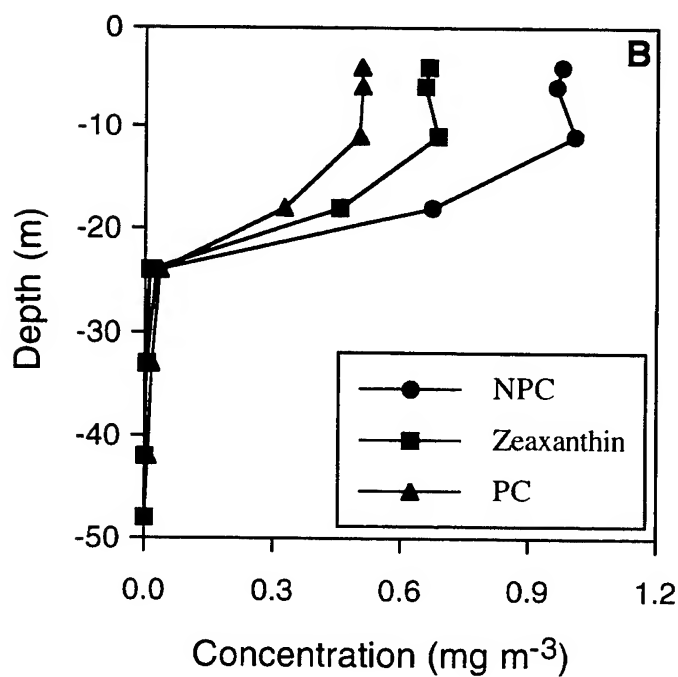
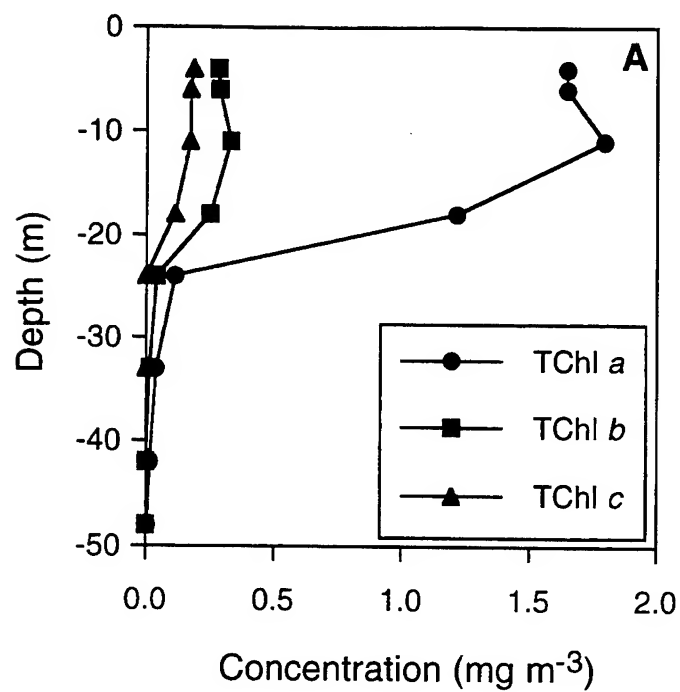


Fig. 1. Distributions of algal pigments within the cyclonic eddy sampled at Station 25: (A) total chlorophyll *a*-related pigments (TChl *a*), total chlorophyll *b*-related pigments (TChl *b*), and total chlorophyll *c*-related pigments (TChl *c*) and (B) total nonphotosynthetic carotenoids (NPC), zeaxanthin, and total photosynthetic carotenoids (PC).

of 17 m. The mixed layer temperature of this feature averaged 26.15°C and the depth of the euphotic zone (i.e. 1% $E_d(0^-, 400-700 \text{ nm})$) coincided with the base of the mixed layer. Nitrate, nitrite, ammonium, phosphate and silicate concentrations averaged 0.3, 0.1, 0.1, 0.6 and 3.7 μM , respectively, in the mixed layer. Nutrient levels were apparently sufficient to support a large phytoplankton crop as the concentration of total chlorophyll *a*-related pigments averaged 1.7 mg m^{-3} in near surface waters (Fig. 1A). Direct microscopic observations and flow cytometric analyses revealed that this algal community was dominated by *Synechococcus* spp. Concentrations of chlorophyll *b*- and chlorophyll *c*-related pigments were low and the nonphotosynthetic carotenoids were dominated by zeaxanthin (Fig. 1B). This pigmentation pattern is consistent with that determined for *Synechococcus*.⁶ Mass balance calculations suggest that *Synechococcus* accounted for approximately 40% of the particulate organic carbon (POC) and 70% of the chlorophyll *a* in the mixed layer of Station 25. HPLC pigment analyses documented additional pigment biomass contributions by *Prochlorococcus*, diatoms, dinoflagellates, prymnesiophytes, cryptophytes, chlorophytes and pelagophytes. This algal community caused a marked attenuation of the blue to bluegreen wavelengths of light, resulting in a preferential transmittance of green light with increasing depth. (Fig. 2).

Phytoplankton absorption and photosynthetic properties were made at depths corresponding to the 75%, 15% and 1% light levels. The phytoplankton absorption spectra show a number of distinct features including the presence of phycoerythrobilin (PEB)-rich phycoerythrin (PE) and large absorption contributions by nonphotosynthetic carotenoids (Fig. 3). As mentioned above, this class of pigments was dominated by zeaxanthin. The spectrally weighted phytoplankton absorption coefficient determined for the

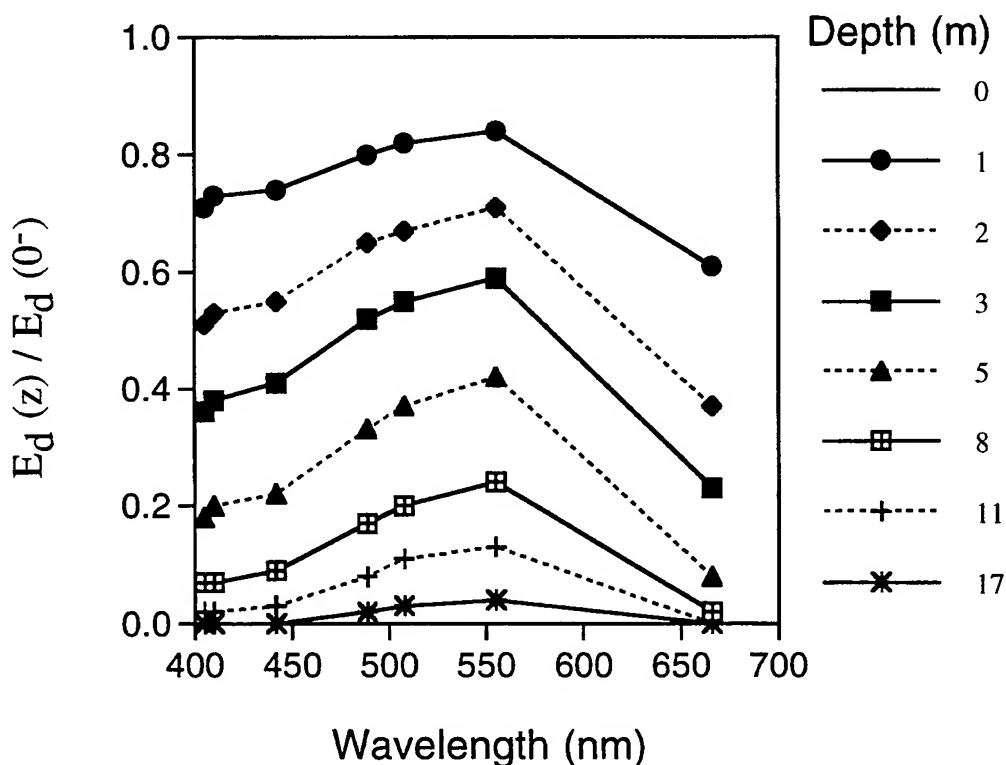


Fig. 2. Distributions of spectral irradiance measured within the cyclonic eddy sampled at Station 25. Values are normalized to those measured just below the sea surface.

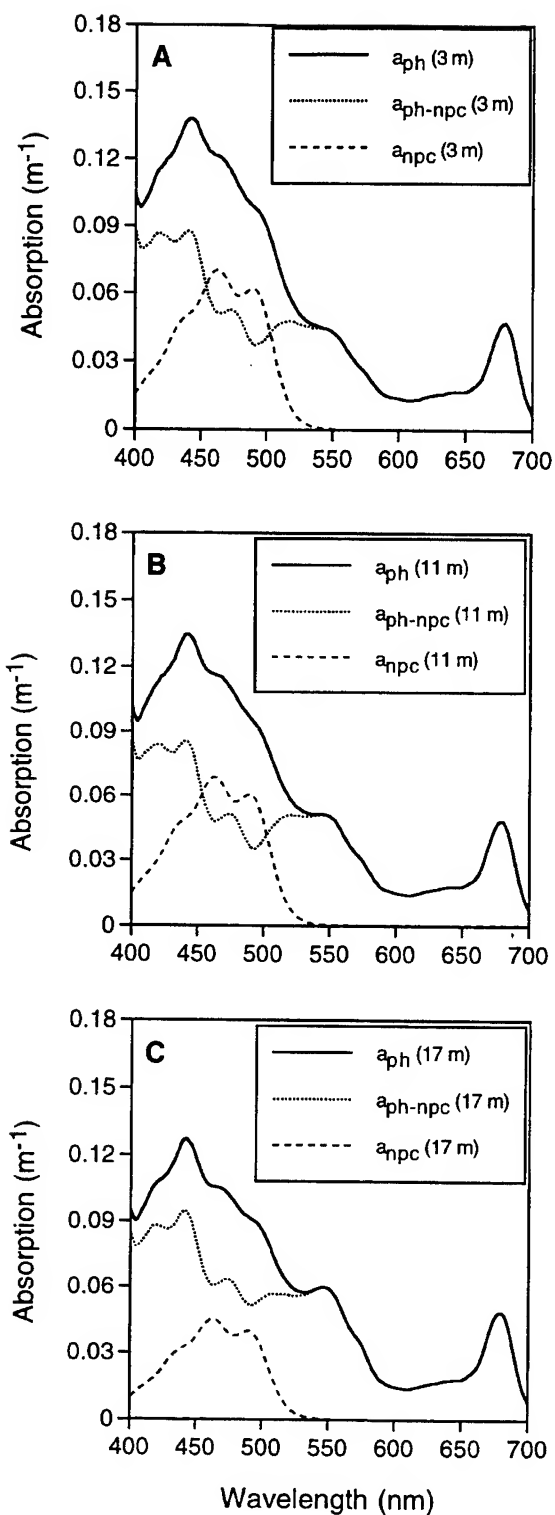


Fig. 3. Spectral absorption coefficients determined for phytoplankton used in the P vs. E measurements: (A) 3 m, (B) 11 m, and (C) 17 m (solid line = total phytoplankton absorption coefficient, dashed line = reconstructed absorption coefficient for nonphotosynthetic carotenoids, and dotted line = total absorption minus contributions by nonphotosynthetic carotenoids).

P vs. E incubations ranged from 0.019 to 0.048 m² mg Chl⁻¹ (Table 1). Most of this variability resulted from differences in light quality used in the photosynthetrons and produced corresponding variations in the rate of light limited photosynthesis (α). The saturation parameter for photosynthesis (E_k) also decreased with increasing depth and varied 4-fold within the "mixed layer." The rate of light saturated photosynthesis (P_{max}) also decreased with increasing depth and the value determined at 17 m was half that measured at 3 m (Table 1). The latter results strongly suggest that the phytoplankton sampled at Station 25 were photoadapted to the ambient light environment within the "mixed layer." The presence of PEB-rich PE further documents that this algal community was chromatically adapted to the green-enriched growth irradiances found within the euphotic zone of Station 25 (Figs. 2 and 3).

The P vs. E responses and corresponding absorption spectra were used to calculate the maximum quantum yield of photosynthesis (Φ_{max} , mol C Ein⁻¹) for phytoplankton sampled within the eddy. The resulting quantum yield values did not appear to vary in a depth-dependent fashion and averaged 0.044 mol C Ein⁻¹ (Table 2). Exclusion of absorption contributions by nonphotosynthetic carotenoids resulted in a 1.25-fold increase in Φ_{max} (mean = 0.055 mol C Ein⁻¹, Table 2).

4. SUMMARY

A *Synechococcus*-dominated phytoplankton bloom significantly altered the optical and chemical properties of a cyclonic eddy sampled in the Arabian Sea. The phytoplankton community was photo- and chromatically-adapted to the light environment within the eddy. Photoadaptation, as evidenced by depth-dependent variations in P_{max} , occurred on time-scales which were faster than that associated with upper ocean mixing. The presence of high concentrations of nonphotosynthetic carotenoids caused a 20% reduction in the maximum quantum yield of photosynthesis. The results of this field work support a previous laboratory study⁶ which found that the nonphotosynthetic carotenoid zeaxanthin produces significant decreases in the maximum quantum yield of photosynthesis for the marine cyanobacterium *Synechococcus*.

5. ACKNOWLEDGMENTS

We gratefully acknowledge R. Arnone (Stennis Space Center); M. Pinkerton and J. Aiken (Plymouth Marine Laboratory); L. Codispoti (Old Dominion University); D. Hansell and R. Parsons (Bermuda Biological Station for Research); H. Ducklow (Virginia Institute of Marine Science) and R. Olson (Woods Hole Oceanographic Institution) for generously providing complementary data. We also wish to thank the captain, crew and scientific personnel of the R/V *Thomas G. Thompson* for their valuable assistance during the cruise. This research was supported by NASA grant NAGW-3439 (RRB) and NSF grant OCE-9311312 (RRB). This is U.S. JGOFS Contribution No. 339.

6. REFERENCES

1. M. Latasa, R.R. Bidigare, M.E. Ondrusek, and M.C. Kennicutt II, "HPLC analysis of algal pigments: A comparison exercise among laboratories and recommendations for improved analytical performance," *Mar. Chem.* **51**, 315-324 (1996).
2. M. Kishino, M. Takahashi, N. Okami, and S. Ichimura, "Estimation of the spectral absorption coefficients of phytoplankton in the sea," *Bull. Mar. Sci.* **37**, 634-642 (1985).
3. L.R. Moore, R. Goericke, and S.W. Chisholm, "Comparative physiology of *Synechococcus* and *Prochlorococcus*: Influence of light and temperature on growth, pigments, fluorescence and absorptive properties," *Mar. Ecol. Prog. Ser.* **116**, 259-275 (1995).
4. R.R. Bidigare, M.E. Ondrusek, J.H. Morrow, and D.A. Kiefer, "In vivo absorption properties of algal pigments," *Proc. SPIE Ocean Opt. X* **1302**, 290-302 (1990).
5. S.T. Lindley, R.R. Bidigare, and R.T. Barber, "Phytoplankton photosynthesis parameters along 140°W in the equatorial Pacific," *Deep-Sea Res. II* **42** (2/3), 441-463 (1995).
6. R.R. Bidigare, O. Schofield, and B.B. Prézelin, "Influence of zeaxanthin on quantum yield of photosynthesis of *Synechococcus* clone WH7803 (DC2)," *Mar. Ecol. Prog. Ser.* **56**, 177-188 (1989).

Chuanmin Hu, Kenneth J. Voss

Department of Physics, University of Miami
Coral Gables, FL 33124

ABSTRACT

Solar Fraunhofer lines are used as indicators of the inelastic light scattering in the sea water. Data from both in-shore and off-shore are presented and compared with results of theoretical modeling. Very good agreement is found between the modeled and measured proportion of inelastic to elastically scattered and direct light at 589nm when the Raman scattering coefficient of Marshall and Smith¹ (1990) (0.00026m^{-1}) is used, as opposed to that of Slusher and Derr² (1975) (0.00078m^{-1}). At 656nm the agreement is not as good, indicating possible interference from other sources such as Chlorophyll fluorescence. Recent work has extended the measurements to include smaller absorption lines, such as 689nm, where significant filling has been measured at the surface due to the Chlorophyll fluorescence. This technique allows the natural fluorescence to be measured, even at the surface where there is still a significant amount of direct solar light.

Key words: Fraunhofer lines, Raman scattering, Chlorophyll fluorescence.

1. INTRODUCTION

Inelastic light scattering plays a very important role in the underwater light field distribution^{1,3,4} and has an influence on the remote sensing signal in the visible⁵ as well. Three main processes are involved in the underwater inelastic light scattering: Raman scattering, fluorescence of chlorophyll a and other phytoplankton pigments^{6,7}, and dissolved organic matter (DOM) fluorescence⁷. Among them, Raman scattering by water molecules typically has a wavenumber shift of 3347 cm^{-1} and a widely accepted value $2.6 \times 10^{-4}\text{m}^{-1}$ for total scattering cross section with 488nm excitation, and has been simulated well using the radiative transfer model^{8,9}; chlorophyll a fluorescence has long been known to contribute to the light field in the 685nm region, while DOM fluorescence is a broad band emission that varies with both the nature and the concentration of the fluorescing compounds⁷.

Direct measurement of inelastic light scattering in natural waters was not found in literature until 1992, when a system with very high spectral resolution ($0.008\text{nm}/\text{CCD pixel}$) was built and solar Fraunhofer lines were used to separate the elastic and inelastic light¹⁰. The basic idea is to measure the spectral irradiance (downwelling E_d or upwelling E_u) at Fraunhofer wavelengths both at the sea surface and in-water, and find out how much the absorption line depth varies (Fig.1). Two parameters, η , which is the ratio of line peak to background, and equivalent width (w), which is the area of line peak divided by background, are used to describe the portion of inelastic light in the total light field:

$$\eta = \frac{E(\lambda_f)}{E_b(\lambda_f)} \quad (1)$$

$$w = \int_{\lambda_1}^{\lambda_2} \left[1 - \frac{E(\lambda)}{E_b(\lambda)} \right] d\lambda \quad (2)$$

where $E(\lambda)$ is the spectral irradiance, $E_b(\lambda)$ is the background irradiance, λ_1 and λ_2 are the starting and ending points of the Fraunhofer line, λ_f is the line peak wavelength (fig. 1a). Thus, at depth z , the ratio of inelastically scattered irradiance to total irradiance, and the ratio of direct transmitted and elastically scattered irradiance to total irradiance, are derived as:

$$\frac{E_{in}(z)}{E_t(z)} = \left(1 - \frac{w(z)}{w_0} \right) \quad (3)$$

$$\frac{E_{el}}{E_t} = \frac{w(z)}{w_0} \quad (4)$$

where $w(z)$ and w_0 are equivalent widths at depth and surface, respectively (fig. 1b).

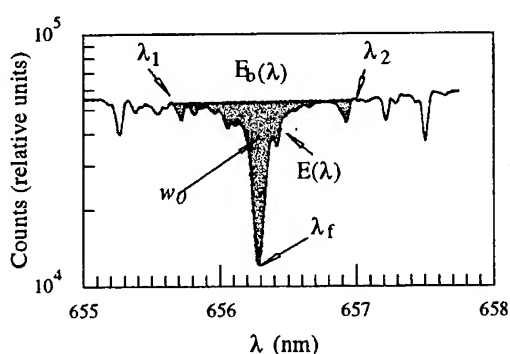


Fig. 1a. Fraunhofer line at 656nm. $E_b(\lambda)$ is the background from λ_1 to λ_2 and the peak wavelength λ_f is 656.28nm. The equivalent width (w) is the shaded area divided by the background.

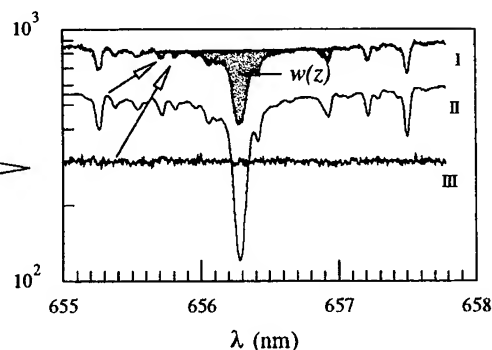


Fig. 1b. Fill-in of the Fraunhofer line. The inelastically scattered light III is added to the direct transmitted and elastically scattered light II (1% of fig. 1a), resulting in I which has a line fill-in.

Figure 1. Fraunhofer line shape at 656nm and the line filling features.

The same technique is used in this paper except that the system is rebuilt to improve its performance. Experiments show that w is a better parameter than η since w is resolution independent and does not depend only on a single point. A least square fitting procedure is used to "clean" any noisy spectra (Fig. 2). Also presented here is the data collected from both off-shore and in-shore waters. Since there is no Fraunhofer line around the 685nm region, smaller absorption lines at 689nm (Fig. 3) caused by oxygen in the atmosphere are used to detect the chlorophyll a fluorescence. This is shown to be a promising technique to measure the natural chlorophyll fluorescence.

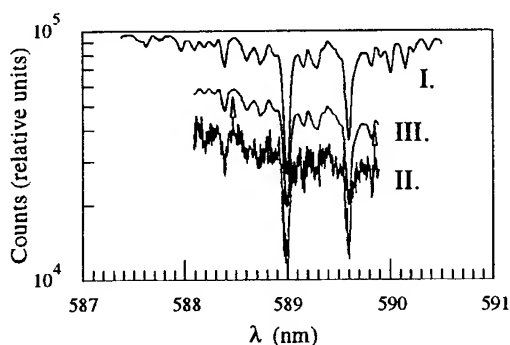


Figure 2. Fraunhofer line at 589nm. I: line at surface; II: line at depth (noisy); III: fitted from II using I as a template.

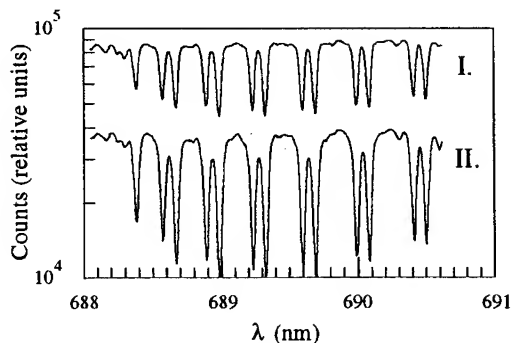
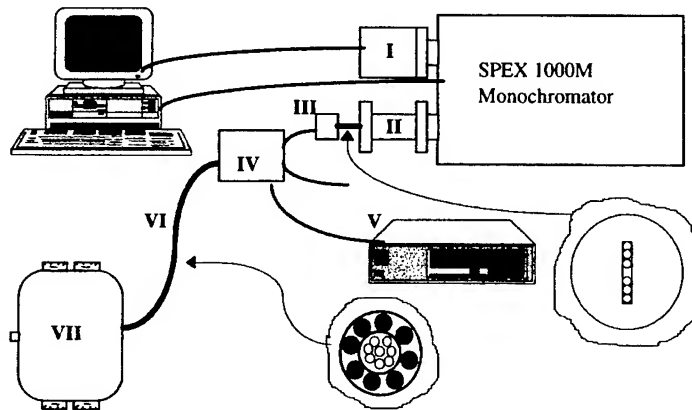


Figure 3. Oxygen absorption line at 689nm. I: measured at 1:13pm with 30s exposure time; II: measured at 6:13pm with 60s exposure time.

2. INSTRUMENTATION AND DATA ACQUISITION

The original Fraunhofer line system described elsewhere¹⁰ has been rebuilt and improved. First, since a single, unprotected fiber is very fragile and not capable of taking measurements during harsh conditions on a cruise (in fact it was broken at least once each time it was on a cruise), a fiber bundle protected by a metal shield together with eight wire conductors is used instead (Fig. 4, part VI). We have the following components built into the instrument head (Fig. 4): two fiber optic cosine irradiance collectors (downwelling and upwelling) for the light input to the monochromator, two cosine

irradiance collectors for photocell detectors which are used to monitor the overall downwelling and upwelling irradiance level, and a depth transducer. Eight 100 μ m core size all silica fibers are used to transmit the light from the two cosine collectors, with four in each one. Only 6 of the 8 fibers are used to measure the Fraunhofer line spectra, the remaining 2 can monitor the overall spectra for the whole visible band. However, they are not used now. A 512x512 TE cooled CCD camera is used to record the spectra. Such a configuration enables us to measure downwelling and upwelling channels simultaneously, which is a very important feature since the reference line shape at sea surface varies with time except around solar noon (Fig. 3) (An alternative way to monitor the surface reference line is to use a deck cell as a separate channel). A cross talk correction algorithm is used to separate the two spectra on the CCD.



- Main parts of the Fraunhofer system:
- I. An OMA 4000 CCD camera;
 - II. Fiber adapter as F-number matcher;
 - III. Fiber array ferrule;
 - IV. Cable splicing box with 3 outputs:
 - 1. 6 fibers as monochromator input;
 - 2. 2 fibers to monitor the overall spectra in visible band, currently not being used;
 - 3. Wire conductors for power supply and depth and photocell readouts;
 - V. Electronic control panel;
 - VI. 130m fiber-wire cable;
 - VII. Detector head which includes:
 - 1. 2 fiber optic cosine collectors;
 - 2. 2 photocell cosine collectors;
 - 3. A depth transducer;
 - 4. 2 photocell electronic boards.

Figure 4. The Fraunhofer system schematic chart.

The instrument was deployed on the research ship RV CALANUS during spring, summer and winter in the Florida Straits and Florida Bay region (Fig. 5). The whole system was aligned and adjusted to achieve its best performance. Six tracks on the CCD were chosen to record the images from the six fibers, three for downwelling and 3 for upwelling. Data were collected both in open ocean blue water and in coastal green and brownish waters where the sea bottom depth is about 6 meters. A floating frame was used to hold the instrument to collect the surface upwelling irradiance data at shallow stations. Care was taken to collect the data only when the sky was clear and the instrument was not in ship shadow. Also the measurements were taken within ± 3 hours around solar noon to make sure that the surface reference line was stable. Wind speed during the measurements was 5m/s to 10m/s and the solar zenith angle was between 15° and 25°. At some stations, pigment concentration data, one of the inputs of the simulation model, were collected by another research group.

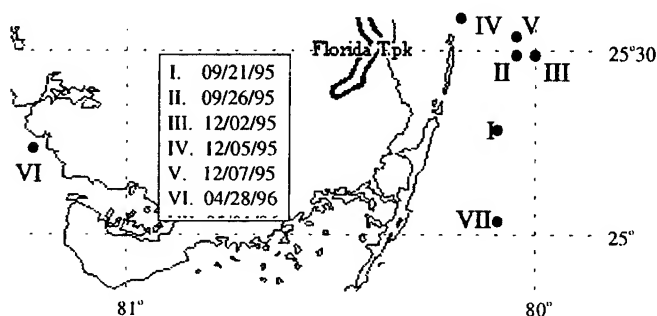


Figure 5. Locations of the data collection stations. Station IV and VI are shallow coastal green waters where the sea bottom can be seen; the other stations are clear ocean waters.

3. RESULTS AND DISCUSSION

The data were reduced by using the fitting procedure and the equivalent width calculation program. Lab experiments show that the maximum error of the algorithm for very noisy spectra is $\pm 5\%$, while another $\pm 5\%$ maximum error is due to the surface reference variation. Thus, the maximum error at depth is about $\pm 10\%$. Forward Monte-Carlo simulation is used to simulate the equivalent width versus depth data⁹ with a correction on the normalization of irradiance level at excitation and emission wavelengths on top of the atmosphere. When pigment concentration data is not available, it is assumed $0.1\text{mg}/\text{m}^3$ for clear ocean water and $1\text{mg}/\text{m}^3$ for coastal green water. DOM is not considered in the model, since the simulation results vary only a little bit even with DOM considered when DOM concentration is low, which is the case for all stations. Chlorophyll fluorescence is not considered in the simulation either. The simulation results together with the reduced data are shown in Figure 6, 7 and 8.

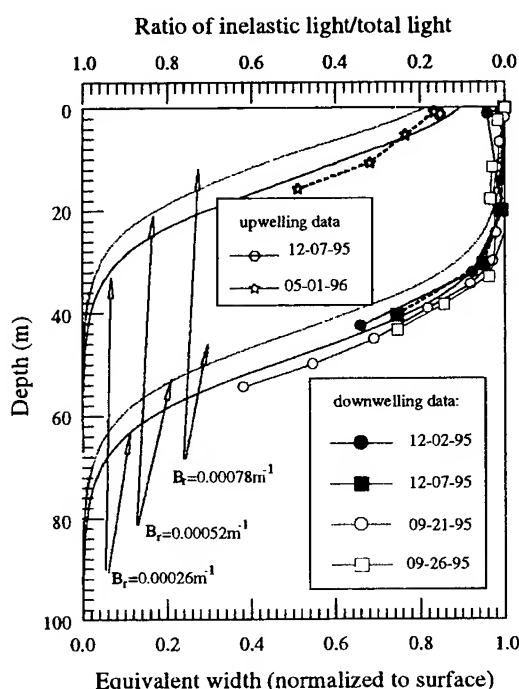


Fig. 6a. Normalized equivalent width ($w(z)/w_0$) for the Fraunhofer line at 589nm at clear water stations, both downwelling and upwelling. The simulation uses the pigment concentration, wind speed and solar zenith angle data from the 12/07/95 station. Only Raman scattering is considered in the model with the excitation wavelength at 492nm. Three different Raman scattering coefficients (B_r) are used.

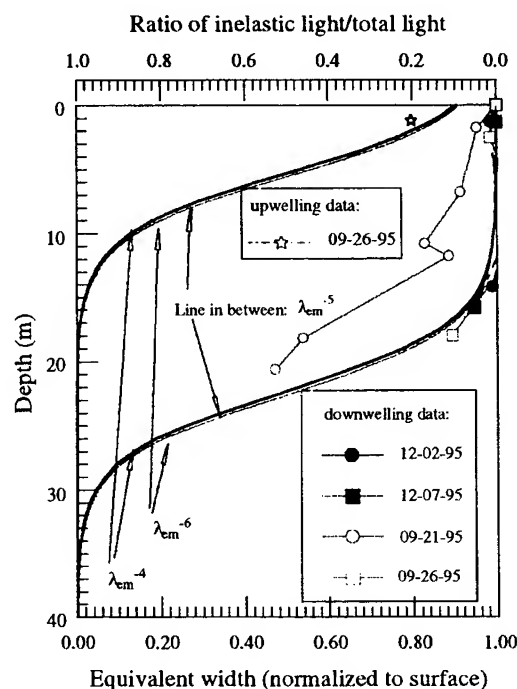


Fig. 6b. $w(z)/w_0$ as a function of depth for the Fraunhofer line at 656nm at clear water stations, both downwelling and upwelling. The simulation uses the pigment concentration, wind speed and solar zenith angle data from the 12/07/95 station. The λ_{em} dependence of the Raman scattering coefficient is assumed to be λ_{em}^{-4} , λ_{em}^{-5} and λ_{em}^{-6} , respectively.

Figure 6. Experimental data and model simulation results for Fraunhofer lines at clear water stations.

From the results in Figure 6a, it is easy to see that when the Raman scattering coefficient, $B_r = 2.6 \times 10^{-4} \text{m}^{-1}$, from Marshall and Smith¹ is used in the simulation, the model results agree very well with the experimental ones. Also shown in the graph is that the experimental data at 589nm for clear water is very stable from station to station. Thus, $B_r = 2.6 \times 10^{-4} \text{m}^{-1}$ for emission at 589nm is confirmed for natural water. In figure 6b, the dependence of the Raman scattering coefficient on the emission wavelength (λ_{em}) is taken to be λ_{em}^{-4} , λ_{em}^{-5} and λ_{em}^{-6} . Negligible difference is found among the results, which means this dependence is not critical in the Raman scattering simulation regardless of the discrepancy in the literature³. From this work, we can see that in clear ocean water, at 50m depth, half of the total downwelling irradiance at 589nm is

from Raman scattering. At 656nm this depth is about 25m. Another interesting feature in Fig. 6b is that the data is not as stable as that for 589nm. The data on 09-21-95 obviously diverge from the general trend and show us more filling, i.e., more inelastically scattered irradiance than the model predicted value. Since the model does not consider chlorophyll or DOM fluorescence, the discrepancy is probably due to one or both of these sources.

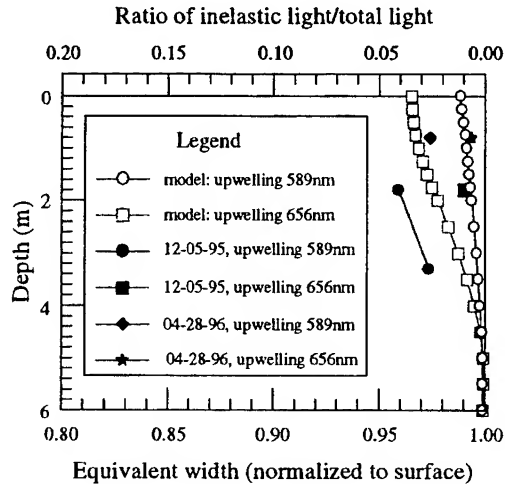


Figure 7. Monte-Carlo simulation and experimental data for coastal green water at 589nm and 656nm. In the model, pigment concentration is taken to be 1mg/m^3 , and a 6m sea bottom with reflectance 0.5 is present. Only Raman scattering is considered in the model.

Note: the x axis is 0.8 to 1.0 instead of 0.0 to 1.0.

In Fig. 7, data from shallow stations are presented together with the model results. One might think that coastal water is very rich in both chlorophyll and DOM and that the inelastic scattered light must be a big portion of the light field. This is incorrect. Not only is the inelastic component in the downwelling light field negligible, but this is also true in the upwelling light field. Even for upwelling, in the total light field, the inelastic light portion is less than 4% at surface, which is less than the instrument error (5%). As a contrast, this value is generally greater than 10% in clear waters (Fig. 6). This difference is due to the bottom effect. The bottom reflected light occupies a big portion in the total upwelling light field. Thus, the inelastic portion is very small. Simulation results show this is also true even when the water is rich in DOM and chlorophyll, or the bottom reflectance is low. So, for shallow waters, the inelastic light is negligible in either downwelling or upwelling light fields.

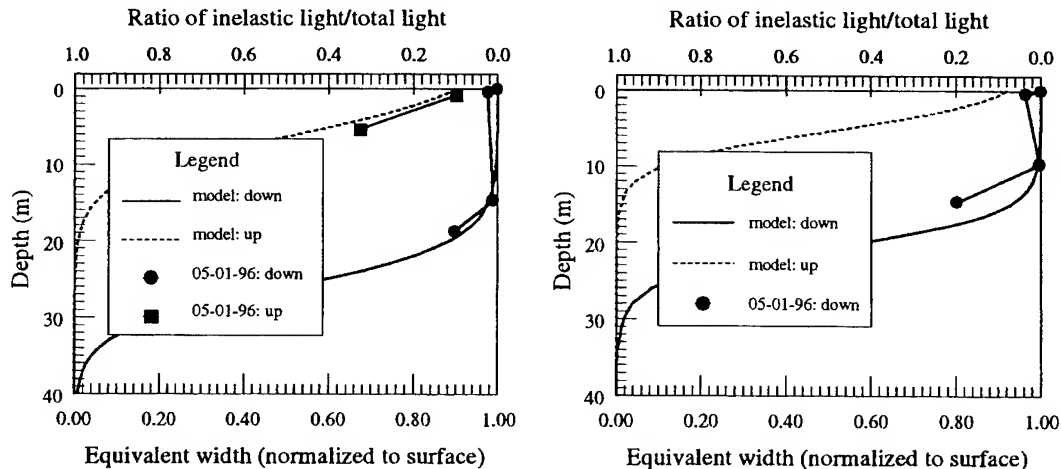


Figure 8. Experimental data from clear ocean water and Monte-Carlo simulation results for the Fraunhofer line at 656nm (left) and for the oxygen absorption line at 689nm (right). Only Raman scattering is considered in the model.

From the results shown above, it can be seen that the technique for using the Fraunhofer lines as inelastic scattering indicators is very powerful in studying *in situ* inelastic light scattering processes in natural waters. Using the same idea, smaller oxygen absorption lines around 689nm (Fig. 3) are utilized to study the *in situ* chlorophyll fluorescence at 685nm. Figure 8 shows that even in clear water where at 656nm the inelastic light is mainly from Raman scattering, the signal from chlorophyll fluorescence is detectable at 689nm. Note that these data were taken at the same station. This will enable us to measure the natural fluorescence in the future.

4. CONCLUSION

The prototype Fraunhofer instrument system¹⁰ has been rebuilt and improved. The correct Raman scattering coefficient at any λ is determined by using the clear water data and the Monte-Carlo simulation and can be used as a basis when other inelastic components, e.g., fluorescence, are considered. Small absorption lines at 689nm are used to detect the chlorophyll fluorescence at 689nm. This has proved to be a promising technique to measure the natural fluorescence.

5. ACKNOWLEDGMENTS

The work is supported by the Ocean Optics program of the Office of Naval Research. The authors want to express their gratitude to Mr. Albert Chapin, who helped a lot in the instrument rebuild, and to Dr. Howard Gordon, Dr. Yuntao Ge and Mr. Marco Monte for very helpful discussions in the simulations.

6. REFERENCES

1. B.R. Marshall and R.C. Smith, "Raman Scattering and In-Water Ocean Optical Properties," Appl. Opt. **29**(1), 71-84 (1990).
2. R.B. Slusher and V.E. Derr, "Temperature Dependence and Cross Sections of some Stokes and Anti-Stokes Raman Lines in Ice Ih," Appl. Opt. **14**(9), 2116-2120 (1975).
3. S. Sugihara, M. Kishino and N. Okami, "Contribution of Raman Scattering to Upward Irradiance in the Sea," Jour. Oceanogr. Soc. Japan **40**, 397-404 (1984).
4. R.H. Stavn and A.D. Weidemann, "Optical Modeling of Clear Ocean Light Fields: Raman Scattering Effects," App. Opt. **27**(19), 4001-4011 (1988).
5. R.H. Stavn, "Raman Scattering Effects at the Shorter Visible Wavelengths in Clear Ocean Water," SPIE Ocean Optics **X 1302**, 94-100 (1990).
6. H.R. Gordon, "The Diffuse Reflectance of the Ocean: The Theory of Its Augmentation by Chlorophyll a Fluorescence at 685nm," Appl. Opt. **18**, 1161-1166 (1979).
7. F.E. Hoge and R.N. Swift, "Airborne Simultaneous Spectroscopic Detection of Laser-Induced Water Raman Backscatter and Fluorescence from Chlorophyll a and Other Naturally Occurring Pigments," Appl. Opt. **20**, 3197-3205 (1981).
8. G.W. Kattawar and X. Xu, "Filling In of Fraunhofer Lines in the Ocean by Raman Scattering," Appl. Opt. **31**(30), 6491-6500 (1992).
9. Y. Ge, H.R. Gordon and K.J. Voss, "Simulation of Inelastic-Scattering Contributions to the Irradiance Field in the Ocean: Variation in Fraunhofer Line Depths," Appl. Opt. **32**(21), 4028-4036 (1993).
10. Y. Ge, K.J. Voss and H.R. Gordon, "In Situ Measurement of Inelastic Light Scattering In Monterey Bay Using Solar Fraunhofer Lines," Journal of Geophysical Research, **100**(C7), 13227-13236 (1995).

The relationship between near-surface chlorophyll and solar-stimulated fluorescence: biological effects

John J. Cullen, Áurea M. Ciotti and Richard F. Davis

Center for Environmental Observation Technology and Research
Dalhousie University, Department of Oceanography
Halifax, Nova Scotia, Canada B3H 4J1

Patrick J. Neale

Smithsonian Environmental Research Center
P.O. Box 28, Edgewater, Maryland USA 21037

ABSTRACT

The fluorescence of chlorophyll *a* (Chl) near 683 nm can be detected in water leaving radiance and related quantitatively to the concentration of Chl. Solar-induced fluorescence has also been related to photosynthesis in deeper waters. However, little is known about the relationships between Chl, fluorescence, photosynthesis, and irradiance near the sea surface. Quantum yields of fluorescence and photosynthesis, as well as the ratio of fluorescence to photosynthesis, change during exposures to bright light. Several physiological processes are at play. Consequently, it is difficult to construct models of near-surface quantum yields. Experimentation and comprehensive sampling in the field are required for critical information. Some approaches are presented here. Radiometer buoys that measure downwelling irradiance at 490 nm, $Ed(490)$, and upwelling spectral radiance, $Lu(\lambda)$ are good tools for measuring solar-stimulated fluorescence during studies of near-surface biology. Results can be compared with experimental measurements using a fluorometer with a very weak measuring beam that does not perturb the balance between fluorescence and photosynthesis. Comparisons indicate that relationships between near-surface Chl, fluorescence, photosynthesis and irradiance can vary widely for reasons that are not yet well resolved. Still, $Lu(683)$, corrected for backscatter and normalized to $Ed(490)$, is a useful measure of near-surface Chl in many environments.

Key words: fluorescence, chlorophyll, photosynthesis, reflectance, upwelling radiance, quenching.

1. INTRODUCTION

Solar-stimulated fluorescence of chlorophyll *a* can be detected in spectra of upwelling radiance or irradiance¹⁻³ and related quantitatively to the concentration of chlorophyll (Chl) in surface waters⁴ and deeper in the water column.^{5,6} Consequently, the fluorescence of Chl can be detected with passive instruments on moorings, profilers, drifters, or remote platforms. These measurements of fluorescence represent an important complement to estimates of Chl concentration from observations of ocean color.^{7,8} To make good use of the data, it is critical to understand the relationship between Chl and solar-stimulated fluorescence as influenced by environmental, physiological and taxonomic factors.

The problem of estimating fluorescence emission (photons $m^{-3} s^{-1}$) from radiance reflectance has been addressed (ref 6 and references therein). However, the biological processes that influence the relationships between Chl, light absorption, photosynthesis, and solar-induced fluorescence are not well studied for high and variable irradiance characteristic of the sea-surface.⁹ It is thus difficult to validate or improve models that describe the relationships between Chl or photosynthesis and the fluorescence signal in upwelling radiance.¹⁰⁻¹² Experimentation, as well as comprehensive sampling in the field under different regimes of solar irradiance and vertical mixing, are required. Some approaches are presented here.

2. METHODS

During several deployments in coastal waters, a tethered spectral radiometer buoy (TSRB) measured downwelling irradiance (490 nm) above the surface [$Ed(490)$] and near-surface upwelling radiance, [$Lu_{TSRB}(\lambda)$] in six wavebands corresponding to the SeaWiFS sensor, plus 683 nm to detect fluorescence of Chl.^{13,14} Meantime, discrete samples were obtained. Only fluorometric determinations of Chl are reported here. More recently, we used an instrument that measures 14 wavebands of Lu and Ed in the UV and visible, with the radiance sensors about 10 cm below the surface vs 45 cm for the TSRB; otherwise, the measurements reported here are essentially the same for both instruments. Data collected at $1 s^{-1}$ were reduced to medians for 60-s bins. The fluorescence signal corrected for backscatter, $Lu(683)_{corr}$, was calculated with linear

baseline correction to $Lu_{TSRB}(683)$, interpolating Lu_{TSRB} at 670 and 700 nm. For the analyses discussed here, no attempt was made to calculate fluorescence emission in photons $m^{-3} s^{-1}$.^{2,6,15}

Fluorescence yield under experimentally controlled irradiance was measured in two ways.¹⁶ For samples from perennially ice-covered Antarctic lakes, fluorescence emission was detected with a Biospherical Instruments PNF-300 natural fluorometer [Lu(683) detector] mounted looking downward from the mouth of a clear container illuminated by a projector lamp filtered through two blue-green (Corning 4-97) filters and neutral density screen. Temperature was near 0°C and samples were dark-adapted for 30 min. Actinic irradiance (PAR) was measured with a submersible scalar irradiance sensor (Biospherical Instruments QSL-100), and steady-state fluorescence as a function of PAR was recorded for individual samples after exposure for about 5 min, when transients had subsided. Relative fluorescence yield was estimated as $Lu(683)/PAR$. Laboratory measurements on a culture of the diatom *Thalassiosira pseudonana* (clone 3H) were made with a PAM fluorometer (Walz, Effeltrich, Germany).¹⁷ Steady-state fluorescence yield under ambient irradiance (F_s) is that measured during stimulation by a very weak, rapidly pulsed, non-actinic measuring beam. Relative fluorescence emission is calculated as F_s times irradiance, as measured with a QSL-100.

3. RESULTS AND DISCUSSION

Although more sophisticated calculations can be made, near surface Chl can be estimated by normalizing the upwelling radiance (or irradiance) signal to downwelling irradiance.⁴ A plot of the fluorescence signal from our radiometer buoys, $[Lu(683)_{corr} / Ed(490)]$ vs surface Chl (Fig. 1A) shows a relationship comparable to what has been observed from aircraft.⁴ The apparent strength of the relationship between Chl and the fluorescence signal comes from the large range of Chl sampled. When the efficiency of fluorescence is approximated with a ratio $[Lu(683)_{corr} / (Ed(490) \cdot Chl)]$ and plotted as a function of irradiance (Fig. 1B),¹⁸ variability is much more prominent (see refs 15,19). In turbid waters, apparent fluorescence yield can vary due to changes in the attenuation of exciting and emitted photons;^{2,6} otherwise, variability in $Lu(683)_{corr} / (Ed(490) \cdot Chl)$ is the consequence of differences in absorption coefficient of phytoplankton ($m^2 mg Chl^{-1}$) and the quantum yield of fluorescence (mol photons emitted \cdot mol photons absorbed $^{-1}$). Variability in absorption coefficient is associated with pigment packaging (a function of cell size and intracellular pigment concentration), and accessory pigmentation, which are linked to differences in species composition, nutrition and photoacclimation.^{15,20-24} Also, there can be changes in the proportion of

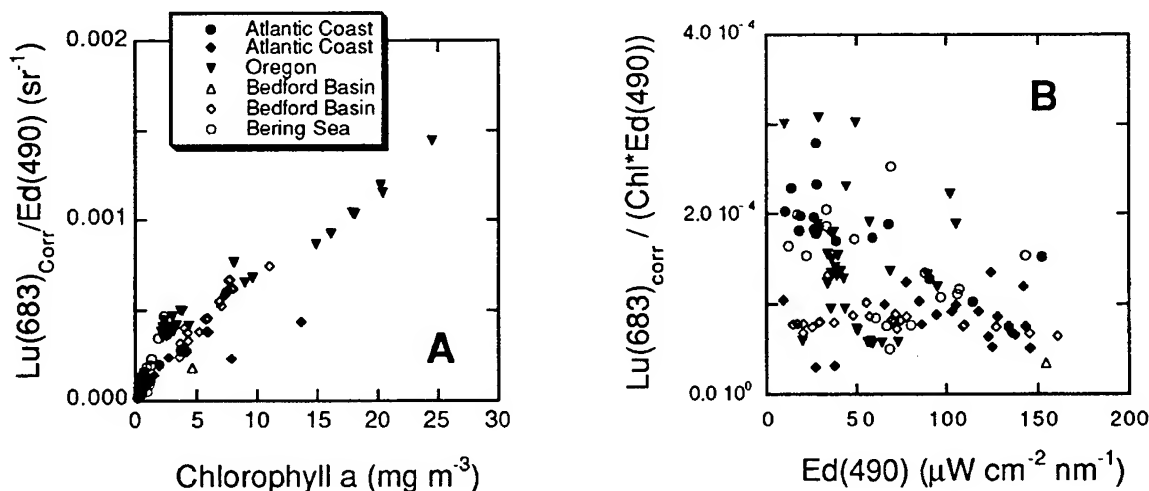


Fig. 1. Relationships between solar-stimulated fluorescence, as measured with radiometer buoys, and surface Chl, extracted and measured fluorometrically. A. The fluorescence signal is $Lu_{TSRB}(683)$, corrected with a linear baseline, normalized to $Ed(490)$ measured above the surface. Samples were collected during two cruises off the Atlantic coast of the US in the summer of 1996, off the Oregon coast in Sept. 1994 (including offshore waters and a diatom bloom in the plume of the Columbia River¹⁴), in the Bering Sea during the spring of 1996, and during August, 1996 in Bedford Basin, Nova Scotia. B. Ignoring for now the attenuation of light that could reduce the fluorescence signal in turbid waters,⁶ we plot a measure related to fluorescence yield, $Lu(683)_{corr} / [Chl \cdot Ed(490)]$, units: $sr^{-1} \cdot (mg m^{-3})^{-1}$.

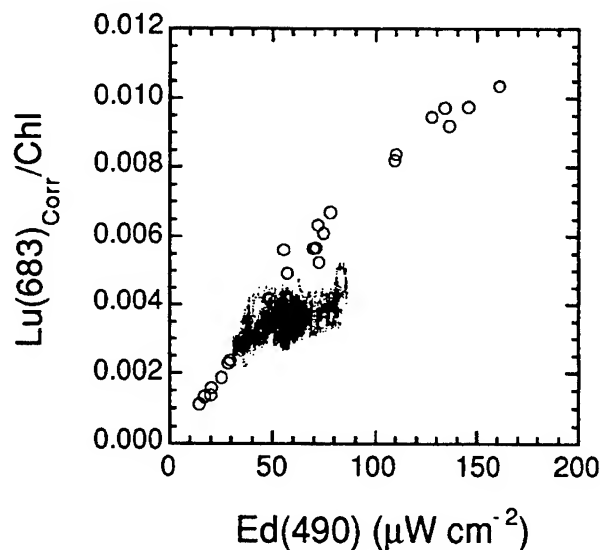


Fig. 2. Relationships between fluorescence per unit Chl [$(\mu\text{W cm}^{-2} \text{ nm}^{-1} \text{ sr}^{-1} (\text{mg m}^{-3})^{-1})$] and $\text{Ed}(490)$ during deployments of radiometer buoys. Open circles: measurements from Bedford Basin, Nova Scotia on 21 and 22 August, 1996. Chlorophyll was measured directly on surface samples. Small points are from a diatom bloom in the plume of the Columbia River off Oregon, Sept. 20, 1994.¹⁴ Each point is a median for 60 records, collected 1 s^{-1} . Chlorophyll was calculated from a power fit to records of $\text{Lu}_{\text{TSRB}}(490)/\text{Lu}_{\text{TSRB}}(555)$ vs Chl during the day ($N = 8$, $R^2 = 0.97$): $\text{Chl} = 9.57 * (\text{Lu}_{\text{TSRB}}(490) / \text{Lu}_{\text{TSRB}}(555))^{-1.96}$. The record from Oregon is consistent with strong quenching of fluorescence at relatively low irradiance.

algorithm for use near the surface, where other physiological processes are at play and where backscattered solar irradiance contributes to $\text{Lu}(683)$ and confounds measurements of fluorescence with a single passive sensor.⁶

Excess irradiance can damage photosynthetic systems, particularly sites associated with the reaction center of PSII.³² It is thus adaptive for plants to reduce excessive "excitation pressure"³³ on PSII. This is accomplished by photoacclimation³⁴ on time scales of hours to days,³⁵ whereby the balance between the rate of light absorption and the rate of utilization is restored.³⁶ On shorter time scales under variable irradiance, responses involve nonphotochemical quenching of absorbed photons, *i.e.*, dissipation of absorbed irradiance as heat.^{29,30} Nonphotochemical quenching reduces the quantum yields of both photosynthesis and fluorescence, complicating the relatively straightforward relationships between photosynthesis, fluorescence and irradiance that hold when only photochemical quenching influences fluorescence yield.³¹ Presently, there is very little information on which to base models of solar-stimulated fluorescence and photosynthesis near the sea-surface (ref 9, but see ref. 28). Where can we look for more information?

One approach is to describe variations in solar-stimulated fluorescence as a function of irradiance in nature (see ref. 18). Solar-stimulated fluorescence yield $[\text{Lu}(683)_{\text{corr}}/(\text{Ed}(490) \cdot \text{Chl})]$, units: $\text{sr}^{-1} (\text{mg m}^{-3})^{-1}$ is determined during deployments of a radiometer buoy. If solar irradiance varies substantially while the phytoplankton assemblage changes little, fluorescence vs. irradiance (F vs E) relationships can be described (see also Fig. 4 in ref. 9). Chlorophyll can be measured directly, or estimated from reflectance ratios.¹⁸ Our records from deployments in coastal waters indicate big differences in F vs E (Fig. 2). It is very likely that nonphotochemical quenching plays an important role in these relationships.

Clearly, there is a need to quantify and understand nonphotochemical quenching under bright and variable irradiance characteristic of surface layers. There are a great many experimental studies that examine changes of fluorescence during

light absorbed by photosynthetically active pigments.^{25,26} In nature, these properties change over time scales of several hours to many days. The quantum yield of fluorescence can change more rapidly, in response to variable irradiance.²⁷⁻²⁹ Under some circumstances, changes in fluorescence yield can be related to changes in the quantum yield of photosynthesis.^{27,30,31}

In the context of the variability in Fig. 1B and related sets of data,^{15,18,19} we focus here on short-term (seconds - minutes) light-induced changes in fluorescence yield that bear directly on the relationships between fluorescence, photosynthesis and Chl in surface waters.^{28,31} The relevant processes are photochemical quenching and nonphotochemical quenching of fluorescence.

Photochemical quenching reflects a trade-off in the fate of photons absorbed by photosynthetic pigments associated with photosystem II (PSII). Absorbed photons can be directed to photosynthesis, fluorescence, or radiationless decay (heat).³⁰ When photon flux is very low, photosynthetic reaction centers are mostly open (*i.e.*, available for photosynthesis) and photosynthetic quantum yield, hence quenching due to photosynthesis, is relatively high; in turn, fluorescence yield is relatively low. As irradiance increases, photons cannot be processed as rapidly as they are absorbed, and a greater proportion of reaction centers are closed: photosynthetic quantum yield declines, photochemical quenching decreases in importance, and fluorescence yield increases. The inverse relationship between photosynthetic quantum yield and fluorescence quantum yield as a function of irradiance is the basis for an algorithm relating photosynthesis to solar-stimulated fluorescence.¹¹ The authors did not intend their

exposures to variable irradiance,^{27,29,37} but it is not always easy to relate yields for stimulated fluorescence to fluorescence emission under natural conditions (ref. 38, but see refs. 28,39). A problem with many instruments is the need to remove samples from the ambient environment to make measurements. Fluorometers with remote probes, LIDAR systems and *in situ* fluorometers don't have that problem, but many of them utilize measuring beams that can induce photochemistry and thereby alter fluorescence yield during the course of the measurement.³⁸ At least two experimental approaches are suitable for studying FI vs *E* relevant to solar-stimulated fluorescence: direct measurement of Lu(683) during exposures to blue-green light,¹⁶ and use of non-actinic (i.e., very weak and very short) measurement beams during active fluorometry (the "probe" during "pump and probe"^{28,40} or the non-actinic measuring beam in pulse-amplitude-modulated (PAM) fluorometry¹⁷).

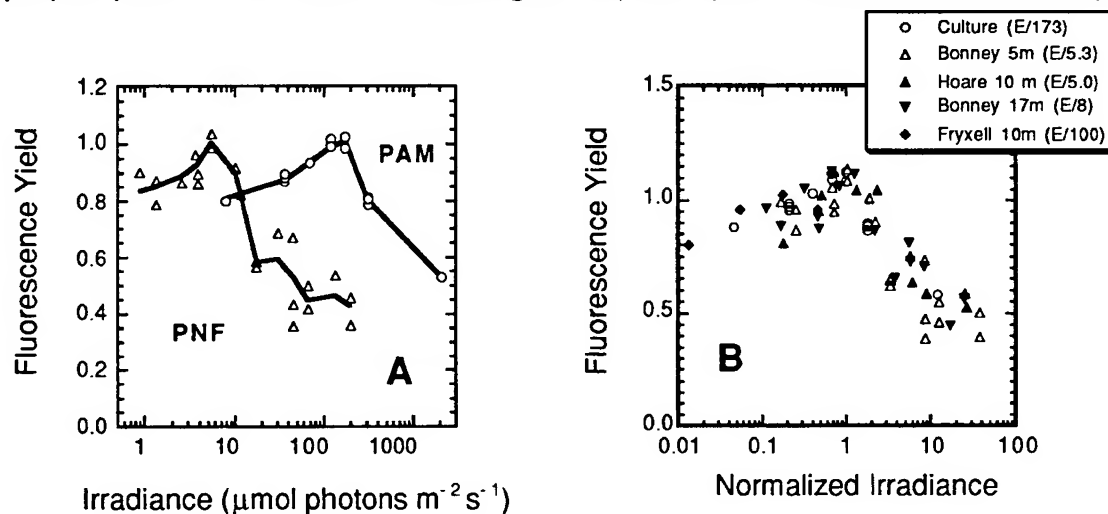


Fig. 3. Relationships between fluorescence and irradiance for phytoplankton, as measured by two different fluorometric systems.¹⁶ A. Fluorescence of natural phytoplankton (relative units, scaled to maximum) from the perennially ice-covered Antarctic Lake Bonney (Δ) was measured with a Biospherical Instruments PNF-300 Lu(683) sensor. A culture of a marine diatom (o) was studied in the laboratory using a PAM fluorometer during illumination with a tungsten-halogen source attenuated with neutral screens. Points represent fluorescence yield for the weak, non-actinic measuring beam (see methods). B. Results for several experiments, scaled to the irradiance of maximum fluorescence (scaling factor, $\mu\text{mol m}^{-2} \text{s}^{-1}$, in legend). Lines are from locally weighted smoothing. Like Lake Bonney, Lakes Hoare and Fryxell are in Antarctica. Nutrient supply was likely higher for the assemblage from L. Fryxell. C. The same data as in B., but fluorescence yield is multiplied by irradiance, so results are comparable to Fig. 2.

Recent experimental results illustrate the influence of photochemical and nonphotochemical quenching on steady-state fluorescence yield (Fig. 3): at low irradiance, fluorescence yield increases with irradiance (photochemical quenching diminishes as photosynthetic quantum yield declines), and at higher irradiance, fluorescence yield decreases because of nonphotochemical quenching. Thresholds for the transition (scaling irradiances in Fig. 3B) are strongly dependent on growth conditions (see also ref. 28). Although it was possible here to find a fairly strong pattern that was largely a function of appropriately scaled irradiance (Fig. 3B), it should be remembered that there are several quenching processes in phytoplankton and that they are time-dependent,⁴¹ a function of preconditioning,⁴² and somewhat species-dependent.²⁹ Much more experimentation is necessary before robust generalizations can be developed. It should be recognized, however, that

extreme, bending in plots of fluorescence (*i.e.*, $\text{Lu}(683)_{\text{corr}} / \text{Chl}$) vs irradiance (compare Fig. 2 with Fig. 3C); even stronger quenching would be required to saturate the FI vs E relationship, as suggested in data from the equatorial Pacific.⁹ Regardless, the slope of fluorescence/Chl vs irradiance (see Fig. 2 and ref 18) can probably be related to quenching under restricted circumstances.

4. CONCLUSIONS

We have shown that several tools can be used to explore the relationships between fluorescence, Chl and irradiance in surface waters. Changes of fluorescence as a function of irradiance, observed experimentally and in the field, indicate that nonphotochemical quenching can be important in surface waters. The significance to photosynthesis is unresolved, however. Direct measurements of short-term carbon assimilation⁴³ or estimates of photosynthesis from special fluorometric methods⁴⁰ could help to improve our extremely sketchy understanding of the relationships between solar-stimulated fluorescence and near-surface photosynthesis.⁹ Indications are that through careful consideration of the expanding literature on fluorescence, along with prudent design of experiments, rapid progress can be made. Meantime, it is encouraging that solar-stimulated fluorescence appears to be a readily detectable and reasonably robust indicator of near-surface chlorophyll.

5. ACKNOWLEDGMENTS

Thanks to ONR, NASA, and NSERC for support. This work is partially supported by the NSERC/Satatlantic Industrial Research Chair in Environmental Observation Technology, awarded to JJC. The arms-length research partnership is open to participation by other manufacturers of instruments. AMC was supported by CNPq, Brazil. CEOTR Publication no. 4.

6. REFERENCES

1. R. A. Neville and J. F. R. Gower, "Passive remote sensing of phytoplankton via chlorophyll fluorescence," *J. Geophys. Res.*, **82**, 3487-3493 (1977).
2. H. Gordon, "Diffuse reflectance of the ocean: the theory of its augmentation by chlorophyll *a* fluorescence," *Appl. Opt.*, **21**, 2489-2492 (1979).
3. A. Morel and L. Prieur, "Analysis of variations in ocean color," *Limnol. Oceanogr.*, **22**, 709-722 (1977).
4. J. F. R. Gower and G. Borstad, "Use of the *in-vivo* fluorescence line at 685 nm for remote sensing surveys of surface chlorophyll *a*," *Oceanography from Space*, J.F.R. Gower, (ed.), pp. 281-294, Plenum Press, New York, 1981.
5. M. S. Kishino, S. Sugihara and N. Okami, "Influence of fluorescence of chlorophyll *a* on underwater upward irradiance spectrum," *La Mer*, **22**, 224-232 (1984).
6. D. A. Kiefer, W. S. Chamberlin and C. R. Booth, "Natural fluorescence of chlorophyll *a*: relationship to photosynthesis and chlorophyll concentration in the western South Pacific gyre," *Limnol. Oceanogr.*, **34**, 868-881 (1989).
7. H. R. Gordon, O. B. Brown, R. H. Evans, J. W. Brown, R. C. Smith, K. S. Baker and D. K. Clark, "A semianalytic radiance model of ocean color," *J. Geophys. Res.*, **93**, 10,909-10,924 (1988).
8. K. L. Carder, S. K. Hawes, K. A. Baker, R. C. Smith, R. G. Steward and B. G. Mitchell, "Reflectance model for quantifying chlorophyll *a* in the presence of productivity degradation products," *J. Geophys. Res.*, **96**(C11), 20,599-20,611 (1991).
9. J. J. Cullen and M. R. Lewis, "Biological processes and optical measurements near the sea-surface: some issues relevant to remote sensing," *J. Geophys. Res.*, **100**(C7), 13,255-13,266 (1995).
10. B. J. Topliss and T. Platt, "Passive fluorescence and photosynthesis in the ocean: Implications for remote sensing," *Deep-Sea Res.*, **33**, 849-864 (1986).
11. W. S. Chamberlin, C. R. Booth, D. A. Kiefer, J. R. Morrow and R. C. Murphy, "Evidence for a simple relationship between natural fluorescence, photosynthesis and chlorophyll in the sea," *Deep-Sea Res.*, **37**, 951-973 (1990).
12. P. M. Stegmann, M. R. Lewis, C. O. Davis and J. J. Cullen, "Primary production estimates from recordings of solar-stimulated fluorescence in the equatorial Pacific at 150° W," *J. Geophys. Res.*, **97**(C1), 627-638 (1992).
13. J. J. Cullen, A. M. Ciotti and M. R. Lewis, "Observing biologically induced optical variability in coastal waters," *SPIE Ocean Optics XII*, **2258**, 105-115 (1994).
14. J. J. Cullen, A. M. Ciotti, R. F. Davis and M. R. Lewis, "Optical detection and assessment of algal blooms," *Limnol. Oceanogr.*, in press (1996).
15. M. S. Kishino, S. Sugihara and N. Okami, "Estimation of quantum yield of chlorophyll *a* fluorescence from the upward irradiance spectrum in the sea," *La Mer*, **22**, 233-240 (1984).
16. P. J. Neale and J. C. Priscu, "Fluorescence quenching in phytoplankton of the McMurdo Dry Valley Lakes (Antarctica): Implications for the function of the photosynthetic apparatus," *Amer. Geophys. Union Ant. Res. Ser.*, submitted, 1996.

17. U. Schreiber, U. Schliwa and B. Bilger, "Continuous recording of photochemical and nonphotochemical chlorophyll fluorescence quenching with a new type of modulation fluorometer," *Photosyn. Res.*, **10**, 51-62 (1986).
18. M. R. Abbott and R. M. Letelier, "Bio-optical drifters — scales of variability of chlorophyll and fluorescence," *SPIE Ocean Optics XIII* (1996).
19. C. Roesler and M. J. Perry, "In situ phytoplankton absorption, fluorescence emission, and particulate backscattering spectra determined from reflectance," *J. Geophys. Res.*, **100**(C7), 13,279-13,294 (1995).
20. W. S. Chamberlin and J. Marra, "Estimation of photosynthetic rate from measurements of natural fluorescence: analysis of the effects of light and temperature," *Deep-Sea Res.*, **39**, 1695-1706 (1992).
21. D. A. Kiefer, "Fluorescence properties of natural phytoplankton assemblages," *Mar. Biol.*, **22**, 263-269 (1973).
22. D. A. Kiefer, "Chlorophyll *a* fluorescence in marine diatoms: responses of chloroplasts to light and nutrient stress," *Mar. Biol.*, **23**, 39-46 (1973).
23. J. J. Cullen, "The deep chlorophyll maximum: comparing vertical profiles of chlorophyll *a*," *Can. J. Fish. Aquat. Sci.*, **39**, 791-803 (1982).
24. A. Morel and A. Bricaud, "Inherent properties of algal cells including picoplankton: Theoretical and experimental results," *Photosynthetic Picoplankton*, T. Platt and W.K.W. Li, (eds.), pp. 521-559, 1986.
25. H. M. Sosik and B. G. Mitchell, "Light absorption by phytoplankton, photosynthetic pigments and detritus in the California Current System," *Deep-Sea Res. I*, **42**(10), 1717-1748 (1995).
26. G. Johnsen, E. Sakshaug and M. Vernet, "Pigment composition, spectral characterization and photosynthetic parameters in *Chrysochromulina polylepis*," *Mar. Ecol. Prog. Ser.*, **83**, 241-249 (1992).
27. P. G. Falkowski and Z. Kolber, "Variations in chlorophyll fluorescence yields in phytoplankton in the world oceans," *Aust. J. Plant Physiol.*, **22**, 341-355 (1995).
28. A. M. Chekalyuk and M. Y. Gorbunov, "Diel variability of in vivo chlorophyll fluorescence in near-surface water layer," *SPIE Ocean Optics XII*, **2258**, 140-151 (1994).
29. B. W. Ibelings, B. M. Kroon and L. R. Mur, "Acclimation of photosystem II in a cyanobacterium and a eukaryotic green alga to high and fluctuating photosynthetic photon flux densities, simulating light regimes induced by mixing in lakes," *New Phytol.*, **128**, 407-424 (1994).
30. G. H. Krause and E. Weis, "Chlorophyll fluorescence and photosynthesis: the basics," *Annu. Rev. Plant Physiol. Plant Mol. Biol.*, **42**, 313-349 (1991).
31. D. A. Kiefer and R. A. Reynolds, "Advances in understanding phytoplankton fluorescence and photosynthesis," *Primary Productivity and Biogeochemical Cycles in the Sea*, P.G. Falkowski and A. Woodhead, (eds.), pp. 155-174, Plenum, 1992.
32. P. J. Neale, "Algal photoinhibition and photosynthesis in the aquatic environment," *Photoinhibition*, D.J. Kyle, C.B. Osmond, and C.J. Arntzen, (eds.), pp. 35- 65, Elsevier, Amsterdam, 1987.
33. D. P. Maxwell, S. Falk and N. P. A. Huner, "Photosystem II excitation pressure and development of resistance to photoinhibition," *Pl. Physiol.*, **107**, 687-694 (1995).
34. P. G. Falkowski and J. LaRoche, "Acclimation to spectral irradiance in algae," *J. Phycol.*, **27**, 8-14 (1991).
35. J. J. Cullen and M. R. Lewis, "The kinetics of algal photoadaptation in the context of vertical mixing," *J. Plankton Res.*, **10**, 1039-1063 (1988).
36. R. J. Geider, H. L. MacIntyre and T. M. Kana, "A dynamic model of photoadaptation in phytoplankton," *Limnol. Oceanogr.*, **41**(1), 1-15 (1996).
37. J. J. Cullen, C. S. Yentsch, T. L. Cucci and H. L. MacIntyre, "Autofluorescence and other optical properties as tools in biological oceanography," *Proc. SPIE Int. Soc. Opt. Eng.*, **925**, 149-156 (1988).
38. P. J. Neale, J. J. Cullen and C. M. Yentsch, "Bio-optical inferences from chlorophyll *a* fluorescence: What kind of fluorescence is measured in flow cytometry?," *Limnol. Oceanogr.*, **34**, 1739-1748 (1989).
39. M. Estrada, C. Marrasé and J. Salat, "In vivo fluorescence/chlorophyll *a* ratio as an ecological indicator in oceanography," *Sci. Mar.*, (1996).
40. Z. Kolber and P. G. Falkowski, "Use of active fluorescence to estimate phytoplankton photosynthesis in situ," *Limnol. Oceanogr.*, **38**, 1646-1665 (1993).
41. C. S. Ting and T. G. Owens, "The effects of excess irradiance on photosynthesis in the marine diatom *Phaeodactylum tricornutum*," *Pl. Physiol.*, **106**, 763-770 (1994).
42. W. Arsalane, B. Rousseau and J. C. Duval, "Influence of the pool size of the xanthophyll cycle on the effects of light stress in a diatom - competition between photoprotection and photoinhibition," *Photochem. Photobiol.*, **60**, 237-243 (1994).
43. J. J. Cullen, M. R. Lewis, C. O. Davis and R. T. Barber, "Photosynthetic characteristics and estimated growth rates indicate grazing is the proximate control of primary production in the equatorial Pacific," *J. Geophys. Res.*, **97**(C1), 639-654 (1992).

Small Scale Optical Structure Measured via Images of Fluorescence Emission

Jaffe, J. S. and P. J. S. Franks

Scripps Institution of Oceanography
La Jolla CA, 92093

Abstract

This article presents the results of analyzing data which were collected in the sea with a structured illumination/fluorescence imaging system. The system employs all lines of an argon ion laser ($< 520nm$) to create a two dimensional slice illumination pattern in the blue-green. A sensitive CCD camera was used to measure the fluorescence emission (in a .67 m x .67 m area) resulting from this stimulation. Under our assumptions, these images are proportional to chlorophyll-a concentration. Inspection of the data reveals a large degree of small scale patchiness with characteristic distances as small as centimeters. In many of the images, the chlorophyll concentration is seen to change by an order of magnitude over several centimeters. Patchiness was characterized via the use of spatial spectral estimation techniques. Preliminary results show that the data follow a $-5/3$ slope at high wave number, consistent with the hypothesis that the patches were formed by turbulent stirring of larger scale gradients of phytoplankton. In addition, repeated vertical profiles demonstrated that the larger scales were extremely constant, even in the presence of this small scale variability. The technique has provided an original data set with important new information about the small scale structure of pigment in the ocean.

Keywords: underwater optics, optical tomography, small-scale structure, phytoplankton, chlorophyll-a.

1 Introduction

Although the basic mechanisms by which light can interact with matter in the ocean have been well characterized, the detailed structure of the ocean optical environment on the order of centimeters to meters has been difficult to measure. Traditional oceanic optical instruments integrate over volumes and scales of centimeters, may disturb the underlying structure of the medium, and may also sample extremely small volumes. It has thus been difficult, if not impossible, to measure the two- or three-dimensional variability in optical properties at this resolution. Over the last decade, efforts in our group have been dedicated to designing new instrumentation systems that use the most modern generation of CCD cameras in conjunction with powerful lasers and structured lighting geometries. These efforts have produced instruments which permit measurement of these multidimensional parameters. Typically, these high grade CCD cameras have excellent linearity over their large dynamic range and extremely sensitivity, with signal-to-noise levels of 1 at tens of photons per pixel.

This article presents the results of analyzing data which were collected at sea with a system called OSST (Optical Serial Section Tomography). The system employs structured lighting to isolate a 2-dimensional slice in

the ocean. Straightforward processing of the data in order to compensate for beam spreading, inherent systematic and stochastic factors, and camera response, has yielded a new view of small-scale structure (cm-to-m) in the ocean.

2 Materials and Methods

Previous publications detailed a theoretical and experimental approach to obtaining small-scale patch information^{3,4} using the OSST system in the present geometry (Figure 1). The method used here yields valid results without resorting to the general inversion procedure which was presented in the above publications. The system was composed of a shipboard argon ion laser, a fiber optic conduit for creating a sheet of underwater illumination, and a sensitive CCD camera for photographing images of the fluorescence emission. The argon laser used all lines below 520 nm for stimulation, and the images were recorded with long passed (> 680 nm) light.

Although previous investigations with the technique had indicated that it could be used successfully as a tomographic method,^{3,4} in this set of experiments a different strategy was employed. Here, the depth of field of the camera system was made extremely small (3 cm) so that all of the out-of-plane light that was fluoresced and/or scattered (at wavelengths > 680) would be out-of-focus. This out of focus light will contribute to the background level of observed fluorescence, however it will not contribute to the observed spatial structure.

Images were processed by correcting for non-uniform illumination by the laser sheet using an internal calibration. The equation governing the light propagation in this system is:

$$I(x, y) = \kappa(x, y) I_s(x, y_0, z_0) c(x, y, z_0) \int \exp(-c[x, y, z, \lambda_s]) dx \int \exp(-c[x, y, z, \lambda_e]) dz. \quad (1)$$

Here, $I_s(x, y_0, z_0)$ is the intensity of the stimulating wavelength of the light at the edge of the viewed field and λ_e is the emission wavelength. As illustrated in Figure 1, the z direction is range from the camera, and the x and y directions are the lateral directions in the plane of the sheet of illumination. The concentration of the (assumed) single fluorescing compound in three dimensions is represented as $c(x, y, z)$. $I(x, y)$ is the intensity of the light recorded by the camera system. The constant $\kappa(x, y)$ is related to the efficiency of the fluorescing process, the spherical spreading of light and the recording efficiency of the camera. The equation states that the intensity of the light recorded in the camera plane is proportional to the intensity of the incident illumination and the concentration of the fluorescent material. The final multiplicative factor (right hand side of the equation) represents the absorption of the fluoresced light after emission and before recording by the camera. An additive factor for the camera dark current also needs to be included:

$$I_{obs}(x, y) = I(x, y) + I_{dc}. \quad (2)$$

The goal of the image processing of the 'raw' collected data was to produce an image in which the intensity of the (i, j^{th}) pixel was proportional to the concentration of fluorescing chemical (here, assumed to be chl-a). Future versions will certainly be absolutely calibrated and allow a computation of the chl-a concentration as a function of location. However, the approach taken here in analyzing the data here was to make several simplifying assumptions and test their validity by examining the images.

Experimentally, we estimate a value for the in-plane concentration at a given range by first averaging the intensity of all of the images over several vertical profiles (after extracting an independently observed value of the dark current measured after every 10 exposures) so that

$$I_{avg}(x, y) = \langle I(x, y, z) - I_{dc} \rangle = \langle \kappa(x, y) I_s(x, y_0, z_0) c(x, y, z) \int \exp(-c[x, y, z, \lambda_s]) dx \int \exp(-c[z, x, y, \lambda_e]) dz \rangle. \quad (3)$$

Dividing equation [1] by equation [3] yields:

$$I_{comp}(x, y, z_0) = I(x, y, z_0) / I_{avg}(x, y, z_0) \propto c(x, y, z_0). \quad (4)$$

Several assumptions are implicit in this procedure. First of all, it assumes that the relative attenuation of the incident light can be represented by a mean value as a function of two dimensions in the plane of illumination. Since the stimulating light is in the blue-green, the absorption and scattering is extremely small over the 1 meter path length that the light must travel in order to stimulate fluorescence. Second, it assumes that the attenuation of the emitted light can be modeled as a mean value over the field of view of the system. Since the camera is 'tuned' to have a very narrow depth of field, including only the area illuminated by the light sheet, the formulation is extremely complex. Sources of light that are out of focus (such as scattered light) can be regarded as virtual sources and their images will be spread over the entire recorded image, thus producing only a mean value for the entire image. On the other hand, differential absorption (in the red) of the light that has been fluoresced by compounds that are between the camera and the stimulated sheet could lead to intensity changes. Assuming a reasonable range of values (.01 - 6 mg/m³) for chl-a concentration, the variation in the received light can be computed and compared to the observed values. The resulting values are approximately an order of magnitude smaller than those observed, which leads us to conclude that this process cannot account for the large changes in intensity that we observe. We believe that the results of this procedure produce images of the relative concentration of emitters that are within the field of view of the system.

As stated, all lines of a shipboard argon ion laser were used to stimulate fluorescence in the blue-green. The illumination intensity used was approximately several watts at the location of the subsurface optical components. The beam divergence in the vertical was large enough that fluorescence emission from a .67 m x .67 m field of view was detectable in all images. The thickness of the slice illumination in the horizontal was approximately several millimeters. Camera, illumination optics, and other sensors for depth, temperature and salinity were all mounted on a frame which was equipped with a vane so that the system pointed into the current. Since the images were recorded at a distance of 1 meter in front of the platform, and the illumination apparatus consisted of a small (5 cm x 10 cm) housing outside the field of view of the camera, the images were considered to be non-invasive. That is to say, we believe that the system did not disturb the distribution of the fluorescent material. Current, estimated by inspecting the mean horizontal displacement of zooplankton targets from 3-dimensional sonar images of zooplankton, was directed toward the instrument package at 10 - 20 cm/s. Exposure of the camera system was approximately 40 ms. The camera thus recorded images of fluorescent chemicals that were distributed within a .5 cm - 1 cm range slice. Images consisted of 102 x 102 arrays of numbers at a resolution of approximately .67 cm x .67 cm. The system resolution was therefore approximately isotropic in x, y, and z, in a range of .5 cm - 1 cm.

Data were processed using the procedure above in order to correct for systematic inhomogeneities in the images. The beam pattern of the stimulating illumination was estimated by averaging over several thousand frames. Assuming an isotropic distribution of scatterers and absorbers in the images, the averaging will yield a picture proportional to the beam pattern of the system. In addition, the dark current of the camera was recorded every 10 images to estimate the transient changes in camera intensity that resulted from the different temperatures that the imaging system was working in. Subtraction of the dark current and then division by the

image of the beam pattern produced images which had no mean trend across the field of view. Therefore, the systematic effects of beam pattern were assumed to be eliminated and the images were treated as if the intensity of the images were proportional to the fluorescing chemicals within the field of view of each camera element, a voxel of dimensions .67 cm x .67 cm x .75 cm.

Processed images were then visually inspected in order to judge the distribution of fluorescing chemicals. In addition, images were integrated spatially to estimate the mean value of the fluorescing material, here judged to be chlorophyll-a. Figure 2 shows a set of four profiles which were the result of this process. Vertical profiles were also performed with a traditional fluorometer (Wet Lab "Wetstar"). Comparison of the profiles of integrated image values with the traditional fluorometer values gave excellent correspondence, implying that our new instrument was performing correctly.

Images were also analyzed to compute spatial power spectra using a spatial version of Welch's method.⁵ Briefly, a set of 25 overlapping (50 %) 32 x 32 images were delineated inside of the 102 x 102 set of computed values. Each of the 32 x 32 subimages was multiplied by a Hanning window and then Fourier transformed. Subsequently, two-dimensional power spectra for each of these images were then averaged to obtain a single averaged power spectrum for the single image. Then, because the images were assumed to have spatially isotropic power spectra, the values of the power spectra were displayed as a one-dimensional function of wave number in Fourier space.

Results reported here are from a set four vertical profiles that were conducted on the RV Sproul on the evening of July 27th from approximately 9:00 - 10:00 pm, Pacific Standard Time. The OSST package consisting of an illumination system (shipboard Argon Ion Laser) with a fiber optic conduit, CCD camera (Photometrics, Tuscon AZ) and ancillary equipment for recording depth temperature and salinity were profiled vertically throughout the water column from a depth of 20 to 80 meters. In addition, a three-dimensional sonar imaging system, FishTV, was used to measure animal abundance, coincident with the optical information. Here, we present analysis of only the OSST data.

3 Results

The vertical profiles contain many interesting features. Two chlorophyll maxima are evident, one at approximately 55 meters and the other at 63 meters depth. The deeper peak is more intense than the shallow one. Many features of the vertical profiles of fluorescence were accurately reproduced from profile to profile. Further inspection of the individual images used to compute these average values reveals a great deal of heterogeneity. An image from 55 m (Figure 3) reveals the presence of many small very bright targets which have intense patches of chlorophyll inside them. The image from 63 m (Figure 4) shows a similar pattern, however the average level of chlorophyll is clearly higher and the patch sizes tend to be larger.

To further analyze the spatial patterns seen in these images, power spectra were computed using the above procedures. Figure 5 shows a power spectra taken from the image displayed in Figure 3 and Figure 6 shows the power spectra taken from the image displayed in Figure 4. Both figures are log-log plots of spectral intensity versus wave number. Here, the wave number axis is in cycles per 32 pixels. As such, a value of 24 corresponds to a frequency of .75 cycles per .67 cms or 1.12 cycles per cm.

Analysis of the spatial spectra of fluorescence fluctuations can give important information on the processes responsible for the patch formation. The first observation from the spectra was that the patches were isotropic, i.e., there was no preferred orientation. The second observation was that the spectra have a slope of $-5/3$ over the well-resolved portion of their range. Both these observations are consistent with the hypothesis that the patches were formed by turbulent stirring of larger scale gradients of phytoplankton.¹ Shown superimposed on both spectra is a line of slope $-5/3$.

4 Discussion

There are two likely hypotheses to explain the occurrence of microscale patchiness of phytoplankton: nucleation and mixing. The nucleation hypothesis suggests that the patches arose from smaller-scale structures through aggregation, while the mixing hypothesis posits that the patches arose from larger-scale structures through stirring across gradients. We feel that the nucleation hypothesis is unlikely to be valid since the spectra of fluorescence variability are very similar, regardless of location in the water column. Aggregation is most likely at high phytoplankton concentrations, leading to larger patch scales in regions of high biomass. This was not observed. On the other hand, the consistency of spectra with depth supports the mixing hypothesis. In particular, the $-5/3$ slope of the spectrum is predicted by turbulence theory for the inertial-convective subrange of passive scalars.¹

These data represent the first *in-situ* observations of the two-dimensional microscale variability of phytoplankton fluorescence in the ocean. The data show that the planktonic environment below the mixed layer is structured by turbulent mixing, driven by the internal wave field. These observations have strong implications for our understanding of the dynamics structuring the planktonic community in the ocean and ocean optics in general.

5 Conclusions

A new instrument called OSST has been used to measure the small-scale spatial distributions of fluorescing chemicals over scales of centimeters to meters in the sea. Images reveal a great deal of repeatability of the average structure with a large degree of small-scale heterogeneity. Relative concentrations of these chemicals (presumed to be chl-a) can change by an order of magnitude over distances as small as several centimeters. The observed power spatial power spectra of the images are the same as that predicted by turbulence theory for the inertial-convective subrange of passive scalars.¹

6 REFERENCES

- [1] Garrett, C. 1989. A mixing length interpretation of fluctuations in passive scalar concentration in homogeneous turbulence. *J. Geophys. Res.* 94:9710-9712.
- [2] Marple, S. Lawrence Jr., *Digital Spectral Analysis with Applications*, Prentice-Hall Signal Processing series, A. V. Oppenheim, Ed. 1987.
- [3] Palowitch, A.W.; Jaffe, J.S. Three-dimensional ocean chlorophyll distributions from underwater serial-sectioned fluorescence images. *Applied Optics*, 10 May 1994, vol.33, (no.14):3023-33.
- [4] Palowitch, A. W. and J. S. Jaffe, "Optical Serial Sectioned Chlorophyll-a Microstructure", *J. of Geophysical Research*, Volume 100, C7, July 15,1995, pp. 13,267-13,278.
- [5] Welch, P.,D., the Use of Fast Fourier Transform for the Estimation of Power Spectra: A Method Based on Time Averaging over Short Modified Periodograms, *IEEE Trans. Audio Electroacoustics*, Vol. AU-15, pp 70-73, June 1967.

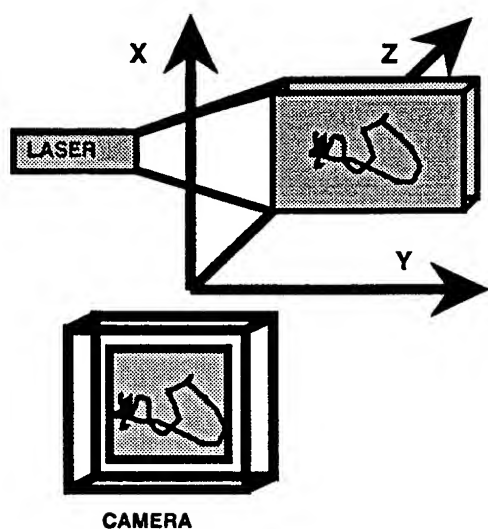


Figure 1: The system geometry.

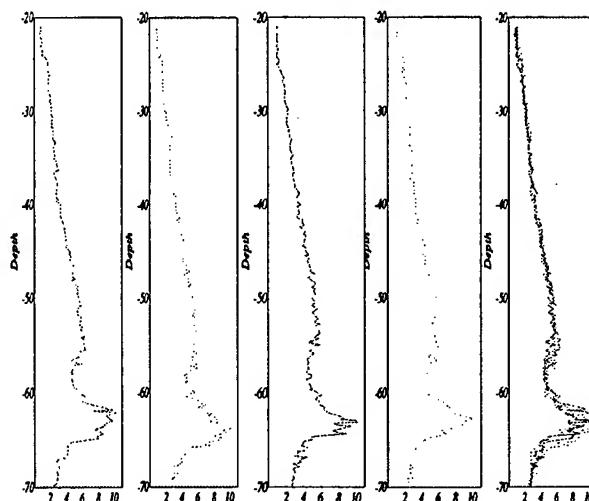


Figure 2: Four vertical profiles.

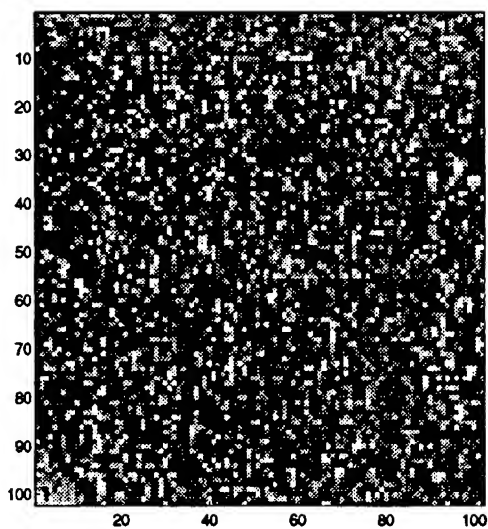


Figure 3: An image from 55 meters.

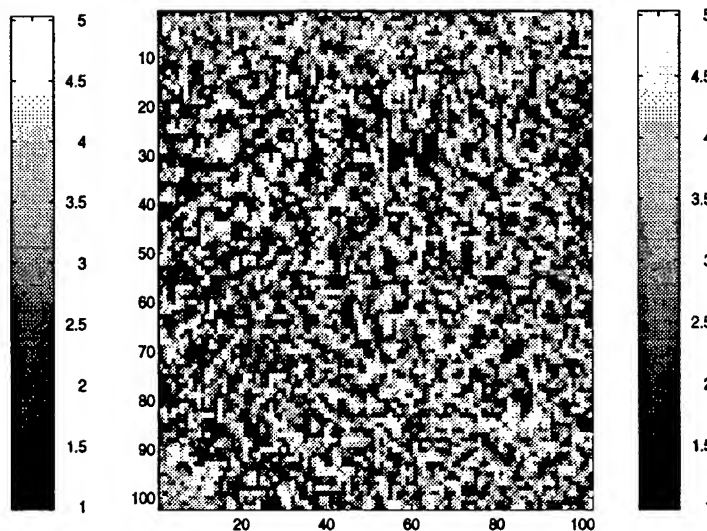


Figure 4: An image from 63 meters.

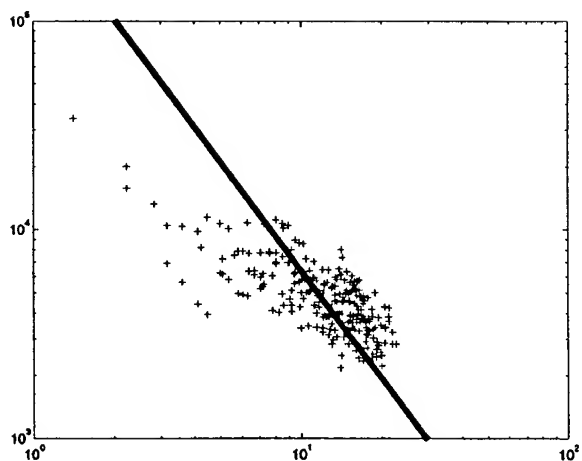


Figure 5: Power spectra of Figure 3.

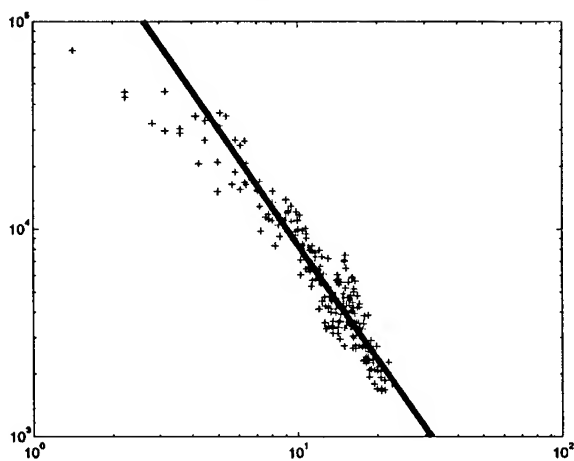


Figure 6: Power spectra of Figure 4.

Depth and wavelength dependence of phytoplankton photosynthesis: implications for the remote sensing of marine primary production

Osvaldo Ulloa

Department of Geophysics
Niels Bohr Institute for Astronomy, Physics and Geophysics
University of Copenhagen
Juliane Maries Vej 30
DK-2100 Copenhagen Ø
Denmark

Nicolas Hoepffner

Space Applications Institute
Joint Research Centre of the European Commission
I-21020 Ispra (Va)
Italy

David Larkin

DJL Software Consultancy Ltd.
63 Fellgate Avenue
Jarrow, Tyne & Wear NE32 4QR
United Kingdom

ABSTRACT

A detailed profile of the photosynthetic parameters and the action spectra was obtained in the Sargasso Sea during late summer, when the upper water column was strongly stratified. Significant depth variation in their magnitudes was present in the lower part of the euphotic zone. The consequences of such vertical structure on the estimation of water column primary production by remote sensing on ocean color are evaluated by sensitivity analysis using a spectral irradiance model. The errors in estimated primary production at depth assuming constant values of the photosynthetic parameters can be of several fold. However, for estimates of daily water-column primary production the errors are generally less than 10%.

Keywords: photosynthesis, phytoplankton, primary production, remote sensing

1. INTRODUCTION

The estimation of water-column primary production from remotely-sensed data on ocean color relies on the parameterization of the response of phytoplankton to the intensity and spectral composition of the light available for photosynthesis, as well as of the processes that determine the light field in the euphotic zone.¹ Although the algorithms that have been developed for this application are, in principle, capable of dealing with depth dependencies in the photosynthetic parameters and in the optical properties, their implementation to date has ignored the vertical structure in these quantities, mainly because of lack of sufficient information.

Here we present detailed measurements of action spectra, photosynthesis versus irradiance (P-I) parameters and phytoplankton pigment concentrations in the Sargasso Sea during late summer, when the upper water column is strongly stratified. We show that below the mixed layer the initial slope α^B of the P-I curves increases significantly with depth, while the assimilation number P_m^B decreases. The implications of such vertical structure for the computation of water-column primary production by remote sensing are evaluated by sensitivity analysis using a spectral irradiance model.²

2. IN SITU OBSERVATIONS

2.1 Methods

Observations were made over a 9-day period at a drift station in the North Sargasso Sea (36.0° N, 64.5°W) during the second leg of the cruise 88-026 of the *C.S.S. Hudson* (September, 1988). Water samples were collected with Niskin bottles or from a submersible pump sampler equipped with a CTD and an *in situ* fluorometer. Chlorophyll-*a* (Chl-*a*) and phaeopigments were measured fluorometrically using a Turner Designs 10-0005R fluorometer. Samples were collected on Whatman GF/F filters and pigments extracted in 90% acetone in the cold and dark for 24 h. Nitrate, phosphate and silicate were measured on board using a Technicon II AutoAnalyzer and standard techniques.

Broad-band (400-700 nm) photosynthesis-irradiance (P-I) experiments were carried out in temperature-controlled incubators illuminated with 250-W tungsten-halogen lamps. Photosynthetic rates were measured with the ¹⁴C method. For each experiment, ~40 μ Ci of ¹⁴C-sodium bicarbonate was added to each of 42 light and 2 dark bottles. The incubation period was 3 h, after which the 100-mL samples were filtered onto Whatman GF/F filters and the filters analyzed by scintillation spectrometry. Photosynthetically Active Radiation (PAR) was measured at each bottle position with a 4 π quantum meter (Biospherical Instruments, model QSL 100). The photosynthetic parameters α^B and P_m^B were obtained by fitting the results to the equation of Platt et al.³

Photosynthetic action spectra were determined for the same water samples as for the broad-band P-I experiments, using the method of Lewis *et al.*⁴ In each experiment, ¹⁴C-sodium bicarbonate was added to the sample (to a final activity of ~18 μ Ci mL⁻¹) and 96 1-mL aliquots were dispensed into 7-mL scintillation vials and incubated for 2 h in the spectrophotosynthetron.⁴ Here, light from ENH-type tungsten-halogen projection lamps is passed through high quality interference filters (12 wavebands, every 25 nm from 400 to 675 nm, 25-nm bandpass) and subsequently through neutral density filters to obtain eight different low light intensities per waveband (in our case $\leq 30 \mu$ E m⁻² s⁻¹). Incubations were terminated and inorganic carbon removed by adding 0.5 mL 6N HCl and shaking the open vials for at least 1 h under the fume hood. Quantum scalar irradiance in each position was measured with a 4 π quantum meter (Biospherical Instruments, model QSL 100), with a modified collector small enough to fit in the bottom of half a 7-mL scintillation vial for the measurements, and calibrated for the different wavebands. The slope of the photosynthetic rate (normalized per unit biomass) versus irradiance relation at each waveband, $\alpha^B(\lambda)$, was determined by linear regression.

2.2 Results

During the 9 days of the study, water column properties remained quite stable. A mixed layer of depth 45 m and temperature of 27°C was present. Nitrate was depleted in the upper 90 m. Mixed-layer Chl-*a* concentrations were $\sim 0.15 \text{ mg m}^{-3}$ and a deep chlorophyll maximum was present and centered at $\sim 90 \text{ m}$, with peak concentrations of 0.64 mg m^{-3} (Fig. 1 a).

In the mixed layer, the initial slope of the broad-band P-I relationship α^B was relatively constant (Fig. 2 b), while P_m^B was somewhat more variable and tended to decrease with depth (Fig. 2 c). Below the mixed layer, α^B increased by a factor of about 4 between 50 and 110 m. Conversely, P_m^B decreased by about the same factor in that depth range.

The general shapes of the action spectra from the different depths sampled (10-110 m, every 10 m) were similar, but some variations were present at particular wavebands. The unweighted spectral averages $\langle \alpha^B(\lambda) \rangle_\lambda = \int_{400}^{700} \alpha(\lambda) d\lambda / \int_{400}^{700} d\lambda$ showed a similar depth structure as the broad-band α^B values.

3. SENSITIVITY ANALYSIS

3.1 Biomass profile

Computations were carried out using a general biomass profile $B(z)$ of the form¹

$$B(z) = B_0 + \frac{h}{\sigma\sqrt{2\pi}} \exp\left[-\frac{(z - z_m)^2}{2\sigma^2}\right], \quad (1)$$

where B_0 is a background concentration, z_m is the depth of the chlorophyll maximum, σ specifies the width of the peak and h specifies the integral under the Gaussian and above the background. Our results (Fig. 1 a) can be described by the following parameter values: $B_0 = 0.132 \text{ mg m}^{-3}$, $h = 22.46 \text{ mg m}^{-2}$, $z_m = 86.16 \text{ m}$ and $\sigma = 18.21 \text{ m}$.

3.2 Primary production model

Primary production at depth was computed with the same P-I model used to obtain the photosynthetic parameters,³ modified to include the dependence of α^B and I on wavelength (P_m^B is considered to be wavelength independent⁵) and assuming, for simplicity, no photoinhibition:

$$P(z) = B(z)P_m^B(z)[1 - \exp(-\Pi(z)/P_m^B(z))], \quad (2)$$

where

$$\Pi(z) = \sec \theta \int_{\lambda_1}^{\lambda_2} \alpha^B(z, \lambda) I_d(z, \lambda, \theta) d\lambda + 1.20 \int_{\lambda_1}^{\lambda_2} \alpha^B(z, \lambda) I_s(z, \lambda) d\lambda. \quad (3)$$

Here θ is the sun's zenith angle in water, I_d and I_s are the direct and diffuse components of the available light at depth z respectively, λ is the wavelength in the spectra range between $\lambda_1 = 400 \text{ nm}$ and $\lambda_2 = 700 \text{ nm}$ and 1.20 is the inverse of the mean cosine for perfectly diffuse skylight after refraction at a flat sea surface.

The underwater light field was computed using the spectral irradiance model of Sathyendranath and Platt.² The light available at the sea surface was obtained from a solar spectral model for direct and diffuse irradiance.⁶ Daily water-column primary production was obtained by integrating Eq. (2) numerically over time and depth.

3.3 Effects of the vertical structure of α^B and P_m^B

To evaluate the effect of depth variations in α^B and P_m^B on primary production estimates, we used a generalized $\alpha^B(z)$ profile, based on our *in situ* results, in which an exponential curve was superimposed on a constant value

$$\alpha^B = \alpha_0^B + A \exp(\omega z). \quad (4)$$

Here, α_0^B is the background constant value of α^B , A is a parameter that specifies the depth at which the second term becomes important and can therefore be related to the mixed-layer depth, and ω is a parameter that describes the rate of change of α^B with depth. We assume that α^B and P_m^B will both change as the euphotic zone becomes stratified, and model the latter as a function of the former:

$$P_m^B(z) = A_2 + A_3[\alpha(z)]^{-\xi}, \quad (5)$$

where A_2 , A_3 and ξ are empirical coefficients. With this representation, as α^B increases with depth (*i.e.*, as ω increases), P_m^B decreases (Fig. 2 a,b).

We computed primary production for different values of the parameters involved and compared the results with the case where the P-I parameters are assumed to be constant with depth. The results for variations in ω are shown in Fig. 2 (c,d). The difference between the primary production values at depth computed assuming constant P-I parameters and those when they vary strongly with depth, can be significant. For example, for $\omega = 0.07274$, representative of our data, the error at the 1% light level (~ 93 m) is $>100\%$ (Fig. 3 c). However, when production values are integrated over time and depth, the relative difference in daily water-column production is only $\sim 5\%$ (Fig. 3 d).

4. Conclusion

The photosynthetic parameters in the ocean can present significant vertical structure below the mixed layer, which, in turn, in many cases is shallower than the euphotic zone. The error introduced in computing primary production at depth by ignoring this vertical structure can be of several fold, particularly at the base of the euphotic zone where the P-I parameters can differ greatly from those at the surface. However, for daily water-column primary production estimates the errors are generally less than 10%.

5. REFERENCES

1. T. Platt and S. Sathyendranath, "Oceanic primary production: estimation by remote sensing at local and regional scales", *Science*, **241**, 1613-1620 (1988).
2. S. Sathyendranath and T. Platt, "The spectral irradiance field at the surface and in the interior of the ocean: a model for applications in oceanography and remote sensing", *J. Geophys. Res.*, **93**, 9270-9280 (1988).
3. T. Platt, C. L. Gallegos and W. G. Harrison, "Photoinhibition of photosynthesis in natural assemblages of marine phytoplankton", *J. Mar. Res.*, **38**, 687-701 (1980).
4. M. R. Lewis, R. E. Warnock, B. Irwin and T. Platt, "Measuring photosynthetic action spectra of natural phytoplankton populations", *J. Phycol.*, **21**, 310-315 (1985).
5. J. M. Pickett and J. Myers, "Monochromatic light saturation curves for photosynthesis in *Chlorella*", *J. Plant Physiol.*, **41**, 90-98.
6. W. W. Gregg and K. L. Carder, "A simple spectral solar irradiance model for cloudless maritime atmospheres", *Limnol. Oceanogr.*, **35**, 1657-1675.

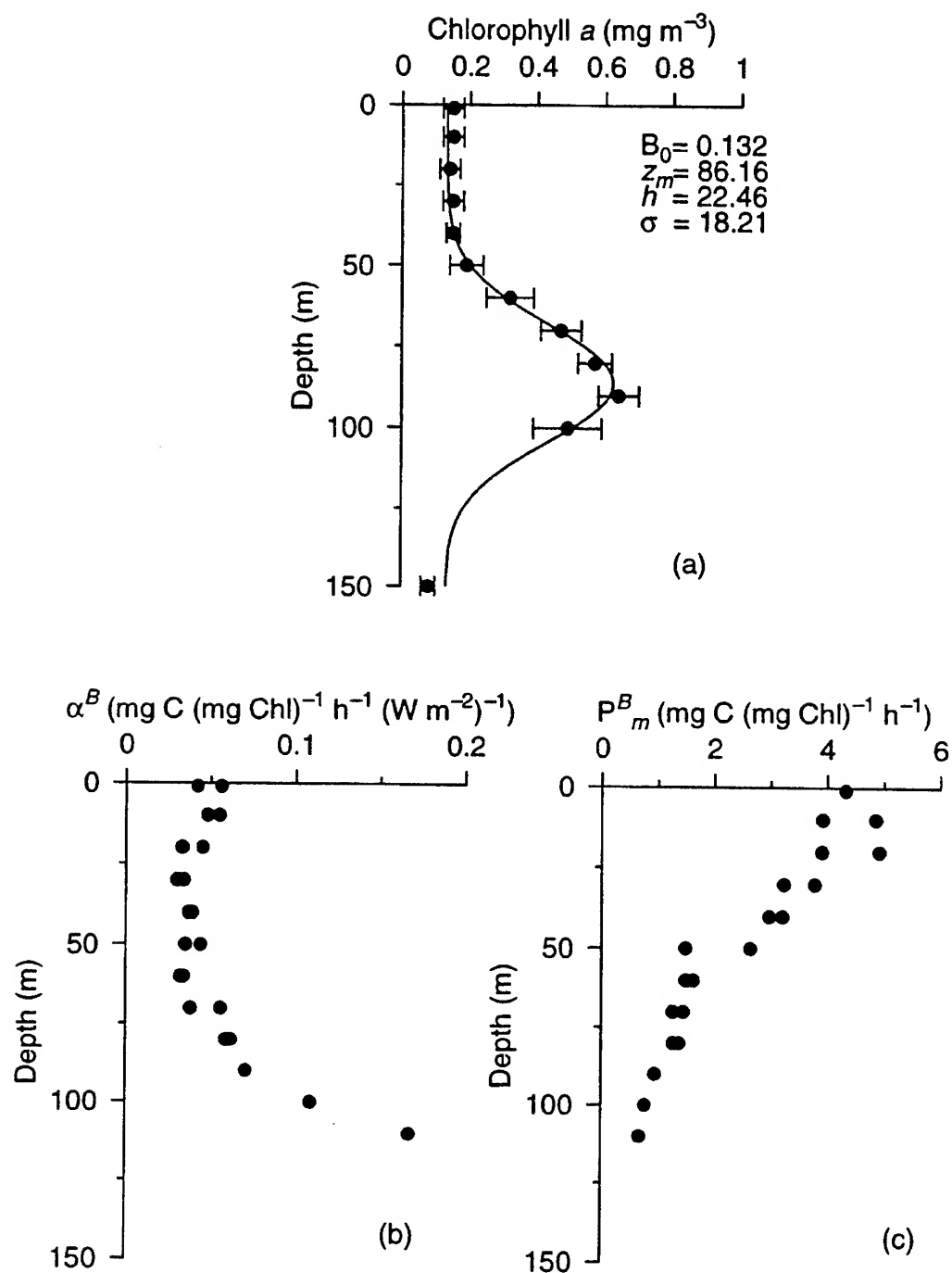


Fig. 1. Profiles of (a) chlorophyll-*a* (errors bars are ± 1 s.d.), (b) α^B and (c) P_m^B in the North Sargasso Sea during a 9-day drift station in September 1988. The curve in a) is the best fit to Eq. (1) in the text.

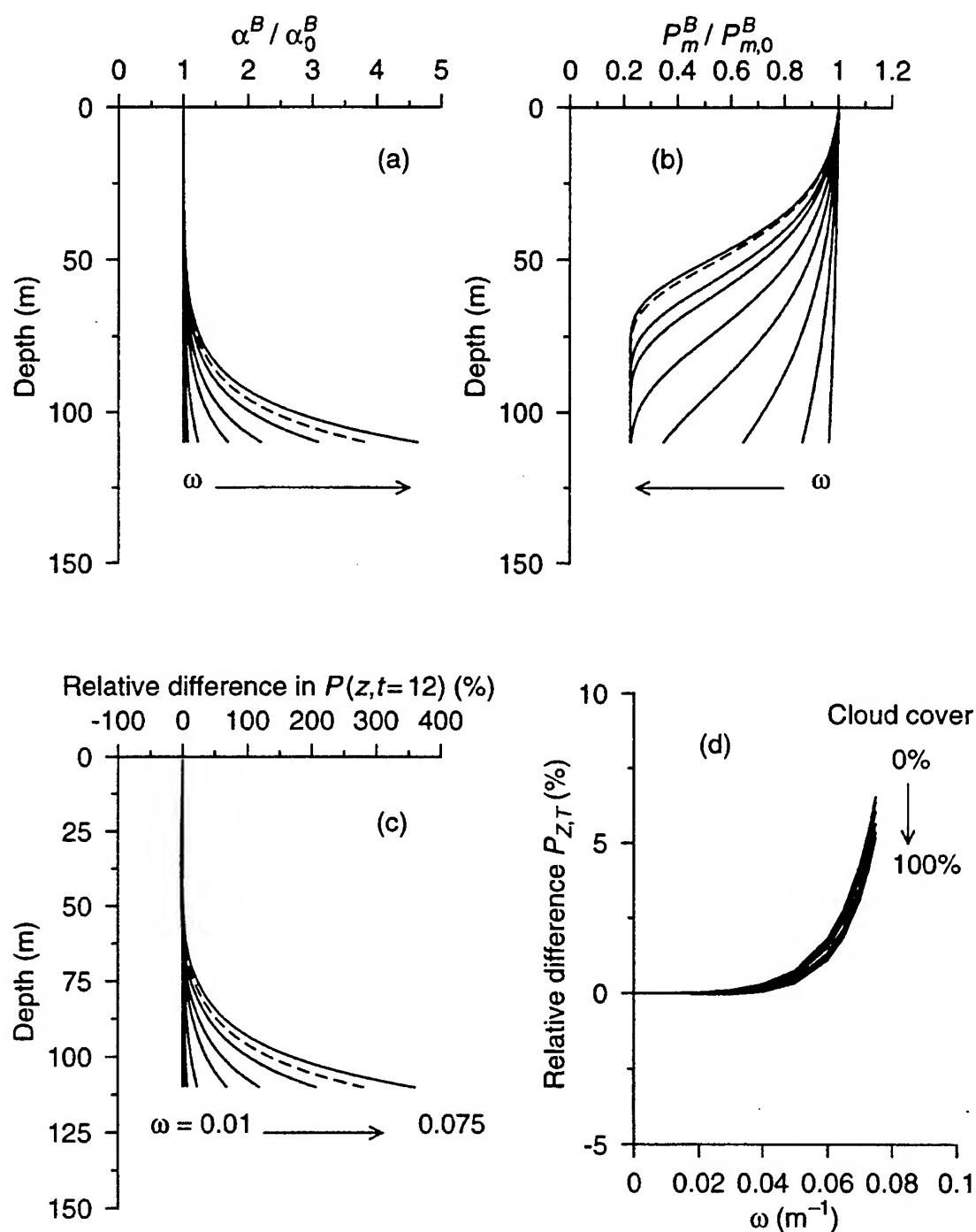


Fig. 2. Modeled profiles of (a) $\alpha^B(z)$ and (b) $P_m^B(z)$ (normalized to their values at the surface) for different values of ω , the rate of change of α^B with depth. Relative difference in estimates of primary production (c) at depth (and noon) and (d) integrated over time and depth ($P_{Z,T}$), when comparisons are made with the case for uniform α^B and P_m^B profiles.

Photosynthetic action spectrum: estimation from phytoplankton absorption spectrum

Margareth N. Kyewalyanga^{1,2}, Trevor Platt³ and Shubha Sathyendranath^{1,3}

¹ Dept. of Oceanography, Dalhousie University, Halifax, Nova Scotia, Canada B3H 4J1

² Institute of Marine Sciences, University of Dar-es-Salaam, P.O. Box 668 Zanzibar, Tanzania

³ Biological Oceanography Division, Bedford Institute of Oceanography, Box 1006, Dartmouth, Nova Scotia, Canada B2Y 4A2.

ABSTRACT

A method is presented for constructing the carbon-based photosynthetic action spectrum which is simple and more economical than conventional methods. The approach uses the *shape* of the phytoplankton absorption spectrum and the initial slope of the photosynthesis-irradiance curve, determined in broad-band illumination. This method assumes that the *shape* of the absorption spectrum is similar to that of the corresponding action spectrum, when non-photosynthetic pigments are absent, or negligible. The method was tested by constructing action spectra at different stations sampled across the North Atlantic, in five biogeochemical provinces. To assess the performance of the method, the constructed action spectra were compared with the results of measurements made at the same stations. The agreement between the measured and the constructed action spectra was good.

Both the measured and constructed action spectra were partitioned into their respective provinces. In each province, a representative spectrum was estimated as the average of all the action spectra measured in the province. Again, the agreement between measured and constructed action spectra was good. It is concluded that the simplified procedure developed here provides an efficient way of estimating the photosynthetic action spectrum for natural phytoplankton populations, and could be used in the computation of primary production at local or large spatial scales.

Keywords: photosynthesis, action spectrum, absorption spectrum, phytoplankton, primary production, biogeochemical provinces

2. METHODS

Samples were collected at twenty stations across the North Atlantic, from Halifax, Canada, to the coast of Morocco (and back); from 41.12°N 49.33°W to 29.00°N 19.16°W (12 transect stations), and at around 31.11°N 10.40°W (8 time-series stations). Sampling took place in the Fall, from 19th September to 21st October, 1992, during a Joint Global Ocean Flux Study (JGOFS) cruise. Water samples for all the relevant measurements were collected at one depth, in the photic zone, using a continuous pump sampler¹. Five biogeochemical provinces² were covered during the cruise, they include: the Northwest Atlantic continental shelf, NWCS, 2 Stns; the Gulf Stream, GFST, 3 Stns; the Western Subtropical Gyre, STGW, 2 Stns; the Eastern Subtropical Gyre, STGE, 5 Stns; and the Eastern Atlantic or Canary, CNRY, 8 Stns.

Biomass (as chlorophyll-*a* concentration) was measured fluorometrically, after extraction in 90% acetone, overnight. The C-based photosynthetic action spectrum, $\alpha^B(\lambda)$, was determined using a spectral incubator³, and the parameters of the broad-band photosynthesis-irradiance

curve, α^B the initial slope and P_m^B the assimilation number, where the superscript B indicates normalization to phytoplankton biomass, were measured using the ^{14}C method⁴. Each α^B value was corrected for the shape of the emission spectrum of the incubator lamp (tungsten-halogen) by multiplying it by a ratio of the unweighted mean phytoplankton absorption coefficient to the mean absorption weighted by the emission spectrum of the lamp³. The phytoplankton absorption spectra were measured using the filter technique, following the method of Hoepffner and Sathyendranath⁵.

3. CONSTRUCTION OF THE ACTION SPECTRUM

Spectrally-resolved primary production models require the action spectrum as one of the inputs. The conventional methods for measuring the C-based photosynthetic action spectrum⁶ are complicated, time consuming and expensive. As a result, data on the action spectrum are few, and there is a need to develop more simple and economical methods. Here we present one such method, which uses the *shape* of the phytoplankton absorption spectrum, and the broad-band α^B to provide the *amplitude*.

To define the *shape* of the absorption spectrum, the absorption coefficients, $a_p(\lambda)$ [m^{-1}], were normalized to their mean value (averaged over the spectral range from 400 to 700 nm). Thus, the action spectrum was constructed as:

$$\alpha_c^B(\lambda) = \frac{a_p(\lambda) \times \alpha^B}{\bar{a}_p}, \quad (1)$$

where, $\alpha_c^B(\lambda)$ is the constructed action spectrum, with the subscript c indicating *constructed*, $a_p(\lambda)$ is the phytoplankton (pigments) absorption spectrum, and \bar{a}_p is the spectrally-averaged mean phytoplankton absorption coefficient. The main assumption in this construction is that the shape of the absorption spectrum represents that of the corresponding action spectrum. However, for this assumption to be valid, the presence of non-photosynthetic pigments has to be negligible. We found this to be the case in the present data set.

4. COMPARISON WITH THE MEASURED ACTION SPECTRA

4.1 Station by station

To test the performance of the method, the constructed action spectra were compared with the measured action spectra, $\alpha^B(\lambda)$, at each of the twenty stations. Figure 1 shows the shapes of some ten action spectra and absorption spectra (which represent the shape of $\alpha_c^B(\lambda)$). Although the shapes varied from one station to another, there was excellent agreement in shapes between $\alpha^B(\lambda)$ and $\alpha_c^B(\lambda)$ at individual stations.

A comparison of amplitudes was made by linear regression of $\alpha_c^B(\lambda)$ on the measured $\alpha^B(\lambda)$. For a perfect agreement, the slope of the regression line would be 1.0; a slope > 1.0 would imply that the magnitude of $\alpha_c^B(\lambda)$ was higher than that of $\alpha^B(\lambda)$, and the reverse would be true for a slope < 1.0 . In 75% of the stations, the slopes were found to be not significantly different from 1.0 (t -test, $p < 0.05$); 20% of the stations had slopes significantly lower than 1.0, and only one station showed a slope greater than 1.0. The intercepts were not significantly different from zero at all the stations and the coefficients of determination (r^2) were high (on average 93%), confirming the good agreement in shapes.

4.2 Provincial representatives

In each of the five biogeochemical provinces, an average action spectrum (one measured and one constructed) was computed as a mean of all the corresponding action spectra in that province. The shapes and amplitudes of the *measured* and *constructed* action spectra were compared in each province. There was good agreement between them for the representative action spectra in all the five biogeochemical provinces; some examples for the GFST, CNRY and STGW provinces are shown in Fig. 2.

As for individual stations (section 4.1), the constructed $\alpha_c^B(\lambda)$ in each province were regressed against their measured counterparts (Fig. 3), to check for an agreement in amplitudes. The slopes for the GFST, STGE and STGW provinces were not significantly different from 1.0 (Student's *t*-test, $p < 0.05$) while those for the NWCS and the CNRY provinces were lower than 1.0. However, the r^2 values were high (e.g., Fig. 3) illustrating that the shapes were well matched.

4.3 Concluding remarks

The *shape* of the phytoplankton absorption spectrum reproduced well the shape of the action spectrum and the α^B provided appropriate normalization of the shape, as shown for both local (stations) and regional (provinces) scales, over the extensive region sampled. The absorption spectra and broad-band α^B are relatively more easy to measure than the C-based action spectra. Therefore, the method developed here provides an efficient way for estimating the photosynthetic action spectra for use in primary production models³ at any spatial scale.

5. ACKNOWLEDGEMENTS

We thank Brian Irwin for helping with the broad-band *P* vs *I* data. This work was supported by the Office of Naval Research, the National Aeronautics and Space Administration, the Department of Fisheries and Oceans, and the Natural Sciences and Engineering Research Council.

6. REFERENCES

1. A. W. Herman, M. R. Mitchell, and S. W. Young, "A continuous pump sampler for profiling copepods and chlorophyll in the upper oceanic layers," *Deep-Sea Res.* **31**, 439-450 (1984).
2. S. Sathyendranath, A. Longhurst, C. M. Caverhill, and T. Platt, "Regionally and seasonally differentiated primary production in the North Atlantic," *Deep-Sea Res.* **42**, 1773-1802 (1995).
3. M. N. Kyewalyanga, T. Platt, and S. Sathyendranath, "Estimation of the photosynthetic action spectrum: Implication for primary production models," *Mar. Ecol. Prog. Ser.* (submitted).
4. B. Irwin, J. Anning, C. Caverhill, and T. Platt, "Primary production on the Labrador Shelf and in the Strait of Belle Isle in May 1988," *Can. Data Rep. Fish. Aquat. Sci.* Vol. 784 (1990).
5. N. Hoepffner and S. Sathyendranath, "Bio-optical characteristics of coastal waters: Absorption spectra of phytoplankton and pigment distribution in the western North Atlantic," *Limnol. Oceanogr.* **37**, 1660-1679 (1992).
6. M. R. Lewis, R. E. Warnock, B. Irwin, and T. Platt, "Measuring photosynthetic action spectra of natural phytoplankton populations," *J. Phycol.* **21**, 310-315 (1985).

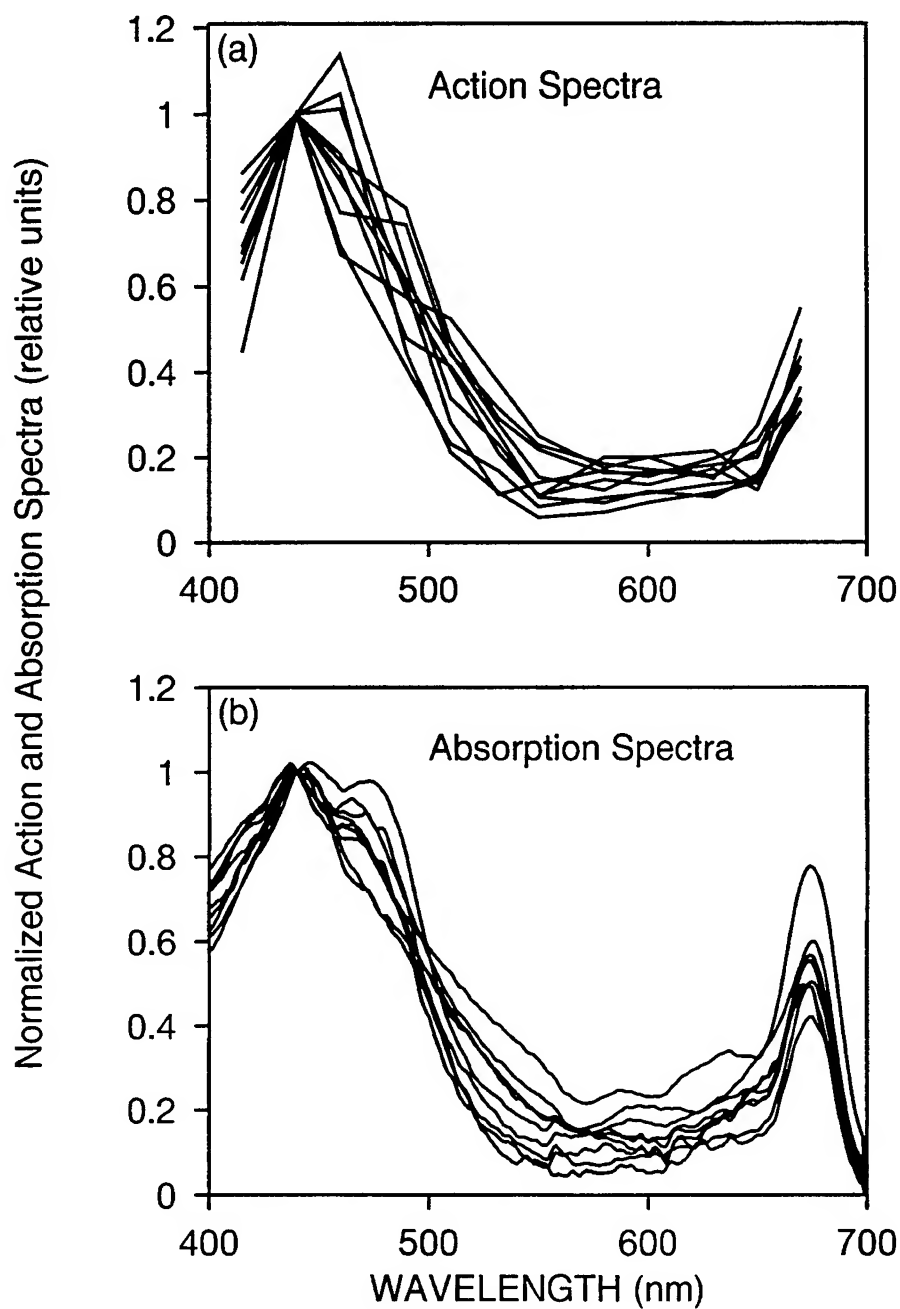


Fig. 1. Shapes of the (a) measured action spectra and (b) phytoplankton absorption spectra from some, randomly selected, ten stations sampled in the North Atlantic. The spectra are normalized to one at 440 nm to compare the shapes.

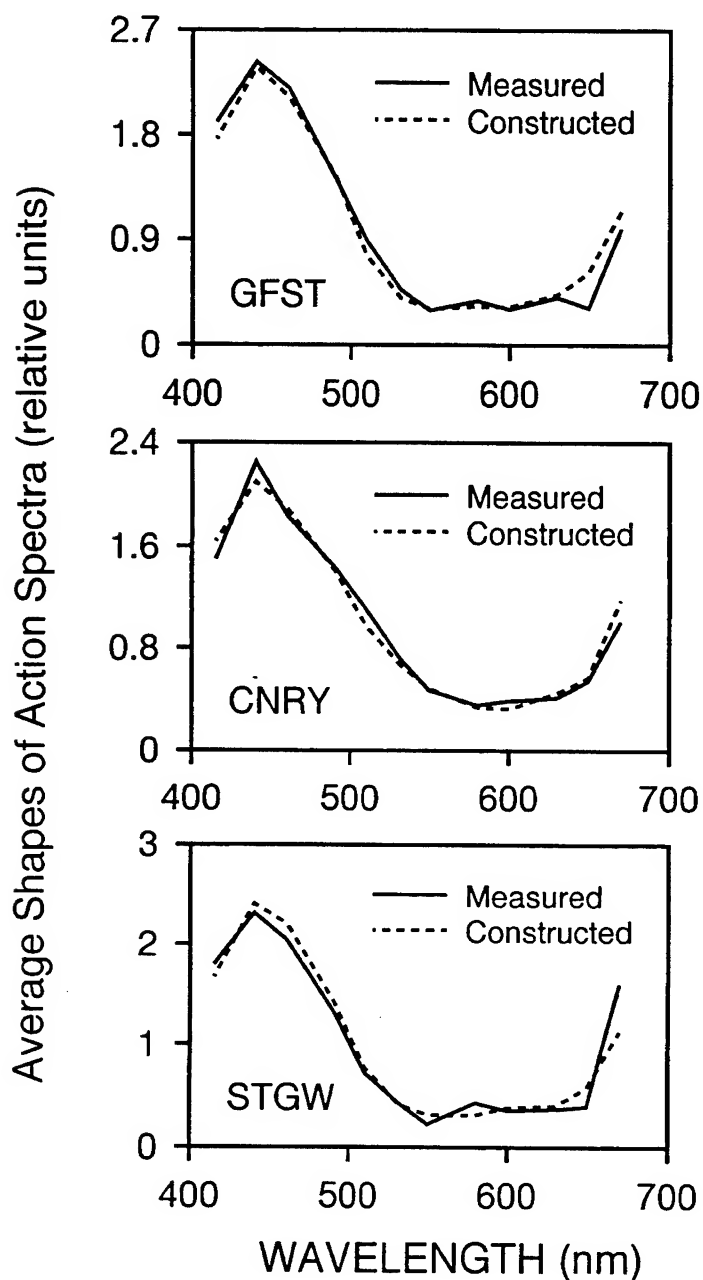


Fig. 2. Comparison of shapes of measured and constructed action spectra in some of the biogeochemical provinces: GFST, the Gulf Stream; CNRY, the Canary; and STGW, the Western Subtropical gyre. Each spectrum is normalized to its mean value, averaged over the spectral range from 400 to 700 nm. The measured action spectra are shown by solid lines, and the constructed ones by the broken lines.

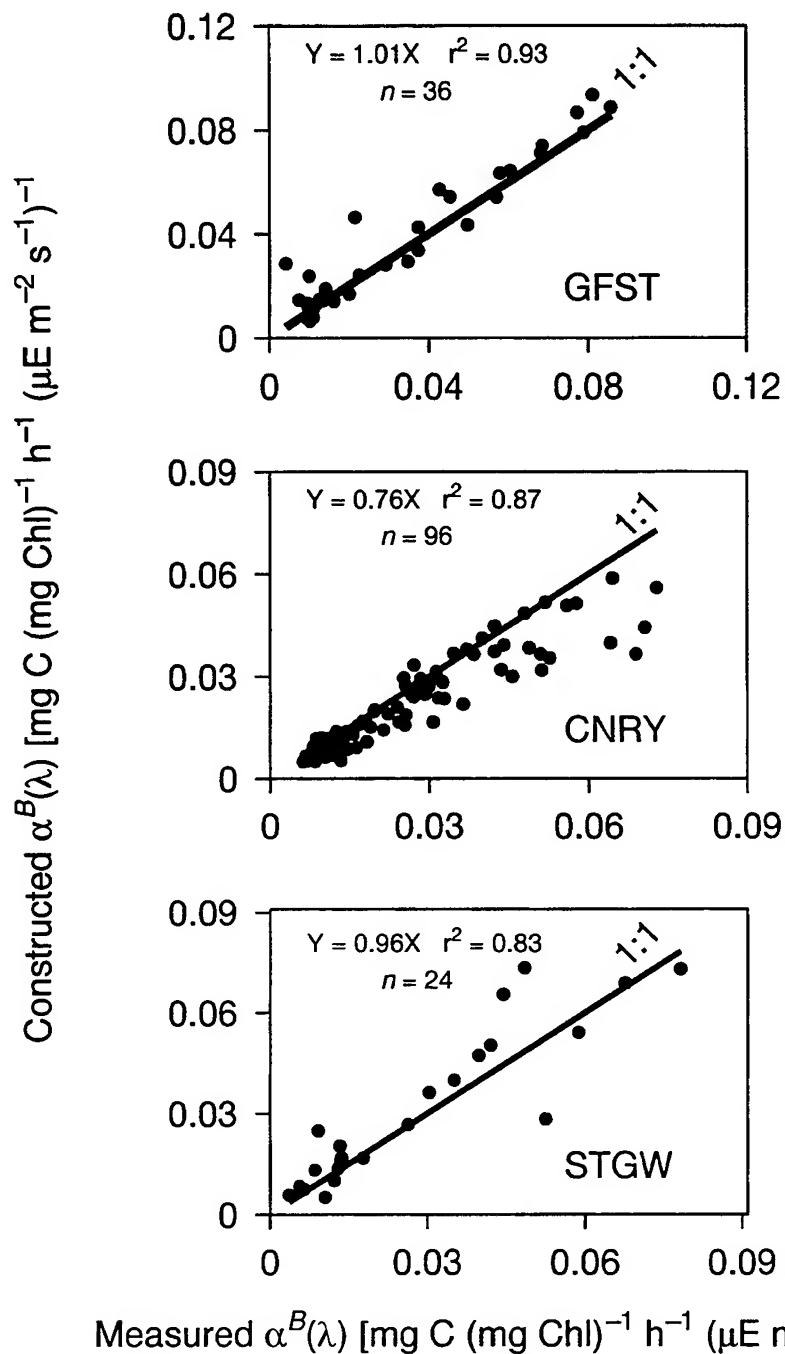


Fig. 3. Regression analysis of constructed $\alpha^B(\lambda)$ on the measured $\alpha^B(\lambda)$, for pooled data, from three biogeochemical provinces referred to in Fig. 2. The respective regression lines, the number of points, the r^2 values and the 1:1 lines are also shown.

In-water algorithms for estimation of chlorophyll *a* and primary production
in the Arabian Sea and the eastern Indian Ocean

Toru Hirawake, Hiroo Satoh, Tsutomu Morinaga, and Takashi Ishimaru

Department of Ocean Sciences, Tokyo University of Fisheries
5-7, Konan 4, Minato-ku, Tokyo, 108, Japan.

Motoaki Kishino

Photosynthesis Research Lab., Solar Energy Research Group
The Institute of Physical and Chemical Research (RIKEN)
2-1, Hirosawa, Wako-shi, Saitama, 351-01, Japan.

ABSTRACT

In-water algorithms to estimate the chlorophyll *a* concentration in the Arabian Sea and the Indian Ocean were set up by computation based on empirical method using subsurface radiance ratio of SeaWiFS bands. A series of investigation for the algorithms was carried out at 16 stations during a cruise in January 1994 from Gulf of Oman to Fremantle, Australia. Photosynthetic productivity of phytoplankton was measured at 12 stations by the stable ^{13}C isotope method. The algorithm of surface chlorophyll *a*, that the strongest correlation was observed, was $\text{Chl.}a + \text{Pheo. (mg m}^{-3}\text{)} = 0.26 \times [\text{Lu}(443)/\text{Lu}(490)]^{-3.35}$ with a coefficient of determination $r^2 = 0.93$. Most of the standing stock was included in the subsurface chlorophyll maximum (SCM) layer found clearly from 15 to 120 m. Primary production of water column in this area depends on it at the upper layer because of low photosynthetic productivity at SCM. Accordingly a linear relationship with $r^2 = 0.90$ between the surface chlorophyll *a* concentration and daily primary production of water column was obtained.

Keywords: in-water algorithm, chlorophyll, primary production, SCM, SeaWiFS, OCTS, Arabian Sea, Indian Ocean

1. INTRODUCTION

The Ocean Color and Temperature Scanner (OCTS) have launched in August 1996. The next sensor, the Sea-viewing Wide Field-of-view Sensor (SeaWiFS) will be launched next February. One of the purpose of these sensors is to determine the magnitude and variability of primary production by marine phytoplankton on a global scale.¹ Gordon *et al.*² showed the global algorithm for the Coastal Zone Color Scanner the (CZCS) to retrieve phytoplankton pigments in subtropical waters. This algorithm parameters are not universal because of a variation in phytoplankton species with region and season. Applying the algorithm to our data induced a large error with its maximum value of 135%. Furthermore, wavelength of the new sensors bands are different from that of CZCS. Thus, local and new algorithm parameters should be required for new sensors.

The CZCS provided a large number of ocean color data. The maps of phytoplankton distribution^{2,3} were made from the image. Based on the CZCS data, primary production was estimated using various algorithms which have a range from simple empirical relationship^{4,5,6} to complex analytical models^{6,7,8}. These algorithms and model have some problem to be resolved. The first is to predict the pigments profiles which were invisible from the satellite. Especially, subsurface chlorophyll maximum (SCM) causes error in estimation of primary production. To resolve this problem, Platt and Sathyendranath⁵ generalized the biomass profile at regional scales.

The Arabian Sea and the Indian Ocean have a wide range of biomass and productivity. The monsoon, SW during June - August and NE during December - February, and currents play a very important part in determining the variability of phytoplankton.^{9,10} Primary production and pigments concentration have measured in these area on board¹¹⁻¹³. These results showed that the occurrence of SCM, productivity and pigments distribution related to nutrients, mixed layer depth and light penetrating. Recent studies used CZCS imagery to derive the phytoplankton chlorophyll concentrations^{10,14,15} and primary production¹⁶ in the Arabian Sea. In the Indian Ocean, however, report of bio-optical observation as the basic research for the study to utilize the SeaWiFS and OCTS have apparently not been published to date.

During the cruises of T/V Umitaka-Marui III of Tokyo University of Fisheries in January 1994, we carried out a series of bio-optical measurements in the Indian Ocean included the Arabian Sea. In this paper, we report the in-water algorithms for retrieving the chlorophyll *a* concentration based on empirical method using subsurface radiance ratio of SeaWiFS bands, and discussed the relationship between surface chlorophyll *a* concentration and primary production in studied area.

2. Materials and Methods

Spectral radiation and chlorophyll *a* concentration at 16 stations, and photosynthetic productivity of phytoplankton at 12 stations, respectively, were measured (Fig. 1) on the cruises from Gulf of Oman to Fremantle, Australia. Profiles of spectral radiation were measured using the MER2020A (Biospherical Instruments Inc.). This instrument measures downwelling irradiance, $Ed(\lambda, z)$, and upwelling radiance, $Lu(\lambda, z)$, at 7 wavelengths (412, 443, 490, 510, 555, 565, and 683 nm) compatible with SeaWiFS and OCTS simultaneously.

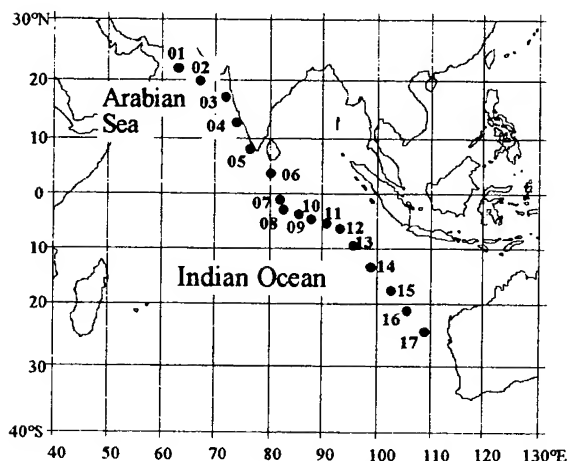


Fig. 1. Location of sampling station in the Arabian Sea and the Indian Ocean.

Water samples for primary productivity were collected using Van Dorn bottles from the sea surface and the depth of SCM. For chlorophyll *a* determination, additional water samples were collected using a Rosette multi sampler equipped with a CTD : OCTOPUS¹⁷ (OCTO-Parameter Underwater Sensor).

The concentrations of chlorophyll *a* were determined fluorometrically¹⁸ with Turner Designs 10-005R fluorometer after extracting the pigments in N, N-Dimethylformamide (DMF)¹⁹.

For measurement of absorption coefficients of total particle, the optical density of total particulate matter concentrated on the filter, OD_{tp} was measured spectrophotometer (UV365, Shimadzu) in the spectral range 350 - 750 nm. The filter was placed in methanol for 24 hours in order to extract pigments²⁰. The bleached filter was dried and then soaked again in filtered seawater. Then the optical density of the bleached material, OD_{fd} , was measured. The absorption coefficients (m^{-1}) were calculated from OD_{tp} and OD_{fd} using an algorithm of the form suggested by Mitchell (1990)²¹.

Photosynthetic productivity of phytoplankton was measured by the stable ^{13}C isotope method²². The samples were incubated for 4 hours in a water bath controlled at surface water temperature under different light levels. The isotope ratios of ^{12}C and ^{13}C were determined by infrared absorption spectrometry²³ with a ^{13}C analyzer (EX-130, JASCO). The photosynthetic rate was calculated by the method of Hama *et al.*²², and the rate at each depth was calculated on the basis of P-I curve fitted to the model of Eilers and Peeters²⁴. Primary production in water column was estimated by integrating the value multiplied the photosynthetic productivity by chlorophyll *a* concentration at each depth over the entire euphotic zone.

For setting up the in-water algorithms, we used two commonest forms,

$$C = A \times [Lu(\lambda_1, 0-) / Lu(\lambda_2, 0-)]^B \quad (1)$$

and

$$C = A \times \left[\frac{Lu(\lambda_1, 0-) + Lu(\lambda_2, 0-)}{Lu(\lambda_3, 0-)} \right]^B, \quad (2)$$

where *C* is the concentration of chlorophyll pigments ($mg\ m^{-3}$) at sea surface, *Lu* is the radiance, λ_1 , λ_2 and λ_3 are wavelengths, *A* and *B* are empirically determined constants, and 0- means that *Lu* was measured at the depth just below the surface. The constants, *A* and *B*, were calculated by least-squares fitting against all two and three bands combinations for the data.

3. Results and Discussion

3.1 Chlorophyll pigments retrieval algorithms

Relationships between surface chlorophyll pigments and radiance ratio expressed by Eq. (1) and (2), that the strongest correlation was observed, were shown in Fig. 2(a) and 2(b). Concentration of surface chlorophyll pigments (chlorophyll *a* + pheophytin), *C* was ranged from 0.05 to 0.72 mg m⁻³ in the studied area. Within the range of low concentration, the algorithms yielded by least-squares fitting were,

$$C = 0.26 \times [\text{Lu}(443, 0-) / \text{Lu}(490, 0-)]^{-3.35} \quad \text{with } r^2=0.93 \quad (3)$$

and

$$C = 1.53 \times \left[\frac{\text{Lu}(412, 0-) + \text{Lu}(443, 0-)}{\text{Lu}(490, 0-)} \right]^{-2.62} \quad \text{with } r^2=0.93. \quad (4)$$

respectively. The maximum relative errors of Eq. (3) and (4) were -32 % and -35 % that satisfied goal value for chlorophyll retrieval from SeaWiFS data in case 1 water²⁵. Usually these ratios have involved wavelength near the maximum in the chlorophyll *a* absorption (440 nm) and the minimum in chlorophyll *a* absorption (560 nm)³ for CZCS. In this study, the wavelength near the minimum in chlorophyll *a* absorption (555 nm) for new sensors was not selected in the ratio with a best correlation. Selected 490 nm was the most penetrable wavelength.

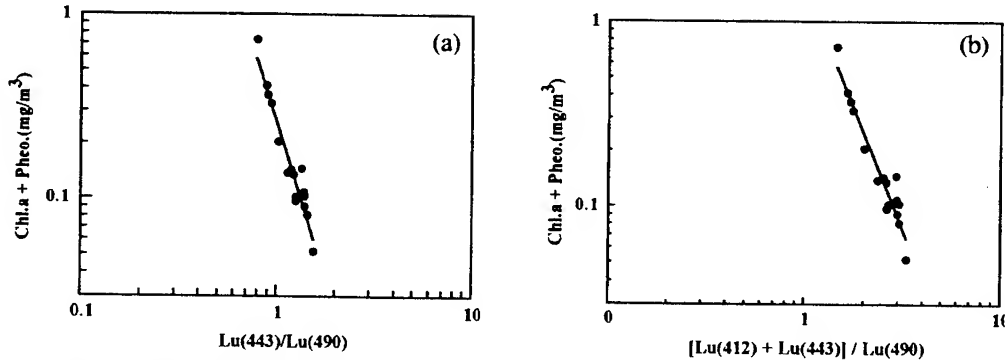


Fig. 2. Scatter plots of chlorophyll pigments concentration versus (a) $\text{Lu}(443)/\text{Lu}(490)$, and (b) $[\text{Lu}(412)+\text{Lu}(443)]/\text{Lu}(490)$.

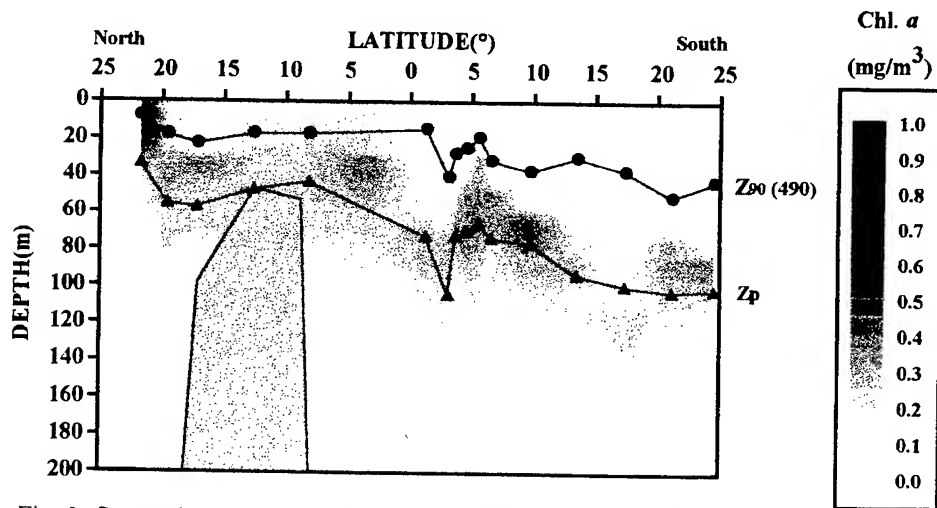


Fig. 3. Comparison of distribution of chlorophyll *a* concentration, Z_p and $Z_{90}(490)$.

3.2 SCM, Z_p and Z_{90}

Comparison of distribution of chlorophyll a concentration (mg m^{-3}), photic depth Z_p (m) (depth where the PAR is reduced to 1% of its surface value) and the penetration depth Z_{90} (m) at 490 nm was shown in Fig. 3. A distinct SCM was observed in the layer at depths of 15 to 40 m in the Arabian Sea ($0.3 - 0.9 \text{ mg m}^{-3}$), and at 50 to 120 m in the Indian Ocean ($0.2 - 0.5 \text{ mg m}^{-3}$). The Z_p was ranged from 34 m at Sta.01 to 105 m at Sta. 08 and the depths of SCM were lower part of the euphotic zone, that were 2 - 3 % penetration of the surface light except Sta.15. The SCM occupied more than 60 % of the standing stocks within the euphotic zone. While the $Z_{90}(490)$ was ranged from 9 to 23 m in the Arabian Sea and from 14 m to 50 m in the Indian Ocean. It was shallower than the depth of the SCM at all stations. This result showed that even at the most penetrable wavelength the information from the SCM was less than 10 % at the sea surface. The SCM included to the reckoning of primary production was invisible to the sensor on the satellites.

3.3 Surface chlorophyll a and primary production

The plots of the daily primary production of water column ($\text{gC m}^{-2} \text{ day}^{-1}$) versus the surface chlorophyll a concentration (mg m^{-3}) was shown in Fig. 4. The daily primary production was ranged from 0.23 to 0.73 in the Arabian Sea and from 0.08 to 0.17 ($\text{gC m}^{-2} \text{ day}^{-1}$) in the Indian Ocean. Although a large amount of standing stocks existed at the SCM, primary production of water column increases linearly with surface chlorophyll a concentration. The relationship obtained by least-squares fitting was,

$$P = 0.93 \times C_0 + 0.064, \quad (5)$$

where P is the daily primary production of water column ($\text{gC m}^{-2} \text{ day}^{-1}$) and C_0 is the surface chlorophyll a concentration (mg m^{-3}), respectively. This simple relationship has a strong correlation with a coefficient of determination $r^2=0.90$.

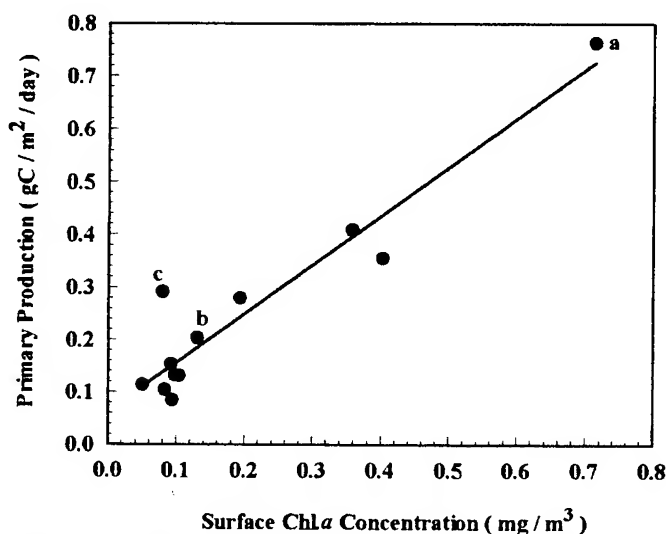


Fig. 4. The plots of the daily primary production of water column versus the surface chlorophyll a concentration. Symbols a, b and c were data at Sta. 02, 10, 17 and correspond to Fig. 5 (a), (b) and (c), respectively.

Photosynthetic productivity ($\text{mgC mg chl.}a^{-1} \text{ h}^{-1}$) versus Irradiance (PAR; $\mu\text{mol quanta m}^{-2} \text{ sec}^{-1}$) curves (P-I curves) at the sea surface and SCM in the Arabian Sea (Sta.2), equatorial area (Sta.10) and at the most southern station (Sta.17) were shown in Fig. 5. Maximum photosynthetic productivity, P_{max} , at the each layers were same level as shown in Fig. 5a. The productivity was very low under the low irradiance corresponded with its level of SCM layer in the Arabian Sea. While the productivity at the SCM in the equatorial area of the Indian Ocean (Fig. 5b) was very low over the all irradiance level, that showed loss of their photosynthetic ability as well as the result by Saijo *et al.*¹¹ In our studied area except the Sta.17, patterns of the P-I curve are similar with Fig. 5a in the Arabian Sea and Fig. 5b in the Indian Ocean. Since the primary production at each depth is the product of the photosynthetic productivity and chlorophyll a concentration, it at the SCM layer was very low. The primary production of water column in this area depends on it at the upper layer (approximately 70 % of the

column) in which the chlorophyll *a* concentration was very nearly constant. Thus a linear relationship with a high coefficient of determination between *P* and *C*₀ was obtained (Fig. 4). At the Sta.17 (Fig. 5c), however, the SCM layer had a *P*_{max} equivalent to it of the surface at near the irradiance level of the SCM. The primary production of the SCM layer was high (approximately 50 % of the column). Therefore *P* was underestimated largely from the equation (5) depended on the surface (Fig. 4, symbol c).

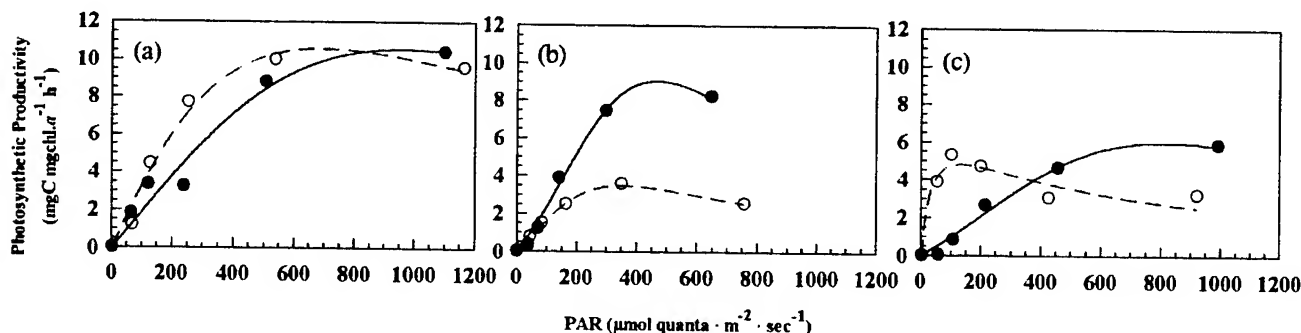


Fig. 5. Photosynthetic productivity versus Irradiance curves at the sea surface (solid lines) and SCM (dashed lines) of (a) Sta.02, (b) Sta.10 and (c) Sta.17.

4. CONCLUSION

In this study we obtained the regional algorithm for the retrieval of surface chlorophyll pigments concentration in the Arabian Sea and Indian Ocean during the NE monsoon season with relative error less than 35 %. The simple and linear relationship between the surface chlorophyll *a* concentration and daily primary production of water column was confirmed. Thus the estimation of primary production in this area will be possible by satellite observation. However it is anticipated that these algorithms can apply to only low pigments concentration area and induce a large error in the site where primary production depends on the standing stock within the SCM layer. To develop these algorithms and to estimate more accurately, we should collect a large number of bio-optical data through a widely range from low productivity area to high productivity area and recognize a variation and pattern in distribution of phytoplankton and characteristics of photosynthesis.

5. ACKNOWLEDGMENTS

We are grateful to Captain T. Isouchi, the officers and crew of the T/V Umitaka Maru III, Tokyo University of Fisheries for their cooperation during the cruises. Thanks are also to Dr. Takeda, Central Institute of Electric Power Industry, for his help in the analysis of ¹³C.

6. REFERENCES

1. S. B. Hooker, W. E. Esaias, G. C. Feldman, W. W. Gregg and C. R. McClain, *SeaWiFS Technical Report Series: Volume 1, An Overview of SeaWiFS and Ocean Color*, S. B. Hooker and E. R. Firestone [Eds.], NASA Technical Memorandum 104566, Vol. 1, 1992.
2. H. R. Gordon, D. K. Clark, J. W. Brown, O. B. Brown, R. H. Evans and W. W. Broenkow, "Phytoplankton pigment concentrations in the Middle Atlantic Bight: Comparison of ship determinations and CZCS estimates," *Appl. Opt.* **22**, 20-36 (1983).
3. H. R. Gordon and A. Y. Morel, *Remote Assessment of Ocean Color For Interpretation of Satellite Visible Imagery: A Review*, R. T. Barber, C. N. K. Mooers, M. J. Bowman and B. Zeitzschel [Eds.], Lecture Notes on Coastal and Estuarine Studies, Vol. 4, Springer-Verlag, New York, 1983.
4. R. W. Eppley, E. Stewart, M. R. Abbott and U. Heyman, "Estimating ocean primary production from satellite chlorophyll. Introduction to regional differences and statistics for the Southern California Bight," *J. Plankton Res.* **7**(1), 57-70 (1985).
5. T. Platt and S. Sathyendranath, "Oceanic primary production: Estimation by remote sensing at local and regional scales," *Science* **241**, 1613-1620 (1988).
6. A. Morel, "Light and marine photosynthesis: a spectral model with geochemical and climatological implications."

Prog. Oceanog. 26, 263-306 (1991).

7. T. Platt, C. Caverhill and S. Sathyendranath, "Basin-scale estimates of oceanic primary production by remote sensing: The North Atlantic," *J. Geophys. Res.* 96(C8), 15147-15159 (1991).

8. N. Hoepffner, T. Barker, L. Nykjaer, M. Estrada and P. Schlittenhardt, "Use of an analytical model to determine the primary production from satellite data in a coastal upwelling environment," *Oceanologica Acta* 17(4), 431-442 (1994).

9. J. Krey, "Primary production in the Indian Ocean I," *The Biology of the Indian Ocean*, B. Zeitzschel [Ed.], Ecological Studies: Analysis and Synthesis Vol. 3, pp. 115-126, Springer-Verlag, Berlin, 1973.

10. C. S. Yentsch and D. A. Phinney, "The effect of wind direction and velocity on the distribution of phytoplankton chlorophyll in the western Arabian Sea," *Oceanography of the Indian Ocean*, B. N. Desai [Ed.], pp. 57-66, A. A. Balkema, Rotterdam, 1993.

11. Y. Saijo, "Summary report on photosynthesis and chlorophyll in the Eastern Indian Ocean observed by Japanese Ships during IIOE," *Inform. Bull. Planktol. Japan* 12, 72-78 (1965).

12. C. S. Yentsch, "Distribution of chlorophyll and phaeophytin in the open ocean," *Deep-Sea Res.* 12, 653-666 (1965).

13. J. H. Ryther, J. R. Hall, A. K. Pease, A. Bakun and M. M. Jones, "Primary organic production in relation to the chemistry and hydrography of the western Indian Ocean," *Limnol. Oceanogr.* 11(3), 371-380 (1966).

14. J. I. Goes, H. do R. Gomes, A. Kumar, A. Gouveia, V. P. Devassy, A. H. Parulekar and L. V. G. Rao, "Satellite and ship studies of phytoplankton along the west coast of India," *Oceanography of the Indian Ocean*, B. N. Desai [Ed.], pp. 67-80, A. A. Balkema, Rotterdam, 1993.

15. K. Banse and C. R. McClain, "Winter blooms of phytoplankton in the Arabian Sea as observed by the Coastal Zone Color Scanner," *Mar. Ecol. Prog. Ser.* 34, 201-211 (1986).

16. J. Brock, S. Sathyendranath and T. Platt, "Modelling the seasonality of subsurface light and primary production in the Arabian Sea," *Mar. Ecol. Prog. Ser.* 101, 209-221 (1993).

17. T. Ishimaru, H. Otake, T. Saino, H. Hasumoto and T. Nakai, "OCTOPUS, an octo-parameter underwater sensor, for use in biological oceanography studies," *J. Oceanogr. Soc. Japan* 40, 207-212 (1984).

18. J. D. H. Strickland and T. R. Parsons, "A practical handbook of seawater analysis," *Bull. Fish. Res. Bd. Can.* 167, pp. 310 (1972).

19. R. Suzuki and T. Ishimaru, "An improved method for the determination of phytoplankton chlorophyll using N, N-Dimethylformamide," *J. Oceanogr. Soc. Japan* 46, 190-194 (1990).

20. M. Kishino, C. R. Booth, N. Okami, "Underwater radiant energy absorbed by phytoplankton, detritus, dissolved organic matter, and pure water," *Limnol. Oceanogr.* 29(2), 340-349 (1984).

21. B. G. Mitchell, "Algorithms for determining the absorption coefficient of aquatic particulates using the quantitative filter technique (QTF)," *Ocean Optics X*, R. W. Spinrad [Ed.], Vol. 1302, pp. 137-148, SPIE, Bellingham, 1990.

22. T. Hama, T. Miyazaki, Y. Ogawa, T. Iwakuma, M. Takahashi, A. Otsuki and S. Ichimura, "Measurement of photosynthetic production of a marine phytoplankton population using a stable ^{13}C isotope," *Mar. Biol.* 73, 31-36 (1983).

23. H. Satoh, Y. Yamaguchi, N. Kokubun and Y. Aruga, "Application of infrared absorption spectrometry for measuring the photosynthetic production of phytoplankton by the stable ^{13}C isotope method," *La mer* 23(4), 171-176 (1985).

24. P. H. C. Eilers and J. C. H. Peeters, "A model for the relationship between light intensity and the rate of photosynthesis in phytoplankton," *Ecol. Modelling* 42, 199-215 (1988).

25. J. L. Mueller and R. W. Austin, *SeaWiFS Technical Report Series: Volume 25, Ocean Optics Protocols for SeaWiFS Validation, Revision 1*, S. B. Hooker, E. R. Firestone and J. G. Acker [Eds.], NASA Technical Memorandum 104566, Vol. 25, 1995.

Primary production and irradiance during an intermonsoon cruise to the Arabian Sea (November, 1995)

John Marra

Lamont-Doherty Earth Observatory of Columbia University
Palisades, NY 10964

R.T. Barber

Duke University Marine Laboratory
Beaufort, NC 28516

C. Trees

Center for Hydrologic Optics and Remote Sensing, San Diego State University
San Diego, CA 92182

Zachary Johnson

Duke University Marine Laboratory
Beaufort, NC 28516

C. Kinkade

Lamont-Doherty Earth Observatory of Columbia University
Palisades, NY 10964

ABSTRACT

The Process-6 cruise, of the Arabian Sea Expedition of the Joint Global Ocean Flux Study (JGOFS), occurred during an intermonsoon, in October-November 1995. A variety of water column conditions were sampled in terms of euphotic zone depths, autotrophic biomass, resident phytoplankton populations, and nutrients. We use measurements of the rate of primary production (in situ), quantities of chlorophyll *a*, the properties of phytoplankton absorption, daily time courses of submarine PAR, and estimates of quantum yield to examine the variability seen. Both phytoplankton absorption and variations in quantum yield contribute to variations in primary production. Offshore populations exhibit a reduction in the apparent maximum quantum yield.

Keywords: primary production, phytoplankton, absorption, quantum yield, Arabian Sea

1. INTRODUCTION

The Arabian Sea is subject to a twice-per-year reversal of winds, the monsoons. The Northeast Monsoon blows off Asia in the months of December and January, and the Southwest Monsoon in the summer months blows dry winds from Africa. Because the Coriolis parameter is relatively weak at the latitudes of the Arabian Sea, the ocean responds quickly to changes in wind, setting up analogous reversals in ocean currents and other wind-driven flows. During the Southwest Monsoon, for example, there exists a generalized offshore flow during the summer months which induces upwelling of colder, nutrient-rich water near the Arabian Peninsula. Offshore, the situation is more complicated, however, evidence also exists for enrichment of surface waters through eddies and Ekman divergence.

The seasonal cycle in the Arabian Sea is therefore unlike that found for example in the North Atlantic. Because it is located in the tropics, there is little seasonal variation in solar radiation, save for cloudiness, and temperature varies by only about 4 or 5°C. Thus, while the monsoons create seasonal signals in surface nutrient concentrations, there are not the confounding changes in solar radiation, temperature, and nutrients as found in the temperate ocean. The seasonal dynamics of the Arabian Sea therefore suggest a means to study the effect of nutrients on primary production to the exclusion of the other factors,

light and temperature.¹

We present here some ongoing analyses of the primary production data from the Arabian Sea, focussing on Process Cruise 6, which took place in October-November, 1995. In a large sense, the analyses here are in the form of a progress report. We do not have all the data in such a form to constitute a complete analysis of the primary productivity of the Arabian Sea during an intermonsoon; indeed not all the data are as yet available. What we have ready are eight in situ primary production (carbon assimilation) experiments, irradiance, nutrient, chlorophyll (fluorometric) and hydrographic data, and data on the absorption properties of phytoplankton.

The question we ask is: What governs the variability of the rate of primary production with the levels of irradiance measured? We analyze the in situ primary production and irradiance data using the basic equation,

$$P = \phi \cdot \bar{a}_{ph} \cdot E \quad (1)$$

which has been used in several studies^{2,3}, albeit with some variation, and where P is the rate carbon assimilation ($\text{mmols C m}^{-3} \text{ d}^{-1}$), ϕ is the quantum yield (mols C per mols photon), \bar{a}_{ph} is the phytoplankton absorption coefficient (m^{-1}) and E is the daily (PAR) irradiance incident on the sample ($\text{mols photons m}^{-2} \text{ d}^{-1}$). We assume, for the purposes of our analysis, that equation (1) applies to the phytoplankton populations at each station as a whole.

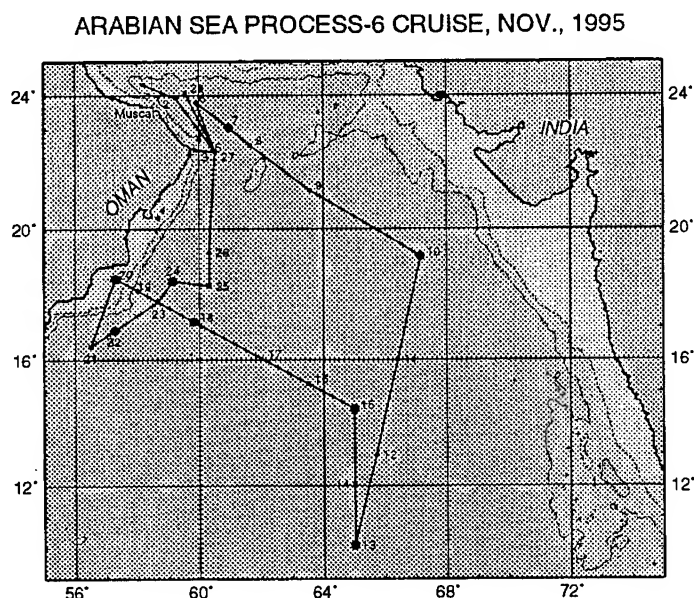


Fig. 1. A station map of Process Cruise 6 of the Arabian Sea Expedition. The larger filled circles represent stations where in situ primary production experiments were done.

Process-6 followed the 1996 Southwest Monsoon by 1-2 months. Although the moorings used in the Forced Upper Ocean Dynamics Experiment had already been recovered by the time of the cruise, the winds had returned to their pre-monsoon velocities, that is, similar to winds characteristic of April and May. Throughout Process-6, winds were light, and sea states calm.

The cruise got underway from Muscat, Oman on 29 October and returned on 26 November, 1996 (Fig. 1). The objective of the cruise was to sample a variety of ocean optical conditions, and secondarily to transit the routine Arabian Sea Expedition station circuit. Thus, at the beginning of the cruise, more time was spent near a front in the Gulf of Oman, and at the end of the cruise, different eddy-like features were investigated, as viewed from AVHRR images for sea-surface temperature.

2. METHODS

The methods followed Joint Global Ocean Flux Study (JGOFS) protocols.⁴ John Morrison and Lou Codispoti oversaw the collection of hydrographic data and nutrients. Chlorophyll *a* was analyzed using a Turner Designs Model 11 fluorometer, which was calibrated using pure chlorophyll *a*. Primary production was estimated from the uptake into particulate matter of ¹⁴C as H¹⁴CO₃. At each productivity station (Fig. 1), two replicates from eight depths in the euphotic zone were suspended from a spar buoy floating free of the ship, from dawn until dusk. The samples were subsequently filtered through GF/F filters, and the filters assayed for their radioactivity aboard ship. Samples to determine the particulate absorption spectrum were also collected onto GF/F filters and scanned over 400-750 nm in a Perkin-Elmer Lambda-3 spectrophotometer. The 'detrital' spectrum was similarly scanned after an extraction in hot methanol,⁵ and the phytoplankton spectrum found by difference. The mean (by wavelength) value for phytoplankton absorption is determined from the equation

$$\bar{a}_{ph} = \frac{\int_{400}^{750} a_{ph}(\lambda) d\lambda}{750 - 400} \quad (2)$$

The method for obtaining the daily subsurface (PAR) irradiance data is as follows. We have added Tattletale Model 5 data logging computers (and batteries) to PAR sensors (model QSP-200) from Biospherical Instruments, producing a self-contained PAR-sensing and data-logging unit. The PAR-loggers are attached to the line of the in situ array at 3-4 depths. PAR is recorded on each, every two minutes throughout the day. We recognize some of the difficulties in interpreting PAR data^{6,7}, however, the QSP-200 combined with a data-logging capability is presently the simplest and most cost-effective means of obtaining detailed time series of submarine irradiance data at sea. Although not a complete test, comparisons we have made with the MER-2040 (unpublished) in determining diffuse attenuation coefficients averaged over the euphotic zone are very good.

3. RESULTS

When primary production is plotted against irradiance, the data seem to fall into three, or maybe four, groups (Fig. 2a). The more offshore stations, 10, 13 and 15, have low rates of production, while two stations, 07 and 18, show about the same high rates. Station 07 is in the Gulf of Oman, while station 18 is about 500 km to the south of station 07. The remainder make up an intermediate group. At any rate, our objective is to try to see how we can collapse the variability, and thereby investigate how primary production is regulated.

The typical means of reducing the variability is to normalize against chlorophyll *a*, and this helps somewhat, particularly in closing the gap between the offshore stations and stations more under the influence of coastal processes. However, we might have expected something better, especially since chlorophyll-specific production is a fundamental parameter being used to develop algorithms by which we compute the rate of primary production, in situ, from satellite imagery. Overall, the variability is worse.

An alternative normalization is to use the absorption coefficient rather than chlorophyll *a*, and the result of that is shown in Fig. 2c. The normalization to \bar{a}_{ph} reduces much of the variability seen with primary production alone (Fig. 2a), or primary production normalized to chlorophyll *a* (Fig. 2b). Only stations 13 and 15 (the stations furthest away from coastlines), remain low compared to the rest of the stations. Notably, station 10, now joins the other stations in terms of its production characteristics. The absorption coefficient, even as the mean by wavelength, has more information about the photosynthetic properties of phytoplankton than just chlorophyll *a*. For example, pigment composition and pigment packaging will be reflected in the absorption coefficient.

Fig. 2c also has information about the quantum yield of production, since re-arranging Eq (1),

$$\phi = \frac{P}{\bar{a}_{ph} \cdot E} \quad (3)$$

Process-6, November, 1995

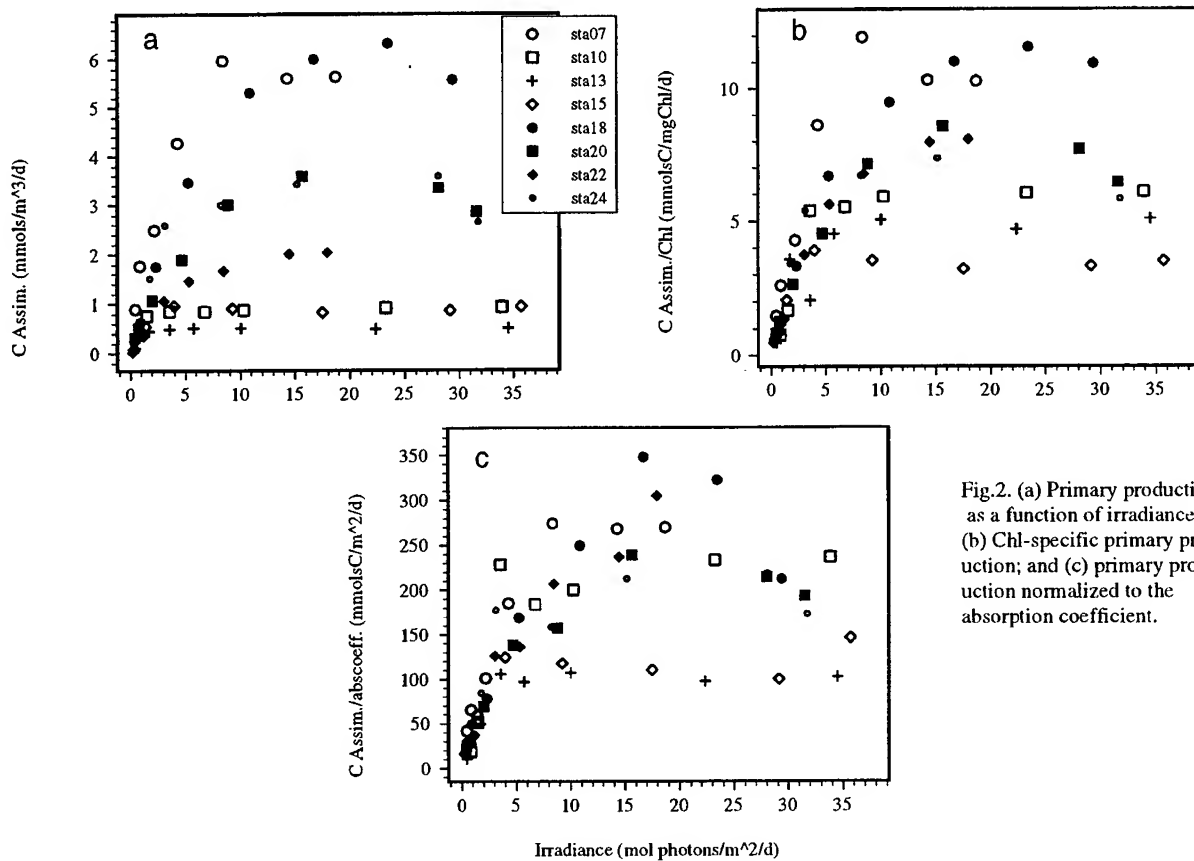


Fig.2. (a) Primary production as a function of irradiance; (b) Chl-specific primary production; and (c) primary production normalized to the absorption coefficient.

The initial slope in Fig. 2c should be equal to the maximum quantum yield, ϕ_{\max} . Since the data in Fig. 2c appear to separate into two groups (the offshore stations 13 and 15, and the rest), we treat them separately for the purposes of non-linear regression to determine the parameters of the relationship between quantum yield and irradiance. The relationship that seems to provide the best fit to the data (based on an analysis of the errors), was a variant of one previously proposed,³

$$\phi = \phi_{\max} \cdot \tanh(K/E) \quad (4)$$

where K is a constant analogous to E_k from $P(E)$ curves, that is, the ratio of ϕ_{\max} to the value of the negative slope at high irradiances. The results are shown in Fig. 3. A clearer picture emerges and suggests that for stations 13 and 15, there appears to be an overall reduction in the quantum yield expressed through the maximum value. For stations 13 and 15, ϕ_{\max} and K take the values 0.039 and 3.2, respectively, while for all the other stations, ϕ_{\max} and K take the values 0.052 mols C (mol photons)⁻¹ and 4.3 mol photons m⁻² d⁻¹.

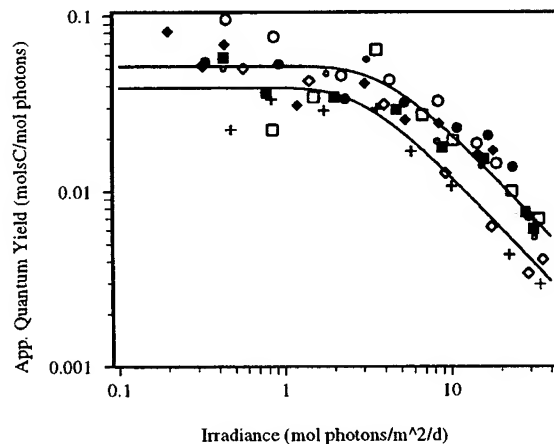


Fig. 3. Quantum yield, calculated as in Eq. (3) in the text, as a function of irradiance. The lines are from non-linear regression using Eq. (4), the parameters of which are in the text. Symbols from Fig. 2

The variability arising from the absorption coefficient, that is, from pigment packaging and pigment composition, is included in the analysis of quantum yield.

4. DISCUSSION

From our analysis, we conclude that both the absorption properties of the phytoplankton and their quantum yields are responsible for the variability in primary production for the intermonsoon period in late 1995. For the stations under the influence of coastal upwelling, and inshore of the Findlater Jet (i.e., north of 15°N), much of the variability can be explained by \bar{a}_{ph} . The offshore stations show a reduction in ϕ_{max} by about 30%.

We are not aware of any studies which routinely employ a normalization of primary production data to the phytoplankton absorption coefficient (however, see ref. 8), however, for our data it appears to work well, and has obvious value to the problem of determining primary production from remote sensing data such as satellite imagery.⁸ The variation in \bar{a}_{ph} can arise from two factors, the pigment composition of the populations, and pigment packaging. We have found little evidence of pigment packaging. One diagnostic is to compare the value of the specific absorption coefficient at 674 nm, $a^*_{ph}(674)$, with that in solution. All our values are equal to or exceed $0.0203 \text{ m}^2 (\text{mg Chl}a)^{-1}$, the “unpacked” specific absorption coefficient at 674 nm.⁹ Our assessment that pigment packaging is unimportant for the time period we sampled in the Arabian Sea agrees with other investigations.¹⁰

The ϕ_{max} estimated in Fig. 3 assumes uniform populations at each of the stations. In fact, ϕ_{max} will probably change as a function of depth, that is, with the stratification of populations. But knowledge of those changes will have to await analysis of the P(E) data. Stations 13 and 15, the offshore stations where we observed reductions in ϕ_{max} have deeper euphotic zones, have greater depth contrasts in density (higher stratification), and lower nutrients (Table 1). In contrast, for Stations 07 and 18 where rates were high, nitrate values usually were $>0.3 \mu\text{Mol}$ in the euphotic zone. However, to devise a relationship between ϕ_{max} and quantities of nitrate¹¹ or nitrate supply¹² that applies to the entire region sampled will be difficult. Nitrate, in particular, shows substantial variability within a day (Table 1), and which cannot be ascribed solely to sampling different water masses during the time the ship was at a particular station.

Table 1: Water column properties for each station. The Depth of Nitracline and Mixed Layer Depths are rough estimates based on the depth where nitrate reaches $0.2 \mu\text{Mol}$ and density increases by $0.2 \sigma_t$ units over the surface value, respectively. The variation in surface nitrate is that occurring over a 24-36 h period on station.

Station	Depth of Nitracline (m)	Euphotic Zone Depth (m)	Mixed Layer Depth (m)	Nitrate at Surface (μMol)
07	0	34	32	0.1-0.4
10	51	75	52	0.00-0.06
13	57	93	38	0.0-0.08
15	52	79	72	0.00-0.05
18	0	44	56	1.1-1.3
20	0-37	53	41	0.0-0.2
22	26	63	29	0.00-0.06
24	0-62	53	63	0.0-1.0

5. ACKNOWLEDGMENTS

This research was supported by the National Science Foundation, NASA, and the Office of Naval Research. We thank our colleagues in the Arabian Sea Expedition for access to data, and to W.B. Balch, Chief Scientist of Process-6. We also acknowledge the assistance of C. Knudson, E. Barber, D. Sullivan, and M. Hiscock throughout the Arabian Sea Expedition. Fig. 1 was produced from the GMT-System software.¹³

6. REFERENCES

1. J. Marra, J. and R.R. Bidigare, "The question of a nutrient effect on the bio-optical properties of phytoplankton." *Proc. SPIE*, 2258, *Ocean Optics XII*, pp. 152-162, 1994.
2. J. Marra, and others, "Estimation of seasonal primary production from moored optical sensors in the Sargasso Sea," *J. Geophys. Res.*, Vol. 97, pp. 7399-7412, 1992.
3. R.R. Bidigare, B.B. Prezelin and R.C. Smith, "Bio-optical models and the problems of scaling," *Primary production and biogeochemical cycling in the sea*, P.G. Falkowski and A.V. Woodhead (Eds.), pp. 175-212., Plenum Press, New York, 1992.
4. JGOFS, "Protocols for the Joint Global Ocean Flux Study (JGOFS) Core Measurements," JGOFS Report No. 19, Bergen, Norway, pp. 169, 1994.
5. M. Kishino, N. Okami and S. Ichimura, "Estimation of the spectral absorption coefficients of phytoplankton in the sea." *Bull. Mar. Sci.* Vol. 37, pp. 634-642, 1985.
6. C.R. Booth, "The design and evaluation of a measurement system for photosynthetically active quantum scalar irradiance." *Limnol. Oceanogr.* Vol. 21, pp.326-336, 1976.
7. J. Marra, W.S. Chamberlin and C. Knudson, "Proportionality between in situ carbon assimilation and bio-optical measures of primary production in the Gulf of Maine in summer." *Limnol. Oceanogr.* Vol. 38, pp.232-238, 1993.
8. Z.P. Lee, K.L. Carder, J. Marra, R.G. Steward and M.J. Perry, "Estimating primary production at depth from remote sensing," *Appl. Optics*, Vol. 35, pp. 463-474, 1996.
9. R.R. Bidigare, M.E. Ondrusek, J.H. Morrow and D.A. Kiefer, "In vivo absorption of algal pigments," *Proc. SPIE*, 2258, *Ocean Optics X*, pp. 290-302, 1989.
10. W.P. Bissett, J.S. Patch, K.L. Carder and Z.P. Lee, "Pigment packaging and chlorophyll-specific absorption in high-light oceanic waters." *Limnol. Oceanogr.*, submitted, 1996.
11. T. Platt, S. Sathyendranath, O. Ulloa, W.G. Harrison, N. Hoepffner and J. Goes, "Nutrient control of phytoplankton photosynthesis in the Western North Atlantic," *Nature* Vol. 356, pp. 229-231, 1992.
12. J.S. Cleveland, M.J. Perry, D.A. Kiefer and M.C. Talbot, "Maximal quantum yield of photosynthesis in the northwestern Sargasso Sea," *J. Mar. Res.* Vol. 47, pp. 869-886, 1989.
13. P. Wessel and W.H.F. Smith, "Free software helps map and display data, EOS Trans. AGU, Vol. 72, pp. 445-446, 1992.

The Bermuda BioOptics Project - BBOP

D.A. Siegel, M.C. O'Brien, S.A. Garver, E.A. Brody, J.C. Sorensen,
Institute for Computational Earth System Science and Department of Geography,
University of California at Santa Barbara, Santa Barbara, CA 93106, USA

A.F. Michaels[†], E.A. Caporelli[†] and N.B. Nelson

Bermuda Biological Station for Research, Ferry Reach, GE 01, Bermuda

[†]Now at Wrigley Institute of Marine Science, University of Southern California,
Los Angeles, CA 90089, USA

ABSTRACT - The Bermuda BioOptics Project (BBOP) has been making bi-weekly to monthly profile observations of bio-optical parameters as a component of the U.S. JGOFS Bermuda Atlantic Time series Study (BATS) since January of 1992. This five year record of apparent and inherent optical observations is, to be the best of our knowledge, the longest quasi-continuous, bio-optical time series made for any oceanic region. The foci for BBOP are to: 1) characterize upper ocean bio-optical property variability; temporally, spatially and spectrally, 2) assess light availability and its utilization, 3) model primary production and other biogeochemical rates using bio-optical quantities and 4) provide the "optical link" between BATS and satellite ocean color observations. Here, we will introduce BBOP, discuss briefly its sampling, data processing procedures and the availability of the BBOP data set. As an example of its utility, we will illustrate the role and implications of colored dissolved organic materials in the absorption and diffuse attenuation of light.

KEYWORDS: bio-optics, time-series, Sargasso Sea, Bermuda, colored dissolved organic material, open ocean

INTRODUCTION

Primary production, the conversion of dissolved inorganic carbon to particulate organic carbon by phytoplankton through their utilization of absorbed light, is a fundamental process in the upper ocean carbon cycle. Its characterization and numerical prediction requires a determination of the ambient light field and its variability. Similarly, our ability to assess ocean biogeochemistry from space is limited by how well we can interpret the water leaving radiance spectrum. As the open ocean represents ~90% the total ocean area (Ryther, 1969), the open ocean *must* be well understood if we are to understand these processes on a global scale. The achievement of these goals provides the focus for the Bermuda BioOptics Project, or BBOP. BBOP has been making high-quality, profile observations of bio-optical parameters as part of the U.S. JGOFS Bermuda Atlantic Time series Study (BATS) since January of 1992. This 5 year long record of bio-optical observations is, to be the best of our knowledge, the longest record of this type made for any oceanic region.

The Sargasso Sea off Bermuda is a unique environment as it may be characterized by both eutrophic and oligotrophic conditions during different times of the year (Menzel and Ryther, 1960; Michaels and Knap, 1996; Siegel *et al.*, 1995a). This provides bio-optical data covering a reasonable dynamic range of possible conditions. The Sargasso Sea off Bermuda has been observed quasi-continuously since 1954 and represents, in our opinion, the best characterized open ocean site on the planet (e.g., Michaels and Knap, 1996). Hydrostation S lies 25 km southeast of Bermuda and the 40+ year time-series record of biweekly hydrographic sampling is continuing at this station. The BATS site is 75 km southeast of Bermuda (31° 50' N; 64° 10' W). Since October 1988, BATS personnel have conducted more than 100 cruises to this site. Other time series observations are conducted off Bermuda, including determinations of deep sediment trap fluxes (since 1977), atmospheric chemistry and aerosol measurements (since 1980) and an interdisciplinary moored science program (since 1994, the Bermuda Testbed Mooring; Dickey, 1994). Clearly, BBOP builds on a long tradition of time-series research at Bermuda.

BBOP GOALS

As the Bermuda BioOptics Project is tightly linked with the U.S. JGOFS BATS observational program, its scientific goals are in many ways compliment the overall BATS efforts. Specifically, the scientific goals of the BBOP are to:

- characterize optical property variations at BATS; temporally, spatially and spectrally,

- assess light availability and its utilization,
- model primary production and other biogeochemically relevant rates using optical quantities, and
- provide the "optical link" between BATS and satellite ocean color observations.

The accomplishment of these goals puts strict requirements on the nature of the sampling program. For instance, providing the optical link between BATS and satellite ocean color data sets requires that noon-time observations of water-leaving radiance be determined while the assessment of light utilization requires day-long observations to match the BATS *in situ* primary production array incubation.

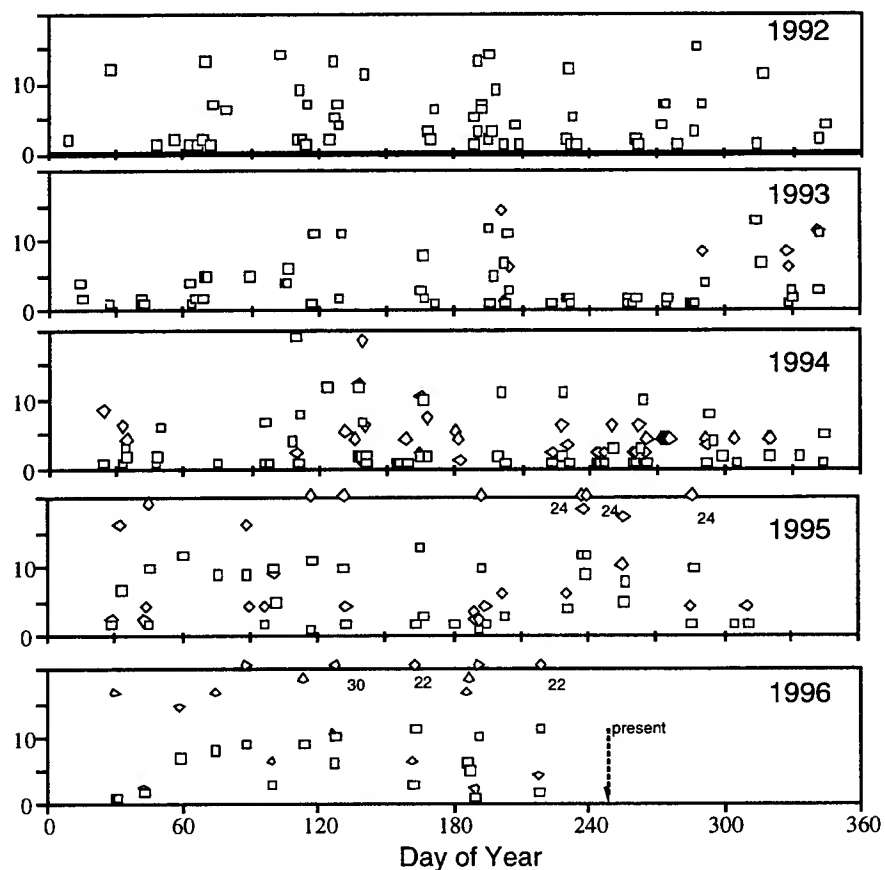


Figure 1 - The BBOP sampling time series. Squares are the number of BBOP AOP casts (2 profiles per cast) while diamonds are the number of individual *in situ* IOP profiles. Typically, 64 noontime casts are made each year.

THE BBOP MEASUREMENT PROGRAM

The optical and biogeochemical measurements made by the BBOP and BATS programs are listed in Table 1. Nearly every measurement recommended in the Ocean Optics Protocols for SeaWiFS Validation for product validation, radiative transfer and bio-optical algorithms (Table 1 in Mueller and Austin, 1995) is sampled as part of the combined BBOP/BATS data set (Table 1). The primary measurement system is a profiling spectroradiometer (MER-2040, Biospherical Instruments, San Diego, CA; Smith *et al.* 1996) which has provided apparent optical property (AOP) observations for use in a wide variety of science questions (Siegel *et al.* 1995a; 1996; Siegel and Michaels, 1996; Garver and Siegel, 1996). The determination of AOP's from optical profiles is well documented (Sorensen *et al.* 1994; Siegel *et al.* 1995b; 1995c), as is our understanding of the ship shadow produced by the *R/V Weatherbird II* (Weir *et al.* 1994) and the calibration history of the primary spectroradiometer used in BBOP (O'Brien *et al.* 1996). Preliminary results from the *in situ* inherent optical property (IOP) profiling instrumentation are presented in this volume (Brody *et al.*, 1996).

TABLE 1: OPTICAL AND BIOGEOCHEMICAL DETERMINATIONS MADE AT BATS

BBOP	
Direct Measurements:	
$E_d(z, \lambda)$	Downwelling vector irradiance (410,441,465,488,510,520,555,565,589,625,665 & 683 nm)
$E_d(0^+, \lambda)$	Incident irradiance (340,390,410,441,465,488,520,545,565,589,625,665 & 683 nm)
$L_u(z, \lambda)$	Upwelling radiance (410,441,465,488,510,520,555,565,589,625,665 & 683 nm)
$a(z, \lambda)$	<i>In situ</i> absorption spectrum using WetLabs AC-9 (410,440,490,520,565,650,676&715 nm)
$c(z, \lambda)$	<i>In situ</i> beam attenuation spectrum (same λ 's as above)
$a_p(\lambda)$	Particulate absorption spectrum by QFT (Mitchell, 1990)
$a_{det}(\lambda)$	Detrital particle absorption spectrum by MeOH extraction
$a_s(\lambda)$	Colored dissolved absorption spectrum
$E_o(z, \lambda)$	Scalar irradiance at 441, 488 and 565 nm
$F_f(z)$	Natural chlorophyll fluorescence using a broadband upwelled radiance sensor
chl-fl(z)	Chlorophyll fluorescence with a SeaTech fluorometer
$c(z, 660)$	Beam attenuation coefficient at 660 nm with SeaTech 25 cm transmissometer
$T(z)$ & $S(z)$	SeaBird temperature and conductivity probes
chl-a(z_0)	Discrete chlorophyll <i>a</i> determinations via Turner fluorometry (for next day delivery)
Primary Derived Products:	
$R_{RS}(0^-, \lambda)$	Remote sensing reflectance (410,441,465,488,510,520,555,565,589,625,665 & 683 nm)
$a_{ph}(\lambda)$	Phytoplankton absorption spectrum ($= a_p(\lambda) - a_{det}(\lambda)$)
$K_d(z, \lambda)$	Attenuation coef. for $E_d(z, \lambda)$ (410,441,465,488,510,520,555,565,589,625,665 & 683 nm)
$\langle PAR(z) \rangle$	Daily mean photosynthetically available radiation at depths of the <i>in situ</i> C^{14} incubations
$b(z, \lambda)$	<i>In situ</i> spectral scattering coefficient ($= c(z, \lambda) - a(z, \lambda)$)
U.S. JGOFS BATS AND RELATED BIOGEOCHEMISTRY SAMPLING PROGRAMS	
Primary Production (<i>in situ</i> ^{14}C incubation)	Sinking flux (sediment trap array)
Phytoplankton pigments (fluorometric & HPLC)	Nutrients (NO_3+NO_2 , SiO_4 , PO_4)
CO_2 system (alkalinity, TCO_2 and pCO_2)	Continuous atmospheric & surface pCO_2
Dissolved oxygen (continuous & discrete)	Zooplankton biomass & grazing
POC & PON (POP infrequently)	DOC & DON (DOP infrequently)
Full water column, WOCE-standard CTD profile	Bacterial abundance and rates
Phytoplankton abundance by flow cytometry	Coccolithophore abundance
Validation spatial cruises (5 days, 4cruises/year)	Deep sea sediment fluxes
BATS-SAT	
Acquisition and analysis of LAC SeaWiFS ocean color and AVHRR sea surface temperature imagery	
BERMUDA TESTBED MOORING	
Spectroradiometry ($E_d(z_0, \lambda)$ & $L_u(z_0, \lambda)$)	Horizontal velocity
<i>In situ</i> chlorophyll and CDOM fluorescence	Beam attenuation at 660 nm
Quasi-continuous <i>in situ</i> nitrate analysis	Air-sea heat and momentum fluxes
<i>In situ</i> absorption & beam attenuation ($a(z_0, \lambda)$ & $c(z_0, \lambda)$)	Dissolved oxygen
Temperature and salinity ($T(z_0)$ & $S(z_0)$)	Natural chl fluorescence ($F_f(z_0)$)
Automated C^{14} productivity incubations	Trace metal clean water sampling

The BBOP sampling time series is shown in figure 1. Over the past five years, BBOP has made more than 2,500 spectroradiometry profiles. A total of 16 BATS cruises are conducted each year and the BBOP profiler is deployed during other cruises of opportunity. This has resulted in a yearly average of 64 noon time casts sampled. The BBOP sampling goals are to 1) make a noon-time AOP/IOP cast every day at sea, 2) sample quasi-continuously when the BATS *in situ* primary production array is deployed and 3) deploy the radiometer every 4 hours (including night) so the diurnal variations in IOP's can be assessed (e.g., Siegel *et al.* 1989). This sampling regimen insures that the BBOP data set will be able to answer a wide variety of scientific questions as well as for ocean color satellite sensor calibration and product validation.

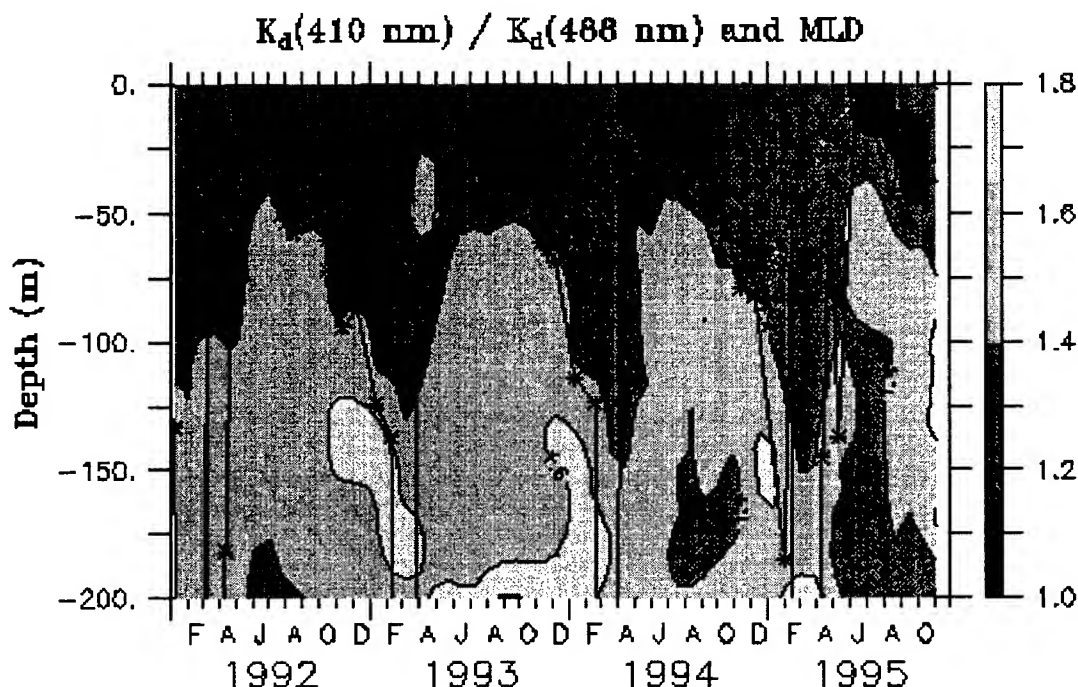


Figure 2 - Time-depth representation of the ratio of $K_d(410)$ to $K_d(488)$, a qualitative indicator of CDM concentrations, the combined effects of CDOM and detrital particulates to light absorption. Higher values indicate higher CDM concentrations and the solid line is the mixed layer depth.

SEASONAL VARIABILITY OF CDOM IN THE SARGASSO SEA

The BBOP data set has been developed to address scientific hypotheses linking ocean optics with marine biogeochemistry. Here, we will use the BBOP data set to assess the optical role and biogeochemical implications of colored dissolved organic materials (CDOM) in the open ocean (Siegel *et al.* 1995a; Siegel and Michaels, 1996; Garver and Siegel, 1996; Nelson *et al.* 1996). Values of the diffuse attenuation coefficient, $K_d(\lambda)$, will be highly influenced by CDOM and detrital particulate materials in the violet region of the spectrum but will be affected to a far lesser degree for the blue-green wavebands. In contrast, spectral differences in light attenuation due to phytoplankton for these wavebands will be roughly the same. By examining the value of the ratio of $K_d(410)$ to $K_d(488)$, the time-depth distributions of the combined effects of CDOM and detrital particulate materials can be ascertained (fig. 2; Siegel *et al.* 1995a; Siegel and Michaels, 1996). We refer to the combined influence of CDOM and detrital particulate materials as colored detrital materials, or CDM. During the summer, CDM concentrations appear to increase within the seasonal pycnocline while they are much lower in the near-surface mixed layer. During the fall and winter, convective mixing homogenizes the CDM profile and this seasonal cycle of CDM abundance repeats (fig. 2). We hypothesize that mixed layer CDM values are reduced due to photo-oxidation while concentrations at depth increase due to *in situ* production.

This CDM signal is an important and often dominant component of the absorption and solar radiation attenuation budget at BATS (e.g., Siegel and Michaels, 1996; Garver and Siegel, 1996; Nelson *et al.* 1996).

Linear regression modeling by Siegel and Michaels [1996] demonstrated that values of light attenuation at 441 nm due to CDM are nearly as large as those due to chlorophyll materials. Semi-analytical, inverse modeling of remote sensed reflectance spectra also illustrates that CDM materials make roughly the same contribution to the absorption coefficient at 441 nm as do phytoplankton materials (Garver and Siegel, 1996; Siegel *et al.* 1996). Finally, *in vivo* estimates of CDM absorption at 441 nm are greater than phytoplankton components (fig. 3; Nelson *et al.* 1996). Thus, several lines of evidence indicate that CDM and algal pigment concentrations contribute nearly equally to the value of the absorption coefficient at 440 nm (and values of $K_d(\lambda)$) observed from the Sargasso Sea.

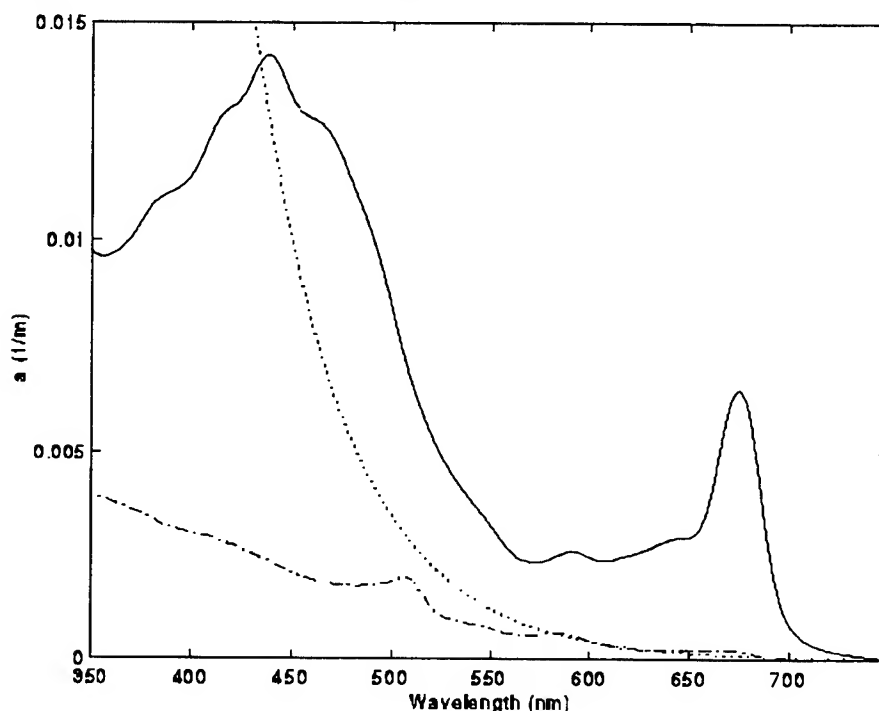


Figure 3 - Representative absorption spectra of 1) phytoplankton ($a_{ph}(\lambda)$, solid line), 2) CDOM ($a_g(\lambda)$, dotted line), and 3) particulate detritus ($a_d(\lambda)$, dashed line). Spectra are from an April 1995 sample taken at 60 m. The $a_g(\lambda)$ spectrum is constructed by extrapolating the measured $a_g(300)$ and spectral slope.

The constituents comprising CDM still need to be determined as *in situ* optical determinations cannot separate particulate from dissolved materials. Recent *in vivo* estimates of particulate and dissolved absorption made by Nelson *et al.* [1996] indicate that the dominant fraction of the CDM signal is due to CDOM (fig. 3). This is particularly true for the blue and violet regions of the spectrum. On the average, CDOM absorption at 440 nm comprised more than one-half of the total non-water absorption coefficient, while detrital particulate absorption was found to be a minor constituent (Nelson *et al.* 1996).

The biogeochemical significance of the observed CDOM variations can also be explored. Concentrations of CDOM and CDM appear to be completely unrelated to dissolved organic carbon (DOC) concentrations (e.g., Siegel and Michaels, 1996; Nelson *et al.* 1996). Mixed layer DOC increases during and just after the spring bloom while CDOM concentrations decrease. Hence, CDOM must contribute only marginally to the total carbon content of the dissolved organic material pool. Further, the seasonal changes of CDOM content in the mixed layers suggests that rates of photochemical reactions will also be modified by the presence or absence of CDOM (e.g., Siegel and Michaels, 1996). Siegel and Michaels [1996] postulate that dimethyl sulfide (DMS) concentrations in surface waters, an important trace gas for the production of cloud condensing nuclei, may regulated by photo-oxidation processes which require CDOM to absorb photons. In the summer mixed layer where CDOM concentrations are low, rates of DMS photo-oxidation will be low resulting in high stocks of DMS as is observed (Siegel and Michaels, 1996). This illustrates a causal link between CDOM variability and biogeochemical transformations in the upper ocean.

SUMMARY AND CONCLUSIONS

We have introduced the Bermuda BioOptics Program (BBOP) and used its data to demonstrate the importance of CDOM in the open ocean. We have shown that CDOM concentrations vary independently throughout the year and independently from chlorophyll concentrations. Hence, simple definitions of Case I waters used in optical oceanography should be reconsidered. More importantly, these data demonstrate that colored dissolved materials are as important in the open ocean as they are in the estuarine environments. We will soon know the global implications of these findings as satellite ocean color missions such as the Ocean Color Temperature Scanner and SeaWiFS will be able to assess CDOM and chlorophyll pigments independently (e.g., Garver and Siegel, 1996; Carder *et al.* in review). Researchers will then be able to make a global assessment of the importance of CDOM to marine bio-optics and ocean biogeochemistry.

ACKNOWLEDGMENTS

The authors would like to thank the BATS technicians and the crew of *R/V Weatherbird II* for their dedication and commitment to the data presented here. Dave Menzies performed the quarterly calibrations of the BBOP radiometer at UCSB. BBOP is supported by NASA (NAGW-3145 and NAGW-3511), the SeaWiFS project office, the U.S. Office of Naval Research and the National Science Foundation (OCE 91-16372 and OCE 90-16990). NSF also supports the core BATS program (OCE 88-01089, OCE 93-01950). The BBOP and BATS data sets are available via the world wide web. For the BBOP data set the URL is <http://www.icess.ucsb.edu/bbop> while for the BATS program it is <http://www.bbsr.edu>.

REFERENCES

- Brody, E.A., D.A. Siegel, E.A. Caporelli, and N.B. Nelson, 1996, Validation of *in situ* inherent optical properties in the Sargasso Sea. This volume.
- Dickey, T., 1994: The Bermuda Testbed Mooring program. *Bull. Amer. Met. Soc.*, **76**, 584.
- Garver, S.A., and D.A. Siegel, 1996, Inherent optical property inversion of remote sensing reflectance and its biogeochemical interpretation. In press, *Journal of Geophysical Research*.
- Menzel, D.W., and J.H. Ryther, 1960, The annual cycle of primary production in the Sargasso Sea off Bermuda. *Deep-Sea Research*, **6**, 351-367.
- Michaels, A.F., and A.H. Knap, 1996: Overview of the U.S. JGOFS Bermuda Atlantic Time-series Study and the Hydrostation S program. *Deep-Sea Research*, **II**, **43**, 157-198.
- Mitchell, B.G., 1990: Algorithms for determining the absorption coefficient for aquatic particles using the quantitative filter technique, *Ocean Optics X, Proc. SPIE*, **1302**, 137-142.
- Mueller, J.L., and R.W. Austin, 1995: Ocean optics protocols for SeaWiFS Validation, Revision 1. *NASA Tech. Memo. 104566*, Vol. 25, NASA Goddard Space Flight Center, Greenbelt, Maryland, 67 pp.
- Nelson, N.B., D.A. Siegel, and A.F. Michaels, 1996: Seasonal dynamics of colored dissolved material in the Sargasso Sea, Submitted to *Deep Sea Research*.
- O'Brien, M.C., D.W. Menzies and D.A. Siegel, 1996, Calibration history of the BBOP radiometer. In preparation for publication in a SeaWiFS Technical Memorandum.
- Ryther, J.H., 1969: Photosynthesis and fish production in the sea. *Science*, **166**, 444-446.
- Siegel, D.A., and A.F. Michaels, 1996: On non-chlorophyll light attenuation in the open ocean: Implications for biogeochemistry and remote sensing. *Deep-Sea Research*, **II**, **43**, 321-345.
- Siegel, D.A., T.D. Dickey, L. Washburn, M.K. Hamilton and B.G. Mitchell, 1989: Optical determination of particulate abundance and production variations in the oligotrophic ocean. *Deep-Sea Res.*, **36**, 211-222.
- Siegel, D.A., A.F. Michaels, J. Sorensen, M.C. O'Brien, and M.A. Hammer, 1995a: Seasonal variability of light availability and its utilization in the Sargasso Sea. *J. Geophys. Res.*, **100**, 8695-8713.
- Siegel, D.A., M.C. O'Brien, J. Sorensen, D. Konnoff, and E. Fields, 1995b, *BBOP Sampling and Data Processing Protocols*. U.S. JGOFS Planning Report Number 19, WHOI, Woods Hole, MA, 77pp.
- Siegel, D.A., M.C. O'Brien, and others, 1995c, Results of the SeaWiFS Data Analysis Round-Robin (DARR-94), July 1994. *NASA Tech. Memo. 104566*, Vol. 26, NASA GSFC, Greenbelt, MD, 58 pp.
- Siegel, D.A., N.B. Nelson, and S.A. Garver, 1996: Modeling inherent optical property characteristics using ocean color spectra from the Sargasso Sea. For *Applied Optics*.
- Smith, R.C., D.W. Menzies and C.R. Booth 1996: Oceanographic Bio-Optical Profiling System II. This volume.
- Sorensen, J.C., D. Konnoff, M.C. O'Brien, E. Fields, and D.A. Siegel, 1994: The BBOP data processing system, In: *Ocean Optics XII, Proc. SPIE*, **2258**, 539-546.
- Weir, C.T., D.A. Siegel, A.F. Michaels and D.W. Menzies, 1994: An *in situ* evaluation of a ship's shadow, In: *Ocean Optics XII, Proc. SPIE*, **2258**, 815-821.

Marcel Babin^{1,2}, Nora Sadoudi¹, Luigi Lazzara⁴, Jacques Gostan³, Frédéric Partensky⁶, Annick Bricaud¹, Marcel Veldhuis⁵, André Morel¹ and Paul G. Falkowski⁷

¹Lab. de Physique et Chimie Marines, U. Pierre et Marie Curie and CNRS, BP 8, 06230 Villefranche-sur-Mer, France

²ACRI S.A., BP 234, 260 Route du Pin Montard, 06904 Sophia Antipolis, France

³Lab. d'Écologie du Plancton Marin, U. Pierre et Marie Curie and CNRS, BP 28, 06230 Villefranche-sur-Mer, France

⁴Laboratorio di Ecologia, Dipartimento di Biologia Vegetale dell' Università, Via Micheli 1, 50121 Firenze, Italy

⁵Netherlands Institute for Sea Research, PO Box 59, 1790 AB Den Burg, Texel, The Netherlands

⁶Station Biologique, Université Pierre et Marie Curie and CNRS, BP 74, 29680 Roscoff, France

⁷Oceanographic and Atmospheric Sciences Division, Brookhaven National Laboratory, Upton, New York 11973, USA

INTRODUCTION

Photoacclimation in prokaryotic phytoplankton species commonly found in the ocean is not as well documented as for eukaryotes. Variations in the pigment cellular content and composition were observed in *Synechococcus*¹ and *Prochlorococcus*² in response to changes in light conditions. These variations lead to changes in the magnitude and spectral shape of light absorption capabilities^{3,4}. Partensky *et al.*² reported a significantly higher photosynthetic capacity in *Prochlorococcus* grown under high light. Besides these signs of the capability of prokaryotic phytoplankton to photoacclimate, it is known that they possess no flagellae and do not operate a xanthophyll cycle⁵. So, keeping in mind the specific character of prokaryotes, it could be thought that the number of photoacclimation strategies is smaller compared with eukaryotes. Nevertheless, prokaryotic phytoplankton dominate large parts of the ocean, especially oligotrophic systems where it grows at high rates⁶. In the present study, we aim at understanding why prokaryotic phytoplankton have such an ecological success in the ocean. Specifically, our objectives are (1) to clearly identify the photoacclimation strategies deployed by these organisms, significant in terms of carbon fixation, and (2) to quantify the timescales on which they are deployed. Finally, we discuss how these strategies are effective in the ocean. To reach our objectives, we studied the photoacclimation kinetics of *Prochlorococcus* sp. We chose this species firstly because it often dominates the prokaryotic phytoplankton communities of oligotrophic systems⁷. Secondly, there is a need for a better documentation on this recently discovered species, which was shown to account for up to 50 % of net primary production⁶ in oligotrophic systems.

2. METHODS

Photoacclimation strategies of *Prochlorococcus* sp. were studied on two different strains, one isolated from Mediterranean surface waters (hereafter denoted MED strain) and another one isolated from the Sargasso Sea deep chlorophyll maximum (hereafter denoted SARG strain). Both strains were grown in batch cultures and submitted to light shift experiments. Light shift up and shift down were applied between 15 and 56 $\mu\text{mol quanta m}^{-2} \text{s}^{-1}$. Shifted batches and controls (shown in Figs. 2-6 as dashed line and plus sign) were then monitored during the following 72 to 96 hours. The following measurements are reported here: pigment cellular content determined from HPLC analyses and flow cytometry cell counting, spectral values of the dv-chl *a*-specific *in vivo* absorption coefficient [$a(\lambda)$], maximum quantum yield of carbon fixation (ϕ_{max}) and saturation parameter (E_k) as determined from P vs. E experiments⁸, and effective optical cross section (σ_{PS2}) and fraction of functional photosystems 2 (f)^{8,9}.

3. RESULTS AND DISCUSSION

$a^*(\lambda)$ decreased in the blue part of the spectrum for all cultures transferred from high to low light, while the reverse was observed for those shifted from low to high light (Fig. 1). The highest values and largest changes in $a^*(\lambda)$ were observed for the SARG strain shifted from low to high light. In this case, the high values at t_0 were related to the high dv-chl *b*-to-dv-chl *a* ratio and the corresponding strong dv-chl *b* absorption band centered around 480 nm. In the second phase of the kinetic, the strong increase of $a^*(\lambda)$ to even higher values accompanied the high increase in the zeaxanthin-to-dv-chl *a* ratio. In fact, in all cases, variations in $a^*(\lambda)$ during the photoacclimation kinetic were dominated by variations in the zeaxanthin-to-dv-chl *a* ratio. Interestingly, for the SARG strain, variations in the specific absorption coefficient from which the contribution of zeaxanthin has been removed [$a^*_{-\text{zea}}(\lambda)$] exhibited variations opposite to those of $a^*(\lambda)$ during the photoacclimation kinetic. In this case, variations in $a^*_{-\text{zea}}(\lambda)$ were accompanied by variations in the dv-chl *b*-to-dv-chl *a* ratio. For the MED strain, the $a^*_{-\text{zea}}(\lambda)$ spectrum remained constant. These results are consistent with the quite stable σ_{PS2} values observed during this experiment (Fig. 3). Variations in zeaxanthin cell content and dv-chl *a*-relative concentration had no significant effect on

σ_{PS2} . Therefore, it can be considered neither as a light harvesting nor as a photoprotecting pigment. Kana *et al.*¹⁰ reached such conclusions for *Synechococcus* as he observed that the zeaxanthin cell content was constant whatever the growth light conditions. He also argued that, given the location of zeaxanthin in cell walls, it could not contribute to any photoprotection process that requires a close interaction with the photosynthetic apparatus. The phylogenic proximity of cyanobacteria and *Prochlorococcus* let us believe that zeaxanthin in *Prochlorococcus* is also located in cell walls. If it is actually the case, Kana's arguments holds also for *Prochlorococcus*. Additionally, even considering the highest zeaxanthin cellular concentration observed during this experiment and found in literature¹, it can be shown from Beer's law, that zeaxanthin located in cell walls can intercept at most 5 and 15 % of light impinging on the cell, respectively. Thus, photoprotection by sunglass effect would be insignificant. This conclusion is again supported by the relative constancy of σ_{PS2} . Given the observed increase in the cell content of zeaxanthin for the SARG LH, it cannot be excluded that zeaxanthin is involved in de-excitation of active oxygen formed under excess irradiance.

Considering the single control points of ϕ_{max} for each of treatment (except for the SARG LH) as the initial value, all strains shifted from high to low light showed a significant decrease in ϕ_{max} over the first 48 hours, and the reverse trend was observed for shifts from low to high light (Fig. 4). The largest variation range was observed for the SARG strain. The maximum quantum yield of carbon fixation, when computed using only photosynthetically active pigments ($\phi_{max-zea}$), significantly varied from close to the maximal theoretical value (0.125) down to 0.01 mol C (mol quanta)⁻¹ (Fig. 5). Variations in $\phi_{max-zea}$ were linearly related to variations in photosystem 2 energy conversion efficiency caused by nutrient limitation and photodamage (Fig. 7). No photoacclimation process thus occurred at the level of energy conversion. E_k tightly followed light conditions (Fig. 6). Because σ_{PS2} was rather constant throughout the experiment, variations in E_k were associated to the minimum time required to transfer an electron from water to CO₂, which is known to vary with the cellular content of photosynthetic units. Variations in the cellular pool of photosynthetic units during this experiment were confirmed by variations in size of cellular pigment pool, while the effective size of photosynthetic units remained stable. It is thus concluded that the only significant photoacclimation strategy observed during this experiment was a change in the cellular pool of photosynthetic units relative to RUBISCO. Results obtained at sea (in Tropical Atlantic and in the Equatorial Pacific) also reveal that the strategy observed in laboratory leads to a tight relationship between mean irradiance within the mixed layer and (1) the contribution of non-photosynthetic pigments to phytoplankton light absorption, and (2) the E_k values. A parameterization of photosynthetic parameters within predictive models of primary production, could be based on the respective depths of the euphotic zone and of the mixed layer.

4. REFERENCES

1. R. R. Bidigare, O. Schofield and B. B. Prézelin, "Influence of zeaxanthin on quantum yield of photosynthesis of *Synechococcus* clone WH7803 (DC2)", *Mar. Ecol. Prog. Ser.* 56, 177-188 (1989).
2. F. Partensky, N. Hoepffner, W. K. W. Li, O. Olloa and D. Vaulot, "Photoacclimation of *Prochlorococcus* sp. (*Prochlorophyta*) strains isolated from North Atlantic and Mediterranean Sea", *Plant Physiol.* 101, 285-296 (1993).
3. A. Morel, Y.-H. Ahn, F. Partensky, D. Vaulot and H. Claustre, "*Prochlorococcus* and *Synechococcus*: A comparative study of their optical properties in relation to their size and pigmentation", *J. Mar. Res.* 51, 617-649 (1993).
4. L. R. Moore, R. Goericke and S. Chisholm, "Comparative physiology of *Synechococcus* and *Prochlorococcus*: influence of light and temperature on growth, pigments, fluorescence and absorptive properties", *Mar. Ecol. Prog. Ser.* 116, 259-275 (1995).
5. B. Demmig-Adams and W. W. Adams III, "Photoprotection and other responses of plants to high light stress", *Annual Rev. of Plant Physiol. Plant Mol. Biol.* 43, 599-626 (1992).
6. D. Vaulot, D. Marie, R. J. Olson and S. W. Chisholm, "Growth of *Prochlorococcus*, a photosynthetic prokaryote, in the Equatorial Pacific Ocean", *Science* 268, 1480-1482 (1995).
7. F. Partensky, J. Blanchot, F. Lantoine, J. Neveux and D. Marie, "Vertical structure of picoplankton at different trophic sites of the subtropical northeastern Atlantic Ocean", *Deep-Sea Res.* (*in press*).
8. M. Babin, A. Morel, H. Claustre, A. Bricaud, Z. Kolber and P. G. Falkowski, "Nitrogen- and irradiance-dependent variations of the maximum quantum yield of carbon fixation in eutrophic, mesotrophic and oligotrophic marine systems", *Deep-Sea Res.* (*in press*).
9. Z. Kolber and P. G. Falkowski, "Use of active fluorescence to estimate phytoplankton photosynthesis *in situ*", *Limnol. Oceanogr.* 38, 1646-1665.
10. T. M. Kana, P. M. Gilbert, R. Goericke and N. A. Welschmeyer, "Zeaxanthin and β -carotene in *Synechococcus* WH7803 respond differently to irradiance", *Limnol. Oceanogr.* 33, 1623-1627.

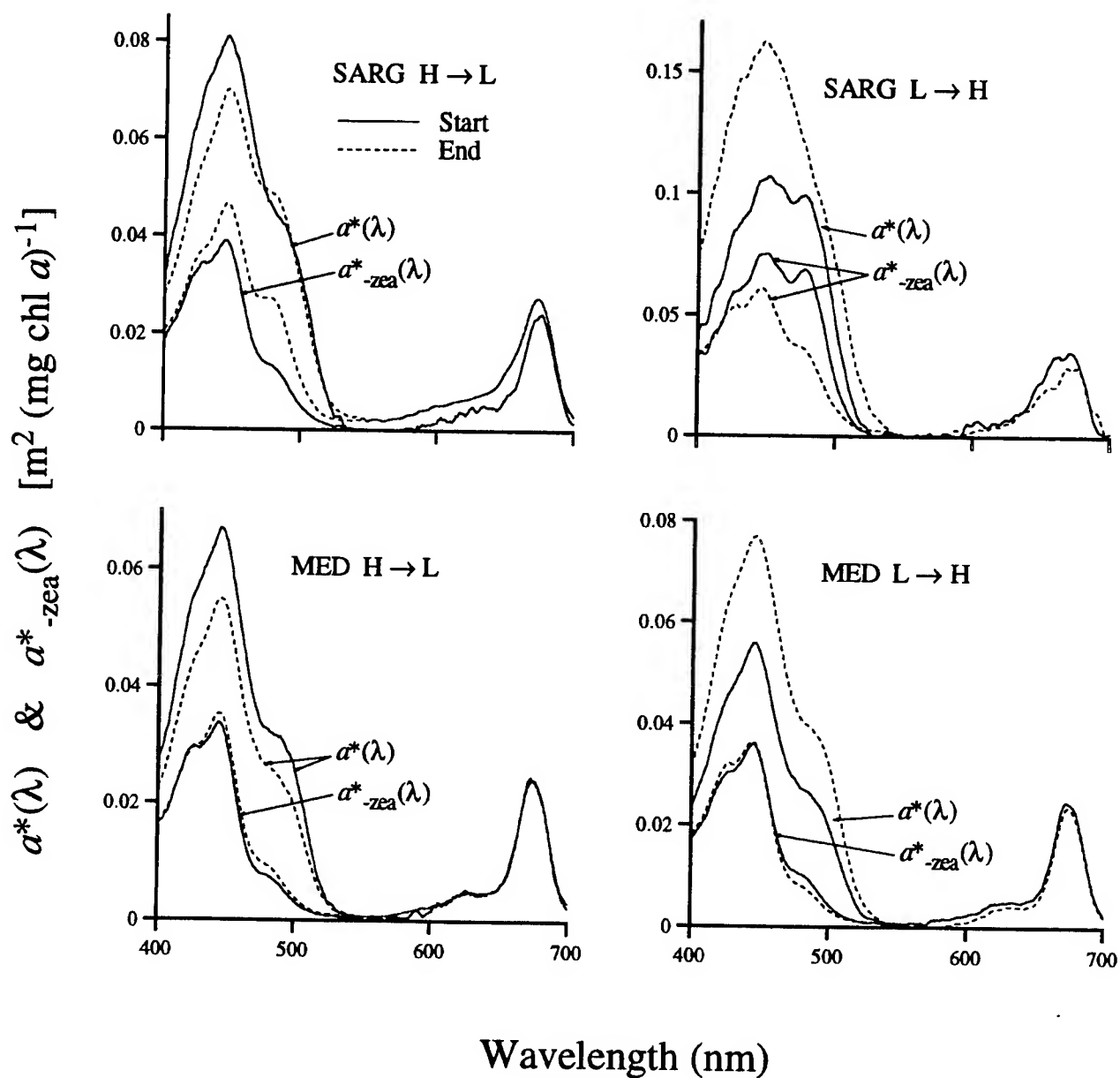


Fig. 1. Spectral values of the *in vivo* absorption coefficient for all pigments [$a^*(\lambda)$] and for photosynthetic pigments only [$a^*_{-zea}(\lambda)$].

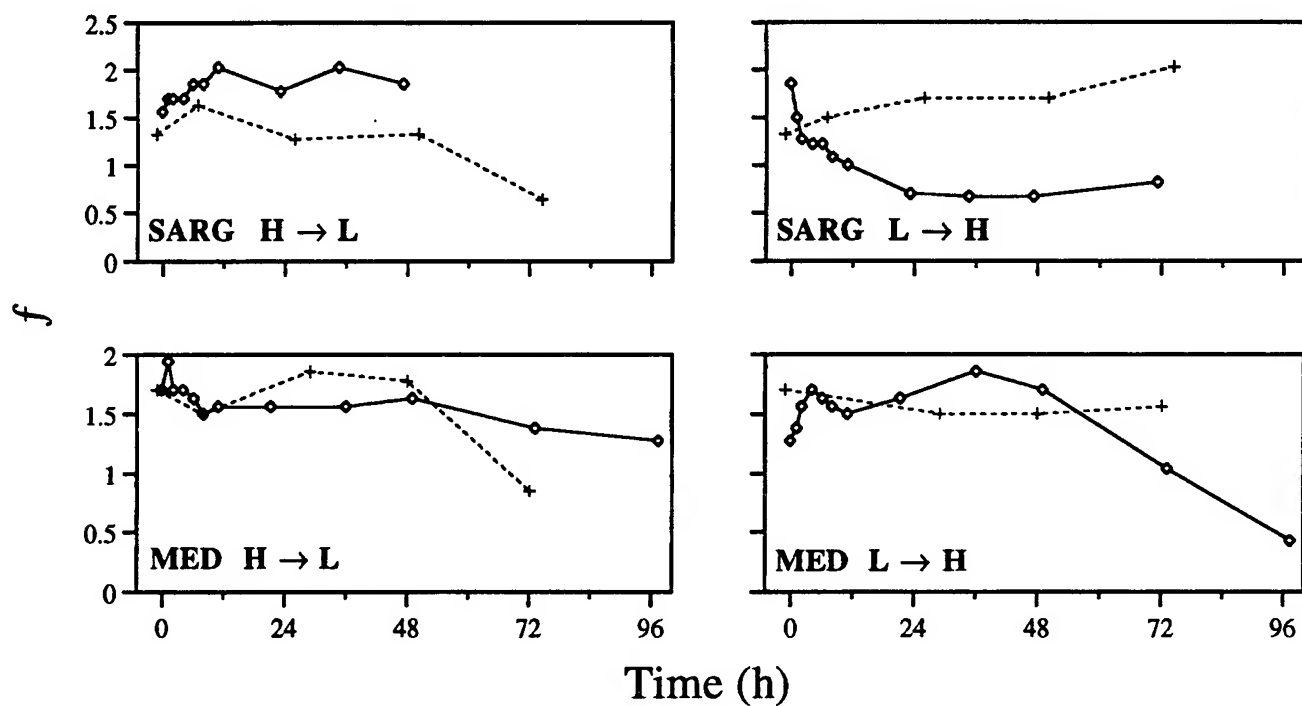


Fig. 2. Variations in the fraction of functional photosystem 2 reaction centers following the light shift.

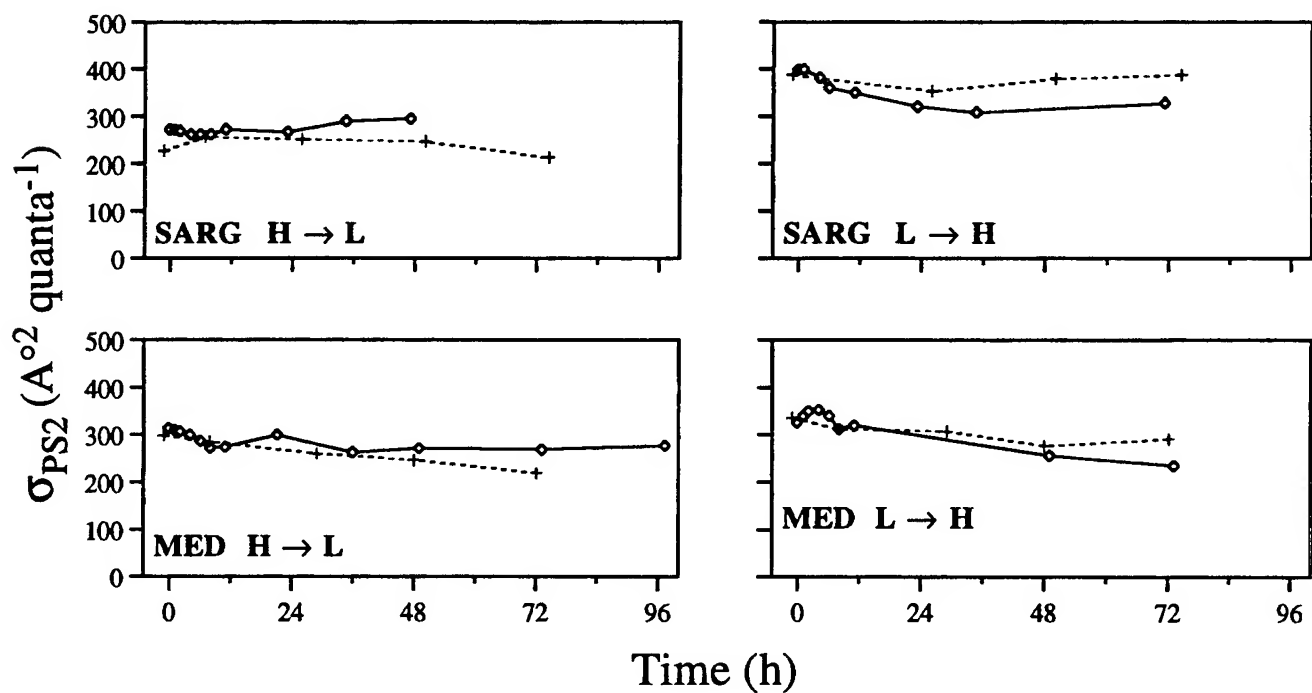


Fig. 3. Variations in the effective optical cross section of photosystem 2 following the light shift.

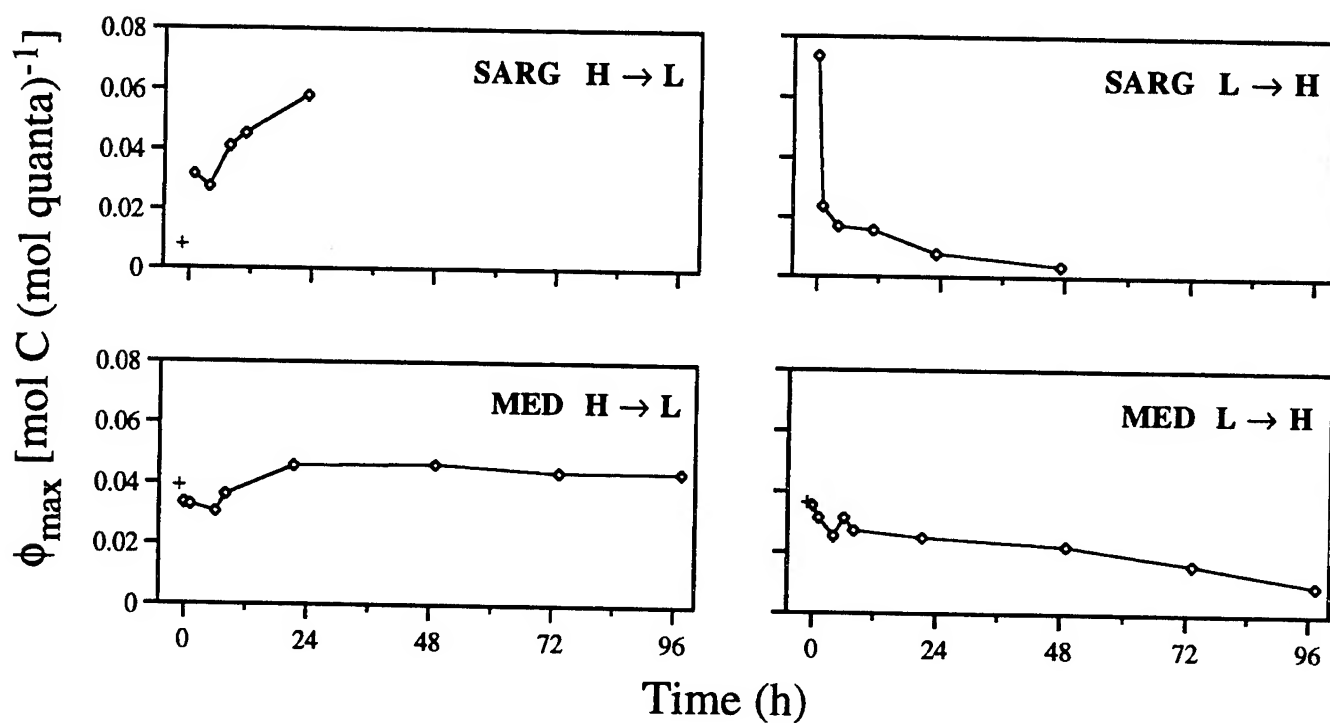


Fig. 4. Variations in the maximum quantum yield of carbon fixation following the light shift.

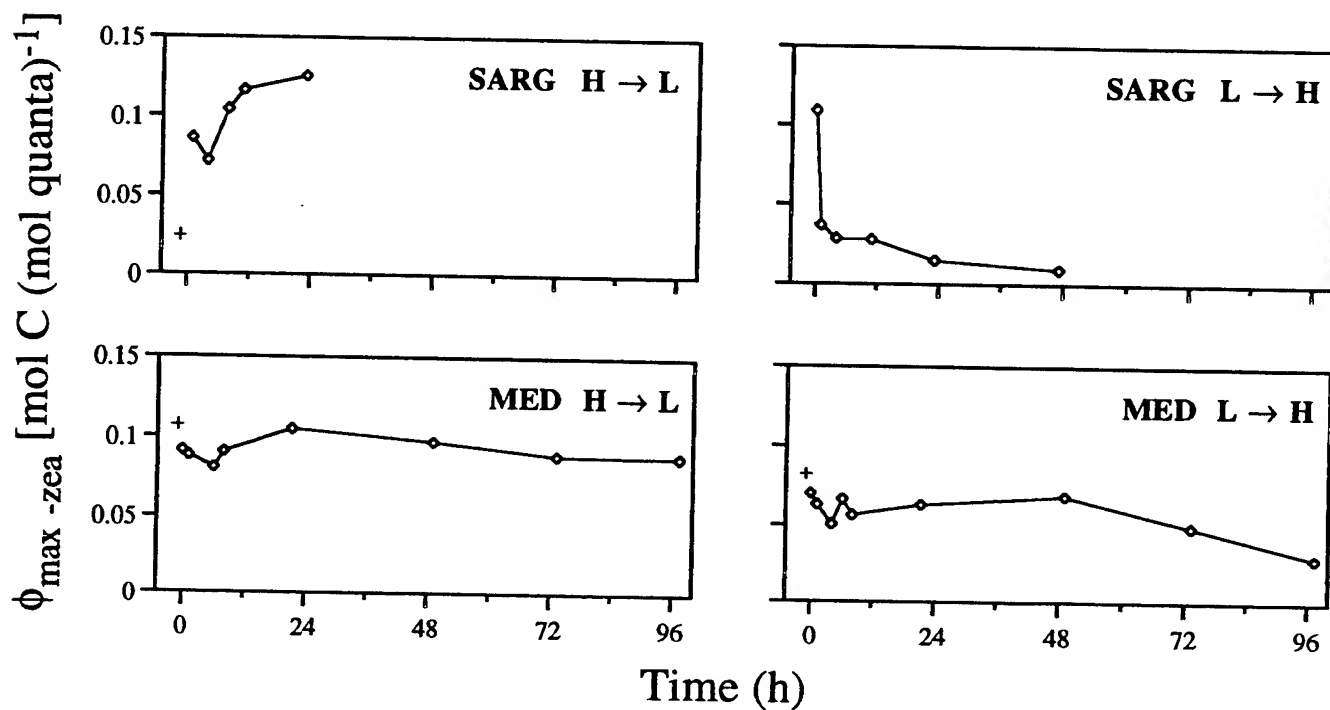


Fig. 5. Variations in the maximum quantum yield of carbon fixation, computed for photosynthetic pigments only, following the light shift.

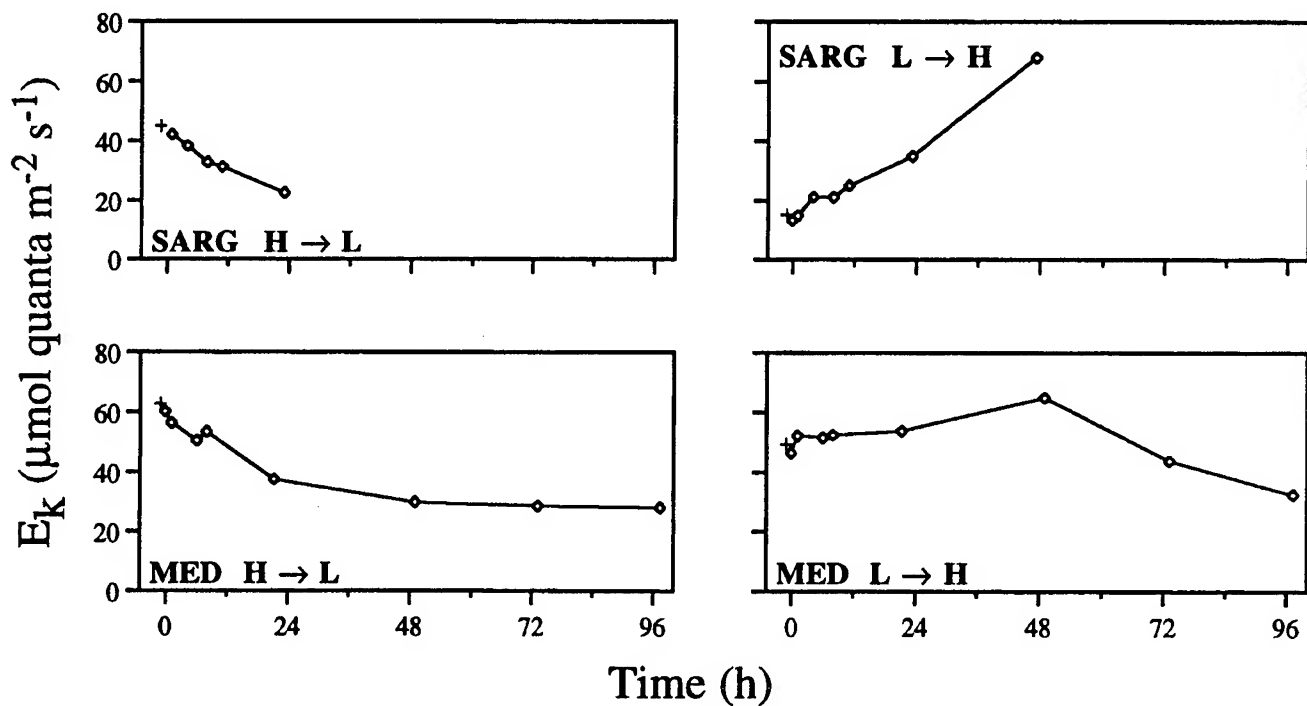


Fig. 6. Variations in the saturation parameter following the light shift.

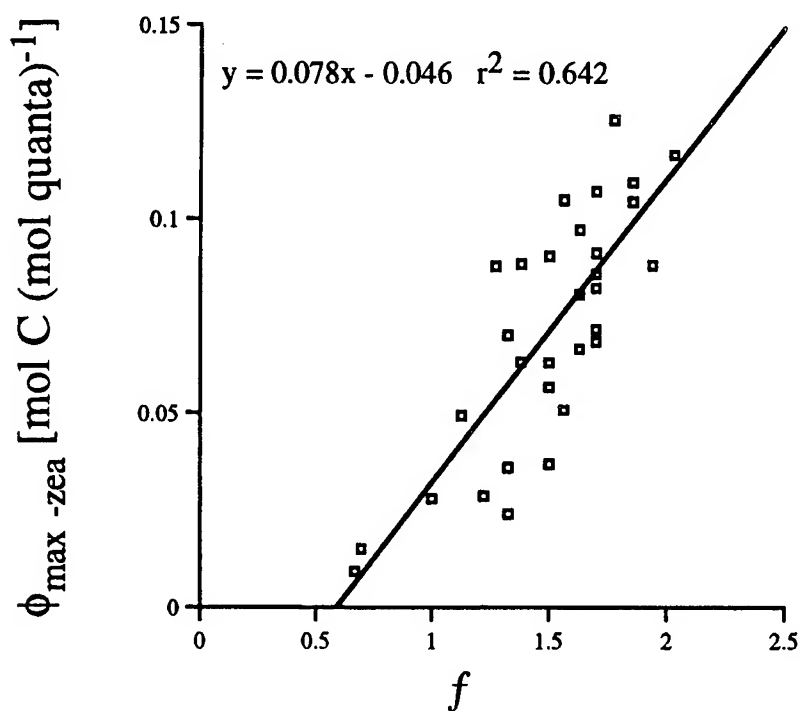


Fig. 7. Relationship between the maximum quantum yield of carbon fixation, computed for photosynthetic pigments only, and the fraction of functional photosystem 2 reaction centers.

Tidal influences on optical variability in shallow water

Alan D. Weidemann

Naval Research Laboratory Code 7331, Stennis Space Center, MS 39529

W. Scott Pegau

Oregon State University, College of Oceanic and Atmospheric Sciences, Corvallis, OR 97331

Laurie A. Jugan and Todd E. Bowers

Planning Systems Incorporated, MSAAP Building 9121, Stennis Space Center, MS 39529

ABSTRACT

Over the past few years, several extensive exercises supported by NRL Optics Programs have taken place in US coastal waters. Analysis of optical data collected has progressed from simply observing high spatial and temporal variability, to linking this variability with physical forcing factors. Data from the most recent exercises off the Oceanside, CA and Le Jeune, NC areas are presented. Optical and oceanographic casts were taken at Oceanside in October 1995 using an ac-9 and an associated CTD. Optical properties were observed to correlate very well with the temperature and density structure of the water column. In turn, the temperature/density structure varied in conjunction with the main component of the local tidal cycle. Optical casts over a 15 hour period when other physical forcing factors are believed to be minimal are presented.

During the two-week Oceanside exercise, an optical mooring recorded absorption, total attenuation, irradiance, and backscattering. Cyclic changes in the optical properties of a factor between two and four were observed, with a base of 0.5 to 1.0 m^{-1} in total attenuation at 532 nm and highs of 2.5 to 5.0 m^{-1} . Phase shifts in the optical data indicate that tidal influences were also modulated and at times overshadowed by large scale meteorological events, local long shore currents, and other physical forces.

At Le Jeune, absorption, attenuation, temperature, and density fields were observed to fluctuate with the tidal cycle at distances of up to 12 mi from New River Inlet. The mean tidal height and density are shown to correlate with a factor of three change in both the absorption and attenuation over a tidal cycle. Warm, high density water with low optical properties advected through the area during the measurement period and overshadowed the variability attributable to tides.

Keywords: optical variability, tidal influences, attenuation, absorption, physical forcing

1. INTRODUCTION

Most work showing the relationship between tidal cycle and optical properties has concentrated either in the near surface or in association with estuarine discharge^{1,2}. The relationship between tidal forcing and optical properties for the near surface has largely been associated with understanding the effects of discharged suspended particulates and Colored Dissolved Organic Matter (CDOM). Strong correlations between optical properties and tidal currents have been shown near the bottom, in association with the resuspension of bottom sediments, dispersion of effluent plumes^{3,4,5}, and resuspension of benthic algae⁶. Isolating tides as having a direct and consistent effect on optical variability has been difficult, as has separating tidal effects from mesoscale, meteorological, or other physical forces. In an attempt to quantify the effects of tides on optical properties in shallow water, we examine the relationship between physical and optical data collected during exercises off Oceanside, CA and Le Jeune, NC in water depths ranging from 7.6 to 28.9 m. Our data indicate that tidal fluctuations in optical properties were observable under conditions when tides were the dominant physical forcing mechanism. Other factors seen to modulate or overshadow the effect of tides on optical properties were resuspended sediments, bathymetry/water depth, the shoaling of long waves from the open ocean, and area conditions (winds, waves, and river discharge).

2. STUDY SITES AND METHODOLOGY

In support of NRL's Littoral Optical Environment (LOE) program, two exercises were conducted off the coasts of Oceanside, CA and Le Jeune, NC. At Oceanside, an optical mooring was deployed, equipped with a WET Labs ac-9 and a Neil Brown inverted Acoustic Current Meter (ACM), both located 1 m off the bottom. The mooring also contained a Sea Tech Optical backscattering sensor (located at mid-depth, 4.65 m from the bottom) and Biospherical irradiance sensors (located at four depths within the water column). A total of five bottom mounted ACMs and seven surface current meters were deployed over a 3 x 3 km box with depths ranging from 7.6 to 28.9 m. Over this box, optical and CTD profiles were collected daily. On 21 October, a 15 hour time series at the optical mooring was taken to observe the tidal influence on the optical variability.

At Le Jeune, optical profiles using an ac-9 and a co-located CTD were made in a 1.5 x 1.5 km box, which was located approximately 12 nmi from the coast and to the SE of New River Inlet. The exercise took place in waters from 19.8 to 28.9 m in depth. Outflow from New River Inlet was observed in conjunction with the passage of a storm that occurred two days prior to the measurements; however, the influence of this outflow was constricted to waters closer to shore.

3. DATA ANALYSIS

Optical variability, as shown as changes in total beam attenuation at 532 nm, and the coincident onshore and alongshore currents recorded 1 m off the bottom at Oceanside are presented in Figure 1. Note that positive current values indicate either northerly alongshore currents (top panel) or shoreward currents (bottom panel). We link these current measurements directly to tidal flow based on correlation with direct tidal measurements taken in the same vicinity using a Sea Bird tide gauge, with flood tide correlated closely with onshore currents (as one would expect). In general, during periods of strong onshore flow (flood tide), values of c were lower than during periods of strong offshore flow (ebb tide). This trend is most evident for Julian days 292 to 298. High values of c , although associated with strong offshore flow (ebb tide), often lagged the peak flow by about one hour. During times of southerly (negative alongshore flow in Figure 1a), values of c were relatively low, with increases seen during times of northerly flow. Deviations from these trends were also observed during the exercise, and were found to be associated with dynamic forces that modified or even overshadowed the effects of the tidal fluctuations in c . These deviations were noted with the onset of storm/high wind events (Julian dates 288-290), advective processes in the area (Julian dates 298-300), and sudden short-lived resuspension of sediments.

In an attempt to quantify the effects of tidal fluctuations on optical properties, hourly ac-9 profiles were taken near the optical mooring at Oceanside; profiles of c at 412 and 440 nm obtained from these casts are shown in Figure 2. Note that times are shown in Pacific Daylight Time (PDT) in this figure. Profiles of a were also analyzed and the structure of a profiles mimicked that seen in the c profiles. These profiles show a definite near-bottom nepheloid layer, with values of c above this feature relatively constant. The analysis of these profiles in relation to tidal fluctuations confirms the results seen above. During ebb tide (1300 hrs), values of c were nearly 0.8 m^{-1} . During flood tide conditions (with peak flood occurring at 0900 and 1900 hrs), values of c were lower at all depths, with the exception of the nepheloid layer. We expect that other physical forces were dominant at this depth.

Two days later at Oceanside, optical profiles were distinctly different; profiles of c taken within hours of each other are shown in the top panel of Figure 3. For each of these profiles, there is a minimum in c at depths between 8 and 14 m. Values of c are higher both above and below this layer. On 23 October, peak flood occurred at 1900 hrs (times in PDT), which corresponds to the lowest values of c at the surface. Two hours later, however, and still under predominantly flood conditions, values of c at the surface were significantly increased. In an attempt to determine the reason for deviation from the trends observed previously, we analyzed the spectra for a and c ; these are shown in Figure 3b and 3c. The spectra (shape and magnitude) for a did not change appreciably during this time frame. The shape of the absorption spectra is consistent with that of a mixture of benthic diatoms, CDOM, and detrital material. The corresponding spectra for c did not show any variation in shape during the sampling period; however, it did vary in magnitude. This indicates that there was an introduction of scatterers into the area.

During the Le Jeune exercise, ac-9 measurements were correlated with tidal heights that were corrected for location such that a high tidal height would be expected at high tide. Analysis of c showed that high values were associated with ebb tide conditions for all stations except two. The density structure of these two anomalous stations indicated an intrusion of oceanic water into the area.

4. CONCLUSIONS

For the two areas studied and under conditions of low physical and meteorological forcing, optical properties fluctuated with the tidal cycle. Although additional statistics must be performed to quantify optical changes seen during these exercise, in general, low values of c are associated with flood tide and high values of c are associated with ebb tide. This relationship holds for all depths, but is modified or even completely overshadowed in the presence of physical or meteorological forcing, such as the presence of internal waves. This has potential applications for the prediction of optical properties in that, for a given area, changes in c can be directly related to physical parameters that may be more easily measured. Algorithms linking optical and physical properties need to be developed and verified under test case scenarios.

5. ACKNOWLEDGMENTS

The authors would like to thank those individuals, too numerous to list here, who gave their time and talents to the at-sea portion of this work. Special thanks is extended to Don Johnson of NRL for the collection and analysis of currents data.

6. REFERENCES

1. M.R. Abbott, K.H. Brink, C.R. Booth, D. Blasco, M.S. Swenson, C.O. Davis, and L.A. Codispoti, "Scales of variability of bio-optical properties as observed from near surface drifters," *JGR* 100 (C7), 13345-13367 (1995).
2. K.L. Carder, Z.P. Lee, and R.F. Chen, "Unmixing of spectral components affecting AVIRIS imagery of Tampa Bay," *SPIE Proc. on Imaging Spectrometry of the Terrestrial Environment*, 1937, 77-90, 1993.
3. T.D. Dickey, L. Washburn, and Y. Wu, "The dispersion of ocean outfall plumes: Physical and biological dynamics," *Proc. 7th Symp. on Coastal and Ocean Management*, 1, 74-85, 1991.
4. L. Washburn, B.H. Jones, A. Bratkovich, T.D. Dickey, and M.S. Chen, "Mixing, dispersion, and resuspension in the vicinity of an ocean wastewater plume," *J. Hydrol. Eng.*, 118, 38-58 (1992).
5. T.D. Dickey, R.H. Douglas, D. Manov, D. Bogucki, P.C. Walker, and P. Petrelis, "An experiment in two-way communication with a multivariable moored system in coastal waters," *J. of Atm. and Oceanic Tech.*, 10, 637-644 (1994).
6. J. Palmer, "Time, tide and the living clocks of marine organisms," *Amer. Scien.*, 84, 570-578 (1996).

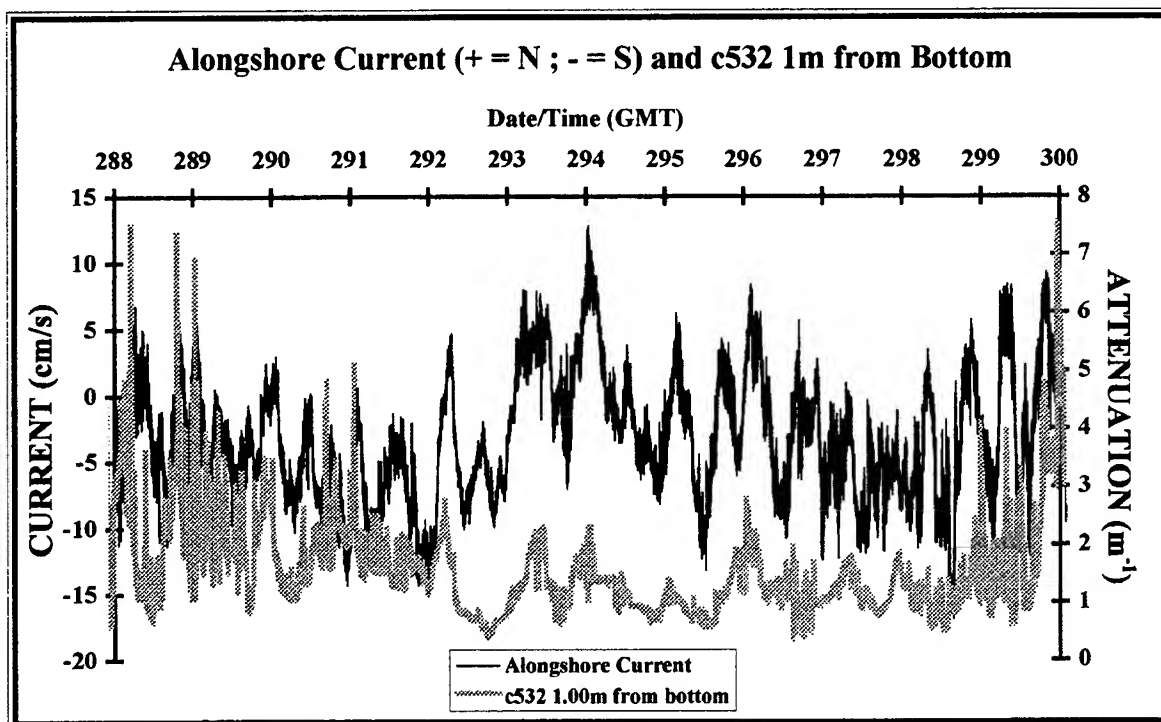


Figure 1a. Alongshore Current Versus Attenuation @ 532 nm.

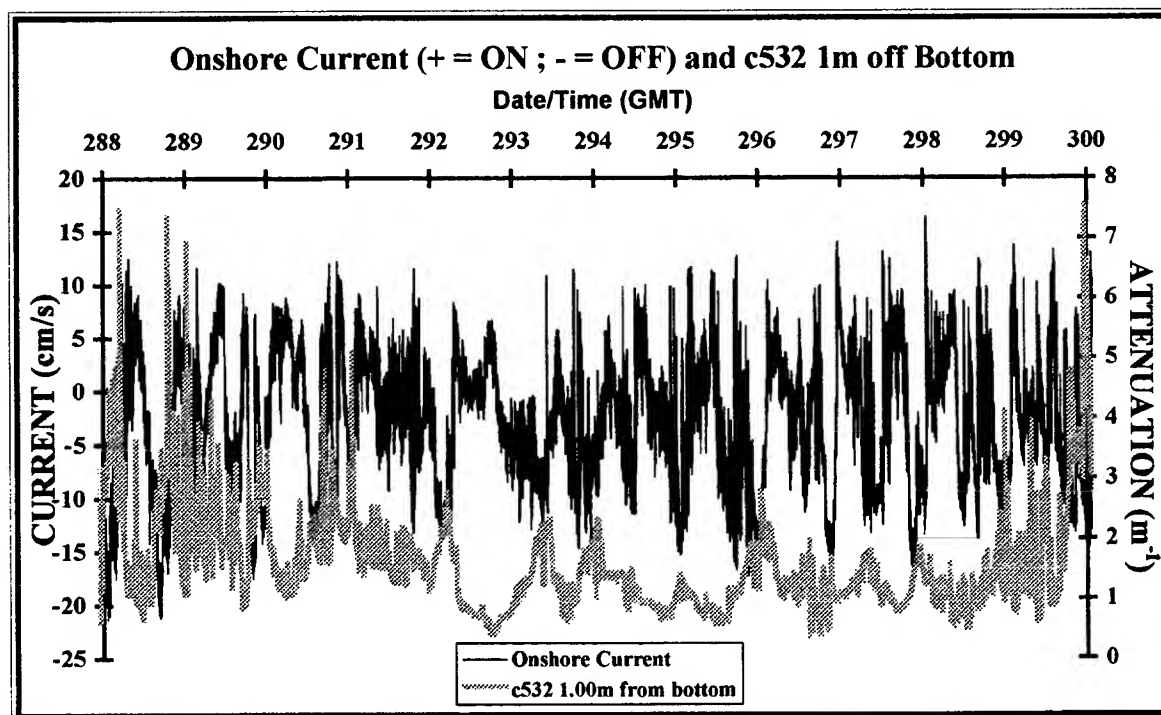


Figure 1b. Onshore Current Versus Attenuation @ 532 nm.

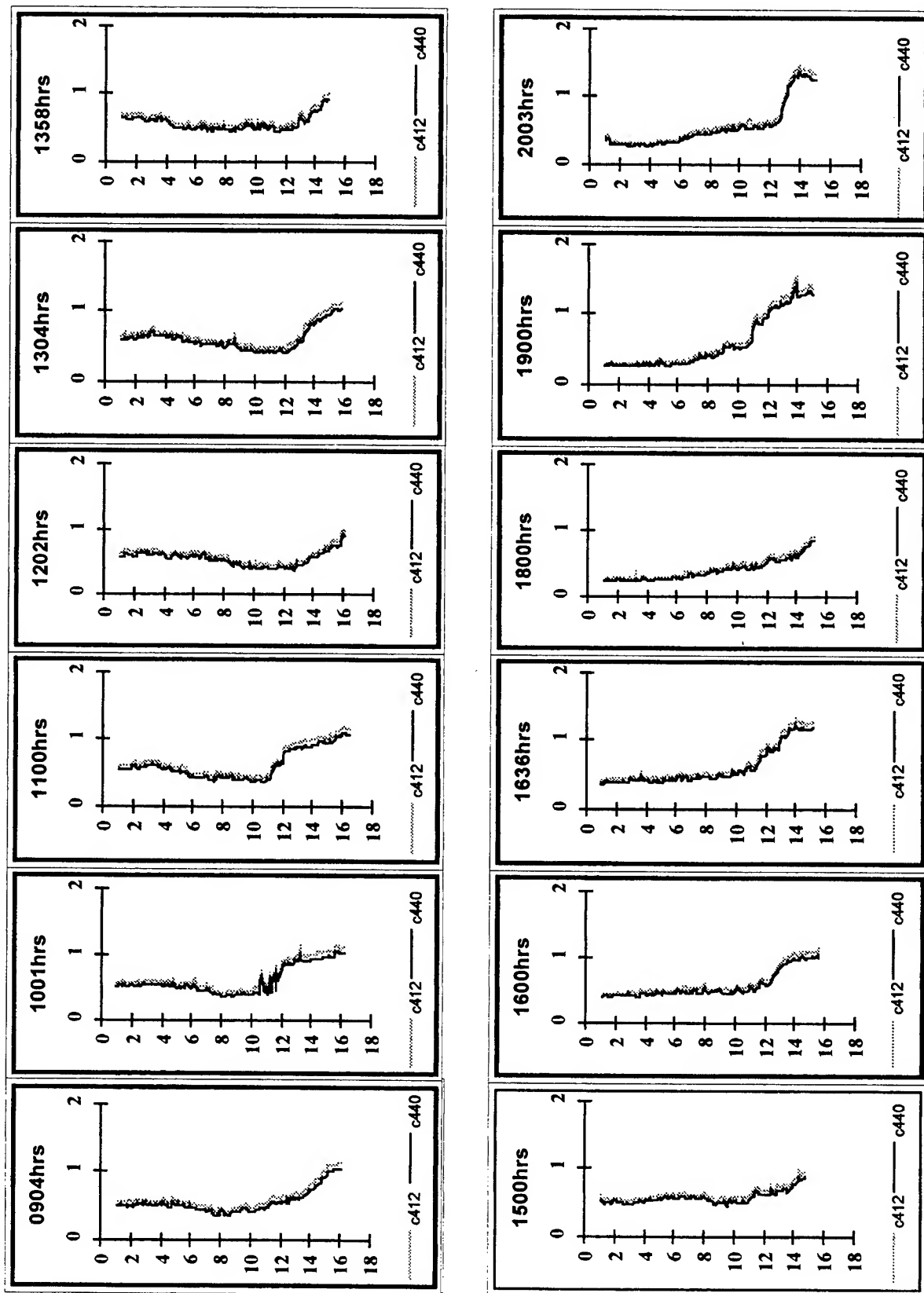


Figure 2-Attenuation (m^{-1}) of 412 and 440 nm as a function of depth (m) on 21 October 95.

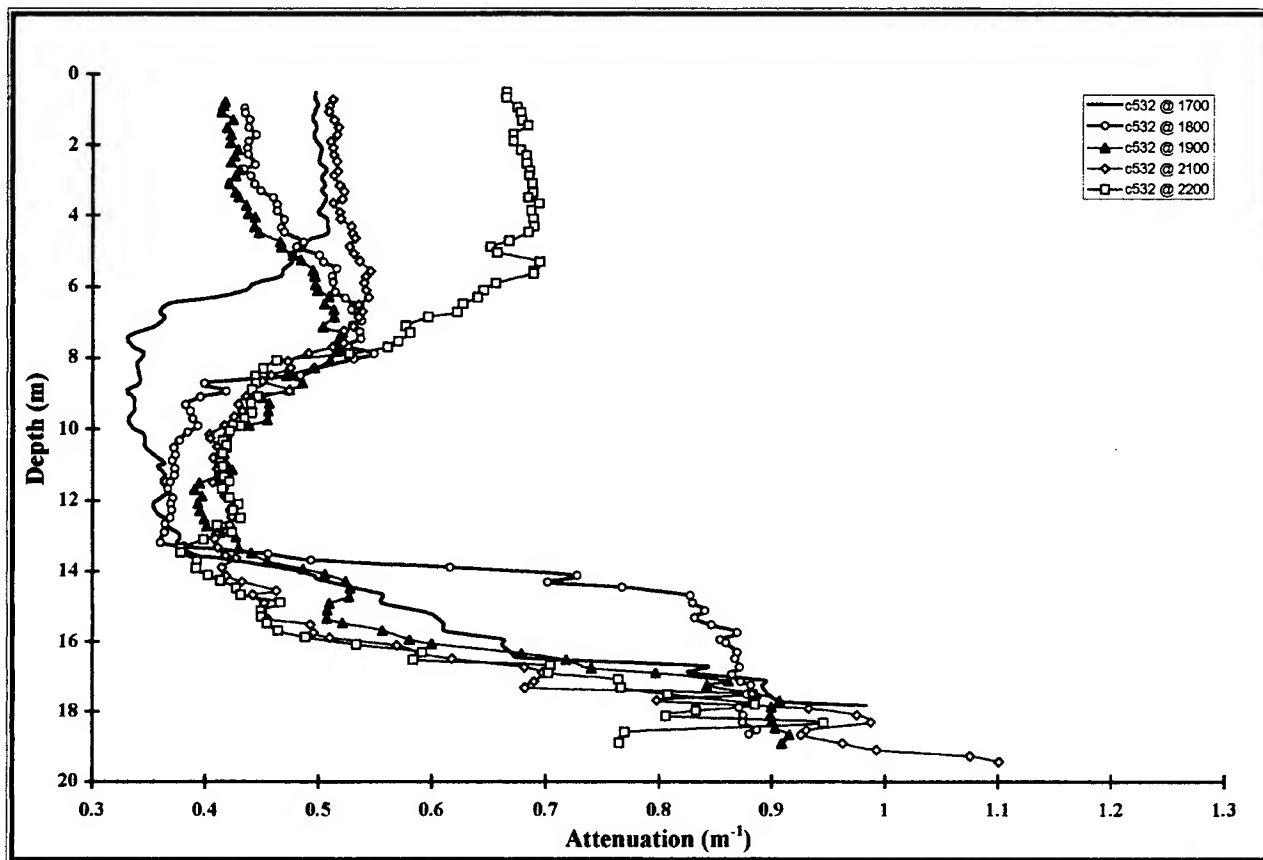


Figure 3a. Vertical Structure of Attenuation as a function of depth/time on October 23, 1995.

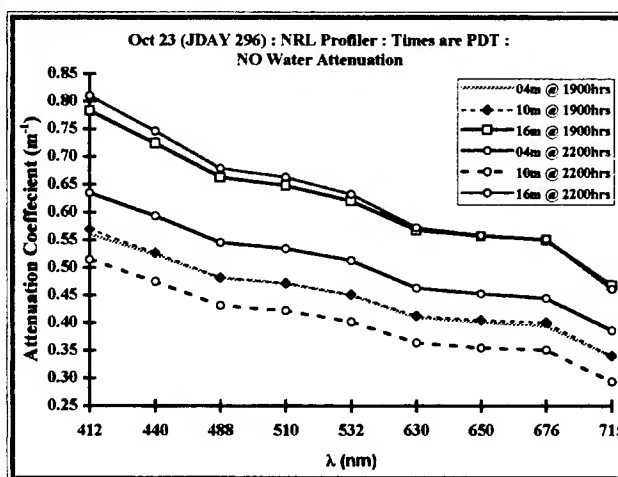
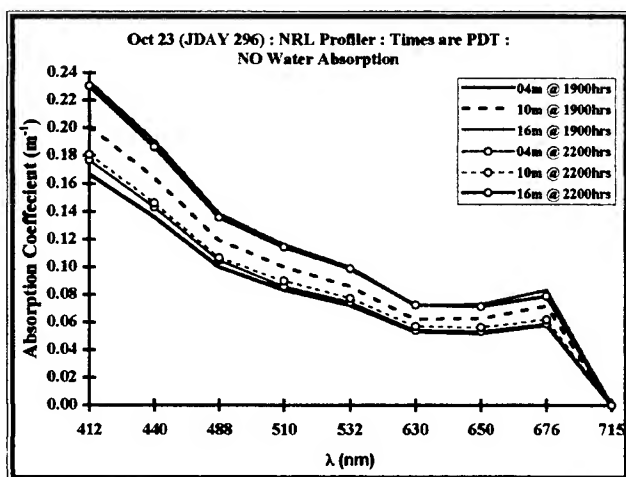


Figure 3b,c. Spectral Absorption and Attenuation for 4 and 10 m from 1900-2200 hrs. on October 23, 1995.

Diffuse attenuation in optically-shallow water: effects of bottom reflectance

Steven G. Ackleson

Office of Naval research, 800 N. Quincy Street, Arlington, VA 22217

ABSTRACT

It is well-known that in the ocean, where the depth of the ocean floor is large compared with the attenuation length of irradiance, the diffuse attenuation coefficients for vector and scalar irradiance (K-functions) are not affected by the optical properties or proximity of the ocean floor. This is the case of an optically deep ocean where the attenuation coefficients are determined solely by the inherent optical properties of the water and the distribution of radiance. Since, within optically-deep water, variability in the K-functions due to radiance distribution are small relative to the effects of the inherent optical properties of water, K-functions have been treated as quasi-inherent optical properties. Furthermore, when the depth of the ocean floor is shallow enough so that it becomes illuminated by downwelling irradiance, i.e. when the ocean is optically shallow, the in-water light field is modified by the optical properties of the ocean floor. The effect decreases with increasing depth and distance from the ocean floor. It is not generally appreciated, however, that the associated K-functions will also be affected by both the optical properties and the proximity of the ocean floor and, therefore, cannot be treated as quasi-inherent optical properties. If these effects are neglected, large errors, exceeding 25% in some cases, can result from modeling the optically shallow scalar irradiance profile as a function of a constant diffuse attenuation coefficient.

Keywords: diffuse attenuation coefficient, optically-shallow water, bottom reflectance

2. INTRODUCTION

The vertical profile of oceanic scalar irradiance, E_0 , is often modeled as a function of the diffuse attenuation coefficient, K (m^{-1});

$$E_0(z) = E_0(0) e^{-Kz} \quad (1)$$

where the operational definition of K is

$$K = -\ln[E(z_2)/E(z_1)]/(z_2 - z_1), \quad (2)$$

and where z is depth (m) and E is irradiance. In the case of optically-deep water, K is primarily a function of the inherent optical properties of water (absorption and, to a lesser extent, light scatter) and radiance distribution and is assumed to be a quasi-inherent optical property of water^{1,2}. In terms of nomenclature, downwelling vector irradiance, E_d , results in K_d , upwelling vector irradiance results in K_u , and scalar irradiance yields K_0 . Excluding the situation where the sky is clear and the sun is very low on the horizon, the in-water radiance distribution does not change significantly with illumination conditions and depth and therefore, to first order, it doesn't matter how E is measured so long as the measurement method does not change with depth. Consequently, in optically-deep water, $K_d \cong K_u \cong K_0$.

When the water column is optically-shallow, significant numbers of photons reach the ocean floor and are reflected upwards, altering the near-bottom radiance distribution^{3,4,5}. In this case, the divergence of irradiance is affected by bottom reflectance, R_b , and the attenuation of diffuse irradiance can no longer be considered a quasi-inherent optical property of water. This is particularly true of K_u and, to a lesser extent, K_0 because both of these K-functions depend on the gradient of the upwelling irradiance field. The downwelling irradiance stream, and therefore K_d , on the other hand, has been shown both in theory and in laboratory and field measurements^{6,7} to be relatively insensitive to reflectance from the ocean floor, even when R_b is large ($R_b \rightarrow .4$).

The purpose of this work is to examine the effect of bottom reflectance on the K-functions in optically shallow water and to examine the magnitude of error introduced by using a constant-K irradiance model, such as Eqn. (1), to estimate scalar irradiance.

3. RANGES AND ASSUMPTIONS REGARDING R_b

While it is well established on theoretical grounds that bottom reflectance can significantly affect the near-bottom radiance distribution, historical studies have not attempted to account for realistic ranges of R_b . Typically, the range of bottom reflectance has always been taken to be $0 \leq R_b \leq 1$. In reality, while the lower limit of R_b for visible light is nearly 0, e.g. in the case of highly absorbing substrates such as mud, measurements of R_b at visible wavelengths have never exceed 0.4, even for pure, non-absorbing quartz and calcareous sediments^{8,9,7,10}. In this work, discussions will be limited to the range $0 \leq R_b \leq 0.4$.

With respect to how light is reflected from the shallow ocean floor, it is customary to assume the angular response of R_b to be Lambertian; e.g. an equal amount of light is reflected into all upwards directions, regardless of illumination direction. In reality, R_b should be modeled as a bi-directional reflectance function (BDRF) that may be a complicated function of the illumination and reflectance angles and the morphology of the ocean floor. Presently, however, little is known about the actual BDRF of the ocean floor, although the potential errors associated with assuming a Lambertian reflectance function are expected to be small⁴. The objectives of this work are not to resolve this issue, but rather to illustrate the effects of the magnitude of R_b on diffuse attenuation. In the interest of simplicity, therefore, R_b will be considered Lambertian.

4. ERRORS IN MODELING SUB-SURFACE IRRADIANCE

Let us first consider the light field directly above the optically shallow ocean floor of depth h where

$$E_o(h) = E_d(h) (1 + R_b) \quad (3)$$

and where the vertical irradiance profile is being modeled as in Eqn. (1). Consider further the situation in optically deep water where the irradiance at depth $z = h$, now at a point in the sun-lit portion of the water column, can be similarly expressed as

$$E_o(z) = E_d(z) (1 + R_w) \quad (4)$$

where R_w is the volume reflectance of the optically-deep water column. If K is calculated with measurements of E_d ($K = K_d$), the absolute error in adopting Eqn. (1) is $\varepsilon = E_o(R_w - R_b)$ and the percent error is $\% \varepsilon = (R_w - R_b) (1 + R_b)^{-1}$. For the situation of clear water having a deep-water reflectance of $R_w = 0.04$ and overlying a highly reflective ocean floor, $R_b = 0.4$, the percent error in modeling the scalar irradiance immediately above the ocean floor using a single- K model is approximately -25%. In other words, the scalar irradiance, e.g. that which is available to drive photosynthesis, will have been underestimated by 25%. On the other hand, if $R_b = 0$, the constant- K model will have overestimated the bottom irradiance by about 4%. An interesting situation occurs when $R_w = R_b$, in which case $\% \varepsilon = 0$.

These error estimates assume that the K ($= K_d$) is equal to the deep-water K . This is a reasonable assumption given the common use of commercially-available submersible radiometers that measure downwelling vector irradiance and since E_d is only weakly affected by R_b . However, it is also common to measure E_o , resulting in $K = K_o$. In this case, the magnitude of $\% \varepsilon$ and the location of the maximum percent error depends on how K_o is calculated.

Consider first the situation where the water is clear, $K_o = 1.0 \text{ m}^{-1}$, $h = 5 \text{ m}$, and $R_b = 0.4$. In this case, the two depths at which E_o is measured to calculate K_o are near-surface and mid-water column. As shown in the vertical profile of $\% \varepsilon$ (Fig. 1A), the modeled scalar irradiance is gradually underestimated with increasing depth until, at the bottom, $\% \varepsilon = -25\%$. This is similar to the situation discussed previously because E_o measured in the near-surface water column is only slightly affected by R_b and $K_o \approx K_d$. Consider next a situation in which K_o is measured near the surface and at the bottom (Fig. 1B). In this case, $K_o = 0.94 \text{ m}^{-1}$, since the near-bottom irradiance intensity increases, relative to the deep water situation, due to the highly-reflective bottom. The maximum percent error is now 20% (overestimated) and occurs at a location in the mid-water column rather than at the bottom.

5. A MODIFIED SINGLE-K MODEL FOR OPTICALLY-SHALLOW WATER

At this point, it should be concluded that a constant- K irradiance model applied to optically-shallow water will produce erroneous results, with the sole exception being the case where $R_w = R_b$. Perhaps the most obvious approach to modeling irradiance

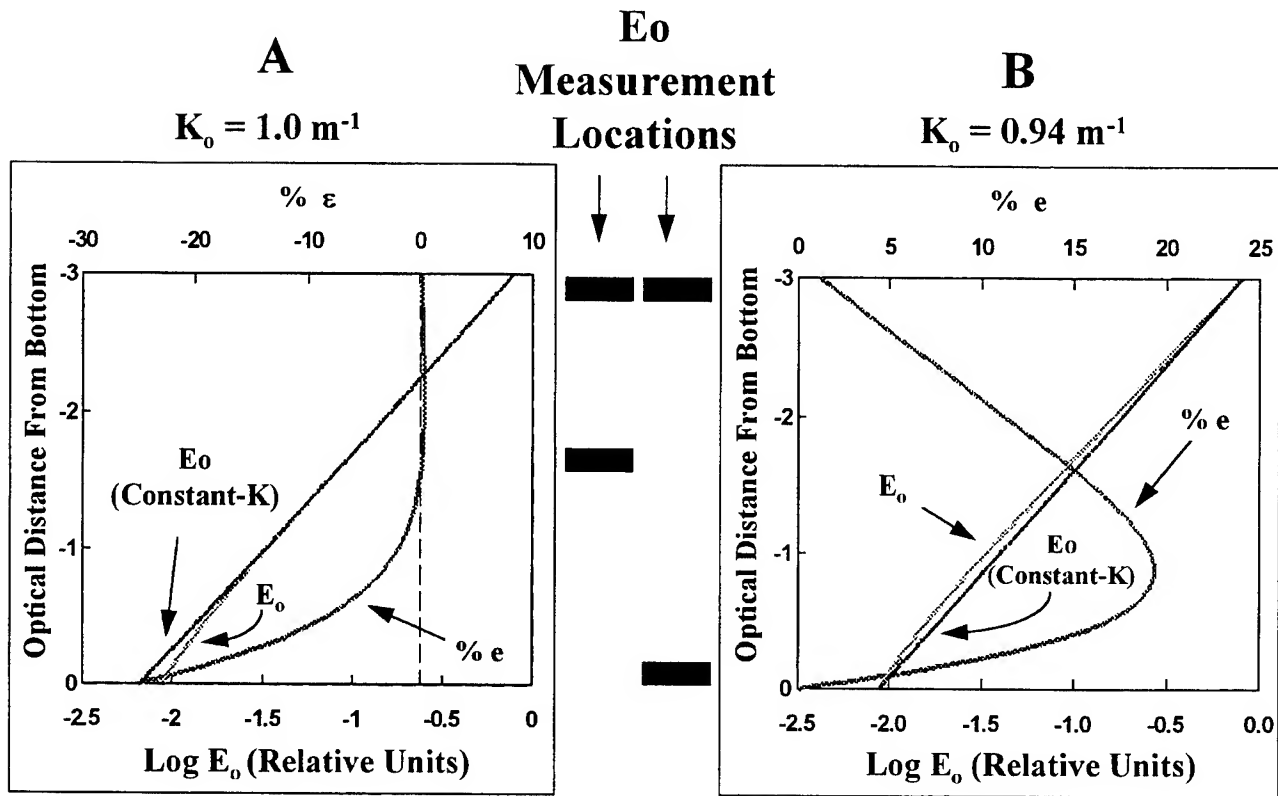


Figure 1. Percent error associated with modeling shallow-water irradiance profiles with a constant-K model where K_0 is calculated from upper water column measurements of E_0 (A), where $K_0 = 1.0 \text{ m}^{-1}$, and K_0 representing the entire water column (B), where $K_0 = 0.94 \text{ m}^{-1}$. In both cases, $R_w = 0.04$ and $R_b = 0.4$.

in shallow water, and certainly the most accurate, is to measure the appropriate inherent optical properties of the water and R_b and use a radiative transfer model that accounts for the bottom boundary condition. Unfortunately, IOP meters are not in wide-spread use and there is no direct method in common use to measure R_b . Irradiance sensors, lowered from the surface and the employment of a constant-K model remains the most common approach to modeling the vertical irradiance profile in optically-shallow water. So, the task at hand is to develop a simple K-based model that accounts for the effects of R_b .

In optically-shallow water, the water column reflectance may be expressed as ^{7, 6, 11}

$$R(z) = R_w + (R_b - R_w) e^{-2K_d(d-z)} \quad (5)$$

Substituting $R(z)$ in for R_b in Eqn. (3), the operational definition of K_0 , Eqn. (2), becomes

$$K_0 = -\ln[Ed(z_2)(1+R(z_2))/Ed(z_1)(1+R(z_1))]/(z_2-z_1). \quad (6)$$

Rearranging Eqn. (6) yields

$$K_0(z) = K_d + -\ln[(1+R(z_2))/(1+R(z_1))]/(z_2-z_1), \quad (7)$$

or $K_0(z) = K_d + K'(z)$. Notice that K_d is the depth-invariant portion of K_0 while all of the effects of R_b are contained in K' . Notice also that Eqn. (7) requires an estimate of R_w as well as R_b . Also, when $R(z)$ is constant, a condition that is assumed for optically-deep water and when $R_w = R_b$, $K_0(z) = K_d$.

To test the validity of Eqn (7), a radiance-based model, HYDROLIGHT¹² was used to calculate attributes of the vertical radiance profile in optically-deep water and in optically shallow water for two illumination conditions; homogeneous ($K_d = 0.64 \text{ m}^{-1}$, $R_w = .008$) and clear sky with a solar zenith angle of 10° ($K_d = 0.56 \text{ m}^{-1}$, $R_w = .006$). In both cases, $R_b = 0.4$. The results (Fig. 2) suggest that the modified model is preserving at least some of the effects of R_b and that the errors associated with a constant-K model are indeed reduced. However, the modified-K model does not completely remove the error in the modeled light field and, in terms of HYDROLIGHT, the errors increase in the vicinity of the ocean surface and the ocean floor. The likely reason for error is that the K model does not account for changes in how radiance is distributed over the upward and downward hemispheres, only the relative amount of light in each. HYDROLIGHT, on the other hand, calculates the depth change in radiance distribution within each hemisphere and the resulting effects are incorporated in the associated calculations of K_o . It should also be noted that while the maximum errors previously estimated are based on assumptions of constant hemispherical radiance distribution, the results of HYDROLIGHT suggest that the actual error associated with a constant-K model may be even larger. However, the differences between the two modeling approaches have yet to be verified with field measurements.

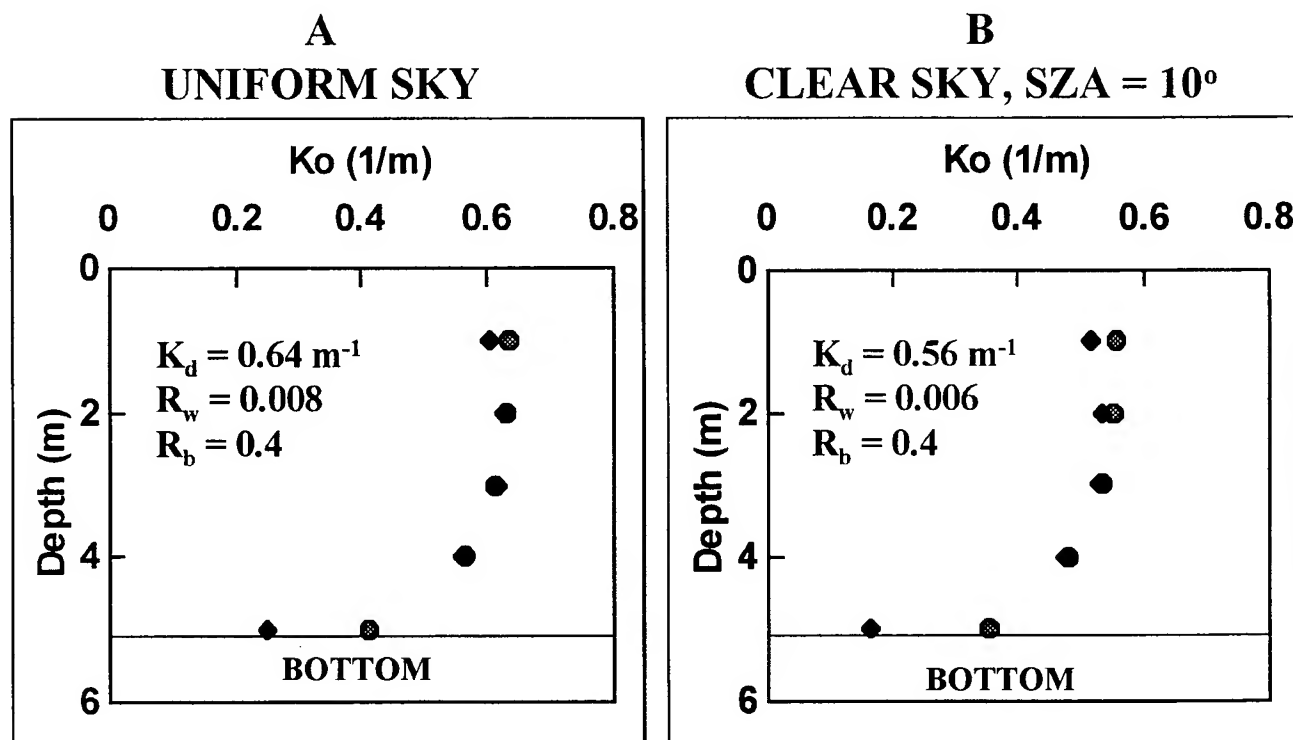


Figure 2. Comparison of K_o computed using the modified K-model (circles, Equ. 7) and the radiance-based model HYDROLIGHT (diamonds) for a uniform sky illumination (A) and a clear sky and solar zenith angle of 10° (B). In both cases, water depth is 5 m.

While Eqn. (7) requires K_d , the use of a vector irradiance meter is not the best method of acquiring the necessary values for Eqn. (7) because the results cannot be verified, especially near the ocean floor, and because measurements of E_d yield no information about R_b required by the model. However, measurements of E_o , made in the upper water column should, in most situations, yield K values close to K_d unless the water is very shallow. At the same time, a near-bottom measurement of K_o can be used to estimate R_b by simply modifying R_b until the modeled near-bottom irradiance matches the measured value.

6. CONCLUSIONS

Modeling the scalar irradiance profile in shallow water as a function of vertically constant K can result in large errors when R_b is large relative to the volume reflectance of optically-deep water ($R_b \gg R_w$). If $K = K_d$, the error increases with decreasing distance from the ocean floor.

The absolute error in E_0 modeled using a constant K model, where $K = K_d$, is equal to $E_0(d) (R_b - R_w)$ and occurs at the ocean floor. The modeled irradiance immediately above a highly reflective sediment ($R_b \rightarrow .4$), can be underestimated by as much as 25%.

If $K = K_s$, computed with irradiance measurements made near the ocean surface and near the ocean floor, the sign of %e is opposite to the situation where $K = K_d$ and the location of the maximum percent error is in the mid-water column, rather than at the ocean floor.

A simple K_d model is presented that incorporates the effects of R_b and can be used to reduce the error in modeled E_0 within an optically-shallow water column.

7. REFERENCES

1. N. G. Jerlov, *Marine Optics*, vol. 14, 1976.
2. R. W. Preisendorfer, "Hydrologic Optics," U.S. Department of Commerce, 1976.
3. G. N. Plass and G. W. Kattawar, "Monte Carlo calculations of radiative transfer within the earth's atmosphere-ocean system: I. flux in the atmosphere and ocean," *J. Phys. Oceanogr.*, **2** : 139-145(1972).
4. H. R. Gordon and O. B. Brown, "Influence of bottom depth and albedo upon diffuse reflectance of a flat homogeneous ocean," *Appl. Opt.*, **13** : 2153-2159(1974).
5. S. G. Ackleson and V. Klemas, "Two-flow simulation of the natural light field within a canopy of submerged aquatic plants," *Appl. Opt.*, **25** : 1129-1136(1986).
6. W. D. Philpot, "Radiative transfer in stratified waters: a single-scattering approximation for irradiance," *Appl. Opt.*, **26** : 4123-4132(1987).
7. S. Maritorena, A. Morel, and B. Gentili, "Diffuse reflectance of oceanic shallow waters: influence of the water depth and bottom albedo," *Limnol. Oceanogr.*, **39** : 1689-1703(1994).
8. D. J. Leu, "Visible and near-infrared reflectance of beach sands: a study on the spectral reflectance / grain size relationship," *Rem. Sens. Environ.*, **6** : 169-182(1977).
9. D. R. Lyzenga and F. Thomson, "Basic Remote Sensing Investigation for Beach Reconnaissance," ERIM Technical Report 108900-11-F, 1978.
10. M. Kuhl and B. B. Jorgensen, "The light field of microbenthic communities: radiance distribution and microscale optics of sandy coastal sediments," *Limnol. Oceanogr.*, **39** : 1368-1398(1994).
11. S. G. Ackleson and V. Klemas, "Remote sensing of submerged aquatic vegetation in Lower Chesapeake Bay: a comparison of Landsat MSS and TM imagery," *Rem. Sens. Environ.*, **22** : 235-248(1987).
12. C. D. Mobley, B. Gentili, H. R. Gordon, Z. Jin, G. W. Kattawar, A. Morel, P. Reinersman, K. Stamnes, and R. H. Stavn, "Comparison of numerical models for computing underwater light fields," *Appl. Opt.*, **32** : 7484-7504(1993).

Radiative transfer within seagrass canopies: impact on carbon budgets and light requirements

Richard C. Zimmerman
Biology Department, University of California, Los Angeles
Los Angeles, CA 90024

Curtis D. Mobley
Sequoia Scientific Inc. Mercer Island WA 98040

ABSTRACT

Seagrasses are ecologically important but extremely vulnerable to anthropogenic modifications of the coastal zone that affect light availability within these unique ecosystems. Strongly pigmented seagrass leaves can extend for more than 1 m above the substrate and biomass is distributed unevenly throughout the canopy. In this study, light attenuation in a 7 m water column that contained a seagrass canopy extending 1.5 m above the bottom was calculated by the radiative transfer model *Hydrolight* using the spectral absorbance of eelgrass (*Zostera marina* L.) leaves and a non-uniform vertical distribution of biomass. Runs were performed in clear ($0.5 \text{ mg Chl } a \text{ m}^{-3}$) and turbid ($3.0 \text{ mg Chl } a \text{ m}^{-3}$) water columns, over sand and mud substrates, and with shoot densities ranging from 25 to 200 m^{-2} using solar angles for both winter and summer solstices. The flux of photosynthetically active irradiance (E_{PAR}) reaching the top of the seagrass canopy (5.5 m) was twice as high in summer compared to winter, and in clear water compared to turbid water. Sediment type (sand versus mud) had a measurable effect on E_{PAR} only within the bottom third of the canopy. Light penetration within the canopy was inversely proportional to shoot density. Introduction of daylength and a sinusoidal distribution of E_{PAR} throughout the day greatly increased the importance of solar elevation (season) on daily integrated production relative to water column turbidity and sediment type. Shoot-specific productivity decreased and the position of maximum shoot productivity within the canopy shallowed as shoot density increased. Positive net photosynthesis for entire shoots was possible only when plant density was lower than $100 \text{ shoots m}^{-2}$ in summer and 50 shoots m^{-2} in winter; values consistent with field observations. Although very simplistic with regard to inherent optical properties of real seagrass leaves, this model was able to generate estimates of maximum sustainable shoot density that were fully testable by, and wholly consistent with, field observations.

Key Words: radiative transfer, seagrass canopy, inherent optical properties, productivity

1. INTRODUCTION

The seaward approach to virtually every shoreline in the world is characterized by optically shallow water and highly variable bottom topography. Radiative transfer models developed for optically deep (bottomless) oceanic waters have little utility for remote characterization of bottom topography or biological characteristics (e.g. the presence of coral reefs or seagrass meadows) in shallow coastal waters. In addition, the ecological importance of seagrasses has generated considerable interest in the production dynamics and light requirements of these unique ecosystems. Much effort has focused on measures of scalar irradiance (E_{PAR}) at the top of the seagrass canopy and on K_{PAR} in the overlying water column¹⁻⁴ and the resulting production models assume an invariant distribution of E_{PAR} throughout the canopy. Even the most casual observations in real seagrass beds reveal that this planar assumption is not valid generally. The leaves are distributed unevenly through a vertical canopy that can extend 1 m or more above the bottom, particularly in mixed-species assemblages in tropical waters where there can be distinct vegetation layers within the canopy. Furthermore, the accumulation of epiphytes (both photosynthetic and non-photosynthetic) can significantly alter the inherent optical

properties (IOP's) and photosynthetic performance of individual seagrass leaves^{5,6}. Taken as a whole, however, seagrass systems are considerably less intricate than the surfaces of coral reefs, where cm-scale spatial variations can often span the full optical range to be encountered across the entire reef system. Seagrass meadows can be relatively homogeneous on spatial scales of 100 m in the horizontal, yet they present properties of reflectance and absorbance that are clearly distinct from unvegetated sediment. Consequently, seagrass meadows provide a relatively simple system in which to begin the development of radiative transfer models for optically shallow waters and benthic ecosystems. The need for better estimates of E_{PAR} distributions within seagrass canopies to drive production models adds additional incentive for the use of seagrasses as experimental systems to develop radiative transfer algorithms within optically shallow marine waters.

Radiative transfer theory can be used to predict (i) canopy reflectance for remote sensing purposes and (ii) canopy photosynthetic rates from measures of above canopy irradiance (E_{PAR}). The aim of this study was to begin the development of a general model of radiative transfer for seagrass canopies and to explore its ability to predict maximum shoot densities within a seagrass meadow in Monterey Bay. Continued refinement will lead to a model of radiative transfer within vegetated benthic habitats of sufficient sensitivity and accuracy for remote sensing of the sea floor, mapping vegetation distributions, habitat resources and for predicting the dynamics of benthic productivity in light limited habitats.

2. SEAGRASS CANOPY IOP MODEL

Solution of the radiative transfer equation (RTE) requires specification of the absorption and scattering properties of the water column (the IOP's)⁷. In the first case, these IOP's are sums of the individual contributions of by water, phytoplankton, dissolved organic matter, and the seagrass itself. We assume that the IOP's depend only on depth and wavelength. Within actual seagrass canopies, the IOP's vary in all three spatial dimensions because of the inhomogeneous distribution of the seagrass leaves. However, with the assumptions that the IOP's depend only on depth and wavelength, the *Hydrolight* radiative transfer model⁸ can solve the RTE from first principles and thereby provide any desired light field quantity - in particular depth profiles of E_{PAR} .

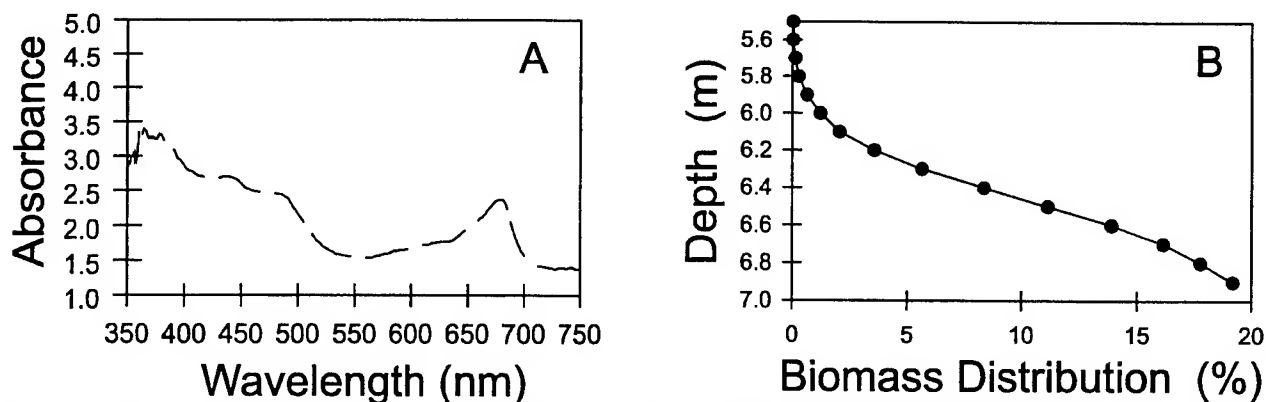


Figure 1. *In vivo* absorbance spectrum of a clean mature eelgrass (*Zostera marina* L.) leaf. B. Relative distribution of leaf biomass (%) as a function of depth.

This one-dimensional approach was used to calculate the vertical distribution of E_{PAR} through an eelgrass canopy and the overlying water column (7 m total depth) in Monterey Bay for the summer and winter solstices. The spectral absorption coefficient a was determined from the *in vivo* absorbance spectrum of a clean young eelgrass leaf (Fig. 1A). The volume fraction of biomass (f) was determined from the measured vertical biomass distribution of eelgrass growing in Monterey Bay (Fig. 1B). The depth- and wavelength-dependent absorption coefficient ($a(z, \lambda)$) was calculated as:

$$a(z, \lambda) = (1 - f)(a_{\text{water}} + a_{\text{phyto}} + a_{\text{cdom}}) + fa_{\text{grass}}$$

Values for a_{water} , a_{phyto} and a_{cdom} were taken from published bio-optical models⁷. Canopy absorption (fa_{grass}) was calculated from the measured leaf absorbance (Fig. 1) and leaf geometry was scaled by the volume fraction of seagrass biomass ($f \leq$

10^{-3}). Although wavelength dependent, the values of a_{grass} are of the order 10^4 , so that the contribution of seagrass to the total absorption is on the order of 10 m^{-1} . Scattering by the seagrass canopy (b_{grass}) was assumed to be $0.05a_{\text{grass}}$ and scattering by seagrass leaves was assumed to be isotropic.

All profiles of E_{PAR} were calculated for local solar noon in Monterey Bay California (Lat. 36.6° N , Long. 121.9° W). Sky conditions were clear, wind speed above the water surface was 5 m s^{-1} . All simulated shoots consisted of 5 leaves. Summer was simulated using a solar zenith angle of 13° and 60° was used for winter. Bottom reflectance for mud was 0.1 and independent of wavelength. Reflectance of sand was wavelength-dependent and ranged from 0.28 at 400 nm to 0.6 at 700 nm . Runs were performed with shoot densities of 25, 50, 100 and $200 \text{ shoots m}^{-2}$.

3. SEAGRASS PRODUCTION MODEL

The resulting vertical noon profiles of E_{PAR} calculated by *Hydrolight* were used to drive the following model of daily gross production of the canopy:

$$P = D \sum_{z=5.5}^7 P_i [1 - \exp(-0.67 E_m/E_k)] \quad \{1\}$$

where P was the daily production integrated through depth z within the seagrass canopy, D was the length of the daily photoperiod, E_m was the maximum instantaneous E_{PAR} at solar noon within depth layer z , E_k was the physiologically determined irradiance required to saturate photosynthesis, P_i was the leaf-specific instantaneous rate of photosynthesis at depth z at noon:

$$P_i = P_m [1 - \exp(-E_m/E_k)] \quad \{2\}$$

P_m was the physiologically determined maximum rate of light-saturated biomass-specific photosynthesis. The temporal distribution of E_{PAR} was assumed to be sinusoidal and depth of the water column was constant (no tides). Respiratory demand of entire shoots was apportioned among leaves, roots and rhizome biomass¹⁰ and a photosynthetic quotient of 1.0 was assumed. Growth was set to 0.

4. RESULTS AND DISCUSSION

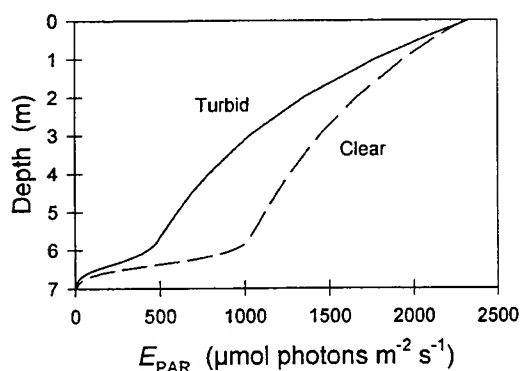


Figure 2. Effect of water column turbidity on vertical distribution of E_{PAR} within the simulated water column. Run conditions: summer, mud substrate, 50 shoots m^{-2} .

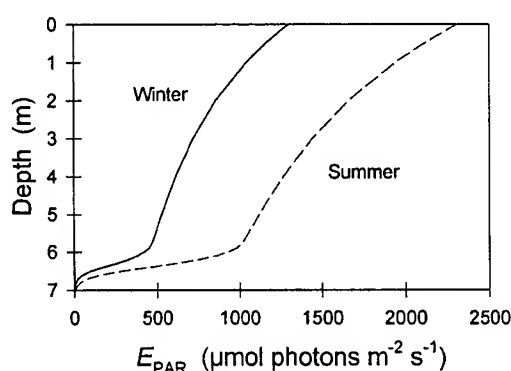


Figure 3. Effect of season (solar zenith angle) on vertical distribution of E_{PAR} . Run conditions: clear water column, mud substrate, 50 shoots m^{-2} .

Water column turbidity had a measurable impact on light availability throughout the simulated water column (Fig. 2). Noon irradiance exceeded $1000 \mu\text{mol photons m}^{-2} \text{ s}^{-1}$ at the top of the simulated seagrass canopy in the clear water

column, but was only 500 $\mu\text{mol photons m}^{-2} \text{s}^{-1}$ in turbid water. Within the canopy, light attenuation was dominated by eelgrass absorption, decreasing rapidly in both turbid and clear water.

Season, as defined by solar zenith angle at noon, also had a strong effect on the vertical distribution of E_{PAR} (Fig. 3). Surface E_{PAR} at noon was 50% lower in winter than summer, and this difference was transferred into the water column. As before, the seagrass canopy markedly increased the rate of E_{PAR} attenuation in the bottom 1.5 m of the water column.

High attenuation from the seagrass canopy prevented sediment type from having a significant impact on the vertical distribution of E_{PAR} (Fig. 4). There was no difference in E_{PAR} above the canopy ($z < 5.5 \text{ m}$). Within the bottom 10 cm layer of the canopy, however, E_{PAR} over the highly reflective sand (11 $\mu\text{mol photons m}^{-2} \text{s}^{-1}$) was 42% higher than over the much less reflective mud (7 $\mu\text{mol photons m}^{-2} \text{s}^{-1}$).

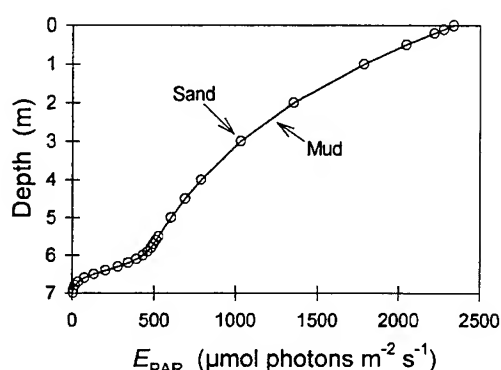


Figure 4. Effect of sediment type on vertical distribution of E_{PAR} . Run conditions: turbid water column, summer, 50 shoots m^{-2} .

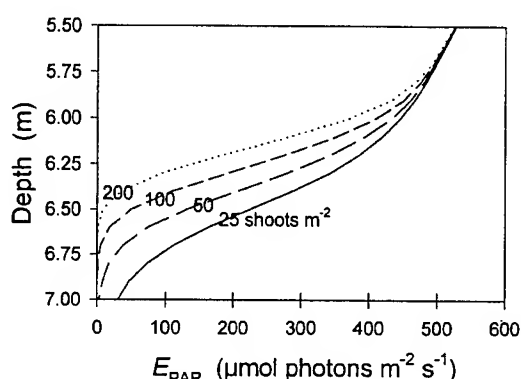


Figure 5. Effect of shoot density on vertical distribution of E_{PAR} within the seagrass canopy. Run conditions: turbid water column, summer, mud substrate.

The distribution of E_{PAR} within the seagrass canopy was strongly affected by shoot density (Fig. 5). The effect of shoot density was minimal in the upper 0.5 m and increased with depth. At 6.5 m, (within the canopy), each doubling in shoot density produced a 50% reduction in E_{PAR} (Fig. 5).

The depth of maximum production within the canopy was strongly affected by shoot density, a consequence of self-shading by the leaves (Fig. 6). Productivity peaked at 6.75 m depth with 25 shoots m^{-2} , and shallowed to 6.25 m at 200 shoots m^{-2} . The peak production value also was reduced 4-fold. Reduced light availability associated with winter decreased overall productivity and increased the effects of self-shading. The region of maximum productivity for any given shoot density was shallower in winter than for comparable summer runs and the difference in depth of maximum production among shoot densities was less than 4.

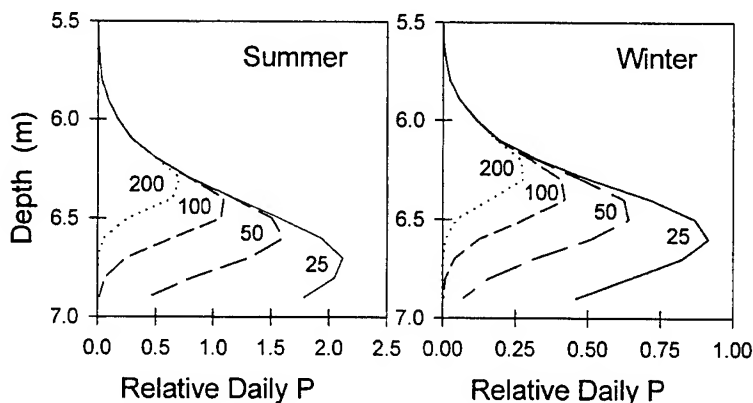


Figure 6. Effect of shoot density on vertical distribution of daily production within the seagrass canopy for summer and winter solar zenith angles. Run conditions: turbid water column, mud substrate.

Area-specific production increased with shoot density between 25 and 50 shoots m^{-2} , but leveled off at higher shoot densities as self-shading became more dominant (Fig. 7A). Biomass-specific productivity, however, declined exponentially as shoot density increased (Fig. 7B). The non-linear P vs. E relationship greatly reduced the impact of water column turbidity on integrated daily production. Season, however, had a much stronger effect on light-driven production. Summer levels of integrated daily P were at least double the winter values whether normalized to area or to biomass. Daily respiration consumes 5.5 units of $P^{4,10}$. Assuming $P = 5.5$ represents the minimum value of daily shoot

-specific production necessary to maintain a stable healthy seagrass population, the model predicted summer light levels should support shoot densities up to 100 shoots m^{-2} , but densities in winter should be limited to 30 shoots m^{-2} . These values are very close to seasonal variations in leaf density observed in the Monterey Bay eelgrass meadow (Zimmerman unpubl.). The results presented here are the first production estimates to include any effects of canopy absorbance on the vertical distribution of E_{PAR} and subsequently on photosynthesis. When the effects of self-shading are ignored, integrated shoot-specific production approaches 14.3 relative production units in summer and 9.7 in winter as the result of Eq. (1) will approach the product DP_m . Thus, our simple model of radiative transfer within the seagrass canopy offers to significantly improve our ability to predict the impacts of E_{PAR} on depth distribution and shoot densities within submerged seagrass meadows.

Development of a more sophisticated model of radiative transfer within seagrass canopies will require considerable knowledge of canopy phytometric properties such as leaf area index, area specific spectral absorbance and reflectance in addition to the inherent optical properties of the water column that are likely to be region- and species-specific. Until those data become available, the relatively simple canopy IOP model developed here provides a reasonable first-order approximation of E_{PAR} within seagrass canopies necessary for accurate production models. Our future efforts will focus on improving the realism of the canopy IOP model by emphasizing (i) the importance of scale with regard to optical heterogeneity of the benthos and (ii) variation among seagrass leaves, including the effects of leaf age and fouling load on leaf absorbance, canopy height, biomass distribution within the canopy and leaf orientation relative to the light field. More sophisticated radiative transfer calculations should also lead to a prediction of upwelling radiance from seagrass canopies that can be used for remote sensing and resource mapping applications, in addition to primary productivity studies and issues of habitat quality.

5. ACKNOWLEDGEMENTS

Support for this study was provided by the Office of Naval Research.

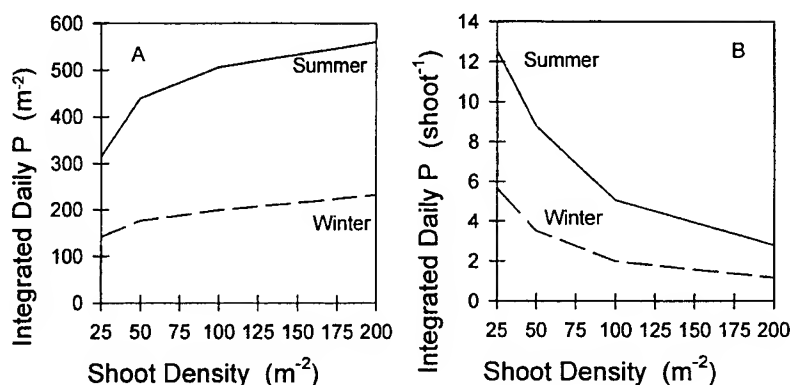


Figure 7. Effect of shoot density on (A) area-specific integrated daily production and (B) shoot-specific integrated daily production. For any particular combination of season and shoot density, water column turbidity and sediment type (sand vs. mud) had no impact on integrated daily production.

6. REFERENCES

1. Dunton, K.H., D.A. Tomasko. 1994. *In situ* photosynthesis in the seagrass *Halodule wrightii* in a hypersaline subtropical lagoon. *Mar. Ecol. Prog. Ser.* **107**:281-293.
2. Dunton, K.H. 1995. Seasonal growth and biomass of the subtropical seagrass *Halodule wrightii* in relation to continuous measurements of underwater irradiance. *Mar. Biol.* **120**:479-489.
3. Zimmerman RC, A. Cabello-Pasini, R.S. Alberte. 1994. Modeling daily production of aquatic macrophytes from irradiance measurements: a comparative analysis. *Mar. Ecol. Prog. Ser.* **114**:185-196.
4. Zimmerman RC, J.L. Reguzzoni JL, R.S. Alberte. 1995. Eelgrass (*Zostera marina* L.) transplants in San Francisco Bay: Role of light availability on metabolism, growth and survival. *Aquat. Bot.* **51**:67-86.
5. Mazzella, L., J.A. Ott. 1984. Seasonal changes in some features of *Posidonia oceanica* (L.) Delile leaves and epiphytes at different depths. In Boudouresque, C.F., de Grissac, A.J. & Olivier, J. (eds), International Workshop on *Posidonia oceanica* beds. G.I.S. Posidonie, Marseille, France.
6. Mazzella, L., R.S. Alberte. 1986. Light adaption and the role of autotrophic epiphytes in primary production of the temperate seagrass *Zostera marina* L. *J. Exp. Mar. Biol. Ecol.* **100**:165-180.
7. Mobley, C.D. 1994. Light and water: radiative transfer in natural waters. Academic Press, San Diego, 592 pp.
8. Mobley, CD. 1995. Hydrolight 3.0 User's Guide. Final report, SRI Project 5632. SRI International, Menlo Park, CA, 65 pp.
9. Maritorena, S., A. Morel, B. Gentili. 1994. Diffuse reflectance of oceanic shallow waters: Influence of water depth and bottom albedo. *Limnol. Oceanogr.* **39**:1689-1703
10. Zimmerman, R.C. D.G. Kohrs and R.S. Alberte 1996. Top-down impact through a bottom-up mechanism: the effect of limpet grazing on growth, productivity and carbon allocation of *Zostera marina* L. (eelgrass). *Oecol.* **107**:560-567.

Poster Session: Optical Properties

UVR attenuation in lakes: Relative contributions of dissolved and particulate material

L. M. Ayoub, B. R. Hargreaves, and D. P. Morris

Lehigh University, Department of Earth and Environmental Sciences
31 Williams Drive, Bethlehem, PA 18015

ABSTRACT

Solar radiation in lakes is attenuated by dissolved material, especially dissolved organic material (DOC), particulate material (PM), and water. DOC is a strong predictor of the attenuation of Ultraviolet Radiation (UVR) in lakes. Phytoplankton and detritus are known to contribute substantially to PAR attenuation but relatively little is known about their role in attenuation of UVR. This study investigated the relative contributions of dissolved and particulate material to the attenuation of UVR in lakes by combining an adapted Quantitative Filter Technique (QFT) with laboratory measurements of absorption by DOC and field measurements of UVR diffuse attenuation. The absorption of filtrate and PM filtered onto glass fiber filters were scanned by a UV-visible dual beam spectrophotometer. Total absorption coefficient (a_t) was computed as the sum of the absorption coefficients for water (a_w), dissolved material (a_d), and PM (a_p).

The value of a_t was compared with the diffuse attenuation coefficient (K_d) measured directly in the lakes by a Profiling UV radiometer (PUV-501, Biospherical Instruments, Inc.). The ratio a_t/K_d ranged between 0.9 and 1.3 for UVR. Ratios less than unity may be attributed to scattering and to sun angle effects, especially at the longer UVR wavelengths. Ratios occasionally were measured above unity, suggesting errors in estimating a_t .

Particles played a significant and seasonally-varying role in lake UVR attenuation. Within oligotrophic, low DOC Lake Giles, the relative contribution of a_p to a_t varied from 30% to 53% for 320 nm UVR. In mesotrophic, higher DOC Lake Lacawac the seasonal range was 7.6% to 57%. In each case, the highest contribution of PM was found during early spring and late fall.

Keywords: particulate material, Ultraviolet Radiation, absorption coefficient, attenuation coefficient

2. INTRODUCTION

UV radiation in aquatic environments is attenuated due to scattering and absorbance by dissolved and particulate material. The beam attenuation coefficient (c) is the sum of the scattering coefficient (b) and the absorption coefficient (a) for collimated light:¹

$$c = a_t + b_t \quad (1)$$

The absorption coefficient a_t of a whole water sample can be calculated from measurements of absorbance by a UV-visible spectrophotometer equipped with an integrating sphere. Field measurements of irradiance reflectance and scalar vs. cosine irradiance for PAR suggest that b_t is much less than a_t in our lakes. The dissolved and particulate components of absorption can also be measured separately. The diffuse attenuation coefficient (K_d) can be calculated from *in situ* irradiance measurements. K_d is expected to exceed c because of the increased pathlength which diffuse light follows compared to the path of a collimated beam. K_d represents the sum of partial diffuse attenuation coefficients of the components of natural waters²

$$K_d = K_{\text{water}} + K_{\text{DOC}} + K_{\text{PM}} + K_{\text{residual}} \quad \text{where} \quad (2)$$

K_{PM} can be further fractionated into K_{pigment} and $K_{\text{nonpigment}}$.

The relative amounts of dissolved and particulate attenuation vary between lakes of different trophic levels and [DOC], and seasonally within lakes. Variations in the relative amounts of dissolved and particulate material cause a change in the attenuation of UVR. Until recently, dissolved matter (principally DOC) has been considered the major determinant for attenuation of UVR.² This study explores the additional role of particulate matter in the attenuation of UVR.

3. EXPERIMENTAL DETAILS

The diffuse attenuation coefficient of UVR measured in situ (K_d) was compared to the total absorbance by dissolved material and PM measured in the laboratory with a UV-visible spectrophotometer. Two lakes in northeastern Pennsylvania of varying trophic status and [DOC] were studied: Lake Giles (41°22'34", oligotrophic, annual average [DOC] = 1.16 mg/l, pH = 5.4, ann. avg. [chl a] = 0.5 µg/l) and Lake Lacawac (41°22'57", mesotrophic, annual average [DOC] = 4.67 mg/l, pH = 6.0, ann. avg. [chl a] = 3 µg/l).³ Measurements were made monthly throughout 1995 - 1996 to determine the effect of changes in the concentrations of dissolved matter, particulate matter and algal biomass on UV transparency. K_d was determined from UVR vs. depth profiles using a profiling Ultraviolet radiometer (PUV-501, Biospherical Instruments Inc.), as the negative slope of Ln(downwelling irradiance) vs. depth (m).

Water samples taken from the middle of each layer (epi-, meta-, and hypolimnion) of each lake were taken to the laboratory and absorbance of dissolved and particulate material was measured from 200 - 800 nm using the Shimadzu UV160U UV-visible spectrophotometer. Since UVR does not consistently penetrate further than the epilimnion in the lakes studied, only epilimnial water samples were compared for this analysis. The PM was separated from dissolved material by filtration with glass fiber filters (GF/C, nominal pore size 1.2 µm) and 0.2 µm nylon membrane filters. The 0.2 µm nylon membrane filters were rinsed with at least 30 ml deionized water (Barnstead NANOpure™) to remove organic substances that might otherwise leach into the filtrate.

The absorption coefficient for PM > 1.2 µm ($a_{p\text{ GFC}}$) was determined by an adaptation of the Quantitative Filter Technique⁵: to obtain OD_f (optical density of material scanned on the filter), PM filtered onto a GF/C filter was scanned by the spectrophotometer, referenced to a clean wet filter. Beta (β) was estimated using the following power function derived by regression from Mitchell's 1990 data⁴:

$$\beta = 1.2857 * OD_f^{-0.1284} \quad (3)$$

OD_f was converted to OD_s (optical density of filtered material as a suspension) using beta:

$$OD_s = OD_f / \beta \quad (4)$$

OD_s was converted to a_p using:

$$a_p = 2.303 * OD_s * l_{\text{geo}} \quad (5)$$

where l_{geo} is geometrical pathlength (m), which is 100 times the filtered volume (ml) divided by the clearance area of filter (cm²). Absorption by 0.2 µm filtrate was subtracted from absorption by 1.2 µm (GF/C) filtrate to determine the absorption due to particles between the sizes of 0.2 µm and 1.2 µm ($a_{p\text{ 0.2-1.2}}$). Thus, $a_{p\text{ total}} = a_{p\text{ 0.2-1.2}} + a_{p\text{ GFC}}$. To determine the absorption coefficient for pigmented particles ($a_{p\text{ pigment}}$), the sample filters were filtered on a filter tower using two 5 ml volumes of hot 90% ethanol for 5 minutes to extract ethanol-soluble pigments. Then the pigment-extracted GF/C filter was scanned in the spectrophotometer as above to determine $a_{p\text{ nonpigment}}$. Thus,

$$a_{p\text{ pigment}} = a_{p\text{ total}} - a_{p\text{ nonpigment}} \quad (6)$$

Absorption by dissolved material (a_d) was determined by scanning the 0.2 µm filtrate in a 10 cm or 1 cm surpersil quartz cuvette referenced to air. An absorption scan of freshly made deionized water in the same cuvette was subtracted to account for cuvette effects. Then the absorption coefficient of pure water⁵ was added, to obtain total absorption due to dissolved materials, a_d . The total absorption coefficient (a_t) was computed as the sum of $a_{p\text{ total}}$ and a_d . Total

absorbance a_t was then compared to K_d at four wavelengths of UVR (305 nm, 320 nm, 340 nm, and 380 nm) and PAR (400 -700 nm).

4. RESULTS AND DISCUSSION

The total absorption coefficient varied with wavelength, with a continuous increase going from visible to shortest wavelength UVR (Fig. 1). In this particular case (June), a_p represented a small and consistent fraction of a_t and most of a_p was greater than 1.2 μm . On top of the graph are listed the ratios of a_t/K_d , which show that most of the UVR attenuation was accounted for by absorbance; there was little effect of sun angle at shorter wavelengths.

From early to late summer, the contribution of a_p to a_t was greater in low [DOC] Lake Giles (Fig. 2). The contribution of a_d to a_t is greater in high DOC lakes.

Figure 3 shows how the relative contributions of a_p and a_d to total UVR attenuation varied seasonally within the lakes studied. Although a different method was used for each summer, the same pattern was observed: gradual increase in % a_p from summer to fall. In oligotrophic, low DOC Lake Giles, comparing August and November, the relative contribution of particulate matter (% a_p) increased from 18.3% to 53.1%, with a proportional decrease in % a_d . In mesotrophic, higher DOC Lake Lacawac, comparing August and April, % a_p increased from 10% to 57%. For Lake Lacawac comparing the two summers, June and July differed in the magnitude of seasonal change perhaps because of differences in the timing of mixing. For each lake, the maximum % a_p occurs in late fall or early spring. The highest values of % a_p tend to underestimate the true maxima because the size fractions 0.2 μm to 1.2 μm or 0.7 μm to 1.2 μm were accidentally excluded from analysis.

Over the course of both summers there was a total decrease in absorption, but the absorption value was greater in 1996 than 1995. Comparing November 1995 and August 1996 for oligotrophic, low DOC Lake Giles, a_p at 320 nm decreased from 0.67 m^{-1} to 0.13 m^{-1} . In higher DOC Lake Lacawac, comparing April 1996 and August 1995, a_p at 320 nm decreased from 10 m^{-1} to 1.2 m^{-1} (Fig. 4). The higher DOC lake showed general dominance in a_t by a_d , except in April, where the lake was thoroughly mixed. The higher DOC lake showed higher a_p as well as higher a_d values, and a_t consistent with the K_d for each lake.

One possible source of error is overestimation of $a_{d\text{ GFC}}$. Since no integrating sphere was available, some attenuation due to scattering by particles might have been detected by the spectrophotometer as absorption. Utilization of an integrating sphere would also increase the accuracy of OD_f measurements and would improve our estimates of beta.

5. CONCLUSIONS

Changes in both particulate and dissolved matter cause variation in the attenuation of UVR ($K_{d\text{ UVR}}$) seasonally as well as among lakes. Understanding these changes will be required to develop models of UVR in natural waters. Based on absorption measurements, particulate material is a significant and variable factor in the attenuation of UVR in lakes. With proper attention to a_p , laboratory spectrophotometric determination of a_t enables the calculation of the diffuse attenuation coefficient for UVR.

6. ACKNOWLEDGEMENTS

We thank Robert Moeller for discussions and field work, B. Greg Mitchell for discussions and Kiersten Dornemann, Carla Gutierrez, Jasmine Gokcen, Kathy Kresge, Dina Leech, Kathy Luzopone, Susanne Metzgar, Spero Michailidis, Olaf Olson, Chris Osburn, Erin Sadlowski, and Craig Williamson for assistance in field work. Logistic support was provided by the Lacawac Sanctuary, the Lake Waynewood Association, and Blooming Grove Hunting and Fishing Club.

7. REFERENCES

1. J. T. O. Kirk, *Light and Photosynthesis in aquatic ecosystems*, 2nd ed., p. 14, Cambridge University Press, Cambridge, 1994.
2. D. P. Morris et. al., "The attenuation of solar UV radiation in lakes and the role of dissolved organic carbon", *Limnol. Oceanogr.*, **40**: 1381-1391, 1995.
3. R. E. Moeller et. al., *Limnology of lakes Lacawac, Giles, and dWayneood 1989-1993: an introduction to the core lakes of the Pocono Comparative Lakes Program*, Lehigh University, Bethlehem, 1995.
4. B. G. Mitchell, " Algorithms for determining the absorption coefficient of aquatic particulates using the quantitative filter technique (QFT). *Ocean Optics X*, SPIE Vol. **1302**, pp. 137-148, 1990.
5. R. C. Smith and K. S. Baker, "Optical properties of the clearest natural waters (200-800 nm)", *Appl. Opt.*, **20**: 177-184.

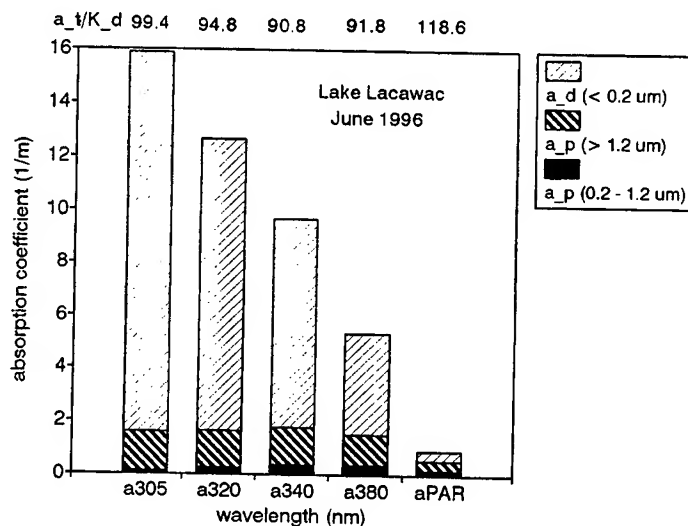


Fig. 1. Fractionation of a_t into a_p nonpigment, a_p pigment, and a_d ; comparison to K_d in Lake Lacawac ($41^\circ 22' 57''$), [DOC] = 4.67 g/m^3 . Pigment is a small part of $a_p > 1.2$ ($\%a_p = 1.3 - 3.6 \%$ in UVR, 7.7% in PAR). Ratios of $a_t:K_d$ exceed 90% in UVR.

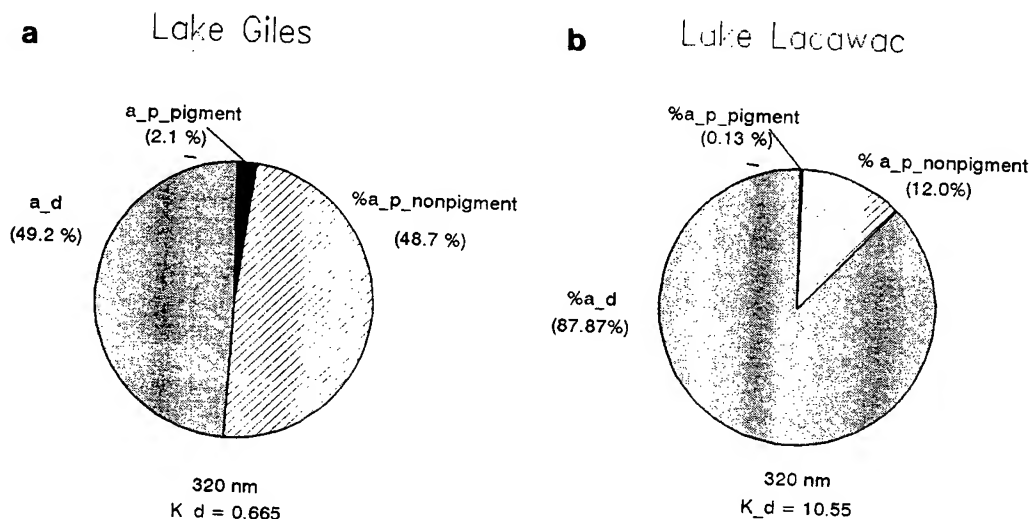


Fig. 2. Variation in relative contributions of epilimnial a_p and a_d to a_t among lakes of different trophic status at 320 nm. (a) $\%a_p = 50.8\%$ in the low [DOC] Lake Giles; (b) $\%a_p = 12.13\%$ in the higher [DOC] Lake Lacawac. a_p is a more significant contributor to a_t in the low [DOC] lake ([DOC] = 1.16 g/m^3 , $K_d = 0.67$) than in the high [DOC] lake ([DOC] = 4.67 g/m^3 , $K_d = 10.55$) during stratification.

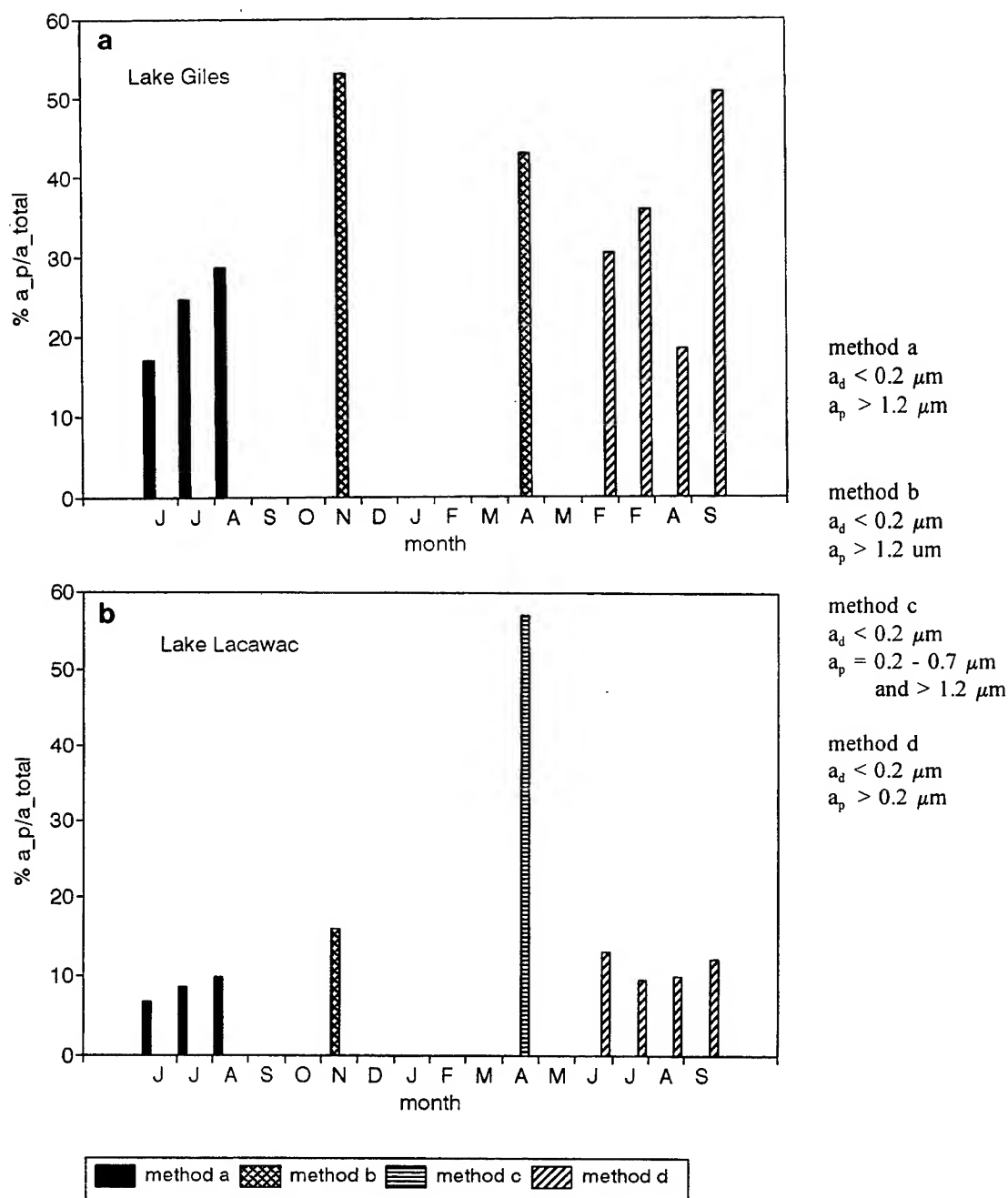


Fig. 3. Seasonal variation of $\%a_p$ at 320 nm in the epilimnion of lakes. (a) low [DOC] Lake Giles, (b) high [DOC] Lake Lacawac: as fall turnover occurs, $\%a_p$ increases. Note that fall turnover occurred earlier in 1995 than in 1996 (June in 1995 vs. August in 1996), due to cooler weather in 1995. Maxima in $\%a_p$ occur in November and April for each lake (see text for methods). At this time of year the lakes are well-mixed, thus particle concentration reaches its maximum. Even in the high [DOC] lake, $\%a_p$ can exceed $\%a_d$: in April 1996 it reaches 57% a_d . For Lake Lacawac comparing the two summers, June and July differ because mixing began later in the second year. The highest values of $\%a_p$ tend to underestimate the true maxima because the size fractions $0.2 \mu\text{m}$ to $1.2 \mu\text{m}$ or $0.7 \mu\text{m}$ to $1.2 \mu\text{m}$ were accidentally excluded from analysis.

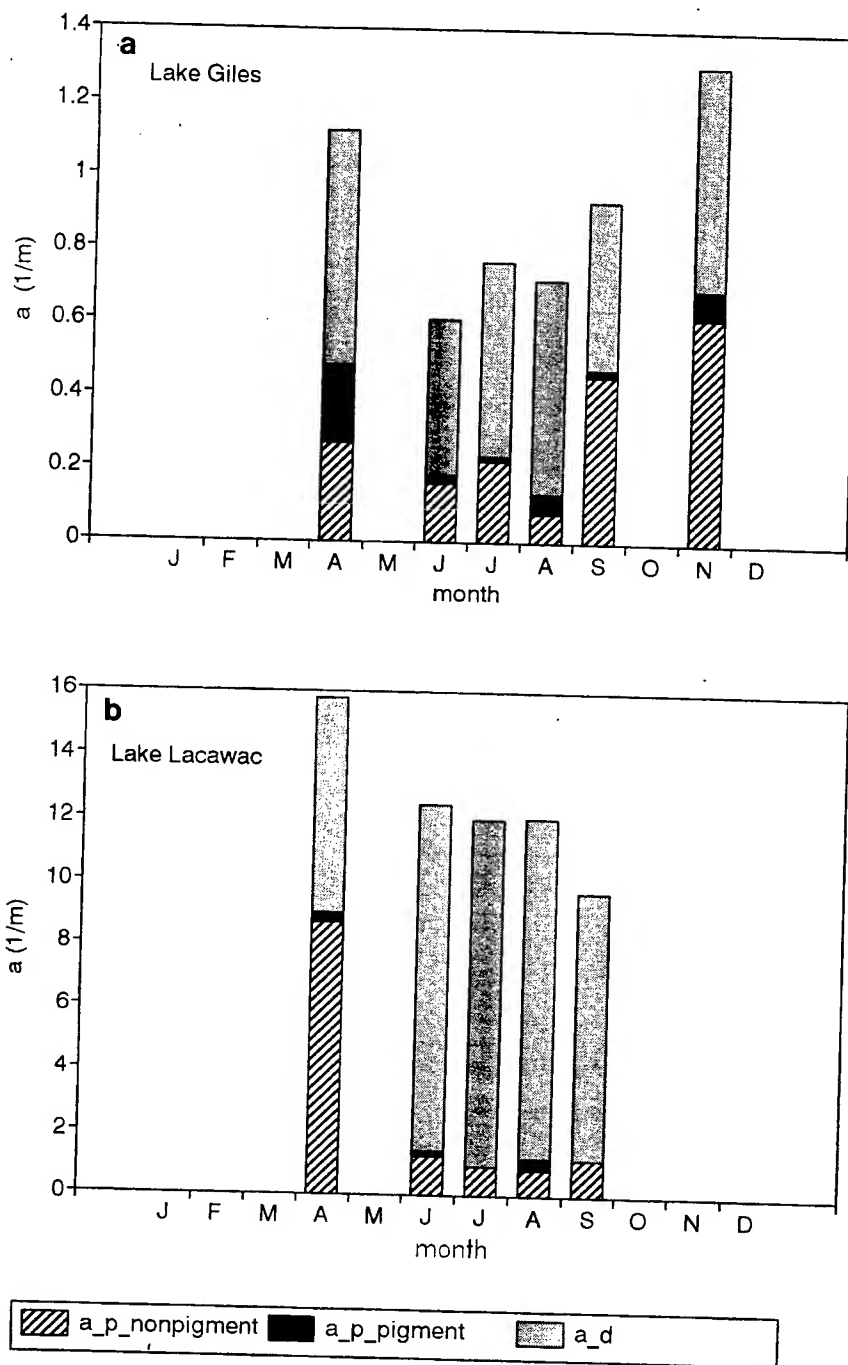


Fig. 4. Seasonal variation in a_p , a_d , and a_t at 320 nm within lakes. (a) low [DOC] Lake Giles, from November to August, a_p decreases from 0.67 m^{-1} to 0.13 m^{-1} . (b) high [DOC] Lake Lacawac, from April to August, a_p decreases from 10 m^{-1} to 1.2 m^{-1} . In each lake, a_t decreases from late spring to late summer. At the maxima, the role of particulates is underestimated due to accidental exclusion of particles of size $0.2 - 1.2 \mu\text{m}$ in Lake Giles (November and April), and Lake Lacawac (November), and exclusion of particles of size $0.7 - 1.2 \mu\text{m}$ in Lake Lacawac in April. Thus, the true maxima are higher than depicted.

Absorption spectra reconstruction using Voigt profiles

R. Aguirre-Gómez*, A. R. Weeks†, S. R. Boxall

University of Southampton
Department of Oceanography
Southampton Oceanography Centre
Waterfront Campus, European Way
SO14 3ZH, U.K.

* Permanent Address: Instituto de Geografia, Universidad Nacional Autonoma de Mexico, Circuito Exterior, 04510, Coyoacan, D.F. Mexico.

† Present Address: Maritime Faculty, Southampton Institute, East Park Terrace, Southampton, SO14 OYN

ABSTRACT

The identification of the components of algal absorption spectra can be made mathematically through either derivative or spectral deconvolution analyses. This work establishes a methodology for identifying phytoplankton pigments from absorption spectra by combining the derivative and spectral deconvolution methods and interpreting the results with the knowledge of the major light absorbing pigments. This was achieved a) by locating the [position of the absorption peaks present in the spectra of different algal groups through the derivative analysis, b) by fitting a combination of Gaussian-Lorentzian or Voigt shaped bands, centred at these peaks, to the original spectra and c) by using pigment analysis via HPLC to provide the biological background for identifying these bands and peaks. The results of this study show that the derivative method can be used successfully in monocultures and natural populations to identify pigments by their individual absorption peaks. Secondly, a good agreement has been found between the original spectra and the reconstructed spectra which were a Voigt combination. The HPLC analysis provided the objective platform for the biological interpretation of the bands.

Keywords: Deconvolution analysis, derivative analysis, phytoplankton pigments, absorption spectra

1. DERIVATIVE AND DECONVOLUTION ANALYSIS

The absorption spectra of photosynthetic organisms in the visible range, from 400 to 700 nanometres, are characterized by a continuous envelope. This makes it difficult to estimate the contribution of each pigment to the total absorption. In this study, high order derivatives are used for decomposing the curves and for locating the absorption peaks.

The derivative algorithm consists of dividing the difference between successive spectral values by the wavelength interval separating them. This provides an approximation of the first derivative at the midpoint between these values whose difference is used to compute the slope. Higher order derivatives are obtained by repeating the process. However, in order to avoid the random noise an optimum differentiating interval was chosen¹.

Gaussian curve-fitting has been used for decomposition of *in vivo* absorption spectra of different algal cultures approximation². Another approach is the Lorentz model which has been applied in molecular biophysics for explaining the electronic excitation energy travelling in a periodic structure, as for example in pigment molecules. Bricaud and Morel³ successfully applied the Lorentzian model to decompose the absorption spectrum of the alga *Platymonas suecica*. In this study a combination of Gaussian and Lorentzian curves are used, along with considerations of the distortion caused by the dispersive slit of the spectrophotometer.

2. THEORETICAL CURVE ANALYSIS

The derivative method was applied to modelled absorption spectra of diatoms and green algae. These curves were constructed by summing up the spectra of their component pigments. The proportion of the different pigments present in each alga and their spectral shape, were determined from literature review⁴. For example, a typical green algae spectrum can be constructed using the following relationship:

$$3(1.6 \text{ Chla} + \text{Chlb}) + \beta\text{-carotene}$$

Applying the derivative algorithm the positions of absorption peaks for the theoretical curve of this algae were found at the following wavelengths: **425, 455, 485, 515, 530, 560, 570, 595, 615, 640, and 660 nm**. Peaks attributable to pigments are in bold.

Figure 1 shows the spectra of the component pigments (chlorophyll-*a*, chlorophyll-*b* and β -carotene) and the combined spectrum. The lower panel shows the peaks obtained using the 4th derivative analysis.

3. MEASURED SPECTRA

3.1. *In vivo*

The derivative method was applied to three algal cultures with different optical properties: a Diatom (*Phaeodactylum tricornutum*); a Prymnesiophyte (*Isochrysis galbana*) and a Chlorophyte (*Tetraselmis suecica*). Absorption spectra of these groups were obtained by spectrophotometry. The absorption peaks found by the fourth derivative analysis are compared (Tables in Figure 2(a) and (b)) with the spectral peaks expected from the individual pigments^{5,2}. There were a number of peaks in the green region which can be attributed to protein-bound molecules.

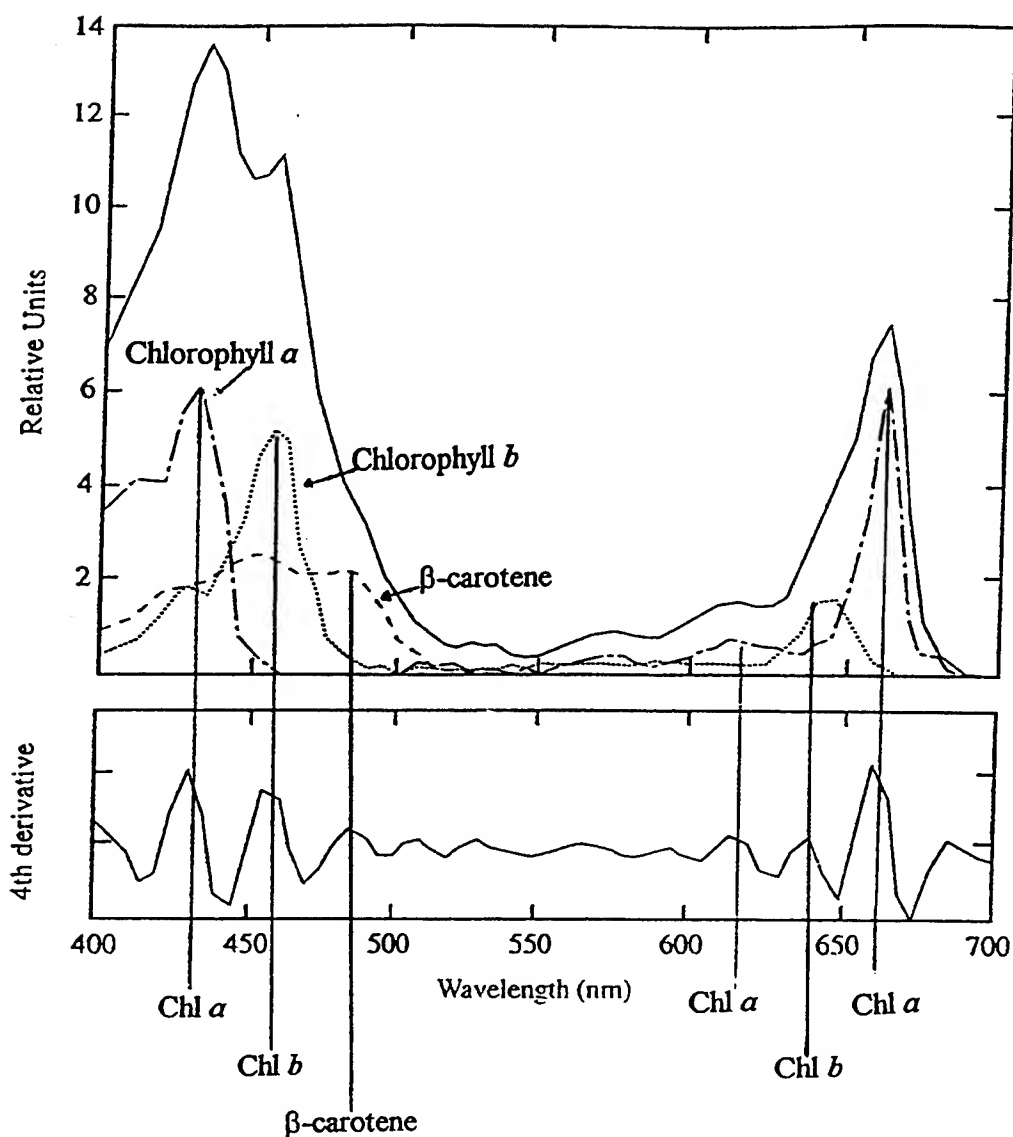


Figure 1. The top panel shows the spectra of the component pigments (chlorophyll-*a*, chlorophyll-*b* and β -carotene) and the combined spectrum. The lower panel shows the peaks obtained using the 4th derivative analysis.

3.2. Acetone-Extracted (*in vitro*)

The derivative method was applied to 4 algal cultures with different optical properties: a Dinoflagellate (*Amphidinium carterae*); two Diatoms (*Phaeodactylum Tricornutum* and *Rhizosolenia delicatula*); and a blue-green alga (*Synechococcus sp.*). The derivative analysis showed conspicuous peaks both in the blue and red regions. These are compared with the spectral peaks expected from the individual pigments (Tables in Figure 3(a) and (b)). Minor peaks also appeared in the green interval, but were much smaller than those observed in the *in vivo* samples.

These results show that mismatches occur when comparisons are made between the peaks attributed to pigments in the *in vivo* and *in vitro* samples, when using the 4th derivative method. Spectral shifts in intact cells are caused by processes such as the protein complexes that bind the pigment molecule, the package effect and the physiological state of the phytoplankton. A method has been developed which uses the peaks from the 4th derivative as input for an iterative procedure to maximise the fit with the absorption spectrum. Previously only Gaussian-shaped curves were used but in this study a combination of Gaussian and Lorentzian shapes are used.

4. GAUSSIAN-LORENTZIAN DECOMPOSITION

For decomposing the absorption spectra with Lorentzian - Gaussian bands the RESOL program⁶ was slightly updated and adapted to the requirements of this study⁷. The initial parameters required by the program were: wavelengths peaks, heights and halfwidths. The first two parameters were obtained through the derivative analysis of absorption spectra of each alga. The third one was estimated based on literature review^{6,2}. Program running specifications for each absorption spectrum, were: a) Gaussian- Lorentzian curves were chosen; b) no weighting factor was applied; c) A maximum of 20 iteration were allowed; d) band centres and the half bandwidths were allowed to change no more than 1 nm per iteration. After each iteration all parameters were adjusted, resulting in rapid convergence. Four parameters are obtained: the central peak, the Gaussian and Lorentzian weights, and the halfwidth. Using these parameters a Gaussian -Lorentzian approximation was obtained. This approach was applied to spectra from *in vivo* and *in vitro* algal cultures and to spectra from *in vivo* natural phytoplankton populations (peaks are shown in brackets in the tables in Figures 2 and 3).

The measured absorption spectra and the peaks found by the iterative procedure for *in vivo* and *in vitro* samples are shown in Figures 2 and 3 respectively. Figure 2(a) shows the absorption spectrum of *Phaeodactylum Tricornutum in vivo* and shows the peaks found by the iterative procedure. The table below shows the adjusted spectral peaks (in brackets) and the pigments that are attributable to them. A second *in vivo* sample *Tetraselmis suecica* is also shown. The lower panel shows the difference between the measured and reconstructed absorption spectrum. Figure 3 shows the absorption spectrum for (a) *Phaeodactylum Tricornutum in vitro* and shows the peaks found by the iterative procedure, and the tables show the spectral peaks and the pigments that are attributable to them. (b) shows a second *in vitro* sample *Synechococcus sp.* As before, the lower panels show the difference between the measured and reconstructed absorption spectrum.

The results from the *in vivo* cultures show a larger spectral shift from the expected peaks due to the pigments, and larger errors between the reconstructed spectra and the measured spectra than for the *in vitro* cultures. This is probably due to the protein complexes binding the pigment molecules, the package effect and the physiological state of the phytoplankton in the *in vivo* cultures.

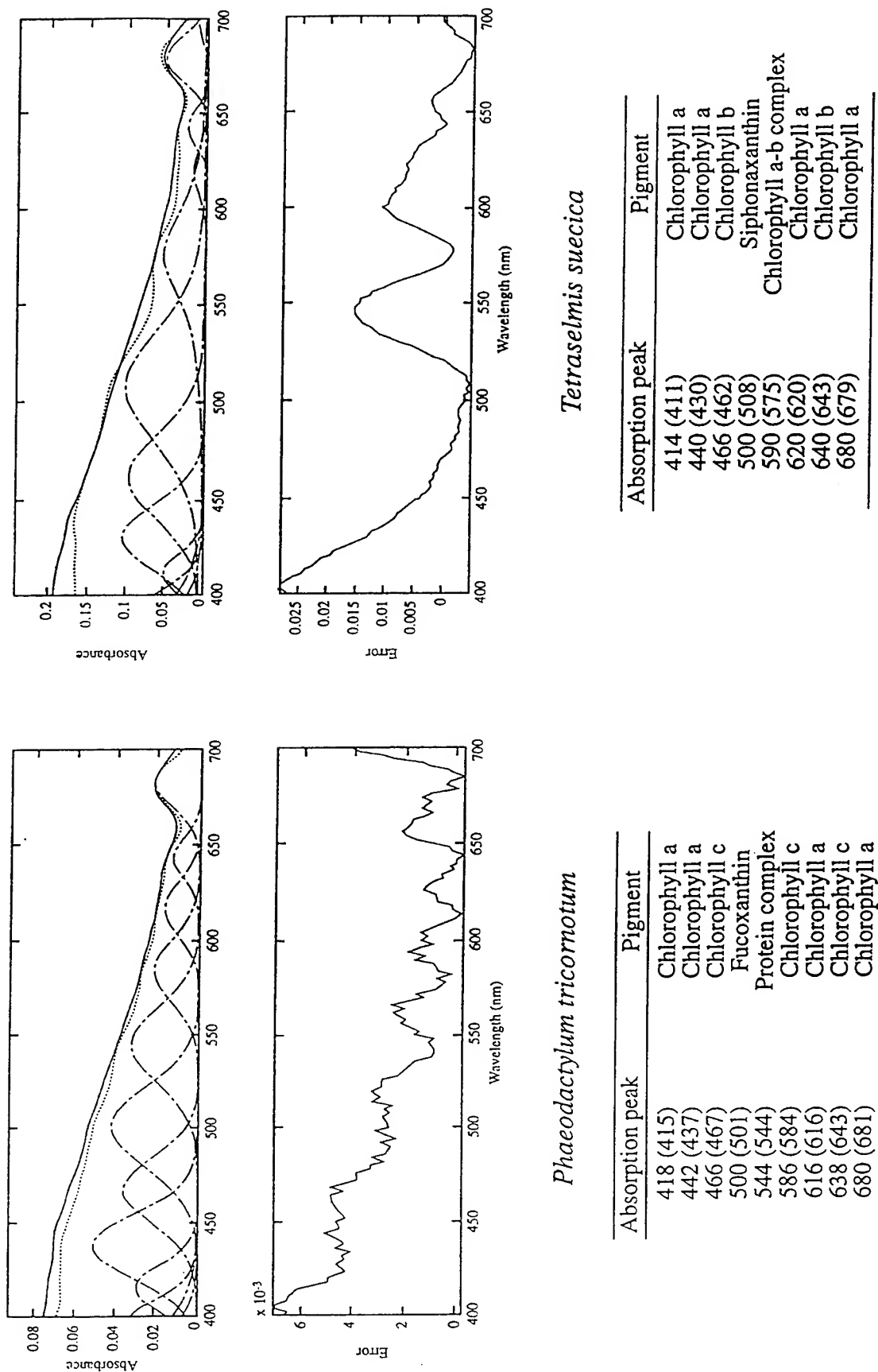
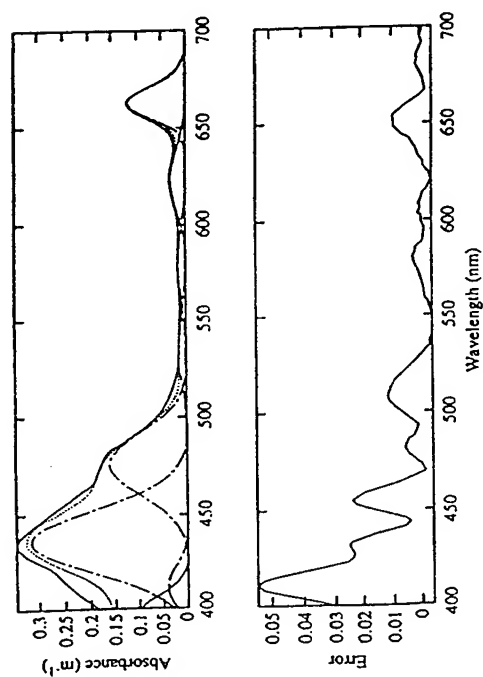
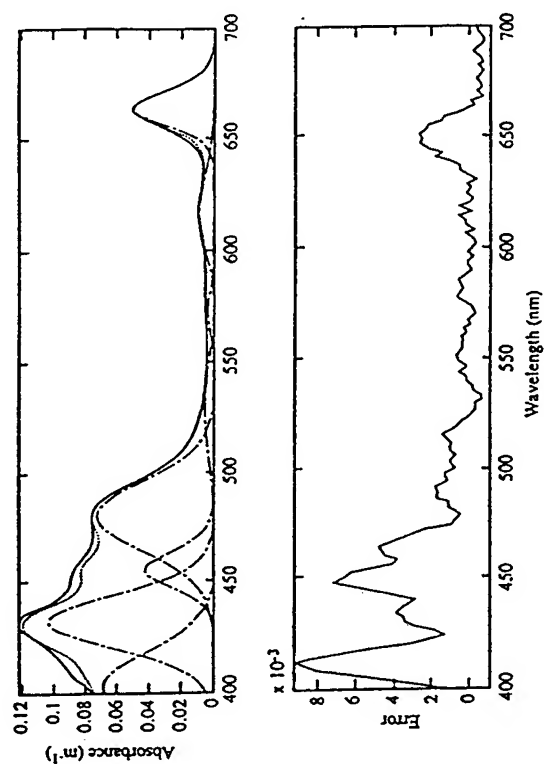


Figure 2. The absorption spectra for 2 *in vivo* phytoplankton cultures; the diatom (*Phaeodactylum tricornutum*) and the Chlorophyte (*Tetraselmis suecica*). Peaks found by the fourth derivative analysis are compared in the tables with the spectral peaks expected from the individual pigments.



Phaeodactylum tricornutum

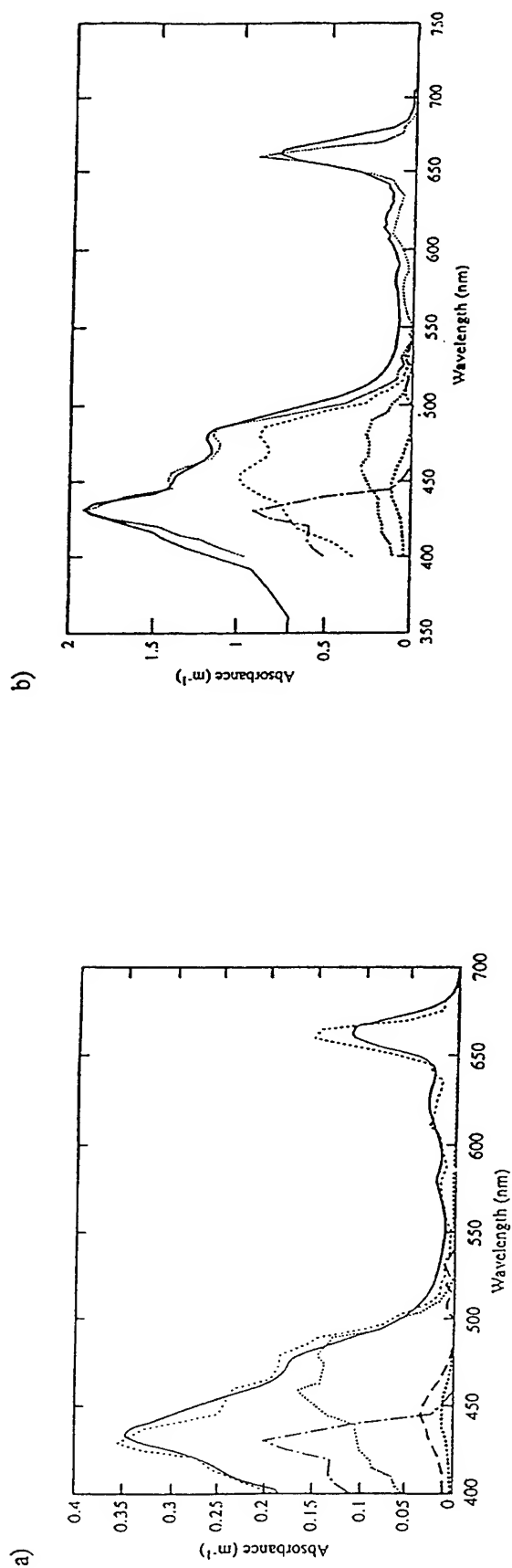
Absorption peak	Pigment
408 (407)	Chlorophyll a
434 (434)	Chlorophyll a
480 (479)	Chlorophyll c
538 (537)	β -carotene
578 (579)	Fucoxanthin
622 (623)	Chlorophyll c
662 (663)	Chlorophyll a



Synechococcus sp

Absorption peak	Pigment
408 (407)	Chlorophyll a
430 (431)	Chlorophyll a
458 (459)	Chlorophyll c
484 (485)	Zeaxanthin
542 (543)	β -carotene
576 (577)	Fucoxanthin
616 (615)	Chlorophyll c
662 (661)	Chlorophyll a

Figure 3. The absorption spectra for 2 *in vitro* phytoplankton cultures; the diatom (*Phaeodactylum tricornutum*) and the blue-green alga (*Synechococcus sp*). Peaks found by the fourth derivative analysis are compared in the tables with the spectral peaks expected from the individual pigments. The bracketed numbers in the tables show the spectral peaks obtained after the Gaussian-Lorentzian deconvolution was carried out.



Phaeodactylum tricornutum

Symbol	
—	Original spectrum
.....	Reconstructed spectrum
- - - -	Chlorophyll a
.....	Fucoxanthin
- - - -	Diadinoxanthin
.....	Chlorophyll c

Synechococcus sp.

Symbol	
—	Original spectrum
.....	Reconstructed spectrum
- - - -	Chlorophyll a
- - - -	β-carotene
.....	Zeaxanthin
.....	Fucoxanthin

Figure 4. The reconstructed absorption spectra for (a) the diatom (*Phaeodactylum tricornutum*); (b) a blue-green alga (*Synechococcus sp.*) using pigments identified and quantified by HPLC analysis. The original spectrum for each of the cultures is shown along with the reconstructed spectrum, and the spectra for the component pigments is also shown.

5. RECONSTRUCTED SPECTRA FROM PIGMENTS

For reconstructing absorption spectra by HPLC analysis, the following steps were performed:

- a) Normalization. Since absorption spectra of algal pigments were obtained from different solvents, a standardization process was required. It was done by assuming that the highest pigment concentration was the norm.
- b) Weighting Factor. Taking the norm as unity, the weighting factor for the other pigments was calculated as the relative proportion of their concentration to that of the norm.
- c) Sum. A weighted sum of the relative proportion of concentrations accounted for the resultant reconstructed spectra.

Examples are shown in Figure 4.

7. SUMMARY

The 4th derivative analysis can be used to identify pigments in modelled spectra when pigment-specific absorption spectra are used to construct the original curve for a particular taxonomic group.

The spectral peaks identified from the absorption spectra of monocultures using the 4th derivative can be identified as pigment bio-markers, although the 4th derivative analysis provides better spectral match to pigment spectra for *in vitro* samples compared to *in vivo* samples.

By applying the deconvolution analysis, the peaks are adjusted to obtain the best fit to the original curves. This approach is logical since linear summation of the component pigment spectra is unlikely to provide a good representation of the interaction of pigments and structures in living cells, where non-linearities from the package affect are well known..

8. ACKNOWLEDGEMENTS

We wish to thank Dr. J.Aiken for the use of facilities at Plymouth Marine Laboratory and Dr. Nicholas Hoepffner for providing a copy of the RESOL program.

9. REFERENCES

1. R.Aguirre-Gomez, A.R.Weeks, and S.R.Boxall, The identification of phytoplankton pigments from absorption spectra. *Proceedings of the International Colloquium of Photosynthesis and Remote Sensing, August 1995*, 191-205, 1995
2. N.Hoepffner, and S. Sathyendranath. Effect of Pigment Composition on Absorption Properties of Phytoplankton, *Marine Ecology Progress Series*, Vol. 73, 11 - 23, 1991.
3. A.Bricaud, and A. Morel. Light Attenuation and Scattering by Phytoplanktonic Cells: a Theoretical Modelling. *Applied Optics*, 25(4), 571-580, 1986.
4. J.T.O.Kirk, Light and Photosynthesis in Aquatic Ecosystems. Cambridge University Press. Cambridge, 1983.
5. R.R.Bidigare, J. H. Morrow and D. A. Kiefer. Derivative Analysis of Spectral Absorption by Photosynthetic Pigments in the Western Sargasso Sea. Vol. *Journal of Marine Research*, 47, 323 - 341, 1989.
6. C.S.French, J. S. Brown, L. Prager and M. Lawrence. Analysis of Spectra of Natural Chlorophyll Complexes. *Carnegie Institute Washington Yearbook* 67, 536 - 546, 1969.
7. R. Aguirre-Gomez, S.R. Boxall and A.R. Weeks. Identification of Algal Pigments Using High Order Derivatives, *Proceedings of the International Symposium "Quantitative Remote Sensing for Science and Applications"*. IGARSS, 1995

Retrieving chlorophyll and non chlorophyllous matter from ocean colour satellite data in Baltic "Case 2Y" waters.

Jean-François Berthon

Baltic Sea Research Institute, Seestrasse 15, D-18119 Rostock-Warnemünde, Germany and Marine Environment Unit, Space Applications Institute, TP272, JRC Ispra, 21020 Ispra, Italy (present address)(jean-francois.berthon@jrc.it).

Mark Dowell

University of Southampton, Southampton Oceanography Centre, European Way, Southampton, SO14 3HZ, UK and Marine Environment Unit, Space Applications Institute, TP272, JRC Ispra, 21020 Ispra, Italy.

Nicolas Hoepffner and Stefania Grossi.

Marine Environment Unit, Space Applications Institute, TP272, JRC Ispra, 21020 Ispra, Italy.

ABSTRACT

Based on *in situ* data collected in the Southern Baltic Proper at three different periods of the year this study investigates the possibility to empirically retrieve Chlorophyllous and Non Chlorophyllous (dissolved and particulate) matter absorption coefficients in the Baltic Sea using "SeaWiFS" type spectral information. It relies on the classical relationship between "remote-sensing" reflectance and the back-scattering and absorption coefficients of the in-water optically active components ($R_{rs} = f/Q \cdot b_b/a$).

The use of reflectance ratios minimizes the effect of the " f/Q " variability if one assume its low wavelength dependency. A reflectance ratio can therefore be expressed as the product of the total absorption ratio and of the total back-scattering wavelength dependency, classically defined as a power law of the wavelength ratio. Empirical relationships, valid for the considered data set, are used to estimate the exponent N of this power law from specific reflectance ratios, the 443/510 and 510/550 ratios being the best candidates. It is thus shown that, in these yellow substances dominated waters ("Case 2Y"), total absorption ratios could allow the estimation of non chlorophyllous matter absorption at 412 nm (using in particular the 665/412 ratio) and of pigment absorption at 443 nm (and consecutively of chlorophyll concentration).

Keywords : ocean colour, SeaWiFS, reflectance, coastal waters, Case2 algorithms, pigments, yellow substances, Baltic Sea

2. INTRODUCTION

Present methods for the inversion of satellite ocean colour measurements generally rely on the classical relationship between the water leaving radiance $L_w(\lambda)$, transformed into reflectance $R(\lambda)$ at the sea surface, and the inherent optical properties (spectral absorption $a(\lambda)$ and back-scattering $b_b(\lambda)$ coefficients) of the water contained dissolved and particulate constituents. Among others, two important problems are encountered, i) L_w is related to b_b and a through the use of the " f/Q " factor which variability can be quite large depending on the water components and the illumination conditions^{1,2}; ii) very little is known on the variability of $b_b(\lambda)$ of particles and especially of non chlorophyllous ones that can play an important role in coastal Case 2 waters.

By using reflectance ratios instead of reflectance alone a part of these variations may be reduced, in particular for f/Q . Empirical relationships between reflectance ratios and water constituents implicitly contain such a simplification. The present study investigates for the Southern Baltic Proper Case 2 waters the possibility to derive information on the total b_b spectral dependency from reflectance ratios. Using this information, reflectance ratios are then simply transformed into total absorption ratios from which estimation of absorption by chlorophyllous and by non chlorophyllous matter at certain wavelengths can be empirically derived.

3. DATA

The *in situ* data set has been collected in the Southern Baltic Proper at three different periods (April, August, September) during 1994 (Figure 1) (Collaboration between the JRC-Ispra and the Institute of Oceanology of Sopot, Poland). The data used in this study include underwater upwelling radiance and downwelling irradiance measured at the six SeaWiFS wavelengths (412, 443, 490, 510, 550 and 665 nm) with a MER-2040 Profiling Spectroradiometer as well as chlorophyllous (a_{ph}), non-chlorophyllous particles (a_d)³ and coloured dissolved organic matter (a_y) absorption spectra (400-700 nm), "spectrophotometric" Chlorophyll a + Pheopigment concentration (Chl), total suspended matter (TSM) and Light beam attenuation at 655 nm ($c(655)$).

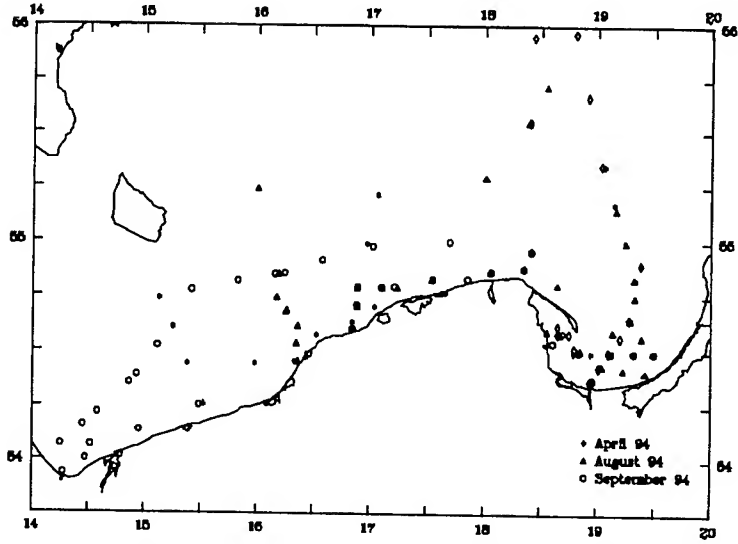


Figure 1: Map of the Southern Baltic Proper and positions of the stations.

4. APPROACH

The classical relationship between the ratio $L_u(0)/E_d(0^+)$ and the optical inherent properties b_b and a of the seawater is⁴

$$L_u(0, \lambda)/E_d(0^+, \lambda) = f/Q \quad b_b(\lambda)/a(\lambda) \quad \text{or} \quad R(\lambda) = f \quad b_b(\lambda)/a \quad (1)$$

For a sake of simplicity we will (erroneously) call our measured $L_u(0, \lambda)/E_d(0^+, \lambda)$ ratio the "remote-sensing reflectance" $R_{rs}(\lambda)$. By assuming that as a first approximation f/Q is independent of λ (as in ref. 5 but see ref. 2) a R_{rs} ratio can be written as

$$R_{rs}(\lambda_i)/R_{rs}(\lambda_j) = [b_b(\lambda_i)a(\lambda_j)] / [b_b(\lambda_j)a(\lambda_i)]$$

If we express the wavelength dependency of the total back-scattering coefficient as

$$b_b(\lambda_i) = b_b(\lambda_j) (\lambda_i/\lambda_j)^N$$

it comes

$$R_{rs}(\lambda_i)/R_{rs}(\lambda_j) = (\lambda_i/\lambda_j)^N \quad a(\lambda_j)/a(\lambda_i) \quad (2)$$

If N could be known or estimated then total absorption ratios would be derived from "remotely-sensed" reflectance ratios. Note that we considered here total b_b including b_b by water (which role may be assumed small in these waters compared to the other components of scattering). Also we only consider the situation where $b_b \ll a$ and then is removed from the denominator of equation (1). For each station N has been estimated by fitting the equation (2) between 412 and 550 nm to the *in situ* measured $R_{rs}(\lambda)$ and $a(\lambda)$.

5. RESULTS

5.1. Variability of the computed exponent N

The resulting N values are presented in Figure 2. Values are ranging between -3. and 2.5 with a few values higher than 0. A rough increase of N with Chl, TSM and specially $c(655)$ is observed. Although these estimations are strongly

depending on the accuracy of the *in situ* measured $R_{rs}(\lambda)$ and $a(\lambda)$, and positive values are doubtful, a part of their variability could result from variations of $b_b(\lambda)$ by particles. For example an increase of Chl accompanied by an increase of the cell size (e.g. a diatoms bloom) can induce an increase (toward 0.) of the slope of the particulate $b_b(\lambda)$.

5.2. Relationships between N and Reflectance ratios

The best reflectance ratios for such relationships should be those for which the total absorption ratios are the less varying. The ratios 443/490, 443/510 and 510/550 have been found to be the best candidates. It has also been observed that the April stations, for which extremely high absorption in the blue ($> 1 \text{ m}^{-1}$ at 412 nm) by dissolved organic matter (DOM) has been measured, were departing from the others whatever the ratio. Figure 3 shows the derived empirical linear relationships between N and reflectance ratios. Even if statistically incorrect (the N values have been partly computed using the same $R_{rs}(\lambda)$ set) this exercise has been tempted since no independent data set was available. No "universal" relationship could be found and the high DOM containing stations of April have been treated separately. The 443/510 ratio showed the best r^2 values for the two groups. The 510/550 ratio could in the extreme case be used for a unique relationship if some stations (the lower N values) were disregarded.

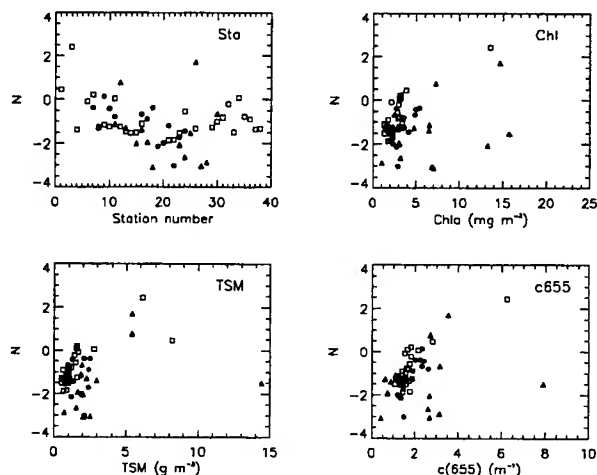


Figure 2 : Distribution of the computed N values with station number, "Chla", Total suspended Matter and Beam attenuation coefficient at 655 nm.

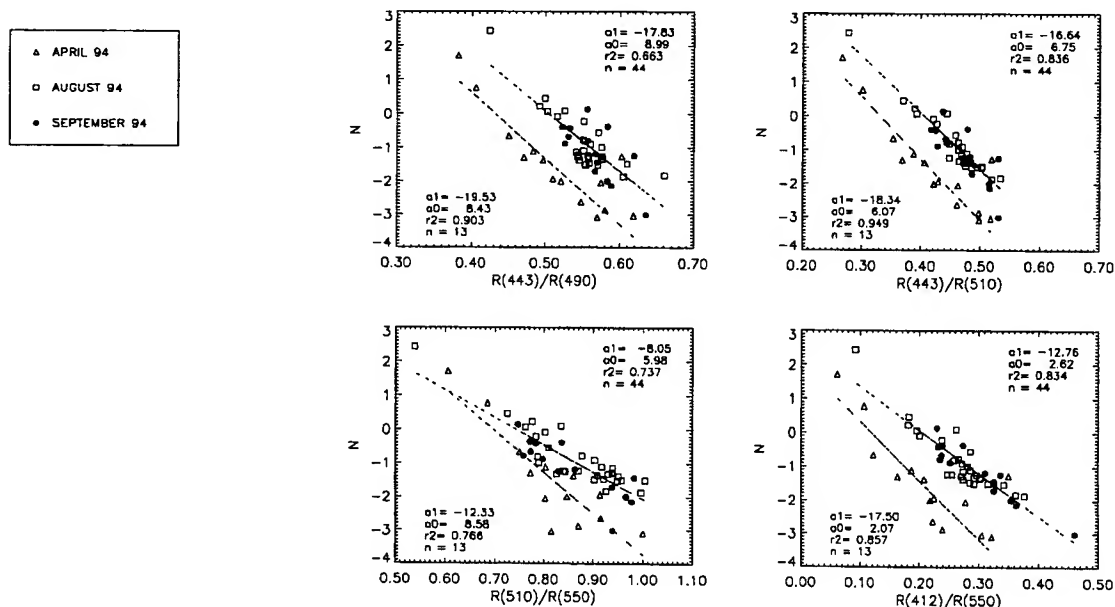


Figure 3 : Computed N values versus $R_{rs}(\lambda)$ ratios and associated linear regressions for April (triangles) and others (see text).

5.3. Estimation of $a_y(\lambda)+a_d(\lambda)$ and $a_{ph}(\lambda)$ from $a_{tot}(\lambda)$ ratios

The 665/412 total absorption ratio has been found to provide the best estimation of (a_y+a_d) at 412 nm (Figure 4a) considering all stations. The 412/443 total absorption ratio provided the best estimation for a_{ph} at 443 nm (Figure 4b) but April stations had to be considered separately once again. In this last case these stations could be identified using the $a_{tot}(412)/a_{tot}(443)$ threshold value of 1.7. The high information content of the 665 nm channel has already been observed for the Baltic Sea in particular for the estimation of the dissolved organic matter using reflectance ratios⁶.

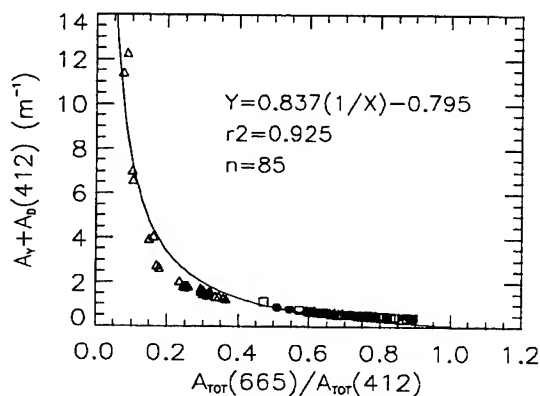


Figure 4a : $(a_y+a_d)(412)$ versus $a_{tot}(665)/a_{tot}(412)$ and computed relationship.

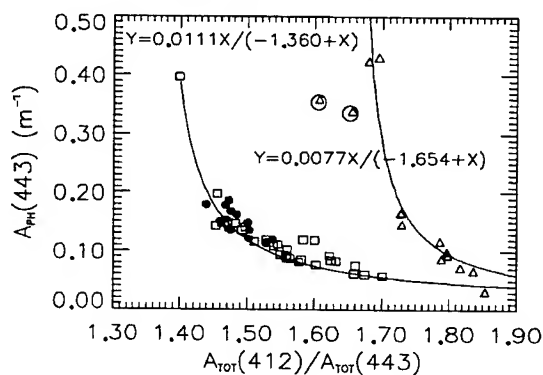


Figure 4b : $a_{ph}(443)$ versus $a_{tot}(412)/a_{tot}(443)$ and computed relationships for April (triangles) and the other cruises. Two April stations (circled) have been disregarded.

5.4. Estimation of Chlorophyll concentration from $a_{ph}(443)$

A reasonably good linear relationship has been found between the Chla+Pheo concentration and the pigment absorption at 443 nm, $a_{ph}(443)$ (Figure 5). It has to be said that the use of $a_{ph}(665)$ resulted in an even better relationship. Nevertheless the value at 443 as derived in the previous section could be used to estimate the chlorophyllous biomass.

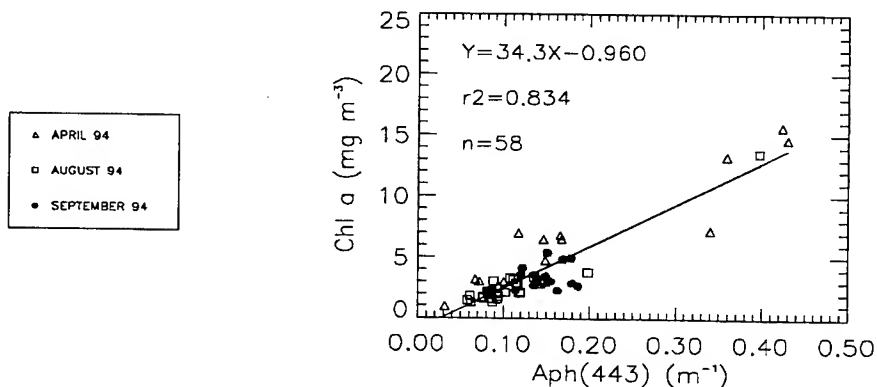


Figure 5 : Chla+Pheo concentration versus $a_{ph}(443)$ and computed linear regression.

6. CONCLUSION

A classical empirical relationship between reflectance $R_{rs}(\lambda)$ ratios and water optical constituents has been here split in different steps. The first one involves the determination of the exponent N of the total back-scattering spectral dependency from reflectance ratios. Rather good relationships between these two quantities have been obtained provided that very high $a_y(412)$ situations (April in the present study) be considered separately. Since the initial computation of our

N values is crucially depending on the accuracy of the measured $R_{rs}(\lambda)$ and $a(\lambda)$ *in situ* back-scattering measurements are needed to really assert the reliability of such an approach.

Once N is estimated $R_{rs}(\lambda)$ ratios can then be transformed into $a_{tot}(\lambda)$ ratios which can provide good empirical estimations of $a_y(412)+a_d(412)$ and, at a lower degree, of $a_{ph}(443)$. In this last case high $a_y(412)$ situations again must be identified and treated separately. The use of $a_{tot}(\lambda)$ ratios "Look-up tables" ^{5,7} could also be envisaged. Finally Chla+Pheo concentration can be estimated using the $a_{ph}(443)$ value.

The sensitivity of the final estimated quantities to these successive empirical steps (in particular to the N estimation) has to be asserted and validation must be effected using independent data sets for the region. The applicability of the presents results is of course restricted to the investigated area.

7. ACKNOWLEDGMENTS

All people involved in the *in situ* measurements campaigns and the subsequent analyses as well as Marinus Ooms who organized the data bank used for this study (information at marinus.ooms@jrc.it) are duly acknowledged.

8. REFERENCES

1. A. Morel and B. Gentili, "Diffuse reflectance of oceanic waters. II Bidirectional aspects", *Appl. Optics* **32**, 6864-6879 (1993).
2. A. Morel and B. Gentili, "Diffuse reflectance of oceanic waters. III Implication of bidirectionality for the remote-sensing problem", *Appl. Optics* **35**, 4850-4862 (1996).
3. S. Tassan and G. M. Ferrari, "An alternative approach to absorption measurements of aquatic particles retained on filters", *Limnol. Oceanogr.* **40**, 1358-1368 (1995).
4. A. Morel and L. Prieur, "Analysis of variations in ocean color", *Limnol. Oceanogr.* **22**, 709-722 (1977).
5. K. L. Carder, "Case 2 Chlorophyll a Algorithm", Modis Ocean Science Team, Algorithm Theoretical Basis Document (1994).
6. H. Siegel, M. Gerth and M. Beckert. "The variations of optical properties in the Baltic Sea and algorithms for the application of remote-sensing data", *Ocean Optics XII, SPIE* **2258**, 894-905 (1994).
7. K. L. Carder, S. K. Hawes, K. A. Baker, R. C. Smith, R. G. Steward and B. G. Mitchell. "Reflectance model for quantifying chlorophyll a in the presence of productivity degradation products", *J. Geophys. Res.* **96**, 20599-20611 (1991).

Pigment Packaging and Chlorophyll a-Specific Absorption in High-Light Oceanic Waters:
a Method, an Algorithm, and Validation

Bissett, W. P., Patch, J. S., Carder, K. L., and Lee, Z. P.

Department of Marine Science, University of South Florida

140 Seventh Ave. South, St. Petersburg, FL 33701

Abstract

The absorption of light by phytoplankton at a single wavelength, $a_{ph}(\lambda)$, is reduced with the increased packaging of the light absorption material. A common method of estimating the "package effect" is to divide $a_{ph}(\lambda)$ by the light absorption of the intracellular material after it has been extracted in an organic solvent. The absorption of the extract is often assumed to be representative of the true absorption of the cellular material in a dissolved state, $a_{sol}(\lambda)$. However, $a_{sol}(\lambda)$ is affected by the process of removing the light absorptive material from the organic matrix of the cell, the destruction of the pigment-protein complexes, and the solvent interference with the excited states of the chromophore. What is actually being measured by these extraction methods to determine $a_{sol}(\lambda)$, is $a_{om}(\lambda)$, i.e., the absorption of light by the pigment material in the organic medium of the experiment (methanol, acetone, Triton-X, etc.). A solvation factor, S , that is the ratio of the true $a_{sol}(\lambda)$ to the measured $a_{om}(\lambda)$ is needed before the package effect can be determined.

We have developed an internally consistent measure of $a_{ph}(\lambda)$, $a_{om}(\lambda)$, chlorophyll a concentration, and pheopigment concentration to determine the ratio $a_{sol}(\lambda):a_{om}(\lambda)$ and the package effect, $Q^*_a = a_{ph} / (S \cdot a_{om})$ at 675 nm. These parameters are used to determine a functional relationship between chlorophyll a concentrations and light absorption for high-light adapted, natural phytoplankton populations in optically clear waters. The packaging effect in these waters is negligible at the red peak of the spectrum. Exclusion of the weight specific absorption of pheopigments and the assumption of a zero $a_{ph}(675)$ at a zero pigment (chlorophyll a + pheopigment) concentration produces a misleading chlorophyll a-specific absorption and a false determination of pigment packaging. An algorithm is developed and validated for predicting chlorophyll a concentration from $a_{ph}(675)$ in high-light, optically clear waters.

Keywords: pigment packaging, chlorophyll a-specific absorption

2. Introduction

One of the driving forces behind the determination of ocean color from remotely sensed data is to derive algal biomass from changes in remote sensing reflectance ratios¹. The most common measure of algal biomass is the amount of chlorophyll a in the water column, as this pigment is ubiquitous to all phytoplankters. However, the determination of chlorophyll a concentration by optical techniques is confounded by the nonlinear changes in light absorption efficiency. This efficiency, $Q_a(\lambda)$ ^{2, 3}, is defined as the ratio of energy absorbed to the energy impinging on the geometric cross section of a particle. As a general rule, $Q_a(\lambda)$ increases at a decreasing rate as intracellular pigment concentration increases. This relationship is evident in the nonlinear flattening of chlorophyll a-specific absorption spectra as size and cellular pigment concentration increases³⁻⁶. These variations in chlorophyll a-specific absorption spectra are typically referred to as the pigment packaging effect⁷.

The reduction of absorption at a single wavelength, λ , can be described by the parameter $Q_a^*(\lambda)$:

$$Q_a^*(\lambda) = \frac{a_{ph}(\lambda)}{a_{sol}(\lambda)} = \frac{a_{ph}^*(\lambda)[conc]}{a_{sol}^*(\lambda)[conc]} = \frac{a_{ph}^*(\lambda)}{a_{sol}^*(\lambda)} \quad (1)$$

where $a_{ph}(\lambda)$ is the absorption of light by the intracellular material of living phytoplankton, and a_{sol} is the absorption of light by the same cellular material dispersed in a dissolved state^{3, 5}. Assuming $Q_a^*(\lambda)$ can be accurately described, one can further substitute for $a_{sol}(\lambda)$:

$$[conc] = \frac{a_{ph}(\lambda)}{Q_a^*(\lambda) \cdot a_{sol}^*(\lambda)} \quad (2)$$

While equations (1) and (2) are true in theory, the methods for deriving $Q_a^*(\lambda)$ generally solve the following equation:

$$[conc] = \frac{a_{ph}(\lambda)}{Q_a^*(\lambda) \cdot S(\lambda) \cdot a_{om}^*(\lambda)} \quad (3)$$

where $a_{om}^*(\lambda)$ is the specific absorption of chlorophyll *a* dissolved in an organic medium, and S is the ratio of true theoretical $a_{sol}^*(\lambda)$ to $a_{om}^*(\lambda)$. $a_{sol}^*(\lambda)$ refers to the specific absorption of the pigments in the organic matrix of the cell; i.e., bound to its pigment-protein complex completely dissolved in a solution of intracellular organic fluid. $a_{om}^*(\lambda)$ will differ depending on the type of organic solvent; i.e., $0.0202 \text{ m}^2 [\text{mg Chl } a]^{-1}$ at 664 nm in 90% acetone⁸ or $0.0171 \text{ m}^2 [\text{mg Chl } a]^{-1}$ at 665 nm in methanol⁹. However, the product of $S(\lambda)$ and $a_{om}^*(\lambda)$ (and by extension $Q_a^*(\lambda) \cdot S(\lambda) \cdot a_{om}^*(\lambda)$) should be constant for the same sample, regardless of the organic solvent used. A major assumption in this formulation (whose validity is rarely questioned) is that all of the cellular absorption is captured in a_{om} .

The primary goal of the present work is to derive a solution for the product of $Q_a^*(\lambda)$ and $S(\lambda)$ at a wavelength that is minimally affected by accessory pigments; i.e., red absorption maximum for high light adapted phytoplankton. This type of empirical solution could then be embedded into remote-sensing algorithms for future ocean-color satellite sensors; i.e., SeaWiFS, to determine chlorophyll *a* concentrations.

3. Methods

Surface water samples were collected on several cruises in the Gulf of Mexico, Arabian Sea, and East China Sea with Niskin bottles, buckets, or from a ship's seachest (Figure 1). The spectral transmissivity of the pads was measured with a 256-channel spectral radiometer (Spectron Engineering - SE 590) at a resolution of 2.7 nm or with a 512-channel spectral radiometer at a resolution of 1.1 nm. Transmissivity measurements of each sample pad were made, in tandem with a wetted blank, within minutes after filtration. The optical densities were corrected for scattering, and converted to particulate absorption, $a_p(\lambda)$, using a correction for the pathlength amplification as functionalized by *Bricaud and Stramski (1990)*¹⁰ for oligotrophic waters.

The pigments were extracted in the shade with methanol, which had been heated to near boiling temperatures in a water bath, for ten to twenty minutes or until all of the color was removed from the pad¹¹. The extracted sample pad was re-wetted before measuring its transmissivity. The resulting $a_d(\lambda)$ was calculated in the same manner as $a_p(\lambda)$. The values for $a_d(675)$ were subtracted from $a_p(675)$ to calculate $a_{ph}(675)$.

The pathlength amplification factor¹², β , is known to be a source of error with the filter pad technique. To minimize the errors associated with an inaccurate description of β for low optical density values, we used only those samples with a

particulate optical density > 0.04 at 675 nm. To test the validity of using the β function of *Bricaud and Stramski (1990)*, we measured the $a_p(\lambda)$ of sample pads obtained using different filtering volumes of seawater, from the same bottle sample (Figure 2a). By rearranging the equation for $a_p(\lambda)$, and setting the low volume absorption, $a_{p1}(\lambda)$, equal to the high volume absorption, $a_{p2}(\lambda)$ an equation for low volume β , $\beta_1(\lambda)$, in terms of the high volume β , $\beta_2(\lambda)$, can be found (Figure 2b). This test suggests that the *Bricaud and Stramski (1990)* β function is robust for our set of instrumentation.

The spectral absorbance of the hot methanol extract filtered with a 0.2 μm syringe filter was measured using a Hewlett Packard 8452A diode array spectrophotometer on the Gulf of Mexico cruises and a Hitachi U-3300 double beam scanning spectrophotometer on the Arabian Sea cruises.

Chlorophyll a and pheopigment concentrations were determined fluorometrically with the standard acidification technique^{13, 14} on a Turner Designs 10-AU fluorometer in 100% methanol (the pheopigment concentration is adjusted by the ratio 593/894 to correct for the lower molecular weight of pheophorbide a relative to chlorophyll a).

A more complete description of these methods can be found in *Bissett et al. (1996)*¹⁵.

4. Results and Discussion

The first step in the development of an algorithm to predict chlorophyll a concentration for high-light subtropical waters was to test our ability to measure the sum of the in vitro chlorophyll a and pheopigment (including all of the degraded products of chlorophyll) absorption and compare it to the expected value of unpackaged chlorophyll a and pheopigment absorption (Figure 3). The specific absorption for chlorophyll a of $0.0171 \text{ m}^2 [\text{mg Chl a}]^{-1}$ in methanol⁹ was used in conjunction with our own measured value of pheopigment specific absorption at 666 nm of $0.0072 \text{ m}^2 [\text{mg Pheo}]^{-1}$. These results imply that over this range of chlorophyll a and pheopigment values, our methodology of measuring fluorometric and spectrophotometric chlorophyll a and pheopigment concentrations was internally consistent, with only a small amount of random error.

Pigment packaging can be determined empirically from a comparison of $a_{ph}(675)$ to $a_{MeOH}(666)$. In this study, we find that there is no curvature to this relationship (Figure 4). Any curvature should be solely the function of $Q^*_a(675)$, as $S(675)$ is expected to be constant. Therefore, there does not appear to be any nonlinear pigment packaging in these samples.

A regression between $a_{ph}(675)$ and $a_{MeOH}(666)$ yields an equation for $Q^*_a(675) \cdot S(675) \cdot a_{om}(666)$, with a slope of 0.904 and an intercept of 0.001 (the latter value significant at the 99.9% confidence level). This suggests that there is some small absorption in the cellular material that is not reflected by the pigment concentration in the particulate absorption measurement; i.e., $a_{ph}(675)$ contains a small amount of absorption resulting from cytoplasm/cell walls³.

Substitution of the $a_{MeOH}(666)$ prediction equation (equation 7) into the regression from Figure 4 (equation 7) yields a predicted $a_{ph}(675)$ from a known concentration of chlorophyll a and pheopigments (equation 8; Figure 5). Substitution of the pheopigment to chlorophyll a ratio versus chlorophyll a regression (equation 9; Figure 6) yields a predicted $a_{ph}(675)$ from a known concentration of chlorophyll a (equation 10). This second order equation can be inverted to yield a quadratic solution for chlorophyll a from a measured value of $a_{ph}(675)$ (Figure 7).

The non-zero intercept from equation (7) becomes very significant at low pigment concentrations. By plotting pigment-specific absorption values against chlorophyll a concentration, there is a downward sloping appearance to the data that would appear to suggest packaging in these samples (Figure 8). However, our results suggest this is the result of absorption by cellular material other than pigments, that becomes increasingly important at low pigment concentrations. Curving-fitting this data would yield a false measure of the package effect.

The $a_{ph}(675)$ data from three additional cruises, which were not used in the development of this algorithm, were used in the quadratic equation to predict chlorophyll a (Figure 9). These results suggest this algorithm, used with our methodology and equipment, is a robust equation to predict chlorophyll a concentration in high-light, optically clear waters.

5. Summary

We have developed an internally consistent method for measuring the relationship between the particulate absorption of light at its red peak, $a_{ph}(675)$, and the absorption of light due to the extracted pigments in a dissolved state at 666 nm, $a_{MeOH}(666)$. The results suggest pigment packaging is insignificant at the red peak in these waters.

Curve fitting the chlorophyll a versus $a^*_{ph}(675)$ relationship will neglect the possibility of a non-zero $a_{ph}(675)$ value at a zero chlorophyll a concentration. This will lead to a false estimation of the pigment packaging effect, especially at low chlorophyll a concentrations.

We have developed an algorithm using our methodology and equipment to derive chlorophyll a concentrations from measurements of $a_{ph}(675)$. This algorithm is validated with additional data collection.

6. Acknowledgements

We wish to thank Robert Steward, Tom Peacock, F. Robert Chen, and Lisa Young for their help with sample processing and lending technical assistance. Research support including ship time were provided by NASA grants NAGU-3483, NAGW-465, NAGW-3459 and GSFC contract NAS5-30779; the Naval Research Laboratory (BONG 1+2); the State University System - Florida Institute of Oceanography (BOSS 1); NSF OCE-9216937 (PELICAN94); JGOFS Arabian Sea Process Study (TN042 and TN048); and the National Taiwan University. Additional support was provided by the John Lake Foundation. We also thank the captains and crews of the *R/V Suncoaster*, *R/V Bellows*, *R/V Pelican*, and *R/V Thomas G. Thompson*.

7.0 References

1. Carder, K.L., R.G. Steward, J.H. Paul, and G.A. Vargo, "Relationships between chlorophyll and ocean color constituents as they affect remote-sensing reflectance models," *Limnology and Oceanography* **31**(2), 403-413, (1986).
2. Duysens, L.N.M., "The flattening of the absorption spectrum of suspensions as compared to that of solutions," *Biochimica et Biophysica Acta* **19**, 1-12, (1956).
3. Morel, A. and A. Bricaud, "Theoretical results concerning light absorption in a discrete medium, and application to specific absorption of phytoplankton," *Deep-Sea Research* **28A**(11), 1375-1393, (1981).
4. Prieur, L. and S. Sathyendranath, "An optical classification of coastal and oceanic waters based on the specific spectral absorption curves of phytoplankton pigments, dissolved organic matter, and other particulate materials," *Limnology and Oceanography* **26**(4), 671-689, (1981).
5. Sathyendranath, S., L. Lazzara, and L. Prieur, "Variations in the spectral values of specific absorption of phytoplankton," *Limnology and Oceanography* **32**(2), 403-415, (1987).
6. Sosik, H.M., S.W. Chisholm, and R.J. Olson, "Chlorophyll fluorescence from single cells: interpretation of flow cytometric signals," *Limnology and Oceanography* **34**(8), 1749-1761, (1989).
7. Kirk, J.T.O., *Light and Photosynthesis in Aquatic Ecosystems*, 2nd ed, 509, University Press, Cambridge, 1994.
8. Lorenzen, C.J. and S.W. Jeffrey, "Determination of chlorophyll in seawater," *UNESCO technical papers in marine science* **35**, 1-20, (1980).

9. MacKinney, G., "Absorption of light by chlorophyll solutions," *Journal of Biological Chemistry* **140**, 315-322, (1941).
10. Bricaud, A. and D. Stramski, "Spectral absorption coefficients of living phytoplankton and nonalgal matter: a comparison between the Peru upwelling area and the Sargasso Sea," *Limnology and Oceanography* **35**(3), 562-582, (1990).
11. Kishino, M., M. Takahashi, N. Okami, and S. Ichimura, "Estimation of the spectral absorption coefficients of phytoplankton in the sea," *Bulletin of Marine Science* **37**(2), 634-642, (1985).
12. Mitchell, B.G. and D.A. Kiefer, "Chlorophyll *a* specific absorption and fluorescence excitation spectra for light-limited phytoplankton," *Deep-Sea Research* **35**(5), 639-663, (1988).
13. Yentsch, C.S. and D.W. Menzel, "A method for the determination of phytoplankton chlorophyll and phaeophytin by fluorescence," *Deep-Sea Research* **10**, 221-231, (1963).
14. Holm-Hansen, O. and B. Riemann, "Chlorophyll *a* determination: improvements in methodology," *OIKOS* **30**(3), 438-447, (1978).
15. Bissett, W.P., J.S. Patch, K.L. Carder, and Z. Lee, "Pigment packaging and chlorophyll *a*-specific absorption in high-light oceanic waters," *Limnology and Oceanography* (**in press**), (1996).

Figure 1(a). Cruise Dates and Locations in the Gulf of Mexico

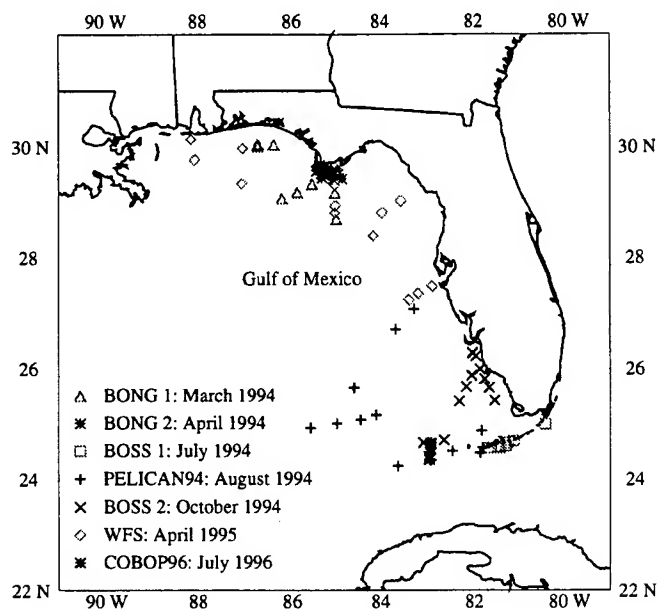


Figure 1(b). Cruise Dates and Locations in the Arabian Sea

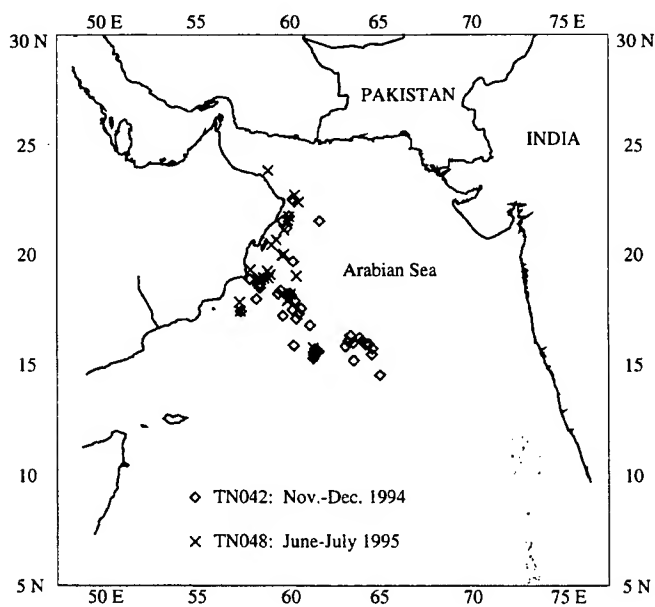


Figure 1(c). Cruise Date and Locations in the East China Sea

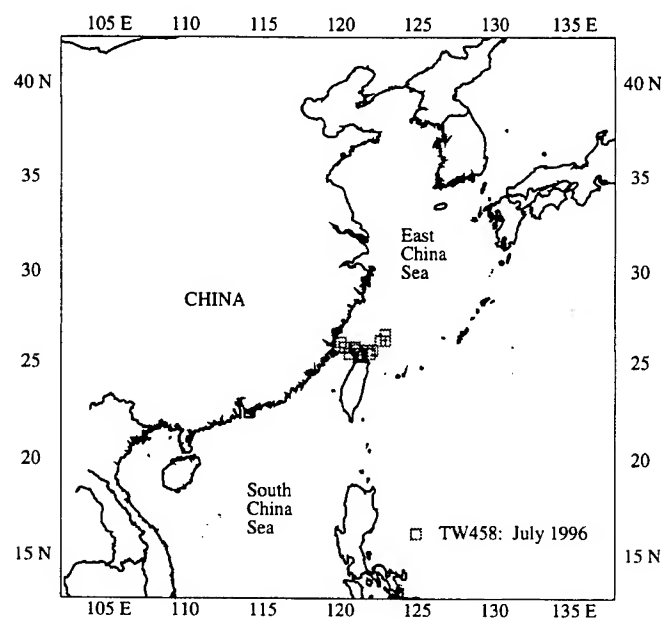
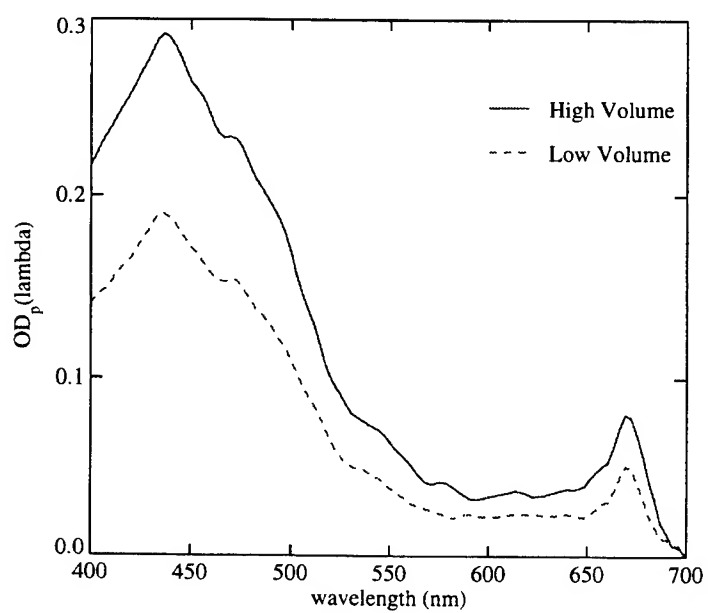


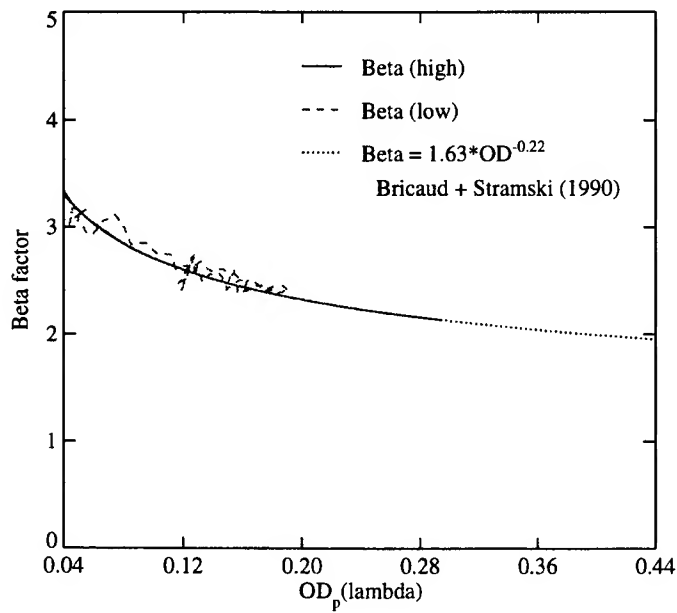
Figure 2(a). High and Low Volume-Filtered $a_p(\lambda)$ from the Same Sample Bottle



$$a_p(\lambda) = \frac{2.3 \cdot OD_p(\lambda) \cdot (\text{filter area})}{\beta(\lambda) \cdot (\text{volume filtered})} \quad (4)$$

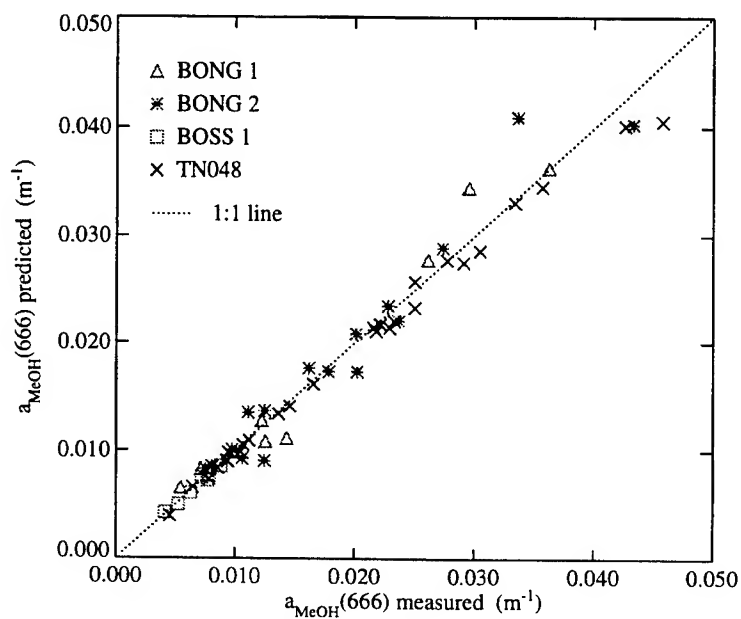
$$\beta_1(\lambda) = \frac{\beta_2(\lambda) \cdot \text{volume}_2 \cdot OD_{p1}(\lambda)}{\text{volume}_1 \cdot OD_{p2}(\lambda)} \quad (5)$$

Figure 2(b). Low Volume-Filtered $\beta(\lambda)$ Function



(a) The $a_p(\lambda)$ from the high and low volume-filtered samples. The right side of equation (4) for the high and low volume samples are set equal to each other to derive equation (5). (b) The derived $\beta_1(\lambda)$ is plotted over the $\beta_2(\lambda)$ as a function of optical density.

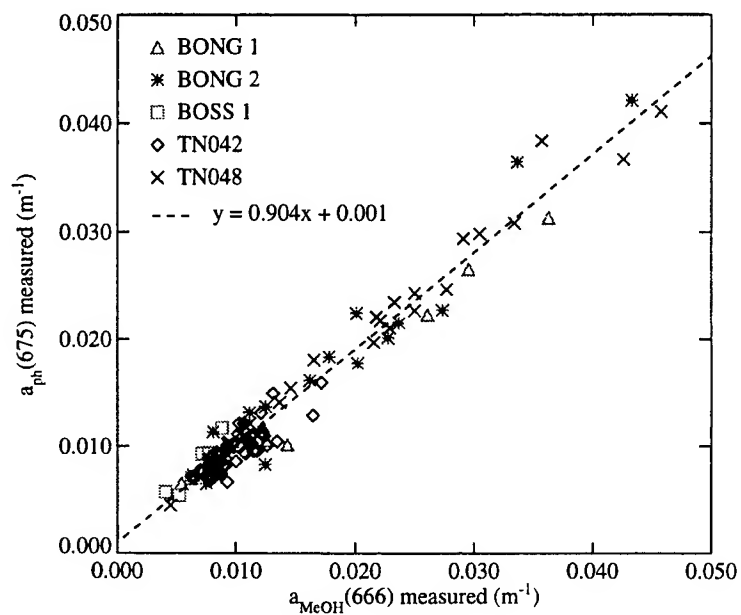
Figure 3. Predicted $a_{\text{MeOH}}(666)$ versus Measured $a_{\text{MeOH}}(666)$



$a_{\text{MeOH}}(666)$ is predicted as a function of the fluorometric chlorophyll a and pheopigment concentrations using equation (6). The predicted values are plotted against the measured values. The coefficients of 0.0171 and 0.0072 represent the chlorophyll a- and pheopigment-specific absorption, respectively.

$$\text{predicted } a_{\text{MeOH}}(666) = 0.0171 [\text{chl a}] + 0.0072 [\text{pheo}] \quad (6)$$

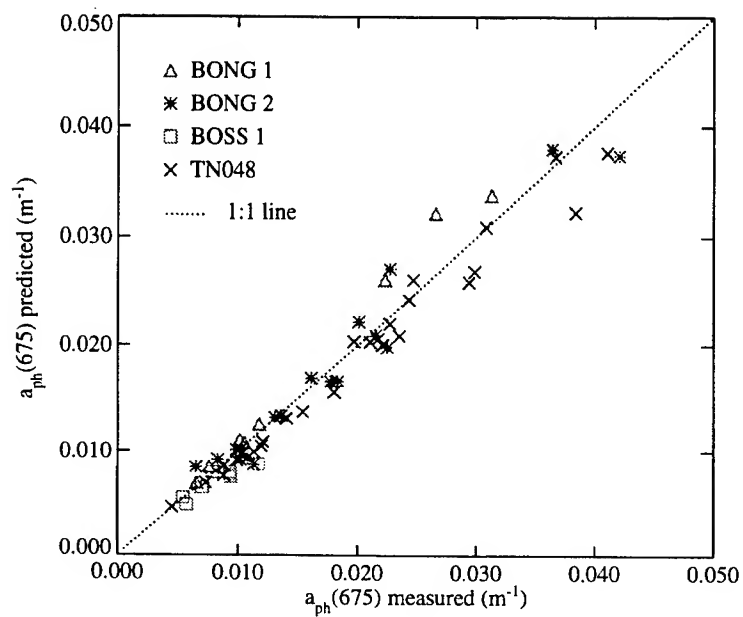
Figure 4. Measured $a_{ph}(675)$ versus Measured $a_{MeOH}(666)$



The measured $a_{ph}(675)$ is plotted against the measured $a_{MeOH}(666)$. The slope and intercept of the regression are shown in equation (7). The intercept is statistically significant at a P value > 0.001.

$$a_{ph}(675) = 0.904 a_{MeOH}(666) + 0.001 \quad (7)$$

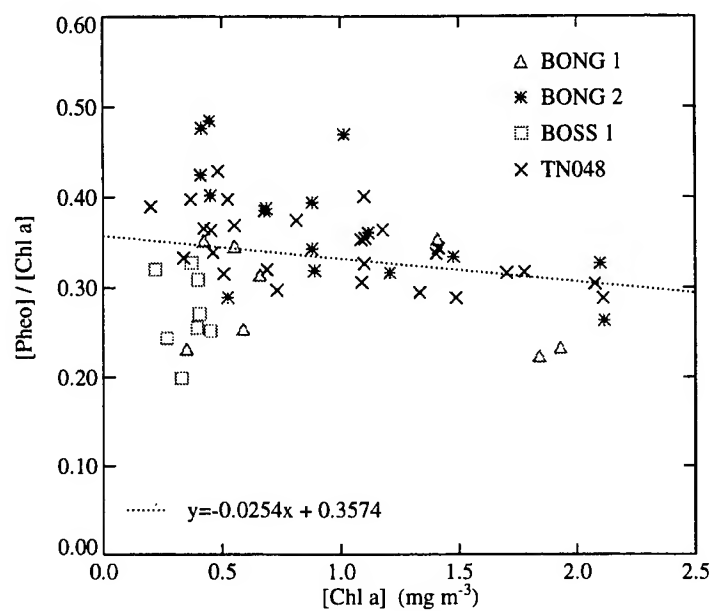
Figure 5. Predicted $a_{ph}(675)$ versus Measured $a_{ph}(675)$



Substituting equation (6) for $a_{MeOH}(666)$ in equation (7) allows for the prediction of $a_{ph}(675)$ from measured concentrations of chlorophyll a and pheopigments.

$$\text{predicted } a_{ph}(675) = 0.904 \cdot (0.0171 [\text{chl } a] + 0.0072 [\text{pheo}]) + 0.001 \quad (8)$$

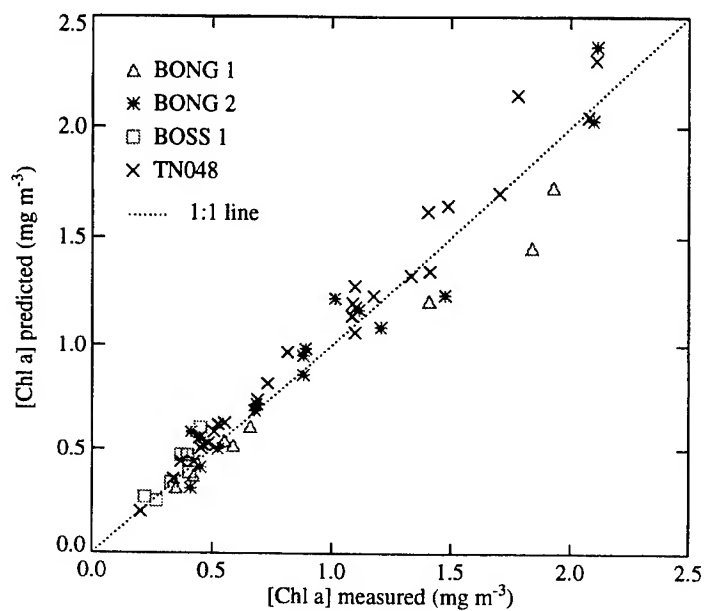
Figure 6. Pheopigment to Chlorophyll a Ratio



Pheopigment to chlorophyll a ratio as a function of chlorophyll a. Equation(9) gives the function used to predict pheopigment concentrations from chlorophyll a.

$$[pheo] = -0.0254[chl a]^2 + 0.3574[chl a] \quad (9)$$

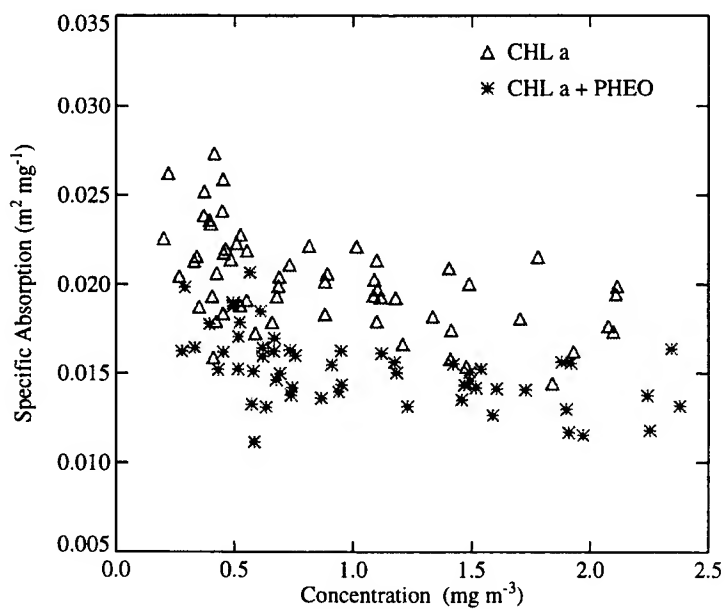
Figure 7. Predicted Chlorophyll a versus Measured Chlorophyll a



The known pheopigment concentration used to predicted $a_{ph}(675)$ in equation (8) is substituted with equation (9) to yield equation (10). Equation (10) can be rearranged to yield a quadratic solution to predict chlorophyll a. This predicted chlorophyll a is plotted against the measured chlorophyll a concentrations from the cruises used in the development of this algorithm.

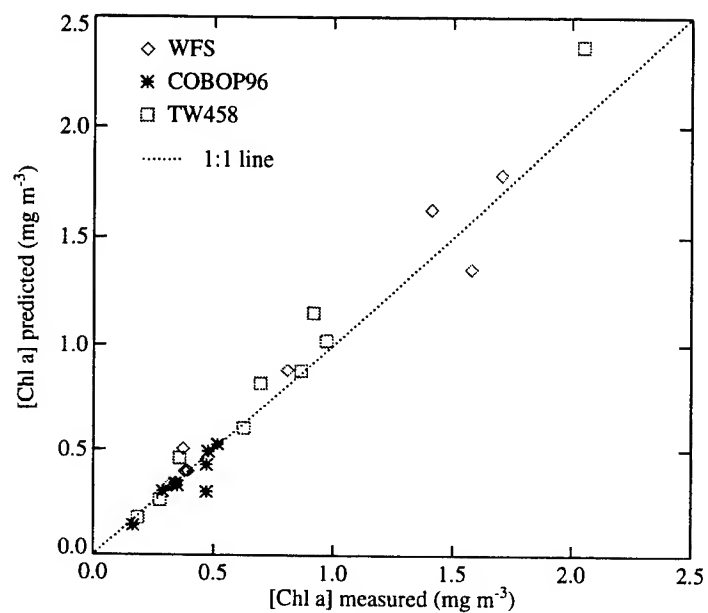
$$\text{predicted } a_{ph}(675) = -0.000165[\text{chl } a]^2 + 0.01778[\text{chl } a] + 0.001 \quad (10)$$

Figure 8. Pigment-specific absorption, $a_{ph}^*(675)$, versus Pigment Concentration



The curvature between the pigment-specific absorption and the pigment concentration results from the non-zero intercept in equation (7). The absorption by material other than extracted pigments; i.e., cell walls, cytoplasm, etc., is an increasingly greater fraction of the specific absorption as the pigment concentration decreases. Curve fitting these parameters would give a false estimate of pigment packaging.

Figure 9. Predicted versus Measured Chlorophyll a from Validation Cruises



Predicted chlorophyll a concentrations derived by solving equation (10) for chlorophyll a as a function of $a_{ph}(675)$ from validation cruises.

Validation of *in situ* inherent optical properties in the Sargasso Sea.

Eric A. Brody, Margaret C. O'Brien, David A. Siegel,
Institute for Computational Earth System Science and Department of Geography
University of California, Santa Barbara, Santa Barbara, California 93106, USA

Elizabeth A. Caporelli and Norm B. Nelson
Bermuda Biological Station for Research, 17 Biological Lane, Ferry Reach, GE01, Bermuda

Abstract

In situ inherent optical properties (IOP) determinations from the U.S. JGOFS Bermuda Atlantic Time-Series (BATS) made from 1994 to 1996 are used to develop processing and correction methods for clear natural waters. Upper bound estimates of precision are 0.0066 and 0.0018 m^{-1} for non-water beam attenuation ($c-c_w(\lambda)$) and absorption coefficient ($a-a_w(\lambda)$) respectively. These are determined by examining the intracruise variability at 190m depth where minimum natural variations exist. The final corrected IOP values show consistent patterns with time, depth and wavelength. A strong correlation is observed between measured beam attenuation and absorption coefficient at 440 nm in the upper 50m ($r^2=0.71$). Whereas lower correlation is observed between the scattering coefficient ($b-b_w(440)$) and absorption coefficient ($r^2=0.52$). In the upper 50m layer, measured values of $a-a_w(440)$ in the upper 50m compare well with chlorophyll-based bio-optical model ($r^2=0.71$, slope=1.17). However measured values of $c-c_w(440)$ and $b-b_w(440)$ do not compare well with the modeled values ($r^2=0.38$ & 0.25 , respectively). In particular, the measured $b/a(440)$ shows an inverse relationship compared with estimated $b/a(440)$ ratio in the upper 50m.

Keywords: inherent optical properties, absorption, scattering, beam attenuation

1. Introduction

Accurate and precise determinations of inherent optical properties (IOP) are important for linking biological components to optical signals for remote sensing platforms (e.g. Dickey and Siegel, 1993). The WET Labs ac-9 spectral absorption and attenuation meter offers much promise in obtaining high resolution, *in situ* determinations of non-water profiles of spectral beam attenuation ($c-c_w(\lambda)$) and absorption ($a-a_w(\lambda)$) coefficients. However, difficulties associated with short time scale bio-fouling, bubbles, calibration uncertainties, and uncollected scattered light by the reflective tube make these *in situ* determinations difficult to obtain in clear natural waters. Our goal is to assess accuracy and precision of IOP measurements from the clear waters at the Bermuda Atlantic Times-Series (BATS) site. First, data processing, calibration, and validation methods as well as comparison with other IOP measurements and modeled IOP will be presented. Then, the results of the IOP determinants for time, depth, and wavelength from 1994 to 1996 will be discussed.

2. Data

In situ IOP profiles are sampled from the surface to 200 m every 2 to 4 weeks from July of 1994 to June of 1996. They are collected in an area 75 km southeast of Bermuda ($31^\circ 50' \text{ N}$, $64^\circ 10' \text{ W}$) as part of the U.S. Joint Global Ocean Flux Study (JGOFS) Bermuda Atlantic Time-series Study (BATS) program. Measurements of IOP's here include non-water beam attenuation ($c-c_w(\lambda)$) and absorption ($a-a_w(\lambda)$) coefficient for nine wavelength (410, 441, 488, 510, 555, 630, 650, 676, and 715 nm) and are collected using a WET Labs ac-9 spectral absorption and beam attenuation meter. Scattering coefficients ($b-b_w(\lambda)$) are derived by subtracting the corrected $a-a_w(\lambda)$ from $c-c_w(\lambda)$. The data are collected concurrently with the Bermuda Bio-Optical Program (BBOP) spectroradiometer package which includes a SeaTech beam transmissometer, SeaTech chlorophyll fluorometer and Seabird temperature and conductivity sensors (Siegel et al., 1995a; 1996b). These auxiliary data sets are used for correcting and validating *in situ* IOP observations collected here.

Water samples drawn from Niskin bottles deployed on the same cruise are used to determine *in vivo* absorption spectra for particulates ($a_p(\lambda)$) and colored dissolved organic materials ($a_{cdom}(\lambda)$). Values of $a_p(\lambda)$ and $a_{cdom}(\lambda)$ are determined using the quantitative filter technique and with a 10 cm long path quartz cylindrical cuvette against pure water blanks, respectively (Nelson et al., submitted). These *in vivo* IOP measurements will be compared with *in situ* IOP signal collected using the WET Labs ac-9 instrument. Fluorometric chlorophyll *a* concentrations (Knap et al., 1993) are also measured and used in bio-optical models for comparison with the *in situ* IOP's. Absorption and scattering coefficients are modeled using the of bio-optical model of Morel (1991):

$$a_{\text{mod}}(\lambda) = [a_w(\lambda) + 0.06 A(\lambda)(C)^{0.65}] [1 + 0.2 \exp -\{0.014 (\lambda - 440)\}],$$

$$b_{\text{mod}}(\lambda) = b_w(\lambda) + 0.3 (550/\lambda)(C)^{0.62}$$

where a_{mod} and b_{mod} are modeled absorption and scattering coefficient, a_w and b_w are absorption and scattering of pure seawater (Morel, 1974), C is chlorophyll pigment concentration, and $A(\lambda)$ is statistically derived chlorophyll-specific absorption coefficient from Prieur and Sathyendranath (1981).

3. Data acquisition, processing, and correction method

The steps for acquiring, processing, calibrating, and correcting *in situ* IOP data are as follows:

(1) Values of $a-a_w(\lambda)$ and $c-c_w(\lambda)$ are acquired with the WET Labs software using the WET Labs preliminary calibration and internal temperature correction (WET Labs ac-9 User's Guide, version 1.0). A sampling rate of 6 Hz is used.

(2) After acquisition, IOP profiles are processed using the BBOP software (Siegel et al., 1995b). The BBOP software screened out any data above the surface, despiked and smoothed the raw profiles before the data is binned to a 1m depth interval.

(3) The beam attenuation measurements are qualified by comparing the ac-9 $c-c_w(650)$ to SeaTech $c-c_w(660)$. If the squared regression coefficient (r^2) is 0.99 between these two estimates, the ac-9 data are selected for further analyses. Many of the vertical profiles were screened out by this qualification procedure (47% of all profiles failed this test). The problem profiles are attributed to various factors ranging from variation in the warm-up time, difference in the flow rates, bubbles, instrument malfunction, and bio-fouling.

(4) A "best" cast profile is selected for each cruise. This cast is the representative average cast for the entire cruise and is normalized to the mean cruise value at 190m. The 190m depth was selected because of its minimum natural variations. The mean and standard deviation for temperature and salinity for the same time period is 18.62 ± 0.32 °C and 36.59 ± 0.04 psu. We define precision for the ac-9 IOP signals as the standard deviation for 190 m IOP signals for each cruise. Typical precision values are 0.0066 and 0.0018 m^{-1} for $c-c_w(\lambda)$ and $a-a_w(\lambda)$ respectively. This is an upperbound estimate as some natural variability must occur.

(5) The *in situ* temperature and salinity correction algorithm provided by Pegau et al., (submitted) is applied to the raw IOP values, or

$$a_{\text{corr}} = a_{\text{meas}} + (T_{\text{ref}} - T_{\text{meas}}) * \psi_T - S * \psi_S$$

where a_{corr} and a_{meas} are absorption corrected and absorption measured, T_{ref} and T_{meas} are the temperature of the water during calibration and the *in situ* temperature of the water, and ψ_T and ψ_S are the linear temperature and salinity slope values. This method corrects IOP values for their temperature and salinity dependence on $a_w(\lambda)$ and $c_w(\lambda)$. Most of the effect is on the absorption and beam attenuation at 410 and 715 nm during the summer months when thermal stratification and a strong temperature gradient forms in the upper 100m water column (figure 1a-c). The uncorrected vertical profile for $a-a_w(715)$ (figure 1a, dashed line) is influenced by temperature in the upper portion of the water column (figure 1c) as compared with $a-a_w(440)$ (figure 1a, solid line). After applying the temperature correction, the vertical profile shape for $a-a_w(715)$ more or less approximates the profile shape at 440 nm (figure 1b).

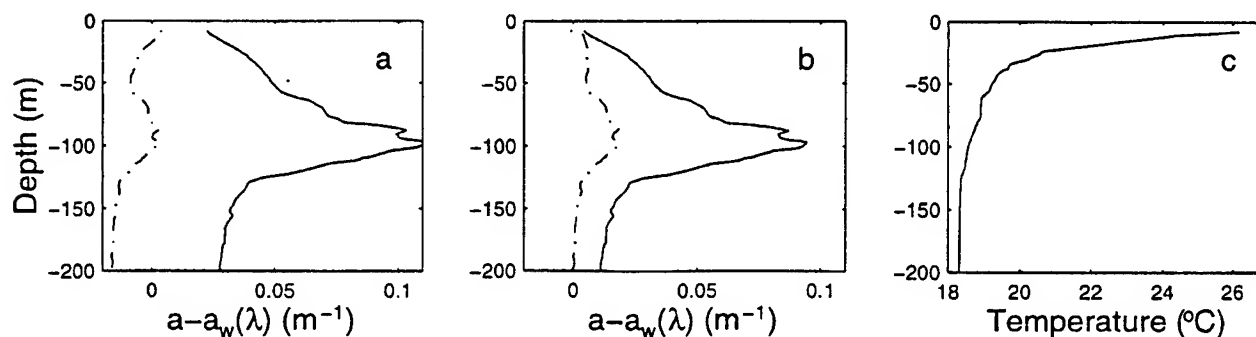


Figure 1-c: Illustration of temperature and salinity dependence on $a-a_w(\lambda)$ collected on August 25, 1995. Dashed line is $a-a_w(715)$ and solid line is $a-a_w(440)$. (a) Profiles before correction, (b) profiles after correction, (c) temperature profile.

(6) Profiles are recalibrated using the average change of the pre and post cruise "pure" water calibration from the WET Labs preliminary calibration. Pre and post cruise "pure" water and air calibrations were performed at the Bermuda Biological Station for Research (BBSR). Production of "pure" water standards and calibration procedures are detailed in the WET Labs

ac-9 user manual. The change in water calibration from WET Labs preliminary calibration is then subtracted from the selected "best" cast profile. However, the clean water system and standardized calibration procedures were only recently implemented. Thus a baseline correction is applied in order to recover the entire IOP data set. This baseline correction method normalized $a-a_w(\lambda)$ at 190m to the mean $a_{cdom}(\lambda)$ estimated at this depth for the period of 1994-1996. Values of $c-c_w(\lambda)$ are normalized to the mean "pure" water calibrated values at 190m from January to June of 1996. This method assumes that at 190m, there is very little seasonality in the absorption and scattering coefficients and that values of $a_p(\lambda)$ are negligible.

The validity of this method is justified by comparison of the variability of $a_{cdom}(\lambda)$ to the cast to cast variability of $a-a_w(\lambda)$ at 200m. Standard deviations are 0.006 and 0.0002 m^{-1} for $a_{cdom}(440)$ and $a_{cdom}(676)$ at 200m respectively. This is much less than the mean cast to cast variability of $a-a_w(\lambda)$. It is also smaller than the standard deviations for recent "pure" water calibration (0.012 m^{-1} for $c-c_w(\lambda)$ and $a-a_w(\lambda)$ from January to June of 1996). The advantage of this method is IOP are no longer subjected to variation in the calibration over time and for individual wavelength.

(7) A scattering correction is applied to the absorption data due to scattered light losses in the reflective tube. Three different scattering correction are applied (Zaneveld et al., 1994). These are:

- (1) Subtraction of a reference wavelength.
- (2) Subtraction of constant proportion of the estimated scattering coefficient.
- (3) Subtraction of a proportion of the scattering coefficient determined using a reference wavelength.

Absorption corrected with these scattering corrections are compared to the uncorrected profiles of $a-a_w(440)$ for Bats 88 and Bats91a, chosen to represent winter and spring bloom periods. For both cases, very little difference is observed spectrally and vertically between scattering correction involving subtraction of $a-a_w(715)$ and a proportion of the scattering coefficient using $a-a_w(715)$. The percentage difference between the uncorrected and corrected absorption in the upper 50m is the same, 12% and 27% percent for Bats88 and Bats 91a respectively. The scattering correction which subtract a constant 11% (S. Pegau, personal comm.) of the scattering coefficient differs substantially from the others. Absorption values are reduced by 25% and 34% for Bats88 and Bats91a. We selected the method that subtract $a-a_w(715)$ from each wavelength for final data and contour plots presented here although more work is required for accessing which scattered correction procedure yields the most accurate results.

4. Results

All "best" cast spectra of $c-c_w(\lambda)$, $a-a_w(\lambda)$, and $b-b_w(\lambda)$ for the 10m depth are shown in figure 2a-c. The basic pattern for spectra of $c-c_w(\lambda)$, $a-a_w(\lambda)$, and $b-b_w(\lambda)$ are consistent with wavelength. Chlorophyll peaks are observed at 440 and 676 nm and values of absorption coefficients increases toward 400 nm where both phytoplankton and CDOM are important. (figure 2b). Spectral distributions of scattering coefficients are also consistent. Values of $b-b_w(\lambda)$ at the surface (figure 2c) ranged from approximately 0.03 to 0.2 m^{-1} and decrease linearly with wavelength.

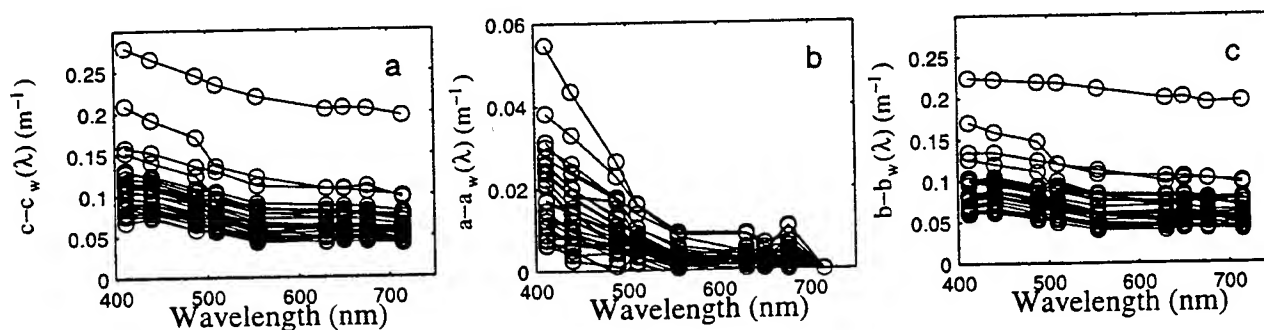


Figure 2a-c: Spectra of $c-c_w(\lambda)$, $a-a_w(\lambda)$, and $b-b_w(\lambda)$ for 10 m depth for all "best" cast profiles from August of 1994 to June of 1996.

Contour plots of $a-a_w(440)$ (figure 3a) show consistent time-depth patterns. Values of $a-a_w(440)$ are high in the surface waters during the spring bloom followed by subsurface maximum at 100 m in the summer. Surface values of $a-a_w(440)$ decrease during the summer possibly as a combined result of reduction of phytoplankton population and stocks of CDOM. In the late fall and early winter, values of $a-a_w(440)$ are low as 0.02 m^{-1} within the upper 200 m of the water column, then increases to approximately 0.03 m^{-1} in the late winter preceding the spring bloom.

Corresponding beam attenuation coefficient estimates compare well with absorption coefficients in the upper 50m ($r^2=0.71$); however, independent variations between scattering and absorption coefficients at 440 nm are observed ($r^2=0.56$). The $b/a(440)$ ratio also shows independent variations and values as low as 1 are observed in January and February (figure 3c). During the spring bloom and summer months, values of $b/a(440)$ reach a maximum of 6 and then decrease to low winter values. Changes in $b/a(440)$ indicate possible changes in the phytoplankton community structure and CDOM stock.

5. Comparison with bio-optical IOP models

The contour of modeled $a-a_w(440)$ compares well with measured $a-a_w(440)$ (figure 3b). The squared regression coefficient and mean slope for the upper 50m of the water column are 0.71 and 1.17, respectively. However, the modeled $c-c_w(440)$, $b-b_w(440)$ and $b/a(440)$ estimates do not compare well with measured data (r^2 are 0.36, 0.24, and 0.38 for $c-c_w(440)$, $b-b_w(440)$ and $b/a(440)$, respectively). This should be expected as the relationship between chlorophyll concentration and scattering coefficient is often not well defined (Kitchen & Zaneveld, 1990). Interestingly, values of the modeled $b/a(440)$ ratio show an inverse relationship compared with measured ratio estimates (figure 3d, $r^2=0.36$, slope = -0.46). This has important consequences for use of chlorophyll based bio-optical model in clear natural water.

6. Conclusion

We show that *in situ* IOP values can be consistently determined in clear natural waters. Estimates of absorption and scattering yield consistent patterns over depth, wavelength, and time. Reasonable precision and accuracy for the absorption and scattering coefficients are achieved with the aid of auxiliary data sets. Standardized "pure" water calibration protocols have been implemented recently and will improve the accuracy of these data. Future validation work will also involve comparison of *in situ* IOP estimates with *in vivo* IOP determinations and IOP estimates made using apparent optical properties.

Acknowledgments

We gratefully acknowledge the support from the U.S. Office of Naval Research (N00014-96-1-0007) and NASA (NAGW-3145 and NAGW-3511). We also would like to thank the BATS technicians and crew of the *R/V Weatherbird II* for their dedication to this effort.

References

- Dickey, T.D. and D.A. Siegel "Bio-optics in the U.S. JGOFS", U.S. Joint Global Ocean Flux Study Planning Report Number 18, WHOI, Woods Hole, Mass, 79pp., 1993.
- Knap, A.H., et al., "BATS Method Manual, version 3", U.S. Joint Global Ocean Flux Study Plann. and Coord. Off., Woods Hole, Mass., 108pp., 1993.
- Kitchen, J.C. and J.R.V. Zaneveld, "On the noncorrelation of the vertical structure of light scattering and chlorophyll-a in case-I waters", *J. Geophys. Res.*, 95, 20237-20246, 1990.
- Nelson, N.B., D.A. Siegel, and A.F. Michaels, "Seasonal dynamics of colored dissolved material in the Sargasso Sea", Submitted to Deep-Sea Research.
- Morel, A., "Optical properties of pure water and pure seawater", N.G. Jerlov and E. Steemann Nielsen, Eds. in *Optical Aspects of Oceanography* (Academic, New York), 1-24, 1974.
- Morel, A., "Light and Marine photosynthesis: a spectral model with geochemical and climatological implications", *Prog. Oceanogr.*, 26, 263-306, 1991.
- Prieur, L. and S. Sathyendranath, "An optical classification of coastal and oceanic waters based on the specific spectral absorption curves of phytoplankton pigments", dissolved organic matter, and other particulate materials, *Limnol. Oceanogr.*, 26(4), 671-689, 1981.
- Siegel, D.A., A.F. Michaels, J.C. Sorensen, M.C. O'Brien, & M.A. Hammer, "Seasonal variability of light availability and utilization in the Sargasso Sea", *J. Geophys. Res.*, 100, 8695-8713, 1995a.
- Siegel, D.A., M.C. O'Brien, J.C. Sorensen, D.A. Konnoff, and E. Fields, "BBOP Data Processing and Sampling Procedures, version 1", U.S. Joint Global Ocean Flux Study Planning Report, 19, Woods Hole, Mass, 79pp., 1995b.
- Siegel, D.A. & A.F. Michaels, "Quantification of non-algal light attenuation in the Sargasso Sea: Implication for biogeochemistry and remote sensing", *Deep-Sea Res.*, II, Vol. 43, 321-345, 1996.
- Pegau, W.S., D. Gray, & J.R.V. Zaneveld, "Absorption of visible and near-infrared light in the water: the dependence on temperature and salinity", submitted to *Applied Optics*.
- Wet Lab ac-9 User's Guide, Version 1.0, WET Labs, Inc., 34pp., 1995.
- Zaneveld, J.R.V., J.C. Kitchen, and C.C. Moore, "Scattering error correction of reflecting-tube absorption meters", *Proceedings of the SPIE, Ocean Optics XII*, Vol. 2258, 44-55, 1994.

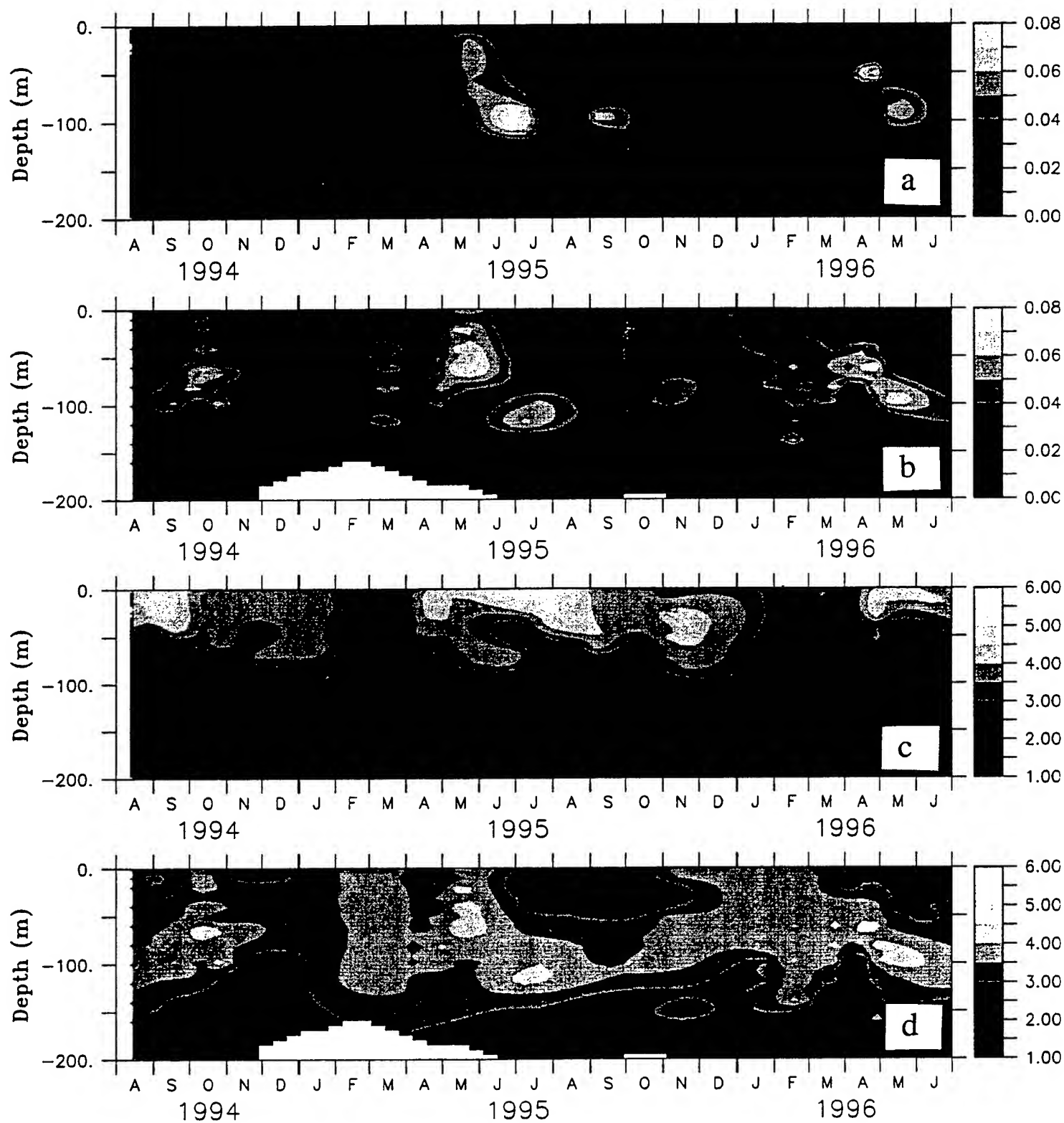


Figure 3a-d: (a) Values of $a-a_w(440)$, (b) Modeled estimates of $a-a_w(440)$, (c) Values of $b/a(440)$, (d) Modeled estimates of $b/a(440)$.

The influence of phytoplankton size structure on the spectral attenuation coefficient in the upper ocean

Áurea M. Ciotti*, John J. Cullen*, Collin S. Roesler⁺ and Marlon R. Lewis*

* Center for Environmental Observation Technology and Research
Department of Oceanography, Dalhousie University
Halifax, N.S., Canada, B3H 4J1

+ Department of Marine Sciences, University of Connecticut
Groton, CT, USA, 06340-6097

ABSTRACT

The influence of the variability in the structure of phytoplankton communities on measurable optical properties of the upper ocean is analyzed for a wide variety of coastal marine environments. Changes in spectral attenuation coefficients in the first optical depth are related to varying levels of dissolved organic matter (DOM) and changes in phytoplankton community structure, operationally defined as changes in the phytoplankton size distributions. Optical measurements include spectral vertical attenuation coefficient and water leaving radiance reflectance. Chlorophyll *a* and particulate absorbance were measured in 4 size fractions: picoplankton (less than 1-2 μm), ultraplankton (2-5 μm), nanoplankton (5-20 μm) and microplankton (>20 μm). By partitioning the contribution of phytoplankton absorbance into 4 size classes, a rational for a quantitative approach for interpreting variations in the relationship between light attenuation and spectral reflectances as a function of different community structures of phytoplankton is developed.

Keywords: phytoplankton community structure, *in situ* optical measurements, attenuation, reflectance

1. INTRODUCTION

The construction of algorithms for retrieving chlorophyll from *in situ* or remote optical measurements involves characterization of the absorption and scattering properties of suspended sediments, detritus, dissolved colored substances and phytoplankton. It was been already extensively illustrated that non-covariance between phytoplankton and the other components makes it difficult to develop simple theoretical and empirical relationships between ocean color, water transparency and phytoplankton abundance,¹ expressed as chlorophyll concentrations. In coastal waters, these simple relationships are even more difficult to obtain, not only because all the other "non-phytoplanktonic" components have a greater influence on the light absorption and scattering² but also because phytoplankton themselves are quite variable particles. Short term variability in mixing and a more direct influence by runoff (i.e. availability of nutrients) allow different communities of phytoplankton to develop and to be replaced in coastal waters on a time scale much shorter than in the open ocean.³ Local nutrient supply, especially nitrate, is reflected in the sizes of the cells present in the community.^{4,5,6} That is, larger sizes are associated with enhanced nutrient availability. Changes in phytoplankton communities are thus directly related to changes in phytoplankton size⁷. Because changes in cell size distributions are expected to alter the bulk optical properties of the phytoplankton, it is expected that measurable optical properties will vary with cell size as well. A simple consequence is that optical properties normalized to chlorophyll will change in some predictable way (see ref. 8). The main questions are: are the differences big enough to be detected with simple measurements of apparent optical properties? If they are, what is the best way to parameterize them?

2. APPROACH

As a first and simple generalization, we will characterize different phytoplankton communities by the distribution of

chlorophyll *a* concentrations (mg m^{-3}) and particulate absorbances (m^{-1}) among 4 size fractions: picoplankton, ultraplankton, nanoplankton and microplankton (Table 1) following Sieburth *et al.*,⁹ having as a base the hypothesis proposed by Yentsch and Phinney⁵ that different communities of phytoplankton are formed when modes of different sizes are added to a relatively constant "background" of smaller cells. The expected scenario is that since packaging effect becomes important as cell size increases, the specific absorption coefficient ($a_{\text{ph}}(\lambda)$; $\text{m}^2 \text{mg chl}^{-1}$) will decrease (see Bricaud *et al.*¹⁰), with enhanced nutrient supply.⁵ Changes in backscattering are also expected, as smaller cells are more efficient backscatterers with a more pronounced spectral signal (i.e. higher in the blue) than bigger cells.¹¹ These changes will affect apparent optical properties because of their dependency on the inherent properties, that is, absorption and scattering.

3. METHODS

From September 15 to 23, 1996, several stations were occupied off the Oregon coast as shown on Fig. 1, aboard the RV Wecoma. The sampling strategy was to compare a variety of waters with a wide range of both chlorophyll and DOM concentrations. Density profiles were computed from a ctd (Seabird) temperature and conductivity sensor. In this extended abstract, we will discuss only data from the mixer layer. Samples were obtained within the mixed layer with Niskin bottles, and at the surface with a clean plastic bucket. Chlorophyll *a* and particulate absorbances were determined for both whole samples and for the 4 size categories, as defined in Table 1.

name	operational definition	size ranges
total	whole sample	all sizes
microplankton	total minus filtrate of 20 μm	bigger than 20 μm
nanoplankton	filtrate 20 μm minus filtrate of 5 μm	5 to 20 μm
ultraplankton	filtrate of 5 μm minus filtrate of 2 μm	2 to 5 μm
picoplankton	filtrate of 2 μm	less than 2 μm

Table 1. Size fractionation of chlorophyll *a* and phytoplankton absorbance as determined by differential filtration. Filtrates from 20, 5 and 2 μm Poretics polycarbonate filters, filtered either by gravity or very low pressure, were concentrated onto GF/F filters. The concentration of each size class was then determined according to the second column.

3.1 Bio-Optical measurements

Chlorophyll *a* was determined fluorometrically using a Turner designs 10-005R, equipped with the following filters: Corning 5-60 (excitation), Corning 3-66 (reference) and Corning 70 and 16 (emission). Filters were extracted at -10°C for at least 24 hours in pre-cooled 90% acetone-DMSO solution (6:4 volume) immediately after the filtration. Samples were corrected for phaeopigments by acidification with 50 μl of 10% HCl.

Particulate phytoplankton absorbance was measured with a Varian Cary3E dual-beam spectrophotometer.¹² Details about the processing of the samples and beta correction can be found in ref. 13 and references therein.

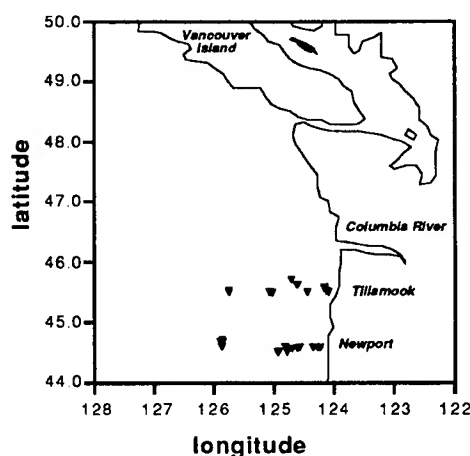


Fig. 1. Stations sampled off the Oregon coast in Sept. 1994.

3.2 Optical measurements

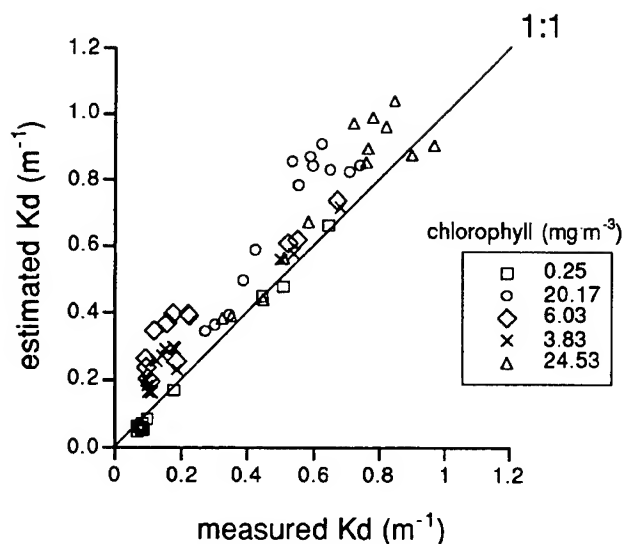


Fig. 2. Comparison between estimated and measured values of K_d for 13 wavebands (same as SPMR). Estimated values according with Morel¹⁴ using an average chlorophyll value for the mixed layer (value indicated on the legend). Measured values are the slope of the normal logarithm of E_d versus depth for the first optical depth of each wavelength.

The diffuse attenuation coefficient ($K_d(\lambda)$; m^{-1}) was measured using a free-falling SeaWiFS Profiling Multichannel Radiometer (SPMR, Satlantic Inc.), which profiled both upwelling radiances and downwelling irradiances in 13 wavebands (10 nm) centered at 406, 412, 435, 443, 456, 490, 510, 532, 555, 590, 670, 683 and 700 nm. The attenuation coefficient for each wavelength was determined, for points within their respective first optical depths, as the slope of the natural logarithm of $E_d(\lambda)$ versus depth, without correcting E_d values from the reference sensor in water. When multiple casts were available, $K_d(\lambda)$ was calculated as above for each cast, then averaged.

Spectral upwelling radiance ($L_u(\lambda)$; $\mu W cm^{-2} nm^{-1} sr^{-1}$) was measured with a Tethered Spectral Radiometer Buoy (TSRB, Satlantic Inc.) at 412, 443, 490, 555, 670, 683 and 700 nm at a depth of 0.5 m, and downwelling irradiance at 490 nm [$E_d(490)$; $\mu W cm^{-2} nm^{-1}$] at 30 cm above the surface (see operational details about the TSRB in ref. 15). The radiance values were then propagated to the surface by using estimated values for the spectral diffuse attenuation coefficient ($K_d(\lambda)$; m^{-1}) computed as a function of chlorophyll concentration,¹⁴ the latter being an average value for the mixed layer. It is important to note that Morel's algorithm for $K_d(\lambda)$ was developed for oceanic waters, and that this relationship tended to overestimate K_d

for chlorophyll values higher than $3 mg m^{-3}$ when compared with concurrent measurements (Fig. 2). However, we have chosen to use estimated values rather than measured ones because SPMR casts were less frequent than TSRB deployments and ctd casts, and also because for a 0.5 meter pathlength the overestimation (approximately 10%) will not produce errors higher than 6-7% on the magnitude of the spectral radiances at the surface. Upwelling radiances at the surface were multiplied by 0.544 to account for reflection at the air-ocean interface,¹⁶ and therefore yielding water leaving radiances ($L_w(\lambda)$; $\mu W cm^{-2} nm^{-1} sr^{-1}$), that were then normalized by $E_d(490)$ to account for changes in the intensity of the incident light. Changes in spectral E_d are expected with different zenith angles and sky conditions (i.e. proportion of diffuse to direct light).^{15,17} We are presently working on independent measurements of spectral downwelling irradiances to derived simple parameterizations for further corrections.

4. RESULTS AND DISCUSSION

The region studied showed a wide variety of surface chlorophyll concentrations varying from less than 0.25 to almost $25 mg m^{-3}$. The chlorophyll size fractionation, when compared to the total chlorophyll, illustrates well the hypothesis that different phytoplankton communities are formed due to the addition of bigger cells (Fig. 3A). As expected, high variability was observed in the specific absorption coefficient ($a_{ph}^*(\lambda)$; $m^2 mg chl^{-1}$) for surface samples (Fig. 3B), with $a_{ph}^*(\lambda)$ decreasing at stations with high chlorophyll concentration due to the presence of bigger cells and consequent increase

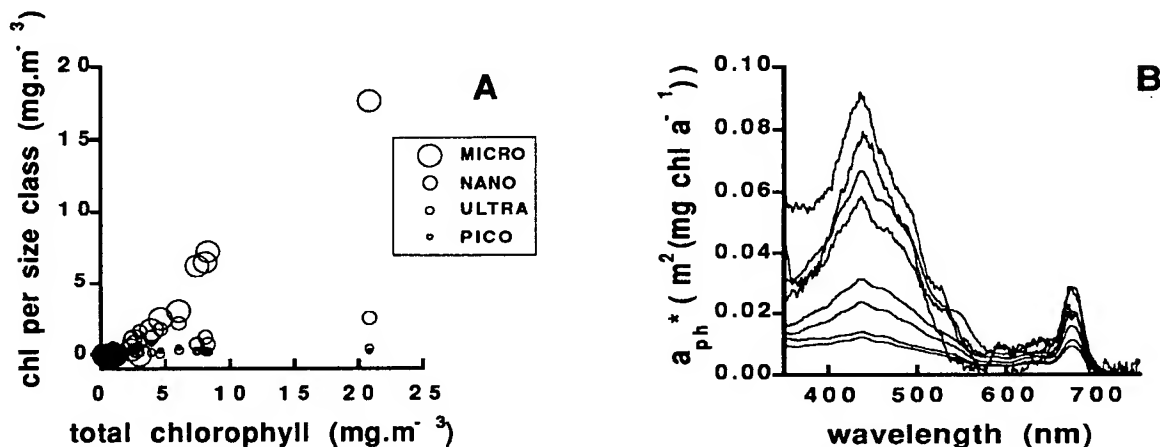


Fig. 3. A- Relationship between total chlorophyll and the chlorophyll content in each size class for surface samples from all stations (symbol size according to size class). Note that chlorophyll in the smaller size classes stay nearly constant, and that the increase in chlorophyll is due to the larger cell sizes. B- Specific absorption coefficient for surface samples from all stations. Highest $a_{ph}^*(\lambda)$ values were found in the low chlorophyll stations.

in the overall package effect. When $a_{ph}^*(\lambda)$ is compared in individual size classes (not shown) the variability is less. However, extremely high values of $a_{ph}^*(\lambda)$ were observed in some samples for the picoplankton class. This was probably a result of the presence of prochlorophytes. When these organisms are abundant (in our case, they are abundant by the exclusion of the other cell sizes), samples will contain high concentrations of chlorophyll b, which by the fluorometric method used here, will underestimate the chlorophyll a concentration and, in turn, overestimate $a_{ph}^*(\lambda)$. Generalized $a_{ph}^*(\lambda)$ for each size class seems to be an achievable goal, but more data has to be combined with the present data set for a more complete picture. It is important to note that the development of a generalized function between size structure and $a_{ph}^*(\lambda)$ for coastal assemblages also depends on how consistently particulate absorbance and chlorophyll measurements are made.

The packaging effect is a well documented source of variability for optical properties of phytoplankton (e.g. specific absorption coefficient, $a_{ph}^*(\lambda)$, (m² mg chl⁻¹) and is directly related to the size of the cells, so simple parameterizations between $a_{ph}^*(\lambda)$ and chlorophyll concentrations seem to be possible.¹⁰ The same trends are observed for spectral diffuse attenuation coefficients normalized to chlorophyll, after correction for attenuation by pure water. Thus, simple parameterizations between $K_d(\lambda)$ and chlorophyll¹⁸ can be reconciled with information on cell size.

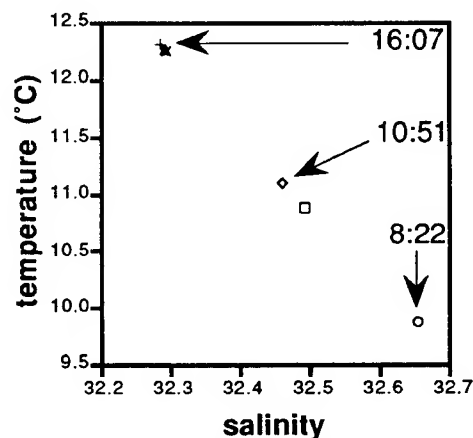


Fig. 4. Changes in temperature and salinity with time, at a coastal station located near the mouth of the Columbia River, in Sep. 20, 1994. Time is indicated by the arrows. These are averaged values in the mixed layer for one station. The chlorophyll increase observed in this location was clearly associated with advection from inshore waters.

During the cruise, we had the opportunity to observe significant changes in phytoplankton size over the course of few hours. In one of the stations, close to the Columbia River mouth, on Sep. 20, we observed an increase in chlorophyll

concentrations from around 8 mg m^{-3} at 0900 h to $18\text{--}20 \text{ mg m}^{-3}$ at 1500 h. The increase in chlorophyll was probably due to advection of cells from inshore waters (see Fig. 4), and perhaps some cell growth. Size fractionated particulate absorption and chlorophyll indicated that the microplankton fraction ($>20 \mu\text{m}$) accounted for more than 80% of the chlorophyll increase, showing that bigger cell sizes became more abundant. Very contrasting phytoplankton absorption spectra among the 4 size classes were measured between 0900 h and 1500 h. Microphytoplankton absorption increased by almost 3-fold, followed by the expected decrease in $a_{\text{ph}}^*(\lambda)$.

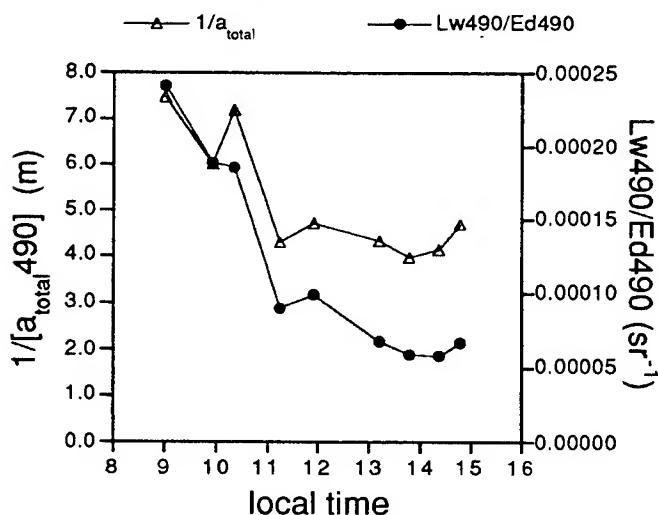


Fig 5. Changes in the total absorption coefficient at 490 nm (i.e., total absorption was estimated as the sum of absorbance by phytoplankton, detritus, DOM and water) and at the reflectance at 490 nm (water leaving radiance over downwelling irradiance at 490) in the time series of chlorophyll sampled close to Columbia River's mouth, on Sep 20, 1994. DOM absorption at 490 nm was measured at 0900 h (0.024 m^{-1}) and at 1500 h (0.020 m^{-1}), so the average value was used for the entire time series; water absorption at 490 nm is 0.022 m^{-1} .¹⁸ Changes in reflectance through time (i.e. increasing chlorophyll and cell size) are clearly the result of both the increase in absorbance and decrease in backscatter, as reflectance is proportional to a constant times the ratio between backscattering and absorption.

During the increase in chlorophyll, spectral water leaving reflectances were also monitored, showing a clear decrease in magnitude, and also the influence from chlorophyll fluorescence (not shown). One example of the influence that changes in cell size has on apparent optical properties, due to changes in the inherent optical properties, is illustrated on Figure 5. The relationship between reflectance (Lw/Ed) and the inherent properties (absorbance and backscattering) are already well known (see ref. 1 and references therein). If $R = \text{constant} \cdot b_b/a$, where R is the reflectance, a is the total absorption coefficient and b_b is the total backscattering coefficient, then by comparing the changes in reflectance and the inverse absorption through time, we can see the effects of increasing cell size. Therefore, both vertical attenuation (by its covariance with phytoplankton absorption) and spectral reflectances contain information on cell sizes via backscattering and absorption.

5-SUMMARY AND FUTURE WORK

For this data set, increases in chlorophyll concentrations were consistently a result of increases in the relative importance of bigger cells in the community. Therefore, a generalization of phytoplankton community structures (i.e. *sensu* Yentsch and Phinney⁵) by changes in chlorophyll content within different size classes seems to be adequate. We also found trends in changes in measurable optical properties that were consistent with changes in cell. These trends were clearly linked to changes in the specific absorption coefficient by the packaging effect, and also inferred changes in backscatter.

For a proper parameterization of different phytoplankton communities by different sizes, however, a larger data set has to be analyzed. We have already collected a extensive data set from coastal waters, and that parameterization will be the focus of our future work.

6-ACKNOWLEDGMENTS

This work was funded by ONR Ocean Optics and NSERC Research Partnerships. AMC was also supported by CNPq (Brazil). The authors would like to thank Richard Davis and Scott McLean for valuable assistance with the data. CEOTR publication no. 005.

7-REFERENCES

1. J. T. O. Kirk, *Light and Photosynthesis in Aquatic Ecosystems*, 2nd ed. Cambridge University Press, Cambridge, 1994.
2. R. P. Bukata, J. H. Jerome, K. Y. Kondratyev and D. V. Pozdnyakov, *Optical Properties and Remote Sensing of Inland and Coastal Waters*, CRC Press, Boca Raton, 1995.
3. R. Margalef, "Life forms of phytoplankton as survival alternatives in an unstable environment," *Oceanol. Acta*, **1**, 493-509 (1978).
4. T. C. Malone, "Algal Size," *The Physiological Ecology of Phytoplankton*, I. Morris, (ed.), pp. 433-463, University of California Press, Berkeley, 1980.
5. C. S. Yentsch and D. A. Phinney, "A bridge between ocean optics and microbial ecology," *Limnol. Oceanogr.*, **34**(8), 1694-1705 (1989).
6. S. W. Chisholm, "Phytoplankton size," *Primary Productivity and Biogeochemical Cycles in the Sea*, P.G. Falkowski and A. Woodhead, (ed.), pp. 213-238, Plenum Press, New York, 1992.
7. T. Kiorboe, "Turbulence, phytoplankton cell size, and the structure of pelagic food webs," *Adv. Mar. Biol.*, **29**, 1-61 (1993).
8. L. Prieur and S. Sathyendranath, "An optical classification of coastal and oceanic waters based on the specific spectral absorption curves of phytoplankton pigments, dissolved organic matter, and other particulate materials," *Limnol. Oceanogr.*, **26**(4), 671-689 (1981).
9. J. M. Sieburth, V. Smetacek and J. Lentz, "Pelagic ecosystem structure: Heterotrophic compartments of the plankton and their relationship to plankton size fractions," *Limnol. Oceanogr.*, **23**(6), 1256-1263 (1978).
10. A. Bricaud, M. Babin, A. Morel and H. Claustre, "Variability in the chlorophyll-specific absorption coefficients of natural phytoplankton: Analysis and parameterization," *J. Geophys. Res.*, **100**(c7), 13,321-13,332 (1995).
11. A. Morel, "Optics of marine particles and marine optics," *Particle analysis in oceanography*, S. Demers, (ed.), pp. 141-188, Springer-Verlag, Berlin, 1990.
12. M. Kishino, M. Takahashi, N. Okami and S. Ichimura, "Estimation of the spectral absorption coefficients of phytoplankton in the sea," *Bulletin of Marine Science*, **37**, 634-642 (1985).
13. C. S. Roesler and M. J. Perry, "In situ phytoplankton absorption, fluorescence emission, and particulate backscattering spectra determined from reflectance," *J. Geophys. Res.*, **100**(c7), 13,279-13,294 (1995).
14. A. Morel, "Optical modelling of the upper ocean in relation to its biogenous matter content (Case I waters)," *J. Geophys. Res.*, **93**, 10749-10768 (1988).
15. J. J. Cullen, A. M. Ciotti and M. R. Lewis, "Observing biologically induced optical variability in coastal waters," *SPIE Ocean Optics XII*, **2258**, 105-115 (1994).
16. R. W. Austin, "Gulf of Mexico Ocean-Color Surface-Truth Measurements," *Boundary-Layer Meteorology*, **18**, 269-285 (1980).
17. W. W. Gregg and K. L. Carder, "A simple spectral solar irradiance model for cloudless maritime atmospheres," *Limn. Oceanogr.*, **35**(8), 1657-1675 (1990).
18. R. C. Smith and K. S. Baker, "Optical Classification of Natural Waters," *Limnol. Oceanogr.*, **23**(2), 260-267 (1978).

Upwelled spectral radiance distribution in relation to yellow substance absorption in the example of Case II waters (Baltic Sea).

Mirosław Darecki
Piotr Kowalczyk

Institute of Oceanology, Polish Academy of Sciences, ul. Powstańców Warszawy 55, 81-712 Sopot, Poland,

ABSTRACT

An extensive data base of in situ measured bio-optical parameters is analysed to examine the influence of absorption of Dissolved Organic Matter on upwelling radiance spectra. The measurements were carried out in the different water masses of the southern Baltic during various seasons of biological activity of the sea basin. Experimental data are the background of statistical relation between spectra of upwelling radiance, absorption of yellow substances and other sea waters constituents in the sea surface. The results allowed to preliminary assess the impact of yellow substance absorption on spectral distribution of upwelled radiance flux in the surface layer of sea water. The spatial and seasonal variability of this relation is considered. Particular attention is given to application of this results in remote sensing determination of water constituents.

Keywords: spectral reflectance, yellow substance, Case II Waters, remote sensing, SeaWiFS

1. INTRODUCTION.

Future global observing systems will use the remotely sensed spectral upwelled radiance to monitor the biophysical processes of the world's oceans. The interpretation of satellite data should be based on multi component model of spectral reflectance. To date, data from ocean colour imagery, such as the Coastal Zone Colour Scanner (CZCS) have been analysed with use of simple model of spectral reflectance^{5, 20, 6, 23}, which based on assumption that, the quantity of significant optically active components of sea water are correlated with chlorophyll concentrations and phytoplankton activity in the basin. This approach has given good result in the Case 1 Waters, but its application to interpretation of data of Case 2 Waters has been unsuccessful. The main reason of this was the impact of absorption of Dissolved Organic Matter (yellow substance) on spectral reflectance, which could not be assessed by this method. The CZCS band selection did not allow the separation of photosynthetically viable chlorophyll a from degradation products. The inclusion of the 412nm band in SeaWiFS should help separate these pigments. Also development of comprehensive bio-optical data sets should enable to formulate more accurate bio-optical algorithms.

A good number of papers presents the importance of yellow substance absorption in modelling the spectral reflectance^{15, 18, 2, 21, 22}. The conclusions present thesis that, in the local condition, relation between three major optically active components: chlorophyll, particulate material, and dissolved organic matter, can be assessed. In recent years there have undertaken intensive experimental research on relations between the spectral distribution of upward radiance and the concentrations of optically active components in the Baltic Sea water. The first preliminary results were presented by Darecki et al.^{3, 4} and Siegel¹⁹. The works of Darecki et al. have not contained the analysis of impact of yellow substance on upward spectral radiance distribution. The principal aim of this paper is to present the results of statistical analysis of relation between yellow substance absorption and spectral upwelling radiance. The study is based on bio-optical data base collected during series of cruises in 1993-1996 and used to investigate various biophysical process.

2. MATERIAL AND METHODS.

The experimental material has been collected during 8 cruises in 1993-1996; details of them are shown on the Fig.1 and in the Tab. 1. For the requirement of this work the following parameters were measured:

1. The upward radiance L_u just below the water surface and downward irradiance at the surface E_d and depth profiles of L_u and E_d in the spectral bands 412, 443, 490, 510, 550, 665, 683, 710 nm with use of the MER 2040 spectroradiometer manufactured by Biospherical Instruments. In September 1995 this instrument has been fitted with additional spectral bands 589 and 625 nm. In the "good sea state" conditions L_u was measured precisely at an infinitesimal depth (practically on 0-0.15m depth) below the surface. Additionally in each case the profile of L_u was measured over the upper few optical depths to determine K_L for L_u . When it was impossible to measure L_u at the infinitesimal depth the diffuse attenuation coefficient K_L was used to calculate propagation of L_u to the surface. To normalise upward radiance measured in different irradiance conditions, coefficient $r = \pi L_u / E_d$ was calculated.
2. The concentration of chlorophyll a, determined spectrophotometrically in acetone extracts of surface water samples.
3. The concentration of total suspended matter (weighed), also determined in surface water samples.
4. Yellow substance absorption spectra of surface waters samples collected, stored and processed according to procedure recommend by Reuter et al.¹⁶.

The light absorption coefficient by yellow substances for specific wavelengths and yellow substance absorption spectra slope coefficient were calculated according to procedure described in paper of Kowalczyk and Kaczmarek¹².

Tab 1. The details of 1993-1996 fields expeditions.

Date of the cruises	Region	Measured Parameters	Notes
Optical cruise 5-14 Sept. 1993	Bay of Gdańsk, Baltic Proper	a_{ys} , E_d , L_u , TSM, Chl a	17 samples.
Optical cruise 10-17 April 1994	Bay of Gdańsk, Baltic Proper	a_{ys} , E_d , L_u , TSM, Chl a	27 samples
Optical cruise 6-15 May 1994	Bay of Gdańsk, Pomeranian Bay, Baltic Proper	a_{ys} , E_d , L_u , Chl a	34 samples
Optical cruise 17-25 Aug. 1994	Bay of Gdańsk, Pomeranian Bay, Baltic Proper	a_{ys} , E_d , L_u , TSM, Chl a	21 samples
Optical cruise 22-29 Sept. 1994	Bay of Gdańsk, Baltic Proper	a_{ys} , E_d , L_u , TSM, Chl a	28 samples
Optical cruise 6-15 Sept. 1995	Bay of Gdańsk, Pomeranian Bay, Baltic Proper	a_{ys} , E_d , L_u , Chl a	12 samples
Optical cruise 7-17 March 1996	Bay of Gdańsk, Pomeranian Bay, Baltic Proper	a_{ys} , E_d , L_u , Chl a	30 samples
Optical cruise 14-26 May 1996	Bay of Gdańsk, Pomeranian Bay, Baltic Proper	a_{ys} , E_d , L_u , TSM, Chl a	31 samples

3. PROPERTIES OF YELLOW SUBSTANCE IN THE BALTIC SEA.

The Baltic Sea is known as the region where yellow substance play very important role in the radiative transfer processes in the water. They have focused the attention of many workers who have studied their chemical and optical properties^{11, 13, 17, 1, 7, 8, 9, 14, 10}. In the recent study of Kowalczyk and Kaczmarek¹² have focused on temporal and spatial variability of yellow substance absorption field in various region of Baltic Sea. They have also assessed the influence of yellow substance of allochthonous origin on absorption conditions by watching the changes in distribution of the yellow substance absorption spectrum slope coefficient. The most important points of their work can be summarised in the Tab. 2 and following points:

1. The statistical distribution of values of a_y ($\lambda=400$ nm) shows that it is log-normal and the statistical distribution of the slope coefficient is nearly normal. The most probable yellow substance absorption spectrum, which could be measured in the Southern Baltic, will be characterised by value a_y ($\lambda=400$ nm) in the range between 0.4- 1.6 m⁻¹ and the value

of the slope coefficient in the range between 0.014- 0.022. The lowest mean value of the absorption coefficient have been observed in the open sea waters, the intermediate in the coastal zone, and the highest in the bay waters.

2. The comparison of the statistical distribution of the slope coefficient with absorption properties of selected fractions of marine humus shows that dominant fraction of marine humus in the Southern Baltic are fulvic acids. The humic acids are present in the river water plums and can change the properties of the absorption field radically in region influenced by it.
3. The temporal variability of mentioned parameter shows the tendency for oscillation around the mean values. This oscillation is clearly visible in case of the absorption coefficient, but less in case of the slope coefficient. The highest values of absorption coefficient in the surface layer of Baltic Sea water are observed in Spring and summer, the lowest in winter.
4. The spatial distribution of a_y ($\lambda=400$ nm) in surface layer of Baltic Sea water shows that during the period of investigation the lowest values of the a_y were noticed offshore. The field of increased absorption was usually met in the near rivers mouths. The horizontal range of increased absorption field was small and decreased with distance from the source (river).

Tab 2. Values of statistical parameters calculated for total sample size collected in three different waters masses.

	Bay waters		Coastal waters		Open sea waters	
	$a_y(\lambda=400\text{nm})$ [m ⁻¹]	S _H VIS	$a_y(\lambda=400\text{nm})$ [m ⁻¹]	S _H VIS	$a_y(\lambda=400\text{nm})$ [m ⁻¹]	S _H VIS
Minimal value	0.16	0.005	0.42	0.012	0.3	0.004
Maximal value	4.55	0.034	4.60	0.029	1.84	0.030
Mean value	1.12	0.018	1.02	0.19	0.76	0.019
Median	0.84	0.019	0.71	0.19	0.67	0.019
Standard deviation	0.73	0.005	0.73	0.002	0.32	0.004
Sample size	225	213	97	97	179	165

4. THE INFLUENCE OF YELLOW SUBSTANCE ON UPWELLED RADIANCE FLUX.

Our data sets have been measured in the different seasons and different water masses to cover the most possible variability of the experimental material. For the purpose of this study the data base have splitted for the time series of subsets of measurement taken in the bay waters, coastal zone and open sea waters. The well known absorption properties of yellow substance have given the clue how to search the impact of them on upwelled radiance. We have calculated ratio of r in the spectral band of maximum absorption of yellow substance (412 nm), to the r measured in the spectral band of the least absorption(665 nm).

The preliminary analysis of collected experimental data, do not allow to formulate the general and objective algorithm for assessment of the yellow substance absorption in the Baltic Sea. But the inclusion of the 412 nm band in SeaWiFS have enable to separate photosynthetically active chlorophyll a from degradation products in specific and stable hydro-meteorological condition. The Fig. 2. shows the plot of the ratio of r in the spectral bands $r(412 \text{ nm})/r(665 \text{ nm})$ against the value of yellow substance absorption coefficient for $\lambda=412$ nm for all data. The weak relation between those two parameters can be seen. On the Fig.3 the same parameter was plotted for chosen seasons. The relation is much better. The upper line in the Fig 3a present the bloom situation in early spring 1994. The lower line in the same plot and Fig 3b. present the post bloom situation in late spring 1994 late summer of 1994. The relation is very similar. So, it is possible to differentiate between periods of high and low biological activity of the marine basin.

The big variability of our data set caused by different hydro-meteorological conditions and biological activity of the phytoplankton have severely influence the result of seasonal comparison of the relation of yellow substance absorption and reflectance. The big number of possible combination of species composition in the algae bloom, their different composition of photosynthetic pigments certainly have impact on the shape of upwelled radiance spectra. The hydrological condition in the investigated area are also very important. During our experiment we met in the spring totally

different conditions; in 1994 an extensive riverin plume containing large amount of mineral suspension and increased yellow substance absorption and associated algae bloom, and in 1996 most of the bay region covered by ice and trace of biological activity. So, we have looked for the period which have most stable hydro-meteorological conditions. The climatological data for the Southern Baltic in May are most stable. We have joined the data sets collected in Mays 1994 and 1996. The results were good (Fig. 4.). We have obtained high correlation between $a_{ys} \lambda=412 \text{ nm}$ and $r(412 \text{ nm})/r(665 \text{ nm})$ in the investigated regions.

5. CONCLUSIONS

The spectral band centred around 412 nm which will be included in the SeaWiFS should enable to construct algorithm for assessment of yellow substance absorption, but we have no circumstances to prepare a good algorithm which will be valid for all seasons in a year. A quite good correlations are obtained for each season. When we take account the same seasons in a different years correlation's are worse but in the stable conditions in each year (e.g. May) they appear still promising. The main clause now is to find a parameter which define these conditions. The authors are working on this problem and will publish farther results of this research soon.

6. REFERENCES

1. Bricaud A., Morel A., Prieur L., 1981, Absorption by dissolved organic matter and of the sea (yellow substance) in the UV and visible domains. *Limnol. Oceanogr.* 26(1) pp 43-53
2. Carder K. L., Hawkes S., K., Baker K., A., Smith R., C., Steward R. G., Mitchell G., 1991, Reflectance model for quantifying chlorophyll 'a' in the presence of productivity degradation products. *Journal Geophys. Res.* Vol. 96 C11 pp 20599-20611
3. Darecki M., Olszewski J., Kowalczyk P., 1994 Spectral characteristics of diffusive reflection coefficient in Southern Baltic- the latest experimental studies. *Proceedings of 19th Conference of the Baltic Oceanographers*, Sopot 29 August-1 September 1994, pp 137-148
4. Darecki M., Olszewski J., Kowalczyk P., 1995 Preliminary study of spectral characteristics of upward radiance field in surface layer of the Baltic. Empirical algorithm for remote detection of chlorophyll concentration. *SiMO 68, Marine Physics* 8, pp. 27-49
5. Gordon H. R., Clark D. K., Mueller J. L., Hovis W. A., 1980 Phytoplankton pigments from Nimbus-7 Coastal Zone Colour Scanner: comparison with surface measurements. *Science* 210 63-66
6. Gordon H. R., Morel A., 1983 Remote assessment of ocean color for interpretation of satellite visible imagery. A review. in: R.T. Barber editor Lecture notes on coastal and estuarine studies. *Springer-Verlag*, New York
7. Højerslev N. K. 1974, Inherent and apparent properties of the Baltic. *Rep. Inst. Phys. Oceanogr., Univ. Copenhagen* No. 24 pp 41
8. Højerslev N. K. 1988, Natural occurrences and optical effects of Gelbstoff. *Rep. Inst. Phys. Oceanogr., Univ. Copenhagen* No. 50 pp 30
9. Højerslev N. K. 1989 Surface water-quality studies in the interior marine environment of Denmark. *Limnol. Oceanogr.* 34(8) pp 1630-1639
10. Højerslev N. K. Holt N., Aarup T., 1996 Optical measurements in the North Sea-Baltic Sea transition zone. On the origin of the deep waters in the Kattegat. *Continental Shelf Research* Vol. 16 No. 10 pp. 1329-1342
11. Kalle K. 1966 The problem of the Gelbstoff in the sea. *Mar. Biol. Annu. Rev.*, 4 pp 91-104
12. Kowalczyk P., Kaczmarek S., 1996 Analysis of temporal and spatial variability of "yellow substance" absorption in the Southern Baltic. *Oceanologia*, No. 38(1) pp. 3-32
13. Nyquist G. 1979 Investigation of some optical properties of sea water with special reference to lignin sulfonates and humic substances. *PhD Thesis Dep. Annal. Mar. Chem. Göteborgs Universitet*, pp 203
14. Pempkowiak J. 1988 Rozmieszczenie, pochodzenie i właściwości kwasów humusowych w Morzu Bałtyckim. *Ossolineum*, pp 146 Wrocław, (in Polish)
15. Prieur L., Sathyendranath S., 1981 An optical classification of coastal and oceanic waters based on the specific spectral absorption curves of phytoplankton pigments, dissolved organic matter, and other particulate material. *Limnol. Oceanogr.* Vol. 26(4) pp 671-689
16. Reuter R., Albers W., Brandt K., Diebel-Langohr D., Doerffer R., Dörre F., Hengstermann T., 1986, Ground truth techniques and procedures for Gelbstoff measurements. in *The influence of yellow substances on remote Sensing of sea water constituents from Space*. Report of ESA Contract No. RFQ 3-5060/84/NL/MD, GKSS Research Centre Geesthacht

17. Samuła-Koszałka T., Woźniak B., 1979 The share of particular sea water component in the light attenuation and analysis of the absorption spectra of yellow taking Bay of Gdańsk as an example. *SiMO* 26 pp 203-216 (in Polish)
18. Sathyendranath S., Prieur L., Morel A., A three-component model of ocean colour and its application to remote sensing of phytoplankton pigments in coastal waters. 1989 *Int. J. Remote Sensing* Vol. 10 No. 8 pp 1373-1394
19. Siegel H., Gerth M., Beckert M., 1994 The variation of optical properties in the Baltic Sea and algorithms for the application of remote sensing data. in *SPIE Proc. Jaffe J. S., ed. Vol. 2258* pp 894-905
20. Smith R. C., Baker K. S., 1982 Oceanic chlorophyll concentrations as determined by satellite (Nimbus-7 coastal zone color scanner). *Mar. Biol.* 66, 269
21. Sturm B., 1994, Water Optical Models. Their role in the interpretation of Ocean Colour Data. *Proceedings of 19th Conference of the Baltic Oceanographers*, Sopot 29 August-1 September 1994, pp 76-90
22. Tassan S., 1994 Local algorithms using SeaWiFS data for the retrieval of phytoplankton, pigments, suspended sediments, and yellow substance in coastal waters. *Applied Optics* Vol. 33, No. 12 pp 2369-2378
23. Volier M., Sturm B., 1984 CZCS data analysis in turbid coastal waters., *J. Geophys. Res.* Vol. 9 4977.

7. Figures

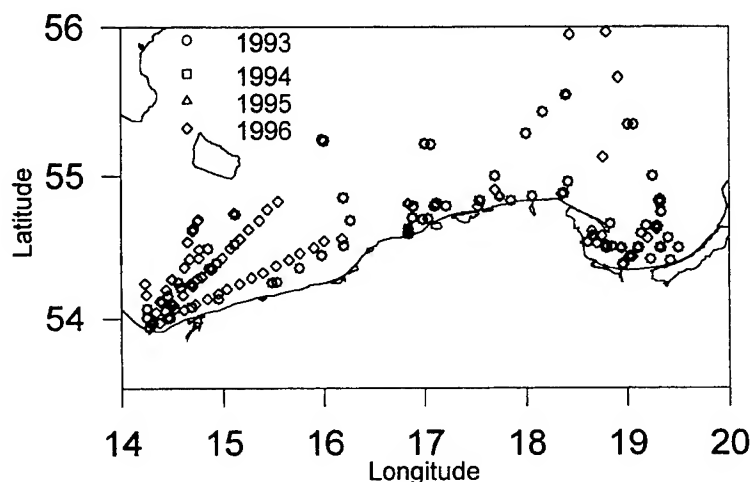


Fig.1. Location of sample stations in the Southern Baltic during measurement campaign in 1993-1996.

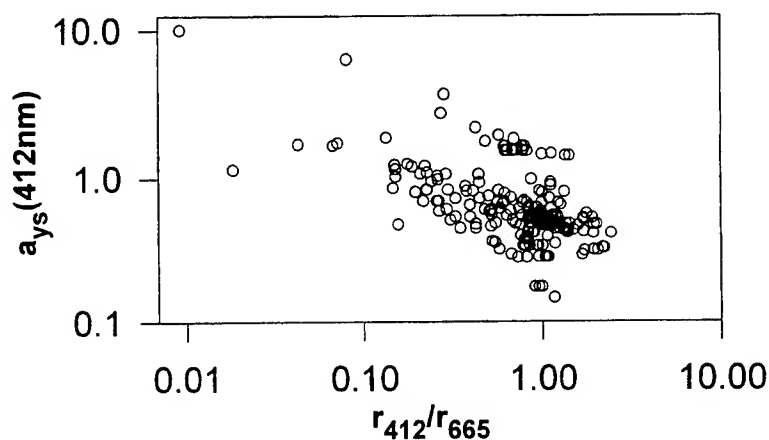


Fig.2. The relation between yellow substance absorption and spectra reflectance ratio for all collected data (log-log scale)

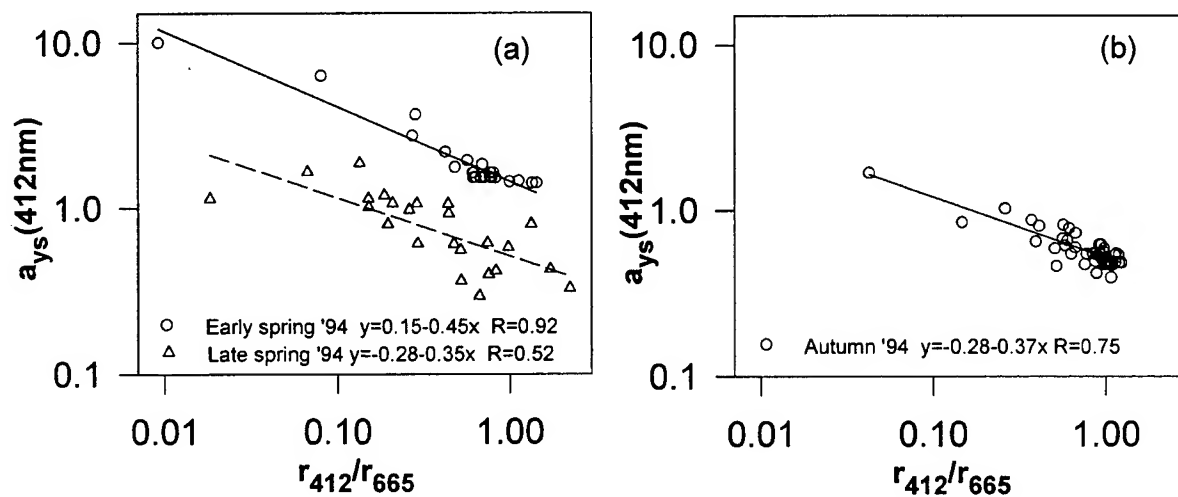


Fig.3. The relation between spectral reflectance and yellow substance absorption during spring (a) and autumn seasons (b) (log-log scale)

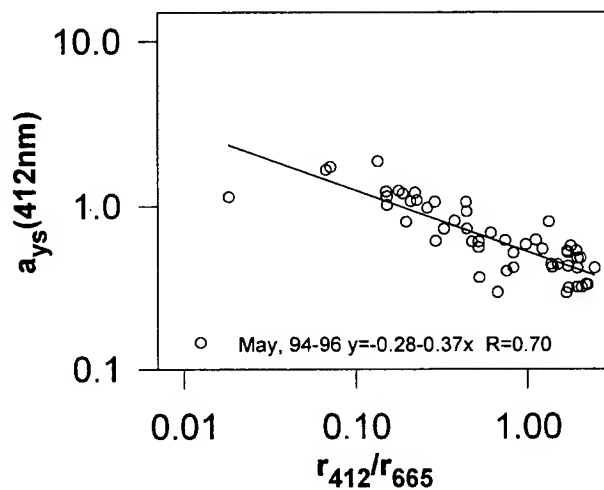


Fig.4. The relation between spectral reflectance and yellow substance absorption for data collected in May 1994 and May 1996 (log-log scale).

Angular scattering functions of algae and silt: an analysis of backscattering to scattering fraction

A.G. Dekker and H.J. Hoogenboom

Institute for Environmental Studies, Vrije Universiteit, De Boelelaan 1115, 1081 HV Amsterdam, The Netherlands
Tel (+31)-20-4449506, Fax (+31)-20-4449553, Email: arnold.dekker@ivm.vu.nl

H. Volten, R. Schreurs and J.F. de Haan

Department of Physics and Astronomy, Vrije Universiteit, De Boelelaan 1081 HV Amsterdam, The Netherlands

ABSTRACT

In order to obtain more information on the angular scattering behaviour of algae and silt research was initiated to determine whether or not the volume scattering functions by Petzold⁷ for the San Diego Harbour are appropriate for use in other types of turbid waters as is often stated in literature. This paper presents a selection of the measured angular scattering distribution functions (ASD; scaled at the 90° scattering angle) over the range 15°-165°, the extrapolated angular scattering distribution functions extended to the range of 0° - 180° by fitting Mie functions and the calculated (partial) backward scattering to total scattering ratios (backscattering fractions). The San Diego Harbour measurements by Petzold⁷ may not be applied to other turbid waters: it is in the backscattering region where the samples deviate most from the San Diego ASD (calculated from his VSF) from Petzold⁷. A large addition to existing literature values for (partial) backscatter probabilities is presented for 14 freshwater and marine algal species samples and 2 estuarine silt samples.

Keywords: angular scattering functions, backscatter ratios, bio-optical modelling, coastal and inland waters, algae, silt.

1. INTRODUCTION

In a comprehensive study² on inherent and apparent optical properties of inland lakes in The Netherlands, a clear dearth of data was identified on volume scattering functions (VSF) for such waters. Often the VSF by Petzold⁷ or by Whitlock¹¹ are, or indeed, have to be, used for research and modelling purposes. In order to obtain more information on the angular scattering behaviour of algae and silt research was initiated by the Institute for Environmental Studies (IVM) in co-operation with the Department of Physics and Astronomy (DPA) (both at the Vrije Universiteit), The Centre for Estuarine and Marine Ecology (NIOO-CEMO) and the Institute for Freshwater Ecology (IFE) in the UK, to carry out a pilot study, to determine whether or not the VSF by Petzold⁷ for the San Diego Harbour is appropriate for use in other types of turbid waters as is often stated in literature. The measurements were performed by a team at the DPA making use of an existing set-up that had been designed and previously used for measuring the scattering behaviour of aerosols. The set-up had to be adapted to be able to measure hydrosols suspended in water. Volten *et al*¹⁰ discusses the set-up and presents all the measurements.

This paper presents a selection of the measured angular scattering distribution functions (ASD; scaled at the 90° scattering angle) over the range 15°-165°, the extrapolated angular scattering distribution functions extended to the range of 0° - 180° by fitting Mie functions and the calculated (partial) backward scattering to total scattering ratios (backscattering fractions). Due to the fact that this was a pilot study a choice of algae and inorganic hydrosols had to be made, large enough to allow an answer to the above mentioned question concerning the validity of the VSF of Petzold for other types of waters, yet limited enough in size to remain workable. The algae measured were culture samples of freshwater algae: *Microcystis ridii*, *Volvox aureus*, *Prochlorothrix hollandica*, *Oscillatoria amoena*, *Oscillatoria agardhii*, *Melosira granulata*, *Anabaena flos-aquae*, *Astrionella formosa*, *Selenastrum capricornutum*; and samples of marine algae *Phaeodactylum*, *Phaeocystis pouchetti* and *Emiliana huxleyi*. Furthermore two samples of Westerschelde silt were measured, one sample with a size of 3 to 5 µm and a sample with a size of 5 to 12 µm. The Westerschelde is a tidal estuary of the river Schelde located in the south-west of The Netherlands.

2. THE ANGULAR SCATTERING DISTRIBUTION MEASUREMENTS OVER 15° - 165°, SCALED AT THE 90° SCATTERING ANGLE (ASD)

2.1. Introduction

To measure the ASD, the experimental set-up developed at the Department of Physics and Astronomy of the Vrije Universiteit in Amsterdam was used. This set-up was originally designed to determine the scattering behaviour, including polarisation, of aerosols, e.g. sand particles^{4,5,9}. With some adaptations¹⁰ this set-up could also be used to perform measurements on hydrosols. The measurements reported in this paper have all been performed with the same instrument under similar

conditions. Therefore, they provide a reliable indication of the differences to be expected in scattering functions. The set-up has been designed to also measure polarisation, further discussed in Volten *et al*¹⁰

The properties of hydrosols that determine their scattering behaviour are their size, shape, internal structure and refractive index. Values for these parameters were obtained either from literature or from additional measurements performed during this measurement campaign, with the exception of some values for the imaginary part of the refractive index, that are estimates obtained from fitting the measurements to the results of Mie-calculations.

Algae have a wide range of possible shapes. Spherical or cylindrical shapes occur frequently, whereby the cylinders may form filaments. The silt particles have irregular shapes. Algae can have a pronounced internal structure. They can for instance possess a kernel, chloroplasts, etc. Some species are surrounded by calcite or silicate mantels. Cyanobacteria usually have less internal structure than true algal species, except for the gasvacuoles that are common in many cyanobacteria species. Gas vacuoles decrease the total density of the cell, and strongly influence the (bulk) refractive index. The size of the algae in the samples range from a few micron up to about a hundred microns for the colonies and filaments. Size distributions have been determined by using a microscope and/or a Coulter counter.

For some of the samples it was possible to estimate the real and imaginary part of the refractive index, using cell size and cell number data and absorption measurements, following the method of Morel and Bricaud⁶. For others values of refractive indices of the real part were taken from the literature. For those samples where no estimate of the imaginary part of the refractive index could be obtained, values obtained from fitting Mie theory to the measurements were used.

2.2. The laboratory set-up

The experimental set-up is configured as follows. Light with a wavelength of 633 nm from a continuous wave HeNe laser passes through a polarizer oriented at 0° between the scattering plane or horizontal plane and its principal axis. The linearly polarised light propagates through a modulator oriented at -45° between the horizontal plane and its principal axis and is scattered by a sample of hydrosol particles. The scattered light is detected by a photomultiplier tube which moves along a ring. The maximum range measurable is a scattering angle range of 15° (nearly forward scattering) up to 165° (nearly backward scattering), however often this range was reduced because the measured values lay below the signal-to-noise levels. This configuration of the optical components in the set-up allowed measurement of the scattering function, as well as the difference between two components of the flux for which the electric field vectors oscillate in directions parallel and perpendicular to the scattering plane^{4,5}.

The hydrosol sample is contained in a cylindrical shaped cuvette with a diameter of 30 mm made of pyrex glass. A magnetic stirrer continuously homogenises the hydrosols. In order to reduce the influence of differing refractive indices, the cuvette has been placed in a cylindrical pyrex glass basin (diameter 22 cm), filled with glycerine (the same refractive index as glass). The glass basin has flat entrance and exit windows, to prevent the reflections of the incident laser beam on the basin to enter the detector and to avoid spherical aberrations of the incident beam. For the remaining reflections a correction as applied¹⁰. Care was taken to avoid multiple scattering in the sample. The changing volume seen by the detector at different angles was also accounted for.

2.3. Results

Figure 1 shows the most reliable ASD measurements of the algae as well as the two silt measurements. Petzold's⁷ San Diego Harbour ASD is also shown. This comparison gives an indication of the differences of the angular scattering behaviour of the investigated water constituents relative to the Petzold⁷ standard.

All samples show a strong peak in the forward direction. Compared to the San Diego ASD function at forward angles *Phaeodactylum* and *Prochlorothrix hollandica* lie higher and *Microcystis* sp. lie lower. The other samples show a more or less similar shape of scattering in near forward directions. The San Diego ASD function is rather flat at backward angles. All samples except silt (3-5 µm) are clearly different: they show an increase at backscatter angles from 120° upwards. Thus it is in the backscattering region where the samples deviate most from the San Diego ASD (calculated from his VSF) from Petzold⁷.

Differences between the algal and silt measurements and the San Diego function at 165° (highest measurement angle) are up to a factor of two or more, especially for *Prochlorothrix hollandica*, *Selenastrum capricornutum* and *Phaeodactylum*. For

forward scattering the differences are from a factor 3 lower (for silt (5-12 μm) to a factor 10 higher for *Phaeodactylum*. For *Microcystis* sp., *Oscillatoria agardhii*, *Prochlorothrix hollandica*, *Selenastrum* and silt (3-5 μm) the differences are within a factor 2.

It is demonstrated that the shapes of the scattering functions for algae are not easily derived from their outer morphology. For instance, the scattering behaviour of the spherical *Microcystis* sp. is similar to that of the cylindrical *Oscillatoria agardhii*. A possible explanation for the oscillations in the scattering pattern of the filamentous *Prochlorothrix hollandica* is the narrow size distribution and uniform shape of the particles, likely causing resonance in the scattering pattern. Due to their tendency to grow in one direction (length) filamentous algae are more apt to have a narrow size distribution than single celled species.

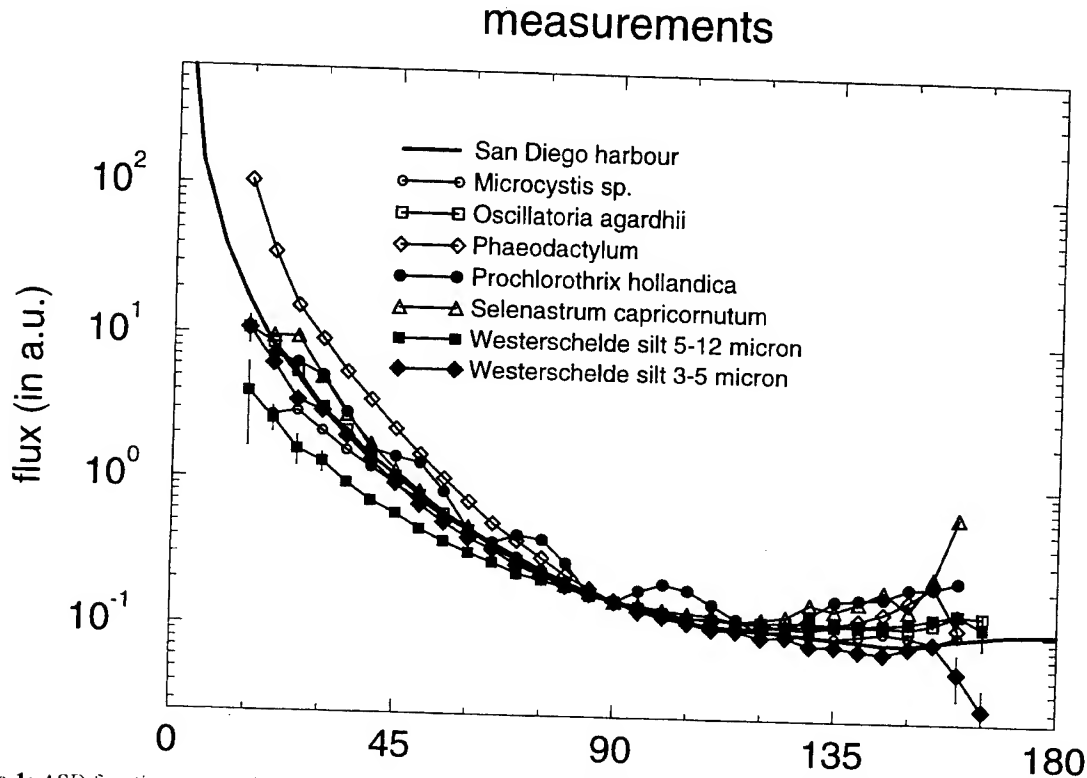


Figure 1: ASD functions, normalised at the 90° scattering angle of five selected algae, 2 silt samples and the Petzold ⁷ San Diego Harbour 1 measurement (data derived from Volten *et al.*¹⁰)

3. THE ASD MEASUREMENTS (15° - 165°) EXTRAPOLATED TO 0° - 180° BY FITTING MIE SCATTERING FUNCTIONS

Because the ASD measurements were limited to within the range of 15° to 165° attempts were made to extrapolate the measurements to the full 0° - 180° range through fitting Mie scattering functions to these measurements⁸. Figure 2 shows the results for these fits (note that the flux log-scale for the ASD is in arbitrary units). For the values given in table 3 the Mie fits were normalised to a value of 1 and therefore are equivalent to the normalised volume scattering function (NVSF). The parameters used for these calculations are size distributions of volume equivalent spheres and the real and complex part of the refractive index. In case no information was available, we chose the values that provided the best fit to the measured data. Since Mie-theory is only valid for homogeneous spherical particles, these are not necessarily realistic values.

In most cases, the results of Mie calculations produce good fits to the measured data. For *Microcystis ridii*(+gv), *Phaeodactylum* and *Astrionella formosa* the Mie fit is lower at angles from 120° to 165°. For *Emiliana Huxleyi* the ASD measurement range was limited to 30° - 150° and therefore a check with the Mie fit was beyond this angle was impossible.

Mie calculations

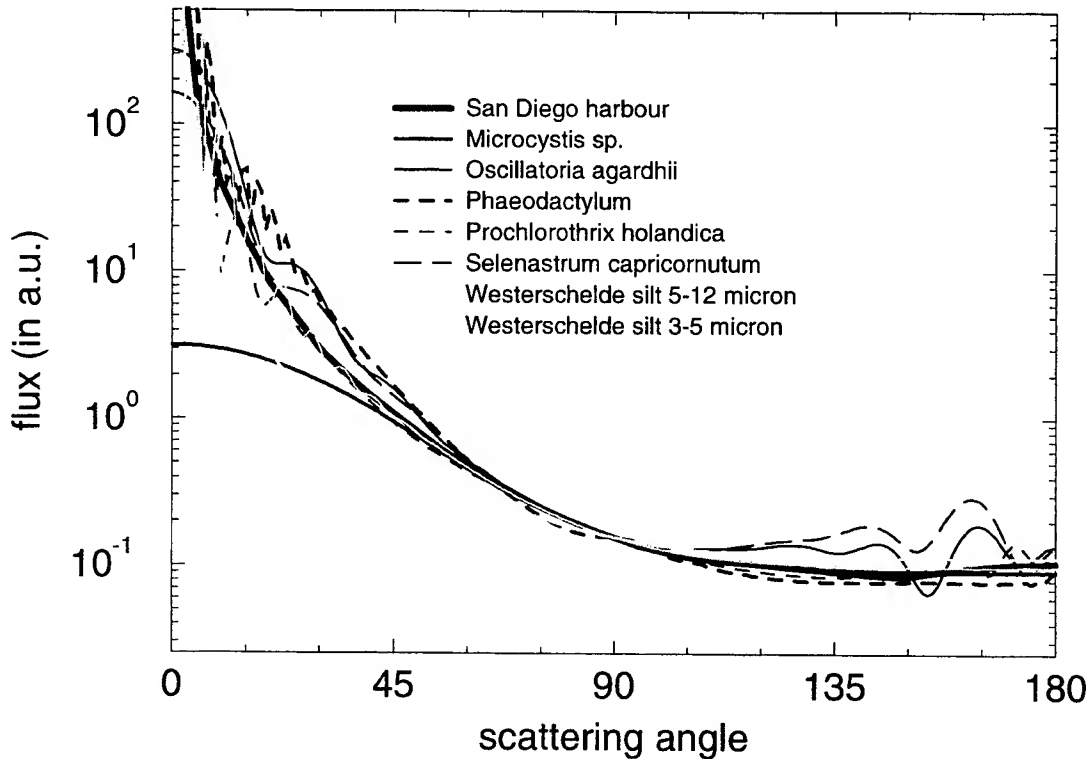


Figure 2: the angular scattering distribution function measurements extrapolated to 0° - 180° by fitting Mie scattering functions to the same data presented in Figure 1.

4. BACKSCATTERING FRACTIONS FROM ASD FUNCTIONS OF ALGAE AND SILT

4.1. Introduction

For bio-optical models, for remote sensing retrieval of water quality algorithms and for many of the laboratory spectrophotometric measurements (especially when using integrating spheres) ratios of scattering at a limited range of smaller angles related to scattering over a larger range of angles are relevant.

The backscatter probability is defined as the proportion of the light scattered at backward angles as compared to the totally scattered amount of light. For this definition it is arbitrary whether an absolute or a normalised VSF is used. In the case of VSF (by definition over the range of 0° - 180°) the general equation becomes:

$$B_{\alpha_1, \alpha_2} = \frac{\int_{\alpha_1}^{180} \tilde{\beta}(\alpha) \sin \alpha d\alpha}{\int_{\alpha_2}^{180} \tilde{\beta}(\alpha) \sin \alpha d\alpha} \quad (1)$$

For the backscattering probability it is:

$$B_{90/0} = B = \frac{\int_{90}^{180} \tilde{\beta}(\alpha) \sin \alpha d\alpha}{\int_{0}^{180} \tilde{\beta}(\alpha) \sin \alpha d\alpha} \quad (2)$$

In a similar fashion $B_{5/0}$ and $B_{40/0}$ etc. may be defined (see table 3). A special case are the partial backscattering fractions B' presented in table 1 and 2: in this case the measurement range was taken from 40° to 140 (or 150 or 160°). Then the partial backscattering probabilities B' are defined as:

$$B'_{90-140/40-140} = \frac{\int_{90}^{140} \tilde{\beta}(\alpha) \sin \alpha d\alpha}{\int_{40}^{140} \tilde{\beta}(\alpha) \sin \alpha d\alpha} \quad (3)$$

	ASD (cubic spline)		
	B _{90-140/40-140}	B _{90-150/40-150}	B _{90-160/40-160}
Freshwater algae			
CHLOROPHYTA-Chlorophyceae			
<i>Selenastrum capricornutum</i>	0.223	0.251	0.282
<i>Volvox aureus</i>	0.210	0.229	0.237
CYANOPHYTA-cyanophyceae			
<i>Anabaena flos-aquae</i>	0.194	0.216	0.226
<i>Microcystis ridii</i> (-gv)	0.226	0.250	0.270
<i>Microcystis ridii</i> (+gv)	0.169	0.188	0.206
<i>Microcystis</i> sp. (+gv)	0.208	0.226	0.239
<i>Oscillatoria agardhii</i>	0.217	0.236	0.251
PROCHLOROPHYTA-Prochlorophyceae			
<i>Prochlorothrix hollandica</i>	0.204	0.229	0.249
CHRYSTOPHYTA-Bacillariophyceae (Diatoms)			
<i>Astrionella formosa</i>	0.136	0.157	0.174
<i>Melosira granulata</i>	0.134	0.157	#
Marine algae			
CHRYSTOPHYTA- Prymnesiophyceae			
<i>Emiliana huxleyi</i> (+c)	0.234	0.268	#
<i>Emiliana huxleyi</i> (-c)	0.220	0.224	#
<i>Phaeocystis pouchetti</i>	0.218	0.238	0.251
CHRYSTOPHYTA-Bacillariophyceae (Diatoms)			
<i>Phaeodactylus</i>	0.131	0.148	0.165
Estuarine mineral particles			
Silt (3-5 μ m)	0.207	0.222	0.234
Silt (5-12 μ m)	0.286	0.310	0.329
average	0.201	0.222	0.239
standard deviation	0.040	0.041	0.041
minimum value	0.131	0.148	0.165
maximum value	0.286	0.310	0.329
San Diego Harbour	0.188	0.204	0.216

Table 1. This table presents the scattering ratios of the ASD as measured by Volten *et al.*¹⁰. A standard cubic spline routine (from MATLAB) was used to enable integration over the given angles. +gv and -gv indicate whether the *Microcystis* samples had intact gas-vacuoles or whether they were collapsed on purpose. +c and -c indicates whether the *Emiliana* had their coccoliths removed or not. # denote calculations which were unreliable due to lack of measurement data at the angles included in the calculation.

4.2. Partial backscattering to scattering fractions over 15° - 165° , scaled at the 90 ° scattering angle: results

Table 1 shows the results of B' calculations based on the ASD measurements (from 40° up to a maximum of 140, 150 and 160°) using a standard (MATLAB) cubic spline routine. for calculating the integrals over the measured angles. Although these calculations are of less use in calculations of the underwater light field, as compared to the ASD that were extended to the full 0°-180° range (see next paragraph), they are more reliable. For forward scattering an angle cut-off of 40° was chosen for its relevance to measurements of attenuation, absorption and scattering using spectrophotometers equipped with integrating spheres with an acceptance angle of 40°.

In table 2 the 14 measured algae (*Oscillatoria amoena* was omitted because the measured values lay within the noise levels) are ordered into their Genus and Species. in order to detect any patterns in the B'. Also the average and the standard deviation was calculated. A rule was applied that all samples falling within the mean +/- 1 standard deviation (σ) are a class and all others belong to another class. This leads to one group of ratios lying between 0.161 - 0.241, one group below this range (all diatoms) and silt (5-12 μ m) with higher values. For the sake of clarity these data have been regrouped in table 2.

samples within 1 σ (table 1)	ASD (cubic spline)		
	B _{90-140/40-140}	B _{90-150/40-150}	B _{90-160/40-160}
<i>Microcystis ridii</i> (+gv)	0.169	0.188	0.206
<i>Anabaena flos-aquae</i>	0.194	0.216	0.226
<i>Prochlorothrix hollandica</i>	0.204	0.229	0.249
Silt (3-5 m)	0.207	0.222	0.234
<i>Microcystis sp.</i> (+gv)	0.208	0.226	0.239
<i>Volvox aureus</i>	0.210	0.229	0.237
<i>Oscillatoria agardhii</i>	0.217	0.236	0.251
<i>Phaeocystis pouchetti</i>	0.218	0.238	0.251
<i>Emiliana huxleyi</i> (-c)	0.220	0.224	#
<i>Selenastrum capricornutum</i>	0.223	0.251	0.282
<i>Microcystis ridii</i> (-gv)	0.226	0.250	0.270
<i>Emiliana huxleyi</i> (+c)	0.234	0.268	#
average	0.211	0.231	0.245
standard deviation	0.016	0.019	0.020
minimum value	0.169	0.188	0.206
maximum value	0.234	0.268	0.282
samples outside 1 σ (table 1)			
Bacillariophyceae (Diatoms)			
<i>Phaeodactylum</i>	0.131	0.148	0.165
<i>Melosira granulata</i>	0.134	0.157	#
<i>Astrionella formosa</i>	0.136	0.157	0.174
average	0.134	0.154	0.170
standard deviation	0.002	0.004	0.005
minimum value	0.131	0.148	0.165
maximum value	0.136	0.157	0.174
others			
San Diego Harbor	0.188	0.204	0.216
Silt (5-12 μ m)	0.286	0.310	0.329

Table 2. This table presents the data from table 1 (arranged in increasing ratios within a block) re-ordered into three groups of data: The first block of data are the values that fall within the range of the average $\pm 1 \sigma$. The second block of data are the diatoms (both from freshwater and marine) that clearly show ratio values below the average. The remaining values are the San Diego Harbour values and the silt(5-12 μ m). # denotes calculations which were unreliable due to lack of measurement data at the angles included in the calculation.

according to their calculated B' values and the groups described above. From table 2 it may be derived that, with the exception of the diatoms, all the freshwater, marine algae and the finer silt sample have a B' of 21 % with a σ of 1.6%. The diatoms have a B' of 13.4 % with a σ of 0.2 %. The San Diego Harbour sample has a B' of 18.8 %.

These values indicate strongly that using only a San Diego harbour B' may introduce errors up to 65 %, with an average error of 11 % for all the algae, except the diatoms: and with an average error of 40 % for the diatoms.

4.3. Backscattering fractions from the ASD measurements extrapolated to 0° - 180° by fitting Mie scattering functions: results

Table 3 presents several values for relevant backscatter to scatter fractions. The backscatter probability values (B) vary from 0.001 to 0.0356, i.e. a backscattering efficiency of 0.1 % to 3.56 %. The San Diego harbour samples range from 1.8% to 2 %. Thus, depending on the accuracy of these Mie fits to the measurements, assuming a San Diego Harbour value of 1.8% to be valid for suspensions of algae or silt may introduce errors of up to 95 % for *Melosira* and errors up to 98% for

(based on) Mie scattering function fit						
	B _{90/0}	B _{5/0}	B _{40/0}	B _{90/5}	B _{90/40}	λ
Freshwater algae						
CHLOROPHYTA-Chlorophyceae						
<i>Selenastrum capricornutum</i>	0.0356	0.8695	0.1346	0.0409	0.2644	633
<i>Volvox aureus</i>	0.0073	0.4423	0.0298	0.0165	0.2443	633
CYANOPHYTA-cyanophyceae						
<i>Anabaena flos-aquae</i>	0.0059	0.4355	0.0250	0.0135	0.2353	633
<i>Microcystis ridi</i> [*] (-gv)	0.0313	0.8647	0.1212	0.0362	0.2580	633
<i>Microcystis ridi</i> [*] (+gv)	0.0029	0.2234	0.0146	0.0128	0.1961	633
<i>Oscillatoria agardhii</i>	0.0205	0.8330	0.0873	0.0246	0.2350	633
PROCHLOROPHYTA-Prochlorophyceae						
<i>Prochlorothrix hollandica</i>	0.0139	0.4404	0.0576	0.0315	0.2406	633
CHRYSTOPHYTA-Bacillariophyceae (Diatoms)						
<i>Astrionella formosa</i>	0.0134	0.7704	0.0691	0.0174	0.1942	633
<i>Melosira granulata</i>	0.0010	0.7572	0.0082	0.0013	0.1226	633
Marine algae						
CHRYSTOPHYTA- Prymnesiophyceae						
<i>Emiliana Huxleyi</i> (+c)	0.0047	0.1294	0.0179	0.0362	0.2614	633
<i>Emiliana Huxleyi</i> (-c)	0.0059	0.1717	0.0216	0.0342	0.2719	633
<i>Phaeocystis pouchetti</i>	0.0236	0.6549	0.0770	0.0360	0.3061	633
CHRYSTOPHYTA-Bacillariophyceae (Diatoms)						
<i>Phaeodactylus</i>	0.0020	0.1109	0.0111	0.0178	0.1799	633
Estuarine mineral particles						
Silt (3-5 μ m)	0.0058	0.2357	0.0214	0.0246	0.2446	633
Silt (5-12 μ m)	0.0153	0.1464	0.0451	0.0105	0.3405	633
average	0.013	0.472	0.049	0.024	0.240	
standard deviation	0.010	0.284	0.039	0.011	0.051	
minimum value	0.001	0.111	0.008	0.001	0.123	
maximum value	0.036	0.870	0.135	0.041	0.341	
other values from literature:						
San Diego Harbor 1,2,3	Petzold ⁷	0.018-0.020			0.23	530
A1, A2,A3	Whitlock ¹¹	0.025-0.070			0.26-0.30	550
<i>Hymenomonas el.</i>	Bricaud ¹	0.0001				
<i>Platmonas sp.</i>	Bricaud ¹	0.0012-0.0016				
<i>Tetraselmis</i>	Bricaud ¹	0.0001-0.0002				

Table 3: the backscattering ratios calculated from the angular scattering distribution function measurements (15° - 165°) extrapolated to 0° - 180° by fitting Mie scattering functions, as well as some values from the literature.

Selenastrum. However, the accuracy of these measurements must be addressed stringently before these values may be used. A value of more interest is the average and the standard deviation of B for the 13 algae and 2 silt samples, which were 0.013 and 0.010 respectively. There is no apparent systematic effect in the distribution of low and high values for B over the various algal types, in contrast to the findings presented in table 1 and 2 and the previous section.

The B_{5/0} values give an indication of the fraction of scattering that is scattered outside of the range of 0° - 5°, e.g. the acceptance angle of a photomultiplier in a spectrophotometer (by calculating B minus 1 the percent of forward scattered light at 0°-5° is calculated). The silt samples, *Emiliana huxleyi*, *Phaeodactylum pouchetti* and *Microcystis* with gasvacuoles intact all have a small value for B_{5/0}, indicating that 75 - 90 % of light is scattered forward between 0° - 5°. For *Volvox*, *Anabaena* and *Prochlorothrix* about 55 % of light is scattered forward between 0° - 5°; for *Phaeocystis* it is around 35%

and for *Selenastrum*, *Microcystis* (with collapsed gasvacuoles), *Oscillatoria*, *Astrionella* and *Melosira* these values are around 15 - 25%.

The $B_{90/5}$ is a value that is often required when calculating backscattering from spectrophotometric measurements. If absorption is known, an attenuation scan of a sample in a cuvette will give $B_{90/5}$. To calculate B from $B_{90/5}$ this value of $B_{90/5}$ is required. These values are highly variable. In contrast the $B_{90/40}$ values are much more stable. The $B_{90/40}$ calculations may be used for a more reliable estimate of backscattering, by measuring a sample in a cuvette with and without an integrating sphere (e.g. an Ulbricht integrating sphere with an acceptance angle of scattering of 40°). For $B_{90/5}$ the average value is 0.024 with a σ of 0.011 amounting to a probable error of 46% and a range of 100%; for $B_{90/40}$ the average value is 0.24 with a σ of 0.051 amounting to a probable error of 21% and a range of 50 %. These last findings corroborate estimates by Dekker² which estimated the value to be 0.25 and the error to be 20% based on data from Petzold⁷ and Whitlock¹¹. The average value for $B_{90/40}$ for the algae dominant in the water of the inland waters study by Dekker² is equal to the average of the algae *Volvox aureus*, *Microcystis ridii* (with and without gasvacuoles), *Oscillatoria agardhii* and *Prochlorothrix hollandica*; i.e. 0.2348. Unfortunately more information is required for measurements or models of light properties in shallow inland waters, because no information is yet available on the ASD or (N)VSF of algal, plant and peat detritus which usually composes 70% of the seston dry weight³ as opposed to 30 % for the algae.

5. CONCLUSIONS AND RECOMMENDATIONS

All measured ASD functions samples show a strong peak in the forward direction. Compared to the San Diego ASD function at forward angles *Phaeodactylum* and *Prochlorothrix hollandica* lie higher and *Microcystis sp.* lie lower. The other samples show a more or less similar shape of scattering in near forward directions. The San Diego ASD function is rather flat at backward angles. All samples except silt (3-5 μm) show an increase at backscatter angles from 120° upwards. Thus it is in the backscattering region where the samples deviate most from the San Diego ASD (calculated from his VSF) from Petzold⁷. Differences between the algal and silt measurements and the San Diego function at 165° (highest measurement angle) are up to a factor of two or more. For forward scattering the differences are from a factor 3 lower (for silt (5-12 μm) to a factor 10 higher for *Phaeodactylum*. For *Microcystis sp.*, *Oscillatoria agardhii*, *Prochlorothrix hollandica*, *Selenastrum* and silt (3-5 μm) the differences are within a factor 2.

The ASD measurements were extrapolated to the full $0^\circ - 180^\circ$ range through fitting Mie scattering functions to these measurements. In most cases, the results of Mie calculations produce good fits to the measured data.

The partial backscattering to scattering fractions (B') over $15^\circ - 165^\circ$, from the ASD measurements show that all the freshwater, marine algae and the finer silt sample have a B' of 21 % with a σ of 1.6%. The diatoms have a B' of 13.4 % with a σ of 0.2 %. The San Diego Harbour sample has a B' of 18.8 %. These values indicate strongly that using only a San Diego harbour B' may introduce errors up to 65 %, with an average error of 11 % for all the algae, except the diatoms; and with an average error of 40 % for the diatoms.

The backscatter probability values (B), calculated using the Mie fitted data, vary from 0.1 % to 3.56 %. The San Diego harbour samples range from 1.8% to 2 %. Therefore assuming a San Diego Harbour value of 1.8% to be valid for suspensions of algae or silt may introduce significant errors. The average and the standard deviation of B for the 13 algae and 2 silt samples, were 0.013 and 0.010 (σ) respectively.

The $B_{5/0}$ values give an indication of the fraction of scattering that is scattered outside of the range of $0^\circ - 5^\circ$, e.g. the acceptance angle of a photomultiplier in a spectrophotometer. The silt samples, *Emiliana huxleyi*, *Phaeodactylum pouchetti* and *Microcystis* with gasvacuoles intact all have a small value for $B_{5/0}$, indicating that 75 - 90 % of light is scattered forward between $0^\circ - 5^\circ$. For *Volvox*, *Anabaena* and *Prochlorothrix* about 55 % of light is scattered forward between $0^\circ - 5^\circ$; for *Phaeocystis* it is around 35% and for *Selenastrum*, *Microcystis* (with collapsed gasvacuoles), *Oscillatoria*, *Astrionella* and *Melosira* these values are around 15 - 25%.

The $B_{90/5}$ is a value that is highly variable. In contrast the $B_{90/40}$ values are much more stable. The $B_{90/40}$ calculations may be used for a more reliable estimate of backscattering, by measuring a sample in a cuvette with and without an integrating

sphere. For $B_{90/5}$ the average value is 0.024 with a σ of 0.011 amounting to a probable error of 46% and a range of 100%; for $B_{90/40}$ the average value is 0.24 with a σ of 0.051 amounting to a probable error of 21% and a range of 50 %.

More information is required for measurements or models of light properties in shallow inland waters, because no information is yet available on the ASD or (N)VSF of algal, plant and peat detritus which usually composes 70% of the seston dry weight³ as opposed to 30 % for the algae.

The laboratory set-up should be improved to enable measurement at more forward and backward angles. Adding a tuneable dye laser to the configuration would enable more analysis of the spectral sensitivity of the measured and calculated values.

Once the simultaneously measured spectrophotometric measurements (of beam attenuation with and without an integrating sphere) have been processed and published, the actual volume scattering may be calculated. Also it then becomes possible to calculate scattering efficiencies, which will play an important role in analytical remote sensing of water quality algorithm development.

6. ACKNOWLEDGEMENTS

The Netherlands Remote Sensing Programme financed parts of this research. R. Wouts of the NIOO-CEMO and F. Charlton of the IFE provided the algal and silt samples.

7. REFERENCES

1. Bricaud, A., Morel, A., and Prieur, L. "Optical efficiency factors of some phytoplankters". *Limnol. Oceanogr.* 28(5):816-832, 1983.
2. Dekker, A.G. *Detection of optical water quality parameters for eutrophic waters by high resolution remote sensing*. Vrije Universiteit, Amsterdam, The Netherlands. PhD.Thesis. 1993.
3. Gons, H.J., Burger-Wiersma, T., Otten, J.H., and Rijkeboer, M. "Coupling of phytoplankton and detritus in a shallow, eutrophic lake (Lake Loosdrecht, The Netherlands)." *Hydrobiologia* 233:51-59, 1992.
4. Kuik, F. *Single scattering of light by ensembles of particles with various shapes*. Vrije Universiteit, Amsterdam, . 1992.
5. Kuik, F., Stammes, P., and Hovenier, J.W. "Experimental determination of scattering matrices of water droplets and quartz particles. *Appl. Opt.*" 30:4872-4881, 1991.
6. Morel, A. and Bricaud, A. "Inherent optical properties of algal cells including picoplankton: theoretical and experimental results". *Can. Bull. of Fish. and Aquat. Sc.* 214:521-559, 1986.
7. Petzold, T.J. "Volume scattering functions for selected ocean waters". San Diego: Scripps Inst. Oceanogr. Visibility Lab. . 1972.
8. Schreurs, R. *Light scattering by algae: fitting experimental data using Lorentz-Mie theory*. Vrije Universiteit, Amsterdam, The Netherlands. :1-68 + app.. MSc.Thesis. 1996
9. Stammes, P. *Light scattering properties of aerosols and the radiation inside a planetary atmosphere*. Vrije Universiteit, Amsterdam, The Netherlands. . PhD.Thesis. 1996
10. Volten, H., De Haan, J.F., Hovenier, J.W., Vassen, W., Schreurs, R., Dekker, A.G., Hoogenboom, H.J., Charlton, F., and Wouts, R. "Laboratory measurements of angular distribution of light scattered by phytoplankton and silt". *submitted to Limnol. & Oceanogr.*
11. Whitlock, C.H., Poole, L.R., Usry, J., Houghton, W.M., Witte, W.G., Morris, W.D., and Gurganus, E.A. "Comparison of reflectance with backscatter and absorption parameters for turbid waters". *Appl. Opt.* 20(3):517-522, 1981.

Absorption modelling in Case II waters: the need to distinguish Coloured Dissolved Organic Matter from Non-Chlorophyllous Particulates.

M.D.Dowell¹*, J-F.Berthon²* and N.Hoepffner*, S.Grossi*

¹University of Southampton, Southampton Oceanography Centre, European Way, Southampton, SO14 3HZ, UK

²Baltic Sea Research Institute, Seestrasse 15, D-18119 Rostock-Warnemünde, Germany.

*Marine Environment Unit, Space Applications Institute, JRC Ispra Site, TP272, Ispra, I-21020, (VA), Italy.

ABSTRACT

The presented study examines, for substantial datasets in different Case II waters, the variability of the spectral absorption of Non Chlorophyllous Particles (NCP) and Coloured Dissolved Organic Matter (CDOM). The investigation has considered the validity of the currently proposed modelling of the absorption of these two components as a single variable, in applications to Case II water environments. In order to encompass a broad range of environmental situations (within coastal Case II waters) in the comparison of NCP and CDOM absorption spectra, two very different sites were selected. The locations investigated were the Southern Baltic Proper and a site in the Northern Adriatic close to the Italian coast. These two regions differ both in their basic oceanographic properties and in their relative proportions of Optically Active Components (OAC). Furthermore, the datasets considered illustrate the variability at different scales in both space and time, combining a series of seasonal oceanographic campaigns in the Baltic with a complete annual timeseries of monthly measurements at a fixed point in the Adriatic. The analysis has shown that, in the selected European Case II waters, the observed variability of the spectral absorption of NCP and CDOM, both with respect to each other as well as to the total absorption, are independent. It is therefore suggested that, in the frame of Reflectance modelling in Case II waters, attention must be placed on accounting for NCP and CDOM individually when defining the absorption segment.

Keywords: Absorption modelling, Case II waters, Inherent Optical Properties, Coloured Dissolved Organic Matter, Non Chlorophyllous Particles, Baltic, Adriatic.

1. INTRODUCTION

A general formulation relating Reflectance (R) to the Inherent Optical Properties: absorption (a) and backscattering (b_b) was defined by Gordon et. al.¹ through Monte Carlo simulation:

$$R = f \times \frac{b_b}{a + b_b}$$

in general $a \gg b_b$ (except in very turbid sediment laden waters e.g. certain parts of the Northern Sea) and therefore, as described by Morel and Prieur² $R = f \times b_b/a$ where these authors found f to be equal to 0.33 (this value has since proven to be variable³ and dependent on water composition and illumination conditions).

The absorption segment of the above relationship has it's own budget, comprising of n components which are linearly related so that:

$$a_{TOT}(\lambda) = \sum_{i=1}^n a_i(\lambda)$$

where the overall budget has been shown to be adequately described by the following components in different investigations (e.g. Sathyendranath et. al. 1989⁴):

$$a_{TOT}(\lambda) = a_{CPIG}(\lambda) + a_{NCP}(\lambda) + a_{CDOM}(\lambda) + a_w(\lambda)$$

the subscripts TOT, CPIG, NCP, CDOM and w refer to different sections of the absorption segment namely Total, Chlorophyll like Pigments, Non-Chlorophyllous Particulates, Coloured Dissolved Organic Matter and water respectively. Some authors have tried to refine this differentiation even further such as Bukata⁵ who proposed a four component model excluding water which he also differentiated the NCP fraction into organic and inorganic particulates.

However, recently several authors have proposed what have been termed as two component models^{6,7} in which the modelisation of the absorption of the above relationship is defined by two components CPIG and DP (Detrital Products),

where DP are a combination of NCP and CDOM. These modelisations of absorption were principally defined for Case I (oceanic) waters however their validity must also be tested in Case II (coastal) waters. The principle rationale behind the grouping together of these two components in the above mentioned model is that apart from the fact (purely by the definition of Case I waters) that in the open ocean these two components covary implicitly with C_{PIGS}, a fact which has recently been explicitly used⁸ in defining an expression for retrieving DP in Case I waters, is that these two components are very similar spectrally in their absorption properties. More specifically both of these components can be adequately (or have been shown to be to date) described by an exponential decay fit (e.g. Roesler (1995)⁹), although recent comparisons with Target Factor Analysis¹⁰ have shown that the RMS error on the determinations of the fit can be improved, with such techniques.

The principle objective of the current study is to present a series of quality datasets for different geographic regions in predominantly Case II waters (although the Adriatic platform is considered as being in certain seasons Case I). The data are continuous measurements of spectral absorption in the range 400 to 700nm for C_{PIG}, NCP and CDOM. These datasets will therefore allow the authors to accomplish the following analyses. An investigation and description of the variability of spectral shape and amplitude for the two sites selected (Baltic and Adriatic) of the three components (C_{PIG}, NCP and CDOM). Subsequently, considerations will be made on the contribution of each of the components to the total $a(\lambda)$ budget, considering site and seasonal variations. Finally the best exponential fits for all CDOM and NCP spectra are determined and a study, of both the slope and a specific value of absorption for the two types of spectra through analyses of variance and covariance for the two locations, is undertaken.

2. METHODS, SITES AND SAMPLING

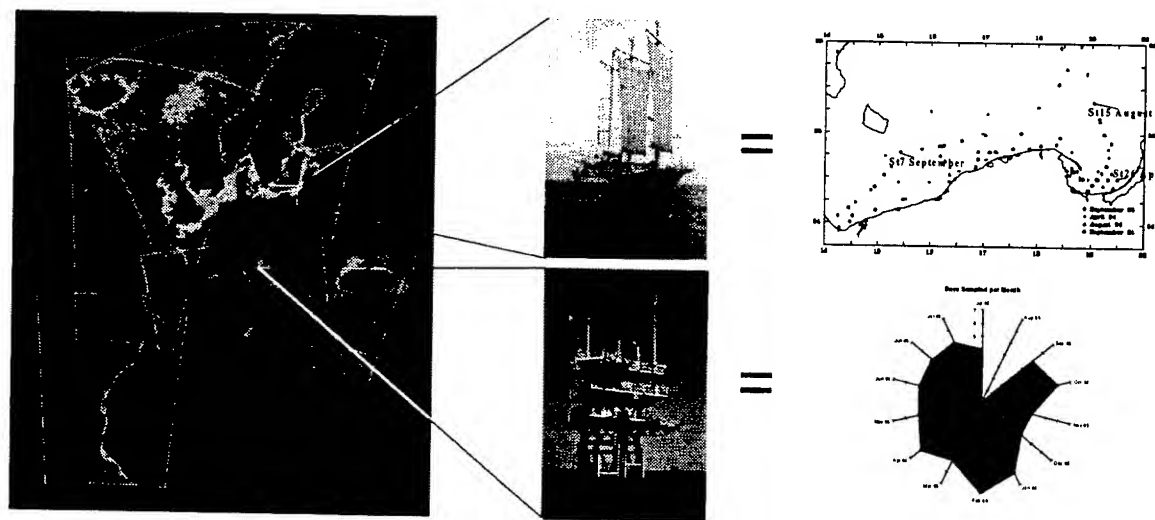


Figure 1: CZCS 7 year composite showing sites, station maps and sampling times

2.1. Methods

The samples for CDOM were filtered through 0.22 μ m Millipore filters and were stored in glass amber bottles at 4°C with the addition of 0.5ml of NaN₃ (sodium azide) as an inhibitor of anaerobic growth all samples were analyzed within one week of collection (within time determined by predefined protocol¹¹). A Perkin Elmer Lambda 19 dual beam spectrophotometer with a 10 cm quartz cuvette was used to determine the absorption spectra of the sample (MilliQ water was used as a blank). In the investigations described here the measurements were made in the range 350 to 700nm, with a spectral resolution of 1nm. Absorbance was subsequently converted into absorption coefficient (m^{-1}) using the expression:

$$a_{CDOM}(\lambda) = 2.3 \times A(\lambda) / L$$

where $A(\lambda)$ is the Absorbance (optical density) and L is the pathlength in metres (i.e. $L=0.1$ in our analyses).

Absorption measurement for CPIG and NCP were not carried out with the standard solvent extraction process for pigment removal on glass fibre filters, but an alternative approach specifically designed for Case II waters was used to account for possibly high suspended sediment concentrations. The filtrations were made on Whatmann GFF (Glass Fibre Filters), the samples were then frozen in liquid nitrogen and put in the freezer at -20°C on return to the laboratory. The measurements were made as for the CDOM with a Perkin Elmer Lambda 19 dual beam spectrophotometer equipped with a 60mm integrating sphere, so as to remove the spurious contribution to the measured absorption caused by the sample backscattering. The Chlorophyll pigment spectra was extracted from the total particulate absorption spectra by bleaching the sample with a NaClO solution allowing for a depigmentation of the particles. The pigment spectra is therefore obtained by subtracting the bleached Non-Chlorophyllous Particles from the total absorption spectra. Further details on this alternative technique are given by Tassan and Ferrari¹². The absorption spectra of the particles retained on the filter are converted into an equivalent particle suspension absorption, using an empirical expression defined in the above mentioned study:

2.2. Sites and Sampling

The dataset presented here for the Southern Baltic Region (as shown in Figure 1) are the result of a collaborative agreement between the Institute of Oceanology of the Polish Academy of Science and the then Institute for Remote Sensing Applications (now Space Applications Institute (SAI)) of the Joint Research Centre in Ispra. Four cruises were carried out on-board *r/v Oceania* one in September 1993 and three in 1994 (April, August and September). Station positions (as in Figure 1) were not fixed before the campaigns, and a principle aim was to collect a dataset representing the largest possible gradients in the measured parameters in order to adequately characterize the notable contribution by terrestrial inputs as well as the marine autochthonous contribution.

The datasets presented for the Northern Adriatic were taken at the fixed platform "Acqua Alta" belonging to the Italian National Research Council. The project under which the measurements were made is the CoASTS (Coastal Atmosphere and Sea Time-Series) project¹³ between SAI JRC and the Institute for the Study of Large Masses, of the Italian National Research Council in Venice. The CoASTS project started in September 1995 (pilot campaign in July 1995) and will continue until September 1997. Monthly campaigns are made involving high quality atmospheric and oceanographic (bio-optic) measurements to support calibration/validation activities for SeaWiFS, OCTS and MOS ocean colour sensors. The site itself is at the geographic position lat. $45^{\circ}19'$ long. $12^{\circ}30'$ at about 30km offshore from the Venice Lagoon. The region is, depending on the prevailing currents, characterised by Case I or Case II waters. The site is considered to be well representative of the entire Adriatic Sea. Some typical values for the location include temperature in the range $4-26^{\circ}\text{C}$, salinity: 32-36 ppt., chlorophyll concentrations in the range $0.1-2 \text{ mg/m}^3$, sediment concentrations in the range $1-5 \text{ g/m}^3$ and CDOM absorption coefficients at 400nm of $0.07-0.45 \text{ m}^{-1}$.

3. RESULTS

3.1. The variability of shape and magnitude of the three components

Figure 2 represents specific and normalised (at 440nm) absorption spectra for the three components. For both the considered sites these show a reasonable degree of variability both in magnitude and for the CDOM and NCP spectra in shape as well. However, the NCP and CDOM spectra do appear to maintain the standard exponential decay general attributed to them. In the CPIG spectra there is less variability in the overall shape and the largest variability in overall magnitude seems to be at the two peaks in the blue 443nm and in the red at about 670 nm. The slight deviation from the mean trend of the CPIG absorption spectra which occurs around 420nm for some particular stations seems to coincide samples during highly productive circumstance.

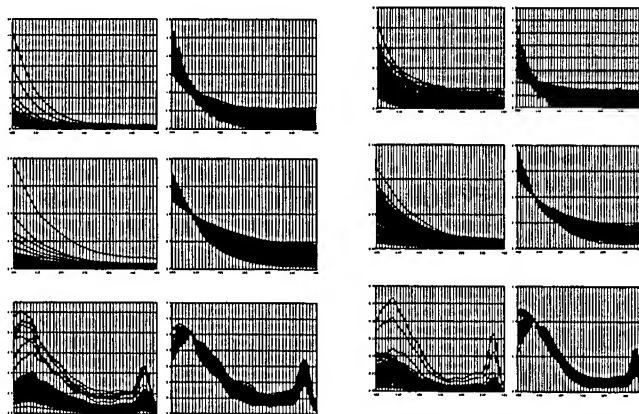


Figure 2a: Baltic absorption spectra

Figure 2b: Adriatic absorption spectra

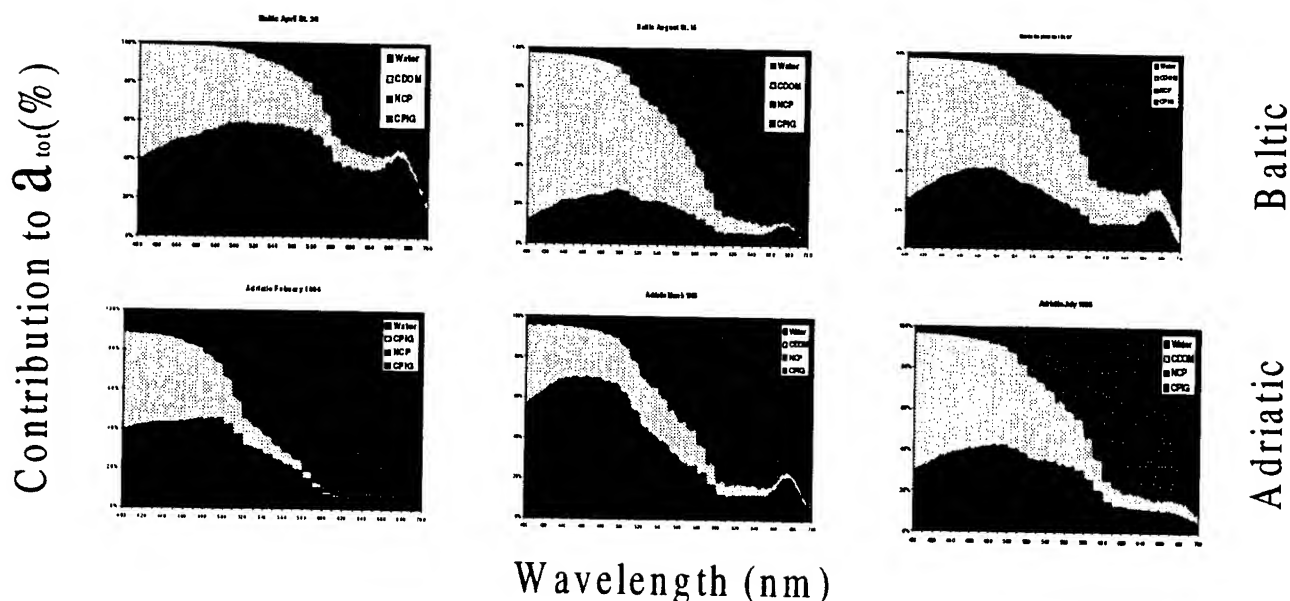


Figure 3: % contribution to the total absorption of the three components

3.2. The relative contribution of the three components to the total absorption

Figure 3 shows plots illustrating the contribution of the three components to the total absorption as a percentage of the total absorption including water (three for the Baltic and three for the Adriatic). The stations included as Baltic examples have been highlighted on the map in Figure 1. Several significant points are quite obvious from these plots: firstly it is apparent that there exists a large variability in the contribution of the individual components to the total absorption. These differences are apparent both on seasonal and geographical (for the Baltic) scales. The dominant component in total absorption budget may vary significantly from one season to another. For example, although CDOM is the dominant constituent in the Baltic, the plot for station 26 in April would seem to suggest that there is a significant contribution by the NCP as well especially in the green area of the spectrum. For the Adriatic plot, an interesting combination is presented. In each of the graphs shown (February, March and July) different dominant constituents are observed. Thus, this highlighting the strong seasonal variation in the absorption budget, with NCP absorption dominating in the Winter month (February), CPMG absorption in spring during the bloom period and CDOM absorbing more during the summer.

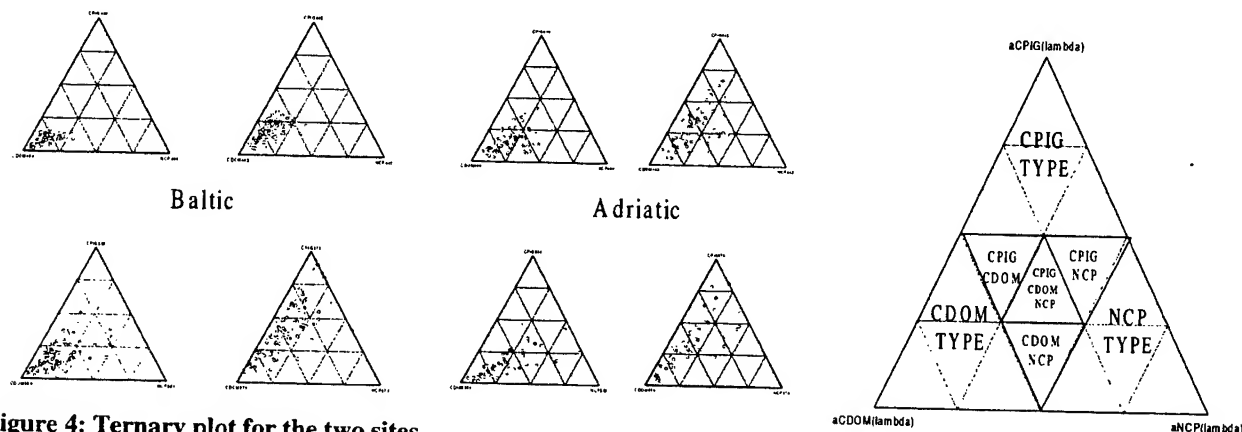


Figure 4: Ternary plot for the two sites

Figure 4 b proposed classification

3.3. Mixture plots: considerations on the absorption budget in different parts of the spectra, a potential method for sub-classifying Case II waters

The investigation using ternary/mixture plots has shown to be most useful in interpretations of the absorption budget for specific wavelengths here coinciding with (or near to) channels from typical ocean-colour sensors. The general picture for the two sites would seem to prominence of the variability shown in the red wavelengths (this may be of significant importance in Reflectance modelling of Case II coastal waters). The dominance of the CDOM absorption at the blue wavelength for the Baltic and to a lesser extent for the Adriatic is quite clearly shown. For both sites, there is a slight

	Baltic						Adriatic					
	A350(CDOM)	S350(CDOM)	A400(CDOM)	S400(CDOM)	A400(NCP)	S400(NCP)	A350(CDOM)	S350(CDOM)	A400(CDOM)	S400(CDOM)	A400(NCP)	S400(NCP)
Mean	3.2763	0.0212	1.1668	0.0188	0.1528	0.0116	0.3498	0.0186	0.1406	0.0176	0.0478	0.0135
Std. Dev.	3.9888	0.0017	1.5682	0.0029	0.2178	0.0026	0.1683	0.0029	0.0583	0.0044	0.0252	0.0026
Variance	15.9107	0.0000	2.4594	0.0000	0.0474	0.0000	0.0283	0.0000	0.0034	0.0000	0.0006	0.0000
Minimum	1.3871	0.0183	0.4781	0.0081	0.0353	0.0049	0.1372	0.0106	0.0520	0.0101	0.0070	0.0088
Maximum	30.2913	0.0280	12.1913	0.0254	1.7977	0.0168	1.0282	0.0281	0.3746	0.0258	0.1267	0.0191
Coeff. of Variation	1.2175	0.0806	1.3441	0.1548	1.4251	0.2288	0.4810	0.1585	0.4145	0.2487	0.5271	0.1898

	Baltic	
	aCDOM(400) vs. aNCP(400)	SCDOM(400-600) vs. SNCP(400-600)
No. Obs.	88	88
F	51.85	3.21
Fcrit	1.42	1.42
	Adriatic	
	aCDOM(400) vs. aNCP(400)	SCDOM(400-600) vs. SNCP(400-600)
No. Obs.	64	64
F	5.35	2.89
Fcrit	1.52	1.52

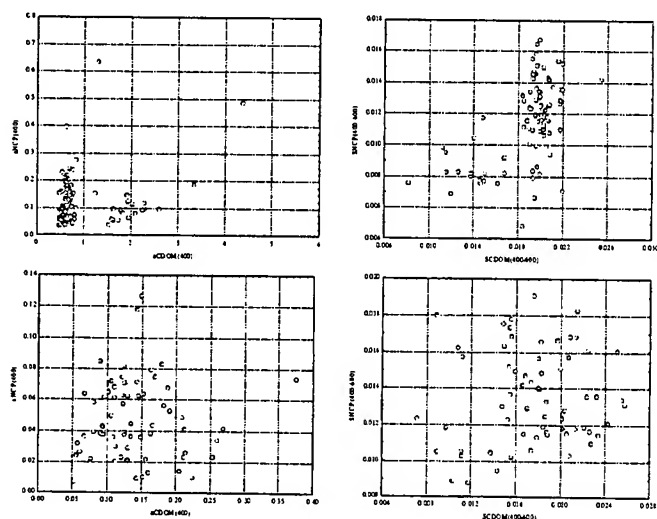
tendency toward NCP at 550nm, although neither of these locations can be considered as sediment dominated waterbodies. As mentioned above, the plot for 670nm shows the largest degree of variability for the datasets considered although the values are concentrated on the CDOM CPIG side of the plot. Ensuing the use of mixture plots in this investigation, it is suggested that, their use may be useful for classification purposes. This technique, already proposed by Prieur and Sathyendranath¹⁴ for a generic marine classification, has here shown its value in sub-classifying Case II waters. Figure 4b shows the proposed classification scheme using the nomenclature adopted in this investigation.

3.4. The variance of a_{CDOM} and a_{NCP} and their covariance with a_{TOT}

Figure 5 shows tables and graphs illustrating the results from the statistical analysis carried out on the CDOM and NCP absorption spectra. The data analysed involve the slope of the exponent and a specific value of absorption retrieved from the fit on the measured absorption spectra. This provided a substantial data set of 88 samples for the Baltic and 64 for the Adriatic. The datasets included distinct values of a_{CDOM}(400), a_{NCP}(400), S_{CDOM}(400-600) and S_{NCP}(400-600) values for a_{CDOM}(350) and S_{CDOM}(350-400) were also included to verify for any large variations in the slope of the CDOM spectra. The exponential fit used for the measured datasets was the following:

$$a_{CDOM}(\lambda) = a_{CDOM}(\lambda_0) \times e^{(-S(\lambda - \lambda_0))} + C$$

Figure 5: 1Scatter plots of the relationship between a_{CDOM} and a_{NCP}



for CDOM, and:

$$a_{NCP}(\lambda) = a_{NCP}(\lambda_0) \times e^{(-S(\lambda - \lambda_0))}$$

for NCP. Here λ_0 and S refer to the values of the specific absorption coefficient and the slope respectively. The value C in the fit for CDOM absorption represents a constant included to improve the fit, and which is proportional to the baseline occurring in the red part of the spectra. This feature is not included in the subsequent analysis as it is interpreted as being an artifactual contribution resulting from instrumental noise or very fine particles (in fact this feature is further minimized by refiltration through 0.1 μm nucleopore filter). The results from the statistical analysis indicate some very clear findings, namely that there is little or no common relationship in variability between the both the specific value of absorption and the slopes of the two datasets (NCP and CDOM). This is shown under many different forms, principally by the large scatter shown in the plots and the results from the F-test in which the calculated values of F are consistently higher than F_{crit} there rejecting the null hypothesis ($\text{varCDOM} = \text{varNCP}$).

4. CONCLUSIONS AND FUTURE WORK

4.1. Conclusions

The presented study has shown the need to independently describe the contributions to the total absorption budget of surface Case II waters by NCP and CDOM. The ranges means and standard deviations found are in some cases substantially different to those presented in literature, indicating that allocating a mean slope in the modelisation of the absorption of these parameters may represent a considerable source of error. The results have further shown the importance of these two components in the composition of Case II waters, where either of these constituents can prove to be dominant in the budget of the total absorption. The analyses of the variance coefficients has shown that it is incorrect to assume the covariability of the two components or that there is a seasonal variability as there are strong gradients in the variables considered for the two datasets showing no relationship whatsoever (within 95% confidence levels).

The results from the ternary/mixture plots has indicated the potential of 670nm, and the red part of the spectra in general, in describing and differentiating the different components (this has already indirectly been observed in Case II waters through the development of empirical algorithms¹⁵). This fact is obviously of considerable importance in the formulation of models for water bodies exhibiting a large degree of variability of the three components. However, assurances must be given on data quality for this part of the spectra, with considerations made on noise and contamination effects.

Therefore in conclusion the results would infer that it is necessary to account for NCP and CDOM absorption distinctly when developing forward reflectance models for waters determined as being Case II. And that although a balance must be maintained between the accuracy of the definition of each individual component in the forward reflectance model with the minimisation of the unknowns in the IOPs for inversion. The considerable importance of terrigenous and atmospheric inputs, both particulate and dissolved, mean that in these coastal regions for an accurate determination and characterisation of the OACs it may be more significant to give priority to the description of the variability of the of NCP and CDOM components and to limit the number of variables used to define the CPIG absorption. In fact it has already been shown⁹ that in models dealing with localized areas which are necessary for these types of Case II waters the CPIG absorption can be adequately defined by a mean spectra and variability at one specific wavelength, Figure 2 here shows this as a possible solution for both the Adriatic and the Baltic spectra.

4.2. Future work

The presented study involves only a first part of a thorough investigation of the absorption budget in the two regions considered. Further investigations will include topics such as investigations of diverse models representing the spectral characteristics of each of the components including approaches similar to that suggested by J. Krijgsman¹⁰ (Target Factor Analysis). A further direction in which the work will progress is a verification that the absorption calculated by the sum of the three components presented here sufficiently describes the total absorption for the areas presented (as well as others). An initial verification of the calculation of the absorption budget could be made through a simple closure experiment using a submersible multispectral absorption meter and comparing the result from this to the summation of the analyses made on the individual components as described here

5. ACKNOWLEDGMENTS

The authors wish to thank all the people who participated in the two activities which were fundamental in creating the datasets used in this investigation. In particular to the staff of the Institute of Oceanology of the Polish Academy of Science and the crew of *r/v Oceania* for the work in the Baltic and G.M.Ferrari for his work on the Baltic datasets, and to G. Zibordi responsible for coordinating the CoASTS project and D. van der Linde for his numerous trips to the platform.

6. REFERENCES

1. H. R. Gordon, O. B. Brown and M. M. Jacobs, "Computed relationships between the inherent and apparent optical properties in a flat homogeneous ocean", *Appl. Optics*, **14**(2), 417-427. (1975).
2. A. Morel and L. Prieur, "Analysis of variations in ocean color", *Limnol. Oceanogr.* **22**, 709-722 (1977).
3. A. Morel and B. Gentili, "Diffuse reflectance of oceanic waters. II Bidirectional aspects", *Appl. Optics*, vol. **32**, no. 33 6865-6879 (1993).
4. S. Sathyendranath, L. Prieur and A. Morel, "A three-component model of ocean colour and its application to remote sensing of phytoplankton in coastal waters." *Int. J. Remote Sensing*, vol. **10**, No. 8, 1373-1394. (1989)
5. R. P. Bukata, J. H. Jerome, J. E. Bruton, S. C. Jain and H. H. Zwick, "Optical water quality model of Lake Ontario. 1: Determination of the optical cross sections of organic and inorganic particulates in Lake Ontario". *Appl. Opt.* **20**(9), 1696-1703, (1981)
6. K. L. Carder, S. K. Hawes, K. A. Baker, R. C. Smith, R. G. Steward and B. G. Mitchell. "Reflectance model for quantifying chlorophyll a in the presence of productivity degradation products", *J. Geophys. Res.* **96**, 20599-20611 (1991).
7. J. Aiken, G. F. Moore, C. C. Trees, S. B. Hooker and D. K. Clark, "The SeaWiFS CZCS-Type Pigment Algorithm." NASA Tech. Memo. 104566, Vol. 29, S. B. Hooker and E. R. Firestone, Eds., NASA Goddard Space Flight Center , Greenbelt, Maryland, 34 pp., (1995).
8. A. D. Giles-Guzmán and S. Alvarez-Borrego, "Covariance of the absorption of phytoplankton, colored dissolved organic matter, and detritus in case I waters, as deduced from the Coastal Zone Color Scanner bio-optical algorithm.", *Appl. Opt.*, **35**(12), 2109-2113, 1996.
9. C.S. Roesler and M.J. Perry, "In situ phytoplankton absorption, fluorescence emission, and particulate backscattering spectra determined from reflectance." *J. Geophys. Res.*, vol. **100**, No. C7, pp. 13279-13294. (1995)
10. J. Krijgsmann, *Optical Remote Sensing of Water Quality Parameters: Interpretation of Reflectance Spectra*. Delft University Press-II1. Thesis Delft University of Technology, p.198. (1994)
11. G. M. Ferrari and S. Tassan, "On the accuracy of determining light absorption by 'yellow substance' through measurement of induced fluorescence." *Limnol. Oceanogr.*, **36**, 777-786, (1991)
12. S. Tassan and G. M. Ferrari, "An alternative approach to absorption measurements of aquatic particles retained on filters", *Limnol. Oceanogr.* **40**, 1358-1368 (1995).
13. G. Zibordi, V. Barale, G. M. Ferrari, N. Hoepffner, D. van der Linde, L. Alberotanza, P. Cova and C. Ramasco, "Coastal Atmosphere and Sea Time-Series Project (CoASTS): an ocean colour remote sensing calibration/validation project." Proc. of Third Thematic Conf. on Remote Sensing for Marine and Coastal Environments, Seattle, Vol. II, pp. 96-100. (1995)
14. L. Prieur and S. Sathyendranath, "An optical classification for coastal and oceanic waters based on specific spectral absorption curves of phytoplankton pigments, dissolved organic matter , and other particulate materials." *Limnol. Oceanogr.*, **26**(4), pp.671-689. (1981)
15. H. Siegel, M. Gerth and M. Beckert. "The variations of optical properties in the Baltic Sea and algorithms for the application of remote-sensing data", *Ocean Optics XII, SPIE* **2258**, 894-905 (1994).

Retrieval of chlorophyll concentration via inversion of ocean reflectance
- a modelling approach.

Peter R.C.S. Fearn and Mervyn J. Lynch.

Remote Sensing and Satellite Research Group,
School of Physical Sciences, Curtin University of Technology,
GPO Box U1987, Perth, Western Australia 6102

ABSTRACT

1996 marks the revival of the production of visible channel imagery of the ocean with the planned launches of Japan's ADEOS Ocean Colour Temperature Sensor (OCTS), SeaWiFS (Sea-viewing Wide Field-of-view Sensor), and the EOS MODIS-N, with launch dates 1996, 1997 and 1998 respectively. At least three other missions are at various stages of planning. The missions will initiate a continuous global time series of ocean colour data that should extend well into the next century.

The classification of water types and application of pigment retrieval algorithms specific to those water types may increase the accuracy of retrieved pigment concentrations. The aim is to develop a pigment concentration retrieval algorithm tuned to local oceanic conditions.

Investigation of the effects of the physical and optical properties of the ocean on the water-leaving radiance, and the development of an inversion scheme for measurement of those physical and optical properties may be achieved through modelling. This approach also aids the design of validation programs.

A simple relationship has been found for predicting the reflectance of the ocean for different optical properties. The applicability of this relationship to chlorophyll concentration retrieval is being investigated.

A multiple channel reflectance inversion has been used to derive pigment concentrations from model results. Preliminary results show that the scheme is sensitive to uncertainty in optical properties of water constituents. The scheme does however provide some indication of the confidence limits applicable to the retrieved concentration.

Keywords: ocean colour, chlorophyll, reflectance, SeaWiFS, absorption, scattering

1. BACKGROUND

Passive remote sensing of ocean colour relies on the sunlight backscattered from the ocean to convey information about optically active marine constituents. Water, dissolved matter and particulate matter scatters as well as absorbs light. Differences in the spectral absorption and scattering properties between various oceanic constituents may allow us to infer the concentrations of a number of pigments from the water-leaving radiance signal¹.

Many workers^{2,3,4} have shown that the reflectance of the ocean just below the surface is given by

$$R(\lambda) = F \frac{b_b(\lambda)}{a(\lambda)} \quad (1.)$$

where $b_b(\lambda)$ is the spectral total backscattering coefficient of the ocean and its optical constituents (including phytoplankton, detritus and sediment), and $a(\lambda)$ is the sum of the spectral absorption coefficients of water and its constituent pigments (including chlorophyll-a, detritus and yellow substance). Each may be expressed as the sum of the coefficients for clear water, and those for each constituent multiplied by the concentration of each respective constituent.

$$b_b(\lambda) = b_{bw}(\lambda) + Cb_{bc}^*(\lambda) + \dots \quad (2.)$$

$$a(\lambda) = a_w(\lambda) + Ca_c^*(\lambda) + Ya_y^*(\lambda) \dots \quad (3.)$$

where the subscripts w , c and y refer to water, chlorophyll and yellow stuff respectively, and the coefficients with superscript asterisks are specific (per unit concentration) values. C is the concentration of chlorophyll, and Y , yellow stuff. Each series of coefficients may be extended to include more constituents and their concentrations.

The constant F in equation 1 is agreed to be reasonably well approximated by the value 0.33 for the situation when the sun is at the zenith, and with this value the spectral reflectance of the ocean may be estimated. The value of F however is not sufficiently well known to permit inversion of the system and retrieval of concentration values.

Gordon⁵ investigated the reflectance of the ocean at various optical depths for different illumination conditions. He shows that the ocean reflectance may be expected to be proportional to $b_b/(a+b_b)$ so that equation 1 may be restated as

$$R = F_G \frac{b_b}{a + b_b} \quad (4.)$$

where F_G is used to differentiate between F in equation 1.

Gordon⁵ used a Monte Carlo model to investigate the relationship between the ratio $b_b/(a+b_b)$, illumination conditions, and the reflectance at various optical depths. His equation for the reflectance of the ocean at optical depth zero and the sun at zenith is,

$$R = 0.001 + 0.3244X + 0.1425X^2 + 0.1308X^3 \quad (5.)$$

where X is $b_b/(a+b_b)$.

2. MONTE CARLO OCEAN OPTICAL MODEL

A Monte Carlo model has been developed and used in preliminary investigations of the spectral reflectance and water leaving radiance distributions of typical ocean waters⁶.

The ocean model determines the spectral reflectance at the ocean surface and with depth, spectral diffuse attenuation coefficient with depth, the spectral three dimensional light field above and below the surface, and the spectral Bi-directional Reflectance Distribution Function (BRDF) for use in the atmospheric model.

The model expects as input a solar beam, or a sky radiance distribution. The ocean surface may be a flat Fresnel surface, or a wind roughened surface⁷. Concentrations of optical constituents (chlorophyll, yellow stuff, sediment) are specified, as well as a volume scattering function (VSF) (at 5° or 1° resolution), to determine total absorption and scattering coefficients. The VSFs are taken from Gordon⁵ and from Petzold⁸.

Fig 1 shows a representation of the three dimensional water leaving radiance distribution as well as the below surface radiance distribution. The model was run with the sun at 40 degrees from the zenith to the left side of the picture.

Knowledge of the three dimensional variation in water-leaving radiance will enable us to more adequately correct the measured radiance for variations due to illumination and viewing geometry.

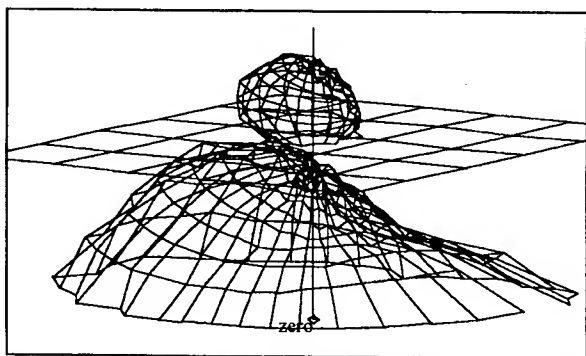


Fig 1 Three dimensional below surface and water-leaving radiance distribution. The surface representing the below surface radiance distribution is created by the tip of the radiance vectors originating at the point marked zero. The surface representing the water-leaving radiance distribution is created by the tips of the radiance vectors originating at the intersection of the vertical axis and the water surface.

A smoothing process is carried out when creating the water-leaving radiance data used to calculate the BRDF. This BRDF may be used by an atmospheric model created by Davies and Lynch⁹ in calculating the top-of-atmosphere radiance field.

3. INVESTIGATION OF REFLECTANCE EQUATIONS

The ocean optical model has been used to investigate the value of F in equation 1 and F_G in equation 4 for a range of water constituents concentrations and different VSFs. The model was run to determine the reflectance just below the surface. The reflectance value was then divided by b_b/a to determine F . Fig 2 shows the value of F in equation 1 as a function of b_b/a .

The ocean optical model was run for water containing chlorophyll concentrations varying from 0.01 to 50 mg m⁻³, and three different volume scattering functions, KA and KB from

Gordon⁵, and “tongue of the ocean” from Petzold⁸. The sun was at the zenith with no atmosphere.

As the backscattering coefficient decreases the error in the Monte Carlo derived reflectance increases. The scatter of data for low values of b_b/a is partly due to Monte Carlo variation, but may also be a function of the VSF and the concentration of constituents. The scatter is greatest for low chlorophyll concentrations at SeaWiFS channels 5 (555 nm) and 6 (670 nm), and for high chlorophyll concentrations for SeaWiFS channels 1 (412 nm), 2 (443 nm), 3 (490 nm), and 4 (510 nm).

The scatter in the data for low values of b_b/a was investigated further by running the Monte Carlo model with

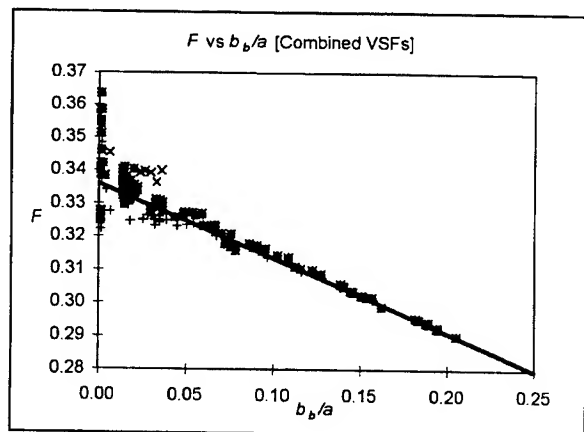


Fig 2. The value of F in equation 1 as a function of b_b/a . The values of constituent concentrations were varied in the model to effect variation in the ratio of the total backscattering coefficient to total absorption coefficient

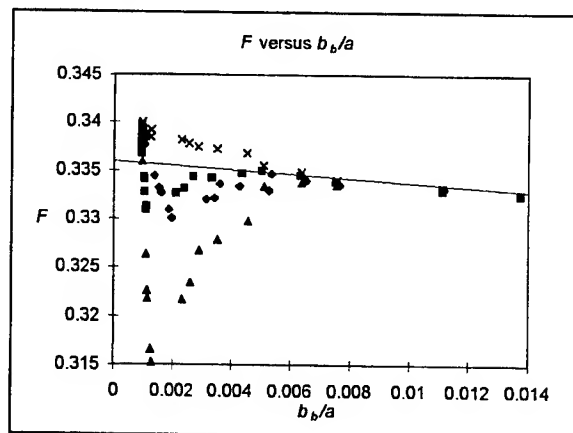


Fig 3. Detail of F study for low values of b_b/a . The model was run at SeaWiFS channels 5 and 6 for chlorophyll concentrations varying from 0 to 2 mg m^{-3} and with four different VSFs.

progressively larger numbers of photons incident on the ocean surface. The model was run at SeaWiFS channels 5 and 6 central wavelengths for chlorophyll concentrations ranging from 0 to 2 mg m^{-3} . The VSFs used for this study were KA from Gordon⁵, and “tongue of the ocean”, offshore southern California and San Diego harbor, all from Petzold⁸. Fig 3 shows the results of the investigation. The figure shows a spread of points for low values of b_b/a , however the deviation from a straight line occurs for lower values of b_b/a than in Fig 2. This may indicate that any deviation is actually due to Monte Carlo error. Fig 3 also shows that there may be a trend to the deviation from a straight line for low values of b_b/a , and that the trend may be different depending on the VSF. Further investigation is required to determine the exact relationship between F and b_b/a for low values of b_b/a . Notwithstanding the fact that there may be some VSF dependent non-linearity for low b_b/a values, the trend may be described as linear, thus allowing an equation to be written for the line that describes this trend.

$$F = -0.225 \frac{b_b(\lambda)}{a(\lambda)} + 0.336 \quad (6.)$$

An equation for the reflectance may then be written which incorporates equation 6.

$$R(\lambda) = \left(-0.225 \frac{b_b(\lambda)}{a(\lambda)} + 0.336 \right) \frac{b_b(\lambda)}{a(\lambda)} \quad (7.)$$

The line described by equation 6 is shown in Fig 2 and Fig 3.

The two previously described Monte Carlo tests were also used to investigate the value of F_G in equation 4. The Monte Carlo derived reflectance was divided by X to determine F_G . Results of this investigation are shown in Fig 4. A study of F_G for low values of X was also undertaken. Graphical results are not shown here, however the conclusions are the same as those for the study of low values of b_b/a .

The assumption has been made that division of a reflectance equation by X would provide a prediction of the value of F_G . This assumption was tested by dividing equation 5 by X .

$$F_G = 0.001/X + 0.3244 + 0.1425X + 0.1308X^2 \quad (8.)$$

Fig 4 shows the curve predicted by this equation for the value of F_G . The extreme value of F_G at low values of X is caused by division of the constant 0.001 in equation 5 by a value approaching zero. Equation 5 predicts a reflectance of 0.1 % for a non-scattering ocean. A simple solution may be to subtract this 0.1% from equation 5.

$$R = 0.3244X + 0.1425X^2 + 0.1308X^3 \quad (9.)$$

Equation 9 is then divided by X

$$F_G = 0.3244 + 0.1425X + 0.1308X^2 \quad (10.)$$

and its corresponding curve is plotted in Fig 4. Neither F_G equation predicts the values of F_G derived from the Monte Carlo ocean optical model.

A curve may be fitted to the Monte Carlo predicted values of F_G in Fig 4. If it is assumed the fit is linear, then

$$F_G = 0.06X + 0.34 \quad (11.)$$

and

$$R = (0.06X + 0.34)X \quad (12.)$$

If however a higher order equation is fitted then this may be described by

$$F_G = 0.336 + 0.116X - 0.23X^2 \quad (13.)$$

which gives an equation for the reflectance

$$R = (0.336 + 0.116X - 0.23X^2)X \quad (14.)$$

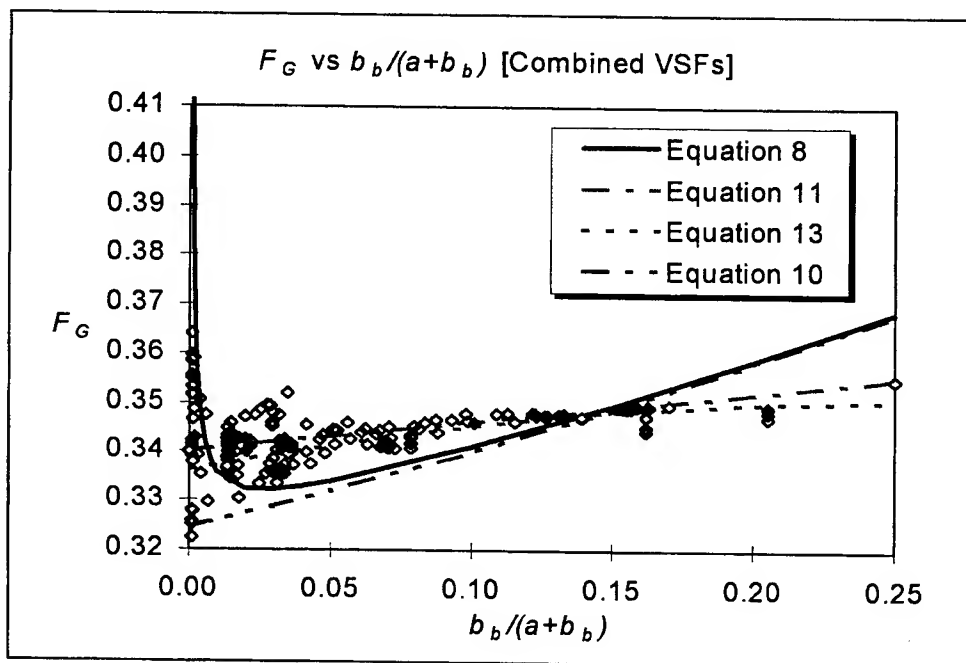


Fig 4. Values of F_G predicted by equations 8, 10, 11 and 13.

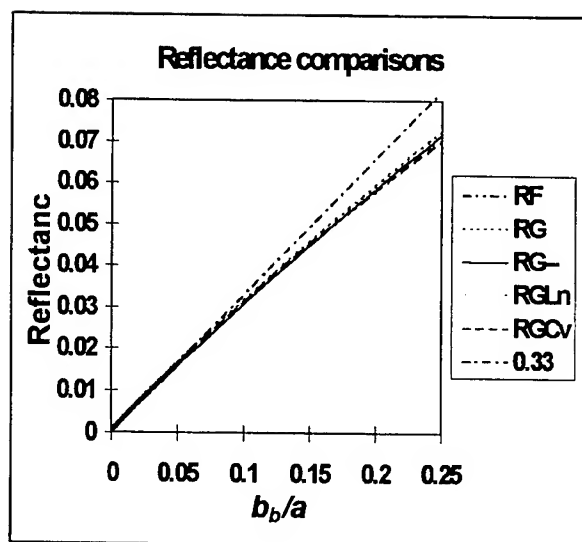


Fig 5 A comparison between the reflectances predicted by equations 1 (0.33), 5 (RG), 7 (RG-), 9 (RGLn), 12(RGCv), and 14 (RF)

$$R = (0.336 + 0.116X - 0.23X^2)X \quad (15.)$$

Fig 5 shows a comparison between the reflectance equations 1, 5, 7, 9, 12 and 14.

4 RETRIEVAL OF CHLOROPHYLL CONCENTRATION

We are investigating the success in inverting the reflectance equation to determine the concentration of ocean optical constituents. The model has been run with just chlorophyll present in the water, or a mix of chlorophyll and yellow stuff. A least squares scheme is used to determine the concentration of the pigments using reflectances at the six visible SeaWiFS channels. The ocean optical model is run to determine the reflectance at each of the six channel central wavelengths (used as the measured reflectance), and equation 7 is used to predict the reflectance values at each channel. The concentration of chlorophyll is varied to minimise the sum of the squares of the difference between the 'measured' reflectances predicted reflectances. A problem that was encountered was that the solution was often attracted to negative values of chlorophyll concentration and yellow stuff absorption

coefficient. This is due to the fact that the reflectance equation is not smoothly varying for negative concentration values. A search routine had to be devised that restricted the search to positive concentrations only

Fig 6 shows a graphical example of how the least squares retrieval finds a solution. In the example the model was run with a chlorophyll concentration of 0.5 mg m^{-3} .

As the noise level in the synthetic measurement data is increased, the curve in Fig 6 becomes wider and flatter but the minimum remains relatively close to the concentration being sought. The width parameter derived from the curve might be used operationally to attach a confidence limit to a retrieved concentration value.

When the inversion is attempted under the assumption that the only pigment present is chlorophyll, when in fact the model had been run with yellow stuff present as well, the retrieved chlorophyll concentration may be in error by a significant amount, depending on the specific values of the concentrations.

Uncertainty in knowledge of the absorption properties of ocean constituents leads to a large uncertainty in retrieved concentrations. However, it appears that the inversion scheme is relatively insensitive to the choice of volume scattering function selected to describe the water type.

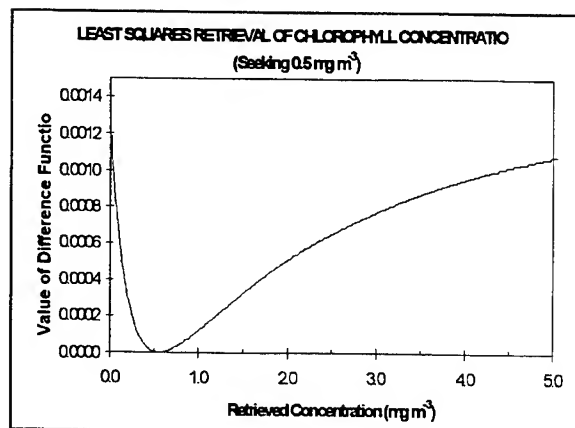


Fig 6 The sum of the squares of the differences between the 'measured' reflectances and the reflectances predicted by equation 7

An attempt has been made to visualise the extent of the uncertainty by using a CZCS image to provide data for retrieval. The CZCS image was used to provide chlorophyll concentration data. Yellow stuff was added to the chlorophyll as an increasing concentration from the west to the east across the image. The absorption coefficient of yellow stuff at 375 nm varied from 0 to 3 m^{-1} . These data were converted to SeaWiFS channel reflectance values via equation 4. Random errors were added to each channel at the following level: reflectance 2%; phytoplankton backscattering coefficient 5%; chlorophyll absorption 5%; water absorption 2%; water scattering coefficient 2%; yellow stuff absorption 1%. The total uncertainty in the b_p/a ratio in each channel is around 10%, depending on the concentrations of constituents. Fig 7 shows the original CZCS image, and Fig 8 shows the retrieved image. Each step down in the concentration log scale is about 30% of the previous level. Although the noise in the image is evident, major features such as the tongue of high concentration water south of Java is clearly visible.

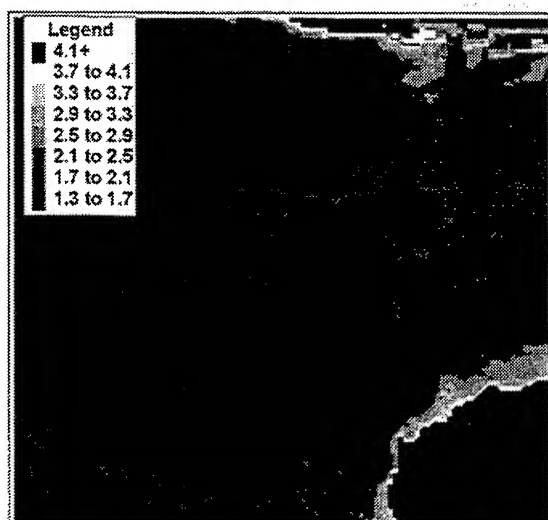


Fig 7 A chlorophyll concentration image derived from CZCS data. This image is used to predict reflectance values at each SeaWiFS central channel wavelength.

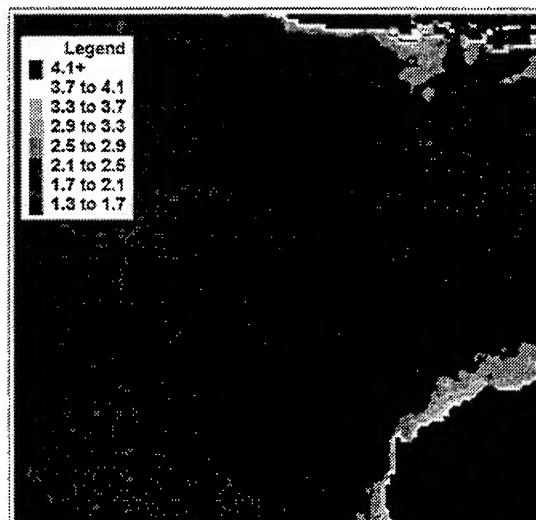


Fig 8 Chlorophyll concentration retrieved after addition of random noise to optical properties of ocean water and its coefficients.

5. CONCLUSION

The chlorophyll concentration retrieval scheme is sensitive to uncertainty, however sampling of local waters may decrease the uncertainty in the optical properties of typical local marine constituents, and therefore increase the confidence in retrieved pigment concentration values. To this end a sampling program has begun off the coast of Perth in Western Australia to provide ground truth measurements for the anticipated SeaWiFS overpasses, as well as data for use in developing and tuning local pigment retrieval algorithms.

6. ACKNOWLEDGEMENTS

Attendance at this conference would not have been possible without generous financial assistance from Curtin University of Technology and the Western Australian Satellite Technology Applications Consortium (WASTAC).

7. REFERENCES

1. S. Sathyendranath, F. E. Hoge, T. Platt, and R. N. Swift, "Detection of phytoplankton pigments from ocean color: improved algorithms", *Appl. Opt.*, **33**(6), 1081-1089 (1994).
2. J. T. O. Kirk, "Monte Carlo study of the nature of the underwater light field in, and the relationships between optical properties of, turbid yellow waters", *Aust. J. Mar. Freshwater Res.*, **32**, 517-532 (1981).
3. R. C. Smith, K. S. Baker, "The bio-optical state of ocean waters and remote sensing", *Limnol. and Oceanog.*, **23**(2), 247-259 (1978).
4. A. Morel, and L. Prieur, "Analysis of variations in ocean color", *Limnol. and Oceanog.*, **22**, 709-722 (1977).
5. H. R. Gordon, "Computed relationships between the inherent and apparent optical properties of a flat homogeneous ocean", *Appl. Opt.*, **14**(2), 417-427 (1975).
6. P. R. Fearn and M. J. Lynch, "Modelling water-leaving radiances for SeaWiFS", *Joint APOC/AMOS conference, Lorne*. (1995).
7. C. Cox and W. Munk, "Measurement of the roughness of the sea surface from photographs of the Sun's glitter", *J. of the Opt. Soc. of Am.*, **44**(11), 838-850 (1954).
8. T. J. Petzold, "Volume scattering functions of selected ocean waters", *Light in the sea, Benchmark Papers in Optics*, 3, Ed J.E. Tyler, 152-174, Dowden, Hutchinson & Ross, Inc., Stroudsburg, Pennsylvania, 1977.
9. J. E. Davies and M. J. Lynch, "Modelling sky radiances for SeaWiFS", *Joint APOC/AMOS conference, Lorne*. 1995.

SCATTERLIB — Light scattering codes library

P. J. Flatau

Scripps Institution of Oceanography
University of California, San Diego
La Jolla, California 92093-0221

ABSTRACT

The SCATTERLIB Internet site is a library of light scattering codes. Emphasis is on providing source codes (mostly FORTRAN). However, other information related to scattering on spherical and non-spherical particles is collected: extensive list of references to light scattering methods, refractive index, etc. The applications include: atmospheric radiative transfer, light scattering by phytoplankton, marine optics, flow cytometry, particle sizing.

Key words: scattering, non-spherical particles, discrete dipole approximation.

1 SCATTERLIB

There is rapid progress in numerical methods for exact solutions to light scattering on particles of interest to marine optics. Advances include exact solutions of light scattering by non-spherical and inhomogeneous particles. Several techniques are being developed including discrete dipole approximation,¹ cluster of spheres,³ new applications of T-matrix method,⁴ and rapid development of Finite Difference Time Domain methods.⁵

The purpose of the SCATTERLIB Internet is to collect classical and modern light scattering codes. Emphasis is on providing source codes (mostly FORTRAN). However, other information related to scattering on spherical and non-spherical particles is collected: extensive list of references to light scattering methods, refractive index, etc. The applications are: atmospheric radiative transfer, scattering on phytoplankton, flow cytometry, particle sizing.

2 CODES AND ALGORITHMS

There are currently several sections in the library including: (a) Spheres ("Mie"), (b) Coated spheres, concentric multispheres ("Mie"-modal), (c) Spheroids, (d) Cylinders, (e) Slabs, (f) Cluster of spheres and spheroids, (g) Discrete dipole approximation (DDA), coupled dipole approximation (CDA), method of moments (MoM), (h) T-matrix, (i) Anomalous diffraction approximation (ADT), high energy approximation (HEA). The codes are distributed via http or ftp access to <http://atol.ucsd.edu/~pflatau>. In addition extensive set of references is provided in hypertext format.

There are several links to related topics and sites including (a) Particle sizing, (b) Flow cytometry, (c) Marine optics, (d) Particle sizing (e) Refractive indices, (f) Related sites.

3 DDSCAT 5a

We have recently (October, 1996) added new version of the DDSCAT code to SCATTERLIB.

DDSCAT.5a is a Fortran software package to calculate scattering and absorption of electromagnetic waves by targets with arbitrary geometries using the "discrete dipole approximation" (DDA). In this approximation the target is replaced by an array of point dipoles (or, more precisely, polarizable points); the electromagnetic scattering problem for an incident periodic wave interacting with this array of point dipoles is then solved essentially exactly.

DDSCAT.5a is a Fortran implementation of the DDA developed by Draine and Flatau. It is intended to be a versatile implementation, suitable for a wide variety of applications ranging from interstellar dust to atmospheric aerosols. As written **DDSCAT** should be usable for many applications without modification, but the program is written in a modular form, so that modifications, if required, should be fairly straightforward.

DDSCAT.5a differs from previous versions in three major respects:

1. Use of the new Generalized Prime Factor Algorithm (GPFA) developed by Clive Temperton for FFT calculations. The GPFA algorithm is generally faster than the previous algorithms, yet requires no more memory than the algorithm of Brenner.
2. Availability of several different algorithms for iterative solution of the system of complex linear equations.² Some of these algorithms are often faster than the algorithm of Petravic and Kuo-Petravic which was used through DDSCAT.4b (and which remains available as an option in **DDSCAT.5a**).
3. Capability to compute the electromagnetic torque (and transverse components of the electromagnetic force) on the target, due to absorption and scattering of light from the incident beam.

4 Acknowledgments

This site is maintained by P. J. Flatau of Scripps Institution of Oceanography with the support from the Office of Naval Research YIP program and DuPont Corporate Educational Assistance.

5 REFERENCES

- [1] B. T. Draine and P. J. Flatau. Discrete dipole approximation for scattering calculations. *J. Opt. Soc. Am. A*, 11:1491–1499, 1994.
- [2] P. J. Flatau. Improvements of the discrete dipole approximation method. Submitted to Optics Communications, 1996.
- [3] D.W. Mackowski. Calculation of total cross sections of multiple-sphere clusters. *J. Opt. Soc. Am. A, Opt. Image Sci. Vis.*, 11(11):2851–2861, 1994.
- [4] M.I. Mishchenko, L.D. Travis, and D.W. Mackowski. T-matrix computations of light scattering by nonspherical particles: a review. *J. Quant. Spectrosc. Radiat. Transf.*, 55(5):535–575, 1996.
- [5] Allen Taflove. *Computational electrodynamics : the finite-difference time-domain method*. Artech House, Boston, 1995.

E.A. Gallie

Laurentian University, Dept. of Earth Science
Ramsey Lake Rd., Sudbury, Ontario, P3E 2C6

ABSTRACT

Triplicate samples were collected from three lakes in order to study variation in the specific absorption of dissolved organic carbon (DOC). Specific absorption was highly correlated with lake pH and DOC concentration, with the DOC in acid lakes absorbing less light at all wavelengths. The slope of the specific absorption curves did not seem to be significantly different in acid and non-acid lakes. This suggests that the decrease in specific absorption as pH declines is not due to change in the fulvic acid fraction, but to changes in the molecules themselves. Sampling variance is reasonably consistent across the range of lakes examined. Thus it may be possible to use an average variance to assign confidence limits when single samples are collected.

Keywords: Specific absorption, dissolved organic carbon, pH, acidification, acid lakes, freshwater, optical modelling, remote sensing.

1. INTRODUCTION

Specific absorption is one of the parameters needed to model the colour and quantity of light leaving a lake or ocean. Such models are important because they enable people to estimate the concentration of certain water quality variables from remote measurements of water colour, such as those obtained by satellite or airborne sensors. Hence the models facilitate remote water quality monitoring.

One of the water quality variables that can be detected remotely is dissolved organic carbon (DOC)¹. DOC has received increasing attention in the last decade² because it strongly affects the light in a lake, including the UV component³, and because it is a large storehouse of carbon with significance for global climate change. In Northern Ontario lakes, DOC is the dominant water colouring agent⁴, and there is considerable interest in developing models to link water colour and DOC concentration.

Such models must be calibrated with optical spectra appropriate for the variables under study. However, the extent to which specific absorption varies under different environmental circumstances is unknown. Thus one cannot assess whether it is appropriate to use off-the-shelf spectra, or which spectra will work best in which lakes. In addition, with limited lab budgets, one is torn between collecting replicate samples in a few lakes, or single samples in more lakes. Thus it would be useful to know whether the sampling variance for specific absorption is sufficiently consistent that an "average" value can be used to place confidence limits on single samples.

To address these issues, triplicate samples were collected from each of three lakes, with two of the lakes sampled again later in the season. The specific absorption of DOC, chlorophyll-a and total suspended solids (TSS) were measured, as well as the specific backscatter of the latter two variables. The measurements for chlorophyll-a and TSS were made because optical models also require calibration for these variables in order to extract accurate estimates of DOC¹. The measurement of the optical properties of chlorophyll-a and TSS are more involved and analyses are not yet complete. Only the results for DOC will be presented here.

2. METHODS

DOC was analyzed according to MOE⁵. Samples for DOC absorption were filtered through Supor 0.45 μm filters. Then transmittance was measured from 350 to 750 nm using a 10 cm cuvette in a single beam, Beckman DU-65 Spectrophotometer. The spectrophotometer was backgrounded on water that was distilled, deionized, and filtered

(Millipore HTTP 0.4 μm filters). Output was stored in digital format at 1.6 nm intervals, smoothed using a 5 nm running average and read at 5 nm intervals.

Transmittance was converted to absorption (a_d) as $-\ln(T)/\text{pathlength}$ where pathlength is in meters. Absorption was forced to zero between 700 and 745 nm by subtracting the lowest value in this range from the whole spectra. This correction is required because the absorption beyond about 700 nm is usually assumed to be due to scattering losses from unfiltered particles rather than true absorption⁷. Then specific absorption (a_d^*) was calculated as a_d / DOC where DOC is in g/m^3 , giving units of m^2/g .

3. RESULTS AND DISCUSSION

3.1 Sampling variation

One of the objectives of this study is to determine whether the variation due to all sources of sampling error (natural water variation, DOC analyses, absorption analyses) is consistent enough that an average value can be used to establish confidence limits for single-sample a_d^* spectra. The standard deviation of four of the triplicate samples is consistent (Figure 1), even though the lakes represent a wide range of DOC concentrations and absorption (Table 1). The Daisy Lake samples, however, have a much higher standard deviation for a_d^* , resulting from variation in the DOC values (Table 1).

Table 1: Specific absorption at 450 nm, slope, pH and DOC concentration for the study lakes. pH for Elbow Lake was measured on 27 Sept, 1996.

	$a_d^*_{450}$	Slope		pH	Avg DOC (mg/L)
		400-440 nm	440-565 nm		
Daisy Lake	0.048	0.0172	0.0141	5.1	2.4
17 Jul 95	± 0.011	± 0.0009	± 0.0019		± 0.61
Swan Lake	0.063	0.0192	0.0145	5.6	3.0
10 Jul 95	± 0.006	± 0.0007	± 0.0006		± 0.12
Swan Lake	0.075	0.0176	0.0139	5.5	2.8
31 Jul 95	± 0.006	± 0.0004	± 0.0007		± 0.06
Elbow Lake	0.313	0.0172	0.0136	6.6	8.3
24 Jul 95	± 0.005	± 0.0000	± 0.0002		± 0.06
Elbow Lake	0.339	0.0171	0.0133	6.6	7.2
14 Aug 95	± 0.004	± 0.0001	± 0.0002		± 0.15

The lab that processed the DOC samples indicates that replicate DOC samples should not vary by more than 0.5 mg/L, and indeed, the range is less than this for the four other triplicates. For Daisy Lake, however, the first sample processed was 1.1 mg/L lower (40% lower) than the other two. The lab suspects that the first sample in the series may have been diluted by rinse water in the DOC equipment. If DOC values within the expected range are substituted for this sample, then Daisy Lake standard deviation falls in line with the other lakes. This suggests that an average value for standard deviation (calculated as the square root of the pooled variance of the samples) based on the four samples excluding Daisy Lake can be used to establish single-sample confidence limits, but that in about 1 case in 15, the average will underestimate the limits.

The standard deviation of a_d^* (Figure 1) declines with wavelength. The reason is partly due to an increase in machine noise toward shorter wavelengths. However, it is also partly due to the shape of the a_d^* spectra which approach zero at longer wavelengths and hence must come closer together. In fact, beyond 700 nm, the only variation that remains is due to spectrophotometer noise, since the small scattering correction removes any variation due to the sample or DOC analyses.

3.2 Environmental variation

The mean a_d^* values for the triplicate samples (Figure 2) show the structureless, exponential decline characteristic of DOC⁷. Paired t-tests were used to ask whether the mean a_d^* spectra are significantly different from one another (Table 2). Daisy and Swan lakes are acid lakes (Table 1) and their spectra differ from those in Elbow Lake which is near-neutral. The two Elbow Lake spectra are significantly different from each other, though the two Swan Lake spectra are not. The Daisy Lake spectra is different at shorter wavelengths from the higher Swan Lake spectra but not the lower spectra.

Table 2: Results of paired t-tests run for each individual wavelength. The range of wavelengths over which the a_d^* spectra are significantly different ($\alpha = 0.05$; $df = 4$) are shown. Lo (low) and hi (high) are used to designate which a_d^* spectra from Figure 2 is being tested.

a_d^* Spectra	Significant Difference
Elbow lo vs Elbow hi	400 - 700 nm
Elbow lo vs Swan hi	400 - 690 nm
Swan lo vs Swan hi	-
Daisy vs Swan lo	-
Daisy vs Swan hi	400 ~ 550

The data suggest that pH is the cause of variation. Indeed, the pH of water is known to affect specific absorption^{8,9,10} with the effect attributed to the ionization state of phenolic and carboxyl groups¹⁰. In the study lakes, the link between a_d^* and pH is strong (Figure 3a). However, a_d^* is also strongly correlated with DOC concentration (Figure 3b). Local freshwater humic acids (HA) precipitate readily at a pH of about 5.5 when aluminum is present, whereas local fulvic acids (FA) do not¹¹. Near Sudbury, aluminum is elevated in most acid lakes due to the widespread sulphate acidification that has occurred in the region. Thus it is reasonable to suggest that a_d^* is low in Daisy and Swan lakes because the more highly coloured HA have precipitated out, leaving only the less coloured FA.

Carder et al.¹² found that there is a strong relationship between the exponential slope of marine absorption spectra and FA as a fraction of humic matter. Therefore slope may provide a method to test whether the differences in a_d^* are due to pH-caused molecular-level changes, or to pH-caused changes in the FA fraction. Slopes are high (Table 1), corresponding to marine FA fractions of over 90% (440-565 nm) to 95% (370-440 nm)¹². The FA fraction in two local lakes with neutral pH was 86%^{† 13}. In acid lakes, it might be higher if HA is precipitating. However, there is no relationship between slope and pH (or DOC) for the study lakes (Figure 4). Thus it appears that the FA fraction is relatively constant in the three lakes studied, assuming the same basic relationship holds for freshwater as marine waters.

[†] FA makes up 86% of the humic material but only about 50% of the total DOC. In marine situations, humic material accounts for virtually all absorption¹². This is probably not true for freshwater.

This implies that the change in a_d^* is a function of pH acting on the ionization state of the molecules.

One of the objectives of this study was to assess whether off-the-shelf spectra can be used to calibrate optical water-quality models. This study shows that different spectra will be required for different lakes, but offers the hope that appropriate spectra can be selected if the pH of a lake is known. Indeed, it may even be possible to estimate both DOC concentration and pH using optical models, by iteratively changing the a_d^* spectra until stable DOC concentration and pH estimates are arrived at.

4. CONCLUSIONS

The standard deviation of a_d^* is reasonably consistent over a range of DOC concentrations from 2.4 - 7.2 mg/L and pH 5.1 - 6.6. Thus it may be possible to use an average value to establish confidence limits for single samples, though errors in DOC measurements may cause variance to exceed the average in about 1 in 15 cases. Although this situation is not statistically ideal, it is commonly encountered because a wider range of lakes can be sampled if replicates are not taken.

Environmental variation in the a_d^* spectra is correlated with pH and DOC concentration. Examination of the slopes of the a_d^* spectra suggests that there is a high fraction of FA in the study lakes, but that there is little variation in that fraction as pH drops. Thus the reduction in a_d^* as pH drops is ascribed to pH acting on the ionization state of the molecules. If off-the-shelf a_d^* spectra are to be used in optical modelling, then pH will have to be taken into consideration when selecting calibration spectra.

5. ACKNOWLEDGEMENTS

The author thanks the Ontario Ministry of the Environment and Energy (MOEE) who provided water chemistry analyses, Bill Keller and Jim Carbone of MOEE who facilitated data collection, Garry Ferroni and Leo Leduc for use of the Beckman spectrophotometer, and Roger Pitblado for discussions on statistics. The work was funded through the Natural Sciences and Engineering Research Council (NSERC).

6. REFERENCES

1. R.P. Bukata, J.E. Bruton and J.H. Jerome, "Application of direct measurements of optical parameters to the estimation of lake water quality indicators," Inland Waters Directorate, Canada Centre for Inland Waters, Scientific Series No. 140, Environment Canada, 45 p (1985).
2. E.M. Perdue and E.T. Gjessing, Eds., "*Organic acids in aquatic ecosystems*," Life Sciences Research Report 48, John Wiley & Sons, Toronto, 1990.
3. N.D. Yan, W. Keller, N.M. Scully, D.R.S. Lean, P.J. Dillon, "Increased UV-B penetration in a lake owing to drought-induced acidification," *Nature*, **381**, 141-143 (1996).
4. B.P. Neary, P.J. Dillon, J.R. Munro and B.J. Clarke, "The acidification of Ontario lakes: an assessment of their sensitivity and current status with respect to biological damage," Ont. Ministr. Environ. Rep., Dorset, Ont. 146 p (1990).
5. E.A. Gallie and P.A. Murtha, "Specific absorption and backscattering spectra for suspended minerals and chlorophyll-a in Chilko Lake, British Columbia," *Remote Sensing of Environment*, **39**, 103-118 (1992).
6. MOE (Ontario Ministry of the Environment), "*Outlines of Analytical Methods*," Ont. Ministr. Environ. Rep., Toronto, Ont. 1981.
7. A. Bricaud, A. Morel and L. Prieur, "Absorption by dissolved organic matter of the sea (yellow substance) in the UV and visible domains," *Limnol. Oceanogr.*, **26**, 42-53 (1981).
8. M. Schnitzer and S.U. Khan. "*Humic substances in the Environment*," Marcel Dekker, New York, 1972.
9. W. Flaig, H. Beutelspacher and E. Reitz, "*Soil Components. Vol I. Organic Components*" J.E. Gieseking, Ed. Springer-Verlag, New York, 97-105, 1975.
10. R.G. Zepp and P.F. Schlottzhauer, "Comparison of photochemical behaviour of various humic substances in

water: III. spectroscopic properties of humic substances," *Chemosphere*, **10**, 479-486 (1981).

11. R.C. Boerschke, "Quantitative isolation and characterization of freshwater dissolved organic carbon and the influence of pH and Al on the absorption spectra of the isolated humic material," MSc. Thesis, Laurentian University, Sudbury, Ontario, 1996.

12. K.L. Carder, R.G. Steward, G.R. Harvey and P.B. Ortner, "Marine humic and fulvic acids: their effects on remote sensing of ocean chlorophyll," *Limnol. Oceanogr.* **34**, 68-81 (1989).

13. R.C. Boerschke, E.A. Gallie, N. Belzile, R.N. Gedye and J.R. Morris, "Quantitative elemental and structural analysis of dissolved organic carbon fractions from lakes near Sudbury, Ontario," *Can. J. Chemistry*, (in press 1996).

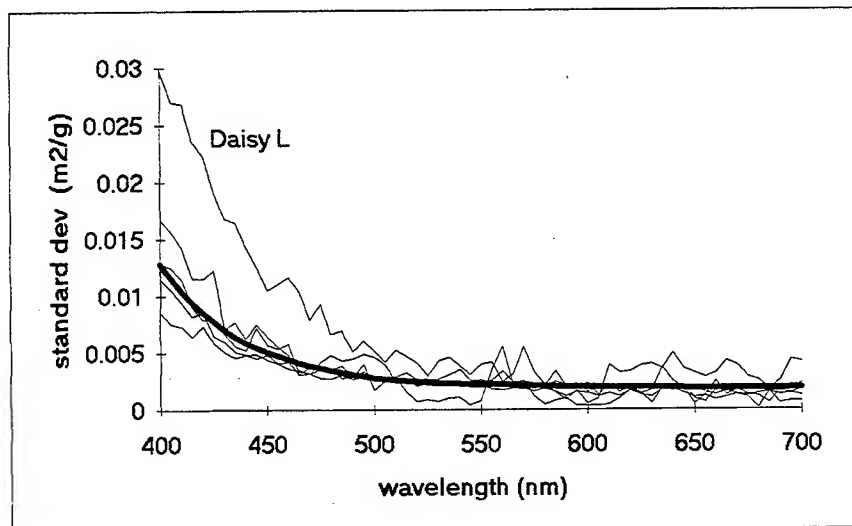


Figure 1 : Standard deviation of ad^* for the triplicate samples from the study lakes. The heavy line is the average for the samples excluding Daisy L.

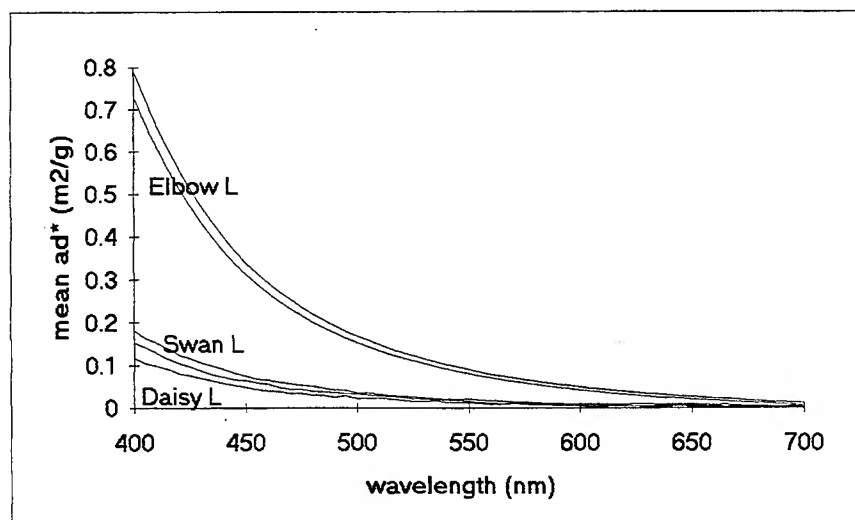


Figure 2 : Mean ad^* spectra for the study lakes. In Table 2, Elbow hi refers to the upper Elbow L. spectra, and Elbow lo to the lower Elbow L. spectra. Equally, Swan hi and lo refer to the upper and lower Swan L. spectra, respectively. There is only one Daisy L. spectra.

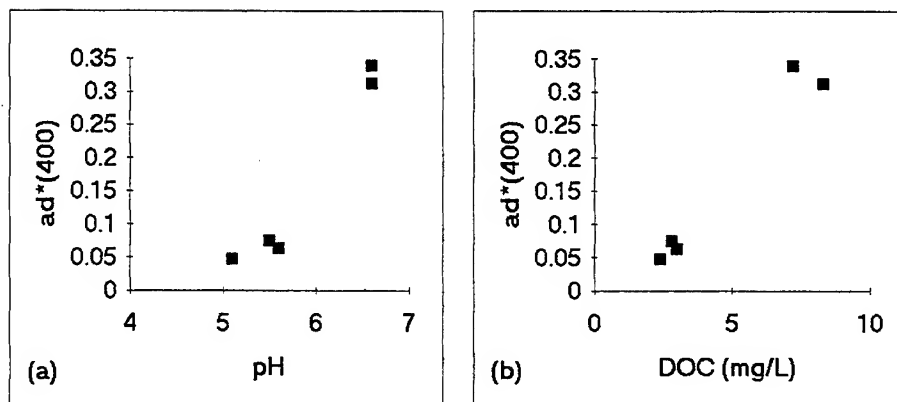


Figure 3 : The relationship between the specific absorption of DOC in m^2/g and (a) pH and (b) DOC in the study lakes.

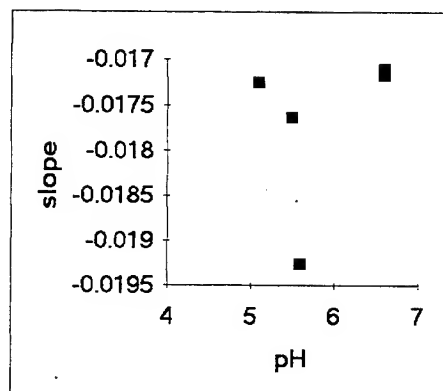


Figure 4: The relationship between the exponential slope of the specific absorption spectra (400-440 nm) and pH in the study lakes.

Classification of Phytoplankton in Lake Constance by Modelling the Albedo

Peter Gege

DLR, Institute of Optoelectronics
P.O.Box 1116
D-82230 Wessling

ABSTRACT

Phytoplankton concentration and species composition in Lake Constance vary markedly over the year, and accordingly the surface albedo also changes. By inverse modelling of albedo spectra, which were measured once per week over a period of 1 ½ years from a ship, the accuracy for retrieving the concentrations of concurring phytoplankton classes was investigated. It was found that 4 classes can be separated with an error between 12 and 25 %, depending on the natural variability of a class's optical properties. The differentiation between 4 classes improves the accuracy of chlorophyll-a determination for remote sensing by 30%.

Keywords: phytoplankton classification, inverse modelling, absorption, albedo, reflectance, remote sensing, Lake Constance.

1. INTRODUCTION

Mapping the distribution of phytoplankton by remote sensing has evolved during the last two decades to a valuable source of information in limnology and oceanography.¹ However, only few attempts have been reported so far for distinguishing algal classes^{2,3} or identifying algal pigments^{4,5} by remote sensing, although such a characterization would be of great importance.⁶

There are three reasons why phytoplankton classes are very rarely distinguished in remote sensing. First, in-situ classification by microscopy is time consuming and requires special taxonomic knowledges, thus it is no routine method in most laboratories. Second, the optical properties of many phytoplankton species are not well documented since pure cultures are often difficult to grow. Third, for several species the optical properties depend considerable on growth conditions such as intensity and spectral composition of the illumination, temperature and nutrients. It is thus difficult to define "spectral classes" of phytoplankton. Such a characterization of the phytoplankton in Lake Constance for concentration determination by remote sensing was the main goal of the present study⁷.

2. MEASUREMENTS

In-situ measurements were performed on a research vessel once per week from April to November 1990 and from April to July 1991. Test site was the deepest place (147 m) of the German Überlinger See, which is the northwestern part of Lake Constance.

2.1 Albedo

Spectral measurements were performed with a Tracor Northern TN 1710 spectrometer of 512 channels in the range 400 to 800 nm. The dispersion is 0.8 nm, the spectral resolution varies from 2 nm in the UV to 4 nm in the red (670 nm) up to 12 nm in the IR. To utilize the radiometric dynamics of 12 bit, the exposure time was adjusted to the actual radiance values. Exposure times up to 30 sec required detector cooling. An accurate calibration was performed⁸ to account *e.g.* for nonlinearities at long exposure times.

For measuring upwelling radiances, the instrument was mounted on a tripod and fixed at the vessel's reling in such a way that it looked almost in nadir direction downwards to the water surface. Disturbances by ship shadow and sunglint were minimized by keeping the ship in a suitable angle relative to the sun. Downwelling irradiances were measured by holding a white teflon plate into the instrument's field of view.

For some measurements from days with variable cloud cover, the spectral signature of the illumination did not vanish when the albedo was calculated. These disturbances are caused by specular reflections at the water surface. A correction algorithm was developed and applied to the disturbed measurements.⁷

2.2 Phytoplankton

For each day of the campaign, 18 water samples were analyzed photometrically with the method of Nusch⁹ to get the concentration profile of chlorophyll-a up to a depth of 30 m at the test site. In addition, two samples averaging the depths 0-8 m were taken, for which a high pressure liquid chromatography (HPLC) analysis and a phytoplankton classification were performed.

From HPLC, the concentrations of different types of chlorophylls, phaeopigments, carotenoids and xanthophylls were derived.

A comparison of 132 HPLC chlorophyll-a values with the corresponding photometric values resulted in a correction factor for the photometric values. All chlorophyll-a values used in the study were taken from the photometric analysis since they are depth resolved. The photometric accuracy was estimated by comparison with HPLC as $\pm 1.3 \mu\text{g l}^{-1}$.

By microscopy, the cell numbers of the different phytoplankton classes or morphotypes per unit sample volume were counted. The biovolume of each species was calculated by multiplying the cell numbers with the average cell volume of that species.

Pure cultures of the phytoplankton species *Cryptomonas marsonii*, *Cryptomonas ovata*, *Cryptomonas rostratiformis*, *Rhodomonas minuta*, *Stephanodiscus hantzschii*, *Fragilaria crotonensis*, *Mougeotia sp.* and *Chlamydomonas sp.* were grown in the laboratory in order to determine their specific absorption spectra. The absorption of samples from the cultures was measured in the range 400 to 800 nm with a resolution of 1 nm using an integrating sphere, the chlorophyll-a concentration was measured by the method of Nusch⁹.

3. ALBEDO MODEL

Remote spectral data were compared with in-situ measurements of chlorophyll-a concentrations and phytoplankton biovolumes by use of a model for the albedo of the water surface. Inputs to the model are the optical properties of water and its ingredients. By varying the concentrations C_i , the calculated albedo spectrum is adjusted to a measured spectrum in a least square fit.

The volume absorption coefficient a and the backscattering coefficient b_b are the relevant inherent optical properties for modelling the light backscattered out of the water. a and b_b are additive parameters, i.e. they are the sum of the contributions of pure water and of the dissolved and suspended substances:

$$a(\lambda) = a_w(\lambda) + \sum_i C_i \cdot a_i^*(\lambda), \quad (1)$$

$$b_b(\lambda) = b_{b,w}(\lambda) + \sum_i C_i \cdot b_{b,i}^*(\lambda), \quad (2)$$

λ = wavelength. The volume absorption coefficient of pure water, $a_w(\lambda)$, is taken from Smith and Baker¹⁰, the backscattering coefficient of pure water is calculated according to Morel¹¹ as $b_{b,w}(\lambda) = 0.000111 \cdot (\lambda/500)^{-4.32}$ (λ in nm, $b_{b,w}$ in m^{-1}).

The optical properties of the dissolved and suspended substances are characterized by their specific absorption coefficients $a_i^*(\lambda)$ and their specific backscattering coefficients $b_{b,i}^*(\lambda)$, where the $*$ -symbol indicates a normalization to a typical concentration. For phytoplankton, the normalization is done to $1 \mu\text{g}$ chlorophyll-a per liter since this pigment is present in all species. Consequently, in spectroscopy the term "phytoplankton concentration" is defined in units of chlorophyll-a concentration. The backscattering of phytoplankton depends more on the cell size than on the species, thus no species-specific backscattering coefficients were used. Instead, the phytoplankton backscattering was lumped together with the backscattering by anorganic particles.

Besides phytoplankton, mainly dissolved organic matter (yellow substance) and suspended anorganic particles determine the water colour. Yellow substance has a characteristic absorption spectrum:¹² high absorption in the UV and exponential decrease towards longer wavelengths.

$$C_Y \cdot a_Y^*(\lambda) = a_Y(450) \cdot e^{S \cdot (450-\lambda)}, \quad (3)$$

The factor S is related to the composition; it was determined for Lake Constance as $S = 0.022 \text{ nm}^{-1}$. The concentration C_Y is defined in terms of absorption at 450 nm, $a_Y(450)$. At moderate concentrations, scattering by yellow substance can be neglected.

Anorganic particles have in general low absorption, but high scattering. Because no information about the optical properties of the anorganic particles in Lake Constance was available, absorption was neglected and backscattering was simplified by assuming that it is the sum of a wavelength independent term and a term proportional to λ^{-1} . This assumption was also made for all the other suspended matter including phytoplankton, hence eq. (2) was replaced by

$$b_b(\lambda) = b_{b,w}(\lambda) + B_0 + B_1 \cdot \lambda^{-1}. \quad (4)$$

Particles larger than $\sim 5 \mu\text{m}$ scatter light nearly wavelength independent; the coefficient B_0 is proportional to their concentration. The backscattering of particles of $\sim 1\text{--}5 \mu\text{m}$ diameter is roughly proportional to λ^{-1} ; the coefficient B_1 takes account of them. B_0 and B_1 were treated as fit variables. Particles with a different backscattering behaviour were neglected.

The light backscattered in the water is described by the subsurface irradiance reflectance, which is approximately proportional to b_b/a .¹³ A sensor above the water surface measures additionally light which is reflected at the water surface. It is given by the Fresnel reflectance σ . The sum is termed albedo ρ and approximated by the equation

$$\rho(\lambda) = \gamma \frac{b_b(\lambda)}{a(\lambda)} + \sigma. \quad (5)$$

The experimental determination of ρ is done by measuring the upwelling radiance L_u and the downwelling irradiance E_d . ρ is the ratio $\pi L_u / E_d$. For a target which reflects light totally diffuse, πL_u is equal to the upwelling irradiance and ρ is only related to the target's optical properties, but it is independent of the illumination. However, if reflection depends on the angle of incidence or on the angle of observation, a radiance measurement cannot replace an irradiance measurement, and the ratio $\pi L_u / E_d$ depends on the angular distribution of the illumination. In the case of water, the requirement of angle independent reflection is fairly fulfilled for the light backscattered out of the water, but not for the radiation specularly reflected at the surface. Consequently, the subsurface reflectance is fairly independent of the illumination, but not the Fresnel reflectance σ . Therefore the value $\sigma = 0.02$ from the Fresnel equations is not valid for that type of measurements. – The factor γ depends on the volume scattering function of the suspended particles¹⁴ and on the Fresnel reflectance for upwelling and downwelling radiation¹⁵, hence for a radiance sensor on the surface roughness. When the albedo was modelled, σ as well as γ were treated as fit variables.

4. RESULTS

4.1 Parameter choice for comparing spectral data with microscopic data

In remote sensing, the parameter of phytoplankton concentration is the chlorophyll-a concentration, which was not measured individually for each species. Instead, microscopy yields cell numbers. When the total cell numbers of water samples are plotted against the independently measured total chlorophyll-a concentrations, the data scatter considerable around the regression line: if cell numbers are calculated from chlorophyll-a concentrations, the error is 90% on average and 736% on maximum.⁷ A better correlation exists for the biovolume, see Fig. 1. If the regression line is used to calculate biovolumes from chlorophyll-a concentrations, the error is 32% on average and 143% on maximum. The equation of the regression line is:

$$\ln B = 12.41 + 0.6488 \cdot \ln C, \quad (6)$$

where the biovolume B is given in units of $\mu\text{m}^3 \text{ ml}^{-1}$ and the chlorophyll-a concentration C in units of $\mu\text{g l}^{-1}$. As the biovolume was found to be the best suited parameter which can be derived from microscopic data, eq. (6) is proposed for comparisons between in-situ measurements and remote sensing data.

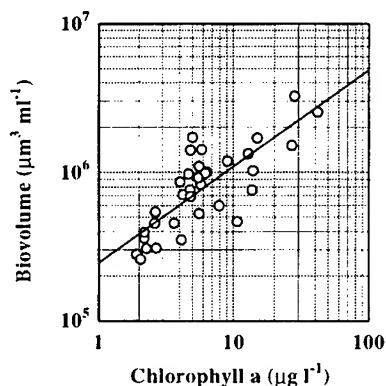


Fig. 1: Relationship between chlorophyll-a concentration and biovolume.

4.2 Assessment of spectral classes

Absorption spectra of individual phytoplankton species are not characteristic enough for a spectral identification, even not all taxonomic classes can be spectrally clear distinguished. A comparison of absorption spectra from the most abundant species in Lake Constance led to the classification of Table 1. The corresponding specific absorption spectra are shown in Fig. 2.

For cryptophyta, two spectra are required to account for the high natural variability of the pigment phycoerythrin. The spectrum for representing the class at low phycoerythrin concentration was measured at a pure culture of *Cryptomonas ovata*, which is by far the most abundant species in Lake Constance. To account for high phycoerythrin concentration, a published¹⁶ absorption measurement of the species *Rhodomonas lens* was digitized and rescaled to $a^*(440) = 0.02 \text{ m}^2 \text{ mg}^{-1}$. Laboratory measurements of the absorption as well as field measurements of the albedo showed that a spectroscopic distinction between species within the class Cryptophyceae is not possible, since absorption differences between species are less significant than absorption variations within a species upon changes of the illumination.

For representing the specific absorption spectrum of diatoms a *Fragilaria crotonensis* measurement was chosen, for green algae a *Mougeotia sp.* measurement, and for dinoflagellates a published¹⁷ spectrum, which averages 5 marine species.

Taxonomic classes	Spectral class
Cryptophyceae	cryptophyta
Bacillariophyceae Chrysophyceae	diatoms
Chlorophyceae Zygnemaphyceae Cyanophyceae	green algae
Dinophyceae	dinoflagellates

Table 1: Spectral classification of the phytoplankton in Lake Constance.

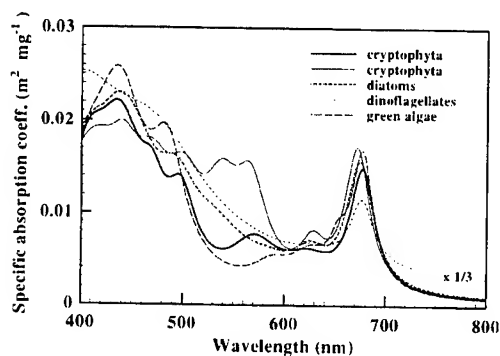


Fig. 2: Specific absorption of the spectral classes of the phytoplankton in Lake Constance.

4.3 Phytoplankton succession

The phytoplankton succession in Lake Constance for the years 1990 and 1991 is shown in Fig. 3. The biovolumes of the classes are shown as accumulated sums, i.e. the upper curve represents the total biovolume. In winter, the concentration is low because of light deficiency. From mid-March onwards, insolation is high enough that phytoplankton can grow and reproduce. The spring blooms are governed by only few species which belong to the same class. During summer and autumn, a great variety of species is concurring, and with few exceptions no single class is dominating.

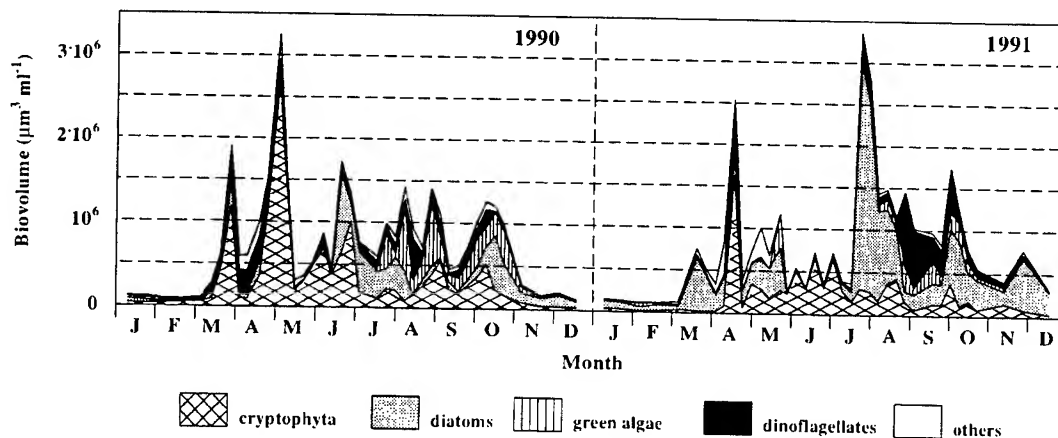


Fig. 3: Phytoplankton succession in Lake Constance.

The changes in phytoplankton concentration and species composition during the year have a significant influence on the albedo spectra. Three examples are given in Fig. 4. They show the albedo for the days of lowest and highest chlorophyll-a concentration and a spectrum at intermediate concentration.

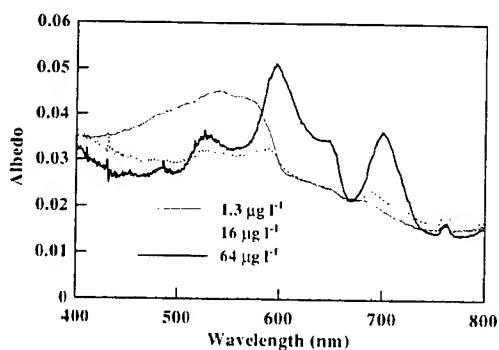


Fig. 4: Albedo at low, moderate and high chlorophyll-a concentration.

4.4 Phytoplankton classification by modelling the albedo

By inverse modelling of albedo spectra according to eq. (5), concentration values for the 4 spectral classes of Table 1 were calculated. They are shown in Fig. 5 as accumulated sums, i.e. the upper curve shows the total chlorophyll-a concentration. For comparison, the average in-situ chlorophyll-a values from the depths 0, 1 and 2 m are also shown (open circles).

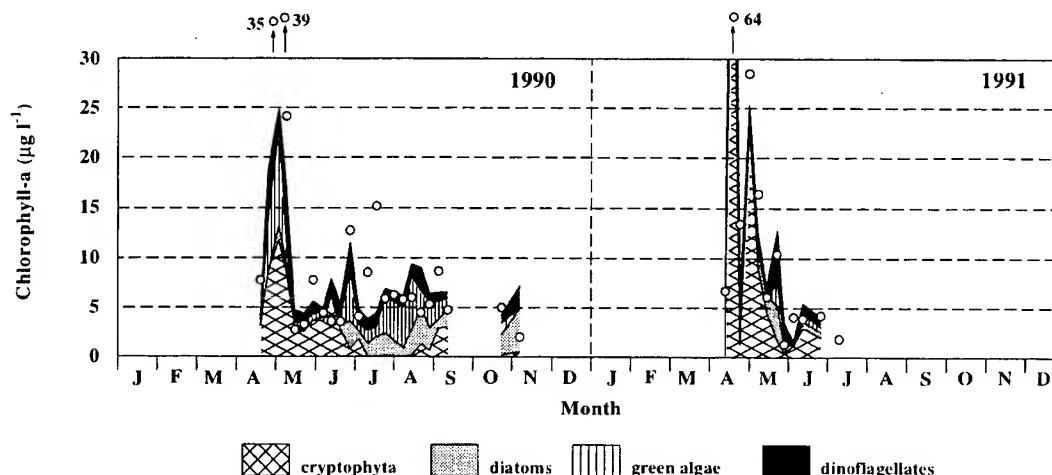


Fig. 5: Phytoplankton succession in Lake Constance (shadowed areas: calculated from albedo; circles: in-situ measurements of chlorophyll-a).

For each day, the relative chlorophyll-a concentrations of the 4 phytoplankton classes were calculated and compared with the corresponding relative biovolumes. The mean differences between the modelled and measured abundancies are listed in Table 2.

Spectral class	Mean error
cryptophyta	25 %
diatoms	14 %
green algae	12 %
dinoflagellates	16 %

Table 2: Accuracy of phytoplankton classification by modelling the albedo spectrum. Since the relative abundance of class i is given from in-situ data in units of biovolumes B_i but calculated from albedo spectra in units of chlorophyll-a concentrations C_i , the difference $|B_i/B - C_i/C|$ was taken to express the error, with $B = \sum B_i$ and $C = \sum C_i$. The mean error is the average over all 33 days of the campaign.

4.5 Accuracy of chlorophyll-a determination

For the total chlorophyll-a concentration values shown in Fig. 5, the mean difference between calculated and measured values is $\pm 2.5 \mu\text{g l}^{-1}$, if the 4 worst results are ignored. A similar error of $\pm 2.6 \mu\text{g l}^{-1}$ results if the chlorophyll-a concentrations are calculated according to eq. (6) from the biovolumes. The accuracy of the model is hence comparable with the correspondence between in-situ data of biovolumes and chlorophyll-a concentrations. The albedo was also modelled without distinguishing between phytoplankton classes; in this case the mean difference was $\pm 3.5 \mu\text{g l}^{-1}$. The differentiation between 4 classes improves thus the accuracy of chlorophyll-a determination by 30 %.

5. DISCUSSION

The model which was used for fitting albedo spectra was kept as simple as possible to minimize the number of fit parameters. The study demonstrated that it is nevertheless able to distinguish between 4 phytoplankton classes and to determine the total chlorophyll-a concentration as accurate as the in-situ data.

A comparison of Fig. 5 with Fig. 3 demonstrates that modelling of albedo spectra is rather well-suited to reproduce in-situ data of phytoplankton succession. Both Figures show correspondingly that in 1990 the spring blooms were dominated by cryptophyta, and that other species turned up at comparable concentrations in the middle of June. Diatoms were the first, green algae followed middle of July. Dinoflagellates were always of minor importance. The cryptophyta dominance ended towards the end of June, when they disappeared almost totally, but they occurred again from end of August to mid of October at concentrations comparable to diatoms and green algae. During the rest of the year, their concentration was very low. A similar succession was observed

in 1991: Starting with a bloom in April, the cryptophyta were the dominating class until mid-July except for some weeks subsequent to the spring bloom.

Although albedo measurements are suited to determine the general trends in phytoplankton succession over the year, the correspondence to in-situ data is not always perfect. Three reasons are responsible for the differences in the relative abundances of classes. First, as Fig. 1 shows, the in-situ parameter "biovolume" (Fig. 3) is not accurately proportional to the spectroscopic parameter "chlorophyll-a" (Fig. 5). Second, the water samples are averages over the depth range 0 to 8 m, while the remote sensing signal decreases with depth and is very low for depths below ~2 m. The phytoplankton composition of the 0-8 m sample may not always be the same as in the upper 2 m. Third, the specific absorption spectra of the 4 classes are not constant. This leads to significant errors, as Table 2 indicates: The highest accuracy in determining the relative concentration was found for green algae. Individual species of this class have very similar absorption spectra, and the spectrum is almost independent from growth conditions. The largest error occurs for cryptophyta whose absorption spectra are changing markedly on illumination conditions.

Differences in the total chlorophyll-a concentration values have two further reasons. As the concentration is not constant with depth, the 0-2 m average may not always represent correctly the "remote sensing" concentration. Second, albedo measurements indicate for some days marked horizontal variations of the chlorophyll-a concentration. Since it was not possible to measure the albedo at the same time as the samples were taken, some albedo measurements may represent other water bodies than in-situ data.

6. ACKNOWLEDGEMENTS

This work is the result of a cooperation between DLR, Institute of Optoelectronics, and the Limnological Institute of the University of Constance. Data were provided generously by M. M. Tilzer, U. Giedke, B. Beese, J. Fürst, A. Schweizer, G. Hartmann and G. M. Ferrari. The author is also grateful to H. Graßl, H. van der Piepen and M. Schroeder for encouraging the work and helpful discussions.

7. REFERENCES

1. V. Barale, P. M. Schlittenhardt (Eds.), *Ocean Colour: Theory and Applications in a Decade of CZCS Experience*, Kluwer Academic Publ. Dordrecht, The Netherlands, 1993.
2. L. L. Richardson, D. Bachoon, V. Ingram-Wiley, C. C. Chow, K. Weinstock, "Remote sensing of the biological dynamics of large-scale salt evaporation ponds," in: *24th Int. Symp. on Remote Sensing of the Environment*, Rio de Janeiro, Brazil, 27-31 May 1991.
3. L.L. Richardson, "Optical properties of naturally occurring populations of algae and photosynthetic bacteria," *Eos* 71, 109 (1990).
4. F. E. Hoge, R. N. Swift, "Airborne dual laser excitation and mapping of phytoplankton photopigments in a Gulf Stream Warm Core Ring," *Appl. Optics* 22, 2272-2280 (1983).
5. A. G. Dekker, M. Donze, "Imaging spectrometry as a research tool for inland water resources analysis," In: J. Hill and J. Miegier (eds.), *Imaging Spectrometry - a Tool for Environmental Observations*, ECSC, EEC, EAEC, Brussels and Luxembourg, 295-317 (1994).
6. E. C. Weaver, R. Wrigley, "Factors Affecting the Identification of Phytoplankton Groups by Means of Remote Sensing," NASA-TM-108799 (1994).
7. P. Gege, "Water analysis by remote sensing: A model for the interpretation of optical spectral measurements," ESA-TT-1324, 231 p., July 1995.
8. P. Gege, "Tracor Northern TN 1710 - Kalibrationsmessungen," DLR Oberpfaffenhofen, IB 552-5/92, 62 p. (1992).
9. E. A. Nusch, "Comparison of different methods for chlorophyll and phaeopigment determination," *Arch. Hydrobiol. Beih. Ergebn. Limnol.* 14, 14-36 (1980).
10. R. C. Smith, K. S. Baker, "Optical classification of natural waters," *Limnol. Oceanogr.* 23, 260-267 (1978).
11. A. Morel, "Optical Properties of Pure Water and Pure Sea Water," In: N. G. Jerlov, E. Steemann Nielsen (Eds.): *Optical Aspects of Oceanography*, Academic press, 1-24 (1974).
12. H. Graßl, R. Doerffer, W. Jäger, "The influence of Yellow Substances on Remote Sensing of Sea-Water Constituents from Space," ESA contract No. RFQ 3-5060/84/NL/MD, GKSS Res. Centre Geesthacht (1986).
13. S. Sathyendranath, L. Prieur, A. Morel, "A three-component model of ocean colour and its application to remote sensing of phytoplankton pigments in coastal waters," *Int. J. Remote Sensing* 10, 1373-1394 (1989).
14. J. T. O. Kirk, *Light and photosynthesis in aquatic ecosystems*, Cambridge University Press (1983).
15. J. H. Jerome, R. P. Bukata, J. E. Bruton, "Determination of available subsurface light for photochemical and photobiological activity," *J. Great Lakes Res.* 16(3), 436-443 (1990).
16. F.T. Haxo, D.C. Fork, "Photosynthetically Active Accessory Pigments of Cryptomonads," *Nature* 184, 1051-1052 (1959).
17. W. von Smekot-Wensierski, B. Wozniak, H. Graßl, R. Doerffer, "Die Absorptionseigenschaften des marinen Phytoplanktons," GKSS Bericht Nr. 92/E/105, Geesthacht - Hamburg - Sopot, 104 p. (1992).

A first look at the particulate absorption coefficient in the surface water of the subtropical East China Sea in spring

Gwo-Ching Gong

National Taiwan Ocean University, Department of Oceanography
Keelung, Taiwan, Republic of China

ABSTRACT

During a KEEP-II (Kuroshio Edge Exchange Processes) expedition in the East China Sea in May 1996, absorption spectra of near surface particulate matters were measured at 38 stations. The total pigment concentrations (chlorophyll *a* plus phaeopigment) ranged from 0.2 to 7 mg m⁻³. The common absorption peaks for chlorophyll *a*, centered at 440 nm and 675 nm, were observed at most stations. However, four exceptions were found in the low salinity China Coastal Water. The 440 nm absorption peak shifted to 410 nm in these four samples. Very high correlation was found between pigment concentration and the particulate absorption coefficient at several visible bands which are often used for satellite spectrometers. It is noted that the relationship between the chlorophyll *a* specific absorption coefficient at 440 nm and the chlorophyll *a* concentration observed in the East China Sea is different from that observed in the central subtropical Pacific and the Gulf of Mexico. The particulate matter in the East China Sea has a slightly higher absorption coefficient than the latter.

Keywords: particulate absorption spectra, absorption coefficient, chlorophyll *a*, East China Sea

1. INTRODUCTION

The color of the ocean is related to the inherent optical properties of the backscattering ($b(\lambda)$) and the absorption coefficient ($a(\lambda)$) in the medium of the ocean.¹ Among the two parameters $a(\lambda)$ is more variable in most marine environments.² As a result, the color of the ocean is mainly determined by the variation of $a(\lambda)$, which may be depicted as follows:

$$a(\lambda) = a_w(\lambda) + a_g(\lambda) + a_p(\lambda)$$

where $a_w(\lambda)$, $a_p(\lambda)$ and $a_g(\lambda)$ are the absorption coefficient of water, colored dissolved organic matters (gelbstof), and total particulates, respectively. The values of $a_w(\lambda)$ had been provided by several researchers.^{1,3,4} The values of $a_g(\lambda)$, although it is comparable to the values of $a_p(\lambda)$ especially in the coastal water, it shows monotonically decreasing with increasing wavelength.^{5,6} The values of $a_p(\lambda)$ are contributed by the phytoplankton ($a_p(\lambda)$) and the detritus ($a_d(\lambda)$). Therefore, the values of $a_p(\lambda)$ are thought to be the most important term needed to be known for the estimation of sea surface pigment concentrations from the algorithm of remote sensing reflectance ($R_{rs}(\lambda)$).⁷

$$R_{rs}(\lambda) = 0.1076 b(\lambda) / a(\lambda)$$

To model $R_{rs}(\lambda)$, $a_p(\lambda)$ was usually expressed as the product of the particulate specific absorption coefficient ($a^*_p(\lambda)$) and the total pigment concentration (TP; Chl *a* plus phaeopigment).

$$a_p(\lambda) = a^*_p(\lambda) \times [\text{TP}]$$

If $a_p^*(\lambda)$ is known and constant, then $a_p(\lambda)$ can be provided from a simple routine measurement of TP. Unfortunately, many studies reported that $a_p^*(\lambda)$ were highly varied with their particles composition, pigment concentrations, phytoplankton growth condition, the physiological state of phytoplankton in the natural marine environment.⁷⁻¹² Therefore, $a_p(\lambda)$ as well as $a_p^*(\lambda)$ should be examined regionally in order to improve the global algorithm of the remote sensing reflectance model.

In this study, I present the first data set of the particulate absorption coefficient spectra of the near surface water where collected from the subtropical East China Sea during a KEEP-II expedition on board the *R/V Ocean Researcher I* in May, 1996. Higher particulate absorption coefficient were observed in the inner shelf waters, lower particulate absorption coefficient were observed in the middle shelf to the offshore waters. Very good correlation was observed between the particulate absorption coefficient and the total pigment concentration at several visible bands which are often used in satellite spectrometry.

2. MATERIALS AND METHODS

The particulate absorption spectra ($a_p(\lambda)$) of the near surface water (2 m below the sea surface) were measured at 38 stations in the East China Sea (Fig. 1). Seawater samples were taken from 20 liter Teflon coated Go-Flo bottles (General Oceanic, USA) mounted on a CTD (Seabird SBE 9/11plus; USA) and Rosette (General Oceanic, USA) assembly. For $a_p(\lambda)$ and Chl *a* measurements, 1.5 L of seawater samples were filtered through 25 mm Whatman GF/F filter and stored immediately in a -20 °C refrigerator for later analysis. Chl *a* and phaeopigment concentrations were determined fluorometrically.¹³⁻¹⁵ For the measurement of the absorption coefficient of total particulates ($a_p(\lambda)$), the glass fiber filter technique was used.¹⁶ The 1% active NaClO solution (15%) was used to bleach the pigment on the sample filter.¹⁷ The quadratic relationship as described by Tassan and Ferrari¹⁷ was used to convert the sample absorbance retained on filter to absorbance (*A*) of total particulates and detritus in suspension. Finally, the absorption coefficient were obtained by:

$$a(\lambda) = 2.3 A(\lambda) / (V/S)$$

where *V* and *S* are the volume filtered and the clearance area of the filter, respectively. $a_p(\lambda)$ was calculated by subtracting $a_d(\lambda)$ from $a_p(\lambda)$. The specific absorption coefficient of total particulates ($a_p^*(\lambda)$) and phytoplankton ($a_p^*(\lambda)$) in the medium are defined as the $a_p(\lambda)$ per unit Chl *a* plus phaeopigment concentration and $a_p(\lambda)$ per unit Chl *a* concentration, respectively.

3. RESULTS AND DISCUSSION

The distribution of total pigment (TP; Chl *a* plus phaeopigment) concentrations is shown in Figure 2. TP concentrations and Chl *a* concentrations were found between 0.4~3.0 mg m⁻³ and 0.2~2.0 mg m⁻³, respectively. The highest TP and Chl *a* concentrations were observed at station 5 (data was not put into contour plot) with values up to about 7.0 mg m⁻³ for TP and 5.1 mg m⁻³ for Chl *a*, respectively. This station was visited at the first day of our investigation (see Fig. 1 for station location). However, the high pigment condition disappeared while the station were revisited (see station 30 in Fig. 1). It probably indicated that a bloom condition occurred in the beginning of our cruise, but faded later. The distribution of Chl *a* almost mimicked the distribution of TP, which showed higher concentrations in waters with salinity less than 34.4 psu. The lower pigment concentrations found in the high salinity waters were resulted from the intrusion of the oligotrophic Kuroshio water onto the shelf.

The results of absorption spectra of total particulates ($a_p(\lambda)$) and phytoplankton ($a_p(\lambda)$) for all stations were plotted in Figure 3. The two common absorption peaks for Chl *a* were observed and centered around 440 nm and 675 nm for most stations except four, where the 440 nm absorption peak shifted to around 410 nm. The four exceptional stations (stations 4, 5, 10 and 30) were located in the

inner shelf close to the mainland China coast. The absorption spectra of $a_d(\lambda)$ all decreased monotonically with increasing wavelength. The magnitude of $a_p(\lambda)$ and $a_d(\lambda)$ at the 440 nm peak were in the ranges of 0.015~0.1 m⁻¹ and 0.012~0.075 m⁻¹, respectively. The magnitudes of $a_p(\lambda)$ and $a_d(\lambda)$ at 675 nm peak were both in the range of 0.005~0.04 m⁻¹. The contribution of detritus on the red peak was relatively small. The highest $a_p(\lambda)$ and $a_d(\lambda)$ were found at station 5, where the blue peak were found to have shifted to 410 nm. In terms of specific absorption coefficient, the magnitude of $a^*_p(\lambda)$ and $a^*_d(\lambda)$ at 440 nm and 675 nm ranged from 0.03~0.85 m² mg⁻¹ and 0.014~0.02 m² mg⁻¹ for $a^*_p(\lambda)$ and 0.035~0.2 m² mg⁻¹ and 0.02~0.035 m² mg⁻¹ for $a^*_d(\lambda)$, respectively. The highest value of $a^*_p(\lambda)$ and $a^*_d(\lambda)$ was found in the deep water station of the Kuroshio Water. The low values of $a^*_p(\lambda)$ and $a^*_d(\lambda)$ were probably the result of the package effect.^{8,11,18,19} The results also indicated that variability of the absorption spectra manifested either in its magnitude or in its peak position. Nevertheless, the absorption coefficient for $a_p(\lambda)$ and $a_d(\lambda)$ always followed the variation of pigment concentration.

Prior to estimation of surface pigment concentration from the remote sensing reflectance algorithm, the relationship between particulate or specific particulate absorption coefficient and the pigment concentration must be known. The relationship between $a_p(\lambda)$ and TP at several visible bands which are usually used in the satellite spectrometer were examined. The results indicated that $a_p(\lambda)$ were in very high correlation ($R^2 \geq 0.92$) with the total pigment concentrations. Figure 4 showed an example of the relationship between $a_p(440)$ and TP. Power function was used to fit the data points due to the pigment packaging effect, but a linear relationship also fitted the data within the data range, except for an outlier at the 410 nm peak. Relatively high correlation coefficient was also found for the relationship between $a_d(\lambda)$ and Chl *a* concentration. The good correlation between pigment concentration and absorption coefficient allows us to estimate total pigment or Chl *a* concentrations independently from the absorption coefficient for waters ranging from coastal to oligotrophic environment in the East China Sea. The relationship between $a^*_p(440)$ and Chl *a* which was proposed by Carder *et al.*²⁰ to develop reflectance model algorithm and to simulate the relationships at 412 and 565 nm based on the feature of the absorption spectra was further examined. The result showed a fairly good relationship between $a^*_p(440)$ and Chl *a* for Chl *a* concentration ranging from about 0.1 to 2.5 mg m⁻³. However, the current relationship was in general slightly higher than that found by Carder *et al.*²⁰ for the central subtropical Pacific and the Gulf of Mexico waters, especially at higher Chl *a* concentrations.

4. CONCLUSION

In this study, the first data set of the surface water particulate absorption coefficient spectra in the subtropical East China Sea was presented. The two common absorption peaks centered at 440 nm and 675 nm were found, but the variability of the absorption coefficients either in their magnitude or in their peak position among stations was high. Nevertheless, the variation of the total particulate absorption coefficient followed that of the pigment concentration closely. As a result, very high correlation coefficients were obtained for the relationships between the total particulates or the phytoplankton absorption coefficient and the total pigment or the Chl *a* concentrations. The results of the relationships are useful for developing the remote sensing reflectance algorithm to the estimation of the pigment concentration.

5. ACKNOWLEDGMENTS

I would like to thank Dr. Yeun-Jung Wu for providing the spectrophotometer for our absorption spectra measurement. I also thanks Mr. Ming-Hsin Liang, Po-Wen Wang and Gong-Jen Liu for chlorophyll measurements, and Dr. Kon-Kee Liu who kindly corrected the manuscript. This work was supported by the National Science Council, Taiwan, Republic of China.

6. REFERENCES

1. A. Y. Morel and L. Prieur, "Analysis of variations in ocean color", *Limnol. Oceanogr.*, 22, 709-722, 1977.
2. H. R. Gordon and A. Y. Morel, "Remote assessment of ocean color for interpretation of satellite visible imagery: A review", *Springer*, 1983.
3. A. Y. Morel, "Optical properties of pure water and sea water", In *Optical Aspects of Oceanography* edited by N. G. Jerlov and E. Steeman Nielsen, pp.1-24, Academic, San Diego, Calif., 1974.
4. R. S. Smith and K. S. Baker, "Optical properties of the clearest natural waters (200-800 nm)", *Appl. Opt.*, 20, 177-184, 1981.
5. A. Bricaud, A. Morel, and L. Prieur, "Absorption by dissolved organic matter in the sea (yellow substance) in the visible domains", *Limnol. Oceanogr.*, 26, 45-53, 1981.
6. C. S. Roesler, M. J. Perry, and K. L. Carder, "Modeling in situ phytoplankton absorption from total absorption spectra in productive inland marine waters", *Limnol. Oceanogr.*, 34, 1510-1523, 1989.
7. K. L. Carder, R. G. Steward, J. H. Paul, and G. A. Vargo, "Relationships between chlorophyll and ocean color constituents as they affect remote-sensing reflectance models", *Limnol. Oceanogr.*, 31, 403-413, 1986.
8. A. Y. Morel and A. Bricaud, "Theoretical results concerning light absorption in a discrete medium and application to the specific absorption of phytoplankton", *Deep Sea Res.*, 28, 1357-1393, 1981.
9. S. Q. Duntley, W. H. Wilson, and C. F. Edgerton, "Detection of ocean chlorophyll from earth orbit", In *Ocean color analysis*, Scripps Inst. Oceanogr. Ref. 74-10, 1974.
10. A. Bricaud, A. Morel, and L. Prieur, "Optical efficiency factors of some phytoplankter", *Limnol. Oceanogr.*, 28, 816-832, 1983.
11. B. G. Mitchell, and D. A. Kiefer, "Variability in pigment specific particulate fluorescence and absorption spectra in the northeaster Pacific Ocean", *Deep Sea Res.*, 35, 665-689, 1988.
12. H. Sosik, and B. G. Mitchell, "Absorption, fluorescence, and quantum yield for growth in nitrogen-limited *Dunaliella tertiolecta*", *Limnol. Oceanogr.*, 36, 910-921, 1991.
13. T. R. Parsons, Y. Maita, and C. M. Lalli (Eds.), "A Manual of chemical and biological methods for seawater analysis", *Pergamon Press*, New York, pp174, 1984.
14. G.-C. Gong, W.-R. Yang, and Y.-H. Wen, "Correlation of chlorophyll *a* concentration and Sea Tech fluorometer fluorescence in seawater", *Acta Oceanographica Taiwanica*, 31, 117-126, 1993.
15. G.-C. Gong, W.-R. Yang, and J. Chang, "In vivo fluorescence-derived chlorophyll *a* concentration in the southern East China Sea", *Acta Oceanographica Taiwanica*, 34, 73-85, 1995.
16. M. Kishino, M. Takahashi, N. Okami, and S. Ichimura, "Estimation of the spectral absorption coefficients of phytoplankton in the sea", *Bull. Mar. Sci.* 37, 634-642, 1985.
17. S. Tassan, and G. M. Ferrari, "An alternative approach to absorption measurements of aquatic particles retained on filters", *Limnol. Oceanogr.*, 40, 1358-1368, 1995.
18. J. T. O. Kirk, "Light and Photosynthesis in Aquatic Ecosystems", *Cambridge University Press*, New York, 1983.
19. C. S. Yentsch, and D. A. Phinney, "A bridge between ocean optics and microbial ecology", *Limnol. and Oceanogr.*, 34, 1694-1705, 1989.
20. K. L. Carder, S. K. Hawes, K. A. Baker, R. C. Smith, R. G. Steward, and B. G. Mitchell, "Reflectance model for quantifying chlorophyll *a* in the presence of productivity degradation products", *J. Geophys. Res.*, 96, 20599-20611, 1991.

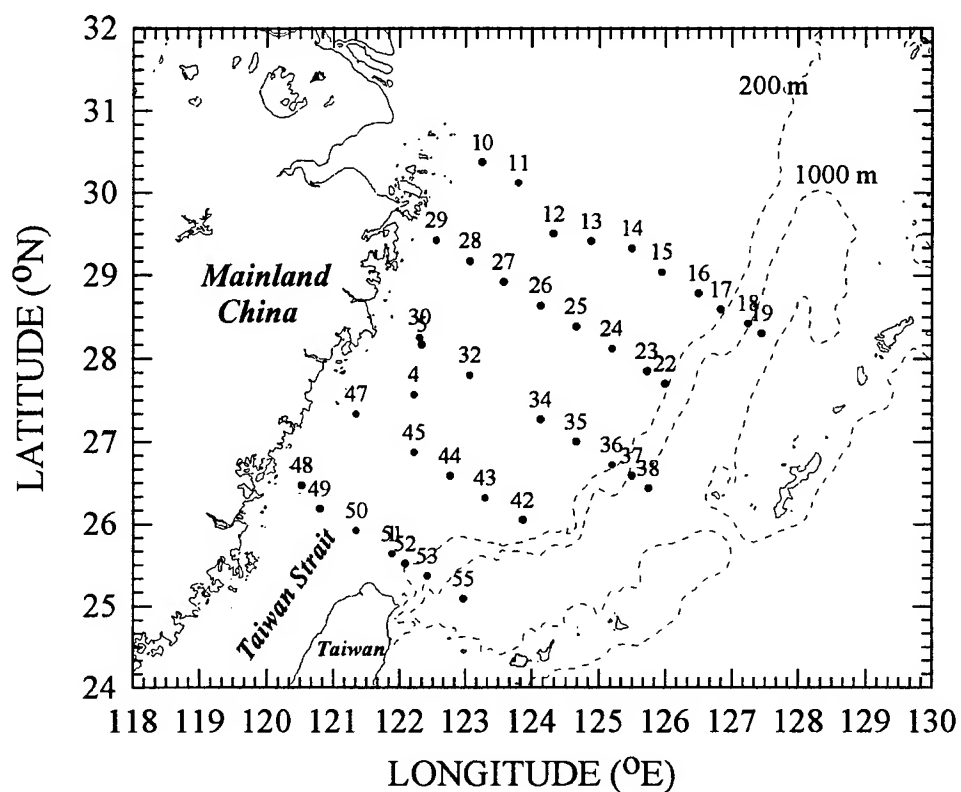


Fig. 1 Sampling stations on the KEEP-II expedition in May 2-15, 1996.

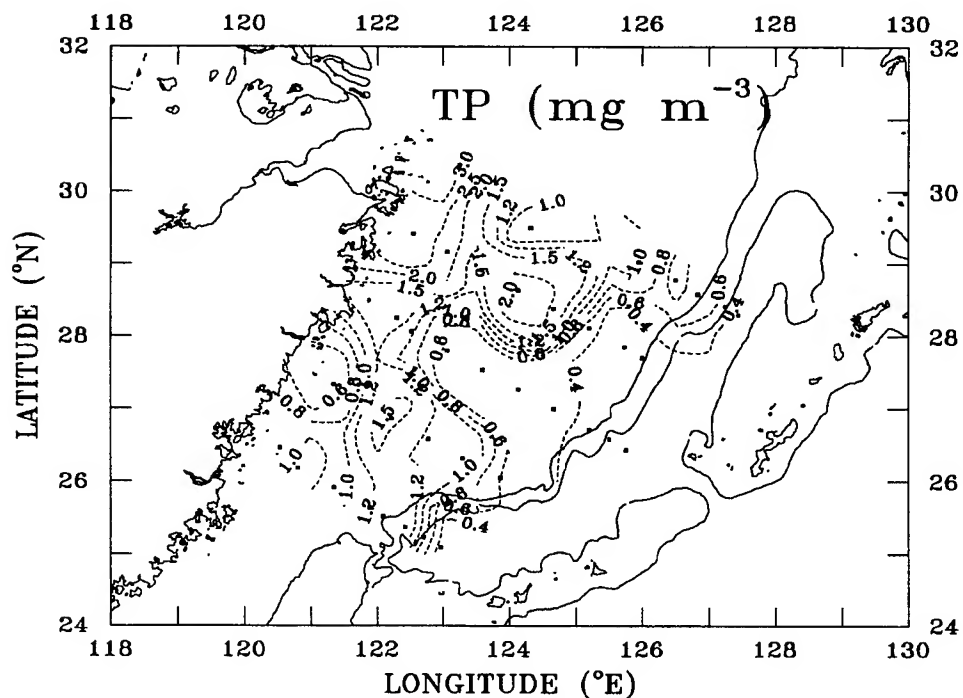


Fig. 2 The distribution of sea surface total pigment (Chl *a* plus phaeopigment) concentration.

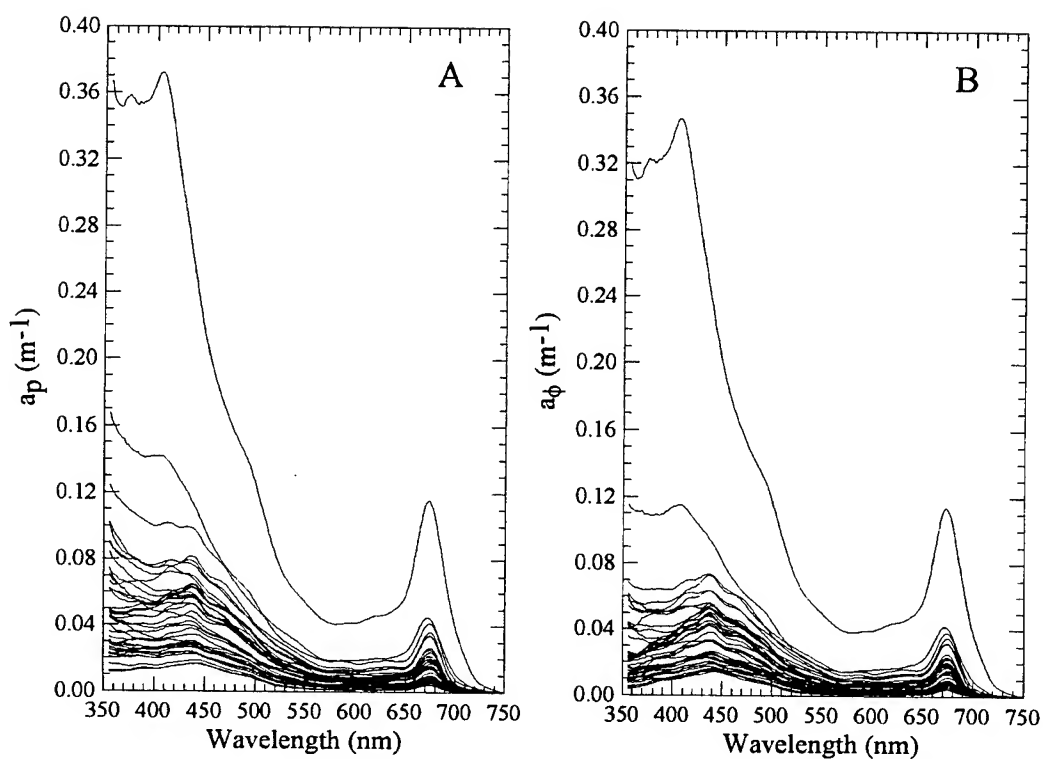


Fig. 3 The absorption spectra of (A) total particulate ($a_p(\lambda)$) and (B) phytoplankton ($a_\phi(\lambda)$)

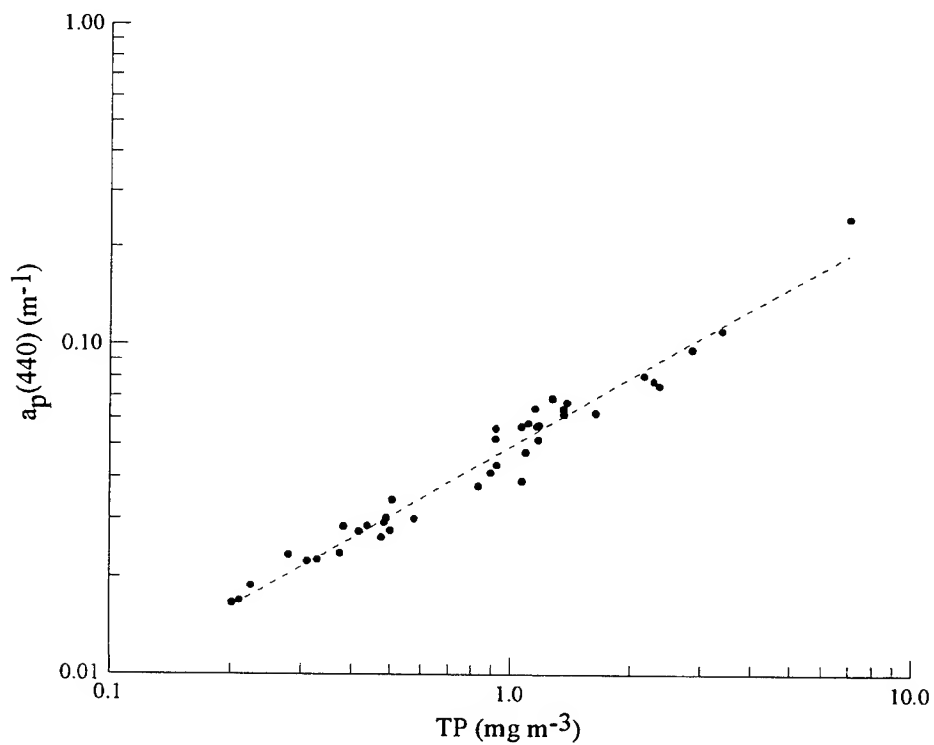


Fig. 4 The relationship between $a_p(440)$ and TP concentrations

Estimation of specific absorption coefficients of turbid coastal water constituents using the AC-9 and asymptotic attenuation coefficients.

Hans Hakvoort and Roland Doerffer

GKSS Research Centre Geesthacht, Bio-Optical Remote Sensing
Max-Planck-Strasse, D-21502 Geesthacht
Germany

ABSTRACT

The inherent absorption coefficients of water constituents in the southern part of the North Sea were spectrally estimated using data from an AC-9 and the asymptotic attenuation coefficients. The 'standard' procedure of Zaneveld was used to calculate the inherent absorption coefficients from AC-9 measurements. The asymptotic attenuation coefficients were obtained from irradiance depth profiles measured with a SeaWiFS Profiling Multichannel Radiometer. The relationship between the single scattering albedo and asymptotic attenuation was calculated with Mobley's radiative transfer model Hydrolight 3.0 for different single scattering albedo using the San Diego volume scattering function. This relation was used to calculate the inherent absorption

The absorption coefficients calculated with both methods matched for water bodies dominated by phytoplanktonic constituents. The 'standard' correction procedure for the AC-9 overcorrected for the scattering error in water bodies having higher concentrations of suspended sediment which is typical for the studied area. A negative absorption in the 500-550 nm wavelength range is obtained. Also, the 'standard' correction assumes a zero absorption at 715 nm and does not distinguish between absorption and the scattering error in this wavelength range. Using the asymptotic attenuation to estimate of inherent absorption occasionally resulted in an underestimation of the absorption in the 600-700 nm wavelength range. Negative absorption may be due to an inaccuracy in the estimation of the asymptotic attenuation in the red wavelength range.

The specific absorption coefficients of the water constituents were calculated from the AC-9 measurements using an optimisation procedure. The specific absorption coefficients as estimated by the different techniques are compared and discussed.

Keywords: inherent absorption, specific absorption, asymptotic attenuation, turbid waters

1. INTRODUCTION

Remote sensed reflectance is used to synoptically estimate the concentrations of water constituents in areas larger than that which can be covered by ship or platform observations. The algorithms used proved to be accurate in clear ocean water containing plankton substances only. However, they do not apply in turbid coastal Case II waters where the remote sensed reflectance is determined by at least three different groups of substances in the water. An new procedure based on inverse modelling of radiative transfer was developed to estimate concentrations of all the groups of substances^{1,2}. This procedure needs specific optical properties of the water constituents for input.

Measurement of the specific optical properties is not trivial. Several methods to measure the inherent absorption coefficient have been introduced and some of them have been inter-compared³. SeaWiFS protocols⁴ suggest the use of the reflective-tube absorption meter *in situ*. However, this does not perfectly gather all scattered light and transmit it to the detector. This scattering error is in the order of 13 percent of the scattering coefficient and can be corrected for⁵. The assumption is that water is the only absorbing component in the near infrared region, which may be false for turbid coastal waters. Alternatively, the absorption may be calculated using the asymptotic attenuation coefficient and the beam attenuation. The asymptotic vertical attenuation coefficient is solely determined by the inherent optical property ω_0 , the volume scattering function β and the beam attenuation c . It is therefore an inherent optical property. So, if K_∞ and c are known and a β is assumed, the inherent optical properties a and b can be calculated. In a first approximation the effects of fluorescence and Raman scattering are neglected.

In the present work estimations of the inherent absorption coefficient from the asymptotic attenuation coefficient and beam attenuation were compared to the absorption as estimated from the AC-9 measurements using the calculation method according to Zaneveld *et al.*⁵. Specific optical properties of the water constituents were calculated using an optimisation procedure.

Table 1. Symbols used.

Symbol	Description	Unit
a	absorption coefficient	m^{-1}
a_h	DOC absorption coefficient	m^{-1}
a_m	measured absorption (AC-9)	m^{-1}
a^*	specific absorption coefficient	m^2mg^{-1}
b	scattering coefficient	m^{-1}
c	beam attenuation coefficient	m^{-1}
c_m	measured beam attenuation (AC-9)	m^{-1}
K_d	downward irradiance attenuation	m^{-1}
K_u	upward radiance attenuation	m^{-1}
K_∞	asymptotic attenuation coefficient	m^{-1}
DOC	Dissolved Organic Carbon	mg l^{-1}
RSR	Remote Sensed Reflectance	-
TSM	Total Suspended Matter	mg l^{-1}
β	Volume scattering function	$\text{m}^{-1}\text{sr}^{-1}$
ω_0	Single scattering albedo	-

Table 2. Spectral bands used in the optical instruments were selected to fit those of SeaWiFS, OCTS and MERIS. Spectral bandwidth is 10 nm.

Parameter to estimate	AC-9	Profiler
DOC	412	412
Chlorophyll (absorption)	440	443
Chlorophyll (other pigments)	488	490
Turbidity, Sediments, Red Tides	510	510
Turbidity, Sediments, Red Tides		520
Chlorophyll reference, Sediments	555	555
Chlorophyll reference, Sediments		565
Phycoerythrin fluorescence		590
Sediments	630	620
Sediments	650	
Chlorophyll a absorption		665
Chlorophyll a absorption	676	670
Chlorophyll fluorescence		683
Chlorophyll base line	715	700

2. METHODOLOGY

2.1 Measurements

The measurements were carried out from Feb. 22 to March 7 and from Aug. 8 to Aug. 13, 1996 at different stations in the German Bight which is a turbid coastal water in the southern part of the North Sea. During the winter the water column in the German Bight is well mixed. Stratification of the water column occurs in the summer. Strong tidal currents cause high fluctuations in the concentrations of water constituents.

Depth profiles of downward vector irradiance and upward radiance were measured simultaneously in 13 spectral wavelength bands (Table 1) using the SeaWiFS Profiling Multichannel Radiometer (SPMR) (Satlantic). This instrument is a free-fall radiometer and has wide dynamic range (24 bit). The depth profiles were measured at a distance more than 50 m away from the ship thus avoiding shadowing effects and reflecting the incident light. Incident vector irradiance was measured simultaneously at the water surface and used to correct for fluctuations in incident light intensity during the profiling. In parallel to these measurements 25 l water samples were taken at 1 m depth in winter and at 10 m depth in summer. The absorption and the beam attenuation of the samples were measured using AC-9 (Wetlabs) in 9 spectral wavelengths bands (Table 1). These measurements were carried out within half an hour after sampling. Sub-samples were filtered over Glass fibre filters (Whatmann GF/F) to collect the particulate matter for measurements of the pigments. The filters were stored at -20°C. Pigments concentrations were measured afterwards using a reversed-phase HPLC technique. Seston was obtained using membrane filters of 0.45 μm (Sartorius). Part of its filtrate was stored in dark bottles at 4°C and used to measure the absorption spectrum of DOC with a Perkin Elmer λ 18 spectrometer and to measure DOC concentration. Highly purified water (Milli-Q Plus) was used as a reference.

2.2 Calculations

The inherent absorption was calculated in three different ways.

1) The asymptotic attenuation coefficients, which is an inherent optical property, was used to calculate the inherent absorption. Therefore, the dependence of K_∞ on ω_0 was calculated with the radiative transfer model Hydrolight 3.0⁶. The c was set at 1. The β was adapted from San Diego Harbor⁷ measured with 75 nm bandwidth. No spectral information on β

was included since for turbid coastal water it is relatively wavelength independent⁸. The optical properties were set at a constant over the depth. All other parameters set in the model have no effect on the K_{∞} . The relation between K_{∞} and the ω_0 given in Equation 1 was calculated using a polynomial fit ($R^2=1$). The K_d and K_u were calculated at 0.5 meter depth interval and the K_{∞} was selected from the measured irradiance profiles (Figure 2). The selection criterion was based on the absence of a drift of K_d and K_u over a 5 meter depth interval, however, this interval was frequently reduced in the red part of the spectrum. The inherent absorption was calculated according Equation 1. The c was taken from the AC-9 measurements. Differences in wavelength bands (Table 2) were corrected for using linear interpolation. The measured c does not include the attenuation caused by pure water, this was corrected for by using measured values of pure water⁹. Therefore, the calculated absorption includes all water constituents including the water itself.

$$\omega_0 = -0.3023\left(\frac{k_{\infty}}{c}\right)^2 - 0.7226\frac{k_{\infty}}{c} + 1.0493 \quad (1)$$

$$b = \omega_0 \cdot c \text{ and } a = c - b$$

2) As a second method the inherent optical properties were calculated according to Zaneveld *et al.*⁵ using the AC-9 measurements. The measured a_m and c_m were corrected for the temperature dependence of the water absorption using the data of Buiteveld *et al.*⁹

3) As a third method the specific absorption spectra were calculated using a non-linear optimisation procedure (simplex)¹⁰. Input data were from the AC-9 and concentrations of pigments and suspended matter. The a_m and c_m were corrected for temperature effects and the absorption spectra of DOC were subtracted. The remaining factors in the spectra are: phytoplankton, other suspended matter and the scattering correction coefficient for the AC-9. This method assumes that the specific optical properties at the stations are constant.

3. RESULTS AND DISCUSSION

3.1 Specific absorption of DOC

The specific absorption coefficient of DOC in the North Sea is variable. Figure 1 shows that the specific absorption of DOC at 412 nm in the winter and in the summer is different. In addition, data obtained during a cruise at the North Sea in summer 1994 showed high variability of specific DOC between the stations. Also, the exponential decrease of DOC absorption with wavelength measured in the summer and winter 1996 was different. The exponential slope parameter was $-0.0132 \text{ nm}^{-1} \pm 0.0029$ in winter and $-0.0096 \text{ nm}^{-1} \pm 0.001$ in summer. The averaged specific absorption coefficient was $0.14 \text{ m}^2 \text{ mg}^{-1}$.

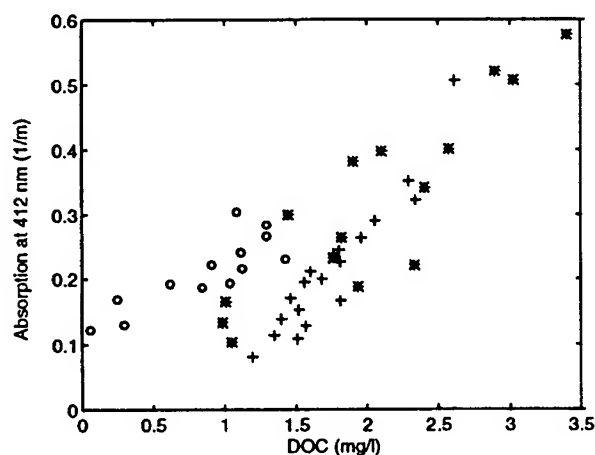


Figure 1. DOC absorption at 412 nm measured in winter (+) and summer (o) 1996. The symbols (*) are values measured in summer 1994. Variation of the ratio between non light absorbing DOC and light absorbing DOC could have caused the scattering of data, however no information on this is presently available.

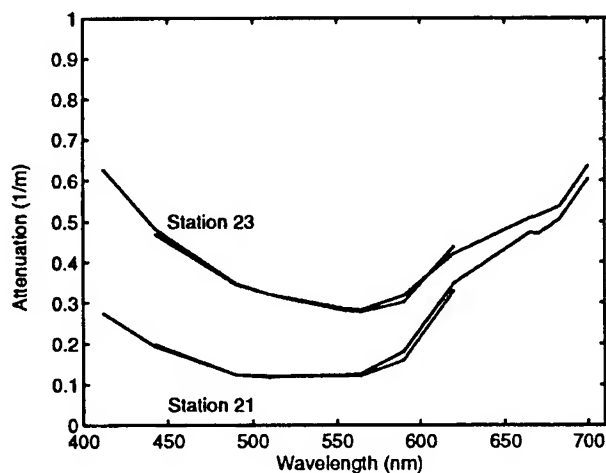


Figure 2. Attenuation coefficients K_d and K_u in the asymptotic region measured at two stations. Chlorophyll a concentration was $1.1 \mu\text{g/l}$ at both stations. DOC absorption at 412 nm was 0.13 m^{-1} at station 21 and 0.27 m^{-1} at station 23. Suspended matter was 0.8 mg/l at station 21 and 9.8 mg/l at station 23.

3.2 Inherent absorption calculated from K_{∞} and AC-9 measurement

The K_{∞} for all wavelengths at most station was reached at 5 m depth and therefore was calculated over the 5-10 m depth interval. However K_{∞} could not be accurately calculated in the red part of the spectrum when the measurements were carried out at 'rougher' weather conditions. Figure 2 shows the K_{∞} spectrally for two stations having different concentration of water constituents. The correspondence between K_d and K_{∞} shows that the asymptotic depth was reached. Parts of the asymptotic upward attenuation spectra are missing due to low light intensities. The absorption spectrum calculated from the K_{∞} is composed of absorption by pure water, DOC, phytoplankton and suspended sediment. The absorption spectra of pure water and DOC were subtracted to obtain absorption caused by suspended matter (Figure 3). About 50 percent of the calculated spectra were found to be reasonable. The other 50 percent underestimated down to 0.05 m^{-1} in the red wavelength range.

The absorption spectra using the AC-9 measurements calculated according to the Zaneveld method showed negative absorption values in the 500-550 nm wavelength range. A disadvantage of the method is its assumption that the absorption at 715 is zero. In turbid coastal water it is not clear what the absorption is in the near infra red part of the spectrum.

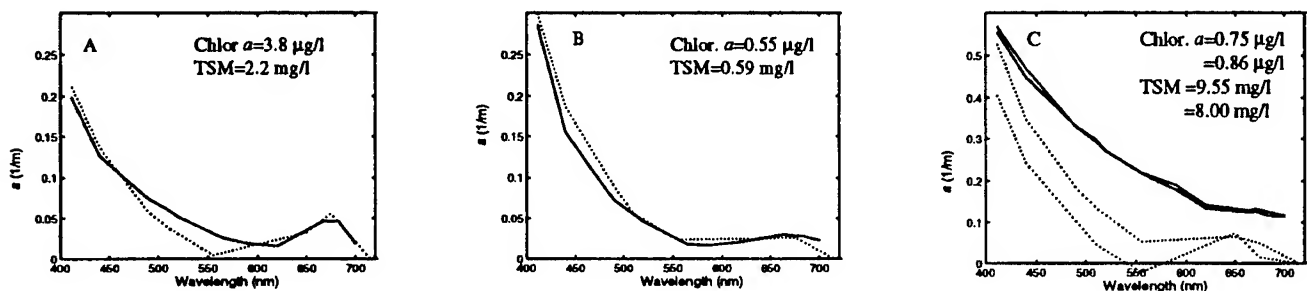


Figure 3. Absorption spectra of total suspended matter as calculated from AC-9 and from the K_{∞} . A) The absorption spectra match at stations dominated by phytoplankton, in this case *Coscinodiscus spp.* Due to high suspended matter concentration the standard correction caused an over-correction for the scattering error which is visible in the 500 nm wavelength region. B) The absorption spectra match at stations with low total suspended matter concentration and low pigment concentration. C) The absorption spectra did not match for stations where the total suspended sediment concentration were high and pigment concentrations were low.

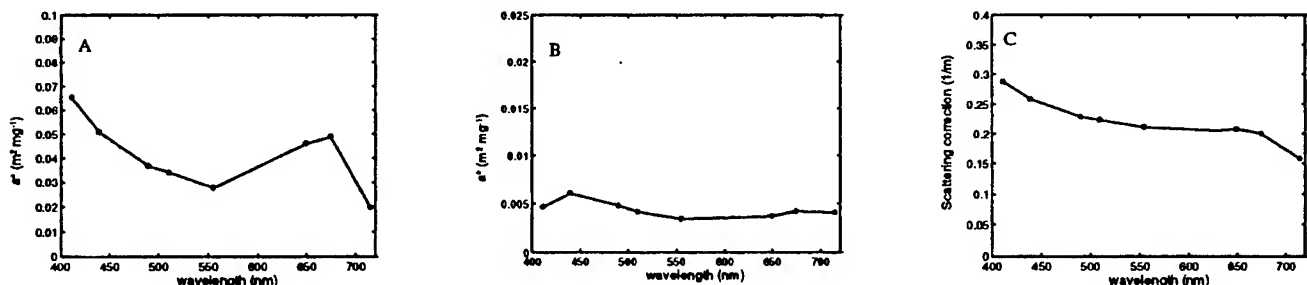


Figure 4. Specific optical properties calculated from AC-9 data using a non linear optimisation procedure. A) Specific absorption coefficient of *Coscinodiscus spp.* B) Specific absorption coefficient of suspended sediment. C) Scattering correction coefficient for the AC-9. This correction coefficient includes the specific absorption of detritus.

3.3 Specific absorption coefficients calculated from AC-9 using an optimisation procedure.

Three components were distinguished in the optimisation procedure i.e. phytoplankton, total suspended matter and the scattering correction for the AC-9. Figure 4 shows their specific coefficients. The specific absorption of *Coscinodiscus spp.* showed absorption in the red part of the spectrum. This spectral 'offset' may be explained by a covariance of the detritus with the chlorophyll *a*. Unfortunately no information is available on the detritus, measuring the concentration of detritus is

difficult. Normally such a 'offset' is corrected for. One simple method is to use an overall subtraction of the 'absorption' value 715 nm. If this subtraction is carried the a^* value is in the range of the chlorophyll-specific absorption coefficient as published by Sathyendranath¹¹.

Comparison of the sum of specific absorption of phytoplankton and suspended matter with the absorption obtained from K_d spectra (in figure 3) will show the spectral signature of the missing component. It is expected that the difference spectrum will have the spectral signature of the detritus absorption spectrum. More work will be done.

4. REFERENCES

-
- ¹ R. Doerffer and J. Fischer. Concentrations of chlorophyll, suspended matter, and gelbstoff in case II waters derived from satellite coastal zone colour scanner data with inverse modelling methods. *Journal of Geophysical Research* 99:7457-7466. (1994).
- ² H. Schiller and R. Doerffer, Submitted. Neural network for emulation of an inverse model- Operational derivation of Case II water properties from MERIS data; Subm. to *Int. Journal of Remote Sensing*.
- ³ W.S. Pegau, J.S. Cleveland, W. Doss, C.D. Kennedy, R.A. Maffione, J.L. Mueller, R. Stone, C.C. Trees, A.D. Weidemann, W.H. Wells and R.V. Zaneveld. A comparison of methods for the measurement of the absorption coefficient in natural waters. *Journal of Geophysical Research* 100:13201-13220. (1995).
- ⁴ J.L. Mueller and R.W. Austin. Ocean optics protocols for SeaWiFS validation, Revision 1. NASA technical memorandum 104566, Vol. 25. (1995).
- ⁵ J.R.V. Zaneveld, R. Bartz and J.Kitchen. A reflective-tube absorption meter. *Proc. SPIE 1302 (Ocean Optics X)* 124-136. (1990).
- ⁶ C.D. Mobley. *Light and water. Radiative transfer in natural waters*. Academic Press, San Diego. pp554. (1994).
- ⁷ T.J. Petzold. Volume scattering functions for selected ocean waters, In: *light in the sea (Benchmark papers in optics: V. 3)* ed. J.E. Tyler, Dowden, Hutchinson and Ross, Stroudsburg, Pennsylvania, 152-174. (1977).
- ⁸ A. Morel. Cited in *Light and Water. Radiative transfer in natural waters*. Edt C.D. Mobley 1994. Academic press. San Diego. (1973)
- ⁹ H. Buiteveld, J.H.M. Hakvoort and M. Donze. The optical properties of pure water. *Proc SPIE 2258 (Ocean Optics XII)* pp 174-183. (1994).
- ¹⁰ J.A. Nelder and R. Mead. A simplex method for function minimization. *The Computer Journal* 7:308-313. (1965).
- ¹¹ S. Sathyendranath, L. Lazzara and L. Prieur. Variations in the spectral values of specific absorption of phytoplankton. *Limnol. Oceanogr.* 32(2): 403-415. (1987).

Simulation of the Medium-Resolution Imaging Spectrometer (MERIS) performance for detecting chlorophyll-a over turbid inland waters.

H.J. Hoogenboom and A.G. Dekker

Institute for Environmental Studies/ Vrije Universiteit
De Boelelaan 1115, 1081 HV Amsterdam, The Netherlands
Tel (+31)-20-4449547, Fax (+31)-20-4449553, Email: erin.hoogenboom@ivm.vu.nl

ABSTRACT

The availability of imaging spectrometers such as the airborne AVIRIS, CASI, ROSIS, HYDICE and future spaceborne instruments such as MERIS and MODIS has created a necessity for spectral methods and models which can predict the performance of these instruments for detecting and estimating chlorophyll-a (CHL) as a water quality indicator. Aim of this study is to gain insight into the performance of MERIS for estimating CHL in turbid inland waters. In such waters with CHL ranging from 10 to over 300 $\mu\text{g l}^{-1}$ estimation of CHL using the fluorescence line height does not apply anymore. The research was carried out by means of bio-optical modelling, which yields the subsurface irradiance reflectance $R(0-)$ from the water constituent concentrations, using the inherent optical properties as parameters. The inherent optical properties are measured with laboratory spectrophotometers and they are applied for simulation of water types ranging from clear drinking water to turbid eutrophic waters. These simulations enabled the quantification of the effect of increasing chlorophyll-a on $R(0-)$. In addition a sensitivity analysis was applied. The change in $R(0-)$ due to a change of 1 $\mu\text{g l}^{-1}$ in CHL was compared to the noise equivalent reflectance as specified for ocean applications of MERIS, which gives an indication of the accuracy for estimating chlorophyll-a. From the simulation results it was concluded that MERIS can estimate chlorophyll-a in turbid inland waters with an accuracy of 1 $\mu\text{g l}^{-1}$ for CHL values of 10 $\mu\text{g l}^{-1}$ and 25 $\mu\text{g l}^{-1}$ for CHL values of 190 $\mu\text{g l}^{-1}$. Furthermore, variations in the backscatter to scatter ratio of 25 %, based on recent measurements of the volume scattering function, yielded a variation of 17-20 % in the reflectance.

Keywords: bio-optical modelling, coastal and inland waters, MERIS, sensitivity analysis, water quality, chlorophyll-a

1. INTRODUCTION

At the Institute for Environmental Studies (IVM) for development and operationalisation of remote sensing of water quality, research focuses on: 1) assessment of remote sensing system requirements for water quality applications and 2) estimation of water quality parameters from remote sensing using an analytical algorithm development and exploring the applicability of inverse modelling, especially in turbid coastal and inland waters.

A quantitative analysis of the relation between water quality parameters and radiometric quantities is facilitated by an bio-optical model for water, which may be linked to models for transferring the underwater light through the air-water interface and the atmosphere to the radiance at the sensor. For the assessment of sensor requirements the model is evaluated in forward direction, i.e. from the water constituent concentrations to a remote sensing signal, whereas for water quality assessment from remote sensing the inverse model is applied.

In the bio-optical model the inherent optical properties (IOP) of the constituents play a key role. The constituents distinguished here are phytoplankton, tripton (dead organic particles and inorganic particles) and aquatic humus (gilvin, Gelbstoff) and their IOP are represented by the absorption coefficient, the scattering coefficient and the normalised volume scattering function (VSF) or a derived quantity such as the backscatter to total scatter fraction. The output of the bio-optical

model used in this study is the underwater irradiance reflectance $R(0^-)$. The input of the model are the representative concentrations of the three constituents: chlorophyll-a (CHL), seston dry weight (DW) and aquatic humus absorption at 440 nm ($a_h(440)$).

This study aims to quantify the effect of variations in CHL on the reflectance. In addition, attention is paid to the sensitivity of $R(0^-)$ due to the backscatter properties of the constituents. The backscatter properties are represented in the model by the backscatter to total scatter fraction, B . From literature values and recent measurements of the VSF it appears that there can be significant difference in B for different water compositions¹⁴ (see also Dekker et al. in these proceedings).

1.1. The Medium Resolution Imaging Spectrometer (MERIS)

MERIS, as part of Envisat-1, is specifically designed for the assessment of marine phenomena. It has fifteen spectral bands for which positions and widths can be programmed. The spectral range is 400 to 1050 nm and the spectral resolution is 2.5 nm. An example¹³ is given in Table 2 and this set was used in the simulations (see also Fig. 2). In this example nine bands are within the visible range the main bands of interest for the assessment of CHL are at 665, 681.25 and 705 nm essentially for measuring the fluorescence peak of CHL. This fluorescence may dominate the reflectance for values in waters containing CHL up to $20 \mu\text{g l}^{-1}$ but for the CHL range found in turbid and eutrophic inland waters (CHL concentrations up to $300 \mu\text{g l}^{-1}$ and higher) the absorption and scattering features of the constituents dominate the reflectance, which means that bands at e.g. 676 and 706 nm may be more appropriate for detecting CHL².

Table 2 The MERIS bands as specified for ocean applications¹³ were used in this study. Only the bands in the visible range are shown.

wavelength in nm			function Rast (1995)
from		to	
407.5	-	417.5	absorption aquatic. humus, turbidity
437.5	-	447.5	CHL
485	-	495	CHL, other pigments
505	-	515	turbidity, DW, red tides
555	-	565	CHL reference, DW
615	-	625	DW
660	-	670	CHL
677.5	-	685.0	CHL fluorescence
700	-	710	aerosol, atmospheric correction, red/near-infrared vegetation ratio

MERIS has a dynamic range up to an albedo of 1 enabling monitoring of land surfaces which have relatively high reflectances compared to water surfaces. In order to assess water quality of the relative dark oceans a radiometric accuracy is specified of 2% of the detected signal relative to the sun. For ocean applications a noise equivalent reflectance, $NE\Delta R$, is specified¹¹ of $5 \cdot 10^{-4}$. In this study the effect small variations of the CHL concentrations on the $R(0^-)$ are investigated. These induced variations in $R(0^-)$ can be compared with the radiometric accuracy of MERIS, indicating MERIS' performance to detect CHL. In Europe there are several large inland and estuarine water bodies that can be monitored by MERIS. Although the simulations in this study are based on existing measurements of small inland waters, the results are also applicable to large inland water bodies in which the constituent types and their (specific) IOP are similar.

2. A BIO-OPTICAL MODEL FOR TURBID COASTAL AND INLAND WATERS

2.1. The relation between inherent optical properties and apparent optical properties

Several authors have shown that the model of Gordon et al.⁷ is applicable to coastal and inland waters^{4,9,14}. It relates the $R(0-)$ to the IOP and is based on a quasi-single scattering approximation of the radiative transfer equation:

$$R(0-) = f \frac{b_b}{a + b_b} \quad (1)$$

where a is the absorption coefficient, b_b the backscatter coefficient and f a multiplication factor, which depends on apparent optical properties of the light field¹⁰. The a and b_b can be written as a superposition of different components, which are phytoplankton, tripton (suspended particles excluding phytoplankton), aquatic humus and water itself:

$$\begin{aligned} a(\lambda) &= a_w(\lambda) + a_{\text{phyl}}(\lambda) + a_{\text{tripton}}(\lambda) + a_h(\lambda) \\ b_b(\lambda) &= B_w b_w(\lambda) + B_{\text{phyl}} b_{\text{phyl}}(\lambda) + B_{\text{tripton}} b_{\text{tripton}}(\lambda) \end{aligned} \quad (2)$$

where the B 's are the backscatter ratios of water, phytoplankton and tripton. For sake of simplicity we assume that the backscatter ratio is not dependent of wavelength and, hence, that all spectral variation is represented by the scattering coefficient. The inherent optical properties of water are assumed constant with a B_w of 0.5. For turbid waters the scattering is dominated by the suspended particles and thus the (back)scattering due to density fluctuations in the water can be neglected. In the next section the measurements of a and b and the water constituents will be considered in more detail.

2.2. The measurement of the constituents and their IOP

The absorption and scattering coefficient can be obtained from beam attenuation measurements with a spectrophotometer and a semi-integrating sphere. Since the spectrophotometer has an acceptance angle of 5° not the true c is measured but an apparent c' which is the sum of the absorption and the scattering from 5 to 180° , $c'_5 = a + b_5$. This measurement is repeated with a semi-integrating sphere with an acceptance angle of 40° , $c'_{40} = a + b_{40}$. If the absorption by the constituents at $\lambda = 750$ nm is neglected an estimate of the absorption can be obtained² and, subsequently, the $b_{40} = B_{40}b$ and $b_5 = B_5b$ can be calculated from a and c'_{40} and c'_5 respectively. Hence, in order to estimate the backscattering coefficient from these measurements a modified backscatter fraction must be used: the relative amount of backscattering compared to the scattering from 5 degrees is now given by:

$$B_{90/5} = \frac{\int_{90}^{180} \tilde{\beta}(\alpha) \sin \alpha d\alpha}{\int_5^{180} \tilde{\beta}(\alpha) \sin \alpha d\alpha} \quad (3)$$

Separate measurements of the inherent optical properties for each of the constituents are not feasible since it is (practically) impossible to separate the phytoplankton fraction from the tripton fraction. Instead, the pigments of the phytoplankton are extracted from the sample with ethanol, yielding the chlorophyll-*a* concentration (CHL) and the absorption of the pigments: a_{pigm} (the scattering by the pigments is neglected). The rest of the phytoplankton (i.e. the cell material) remains with the tripton fraction, and this combination will be referred to as apparent tripton. Its concentration is represented by the dry weight (DW) and the IOP by absorption and scatter coefficients, a_{trip} and b_{trip} , respectively. Due to these constraints in measuring the IOP and constituent concentrations we arrive at the following relation for the total absorption and backscatter coefficient

$$\begin{aligned} a(\lambda) &= a_w(\lambda) + a_{\text{pigm}}^*(\lambda) \text{CHL} + a_{\text{trip}}^*(\lambda) \text{DW} + a_h^*(\lambda) a_h(440) \\ b_b(\lambda) &= B_w b_w(\lambda) + B_{90/5, \text{trip}} b_{5, \text{trip}}^*(\lambda) \text{DW} \end{aligned} \quad (4)$$

where the IOP with a subscript * are specific quantities, i.e. per unit concentration. The inherent optical properties of a deep mesotrophic lake, lake Wijde Blik, together with the water absorption are shown in Figure 1a. These IOP represent a water type that is considered valid for most large inland and coastal waters with low resuspension of sediments. The specific scattering coefficient of the constituents and the specific absorption coefficient of aquatic humus are plotted on a separate axis on the right hand side.

The correlation between the CHL and the DW is taken into account in the bio-optical model, because of the high values of CHL. From measurements with algae cultures representing algae in inland waters, an empirical relation was found between the CHL and the DW of the phytoplankton, $DW_{\text{phyt}} = 0.07 \cdot \text{CHL}$. This was used to estimate the dry weight of the tripton fraction, $DW_{\text{tript}} = DW - DW_{\text{phyt}}$. In the simulation this tripton DW was fixed so the DW concentration varies only with CHL: $DW_{\text{model}} = DW_{\text{tript}} + 0.07 \cdot \text{CHL}_{\text{model}}$.

In contrast to the a and b , backscatter ratios, such as B and $B_{90/5}$, are not determined regularly, because they must be derived from the volume scattering function which is difficult to measure. Instead literature values are taken, e.g. $B = 0.019$ from the San Diego measurement by Petzold¹². Kirk¹⁰ points out that the VSF of different samples reported in literature, including coastal waters, have a similar shape and therefore one value of B suffices for many applications. However, the question arises whether this value is also applicable to turbid coastal and inland waters since the VSF may differ at backscatter angles. Volten et al.¹⁴ measured normalised VSF of several algae species of coastal and inland waters together with sample of silt. From these measurements Dekker et al. (these proceedings) found a $B_{90/5}$ of 0.025 for the freshwater algae. In the sensitivity analysis an average $B_{90/5}$ of 0.025 was used with a standard deviation of 0.005 (25 %).

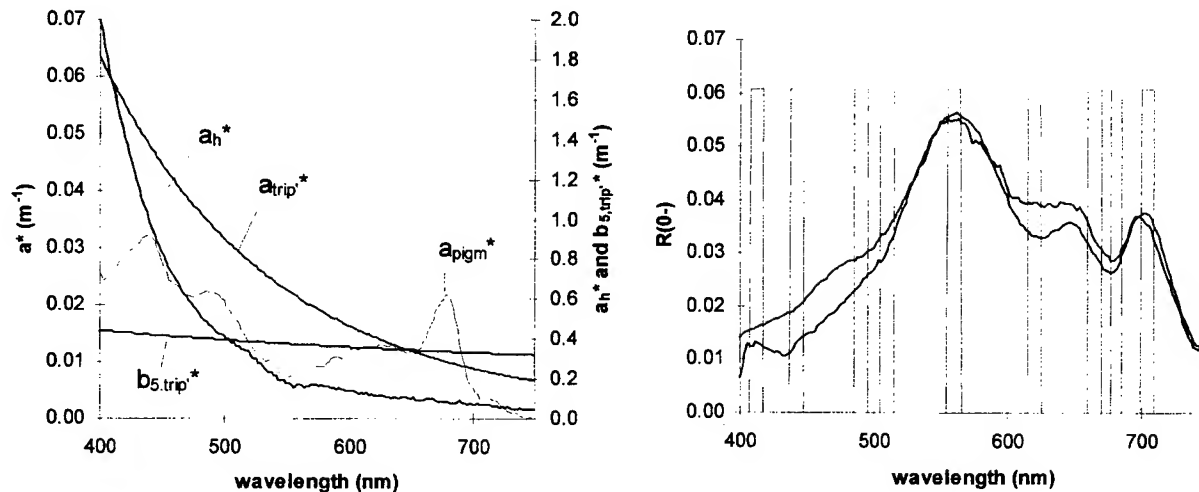


Figure 1a (left) The specific absorption of pigments, apparent tripton (seston without pigments) of lake Wijde Blik, a deep mesotrophic water, and the absorption of water (left axis) and the specific absorption of aquatic humus (Gelbstoff) and the specific scattering of apparent tripton (right axis). Figure 1b (right) The measured and modelled $R(0-)$; the measurements were carried out on 12 Sept 1990 ($\text{CHL} = 25 \mu\text{g l}^{-1}$, $\text{DW} = 8.5 \text{ mg l}^{-1}$).

3. RESULTS

A series of simulations were carried out in which the CHL concentration was varied. The simulations represent a situation of developing algae bloom in a short period of time, i.e. the CHL increases from 10 to 190 $\mu\text{g l}^{-1}$ while the tripton concentration remains constant. The specific inherent optical properties obtained for lake Wijde Blik were used as model parameters, since its water type (relative low mineral fraction and a mesotrophic state) is comparable to the type found in large inland and coastal waters with low resuspension of bottom material. The backscatter ratio $B_{90/5}$ was fixed to 0.041 based on the San Diego Harbour measurement of Petzold (1972).

3.1. A comparison of modelled and measured reflectance spectra

Before the actual simulations were carried out, the measured constituent concentrations were used as input in order to fit the modelled $R(0-)$ to the measured $R(0-)$, since the multiplication factor f in eq. 1 was unknown. The measured concentrations of the constituents in Lake Wijde Blik sampled at the time of the $R(0-)$ measurement were: CHL=25 $\mu\text{g l}^{-1}$, DW=8.5 mg l^{-1} and $a_h(440)=2.45 \text{ m}^{-1}$. From these a DW_{phyt} of 1.75 mg l^{-1} and a DW_{trip} of 6.65 mg l^{-1} were obtained. The $R(0-)$ was determined from radiance measurements of the upwelling and downwelling light above the surface using a Spectron spectroradiometer. The determination of $R(0-)$ involves correction for the air-water interface assuming a flat surface².

The multiplication factor f was estimated by fitting the modelled and measured $R(0-)$ in the region 670 to 720 nm, yielding a value of 0.31. This value lies with the range of 0.14-0.56 found in 31 samples in the same study area. The results are shown in Figure 1b together with bands of MERIS. It appears that the model yields a higher reflectance than the measurement, with a maximum difference of 0.01. Comparing the positions of the MERIS bands specified for CHL retrieval (see Table 1) with the spectral features of the $R(0-)$ it appears that these bands may not be appropriate for more eutrophic turbid waters. For instance, instead of a fluorescence peak at 681 nm the $R(0-)$ has a minimum at 676 nm and a maximum at 705 nm.

3.2. Simulations of an algae bloom in inland waters

In the first series of simulations the effect of increasing CHL was illustrated by varying the CHL from 10 to 190 $\mu\text{g l}^{-1}$ with increments of 20 $\mu\text{g l}^{-1}$. The DW was varied according to the correlation with CHL. The aquatic humus and DW_{trip} were kept constant. Figure 2a shows the high spectral results (2 nm resolution), where the arrows give the direction of changes in $R(0-)$ with increasing CHL. At 697 nm a hinge point appears where the increase in absorption is balanced by the increase in backscattering (and fluorescence). Simulations for other concentrations of the constituents (e.g. high tripton but relative low CHL) show that such hinge points are a common feature for this range of CHL, although the position depends on the water composition^{3,8}. From 400 to 697 nm the $R(0-)$ decreases with increasing CHL due to absorption by the pigments. However, since the absorption is in the denominator of the bio-optical model (see eq. 1) this decrease is not linear with CHL so that further decrease of $R(0-)$ is limited for high values of CHL ($> 200 \mu\text{g l}^{-1}$). From 697 to 750 nm the $R(0-)$ increases with increasing CHL due to a relative high backscattering compared to the absorption of the constituents.

In Figure 2b the $R(0-)$ are evaluated at the MERIS bands as specified in Table 1 in the range of 400 to 750 nm. Since the wavelength resolution of the simulated $R(0-)$ was coarse (2 nm) with respect to some band definitions of MERIS (0.25 nm see Table 1) the $R(0-)$ results were first splined to 0.25 nm using the standard spline function of Matlab. Subsequently, the $R(0-)$ values within a MERIS band were averaged. The MERIS reflectances show the same spectral features as the high spectral $R(0-)$. However the shoulder at 600-624 nm caused by the absorption of cyanophycocyanin (pigment present in cyanobacteria) is less pronounced which will probably limit the capability of MERIS for retrieval of cyanobacteria pigment concentrations.

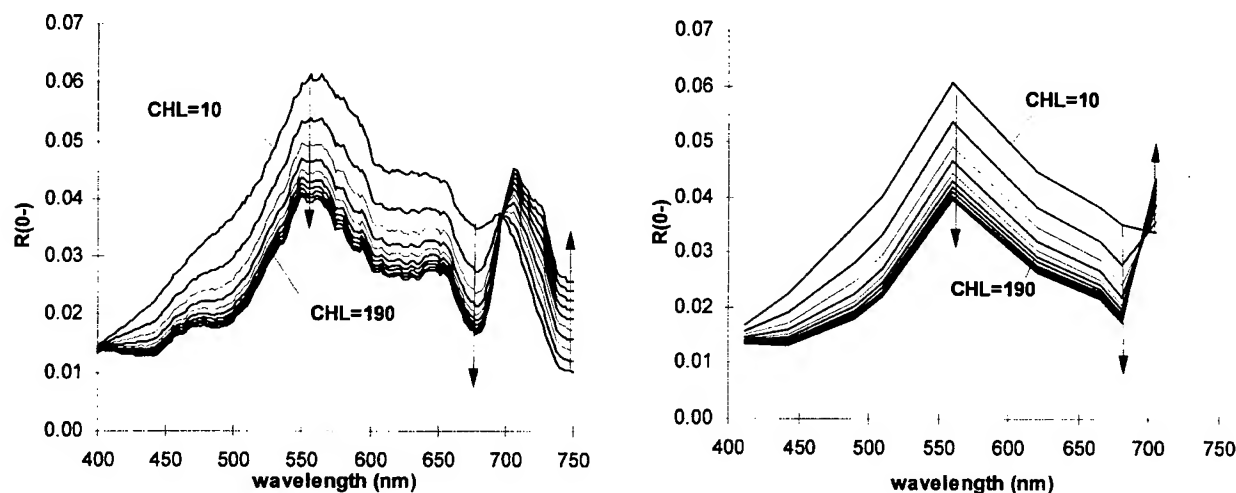


Figure 2a (left). The modelled $R(0-)$ for a range of CHL concentrations from 10 to 190 $\mu\text{g l}^{-1}$. In Fig. 2b (right) the high spectral results (resolution 2 nm) were evaluated at the MERIS bands in Table 1. The arrows indicate the change of $R(0-)$ induced by increasing CHL. Note the hinge point at 697 nm.

3.3. The sensitivity of $R(0-)$ for CHL and backscatter ratio

The sensitivity of $R(0-)$ with respect to CHL is important for assessment of the accuracy with which the CHL can be estimated from (remotely sensed) $R(0-)$. In this study the change of $R(0-)$ per unit change of CHL is used as a measure of the sensitivity. Mathematically, this definition of sensitivity is equal to the first derivative of $R(0-)$ with respect to CHL. The first derivative and, hence, the sensitivity depends on the concentration of CHL. The derivative was calculated from the bio-optical model for several CHL from 10 to 190 $\mu\text{g l}^{-1}$ and plotted in Figure 3a. The spectra can be interpreted as (the absolute value of) the change in $R(0-)$ induced by adding 1 $\mu\text{g l}^{-1}$ to the CHL which was used to calculate $R(0-)$. At the hinge point at 697 nm (see Fig 2) the increase in absorption balances the increase in backscattering and consequently the derivative is zero.

In the initial assessment of the performance of MERIS the sensitivity of $R(0-)$ for different CHL can be compared with the noise equivalent reflectance at sea level, $\text{NE}\Delta R$, specified for MERIS. The $\text{NE}\Delta R$ specified for ocean applications¹¹, $5 \cdot 10^{-4}$ was also plotted in Fig. 3a. It indicates that MERIS will be able to discriminate 1 $\mu\text{g l}^{-1}$ for $\text{CHL}=10 \mu\text{g l}^{-1}$ but can only discriminate 25 $\mu\text{g l}^{-1}$ for $\text{CHL}=190 \mu\text{g l}^{-1}$.

The sensitivity of $R(0-)$ due to variations in the modified backscatter to scatter fraction, $B_{90/5}$, was also considered in this study. Five thousand samples were taken from a normal distribution with a mean of 0.025 and standard deviation of 0.005, thus assuming that 95% of the $B_{90/5}$ in actual waters is within the range 0.015–0.035 based on Dekker et al. in these proceedings. The $R(0-)$ was calculated for each value of $B_{90/5}$ and then mean and standard deviation of all $R(0-)$ spectra were calculated. The standard deviation can be considered as a measure for the sensitivity of $R(0-)$ for variations in backscatter ratio's. Figure 3b shows the results for $\text{CHL}=25, 100$ and $200 \mu\text{g l}^{-1}$. Due to the relative large variation in $B_{90/5}$ (25%) the variations in $R(0-)$ are smaller (17–19 %) but still substantial. Further analysis of the variation in B and its effect on $R(0-)$ and, more importantly, the retrieval of CHL and DW is required.

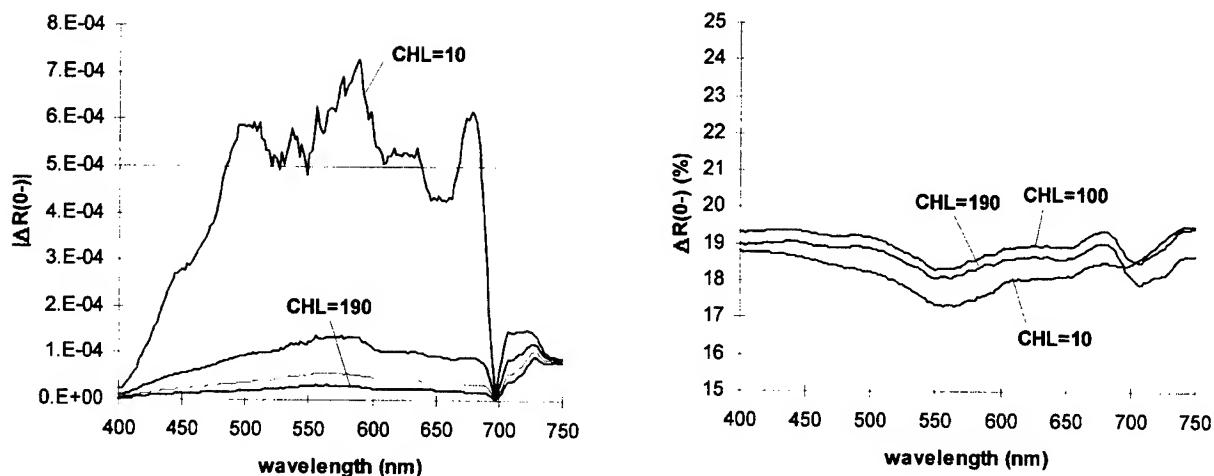


Figure 3a (left) The sensitivity of $R(0-)$ for $1 μg l^{-1}$ CHL at CHL=10, 70, 130 and 190 $μg l^{-1}$. The horizontal line indicates the required noise equivalent reflectance, NEAR, as was specified for ocean applications. Figure 3b (right) The sensitivity of $R(0-)$ due to variations in the backscatter ratio.

4. DISCUSSION AND CONCLUSIONS

This paper illustrates how variations in chlorophyll-a (CHL) and backscatter properties of tripton effect the accuracy with which MERIS can retrieve CHL in turbid inland waters, for CHL ranging from 10 to 200 $μg l^{-1}$, several times higher than in most ocean and coastal waters. The combination of absorption and scattering of the constituents in turbid waters results in reflectances for which spectral shape can deviate significantly from typical reflectances found in case I and II waters. For example, the fluorescence peak at 681 nm was not present in the simulated spectra. As a consequence, the band set defined for retrieval of CHL in oceans and the radiometric requirements may not be applicable for turbid water types. This pilot study aims to get an indication of MERIS' performance in discriminating CHL in turbid inland waters.

In this study bio-optical modelling was used to calculate the subsurface reflectance $R(0-)$. In the bio-optical model the variability of the inherent optical properties needs to be analysed, especially the estimation of the backscatter coefficient for different algae and sediment types. The propagation through the air-water interface and atmosphere may effect the resolving power of MERIS significantly. Variations in these effects due to variability/uncertainty in the transfer should be evaluated.

Although the parameters of the bio-optical model need to be validated, some important conclusions can be drawn from the initial simulations of this study. The simulations showed significant influence on the size and shape of the $R(0-)$ spectra, e.g. the identification of hinge points in the $R(0-)$ that indicate spectral areas where increases in absorption are compensated by increases in backscattering. Some of the spectral features that appeared from the simulation results may be important for developing new algorithms, such as the shoulder at 620 nm due to cyanophycocyanin and the constant increase of $R(0-)$ at 750 nm with increasing CHL.

Another conclusion drawn from the modelling results is that MERIS has a sufficient NEAR for detecting concentration differences of CHL: based on the 1995 specifications of MERIS can detect $1 μg l^{-1}$ CHL at concentration levels of 10 $μg l^{-1}$

and $22 \mu\text{g l}^{-1}$ CHL at $190 \mu\text{g l}^{-1}$ CHL. Using smart algorithms this accuracy may even improve. Of course in a real remote sensing mission these values will deteriorate due to the influence of the atmosphere and a rough water surface.

From the sensitivity of $R(0-)$ induced by variations in the backscatter fraction it can be concluded that the observed variation in B (25 %) yields a smaller but still substantial variation in $R(0-)$ (17-20%). Further research should preferably focus on separation of the back scatter fractions for each type of constituent and the expected reduced variation in normalised $R(0-)$ spectra.

5. REFERENCES

1. Althuis, I.A., J. Vogelzang, M.R. Wernand, S.J. Shimwell, W.W. Gieskes, R.E. Warnock, J. Kromkamp, R. Wouts, W. Zevenboom, (1995) *On the colour of Case 2 waters: particulate matter North Sea: Part 1-Results and conclusions*, RIKZ, RIKZ, Den Haag, The Netherlands, 161 p.
2. Dekker, A.G. (1993) *Detection of optical water quality parameters for eutrophic waters by high resolution remote sensing*. PhD. Thesis, Vrije Universiteit, Amsterdam, The Netherlands; 240 p.
3. Dekker, A.G. and H.J. Hoogenboom. (1996) Predictive modelling of AVIRIS performance over inland waters. In: R.O. Green, editor. *JPL Airborne Earth Science Workshop Proceedings*, 3 -1996, JPL Laboratory, Pasadena, California, USA. p. 1-10.
4. Dekker, A.G., H.J. Hoogenboom, L.M. Goddijn, S.W.M. Peters, (1996) The relationship between inherent optical properties and reflectance spectra in turbid inland waters. *Remote Sens. Reviews*, Vol. 19, p. ??
5. Doerffer, R. and H. Schiller. (1994) Inverse modelling for retrieval of ocean color parameters in Case II coastal waters: an analysis of the minimum error. In: J.S. Jaffe, editor. *Ocean Optics XII*, 6 -1994, SPIE, Bellingham, Washington, USA, p. 887-893.
6. Doerffer, R., K. Sorensen, and J. Aiken. (1995) MERIS: Potential for coastal zone application. In: P.J. Curran and Y.C. Robertson, editors. 9 -1995, Remote Sensing Society, Southampton, p. 157-165.
7. Gordon, H.R., O.B. Brown, M.M. Jacobs, (1975) Computed relationships between the inherent and apparent optical properties of a flat homogeneous ocean. *Appl. Opt.* Vol. 14, No. 2, p. 417-427.
8. Hoogenboom, H.J., A.G. Dekker, I.A. Althuis, Simulation of AVIRIS performance for detecting chlorophyll over coastal and inland waters. [In Press] *Remote Sens. Environ.* (1996)
9. Jupp, D.L.B., J.T.O. Kirk, G.P. Harris, (1994) Detection, identification and mapping of cyanobacteria-using remote sensing to measure the optical quality of turbid inland waters. *Australian Journal of Marine and Freshwater Research*, Vol. 45, p. 801-828.
10. Kirk, J.T.O. (1994) *Light & photosynthesis in aquatic ecosystems*, 2nd ed., 509 p.
11. MERIS Science Advisory Group, (1995) *The Medium Resolution Imaging Spectrometer MERIS; Report of the MERIS Scientific Advisory Group*, SP-1184, ESA Publications Division, ESTEC, Noordwijk, The Netherlands, 62 p.
12. Petzold, T.J. (1972) *Volume scattering functions for selected ocean waters*, San Diego: Scripps Inst. Oceanogr. Visibility Lab.
13. Rast, M. and J.L. Bezy. (1995) The ESA Medium Resolution Imaging Spectrometer(MERIS): Requirements to its mission and performance of its system. In: P.J. Curran and Y.C. Robertson, editors. 9 -1995, Remote Sensing Society, Southampton, p. 125-132.
14. Volten, H., J.F. De Haan, J.W. Hovenier, W. Vassen, R. Schreurs, A.G. Dekker, H.J. Hoogenboom, F. Charlton, R. Wouts, Laboratory measurements of angular distribution of light scattered by phytoplankton and silt. [In Press] *submitted to Limn. Ocean.* (1996)

A neural network to extract size parameter from light scattering data

Patricia G. Hull

Tennessee State University, Department of Physics and Mathematics
3500 John Merriitt Blvd., Nashville, TN 37209-1561

Mary Quinby-Hunt

Lawrence Berkeley National Laboratory, Energy and Environment Division
One Cyclotron Road, Berkeley, CA 94720

Keywords: polarized light scattering, neural networks, size parameter, microscopic size distributions

ABSTRACT

A computer-simulated neural network is described that successfully identifies the size parameter of particles in a sample of ocean water from its S34 Mueller matrix element. In the Mueller matrix formalism, the polarization states of the incident and scattered light are described by four-element Stokes vectors, and the effect of the scattering medium on the incident beam is described by the sixteen-element Mueller or scattering matrix. The experimental measurements of the Mueller matrix elements as functions of the scattering angle contain all the information on optical properties, size parameter, and shape of the particles that make up the scattering medium, although it is not a simple task to retrieve it. The pattern recognition and classification properties of an artificial neural network, such as that described here, offer a new and powerful approach to retrieving the information.

1. INTRODUCTION

The problem of determining the size distribution of a sample of microscopic particles has long received attention from the scientific community. Kerker¹ devoted a chapter in his popular text on light scattering to modeling and measuring particle size distributions using light scattering data, specifically, total scattered light intensity as a function of scattering angle. More recently, because of its strong dependence on particle size, Bronk, *et al*, used a polarized light scattering function to determine size distribution in bacteria samples.²

Solutions to an impressive list of problems in both science and industry are currently being found using the unique and powerful pattern-recognition abilities of artificial neural networks. In fact, a neural network analysis of the intensity of scattered light has been used to characterize bubbles in bioreactors and in water quality assessment.^{3,4} Whereas traditional problem-solving methods, even computer programs, must be provided manually-determined solution algorithms, artificial neural networks do not. From the training data, mapping input to known output, and a few simple instructions, the network itself can determine the adjustment needed on each input to map it to its corresponding output. It can then interpolate that knowledge to apply to input for which it must calculate the output.

The object of the work presented here was to develop an artificial neural network to recognize in the scattering matrix elements, those features associated with the optical properties of ocean scatterers. That is, given the Mueller matrix elements, what are the optical properties, size parameters, and shapes, of the particles that scatter the light? The complex, relationships between the inputs and outputs of the light-scattering process make this problem seemingly intractable by conventional methods, but ideally suited for solution by an artificial neural network.

2. THEORY

Stokes vector and Mueller matrix formalism

The Stokes vector and Mueller matrix formalism is well suited to the study of the scattering of polarized light. The complete polarization properties of a beam of light can be described by a four element Stokes vector $F = [I, Q, U, V]$, where I is the total intensity of light, Q represents the degree of vertical or horizontal polarization, U represents the degree of 45° or 135° polarization, and V represents the degree of left or right circular polarization. The effect of the scattering medium on the incident beam is described by the sixteen-element Mueller or scattering matrix, M . The Mueller matrix for a given medium depends on the scattering angle and contains all the elastic scattering information available at a given wavelength on the size, structure, symmetry, orientation, complex refractive index, and ordering of the particles that make up the scattering medium. In this formalism, the scattering event is represented by the matrix equation, $F' = M F$, shown in terms of the matrix elements below:

$$\begin{pmatrix} I_s \\ Q_s \\ U_s \\ V_s \end{pmatrix} = \frac{1}{k^2 r^2} \begin{pmatrix} S_{11} & S_{12} & S_{13} & S_{14} \\ S_{21} & S_{22} & S_{23} & S_{24} \\ S_{31} & S_{32} & S_{33} & S_{34} \\ S_{41} & S_{42} & S_{43} & S_{44} \end{pmatrix} \begin{pmatrix} I_i \\ Q_i \\ U_i \\ V_i \end{pmatrix}$$

The experimental determination of all sixteen of the Mueller matrix elements requires a number of measurements. Generally, a detector is set up to measure the total intensity of light scattered from a sample illuminated with a laser beam. A filter in front of the sample determines the polarization state of the incident beam and a filter in front of the detector determines the polarization state to be measured. A number of measurements of intensity vs. scattering angle with different combinations of input and exit filters are made. An algebraic manipulation of these intensities then yields the 16 matrix elements. Not all the matrix elements are independent, so in most cases, fewer than sixteen intensity measurements vs. scattering angle are necessary. In the case of spherical particles, for example, there are only four independent matrix elements.

Analytical values of the Mueller matrix elements for light scattering by spherical particles are generally determined by Mie calculations, but for non-spherical particles, they must be determined by an approximation method such as the coupled-dipole model.^{5,6,7,8}

An artificial neural network

Despite its provocative name, an artificial neural network does not necessarily mimic a network of biological neurons. Rather, it is a computing system composed of a number of simple, interconnected processing elements, typically referred to as neurons or nodes, operating in parallel. The network may be 'hard-wired' (constructed of electronic components) or created by a computer simulation. The artificial neural network described in this work was a computer simulation using a Power Macintosh desktop computer.

A given neuron, or node, may have any number of inputs, but it always has only one output. In the neuron/node, each input value is multiplied by an assigned corresponding weight, and these extended values are then summed to a single total. This total is passed to a transfer function, which may be linear or non-linear, and which may or may not perform some calculation on the data. The transfer function may also contain a bias that adds a degree of freedom in training the network. The several types of transfer functions used in neural network architecture include 1) a function that restricts the output of the neuron to be either zero or one (hard-limit function), 2) a function that restricts it to being a number ranging between zero and one (log-sigmoid function), and 3) a function that simply generates output numbers proportional to the input numbers (linear function).

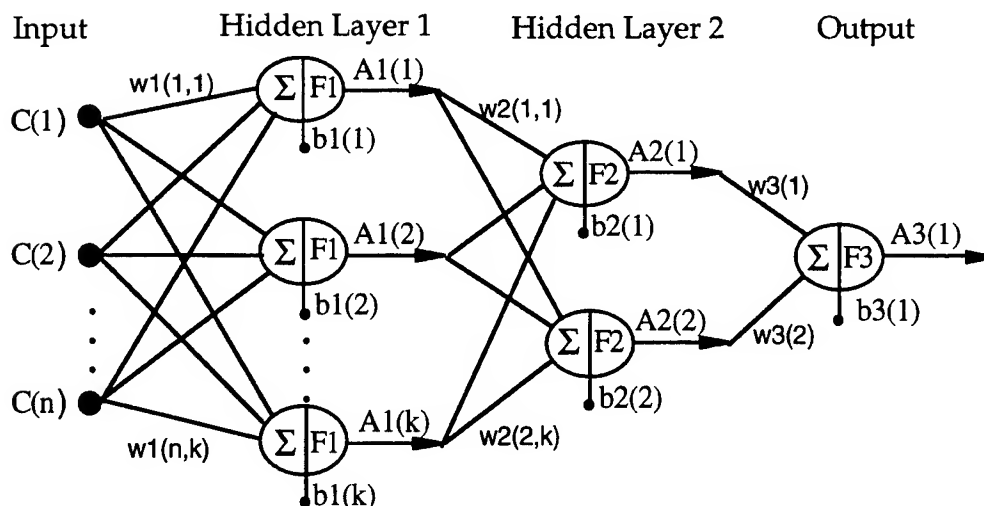


Figure 1. A multi-layer artificial neural network. The network shown is fully connected. In this network, there are n inputs values, k processing elements (nodes) in the first hidden layer, two nodes in the second hidden layer, and one output node.

A number of identical processing elements functioning in parallel constitute a layer. The layer that receives inputs is called the *input* layer. It performs no function other than buffering the input signal. The network outputs are generated from the *output* layer. A layers whose outputs are passed to the next layer is called a *hidden* layer. The network is *fully connected* if every output from one layer is passed along to every node in the next layer. When weight adjustments are made in preceding layers of feed forward networks by "backing up" from outputs, the term *back propagation* is used. The back propagation allows for the training of a network to produce the correct output. The architecture of the artificial neural network we have selected for our light scattering analysis is a fully connected, 2 hidden-layer, back propagation neural network. A diagram of a simple artificial neural network is shown in Figure 1.

3. APPROACH

The initial approach to developing the desired neural net was to target one property of a scatterer, its size parameter. The size parameter is typically defined to be equal to $2\pi r/\lambda$, where r is the radius of the spherical particle and λ is the wavelength of the incident light in the medium. Since samples of ocean waters contain a distribution of particle sizes, the value of the radius used in the definition will be its mean value. For non-spherical particles, r , is taken to be the radius of a sphere of equivalent volume. The Mueller matrix element, S_{34} , has been used to predict the sizes of bacteria,² so it seemed to be a good candidate for the input to the network. If the network is given the S_{34} matrix element as a function of scattering angle, can it determine the size parameter of the scattering particles? In order to construct a network that could be evaluated for different learning strategies and error determination methods, it was important to keep the number of input data points as small as possible so that the calculations could be carried out on a Macintosh computer. It has been shown that at least 3 or 4 processing elements for each input node (data point) is required for a network to have sufficient power to solve a problem of this type.^{9,10,11,12} Since the Mueller matrix elements have a period of 2π and are even functions of the scattering angle, it proved to be convenient to describe the functional form of these elements by a simple Fourier series of cosine terms. For example, the S_{34} element as a function of scattering angle can be written as;

$$S_{34}(\theta) = c_0 + \sum_{k=1}^{\infty} c_k \cos(k\theta)$$

where,

$$c_0 = \frac{1}{\pi} \int_0^{\pi} S_{34}(\theta) d\theta \quad \text{and} \quad c_k = \frac{2}{\pi} \int_0^{\pi} S_{34}(\theta) \cos(k\theta) d\theta$$

Examination of the S_{34} matrix element calculated from Mie theory indicated that it could be duplicated extremely well with a Fourier series of about 12 terms for size parameters up to 20. Therefore, for small particles, as much useful information about the functional form of S_{34} could be supplied to the network using the twelve Fourier coefficients as with using forty or fifty data points. Instead of one or two hundred processing elements, a trainable network with as few as 36 processing elements was feasible. The simple network design described here is similar that shown in Figure 1. The network had 12 input nodes (the Fourier coefficients) and one output node (the size parameter.) The first hidden layer had 48 nodes and the second hidden layer had 16 nodes. The output layer had a linear transfer function (F3 with a bias b_3) and the two hidden layers both had log-sigmoid transfer functions (F1 and F2 with bias b_1 and b_2 , respectively). Computations such as selection of initial weight matrices, summing weighted inputs (matrix inner product), calculations of the transfer functions, applying learning rules, and assessing the network's learning rate and performance were carried out using algorithms in the MATLAB library and its associated Neural Network Toolbox.¹³

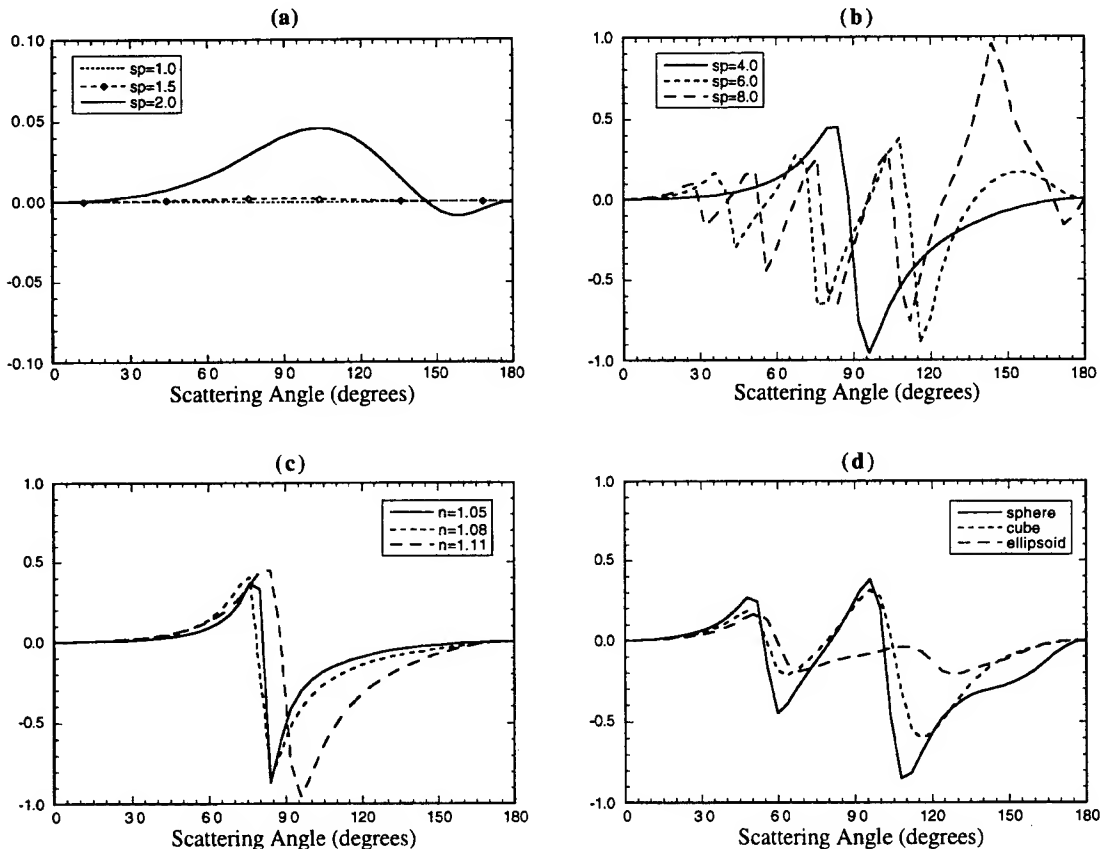


Figure 2. The Mueller matrix element, S_{34} as a function of scattering angle. Figures 2(a) and (b) show S_{34} for spheres of various size parameters. Figure 2(c) shows the variation of S_{34} for spheres with relative index of refractive for a constant size parameter of 5.0, and Figure 2(d) illustrates the effects of particle shape on S_{34} . In all figures other than (c) the relative index of refraction of the scattering particles is kept constant at 1.11.

4. RESULTS

In order to provide well-characterized training data to the neural network, analytical rather than experimental data were used. Unlike analytical calculations, experimental data are often 'noisy.' In addition to the electronic noise in the instrument, the effects of scattering samples made up of a mixture of particles of different sizes, shapes and refractive indices contribute to the 'noise' in the data. A reasonable evaluation of a neural net cannot be made without taking into account 'noisy' input data. In order to simulate the features of experimental data, Mie calculations were made using a Gaussian distribution of spheres and by varying the index of refraction. Producing data in this way seemed reasonable since, it has been shown that light scattering by marine *Chlorella* predicted by Mie calculations using a Gaussian distribution exhibits good agreement with experimental measurements.¹⁴ Coupled-dipole calculations with orientational averaging were made for ellipsoids, cubes and cylinders for different size parameters and index of refraction.¹⁵ Although no experimental data was included in the training sets, some experimental data of polarized light scattering by samples of bacteria were included in the test set.¹⁶ Examples of the resulting S34 matrix elements are shown as a function of scattering angle for particles of different size parameters, indices of refraction and shape in Figure 2. The figure clearly shows why S34 was chosen as a predictor of size parameter. Figures 2(a) and 2(b) illustrate the strong dependence of S34 on size parameter. The index of refraction is kept constant in both (a) and (b). Figure 2(a) also shows how rapidly S34 goes to zero in the Rayleigh limit. Figure 2(c) depicts the change in S34 as the index of refraction is changed while keeping the size parameter fixed at 5.0. Finally, Figure 2(d) illustrates differences that might be expected in S34 for particles of different shapes.

The 'noisy' data (different shapes and relative refractive index) shown in Figure 2 were presented to the network to test the network's ability to distinguish size parameter from shape and index of refraction variations. It was necessary to train that neural net to be insensitive to the variations in S34 due to index of refraction. This was accomplished by including S34's calculated for different indices of refraction in the training set. Figure 3 shows an example of a training session in which 50 data sets from Mie calculations with a range of refractive indices were introduced to the network. The size parameters in this set ranged from 1.0 to 20.0. A sum-square error goal of 0.01 between network output and target size parameter was selected for this session, and about eighteen thousand epochs (iterations back through the network) were required to reach the goal. The calculations required about 40 minutes of computer time. As the network carried out the calculations, a record of the sum-squared error as a function of number of epochs was displayed on the computer screen. The top graph of Figure 3 is a copy of that display after it had reached the target goal. A test set consisting of data not used in the training was then presented to the network. The bottom graph of Figure 3 is a record of that outcome. The + 's mark the value of each size parameter as predicted by the network. Points on the dashed line are correct (or target) values of the size parameter. This graph is shown for purposes of illustration only. Clearly, the error is much too large to consider this "first generation" network properly trained. Examination of the graph, however, provides valuable information as to how to proceed with the next generation training. The points that are in the greatest error (points at 16 and 17 near the top end of the graph) are for experimental data for bacteria. This error is on the order of 20%. The network, however, did reasonably well at identifying size parameters for cubes (points at 5.0 and 6.0) and better for spheres (all other points.) The large error for the bacteria data may be due to an unsatisfactory definition or knowledge of the appropriate value to assign for the size parameter. Successive generations of training data included data for cubes from coupled-dipole calculations in addition to the Mie calculations. After three generations, all data points for the test set fell within the desired error limit of 1% except the two points for the experimental data. In fact, the agreement got worse in this case. Possibly the number of training sets and/or the number of neurons could be increased to improve the network's performance, or other additional matrix elements (S11, S12 and S33) used in the training and testing data. The most obvious way to improve the network's ability to recognize features in experimental data is to include many samples of experimental data in the training sets. Much work needs to be done to increase the availability of experimental data for polarized light scattering for well-characterized samples.

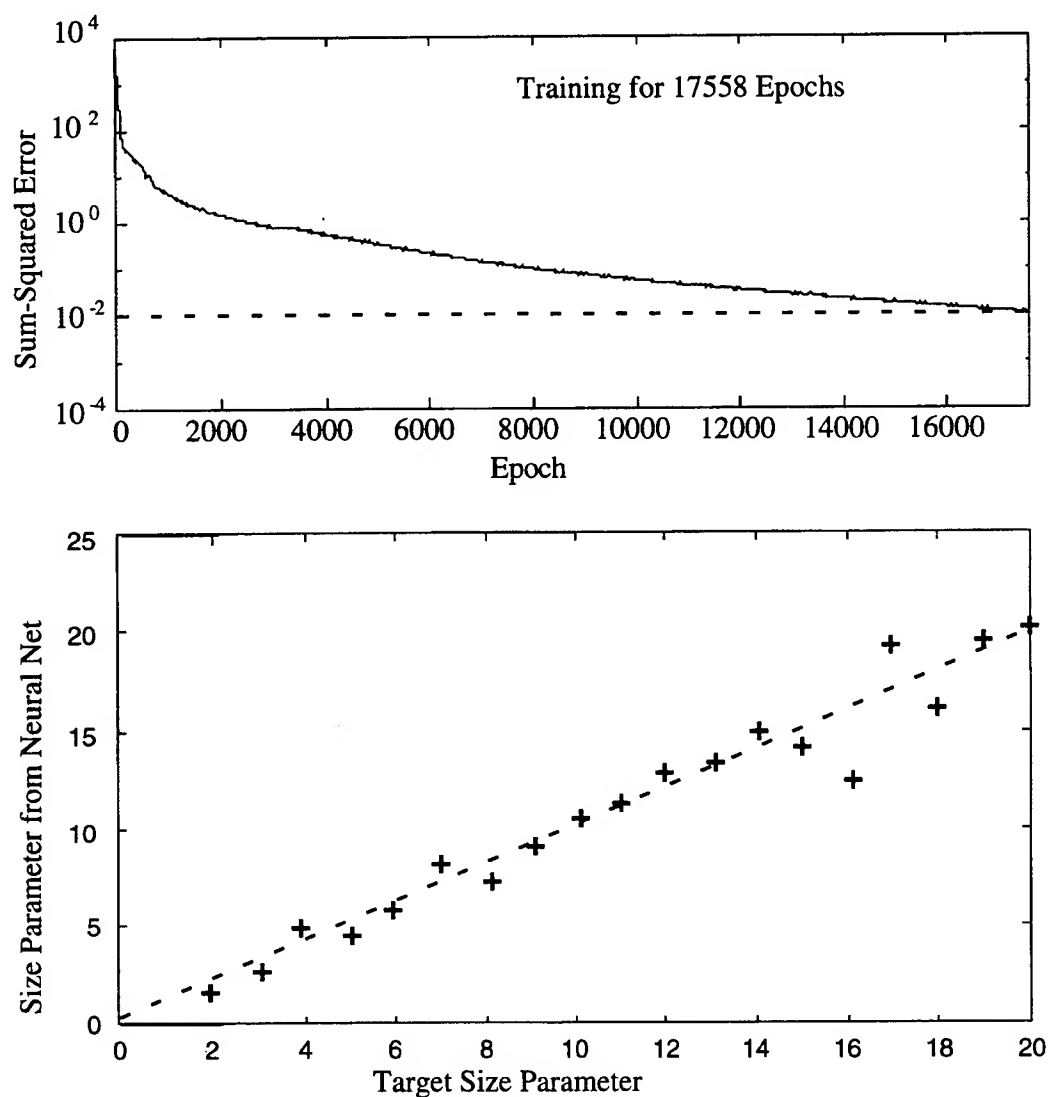


Figure 3. Graphs showing a training and testing session for a back-propagation neural network. Input data consisted of Fourier coefficients for each of 50 sets of S34 matrix elements. Dashed line in the training graph (top) is error goal, and dashed line in testing graph (bottom) is the actual value of the size parameter.

4. CONCLUSIONS

In our inverse problem approach, a simple artificial neural network has been designed and tested that predicts the size parameter of a scatterer based on its S34 matrix element. The success of this simple network is an important first step in our goal of predicting the optical properties, size parameter, and shape of the particles that make up the scattering medium from experimental measurements of light scattering. Furthermore, the experience we have gained in designing, training and testing this simple neural network has given us insight into its potential applications.

5. ACKNOWLEDGEMENT

This work was sponsored by the Office of Naval Research, Grant No. N00014-96-1-0307, Steven Ackleson, Project Manager.

6. REFERENCES

1. Kerker, M., *The Scattering of Light and Other Electromagnetic Radiation*. Academic Press, New York. (1969)
2. Bronk, B., Van De Merwe, W. and Stanley, M., "InVivo Measurement of Average Bacterial Cell Size from a Polarized Light Scattering Function," *Cytometry*, Vol.13, 155. (1992)
3. Bugman, G., Lister, J.B., and von Stockar, U., "Characterizing Bubbles in Bioreactors Using Light or Ultrasound Probes: Data Analysis by Classical Means and by Neural Networks." *Canadian Journal of Chemical Engineering*, Vol. 69, 474-480, (1991)
4. Smith, P.R., Green, D., and Naimimohasses, R., "Some Investigations on neural processing of scattered light in water quality assessment." *IEE Proc.-Vis Image Signal Process.*, Vol 141, No.4, 261. (1994)
5. Purcell, E.M. and Pennypacker, C.R. Scattering and Absorption of Light by Non spherical Dielectric Grains, *Astrophys. J.* Vol.186, 705. (1973)
6. Singham, M., Singham, S. and Salzman, G. 1986: The scattering matrix for randomly oriented particles, *J. Chem. Phys.* Vol.85, 3807. (1986)
7. Hull, P., Hunt, A., Quinby-Hunt, M., and Shapiro, D., "An analytical model for predicting light scattering from marine micro-organisms," *Proc. SPIE*, Vol. 1537, San Diego, July 1991.
8. Shapiro, D., Hull, P., Hunt, A., Quinby-Hunt, M., and Maestre, M., "Theoretical and experimental study of polarized light scattering on helices," *Ocean Optics XI Proc. SPIE*, Vol. 1750, San Diego. (1992)
9. McCord, M. and Illiangworth, W., *A Practical Guide to Neural Nets*, Addison-Wesley Publishing Co., Reading, Mass. (1991)
10. Lippman, R.P., "An Introduction to Computing with Neural Nets", *IEEE ASSP Magazine* Vol.4 (2) 4, (1987)
11. Beale, R., and Jackson, T., *Neural Computing: an Introduction*. Institute of Physics Publishing, Philadelphia, PA. (1990)
12. Hagan, M., Demuth, H., and Beale, M., *Neural Network Design*. PWS Publishing Co., Boston, MA. (1996)
13. Demuth, H. and Beal, M., *Neural Network Toolbox User's Guide*, The Math Works, Inc., Natwick, Mass. (1993) MATLAB is a registered trademark of The Math Works, Inc.
14. Quinby-Hunt, M., Hunt, A., Lofftus, K., and Shapiro, D., "Polarized-Light Scattering Studies of Marine *Chlorella*," *Limnol. Oceanogr.*, 34, 1587. (1989)
15. Hull, P., Hunt, A., Quinby-Hunt, M., and Shapiro, D. "Coupled-dipole Approximation as an analytical Model for Predicting Scattering from Marine Micro-organisms," *American Geophysical Union*, San Francisco. (1990)
16. Hull, P., Shaw, F., Quinby-Hunt, M., Shapiro, D. Hunt, A., and Leighton, T., "Comparison of analytical calculations with experimental measurements for polarized light scattering by marine micro-organisms," *Ocean Optics XII, Proc. SPIE*, Vol. 2258. (1994)

A new technique for the determination of spectral reflectance of individual and bulk particulate suspended matter in natural water samples.

Rodolfo Iturriaga
Juli Berwald

Hancock Institute of Marine Sciences and Department of Biological Sciences
University of Southern California
Los Angeles, CA 90089-0371

Gregory J. Sonek
Department of Electrical and Computer Engineering
Beckman Laser Institute and Medical Clinic
University of California, Irvine
Irvine, CA 92717

ABSTRACT

The behavior of real scattering surfaces is often specified by measuring the bidirectional reflectance factor (BRF), defined as the ratio of the flux scattered into a given direction by a surface under given conditions of illumination to the flux scattered in the same direction by a Lambertian scatterer under identical conditions. The utility of this factor is that measurements on surfaces can be related to known standards (e.g. Spectralon), which have a BRF greater than 99% for a broad range of wavelengths. In addition to the incidence angle and spectral features of the incident flux, the reflectance properties of a surface are affected by the intrinsic composition and roughness properties of the surface. Therefore, the spectral reflectance of different targets will generally yield spectral reflectance curves of different shapes, forming the basis for identification of materials. For example, optical principles developed for the determination of reflectance properties of marine particles facilitate the determination of the BRF of oceanic samples.

We have recently developed and implemented a system for determining the BRF composed of a Zeiss photomicroscope equipped with a reflective system. In this system, excitation is provided over a large field of view while reflection collection is acquired over a slightly smaller solid angle. Multi-wavelength measurements allow the determination of the effect of the excitation wavelength on both the reflectance and fluorescence properties of the sample, whereas monochromatic measurements exclude fluorescence effects. This new technique provides the advantages of determination of the BRF for different types of individual and bulk particulates transferred onto an optical embedding medium or collected on an Anopore filter. Abundance and other optical properties (e.g. absorption) of dominant particle types can also be determined by individual particle analysis on the same sample.

1. INTRODUCTION

The reflectivity R of a surface is the ratio of the energy scattered by the surface in the direction of the detector, I , to the total energy incident on a surface, I_0 ,

$$R = \frac{I}{I_0}, \quad (1)$$

where the direction of the detector is in the backwards direction relative to the incident light. Lambertian scatterers represent idealized surfaces with near perfect reflectivity. Reflectivity from natural surfaces can be specified in relation to such ideal surfaces.

For a natural surface, the bidirectional reflectance factor BRF is defined as the ratio of the reflectivity of a natural surface, R_s , to the reflectivity of a Lambertian scatterer, R_L under identical conditions,

$$\text{BRF} = \frac{R_s}{R_L}. \quad (2)$$

The utility of the BRF is that measurements on surfaces can be related to known standards (e.g. Spectralon), with a well calibrated reflectance coefficient, greater than 99% for a broad band of wavelengths. The reflectivity of a surface is affected by the intrinsic composition of the surface, the roughness properties of the surface and the spectral characteristics of the incident

flux. Therefore, the spectral reflectivity of different surfaces will, in general, yield spectral reflectivity curves of different shapes, forming the basis for identification of different materials.

In aquatic systems, particles must be concentrated onto a surface such as a glass fiber or Anopore filter before reflectivity measurements can be made. In general, these filters are strongly scattering and weakly absorbing. The BRF for the bulk particle assemblage, BRF_{bp} , can be calculated by the ratio of the filter with the particles concentrated on it, BRF_{bpf} , to the BRF of the filter alone, BRF_f ,

$$BRF_{bp} = \frac{BRF_{bpf}}{BRF_f} = \frac{\frac{R_{bpf}}{R_L}}{\frac{R_f}{R_L}} \quad (3)$$

For an individual particle transferred onto a gelatin coated slide, the reflectivity of the gelatin is nearly negligible. Therefore, the reflectivity of an individual particle, R_p , is determined by the ratio of the energy scattered into the detector by the particle, I_p , to the incident energy impinging on the geometrical cross section of the particle, I_{op} ,

$$R_p = \frac{I_p}{I_{op}} \quad (4)$$

A bidirectional reflectance factor for the particle, BRF_p , with respect to a standard of known reflectivity can be calculated,

$$BRF_p = \frac{R_p}{R_L} \quad (5)$$

In this study, we discuss a microphotometric technique for the determination of the reflectivity of suspended particulate matter or sediments from aquatic systems at both the bulk, BRF_{bp} , and the individual particle level, BRF_p .

2. METHODS

2.1 Particle concentration

Different types of filters were chosen depending on the type of sample and analysis to be performed. For individual particle analysis, the gelatin transfer technique was used.^{1,2,3}

For measurements which were restricted to bulk particulate matter, the most favorable results were achieved using Anopore filters. Samples for bulk analysis were filtered at low vacuum pressure onto Anopore filters which were then placed flat on a microscope slide. The Anopore filters were then covered with one or two drops of gelatin previously dissolved and maintained close to the gelling temperature of the mixture (~23-24°C) and a thin glass cover slip was placed on top of the gelatin and filter. The prepared samples were then stored frozen (-20°C or lower temperatures).

The use of glass fiber filters (GF/F) has proven useful for determinations of absorption by resuspended particles, including phytoplankton and minerals, or samples treated with methanol as described by Kishino.⁴ These type of preparations do not require embedding of the sample in gelatin and may be used to determine reflectivity on freshly collected samples. Embedding glass fiber filters in gelatin for storage is not recommended for reflectivity measurements.

2.2 Microphotometric determinations

Reflectivity measurements were performed on a Zeiss microphotometer-03 equipped with a full reflecting mirror system for bulk measurements and a reflecting dark field configuration for individual particles.⁵ The illumination system consisted of a 150W Tungsten-Xenon lamp (Xenophot, Osram), focusing optics and special reflecting objectives. The description of light ray paths for the optical illumination system are described in Figure 1A and B. The samples were illuminated with a full spectrum of light and the emission was recorded continuously using a scanning monochromator of 0.5 nm resolution placed in front of the PMT and interfaced to a robotics unit and a personal computer.

Spectralon reflectance standards (99% and 10% reflectivity) were used as references. In order to make microphotometric measurements reproducible, the diameter of the measuring optical slit was set according to the particle size for individual particle analysis or at a fixed diameter for bulk measurements and kept constant until measurements of the samples, blank and reflectance standard were completed. Before measurements of the standard (Spectralon) were made, the microscope was focused

until a sharp image of the surface was reached. In such a manner, the focal distance for the standard was the same as that for the sample in all analyses.

3. RESULTS

For individual particulate reflectance measurements the dark field reflective system (Figure 1B) provided higher image resolution and reflectance signals, due to the low background noise with the gelatin transfer method. Figure 2 shows a typical red tide dinoflagellate (*Lingulodinium* sp.) under reflectance illumination. Figure 3 shows the reflectance and absorption of this single cell. The decrease in reflectance near 450 nm corresponds to increased absorption in this region. The reflectance peak at 683 nm (Fig. 3A) includes the effects of chlorophyll a fluorescence.

Spectral reflectance data for different types of samples concentrated on either GF/F, Anopore filters, or transferred onto gelatin-coated microscope slides were measured at the bulk and at the individual level. Bulk reflectance and absorption measurements for suspended particulate matter were performed on GF/F filters, the results of which are shown in Figure 4. Mineral particulates appeared to be the main components of the Yellow Sea samples. These samples were treated with methanol before measurements were performed so as to remove phytoplankton pigments or other methanol extractable products (e.g. lipids). Mineral dust from the Gobi desert found at the surface showed different reflectance properties compared to samples collected at 20 m depth, where the presence of resuspended sediments was apparent for some regions of the Yellow Sea. As expected, a higher absorption in the blue region of the spectrum for the Gobi desert dust corresponds to a low BRFBp.

The reflectance technique have been also applied to different types of cells. Measurements have been performed on mammalian tissue treated with melanin precursors (ALA) for the differentiation between pre-cancerous and normal epithelial tissue. This method has also recently been used to image and detect intracellular activity on *Giardia* cysts, a common intestinal parasite (Figure 5). The high imaging resolution of the dark field reflective system allows fingerprinting of cells in order to assess their cellular activity when stained with enzymatic activity markers. Currently, two micro-techniques, Optical tweezers and microphotometry, are being used to assess the viability of *Giardia* and *Cryptosporidium* cysts.

4. SUMMARY

This study demonstrates the use of the bidirectional reflectance factor BRFB to determine the reflectivity of particulate matter at the bulk and individual level. Concentrating bulk suspended matter on Anopore filters and embedding individual particles in gelatin provides good sample preservation of field samples where BRFB measurements are performed later in the laboratory. These techniques are currently being used for both the characterization of marine particulate matter and also for assessing the physiological state of other aquatic microbial cells, such as the intestinal parasite, *Giardia*.

5. ACKNOWLEDGMENTS

This research was supported by NASA (Grant # NAGW-3795), the University of Southern California Sea Grant Program and ONR (Grant # N00014-95-1-1096).

6. REFERENCES

1. R. Iturriaga, B.G. Mitchell and D.A. Kiefer, " Microphotometric analysis of individual particle absorption spectra". *Limnol. Oceanogr.* **33**: 128-135 (1988).
2. R. Iturriaga, S. Bower, "Microphotometric analysis of the spectral absorption and fluorescence of individual phytoplankton cells and detrital matter". *Current Methods in Aquatic Marine Ecology*. Lewis Publishers, New York (1993).
3. R. Iturriaga, and D. A. Siegel, " Microphotometric characterization of phytoplankton and detrital absorption properties in the Sargasso Sea". *Limnol. Oceanogr.* **34**:1706-1726 (1989).
4. M. Kishino, M. Takahashi, N. Okami and S. Ishimura, " Estimation of the spectral absorption coefficients of phytoplankton in the sea". *Bull. Mar. Sci.* **37**: 634-642 (1985).
5. H. Piller, *Microscope Photometry* Springer Verlag, Berlin, (1977).

Figure 1. Ray paths in the microscope for bulk reflected light (A) and individual particle measurements (B). The optical system in (A) consists of bright field illumination with a glass plate reflector and a mirror condenser. The optical system in (B) for reflected light, dark field illumination requires an ellipsoidal ring mirror condenser and a concave ring-mirror condenser.

Col - Collector
 CAD - Condenser-aperture diaphragm
 OAD - Objective-aperture diaphragm
 Obj - Objective
 Con - Condenser
 St.L' - Image of condenser-aperture diaphragm (CAD') in the objective aperture area
 L - Luminous surface of the lamp

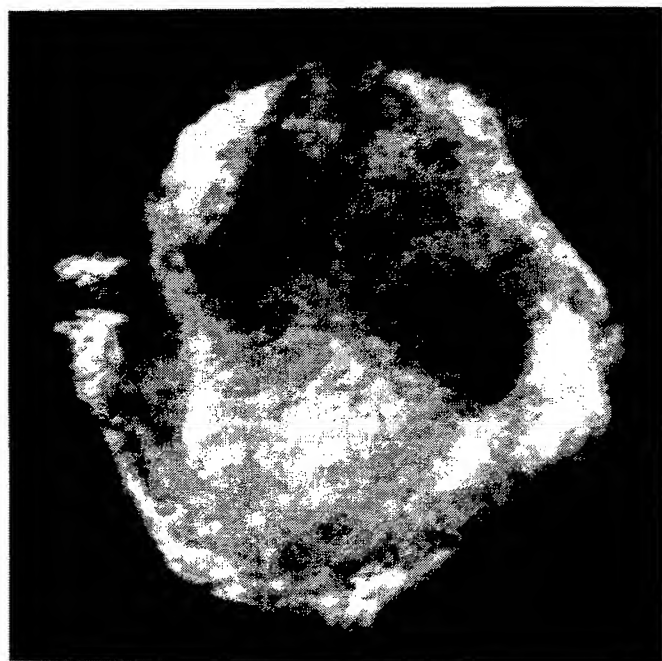
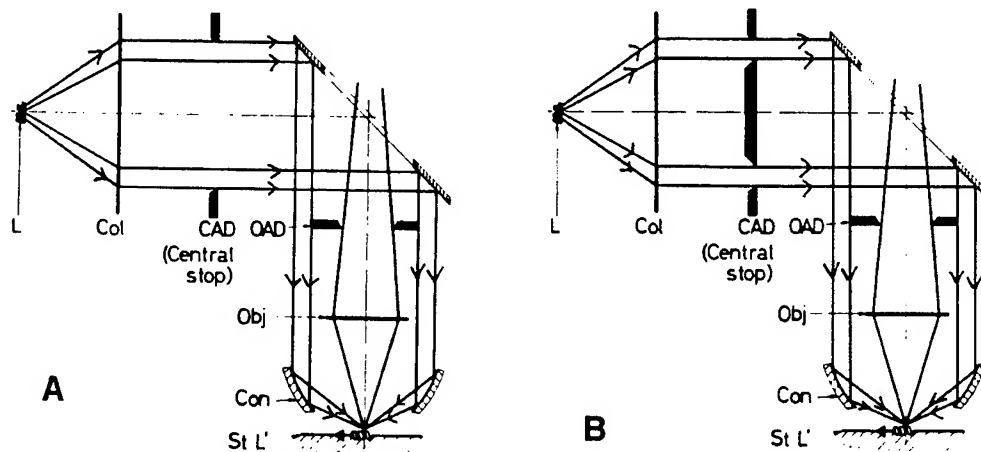
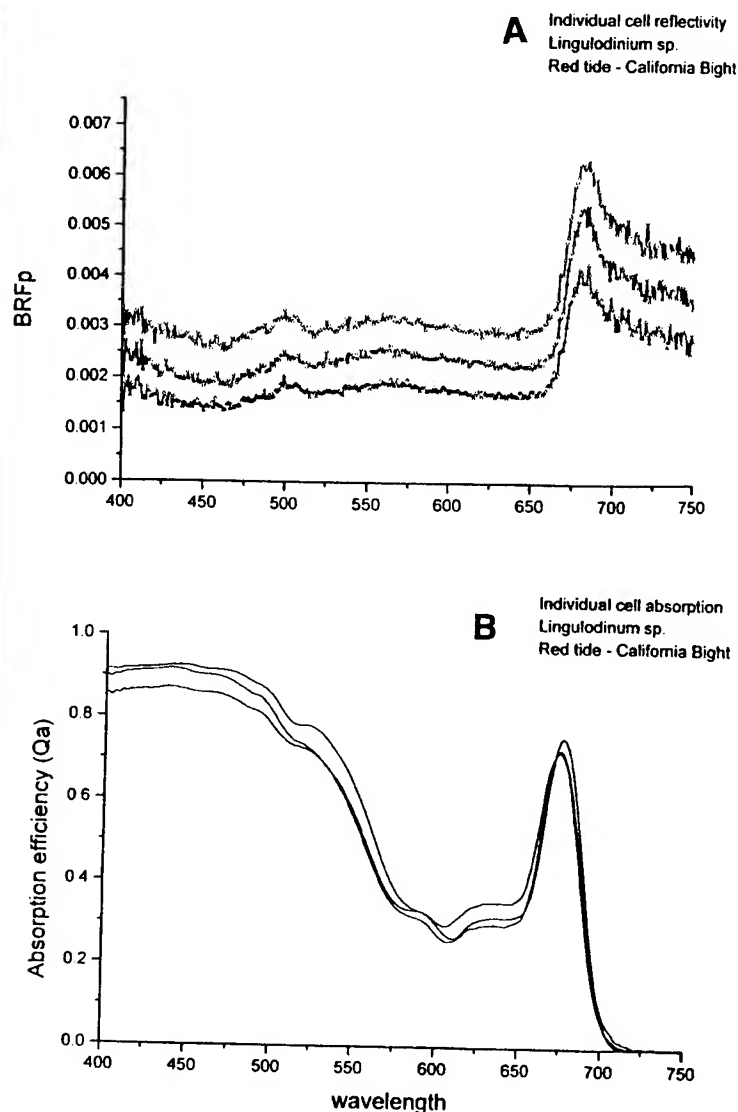


Figure 2. Red tide dinoflagellate (*Lingulodinium* sp.) imaged with dark field reflective system.

Figure 3. The reflectivity (A) and absorption (B) spectra for *Lingulodinium* sp. Cells of this type are strongly absorbing as demonstrated by their high Q_a values.



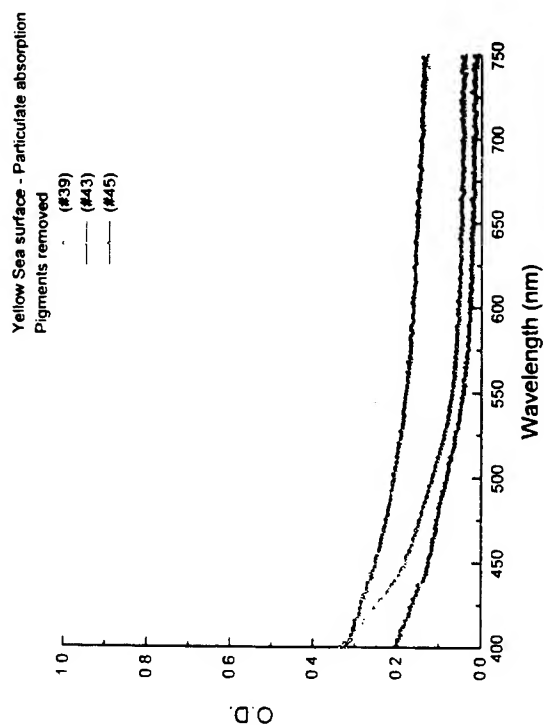
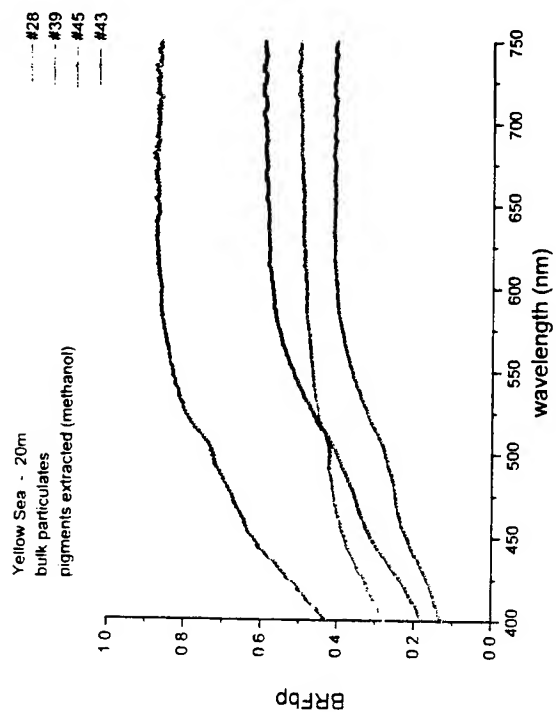
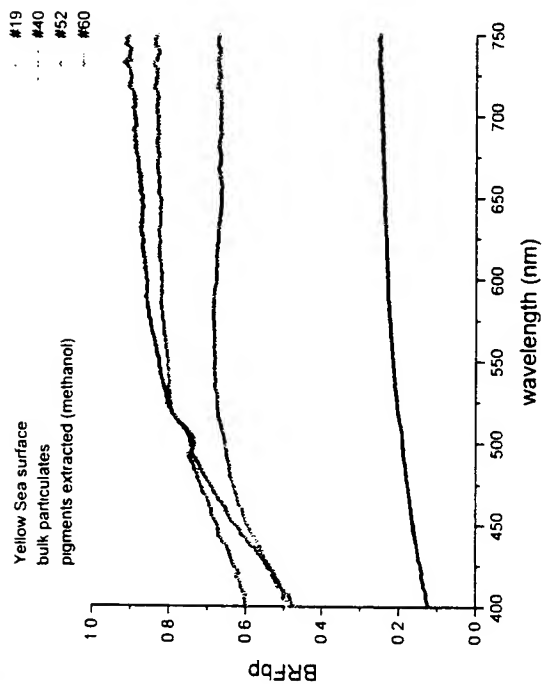
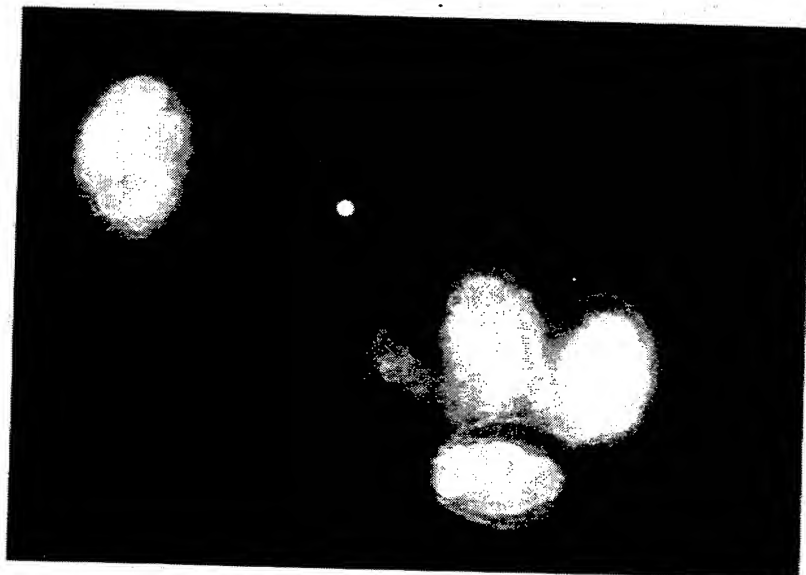


Figure 4. Yellow sea particulate matter collected at surface and 20 m depth during May 1996, concentrated onto GF/F filters and treated with methanol to remove pigments. The characteristic yellow color (Gobi desert dust) corresponds to surface samples (#28, 39, 45, 43). The grey color corresponds to 20 m depth samples (#19, 40, 52, 60) which are characterized by resuspended bottom sediments.

Figure 5. *Giardia* cyst (approximately 15 μm diameter) transferred onto a gelatin coated slide imaged with a dark field reflective optical system. Currently, two micro-techniques, optical tweezers and microphotometry, are being used to assess the viability of *Giardia* and *Cryptosporidium* cysts in natural systems. These two intestinal parasites are of major concern for drinking water supplies.



Bypass method for estimating backward scattering coefficient

*Jodai, Y., *T.Oishi, *Y.Saruya, **M.Kishino

* School of Marine Science and Technology, Tokai Univ.,
Orido 3-20-1, Shimizu City, Shizuoka Pref., Japan, Postal Code 424

** Institute for Physical and Chemical Research,
Hirosawa 2-1, Wako City, Saitama Pref., Japan, Postal Code 351-01

ABSTRACT

The bypass method to estimate the backward scattering coefficient using the scatterance at 120 deg. was confirmed. The regression analysis gives $b_b = 7.48\beta(120)$ with the maximum error of 6%. The relation is held for all wavelength and for all water from open sea to coastal area. Further, the relation seems to be also applicable to water being rich of phytoplankton, except for some species of phytoplankton. It is concluded that the method is practical and promising for routine works.

2. INTRODUCTION

The backward scattering coefficient is an import parameter for many problems concerned with marine optics, for instance, ocean color remote sensing, two flow model¹ and so on. The backward scattering coefficient can be estimated either by irradiance measurements in the natural light field, or obtained by integrating the volume scattering function from 90 to 180 deg. However, because the work is complex and time consuming, it is difficult to use either of these above measurements as a routine method.

Recently, Oishi(1990)² shows that there exists the direct relation between the backward scattering coefficient and the scattering at 120 deg. with the error of 6%, and it was also demonstrated later that the relation is held in Baltic Sea³. So that, Oishi relation seems to be one of promising and practical approaches to estimate the backward scattering coefficient.

However, there are still unclear parts which should be confirmed, if the relation is held through all visible range of spectrum and for water sample being rich in phytoplankton, and it is independent of sea areas. In this paper, above questions are concerned.

3. INSTRUMENT

The volume scattering function is defined⁴ by

$$\beta(\theta) = dI(\theta)/EdV \quad (1)$$

where $dI(\theta)$ is the scattered intensity in the direction θ by scattering volume dV irradiated by the irradiance E . The backward scattering coefficient is obtained by integrating over the whole backward hemisphere:

$$b_b = 2\pi \int_{\frac{\pi}{2}}^{\pi} \beta(\theta) \sin(\theta) d\theta \quad (2)$$

The laboratory type scattering function meter is developed and applied for this study (Fig.1). 300W short arc Xe lamp with ellipsoidal reflector is used as a light source. A monochromator is placed between Xe lamp and the collimator. The water sample is irradiated by the collimated beam, 5mm in diameter, with any wavelength in the range between 350 and 800 nm of which half band width is 10 nm. The uniform collimated beam with the divergence of 0.6 deg. is obtained by the lens pinhole system applying the diffuser placed at the behind of pinhole. The detector of which half angle of acceptance is also 0.6 deg. pivots around the center of the glass sample chamber, which has the diameter of 110mm. The chamber has the flat quartz glass entrance window. Further, in order to reduce the re-irradiation of sample by the reflection of un-scattered light at the glass-air interface, the absorbing type neutral density filter, of which transmittance is 0.01, is placed at the exit window of the chamber.

The scattering volume correction was carried out measuring the angular intensity of fluorescence. It was found that the distribution was very close to sine curve in forward angles. On the other hand, it was found that there is small but not negligible difference between sine curve and the measured volume correction factor in backward angles. So that, the

scattering volume correction was made by the measured angular intensity of fluorescence. The absolute scattering function was obtained by taking the ratio between output signal of methanol at 90 deg. and that of water sample. The Rayleigh ratio of methanol was taken from Oishi(1987)⁵. The spectroscopic purpose methanol was used for this study. Methanol has the refractive index of 1.33 which is very close to that of water, so that it is not necessary to make the volume correction due to the difference of refractive index between the standard and water samples.

4. WATER SAMPLE SCATTERING FUNCTION MEASUREMENTS

Natural water samples were collected from coastal and harbor waters, Suruga Bay and Shimizu Port, Japan, respectively. Suruga Bay faces to Pacific ocean, and has the width of 55km at the mouth, 50km long and maximum depth of 2800m. So that, depending on the hydrographic condition of Kuroshio, optical properties of Suruga Bay water change its character from with open sea to coastal waters. In this study, Secchi disk depths were in the range between 1.0~ 15m. Totally 25 water samples were collected from May to August, 1996, and all measurements were completed within 6 hours.

The scattering functions were obtained at 7 wavelength(412, 443, 490, 510, 555, 665, 683nm) in the visible range of spectrum on the same water sample. (See Table 1.)

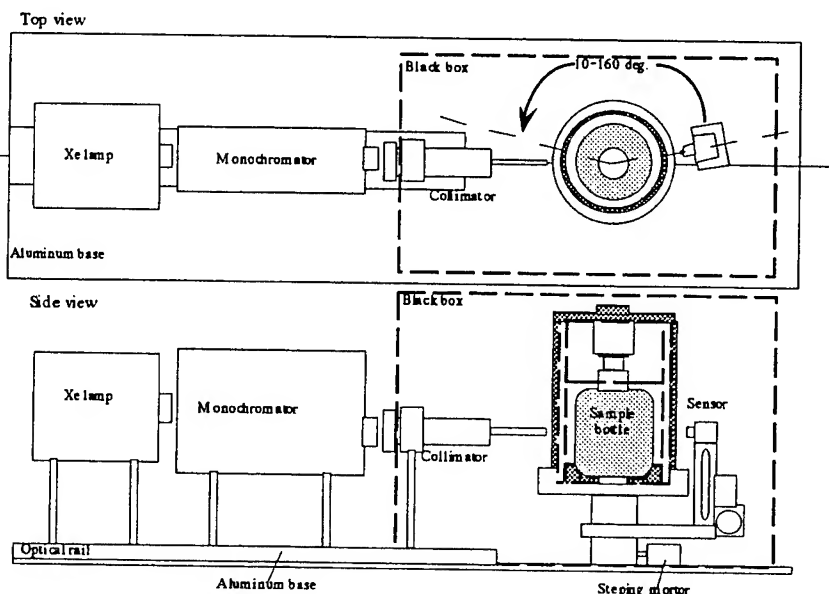


Fig.1 Over view of the scattering meter.

Table 1. Sample list of natural waters

Area	date	Depth(m)	Secchi disk depth(m)
Uchiura Bay	16 May 1996 Am	0,5,15,25	
	16 May 1996 Pm	0	
	17 May 1996 Am	0,5,15,25	
	17 May 1996 Pm	0	
Suruga Bay	20 June 1996	0,5,10	
Off Okitu River	20 June 1996	0,5,10	
Suruga Bay	1 August 1996	0	3.5
Off Okitu River	1 August 1996	0	2.5
Shimizu Port	1 August 1996	0	2.1
Suruga Bay	22 August 1996	0	5
Off Okitu River	22 August 1996	0	4
Shimizu Port	22 August 1996	0	2.3
Suruga Bay	29 August 1996	0	15
Off Okitu River	29 August 1996	0	10
Shimizu Port	29 August 1996	0	3

Total: 25 water samples

One of our interest concerned with the application of remote sensing technology to ocean is the study of primary production. Based on this point of view, we measured the scattering function of 5 species of cultured phytoplankton for different concentration at 11 wavelength(400, 412, 443, 450, 490, 500, 520, 550, 565, 600, 650nm) in visible range of spectrum and studied the relation between the backward scattering coefficient and scatterance at 120 deg. Sample of plankton is *Nannochloropsis*, *Pavlova lutheri*, *Phaeodactylum*, *Skeletonema*, *Tetraselmis tetrathele*.

5. RESULTS

The normalized scattering function for natural water and cultured phytoplankton at 90 deg. are shown in Fig.2, and Fig.3, respectively. The shape of scattering function in forward angles are almost coincident each other. On the other hand, there are large deviations in the backward angles, in particular >130 deg., and the minimum of the scatterance appears around 120 deg. (110~130 deg.) for natural waters. Considering the general behavior of the scattering function, it is easy to imagine that the information concerned with the properties of suspended matter is involved in backward scattering angles rather than in forward angles. The shapes of the scattering functions by cultured phytoplankton vary remarkably depending on phytoplankton, in particular in the backward angle. Some phytoplankton have remarkable increase of scatterance in large angle, and other are not (Fig.3).

The instrument used for this study can measure the scattering function between 10 and 160 deg. In order to obtain b_b , it needs to estimate the scattering function between 160 and 180 deg. The extrapolation was carried out using scatterance values from 90 to 160 so as to gradually dump in missing angle and to become zero gradient at 180 deg. by a flexible ruler. The backward scattering coefficient were calculated by the trapezoidal method.

Fig.4, 5 and 6 show the relation between b_b and scatterance of all wavelength and all natural water samples at 90, 120 and 150 deg. as examples, respectively. As shown in the figures, the highest correlation ($r=0.996$) was found at 120deg. with the maximum error of 6%. On the other hand, the correlations are high at other angles as well. However, the maximum error is much larger than the case of 120 deg., i.e. 10 ~ 15%. These relation is the same as that obtained by Oishi(1990).

Fig.7, 8 and 9 show the same relation as shown in Fig.4, 5 and 6, but for cultured phytoplankton, respectively. Although the gradients of the relation for phytoplankton are similar to the case of natural waters, the maximum errors are much larger through all scattering angles. Further, the figures show the interesting feature. Thus, it is easily recognize that there exists the clear dependence of phytoplankton species (see Fig. 7 and 8). However, again the estimation using the scatterance at 120 deg. seems to be much better than others, i.e. high correlation and small deviation, expect for the scattering data of *Skeletonema*. (indicated by circle). The regression analysis gives $b_b = 7.43 \cdot \beta(120) - 1.7 \cdot 10^{-3}$, which was obtained by eliminating the scatterance data of *Skeletonema*. Again, the gradient of the relation is almost the same gradient of as that obtained by natural water sample.

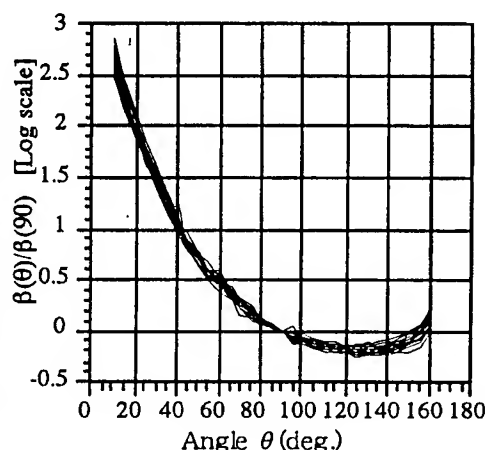


Fig.2 Normalized scattering function at 90 deg for 25 water samples. Wavelength is 510 nm.

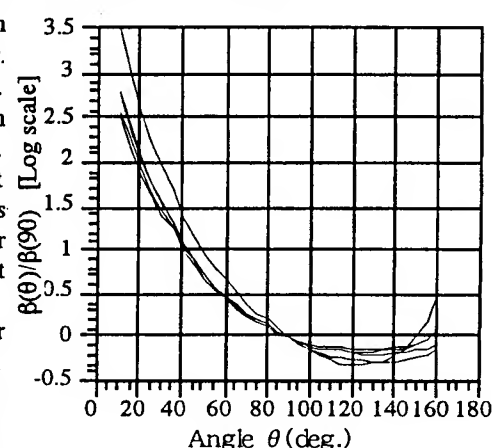


Fig.3 Normalized scattering function at 90 deg for 5 species of cultured phytoplankton. Wavelength is 510 nm.

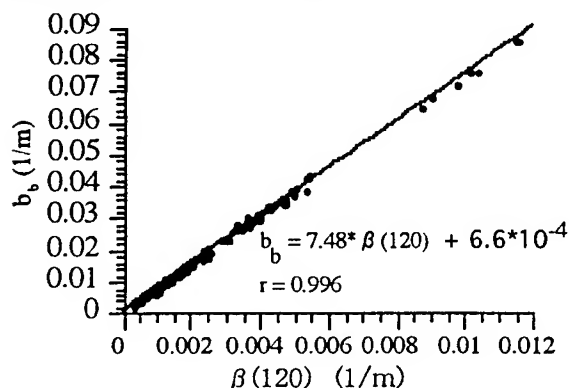


Fig.4 Relationship between the backward scattering coefficient and scatterance at 120 deg.

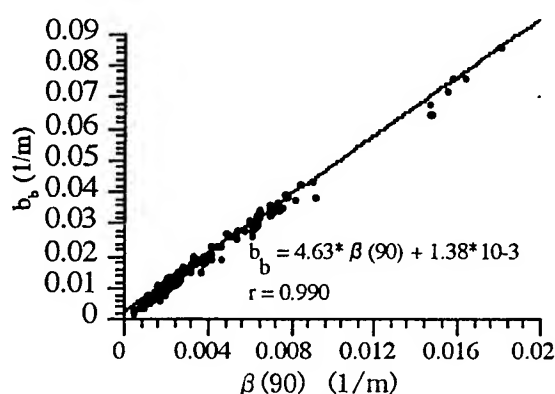


Fig.5 Relationship between the backward scattering coefficient and scatterance at 90 deg.

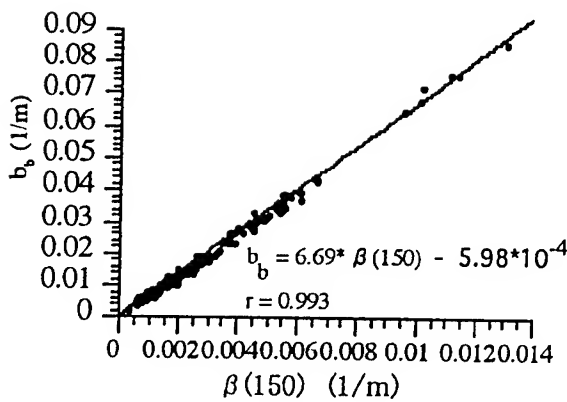


Fig.6 Relationship between the backward scattering coefficient and scatterance at 150 deg.

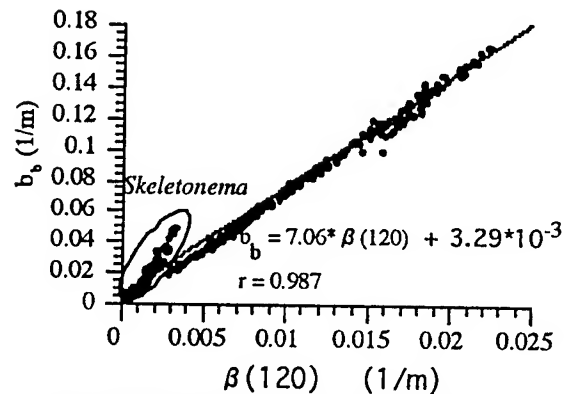


Fig.7 Relationship between the backward scattering coefficient and scatterance at 120 deg. for phytoplankton.

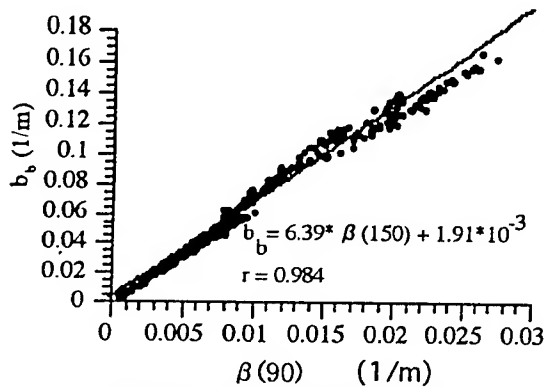


Fig.8 Relationship between the backward scattering coefficient and scatterance at 90 deg. for phytoplankton.

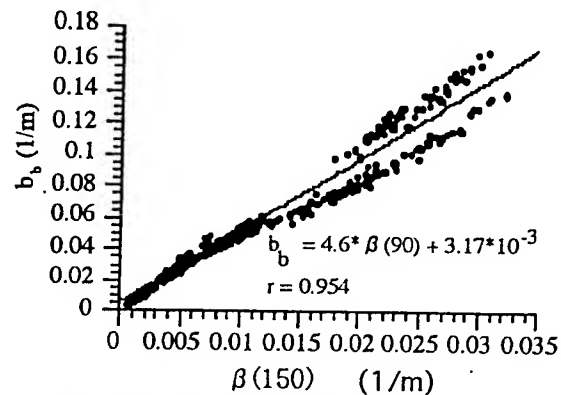


Fig.9 Relationship between the backward scattering coefficient and scatterance at 150 deg. for phytoplankton.

6. DISCUSSION AND CONCLUSION

In this study, the scattering function between 160 and 180 were extrapolated. However, this procedure does not introduce the significant error for the estimation of b_b . Fig.11 shows the angular contribution of scattered energy on b_b computed by

$$P_{(\theta_i)} = \frac{2\pi \int_{\theta_i}^{\theta_i + \Delta\theta} \beta(\theta) \sin(\theta) d\theta}{b_b} \quad (3)$$

where $\Delta\theta$ is the angle increment, $\Delta\theta = 5\text{deg}$. As shown in the figure, the contribution of scattered energy between 160~180 deg. on b_b is small, less than 12%, comparing other angles, because of small solid angle. So that, even if the estimated scatterance in this angle range have relatively large error, the error does not reflect directly to b_b .

Although the contribution of the scatterance, angle range of 90~110 deg., are large, there are the large deviations. Further,

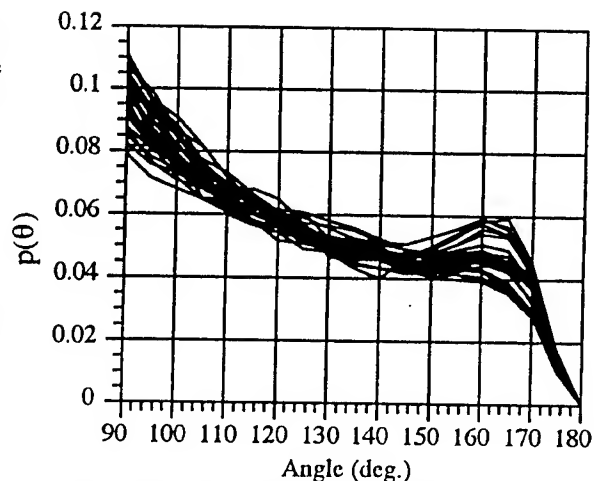


Fig.11 Angular contribution of scattered energy on b_b .

the scatterance at larger angle, let us say >130 deg., have much smaller deviations, but smaller contribution to b_b . So that even if it has small deviation, it introduce large estimation error of b_b . Contrary to above two cases, the scatterance at around 120 deg. has relatively large contribution as well as small deviation. Note that the increases of $P(\theta)$ around 150~170 deg. are from scatterance of relatively clean sea water samples.

Fig.(11) and Fig.(12) show the typical example of the normalized scattering function at 90 deg. for phytoplankton, *Nannochloropsis* and *Phaeodactylum*, respectively. One has the wavelength dependence of the shape of the function in backward angles. Another has no or very little dependence. Further their investigation is necessary for this problem.

The water samples used for the present study had wide range of Secchi disk depth, 1.0~15m. As shown in Fig.4, although there is some deviation, there is no wavelength dependence on the relation between $\beta(120)$ and b_b . So that, it can be concluded that b_b can be safely estimated by $\beta(120)$:

$$b_b = 7.48 \cdot \beta(120) + 6.6 \cdot 10^{-4} \quad (4)$$

However, the gradient was little larger than that obtained by Oishi. The reflection at glass wall might not be perfectly eliminated.

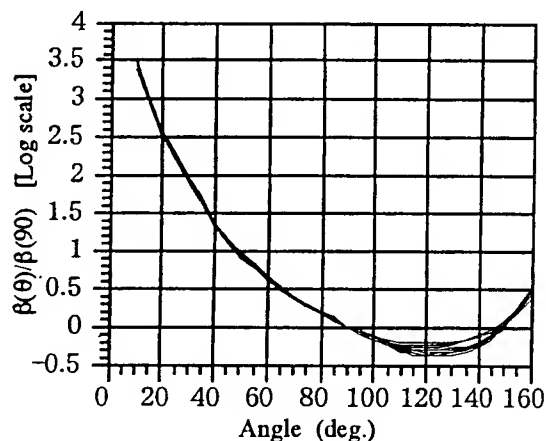


Fig.11 Normalized scattering function at 90 deg for 11 wavelength in visible light. (*Nannochloropsis*)

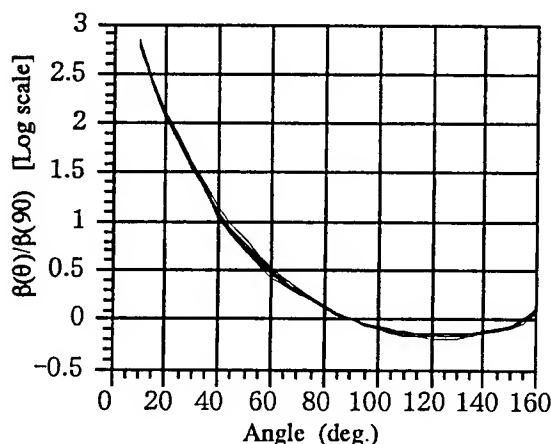


Fig.12 Normalized scattering function at 90 deg for 11 wavelength in visible light. (*Paeodactylum*)

7. ACKNOWLEDGMENTS

This work was partly supported by School of Marine Science and Technology, Tkai Univ., Japan. Authors would like to express their cordial thanks to M. Hagiwara and N. Akiyama, Tokai Univ., for providing cultured phytoplankton. Finally, thanks go to K. Kadokura, Tokai Univ., for the Instrumentation.

8. REFERENCES

1. E.Aas, "Two stream irradiance model for deep waters," *Appl.Opt.*, **26**, 2095-2101 (1987).
2. T.Oishi, "Significant relationship between the backward scattering coefficient of sea water and the scatterance at 120," *Appl.Opt.*, **20**, (31), 4658-4665 (1990).
3. H.Siegel, M.Gerth, and M.Beckert, "The variation of optical properties in the Baltic Sea and algorithms for the application of remote sensing data," *Ocean Optics XII*, **2258**, 894-905 (1994).
4. N.G.Jerlov, *Marine Optics*, 13-45, Elsevier, Amsteldam (1976).
5. T.Oishi, "Light scattering and polarization by suspended particle matter in sea water," *Rep. Inst. Fysisk. Oceanografi*, **49**, U.Copenhagen (1987).

Sea Water Optical Characteristics near the Ryukyu Islands in Japan

Kiyoshi Kawasaki

National Research Institute of Fisheries Science

12-4, Fukuura 2 chome, Kanazawa-ku, Yokohama-shi, Kanagawa, 236 Japan

ABSTRACT

Phytoplankton pigments and water optical properties were investigated around the Ryukyu Islands on April, 1996. The ratio of β -carotene and chlorophyll-*a* increased as proportional to the sampling depth at the southeast off the Ryukyu Islands. The concentration of chlorophyll-*b* increased the absorption coefficient.

Keywords: chlorophyll-*a*, chlorophyll-*b*, β -carotene, optical properties, absorption coefficient, Western North Pacific

INTRODUCTION

Recent developments in visible remote sensing technology allow global mapping the near surface phytoplankton pigment concentration from space. The concentration of phytoplankton pigment is low south of Japan, especially low around the Ryukyu Islands (Fig. 1). The chlorophyll peak generally appears at subsurface in this subtropical area. The relationship between the water leaving irradiance and chlorophyll-*a* may not be the same in mid latitude. Other pigments

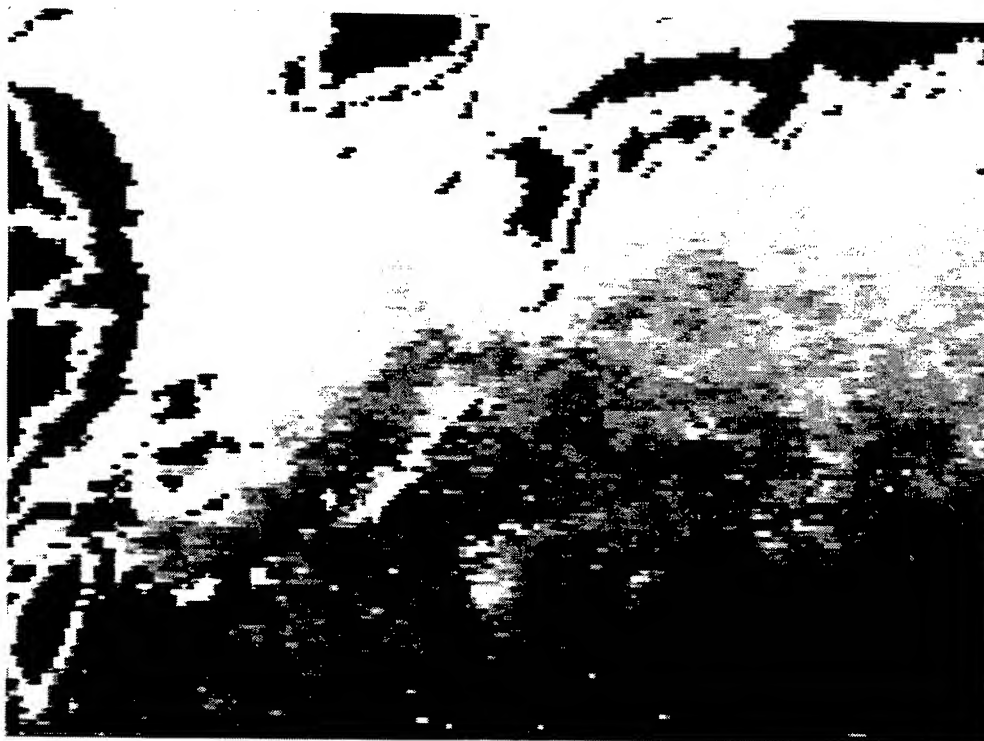


Fig.1
Phytoplankton
pigment
concentration map
in spring around
the Ryukyu Islands
(Takagi *et al.*,
1993)

like chlorophyll-*b* may affect water optical properties. In this study, the concentration of chlorophyll-*a*, chlorophyll-*b*, and β -carotene was preliminarily examined the relation to the water optical properties such as absorption coefficient south of Japan.

Methods

Oceanographic observations were conducted around the Ryukyu Islands (Fig. 2) from 13 to 25 April, 1996 by the RV Soyo-maru of National Research Institute of Fisheries Science. CTD observation and 10/ GO/FLO sampler were made. Five liters was filtered on Wattman GF/F filters for chlorophyll-*a*, chlorophyll-*b*, and β -carotene determination. The profiling reflectance radiometer MER2040 observation was also made.

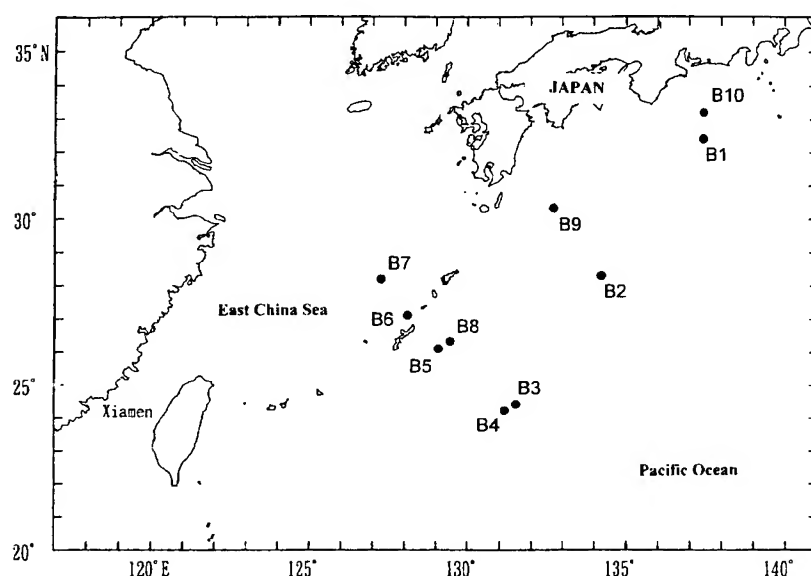


Fig.2 Location of the stations for reflectance and water sampling

RESULTS

The vertical profiles of pigments, chlorophyll-*a*, chlorophyll-*b*, and β -carotene, are shown in Fig.3. St.B10 was located the coastal water area. The concentration of chlorophyll-*b* is as high as that of chlorophyll-*a*. The chlorophyll-*a* maximum is 30m deep. St.B1 was located outside of the Kuroshio. The concentration of chlorophyll-*b* is low compared with that of chlorophyll-*a*. The ratio of the concentration of β -carotene to that of chlorophyll-*a* is about 1 at st. B1 and st.B10. St.B2 and st.B7 were located about 28N. The ratio of the concentration of β -carotene to that of chlorophyll-*a* is about 1.2 at st.B2 and 1.8 at st.B7. This ratio is about constant in each station north of 28N. Whereas this ratio increases in proportion to observation depth at the station southeast of the Ryukyu Islands such as st.B5 and B3.

The attenuation coefficient (*K*) was calculated downwelling irradiance corrected by solar irradiance. Fig.4 shows the chlorophyll-*a* concentration as a function of attenuation coefficient. Bold line shows the autocorrelation with all data except st.B10 and dotted line shows that with all data. As the characteristics of st.B10 was rich chlorophyll-*b* concentration,

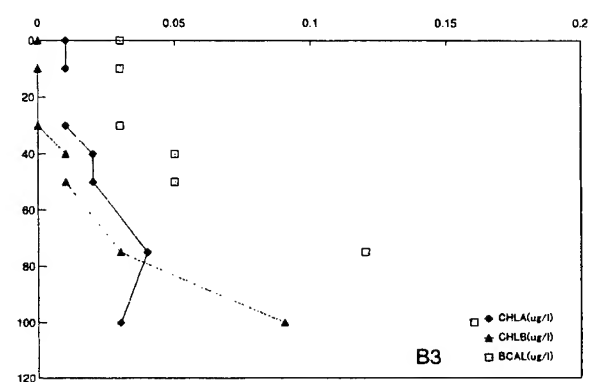
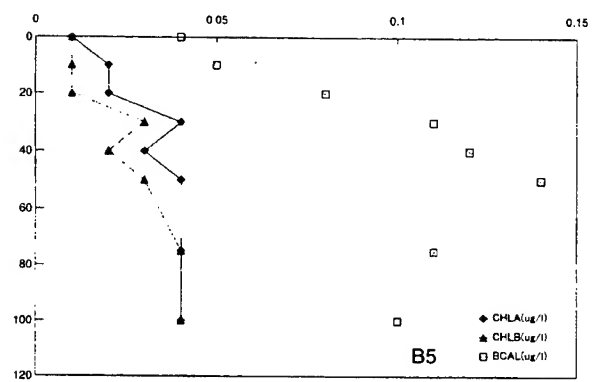
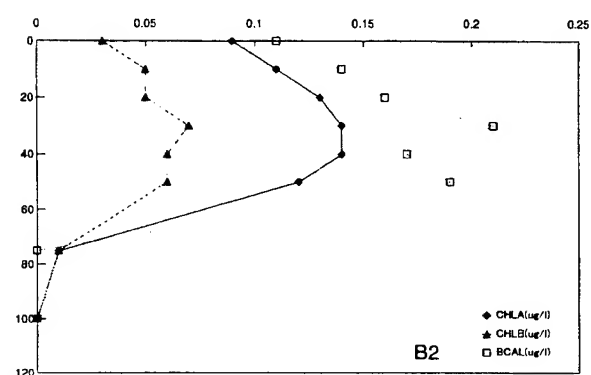
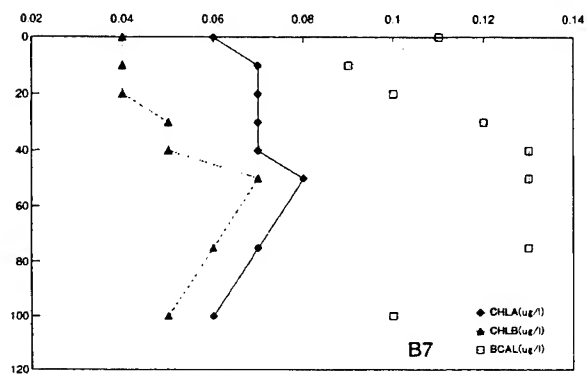
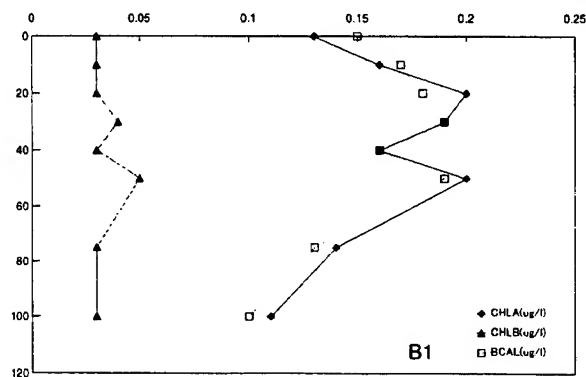
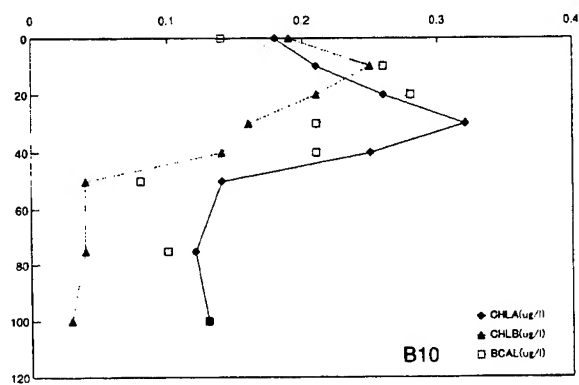


Fig.3 Vertical profiles of Pigments, chlorophyll-*a* (◆), chlorophyll-*b* (▲), and β -carotene (□)

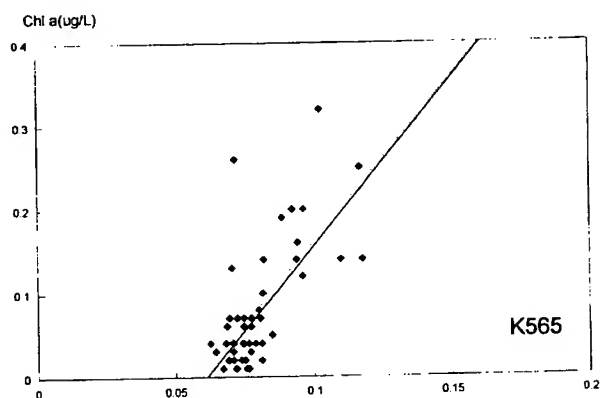
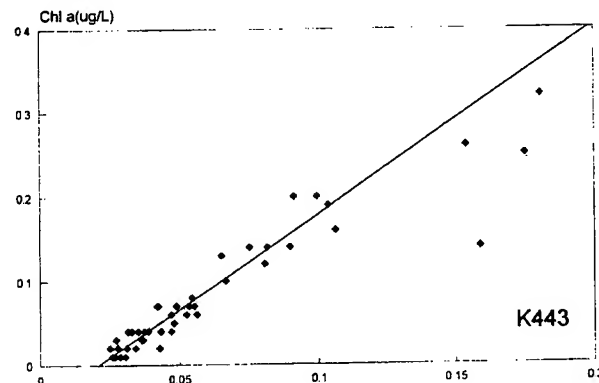
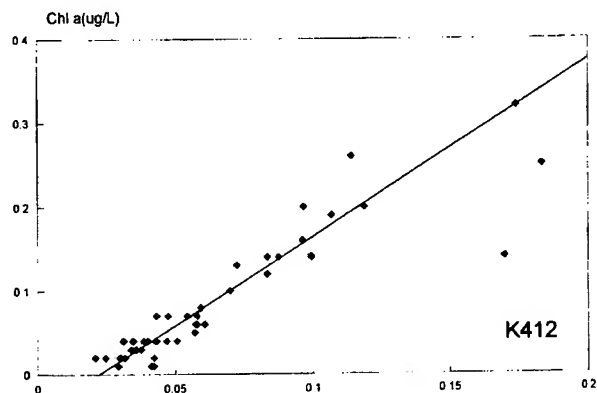


Fig.4 Chlorophyll-*a* concentration as a function of attenuation coefficient (*K*) at 412nm, 443nm, 465nm.

the presence of chlorophyll-*b* will change the relationship between chlorophyll-*a* and attenuation coefficient.

Fig.5 shows the chlorophyll-*a* concentration (*Chla*) as a function of Ed/Lu (downwelling irradiance, *Ed*, by upwelling radiance, *Lu*) at 412nm. *Chla* is proportional to the square of Ed/Lu .

CONCLUSION

In this paper, aspects of phytoplankton pigments, chlorophyll-*a*, chlorophyll-*b*, and β -carotene, associated to water optical properties were reported. The ratio of pigments concentrations was greatly changed, and the pigment concentration changed the relationship between the chlorophyll-*a* concentration and water optical properties. It is important to observe the phytoplankton pigments like chlorophyll-*a* and β -carotene as well as chlorophyll-*a* for good understanding of optical properties of water.

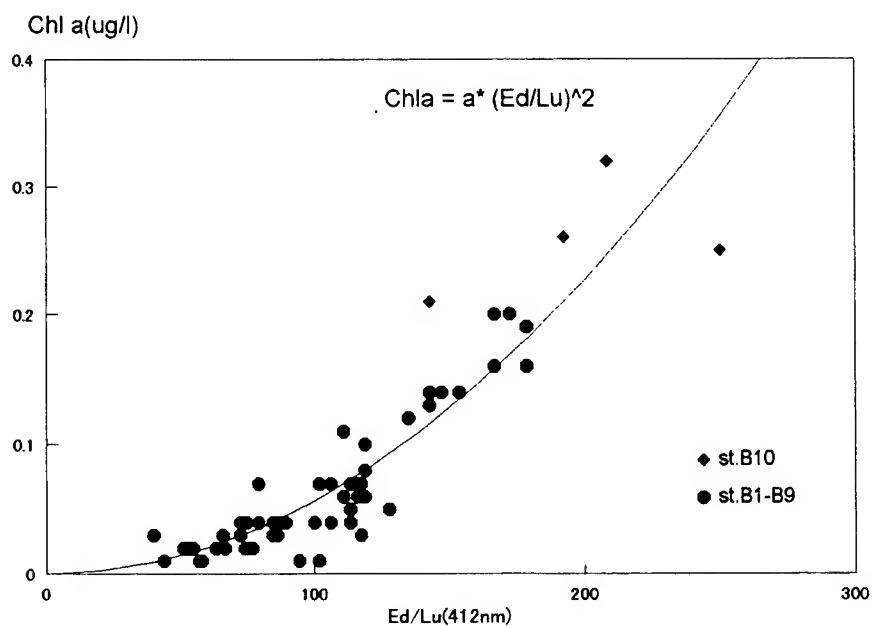


Fig.5 Chlorophyll-*a* concentration as a function of downward irradiance (Ed) by upward radiance (Lu) at 412nm

ACKNOWLEDGMENT

This study was supported with the funds by the Science and Technology Agency as a part of "Technology Development on Remote Sensing". I would like to thank K. Nakayama for analyzing pigments.

REFERENCE

1. Takagi M., H.Fukushima, I.Asanuma and J.Ishizaka, "Northwestern Pacific Coastal Zone Color Scanner Monthly Composite, a CD-ROM publication", 1993.

Estimating new production from the quantum yield of nitrate uptake

Raphael M. Kudela and Francisco P. Chavez

Monterey Bay Aquarium Research Institute
P.O. Box 628, Moss Landing, CA, 95039, USA.

ABSTRACT

Under most conditions nitrate uptake is light-dependent and may be characterized using the same uptake-irradiance response parameters as carbon. This suggests that the quantum yield of nitrate may be determined, which in turn allows for the determination of new production using existing quantum-based models of primary production. Balanced growth conditions are rare in upwelling phytoplankton assemblages (in terms of carbon and nitrogen), which makes it difficult to gauge new production from primary production. During the spring of 1995, a multi-investigator initiative was carried out to assess the role of biology in the air-sea exchange of carbon dioxide in coastal Central California. During the upwelling season this region is highly variable in space and time and provides the opportunity to study phytoplankton exhibiting a variety of physiological states and occurring in a variety of environmental milieus. Measured bio-optical parameters demonstrated no correlation to the corresponding environmental characteristics, and comparison of the calculated quantum yields demonstrated that phytoplankton carbon and nitrogen metabolic processes were not in a balanced state, as would be expected. Determination of new production rates using a simple bio-optical model was in good agreement with traditional estimates of new production using ^{15}N incubations.

Keywords: new production, quantum yield, photosynthesis, nitrate, Monterey Bay

1. INTRODUCTION

A central goal of biological oceanography is to characterize and predict primary productivity and new production in the world's oceans. This effort is often hampered by the inherent variability associated with temporal and spatial scales of phytoplankton ecology and physiology. To overcome this problem, models which mechanistically link the physiological processes of the phytoplankton with the physical and bio-optical properties of the water column and which may be measured both synoptically (via satellite) and with high frequency (via moorings and drifters) are often utilized.^{1,2} Characterization of the response of phytoplankton to dynamic physical forces directly or indirectly involves measurement of the indices of photoadaptation, which assay the ability of the phytoplankton to utilize available energy to meet the nutritional demands of growth. These indices are typically derived from photosynthesis versus irradiance (P vs. E) experiments for carbon uptake. Nitrogen uptake indices have been calculated in a similar manner by application of the Michaelis-Menten relationship to the nitrogen uptake versus irradiance response^{3,4,5}, or by a modification of the various P vs. E curve fitting methods.^{6,7} However to date, very little attention has been directed towards the interactions and variability of nitrogen, carbon and light in upwelling systems, where rapid changes in the physical environment will cause dramatic changes in phytoplankton physiology.

Oxygenic photosynthesis involves the absorption of light energy, and the subsequent utilization of this energy to produce reducing power via NAD(P)H and ATP. After carbon, the most reducing-energy dependent reaction carried out by phytoplankton is the uptake and assimilation of NO_3^- .⁸ Since it is possible to apply P vs. E type curve parameters to NO_3^- uptake, it follows that it should also be possible to calculate a quantum yield (ϕ_{NO_3} ; moles NO_3^- reduced per moles quanta absorbed) for this process. This would allow the direct estimation of new production⁹ on the same spatial and temporal scales as primary production, using quantum yield models with the same underlying physiological assumptions. In the spring of 1995, we conducted a series of measurements within an upwelling plume in Monterey Bay, California to estimate ϕ_{C} and ϕ_{NO_3} . These data represent the first attempt to estimate ϕ_{NO_3} for a natural phytoplankton assemblage. We applied a simple model to directly estimate new production values from the bio-optical data. Estimates of ϕ_{C} have demonstrated that quantum yields are highly variable, and are not well correlated with any single environmental parameter.¹⁰ We would predict that ϕ_{NO_3} is also spatially and temporally highly variable, and that ϕ_{NO_3} may not be well correlated to ϕ_{C} . By modeling these processes independently, we can directly estimate new and primary production, and evaluate the relative variability in these parameters and in the underlying model assumptions.

2. MATERIALS AND METHODS

2.1 Field area and sample collection

Experiments were conducted in Monterey Bay, CA aboard the R/V *Point Sur* during April-May 1995 during a vigorous upwelling event. The upwelled water was tracked using a series of 3 drifters deployed along the axis of the upwelling plume; the data reported represent samples collected during 6 days. In addition to the drifter stations, a series of surface and vertical-profile stations were occupied at the beginning of the cruise to provide a quasi-synoptic picture of the physical, chemical and biological variability for the region. At all stations routine measurement of pigments, nutrients, and physical properties (temperature, salinity, particle distribution, etc.) were conducted,¹¹ while at select stations the vertical structure of the light field within the water column was determined with a profiling spectroradiometer (PRR-600; Biospherical Instruments) and the downwelling and water-leaving radiances were determined with a hand-held spectroradiometer (PSII; Analytical Spectral Devices Inc.). Water samples for estimation of ϕ_C and ϕ_{NO_3} were collected from the mixed layer and occasionally from the base of the euphotic zone to estimate variability with depth.

2.2 Uptake versus irradiance parameters

At each station where quantum yields were estimated, short-term (0.5-4 h) ^{14}C and ^{15}N incubations were conducted with whole water samples to estimate 'instantaneous' uptake vs. irradiance relationships for carbon¹¹ and nitrogen.¹² Incubations were carried out using 14 discrete light levels (including a dark bottle) at constant temperature (maintained with either a circulating water bath or with near-surface seawater). Two types of incubator were utilized: deck incubations were conducted under ambient sunlight with neutral density film (Courtauld Performance Films) while photosynthetron incubations used a halogen light source and blue filters to achieve the correct irradiance levels. The spectral quality of the light sources was determined for each experiment using the PSII spectroradiometer. Curve fitting parameters were completed using a computerized, iterative non-linear least-squares technique (Deltagraph, Deltapoint Inc.). A 3-parameter P vs. E equation¹³ was fitted to both the carbon and nitrogen data, with the inclusion of a dark-uptake parameter for the nitrogen uptake rates (equation. 2):

$$P^B = P_s^B \left(1 - e^{\frac{-\alpha \cdot E}{P_s^B}} \right) \left(e^{\frac{-\beta \cdot E}{P_s^B}} \right) \quad (1)$$

$$V_{NO_3}^{CHL} = V_s^{CHL} \left(1 - e^{\frac{-\alpha \cdot E}{V_s^{CHL}}} \right) \left(e^{\frac{-\beta \cdot E}{V_s^{CHL}}} \right) + V_D^{CHL} \quad (2)$$

where P^B and $V_{NO_3}^{CHL}$ refer to biomass-specific carbon and nitrogen uptake rates, P_s^B and V_s^{CHL} are the maximal rates in the absence of photo-inhibition, α and β are the light-limited and light-saturated slopes of the uptake vs. irradiance curves, and E represents the irradiance (quanta) between 400-700 nm for each experiment. The V_D^{CHL} term in (2) accounts for dark-uptake of nitrogen. All units were chosen to be consistent with the literature.

2.3 Absorption spectra and quantum yields

Whole-cell absorption spectra ($a_{ph}(\lambda)$, $m^2 \cdot mg \text{ chl } a^{-1}$, 400-700 nm) were measured using a Hewlett-Packard HP8452A diode-array spectrophotometer equipped with a LabSphere integrating sphere attachment, using the quantitative filter-pad technique.¹⁴ Samples were corrected for detritus using cold methanol extraction¹⁵ and for pathlength amplification using an empirical correction.¹⁶ The total spectral irradiance absorbed by the phytoplankton assemblage (AQ_{ph} , $\text{Ein} \cdot mg \text{ chl } a^{-1}$, 400-700 nm) was determined from the product of $a_{ph}(\lambda)$ and Q , the spectral irradiance:

$$AQ_{ph} = \int_{400}^{700} a_{ph}(\lambda) \cdot Q(\lambda) d\lambda \quad (3)$$

To estimate the quantum yield values, it is also necessary to determine the spectrally weighted absorption coefficient (\bar{a}_{ph} , m^2 mg chl a^{-1}), calculated as

$$\bar{a}_{ph} = \frac{\int_{400}^{700} a_{ph}(\lambda) \cdot Q(\lambda) \cdot d\lambda}{\int_{400}^{700} Q(\lambda) \cdot d\lambda} \quad (4)$$

Estimates of the maximal quantum yields for carbon (ϕ_C) and nitrate (ϕ_{NO_3}) were determined by dividing the light-limited slope of carbon or nitrate uptake (α) by \bar{a}_{ph}

$$\phi = \frac{\alpha}{\bar{a}_{ph}} \quad (5)$$

where carbon- or nitrate-based values are substituted for the calculation. This value represents a maximal quantum yield; to calculate new production values at depth, it is necessary to define the operational quantum yield, at depth z , where the depth corresponds to new production estimates using traditional ^{15}N techniques.¹² The operational quantum yield was calculated as

$$\phi(z) = \frac{V_{max}^{CHL}(z)}{AQ_{ph}(z)} \cdot \tanh\left(\frac{Q_{PAR}(z)}{E_k(z)}\right) \quad (6)$$

where V_{max}^{CHL} and E_k were derived from the uptake vs. irradiance curves. New production values were then estimated as the product of the chlorophyll concentration, equation (3) and equation (6). Since the traditional ^{15}N measurements from discrete depths were estimated in deck incubators, no attempt was made to correct for the spectral quality of the light field *in situ*. Comparisons of quantum yield-based new production and traditional estimates of new production were made for those stations where both estimates were conducted (5 stations).

3. RESULTS AND DISCUSSION

During this field program, a massive upwelling event produced by strong and persistent NW winds (>20 knots) which blew from April 14-27 resulted in a pronounced upwelling plume centered off Davenport, CA and generated a strong frontal system consisting of the cold, nutrient rich plume waters and the warmer waters trapped within the Bay and advected in from offshore. The drifters which were released in this plume tracked these waters more or less continuously as the plume moved south, gradually warming as surface heating and mixing occurred. The occupied stations, located along the axis of this plume, demonstrate a wide variety of conditions, with a 40-fold variation in NO_3 and a 10-fold variation in chlorophyll (Table 1). Changes in species composition can potentially influence changes in the quantum yield calculations.¹⁷ Examination of discrete samples demonstrates that within the upwelling plume, diatoms consistently represented >90% of the biomass, which leads us to conclude that this factor was not an issue for these data.

A second factor which could influence the calculation of ϕ_{NO_3} involves the application of uptake vs. irradiance curves to N data. One of the assumptions made in determining nitrogen uptake versus irradiance kinetics parameters is that there is a direct dependence of nitrogen uptake on light (i.e. it's a first-order process). Nitrogen, however, is often transported across the cell membrane and incorporated in the dark at substantial rates,⁵ which negates this assumption provided dark-uptake rates are a significant proportion of total uptake rates. Although significant, the dark uptake of nitrogen in this study was lower than those values reported for other areas (e.g. 50%),⁵ and was consistently <20% of V_{max}^{CHL} with most values approaching zero. This is consistent with previous findings which have shown that dark uptake is indicative of nutrient stress.¹⁸ Clearly, if N uptake is nutrient limited, there will not be a direct dependence on irradiance, and the quantum yield calculations will not hold. However, the high ambient N concentrations and the good curve fits for the uptake vs. irradiance data ($r^2 > 0.80$) suggest that light availability was the limiting factor in N utilization for this study.

We have predicted new production values based on our estimate of ϕ_{NO_3} and a knowledge of the *in situ* irradiance and pigment fields. Using a relatively simple quantum yield model¹⁰ we predict new production values that are in good

Table 1. Physical, chemical and bio-optical (production) values for the stations where quantum yield determinations were conducted in Monterey Bay, CA. Units are a^*_{ph} ($m^{-2} mg Chl^{-1}$), Carbon α ($mg C mg Chl^{-1} (\mu E m^{-2} s^{-1})^{-1}$), P^B_{max} ($mg C mg Chl^{-1} h^{-1}$), Nitrogen α ($mg-at N mg Chl^{-1} (\mu E m^{-2} s^{-1})^{-1}$), V^{CHL}_{max} ($mg-at N mg Chl^{-1} h^{-1}$).

Lat. (°N)	Long. (°W)	Depth (%E ₀)	[NO ₃] (μM)	Chl <i>a</i> (mg m ⁻³)	Temp. (°C)	Salin. (ppt)	a^*_{ph}	Carbon α	P^B_{max}	ϕ_C	Nitrogen α	V^{CHL}_{max}	ϕ_N
37.00	122.22	30	20.93	4.85	9.70	33.45	0.0101	0.106	4.41	0.106	3.69E-4	0.044	0.004
37.00	122.22	50	20.93	4.85	9.70	33.45	0.0101	0.059	6.35	0.068	1.02E-3	0.062	0.014
36.98	122.20	50	5.46	13.31	10.80	33.52	0.0073	0.030	4.44	0.035	6.35E-4	0.043	0.009
36.98	122.21	5	12.94	3.47	9.35	33.74	0.0088	0.055	5.76	0.089	6.50E-4	0.024	0.013
36.78	122.09	50	22.99	2.58	9.66	33.66	0.0057	0.021	3.04	0.037	3.45E-3	0.063	0.073
36.82	122.08	50	13.63	19.38	10.28	33.72	0.0047	0.014	2.19	0.030	3.75E-4	0.036	0.010
36.79	122.04	50	22.27	5.49	9.95	33.66	0.0035	0.006	1.33	0.017	3.24E-4	0.053	0.011
36.77	122.13	50	19.96	8.06	9.92	33.69	0.0078	0.020	3.49	0.026	3.96E-4	0.048	0.006
36.77	122.13	1	19.96	7.23	8.98	33.80	0.0079	0.026	3.21	0.035	3.94E-4	0.039	0.006
36.67	122.62	50	0.60	2.66	12.51	32.88	0.0133	0.028	2.73	0.019	2.32E-4	0.042	0.002
36.67	122.62	50	0.60	2.66	12.51	32.88	0.0133	0.068	5.48	0.059	1.22E-3	0.049	0.013
37.00	122.22	50	5.51	13.89	11.01	33.63	0.0067	0.066	3.07	0.102	7.79E-4	0.069	0.014
37.00	122.22	5	14.40	11.28	10.43	33.67	0.0116	0.066	3.07	0.059	4.30E-4	0.047	0.005

agreement with values determined from discrete depths within the water column using traditional ¹⁵N techniques (Fig. 1). Our modeled values appear to underestimate the measured values at the higher new production rates; this is likely due to our use of one or two quantum yield values, from the near surface and from the bottom of the euphotic zone, for the entire water-column. The good agreement between modeled and measured new production values is particularly encouraging, given the disparate measurement conditions. The "traditional" measurements were conducted with samples incubated for 6-8 hours, and were often collected at different times and locations from the samples used for parameterization of the model. Examination of the predicted new production values with depth (data not shown) demonstrates that this model accurately reproduces the vertical structure of the traditional new production measurements, but modeled values are often consistently higher (or lower) than the direct estimates for a given vertical profile. This supports our belief that the discrepancy between measured and modeled values is related to the disparate measurement conditions and use of an unoptimized quantum yield model, rather than an underlying problem in the use of quantum yields for prediction of nitrate uptake. Our results demonstrate that calculation of ϕ_{NO_3} provide a useful and robust method for prediction of new production in physiologically relevant time and space scales.

The ability to predict productivity values from mooring or satellite data requires that we be able to estimate or model photosynthetic parameters based on hydrographic or biological data which can be remotely sensed. Numerous models have been formulated to predict primary production from such data; to date, it has been assumed that new production could then be derived from these primary production models.¹⁹ It has been demonstrated that ϕ_C values are not well predicted from any of the commonly measured oceanographic variables, and that there is significant small-scale (spatial and temporal) variability in these values,¹⁷ although others have argued that models based on oceanic provinces with constant or predictable values for ϕ_C (or alternatively P^B_{max} and α) provide an acceptable method for determining primary production from remotely sensed data.²⁰ We found no significant correlations between maximum quantum yields and any of the other measured variables (excluding α , V^{CHL}_{max} and P^B_{max}) which is consistent with what others have found in upwelling regions and highlights the difficulty of estimating productivity from global variables. We also found that ϕ_C and ϕ_{NO_3} demonstrated no significant correlation.

The assumption of balanced growth implies that the ratio between ϕ_C and ϕ_{NO_3} should be similar to Redfield proportions for phytoplankton composition, or about 7:1 (C:N by atoms). For the 13 stations where we obtained data for both ϕ_C and ϕ_{NO_3} , only two values were near Redfield proportions, with the ratio ranging from 0.5 to 24 for the whole data set. Some of this discrepancy may be explained by the lack of measurements for NH₄ uptake, which could provide a significant amount of the total N requirements for the phytoplankton, and thereby raise the total $\phi_C:\phi_N$ values. However, independent estimates of the *f*-ratio (an estimate of relative N utilization) during this cruise demonstrate that NO₃ was the predominant

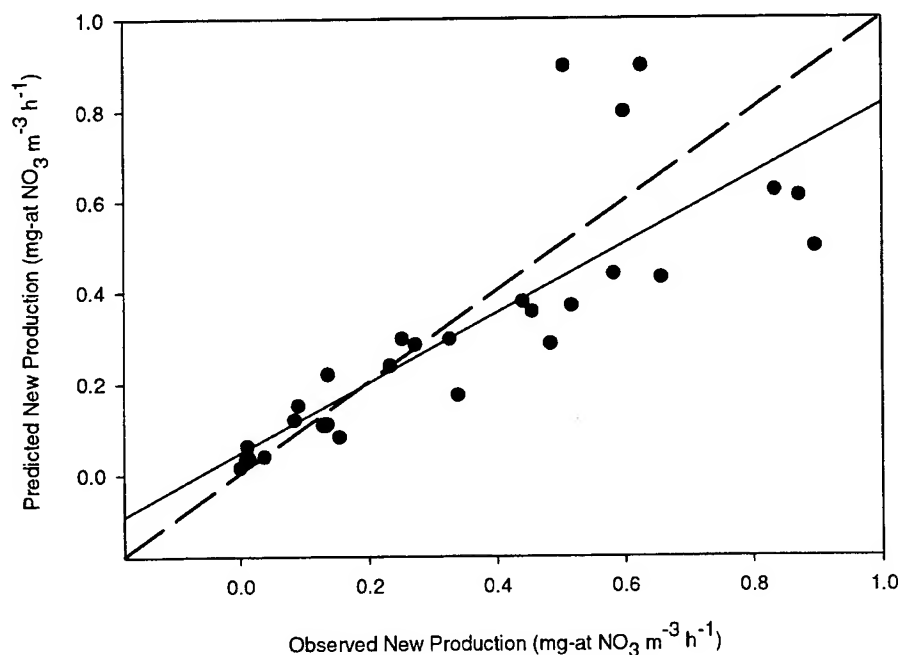


Figure 1. Observed vs. Predicted new production values for Monterey Bay, CA. Observed values were measured using ^{15}N with discrete water samples at 6 depths; predicted values were calculated using a quantum-yield model. The dashed line represents a 1:1 correspondence, the solid line represents a linear regression estimate ($r^2=0.68$) for the data.

source of nitrogen utilized by the phytoplankton. Furthermore, the mean value for this ratio (for all data) was 6.85, not significantly different from Redfield proportions. This suggests that imbalances in carbon and nitrogen processes are averaged out over sufficiently large spatial and temporal scales. Our results indicating short-term uncoupling of carbon and nitrogen metabolism are consistent with the shift-up hypothesis²¹, which predicts that maximal carbon and nitrogen utilization are temporally uncoupled in dynamic regions such as upwelling zones. According to this hypothesis, it takes phytoplankton several days to maximize nitrogen metabolism after exposure to high light and nutrient conditions, due to the requirement to synthesize essential biochemical components. According to this model, C:N utilization should initially be higher than Redfield (freshly upwelled), drop to below Redfield (shifted-up N metabolism) and then return to above Redfield (nutrient depletion) as a function of the age of the upwelling plume.²¹ When our $\phi_{\text{C}}:\phi_{\text{NO}_3}$ data are plotted versus temperature (a proxy for the age of the water) the data approximately correspond to this pattern (not shown), with maximal ratios occurring at low and high temperatures (indicative of more carbon being utilized in freshly-upwelled and nutrient depleted waters). These results highlight the importance of modeling carbon and nitrogen metabolic processes independently if the small-scale variability associated with these parameters is to be determined.

4. CONCLUSIONS

We have demonstrated that NO_3 uptake approximates a first-order response to irradiance, and that application of a modified 3-parameter P vs. E curve fit adequately predicts this relationship. We have also demonstrated that this first-order relationship between NO_3 uptake and irradiance makes it possible to calculate the quantum yield of NO_3 uptake, and that this yield can not be predicted from either a knowledge of primary production, the carbon quantum yield, or commonly measured oceanographic variables over small spatial and temporal scales. With a knowledge of ϕ_{NO_3} we have shown that it is possible to directly estimate new production through the use of previously published quantum yield models of primary production. Utilization of this model provides an opportunity to directly estimate new production on the same temporal and spatial scales as primary production, and to provide an indication of the underlying phytoplankton physiological processes in dynamic oceanographic regions.

5. ACKNOWLEDGEMENTS

We thank the crew of the R/V *Pt Sur* and the other members of the CoOP95 cruise program for support during the field investigation, Mike Kelley for the particulate absorption measurements, and Dick Dugdale for access to his mass spectrometry equipment. The ^{15}N -new production estimates were kindly provided by Dick Dugdale and Frances Wilkerson. Support for the CoOP field program was provided by the National Science Foundation through grants to F.P. Chavez (OCE-9419322) and R.C. Dugdale (OCE-9410445).

6. REFERENCES

1. W. Balch, R. Evans, J. Brown, G. Feldman, C. McClain, and W. Esaias, "The remote sensing of ocean primary productivity: Use of a new data compilation to test satellite algorithms," *J. Geophys. Res.*, **97**, 2279-2293, 1992.
2. J. Marra et al., "Estimation of seasonal primary production from moored optical sensors in the Sargasso Sea," *J. Geophys. Res.*, **97**, 7399-7412, 1992.
3. J.J. MacIsaac and R.C. Dugdale, "Interactions of light and inorganic nitrogen in controlling nitrogen uptake in the sea," *Deep Sea Res.* **19**, 209-232, 1972.
4. D. Kanda, D.A. Ziemann, L.D. Conquest, and P.K. Bienfang, "Light-dependency of nitrate uptake by phytoplankton over the spring bloom in Auke Bay, Alaska," *Mar. Biol.* **103**, 563-569, 1989.
5. W.P. Cochlan, N.M. Price and W.P. Harrison, "Effects of irradiance on nitrogen uptake by phytoplankton: comparison of frontal and stratified communities," *Mar. Ecol. Prog. Ser.* **69**, 103-116, 1991.
6. J.C. Prisco, M.P. Lizotte, G.F. Cota, A.C. Palmisano, and C.W. Sullivan, "Comparison of the irradiance response of photosynthesis and nitrogen uptake by sea ice microalgae," *Mar. Ecol. Prog. Ser.*, **70**, 201-210, 1991.
7. W.O. Smith and W.G. Harrison, "New production in polar regions: the role of environmental controls," *Deep-Sea Res.*, **38**, 1463-1479, 1991.
8. P.J. Syrett, "Nitrogen metabolism in microalgae," *Physiological Basis of Phytoplankton Ecology*, T. Platt [Ed.], *Can. Bull. Fish. Aquatic. Sci.*, **210**, 182-210, 1981.
9. R.C. Dugdale and J.J. Goering, "Uptake of new and regenerated forms of nitrogen in primary productivity," *Limnol. Oceanogr.*, **12**, 196-206, 1967.
10. O. Schofield, B.B. Prézelin, R.R. Bidigare, and R.C. Smith, "In situ photosynthetic quantum yield. Correspondence to hydrographic and optical variability within the Southern California Bight," *Mar. Ecol. Prog. Ser.*, **93**, 25-37, 1993.
11. F.P. Chavez et al., "Growth rates, grazing, sinking, and iron limitation in the eastern tropical Pacific," *Limnol. Oceanogr.*, **36**, 1816-1827, 1991.
12. R.C. Dugdale and F.P. Wilkerson, "The use of ^{15}N to measure nitrogen uptake in eutrophic oceans; experimental considerations," *Limnol. Oceanogr.* **31**, 673-689, 1986.
13. T. Platt and C.L. Gallegos, "Modelling primary production," *Primary Productivity in the Sea*, P.G. Falkowski [Ed.], Plenum Press, New York, pp. 339-351, 1980.
14. H.G. Trüper and C.S. Yentsch, "Use of glass-fiber filters for the rapid preparation of in vivo absorption spectra of photosynthetic bacteria," *J. Bacteriol.*, **94**, 1255-1256, 1967.
15. M. Kishino, N. Okami, M. Takahashi, and S. Ichimura, "Light utilization efficiency and quantum yield of phytoplankton in a thermally stratified sea," *Limnol. Oceanogr.*, **31**, 557-566, 1986.
16. S. Tassan and G.M. Ferrari, "An alternative approach to absorption measurements of aquatic particles retained on filters," *Limnol. Oceanogr.*, **40**, 1358-1368, 1995.
17. O. Schofield, B.B. Prézelin, R.C. Smith, P.M. Stegmann, N.B. Nelson, M.R. Lewis, and K.S. Baker, "Variability in spectral and nonspectral measurements of photosynthetic light utilization efficiencies," *Mar. Ecol. Prog. Ser.*, **78**, 253-271, 1991.
18. E. Paasche, I. Bryceson and K. Tangen, "Interspecific variation in dark nitrogen uptake by dinoflagellates," *J. Phycol.* **20**, 394-401, 1984.
19. T. Platt, P. Jauhari, and S. Sathyendranath, "The importance and measurement of new production, *Primary Productivity and Biogeochemical Cycles in the Sea*, P.G. Falkowski and A.D. Woodhead [Eds.], Plenum Press, New York, pp. 273-284, 1992.
20. T. Platt, S. Sathyendranath, O. Ulloa, W.G. Harrison, N. Hoepffner, and J. Goes, "Nutrient control of phytoplankton photosynthesis in the Western North Atlantic," *Nature*, **356**, 229-231, 1992.
21. R.M. Kudela, W.P. Cochlan, and R.C. Dugdale, "Carbon and nitrogen uptake response to light by phytoplankton during an upwelling event," *J. Plankton Res.*, submitted, 1996.

Optical inverse problem in turbid waters

Tiit Kutser, Helgi Arst, Sirje Mäekivi

Estonian Marine Institute, Lai 32, Tallinn, EE-0001, Estonia

Alberto Blanco-Sequeiros

Department of Geophysics, University of Helsinki, Fabianinkatu 24A, Helsinki, Finland

ABSTRACT

Two methods have been used for solving the inverse problem of remote sensing in case of turbid coastal and inland waters. Color indices are elaborated for estimation of Secchi depth, chlorophyll, yellow substance, suspended matter and total phosphorus concentrations and mean beam attenuation coefficient using passive optical remote sensing data. The second method is spectral modelling. A simple mathematical model is elaborated for simulating the diffuse reflectance spectra beneath and just above the water surface.

Keywords: Passive optical remote sensing, spectral modelling, optically active substances

1. INTRODUCTION

Modern Earth science is beginning to examine interactions among the different terrestrial components at all temporal and spatial scales. It is obvious that the use of satellite measurements is inevitable for operative information on global scale. However, the interpretation of the satellite data is sometimes connected with difficulties, which appear especially in the case of waters with high turbidity and areas where great optical variability inside a small territory occurs. Therefore, further development of remote optical measurements from aircraft or ships is necessary. For the elaboration and application of any method of remote sensing one must proceed through intermediate stages, where also underwater contact measurements and numerical experiments are made simultaneously with remote measurements.

2. METHOD

Remote sensing and underwater spectral measurements have been carried out in the Baltic Sea, Estonian and Finnish lakes using telespectrometer "Pegasus". This device enables to measure the downwelling irradiance, E_d , upwelling radiance, L_u , and downwelling radiance, L_d , in the waveband 400-700 nm with spectral resolution approximately 6 nm. The remote sensing measurements were performed on board a research vessel or boat. Simultaneously the measurements of upward and downward irradiance (E_u and E_d correspondingly) were carried out by Li-1800UW spectrophotometer. Concentrations of chlorophyll a , C_{CHL} , and suspended matter, C_{SM} , were determined from water samples. Spectral beam attenuation coefficients were estimated from water samples by spectrophotometer Hitachi-U1000. Yellow substance concentrations, C_{DOC} , were calculated from the Hitachi data by following formula¹:

$$C_{DOC} = \frac{c'_f(\lambda)}{a^*_{DOC}(\lambda)}, \quad (1)$$

where $c'_f(\lambda)$ is the difference between the beam attenuation coefficient of filtered and distilled water and $a^*_{DOC}(\lambda)$ is the specific absorption coefficient of the yellow substance at the wavelength λ . Here is assumed, that scattering coefficient of the yellow substance at this wavelength is negligible in comparison with the absorption coefficient.

The remote sensing reflectance, $r(\lambda)$, can be calculated by formula $r(\lambda) = L_u(\lambda)/E_d(\lambda)$. In case of measurements directed to the nadir point on board a ship or low flying aircraft the influence of the air layer between the water surface and the reservoir on the measured signal is small and the upwelling radiance consists of two main components: 1) solar radiance reflected from the wavy water surface, $L_R(\lambda)$; 2) solar radiance backscattered from the water mass, $L_D(\lambda)$. We can estimate the component $L_R(\lambda)$ by approximate formula $L_R(\lambda) \approx 0.02L_d(\lambda)$ and determine separately two components of $r(\lambda)$:

$$r(\lambda) = \frac{\pi L_u(\lambda)}{E_d(\lambda)} = \frac{\pi L_R(\lambda)}{E_d(\lambda)} + \frac{\pi L_D(\lambda)}{E_d(\lambda)} = r_R(\lambda) + r_D(\lambda). \quad (2)$$

It is possible to estimate remote sensing reflectance from the data of diffuse reflectance just beneath the water surface, $R_D(\lambda)$. Gordon, Brown and Jacobs² have shown that diffuse reflectances just beneath and above the water surface are related by approximate formula: $r_D(\lambda) \approx 0.544 R_D(\lambda)$.

Kirk³ proposed a formula for computing the diffuse reflectance just beneath the water surface:

$$R_D(\lambda) = (0.975 - 0.629\mu_0) \frac{b'(\lambda)}{a(\lambda)}, \quad (3)$$

where $a(\lambda)$ is the total spectral absorption coefficient, $b'(\lambda)$ is total spectral backscattering coefficient and μ_0 is the cosine of direct solar beam in the water after refraction. Consequently, we can write:

$$r_D(\lambda) \approx 0.544(0.975 - 0.629\mu_0) \frac{b'(\lambda)}{a(\lambda)}. \quad (4)$$

Diffuse reflectance beneath the water surface, $R_D(\lambda)$ can be calculated from underwater spectral data: $R_D(\lambda) = E_u(\lambda)/E_d(\lambda)$, where E_u and E_d are upward and downward spectral irradiance in the water.

3. COLOR INDEX METHOD

Spectral ratios in form $C_{chl} = A[r(\lambda_1)/r(\lambda_2)]^B$, where A and B are empirical constants, have been widely used^{4,5} in estimation of chlorophyll *a* concentration in Case I waters. The same or different kind of algorithms can be elaborated for estimation of other characteristics of water environment from optical remote sensing data. However, our calculations (using different algorithms^{6,7,8}) and also the results of other authors⁵ show that algorithms elaborated for Case I waters cannot be used in interpretation of remote sensing data collected for turbid coastal and inland waters. Here is difficult to separate influence of different optically active substances on remote sensing reflectance (obtained on turbid waters) whereas their concentrations vary dramatically in space and time, and the optical properties are often site specific.

Nevertheless, we have made an attempt to elaborate remote sensing algorithms for turbid waters using the data of measurements carried out in the Baltic Sea and at some Estonian and Finnish lakes. The simple spectral ratios $r(\lambda_1)/r(\lambda_2)$, their combinations and also integral characteristics of the remote sensing spectra were used for interpreting of our data.

The water characteristics that we tried to estimate are: chlorophyll *a*, yellow substance, suspended matter and total phosphorus concentrations; the mean value of $c'(\lambda)$ in the range 400-700 nm and Secchi depth.

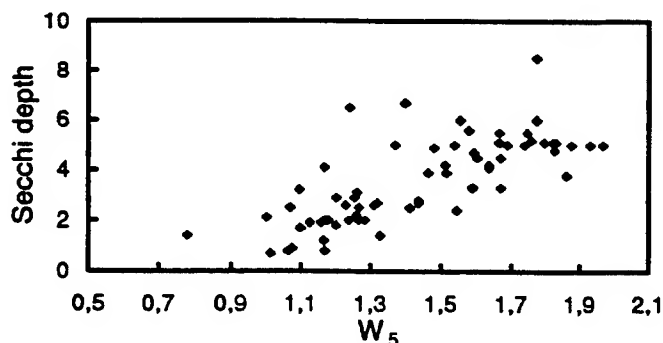


Figure 1. Correlation between Secchi depth and the remote sensing characteristic W_5 . A sum of two color indices, $W_5 = r(480)/r(620) + r(620)/r_{max}$ was used for interpretation of remote sensing data. $R=0.78$

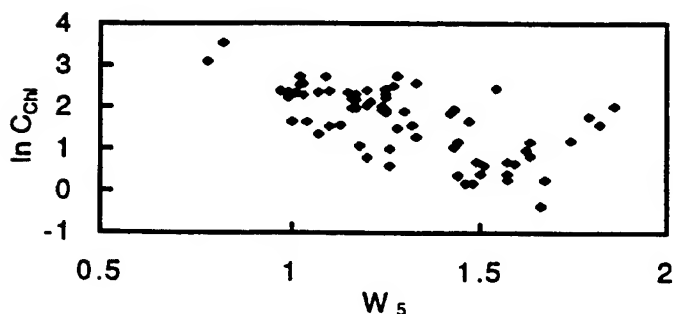


Figure 2. Correlation between $\ln C_{chl}$ and remote sensing characteristic W_5 . $R=0.72$

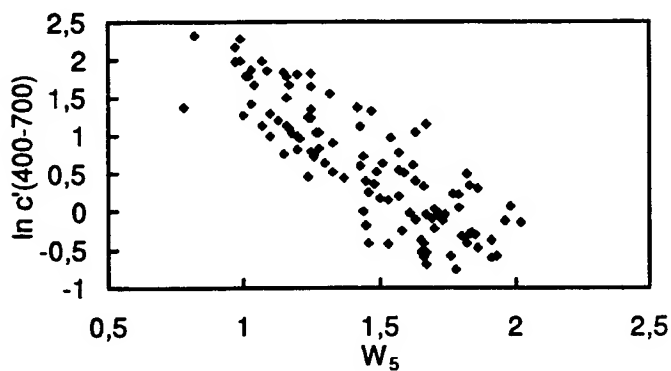


Figure 3. Correlation between mean beam attenuation coefficient and remote sensing characteristic W_5 . $R=0.84$

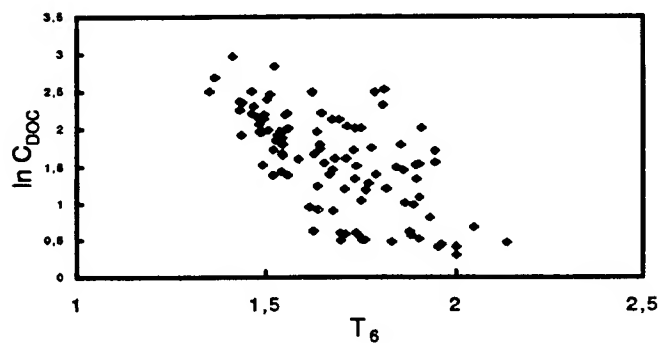


Figure 4. Correlation between measured and calculated by means of remote sensing characteristic T_6 yellow substance concentrations. $R=0.80$
 $T_6 = [r(440) + r(600)] / r(600)$.

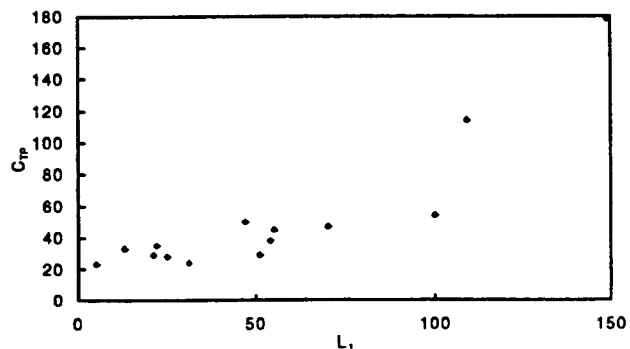


Figure 5. Correlation between measured and estimated by means of remote sensing characteristic L_1 concentrations of total phosphorus in Lake Peipsi in May 1990. $R=0.78$

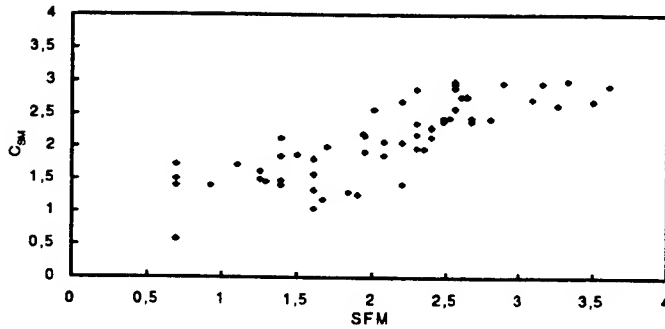


Figure 6. Correlation between measured and estimated by remote sensing characteristic SFM concentrations of suspended matter. $SFM = r(430)/r(530) + r(530)/r(620) + [r(520)/r_{max}]A$. $A=1$ if r_{max} is in spectral region $\lambda > 480nm$, elsewhere $A=-1$.

4. MODEL

The second, alternative method for the interpretation of optical remote sensing data we call the "similarity method". The basis of this method is the comparison of the measured full spectrum of $r_D(\lambda)$ with the multitude of the corresponding spectra determined by means of model calculations. From this group of spectra we try to identify the one which is the closest to the measured spectrum. Thereafter we can determine the concentrations of the optically active substances in the water for the experimental spectrum under consideration, assuming them to be the same as the corresponding initial data for computing the "most similar" theoretical spectrum. Note that for this kind of comparison normalized spectral curves may also be used.

The efficiency of this method depends essentially on the validity of the mathematical model describing the spectra of $r_D(\lambda)$. The principal difficulty is with the detailed description of the absorptive and scattering properties of optically active material in the water (e.g., different types of phytoplankton pigments, organic and inorganic substances, detritus, etc.), especially the determination of the backscattering coefficients. Our estimations show that the scattering (and backscattering) coefficients presented in handbooks and monographs (mainly for the open ocean waters) are unsuitable for turbid coastal and inland waters.

We used a simple model (4) on assumption that there are three optically active components in the water: phytoplankton pigments, yellow substance and suspended matter. Under these conditions the total spectral absorption coefficient of the water, $a(\lambda)$, is described by the following formula:

$$a(\lambda) = a_w^*(\lambda) + a_{ph}^*(\lambda)C_{ph} + a_{DOC}^*(\lambda)C_{DOC} + a_{SM}^*(\lambda)C_{SM} \quad (5)$$

where $a_w^*(\lambda)$ is spectral absorption coefficient of pure water, $a_{ph}^*(\lambda)$, $a_{DOC}^*(\lambda)$ and $a_{SM}^*(\lambda)$ are the spectral specific absorption coefficients of phytoplankton, yellow substance and suspended matter respectively; and C_{ph} , C_{DOC} and C_{SM} are concentrations of phytoplankton, yellow substance and suspended matter. The spectral chlorophyll-specific absorption coefficient of phytoplankton is calculated using the power function⁹:

$$a_{ph}^*(\lambda) = A(\lambda)C_{chl}^{-B(\lambda)}, \quad (6)$$

where $A(\lambda)$ and $B(\lambda)$ are positive, wavelength-dependent parameters.

The values of $a_{DOC}^*(\lambda)$ were calculated by the formula¹⁰:

$$a_{DOC}^* = 0.565 \exp[-S(\lambda - 380)], \quad (7)$$

where $S=0.013 \pm 0.005$. By our estimations¹ $S=0.017$ gives the best result in case of the Baltic Sea, Estonian and Finnish lakes. Specific absorption coefficients, $a_{SM}^*(\lambda)$, are taken from Prieur and Sathyendranath¹¹ as normalized specific absorption spectra for non-chlorophyllous particles.

The total spectral backscattering coefficient $b'(\lambda)$ can be described by formula:

$$b'(\lambda) = 0.5b_w(\lambda) + b_{ph}^*(\lambda)\tilde{b}_{ph}(\lambda)C_{chl} + b_{SM}^*(\lambda)\tilde{b}_{SM}(\lambda)C_{SM}, \quad (8)$$

where b_w is scattering coefficient of pure water obtained from Smith and Baker¹² and it is assumed that backscattering probability is 50% in clear water. Chlorophyll-specific spectral scattering coefficient $b_{ph}^*(\lambda)$ and spectral backscattering probability, $\tilde{b}_{ph}(\lambda)$ are taken from Ahn, Bricaud and Morel¹³. The spectral scattering coefficient spectra of non-chlorophyllous particles found in literature are either linearly or exponentially decreasing with increasing of wavelength or even taken as constant. Presented in literature $b_{SM}(\lambda)$ and \tilde{b}_{SM} values are obtained in Case I waters and are not suitable for turbid waters. We used the simultaneous underwater measurement data by Li-1800UW for estimating the approximate values and spectral

dependence of $b_{SM}(\lambda)$ on $b_{SM}(\lambda)$. Underwater spectral radiation data help us to test our model and comparison of the model spectra with corresponding Li-1800UW spectra is the first stage of the investigation.

5. RESULTS AND DISCUSSION

Our results confirm that it is possible to estimate concentrations of chlorophyll *a*, yellow substance, suspended matter and even optically invisible total phosphorus concentration as well as Secchi depth and mean beam attenuation coefficient in turbid coastal and inland waters using color index method. However, it is practically impossible when the concentration of the substance we are seeking for is relatively small in comparison of other optically active substances.

Positive side of this method is the simplicity - only remotely measured data and simple algorithms are needed to describe the water environment. It is possible to search for different characteristics of the water that are in correlation with water color, but cannot be estimated by modelling or other methods (total phosphorus concentration, Secchi depth etc.). The correlation pictures show also some instability referring that the algorithms are in some degree site specific and seasonal. Correlation between measured and estimated characteristics of the water are higher ($R > 0.9$) for some expeditions, but whole data complex may not give a good correlation¹⁴. It often happens that we are able to elaborate a remote sensing algorithm for estimation of a water characteristic in certain region of the Baltic Sea, but we cannot find an universal algorithm for whole sea, or for all water bodies under investigation.

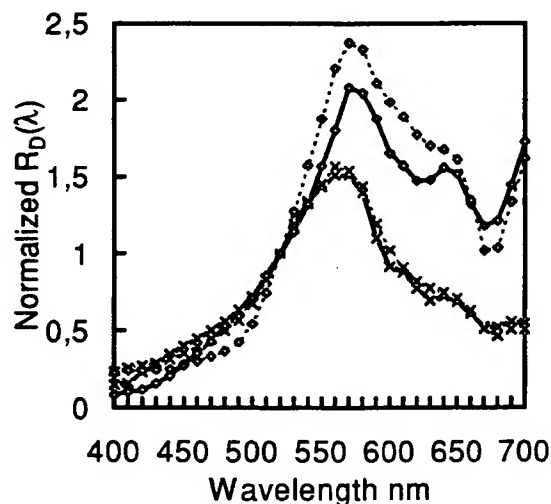


Figure 7. Comparison between measured (solid line) and calculated (dashed line) normalized to 520 nm diffuse reflectance spectra.

Empty diamonds - Lake Tuusula;

X - Lake Vesijärvi

	C_{chl}	C_{DOC}	C_{SM}
Tuusula	16.17	17.03	14.1
Vesijärvi	5.84	3.73	2
	mg/m ³	mg/l	mg/l

As was told above the first step is to test our model by using the underwater radiation spectra measured by Li-1800UW. The values of $R_D(\lambda)$ were calculated by measured $E_u(\lambda)$ and $E_d(\lambda)$ and the spectrum obtained were compared with the model spectrum. The results show quite good coincidence. Correlation between measured and estimated concentrations of chlorophyll and yellow substances are 0.97 and 0.98 correspondingly, but the correlation coefficients for suspended matter are low. Fig.7 demonstrates two examples of simulated and measured spectra. In most cases these spectra fit well with each other, except some extremal cases (very turbid water and the water with very low backscattering coefficient).

One of the reasons of non-coincidence of measured and calculated results may be selection of grid steps in model calculation. For example if the grid step of yellow substance concentration is too big compared with chlorophyll grid step then the adequate estimating of the chlorophyll concentration is practically impossible. For that reason model calculations are carried out using the variable grid steps, increasing steps with increasing concentrations.

The other reason of weak correlation for C_{SM} is nature of the suspended matter itself. We have a dry weight of material remaining on filter pad after filtration. This material consists of phytoplankton and detritus. We do not know dry weight of phytoplankton corresponding to unit of chlorophyll *a*. Therefore we cannot separate the part of weight caused by plankton as it is in our model.

The selection of proper set of grid steps is important also from point of view of computing time. Time used for one run may rise from minute to hours if to use smaller grid step. Instead of getting more precise estimations we will get a set of

concentrations where only one concentration is changing and others may be far from reality whereas number of combinations of concentrations giving approximately the same remote sensing spectrum is increasing.

Aiken et al.⁶ have shown that concentration of phytoplankton pigments, C_{Ph} , is related to chlorophyll *a* concentration $C_{TP}=2.17C_{Chl}+0.021$. Our model calculations show for the Estonian and Finnish lakes relationship $C_{TP}\approx 3C_{Chl}$ gives better results. This result agrees with data presented in above mentioned paper.

6. REFERENCES

1. S. Mäekivi and H. Arst, "Estimation of the concentration of yellow substance in natural waters by beam attenuation coefficient spectra," *Proc. Estonian Acad. Sci. Ecol.*, **6** (3/4), 108-123, (1996).
2. H.R. Gordon, O.B. Brown and M.M. Jacobs, "Computed relationships between the inherent and apparent optical properties of a flat homogenous ocean," *Appl. Opt.* **14**, 417-427, (1975).
3. J.T.O. Kirk, "The assessment and prediction of optical water quality," Australian Water and Wastewater Association 13th Federal Convention, 504-507, (1989).
4. H.R. Gordon, O.B. Brown, R.H. Evans, J.W. Brown, R.C. Smith, K.S. Baker and D.K. Clark, "A semianalytic radiance model of ocean color," *J. Geophys. Res.*, **93**(D9), 10909-10924, (1988).
5. R.P. Bukata, J.H. Jerome, K.Y. Kondratyev and D.V. Pozdnyakov, "Satellite monitoring of optically-active components of inland waters: an essential input to regional climate change impact studies," *J. Great Lakes Res.*, **17**, 470-478, (1991).
6. J. Aiken, G.F. Moore, C.C. Trees, S.B. Hooker and D.K. Clark, "The SeaWiFS CZCS type pigment algorithm," *SeaWiFS Technical Report Series, NASA Technical Memorandum 104566*, **29**, (1995).
7. J.W. Campbell, J.M. Blaisdell, M. Darzi, "Level-3 SeaWiFS data products: spatial and temporal binning algorithms," *SeaWiFS Technical Report Series, NASA Technical Memorandum 104566*, **32**, (1995).
8. S. Tassan, "Local algorithms using SeaWiFS data for the retrieval of phytoplankton pigments, suspended sediment, and yellow substance in coastal waters," *Appl. Opt.*, **33**(12), 2369-2378, (1994).
9. A. Bricaud, M. Babin, A. Morel and H. Claustre, "Variability in the chlorophyll-specific absorption coefficients of natural phytoplankton: analyses and parametrization," *J. Geophys. Res.* **100**(C7), 13321-13332 (1995).
10. K.S. Baker and R.C. Smith, "Bio-optical classification and model of natural waters. 2.," *Limnol. Oceanogr.*, **27**(3), 500-509, (1982).
11. L. Prieur and S. Sathyendranath, "Optical classification of coastal and oceanic waters based on specific spectral absorption curves of phytoplankton pigments, dissolved organic matter, and other particulate materials," *Limnol. Oceanogr.* **26**(4), 671-689, (1981).
12. R.C. Smith and K.S. Baker, "Optical properties of the clearest natural waters (200-800 nm)," *Appl. Opt.* **20**(2), 177-184, (1981).
13. Y.-H. Ahn, A. Bricaud and A. Morel, "Light backscattering efficiency and related properties of some phytoplankters," *Deep-Sea Res.* **39**(11/12), 1835-1855, (1992).
14. T. Kutser, H. Arst, T. Miller, L. Käärmann and A. Milius, "Telespectrometrical estimation of water transparency, chlorophyll *a* and total phosphorus concentration of Lake Peipsi," *Int. J. Remote Sensing*, **16**, 3069-3085, (1995).

Remote-sensing reflectance measured with and without a vertical polarizer

Z. P. Lee, K. L. Carder, T. G. Peacock, and R. G. Steward

Department of Marine Science
University of South Florida
St. Petersburg, FL 33701

ABSTRACT

Remote-sensing reflectance (R_{rs} , ratio of the water-leaving radiance to the downwelling irradiance above the surface) with and without a vertical polarizer in front of the sensor were derived for measurements made at 90° to the solar plane and in a direction 30° to nadir. These measurements were carried out to see if a vertical polarizer mounted in front of a sensor would improve the R_{rs} results. For 28 pairs of measurements with chlorophyll *a* concentrations ranging from 0.07 to 38 mg/m^3 , solar zenith angles from 18° to 66° , clear to cloudy skies, and for optically shallow and deep waters, there was no significant variation between the polarized and unpolarized R_{rs} values. Statistical comparisons of polarized to unpolarized results provided R^2 values of 0.987, 0.987, 0.994, and 0.999 with slopes 1.007, 1.005, 0.983 and 0.998 for wavelengths at 410, 440, 550 and 630 nm, respectively. These results suggest that although the underwater light field is partially polarized, a vertical polarizer in front of a sensor will provide close results ($\sim 9\%$ difference for $R_{rs}(440)$) to unpolarized sensor, if the measurements were made in a direction 90° to the solar plane and 30° ($\sim 22^\circ$ underwater) to the nadir.

Key words: remote-sensing reflectance, polarizer

1. INTRODUCTION

In the field measurements of water color, Clarke et al.¹ and Carder et al.² used a vertical polarizer in front of the radiance sensor to reduce the sea-surface reflected skylight. These measurements can lead to the calculation of remote-sensing reflectance (R_{rs} , ratio of the water-leaving radiance to downwelling irradiance just above the sea surface). As the skylight is partially polarized³ and in non-uniform distribution, concerns have arisen about the skylight correction in the R_{rs} derivation. Also, as the subsurface light field is partially polarized^{3,4}, it is not known if the polarized sensors will provide the same remote-sensing reflectance values to unpolarized sensors, as satellite calibration relies on the accurate measurements of the remote-sensing reflectance. To examine the affects of a vertical polarizer, a series of field measurements were carried out in June 1993 and March 1994 in the West Florida Shelf and the Gulf of Mexico. Figure 1 shows the locations of the measurements. The experiment sites covered chl *a* concentrations from 0.07 to 38 mg/m^3 , waters with optically shallow and deep bottom, and clear to cloudy sky conditions (Table 1 summarizes the station information). Results of the R_{rs} values were presented.

2. METHOD

The measurement methods were summarized in Lee et al.⁵ Briefly, above-water upwelling radiance, downwelling sky radiance, and downwelling irradiance above the surface were measured using Spectron Engineering SE-590⁶. The SE-590 is insensitive to polarization as it has no folding mirrors or other optical surfaces to enhance or degrade a polarized source field. Only difference here was that for the same stations, these measurements were made with and without a vertical polarizer in front of the sensor. All the measurements were finished within a few minutes, which guaranteed the stability of the incoming solar irradiance.

R_{rs} were derived using the full-spectral optimization algorithm in Lee et al.⁵, with a term for bottom reflectance added for the possible optical shallow waters. We used the term in Lee et al.⁷ for the description about the bottom contributions. Cloud covered Sun data were not included, because the illumination was too variable even during the short sampling period. Cloudy sky data was retained where the Sun was not covered and the illumination was constant.

3. RESULTS AND DISCUSSION

Figures 2 - 5 present the derived R_{rs} values for wavelengths 410, 440, 550, and 630 nm, respectively. For the four wavelengths, the R^2 values are 0.987, 0.987, 0.994, and 0.999 with slopes of 1.007, 1.005, 0.983 and 0.998, respectively. Although the R_{rs} values did not match each other exactly, these results suggest that there are no significant or systematic variations between the polarized and non-polarized R_{rs} values. The ~ 9% variation in the R_{rs} values could come from the polarization introduced by the waters^{3, 4}, or from the sky correction procedure⁵, especially those results using polarized sensors, as skylight is partially polarized and in non-uniform distribution. Rigorously controlled experiments are needed in order to determine the source of the 9% difference.

Intuitively, it seems a good idea to add a vertical polarizer in front of a sensor to cut off the unwanted reflected skylight, especially when viewing the water at the Brewster's angle (~53° from nadir). However, in the field, due to the uneven sea surface, waves reflected skylight can come from a large effective solid angle, which makes it impossible to cut off all the reflected skylight, even at the Brewster's angle. And, the inclusion of a polarizer reduces the signal by ~50% due to transmission losses through the filter. This increases the uncertainties for coastal water R_{rs} , where the blue signals are very low. Also, there was an averaged ~ 9% difference between polarized and unpolarized R_{rs} values. Thus, to calibrate satellite sensor, it is better to use unpolarized sensors for shipboard measurements.

4. CONCLUSIONS

When viewing the water at 90° to the solar plane and 30° from nadir, sensors with and without a vertical polarizer provided close R_{rs} results.

To be consistent with satellite sensors, and to increase the signal entering into the field sensors, it is better to use unpolarized sensors.

5. ACKNOWLEDGMENTS

Financial support was provided by NASA through grant NAGW-465 and GSFC contract NAS5-30779, and by ONR through grants N00014-89-J-1091. Ship support was provided by the *R/V Suncoaster* through the Florida Institute of Oceanography.

6. REFERENCES

1. G. L. Clarke, G. C. Ewing, C. J. Lorenzen, "Spectra of backscattered light from the sea obtained from aircraft as a measure of chlorophyll concentration", *Science* **167**, 1119-21 (1970).
2. K. L. Carder, P. Reinersman, R. F. Chen, F. Muller-Karger, C. O. Davis, and M. Hamilton, "AVIRIS calibration and application in coastal oceanic environments", *Remote Sens. Environ.* **44**, 205-16 (1993).
3. G. W. Kattawar, "Polarization of light in the ocean", in *Ocean Optics*, ed. by R. W. Spinrad, K. L. Carder and M. J. Perry, pp. 202-225, Oxford University Press, New York, 1994.
4. T. H. Waterman, "Polarization of scattered sunlight in the deep water", *Deep-Sea Research Supp.* **3**, 426-434 (1961).
5. Z. P. Lee, K. L. Carder, R. G. Steward, T. G. Peacock, C. O. Davis and J. L. Mueller, "Protocols for measurement of remote-sensing reflectance from clear to turbid waters", this volume.
6. K. L. Carder and R. G. Steward, "A remote-sensing reflectance model of a red tide dinoflagellate off West Florida. *Limnol. Oceanogr.* **30**, 286-98 (1985).
7. Z. P. Lee, K. L. Carder, S. K. Hawes, R. G. Steward, T. G. Peacock, and C. O. Davis, "Model for the interpretation of hyperspectral remote-sensing reflectance", *Appl. Opt.* **33**, 5721-5732 (1994).

Table 1. Summary of the station conditions.

stations	solar zenith angle (°)	[chl_a] (mg/m ³)	sky	bottom depth (m)
*BN1	58	3.71	Clear	~ 11
2	31	2.01	CLOUDY	~ 17
3	63	0.62	CLOUDY	~ 25
6	49	1.42	Clear	Deep
7	37	0.64	Clear	Deep
12	38	2.14	CLOUDY	Deep
14	36	0.45	CLOUDY	Deep
16	34	0.7	Clear	Deep
17	66	2.19	Clear	Deep
19	45	0.32	Clear	~ 30
20	36	0.26	Clear	Deep
21	65	0.52	Clear	Deep

stations	solar zenith angle (°)	[chl a] (mg/m ³)	sky	bottom depth (m)
22	47	0.25	CLOUDY	Deep
23	37	0.17	CLOUDY	Deep
24	56	0.19	CLOUDY	Deep
28	56	0.22	CLOUDY	Deep
*CO1	44	4.22	CLOUDY	Deep
3	63	0.07	CLOUDY	Deep
4	34	0.08	CLOUDY	Deep
5	46	8.69	Clear	Deep
7	18	9.45	Clear	Deep
11	49	5.98	CLOUDY	Deep
12	43	38.6	Clear	Deep
15	50	22.82	CLOUDY	Deep
16	21	19.57	CLOUDY	Deep
18	66	0.1	CLOUDY	Deep
19	54	0.22	Clear	33
20	28	0.43	Clear	~ 14

+: BONG cruise, March 1994, West Florida Shelf;

*: COLOR cruise, June 1993, Gulf of Mexico.

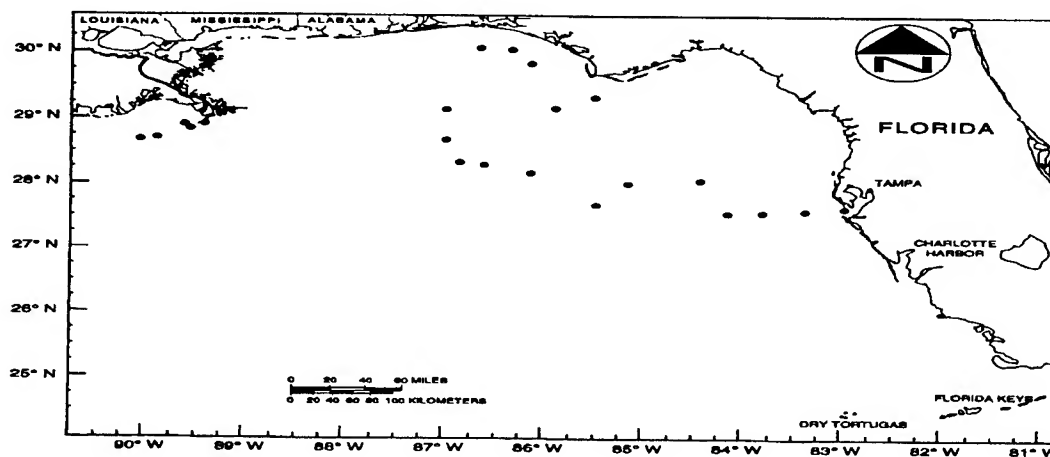


Figure 1. Measurement sites in the Gulf of Mexico and West Florida Shelf.

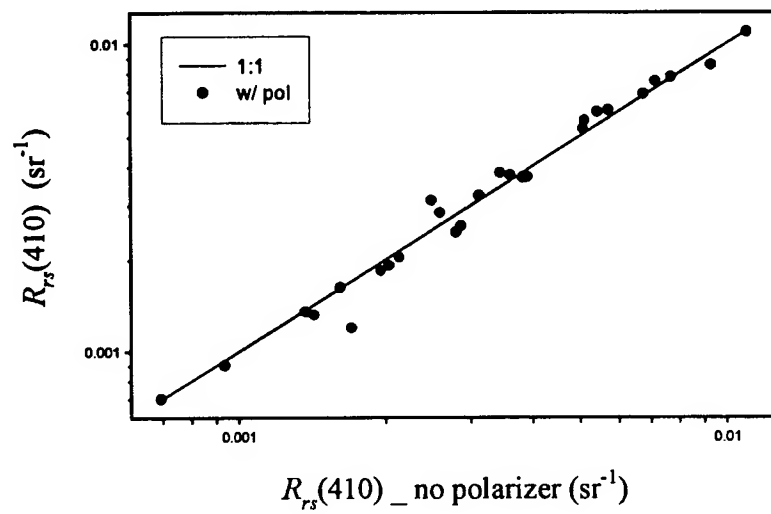


Figure 2. Comparison of $R_{rs}(410)$ values.

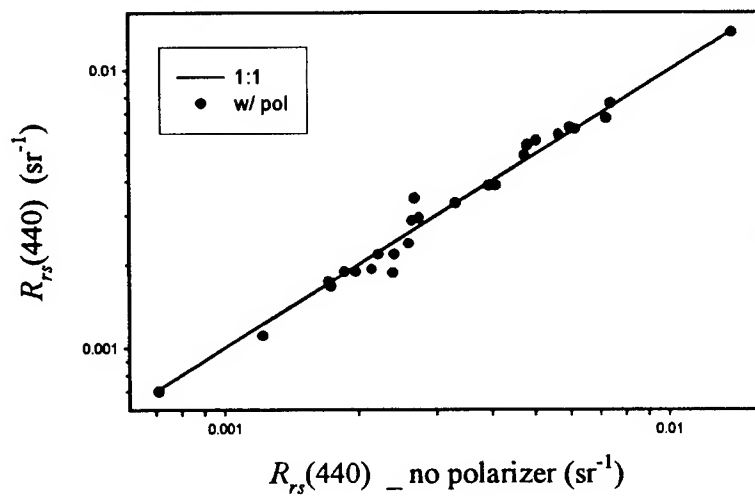


Figure 3. Comparison of $R_{rs}(440)$ values.

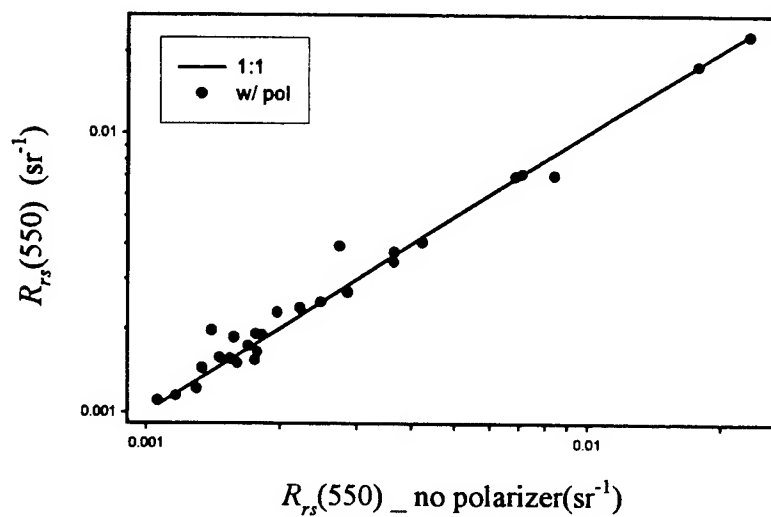


Figure 4. Comparison of $R_{rs}(550)$ values.

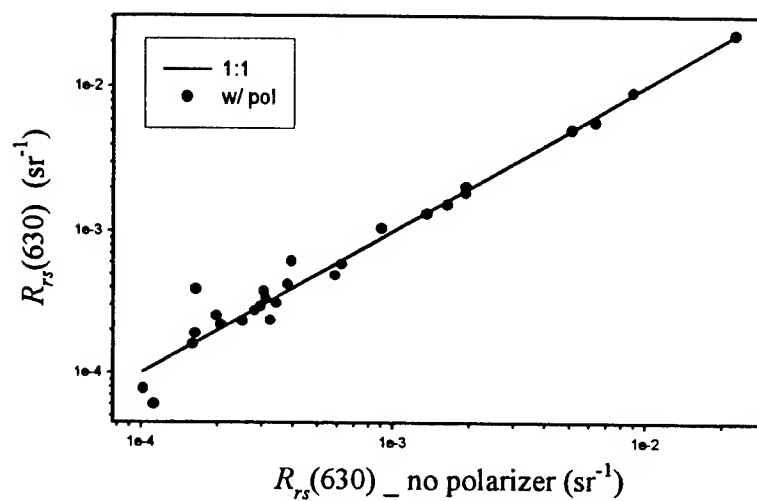


Figure 5. Comparison of $R_{rs}(630)$ values.

Comparison of measured inherent optical properties with estimates determined from reflectance in coastal waters off Cape Hatteras, North Carolina, USA

Steven E. Lohrenz^a, Donald G. Redalje^a, Ken M. Matulewski^a, James E. Ivey^a and Alan D. Weidemann^b

^aInstitute of Marine Sciences, University of Southern Mississippi, Stennis Space Center, Mississippi, 39529, USA

^bNaval Research Laboratory, Stennis Space Center, Mississippi, 39529, USA

ABSTRACT

The ability to acquire information about inherent optical properties such as total spectral absorption ($a(\lambda)$, m^{-1}) and scattering ($b(\lambda)$, m^{-1}) from reflectance properties of oceanic waters is fundamental to the development of remote sensing algorithms. While considerable success has been achieved in relatively clear oceanic waters, inversion methods to determine $a(\lambda)$ and $b(\lambda)$ from reflectance properties in coastal waters is a more complex problem. We conducted measurements of $a(\lambda)$ and $b(\lambda)$ in conjunction with profiles of *in situ* radiance reflectance at various locations off Cape Hatteras, North Carolina during spring 1996. Our objective was to evaluate measurement and model closure among the different methods that were applied. Spectral a and b were determined using a WETLabs ac-9. Independent estimates of a were also determined in discrete samples using a spectrophotometer. *In situ* upwelling radiance (L_u) and downwelling irradiance (E_d) were determined using a Satlantic SeaWiFS Profiling Multichannel Radiometer. Inverse methods provided estimates of a and b from reflectance (L_u/E_d). For the mid-shelf station characterized by relatively low b/a ratios, agreement among the different methods for estimating $a(\lambda)$ was quite good. At the inner shelf station, higher b/a ratios were encountered and larger discrepancies were observed between the different methods. The results illustrate the utility of multi-faceted measurement strategies for evaluating the reliability of estimates of optical properties.

Keywords: inherent optical properties, absorption, scattering, reflectance, backscattering, remote sensing, coastal, Case 2 waters, inverse methods, ocean color

1. INTRODUCTION

Determination of optical properties of coastal waters is important for efforts to characterize the, as yet, undefined role of continental shelf ecosystems in global biogeochemical cycles. Information about inherent optical properties (e.g., total spectral absorption [$a(\lambda)$] and scattering [$b(\lambda)$] coefficients) can be used in support of algorithms to determine chlorophyll and dissolved organic matter concentrations, photosynthetically available radiation and its absorption by phytoplankton. The ability to estimate inherent optical properties from reflectance properties is fundamental to the development of remote sensing algorithms. While considerable success has been achieved in relatively clear oceanic waters, inversion methods to determine a and b from reflectance properties in coastal waters is a more complex problem. A prerequisite to dealing with this problem is the establishment of reliable methods for determining inherent and apparent optical properties in coastal environments. As part of the Department of Energy's Ocean Margins Program, we made observations of inherent optical properties and spectral radiance reflectance in continental shelf waters off Cape Hatteras, North Carolina, USA. This study provided one of the few available data sets in this region involving simultaneous measurements of spectral radiance reflectance and *in situ* and *in vitro* determinations of inherent optical properties. Simple inverse methods were applied to derive estimates of inherent optical properties from reflectance. Our objective was to evaluate measurement and model closure among the different methods that were applied.

2. METHODS

Measurements were conducted during the R/V *Endeavour* cruise EN280 from 12-20 March 1996. Comparisons among the different methods were made at three stations including an inner shelf station (St. 26, 16 m bottom depth), and two stations located in the mid- to outer shelf region (St. 43, 39 m and St. 49, 34 m). Vertical profiles of $a(\lambda)$ and $c(\lambda)$ (spectral beam attenuation coefficient) were determined at nine wavelengths using a WETLabs ac-9. Pre- and post-deployment calibration of the ac-9 was done in the laboratory using dry air to determine zero absorption and attenuation. Custom-designed compression fittings, designed to minimize torque, were used to attach the instrument to a lowering frame. A wavelength-dependent scattering correction was applied to absorption values¹ using temperature- and salinity-corrected² values of absorption at 715 nm. Initial estimates of $a(\lambda)$ obtained from the ac-9 were systematically higher than those derived from the spectrophotometric and reflectance methods (see below). This was attributed to a possible modification in the optical path of the instrument due to torsion or compression as a result of mounting on the lowering

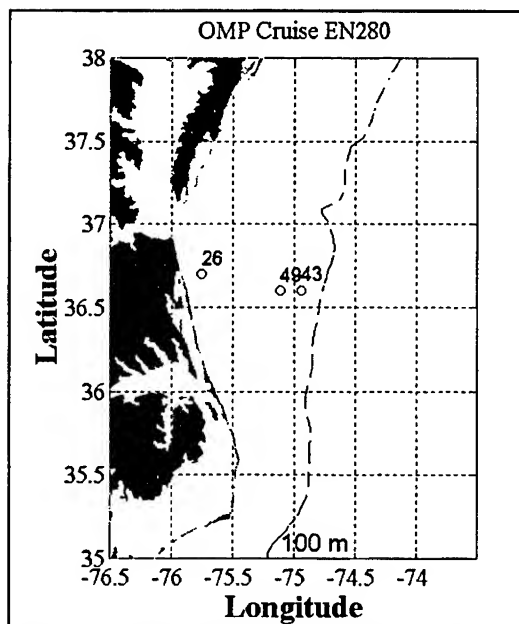


Figure 1. Location of sampling stations during R/V Endeavour cruise EN280.

frame. Air calibration values for absorption were adjusted at selected wavelengths to optimize agreement (minimize the root mean square deviation) between ac-9 and the other methods. Once an optimum was established, the same calibration was used in all cases. The total scattering coefficient, $b(\lambda)$, was estimated by subtraction of the corrected values of $a(\lambda)$ from $c(\lambda)$.

Independent estimates of $a(\lambda)$ were also determined *in vitro* by analysis of discrete samples using a Kontron dual beam spectrophotometer. Water samples were collected using the ship's CTD/Niskin rosette system. Particulate absorption spectra were measured on Whatman GF/F filters by the filter pad method^{3,4}. Non-pigmented particulate absorption was measured on filters extracted with boiling methanol for 15 min and subsequently rinsed with deionized water. Pigment absorption was estimated by subtracting non-pigmented particulate absorption from the total particulate absorption. Path length amplification, β , was estimated using the method of Arbones et al. (1996)⁵. Absorption spectra of the GF/F filtrates were measured in 10 cm glass cuvettes. Chlorophyll concentrations were determined by extraction of filtered samples with 90% acetone and subsequent analysis by the fluorometric method⁶ using a Turner Designs Model 10 fluorometer.

Vertical profiles of *in situ* upwelling spectral radiance [$L_u(\lambda, z)$] and downwelling irradiance [$E_d(\lambda, z)$] were determined using a Satlantic SeaWiFS Profiling Multichannel Radiometer. Profiles were conducted between 0900 and 1400 h local time. Our study was one of the first to deploy this free falling profiling instrument in relatively shallow (< 50 m) coastal waters. Near-surface (upper 3 m) spectral radiance reflectance (L_u/E_d) was related to $a(\lambda)$ and the total backscattering coefficient, $b_b(\lambda)$, by the relation of Gordon et al. (1988)⁷:

$$\frac{L_u}{E_d} \approx 0.095 \frac{b_b}{a + b_b} \quad (1)$$

where

$$\frac{L_u}{E_d} \approx 0.11 \frac{b_b}{K_d} \quad (2)$$

Rearranging these equations we obtain:

$$b_b \approx \frac{L_u K_d}{E_d 0.11} \quad (3)$$

and

$$a \approx \frac{K_d}{0.11} \left(0.095 - \frac{L_u}{E_d} \right) \quad (4)$$

The wavelength notation has been omitted for convenience. The spectral downwelling diffuse attenuation coefficient, $K_d(\lambda)$, was estimated from irradiance profiles. Absorption due to pure water was subtracted from the values of $a(\lambda)$ determined by equation 4 to facilitate comparisons with the other methods.

In addition to the determinations of the total scattering coefficient, $b(\lambda)$, made with the ac-9 as described above, estimates were made using two other methods. One approach was to assume a constant b_b/b ratio equal to 0.01, which is reasonable for these coastal waters. This permitted the estimation of $b(\lambda)$ from equation 3 as follows:

$$b = \frac{b_b}{0.01} \quad (5)$$

An alternative method used was that based on the relation given by Gordon and Morel (1983)⁸:

$$b(\lambda) = \left(\frac{550}{\lambda}\right) 0.3C^{0.62} \quad (6)$$

where C is the total pigment concentration in mg m^{-3} .

3. RESULTS

The comparison of total absorption coefficients estimated by the three different approaches revealed different levels of agreement at the different stations (Table 1). At the inner shelf station (St. 26), spectrophotometric estimates of $a(\lambda)$ tended to be lower than estimates derived from the reflectance profile for some wavelengths (Fig. 2a) and a comparison of the two spectra showed the highest root mean square (rms) deviation (Table 1). Agreement between reflectance and

Table 1. Root mean square deviation between estimates of total spectral absorption by *in vitro* (spectrophotometric) and *in situ* (ac-9 and equation 4) techniques.

Station No.:	26	43	49
RMS Deviation (equation 4 vs. spec.)	0.073	0.013	0.021
RMS Deviation (ac-9 vs. spec.)	0.038	0.022	0.068

spectrophotometric methods was better at the outer and mid-shelf locations, Stns. 43 and 49 respectively. The ac-9 estimates of $a(\lambda)$ were generally consistent with the spectrophotometric determinations, although scatter in the measurements was larger, particularly at Stns. 26 and 49. This contributed to larger rms deviations between spectrophotometric and ac-9 measurements at these stations (Table 1).

Estimates of total scattering coefficients determined with the ac-9 and from equation 5 were highest at the inner shelf station, possibly related to the higher relative contribution of non-pigmented particulate matter (Fig. 2a). Values of $b(\lambda)$ determined using equation 5 displayed a wavelength dependence with a maximum around 500 nm that was greater than corresponding estimates made with the ac-9. At the mid-shelf and outer shelf stations (Figs. 3b and 3c), estimates of $b(\lambda)$ from both the ac-9 and equation 5 were generally lower than observed at the inner shelf station. The ac-9 determinations of $b(\lambda)$ at these stations ranged slightly higher than those estimated from equation 5 for intermediate wavelengths. Values of $b(\lambda)$ determined from equation 5 were relatively invariant at intermediate wavelengths, but exhibited a tendency towards higher values at longer and shorter wavelengths. At the inner shelf station (Fig. 3a), both the ac-9 estimates of $b(\lambda)$ and those determined from equation 5 were higher than the estimates based on chlorophyll concentration given by

equation 6. In contrast, values of $b(\lambda)$ estimated from equation 6 were generally higher than the instrument-derived estimates of $b(\lambda)$ at the mid-shelf and outer shelf stations (Figs. 3b and 3c). The differences between stations in values of $b(\lambda)$ estimated from equation 6 were reflected in the pattern of variation in chlorophyll concentrations (Table 2).

Table 2. Chlorophyll and pheopigment concentrations (mg m^{-3}).

Station No. and sample depth:	26 13.5 m	43 3.4 m	49 3 m
Chlorophyll	3.0	3.8	5.9
Pheopigment	n.d.	0.16	0.86

n.d.=not detected

4. DISCUSSION

Within the limits of our data, it can be concluded that measurement and model closure was achieved in the case of absorption at the mid-shelf and outer shelf locations. At the inner shelf station, estimates of $a(\lambda)$ made with the ac-9 were comparable to the *in vitro* spectrophotometric determinations, but values of $a(\lambda)$ estimated from reflectance (i.e., equation 4) were higher at some wavelengths. The rms deviation between the *in vitro* and reflectance-based estimates of $a(\lambda)$ at St. 26 was the largest observed (Table 1). Furthermore, the true difference was underestimated because our sample for the spectrophotometric analysis was taken from deeper in the water column where chlorophyll concentrations were slightly higher than surface waters (3.0 mg m^{-3} at 13.5 m as compared to 1.2 mg m^{-3} at 4 m). A comparison using the *in vitro* estimate of $a(\lambda)$ at 4 m (data not shown) yielded a larger rms deviation of 0.13. Values of $a(\lambda)$ estimated from equation 4 may have been overestimated if assumptions regarding the downwelling distribution function, $D_o (= 1/\bar{\mu}_d)$, were violated. Because of overcast conditions and rough seas, actual values of D_o may have exceeded the desired range of 1.0-1.2⁷. Nevertheless, environmental conditions were similar for the different stations, so this would not explain why the differences were so much greater for St. 26. The presence of relatively high dissolved organic matter and non-pigmented particulate matter (Fig. 2a) may have contributed to the greater deviation at this station.

Better agreement between the *in vitro* and reflectance-based (equation 4) estimates of $a(\lambda)$ was achieved at Stns. 43 and 49 (Figs. 2b and 2c). In contrast, the deviation between the *in vitro* and ac-9 estimates of $a(\lambda)$ was larger at the mid-shelf station, St. 49 (Table 1). A problem in the interpretation of these data was the degree of scatter in some of the instrument observations. In the case of the ac-9 measurements, this could be at least partially attributed to interference by bubbles in the flow cell. These tend to produce anomalously high absorption and beam attenuation values.

Our efforts to achieve closure among different methods for estimating scattering were less successful. For the inner shelf station, estimates of $b(\lambda)$ from equation 5 were higher than the ac-9 estimates at intermediate wavelengths. The opposite was true for the other two stations. One explanation for this pattern was that the backscattering probability (b_b/b) may have varied between stations as a function of the composition, size and concentration of particles. An explanation for the wavelength dependence observed in estimates of $b(\lambda)$ from equation 5 (Fig. 3) was unclear. A comparison of the *in situ* estimates of $b(\lambda)$ with those estimated from equation 6 revealed substantial differences. Equation 6 is an empirical relation developed for Case 1 waters. Implicit assumptions in this equation are that constituents contributing to scattering co-vary with chlorophyll concentrations. The results presented here apparently illustrate a case where this assumption was invalid.

This study has illustrated the utility of multiple measurement approaches in evaluation of methods for the determination of optical properties of coastal waters. An important prerequisite for the successful application of remote sensing as a tool for studying biogeochemical processes in coastal waters will be to achieve closure among ground truth measurement techniques and optical theory. We have made some progress towards that goal, and identified areas that need improvement.

5. ACKNOWLEDGEMENTS

We are grateful to the captain and crew of the R/V *Endeavour* for their assistance. We also thank C. D. Kennedy for data processing. R. A. Arnone provided helpful comments. Support for this research was provided by the Department of Energy (#DE-FG05-95ER62071 and #DE-FG02-92ER61443) and by the US Naval Research Laboratory.

6. REFERENCES

1. J. R. V. Zaneveld, J. C. Kitchen, and C. Moore, "Scattering correction of reflecting tube absorption meter," *Proc. Soc. Photo-Opt. Instrum. Engineer., Ocean Optics 12*, vol. 2258, pp. 44-55, 1994.
2. W. S. Pegau and J. R. V. Zaneveld, "Temperature dependence of the absorption coefficient of pure water in the visible portion of the spectrum," *Proc. Soc. Photo-Opt. Instrum. Engineer., Ocean Optics 12*, vol. 2258, pp. 597-604, 1994.
3. M. Kishino, N. Okami, M. Takahashi, and S. Ichimura, "Light utilization efficiency and quantum yield of phytoplankton in a thermally stratified sea," *Limnol. Oceanogr.*, vol. 31, pp. 557-566, 1986.
4. A. Bricaud and D. Stramski, "Spectral absorption coefficients of living phytoplankton and nonalgal biogenous matter: a comparison between the Peru upwelling area and the Sargasso Sea," *Limnol. Oceanogr.*, vol. 35, pp. 562-582, 1990.
5. B. Arbones, F. G. Figueiras, and M. Zapata, "Determination of phytoplankton absorption coefficient in natural seawater samples: evidence of a unique equation to correct the pathlength amplification on glass-fiber filters," *Mar. Ecol. Prog. Ser.*, vol. 137, pp. 293-304, 1996.
6. O. Holm-Hansen, C. J. Lorenzen, R. W. Holmes, and J. D. H. Strickland, "Fluorometric determination of chlorophyll," *J. Cons. Perm. Int. Exp. Mer*, vol. 30, pp. 3-15, 1965.
7. H. R. Gordon, O. B. Brown, R. H. Evans, J. W. Brown, R. C. Smith, K. S. Baker, and D. K. Clark, "A semianalytical radiance model of ocean color," *J. Geophys. Res.*, vol. 93, pp. 10,909-10,924, 1988.
8. H. R. Gordon and A. Y. Morel, Eds., *Remote assessment of ocean color for interpretation of satellite visible imagery*. New York: Springer-Verlag, 1983.

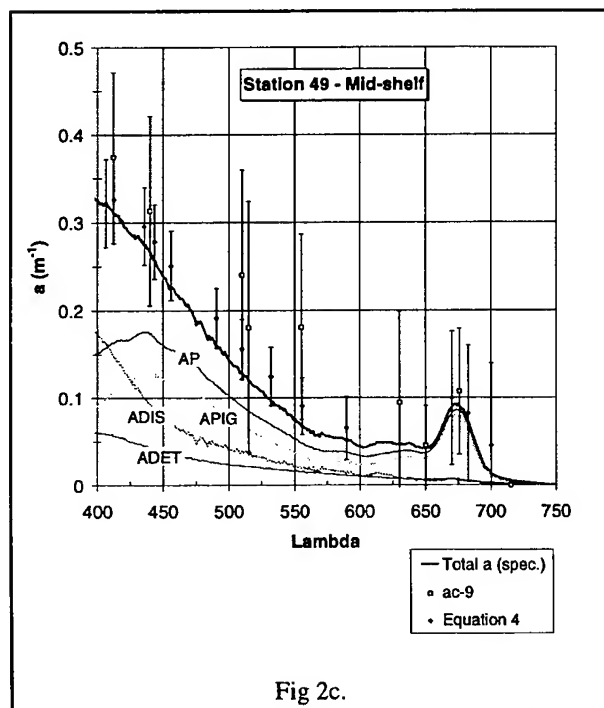
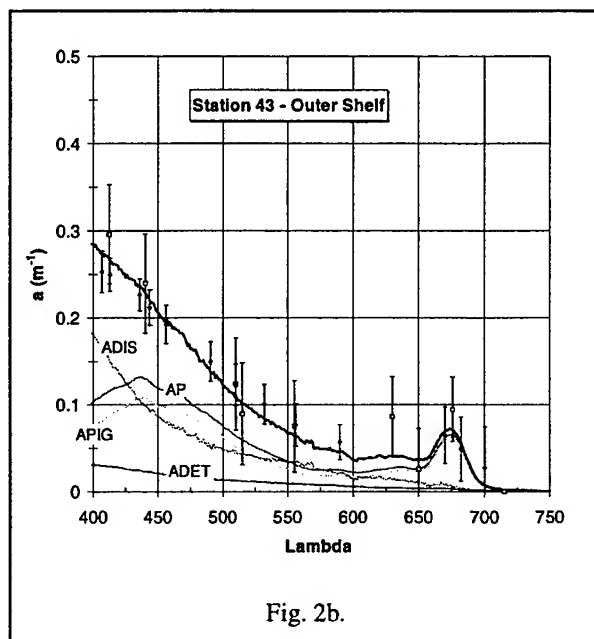
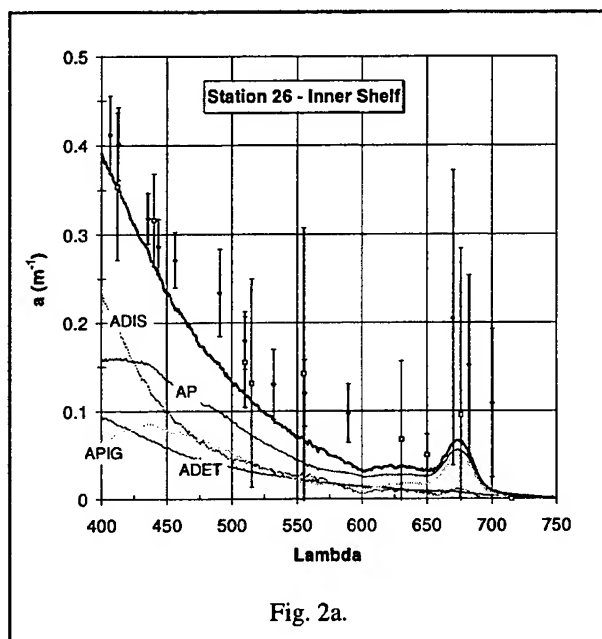


Figure 2. Total and constituent absorption coefficients estimated from spectrophotometric analysis of discrete samples, ac-9 and reflectance (equation 4) at Stations 26, 43 and 49. Sample depths for spectrophotometric analyses are given in Table 2. Measurements from the ac-9 were depth-averaged over the upper 5 m except at St. 26. Because of interference by bubbles at near-surface depths, ac-9 data from 12 - 16 m were used for St. 26. Error bars represent 1 standard deviation. Legend: AP-particulate absorption, ADET-non-pigmented particulate absorption, APIG-pigment absorption equal to (AP-ADET), ADIS-dissolved absorption.

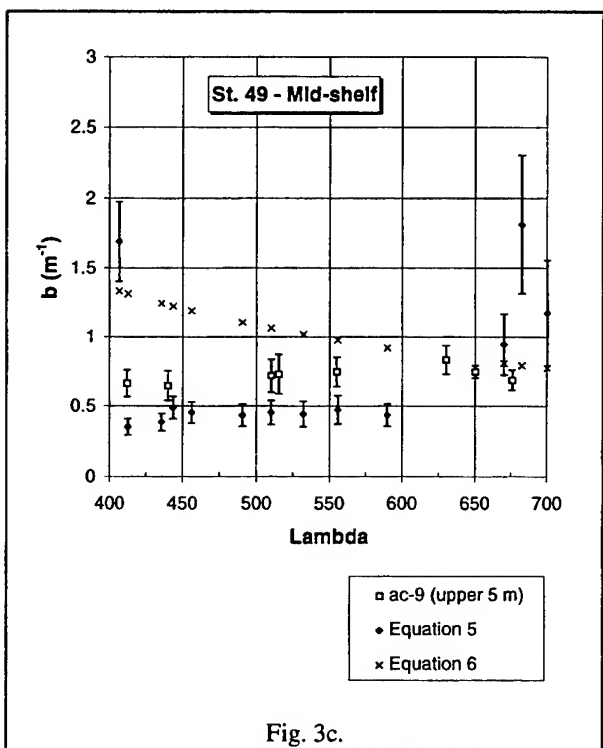
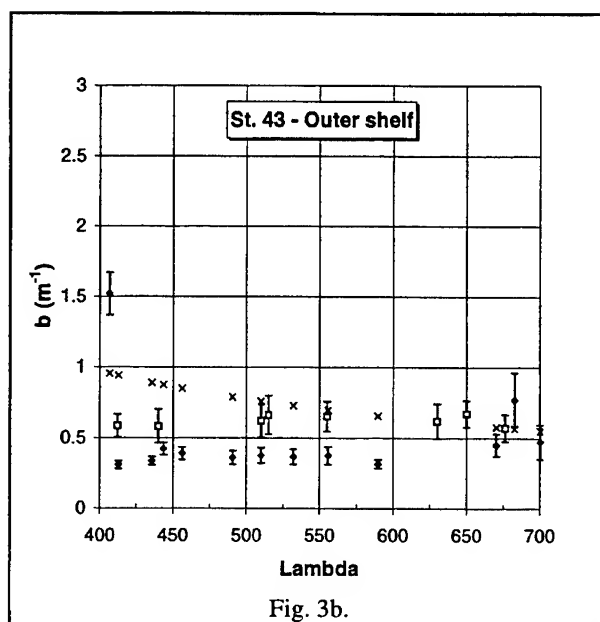
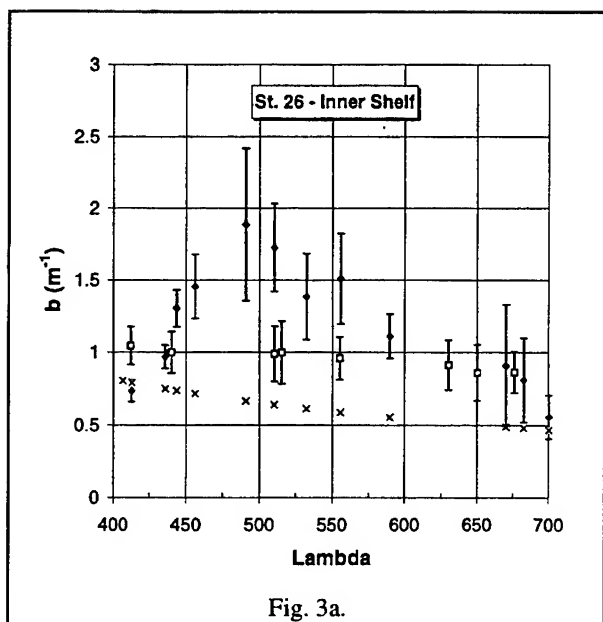


Figure 3. Total scattering coefficients determined by three approaches as described in Methods. Error bars represent 1 standard deviation. Pigment concentrations used with equation 6 are given in Table 2.

Kedarnath Mahapatra*, Satsuki Matsumura**, So Kawaguchi** and Yasuhiro Senga*

*School of Marine Science and Technology, Tokai University, 3-20-1 Orido, Shimizu, Shizuoka, 424 Japan

**National Research Institute of Far Seas Fisheries, 7-1-5 Orido, Shimizu, Shizuoka, 424 Japan

ABSTRACT

Optical and Phytoplankton pigment data collected from around 80 stations in the south-west Atlantic sector of Antarctic ocean between the Drake Passage and Antarctic Peninsula during three Antarctic Expeditions of Japan Fisheries Agency in Austral summer were analyzed for bio-optical characterization. Three optical water types were identified based on the spatial variability of phytoplankton pigment in the euphotic zone and corresponding profile of physical parameters along with total beam attenuation coefficient, c_t (m^{-1}) and diffuse attenuation coefficient, K_d (m^{-1}). The derived pigment specific particulate beam attenuation coefficient (c^*) and diffuse attenuation coefficients (K^*) were effectively used to identify optical stations under dominant influence of non-chlorophyll substances. The pigment specific coefficients were compared with the coefficients reported from typical case I waters (mostly temperate) and polar waters as well. Significant variations from temperate model and agreement with polar region model are discussed. Chlorophyll remote sensing model was examined with two sets of reflectance, $R(\lambda)$ and sub-surface upwelling radiance, $L_u(\lambda)$ ratios (441/565 and 520/565). The typical case I water remote sensing algorithm and the algorithm derived from present analysis were implemented on the CZCS image, and satellite derived chlorophyll values were compared with *in situ* estimates available in the same area from the Polish BIOMASS - FIBEX expedition. The results point to the need of more critical study on the bio-optical aspects before implementation of local algorithms for this region on ocean color image.

Keywords: Antarctic ocean, ocean color, bio-optical relationships, regional variability, pigment algorithms, remote sensing, CZCS

1. INTRODUCTION

The unique photo-biological condition in Antarctic ocean has prompted satellite oceanographers in the recent years to investigate bio-optical properties of these waters.¹⁻² The results from these studies points at the need of considering Antarctic ocean waters separately from the typical case I water of the world ocean for development of bio-optical model. The variation in pigment specific absorption and pigment 'package effect' due to low light adaptability of Antarctic phytoplankton have been hypothesized as the most important attributable factors for such regional variation. Mitchell and Holm-Hansen¹ have pointed out that the underwater bio-optical algorithm used for processing of global CZCS data³⁻⁴ for estimating phytoplankton pigment concentration underestimates the Antarctic pigment concentration by approximately factor of 3. However, the validity of this algorithm for the entire Southern ocean is yet to be confirmed as local variability of biological and other water constituents can significantly change bio-optical characteristics.

Under the present study we present results from the bio-optical data analysis of over 80 stations covered during the fifth, the sixth and the seventh Antarctic Expeditions of Japan Fisheries Agency undertaken during Austral summer of 1987-88, 1990-91 and 1994-95 respectively. We characterize the study area into different bio-optical zones based on apparent and inherent optical properties such as diffuse attenuation coefficient, $K_d(\lambda)$ and beam attenuation coefficient C_t and their relationship with the pigment concentrations. We also present the bio-optical regression model using reflectance $R(\lambda)$ and sub-surface upwelling radiance $L_u(\lambda)$ at wavelengths closer to CZCS channels. We have implemented the bio-optical algorithm developed from the present dataset on one CZCS image covering the study area and compared the pigment estimates with the estimates derived from the global processing algorithms of Gordon *et al.*³ and the Southern ocean algorithm proposed by Mitchell and Holm-Hansen¹ to find out the discrepancy in CZCS estimates of pigment concentration using different models. Finally these estimates were validated using the ship-board data as available from Polish BIOMASS-FIBEX program.

2. MATERIALS AND METHODS

This study is based on three sets of bio-optical data collected during 1987-88, 1990-91 and 1994-95 cruises. The study area covered during 1987-88 spreads over a larger area starting from Antarctic Peninsula in south to Falkland Island in north (Fig. 1a). A small part of this area as shown in the Fig. 1a was covered during 1990-91 and 1994-95 including the Antarctic Peninsula region and southern part of the Drake Passage (Fig. 1b). The bio-optical data were

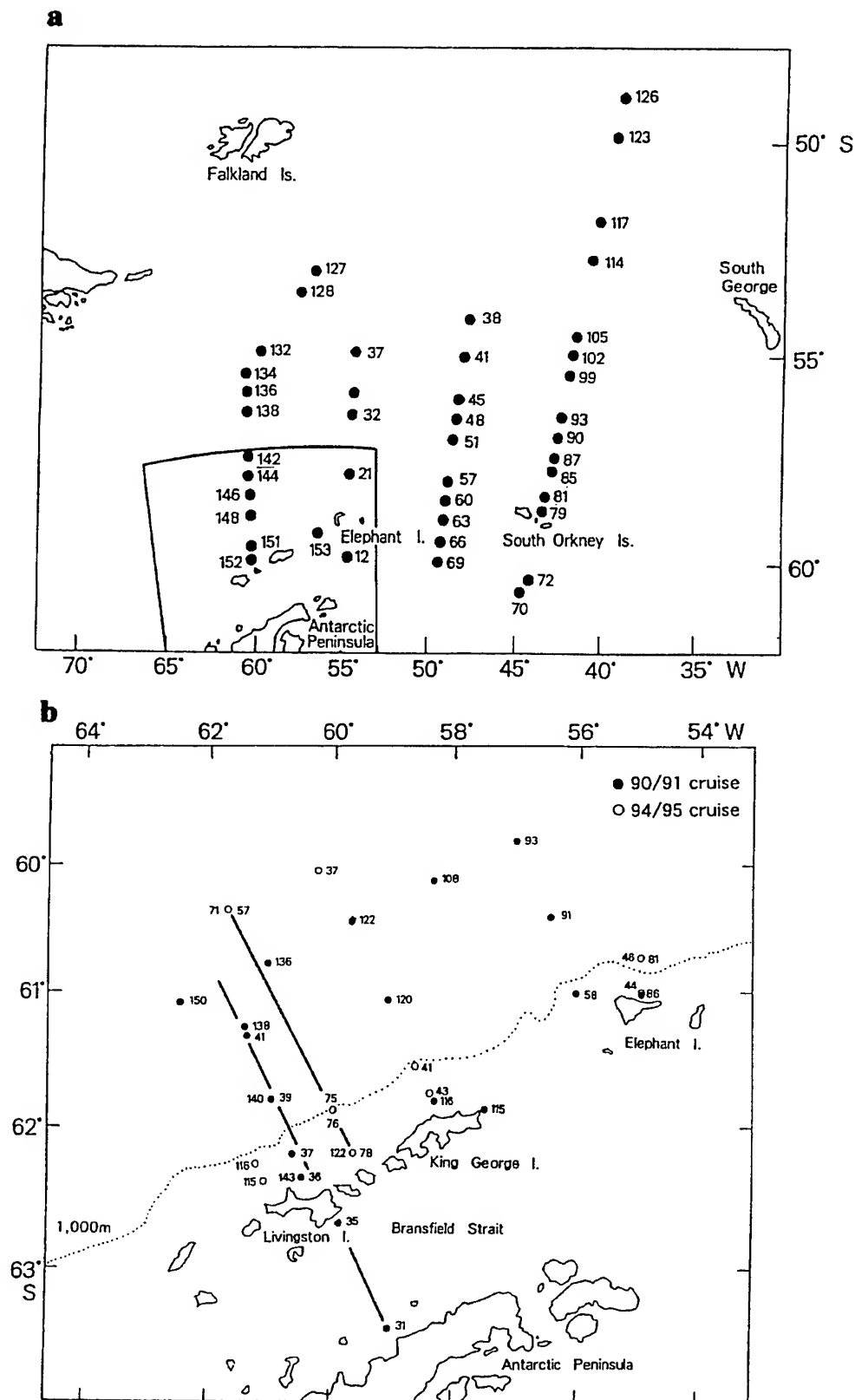


Fig. 1. Map of the south-west Atlantic sector of the Antarctic ocean covered during 1987-88, 1990-91 and 1994-95 showing the stations covered for bio-optical data collection. Fig. 1a shows the region covered during 1987-88 cruise and Fig. 1b show the bio-optical stations of 1990-91 and 1994-95 cruise in Antarctic Peninsular water. Transacts are indicated with line in Fig. 1b.

collected from 4 transects during 1987-88, out of which 2 transects passes through the Antarctic Peninsular waters. Bio-optical observations were made along the transects off the Livingston island and off the Elephant island during 1990-91 and 1994-95. The type of data collected during three investigations and instrumentation used for measurements are presented in the Table 1.

All bio-optical and pertinent physical oceanographic data were sorted by depth from surface to 100m under present investigation. The underwater $E_d(\lambda)$, $E_u(\lambda)$ and $L_u(\lambda)$ were appropriately corrected by relating the variable incident sunlight measured above the sea surface. Since the optical data of the sea surface and immediately below the surface were subjected to erratic profiling, the data for this upper layer of the water column have been extrapolated using linear regression of $E_d(\lambda)$, $E_u(\lambda)$ and $L_u(\lambda)$ as a function of depth for immediately below the disturbed column of water. The stations with observations affected by ship shadow, sensor tilt and lack of sufficient illumination for irradiance and radiance measurements were removed from the optical dataset.

Table 1 Instrumentation

Parameters	1987-88	Year 1990-91	1994-95
<u>Beam Attenuation C_d (600nm)</u>			
Instrument type	Transmissometer (Sea Tech)	Transmissometer (Sea Tech)	Transmissometer (Sea Tech)
Path length(cm)	25	10	25
<u>Downwelling and Upwelling Irradiance [$E_d(\lambda)$ & $E_u(\lambda)$]</u>			
Instrument	MER-1010	MER-1032	MER-1032
Number of channels	12 (E_d) 12 (E_u)	12 (E_d) 7 (E_u)	12 (E_d) 7 (E_u)
<u>Upwelling Radiance [$L_u(\lambda)$]</u>			
Number of channels	-	7 (L_u)	7 (L_u)
<u>Chlorophyll a & Phaeopigment concentration</u>	spectrofluorometer*	spectrofluorometer*	spectrofluorometer*
*spectrofluorometer:	SHIMADZU RF5100		
cuvette length :	1 cm		
sampling volume:	300~1000 ml		
pigment extraction:	85-90% Acetone		
excitation wavelength:	436nm		
emission wavelength:	659.8nm-670nm		
calibration:	Spirulina Chl. a (Wako Chemicals Co)		

3. RESULTS AND DISCUSSION

The bio-optical data derived from three different cruises were considered as a single dataset for the purpose of present analysis since all the three investigations were conducted during the Austral summer. Based on the physical and bio-optical characteristics, the study area was divided into three zones viz. open ocean, southern Drake passage and Antarctic Peninsula area. While the southern Drake passage and Antarctic peninsula area were covered during all three cruises, the stations in the open ocean were covered only during the 1987-88 investigation. Since one transect off Livingston island was covered during all the three cruises (Fig.1), the physical and bio-optical variability along this transect was examined and the vertical profile of the physical and bio-optical parameters were found to have maintained almost the same trend during three investigations. It was very well noticed that the mixed layer was

shallow towards the Antarctic peninsula and deeper towards the southern Drake passage. The vertical distribution of bio-optical characteristics closely followed the other physical parameters.

The total beam attenuation coefficient C_t (m^{-1}) was calculated using the following formula:

$$C_t (m^{-1}) = -\ln(1-C)/r \quad (1)$$

Where C is measure of proportion of the incident beam(660nm) that is lost by absorption and scattering in a path length, r . The attenuation coefficient of pure water (0.364)¹ was used to estimate the particulate beam attenuation coefficients ($C_t - C_w$) assuming that there is no contribution by the dissolved constituents. The pigment specific particulate beam attenuation coefficient C^* is calculated as the ratio of ($C_t - C_w$) / (Chl a +Phaeo). This parameter is considered to be an important index of water type. If value of C^* becomes >0.5, the water type is considered as case II, however, <0.5 indicates case I water.¹

Under the present study statistical analysis was carried out between $C_t - C_w$ and Chl a + Phaeo (Fig. 2) and C^* and diffuse attenuation coefficient, K_d (488 nm) (Fig. 3) for three zones to find out the relationships between these parameters. The covariance of phytoplankton pigments with beam attenuation was determined by applying linear regression analysis. The relationship for open ocean stations was found to be more significant than that of the southern Drake passage and Antarctic Peninsula stations. A cluster of stations as found in the Antarctic peninsula region shows $C_t - C_w$ as independent of phytoplankton pigment concentrations(Fig. 2c). The similar phenomena was noticed in Bellingshausen sea, adjacent to the present study area by Sagan et al.² This can be attributed to influence of the non-pigment constituents in this region. It was found out that out of 29 stations under this zone 12 stations have C^* values > 0.4. Fig. 3 shows the relationship between K_d (488 nm) and C^* at three different zones. There seems to be no significant relationship between these two properties unlike the inverse relationship reported by Mitchell and Holm-Hansen¹ for the open ocean stations of southern Drake passage area during the same season. Moreover during their investigation they have noticed C^* values in the Antarctic region is usually lower than 0.4. However during the present study the C^* values were found to be quite higher at many stations in all the three zones including the Antarctic peninsular waters. Anticipating the possible influence of such discrepancy between our results and that of Mitchell and Holm-Hansen¹ on bio-optical algorithms, an attempt was made to compare the regional algorithms for different zones in the Antarctic ocean and find out the extent of variation in the coefficients. Reflectance ratios such as $R(441)/R(565)$ and $R(520)/R(565)$ were considered for development of pigment algorithms for two different areas such as Antarctic Peninsular region and open ocean waters. Significant variation was noticed between these local algorithms(Table 2). Algorithms were also developed based on upwelling radiance (L_u) collected during 1994-95 investigation to compare with results of L_u (λ)-based algorithms of Mitchell and Holm-Hansen¹. The results are shown in the Table 3. Finally the algorithms derived from the present study and those of Gordon et al.³ and Mitchell and Holm-Hansen¹ were implemented on the CZCS image of February 27, 1981 to derive the pigment estimates for assessing performance of different algorithms. The CZCS estimates show that although the algorithms of Mitchell and Holm-Hansen¹ as well as the one from the present study produce higher concentration of phytoplankton pigment compared to Gordon et al.³ in low pigment concentration area, it produces quite lower estimates in bloom area. The ship estimate of Chlorophyll a pigment concentration for the corresponding CZCS image was available from only one station (Station 60) from the Polish BIOMASS-FIBEX database⁵. The CZCS pigment estimate derived from using the algorithm of Gordon et al.³ (0.20 mg/m³) was found to closely agree with the *in situ* estimate (0.14 mg/m³), however our algorithm and that of Mitchell and Holm-Hansen¹ produced distinctly overestimates, 0.68mg/m³ and 0.45 mg/m³ respectively.

4. CONCLUSION

The results from the present study underlines the need for more planned bio-optical investigations in the Antarctic waters to critically understand the phenomena for more accurate estimation of phytoplankton pigment concentrations in these waters. This is felt more relevant in the background of recent launching of ADEOS/OCTS and forthcoming SeaWiFS.

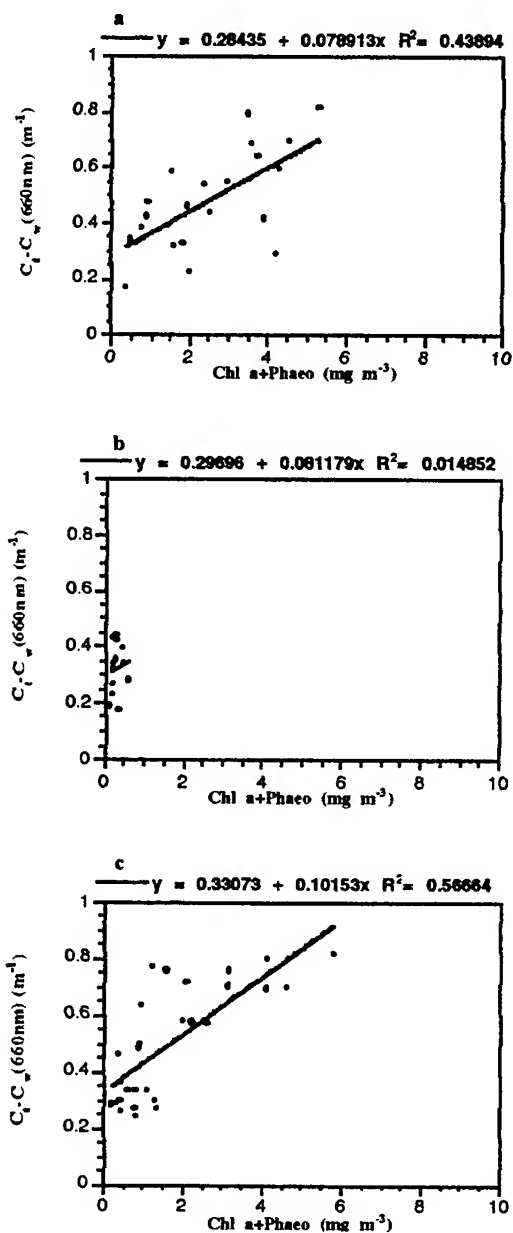


Fig. 2 Relationship between the beam attenuation coefficient, $C_t - C_w$ (660nm) and Phytoplankton pigment. (a) Open ocean region; (b) southern Drake Passage; (c) Antarctic Peninsular waters.

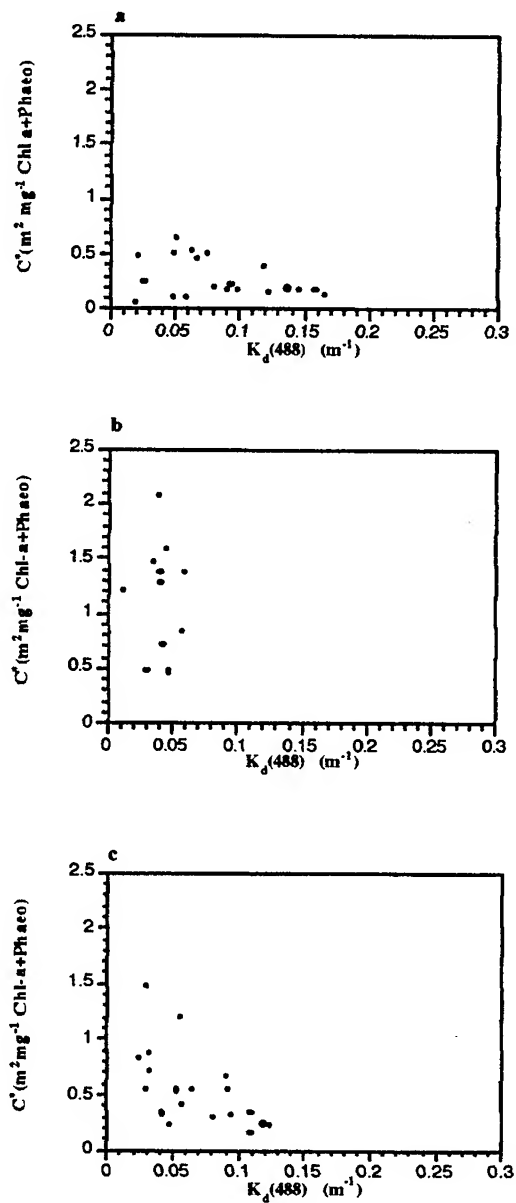


Fig. 3 Relationship between $K_d(488\ nm)$ (m^{-1}) and Pigment specific particulate beam attenuation coefficient, C^* . (a) Open ocean region; (b) southern Drake passage; (c) Antarctic Peninsular waters.

Table 2. Results of the regression analyses between ratios of reflectance (R) and phytoplankton pigment concentration in open ocean and Antarctic Peninsula waters

Ratios	N	a (intercept)	Error	b (slope)	Error	r^2
<u>R(441/565)</u>						
Open ocean	19	0.46	0.07	-1.20	0.26	0.55
Antarctic Peninsula	32	0.55	0.07	-1.62	0.15	0.80
<u>R(520/565)</u>						
Open ocean	19	0.44	0.13	-1.05	0.64	0.13
Antarctic Peninsula	32	1.03	0.17	-4.02	0.58	0.62

Table 3. Bio-optical algorithms (L_u) for Antarctic Peninsula waters derived from present study along with algorithms proposed by Mitchell and Holm-Hansen¹ for Southern ocean and Gordon *et al.*³ for global ocean case I waters. CZCS image processing was carried out using these algorithms

Ratios	N	a (intercept)	Error	b (slope)	Error	r^2
<u>$L_u(441/565)$</u>						
Present study	12	0.66	0.05	-1.54	0.11	0.95
Mitchell and Holm-Hansen ^{1*}	122	0.53(+/-0.32)		-1.63(+/-0.12)		0.83
Gordon <i>et al.</i> ^{3*}	33	0.14		-1.55		0.97
<u>$L_u(520/565)$</u>						
Present study	12	1.11	0.16	-4.33	0.62	0.83
Mitchell and Holm-Hansen ^{1*}	122	0.48(+/-0.38)		-3.32(+/-0.38)		0.61
Gordon <i>et al.</i> ^{3*}	33	0.63		-4.72		0.94

* Algorithms were developed based on upwelling radiance (L_u) values at 560 nm under these investigations.

5. ACKNOWLEDGMENT

The authors wish to thank the Captain and crew of *Kaiyo Maru* for their active co-operation in ship-board measurements during three cruises. They also thank Ogishima for MER-1032 data collection during 1994-95 cruise. They gratefully acknowledge help from G. Feldman and J. L. Green of NASA/GSFC in making available the CZCS data. They are also thankful to M. Toratani of School of High Technology for Human Welfare, Tokai University for his kind support during CZCS image processing. The authors are also grateful to Prof. Y. Sugimori of Tokai University for his helpful advice during the course of work. This work was carried out during the tenure of Science and Technology Agency (STA) Fellowship awarded to K. M. by Japan International Science and Technology Exchange Center (JISTEC). The author expresses his profound gratitude to the JISTEC for financial support and hospitality.

6. REFERENCES

1. B. G. Mitchell and O. Holm-Hansen, "Bio-optical properties of Antarctic Peninsula waters: differentiation from temperate ocean models," *Deep-Sea Research*, 38(8/9), 1009-1028 (1991).
2. S. Sagan, A. R. Weeks, I. S. Robinson, G. F. Moore and J. Aiken, "The relationship between beam attenuation and chlorophyll concentration and reflectance in Antarctic waters," *Deep-Sea Research II*, 42(4-5), 983-996 (1995).
3. H. R. Gordon, D. K. Clark, J. W. Brown, O. B. Brown, R. H. Evans and W. W. Brown, "Phytoplankton pigment concentrations in the Middle Atlantic Bight: comparison ship determinations and CZCS estimates," *Applied Optics*, 22, 20-35 (1983).
4. H. R. Gordon, O. B. Brown, R. H. Evans, J. W. Brown, R. C. Smith, K. S. Baker and D. K. Clark, "A semianalytical radiance model of ocean color," *Journal of Geophysical Research*, 93, 10,909-10,924 (1988).
5. M. Lipski, "The distribution of chlorophyll a in relation to the water masses in the southern Drake passage and the Bransfield strait (BIOMASS-FIBEX, February-March 1981)," *Pol. Polar Res.*, 3(3-4), 143-152 (1982).

Remote sensing reflectance: preliminary comparisons between in-water and above water measurements, and estimates modelled from measured inherent optical properties.

James L. Mueller

San Diego State University, Center for Hydro-Optics and Remote Sensing
6505 Alvarado Rd, Ste 206, San Diego, CA 92120

J. Ronald V. Zaneveld, Scott Pegau

Oregon State University, College of Oceanography
Corvallis, OR 97331

Eduardo Valdez, Helmut Maske, Saul Alvarez-Borrego & Ruben Lara-Lara
CICESE (Apdo Postal 2372)
Ensenada, BC, Mexico

ABSTRACT

Remote sensing reflectances measured underwater and above-water in the Gulf of California are compared to evaluate the equivalence between methods. Each form of reflectance is also compared to concurrently measured ratios of scattering to absorption, and the mean backscattering fraction is estimated. Above-water and in-water remote sensing reflectance estimates differ by more than 20%, with absolute RMS difference ranging from 0.001 to 0.005. Standard deviations of estimated backscattering fractions are between 15% and 20% of the mean at each wavelength.

Keywords: remote sensing reflectance, water-leaving radiance, ocean bidirectional reflectance

1. INTRODUCTION

Remote sensing reflectance $R_{Lw}(\lambda)$ is defined as the ratio of water-leaving radiance to incident surface irradiance $L_w(\lambda)/E_s(\lambda)$. Two methods of determining $R_{Lw}(\lambda)$ are currently in use¹. Traditionally, upwelled radiance just beneath the sea surface $L_u(\lambda, 0^-)$ is determined from an underwater profile of $L_u(\lambda, z)$ and is propagated through the sea surface by the Fresnel transmittance to determine nadir water-leaving radiance. An alternative approach is to measure surface radiance at a nadir-angle θ and zenith angle relative to the sun ϕ , together with incident sky radiance at ϕ and zenith angle θ . In the latter case, it is necessary to account for the ocean bidirectional reflectance distribution function, and its dependence on solar zenith and azimuth angles, θ_s and ϕ_s , to adjust the measured water-leaving radiance at angle θ to correspond to nadir radiance². In either case, reflectance is determined by dividing the nadir water-leaving radiance by incident spectral irradiance measured by a cosine-response radiometer. The alternative above-water method of approximating incident spectral irradiance by measuring radiance reflected from a grey plaque³ is not considered here.

Radiance measurements below and above the water surface are subject to different sources of uncertainty. To derive $L_u(\lambda, 0^-, 0^-)$ from an underwater profile, it is necessary to extrapolate the measurements from a few m below the surface to the surface, and in strongly absorbing waters instrument self-shading becomes a significant source of uncertainty as well. Above-water measurements of surface radiance $L_s(\lambda, \theta, \theta_s, \phi)$ must be corrected both for reflected sky radiance, and for the ocean BRDF, to derive $L_w(\lambda, 0^+)$; surface wave introduce serious sky and cloud glint fluctuations into these corrections under all but ideal clear-sky conditions. The uncertainty in determining $L_w(\lambda, 0^+)$ from underwater profiles is thought to be approximately 5% for Case 1 waters and low variability in $E_s(\lambda)$. The uncertainty associated with the above water measurement has not been well quantified. This paper is a preliminary attempt to estimate the magnitude of that uncertainty through direct comparisons between above-water and in-water measurements.

We also examine the relationship between each form of reflectance and the ratio of scattering to absorption coefficients, $b(\lambda)/a(\lambda)$, as a preliminary test of consistency in these data with reflectance models based on inherent optical properties.

2. DATA AND METHODS

In December 1995, we measured inherent and apparent optical properties in the central Gulf of California aboard the Mexican research vessel *El Puma*. Over a period of 8 days, we acquired data at 12 stations over the continental shelf near Guaymas, Mexico, and additional stations over the sill separating the northern and central basins of the Gulf of California.

Vertical profiles of spectral irradiance and radiance $E_d(\lambda, z)$, $L_u(\lambda, z)$, and surface irradiance $E_s(\lambda)$, were measured using a PRR-600 radiometer system manufactured by Biospherical Instruments, Inc. $L_u(\lambda, 0^-)$ was derived through analysis of the upwelled radiance profile and combined with deck cell irradiance to form the in-water estimate of nadir remote sensing reflectance as

$$R_{Lw}(\lambda, 0^\circ, \theta_o) = L_u(\lambda, 0^-) * [1 - \rho(0^\circ)] / [m^2 * E_s(\lambda)] \quad (1)$$

where $\rho(0^\circ)$ is Fresnel reflectance of the sea surface for normal incident and m is the refractive index of water relative to air (approximately 1.34).

Surface radiance $L_s(\lambda, \theta, \phi)$ and sky radiance $L_{sky}(\lambda, \theta, \phi)$ were measured with a prototype radiometer assembled at SDSU CHORS. A 35mm camera, with a 5mm $f/1.4$ lens, was modified by installing an aperture plate in the focal plane to limit the field of view to 5° (full width). A Light-Shaping Diffuser (40° FWHM) is placed over the aperture to disperse the flux uniformly to 7 filter/detectors (a Satlantic OCR-100 detector array). The camera was mounted on a handle with a horizon-sighting telescope to fix the viewing nadir/zenith angle at $\theta = 30^\circ$ in all measurements. Azimuth relative to the sun was varied between $\phi = 90^\circ$ and $\phi = 135^\circ$ to allow evaluation of azimuth sensitivity in the measurements. The surface and sky radiances were then combined to calculate remote sensing reflectance (off nadir) as

$$R_{Lw}(\lambda, \theta, \theta_o, \phi) = [L_s(\lambda, \theta, \phi) - \rho(\theta) * L_{sky}(\lambda, \theta, \phi)] / E_s(\lambda), \quad (2)$$

where $\rho(\theta)$ is the average (unpolarized) Fresnel reflectance for incidence angle θ (30° in these data). A polarizing filter was also placed over the radiometer lens to measure the vertically and horizontally polarized components of $L_s(\lambda, \theta, \phi)$ and $L_{sky}(\lambda, \theta, \phi)$. These data were then combined to form a polarized reflected skylight correction to remote sensing reflectance as

$$R_{Lw}(\lambda, \theta, \theta_o, \phi) = [L_s(\lambda) - \{\rho_v(\theta) * L_{sky,v}(\lambda) + \rho_h(\theta) * L_{sky,h}(\lambda)\}] / E_s(\lambda), \quad (3)$$

where subscripts v and h refer to vertical and horizontal polarizations, respectively.

The variation of the incident radiance distribution and ocean BRDF with solar elevation and relative zenith angle must be taken into account to compare reflectances calculated from above-water data using (2) or (3) with nadir reflectance calculated from in-water data with (1). One approach, for Case 1 waters with chlorophyll concentrations $< 3 \text{ mg m}^{-3}$, is the scaling

$$R_{Lw}(\lambda, 0^\circ, \theta_o) = (f/Q_n)(f/Q)^{-1} R_{Lw}(\lambda, \theta, \theta_o, \phi) \quad (4)$$

where (f/Q_n) and (f/Q) are the correction factors for nadir radiance and radiance at θ , respectively, as introduced by Morel and Gentili². These factors vary as a function of λ , θ , θ_o , ϕ , and b_b/a (where b_b is the backscattering coefficient).

We also measured spectral absorption and beam attenuation coefficients $a(\lambda)$ and $c(\lambda)$ at each station, and then calculate the scattering coefficient as $b(\lambda) = c(\lambda) - a(\lambda)$. These data were acquired using an AC-9 manufactured by WetLabs Inc. Defining the backscattering fraction as $F_B(\lambda) = b_b(\lambda) / b(\lambda)$, we may write reflectance as a function of inherent optical properties as²

$$R_{Lw}(\lambda, 0^\circ, \theta_o) = (f/Q_n) [F_B(\lambda) * b(\lambda) / a(\lambda)]. \quad (5)$$

By combining (5) with (1), and with (4) [together with (2) and (3)] we may estimate a value of the backscattering fraction for each station and form of reflectance estimate as

$$F_B(\lambda) = R_{Lw}(\lambda, 0^\circ, \theta_o) / [(f/Q_n) * b(\lambda) / a(\lambda)]. \quad (6)$$

3. RESULTS

Comparisons between in-water and above water reflectance (1) versus (4), combined with (2) for the unpolarized surface radiance corrections, are illustrated in Fig. 1 for 555 nm. The RMS differences between the above water and in-water reflectance determinations are approximately 25%. The differences are larger at 412 nm (not illustrated here). There is little difference between the polarized and unpolarized skylight reflectance corrections, as is illustrated in Fig. 2. Results for other wavelengths are similar, with increased scatter at short wavelengths.

The average backscattering fractions computed from AC-9 data with (6) in combination with the in-water and above water reflectance determinations are illustrated in Fig. 3. Relative uncertainties with respect to these means are between 15% and 20% for the in-water and $\phi = 90^\circ$ above water reflectances (assuming constant $F_B(1)$ in the region), and are approximately 30% for $\phi = 135^\circ$.

4. DISCUSSION AND CONCLUSIONS

These preliminary results suggest that it will be very difficult to reduce the uncertainty in above-water determinations of remote sensing reflectance to the 5% level, considering the present uncertainties of approximately 25%. We attribute the bulk of this uncertainty to variability in sky radiance reflections (due to surface waves) coupled with relatively bright patches of wispy clouds (even under relatively clear-sky conditions). The BRDF corrections used here certainly reduced the scatter in the data, but we need to pursue this aspect further, particularly since errors in this adjustment could certainly account for the biases observed in our present comparisons. Further analysis and research are needed to better quantify the sources and magnitudes of these uncertainties under general conditions. We have also not yet considered whether smaller uncertainties can be realized for reflectance ratios between different wavelengths, a question of critical importance for remote sensing algorithm development.

Finally, we are encouraged by the internal consistency in backscattering fractions estimated by combining the measured reflectances with absorption and scattering. In future work we hope to obtain direct measurements of backscattering as a basis for independently deriving reflectance from inherent optical properties. This capability would greatly advance our ability to apply satellite remote sensing reflectances to Case 2 waters, where *in situ* radiometry is especially difficult.

5. ACKNOWLEDGEMENTS

This research was supported by the National Aeronautics and Space Administration Biogeochemistry Program, the Office of Naval Research Environmental Optics program, and by CICESE institutional programs (including ship support).

6. REFERENCES

1. Mueller, J.L. and R.W. Austin, *Ocean Optics Protocols for SeaWiFS Validation, Revision 1*, NASA TM 104566, Vol. 25, S.B. Hooker, E.R. Firestone and J.G. Acker, [Eds.], NASA Goddard Space Flight Center, Greenbelt, MD, 1995.
2. Morel, A. and B. Gentili, "Diffuse reflectance of oceanic waters. III. implication of bidirectionality for the remote-sensing problem," *Appl. Opt.* **35**(24), 4850-4862 (1996).
3. Carder, K.L. and R.G. Steward, "A remote-sensing reflectance model of red-tide dinoflagellate off West Florida", *Limnol. Oceanogr.* **30**, 286-298, (1985).

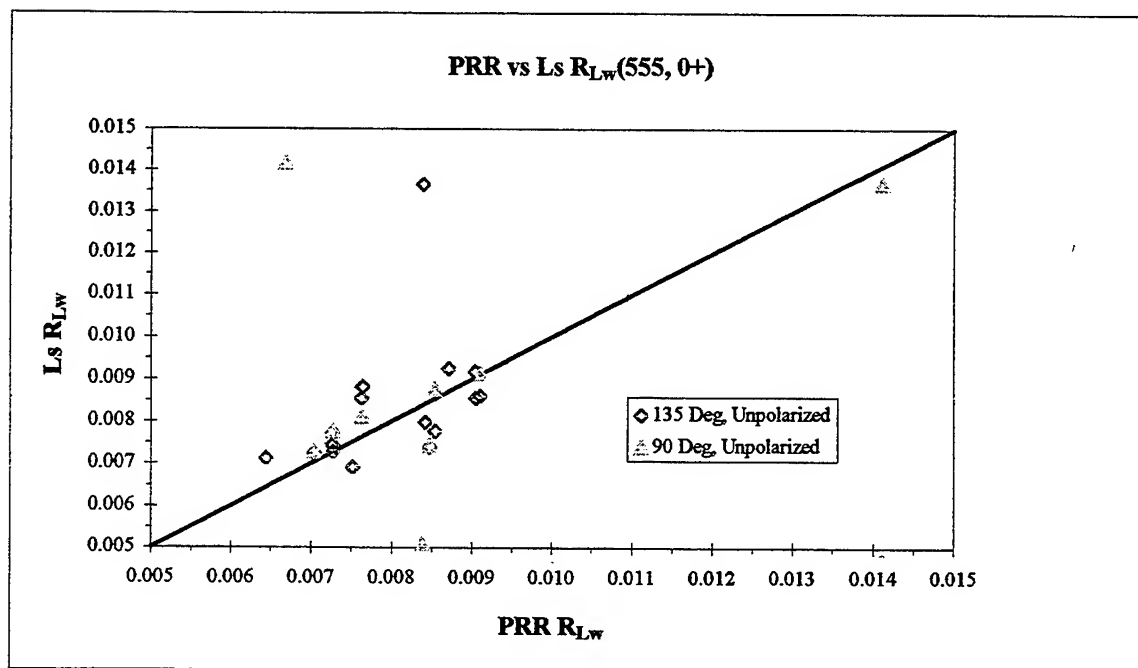


Figure 1. Remote sensing reflectances at 555 nm calculated from in-water radiances (PRR data) and above water radiance measurements $L_s(\lambda)$ at relative solar zenith angles of 90° and 135° and a nadir angle of 30°.

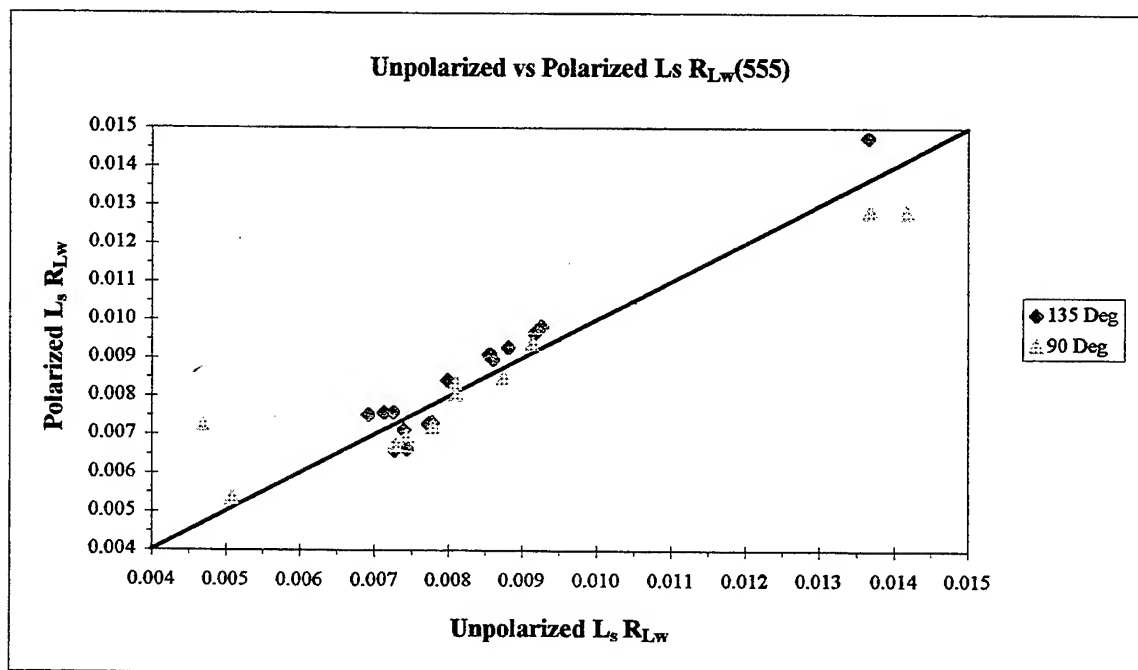


Figure 2. Above water reflectance determined using unpolarized and polarized surface reflectance and skylight measurements, compared with reflectances computed from unpolarized measurements using the average Fresnel reflectance.

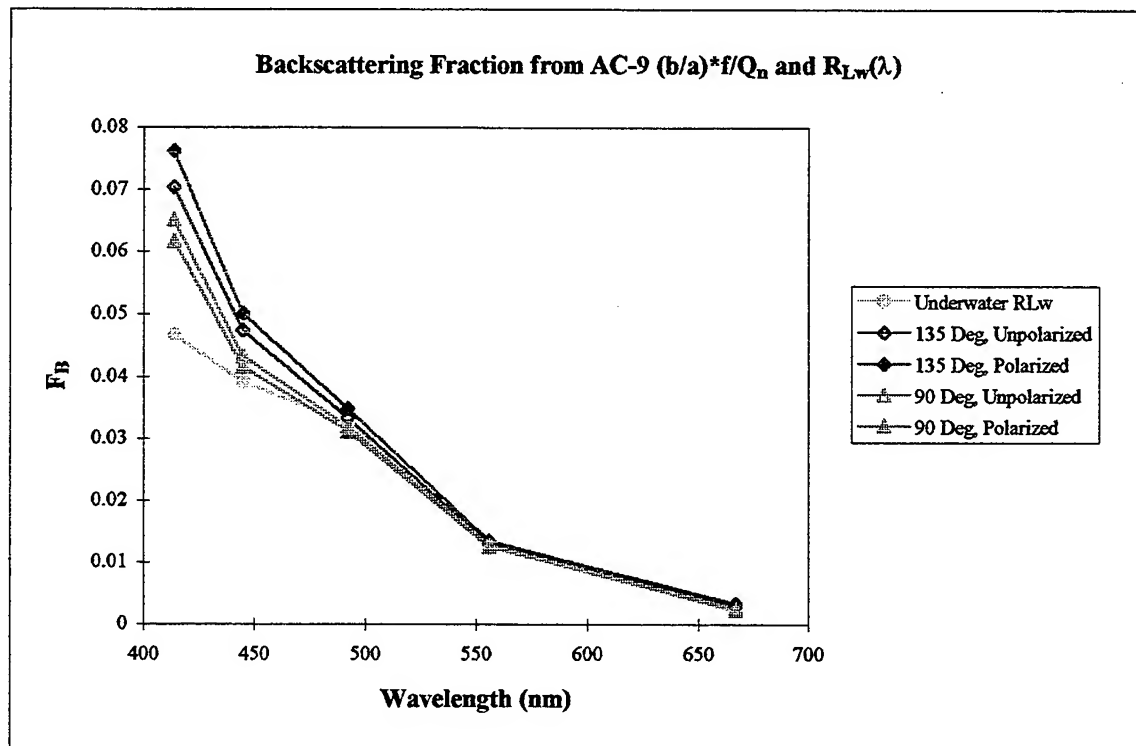


Figure 3. The backscattering fraction $b_b(\lambda) / b(\lambda)$ computed by combining the measured ratio $b(\lambda)/a(\lambda)$ with in-water and above water reflectance determinations.

The distribution of colored dissolved organic matter (CDOM) in the Equatorial Pacific

W. Scott Pegau

College of Oceanic and Atmospheric Sciences, Oregon State University, Corvallis, Oregon 97331

ABSTRACT

Optical properties of dissolved and particulate matter were measured in the surface waters of the Equatorial Pacific between 165°E and 150°W. In this area upwelling provided nutrient-rich water creating a mesotrophic environment. Below the surface mixed layer runs the Equatorial Undercurrent, which was marked by increases in salinity and absorption by CDOM. The magnitude of the absorption appears to be correlated with salinity even though there are no terrigenous inputs into this region. In the surface water the CDOM absorption is an important portion of the total absorption in the blue portion of the spectrum. Below the mixed layer the dissolved component absorption was the dominant non-water optical component.

Keywords: CDOM, yellow matter, absorption, equatorial pacific

1. INTRODUCTION

The absorption coefficient of colored dissolved organic matter (CDOM) can be the major optical property in the blue portion of the spectrum. CDOM has terrigenous and marine sources¹⁻⁷ that determine its distribution in the ocean. Mixing of river water with high CDOM content into the ocean leads to the absorption by CDOM being related to salinity in coastal environments (Figure 1). In the open ocean, decay products of phytoplankton are the major source of CDOM. In the Equatorial Pacific it is expected that terrigenous sources of CDOM are negligible and the CDOM distribution is determined by the primary productivity of the source water. For the Equatorial Undercurrent the source waters are hundreds of kilometers to the south-east of the area where we sampled⁸. The upwelling along the equator creates a circulation above the Equatorial Undercurrent^{9,10} that may add to the physical and optical structure of the water (Figure 2).

The relationships between the distribution of CDOM and salinity as well as particulate absorption are explored. The role of CDOM in determining the optical properties of the water column in this region are also investigated.

2. METHODS

During an April-May 1996 cruise along the Equatorial Pacific between 165°E and 150°W two WET Labs ac-9 (nine wavelength absorption and attenuation meter) were used to measure CDOM absorption coefficients and total absorption and attenuation coefficients. To determine the contribution of dissolved materials to the total absorption coefficient a 0.2 μm pore-size filter (Gelman Suporcap 100) was attached to the inlet of one ac-9. Determination of the particulate absorption coefficient was made by subtracting the dissolved measurement from the scattering-corrected, unfiltered ac-9 absorption measurement. Both instruments had been calibrated with optically pure water as a reference. To obtain total absorption and attenuation, pure water absorption and attenuation coefficients were added to the unfiltered ac-9 measurements. Physical properties were measured on the same cage using a SeaBird Electronics SBE-25 CTD. Data from the three instruments were then merged to provide a single data set with physical and optical properties.

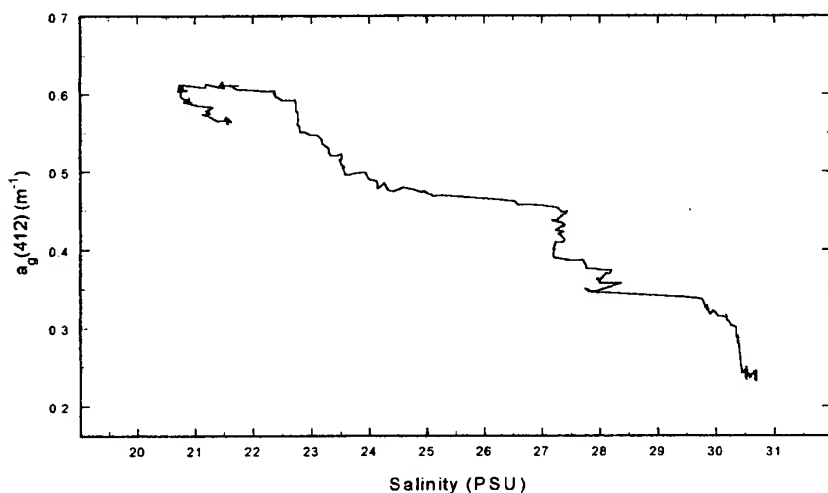


Figure 1. The CDOM absorption coefficient at 412 nm versus salinity. The measurements are from the Chesapeake Bay Plume and show the strong relationship between CDOM absorption and salinity. This relationship is caused by mixing of high-CDOM, low-salinity water from the bay with low-CDOM, high-salinity ocean water.

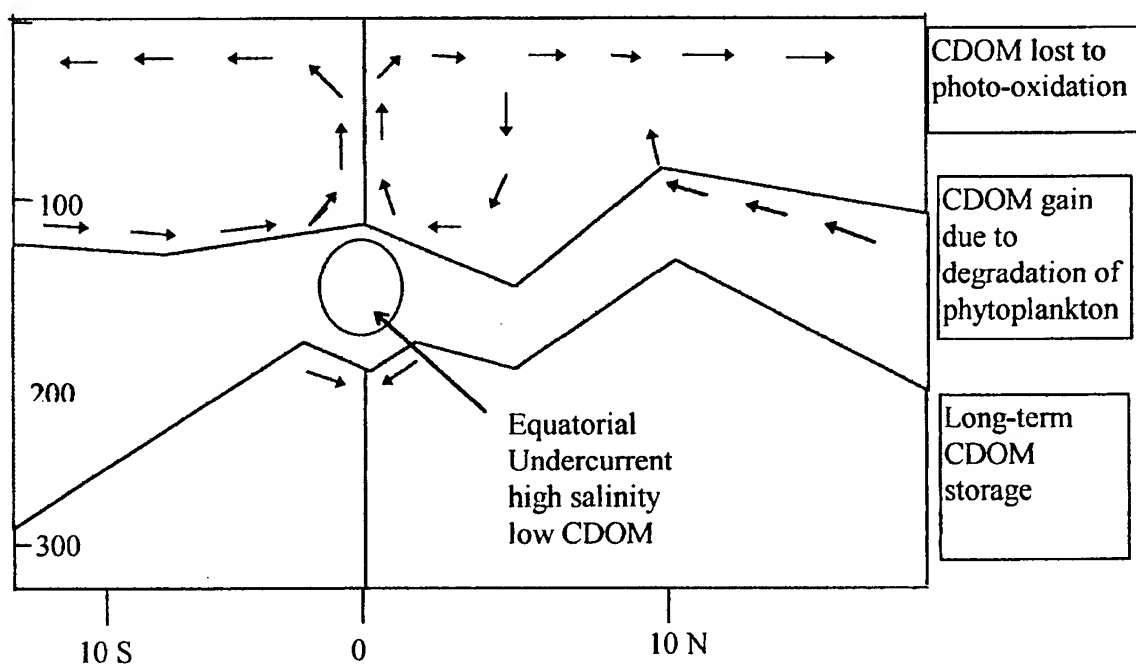


Figure 2. Expected current structure for the Equatorial Pacific¹⁰ and regions with expected sources and sinks of CDOM. The Equatorial Undercurrent would be expected to have low CDOM levels because its source waters are oligotrophic so there would be little source of dissolved materials.

3. RESULTS AND DISCUSSION

Profiles taken in the Equatorial Pacific suggest that there may be a relationship between the CDOM distribution and salinity of the water even though there are no nearby terrigenous sources of water (Figure 3). The Equatorial Undercurrent is denoted by the high-salinity, low-CDOM water that exists near the top of the pycnocline. The lower salinity water between 70 and 100 m may be a portion of the water circulation driven by the equatorial upwelling. The profile in Figure 3 shows a relatively low surface value of the dissolved component absorption coefficient (a_g) with an increase near the particle absorption maximum near 70 m. Near the surface the CDOM level is reduced by photo-oxidation. The largest increase in a_g being just below the particle maximum. The increase in a_g below the particle maximum is a common feature seen during the two cruises in this region in which we have participated and is related to production of CDOM from phytoplankton degradation.

Contour plots of the physical (temperature and salinity, Figure 4) and optical parameters (dissolved and particulate component absorption, Figure 5) show the complexity of the relationship between the various parameters. Figure 4 shows the shoaling of the thermocline and associated pycnocline towards the eastern portion of the transect. The high-salinity, low-CDOM waters were only observed intermittently along the transect. The high-salinity waters were located near the top of the thermocline when they were observed. Figure 5 shows that the higher values of the dissolved component absorption coefficient also shoaled towards the east. The particulate absorption coefficient did not show any strong zonal structure. From Figures 3-5 it appears that the dissolved absorption is greatest below the pycnocline. The shoaling of the pycnocline towards the east increases the absorption by CDOM in the waters below 100 m. For individual locations the distribution of CDOM appears to be modified by primary production, and currents as marked by the salinity structure.

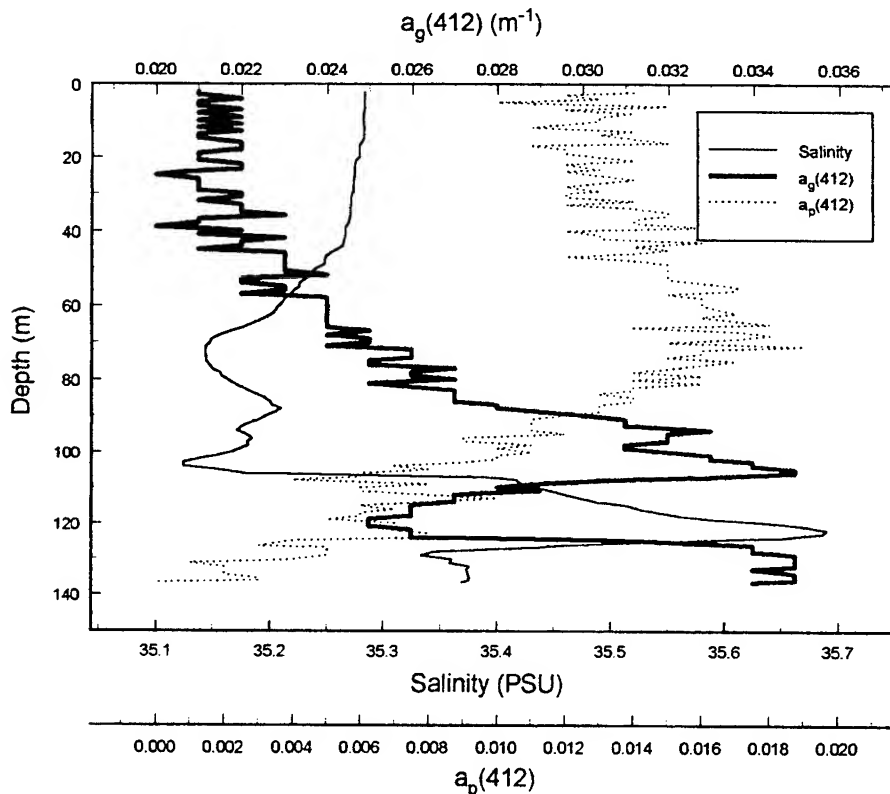


Figure 3. Vertical profiles of salinity, $a_g(412)$, and fluorescence voltage from 165°W (station 12). Note the layer between 110 and 130 m where $a_g(412)$ decreases and salinity increases suggesting a possible relationship between CDOM and salinity.

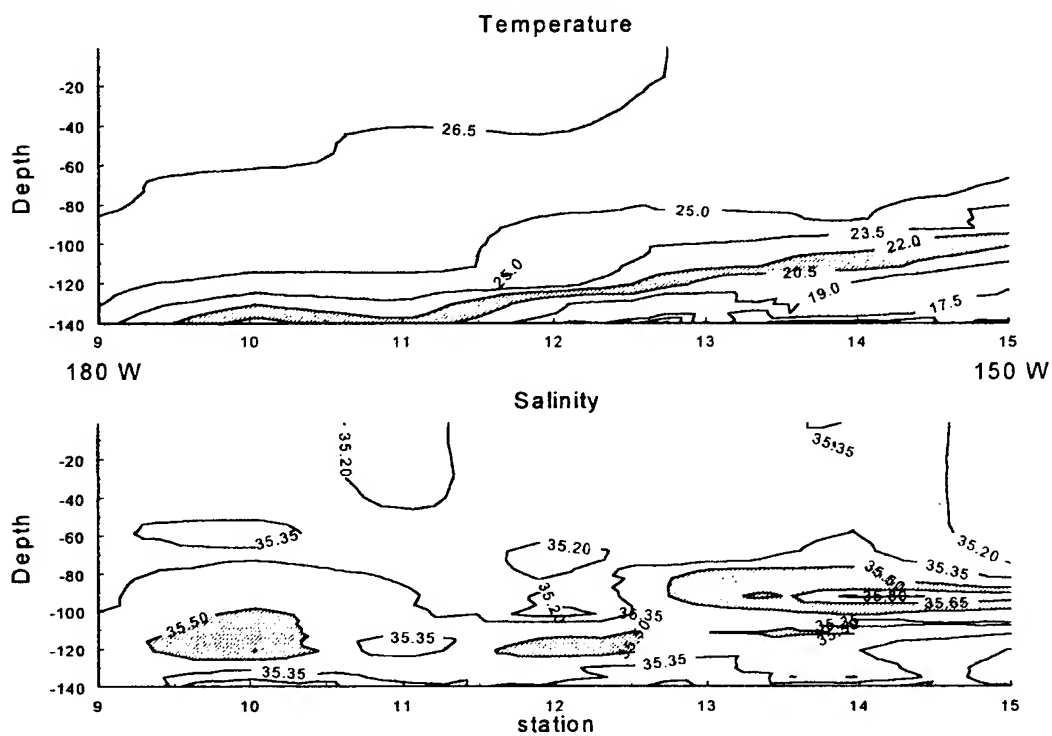


Figure 4 Contours of temperature and salinity along the cruise line. Stations are five degrees apart. A contour is shaded to help visualize the zonal pattern in the parameters.

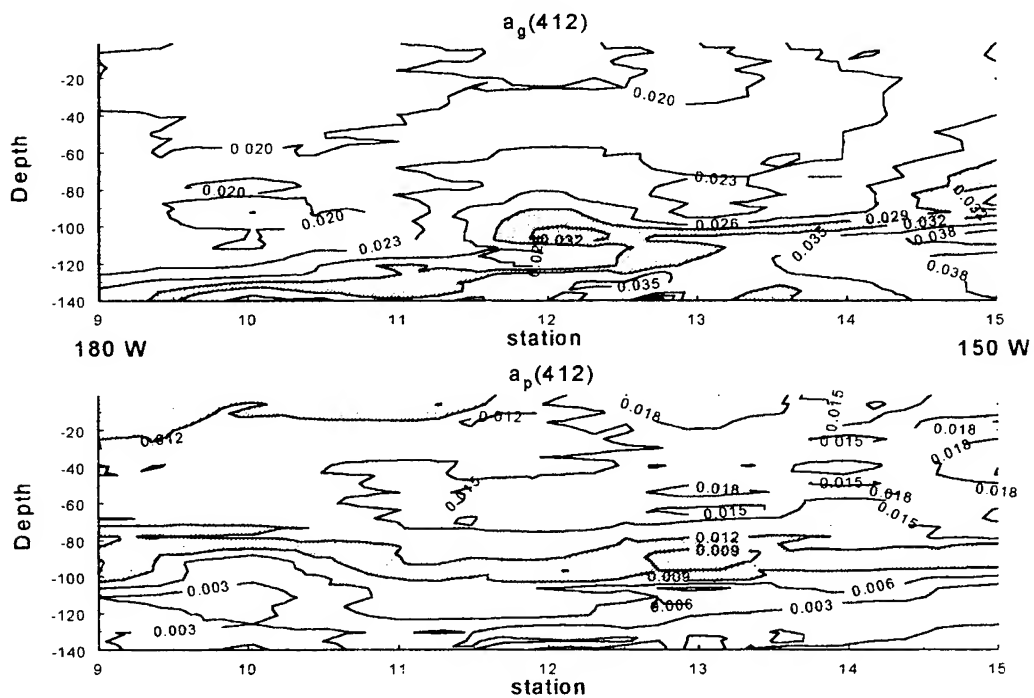


Figure 5. Contours of dissolved and particulate absorption along the cruise line.

The importance of CDOM in determining the optical properties of the water in the blue portion of the spectrum can be seen in Figure 6. The relative contribution of CDOM to the total absorption and attenuation coefficients has a simpler zonal distribution than that of CDOM itself. The CDOM absorption coefficient is generally half of the total absorption coefficient to the bottom of the particulate absorption maximum. When the particulate absorption begins to decrease the dissolved absorption becomes increasingly important due to the much larger half-life of yellow matter compared to particulate matter. This is most evident below the thermocline where, in areas, the dissolved absorption made up over 90 % of the total absorption. In this area the absorption by CDOM also made up as much as 50% of the total attenuation coefficient at 412 nm. The increased contribution by CDOM to the total attenuation coefficient shoals towards the east in a manner similar to the thermocline.

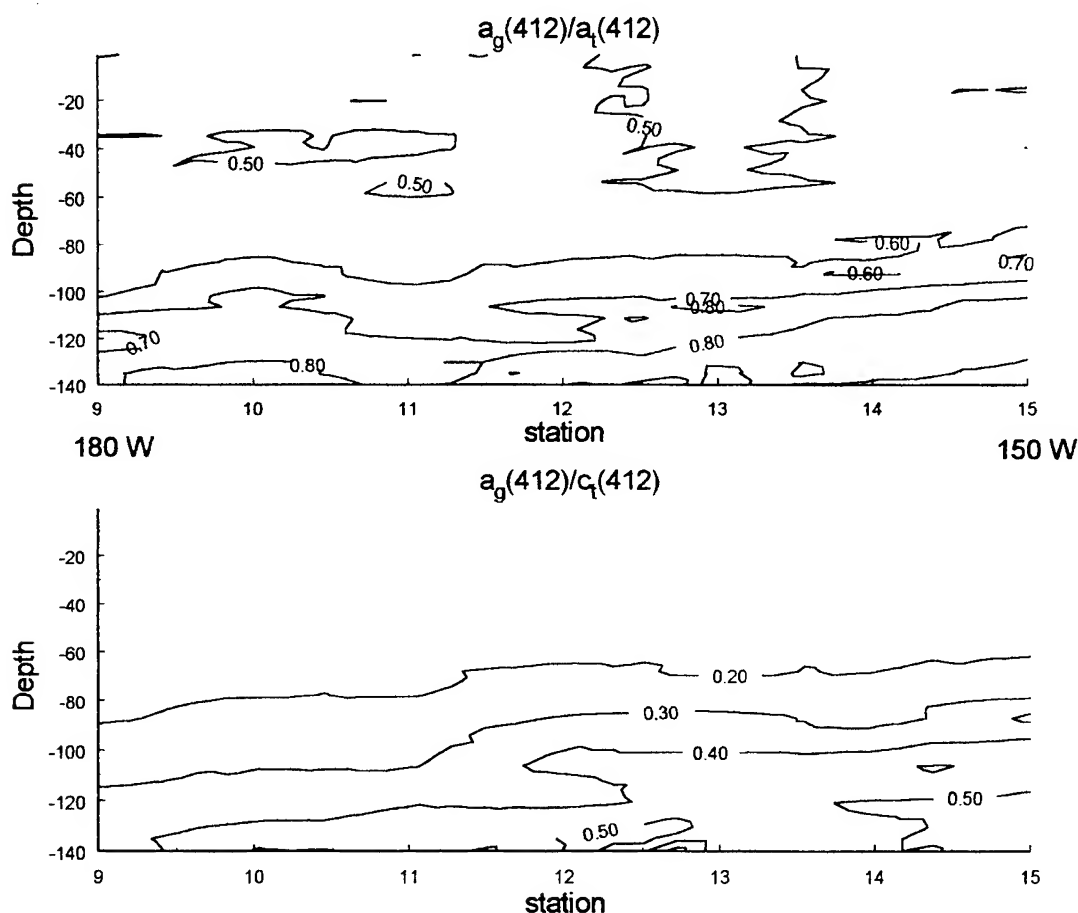


Figure 6. The contribution of CDOM absorption (a_g) to the total absorption (a_t) and attenuation (c_t) coefficients.

4. CONCLUSION

In the near-surface waters of the Equatorial Pacific the distribution of CDOM is dependent mainly on the depth of the pycnocline, with high values of a_g existing below the pycnocline. The distribution of CDOM above the pycnocline appears to be modulated by the productivity of the water and currents, such as the Equatorial Undercurrent which is in the pycnocline. The existence of CDOM is important in determining the optical properties in the blue portion of the spectrum. In most instances the absorption coefficient at 412 nm of the dissolved component makes up over half of the total absorption coefficient and up to half of the total attenuation coefficient in this region.

5. ACKNOWLEDGEMENTS

I thank Jim Washburn, Jennifer Simeon, and the crew of the R.V. Thomas Thompson for their assistance in making the measurements. I thank Andrew Barnard for his help with analysis of the data and Ron Zaneveld for his assistance with this project. This work was supported by the National Aeronautics and Space Administration Ocean Biogeochemistry program. The data for Figure 1 was collected under a program supported by the Office of Naval Research Environmental Optics program.

6. REFERENCES

1. Bricaud, A. A. Morel, and L. Prieur, "Absorption by dissolved organic matter of the sea (yellow substance) in the UV and visible domains", *Limnol. Oceanogr.*, **26**, 43-53, (1981).
2. Carder, K. L., R. G. Steward, G. R. Harvey, and P. B. Ortner, "Marine humic and fulvic acids: Their effects on remote sensing of ocean chlorophyll", *Limnol. Oceanogr.*, **34**, 68-81, (1989).
3. Carder, K. L., S. K. Hawes, K. A. Baker, R. C. Smith, R. G. Steward, and B. G. Mitchell, "Reflectance model for quantifying chlorophyll *a* in the presence of productivity degradation products", *J. Geophys. Res.*, **96**, 20,599-20,611, (1991).
4. Davies-Colley, R. J., "Yellow substance in coastal and marine waters round the South Island, New Zealand", *New Zealand J. Mar. and Freshwat. Res.*, **26**, 311-322, (1992).
5. Green, S. A., and N. V. Blough, "Optical absorption and fluorescence properties of chromophoric dissolved organic matter in natural waters", *Limnol. Oceanogr.*, **39**, 1903-1916, (1994).
6. Højerslev, N. K., "On the origin of yellow substance in the marine environment", in *Studies in physical oceanography: Papers dedicated to professor Nils G. Jerlov in commemoration of his seventieth birthday*, Inst. Phys. Oceanogr., Report 42, University of Copenhagen, (1980).
7. Kirk, J. T. O., *Light and photosynthesis in aquatic ecosystems*, 2 nd edition, pp.509, Cambridge University Press, Cambridge, (1994).
8. Tsuchiya, M., R. Lukas, R. A. Fine, E. Firing, and E. Lindstrom, "Source waters of the Pacific Equatorial Undercurrent", *J. Phys. Ocean.*, 101-148, (1991).
9. The Open University, *Ocean circulation*, pp. 238, Pergamon Press, New York, (1989).
10. Pickard, G. L., and W. J. Emery, *Descriptive physical oceanography*, 5 th edition, pp. 320, Pergamon Press, New York, (1990).

Short-Period photophysiological responses of *Thalassiosira pseudonana* during photoacclimation to near surface irradiance

Robert E. Reed

Dept. of Marine, Earth, and Atmospheric Sciences
North Carolina State University, Raleigh, N.C. 27695

Gary J. Kirkpatrick

Mote Marine Laboratory
1600 Ken Thompson Parkway, Sarasota, FL 34236

Dan Kamykowski

Dept. of Marine, Earth, and Atmospheric Sciences
North Carolina State University, Raleigh, N.C. 27695

ABSTRACT

A two day deployment of the Self-Contained Underwater Photosynthetic Apparatus (SUPA) was conducted to examine the effects of high and variable natural irradiance on the optical properties and primary productivity of the diatom *Thalassiosira pseudonana* (clone 3H). Study objectives included the determination of short time responses in the cycling of diadinoxanthin(DD) and diatoxanthin(DT), and associated changes in the rates of primary production, and quantum yield, and in cell absorption characteristics over a two day period.

A nutrient replete, low light acclimated diatom culture was placed in SUPA and in a collocated culture reservoir fitted with a quartz top. The instrument was deployed in shallow water in Sarasota Bay under fluctuating, high irradiance typical for June. A pigment sampling series reveals a correlation of DD to DT cycling with exposure to high irradiance. Net quantum yields, determined by cell absorption spectra and minute-to-minute SUPA net primary productivity values, exhibit high values initially which decay to lower values upon exposure to high light. Short time scale changes in quantum yield are observed due to changes in DD/DT cycling and fluctuating irradiance.

1. INTRODUCTION

The ability of a phytoplankter to acclimate to high and variable irradiance levels is an important factor in determining growth rates and overall success.^{10,16} Short time scale responses due to fluctuating light are not easily determined by traditional methods (e.g. radioactive carbon uptake) because the sample handling time exceeds the time scale of response. The biophysical instrument SUPA simultaneously can determine minute-to-minute changes in carbon uptake rates and oxygen evolution rates by a unialgal culture *in situ*.² Since, the light (oxygenic photosynthesis) and dark (Calvin cycle) reactions of photosynthesis are not directly coupled, divergences can occur in the rates of the two photosynthetic reactions. This research attempts to accurately determine changes in the *T. pseudonana* photosynthetic rates as measured by SUPA on a per minute basis and pigment complement as measured on periodic samples for two consecutive diurnal cycles under high and variable irradiance.

2. METHODS

Unialgal batch cultures of *T. pseudonana* (clone 3H) were grown on a 12:12 hour light-dark cycle in F/2 growth media.¹ A mixture of cool-white, and Vita-lite fluorescent lamps provided approximately 135 $\mu\text{Ein m}^{-2} \text{s}^{-1}$ of photosynthetically active radiation (PAR). All PAR measurements were made with a Biospherical Instruments, Inc. model QSL-100 quantum scalar irradiance sensor. The cultures were diluted to F/20 prior to loading into SUPA and the 18 liter reservoir. The SUPA dome and top of the enclosure was constructed of quartz glass to allow the penetration full spectrum irradiance. Changes in ambient irradiance, culture temperature, pH and dissolved oxygen are recorded by SUPA on a one-minute basis. All rates of change were calculated by algorithms developed for the specific parameters.² *In vivo* OD spectra collected on glass fiber filters were determined using a Varian model DMS-80 UV-VIS spectrophotometer. The resulting

spectra were corrected for multiple scattering using the method of Cleveland and Weidemann³. The spectral fourth derivative was then computed for each spectrum to resolve the position and any shifts in absorption peaks.⁴ Pigment analysis methods follow Mantoura and Llewellyn⁵ with detection on a Shimadzu SPD-M6A photo-diode array detector and quantification at 440nm. Cell numbers were enumerated using both Coulter Counter and hemacytometer methods.

The SUPA and associated enclosure were deployed in Sarasota Bay on June 25, 1995 off the Mote Marine Laboratory dock. The sample chamber was approximately at 1 meter depth at high tide. The array was sampled at deployment and approximately every two hours thereafter via a darkened tube connected to a peristaltic pump. A 3m x 3m neutral density screen was constructed to provide some protection to the shade adapted culture if deemed necessary. Surface irradiance was recorded by the Mote Marine Laboratory weather station. In order to determine the fine scale changes in pigment complement due to short term irradiance fluctuations, the HPLC and cell absorption samples received the highest priority for processing. Both were immediately filtered with low vacuum and frozen in liquid nitrogen.

3. RESULTS

3.1 Photosynthetic rate response to irradiance fluctuations

A two day, minute-to-minute record of oxygen evolution and carbon uptake by *T. pseudonana* was collected by SUPA. If one takes the light field experienced as the input and the rate of carbon uptake or oxygen evolution in the context of variable and high irradiance exposure as the output of the system, the rates either mimic the light field or spikes and noise seem to predominate. For example, the carbon uptake rate (Fig. 1A & 1B) after 1720 min. elapsed time, closely resembles the light input signal. Prior to this time, large swings in uptake occur on a regular basis that appear independent of the light. Also, the oxygen evolution data (Fig. 1C & 1D) exhibit noise during the first day; however, the second day seems more stable and rate features more closely match the light signal. These gross features will be examined later in the context of cellular photoadaptive responses.

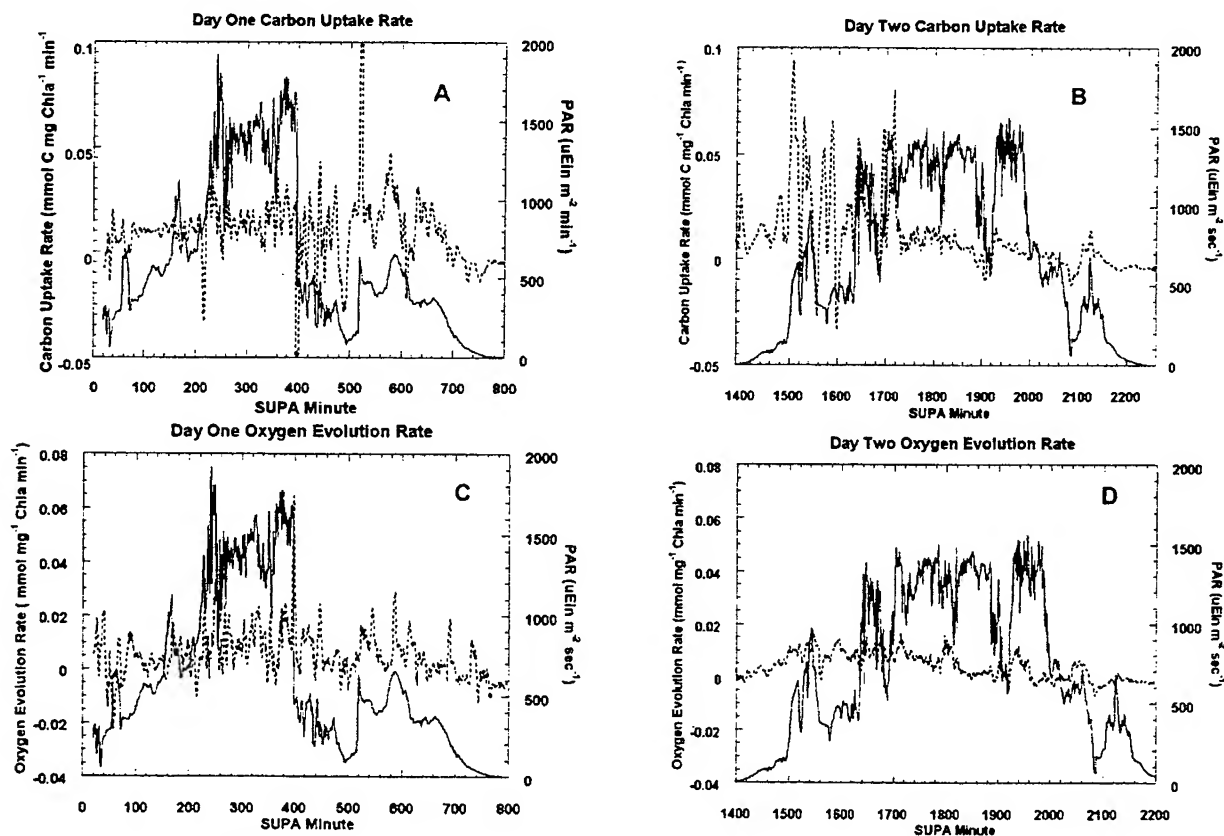


Fig 1. Photosynthetic rate response, solid lines-PAR, dashed lines-photosynthetic rate (carbon or oxygen)

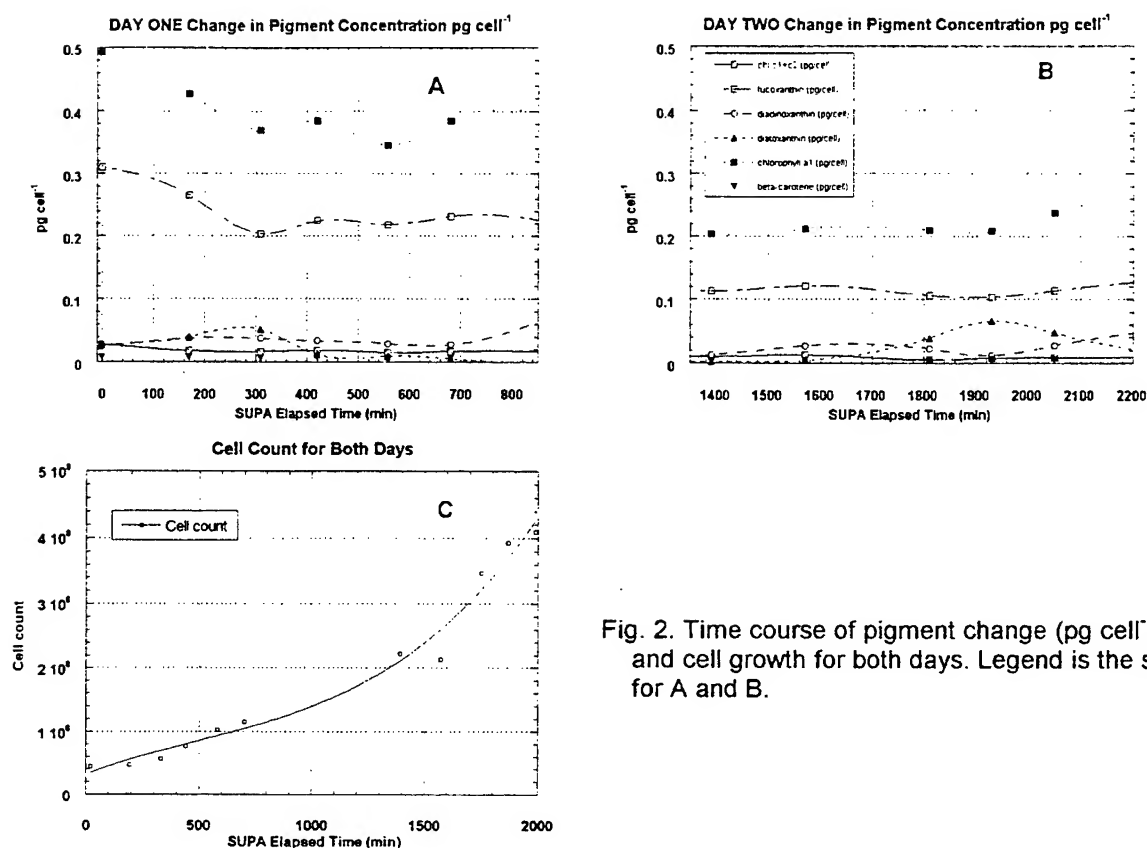


Fig. 2. Time course of pigment change (pg cell^{-1}) and cell growth for both days. Legend is the same for A and B.

3.2 Changes in pigment complement

The various components of the pigment complement responded to the increased irradiance over the two day deployment. A time course of pigment change and cell growth is illustrated in Figure 2. Chlorophyll a and fucoxanthin both decreased on a per cell basis for the first two sampling periods after deployment; however, DD and DT (photoprotective pigments) both increased in response to the high irradiance levels (Fig 2A). Light levels dropped significantly after 400 minutes elapsed time when a neutral density (47%) filter was floated above the SUPA. A decrease in the cellular DT concentration was noted soon after. The per cell concentration of the other pigments did not vary throughout the rest of the first day. The second day time course of per cell pigment concentration showed an increase in DD during the morning followed by a decrease in the afternoon. Diatoxanthin, the epoxy free product of DD, increased at the expense of its parent during the times of highest irradiance. The last sampling period showed a decrease in DT and an increase of DD, most likely due to lower irradiance levels. Cell numbers (Fig. 2C) steadily increase throughout the first day; with the exception of one sampling period, cell division was vigorous the second day.

Cell absorption spectra were determined for each sample throughout the deployment³ and HPLC pigment concentrations were spectrally reconstructed⁷. Figures 3A and 3B are composites of the 480 to 520 nm region of the fourth derivative analyses performed on each of the sample periods for day one and two. A downward shift from near 495 to 500nm should be observed when DD is converted to diatoxanthin. In Figure 3A, no shift is noted for the five samples examined (each trace was determined from triplicates). However, a distinctive shift down in wavelength is seen for the two samples taken during times of highest irradiance when DT concentrations were highest. A comparison of the beta-corrected cell absorption spectra and HPLC pigment reconstructed spectra of the two endpoint samples (the first on the first day and the fourth on the second day) revealed an increase in the absorption peaks near 435 and 670 nm over time. The percentage difference of the reconstructed spectrum in comparison to the cell absorption spectrum for the shade adapted sample was 31% at 435nm and 13% at 670 nm (Figure 3C). The high light adapted sample showed an increase of 45% at 435nm and

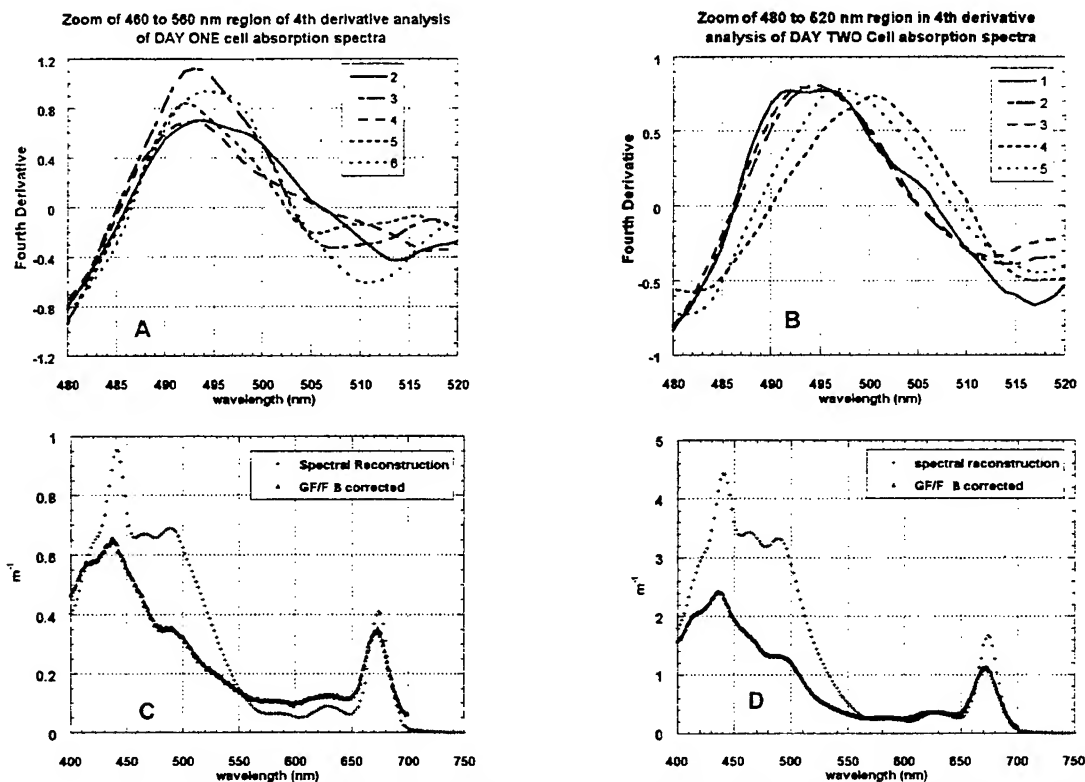


Fig. 3. A & B, fourth derivative analyses for day one and two. C & D, package effect for high and low light exposure sample periods

33% at 670 nm (Figure 3D). The decrease at these wavelengths by the whole cell spectra suggests an increase in the package effect by *T. pseudonana*⁵.

3.3 Changes in net quantum yield

The $\Phi_c(z)$ equation as set forth by Bidigare⁸ was used to calculate quantum yield using the minute by minute Pmax values from SUPA and Φ max value of 0.06 mol C mol Ein⁻¹. The quantum yields are plotted against both the phytoplankton absorbed quanta (AQph) (Figs. 4A-4D, note different scales for X axes) and SUPA elapsed time (Figs 4E-4H) to reveal different features. The quantum yields for both oxygen and carbon compared to AQph display the pattern described by Kroon *et al.*⁹ An initial high quantum yield at low levels of AQph decays to lower values when higher irradiance levels are encountered until leveling off. The striking difference in the SUPA determined quantum yields vs. AQph when compared to the Kroon data are the negative values which mirror the high positive values. These negative values are recorded at discrete times of the day as seen in Figs. 4E-4H, with a general trend toward the end of the day, however there are times when large negative spikes occur in the quantum yield vs. elapsed time figures (4E-4H). At 400 minutes elapsed time (Figs. 4E & 4F), an increase in quantum yield begins and remains high until near 700 minutes. This coincides with the placement of a neutral density screen over SUPA. In Figs. 4G & 4H, the quantum yield initially starts out high and decays to a minimum at 1700 minutes where it remains steady until the end of the day. It is also noteworthy that the 1700 minute mark of the second day is when DT concentration begins to increase (see Fig. 2B).

4. DISCUSSION

The photophysiological response of *T. pseudonana* to variable and high irradiance determined by the bio-optical instrument SUPA and pigment based laboratory techniques strongly suggests the manifestation of the 'sunglass' effect of Sakshaug *et al.*¹⁰. These researchers note that this mechanism acts on the same time scale as the DD/DT cycle in diatoms. The importance of the DD/DT cycle in a photoprotective role in phytoplankton is well documented^{11,12,13,14}. The interconversion of DD to DT due to high irradiance levels provides protection until other adaptive strategies can occur. The DD/DT response and associated changes in quantum yield by *T. pseudonana* to high light seen in this deployment suggests

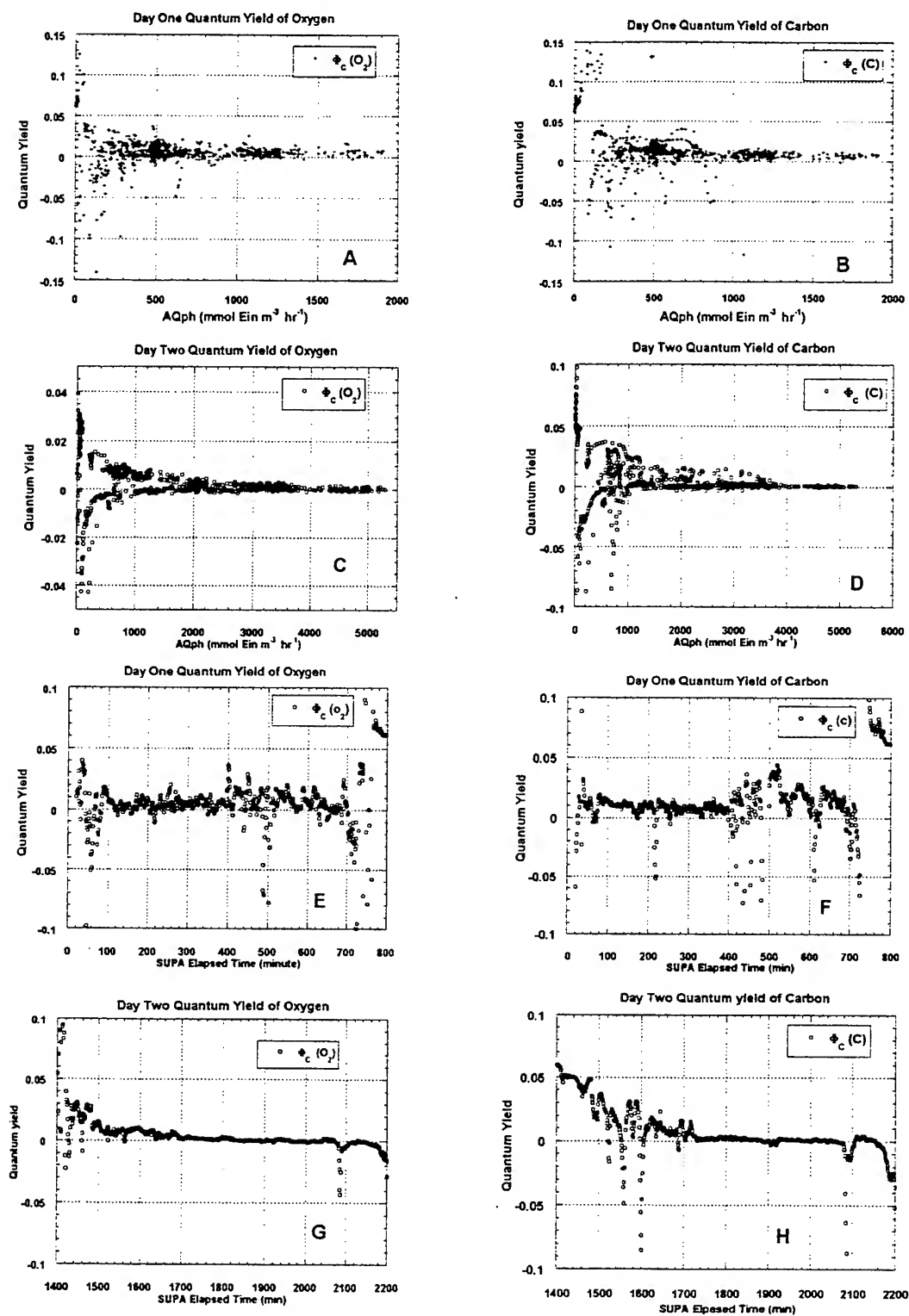


Fig. 4 SUPA determined net quantum yields for oxygen and carbon

that this mechanism provided protection allowing the cell to grow and thrive. It is also noted that the chlorophyll values for this deployment, near or slightly above 0.2 pg cell^{-1} , are similar to the high light values obtained by Sakshaug *et al.* ($0.20\text{--}0.22 \text{ pg cell}^{-1}$). An increased carbon uptake in strong light appears related to the 'sunglass' effect that may have occurred in the SUPA culture. Carbon uptake rate spikes are seen in Figs. 1A and B. and are related to high light. The minute sample rate by SUPA gives excellent resolution in determining short time scale patterns of quantum yield change. The day one quantum yield of oxygen and carbon show increases when light levels decreased¹⁷ due to the placement of a neutral density filter over SUPA. Thus, the patterns exhibited in Fig. 4 can be correlated to specific events in the cells growth history. The diminished noise in the quantum yield trace for both oxygen and carbon after 1700 minutes elapsed time during day two is coincident with the increase in DT levels. A change in the cellular package effect could also give some photoprotection to the phytoplankter¹⁴. The increase in the difference of the reconstructed and cell absorbance spectrum wavelength maximums suggest that this change did occur during high irradiance exposure (Figs. 3C & 3D).

5. ACKNOWLEDGMENTS

This research was supported by NASA grant NAGW 3575 (D.K. & G.J.K.) and an ONR AASERT grant (R.R). The authors wish to thank Mote Marine Laboratory, Sarasota, Florida for providing lab and field space to conduct the research.

6. REFERENCES

1. R.R.L. Guillard and J.H. Ryther, "Studies of marine planktonic diatoms. I. *Cyclotella nana* Hustedt and *Detonula confervacea* (Cleve) Gran." *Can. J. Microbiol.* 8, 229-239 (1962).
2. G.J. Kirkpatrick, T.B. Curtin, D. Kamykowski, M.D. Feezor, M.D. Sartin and R.E. Reed. "Measurement of photosynthetic response to euphotic zone physical forcing," *Oceanography*, 3(1), 18-22 (1990).
3. J.S. Cleveland and A.D. Weidemann, "Quantifying absorption by aquatic particles: A multiple scattering correction for glass-fiber filters," *Limnology and Oceanography*, 38(6), 1321-1327 (1993).
4. W.L. Butler and D.W. Hopkins, "An analysis of fourth derivative spectra," *Photochem. Photobiol.* 12, 451-456 (1970).
5. R.F.C. Mantoura and C.A. Llewellyn, "The rapid determination of algal chlorophyll and carotenoid pigments and their breakdown products in natural waters by reverse-phase high performance liquid chromatography," *Analyt. Chim. Acta*, 151,297-314 (1983).
7. R.R. Bidigare, M.E. Ondrusek, J.H. Morrow, D.A. Kiefer, "In vivo absorption properties of algal pigments," *Ocean Optics X. SPIE Vol. 1302*, 290-302 (1990).
8. R.R. Bidigare, B.B. Prezelin and R.C. Smith, "Bio-optical models and the problems of scaling," *Primary Productivity and Biogeochemical Cycles in the Sea*, Edited by P.G. Falkowski and A.D. Woodhead, Plenum Prss, New York, (1992).
9. B. Kroon, B.B. Prezelin, and O. Schofield, "Chromatic regulation of quantum yields for photosystem II charge separation, oxygen evolution, and carbon fixation in *Heterocapsa pygmaea* (Pyrrophyta)," *J. Phycol.*, 29, 453-462 (1993).
10. E. Sakshaug, S. Demers, C.M. Yentsch, "Thalassiosira oceanica and T. pseudonana: two different photoadaptational responses," *Mar. Ecol. Progr. Ser.* 41, 275-282 (1987).
11. S. Demers, S. Roy, R. Gagnon, and C. Vignault, "Rapid light-induced changes in cell fluorescence and in xanthophyll-cycle pigments of *Alexandrium excavatum* (Dinopyceae) and *Thalassiosira pseudonana* (Bacillariophyceae): a photo-protection mechanism," *Mar. Ecol. Progr. Ser.* 76, 185-193 (1991).
12. M. Olaizola, J. LaRoche, Z. Kolber, and P.G. Falkowski, "Non-photochemical fluorescence quenching and the diadinoxanthin cycle in a marine diatom," *Photosynthesis Research*, 41, 357-370 (1994).
13. M. Olaizola and H.Y. Yamamoto, "Short-term response of the diadinoxanthin cycle and fluorescence yield to high irradiance in *Chaetoceros muelleri* (Bacillariophyceae)," *J. Phycol.* 30, 606-612 (1994).
14. R.J. Geider and B.A. Osborne, "Light absorption by a marine diatom: experimental observations and theoretical calculations of the package effect in a small *Thalassiosira* species," *Marine Biology*. 96, 299-308 (1987).
15. B.M.A. Kroon, "Variability of photosystem II quantum yield and related processes in *Chlorella pyrenoidosa* (Chlorophyta) acclimated to an oscillating light regime simulating a mixed photic zone," *J. Phycol.* 30, 841-852 (1994).
16. P.G. Falkowski and J. La Roche. "Acclimation to spectral irradiance in algae," *J. Phycol.* 27, 8-14 (1991).
17. A. Morel. "Available, usable and stored radiant energy in relation to marine photosynthesis," *Deep Sea Research*, 25,673-88 (1978).

Calculation of the Q factor for Case 2 waters

Susan J. Shimwell¹
Marcel R. Wernand²
Simon R. Boxall¹

¹ Department of Oceanography, University of Southampton, Southampton Oceanography Centre, Waterfront Campus, European Way, Southampton, SO14 3HZ, England, UK.

² Netherlands Institute for Sea Research, PO BOX 59, 1790 AB Den Burgh, Texel, The Netherlands.

ABSTRACT

An intensive data collection campaign has been conducted in the coastal waters of the southern North Sea during which a variety of marine optical parameters have been measured. This has enabled the angular distribution factor of spectral radiance or Q factor to be calculated from *in situ* measurements. The Q factor relates upwelled spectral radiance to upwelled spectral irradiance and its precise determination is of importance in ocean colour remote sensing. Previous modelling studies, often based on the optical properties of Case 1 waters, have proposed a value of 5 for Q. However, this study suggests that more turbid coastal waters may approach the Lambertian case of Q close to π .

Keywords: Case 2 waters, Q factor, ocean colour remote sensing

1. INTRODUCTION

For natural waters Q is the angular distribution factor of spectral radiance¹ and can be used to relate upwelled spectral radiance (Lu) to upwelled spectral irradiance (Eu) just below the water surface. It is important for optical remote sensing studies that such a relationship is well-established. It is often assumed that the radiance distribution of the upwelling flux is completely diffuse and that the water body acts as a Lambertian reflector (i.e. the same radiance values at all angles), in which case Eu would equal πLu . However, in reality, the radiance distribution is not Lambertian². In the literature Q has been assigned values ranging from 3 to 5 for solar and viewing angles typical of those involved in satellite-based ocean colour observation, with an increased range from 1 to 7 if solar angles from 0 to 90° are considered³. Gordon and Morel⁴ predict that Q would also be dependent on the wavelength. Tyler⁵ showed that at a solar altitude of 57° in Lake Pend Oreille the Eu was equal to $5.08Lu$ near the water surface. Bukata *et al*⁶ used Monte Carlo simulations to estimate values of Q using the inherent optical properties of Great Lakes waters. They present curves of the variation of Q with solar zenith angle in which Q varies between 2.6 and 5 for solar zenith angles between 0° and 80° respectively. Morel and Gentili⁷ used Monte Carlo simulations to calculate Q for a variety of water optical characteristics and found that Q varied between 3 and 5 for Case 1 waters. These calculated values of Q were compared with those derived from measurements made by the radiance distribution camera system (RADS)³. This instrument allows a complete up and downwelling radiance distribution to be simultaneously captured at various depths and wavelengths. They found strong agreement between the measured and predicted Q values over the full range from <1 to 5 in Case 1 oceanic waters under clear skies. Kirk² also used Monte Carlo modelling to calculate a Q value of approximately 4.9 for waters with b/a (scattering/absorption coefficient) values in the range 1 to 5 at a solar altitude of 45°. He concluded that for intermediate solar altitudes it is reasonable to assume that the ratio Eu/Lu is 5 and that this ratio would not vary greatly at other solar altitudes.

It is therefore not clear from the literature the precise value of Q or if it varies significantly with the solar zenith angle, wavelength, or water case type. The aim of the present work is to calculate the Q factor from *in situ* optical measurements made in North Sea coastal waters (Case 2).

2. DATA COLLECTION

2.1 Research area and sampling programme

The research area was the coastal water of the southern North Sea and extended from the Dover Strait in the south to the Frisian Front in the north (Figure 1). This area is characterised by shallow depths of around 30m with a sand and mud sea bed. Elongated sand banks are present in the south of the region called the Flemish Banks. The residual water circulation is from the English Channel, through the Dover Strait and into the southern North Sea. Concentrations of suspended material vary from as high as 100mg/l very close to the coast near the Flemish Banks, to less than 2mg/l in the clear Channel water. Concentrations vary widely in the coastal zone as a result of tides, weather conditions and seasonal influences. In the north of the region is the Frisian Front which forms the boundary between water from the English Channel and water from the North Atlantic. Temperature and salinity measurements made during the programme showed that the coastal waters sampled were well mixed, except in the Frisian Front area.

Sampling was undertaken in April, June, September and December 1993 and July 1994. Several transects were chosen which were sampled at regular intervals, commencing at the coast and extending 30 to 70 nautical miles offshore in relatively clear water (Figure 1). Transects were carried out from Texel where the water has a relatively high chlorophyll concentration, (up to 38 μ g/l during bloom periods), from Walcheren near the Flemish banks where the water has a relatively high sediment load, (up to 50mg/l) and Noordwijk where the water has intermediate characteristics, (1-14 μ g/l chlorophyll and 1-30mg/l suspended sediment). Occasionally a transect was sampled across the Dover Strait to enable sampling of English and French coastal waters which have an input to Dutch coastal waters. A total of 138 stations were sampled during the five cruises.

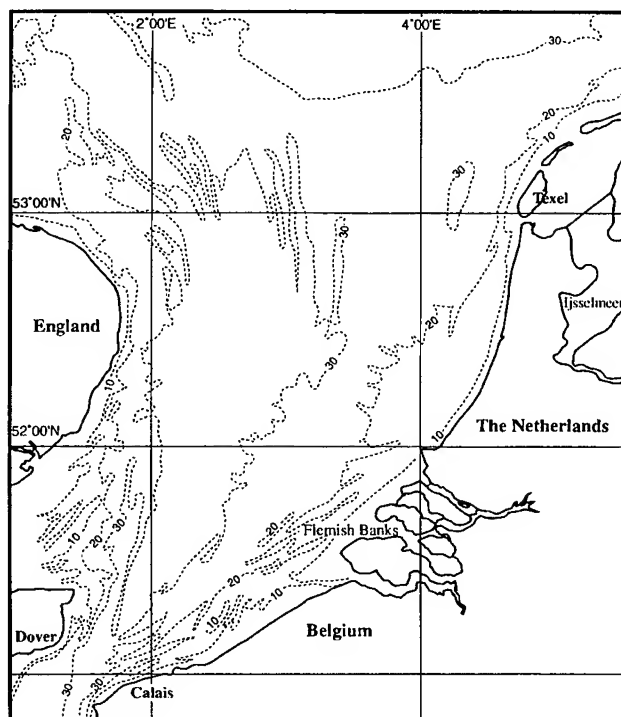


Figure 1: The research area in the southern North Sea extending from the Dover Strait in the south to the Frisian Front in the north. Depth contours are in metres.

2.2 Instrumentation

Sub-surface upwelling and downwelling irradiance $E_u(\lambda)$ and $E_d(\lambda)$ were measured simultaneously with the multi-spectral irradiance meter, ASIR, in 22 channels from 400-700nm. From these two measurements the attenuation coefficient of upwelling diffuse irradiance $K_u(\lambda)$ and the attenuation coefficient of downwelling diffuse irradiance $K_d(\lambda)$ could be derived:

$$K_{z_2-z_1} = -\ln(E_{z_2}/E_{z_1})/(z_2-z_1) \quad (1)$$

where z_1 and z_2 are the different depths of the water column where the up or downwelling irradiance (E_u or E_d) was measured.

The PR650 Spectrascan multi-spectral radiometer was used to measure the water-leaving radiance $L_w(\lambda)$ and was focused on the water surface from a height of 4 metres. This instrument has a spectral range from 380 - 780nm with a FWHM of 8nm and a spectral accuracy of 2nm. The instrument was tilted 20° off nadir away from the sun during measurements to minimise direct surface reflectance. The L_w at 752nm was also subtracted from each spectrum to reduce errors by direct reflection of the sun into the sensor.

3. CALCULATION OF Q

We have seen that if the water surface was Lambertian, E_u would equal πL_u . For non-Lambertian surfaces $E_u = Q L_u$. Throughout this study the up and downwelling irradiances (E_u , E_d) were measured below the water surface together with the water leaving radiance (L_w) just above the water surface, for a variety of water types and under a variety of downwelling light conditions. In order to derive Q it is necessary to convert the water leaving radiance above the surface (L_w) to the upwelling radiance just below the water surface (L_u). Furthermore E_u was usually measured at a depth of between 0.1 and 2m below the surface and it is necessary to convert this to E_u just below the water surface.

3.1 Derivation of L_u

The derivation of L_u from L_w can be achieved by making a few simple approximations. As light passes through the water/air boundary, travelling upwards, it undergoes refraction and as a consequence the light flux contained within a small solid angle below the surface spreads out to a larger solid angle above the surface. Therefore the value of emergent radiance at any given angle is about 55% of the corresponding subsurface radiance². A factor of 0.544 has been proposed by Austin¹ for relating radiance just above the surface $L_w(\theta', \phi)$ to the corresponding radiance just below the surface $L_u(\theta, \phi)$

$$L_w(\theta', \phi) = 0.544 L_u(\theta, \phi) \quad (2)$$

where θ is the nadir angle within the water and θ' is the angle in air after refraction at the surface.

Therefore if $L_w(\theta', \phi)$ is determined from remote sensing instruments such as the PR650, then it can be multiplied by 1.84 to give $L_u(\theta, \phi)$. As $L_u(\theta)$ does not change much with nadir angle in the range 0-30°, the value of $L_u(\theta)$ can be taken as an estimate of the radiance, L_u , in the vertically upward direction². Using this information the L_w measured by the PR650 can be converted to L_u .

Hence:

$$L_u = 1.84 L_w \quad (3)$$

It is assumed for the above calculation that L_w is measured just above the water surface which in this case was 4m. The variation in L_w caused by path radiance is assumed to be negligible at this distance and if measurements were taken at a lesser distance errors could be caused by the irregular wave surface.

3.2 Derivation of Eu

It is essential that the Eu used in deriving Q is that just below the surface as there can be considerable difference between the Eu just below the surface and that measured, for example, 1m below the surface. Therefore the Eu at 1cm below the surface was calculated from the measured Eu , whether at 0.1m or 1m, using the diffuse upwelling attenuation coefficient (Ku is normally derived using equation 1).

Re-arranging this equation to extract E_{z1} gives:

$$E_{z1} = E_{z2} / \exp(-Ku(z_2 - z_1)) \quad (4)$$

where E_{z1} is taken to be 0.01m and E_{z2} is the Eu at the measured depth of usually between 0.1 and 1m. Ku had previously been calculated for each station. Using equation 4, Eu was calculated for each station at a depth of 0.01m below the surface.

4. RESULTS

Both the Lu and Eu at just below the surface were calculated for each station. This enabled the Q factor to be calculated spectrally:

$$Q = Eu(\lambda) / Lu(\lambda) \quad (5)$$

The calculated spectral Q factor is shown for every station for some of the cruises in Figures 2 and 3. It can be seen that there is a large variation between stations and some variation between wavelength. However it is clear that for the majority of stations the Q factor calculated from *in situ* measurements is below 5 and closer to π .

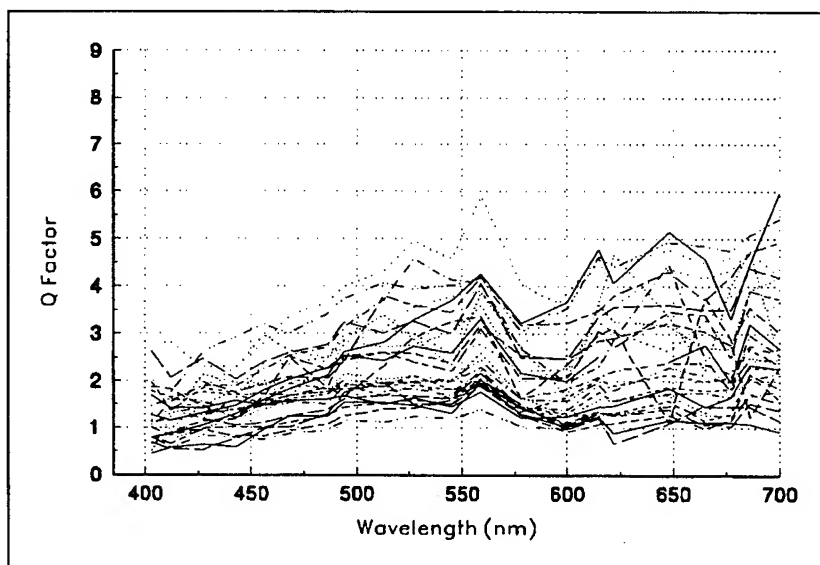


Figure 2: The calculated spectral Q factor for each station during June 1993 to show the spread of data.

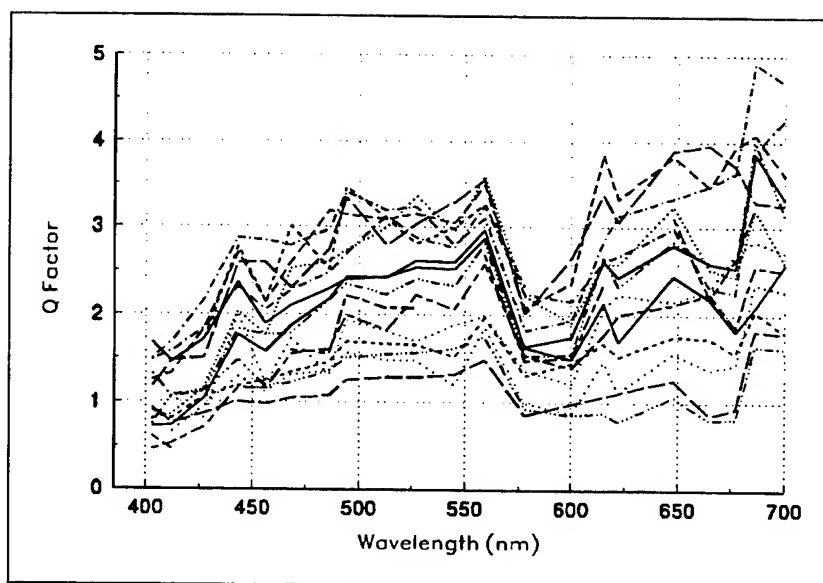


Figure 3: *The calculated spectral Q factor for each station during September 1993.*

Despite some variation between stations it was decided to establish a mean Q factor for each cruise. This is shown spectrally for each cruise in Figure 4.

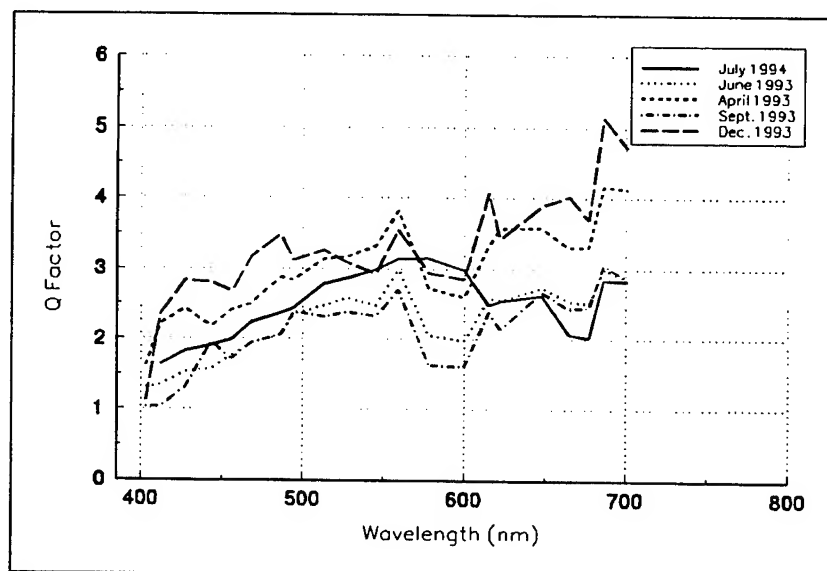


Figure 4: *The mean spectral Q factor for each cruise.*

It can be seen that Q is lower in the blue part of the spectrum (400-500nm). This is probably caused by the reflection of skylight at the surface into the sensor as it was not possible to make a correction for this. However the values in the red part of the spectrum above 550nm will be minimally affected by skylight reflection and it is clear that even here Q is much lower than the predicted value of 5 and is closer to π .

5. DISCUSSION

The angular distribution factor of spectral radiance or Q factor has been calculated for all available *in situ* measurements in North Sea coastal waters. The average value for each cruise was found to vary between 1 and 4, although values in the blue will be adversely affected by reflected skylight. However those in the red will be much less affected. These values are close to π for a Lambertian surface and are significantly less than the value of 5 which has been recommended by modelling research^{2,5}. Indeed there is no evidence within these results to show that 5 is valid for Q in Case 2 waters. It appears that in turbid waters increased scattering causes a more diffuse light field and therefore a more Lambertian surface. This seems to suggest that π is a more accurate value for Q than 5 for Case 2 waters. It should be emphasised that previous modelling studies and *in situ* measurements have focused almost entirely on Case 1 Waters. This is the first detailed study in Case 2 waters where the underwater light regime is significantly altered by the increased number of scatterers in the water. An improved estimate of Q will be obtained when a correction for skylight is included in this data set.

6. ACKNOWLEDGEMENTS

The data used in this study were collected within the Particulate Matter North Sea (PMNS) programme. This was a joint research programme funded by the Netherlands Remote Sensing Board, together with the Rijkswaterstaat, (NL) and participants included the Netherlands Institute for Sea Research (NIOZ), the University of Groningen, and the Rijkswaterstaat in the Netherlands and the University of Southampton in England. The authors would like to thank the Captain and crew of the r.v. *Pelagia* for their help and co-operation during each cruise.

7. REFERENCES

1. Austin, R.W. "Gulf of Mexico, ocean colour surface-truth measurements". *Boundary-Layer Meteorology*, **18**, 269-285 (1980).
2. Kirk, J.T.O. *Light and photosynthesis in aquatic ecosystems*. pp 508. Cambridge University Press, 2nd Edition (1994).
3. Morel, A., K.J. Voss, and B. Gentili. "Bidirectional reflectance of oceanic waters: A comparison of modeled and measured upward radiance fields". *Journal of Geophysical Research*, **100**, C7, 13143-13150 (1995).
4. Gordon, H.R. and A.Y. Morel. *Remote assessment of ocean colour for interpretation of satellite visible imagery: a review Lecture notes on Coastal and Estuarine Studies 4*, pp 114. Springer-Verlag, New York (1983).
5. Tyler, J.E. "Radiance distribution as a function of depth in an underwater environment". *Bulletin of Scripps Institute of Oceanography*, **7**, 363-411 (1960).
6. Bukata, R.P., J.H. Jerome, and J. Bruton "Particulate concentrations in Lake St. Clair as recorded by a shipborne multispectral optical monitoring system". *Remote Sensing of the Environment*, **25**, 201-299 (1988).
7. Morel, A. and B. Gentili. "Diffuse reflectance of oceanic waters. II. Bidirectional aspects." *Applied Optics*, **32**, No.33, 6864-6879 (1993).

Variation of specific optical properties and their influence on measured and modelled spectral reflectances in the Baltic Sea

Herbert Siegel, Monika Gerth, Marko Beckert
Baltic Sea Research Institute Warnemünde
Seestrasse 15, D-18119 Rostock, Germany

ABSTRACT

Spatial and temporal variations due to seasonal and regional development of phytoplankton and the freshwater inflow in river mouth areas influencing the optical properties in the Baltic Sea. The phytoplankton blooms in different seasons are dominated by special taxonomical groups. The variation intervals for the concentration of different optical active water constituents are presented. Regional and seasonal variations in the absorption of phytoplankton, detritus and gelbstoff are discussed in relation to the sources. The specific absorptions of chlorophyll show more regional differences than temporal. Measured volume scattering functions from the open Baltic and Pomeranian Bight are compared with published data. The b_p/b_v -ratio delivers the known values for different dominating water constituents, which influences also the spectral shape the backscattering coefficient. Derived spectral specific absorption and backscattering coefficients were used to control the reflectance model by comparison to measurements of the total internal reflectance. Selected inherent optical properties for the spring bloom were included in the inverse procedure by Krawczyk et al. for the derivation of water constituents from simultaneous satellite data of the Modular Optical Scanner (MOS) at the Indian Satellite IRS- P3.

2. INTRODUCTION

The Baltic Sea is a tideless marginal sea with a limited water exchange to open ocean. In optical sense the Baltic is a case II water where the optical properties are dominated by different water constituents depending on region and season. In central parts temporal and spatial variations in the phytoplankton development occur and in coastal areas rivers transport high concentrations of organic and inorganic suspended and dissolved materials into the Baltic. The river water also contains high concentration of terrigenous yellow substances due draining of swampy areas. The phytoplankton blooms in different seasons are dominated by special taxonomical groups.

The application of satellite data of ocean colour for the investigation of temporal and spatial distribution of the concentrations of water constituents requires ground truth algorithms on the basis of reflectances or specific optical properties. Therefore regional and seasonal variations in the absorption of phytoplankton, detritus and gelbstoff as well as in scattering properties are discussed and first attempt for a reflectance model are presented. For retrieving specific optical properties different methods are compared. The reflectance model shall be included into the inverse procedure by Krawczyk et al. for the derivation of water constituents from simultaneous satellite data of the Modular Optical Scanner (MOS) at the Indian Satellite IRS- P3.

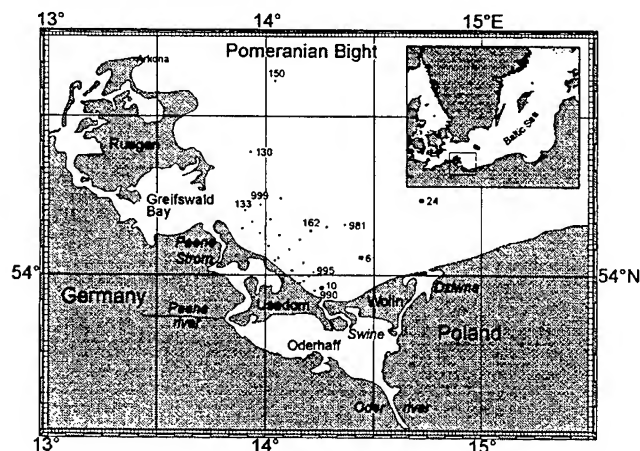


Fig. 1: Map of the Pomeranian Bight in the southern Baltic Sea

2. Experimental Details

The concentration and composition of water constituents, their inherent optical properties and the influence on the spectral reflectance at the sea surface were studied in different regions of the Baltic during different seasons. The reflectances were calculated from measurements of upward radiance L_u just beneath the sea surface and downward irradiance E_s above the surface using the equation $\mathcal{R}(\lambda) = \pi L_u(\lambda) / E_s(\lambda)$. The radiometric measurements were carried out at 25 wavelength in the spectral interval between 400 and 735 nm with a spectral resolution of $\Delta\lambda = 10$ nm using the radiometric calibrated spectrometer BAS-W¹.

As inherent optical properties we determined absorption of yellow substances from filtered water samples $a_y(\lambda)$ and absorption of particulate material $a_p(\lambda)$ using the filter method² with a Perkin Elmer Lambda II Spectrophotometer. From $a_p(\lambda)$ we calculated the absorption of chlorophyllous particle and detritus $a_{Ch}(\lambda)$ and $a_d(\lambda)$.

Measurements of the volume scattering function at 633 nm between 5° and 165° by means of a laboratory light scattering photometer³ were used to study the variability of the scattering properties and the relationship between the backscattering and the total scattering coefficient. From measurements of the beam attenuation $c(\lambda)$ and the absorption $a(\lambda)$ using a AC-9 Instrument from Wetlabs Inc. the spectral scattering coefficients were calculated.

The water constituents taken into account were chlorophyll and phaeopigment concentrations⁴, suspended matter and, in some cases, phytoplankton composition. From suspended matter the organic and inorganic part was partly determined. The measurements were carried out in the whole Baltic Sea as well in central parts as in coastal areas in different seasons (Fig. 1).

3. The reflectance model

The total internal reflectance $\mathcal{R}(\lambda)$ determined from measurements of upward radiance just beneath the sea surface $L_u(\lambda)$ and downward irradiance $E_s(\lambda)$ just above the surface is related to the water reflectance R_w according to equation (1).

$$\mathcal{R}(\lambda) = \frac{\pi L_u(\lambda)}{E_s(\lambda)} = \frac{t_d(R_w)}{1 - r_u(R_w)} \quad (1)$$

where $t_d = 0.98$ is the transmittance of the surface for downward irradiance and $r_u = 0.48$ denotes the reflectance of the surface for upward irradiance as proposed for diffuse conditions.⁵ $R_w(\lambda)$ is produced by the backscattering of the natural water and modified by the total absorption coefficient $a(\lambda)$.

$$R_w(\lambda) = 0.33 \frac{b_b(\lambda)}{a(\lambda)} \quad (2)$$

The spectral absorption and backscattering coefficient consist of the contributions of the water and different water constituents.

$$b_b(\lambda) = b_{bw}(\lambda) + b_{bc}(\lambda) + b_{bp}(\lambda) \quad (3)$$

$$a(\lambda) = a_w(\lambda) + C_{Ch} a_{Ch}^*(\lambda) + a_d(440) a_d^*(\lambda) + a_y(440) a_y^*(\lambda) + f C_s a_s^*(\lambda)$$

where a and b_b are the absorption and backscattering coefficients, the indices indicate w- water, Ch- chlorophyll, d- detritus, y- yellow substances, s- inorganic suspended matter, c- phytoplankton, p- non-chlorophyllous particles. The actual absorption of different components are determined as the product of specific absorption coefficients $a_i^*(\lambda)$ and the concentration. The factor f introduces the portion of the inorganic material in the suspended matter. The contributions of different constituents were adapted to the conditions of the Baltic using own measurements from different cruises.

4. RESULTS

4.1 Variation of water constituents

The optical active water constituents are dominated by the phytoplankton and river discharge. Spring bloom of Bacillariophyceae and Dinophyceae starts in March in the western Baltic and develops eastward with a maximum in the end of May in the northern Gotland Sea. The summer bloom of Cyanobacteria occurs in July to August in the central Baltic Sea. Due to the nutrient input by the river and the residence time of river water in lagoons the water reaching the Baltic contains a high portion of organic suspended material. The concentration of chlorophyll varies in the central part between 0.3 mg/m^3 in winter and stagnation periods and 20 mg/m^3 during the bloom. In river mouth areas values up to 50 mg/m^3 are often reached. The total suspended matter is in a range of 0.5 up to 30 mg/dm^3 . The ratio of organic to inorganic material depends on the region and the presence of phytoplanktons. In the central part of the Baltic the portion of organic material varies between 60% and 90% during blooms. In the river discharge the ratio depends on the development of the river plume and the wind mixing. Values of about 40 - 60 % are normal. In well mixed areas in the inner lagoons for the portion of organic material the same values of about 25 % were measured as of muddy sediments.

4.2. Inherent optical properties

The humic yellow substances in the Baltic Sea water are mainly of a terrigenous origin due to drainage of swamp areas and transported by river water. Mean spectral absorption coefficients show the north-south decrease and increase in the river mouth areas of the Pomeranian Bight with highest values in the Peene River mouth. The normalized mean curves of different regions confirm the applicability of the known wavelength dependence $a_y(\lambda) = a_y(440) \cdot e^{-s(\lambda-440)}$ with a coefficient s of about 0.014. The absorption at 440 nm, $a_y(440 \text{ nm})$, varies in the open Baltic between 0.2 m^{-1} and 0.4 m^{-1} and increases in the Pomeranian Bight up to 0.6 m^{-1} . The highest absorption coefficients of about 1.2 m^{-1} were found in the Peene River.

The specific absorption of chlorophyll derived from measurements of the absorption of particulate matter is characterized by regional and seasonal variations. Main differences occur between open Baltic and river mouth areas and inbetween the mixed water of the Pomeranian Bight as shown in Fig. 2. Regional differences are more important than seasonal variations due to blooms of different phytoplankton taxonomical groups.

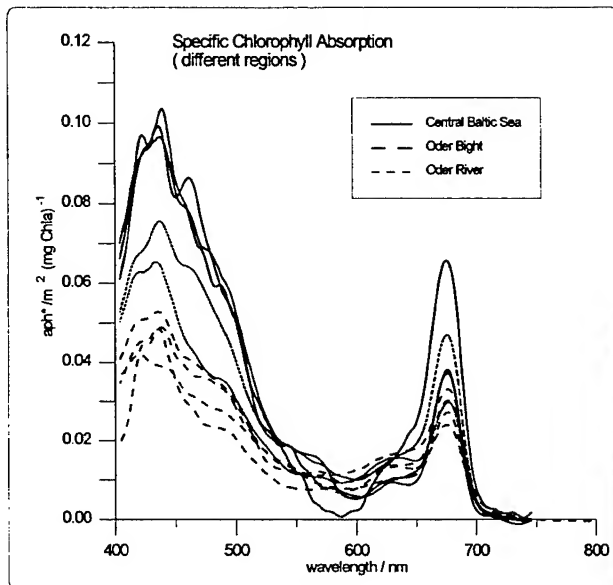


Fig. 2: Specific absorption coefficients of phytoplankton for different regions and seasons

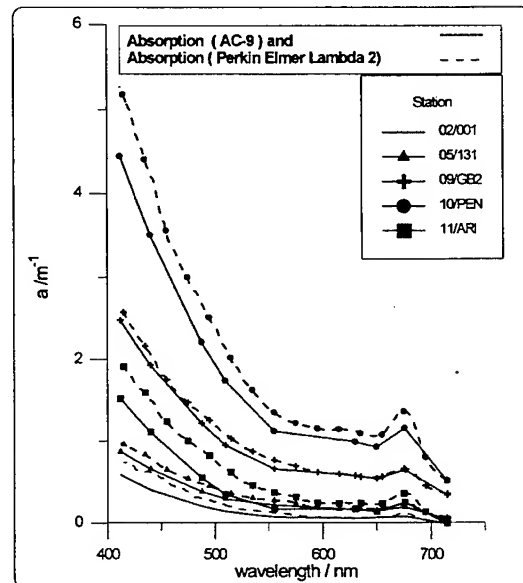


Fig. 3: Comparison for $a-a_w$ between filter method and AC-9

The detritus as the degradation product of the phytoplankton is in the Baltic normally produced in the water body. The absorption of detritus a_d determined by the filter method is correlated to the chlorophyll + phaeopigment concentration. The highest a_d per chlorophyll unit were found in the Pomeranian Bight and especially in the wind mixed bight water with high portions of resuspended materials. These correlations allow to determine specific spectral absorptions of detritus per Ch+Ph. A mean specific $a_d^*(\lambda)$ was used for the model calculations. The variable $a_d(440\text{nm})$ varied for the open Baltic between 0.02 and 0.13 m^{-1} and for the Pomeranian Bight between 0.13 and 0.8 m^{-1} .

The WETLABS instrument AC-9 was used to determined the absorption of natural water to prove the filter method and the spectral dependence of scattering. The scattering correction recommended was not usable for the Baltic because of the detritus absorption. In the correction procedure we took into consideration the detritus absorption at 715 nm measured with the filter method. Absorption coefficients of natural water $a_p(\lambda)+a_d(\lambda)$ without pure sea water calculated from both methods show comparable results in Fig. 3.

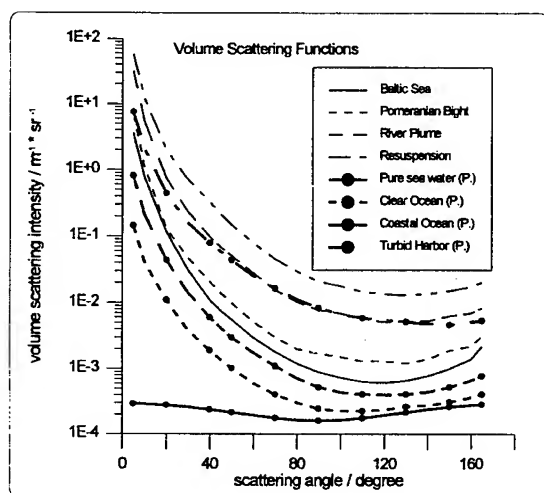


Fig. 4: Volume scattering function

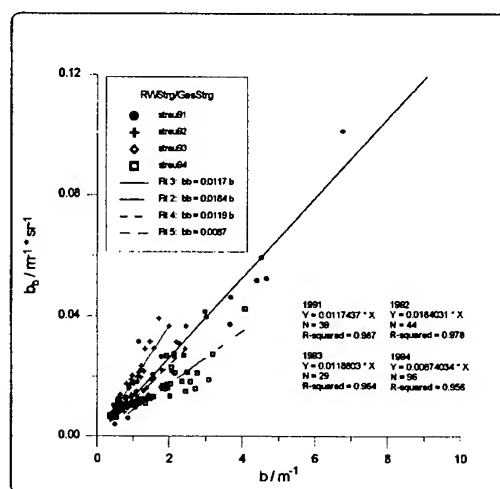
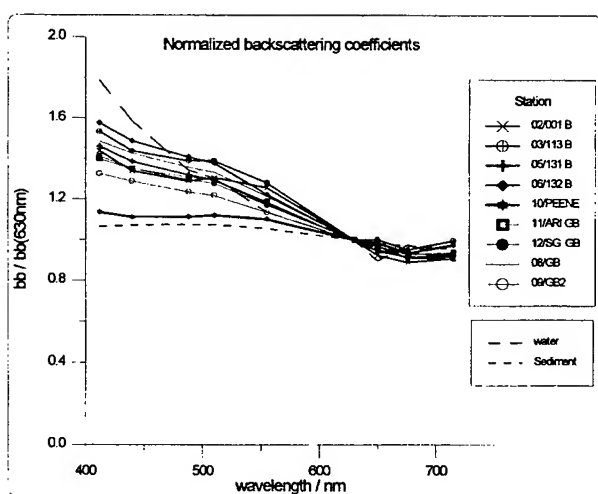


Fig. 5: Relationship between b_b and b



Measured volume scattering function $B(\theta)$ for the open Baltic, the Pomeranian Bight, the river plume area and a station with high concentration of resuspended material in Fig. 4 are comparable to published results and show already the different ratios between low and large angle range due to the particle size distribution.⁶

The b_b/b -ratio approaches showed in Fig. 5 differences in dependence on the area and season. For a phytoplankton bloom with larger particles we found values of about 0.008, for the Pomeranian Bight during 2 cruises and low wind periods 0.012 and for strong wind periods in this region of about 0.018 which confirm data from other areas.⁷

Fig. 6: Normalized backscattering coefficients of different stations, filtered water and sediment

Backscattering coefficients calculated from AC-9 measurements of b and the determined b_b/b -ratio normalized to the wavelength of 630nm for open Baltic, Greifswald Bay and Peene River are presented in Fig. 6. Differences occur between open Baltic and Bight and especially to River Peene with the same shape as for sediments with a portion of 75% of inorganic material.

4.3 Model

For the modelling of spectral reflectance at the sea surface different approaches for the relationship between the reflectance and the inherent optical properties were used.⁸ The differences delivered by the models solved not the problems in comparison to measured reflectances, so that we decided to continue with $R_w = 0.33 b_b / a$. Therefore the radiometric calibrated upward radiance just beneath the sea surface $L_u(\lambda)$ and downward irradiance $E_s(\lambda)$ just above the surface as well as the above mentioned optical properties with two different methods were measured in September 1996 in the open Baltic and in the Greifswald Bay to cover the range of variation. The inherent optical properties and the concentration of water constituents have shown, that we have to take into consideration besides the absorption of yellow substances the variable specific absorption of chlorophyll, the variation in absorption of the suspended matter and its origin from detritus, muddy or mineralic resuspended material. Furthermore the spectral differences in the backscattering coefficient have to be considered.

The analysis are not completely finished. First results are shown in Fig. 7 and Fig. 8.

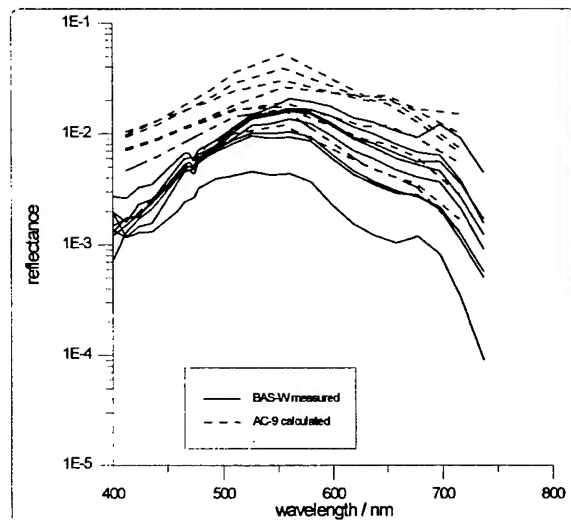


Fig. 7: Variation of measured (BAS-W, solid) and calculated (AC-9) reflectances

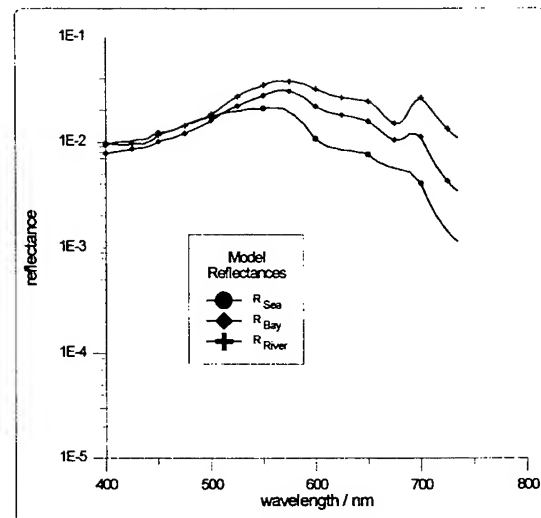


Fig. 8: Modelled reflectances

The measured reflectances of the BAS-W (solid lines) show strong variations in the long wavelength with the lowest values in the open Baltic and the highest in the Peene River. The strong slope in the short wavelength range is caused by the absorption of yellow substances and detritus. The reflectances calculated from b and a of AC-9 including the b_b/b ratio and the water absorption are drawn for the same stations as dashed lines. These values are higher and especially the slope in the short wavelength range is not so strong developed. The modelled reflectances in Fig. 8 deliver comparable results. Two reasons could be responsible for these result. The water constituents and their inherent optical properties are not right measured and modelled or not fully considered. Incorrect radiation measurements we may exclude because of the radiometric calibration of the BAS-W and the comparison to other instruments. In the future more attention has to be focused on the Q-factor the relation between the upward radiance and upward irradiance.

5. CONCLUSIONS

In the Baltic Sea, concentrations and compositions of water constituents and their optical properties are subject to seasonal and regional variations. The natural range of variation of the optical active materials are presented. Seasonal variations occur in the central parts due to temporal differences in the development of plankton blooms. Regional differences are dominated by river discharge. In the specific absorption of phytoplankton the regional influence is dominant leading to special curves for the open Baltic, the Pomeranian Bight as well as for river plumes and inner lagoon.

For detritus a specific spectral absorption was retrieved but the investigations should be continued.

The total suspended matter varied also especially in the river mouth area. The portion of the organic part varies between 90% during the plankton bloom and 25% in river water with resuspension comparable values to the muddy sediment at the sea bottom.

The spatial distribution of the absorption of yellow substances is characterized by a north-south decrease and an increase to river mouth areas with maximum in river water and inner lagoons due to their origin the swamp areas. The known mean spectral dependence is usable.

The shape of the volume scattering function is comparable to results of Petzold. The b_p/b -ratio varies between 0.8% during plankton blooms and 1.8% during wind induced resuspension with mean values of about 1.2%. The spectral dependence of the backscattering coefficient varies between open Baltic and bight water, but especially to river water with high percentage of inorganic suspended material.

These dissolved and suspended constituents, as phytoplankton, detritus, yellow substances and inorganic constituents are considered in reflectance models, but their effect in the calculated reflectances is not completely in agreement with the measurements. Calculated reflectances from AC-9 data are comparable with the model results.

6. ACKNOWLEDGEMENT

This work was partly supported by projects of the Deutsche Forschungsgemeinschaft (DFG) and the Deutsche Agentur für Raumfahrtangelegenheiten (DARA).

7. REFERENCES

1. SIEGEL, H. und U. LEITERER, "Die Wasservariante des Spektralfotometers BAS (BAS-W)". Feingerätetechnik, 35, 279-281, 1986
2. BRICAUD, A., and D. STRAMSKI, "Spectral absorption coefficients of living phytoplankton and nonalgal biogenous matter: A comparison between the Peru upwelling area and the Sargasso Sea". Limnol. Oceanogr., 35(3), 562-582, 1990
3. PRANDKE, H., "Konstruktion eines Laborstreulichtphotometers für den Einsatz in der Meeresforschung", Beitr. Meeresk., 43, 109-122, 1980
4. LORENZEN, C.J. and S.W. JEFFREY, "Determination of chlorophyll in seawater", UNESCO Technical Papers in Marine Science, 35, 20 p, 1980
5. AUSTIN, R.W., The remote sensing of spectral radiance from below the ocean surface. In: Optical Aspects of Oceanography. Ed. by N.G. Jerlov and E. Steemann Nielsen, Academic Press, London (1974), 317-344
6. PETZOLD, T. J., "Volume scattering functions for selected ocean waters", In: Light in the Sea. Ed. J. E. Tyler et al. 152-174, 1977.
7. SATHYENDRANATH, S., L. PRIEUR and A. MOREL, "A three-component model of ocean colour and its application to remote sensing of phytoplankton pigments in coastal waters". Int. J. Remote Sensing, V. 10, No 8, 1373-1394, 1989
8. SIEGEL, H., "On the relationship between the spectral reflectance and inherent optical properties of oceanic water", Beitr. Meeresk., 56, 73-80, 1987

The optical determination of phytoplankton floristic composition

P.S.D. Smith, D.G. Bowers, and E.G. Mitchelson-Jacob

School of Ocean Sciences, University of Wales, Bangor,
Gwynedd, U.K., LL59 5EY

ABSTRACT

Radiance and irradiance measurements are collected using a seven channel profiling radiometer and a four channel moored irradiance sensor which both use Sea-viewing Wide Field-of-view Sensor (SeaWiFS) wavebands. The instruments were deployed as part of the Land-Ocean Interaction Study (LOIS), Shelf Edge Study (SES) on the Malin Shelf, off the west coast of Scotland, during spring and summer 1995 and 1996. Changes in *in-situ* reflectance ratios, calculated from the blue, cyan and green wavebands of the moored colour sensors, suggest a diatom-dominated spring bloom, followed by an early summer coccolithophore bloom, with a flagellate-dominated phytoplankton population during the summer. Similar changes are also seen in attenuation ratios and specific attenuation coefficients calculated from the profiling radiometer data. The use of these optical properties to determine phytoplankton floristic composition is discussed.

Keywords: phytoplankton, diatom, flagellate, coccolithophore, attenuation, absorption, irradiance, reflectance

2. INTRODUCTION

Absorption and scattering by phytoplankton are considered to be responsible for most variations in the optical properties of open-ocean waters. All photosynthetic plankton are equipped with a variety of light absorbing pigments. Chlorophyll-*a* is the major pigment present, and is therefore used as a convenient measure of phytoplankton biomass.¹ In addition, phytoplankton contain a number of accessory pigments that absorb light in distinct spectral regions.

The shape of the absorption spectrum of a phytoplankton population is determined mainly by its pigment composition.^{2,3} Also cell size (*i.e.* package or flattening effect) affects the absorption due to the tendency for the pigments to coalesce into discrete units.⁴ This lessens the efficiency of photon collection and thereby reduces absorption. Thus changes in species composition and cell physiology will affect the absorption coefficient of phytoplankton, $a_{ph}(\lambda)(m^{-1})$ and consequently the attenuation of light, $k_d(\lambda)$.⁵

In-situ bio-optical measurements were made during four cruises, undertaken as part of the U.K. LOIS SES research programme in the Malin Shelf region, located to the north of Ireland and to the west of the Scottish Outer Hebrides (Fig. 1). In these case-1 waters, phytoplankton are the principal absorbers of light, with yellow substance and suspended particulates having a secondary influence on the in-water radiance field.

The instrument suite used on these cruises comprised:

- (i) Profiling Reflectance Radiometer with surface sensor (PRR600 / 610); a seven waveband irradiance and seven band radiance instrument tuned to the SeaWiFS wavebands (412, 443, 490, 510, 555, 670/683 nm, and PAR).
- (ii) Integrating Natural Fluorometer (INF300); measuring scalar PAR and natural stimulated fluorescence at 683 nm.
- (iii) Four-band radiometers deployed on moorings in LOIS SES region April - July 1995/ 1996; measure irradiance in the following bands: 410, 440, 490, and 670 nm.
- (iv) Spectrophotometric analysis of particulates from 350 to 750 nm, and complementary water quality measurements.

Radiometer profiles were used to calculate $k_d(\lambda)$ whilst $a_{ph}(\lambda)$ was measured spectrophotometrically. In addition, moored colour sensors, fluorometers and current meters provided time series of reflectance, chlorophyll fluorescence, beam transmittance and currents from early spring through to late summer during 1995 and 1996. These measurements have allowed the investigation of species succession from spring diatoms to a flagellate-dominated population in summer.

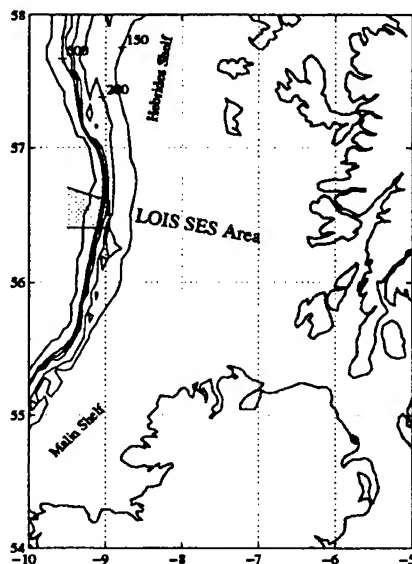


Figure 1: Map showing the location of the SES survey area on the Malin Shelf off the west coast of Scotland.

3. METHODS OF ANALYSIS AND RESULTS

3.1 Chlorophyll specific absorption.

Absorption spectra measured for aquatic particles concentrated onto a glass fibre filter were measured using a spectrophotometer after the method developed by Cleveland and Weidemann.⁶ To identify the absorption coefficient of phytoplankton at any wavelength λ , it is usual to express the total absorption coefficient, $a_p(\lambda)$ in terms of a specific absorption coefficient, $a_*(\lambda)$ and C , the concentration of chlorophyll a , the main pigment in phytoplankton:

$$a_p(\lambda) = C \cdot a_*(\lambda) \quad (1)$$

Since phytoplankton absorption is due to absorption not just by chlorophyll a but also by all the auxiliary pigments present, $a_*(\lambda)$ is not a true specific absorption by chlorophyll a , but only an apparent one. The composition of the auxiliary pigments and the relative importance of their absorbance and therefore the attenuation is variable. This variability in pigment composition, and therefore phytoplankton group is the major factor for the observed variability in magnitude and spectral form of $a_*(\lambda)$.

The specific absorption coefficient, $a_*(\lambda)$ was calculated spectrally from 350 to 750 nm for all cruise data. Differences in phytoplankton groups were apparent with diatoms absorbing more light per unit chlorophyll than the flagellate-dominated populations. The variability in spectral shape was most pronounced in the blue-green region (440 - 550 nm), where accessory chlorophylls and carotenoids have their maximum absorption. All diatom-dominated spectra had a shoulder centred around 510 nm caused by absorption by the accessory pigment fucoxanthin. However, the changes in spectral shape were less significant than the differences in the specific absorption of phytoplankton. Fig. 2 shows the chlorophyll specific absorption and attenuation spectra for two Malin

Shelf cruises, April 1995 and July 1996. The results are contrary to previous work by Morel and Bricaud⁷ who found that specific absorption coefficients decrease with increasing cell size and intracellular pigment concentration, although in this case phytoplankton physiology may be an important factor.

3.2 Chlorophyll specific attenuation.

All PRR irradiance profiles were surface-normalised to eliminate changes in the surface incident irradiance. Natural logarithms were taken to determine the attenuation coefficient, k_d for each of the seven radiometer channels at pre-determined optical depths. The chlorophyll specific attenuation coefficient $k_*(\lambda)$ was then calculated as for the specific absorption, $a_*(\lambda)$ by regressing the attenuation coefficient at each channel against the measured chlorophyll concentration.

The chlorophyll specific attenuation (k_*) spectra from the Malin dataset show consistently higher values for diatoms than for flagellates or mixed populations, in agreement with the particulate filter results (Fig. 2). However, due to the lack of resolution, small changes in the overall spectral shape due to differing pigment composition could not be seen. The attenuation values were found to be higher than absorption at each waveband consistent with the Gershun equation which gives an estimation of the mean cosine, μ . Values for the mean cosine downwelling flux μ_d ranging from 0.7 to 0.9 for the SeaWiFS wavebands from the Malin Shelf compare well with Monte Carlo calculations.²

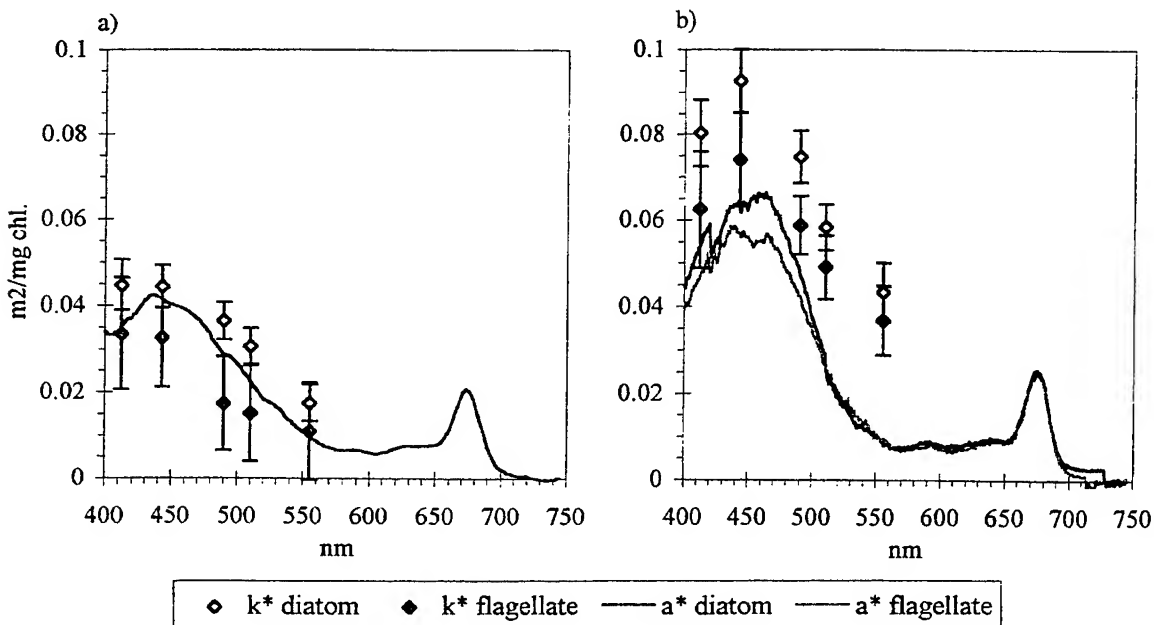


Figure 2: Chlorophyll specific absorption (a_*) and attenuation (k_*) coefficients ($\text{m}^2 / \text{mg chl.}$) plotted against wavelength (nm) from two Malin Shelf cruises: a) April 1995 and b) July 1996. Both cruises encountered diatom- and flagellate-dominated populations.

3.3 Moored Colour Sensor Data.

The moored colour sensor measured near-surface upwelled irradiance from April to July 1995 and 1996. These data were converted into chlorophyll concentrations by plotting the logarithm of fluorometrically-measured chlorophyll against the ratio of both the cyan (490 nm) to green (570 nm) and the blue (440 nm) to green (570 nm) irradiance channels to obtain two calibrations for the moorings.

Fig. 3 shows the resulting chlorophyll time series for 1995 and 1996 using both algorithms. The plots show the observed spring bloom in 1995 and 1996. A second chlorophyll peak in mid-June is also seen in both years. Visible imagery from the Advanced Very High Resolution Radiometer (AVHRR) for mid-June 1995 and 1996 shows a region of high surface-leaving reflectance at the shelf edge, which correlates with areas of higher sea surface temperature (Fig. 5). This is likely to be a coccolithophore bloom, a common feature in this region during early summer.⁸

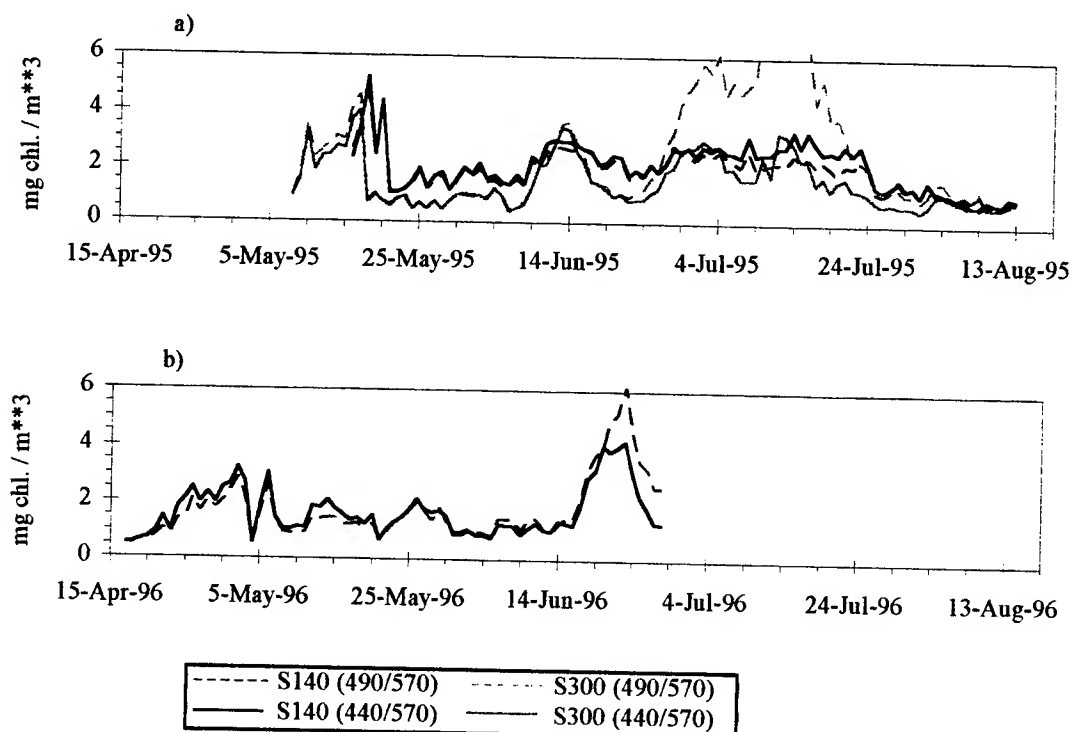


Figure 3: Chlorophyll time-series derived from the moored colour sensors from the Malin Shelf for a) 1995 and b) 1996. The colour sensors were deployed on surface moorings at 1 metre depth, at the 140 metres contour (S140) and at the 300 metres contour (S300). The data are midday averages, and are surface-normalised.

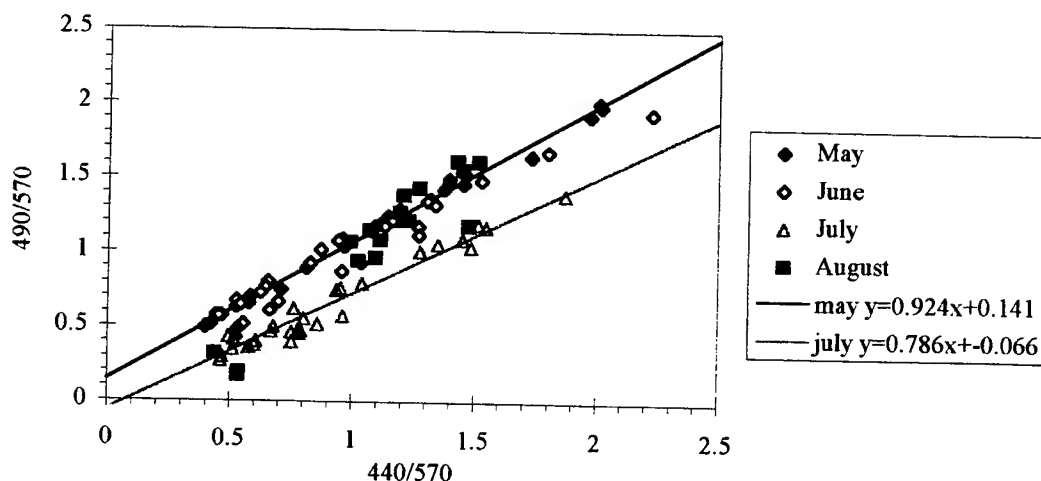


Figure 4: S300 1995 mooring time-series plotted as irradiance calibration ratios, showing the spectral shift in July.

The longer 1995 time series shows another chlorophyll peak at station S300 in July, in the cyan-green plot, reaching maximum concentrations of 12 mg.m^{-3} . However this is not mirrored in the corresponding blue-green time-series, or at S140. Using the irradiance ratio $440 \text{ nm} / 570 \text{ nm}$ as a chlorophyll indicator and plotting this against $490 \text{ nm} / 570 \text{ nm}$ (Fig. 4), the spectral shift in July at S300 can be clearly seen. This may be caused by a change in the accessory pigment composition of the phytoplankton at this site.

Coincident imagery for July 1995 from the visible channel of the AVHRR shows no increase in reflectance, implying this is not a coccolith bloom. Since chlorophyll concentrations of 12 mg.m^{-3} are unlikely for the shelf edge during July, it could be that the event seen was a spectral shift caused by a change in the dominant phytoplankton species. This change may have been caused by a localised mixing event, such as the internal tide, bringing nutrients into the mixed layer, or more likely by a different water mass at the shelf edge passing the moored instrument. The latter is the more likely scenario, since the spectral shift was not observed on the shelf at S140. However, the rate of bio-fouling and the effect on the spectral signal needs to be addressed before this latter part of the long time-series can be analysed further.

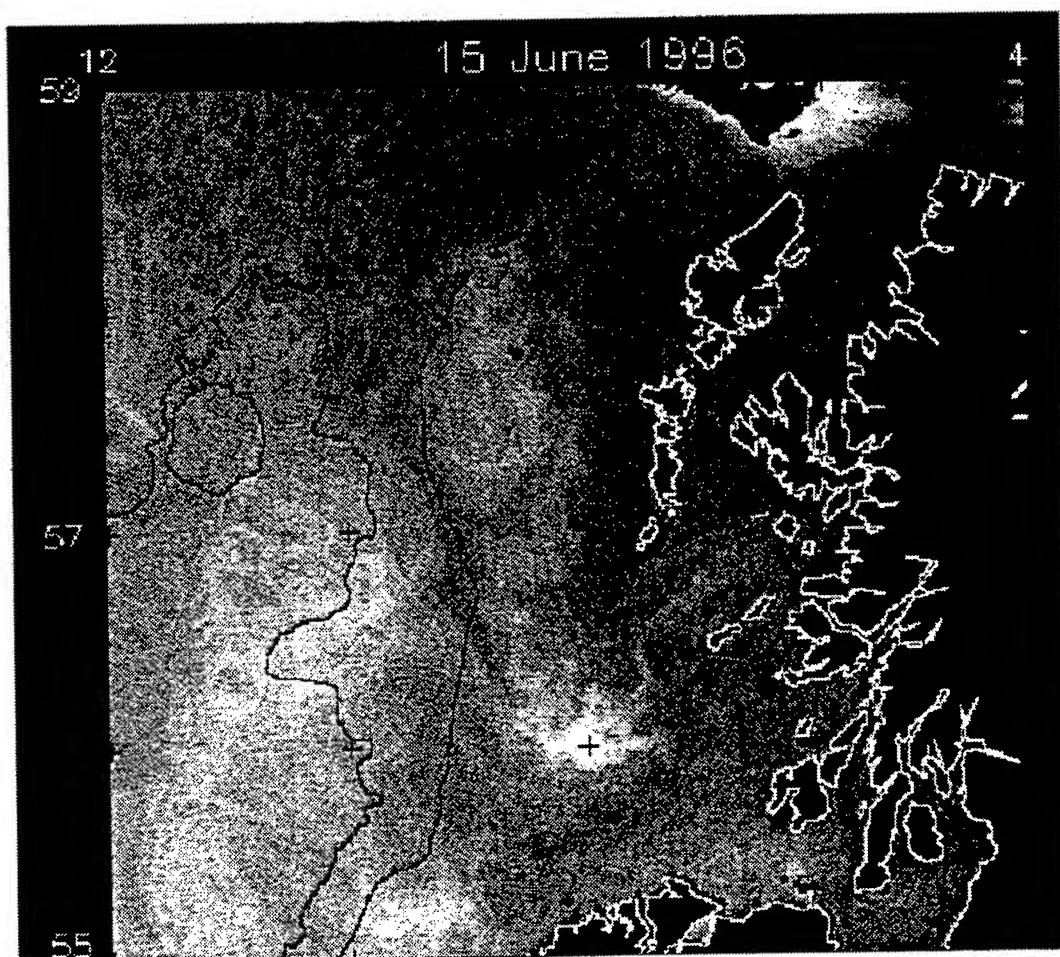


Figure 5: AVHRR visible satellite image showing a coccolithophore bloom in the Malin Shelf region on 15 June 1996. The light shades indicating regions of high reflectance, caused by the coccolithophores, can be seen on- and off-shelf.

4. DISCUSSION

The absorption spectra show diatoms absorb more light per unit chlorophyll than flagellates, in the 450 - 550 nm range. Changes in spectral shape due to accessory pigment composition are less significant. The in-water attenuation measurements correlate well with the laboratory spectra, although the limited wavebands are not sufficient to resolve the spectral form.

Analysis of the moored colour sensor data has shown the importance of using several calibration ratios in order to give an accurate chlorophyll time series, as well as information on pigment shifts in the phytoplankton population. This enables a more accurate estimation of phytoplankton biomass, and may offer an insight into the dominant phytoplankton group, which in turn could be used to improve remote sensing algorithms for primary productivity.

5. ACKNOWLEDGMENTS

This work has been funded by a Natural Environment Research Council (NERC) SeaWiFS Special Topic Research Grant (No. GT12/94/LOIS/52). The authors would also like to thank Steve Groom and Mike Hughes from the NERC Remote Sensing Data Analysis Service (RSDAS) at the Plymouth Marine Laboratory, U.K. for supplying the processed AVHRR imagery in this paper.

6. REFERENCES

1. J.R. Apel "Optics of the sea," In: *Principles of ocean physics*, ed. Apel, J.R., pp. 511-605, Academic Press, (1982)
2. J.T.O. Kirk, "Light and photosynthesis in aquatic ecosystems," Cambridge University Press, Cambridge (1983).
3. S. Sathyendranath, L. Lazzara, and L. Prieur, "Variations in the spectral values of specific absorption of phytoplankton," *Limnol. Oceanogr.*, **32**, 403-415 (1987).
4. N. Hoepffner and S. Sathyendranath, "Effect of pigment composition on absorption properties of phytoplankton," *Mar. Ecol. Prog. Ser.*, **73**, 11-23 (1991).
5. V.A. Lutz, S. Sathyendranath, and E.J.H. Head, "Absorption coefficient of phytoplankton: regional variations in the North Atlantic," *Mar. Ecol. Prog. Ser.*, **135**, 197-213 (1996).
6. J.S. Cleveland and A.D. Weidemann, "Quantifying absorption by aquatic particles: A multiple scattering correction for glass-fiber filters," *Limnol. Oceanogr.*, **38**, 1321-1327 (1993).
7. A. Morel and A. Bricaud, "Theoretical results concerning light absorption in a discrete medium, and application to specific absorption of phytoplankton," *Deep Sea Res.*, **28**, 1375-1393 (1981).
8. P.M. Holligan and S.B. Groom, "Phytoplankton distributions along the shelf break," *Proc. R. Soc. Edinburgh Sect B*, **88**, 239-263.

Role of pigments and species composition in modifying the absorption spectra of natural phytoplankton populations

Venetia Stuart¹, Shubha Sathyendranath^{1,2}, Trevor Platt², Heidi Maass¹ and Brian D. Irwin²

1. Department of Oceanography, Dalhousie University, Halifax, Nova Scotia, Canada, B3H 4J1.
2. Biological Oceanography Division, Bedford Institute of Oceanography, Box 1006, Dartmouth, Nova Scotia, Canada, B2Y 4A2.

ABSTRACT

Absorption spectra from three cruises with diverse phytoplankton assemblages were decomposed into 13 Gaussian bands, representing absorption by the major chlorophylls and accessory pigments. The relationship between Gaussian peak height and the concentration of the pigment responsible for the absorption band reflects changes in the packaging effect, which were most apparent at Gaussian bands of high absorption (400 – 490 nm) but were close to zero for the Gaussian band centered around 623 nm, associated with chl-*a*. The specific peak height of this Gaussian band was used to obtain reliable estimates of chl-*a* for any phytoplankton assemblage, unaffected by variations caused by the package effect. Specific peak heights of the blue (440 nm) and red (676 nm) chl-*a* absorption bands were highest for the Arabesque 2 cruise (small cells) and lowest for the Vancouver Island cruise (large cells), which is consistent with an increase in the package effect with increasing cell size. We estimated that 69% of the total variability in a_{ph}^* at 440 nm was due to changes in the package effect while the remaining 31% was due to changes in pigment composition.

Keywords: package effect, absorption coefficients, accessory pigments, phytoplankton composition

2. METHODS

Samples from three different cruises were used to cover a wide variety of natural phytoplankton assemblages. Two cruises were conducted in the NW Indian Ocean: the first sampled the region during the SW monsoon (August – December 1994, Arabesque 1 cruise) while the second was undertaken during the intermonsoon period (November – December 1994, Arabesque 2 cruise). The third cruise (Vancouver Island) sampled the shallow eutrophic waters of Saanich Inlet and around the Gulf Islands of Vancouver Island, British Columbia. Pigment concentrations were quantified with reverse-phase, high-performance liquid chromatography (HPLC)¹, and the absorption spectra were measured according to the filter technique^{2,3}. Each absorption spectrum of photosynthetic pigments was decomposed into 13 Gaussian bands representing absorption by the major phytoplankton pigments (chls *a*, *b* and *c*, and carotenoids)⁴. The relationship between the peak height (p_i , for the *i*th Gaussian band) and the corresponding pigment concentration, C_i (mg m⁻³), was generally non-linear, (reflecting an increased package effect with increasing pigment concentration) and was fitted with a rectangular hyperbolic function:⁵

$$p_i(\lambda_i) = \frac{p_m(i)p_m^*(i)C_i}{C_i p_m^*(i) + p_m(i)} \quad (1)$$

where $p_m^*(i)$ is the maximum specific peak height and $p_m(i)$ is the maximum asymptotic value of the absorption coefficient. The parameter $p_m^*(i)$ describes the initial slope of the curve at low pigment concentrations and represents the maximum specific absorption for the p_i - C_i pairs for each Gaussian band.

3. RESULTS AND DISCUSSION

3.1 Phytoplankton composition

Phytoplankton composition varied considerably between cruises: samples from the Arabesque 2 cruise had very low chl-*a* concentrations and were comprised predominantly of small prochlorophytes and cyanobacteria, as evidenced by the high proportion of divinyl chl-*a* (up to 74% of the total chl-*a*) and zeaxanthin (up to 82% of total carotenoids). Samples from the Vancouver Island cruise, on the other hand, had very high chl-*a* concentrations (up to 30 mg m⁻³) and were dominated almost entirely by large-celled diatoms, with fucoxanthin being the major carotenoid. Samples from the Arabesque 1 cruise contained a mixture of small and large cells, (prokaryotes, chlorophytes, prymnesiophytes and diatoms) and had intermediate chl-*a* concentrations.

3.2 Decomposition of absorption spectra

The parameters of the rectangular hyperbolic function are given in Table 1 for the main chl-*a* and carotenoid absorption bands. Non-linearity between absorption and chl-*a* concentration, as well as differences in slopes between cruises may be ascribed to packaging effects. With the exception of one Gaussian band (623nm), the maximum specific peak heights were noticeably higher (least package effect) for the Arabesque 2 cruise than for the other two cruises. At 623 nm there was no obvious package effect. A linear relationship provided the best fit to the data for all three cruises, and the coefficients ($p_m^*(i)$ values) of all three cruises were very similar. The mean specific absorption coefficient at this Gaussian band could be used to predict accurately the chl-*a* concentration in all three cruises from the phytoplankton absorption spectrum alone. The lack of a packaging effect at 623 nm may be useful when developing algorithms for estimating phytoplankton biomass from remotely-sensed ocean-colour data, since the optical effects of variations in cell size can be ignored. On a practical basis, however, collecting measurements at the red end of the spectrum are difficult because of the high attenuation of light at these wavelengths by pure seawater.

Table 1. Values of the parameters $p_m(i)$ (maximum value of absorption in m⁻¹) and $p_m^*(i)$ (maximum specific peak height in m² (mg chlorophyll-*a*)⁻¹) for the rectangular hyperbolic equation (Eq. 1) relating peak height of the Gaussian bands associated with chlorophyll-*a* and total carotenoids to pigment concentration (determined by HPLC analysis). Data are presented for the three cruises (Vancouver, $n = 34$; Arabesque 1, $n = 109$ and Arabesque 2, $n = 95$). The coefficient of determination (r^2) is also given.

Band center	Vancouver			Arabesque 1			Arabesque 2		
	p_m	p_m^*	r^2	p_m	p_m^*	r^2	p_m	p_m^*	r^2
384 (chl- <i>a</i>)	5.403	0.032	0.90	0.998	0.051	0.92	0.512	0.083	0.87
413 (chl- <i>a</i>)	0.421	0.020	0.90	0.177	0.030	0.93	0.196	0.050	0.85
440 (chl- <i>a</i>)	1.365	0.034	0.92	0.761	0.053	0.93	0.285	0.108	0.92
623 (chl- <i>a</i>)	-	0.006	0.94	-	0.006	0.97	-	0.007	0.87
676 (chl- <i>a</i>)	2.043	0.024	0.95	0.373	0.029	0.97	0.352	0.048	0.96
490 (carot)	6.600	0.028	0.95	0.388	0.040	0.93	0.220	0.099	0.89
532 (carot)	-	0.020	0.95	0.079	0.021	0.93	0.118	0.034	0.82

3.3 Estimation of the magnitude of the package effect

Since inter-cruise variations in absorption characteristics are most pronounced at wavelengths of maximum absorption (400 – 500 nm) but are close to zero at 623 nm, the magnitude of the package effect can be estimated by normalizing the chl-*a* peak heights to $p_i(623)$. In the blue region of the spectrum, the average $p_i^*(440)/p_i^*(623)$ for the Vancouver cruise (large cells, high package effect) was approximately 61% lower than that of the Arabesque 2 cruise (small cells, minimal package effect), while in the red region of the spectrum (676 nm) differences between cruises were less pronounced (Vancouver cruise approximately 42% lower).

Samples from the three cruises are clearly separated on the basis of specific peak heights in the blue (440 nm) and red (676 nm) regions of the spectrum (Fig. 1). Vancouver Island samples have the lowest specific peak heights while the Arabesque 2 samples have the highest, which is consistent with an increase in the package effect with increasing cell size between the cruises.

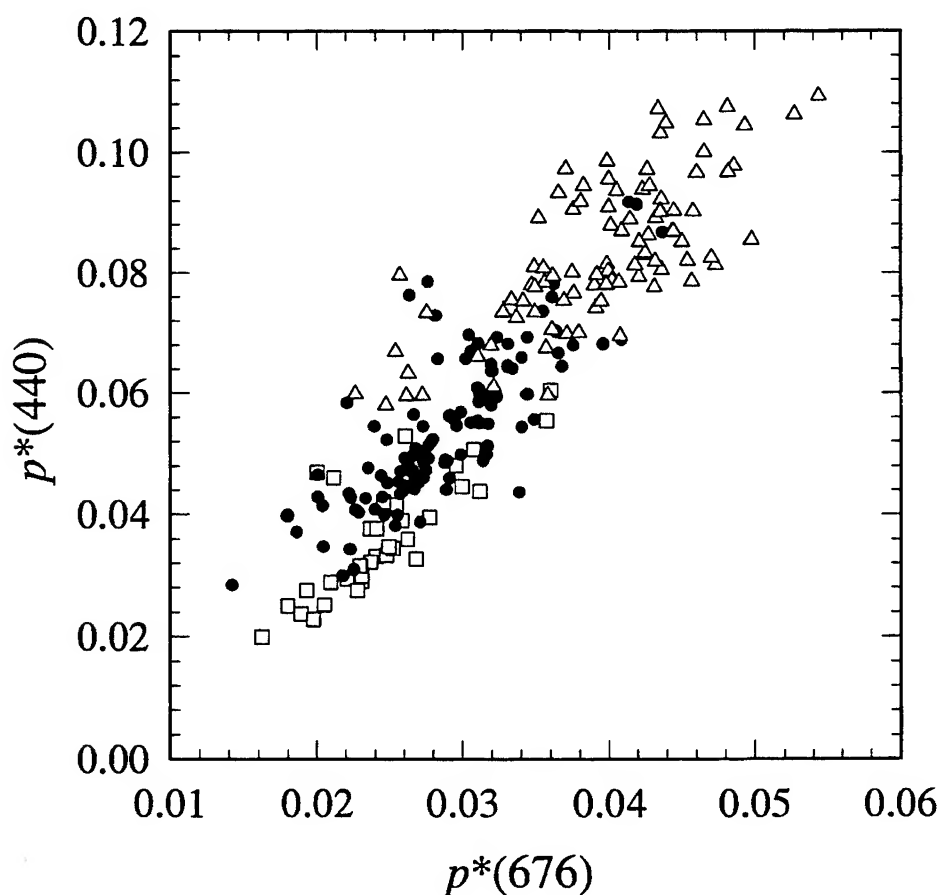


Fig. 1. Specific peak heights of chl-*a* in the blue (440 nm) versus the red (676 nm) regions of the spectrum. Vancouver cruise, open squares; Arabesque 1 cruise, solid circles; Arabesque 2 cruise, open triangles.

3.4 Pigment versus package effects

We estimated the contribution of the package effect to the total variability in the specific absorption coefficient of phytoplankton ($a_{ph}^*(\lambda)$) at the two major chl-*a* wavebands from the difference in specific peak heights ($p_i^*(\lambda)$) between cruises. Differences in peak heights may be attributed entirely to the package effect since the influence of other pigments has been systematically removed, while differences in phytoplankton absorption ($a_{ph}(\lambda)$) may be due to both the package effect plus variations in pigment composition. For the Arabesque 2 cruise, the mean $p_i^*(440)$ was 0.083 while for the Vancouver cruise it was 0.036 (a difference of 0.047). On the other hand, $a_{ph}^*(440)$, was 0.114 for the Arabesque 2 cruise and 0.046 for the Vancouver cruise (a difference of 0.068). Thus, flattening alone was responsible for 0.047/0.068 or 69% of the variability in $a_{ph}^*(440)$, with the remaining 31% being attributed to changes in pigment composition. In the same way we estimated that package effects were responsible for nearly all the change in a_{ph}^* at 676 nm (92%). Since there is a relatively small contribution by other pigments to the total absorption in this region of the spectrum (mean of 8%), the influence of accessory pigments is minimal here.

3.5 Variations in carotenoid composition

In principle, variations in absorption characteristics due to changes in pigment composition are not an issue when we are dealing with specific absorption coefficients of individual pigments. However, small changes in absorption characteristics within a Gaussian band as a result of variations in pigment composition should not be overruled, especially in those bands assigned to absorption by carotenoids. Carotenoids serve two distinct functions within the cell: i.e. harvesting light (photosynthetic carotenoids) or protecting the cells against photooxidation (non-photosynthetic carotenoids, NPC). For our data set, there was a much higher proportion of non-photosynthetic carotenoids at low ambient chl-*a* concentrations than in chlorophyll-rich waters.

We used multiple-linear regression to examine the influence of the major carotenoids on the peak height of the Gaussian bands centered around 490 nm and 532 nm, omitting samples with high total carotenoid concentrations to avoid biased data. We found that the concentrations of fucoxanthin, zeaxanthin and 19'-butanoyloxyfucoxanthin were able to explain 72 – 79% of the variance in the Gaussian peak heights. At both Gaussian bands, the coefficients obtained for zeaxanthin (a non-photosynthetic carotenoid) were much higher than the coefficients for the other photosynthetic carotenoids, especially fucoxanthin, implying that non-photosynthetic carotenoids have a much higher specific absorption. This is in agreement with known extinction coefficients of these carotenoids in ethanol and would help explain the high specific absorption coefficients obtained for the carotenoid absorption bands in the Arabesque 2 cruise (Table 1). These findings also suggest that variations in absorption coefficients at this Gaussian band may also be partially attributed to changes in the relative proportions of non-photosynthetic and photosynthetic carotenoids. However, since there is a strong (inverse) relationship between the proportion of non-photosynthetic carotenoids and chl-*a* concentration, and between chlorophyll concentration and cell size (large cells are generally found in eutrophic waters), the influence of cell size on carotenoid absorption peaks cannot be ignored.

4. CONCLUDING REMARKS

Changes in the package effect with cell size were responsible for most of the variability in peak heights of the two major chl-*a* absorption bands. At the carotenoid absorption band, variations in the specific absorption coefficients were partially attributed to changes in the relative proportions of photosynthetic and non-photosynthetic pigments. However, we should not rule out the possibility that there may also be species-dependent differences in absorption coefficients for the various

pigment-protein complexes, which would account for some of the scatter in our data.

We estimated that the package effect was responsible for 69% of the variability in absorption at 440 nm, while changes in pigment composition were responsible for the remaining 31%. Since our study incorporates a wide range of cell sizes, from minute prochlorophytes (0.5μ in diameter) to large diatoms (up to 45μ in length), one would expect that the role of flattening would be of major importance in the variability of $a_{ph}^*(\lambda)$. We have assumed that package effects are predominantly caused by changes in cell size of the phytoplankton populations between the cruises, although package effects may also be attributed to variations in the intracellular pigment concentration, often through photoacclimation responses.

Large variations in the optical characteristics of the phytoplankton assemblages, attributed to changes in cell size and community composition, may have far-reaching implications. For example, Sathyendranath, *et al.*⁶ found that strong differences in the chl-specific absorption coefficients between the intermonsoon (Arabesque 2) and monsoon (Arabesque 1) cruises were responsible for substantially increasing the maximum quantum yield for photosynthesis during the monsoon season and could explain the occurrence of the phytoplankton blooms observed in the Arabian Sea following the start of the monsoon season. Changes in the parameters of the photosynthesis-light curve alone (α^B , the initial slope and P_m^B , the assimilation number) could not account for the incidence of these blooms.

5. ACKNOWLEDGMENTS

The work presented in this paper was supported, in part, by the Office of Naval Research, U.S.A and the Department of Fisheries and Oceans, Canada. Additional support was provided by the Natural Sciences and Engineering Research Council through operating grants to S.S. This work was carried out as part of the Canadian contribution to the Joint Global Ocean Flux Study (JGOFS).

6. REFERENCES

1. E.J.H. Head and E.P.W. Horne, "Pigment transformation and vertical flux in an area of convergence in the North Atlantic", *Deep-Sea Res. II.* **40**, 329-346 (1993).
2. C.S. Yentsch, "Measurement of visible light absorption by particulate matter in the ocean", *Limnol. Oceanogr.* **7**, 207-217 (1962).
3. B.G. Mitchell and D.A. Kiefer, "Determination of absorption and fluorescence excitation spectra for phytoplankton". In: *Marine Phytoplankton and Productivity*, O. Holm-Hansen, L. Bolis and R. Giles (eds.) pp. 157-169, Springer-Verlag, Berlin, (1984).
4. N. Hoepffner and S. Sathyendranath, "Effect of pigment composition on absorption properties of phytoplankton", *Mar. Ecol. Prog. Ser.* **73**, 11-23 (1991).
5. V.A. Lutz, S. Sathyendranath, and E.J.H. Head, "Absorption coefficient of phytoplankton: Regional variations in the North Atlantic", *Mar. Ecol. Prog. Ser.* **135**, 197-213 (1996).
6. S. Sathyendranath, V. Stuart, B.D. Irwin, H. Maass, G. Savidge, L. Gilpin, and T. Platt, "Seasonal variations in bio-optical properties of phytoplankton in the Arabian Sea", *Deep-Sea Res.* In press. (1996).

Spatial variability in optical properties of the waters around the Ambrose light tower

Ajit Subramaniam, Kirk Waters, Edward Armstrong

**Technology Planning and Management Corporation
NOAA Coastal Services Center
2234 Hobson Avenue, Charleston SC 29405**

John Brock

**NOAA Coastal Services Center
2234 Hobson Avenue
Charleston, SC 29405**

Robert Ranheim

**New York City Department of Environmental Protection
Wards Island, Room 213
New York, NY 10035**

ABSTRACT

The Ambrose Light Tower, situated at the New York Bight Apex near the entrance to New York Harbor, will be equipped with a suite of optical instruments designed to make high temporal resolution optical measurements. The resulting measurements of subsurface upwelling radiance and downwelling irradiance, spectral absorption and attenuation will be used to validate algorithms for retrieval of chlorophyll biomass and k_{490} from satellite data in case II waters.

The Hudson River, a major source of freshwater to the coastal ocean of the northeastern United States flows into the New York Bight Apex and has a very well defined buoyant freshwater plume that can be as large as 500 km². Optical measurements of spectral absorption, attenuation, upwelling radiance and downwelling irradiance were made across the plume during a cruise in May 1996 during a period of high discharge. These showed that there was a 5 fold increase in absorption and attenuation inside the plume. The plume could be seen in reflectance difference images constructed using bands 1 and 2 of the AVHRR.

Keywords: Hudson river plume, New York Bight Apex, Ambrose light tower, spatial variability, coastal water optics, validation of case II algorithms, absorption, attenuation, reflectance difference, AVHRR

1. INTRODUCTION

The coastline along the New York Bight is home to more than 20 million people. Green tides, red tides, and other strange phytoplankton blooms are recurrent features throughout the New York Bight, particularly off the New Jersey coast¹. The economic impact of these phytoplankton blooms are difficult to quantify but have lead to beach closures and fish kills due to hypoxia. Hypoxia events in the New York Bight Apex, especially in the Christiaensen Basin have been identified as major concerns to the health and management of this ecosystem². These phytoplankton blooms could be caused by nutrient enrichment due to either anthropogenic activity or as response to natural events such as coastal upwelling or a combination of both. The exact frequency, location, and causes of these events are poorly understood. Ocean color satellites are ideal instruments for routine monitoring of phytoplankton biomass and primary production since they cover large areas synoptically and at regular intervals. However, determining chlorophyll biomass from ocean color satellite data has had very limited success in "case II" waters such as the New York Bight that have high concentrations of colored dissolved organic material and suspended solids.

The National Data Buoy Center will be outfitting the Ambrose Light Tower, situated near the entrance to New York Harbor, with a suite of instruments designed to make high temporal resolution optical measurements of the underwater light field (C. Woody, personal communication). These measurements of subsurface upwelling radiance and downwelling irradiance, spectral absorption and attenuation will be used to validate the case II algorithms. The optical variability of the waters in the New York Bight Apex is not well known. The Hudson River, a major source of freshwater to the coastal ocean of the northeastern United States flows into the New York Bight Apex. We anticipated that this freshwater plume has optical properties quite different from the surrounding oceanic continental shelf waters. It will be necessary to characterize the optical properties of the plume and surrounding waters to use the high resolution optical data for validation of satellite algorithms.

2. METHODS

Scientists from the Coastal Remote Sensing program at the NOAA Coastal Services Center organized a research cruise in this area on 14 and 15 May 1996 in cooperation with scientists from the National Data Buoy Center and the New York City Department of Environmental Protection. Ten stations were occupied, five on each day (Figures 1a & b). Measurements at each station included profiles of the downwelling irradiance at 380, 412, 443, 490, 510, 555 nm, PAR, upwelling radiance at 380, 412, 443, 490, 510, 555, 683 nm, temperature, beam attenuation, and chlorophyll fluorescence. Measurements were also made of surface temperature, salinity, spectral absorption and attenuation (Figures 2 & 3). The remote sensing reflectance was calculated from the measurements of upwelling radiance and downwelling irradiance just below the surface (Figure 4).

3. DISCUSSION AND SUMMARY

The reflectance difference images (Figures 1a & b) do not map the entire extent of the Hudson river plume, they show only the most turbid waters. The extension of the highly turbid waters to the Ambrose light tower occurred on only eight days of the twelve clear AVHRR images for the month of May, 1996. This is consistent with other observations³ that the direction and extent of the plume was influenced by local wind stress, prevailing shelf currents, tides and the rate of discharge. The plume was described as being very dynamic, reversing itself in less than six hours due to changes in local wind stress³.

The surface absorption and attenuation measurements were well correlated with surface temperature and salinity, demonstrating that the freshwater plume had distinct optical properties. Track AT2 showed the sharp increase in absorption and attenuation as the boat steamed from a station dominated by continental shelf water, up the Hudson river. At some stations (especially 1A) the colored dissolved organic material completely absorbed all upwelling radiance below 443 nm. Station 1B, inside New York Harbor, appeared to have a very high beam attenuation, due to both high chlorophyll and sediments. These results show that the Hudson river plume forms quite a sharp front that moves rapidly in the New York Bight Apex, past the Ambrose light tower. These results suggest that local optical variability due to the Hudson river plume must be considered in any efforts to use optical measurements at the Ambrose light tower for validation of case II bio-optical algorithms. This optical variability also provides the opportunity for fusing of data from different satellite sensors to examine problems such as sub-pixel variability.

5. REFERENCES

1. J. Ohla, "Novel algal blooms: common underlying causes with particular reference to New York and New Jersey coastal waters," M.S. thesis, Marine Sciences Research Center, SUNY at Stony Brook, NY 11794-5000, 1990.
2. R.L. Swanson, T.M. Bell, J. Kahn and J. Ohla, "Use impairments and ecosystem impacts of the New York Bight," *Chemistry and Ecology*, 5, 99-127, 1991.
3. M. Bowman, "Spreading and mixing of the Hudson river effluent into the New York Bight," *Hydrodynamics of Estuaries and Fjords*, J.C.J. Nihoul, 373-385, Elsevier Scientific Publishing Company, Amsterdam, 1978.

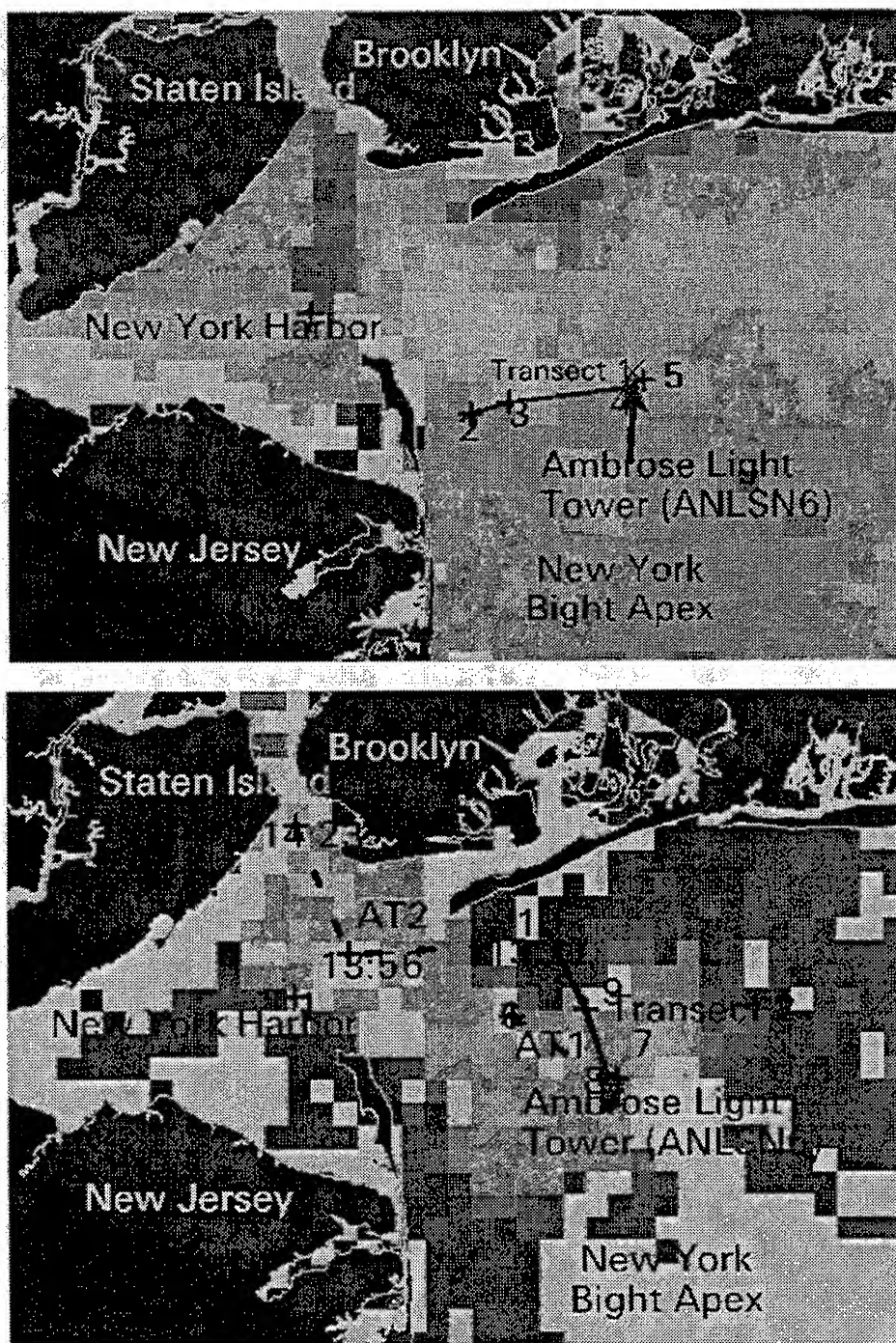


Figure 1: Reflectance difference image calculated using bands 1 and 2 of the AVHRR⁴ on board NOAA14 for 14 (a) 15 (b) May 1996. The turbid water associated with the Hudson River plume has a higher reflectance difference. The location of the stations occupied is shown, as is the Ambrose Light Tower. AT1 and AT2 in Fig. (b) refer to the along track surface absorption and attenuation measurements shown in Figures 2 & 3.

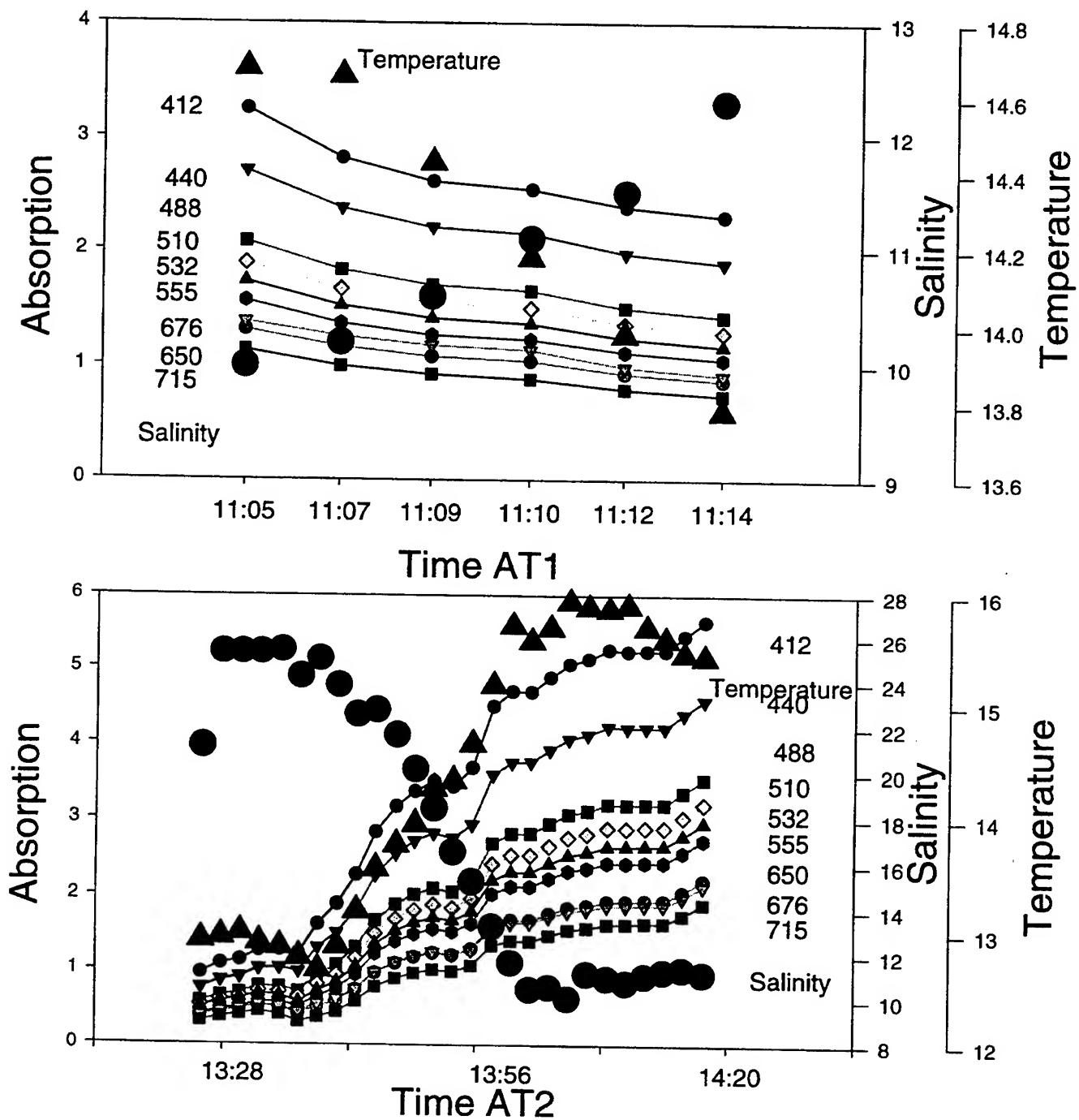


Figure 2: Surface absorption measured by an AC-9 attached to the vessel's flow-through system. AT1 was a transect between stations 6 and 7. AT2 was a transect from station 10 back to port. Note the sharp increase in absorption as the vessel entered the center of the plume at 13:56.

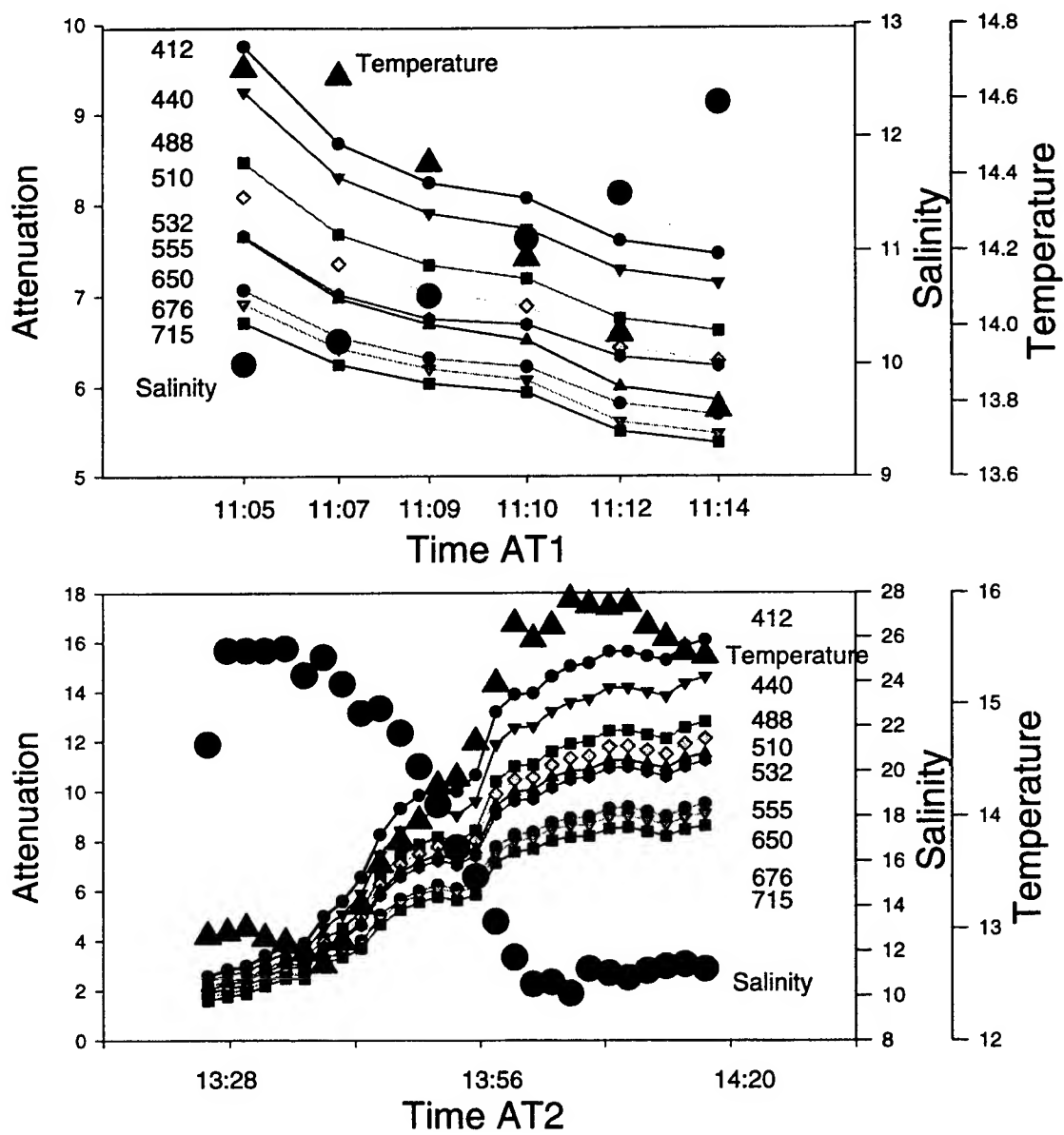


Figure 3: Same as Figure 2, but showing surface attenuation.

Subsurface Reflectance

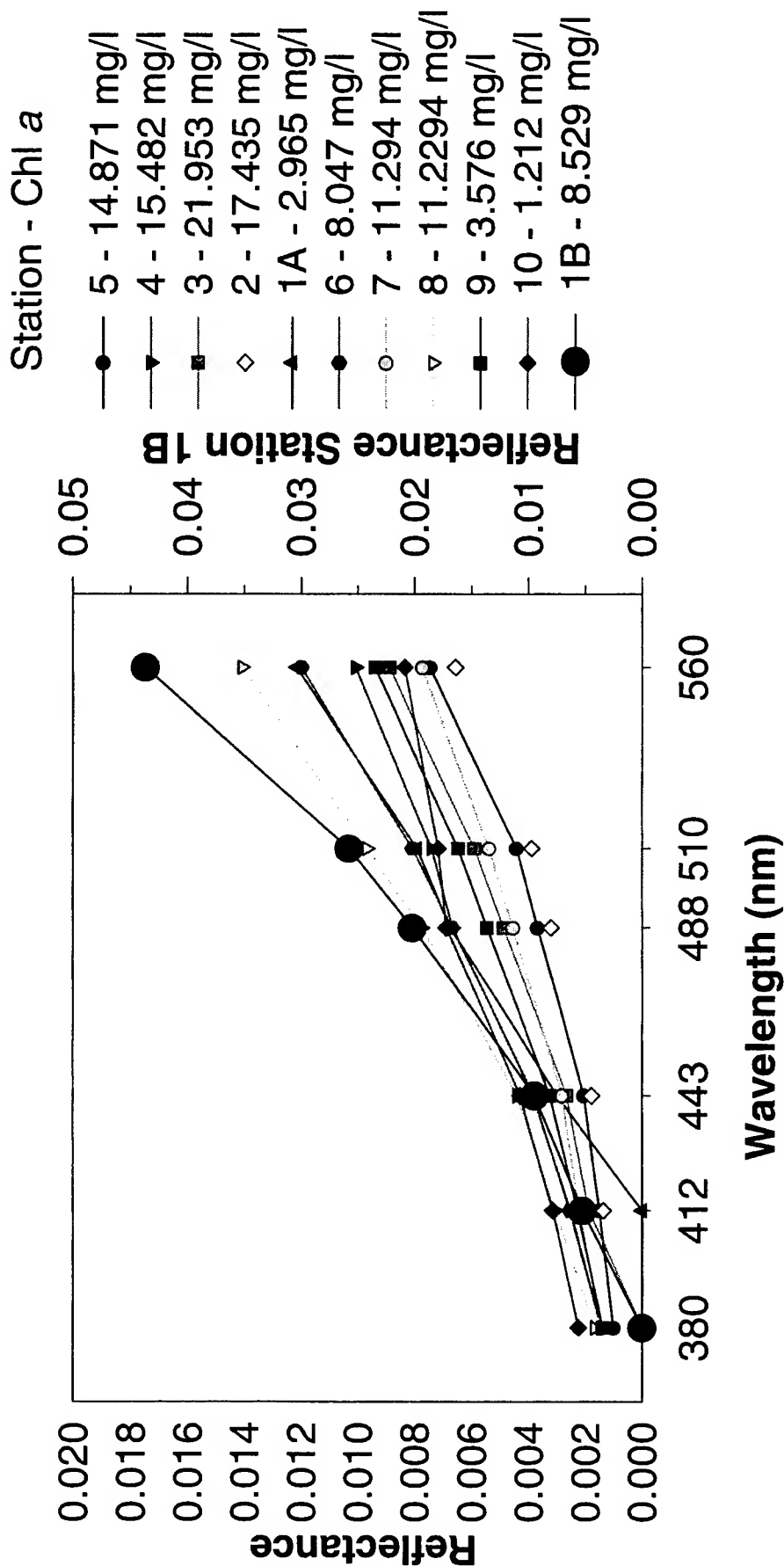


Figure 4: Subsurface remote sensing reflectance calculated for each station as a ratio of upwelling radiance to downwelling irradiance. The station name and the chlorophyll concentration measured at that station is also indicated. Note that the reflectance for station 1B is referenced to the scale on the right. While the reflectance for all other stations ranged from 0-0.015, the reflectance for station 1B ranged from 0-0.045.

Effects of suspended sediment concentration on the absorption and scattering coefficients

Gregory Terrie

Naval Research Laboratory, Code 7243, Stennis Space Center, MS 39529

Sherwin Ladner and Richard Gould

Planning Systems, Inc., 115 Christian Lane, Slidell, LA 70458

ABSTRACT

The scattering coefficient (b) for the nearshore waters off the coast of North Carolina near Camp Lejeune is strongly influenced by suspended sediment concentration and total particulate cross-sectional area (x_g). In-situ measurements of a and b were made using a WET Labs AC9 meter. Estimates of suspended sediment concentration and total particulate cross-sectional area were determined from laser particle size analyses of surface water samples. The SeaWiFS bio-optical algorithm was modified for Case II waters and used to estimate a and b_b from remote sensing reflectance (R_{rs}). After conversion from backscattering (b_b) to total scattering (b), modeled a and b values from the modified SeaWiFS algorithm were compared to the measured values. The differences between the measured and estimated values appear to be directly related to increases in suspended sediment concentration and x_g . Correlations of about 0.90 were obtained for b vs x_g and b_b vs x_g .

Keywords: water optical properties, suspended sediment concentration, particle size distribution

2. INTRODUCTION

In-situ optical measurements were collected on April 25, 1996, at 18 stations in the nearshore coastal waters off the coast of North Carolina near Camp Lejeune. These waters contained areas with high surf conditions where resuspended sediments produce a very high scattering environment. DOM concentrations and the absorption coefficients were relatively low in this area. The measurements included, remote sensing reflectance (R_{rs}), absorption (a), beam attenuation (c) of the water. Additionally, surface water samples were also collected at 10 of the 18 stations, which were analyzed to determine particle size distribution and suspended sediment concentration. The data collected in this exercise will support ongoing satellite and airborne remote sensing applications for estimating and modeling surface water optical properties. The Case II waters found in this region are characterized by strong signals of suspended sediments and inorganic particles with a high degree of variability. This variability is believed to be strongly associated with the physical processes occurring in the littoral environment.

The objective of this paper is to characterize how the suspended sediments influence the inherent optical properties of scattering and absorption in Case II waters. Because these

IOP's are important for remote sensing algorithms, we apply the $R_{rs} = C b_b/a$ relationship to a high scattering, low absorption environment.

3. MEASUREMENTS

3.1 Absorption, beam attenuation, and scattering

The inherent optical properties, a and c , were measured using a WET Laboratories, Inc. AC9 instrument at $\lambda = 412, 440, 488, 510, 532, 555, 650, 676$, and 715 nm. Scattering is obtained from the difference between c and a . Following the algorithm suggested by Zaneveld¹ et al, a scatter correction is applied to the absorption measurements. The AC9 was used to profile the water column, but, only the near surface measurements are examined in this paper.

3.2 Remote sensing reflectance

The R_{rs} measurements were acquired using an Analytical Spectral Devices (ASD) VNIR 512 FieldSpec spectral radiometer. The ASD measures radiance at 512, 1.4 nm bands in the 350-1100 nm range. Spectral measurements of the sky (S_s), water (S_{w+s}), and calibrated reflectance standard (S_g) were made by the ASD. R_{rs} will be computed according to equation (1):

$$R_{rs} = \frac{S_{w+s} - 0.021 * S_s}{\pi * S_g / r_g} \quad (1)$$

Note that r_g is the known reflectance of the calibrated reflectance standard. R_{rs} will be related to a and backscattering (b_b) according to the SeaWiFS algorithm developed by Lee et al².

3.3 Particle size analysis

Surface water bottle samples were analyzed for particulate size distributions and suspended sediment concentrations using a Spectrex Laser Particle Counter (LPC). The system employs forward scattering interference pattern analysis to enumerate and size the particles into 32 size bins from 1 - 99 μm . The results of this analysis will provide not only the total suspended sediment concentration but also the total cross sectional area (x_g) of the particles as well. This parameter is related to the volume scattering function (β) and therefore b .

4. ALGORITHMS

The SeaWiFS bio-optical algorithm developed by Lee et al² was modified to output total a and b_b from R_{rs} . Note that this algorithm is more applicable in Case I waters where the R_{rs} signal is dominated by chlorophyll absorption and less by particulates and suspended sediments. Simply stated, R_{rs} is related to a and b_b by

$$R_{rs} = C \frac{b_b}{a} \quad (2)$$

Generally, C is considered a constant that is independent of wavelength, however, more recent studies have suggested that this "constant" varies with water turbidity and wavelength³. Furthermore, b_b is difficult to measure directly and is not always directly related to b . Arnone et al⁴ indicate that for Case II waters b_b/b may be constant and b can be related to the cross sectional area of particulates (x_g). By exploiting the relationship between x_g and b , a relationship between x_g and b_b can be determined, thus a direct relationship between the concentration of particulates and backscattering and ultimately R_{rs} will be established.

5. RESULTS

The highest concentrations of suspended sediments particles were observed at those stations closest to shore (i.e. 8, 9, 14). The x_g results as shown in figure 1 show a similar result. AC9 measurements of b showed strong correlation with changes in sediment concentration and x_g (i.e. $r^2 \approx 0.90$). Likewise, variability in the magnitude and shape of R_{rs} spectra was also seen.

The total absorption and backscattering coefficients derived from R_{rs} using the SeaWiFS algorithm were compared to the AC9 measured a and b_b for each of the 18 stations. Note that b_b was estimated from b using Petzold's relationship⁵. In general, measured and modeled absorption values agreed closely with low sediment loads, but differed increasingly as sediment concentrations increased, particularly in the blue wavelengths. Likewise, measured and modeled backscattering coefficients differed according to the amount of sediments present. At stations 1, 11, and 12, where the concentrations of sediments was relatively low, good agreement was achieved for both a and b_b .

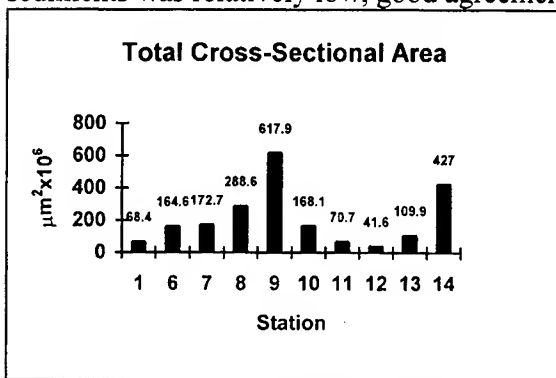


Figure 1. Total cross-sectional area (x_g) results from Laser Particle Counter measurements at Camp Lejeune, NC.

As illustrated by figure 2, a near linear relationship exists between b_b and x_g with $r^2 \approx 0.90$ for all wavelengths. The slopes of the regression lines varied slightly with wavelength with the average about 0.028. Rewriting equation (2) in terms of x_g gives

$$R_{rs} = C' \frac{x_g}{a} \quad (3)$$

where $C' = C \cdot G$, and $G = b_b/x_g$. A linear relationship, C' , does exist between R_{rs} and x_g/a that varies with wavelength as illustrated in figure 3. Knowing C' and G we can now solve for C . The values of C

ranged from 0.022 to 0.033, thus illustrating that C is not a constant, but is wavelength dependent.

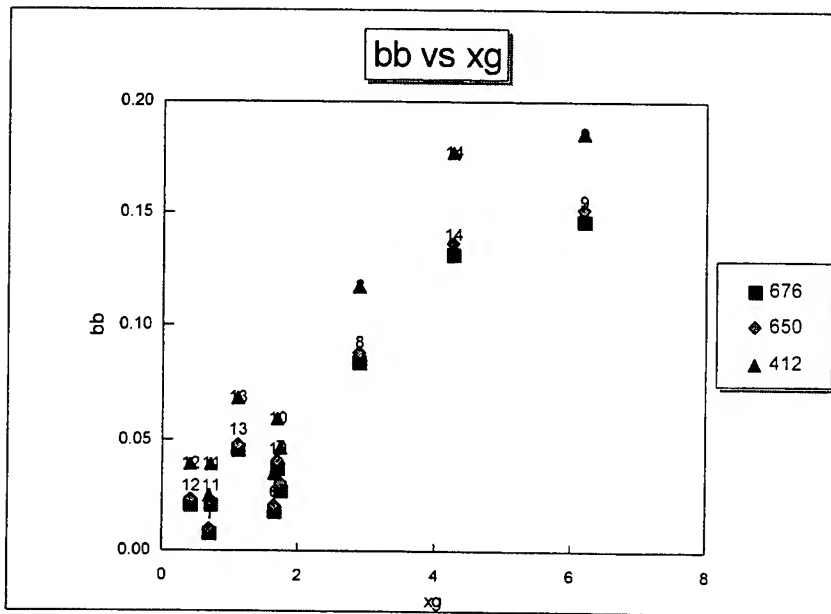


Figure 2: : b_b and x_g are linearly related with $r^2 = 0.90$. The slope varies slightly with wavelength.

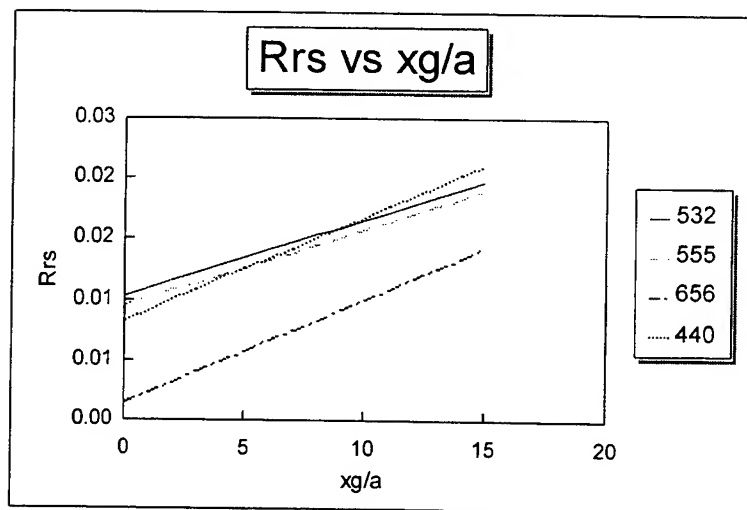


Figure 3 The regression lines for $R_{rs}(\lambda)$ vs x_g/a for $\lambda=440, 532, 555$, and 656 .

6. CONCLUSIONS

This paper illustrates the influence that the concentrations of suspended sediments and particulate cross-sectional area have on the changes in the IOP's of Case II waters. The total cross-sectional area of the particles correlated quite well ($r^2 \approx 0.90$) with the backscattering coefficient for all wavelengths. This suggests that the DOM and phytoplankton absorption was low for this data set and the particulate scattering was dominant. This relationship was extended to R_{rs} and x_g . We observed high correlations between R_{rs} and x_g since absorption was minimized. The nature of the constant C (equation 2), in the SeaWiFS algorithm, was shown to be wavelength dependent for the Case II waters. This suggests that ratios of spectral channels should be examined further for Case II waters.

7. ACKNOWLEDGMENTS

The authors wish to thank R. Arnone and M. Sydor for their insight and contributions to this work. This work was performed for the NRL Spectral Signatures ARI and sponsored by ONR Program Element 61153N 31.

8. REFERENCES

1. Zaneveld, J.R.V., J.C. Kitchen and C.C. Moore, "Scattering error correction of reflecting tube absorption meter," *Ocean Optics XII, Proc. Soc. Photo-Optical Instrum. Eng. (SPIE)*, Vol. 2258, pp. 44-55, 1994.
2. Lee, Z.P., K.L. Carder, S.K. Hawes, R.G. Steward, T.G. Peacock, and C.O. Davis, "A model for interpretation of hyperspectral remote-sensing reflectance," *Appl. Opt.* **33**, 5721-5732, 1994.
3. Morel A., B. Gentili, "Diffuse reflectance of oceanic waters III: Implication of bidirectionality for the remote sensing problem," *Appl. Opt.* **35**, 4850-4862, 1996.
4. Arnone R., M. Sydor, R. Gould, "Remote sensing reflectance in case 2 waters," *Ocean Optics XIII, Proc. SPIE*, 1996.
5. Petzold, T.J. *Volume Scattering Functions for Selected Ocean Waters*, SIO Ref. 72-78, 79 pp. 1972.

How do coccoliths affect light in the sea?

Toby Tyrrell and Patrick M. Holligan

Southampton Oceanography Centre, Southampton University,
European Way, Southampton SO14 3ZH, UK.

ABSTRACT

Recent work has characterised the effect of coccoliths on the scattering coefficient at different wavelengths^{1,2}. This relationship has now been used in a sophisticated multi-component, multi-spectral Monte Carlo optical model to estimate the effects of coccoliths on scalar irradiance, heating rate, vertical attenuation rate and emergent flux. The main effects of the coccoliths are outlined, and implications of these effects for phytoplankton productivity and biogeochemistry are discussed.

Keywords: coccoliths, *Emiliana huxleyi*, phytoplankton, coccolithophores, optics, light, scattering, blooms, white waters, energy trapping.

1. INTRODUCTION

Coccolithophores are phytoplankton which produce calcium carbonate platelets called coccoliths in a layer around the surface of the cell. Coccoliths are important for ocean optics because they act somewhat like little mirrors, causing an increase in the value of the scattering coefficient (b), without causing a consequent increase in the value of absorption coefficient (a). During coccolithophore blooms, when there are high concentrations of coccoliths in the water, extreme optical effects can be produced due to high (b/a) ratios. These optical effects manifest themselves (1) within the top 2-3m of the water (brighter, warmer water), (2) in deeper water (intense shading leading to darker cooler water), (3) above the water with the appearance to ship-board observers of 'white waters', and (4) in space (remote sensing of blooms).

Coccolithophores are widespread, present in all oceans except the polar ones³. However, bloom proportions ($> 1,000$ cells ml^{-1}) are only attained in a few areas, most notably the subarctic North Atlantic and adjacent seas⁴, and most blooms are of the species *Emiliana huxleyi*. Blooms of this species can cover large areas of over 100,000 km^2 (ref 4), with significant environmental impacts: via increased water albedo (reflectance), altered air-sea heat fluxes, DMS production and cloud albedo, large fluxes of calcium carbonate out of the surface waters and changes in the oceanic uptake of CO_2 .

Previous work has estimated the spectral variation of the impact of coccolith calcite on b (fig 8, ref 1), and the variation in b with calcite concentration at 440 and 550nm (ref 2). These data are for coccoliths of *Emiliana huxleyi*. During blooms of *Emiliana huxleyi*, many coccoliths become detached from the cell surfaces and are left to float independently in the water. The free-floating coccoliths have been thought to contribute more strongly to the scattering than the coccoliths still attached to cells, but it has recently been calculated that particulate inorganic carbon (PIC), i.e. calcite, is a better predictor of the amount of scattering than is detached coccolith number². In this work, the relationships between calcite concentration and b are used to set some parameter values in a sophisticated Monte Carlo model, in order to estimate the effects of coccoliths on in-water irradiances and other optical properties.

2. MODEL DESCRIPTION

2.1 Model structure

A multi-spectral, multi-component Monte Carlo model was constructed in order to examine coccolith optical impacts. The model is based on Kirk's simple multi-spectral model⁵, but has been improved in several ways. The equations have been modified to calculate azimuth as well as zenith angles of photons in the water (making it 3D rather than just 2D), and more components (including coccoliths) have been added to the factors affecting a and b . Incoming irradiance from above the sea surface has been changed from a simple point source representing the sun to a full representation of the skylight (diffuse light) in addition to the direct solar beam. This has been implemented exactly according to the formula of Harrison & Coombes⁶, which takes account of sun zenith angle

and cloud cover to calculate the full 3D radiance distribution of the light arriving at the sea surface from the atmosphere.

Kirk's basic model was also extended by the inclusion of a wind-roughened sea surface, to replace the original flat sea surface. This was achieved by generating wave facets with slopes chosen probabilistically from a distribution dependent on the wind speed, but not dependent on the wind direction, according to the formula⁷:

$$\sigma^2 = 0.003 + 0.00512 \times U \quad (1)$$

where σ is the standard deviation of the normal distribution of wave slopes ($N = 0.0$), and U is the wind speed (m s^{-1}). This formula, together with consideration of the 'apparent area' of a facet when looking along the line of travel of a particular photon (for instance, a facet whose normal is perpendicular to the incoming photon has no chance of intercepting it), was used to generate probabilities of photons at different orientations impinging on wave facets at different orientations. Once a photon was matched to a wave facet using a random number, Fresnel's Formula was then applied to calculate the probability of reflection of the photon from the air-sea interface. The resulting reflection probabilities (averaging over many photons) for photons travelling from air to sea and from sea to air, and at different angles to the vertical, and at different wind speeds, agree well with the desired probabilities (fig 2.10, ref 8; fig 4.3, ref 9).

2.2 Inherent optical properties (IOPs)

Contributions to absorption and scattering are summed to give the values of the total absorption and scattering coefficients. The absorption coefficient ($a(\lambda)$) in the model is calculated as

$$a(\lambda) = a_w(\lambda) + (chl \times a_{chl}(\lambda)) + a_g(\lambda) + a_d(\lambda) \quad (2)$$

where $a_w(\lambda)$ is the contribution due to pure seawater at each wavelength, chl is the concentration of chlorophyll-*a*, $a_{chl}(\lambda)$ is the effect on absorption of $1 \text{ mg chl-}a \text{ m}^{-3}$, $a_g(\lambda)$ is the contribution due to gilvin, and $a_d(\lambda)$ is the contribution due to detritus.

The scattering coefficient at each wavelength ($b(\lambda)$) is similarly calculated as

$$b(\lambda) = b_w(\lambda) + (CaCO_3 \times b_{CaCO_3}(\lambda)) + (chl \times b_{chl}(\lambda)) + b_p(\lambda) \quad (3)$$

where $b_w(\lambda)$ is the very small contribution due to pure seawater at each wavelength, $b_{chl}(\lambda)$ is the effect on scattering of $1 \text{ mg chl-}a \text{ m}^{-3}$, $CaCO_3$ is the concentration of calcite in the water, $b_{CaCO_3}(\lambda)$ is the effect on scattering of $1 \text{ mg CaCO}_3 \text{ m}^{-3}$, and $b_p(\lambda)$ is the contribution due to other particulates.

The contributions of pure seawater to a and b at different wavelengths are taken from ref 10, the spectral variations in impact of $1 \text{ mg chl-}a \text{ m}^{-3}$ on a are taken from ref 11, and the spectral variations in impact of $1 \text{ mg chl-}a \text{ m}^{-3}$ on b are calculated as $(118.0 \times \frac{1}{\lambda})$. Absorption due to gilvin is calculated according to the equation in Table 1, scattering due to non-coccolith particulates is calculated as $(90.0 \times \frac{1}{\lambda})$, and contributions from other minor components are calculated based on descriptions and data in ref 8. Coccolith impacts on b are calculated using data in refs 1 and 2, as discussed above. A standard particle scattering phase function (column 6, Table 3.10, ref 9) is used for all scattering components. A homogeneous mixed layer is assumed.

2.3 Tests of model

Numerous aspects of the photon dynamics in the model were checked (including generating full radiance plots at many different depths under several different conditions). The model was also tested for some canonical water cases to check that it gave the same results as other tried and tested models in a published comparison¹², which it did. Finally, the *HYDROLIGHT* model¹³, an invariant imbedded (mathematical) model rather than a ray tracing Monte Carlo one, was installed and given the same IOPs as the Monte Carlo one. The Monte Carlo and *HYDROLIGHT* results (all irradiances and apparent optical properties) compared favourably for the situation described in Table 1, with a high coccolith concentration. Because the results from the two very different modelling approaches show the same phenomena, and are numerically similar, we can be more confident of their veracity.

Parameter	Value	Reference
Sun zenith angle (θ)	37°	standard formula
Cloudiness	0.0 (no cloud)	(fig 1a, ref 14)
Wind speed	7 m s^{-1}	(fig 1b, ref 14)
Incident irradiance ($E_d(\text{PAR})$)	$1500 \mu\text{Ein m}^{-2} \text{ s}^{-1}$	(BOFS CD-ROM)
Chlorophyll- <i>a</i>	$1.0 \text{ mg chl-}a \text{ m}^{-3}$	(fig 6a, ref 15; fig 5a, ref 14)
Absorption due to gilvin ($a_g(\lambda)$)	$0.05 \times e^{-0.0135 \times (\lambda - 400)}$	(section 3.3, table 3.2, ref 8)

Table 1: Water parameters for NE Atlantic ($60^\circ\text{N}, 20^\circ\text{W}$) during typical day in June, 1991. BOFS is the Biogeochemical Ocean Flux Study.

3. MODEL RESULTS FOR TYPICAL COCCOLITHOPHORE BLOOM

3.1 Water parameters for typical bloom

The effects of a given concentration of coccoliths on optics are dependent on other parameters of the water: sun zenith angle, cloudiness, chlorophyll and wind speed, among other factors. Model results are shown here for one particular set of conditions (one set of parameter values), representative of the water state during the most thoroughly studied natural coccolithophore bloom -- one of *Emiliana huxleyi* which occurred south of Iceland in June, 1991¹⁵. Blooms of *Emiliana huxleyi* frequently occur in this part of the Atlantic Ocean during June and July⁴. This bloom in 1991 was extensive ($\sim 250,000 \text{ km}^2$), with high concentrations of coccoliths (up to $300,000 \text{ coccoliths ml}^{-1}$, up to $350 \text{ mg CaCO}_3 \text{ m}^{-3}$) (ref 15). More intense blooms can occur in other areas, in particular in the Norwegian fjords.

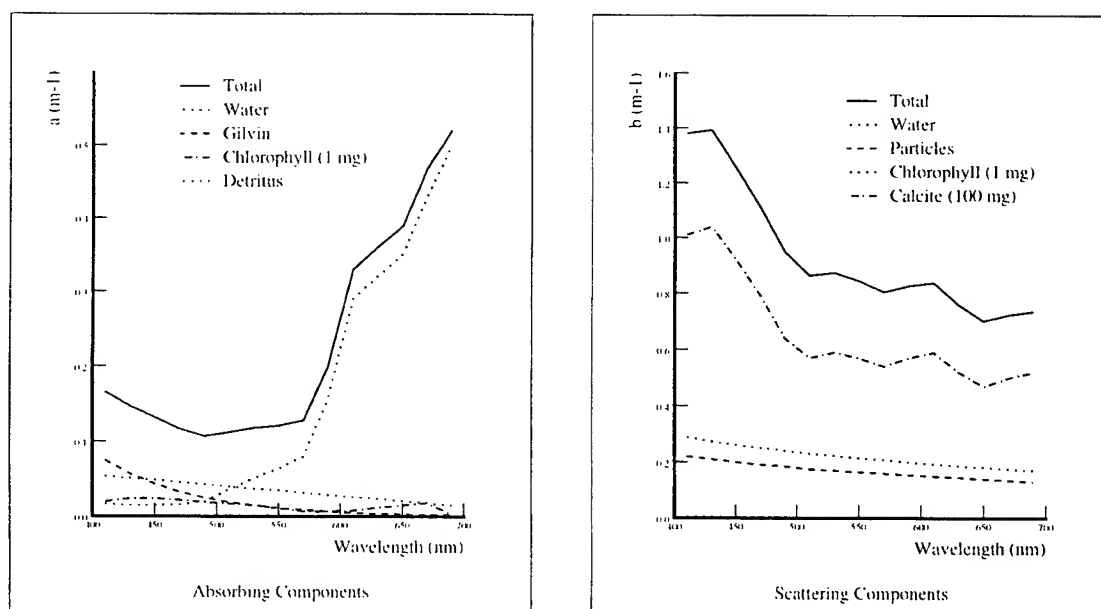


Figure 1: Inherent optical properties: **(a):** variation of a with λ , with $1.0 \text{ mg chl-}a \text{ m}^{-3}$; **(b):** variation of b with λ , with $1.0 \text{ mg chl-}a \text{ m}^{-3}$ and $100 \text{ mg CaCO}_3 \text{ m}^{-3}$. Both graphs show contributions from individual components (dashed, dotted and stippled lines) together with the total (solid line). $a_w(\lambda)$ is the generally higher of the two dotted lines in (a); $b_w(\lambda)$ is the lower of the two dotted lines in (b), almost completely obscured by the x -axis. Note the different y -axis scales in (a) and (b).

Scalar Irradiance vs. Depth

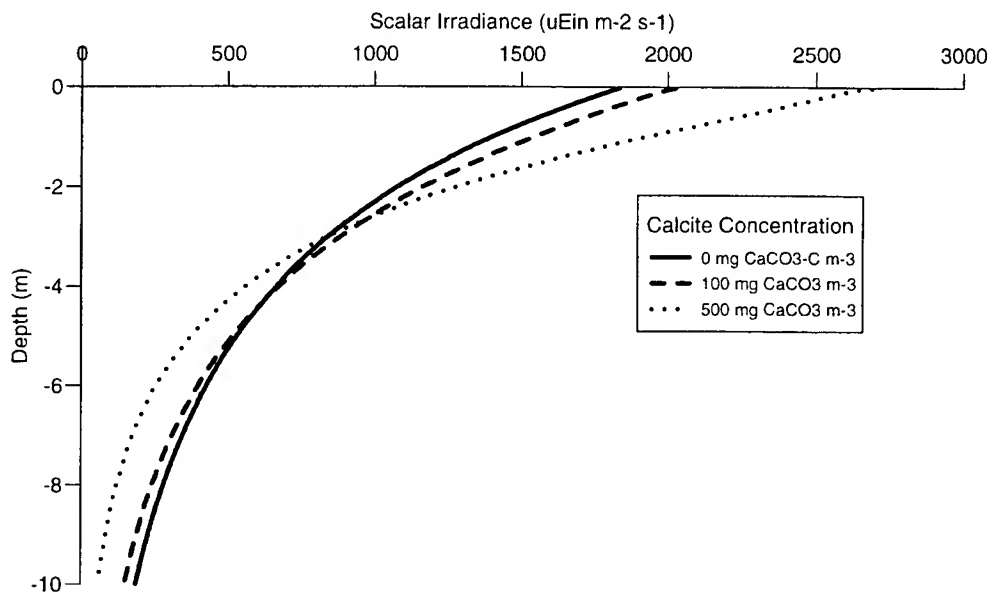


Figure 2: Scalar irradiance depth profiles for a typical NE Atlantic mid-summer water state with different concentrations of coccolith calcite. The solid line shows the scalar irradiance profile for 0 mg $\text{CaCO}_3 \text{ m}^{-3}$; the dashed line for water containing 100 mg $\text{CaCO}_3 \text{ m}^{-3}$; and the dotted line for water containing 500 mg $\text{CaCO}_3 \text{ m}^{-3}$.

The parameter values used in the model to represent these conditions are shown in Table 1. Only one parameter was varied to produce different model runs: the concentration of calcite, i.e. coccoliths. The values of a and b in the model at different wavelengths are shown in Figure 1, with the scattering being that obtained with 100 mg $\text{CaCO}_3 \text{ m}^{-3}$ in the water.

3.2 Model results

Figure 2 shows three model scalar irradiance (E_0) depth profiles, for different concentrations of coccoliths. As the concentration of coccoliths increases it can be seen that (1) light intensities near the surface (top 2-3m) increase, in accordance with the theory of *energy trapping*¹⁶ in high (b/a) surface waters, creating a super-bright zone near to the surface; (2) attenuation of light with depth is still exponential, but starts from a higher initial (surface) value; (3) light attenuation rate is increased; and (4) light intensities beneath the very surface waters (deeper than 2-3m or so) decrease. Heating rates (photon absorption by water molecules) are proportional to scalar irradiances and so possess similar profiles to those shown in Figure 2.

The vertical attenuation coefficient for downward irradiance (K_d) increases with increasing coccolith concentration. For the three cases in figure 2, $K_d(\text{PAR})$ at 5m depth was 0.22 m^{-1} with 0 mg $\text{CaCO}_3 \text{ m}^{-3}$, 0.27 m^{-1} with 100 mg $\text{CaCO}_3 \text{ m}^{-3}$, and 0.40 m^{-1} with 500 mg $\text{CaCO}_3 \text{ m}^{-3}$. Increasing coccolith concentration also causes an increased emergent flux, i.e. an increased scattering and re-emission of photons which have previously entered the water. The radiance distributions of that flux for 0 and 500 mg $\text{CaCO}_3 \text{ m}^{-3}$ are shown in figure 3. For these two cases 0.63% and 6.8% respectively of the total number of photons entering the water were reflected back out to the atmosphere again.

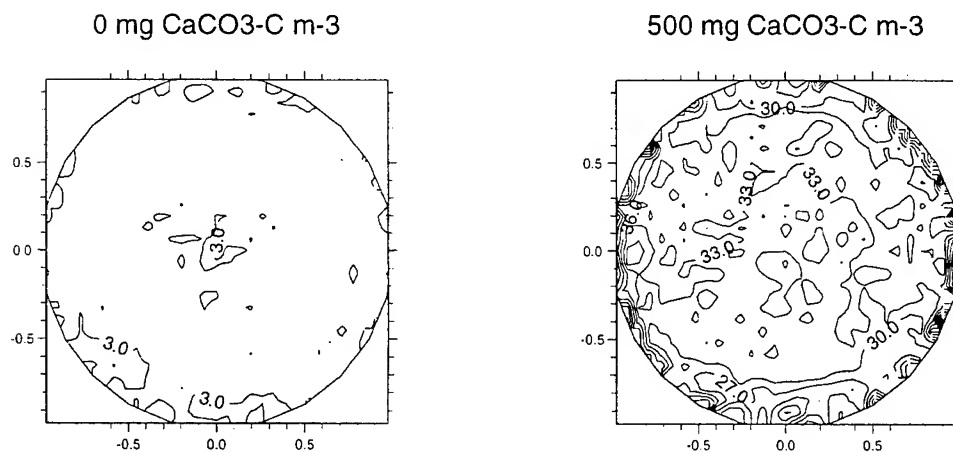


Figure 3: Emergent flux radiance distribution ($\mu\text{Ein m}^{-2} \text{s}^{-1} \text{sr}^{-1}$) for a typical NE Atlantic mid-summer water state: (a) with $0 \text{ mg CaCO}_3 \text{ m}^{-3}$; (b) with $500 \text{ mg CaCO}_3 \text{ m}^{-3}$. The contour plots show hemispherical radiance plotted in a 2D-circle, as described in ref 6. Variability in the plots is due to not averaging over enough photons in the Monte Carlo program.

3.3 Comparisons with data

Light amplification (creation of an intensely illuminated surface layer with scalar irradiances that are higher than those in the atmosphere and higher than those in clear water of the same depth) has been observed following kaolin (china clay) particle additions to a pond¹⁶, but has not been observed (mainly because very few near-surface measurements have been taken) during coccolithophore blooms. Future field work should be targetted at testing this explicit model prediction. However, increased surface heating correlated with coccolith concentration has been observed (fig 12E, ref 15), as has the intense shading of water beneath a coccolithophore bloom (fig 6A, ref 14). Increased K_d values (fig 12B, ref 17; CTD casts, BOFS CD-ROM) and increased emergent flux^{15,17} have also been observed.

4. DISCUSSION

4.1 Super-illumination of the near surface

The super-illumination of the near-surface waters during a bloom of *Emiliana huxleyi* has only been appreciated as a result of this modelling study, and full confirmation with observational data is still required. If true (and both types of model predict that it is) then this phenomena has important ramifications, for instance for the ecology of *Emiliana huxleyi*. Most blooms of *Emiliana huxleyi* occur in shallow mixed layers¹⁸, and most other phytoplankton will be even more strongly photoinhibited than normal in these thin surface layers if the light is amplified due to the presence of coccoliths. *Emiliana huxleyi* appears to be adapted to tolerate high light intensities¹⁸. Could the production and detachment of coccoliths by *Emiliana huxleyi* be a mechanism for producing conditions under which it thrives?

4.2 Changes to water heating

It has been observed that turbid reservoirs are cooler than clear ones¹⁶. Several of the coccolith-induced optical effects seem to point in this same direction: (1) reduced total energy input due to higher albedo (greater emergent flux); (2) decreased energy input to depth and increased energy input to the surface, where the heat is more easily lost again to the overlying atmosphere; and (3) production of stronger and shallower stratification due to the steeper depth gradient in heating rates, which will inhibit wind-induced mixing of warmer water to depth. It needs to be clarified how important these effects are for cooling the ocean during blooms of coccolithophores.

5. CONCLUSIONS

Coccoliths in high concentrations cause radical changes in the behaviour of light in the sea. We have used models to characterise the nature of these changes and to provide quantitative estimates of the sizes of some of these

changes under a specific set of realistic conditions. The model results show that the most notable effects of increased coccoliths are (1) light amplification in the top 2–3m; (2) light diminution further down; (3) parallel changes to the heating rates; and (4) increased emergent flux.

These changes have implications for the stratification (thermal structure) of the surface ocean, and the capacity of the ocean to accept and to retain heat energy. The changes in the light profile with depth, and the changes in stratification must also impinge heavily on phytoplankton ecology and productivity. The surface heating during a bloom also affects the partial pressure of CO_2 in the water and will thereby alter the air-sea flux of CO_2 .

6. ACKNOWLEDGEMENTS

This research is part of the UK *PRIME* funding initiative, funded by the UK Natural Environment Research Council (NERC). We would like to thank Barney Balch for assistance with the relationship between coccoliths and scattering, Gerald Moore and Jill Schwarz for discussions on the theory of optics, and Curtis Mobley for distributing *HYDROLIGHT* without charge and for assistance in installing it.

7. REFERENCES

1. Balch WM, PM Holligan, SG Ackleson, KJ Voss, "Biological and optical properties of mesoscale coccolithophore blooms in the Gulf of Maine", *Limnology & Oceanography*, **36**(4), 629–643 (1991).
2. Balch WM, KA Kilpatrick, PM Holligan, D Harbour, E Fernández, "The 1991 coccolithophore bloom in the central North Atlantic: II – relating optics to coccolith concentration", *Limnol. Oceanogr.*, in press (1996).
3. Winter A, Jordan R, Roth P, "Biogeography of living coccolithophores in ocean waters", In: *Coccolithophores*, (eds. Winter A, Siesser WG), Cambridge University Press, Cambridge, UK, pp. 161–177, 1994.
4. Brown CW, Yoder JA, "Coccolithophorid blooms in the global ocean", *Journal of Geophysical Research*, **99**(C4): 7467–7482 (1994).
5. Kirk JTO, *A Monte Carlo procedure for simulating the penetration of light into natural waters*, CSIRO Division of Plant Industry, Technical Paper No. 36, 1981.
6. Harrison AW, Coombes CA, "An opaque cloud cover model of sky short wavelength radiance", *Solar Energy*, **41**(4): 387–392 (1988).
7. Cox C, Munk W, "Measurement of the roughness of the sea surface from photographs of the sun's glitter", *Journal of the Optical Society of America*, **44**(11): 838–850 (1954).
8. Kirk JTO, *Light and Photosynthesis in Aquatic Ecosystems*, 2nd Edition, Cambridge University Press, Cambridge UK, 1994.
9. Mobley CD, *Light and Water: radiative transfer in natural waters*, Academic Press, San Diego CA, 1994.
10. Smith RC, Baker, KS, "Optical properties of the clearest natural waters (200–800nm)", *Applied Optics*, **20**(2): 177–184 (1981).
11. Morel A, Prieur L, "Analysis of variations in ocean colour", *Limnol. Oceanogr.*, **22**: 709–722 (1977).
12. Mobley CD, Gentili B, Gordon HR, Jin Z, Kattawar GW, Morel A, Reinersman P, Stamnes K, Stavn RH, "Comparison of numerical models for computing underwater light fields", *Applied Optics*, **32**(36): 7484–7504 (1993).
13. Mobley CD, *HYDROLIGHT 3.0 User's Guide*, Project Report Number 5632, SRI International, California, USA, 1995.
14. Stramska M, Dickey TD, Plueddemann A, Weller R, Langdon C, Marra J, "Bio-optical variability associated with phytoplankton dynamics in the North Atlantic Ocean during spring and summer of 1991", *J. Geophys. Res.*, **100**(C4): 6621–6632 (1995).
15. Holligan PM, E Fernández, J Aiken, WM Balch, P Boyd, PH Burkhill, M Finch, SB Groom, G Malin, K Muller, DA Purdie, C Robinson, CC Trees, SM Turner, and P van der Wal "A biogeochemical study of the coccolithophore *Emiliania huxleyi* in the north Atlantic", *Global Biogeochemical Cycles*, **7**(4): 879–900 (1993).
16. Stavn RH, FR Schiebe, CL Gallegos, "Optical controls on the radiant energy dynamics of the air/water interface: the average cosine and the absorption coefficient", *Ocean Optics VII, SPIE Vol. 489*, pp. 62–67 (1984).
17. Garcia-Soto C, Fernández E, Pingree RD, Harbour RS, "Evolution and structure of a shelf coccolithophore bloom in the Western English Channel", *Journal of Plankton Research*, **17**(11): 2011–2036 (1995).
18. Nanninga HJ, Tyrrell T, "The importance of light for the formation of algal blooms by *Emiliania huxleyi*", *Marine Ecology Progress Series*, **136**: 195–203 (1996).

Optical parameters of the Black Sea waters: long-term variability and present status

Vladimir L. Vladimirov, Viktor I. Mankovsky, Mark V. Solov'ev, Alexey V. Mishonov

Marine Hydrophysical Institute, National Academy of Sciences of Ukraine,
2 Kapitanskaya Str., Sevastopol, Crimea, 335000, Ukraine

Sukru Besiktepe, Emin Ozsoy

Institute of Marine Sciences, Middle East Technical University, Erdemli, Icel, Turkey, 33731

ABSTRACT

Seasonal and long-term variability of the Black sea optical parameters are analyzed using valuable data set from the data bases of Marine Hydrophysical Institute and Institute of Marine Sciences. The drastic decrease of the water transparency was observed during 1986-1992. It coincided with the big changes of the spectral distribution of water optical parameters. The main causes of these changes are eutrophication, influence of biological invader *Mnemiopsis leidyi* on the sea ecosystem, and the natural 11-years cycle.

Keywords: marine optics, Black Sea, water transparency, Secchi disk, attenuation coefficient, climatic changes, spectra of optical properties, yellow substance

1. INTRODUCTION

In situ measurements of optical characteristics are conducted in the Black Sea since 1960s and Secchi disk measurements are conducted since 1920s. A valuable data set of the optical characteristics is available at present at Marine Hydrophysical Institute (MHI) and Institute of Marine Sciences (IMS). There are, in total, more than 13000 Secchi disk measurements, 2500 profiles of light attenuation coefficient, etc. These data permit to estimate vertical, spatial, seasonal and long-term variability of some optical characteristics of the Black Sea and to analyze their relations with biological variables and water dynamics.

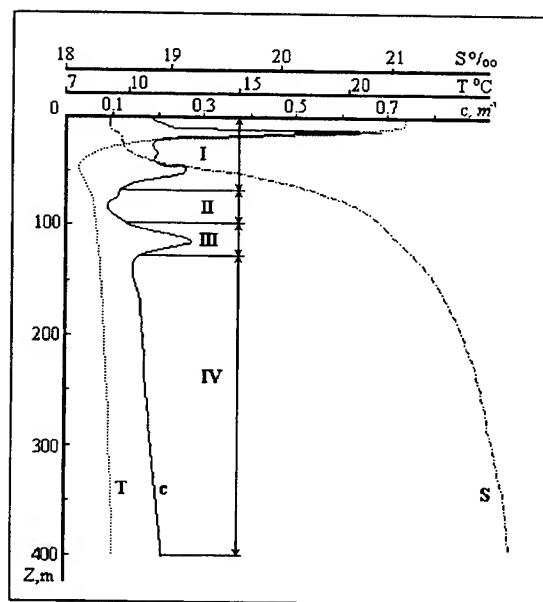


Fig. 1. Typical vertical distribution of the attenuation coefficient (c), temperature (T) and salinity (S) in the deep region of the Black Sea in summer.

2. VERTICAL OPTICAL WATER STRUCTURE AND ITS SEASONAL VARIABILITY

Vertical distribution on the optical water properties is determined by the peculiarities of the distribution of physical, chemical and biological properties and by the water dynamics. Main of those in the Black Sea are: existence of the anaerobic hydrogen sulfide zone deeper 120 --140 meters, cold intermediate layer at depths 40 --75 meters, cyclonic current system containing rim current along all the sea coast and some eddies.

There are four typical layers of the vertical profiles of the light attenuation coefficient ($c(z)$) in the deep area of the sea: upper, intermediate, boundary and deep (Fig. 1), which correspond to the layers with different hydrological, chemical and biological properties.¹ The upper layer locates in the euphotic zone. The intermediate layer housing the most transparent water, centered near the low boundary of the cold intermediate layer. The boundary turbid layer exists at the oxic/anoxic interface. The deep layer is spreading over the hydrogen sulfide zone. Seasonal variability of $c(z)$ is best pronounced in the up-

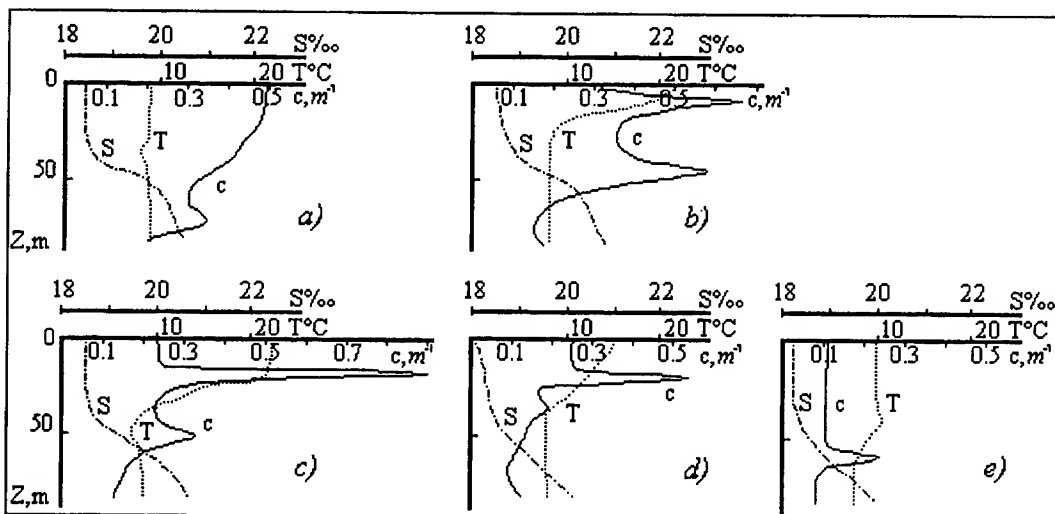


Fig.2. Seasonal variability of the vertical profiles of attenuation coefficient (c), temperature (T) and salinity (S) in the upper layer: a) - April, b) - June, c) - August, d) - October, e) - December.

per layer (Fig. 2). Two typical maximums of $c(z)$ occur within this layer in summer, which are connected with the vertical distribution of the phytoplankton. One of those is connected with the upper part of the seasonal thermocline and the other - with upper part of the permanent halocline. Often, some maximums of the second order of magnitude occur in the thermocline in summer, which are connected with the fine structure of the seasonal thermocline. There is only one maximum of $c(z)$ in winter (after the destruction of the seasonal thermocline), which connected with halocline and which is deeper then in summer. An intermediate layer with minimum values of $c(z)$ exists throughout the year, its seasonal variability being low. The boundary turbid layer is more powerful on the periphery of the sea within the Black Sea Rim current area and it is absent at the centers of the main cyclonic circulation cells. This layer is more pronounced in winter, with its depth also being larger. Within the deep layer, a seasonal variability is very small. The attenuation coefficient is changing monotonous with depth in this layer depending on the wavelength. It is approximately constant at the long wavelength and it increases with depth at the short ultraviolet spectral band. This fact shows the growth of the "yellow substance" concentration with depth.

3. SEASONAL AND LONG-TERM VARIABILITY OF WATER TRANSPARENCY

Figure 3 shows the seasonal variability of the Secchi disk depth (Z_d) analyzed using monthly mean values, calculated for 1922-1985 for the central deep part of the Black Sea, limited by the latitudes $42^{\circ}20'$ and $44^{\circ}15'N$ and longitudes 31° and $38^{\circ}E$. There are two minimum in the interannual variability of Z_d namely in spring and at the end of autumn and two maximums, namely in summer and at the end of winter. The difference between maximum and minimum mean month values is about 6.2 meters or 37% of mean annual value (16.8 m).

Very interesting phenomenon is the strong changes occurred in the Black Sea recent years.² From the early 1920s to the mid-1980s, the weakly pronounced transparency decrease was observed. Over 60 years, Secchi disk visibility depth had decreased from 20-21 to 15-16 meters (mean values in the deep central part of the sea), however, single values up to 25 meters were occasionally observed. The Black Sea water transparency has decreased dramatically since 1985. In 1990-1993, the values in excess of 15 meters were no longer observed and mean values were only 6-10 meters (Table 1). It is worth to mention that the water transparency in the Black Sea started to increase since 1993.

Water transparency measurements using *in situ* sounding instruments, which were performed by MHI during Black Sea surveys, also indicate the same decrease of transparency. Mean, maximum, minimum values and standard deviation of the attenuation coefficients (wavelength 410-420 nm) in the surface layer of the central, deep part of the sea for summer are shown in Table 2. Values for 1977-85 which are considered as the "background" data show large changes compared to 1990, 1991, and 1992 data.

Spectral optical properties of the Black Sea water had also changed. In 1990s compared with 1984, not only the values of the light attenuation coefficient strongly increased, but as well, the shape of spectral curves changed, due to the initial enhanced increase in the short wavelength band. The minimum values, which were at 480 nm in 1984, shifted to the 550-570 nm in 1992. Spectra of the light attenuation coefficient $c(\lambda)$ for 1984, 1991, 1992, 1995, and for the optical pure sea water³

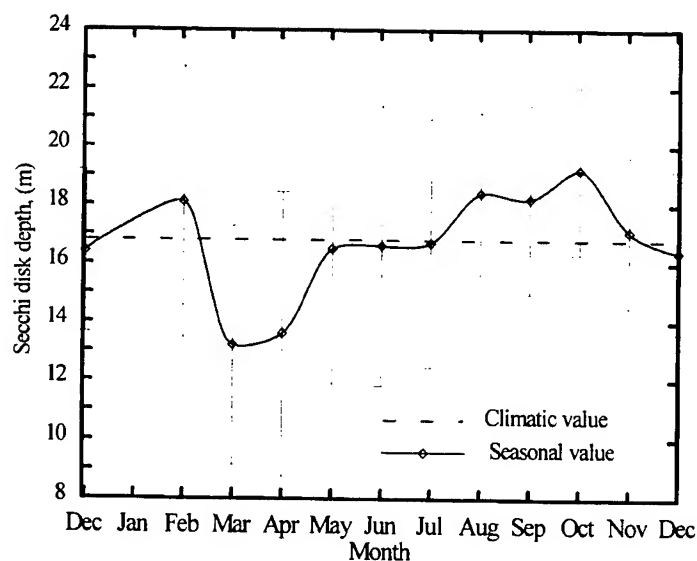


Fig. 3. Monthly variation of the mean Secchi disk depth in the central part of the Black Sea in 1922-1985. Vertical bars show the standard deviations.

fact caused an increase in the radiance index values and a shift in the maximum of radiance index to the longer wavelengths due to the increase in the dissolved organic matter concentration, especially of yellow substance.

Table 1. The annual mean, maximum, minimum Secchi disk depth values and standard deviations for each year for the central part of the Black Sea

Year	Mean	Max	Min	STD	Number of data points
1923	20.2	23.0	19.0	1.44	5
1924	19.9	28.0	13.5	4.18	20
1925	19.8	30.5	11.0	4.32	24
1927	20.9	25.0	16.0	2.70	10
1953	18.0	20.0	17.0	1.22	4
1956	13.8	20.0	8.0	3.99	10
1957	19.5	25.5	13.0	3.53	22
1958	21.5	30.0	10.0	7.31	14
1960	19.9	22.0	19.0	0.99	9
1961	17.1	20.0	13.0	2.08	10
1962	21.1	27.0	16.6	2.92	11
1963	17.0	22.0	11.0	3.74	9
1964	17.4	24.0	3.5	4.21	29
1965	13.7	20.5	9.0	3.78	10
1966	15.4	22.0	9.0	4.58	10
1967	16.7	23.0	10.0	5.31	3
1968	17.4	26.0	9.0	5.69	5
1969	13.0	15.0	10.0	2.12	4
1970	20.0	22.0	18.0	2.00	2
1972	20.1	28.0	13.0	4.10	11
1973	14.1	20.0	6.0	4.22	7

Year	Mean	Max	Min	STD	Number of data points
1974	19.0	27.0	15.0	3.12	15
1975	18.8	24.0	9.0	2.86	58
1978	17.7	23.0	14.0	2.35	18
1979	19.3	20.0	18.0	0.94	3
1980	16.1	21.0	7.0	4.31	14
1981	16.9	29.0	12.0	4.33	12
1982	14.0	18.0	9.0	2.92	29
1983	13.9	20.0	10.0	2.82	15
1984	16.2	24.0	5.0	3.29	113
1985	15.1	27.0	6.0	4.87	38
1986	17.5	25.0	6.0	5.10	14
1987	12.5	19.0	7.0	3.11	65
1988	12.5	18.0	8.0	2.45	54
1989	12.0	25.0	2.0	4.73	179
1990	8.2	13.0	3.0	2.16	53
1991	8.7	14.0	5.5	1.92	90
1992	6.2	11.0	2.0	2.51	51
1993	10.0	16.0	7.0	1.76	94
1994	12.7	16.0	9.0	1.52	33
1995	13.9	21.0	6.7	3.89	13

Table 2. Attenuation coefficients (wavelength 410-420 nm) in the upper water layer in the central deep part of the Black Sea in summer, $c(\lambda)$ [m^{-1}]

Year	Mean	Max	Min	STD.
1977-1985	0.55	1.38	0.23	0.32
1990	1.17	1.86	0.78	0.23
1991	1.03	2.16	0.69	0.21
1992	1.70	2.76	0.55	0.60

are presented in the Figure 4 for the subsurface water of the deep central part of the sea. The Secchi disk depth values corresponding to the each spectrum are showed in a legend.

Similar shift in the spectral minimum was also observed recent years in the spectra of the vertical attenuation coefficients, $K(\lambda)$, of the sunlight. Measurements of $K(\lambda)$ were performed by the authors of [11] in the central part of the sea in February-March of 1991 at the Secchi disk depth of 5-6 meters. The spectral minimum of $K(\lambda)$ at 520-560 nm calculated for these measurements was observed at 490-530 nm in the central part of the Black Sea before 1979 (Table 3).

Parallel changes have occurred in the radiance spectra of the sea. The radiance index increased four-five times in the band of spectral maximum, and the maximum proper displaced from 480 nm to 540-560 nm in 1992, as compared with 1984.

Such changes in the spectra of radiance index show that the concentration of particulate matter, which scatter the light, increased in the upper layer of the sea. This

4. CLIMATIC DISTRIBUTION OF WATER TRANSPARENCY

The climatic characteristics of the Black Sea Secchi disk depth in the years preceding the large changes of water transparency were calculated and evaluated for summer and autumn seasons since the most part of the Secchi disk measurements were done during these seasons (Fig.5). The cli-

matic transparency field has the following features. Water with $Z_d < 6\text{m}$ is found only in a narrow band in the regions of big river mouths: Danube and Dnieper on the northwest shelf, Inguri and Rioni near the Caucasus, and near the Kerch strait. Transparency in nearly 60% of the deep regions of the sea, is more than 16 m. The most transparent waters ($Z_d > 22\text{m}$) occur in the middle part of the sea where eastern and western cyclonic rings come into contacts with each other and where surface waters with low concentration of nutrients downwells. Relatively higher transparencies (up to 10-20 m) occurs in the shelf zone and often near the coast; for example, near the Bosphorus Z_d exceeds 18 m. There is a difference in the transparency of the eastern and western deep regions of the sea: the eastern part shows considerably lower Z_d values due to higher biological productivity.

Table 3. Minimum values of the vertical attenuation coefficients and corresponding wavelengths

Time of measurements	$\lambda(k_{\min})$, nm	k_{\min} , m^{-1}
1962-1963, March-August	490 - 530	0.069
1984, April-May	500 - 525	0.099
1989, July-August	525 - 554	0.104
1991, February-March	525 - 554	0.115

connected with the long-term increasing input of nutrients of anthropogenic origin. For example, an input of biogenic compounds of nitrogen and phosphorus by the Dnieper and Danube waters, which are responsible for 3/4 of the overall river input to the Black Sea, increased 5-7 times from the 1960s to the 1980s.⁶ The mean chlorophyll concentration has become one and a half time larger in deep part of the sea throughout the same period (Fig. 6).⁷

Water transparency gradually declined due to the increase of the content of optically active matter in the sea. Over 20 years, from the mid-1960s to the mid-1980s, the mean annual decrease of the Secchi disk depth has attained about two meters.

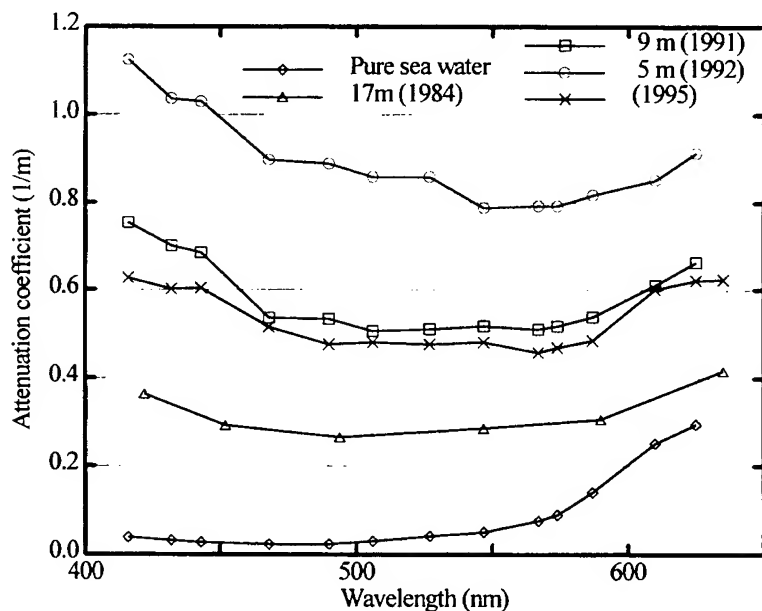


Fig. 4. Spectra of the light attenuation coefficient $c(\lambda)$ for the subsurface water of the deep central part of the sea for the different years and for the pure sea water. The Secchi disk depth values measured at the same station are included in a legend.

Phytoplankton structure was also strongly impacted by the biological invaders, such as *Mnemiopsis leidyi* which appeared in the Black Sea in the early 1980s and its biomass amounted to one billion tons in 1989.⁸ As a result, the amount of

5. FACTORS INFLUENCED ON THE DRASTIC DECREASE OF WATER TRANSPARENCY

Analysis of the total collected information has enabled to understand the main causes of the drastic transparency decrease in the deep basin of the Black Sea from 1986 to 1992 and to reach the conclusions stated below.⁵

Significant eutrophication occurs both in the near-shore areas of the Black Sea and in the deep ones, being

However, the direct cause of the drastic transparency decrease from 1986 to 1992 was the enhanced bloom of *Peridinium* and *Coccolithophores*. Their number in the Black Sea was 1.5 - 2 orders of magnitude larger than in previous years and reached 2-3 billions per cubic meter. A significant increase in the biomass of these planktonic organisms has changed the structure of the plankton community. Now nanoplankton, which contributes immensely to the light scattering, accounts for 90% of the phytoplankton content.⁵

The intense blooms of *Peridinium* might have been also caused by the increased concentration of particulate organic matter, as *Peridinium* can switch to heterotrophic nutrition.

Coccolithophores also play a significant role in the changes of water transparency, due to their crustal structure containing a number of disks, namely, coccoliths, which can be separated. These disks cause an intensive scattering of light. That is why, when the *Coccolithophores* concentration is high, sea water becomes whitish. This effect has been observed in the Black Sea over the last few years.⁵

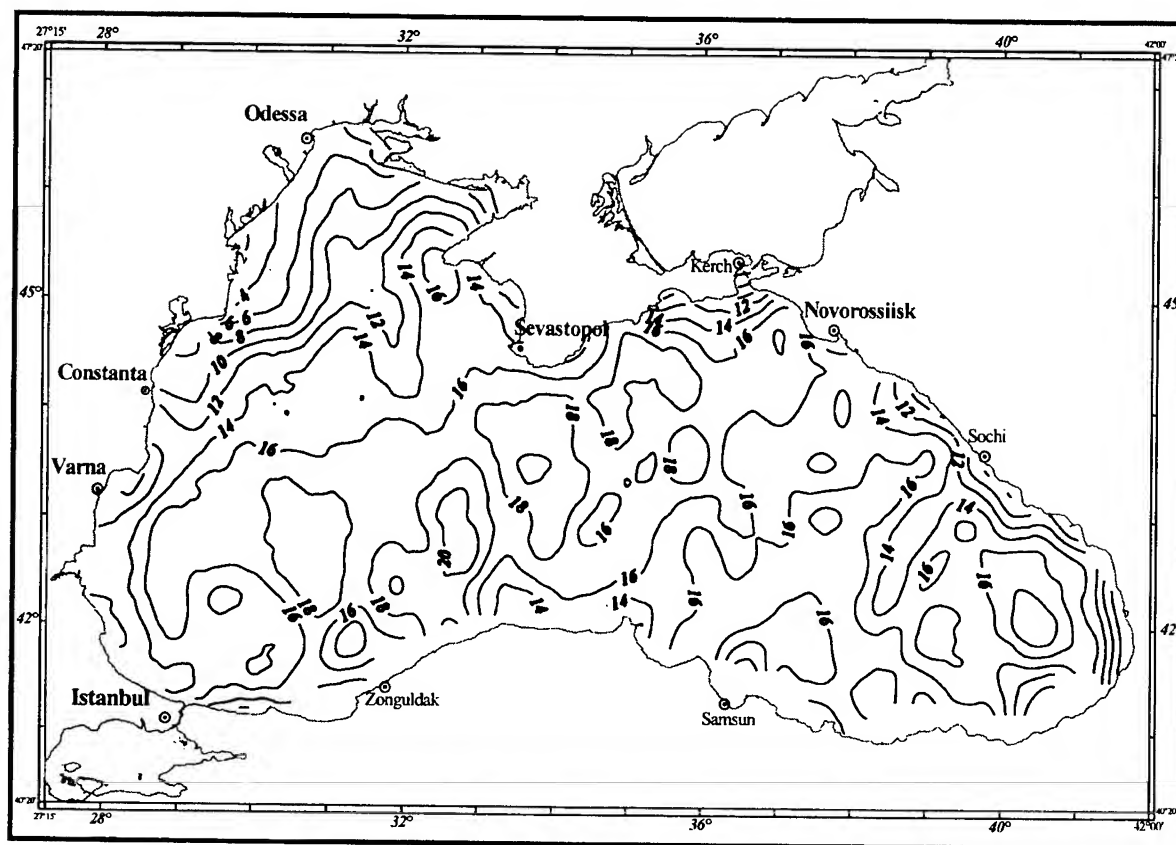


Fig. 5. The climatological field of mean Secchi disk depths in the Black Sea for June - October 1922-1985.

herbivorous microzooplankton, which is a part of the *Mnemiopsis* food, has decreased by several times, whereas the phytoplankton content conversely, increased. The great amount of dissolved organic matter released by *Mnemiopsis* also facilitated the increase of some types of phytoplankton and bacteria.

Long-term periodical oscillations in the Black Sea water transparency have been found to occur, which seems to be correlated with the 11-year cycle of solar activity. Water transparency increases during the second half of the cycle and decreases during the first one. This fact shows the same cyclicity is inherent to the planktonic community.

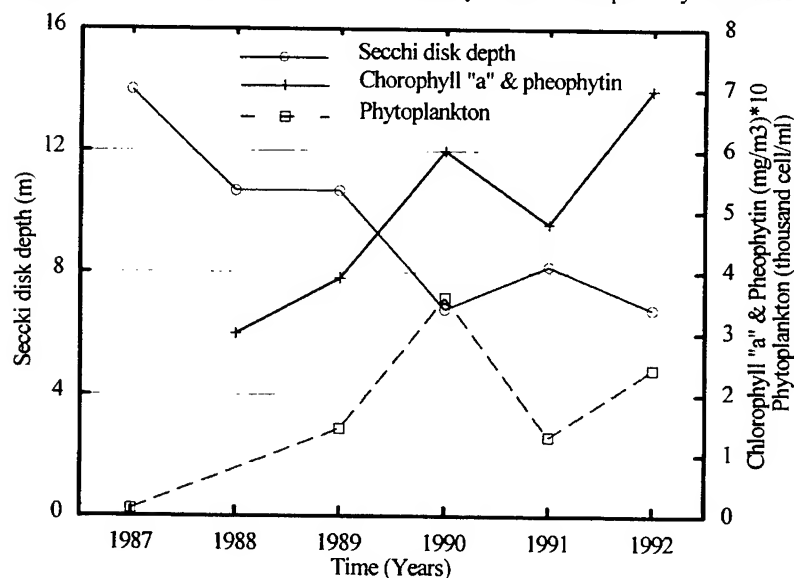


Fig. 6. Secchi disk depth, chlorophyll "a" + pheophytin, and phytoplankton concentration in the western deep part of the sea for 1987-1992. Mean values for May-September.

drastic decrease in the transparency in late 1980s coincided with the second half of the 1980-1991 solar activity cycle. However, the magnitude of the transparency decrease was more intense during this cycle than those during the previous cycles.

Analyses of the collected data, it may be concluded that the catastrophic transparency decrease in 1990-1992 took place due to the combined effect of three factors coinciding in time and sign: (1) the natural 11-year cycle, (2) increased eutrophication, and (3) the influence of the biological invader *Mnemiopsis leidyi* on the ecosystem structure.

It is important to emphasize that the intense decrease in water transparency dis-

continued in the Black Sea in 1992, and in 1993 water transparency started slightly to improve. As a result, already by the end of 1995, the mean Secchi disk depth in the deep central part of the Black Sea had reached to the levels observed for the early 1980s, i.e. about 17 meters. Regretfully, we have no evidence on the changes that took place in the ecosystem of the sea during these years, which made this transparency to increase.

6. ACKNOWLEDGMENTS

We thank all the scientists and crew of the research vessels participated in data collecting in the Black sea. We wish to thank also Drs. O.Yunev, L.Georgieva and B.Anninsky from Institute of Biology of the Southern Seas NASU for the very useful discussion on the reasons of catastrophic transparency decrease in the Black Sea. The research described in this publication was made possible in part through the TU-Black Sea Project of the NATO Science for Stability Program and by Grant No. U1V200 from the Joint Fund of the Government of Ukraine and International Science Foundation.

7. REFERENCES

1. V.I. Mankovsky, "Optical structure of the Black Sea waters and regularities of its formation," *Hydrophysical and hydrochemical investigations of the Black Sea*, pp. 7-28, MHI of the Ukr. Acad. of Sci., Sevastopol, 1992.
3. V.N. Eremeev, V.L. Vladimirov, B.N. Krashenninnikov, "Long-term variability of the Black Sea water transparency," *Hydrophysical and hydrochemical investigations of the Black Sea*, pp. 28-30, MHI of the Ukr. Acad. of Sci., Sevastopol, 1992.
3. A. Ivanov, *Introduction a l'oceanographie. Proprietes physiques et Chimiques des eaux de mer*. Vol. II, Librairie Vuibert, Paris, 1975.
4. V.P. Nikolaev, "New results of the measurements of vertical attenuation of the underwater irradiance in the Black Sea," *Oceanology*, **36**(3), 377-383 (1996).
5. V.I. Mankovsky, V.L. Vladimirov, E.I. Afonin, A.V. Mishonov, M.V. Solov'ev, B.E. Anninskiy, L.V. Georgieva, and O.A. Yunev, *Long-term variability of the Black Sea water transparency and factors determined its strong decrease in the late 1980s early 1990s*, pp.1-32, MHI of the Ukr. Acad. of Sci., Sevastopol, 1996.
6. E.N. Altman, A.A. Bezborodov, Yu.I. Bogatova, et al. "Black Sea Hydrobiology," *Practical ecology of sea regions. Black Sea*. V.P. Keondgyan, A.M. Kudin, Yu.A. Terekhin, (eds.), pp.1-252, Nauk. dumka, Kiev, 1990.
7. V.I. Vedernikov and A.B. Demidov, "Primary production and chlorophyll in the deep regions of the Black Sea," *Oceanology*, **33**(2), 229-235 (1993).
8. M.E. Vinogradov, V.V. Sapozhnikov, E.A. Shushkina, *The Black Sea ecosystem*, Nauka, Moscow, 1992.

Aspects of the Point Spread Function in the Coastal Zone

Kenneth J. Voss and Brian J. Frew

Physics Department, University of Miami
Coral Gables, Fl. 33124

ABSTRACT

Measurements of the point spread function in the coastal zone will be presented. While measurements appear to be very similar to the deeper ocean measurements, other factors in the coastal zone that could influence the point spread function (PSF) were investigated. Laboratory experiments were performed to look at the effect of inhomogeneities, or layering, on the point spread function, and the layering was found to have a significant effect on the PSF.

Keywords: Point spread function, forward scattering, ocean optics

2. INTRODUCTION

The point spread function (PSF) is an important factor in predicting the system performance of in-water imaging systems. The PSF is defined as the radiance distribution at some range, R , resulting from a point, lambertian, source.¹ In homogeneous waters the PSF is equivalent through reciprocity² to the beam spread function (BSF), which is the irradiance distribution on a sphere of radius R , resulting from a source initially collimated at the origin.¹ In this paper we will concentrate on the PSF, but much of the same discussion could be related to the BSF.

The PSF at a given range is influenced mainly by the small angle scattering of particulates in the water, but also can be affected by the single scattering albedo (scattering/attenuation).³ Theory relating the volume scattering function to the PSF, using the small angle approximation, has been developed.⁴ For imaging purposes, the PSF for small angles, on the order of milliradians, is desired. But in this region it is difficult to measure the scattering function. Thus, if the PSF is desired for investigation of imaging systems, the PSF should be measured directly. Instrumentation to measure the PSF in the open ocean was originally developed by Honey.⁵ A modern version has been fielded to make these measurements in the open ocean and coastal areas.⁶

The open ocean PSF has been investigated,⁷ but with new interest in optical imaging in coastal waters, aspects of the PSF relating to coastal areas become important. Two main features of the coastal environment that affect the PSF are the large variations in particle type and quantity, and the large inhomogeneities in water properties, vertically and horizontally, that can exist. We have modified our ocean instrumentation to make measurements of the PSF in shallow waters, including the surf zone, to investigate the effects of the different particles on the PSF. To investigate the PSF for a inhomogeneous water column a laboratory facility was built which allows the water properties to be varied along the measurement path. Thus, the PSF for layered systems could be investigated in a controlled manner. Our preliminary results from these two measurement programs will be outlined in this paper.

2. INSTRUMENTATION

The basic system to measure the PSF has been described in detail elsewhere.⁶ Several modifications were required for measurement in the coastal zone. The basic system has a cosine source to simulate a lambertian source, and a cooled CCD camera, focused at infinity. The spectral region of the measurements, 500 nm, is selected by an interference filter on the front of the camera lens. In open ocean measurements the system is typically separated by ranges between 10 and 150m. In the shallow coastal region the attenuation properties of the water are typically much greater than in the open ocean. Thus, we make measurements of the PSF over ranges from 0.5 - 3 meters. Also, since we wanted to make measurements in very shallow water, an alternative mounting scheme was required. In our coastal measurements we mounted the flashlamp source and camera on an aluminum bar. The two devices were held horizontally so that profiles of the PSF at specific depths could be measured, or measurement of the PSF in very shallow water could be performed. In one case, we wanted to

make measurements of the PSF as a function of distance offshore, so floats were attached to each end of the aluminum bar to suspend the instrumentation at a constant depth of 1 m below the surface.

The cosine source has a 5 cm diameter. At the longer ranges used in the open ocean this could approximate a point source. With the shorter ranges used in the coastal zone and in the laboratory, a smaller source was needed, thus a pinhole aperture (1 mm diameter) was placed over the cosine source to approximate a point lambertian source. While this probably does not have as accurate a cosine emission profile over the angular range of our measurements, 0-12 degrees at most, the non-lambertian properties will not affect the results.

The laboratory measurements were performed in a specially built tank. This tank was approximately 4 meters long and constructed so that Plexiglas separators could be placed at 0.5 m intervals along the measurement path. This allowed the water scattering properties of segments of the measurement path to be varied in an independent and controlled fashion. The inside of the tank was painted with a black epoxy to reduce reflections and the surface of the water was covered with a black neoprene to reduce surface effects at the air-water interface.

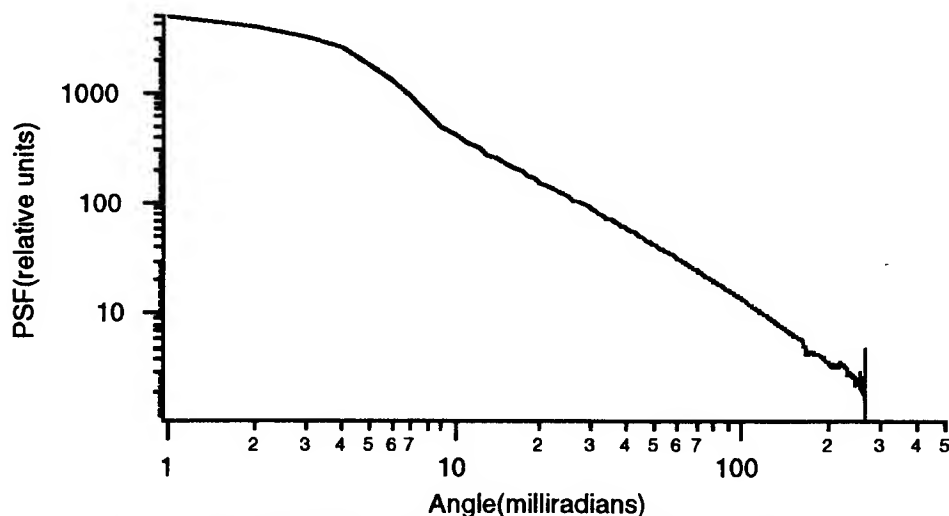


Figure 1) Example PSF measurement. This measurement was over a 1m pathlength. The total optical pathlength (τ) was 3.03. The measurement depth was 1 m, and the measurement was made off of Oceanside, Ca.

3. RESULTS

We have made measurements of the PSF in two littoral zones, off of Ft. Walton Beach, Fl. on two occasions and off of Oceanside, Ca. A typical PSF measurement is shown in Fig. 1. Two general features are worth noting in this measurement. First the region between 0 and 6 milliradians is the area in which the physical size of the source dominates the measurement. Next the region between 10 and 100 milliradians is typically fairly linear in this log (PSF) - log(angle) representation. We have used this to parameterize and represent the PSF in this angular range as:

$$\text{PSF}(\theta) = B \theta^{-m} \quad (1)$$

For a specific measurement series in the water column in the open ocean, we have found that the m varies with optical pathlength ($\tau = c * l$, where l is geometrical pathlength and c is the beam attenuation) in a regular manner. Our coastal measurements show the same general pattern. In fact if one plots the optical pathlength vs slope, m , for all of our measurements a general pattern emerges. Figure 2 shows the totality of our field PSF measurements, both coastal and open ocean. The open ocean measurements include measurements in the Sargasso Sea, clear water off Hawaii, Tongue of the Ocean (Bahamas), and off San Diego, Ca.

While the general trend is fairly constant, getting accurate predictions in coastal water is more difficult than oceanic measurements. In the open ocean, more accurate predictions can be made if the optical pathlength for a specific cast is plotted against the slope as a very regular pattern exists. For example, the small angle scattering theory of Wells⁴ can be used to predict the PSF for other ranges very accurately.⁸ In the littoral zone, groups of measurements for a single station or day show much more variation due to the local inhomogeneities of the water column, both horizontal and vertical. To get a more quantitative measure of the effect of layering on the PSF, laboratory measurements were made in the specially constructed tank described above.

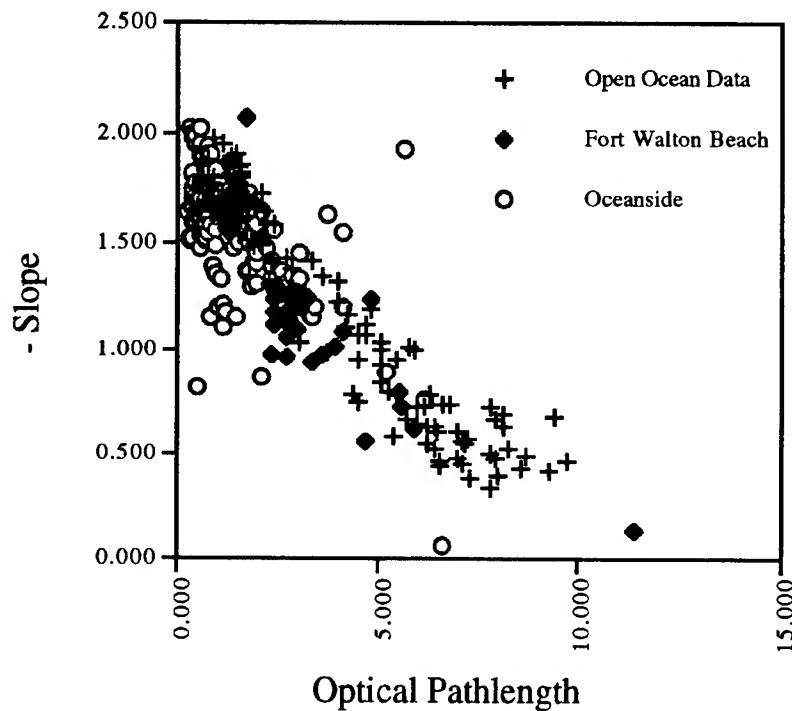


Figure 2) Slope of $\log(\text{PSF}) - \log(\text{angle})$ vs optical pathlength for measurements in open ocean and two littoral sites.

These measurements are described in more detail elsewhere,⁹ but the general trend was that if inhomogeneities of the water path exist, the structure of the water path can have a significant affect on the overall PSF. Figure 3 shows the slope vs total optical path for three different water structures. As can be seen, the scattering layer has the greatest effect on the PSF if it is closer to the camera (imaging side) rather than the flashlamp. Also, it can be seen that the scattering layer positioned in the center is very close to the case of a homogeneous water path. This data shows that the structure of the water path is an important factor. We will be using this data to investigate models to predict the effect of the structured water path.

4. CONCLUSION

These measurements show that while the PSF for coastal waters generally fits the trend of the oceanic measurements, various effects specific to the littoral zone (vertical and horizontal variability) can be important. More work needs to be done to improve understanding of the water path structure effects. We will be making additional measurements in our tank system and modeling these results in the near future.

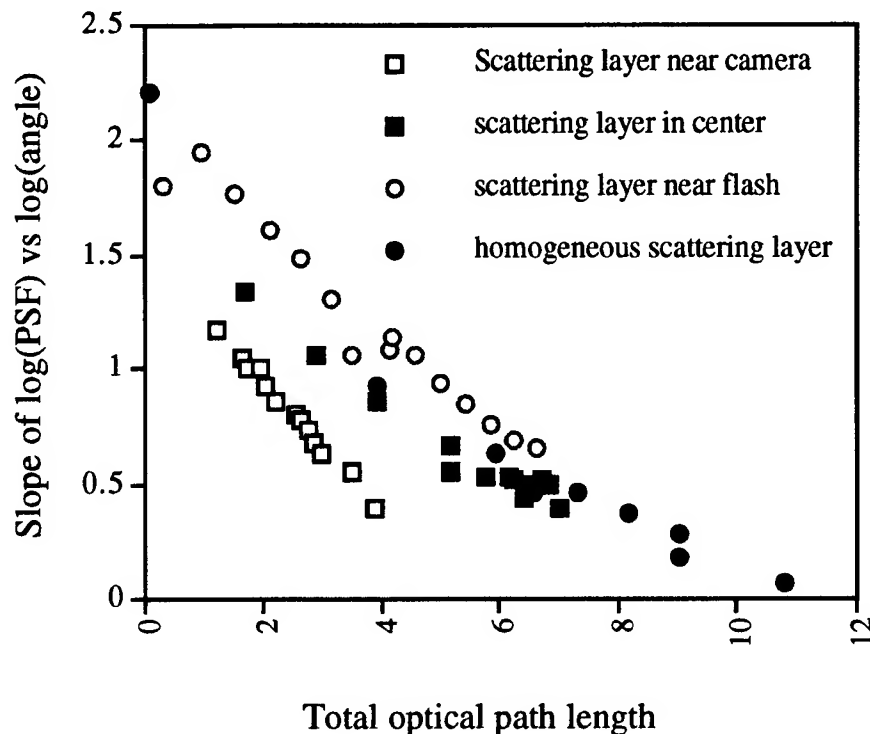


Figure 3) Illustrates the effect of an inhomogeneous measurement path on the PSF. In each case the scattering layer was confined to 1/3 the total pathlength in a region specified as near the camera, in the center or near the flash (source).

5. ACKNOWLEDGMENTS

This work was supported by NRL/Stennis (Dr. Alan Wiedemann) and ONR Ocean Optics (Dr. Steve Ackleson). We also thank Mr. Albert Chapin for his help in the measurement program and constructing the water tank.

6. REFERENCES

- 1) L. E. Mertens and F. S. Replogle, Jr., "Use of Point Spread and Beam Spread Functions for Analysis of Imaging Systems in Water," *J. Opt. Soc. Am.* **67**, 1105-1117 (1977).
- 2) H. R. Gordon, "Equivalence of the Point and Beam Spread Functions of Scattering Media: a Formal Demonstration," *Applied Optics* **33**, 1120-1122 (1994).
- 3) S. Q. Duntley, "Underwater lighting by submerged Lasers and incandescent sources," SIO Ref. 71-1, Scripps Institution of Oceanography, U. California, San Diego (1971).
- 4) W. H. Wells, "Theory of Small Angle Scattering," in *Optics of the Sea*, AGARD Lecture Series 61 (NATO, 1973).
- 5) R. C. Honey, "Beam Spread and Point Spread Functions and Their Measurement in the Ocean," *Proc. Soc. Photo-Opt. Instrum. Eng.* **208**, 242-248 (1979).
- 6) K. J. Voss and A. L. Chapin, "Measurement of the Point Spread Function in the Ocean," *Applied Optics* **29**, 3638-3642 (1990).
- 7) K. J. Voss, "Simple Empirical Model of the Oceanic Point Spread Function," *Applied Optics* **30**, 2647-2651 (1991).
- 8) K. J. Voss, "Variation of the point spread function in the Sargasso Sea," *Proc. Soc. Photo-Opt. Instrum. Eng.* **1537**, 97-103 (1991).
- 9) B. J. Frew and K. J. Voss, "Measurement of the Point Spread Function in a layered system," Submitted to *Applied Optics*.

Optical Properties of the upper ocean in the Arabian Sea in August 1994

Alison Weeks, Daniel Ballester* and Ian Robinson*

Maritime Faculty, Southampton Institute,
East Park Terrace, Southampton, SO14 OYN

* University of Southampton
Department of Oceanography
Southampton Oceanography Centre
Waterfront Campus, European Way
Southampton, SO17 1BJ

ABSTRACT

Upwelling was observed close to the Omani shelf during August 1994, and high values of chlorophyll concentration were observed in the upper mixed layer on the offshore region of the raised isopycnals. A rapid increase of phytoplankton biomass was observed over the whole area of the survey 7 days later. Values of the diffuse attenuation coefficient and beam transmittance were closely related to the phytoplankton concentrations, but spatial variations were observed. Spectral variations in reflectance were also observed. These observations are considered in relation to the distribution of the major phytoplankton taxonomic groups and light absorbing pigments.

Keywords: Optical properties, Arabian Sea, reflectance, phytoplankton, upper ocean

1. INTRODUCTION

Interprovince variability in the chlorophyll to carotenoid ratio is thought to limit the accuracy of two band single pigment algorithms¹. This study describes the optical properties and phytoplankton distribution in the upper ocean during a period of coastal upwelling off the coast of Oman between 3-22 August 1994. The work explores how spectral reflectance may differ where there are variations in major phytoplankton taxonomic groups, and different chlorophyll to carotenoid ratios, in a spatially and temporally dynamic region.

2. METHODOLOGY

Seasoar was deployed to a depth of 350 m with downwelling irradiance and upwelling radiance sensors (Satlantic Inc, wavelengths: 411, 443, 490, 510, 556, 670, 682 nm (± 10 nm)) to measure the diffuse attenuation coefficient (K_d); Lightfish was deployed at a fixed depth of 5 m with downwelling and upwelling irradiance sensors², wavelengths: 410, 440, 490, 520, 550 and 670 (± 10 nm) to provide subsurface spectral reflectance. Transmittance (Sea-Tech) and in vivo fluorescence (Chelsea Instruments) were sampled from an underway pumped supply (3 m).

Water samples were taken from the underway supply and microscopic analysis was carried out for phytoplankton species (cells l⁻¹, and converted to mg C l⁻¹)³ and for the major light absorbing pigment concentrations, by High Performance Liquid Chromatography (HPLC) (ng l⁻¹)⁴. Calibration of fluorometers measuring in vivo fluorescence was carried out by comparison with underway samples measured by in vitro fluorescence, on a calibrated bench fluorometer².

3. RESULTS

Seasoar surveys were carried out between 10-12.8.94 (Survey 1) and 17-18.8.94 (Survey 2) (Figure 1). Survey 1 showed upwelling near the coast; 1 week later the slope in the isopycnals had diminished. Surface temperature increased by 1 °C over the period, and σ_t by 0.2. Chlorophyll concentrations in the upper 50 m increased from 1.75-2.0 mg m⁻³ to 2.5-3.0 mg m⁻³, except for the region outcropping of raised isopycnals in Survey 1 where values reached 2.5 mg m⁻³. Phytoplankton cells converted to carbon measured at A1 (59°N, 19°W) doubled in quantity between 5-21.8.94 with more heterotrophic Dinoflagellates on 21st August).

There was considerable spatial variability in the concentration of chlorophyll during the 2 surveys. This is shown for Survey 2 where there were lower concentrations in the central region (Figure 2(a)). The isolines of downwelling irradiance are deeper and K_d is lower in this region during leg 2 (Figure 2(b) and (c)). Transmittance is inversely related to subsurface chlorophyll, as might be expected off the coast of Oman, where concentrations of suspended particulates from river runoff are low. However there was considerable variation in the relationship during the period of the cruise, over the region sampled (Figure 3).

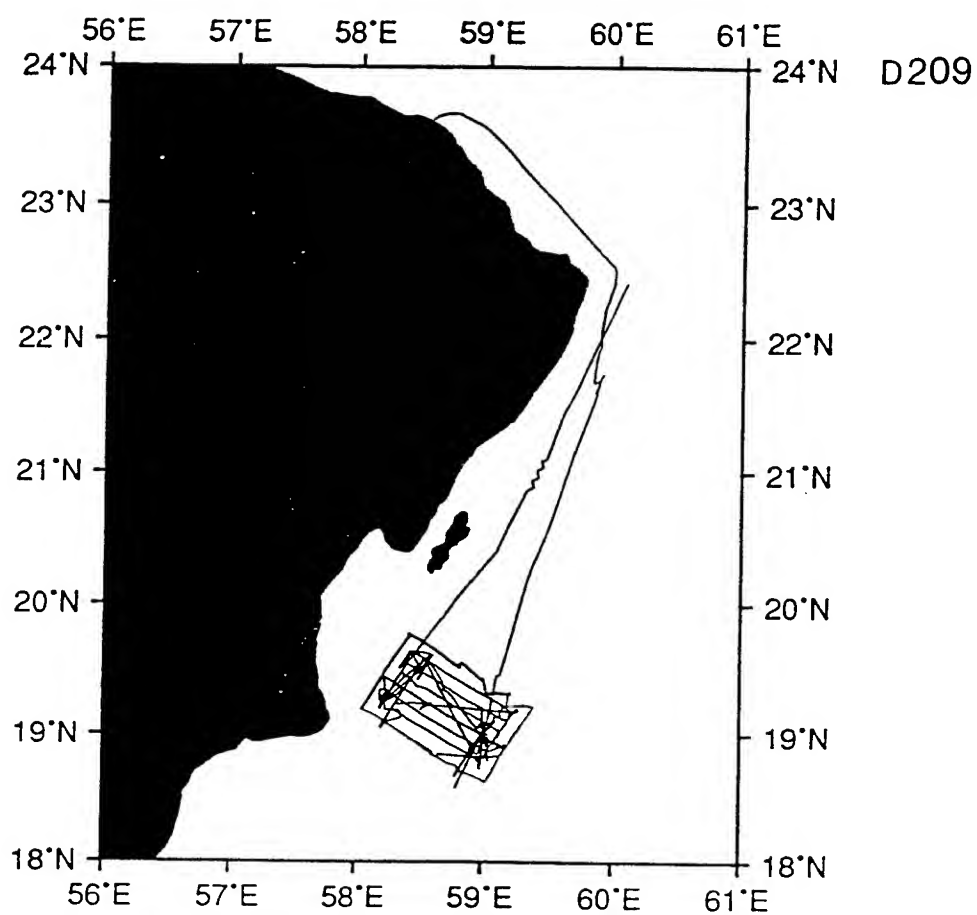


Figure 1. The cruise track for D209. Seasoar surveys were carried out between 10-12.8.94 (Survey 1) and 17-18.8.94 (Survey 2).

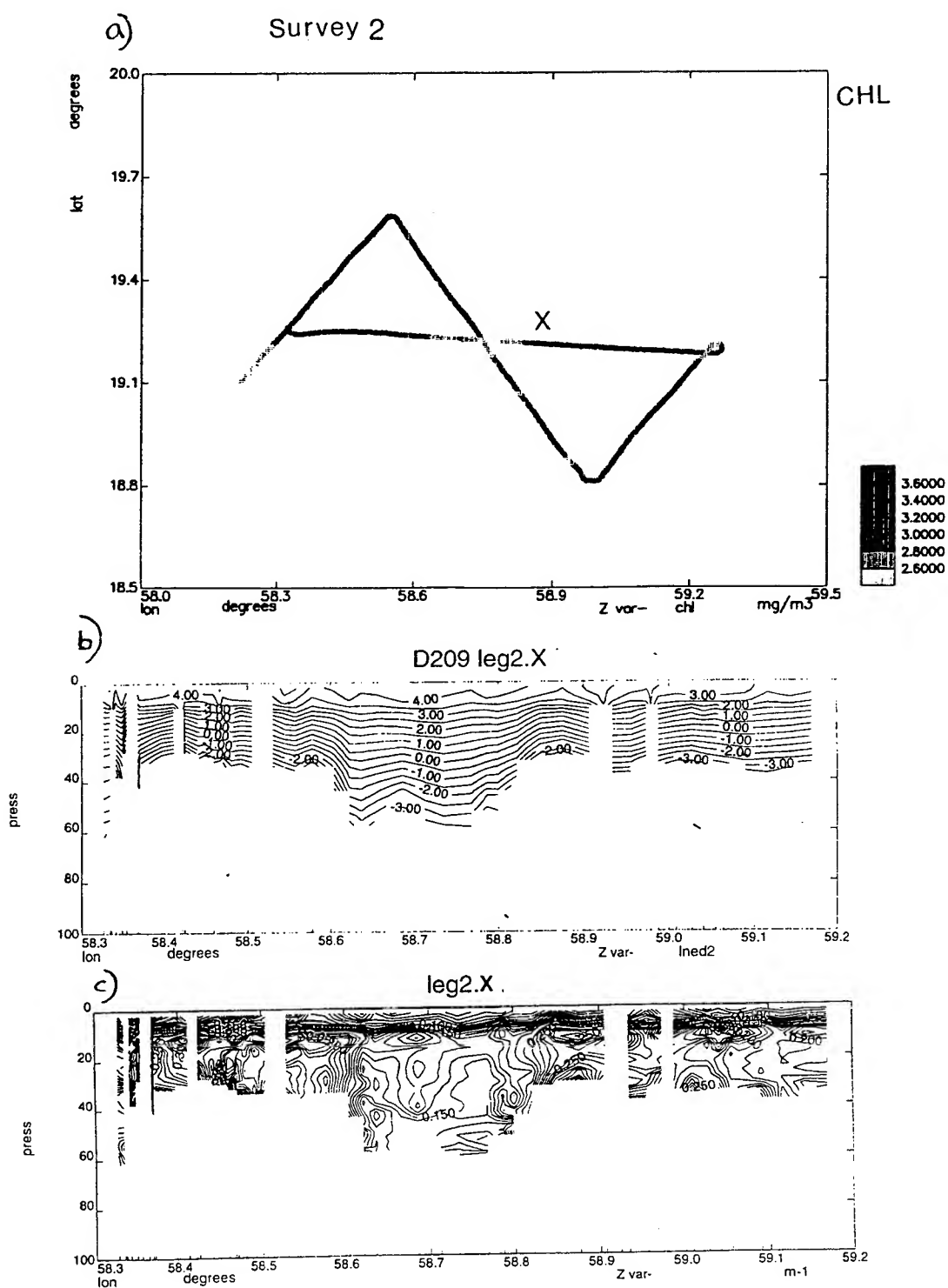


Figure 2 (a). The plot shows spatial variability in sub-surface chlorophyll concentration (mg m^{-3}) from Seasoar Survey 2. There were lower concentrations of chlorophyll in the central region; (b) Leg X downwelling irradiance (443 nm) is attenuated more slowly in the central region, and (c) K_d (443 nm) is lower.

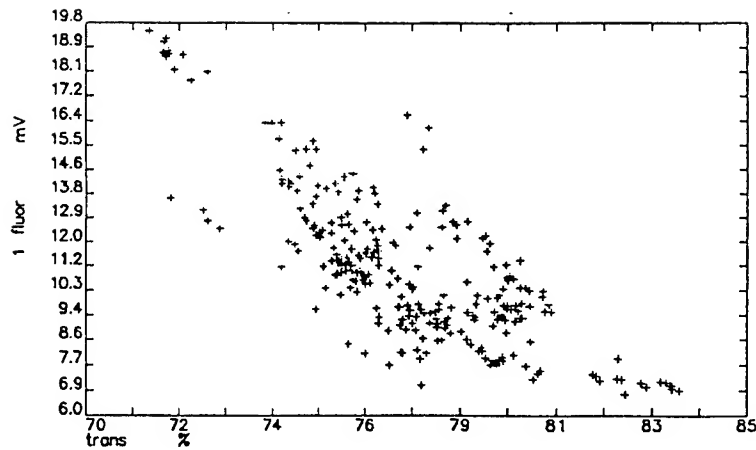


Figure 3. Fluorescence (mV) versus transmittance (%) for the sub-surface data for the whole cruise.

Spectral reflectance measured during the Lightfish survey (carried out on 9th, 10th and 12th August) was closely related to the concentration of chlorophyll. This is shown by plotting $\log(R_{440}/R_{550})$ and $\log(R_{520}/R_{550})$ against log pigment for each of the 3 days (Figure 4). This shows a departure from the relationship on 12.8.94, in the south-west of the survey where relatively low values (R_{520}/R_{550}) were observed.

This departure from the simple 2 band remote sensing algorithm for pigments can be observed more clearly in the plot of the ratio of the reflectance ratios (eg $((R_{440}/R_{550})/(R_{520}/R_{550}))$) (Figure 5). This reveals a body of 'bluer' water in the survey, and this was in south eastern part of the survey (Region X).

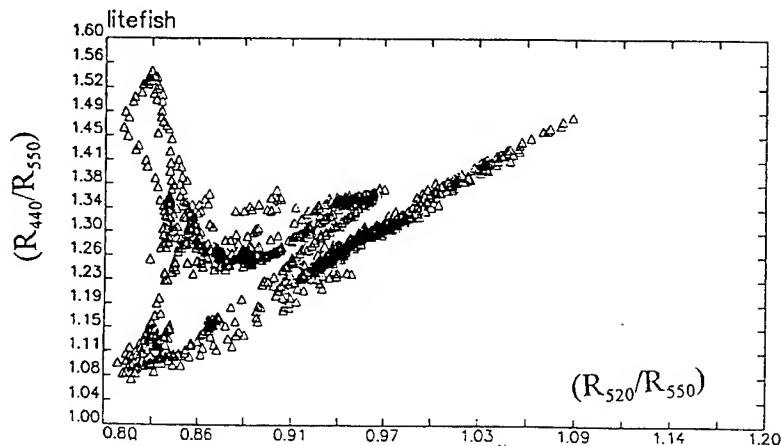
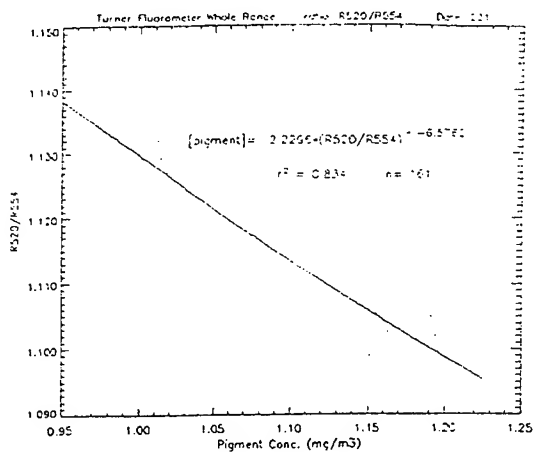
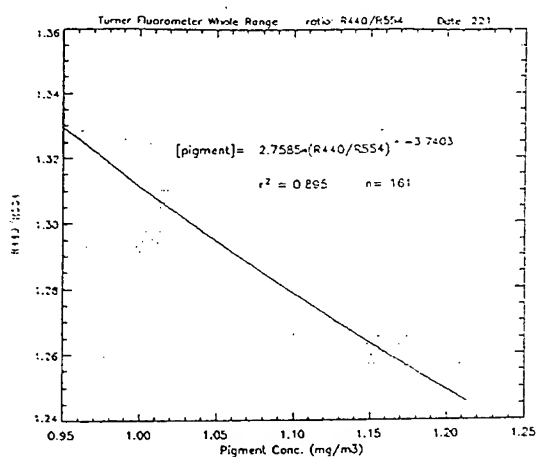
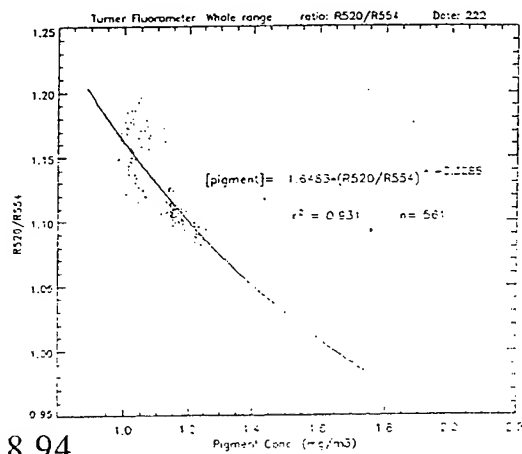
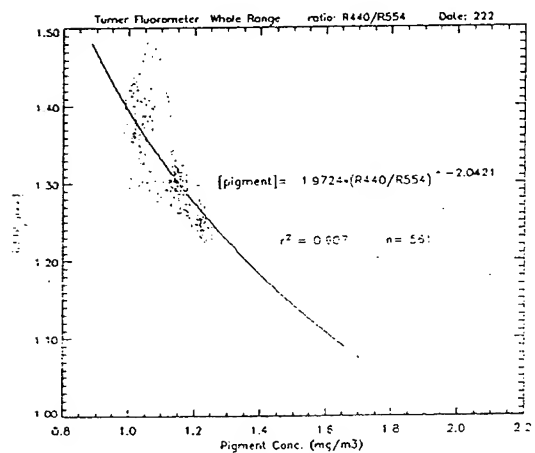


Figure 5. The ratio of the reflectance ratios (eg $((R_{440}/R_{550})/(R_{520}/R_{550}))$), showing the departure from the general trend in part of the data with relatively high values of (R_{440}/R_{550}) .

9.8.94



10.8.94



12.8.94

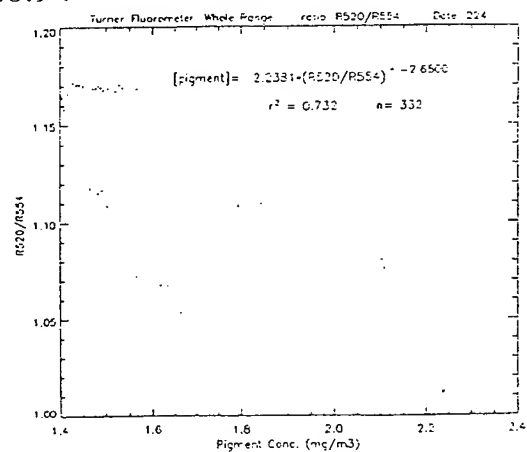
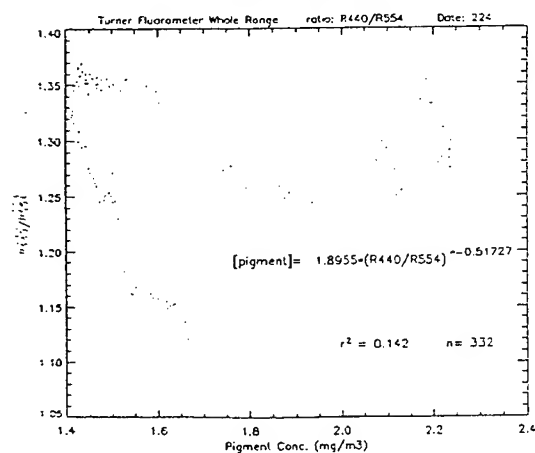


Figure 4. R440/R550 and R520/R550 plotted vs. pigment for each of the 3 days. This shows a departure from the relationship on 12.8.94, in the south-west of the survey where relatively low values (R520/R550) were observed.

Phytoplankton taxonomic groups are shown below (Figure 6(a) and (b)) for two regions during the Lightfish survey. In the south eastern part of the survey (X) there were proportionally more cyanobacteria and microflagellates (Sample 25), than in the 'greener' water (Y) (Sample 33). Sample 33 shows that diatoms were the dominant group, and cryptophytes and prymnesiophytes were there in larger proportions than in the sample from the southeast Sample 25). The pigment data is also shown below (Figure 6c) and (d)): Region Y=Sample 1; Region X=Sample 3; (e) shows Lightfish (sub-surface) reflectance spectra for 3 stations; solid line = station in region X; dotted lines = samples in region Y.

The ratio of total carotenoids to total chlorophylls may provide some insight into the cause of the spectral variation. This is expected to show a linear relationship, since carotenoids absorb longer wavelengths of light, thus reflecting shorter wavelengths. These pigment ratios are compared with the spectral ratios for the two areas (table below). This showed the expected trend, but cannot be proven with so few data. Furthermore, other factors should be considered in respect to the spectral change in reflectance (eg phytoplankton physiology and senescence; spatial variations in yellow substance; suspended particulates, etc).

carotenoid/chlorophylls		((R440/R550)/(R520/R550))	
sample 1	0.6	sample 33	1.35
sample 3	0.8	sample 25	1.62

The pigment data has been used to reconstruct the absorption spectrum for station 1 (Figure 6(f))(using a method described by R. Aguirre Gomez⁵. It should be noted that the absorption spectrum has not been modelled to include the spectral shifts caused by packaging, cell shape, size, physiological state and the extraction media of the individual pigments. The reflectance spectrum for the sample, and for a neighbouring station is also shown (e), along with the reflectance for a station in Region Y.

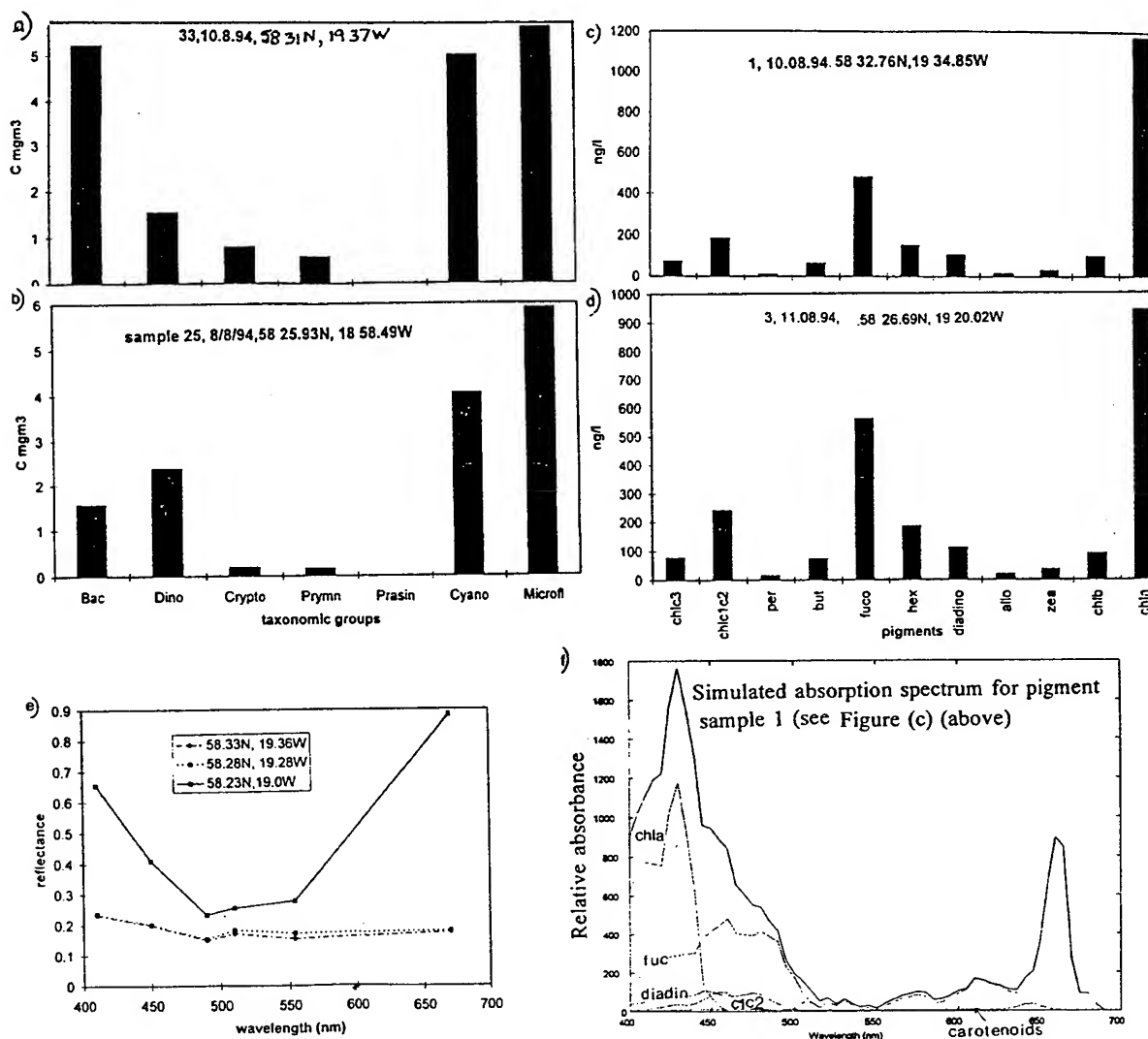


Figure 6. Phytoplankton taxonomic groups are shown in (a) and (b) for two regions sampled during the Lightfish survey. In the south eastern part of the survey (X) there were proportionally more cyanobacteria and microflageallates (Sample 25), than in the 'greener' water (Y) (Sample 33). Sample 33 shows that diatoms were the dominant group, and cryptophytes and prymnesiophytes were there in larger proportions than in the sample from the southeast Sample 25). The pigment data is also shown in (c) and (d): Region Y=Sample 1; Region X=Sample 3; (e) shows Lightfish (sub-surface) reflectance spectra for 3 stations; solid line = station in region X; dotted lines = samples in region Y; (f) The pigment data has been used to reconstruct the absorption spectrum for station 1.

4. SUMMARY

A coastal upwelling event is associated with a rapid increase in phytoplankton biomass over a period of 7 days. Doubling of phytoplankton carbon and a change in phytoplankton composition is observed over within 15 days. The optical properties of the water column are strongly influenced by the increase in phytoplankton biomass, although there is a high degree of spatial and temporal variation. The spectral reflectance of the sub-surface waters are compared with the phytoplankton taxonomic groups, and the relative proportions of the light absorbing pigments. Simulation of the spectrum of absorbance by phytoplankton is made using pigment concentrations.

5. ACKNOWLEDGEMENTS

Dr. Peter Herring was the Principal Investigator on cruise D209; John Hemmings calibrated the fluorometers; Derek Harbour and J O'Mahony carried out the analysis of the phytoplankton; Ray Barlow and Denise Cummings analyzed the pigment concentrations by High Performance Liquid Chromatography (HPLC); Raul Aguirre Gomez reconstructed the absorption spectrum from pigment data. We acknowledge the help of all those participating in the NERC RRS Discovery cruise D209; the work was supported by the WOCE NERC Special Topic, Grant No. GST/02/0578 which is gratefully acknowledged.

6. REFERENCES:

1. J.A.Aiken, G.F. Moore and C.Trees, The SeaWiFS CZCS-Type Pigment Algorithm, *SeaWiFS Technical Report Series NASA Technical Memorandum 104566, Volume 29*, pp 34.1995.
2. I.S. Robinson, B.Booty and A.R.Weeks, A towed near-surface optical reflectance meter for measuring ocean colour in support of remote sensing, *Deep Sea Research I*, **42**, 2093-2111, 1995.
3. A.R.Weeks, J.A., Aiken, M.Fasham, J.Read, D.Harbour and I.Bellan, The spatial and temporal development of the spring bloom during the JGOFS North Atlantic Experiment, 1989, *Journal of the Marine Biological Association of the UK*, **73**, 253-282, 1993
4. R.F.C.Mantoura and C.A.Llewellyn, The rapid determination of algal chlorophyll and carotenoid pigments and their breakdown products in natural waters by reverse-phase high-performance liquid chromatography, *Analytica Chimica Acta*, **151**, 297-314.
5. R.Aguirre-Gomez, A.R.Weeks and S.Boxall, The identification of phytoplankton pigments from absorption spectra, In: *Proceedings of the International Colloquium of Photosynthesis and Remote Sensing, August 1995*, 191-205, 1995.

Scattering phase function of very large particles in the ocean

Weilin Hou, Kendall L. Carder, David K. Costello

University of South Florida, Department of Marine Science
140 7th Ave South, St. Petersburg, FL 33701

ABSTRACT

Scattering properties of large particles are mostly unknown, either in theory or measurement, primarily due to the significant variations of large particle characteristics in the natural environment and the inability to sample non-invasively. The Marine-Aggregated, Profiling and Enumerating Rover (MAPPER), measures scattering angles in the vicinity of 50, 90 and 130° caused by very large particles ranging from 280µm and up. Measurements were made during SIGMA cruise (Significant Interactions Governing Marine Aggregation), April 13-21, 1994 in East Sound, Washington, using Structured Light Sheet formed by 4 diode lasers of 660nm wavelength. The results fit the analytic phase function used by Beardsley and Zaneveld, and indicate a significant elevation of back-scattering efficiency throughout the water column for all downcasts during our multi-day experiments. Some of this increase in efficiency can be explained by multiple scattering, using Monte Carlo simulation, assuming independent scattering. Measured in-situ particle size distributions, in conjunction with Mie theory, demonstrate that large particles are significant scatterers in the ocean and contribute up to 20% of total scattering. These measurements support previous theories that large, marine-snow types of particles enhance back scattering efficiency and, when present, contribute significantly to remote sensing signals.

Keywords: scattering, large particle, phase function, marine snow, aggregates

1. INTRODUCTION

Light scatterers in the ocean are usually small and invisible to naked eyes yet with vast quantity in any unit volume, such as phytoplankton cells and small bacteria. Larger ones measuring hundreds of microns and up in diameter, such as marine snow type particles (0.5mm and up), are often ignored since they are relatively rare^{1,2} and do not affect much of our routinely measured optical properties such as absorption, attenuation and scattering; these are inherent to the medium (sea water and its components), and termed inherent optical properties (IOP, Preisendorfer, 1961). IOP's can be used to predict such frequently used quantities as remote sensing reflectance (R_{rs}), water leaving radiance (L_u), irradiance attenuation (K_d), which vary with location of light source and termed apparent optical properties (AOP). This approach, usually referred to as model closure, would be successful if the derived AOP match those directly measured AOP. However, IOP measurements like those of beam attenuation (c-meter) or scattering meter typically involve water samples no more than a few cubic centimeters, hence unlikely to include those large, "rare" marine snow type particles which appear a few times per liter, while on the other hand, AOP measurements such as water leaving radiance L_u involve back-scattered signals from tens of cubic meters of water and would definitely include the effect of marine snow particles. It has been estimated that 1,000 samples need to be taken on average, for 25cm pathlength c-meter to include one 1-mm-size particle, assuming flat volume distribution or a hyperbolic slope of -3, for cumulative particle size distribution².

These discrepancies could pose a significant problem to model closure if indeed these large particles exist in abundance. It is therefore necessary to either include the effect of large particles in IOP measurement, or exclude their effect from AOP. Since it is not feasible to scale up instruments that measures IOP², direct measurement of these very large particles and their optical properties is desirable. The Marine Aggregated Particle Profiling & Enumerating Rover (MAPPER) system⁴ (Figure 1) fills this need by measuring large particle scattering in forward (near 50°), near 90 and backward (near 130) directions, and continuous spatial particle size distribution. Data results from SIGMA Friday Harbor experiment are used here. Single particle scattering phase functions which describe the angular scattering behavior are derived based on Monte Carlo simulations, and compared to measurement, leading to an empirical phase function in Beardsley and Zaneveld form (Beardsley and Zaneveld, 1969).

2. MEASUREMENTS

Great morphological diversity has been observed for these large, fluffy or "marine snow" type particles¹, indicating different origins or pathways of particle formation, such as physical contact (Brownian movement, differential settling, shear), biological excretion and degradation. The fragile nature of these particles often poses significant difficulties to sampling and measurements as handling could easily break them apart.

To measure large-particle optical properties such as scattering, a multi-camera system was developed in Marine Science Department, University of South Florida to measure the abundance, distribution, and optical information of these large particles⁴. A hyper-stereo mirror module (HMM) consists of two tilted mirrors mounted on MAPPER gives the images of particles at different scattering angles, when only one laser is used (Figure 2).

MAPPER

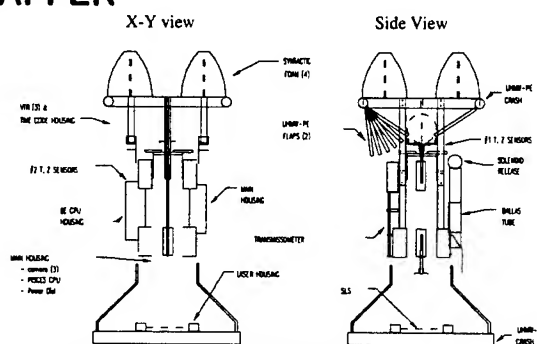


Figure 1 Sketch of MAPPER

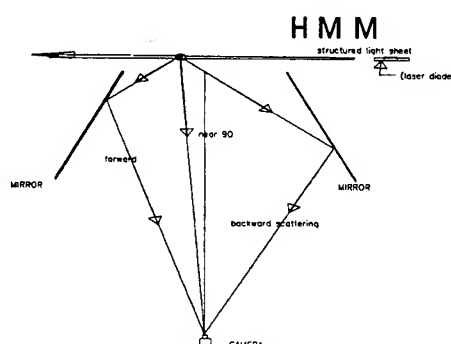


Figure 2 Hyperstereo Mirror Module

To overcome the difficulties associated with data reduction and image processing, a PC-based, automated image control and examination (ICE) system has been implemented^{4,5}. The system is capable of automatic image capturing, digitization, measurement and classifying particles based on pattern recognition and optical characteristics. Single large particle scattering in HMM gives the forward (near 50 to 60°), side (near 90°) and backward (near 130°) scattering which has yet been done for large particles.

We choose to measure fixed windowing positions and average their value over depth. With measured particle concentration at >100 per liter for large particles (100µm), any average over 5 meter range should give a sample size that is statistically sufficient, since each window samples a water volume of 35.3 liters.

Each data point is corrected for its path attenuation; namely, from laser to the scattering center and from scattering center to the forward, near 90°, and backward directions. Final plots are those normalized to 90° scattering, in order to ease comparison with other functions.

Figure 3 and 4 shows the measured single particle phase functions for two downcasts carried out on April 20 (20:00, denoted as 4/20 H, and 6:00 as 4/20 D), and April 21 (0:00, as 4/21 B), 1994, at East Sound, WA., normalized to 90°. The phase function for scattering in larger angles used by Beardsley and Zaneveld (1969)

$$\tilde{\beta}_{BZ} \sim \frac{1}{(1 - \epsilon_f \cos \phi)^4 (1 + \epsilon_b \cos \phi)^4} \quad (1)$$

proved to closely match our measurements, where ϕ is scattering angle and this 90° normalized phase function seems working out nicely in our cases, though small scattering obviously biased (Mobley, 1995).

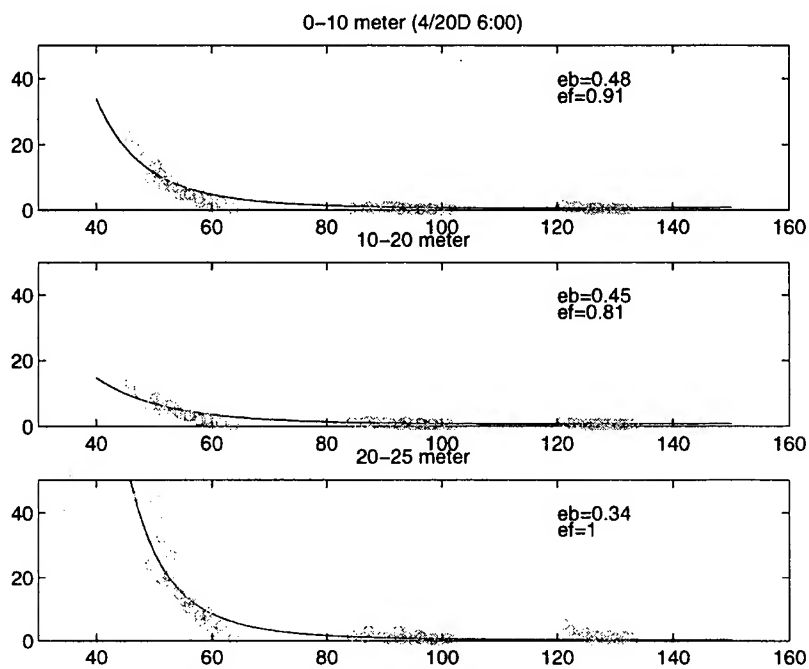


Figure 3. Single Particle Scattering (4/20/94)

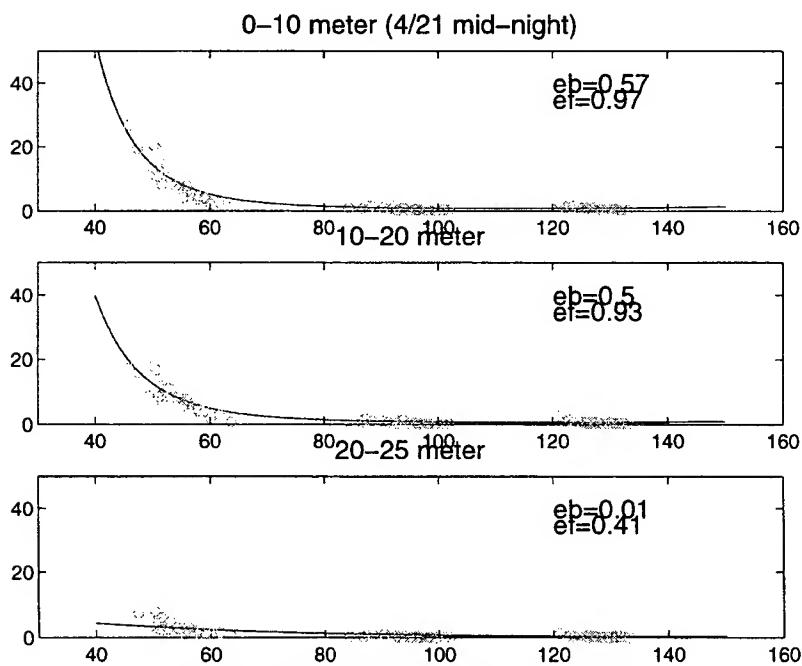


Figure 4. Single Particle Scattering (4/21/94)

Measurements taken from other down casts are presented in Table 1. Each value is averaged over either whole water column or part, for every 1/30 second continuous measurement (in which each data point corrected for corresponding beam attenuation and individual geometry). Beam attenuation at 660nm, almost exclusively caused by scattering, also measured by MAPPER, is listed in the table 1, with the slope of

differential particle size distribution (k), measured for each depth. k is derived from the hyperbolic-shaped differential particle size distribution, or Junge type:

$$\frac{d^2N}{dD * dV} = A * D^{-k} \quad (2)$$

D is the diameter of the particle, k the slope of the distribution, A the constant that associated with particle concentration, N the number of particles in the volume measured, and V the sample volume.

	ϵ_b	ϵ_f	$c \text{ (m}^{-1}\text{)}$	$A \text{ (x10}^4\text{)}$	k
4/19 D	0.4	0.83	1.47	4.22	3.20
4/20 D	0.47	0.87	1.38	5.53	3.09
4/20 H	0.49	0.9	1.63	4.64	3.15
4/21 B	0.51	0.91	1.74	6.21	3.15
4/21 H (0-10m)	0.57	0.97	2.52	6.56	3.15
4/20 H (0-6m)	0.54	1	2.76	2.91	3.09
4/20 D (10-20)	0.45	0.81	0.99	6.06	3.07

Table 1. Parameter of single particle scattering (units in cm)

3. DISCUSSION

When $0 < \epsilon_b, \epsilon_f \leq 1$, in Bredlesy and Zaneveld phase function, each constant controls the level of backward ($>90^\circ$, ϵ_b) or forward ($<90^\circ$, ϵ_f) scattering almost separately, and could be used as a descriptive measure to the degree of scattering in those general directions. For example, using Mie scattering code³, a 100 μm diameter particle ensemble (with Gaussian distribution centered at 100 μm , 7 size groups and a standard deviation of 20 μm), displays a scattering phase function (Figure 5, curve "Mie") that could be described very well (in larger angles), by $\epsilon_b = 0.36$ and $\epsilon_f = 0.81$ (curve "BZ" in Figure 5). These numbers can serve as a general guideline to describing the scattering behavior of large particles. A layer of large particles existed at the surface of the water during April 20 night downcast ($k = 3.06$). Although the total particle concentration is lower ($A = 2.91 \times 10^{-4}$), a high beam attenuation ($c = 2.76$) is seen, indicating that the total scattering is strong. This is confirmed by high values of $\epsilon_b = 0.54$, $\epsilon_f = 1$. However, when these values drop, as in April 20 morning cast (D, 10 to 20m), we notice significant drop in corresponding c -meter value (0.99 m^{-1}), although we have a similar particle size distribution and higher particle concentration (these particles might have different scattering properties such as lower index refraction). This indicates that our ϵ_b and ϵ_f are indeed good descriptors for particle scattering and, in our case, our measured ϵ_b and ϵ_f for the large particles.

Scattering of light by large particles are dominant in forward direction, as seen by Mie scattering calculations (Figure 5). Notice if we overlay our measurements (circles) on top of calculated Mie scattering, enhanced backward scattering occurs. This, in part, could be explained by independent multiple scattering simulation. If assume each photon scatters up to 3 times before reaches the collector, Monte Carlo simulations show elevated back-scattering ("multi Mie" as in Figure 5). Intuitively, when a photon gets scattered by a large particle, chances are greater that its direction will be changed little (stronger forward scattering) with only a slim possibility of back-scattering. However, once it gets scattered backward, it will have a better chance stay in that direction. It is this imbalance that will "drain" photons from forward direction into larger scattering angles and hence enhance backscattering. In natural environment, multiple scattering should be mostly considered, even when particle concentration is low. The discovery of high abundance of transparent exopolymer particles (TEP) in natural water and in aggregates¹, seems to indicate that such particles may possess complex structures and make multiple scattering much more likely. If so, the role of large particle scattering may be much greater than previously believed.

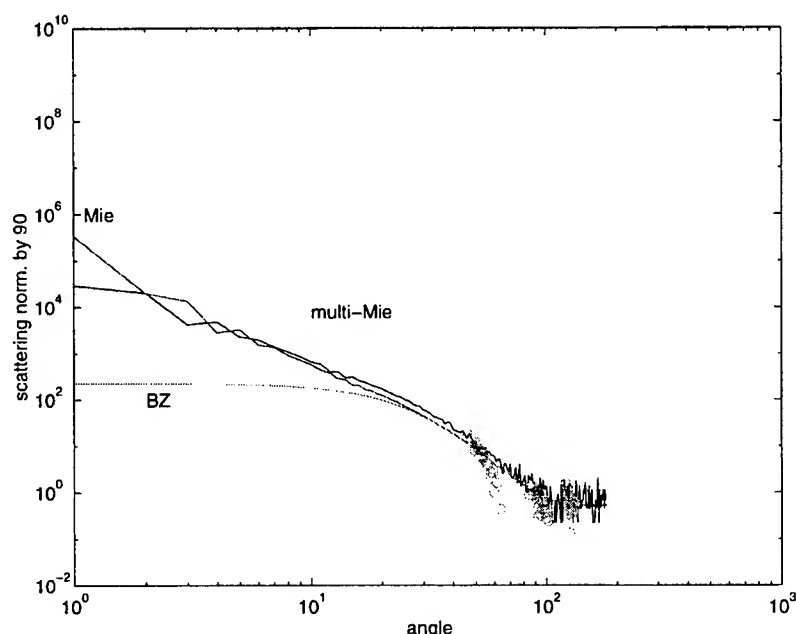


Figure 5 Measured vs calculated

The slope of differential particle size distribution describes the relative abundance of large to small sized class particles; if each particle size bin has equal volume particles, the slope would be $k=4$ as in Equation 2, or 3 for cumulative particle size distribution. If $k < 4$, the "excessive" large particles could come in from various sources, like biogenic, or resuspension, or even the method of describing the size⁵. This "enlarged" value gives large particle scattering more importance as we previously perceived. A simple example is shown below using our measured particle size distribution, and single particle scattering efficiency calculated using anomalous diffraction theory (van de Hulst, 1957). Thus, the total scattering within certain size range D_1 and D_2 is given by,

$$b = \int_{D_1}^{D_2} f(D) * Q_c(D) * dD \quad (3)$$

The relative contribution of particles in certain size range are examined using this integral, as listed in Table 2, with relative index refraction $n_r=1.05$ (typical for phytoplankton cells):

Slope	0-1 μ m	1-10 μ m	10-100 μ m	0.1-1mm	1-10mm	1-10cm
3	0.5	18.6	21.4	20.7	19.8	18.9
3.5	4.1	56.9	26.7	8.60	2.72	0.86
4	15.7	70.3	12.6	1.24	0.12	0.01
4.5	43.2	52.7	3.9	0.13	0.004	0.00

Table 2 Contribution of Scattering in Size Group for $n_r=1.05$

This calculation illustrates that the slope of size distribution is very sensitive to scattering contribution. When the slope is less than 3, only the large particles contribute to the total scattering. This changes when approaches 3, the size group from 1 μ m and larger shows about equal contribution in each group. As the slope increases, less contribution results from large particle scattering.

These calculations assume the particle size distribution is continuous over the entire particle size spectrum and the same slope is applicable over the whole range. Other research suggests that the slope is not single valued and is larger at the small particle end⁷. If so, the contribution of particle scattering would be exclusively attributed to small particles less than 10 μ m in diameters (Table 3). In Table 3, the first three

size groups (up to 10 μ m) are assigned varying slopes (first column), and the remaining size groups have a fixed slope of 3.5. In this case, 89% contribution comes from 0 to 1 μ m range and it jumped to 99% when the slope just turned to -5.3.

slope*	0-0.1 μ	0.1-1 μ	1-10 μ	10-100 μ	0.1-1mm	1-10mm	1-10cm
3.5	0.13	4.07	56.9	26.7	8.60	2.72	0.86
4.0	1.31	11.9	61.2	17.6	5.67	1.79	0.57
4.5	14.4	25.6	48.5	7.86	2.53	0.802	0.25
5.0	75.4	14.0	9.51	0.797	0.26	0.081	0.026
5.3	94.9	3.69	1.34	0.073	0.02	0.007	0.002

Table 3 Contribution of Scattering in Size Group for $n_r=1.05$

However, the above slope for smaller particles is questionable. A connected slope of -6 will generate 10^{19} particles per m^3 in our case (0.1 to 0.2 μ m). Even assuming a slope of -4, the total number would be $10^{16.5}$ by using slope of -3 connection as 10 μ m size point, while a slope of -3.5 and $A \sim 10^{-4}$ (Table 3) will show $10^{13.5}$ per m^3 . Friday Harbor data (unpublished) ($A=3.792 \times 10^{-4}$, $K=-3.29$) show an average concentration 9.27×10^{13} per m^3 for 0.1 μ m size particles (0.1 μ - 0.2 μ m), comparable to measured sub-micron particle measured on order 10^{13} from 0.38 to 1 μ m⁷.

4. ACKNOWLEDGEMENT

Financial support was provided by the Office of Naval Research to the University of South Florida through Grant N00014-88-J-1017, N00014-94-0963 and N00014-96-1-5013.

5. REFERENCES

1. Alldredge, A. L., U. Passow, and B.E. Logan, "The abundance and significance of a class of large, transparent organic particles in the ocean," *Deep-Sea Res.* 40, pp.1131-1140, 1993
2. Carder, K.L. and D.K. Costello. "Optical effects of large particles," *Ocean Optics*, R.W. Spinrad, K. L. Carder and M.J. Perry (eds). Oxford University Press, New York, N.Y. pp.243-257, 1994
3. Bohren, C. F. and D. R. Huffman, *Absorption and scattering of light by small particles*, Wiley-Interscience, 1983
4. Costello, D.K., K.L. Carder and R.G. Steward, "Development of the Marine Aggregated Particle Profiling and Enumerating Rover (MAPPER)," *Underwater Imaging, Photography, and Visibility*, Richard W. Spinrad, Editor, Proc. SPIE 1537, 161-172, 1991
5. Hou, W. (*In Prep.*) "Characteristics of large particles and their effects on the submarine light field," *Dissertation*, University of South Florida, Marine Science Department.
6. Hou, W., D. K. Costello, K. L. Carder and R.G. Steward, "High-resolution Marine Particle data from MAPPER, a new, in situ optical ocean instrument," *EOS AGU/ASLO* (75), 3, 21, 1994
7. Koike, I. S. K. Terauchi and K. Kogure, "Role of sub-micrometre particles in the ocean," *Nature*, London, 345, 242-243, 1990

Prediction of euphotic depths and diffuse attenuation coefficients from absorption profiles: a model based on comparisons between vertical profiles of spectral absorption, spectral irradiance, and PAR.

J. Ronald V. Zaneveld, W. Scott Pegau, and Andrew H. Barnard

College of Oceanic and Atmospheric Sciences, Oregon State University, Corvallis, Oregon 97331

James L. Mueller

Center for Hydro-Optics and Remote Sensing, San Diego State University, San Diego, California 92120

Helmut Maske, Eduardo Valdez, Ruben Lara Lara, and Saul Alvarez Borrego

Centro de Investigación Científica y de Educación Superior de Ensenada, Ensenada 2732, Baja California, Mexico

ABSTRACT

A model is presented which predicts the diffuse attenuation coefficient of downwelling irradiance as a function of depth and the depth of the euphotic zone as based on the one percent level of Photosynthetically Active Radiation from vertical profiles of spectral absorption and attenuation. The model is tested using data obtained in the Gulf of California. The modeled diffuse attenuation coefficients and PAR levels are shown to have average errors of less than five percent when compared to the measured values.

Keywords: absorption, attenuation, irradiance, diffuse attenuation, average cosine, PAR, night time K meter.

1. INTRODUCTION

Recent instrument development efforts at WET Labs, Inc. and Oregon State University^{1,2,3} have made the *in situ* measurement of inherent optical properties (IOP) such as spectral absorption and attenuation coefficients routine. Since these parameters can now be measured accurately it is of interest to use these IOP to predict apparent optical properties (AOP) such as irradiance levels, diffuse attenuation coefficients of irradiance, and PAR levels. The connection between these inherent and apparent optical properties is via the equation of radiative transfer, which solves for the radiance distribution as a function of depth when the absorption and scattering properties of the sea water as well as the incident radiance distribution are known.

2. MODELS

2.1 K(z) model

The integration of the equation of radiative transfer is given by Gershun's equation (unless indicated otherwise, the wavelength is assumed to be constant):

$$\frac{dE(z)}{dz} = -a(z) E_O(z), \text{ or } K(z) E(z) = a(z) E_O(z), \quad (1)$$

where $E(z)$ is the plane irradiance, $E_O(z)$ is the scalar irradiance, $a(z)$ is the absorption coefficient, and $K(z)$ is the diffuse attenuation coefficient of irradiance, given by:

$$K(z) \equiv -\frac{dE(z)}{E(z) dz} \quad (2)$$

If we define the average cosine of the light field as

$$\bar{\mu}(z) \equiv \frac{E(z)}{E_O(z)}, \quad (3)$$

we get that

$$K(z) = a(z) / \bar{\mu}(z) \text{ and } \bar{\mu}(z) = a(z) / K(z). \quad (4)$$

If we can model the average cosine of the light field we can thus predict the vertical structure of $K(z)$ if $a(z)$ is known. Starting with Zaneveld (1989) a number of models of the vertical structure of the average cosine of the light field in homogeneous media with flat surfaces have been presented^{4,5,6,7,8,9}. As will be shown below using data from the Gulf of California, none of these models are applicable to our data because the waters of the Gulf (and those of most other natural water bodies) are not homogeneous. Significant surface effects furthermore invalidate the flat surface assumption of the models. The simplest model is then to assume that the light field is sufficiently diffuse to allow $\bar{\mu}(z)$ to be approximated by

the average cosine of the asymptotic light field, $\bar{\mu}_{\infty}(z)$, that would exist if the entire water column had the IOP's present at the local depth z . We thus set:

$$\bar{\mu}(z) \approx \bar{\mu}_{\infty}(z). \quad (5)$$

A model for $\bar{\mu}_{\infty}(z)$ that fits experimental data very well⁴ is given by:

$$\bar{\mu}_{\infty}(z) = \frac{1 - b(z)/c(z)}{1 - 0.52 b(z)/c(z) - 0.44 (b(z)/c(z))^2}, \quad (6)$$

where $b(z)$ is the scattering coefficient and $c(z)$ is the beam attenuation coefficient at depth z . A combination of equations 4, 5, and 6 thus describes our model for the determination of $K(z)$ from $a(z)$, $b(z)$, and $c(z)$.

2.2 K_{PAR} and euphotic depth model

Once $K(z)$ has been modeled we can determine irradiance levels from:

$$E(z) = E(0) \exp\left[-\int_0^z K(z) dz\right] = E(0) \exp[-\tau(z)], \quad (7)$$

where $\tau(z)$ is the optical depth at a given wavelength. For the above development, the wavelength has not been expressly stated. The expressions are assumed to be correct at any wavelength in the visible region. Equations 4, 5, and 6 can thus be carried out at a number of wavelengths. PAR levels can then be obtained from

$$\text{PAR}(z) = \text{PAR}(0) \int_{400}^{700} E(\lambda, z) d\lambda. \quad (8)$$

The euphotic depth is then given by the depth at which $\text{PAR}(z) / \text{PAR}(0) = 0.01$. A simpler approach is to assume that there is a one to one relationship between $\tau(z)$ and $\tau_{\text{PAR}}(z)$ as was demonstrated in Zaneveld et al. (1993). In that paper a piece wise linear relationship was deduced. Here we model the relationship with a second order polynomial.. This second order equation is given by:

$$\tau_{\text{PAR}}(z) = -0.0308 \tau^2(488, z) + 1.325 \tau(488, z) \quad (9)$$

If the optical depth at 488 nm has been calculated from the IOP, the PAR optical depth can then be calculated from Eq. 9. To determine a given PAR light level such as the euphotic depth, for which PAR is 1% of its surface value (so that $\tau_{\text{PAR}}(z) = 4.6$), we can then calculate a number of $\tau(z)$, and interpolate to obtain the desired depth.

A slightly less accurate, but much faster method for calculating a number of PAR levels is as follows. It is assumed that we want to calculate those depths at which PAR has been reduced for example to 30, 10, 3, and 1% of its surface value ($z_{0.3}$, $z_{0.1}$, $z_{0.03}$, and $z_{0.01}$). We invert the relationship in Eq. 9:

$$\tau(488, z) = 0.0266 \tau_{\text{PAR}}^2(z) + 0.6924 \tau_{\text{PAR}}(z). \quad (10)$$

Eq. 10 is assumed to be a universal relationship. For example, the euphotic depth, $z_{0.01}$, is at the depth for which $\tau_{\text{PAR}}(z) = 4.6$, so that $\tau(488, z) = 3.75$. The results of Eq. 7 for a given profile can similarly be expressed as a second order inverse polynomial:

$$z(\tau, x, y) = A_1(x, y) \tau^2(488, z) + A_2(x, y) \tau(488, z). \quad (11)$$

A_1 and A_2 are different for each station and depend on the vertical structure of the IOP, as calculated above. $\tau_{\text{PAR}}(z)$ versus depth profiles are obtained by substitution of Eq. 9 into 10 and 10 into 11.

3. METHODS

During November of 1995 we carried out a research cruise in the central Gulf of California aboard the R/V El Puma. Stations were taken on the shelf near Guaymas, Sonora. These are labeled "CS." A large grid of stations was carried out in the central Gulf in deep water. These are labeled "EST." A number of stations were also taken on the sill just southwest of the central band of islands in the Gulf. These are labeled "UM." The spectral absorption and attenuation coefficients were determined by means of a WET Labs ac-9. The instrument was calibrated daily by means of a Barnstead Nanopure pure water system. Spectral irradiance was determined by means of a Biospherical PRR sensor. Profiles of IOP and AOP were typically taken half an hour apart. Diffuse attenuation coefficient profiles for the downwelling irradiance were determined from the irradiance profiles by the Hermetian polynomial method of Mueller (1991). PAR levels were obtained by spectral integration of the irradiance as in equation 8.

4. RESULTS

The data shown for IOP were obtained at 488 nm, and for the IOP at 491 nm. Fig. 1 shows the measured average cosine calculated from $\bar{\mu}(z) \approx a(z) / K_d(z)$. $K_d(z)$ is used here as this is the parameter determined from the measured $E_d(z)$. This is in error by approximately the irradiance reflectance, which is a few percent. $\bar{\mu}(z)$ is seen to be highly variable with depth, and the profiles do not display the smooth transition from a surface value to an asymptotic value as predicted by theory^{4,5,6,7,8,9}. We believe this departure from theory to be due to vertical inhomogeneities in the IOP, and the observation that the light field in the surface layer of the ocean is often probably far more diffuse than theoretical models assume. This diffuse light field is due to haze and clouds in the atmosphere, relatively low solar zenith angles, and surface waves. The modeled average cosine, from Eq. 6 is shown on Fig. 2. Fig. 3 shows profiles of measured and modeled (from Eq.'s 4,5, and 6) $K(z)$ for various stations. Measured and modeled (from Eq. 8) optical depths for 488 nm are shown on Fig. 4. Measured and modeled PAR optical depths are shown on Fig. 5 and measured and modeled $z_{0.3}$, $z_{0.1}$, $z_{0.03}$, and $z_{0.01}$ are shown on Fig. 6.

5. DISCUSSION AND CONCLUSIONS

We found that the average cosine of the light field in natural waters tends not to conform to modeled^{4,5,6,7,8,9} profiles. Due to surface roughness, clouds, and inhomogeneities, the light field is quite diffuse, so that it may be modeled by the asymptotic average cosine⁴ for the local IOP. The dependence of the asymptotic diffuse attenuation coefficient, K_∞ , on the IOP can be presented¹² as a graph of K_∞/c versus b/c . The measured K/c as a function of b/c data corresponds quite well to Zaneveld's (1989) curve for K_∞/c versus b/c . This supports the notion that $\bar{\mu}(z)$ can be modeled as $\bar{\mu}_\infty(z)$.

Generally excellent agreements were obtained between measured and modeled $K(z)$. The modeled $K(z)$ contain the vertical structure of $a(z)$, and so are more detailed than the measured $K(z)$. Excellent $K(z)$ fits translated into excellent modeled $\tau(z)$ versus measured $\tau(z)$ regressions ($r^2 = 0.988$). It was thus shown that the absorption and attenuation data can be used to determine expected daytime $K(z)$ at night.

Expected daytime $\tau_{PAR}(z)$ versus depth profiles are very good, considering that the irradiance data was usually collected about half an hour after the IOP data. Any discrepancies could thus be ascribed to spatial variations alone. Other sources of error exist, of course, in all approximations. Instrumental errors are also present. Considering these, the results are surprisingly good. This indicates that the expected daytime PAR levels can be determined with sufficient accuracy to allow appropriate depths to be determined at night, so that samples can be obtained for C-14 primary productivity incubations the following day light period.

6. ACKNOWLEDGMENTS

This work was supported by the National Aeronautics and Space Administration Ocean Biogeochemistry program and the Office of Naval Research Environmental Optics program.

7. REFERENCES

1. J. R. V. Zaneveld, J. C. Kitchen, A. Bricaud and C. Moore, "Analysis of *in situ* spectral absorption meter data," *Ocean Optics XI*, G. D. Gilbert, Ed., Proc. SPIE **1750**, 187-200 (1992)
2. C. Moore, J. R. V. Zaneveld, and J. C. Kitchen, "Preliminary results from an *in situ* spectral absorption meter," *Ocean Optics XI*, G. D. Gilbert, Ed., Proc. SPIE **1750**, 330-337 (1992)
3. J. R. V. Zaneveld, J. C. Kitchen, and C. C. Moore, "Scattering error correction of reflecting tube absorption meters," *Ocean Optics XII*, S. Ackleson, Ed., Proc. SPIE Vol. **2258**, 44-55 (1994)
4. J. R. V. Zaneveld, "An asymptotic closure theory for irradiance in the sea and its inversion to obtain the inherent optical properties," *Limnol. Oceanogr.* **34** 1442-1452 (1989)
5. J. T. O. Kirk, "Volume scattering function, average cosines, and the underwater light field," *Limnol. Oceanogr.* **36** 455-467 (1991)
6. T. T. Banister, "Model of the mean cosine of underwater radiance and estimation of underwater scalar irradiance," *Limnol. Oceanogr.* **37**(4) 773-780 (1992)
7. H. R. Gordon, K. Dong, and W. Gong, "Radiative transfer in the ocean: computations relating to the asymptotic and near-asymptotic daylight field," *Applied Optics* **32**(9) 1606-1619 (1993)

8. N.J.McCormick, "Mathematical models for the mean cosine of irradiance and the diffuse attenuation coefficient," *Limnol. Oceanogr.* **40**(5):1013-1018 (1995)
9. J.Berwald, D.Stramski, C.D.Mobley, and D.A.Kiefer, "Influences of absorption and scattering on vertical changes in the average cosine of the underwater light field," *Limnol. Oceanogr.* **40**(8):1347-1357 (1995)
10. J.R.V.Zaneveld, J.C.Kitchen, and J.L.Mueller, "The vertical structure of productivity and its vertical integration as derived from remotely sensed observation," *Limnol. Oceanogr.* **38**:1384-1393 (1993)
11. J.L.Mueller, "Integral method for irradiance profile analysis," *CHORS Tech. Memo.* 007-91, San Diego State University, 10pp. (1991)
12. L.Prieur and A.Morel, "Etude théorique du régime asymptotique: relations entre caractéristiques optiques et coefficient d'extinction relatif a la pénétration de la lumière du jour," *Cah. Oceanogr.* **23**:35-48 (1971)

8. FIGURES

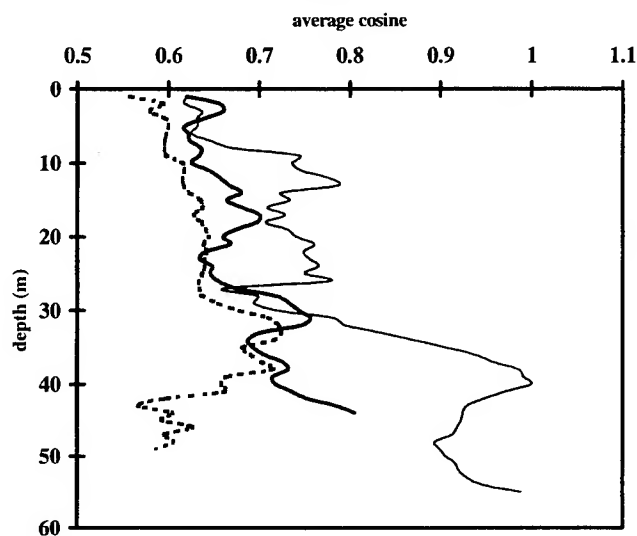


Fig. 1 - The measured average cosine obtained from Eq. 4. The thin solid line is for station CS4, the dashed line is for station EST6, and the thick solid line is for station UM209.

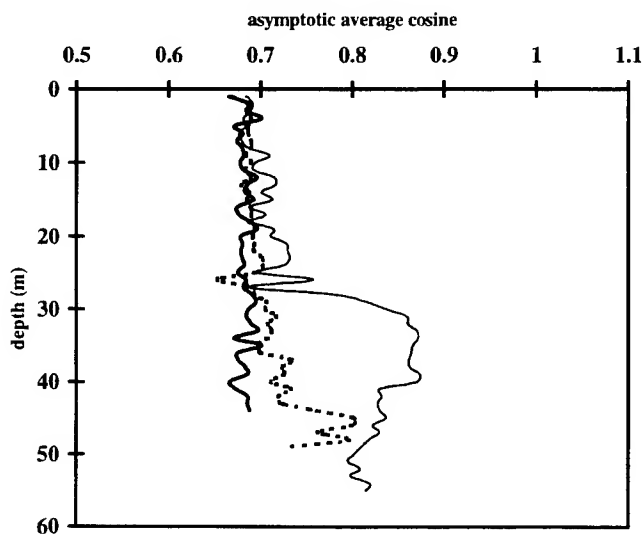


Fig. 2 - The modeled asymptotic average cosine obtained using Eq. 4 and measured $b(z)/c(z)$. Profile indicators are the same as in Fig. 1.

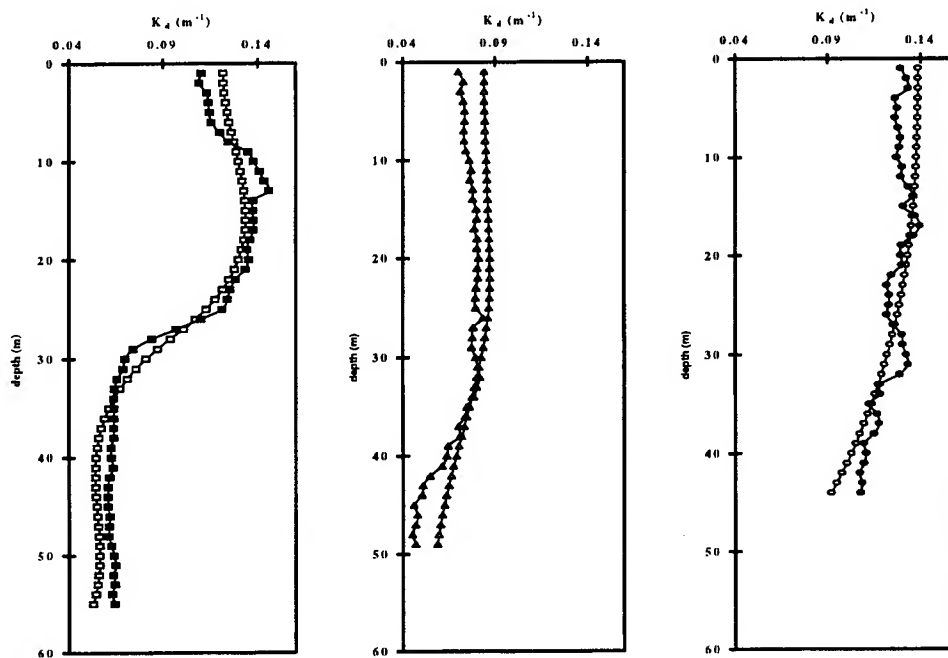


Fig. 3 - Profiles of measured $K_d(z)$ (open symbols) and modeled $K_d(z)$ (filled symbols) from Eq.'s 4,5 and 6. Left panel is for station CS4 (squares), middle panel is for station EST6 (triangles), and the right panel is for station UM209 (circles).

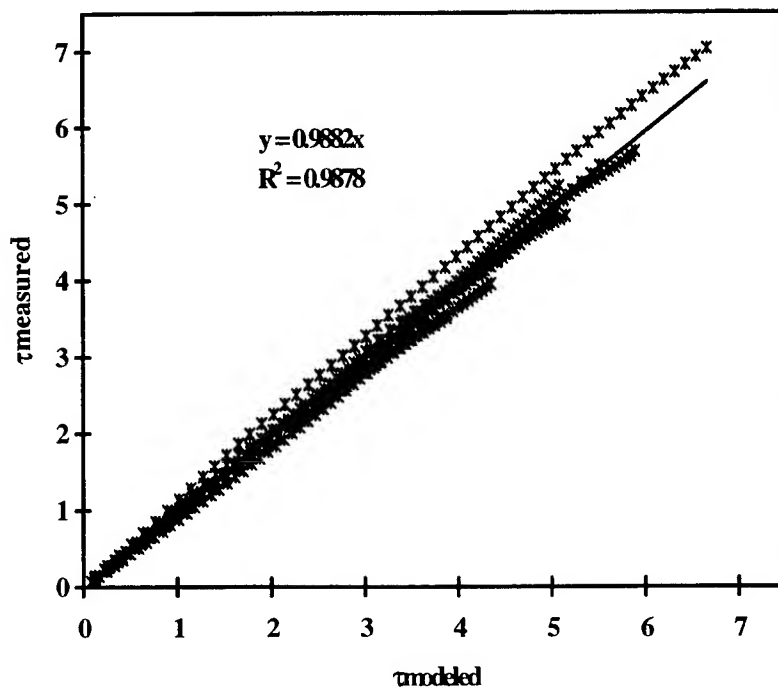


Fig. 4 - Measured optical depth versus modeled optical depth at 488nm with linear regression shown as solid line.

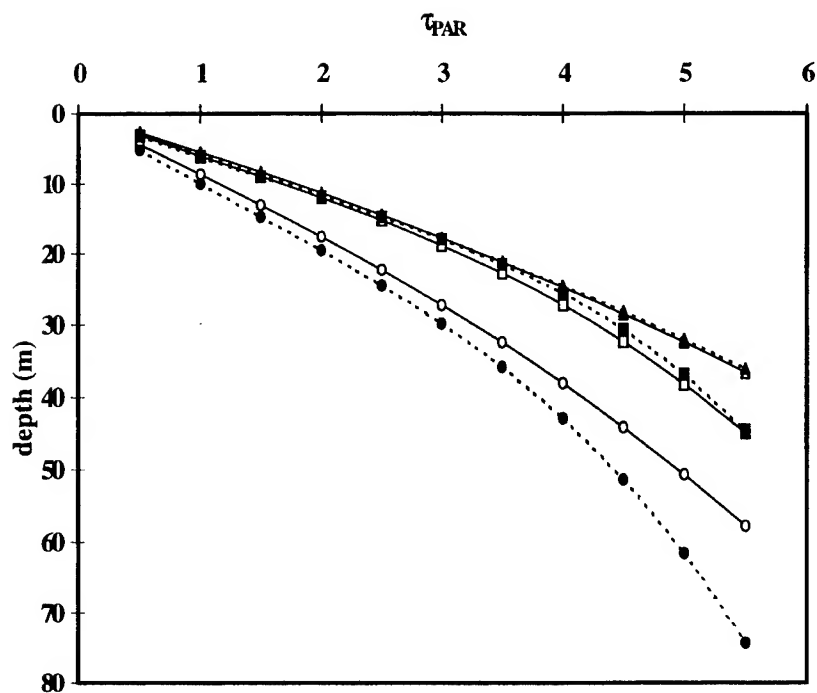


Fig. 5 - Measured and modeled PAR optical depths. Symbols are the same as in Fig. 3.

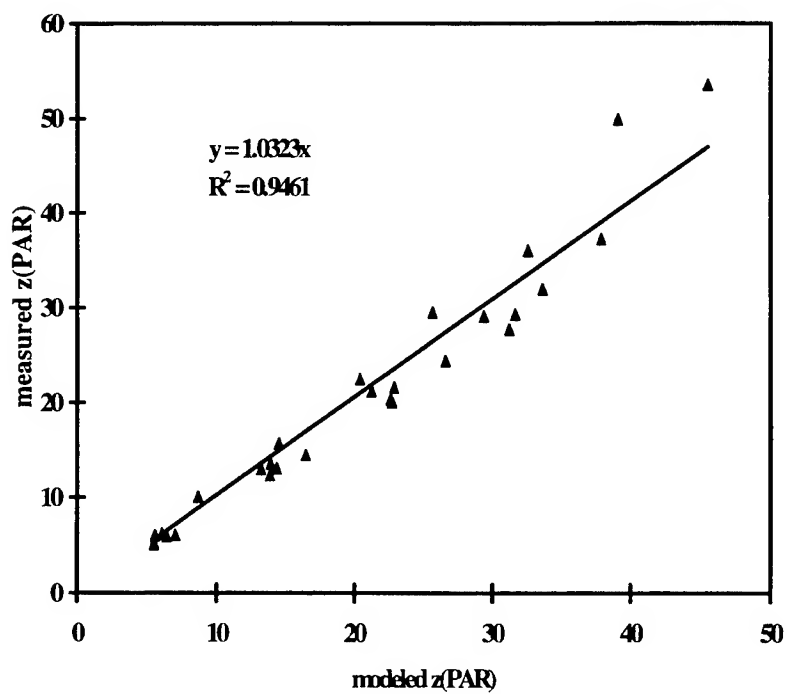


Fig. 6 - Measured versus modeled PAR depths. Points are for $\text{PAR}(z)/\text{PAR}(0) = 0.37, 0.10, 0.03, \text{ and } 0.01$ (euphotic depth).

Poster Session: Radiative Transfer Theory

A comparison of models of sea-surface reflectance incorporating Raman scattering by water

Jasmine S. Bartlett

Dept. of Oceanography, Dalhousie University,
1355 Oxford St., Halifax, N.S., Canada B3H 4J1

ABSTRACT

Reliable estimates of sea-surface optical properties from irradiance reflectance at the sea surface require algorithms and models that accurately describe optical processes in the ocean. One important process not explicitly included in most remote-sensing algorithms is Raman scattering by water. This inelastic process can be a significant contributor to sea-surface reflectance. In this study, four models of sea-surface reflectance, incorporating Raman scattering by water, are compared. The aim is to determine the degree of equivalence of the models and their relative benefits. After analytical simplification, three of the four models are shown to yield results of similar magnitude. The suitability of each of the models for remote sensing applications is then discussed.

Keywords: Raman scattering by water, sea-surface reflectance, remote sensing.

1. INTRODUCTION

The color of the ocean is affected by particles in suspension, such as phytoplankton, and by dissolved organic matter (DOM) in the water column, as well as by the water molecules themselves. This ocean color can be described by spectral variations of reflectance at the sea surface, $R(\lambda, 0)$, where λ is the wavelength and 0 denotes zero depth. Global estimates of the concentration of chlorophyll *a* plus phaeophytin (*C*) at the sea surface are often calculated from empirical relationships linking ratios of $R(\lambda, 0)$ at two wavelengths, calculated from remotely-sensed data, to C^{1-4} . One of the limitations of these empirical relationships is that inelastic processes, such as Raman scattering, are not included explicitly. Recently, it has been shown that these inelastic processes can make significant contributions to the sea-surface reflectance⁵⁻⁸.

Raman scattering occurs when a photon of a given energy interacts with a molecule, causing the scattering of a second photon with a different energy. Since the scattered photon can have either a higher or a lower energy than the incident photon, the scattering molecule will either lose or gain energy accordingly. This energy change in the molecule is equivalent to the difference between two energy levels characteristic of the molecule. The Raman scattering process for water considered here is the one that transfers light from shorter wavelengths to longer wavelengths, with a frequency shift of approximately 3400 cm^{-1} . This process has a relatively low probability of occurrence: Raman scattering by water occurs approximately one-tenth as often as elastic scattering by water. However, it has been shown that Raman scattering by water molecules may be responsible for up to 25% of $R(\lambda, 0)$ at long wavelengths (500–700 nm) in waters with low concentrations of phytoplankton^{5,7-9}. Hence, the incorporation of Raman scattering by water is essential in remote-sensing algorithms, to improve the accuracy of retrievals of oceanic properties such as *C*. The appropriate algorithm should be based on a simple, analytic model that accurately describes the effect of Raman scattering by water on the underwater light field.

Several models of sea-surface reflectance incorporating Raman scattering have been developed recently^{5,6,10,11}. Marshall & Smith⁵ incorporate Raman scattering by water into a clear-water model. The model of Lee *et al.*⁶ incorporates both Raman scattering by water and fluorescence by DOM. Haltrin & Kattawar¹¹ have developed a model to describe the combined effects of Raman scattering by water and fluorescence by both phytoplankton and DOM on reflectance. More recently, Sathyendranath & Platt¹⁰ derived a simpler analytic model to describe the effects of fluorescence and Raman scattering by water on the sea-surface reflectance.

This study compares the Raman scattering term from each of these four models. The suitability of each of the four models to remote sensing applications is then discussed.

2. INTER-COMPARISON OF THE MODELS

The four models discussed here are: the Marshall & Smith model⁵, the Lee *et al.* model⁶, the Haltrin & Kattawar model¹¹, and the Sathyendranath & Platt model¹⁰. Each of these models is briefly described below. To ease comparison, all of the solutions were rearranged in a general form. Finally, the models are compared.

2.1 The Marshall & Smith model

Marshall & Smith derived the following expression for the total reflectance (including elastic and Raman scattering), as the depth approaches zero⁵:

$$R(\lambda, 0) = R_s(\lambda, 0) + \frac{b_{rw}(\lambda')E_o(\lambda', 0)}{4(1.5K(\lambda) + K_o(\lambda'))E_d(\lambda, 0)}, \quad (1)$$

where $R_s(\lambda, 0)$ is the reflectance resulting from elastic scattering processes only, λ' is the Raman source wavelength for Raman-scattered light at λ , $b_{rw}(\lambda')$ is the Raman scattering coefficient for pure water, $E_o(\lambda', 0)$ is the scalar irradiance at the sea-surface, $K(\lambda)$ is the total diffuse attenuation coefficient, $K_o(\lambda')$ is the diffuse attenuation coefficient for the scalar irradiance, and $E_d(\lambda, 0)$ is the downwelling irradiance at the sea surface. By definition, the attenuation coefficients describe the attenuation of irradiance through a thin layer of medium, per unit incident irradiance, and the scalar irradiance is the total radiance at a point in space from all directions. The reflectance near the sea-surface resulting from Raman scattering by water, $R_r(\lambda, 0)$, is given by the second term on the right-hand-side (RHS) of Eqn. 1⁶.

By expressing the second term of Eqn. 1 as a function of $\kappa(\lambda)$, the vertical diffuse attenuation coefficient for light scattered upwards, and $K_d(\lambda)$, the vertical diffuse attenuation coefficient for downwelling light, and substituting for $E_o(\lambda', 0)$ (see Bartlett⁸ for details), the Raman reflectance can be approximated by:

$$R_r(\lambda, 0) = \frac{b_{rw}(\lambda')E_d(\lambda', 0)}{2\mu_d(\kappa(\lambda) + K_d(\lambda'))E_d(\lambda, 0)} \left(\frac{1}{2} + \frac{\mu_d}{2\mu_u} R(\lambda', 0) \right), \quad (2)$$

where μ_d and μ_u are the mean cosines for the downwelling and upwelling light fields respectively. Note that the form of this equation implies that to evaluate $R_r(\lambda, 0)$, it is necessary to know $R(\lambda', 0)$, the total reflectance (including the effects caused by Raman scattering) at the Raman source wavelength λ' .

2.2 The Lee *et al.* model

In a more recent study, Lee *et al.*⁶ expressed $R(\lambda, 0)$ as a sum of contributions from elastic scattering, fluorescence by DOM, Raman scattering by water, and scattering by the sea floor. The following expression for $R_r(\lambda, 0)$ was obtained⁶:

$$R_r(\lambda, 0) = \frac{b_{rw}(\lambda')E_d(\lambda', 0)}{(2a(\lambda) + a(\lambda'))E_d(\lambda, 0)} \left(\frac{1 + 2R(\lambda', 0)}{2} \right), \quad (3)$$

where $a(\lambda)$ is the total absorption coefficient. Dropping several assumptions made by Lee *et al.*⁶, one of which limits the use of their model to absorption-dominated waters, yields⁸:

$$R_r(\lambda, 0) = \frac{b_{rw}(\lambda')E_d(\lambda', 0)}{2\mu_d(\kappa(\lambda) + K_d(\lambda'))E_d(\lambda, 0)} \left(1 + \frac{\mu_d}{\mu_u} R(\lambda', 0) \right). \quad (4)$$

Again, to evaluate this expression at λ , it is necessary to know $R(\lambda', 0)$, the total reflectance at the Raman source wavelength λ' .

2.3 The Haltrin & Kattawar model

Later still, Haltrin & Kattawar¹¹ derived the following model for $R_r(\lambda, 0)$ based on the two-stream method:

$$R_r(\lambda, 0) = \frac{1 + \left(\frac{1 - \mu}{1 + \mu} \right)^2}{2\mu_s L(\lambda, 0)} \int_{\lambda'} \sigma^r(\lambda', \lambda) L(\lambda', 0) \left[\frac{1}{\epsilon(\lambda)\mu(4 - \mu^2) + \epsilon(\lambda')/\mu_s} \right. \\ + \frac{1}{\epsilon(\lambda)\mu(4 - \mu^2) + a(\lambda')/\mu} \left(\mu_s R_s(\lambda', 0)(2 + \mu') \left(\frac{(1 + \mu')^2}{1 + (\mu')^2} \right) R_s(\lambda', 0)\epsilon(\lambda') \right. \\ \left. \left. \times \left(\mu_s(4 - (\mu')^2) - \mu' \right) \left(\frac{1}{\epsilon(\lambda)\mu(4 - \mu^2) + \epsilon(\lambda')/\mu_s} \right) \right) \right] d\lambda', \quad (5)$$

where $L(\lambda, 0)$ is the radiance at the sea surface, $\sigma^r(\lambda', \lambda)$ is the differential emission coefficient for Raman scattering, $\epsilon(\lambda) = a(\lambda) + 2b_b(\lambda) + b_{rw}(\lambda)$ is an approximation to the beam attenuation coefficient, $b_b(\lambda)$ is the total backscattering coefficient, μ and μ' are the mean cosines for the irradiance at wavelengths λ and λ' respectively, and μ_s is the mean cosine for downwelling light caused by direct sunlight only.

To reduce Eqn. 5 to a form compatible with the other three models, it is necessary to make a number of approximations. One of the most significant of these is that the contribution to the Raman reflectance at wavelength λ is a result of Raman scattering from only one incident wavelength (λ'), thereby eliminating the need for the integral in Eqn. 5. Details of the remaining assumptions made can be found in Bartlett⁸. The resulting simplified expression for $R_r(\lambda, 0)$ is:

$$R_r(\lambda, 0) \approx \frac{b_{rw}(\lambda') E_d(\lambda', 0)}{2\mu_d(\kappa(\lambda) + K_d(\lambda')) E_d(\lambda, 0)} \left(1 + \frac{\mu_d}{\mu_u} R_s(\lambda', 0) + \frac{4}{3} \frac{b_b(\lambda')}{\kappa(\lambda) + K_d(\lambda')} \right). \quad (6)$$

2.4 The Sathyendranath & Platt model

The most recent model of the sea-surface reflectance incorporating Raman scattering by water is that of Sathyendranath & Platt¹⁰:

$$R_r(\lambda, 0) = \frac{b_{brw}(\lambda') E_d(\lambda', 0)}{\mu_d(\kappa(\lambda) + K_d(\lambda')) E_d(\lambda, 0)} \left(1 + \frac{b_b(\lambda')}{\mu_u(K_d(\lambda') + \kappa(\lambda'))} + \frac{b_b(\lambda)}{2\mu_u \kappa(\lambda)} \right), \quad (7)$$

where $b_{brw}(\lambda)$ is the Raman backscattering coefficient for water. This expression can be approximated by⁸:

$$R_r(\lambda, 0) = \frac{b_{rw}(\lambda') E_d(\lambda', 0)}{2\mu_d(\kappa(\lambda) + K_d(\lambda')) E_d(\lambda, 0)} \left(1 + \frac{\mu_d}{\mu_u} R_s(\lambda', 0) + \frac{b_b(\lambda)}{2\mu_u \kappa(\lambda)} \right). \quad (8)$$

2.5 The comparison

Four models have been manipulated to yield relationships of similar structure (Eqns. 2, 4, 6 & 8). These models describe the contribution of Raman scattering by water to reflectance at the sea surface. Each of the simplified relationships for $R_r(\lambda, 0)$ can be expressed in the form:

$$R_r(\lambda, 0) = F(\lambda', \lambda)(t_1(\lambda', \lambda) + t_2(\lambda', \lambda) + t_3(\lambda', \lambda)), \quad (9)$$

where $t_1(\lambda', \lambda)$, $t_2(\lambda', \lambda)$ and $t_3(\lambda', \lambda)$ are dimensionless functions, and

$$F(\lambda', \lambda) = \frac{b_{rw}(\lambda')E_d(\lambda', 0)}{2\mu_d(\kappa(\lambda) + K_d(\lambda'))E_d(\lambda, 0)}. \quad (10)$$

Values for $t_1(\lambda', \lambda)$, $t_2(\lambda', \lambda)$ and $t_3(\lambda', \lambda)$ are listed for each model in Table 1.

Quantity	Marshall & Smith	Lee <i>et al.</i>	Haltrin & Kattawar	Sathyendranath & Platt
$t_1(\lambda', \lambda)$:	1/2	1	1	1
$t_2(\lambda', \lambda)$:	$(\mu_d/2\mu_u)R(\lambda', 0)$	$(\mu_d/\mu_u)R(\lambda', 0)$	$(\mu_d/\mu_u)R_s(\lambda', 0)$	$(\mu_d/\mu_u)R_s(\lambda', 0)$
$t_3(\lambda', \lambda)$:	—	—	$4b_b(\lambda')/[3(\kappa(\lambda) + K_d(\lambda'))]$	$b_b(\lambda)/(2\mu_u\kappa(\lambda))$

Table 1: Terms in the relationships for $R_r(\lambda, 0)$ (after simplification) by various authors

From Table 1, it can be seen that the first term in all of the models, except that of Marshall & Smith, are in perfect agreement. The first term in the Marshall & Smith model is half the magnitude of that of the other models. Comparing the second term of the Marshall & Smith model with the second term of the Lee *et al.* model again shows a disagreement by a factor of two; the Lee *et al.* term is twice as large as the Marshall & Smith term. This may be a consequence of the value of the source term, which describes the addition to irradiance of light at wavelength λ from Raman scattering at wavelength λ' , used by Marshall & Smith. The second term of the Haltrin & Kattawar model and that of the Sathyendranath & Platt model are identical, in these simplified forms of both the models. This term is smaller than $(\mu_d/\mu_u)R(\lambda', 0)$, the second term in the Lee *et al.* model. The third terms, which appear only in the Haltrin & Kattawar model and the Sathyendranath & Platt model, appear to be of the same order of magnitude as each other. This third term has a magnitude of between 1 and 27.5 times smaller than the second term⁸. Hence, the models of Lee *et al.*, Haltrin & Kattawar and Sathyendranath & Platt may yield values for $R_r(\lambda, 0)$ of similar magnitude. However, the Sathyendranath & Platt model is easier to implement than both the Lee *et al.* model and the Haltrin & Kattawar model. Implementation of the second term in the Lee *et al.* model requires knowledge of $R(\lambda', 0)$, the total reflectance at the Raman source wavelength, which will be always unknown. In the application of their model, Lee *et al.*⁶ assumed that the term containing $R(\lambda', 0)$ is relatively small, and hence neglected it. The Haltrin & Kattawar model, in its original form, would be difficult to use in remote sensing applications because of its complexity. In contrast to both of these models, all the terms in the Sathyendranath & Platt model (Eqn. 8) are easily computed.

Comparisons of the Sathyendranath & Platt model with measurements⁸ have shown that, given appropriate parameterizations of local optical properties, the model is able to simulate oceanic values of the sea-surface reflectance to within 10% in the 400–575 nm region, and qualitatively mimic the sea-surface reflectance in the 575–700 nm region. The increased agreement observed between measured and modelled reflectance after incorporating Raman scattering indicates that the explicit inclusion of this process in models may be a step towards increased accuracy in the estimation of sea-surface reflectance.

3. CONCLUSIONS

Four models of sea-surface reflectance incorporating Raman scattering by water were compared analytically. The Marshall & Smith model⁵ disagrees with generalised forms of the other three models studied here^{6,10,11} by a factor of two. The remaining three models appear to yield results of similar magnitude to each other. The Lee *et al.* model requires knowledge of the total sea-surface reflectance, incorporating both elastic scattering and Raman scattering, at wavelength λ' to determine the Raman reflectance at λ . Since $R(\lambda', 0)$ is generally unknown in remote-sensing applications, the implementation of this model may require neglecting the term incorporating $R(\lambda', 0)$, resulting in an error of approximately 10%⁸. The Haltrin & Kattawar model does not have this problem, however the unsimplified form of their model is very complicated. For this reason, their model does not appear to be suitable for remote-sensing applications. The Sathyendranath & Platt model overcomes both of these problems; it has a relatively simple form, and all of its terms can be computed. It also appears that this model is capable of simulating measurements of the sea-surface reflectance, given appropriate parameterizations. It is therefore suggested that, of the models studied here, the Sathyendranath & Platt model is the most appropriate one for remote-sensing applications.

4. ACKNOWLEDGMENTS

I would like to acknowledge the support and suggestions provided by Shubha Sathyendranath. The helpful comments provided by Carl Boyd, Trevor Platt, John Coxon and Ian Folkins were also appreciated. Thanks also to Aurea Ciotti, Richard Davis and Kevin MacIsaac for comments on the manuscript.

5. REFERENCES

1. H. R. Gordon and A. Y. Morel, *Remote Assessment of Ocean Color for Interpretation of Satellite Visible Imagery: A Review*, Springer-Verlag, New York, 1983.
2. G. L. Clarke, G. C. Ewing and C. J. Lorenzen, "Spectra of backscattered light from the sea obtained from aircraft as a measure of chlorophyll concentration," *Science* **167**, 1119-1121 (1970).
3. A. Morel and L. Prieur, "Analysis of variations in ocean color," *Limnol. Oceanogr.* **22**(4), 709-722 (1977).
4. H. R. Gordon and D. K. Clark, "Atmospheric effects in the remote sensing of phytoplankton pigments," *Boundary-Layer Meteorol.* **18**, 299-313 (1980).
5. B. R. Marshall and R. C. Smith, "Raman scattering and in-water ocean optical properties," *Appl. Opt.* **29**(1), 71-84 (1990).
6. Z. Lee, K. L. Carder, S. K. Hawes, R. G. Steward, T. G. Peacock and C. O. Davis, "An interpretation of high spectral resolution remote sensing reflectance," in *Optics of the Air-Sea Interface: Theory and Measurement*, L. Estep, ed., Proc. SPIE **1749**, 49-64 (1992).
7. V. I. Haltrin and G. W. Kattawar, "Self-consistent solutions to the equation of transfer with elastic and inelastic scattering in oceanic optics: 2. model calculations," (in prep).
8. J. S. Bartlett, "The influence of Raman scattering by seawater and fluorescence by phytoplankton on ocean colour," M.S. thesis, Dalhousie University (Halifax, 1996).
9. K. J. Waters, "Effects of Raman scattering on the water-leaving radiance," *J. Geophys. Res.* **100**(C7), 13151-13161 (1995).
10. S. Sathyendranath and T. Platt, "An ocean-colour model incorporating trans-spectral processes," submitted to *Appl. Opt.*
11. V. I. Haltrin and G. W. Kattawar, "Self-consistent solutions to the equation of transfer with elastic and inelastic scattering in oceanic optics: 1. model," *Appl. Opt.* **32**(27), 5356-5367 (1993).

Modeling of elastic and inelastic scattering effects in oceanic optics

Vladimir I. Haltrin[†], George W. Kattawar^{††}, and Alan D. Weidemann[†]

[†] Naval Research Laboratory, Ocean Sciences Branch, Code 7331
Stennis Space Center, MS 39529-5004, USA. e-mail: <haltrin@nrlssc.navy.mil>

^{††} Center for Theoretical Physics, Department of Physics, Texas A&M University,
College Station, Texas 77843-4242, USA. e-mail: <kattawar@silly.tamu.edu>

ABSTRACT

The results of model calculations of apparent optical properties for realistic marine waters with inclusion of Raman scattering and fluorescence are presented. It is shown that the underwater light spectrum can be divided, by a threshold wavelength, into two regions with different behavior of apparent optical properties, and also that inelastic effects are significant and should be considered in ocean optics measurements.

Keywords: ocean optics, optical properties, light propagation, scattering, absorption, diffuse reflectance, sea water, Raman scattering, chlorophyll fluorescence, CDOM fluorescence.

1. INTRODUCTION

A rigorous derivation of all the equations needed to perform ocean model calculations involving both elastic and inelastic processes was presented by Haltrin and Kattawar [1]. In order to determine the importance of inelastic effects in the ocean, we need quantitative results for different realistic water types at different depths for wavelengths throughout the visible spectrum. On the basis of algorithms developed in Ref. [1], an ANSI FORTRAN-77 code was written and tested [2]. The compiled version runs in about 23 seconds on a 120MHz Apple Power Macintosh 9500 or 19 seconds on 150MHz SGI Indy and produces results for 31 depths between 0–200 m, and 109 wavelengths in the spectral range from 380 to 780 nm.

In order to make this paper convenient to readers who don't wish to involve themselves in the mathematics of Ref. [1], we present here a brief qualitative description of the approach used for deriving the equations which were coded to obtain the results.

As a basis for our calculations we chose the scalar equation of transfer for radiation with an inelastic source term. This approach is not new in optics and has been widely used in the physics of multi-speed neutron transport. All we do is to adjust the inelastic term to include both Raman scattering and fluorescence in marine water, which can easily be done on the basis of investigations by such authors as Walrafen [3] and Gordon [4].

The objectives of our approach are as follows: a) the solutions should be valid for the complete range of variability of inherent optical properties, *i. e.* equally applicable for both very clear and extremely turbid marine waters, in the complete range of the visible spectrum (380–780 nm); b) the precision of the results should be in the range of 6–8%, *i. e.* comparable with the precision of *in situ* marine optical measurements, and c) we should be able to calculate downward and upward irradiances and such apparent optical properties as diffuse reflectance, downward and upward irradiance attenuation coefficients, euphotic zone depth, *etc.* in the whole range of the visible spectrum, for a complete range of inherent optical properties and for any depth (when applicable).

On the basis of these criteria we have chosen a self-consistent two-flow approach [1] to simplify the original inelastic equation of transfer for radiance. This approach was originally used for elastic-scattering calculations [5], it is non-restrictive on values of optical parameters and gives the requisite precision for most ocean optics studies.

It is not clear from the description of this method how precise it is, and it is impossible to derive any proof of precision theoretically. The estimate of precision was made by comparison with Monte-Carlo calculations and the agreement in the results was sufficient to satisfy our objectives formulated above.

In the calculations, presented in Ref. [1], we reduced the complexity of the final computations by only considering a homogeneous, optically infinitely deep ocean illuminated by plane-parallel sun rays. The generalization to arbitrary illumination, finite depth and vertical inhomogeneity can easily be made, but it will increase the complexity of the final equations and significantly increase the computation time.

2. MODEL OF OPTICAL PROPERTIES

Recent studies [6] show that Raman scattering and fluorescence cause significant changes in the apparent optical properties of sea water. The magnitude and spectral shape of these effects depend not only on the inelastic components themselves but also, to a significant degree, on the spectral distributions and magnitudes of the elastic inherent optical properties. For that reason it is very important to model realistic ocean optics situations in order to estimate the significance of inelastic effects at different wavelengths and depths in the ocean.

We have adopted the following model [7-10] for the calculations presented: The absorption coefficient $a(\lambda)$ (m^{-1}) is taken to be:

$$\left. \begin{aligned} a(\lambda) &= a_w(\lambda) + a_c(C_c, \lambda) + a_f(C_f, \lambda) + a_h(C_h, \lambda), \quad a_c(C_c, \lambda) = a_c^0(\lambda) C_c^{0.602} \\ a_f(C_f, \lambda) &= a_f^0 C_f \exp(-k_f \lambda), \quad a_h(C_h, \lambda) = a_h^0 C_h \exp(-k_h \lambda) \end{aligned} \right\}, \quad (1)$$

where $a_w(\lambda)$ is the pure water absorption coefficient [8], λ is the vacuum wavelength of light in nm , $a_c^0(\lambda)$ is the specific absorption coefficient of chlorophyll [9] (m^2/mg), C_c is the total concentration of chlorophyll (mg/m^3), $a_f^0 = 35.959 m^2/mg$ is the specific absorption coefficient of fulvic acid (the first component of colored dissolved organic matter (CDOM) or yellow substance); $k_f = 0.0189 nm^{-1}$; $a_h^0 = 18.828 m^2/mg$ is the specific absorption coefficient of humic acid (the second component of CDOM); $k_h = 0.01105 nm^{-1}$; C_f and C_h are, respectively, the concentrations of fulvic and humic acids (mg/m^3). The values for $a_w(\lambda)$, and $a_c^0(\lambda)$ are given in Ref. [9], and values for CDOM are taken from Refs. [10, 11].

The elastic scattering ($b^E(\lambda)$) and backscattering ($b_B(\lambda)$) coefficients are calculated according to Kopelevich [7]:

$$b^E(\lambda) = b_w(\lambda) + b_s^0(\lambda) C_s + b_l^0(\lambda) C_l, \quad (2)$$

$$b_B(\lambda) = 0.5 b_w(\lambda) + B_s b_s^0(\lambda) C_s + B_l b_l^0(\lambda) C_l, \quad (3)$$

$$B_s = 0.5 \int_{-1}^0 p_s(\mu) d\mu = 0.039, \quad B_l = 0.5 \int_{-1}^0 p_l(\mu) d\mu = 6.4 \cdot 10^{-4}, \quad (4)$$

where $b_w(\lambda)$ is the scattering coefficient of pure water, $b_s^0(\lambda)$ and $b_l^0(\lambda)$ are the specific scattering coefficients for the small and large particulate matter respectively [7], B_s is the backscattering probability for the small particles, $p_s(\mu)$ is the scattering phase function for the small particles, B_l is the backscattering probability for the large particles, $p_l(\mu)$ is the scattering phase function for the large particles, C_s and C_l are the concentrations (g/m^3) of small and large particles respectively. We derived the equation for $b_w(\lambda)$ by interpolating the data given in Ref. [12]:

$$b_w(\lambda) = (5.826 \cdot 10^{-3} m^{-1}) (\lambda_0/\lambda)^{4.322}, \quad \lambda_0 = 400 nm, \quad (5)$$

and adopted the scattering coefficients for small and large particulate matter from Ref. [7]:

$$b_s^0(\lambda) = (1.1513 m^2/g) (\lambda_0/\lambda)^{1.7}, \quad b_l^0(\lambda) = (0.3411 m^2/g) (\lambda_0/\lambda)^{0.3}. \quad (6)$$

For the inelastic part of the optical model we used the approach given in the paper by Haltrin and Kattawar [1].

3. ILLUSTRATIONS

Results from model calculations are presented in figures 1 to 4 for different optical water types. We present here only a few illustrations, but we use all available data to formulate the results and conclusions. For the purposes of convenience we have chosen the chlorophyll concentration C_c as our main parameter in the computations. The concentration of scattering particles $C_p = C_s + C_l$ was estimated from the regression given in paper by Clark, Backer and Strong [13]: $C_p = 0.5 C_c^{0.75}$. Following Carder *et al.* [11], we adopted a fixed ratio of humic to fulvic acid: $C_h/(C_h + C_f) = 0.1$. All other concentrations were found by minimizing the difference between an actual and remotely estimated chlorophyll concentrations: $C_c - 1.92 [R(550)/R(440)]^{1.8}$.

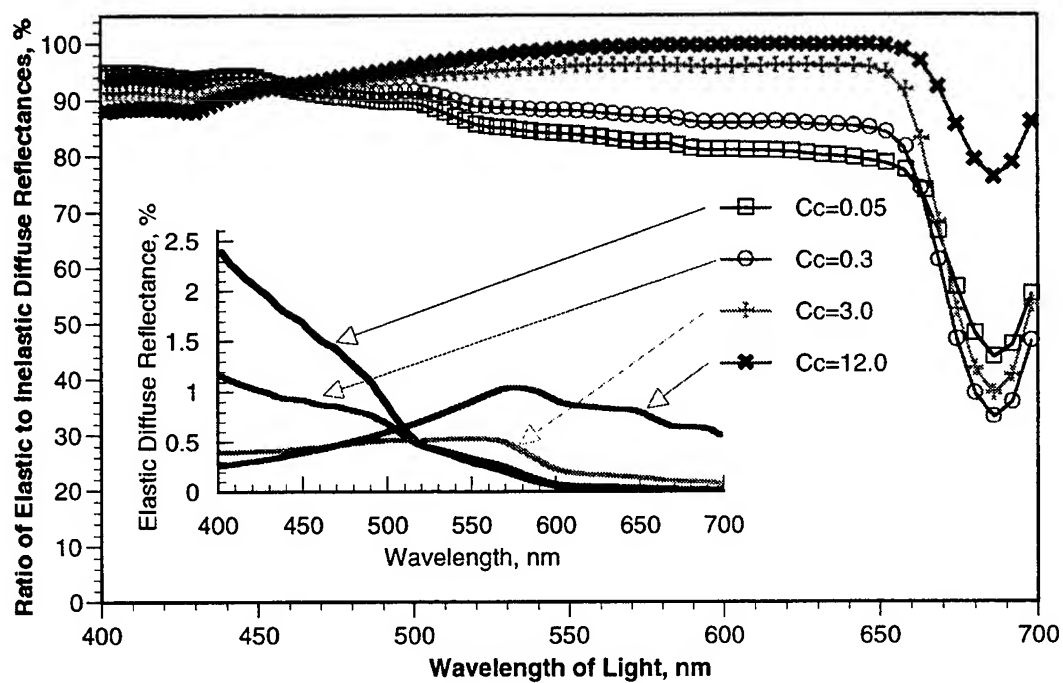


Fig.1. Ratio of elastic to inelastic diffuse reflectances as a function of wavelength for chlorophyll concentrations from 0.05 to 12 mg/m^3 .

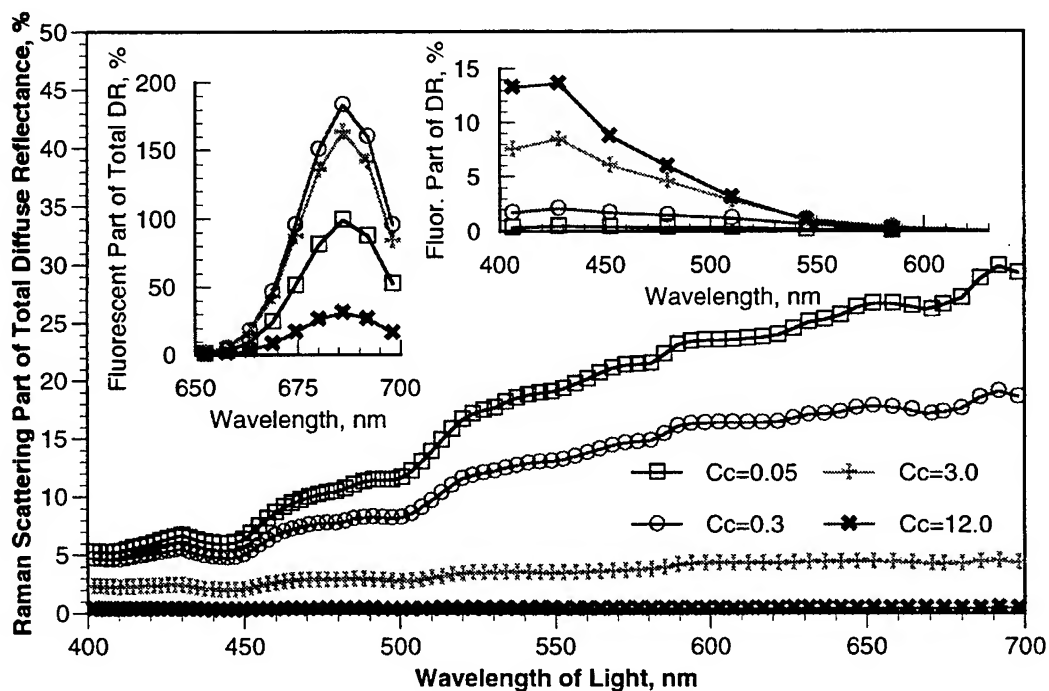


Fig.2. Raman scattering part of total diffuse reflectance as a function of wavelength for chlorophyll concentrations from 0.05 to 12 mg/m^3 .

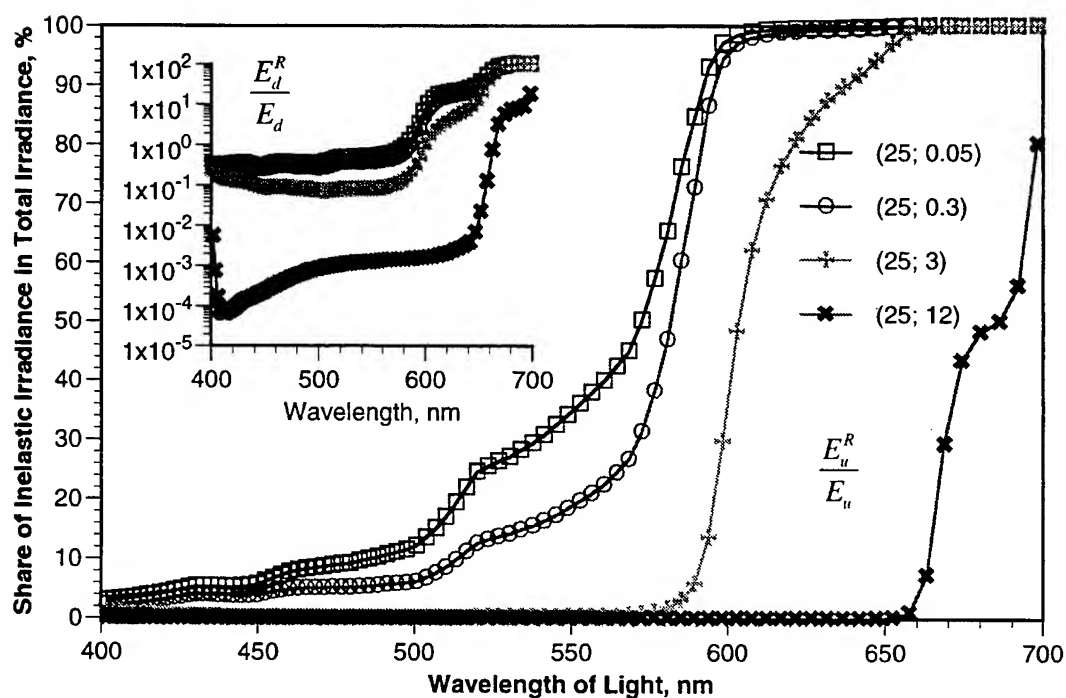


Fig.3. Share of inelastic irradiance in total irradiance as a function of wavelength for 25 m depth and chlorophyll concentrations from 0.05 to 12 mg/m^3 .

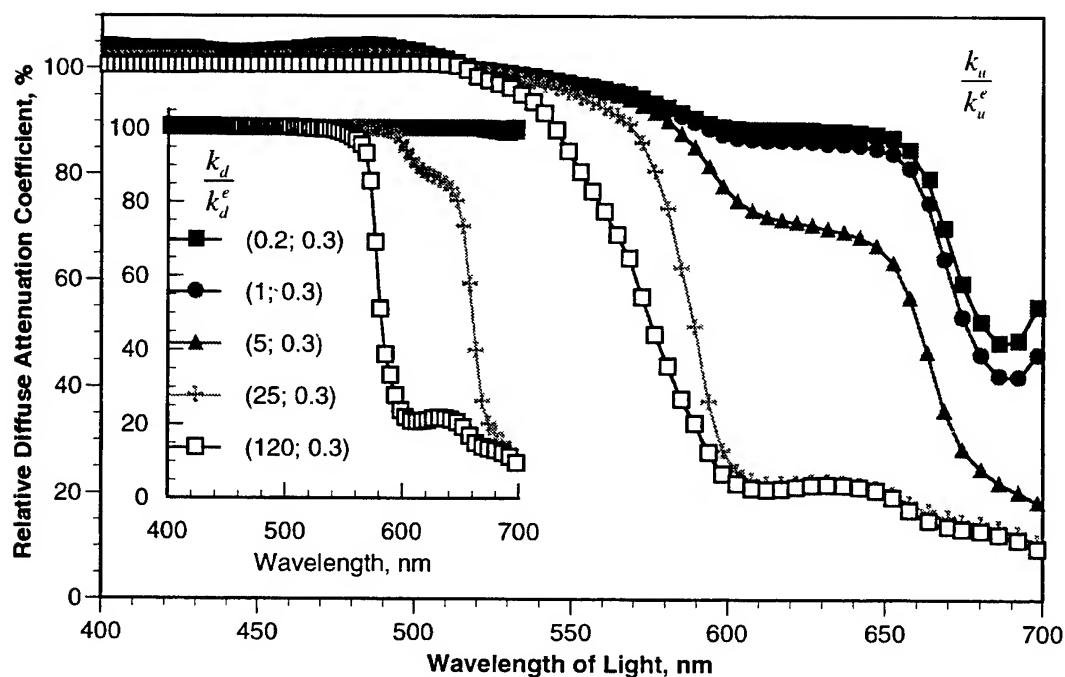


Fig.4. Relative to elastic inelastic diffuse attenuation coefficient as a function of wavelength for depths from 0.2 to 120 m and chlorophyll concentration 0.3 mg/m^3 .

We used the following sets of concentrations (C_c, C_f, C_h, C_s, C_l): (0.05, 0.1385, 0.0154, 0.0019, 0.0114), (0.3, 0.8134, 0.0904, 0.0109, 0.0869), (3.0, 7.5339, 0.8371, 0.0713, 2.5287), and (12.0, 91.7042, 10.1942, 0.8207, 13.2652).

Fig. 1 shows the ratio of elastic diffuse reflectance (DR) to the inelastic DR for four types of marine water with different chlorophyll concentrations C_c . The insert of Fig. 1 shows the spectral dependence of the elastic total DR for waters with these concentrations of chlorophyll. Note the strong dependence of DR on C_c in the blue part of the spectrum $400 \leq \lambda \leq 500 \text{ nm}$. The general behavior of modeled dependencies correspond to the experimental curves including the pivotal point at $\lambda \sim 520 \text{ nm}$.

Fig. 2 shows the spectral dependence of the Raman scattering contribution to total DR as well as the fluorescent portion (insets) for four chosen concentrations of chlorophyll. Both figures demonstrate significance of inelastic scattering effects on the diffuse reflection coefficient. The Raman scattering correction to DR increases from 6% at 400 nm to about 30% at 700 nm. It is most significant at small concentrations of chlorophyll and decreases with increasing values of C_c .

Fig. 3 shows the share of upward and downward (the inset) inelastic (Raman scattering plus fluorescence) irradiances to the total irradiance at a depth of 25 m for four different concentrations of chlorophyll. Changes in the spectral shape of the curves for the cases considered here are determined not only by the spectral characteristics of the attenuation coefficient but also by the transfer of energy from the blue to the red end of the spectrum by Raman scattering and fluorescence. With increasing depth, it is clearly seen that the portion of inelastic scattering increases at wavelengths greater than 580 nm causing a predominance of the inelastic light at chosen depths ($z > 25 \text{ m}$). At smaller depths ($z \leq 25 \text{ m}$) the relative upward component is significantly higher than the corresponding downward component and with increasing depth experiences the same saturation phenomenon as the downward component.

Fig. 4 shows the relative to elastic upward and downward (the inset) diffuse attenuation coefficient (DAC) as a function of wavelength for five different depths and $C_c = 0.3 \text{ mg/m}^3$. The results of computations shown in Fig. 4 reveal the remarkable effect that the upward and downward diffuse attenuation coefficients in the red-green part of the spectrum are far less than the corresponding elastic diffuse attenuation coefficients. This would imply of course that the measured DAC, under conditions of natural illumination, is actually smaller than the DAC computed using only elastic scattering. This effect has been observed *in situ* by Sugihara *et al.* [6].

4. CONCLUSIONS

Raman scattering corrections are higher for pure water and decline with increase in productivity or chlorophyll concentration. The highest value for the Raman scattering correction in terms of upward irradiances is about 30% at about 430 nm which constitutes about 5% of the total diffuse reflectance at this wavelength. The highest relative Raman correction to DR is about 25% at 700 nm. In eutrophic waters with chlorophyll concentration of 3 mg/m^3 , the relative Raman correction to the diffuse reflectance is about 3% throughout the entire range of the visible spectrum.

Fluorescent corrections are proportional to the concentrations of chlorophyll (red fluorescence at 685 nm) and CDOM or yellow substance (blue fluorescence at 425 nm). In pure water there is no fluorescence. The relative values of fluorescent corrections to DR in eutrophic water (3.0 mg/m^3 of chlorophyll) are 8% and 150% for the blue and red fluorescence peaks of chlorophyll respectively.

4.1 Threshold wavelength

There is a threshold wavelength approximately equal to the minimum wavelength in the spectral distribution of the irradiance attenuation coefficient plus one half of the Raman shift wavelength ($\sim 35 \text{ nm}$). This threshold wavelength divides the underwater light spectrum into two different parts. In the red part of the spectrum the inelastic part of the underwater light field increases with depth eventually reaching 100% of the total if the ocean is optically deep. In the blue part of the spectrum the inelastic part of the light exponentially decreases with depth. In optically deep oceans, at sufficient depths, the relative inelastic spectrum has the form of a step function with a zero value on the blue side of the threshold wavelength and a value of unity on the red side.

This phenomenon affects the behavior of the total irradiance attenuation coefficient. On the blue side of the threshold wavelength the total irradiance attenuation coefficients almost coincide with the elastic ones. To the red side of the threshold wavelength the total irradiance attenuation coefficients begin to decrease. Thus the apparent effect of water clarification in the red part of the spectrum is achieved.

4.2 Importance of this work for ocean optics

The three components of inelastic light can be categorized by their relative importance as follows: Raman scattering, the most important component, is the major cause for dividing the spectrum into two different regions, a blue region dominated by elastic light, and a red region dominated by inelastic light.

Red fluorescence (caused by chlorophyll), the second in importance, plays a predominant role in the vicinity of its emittance peak near 685 nm, especially when the concentration of chlorophyll is large. Blue fluorescence (caused by CDOM), although the least important, should definitely be taken into account in the spectral region near its peak at 425 nm, especially when the concentration of yellow substance is large.

The importance of all these components depends primarily on the value and spectral shape of the elastic absorption coefficient of water. The existence of the threshold wavelength is a combined result of Raman scattering and the shape of the absorption curve which has a minimum in the blue part of the spectrum.

For optical remote sensing both the blue and red portions of the spectrum should be reconsidered. The 3-7% corrections to the diffuse reflectance in the blue part of the spectrum and 50% or more in the red part are very important to the effectiveness of the algorithms dealing with the inversion of concentrations of dissolved and suspended substances.

Analysis of underwater light fields given in this presentation show that it is no longer possible to ignore inelastic effects in the analysis of oceanographic measurements of apparent optical properties of marine water, especially in the part of the spectrum to the red of 500 nm and at depths exceeding several optical depths.

ACKNOWLEDGMENTS

The authors wish to thank continuing support at the Naval Research Laboratory through the Littoral Optical Environment (LOE 6640-06) and Optical Oceanography (OO 73-5051-05) programs. This work was partially supported by the Office of Naval Research under contract number N00014-89-J-1467. This article represents NRL contribution NRL/PP/7331-96-0011.

REFERENCES

1. V. I. Haltrin, and G. W. Kattawar, "Self-Consistent Solutions to the Equation of Transfer with Elastic and Inelastic Scattering in Oceanic Optics: I. Model", *Applied Optics*, 32, pp. 5356-5367, 1993.
2. The commented FORTRAN code used here is available on an anonymous account at <indyvih.nrlssc.navy.mil>.
3. G. E. Walrafen, a) "Raman Spectral Studies of the Effects of Temperature on Water Structure", *J. Chem. Phys.*, 47, pp. 114-126, 1967; b) "Continuum Model of Water - An Erroneous Interpretation", *ibid*, 50, pp. 567-569, 1969.
4. H. R. Gordon, "Diffuse Reflectance of the Ocean: The Theory of Its Augmentation by Chlorophyll *a* Fluorescence at 685 nm", *Appl. Opt.*, 18, pp. 1161-1166, 1979.
5. V. I. Haltrin, "Propagation of Light in Sea Depth", in *Optical Remote Sensing of the Sea and the Influence of the Atmosphere* (in Russian), eds. V. A. Urdenko and G. Zimmermann, GDR AS, Berlin, pp. 20-62, 1985.
6. S. Sugihara, M. Kishino, and N. Okami, "Contribution of Raman scattering to Upward Irradiance in the Sea", *J. Ocean. Soc. of Japan*, 40, pp. 397-403, 1984.
7. O. V. Kopelevich, "Small-Parameter Model of Optical Properties of sea water", in *Ocean Optics*, Vol. 1: Physical Ocean Optics (in Russian), ed. A. S. Monin, Nauka, Moscow, pp. 208-234, 1983.
8. R. C. Smith, and K. S. Baker, "Optical Properties of Clearest Natural Waters", *Appl. Opt.*, 20, pp. 177-184, 1981.
9. L. Prieur, and S. Sathyendranath, "An Optical Classification of Coastal and oceanic waters based on the specific spectral absorption curves of phytoplankton pigments, dissolved organic matter, and other particulate materials", *Limnol. Oceanogr.*, 26(4), pp. 671-689, 1981.
10. Hawes, S. K., Carder, K. L., and Harvey, G. R. "Quantum fluorescence efficiencies of fulvic and humic acids: effect on ocean color and fluorometric detection", in SPIE, Vol. 1750, *Ocean Optics XI*, pp. 212-223, 1992.
11. Carder, K. L., Stewart R. G., Harvey, G. R., and Ortner P. B., "Marine humic and fulvic acids: Their effects on remote sensing of ocean chlorophyll", *Limnol. Oceanogr.*, 34(1): pp. 68-81, 1989.
12. A. Morel, and L. Prieur, "Analysis of Variations in Ocean Color". - *Limnol. Oceanogr.*, 22, pp. 709-722, 1977.
13. D. K. Clark, E. T. Backer, and A. E. Strong, "Upwelled spectral radiance distribution in relation to particular matter in water." - *Boundary-Layer Meteorol.*, 18 (3), pp. 287-298, 1980.

The use of a four-channel colour sensor to measure chlorophyll and carotenoid concentration

Kratzer, S.^{*}, Tett, P.⁺ and Wilton, R.^{*}

^{*} School of Ocean Sciences, University of Wales, Bangor, Menai Bridge, Gwynedd, LL59 5EY, UK

⁺ Department of Biological Sciences, Napier University, 10 Colinton Road, Edinburgh EH10 5DT, UK

ABSTRACT

A self-contained 4-channel sub-surface colour sensor built by the School of Ocean Sciences is tested for the use of measuring phytoplankton pigments. The four 10 nm wide wavebands are centred at 435 nm (blue), 485 nm (cyan), 565 nm (yellow) and 665 nm (red). The instrument can be used for estimating chlorophyll a concentration from changes of the ratio of upwelling irradiances in the cyan and yellow wavebands and has been successfully calibrated for optical case-1 waters, where phytoplankton play a key role in the absorption of light. However, the main absorbing pigments in the cyan waveband are not chlorophyll a but carotenoid pigments. These also show a good correlation using the same ratio. The strong relationship between chlorophyll a and carotenoid concentrations in the phytoplankton cells explains the apparent chlorophyll a - cyan:yellow relationship. Application to Case-2 waters is being examined.

Keywords: colour sensors, chlorophyll, carotenoids, HPLC, case-1 / case-2 waters, colour ratios

1. INTRODUCTION

Optical measurements from in situ profiling radiometers, moorings, aircraft and satellites provide information about phytoplankton distribution at a temporal and spatial resolution that is not possible with traditional techniques in biological oceanography. Satellite measurements of sea-leaving radiance have been widely used to map concentrations of phytoplankton pigments. Gordon and Morel¹ used the blue-green (440, 560 nm) reflectance ratio to derive chlorophyll concentration from CZCS (Coastal Zone Colour Scanner) data. The ratio of reflection coefficients in the green and in the blue part of the spectrum was related to the pigment concentration, usually on a log-log plot. This worked very well for Case-1 waters (mostly oceanic waters) where there is little absorbance from other constituents but phytoplankton.

The School of Ocean Sciences, University of Wales, Bangor (UWB), developed a 6-channel profiling radiometer in 1981² which copied some of the features of the CZCS. It was shown that in case-2 waters, the blue-green reflectance ratio is less sensitive to changes in chlorophyll a concentration than in the open sea. Brown and Simpson³ showed empirically that the slope of the log of chlorophyll a concentration against the log of the blue-green ratio (440, 550 nm) changed in proportion to the concentration of inorganic sediments. In 1991 another colour sensor (CS1) was developed by UWB with only two channels to estimate the phytoplankton chlorophyll concentration from the ratio of the blue to green (440, 524 nm) submarine irradiance. It was compared with two recording Chelsea Instruments Aquatracka I fluorimeters and proved to be as reliable as the *in vivo* fluorimeters for the estimation of chlorophyll concentration⁴. The aim was to develop simple (hence cheap) and robust instruments for use at moorings and thus complement remotely sensed observations.

In 1993, studies were begun with 4-channel versions of this colour sensor. The first two instruments were denoted CS2 and CS3⁵. They have four 10 nm wide wavebands, centred at 435 nm (blue), 485 nm (cyan), 565 nm (yellow) and 665 nm (red). These wavebands were chosen to be in close agreement with some of the channels of the SeaWiFS satellite⁶. The 435 nm waveband is close to the *in vivo* peak of absorbance of chlorophyll a, but can also be influenced by high concentrations of yellow substances and suspended particulate matter which absorb highly in the blue part of the visible spectrum. The 485 nm channel represents the peak of absorbance of carotenoid pigments. The channel at 565 nm, corresponding to the waveband at 570 nm originally selected for SeaWiFS, is used as a reference channel as chlorophyll a has weak absorbance in this waveband. The channel at 665 nm represents the second peak of chlorophyll absorption.

The colour sensors are 40 cm high and 15 cm in diameter. At the top of each instrument there is a flat diffusing Perspex window which behaves as a cosine collector. Under the diffuser there are four short tubes to collimate the light. At the bottom of each tube is an interference filter and a photodiode. A 9V battery pack with an operational lifetime of about three months is used as power supply and is situated at the bottom of the instrument. The instruments were designed to be used on a mooring or a drifter, measuring upwelling light near the surface or downwelling irradiance at several optical depths.

2. MATERIALS AND METHODS

CS2 and CS3 use four 1 cm² silicon photodiodes each with a built-in amplifier. The signals from these are passed to a gain controlled amplifier and then to a A-D converter with a conversion time of about 250 μ s. Sampling is controlled by a 16 bit microcomputer. Each sensor is initially sampled to determine the light level and the gain of the amplifier is adjusted for maximum signal without swamping the A-D converter. 20 discrete samples over a period of one second are taken together with the gain settings. The average of these samples is stored for each colour filter. The CS4 versions of the colour sensor have improved sensitivity compared to CS2 and CS3.

By using long sample periods (~30-60 sec) very low light levels can be monitored which makes CS4 a better instrument for measuring upwelling light than the previous models. The instrument of the CS4 series also contain an internal pressure sensor to determine water depth when lowered into the water. With care, it allows CS4 to be used in profiling mode when measuring downwelling irradiance. CS4 was also developed to simplify the electronics of CS2/3. It utilises a large area photodiode with a built-in current-to-frequency converter. The output of the sensor is a pulse train whose frequency is directly proportional to the irradiance on the photodiode. The pulses are counted and stored by the microcomputer for a predetermined sample period, which is set by the user before the deployment.

The colour sensors have not been calibrated to measure absolute values of irradiance, since their function is to provide colour ratios from which to estimate the changes in pigment concentration. We sought a relationship between the logarithm of the colour ratios and the logarithm of pigment concentrations. Unlike Gordon & Morel¹, who took the surface reflectance ratios, we took the ratio of upwelling irradiance at depths of between 0.2 and 2 m, depending on the platform used to support the instrument. Data from 5 different sensors is reported here. Despite differences in their absolute sensitivity, all were constructed to have the same relative response when the output from one channel was compared with another.

The instruments have been deployed in a wide range of different water types: in the subtropical Atlantic Ocean South West of Gran Canaria, where CS3 was deployed on a drifting buoy⁷; in Loch Striven (W. Scotland) CS2 and CS3 were deployed on a mooring during a phytoplankton spring bloom in April 1994, and during the Summers of 1993 and 1994 in the Menai Strait, North Wales. The sensors were deployed looking downwards in order to measure the ratios of upwelling irradiance. Several, notionally identical, versions of CS4 were used from the RRS Charles Darwin in the Malin Shelf (Outer Hebrides, Scotland) in May 1995, and from RV Cirolana (MAFF) in the Irish Sea and the North Sea (May and July 1996), deployed on a floating frame, looking downwards. In summer 1995 one of the CS4 sensors was used from the pier in Menai Bridge and since March 1996 CS3 is deployed on a floating raft in the Menai Strait.

Because continuous time-series show a systematic daily change in colour ratios^{7,8}, we took colour ratios only for times within 3 hours of local noon.

At corresponding times, water samples were taken for measurement of chlorophyll a and total carotenoid concentrations. 1-2 l of sea water were filtered onto a GF/F filter and extracted into 90% acetone. The filters were kept in a refrigerator overnight and the extracts were scanned (350-750 nm) in a 1 cm cuvette the following day. Chlorophyll a, b and c and carotenoid concentrations were calculated using the algorithms given by⁹. In order to comply with the SeaWiFS protocols, the pigments of the later observations (from May 1995) were also measured by reverse-phase HPLC in PML after storage in liquid nitrogen¹⁰. The chlorophyll a concentration was also measured fluorometrically¹¹ as a standard method, and for inter comparison of the techniques.

3. RESULTS

Because the instrument were used across a wide range of pigment and suspended sediment concentrations, we sometimes obtained readings in the blue channel which were too low for the satisfactory calculation of colour ratios. We found, however, a good correlation between spectrophotometrically determined chlorophyll a concentrations and the ratio of upwelling irradiances in the cyan (485 nm) and yellow (565 nm) wavebands over a wide range of concentrations in optical Case-1 waters (see Fig 1), where phytoplankton play a key role in the absorption of light.

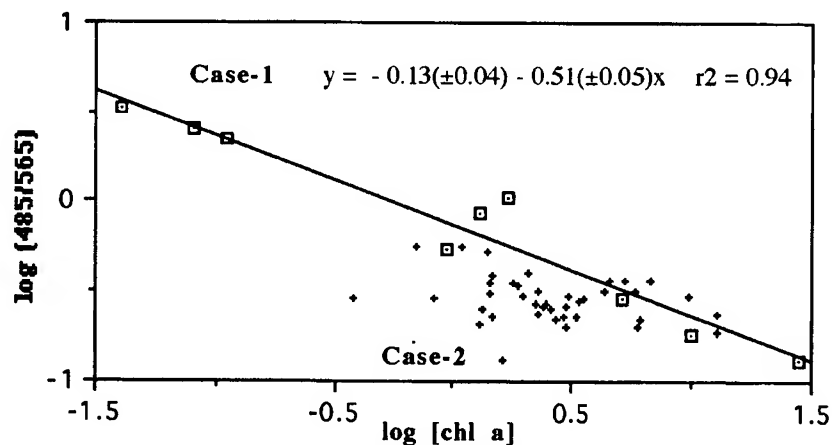


Fig. I For Case-1 () waters (Canary Islands, Outer Hebrides, spring bloom in Loch Striven), there is a good correlation between the logarithm of the cyan:yellow ratio and the logarithm of the chlorophyll concentration. For Case-2 (+) waters (Menai Straits, Irish Sea, North Sea), there was no significant correlation.

The regression equation (for Case-1 data) was:

$$\log(485:565) = -0.13(\pm 0.04) - 0.51(\pm 0.05) * \log[\text{chl}] \quad r^2 = 0.94; \text{df} = 8$$

The main absorbing pigments in the cyan waveband, however, are not chlorophyll a but the carotenoid pigments. These, as measured by spectrophotometry, also showed a good correlation to the cyan:yellow ratio:

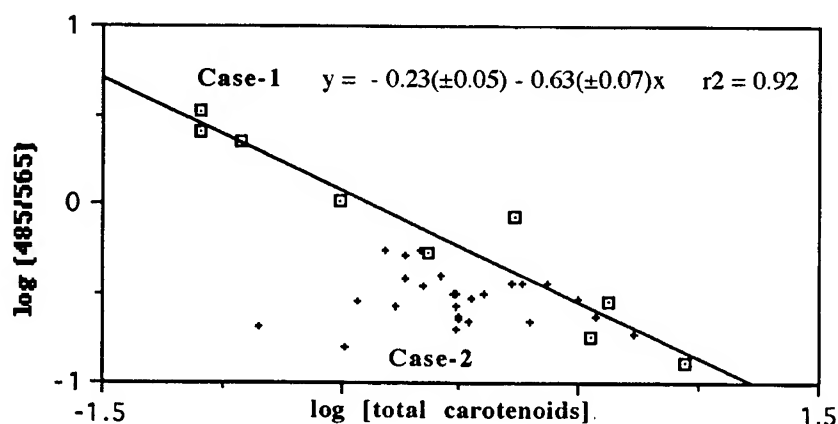


Fig. II Case-1 waters show a similar correlation between the logarithm of the cyan:yellow ratio and the logarithm of the carotenoid concentration for the same sites as in Fig I

The regression equation (for Case-1 data) was:

$$\log(485:565) = -0.23(\pm 0.05) - 0.63(\pm 0.07) * \log[\text{carot}] \quad r^2 = 0.92; \text{df} = 8$$

Fig. III shows that there was a strong correlation between chlorophyll a and carotenoid concentrations., as might be expected in the case of phytoplankton communities dominated by Chromophyta (i.e. algae with brown plastids, also referred to as 'phaeoplasts' in German literature).

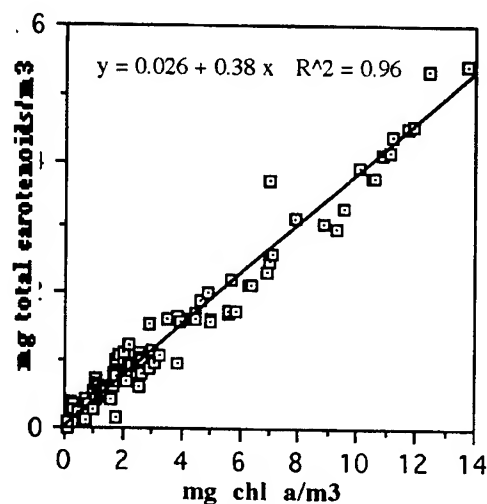


Fig. III There was a good correlation between the chlorophyll and carotenoid concentration measured by the trichromatic method (data from Canary Islands, Loch Striven, Outer Hebrides, Menai Strait, Irish Sea North Sea)

A whole range of carotenoid pigments absorb at 480 and 510 nm. However, the carotenoid pigments measured by the spectrophotometric method showed a good correlation with the correspondent samples measured by HPLC:

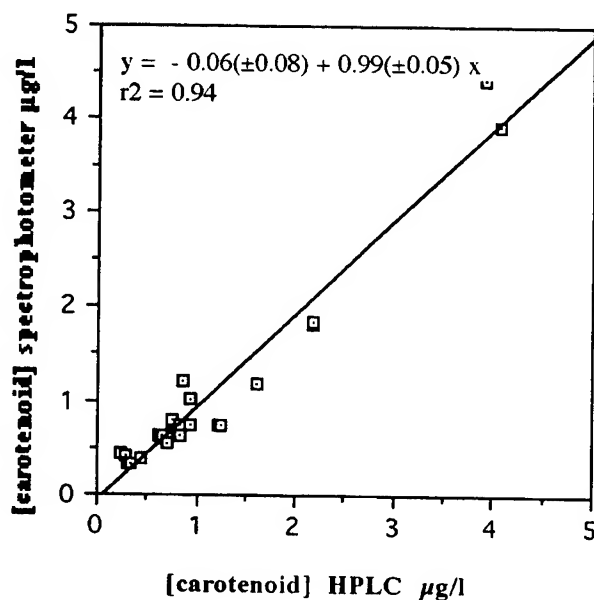


Fig. IV A regression of carotenoid concentration as measured by the spectrophotometric method, using the absorbance at 480nm and 510 nm, on total carotenoid concentration measured by HPLC. Data from SES cruise, May 1995.

The regression equation was: $[\text{carotenoid}]_{\text{spec}} = -0.06(\pm 0.08) + 0.99(\pm 0.05) * [\text{carotenoid}]_{\text{HPLC}}$

There was also a good correlation between the chlorophyll a concentration measured by HPLC and the chlorophyll a measured by the standard fluorometric method ($r^2 = 0.88$, $p < 0.001$, $df = 25$, data SES cruise, May 1995).

In respect of the optical Case-2 waters of the Menai Strait, the Irish Sea, and the North Sea the correlation between colour ratio and either chlorophyll or carotenoid was not significant (see Fig. II: $r = -0.18$, $p = 0.26$; $df = 39$ and Fig. III: $r = -0.093$; $p = 0.051$; $df = 24$).

4. DISCUSSION

Much current bio-optical work^{12,13} is aimed at providing algorithms or models for remote sensing of ocean colour by the SeaWiFS and similar sensors, once these are operational. Another body of work focuses on the absorption spectra of seston retained on a filter^{14,15}, with aims which include the decomposition of fully resolved spectra into components due to each particulate fraction. Our aim is intermediate between these approaches. We have made efficient and relatively simple instruments for deployment at moorings and on drifters in order to provide time series with the daily resolution that is unlikely to be obtained by satellites in regions subject to frequent cloud cover.

As with remotely sensed ocean colour, the interpretation of *in situ* optical data poses many difficulties, although these do not include atmospheric effects. The work reported here is part of a, mainly, empirical, study with the objective of a universal calibration of our colour sensors. Such a calibration should apply across a range of pigment concentrations and in waters with high and fluctuating concentrations of suspended non-phytoplankton particles, as well as in optical Case-1 waters.

Our first step was to consider the power of simple ratios of two reflected colours to explain variation in 'chlorophyll-like' pigments over a range of conditions in Case-1 waters. We have made observations over the widest range of concentrations likely to exist outside of a Red Tide, from oligotrophic sub-tropical waters to a eutrophic fjord during the spring bloom. Because high concentrations of chlorophyll attenuate blue light strongly, we found the cyan:yellow ratio a better single index than blue:yellow, in that it could be used over the whole of this range. This paper has largely been concerned with explaining the observed correlation between chlorophyll concentration and cyan:yellow ratio, when the latter should not be directly sensitive to chlorophyll a.

The pigments absorbing in the blue to green part of the spectrum are part of light harvesting complex II (LHC II). This contains chlorophyll a together with an accessory chlorophyll b or c, and in addition the major light-harvesting xanthophyll carotenoid(s) characteristic of the algal class. Its main absorption is that of the chlorophyll Soret band. The absorption in the cyan waveband, however is not caused by chlorophyll a, but by a mixture of carotenoid pigments¹⁶. Chlorophyll b also absorbs in this waveband but can be neglected as all the phytoplankton communities we encountered in this survey were dominated by Chromophyta which do not contain chlorophyll b.

Work is in progress to investigate the spectral influence of individual carotenoid pigments onto the cyan:yellow ratio using the results from the HPLC measurements. Furthermore, the nutrient status is also being assessed which may be found to influence the carotenoid to chlorophyll a content of phytoplankton cells¹⁷. Fig. II and III show that the difficulties of developing a calibration of colour ratios for Case-2 waters, where the pigment signal may be overwhelmed by that due to yellow substances and suspended particulate matter. Colour sensor calibration for case-2 waters may be possible using data from additional channels or by complementing the measurements with those from additional optical instruments, and we are presently investigating this possibility in the Menai Strait, with the aid of a optical model of Bowers et al.¹⁸.

5. ACKNOWLEDGEMENTS

We are grateful to NERC (GST/02/664, part of the SIDAL special topic) and to MAFF for the funding of this project. Many thanks to Dr. Ray Barlow and Denise Cuning for access to and advice on the PML HPLC system. Thanks to Dr. Dave Bowers, Dr. Tony Walne and Dr. Karen Wild-Allen who were heavily involved in the deployment of various sensors. Thanks to Anne Hammerstein who is currently involved in the technical servicing of the sensors.

6. REFERENCES

1. Gordon, H.R. and A.Y. Morel, Remote assessment of ocean colour for interpretation of satellite visible imagery: A review. 1983, New York: Springer Verlag.
2. Mitchelson, E.G., N.J. Jacobs, and J.H. Simpson, Ocean colour algorithms from the case II waters of the Irish Sea in comparison to algorithms from case I waters. *Continental Shelf Research*, 1986. 5: p. 403-415.
3. Brown, J. and J.H. Simpson, The radiometric determination of total pigment and seston and its potential use in shelf seas. *Estuarine, Coastal and Shelf Science*, 1990. 31: p. 1-9.
4. Tett, P.B., *et al.*, A blue-green ratio sensor for recording phytoplankton chlorophyll. 1994 ms.
5. Bowers, D.G. and P.B. Tett, Development of recording bio-optical sensors, 1995, University of Wales, Bangor, School of Ocean Sciences
6. Hooker, S.B., *et al.*, An overview of SeaWiFS and ocean colour. *NASA Technical Memorandum* 104566, 1992. 1: p. 24 pp.
7. Wild-Allen, K., P.B. Tett, and D. Bowers, Observations of diffuse upwelling irradiance and chlorophyll in case I waters near the Canary Islands (Spain). *Optics & Laser Technology*, accepted, 1996. (special issue on Underwater Optics).
8. Abbott, M.R., *et al.*, Scales of variability of bio-optical properties as observed from near-surface drifters. *Journal of Geophysical Research*, 1995. 100: p. 13345-13367.
9. Parsons, T.R., Y. Maita, and C.M. Lalli, A manual of chemical and biological methods for sea water analysis. 1984, Pergamon Press. pp. 101-104.
10. Barlow, R.G., Mantoura, R.F.C., Gough, M.A. and Fileman, T.W., Pigment signatures of the phytoplankton composition in the north eastern Atlantic during the 1990 spring bloom. *Deep Sea Research*, 1993. II(40): p. 459-477.
11. Tett, P., Plankton, in Biological Survey of Estuaries and Coasts, J. Baker and W.J. Wolff, Editors. 1987, Cambridge University Press: p. 280-341.
12. Gordon, H.R., Remote-sensing of ocean color - a methodology for dealing with broad spectral bands and significant out-of-band response. *Applied Optics*, 1995. 34(36): p. 8363-8374.
13. Doerffer, R. and J. Fischer, Concentrations of chlorophyll, suspended matter, and Gelbstoff in Case-II waters derived from satellite coastal zone color scanner data with inverse modelling methods. *Journal of Geophysical Research-Oceans*, 1994. 99(C4): p. 7457-7466.
14. Bricaud, A., *et al.*, Variability in the chlorophyll-specific absorption-coefficients of natural phytoplankton - analysis and parameterization. *Journal of Geophysical Research-Oceans*, 1995. 100(C7): p. 13321-13332.
15. Cleveland, J.S., Regional models for phytoplankton absorption as a function of chlorophyll-a concentration. *Journal of Geophysical Research-Oceans*, 1995. 100(C7): p. 13333-13344.
16. Johnson, G., *et al.*, *In vivo* absorption characteristics of 10 classes of bloom-forming phytoplankton: taxonomic characteristics and responses to photoadaptation by means of discriminant and HPLC analysis. *Marine Ecology Progress Series*, 1994. 105: p. 149-157.
17. Heath, M.R., K. Richardson, and T. Kiørboe, Optical assessment of phytoplankton nutrient depletion. *J. Plankton Research*, 1990. 12: p. 381-396.
18. Bowers, D.G., G.E.L. Harker, and B. Stephan, Absorption spectra of inorganic particles in the Irish Sea and their relevance to remote sensing of chlorophyll. *Int. J. Remote Sensing*, 1996. 17(12): p. 2449-2460.

Peter E. Land and Joanna D. Haigh

ABSTRACT

It is generally assumed that the spectral variation of aerosol optical depth is characterized by an Ångström power law or similar dependence. In an iterative fitting algorithm for atmospheric correction of ocean color imagery over case 2 waters previously described, this leads to an inability to retrieve the aerosol type and the attribution of spectral effects due to the water contents to aerosol spectral variations. An improvement to this algorithm is described in which the spectral variation of optical depth is calculated as a function of aerosol type and relative humidity, and the relative humidity is retrieved as well as aerosol type. The aerosol is treated as a mixture of aerosol components (e. g. soot), rather than of aerosol types (e. g. urban). We demonstrate the improvement over the previous method by using simulated case 1 and case 2 SeaWiFS data.

Key words: Ocean color, SeaWiFS, optical properties, multiple scattering, error minimization.

1. MOTIVATION

Standard methods of atmospheric correction over water (e.g. Gordon and Wang 1994¹) assume zero water leaving reflectance in the near infrared, an assumption that can fail badly in the presence of suspended inorganic sediment (see Fig. 1). Other methods often assume the water leaving reflectance to be dominated by sediment, resulting both in poor correction of pixels partially affected by sediment and in discontinuities in the correction across an image due to transitions between the case 1 and case 2 algorithms. There is a need for an atmospheric correction method that can be applied to all waters, allowing a smooth correction across mixed case images and dealing with gelbstoff affected waters as well as sediment affected waters. Such an algorithm was described by Doerffer and Fischer (1994)² for Coastal Zone Color Scanner (CZCS) images over the North Sea.

2. METHOD

Here we describe a development of the method of Doerffer and Fischer utilizing the capabilities of the new generation of sensors such as Sea viewing Wide Field of view Sensor (SeaWiFS) to extract information about the nature of the aerosols as well as the water contents. In a previous paper using this method³ we described the aerosols as a mixture of three types (maritime, continental and urban), the proportions of which determined the overall aerosol single scattering albedo and phase function. Single scattering theory with an implicit multiple scattering correction was used to determine the satellite measured radiance from the water and atmospheric model parameters, which were then varied to minimize the error. The spectral variation of aerosol optical depth was characterized by an Ångström power law. This was because this variation is dependent both on the aerosol type and on the relative humidity, which is unknown. This assumption was found to be detrimental to the retrieval, since it allowed physically unrealistic spectral optical depths which could be confused with the spectral signature of the water.

The effect of relative humidity on aerosol properties is well documented⁴ and may be used to calculate the spectral variation of aerosol extinction given the dry aerosol characteristics and the relative humidity.⁵ The aerosol model described previously is improved by using four components (sea salt, dust like, water soluble and soot, of which dust like and water soluble are in fixed proportion⁵) in place of the three aerosol types and by including relative humidity as a model parameter in place of the Ångström exponent. The algorithm works on a pixel by pixel basis. At each pixel, the following steps are executed:

SeaWiFS band 1 2 3 4 5 6 7 8

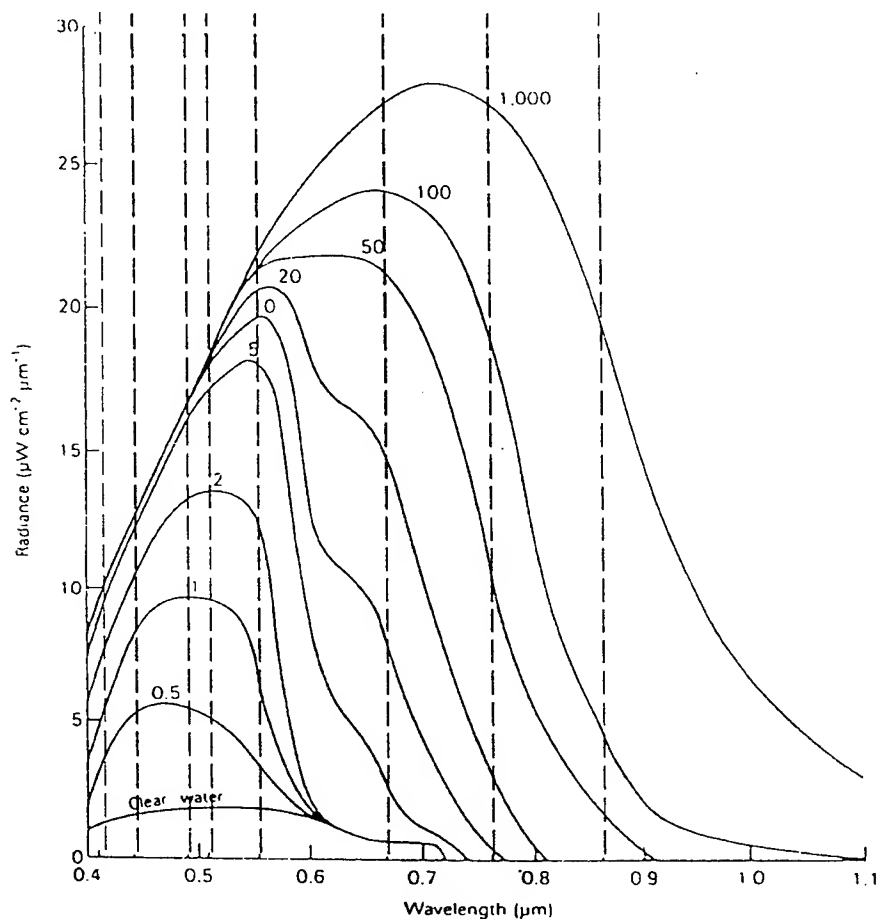


Figure 1. Relationship between water leaving radiance and wavelength for ten levels of sediment in milligrams per litre (Curran and Novo, 1988)

1. Correct reflectances at a pixel for molecular scattering (Rayleigh) and absorption (O_3 , O_2 , H_2O).
2. Initialize the parameters of the water model (chlorophyll and sediment concentrations, gelbstoff attenuation) and the atmospheric model (optical depth of oceanic, continental and soot aerosol components and the relative humidity).
3. Calculate the water leaving reflectance from the water model, and the molecular corrected reflectance from the water leaving reflectance and the atmospheric model.
4. Minimize the error in molecular corrected reflectance by iterating step 3 with changed model parameters.
5. Randomize the model parameters and repeat steps 3 and 4 until convergence criteria are met.

6. Go to step 1 for the next pixel.

Step 2 can be achieved by using the reflectances alone (independent initialization) or by using the values found at a neighbouring pixel (contextual initialization). Independent initialization starts by assuming a climatological aerosol type and relative humidity. It then uses single scattering theory (with the implicit multiple scattering correction) to calculate the aerosol optical depth in each band assuming zero water leaving reflectance. The largest possible optical depth with the correct spectral variation is used and the remaining signal is assumed to be due to water leaving reflectance, from which the water contents are estimated.

Step 3 is achieved using single scattering theory with an implicit correction for multiple scattering based on lookup tables generated with a multiple scattering code (DISORT) for each aerosol component at selected relative humidities and geometries.⁶ The correction is interpolated between components (weighted by optical depth at each wavelength), humidities and geometries. The spectral optical properties of the aerosols (spectral attenuation, single scattering albedo and phase function) are also stored in lookup tables at selected humidities for each component and interpolated between components and humidities.

Step 4 is achieved using the simplex algorithm of Nelder and Mead, creating a polyhedron in parameter space on which simple geometric operations based on the error at each vertex are performed.

Step 5 is necessary because multiple local minima of the error occur, so the true (global) minimum must be found by repeated minimization.

3. RESULTS

The algorithm was tested by generating reflectances from various regimes. These were chlorophyll only (case 1), sediment only, gelbstoff only and combinations, each combined with two atmospheres (maritime and polluted maritime) at three humidities. The above inversion technique was then used to retrieve the model parameters. All pixels were initialized independently, as no attempt was made to simulate the continuity of real data. Examples of the results from these regimes are shown in Fig. 2.

This shows to what extent different water and atmospheric conditions can give rise to the same reflectances. A stated goal of satellite ocean colour retrieval is to obtain chlorophyll concentration to within 35% and water leaving reflectance R_w to within 5%. The latter is often impossible due to instrument noise. If a 5% variation in R_w propagated through the atmosphere results in a variation in satellite reflectance less than the instrument noise level, then it cannot be distinguished from noise.

1. Case 1 waters. In all cases chlorophyll was retrieved to within the required 35% accuracy, mostly to 10%. Retrieved sediment was minimal, but gelbstoff was occasionally detected (see Fig. 2a). R_w retrieval was erratic, often within 5% but sometimes with errors over 10% at high chlorophyll concentrations.

2. Sediment laden waters. Sediment was typically retrieved to well within 10%, often to 1%. Up to 0.05 mg m^{-3} of chlorophyll was occasionally detected, but retrieved gelbstoff was minimal. R_w was very well retrieved, with all errors within 2%.
3. Gelbstoff laden waters. Gelbstoff retrieval was variable but usually within about 20%, with very little chlorophyll or sediment detected. As R_w approached zero, errors fluctuated widely, sometimes near 100%.
4. Chlorophyll and sediment. Chlorophyll was typically retrieved to within 10%, and sediment usually to within 5% but occasionally up to 20%. Gelbstoff was sometimes detected. R_w was often retrieved to within 5% but sometimes with errors up to 10%.
5. Chlorophyll and gelbstoff. Chlorophyll was usually retrieved to within 15% with errors near 100% at the highest humidity. Gelbstoff retrieval was highly erratic, with zero gelbstoff often detected. up to 0.06 g m^{-3} of sediment was detected.

Aerosol optical depth was retrieved typically to within 5% with the unpolluted atmosphere, and to within 10% with the polluted atmosphere. With the polluted atmosphere it was underestimated by an average of 9%, increasing with humidity.

Aerosol proportions were retrieved within about 0.05 at low humidity, and a bias of about 0.15 appeared at high humidity in favour of oceanic aerosol and against continental.

Humidity values had large scatter and appeared often to be essentially uncorrelated with the actual humidity.

4. REFERENCES

1. H. R. Gordon and M. H. Wang, "Retrieval of water leaving radiance and aerosol optical-thickness over the oceans with SeaWiFS - a preliminary algorithm," *Appl. Opt.* **33**, 443-452 (1994).
2. R. Doerffer and J. Fischer, "Concentrations of chlorophyll, suspended matter and gelbstoff in case 2 waters derived from satellite Coastal Zone Color Scanner data with inverse modeling methods," *J. Geophys. Res.* **99** C4, 7457-7466 (1994).
3. P. E. Land and J. D. Haigh, "Atmospheric correction over case 2 waters with an iterative fitting algorithm," *Appl. Opt.* **35** 27, 5443-5451 (1996).
4. G. Hanel, "The properties of atmospheric aerosol particles as functions of the relative humidity at thermodynamic equilibrium with the surrounding moist air," in *Advances in Geophysics* **19**, H. E. Landsberg and J. Van Mieghem, eds. (Academic Press, New York, 1976) pp. 73-188.
5. E. P. Shettle and R. W. Fenn, *Models for the aerosols of the lower atmosphere and the effects of humidity variations on their optical properties* (Air Force Geophysics Laboratory, Hanscomb AFB, MA 01731, AFGL-TR-79-0214, 1979).
6. R. J. Flowerdew and J. D. Haigh, "Retrieving land surface reflectances using ATSR-2," *J. Geophys. Res.*, in press.

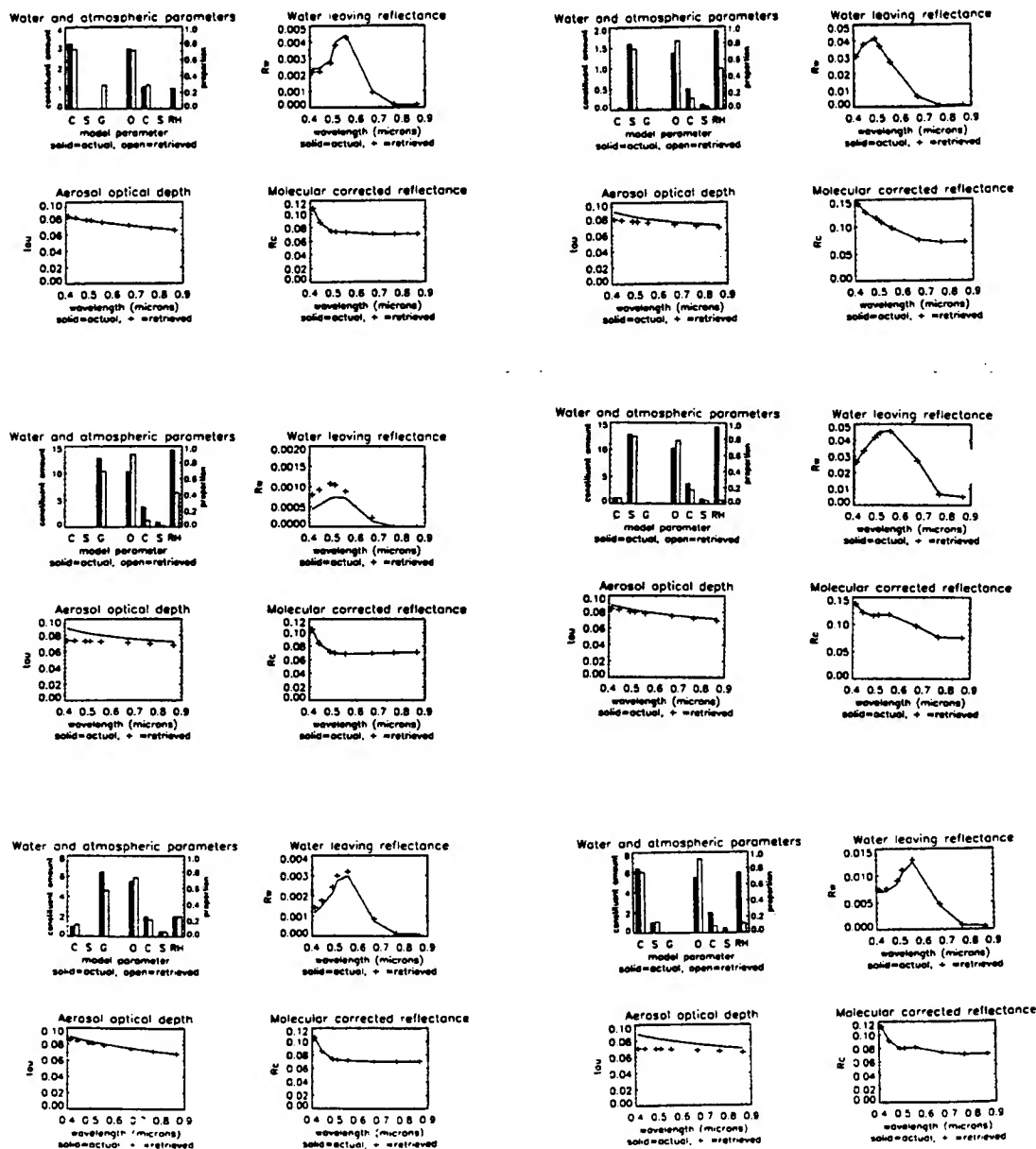


Figure 2. Results for six examples (one case 1, five case 2). Each example has four graphs.

The upper left graph shows actual (solid) and retrieved (open) values of:

the amounts of the three water constituents (C=chlorophyll in mg m^{-3} , S=sediment in g m^{-3} , G= $10 \times \{\text{gelbstoff diffuse attenuation at } 380\text{nm in } \text{m}^{-1}\}$); the proportions of the optical depths at 555nm (SeaWiFS band 5) of three aerosol constituents (O=oceanic, C=continental, S=soot); the relative humidity.

The upper right graph shows actual (solid) and retrieved (+) values of water leaving reflectance.

The lower left graph shows actual (solid) and retrieved (+) values of aerosol optical depth.

The lower right graph shows actual (solid) and retrieved (+) values of top of atmosphere reflectance corrected for molecular scattering and absorption effects.

Toward optical closure in coastal waters

Jill Schwarz^{a†}, Alison Weeks^b, Keith Trundle^c, Ian Robinson^a.

^a Dept. of Oceanography, Southampton Oceanography Centre, European Way, Southampton, SO14 3ZH.

wim@soton.ac.uk; isr@soc.soton.ac.uk

^b Southampton Institute, East Park Terrace, Southampton, SO9 4WW.

weeks_a@southampton-institute.ac.uk

^c Optoelectronics Research Centre, Southampton University, Highfield, Southampton, SO17 1BJ.

kjt@orc.phys.soton.ac.uk

†Jointly funded by the University of Southampton and the Defence Research Agency.

ABSTRACT

An instrument has been developed for the simultaneous *in situ* measurement of inherent and apparent optical properties, enabling various radiative transfer models to be tested. The Southampton Underwater Multi-parameter Optical Spectrometer System (SUMOSS) measures up- and downwelling irradiance, beam transmission and forward, side and backward scatter. These inherent optical properties can be measured both at 670nm using a laser diode, or spectrally using a white light. The instrument resolution ranges from 0.47nm to 6.7nm.

This extended abstract describes the new instrument, and presents preliminary data from an experiment to monitor the optical properties at the mouth of the Hamble river (Southampton Water, UK) over a spring tidal cycle. Optical data are compared with measurements of suspended particulate matter and chlorophyll concentrations.

Keywords: hyperspectral, *in situ* sensors, inherent optical properties, apparent optical properties, river Hamble (UK).

1 INTRODUCTION

The problem of interpreting ocean colour images of turbid coastal waters in terms of water quality parameters is complex and intriguing: man's activities are focused on coastal regions, and these often contain delicate, productive ecosystems.

Data from the CZCS have successfully been used to estimate primary productivity in Case I waters. In turbid waters, however, large errors arise in productivity estimates, owing to the presence of gelbstoff, sediments and pollutants (Hochman *et al.*, 1994)¹.

The work of Mayo (1993)² demonstrated the use of local, empirical algorithms to extract sediment load data from CZCS images, but with only a few available wavebands, the method is inversatile and limited in the parameters to which it is sensitive.

The question then arises whether increased spectral resolution will yield richer water quality information, and allow use of general rather than local algorithms. That the former is possible may be inferred from studies such as the deconvolution of reflectance spectra into identifiable pigment signatures (Aguirre-Gomez, 1996)³, and the resolution of distinctive spectra for land- and ocean-derived gelbstoff (Carder *et al.*, 1989)⁴.

The instrument described here is being used to explore the possibilities of hyperspectral satellite data, by measuring inherent and apparent optical properties *in situ* across the visible spectrum. These data, along with water quality measurements, will be used in various optical closure models, which may be inverted to yield water quality parameters from remotely sensed data.

2 TECHNICAL DETAILS OF THE NEW INSTRUMENT

2.1 The Southampton Underwater Multi-parameter Optical Spectrometer System (SUMOSS)

The SUMOSS comprises a 1.5m high sealed aluminium cylinder, to which two optical sensor frames are attached. The sealed housing contains a computer, light sources and a spectrometer system, and has been pressure tested to 200m depth.

Beneath the cylinder is a 25cm pathlength transmissometer and nephelometer frame, to which either laser or white light is carried by optical fibres from inside the housing. Lens cells are positioned to receive the transmitted light, as well as that scattered at 25°, 90° and 155°.

Cosine collectors for measuring up- and downwelling irradiance are attached to a 1m long hinged arm which is automatically deployed by the float system as the instrument enters the water.

The float system comprises two pipes with holes at the bottom, containing heavy floats. Strings join the top of each float to the irradiance sensor arm, via a hole in the top of each pipe. When the instrument is lowered into the water, the pipes are flooded and the floats rise, allowing the irradiance arm to descend to a horizontal position.

2.2 Internal workings

The irradiance and scatter signals are carried to a grating spectrograph by optical fibres. The transmission and reference signals travel to the spectrograph via fibre switches, allowing them to be measured separately when the signals are large (avoiding cross-talk on the CCD array). The resulting spectra (cut off at 375nm to eliminate second-order diffraction) are focused onto a 256 x 1024 pixel CCD array (Oriol Instaspec IV), and the digital read-out is stored on hard disk. The instrument can be powered either by an on-board 13V battery, or through a power cable.

2.3 Spectral resolution

The spectral resolution is determined by the size of the fibre image on the CCD array, and is limited by the dynamic range of the CCD array: for high intensity signals, the effective fibre diameter can be reduced by placing a mask in front of the spectrograph entrance (as shown below). In this way, the resolution may be varied between 0.45nm (bright environment; pixel-limited resolution) and 6.7nm (dull environment; light-limited resolution). Figure 2.1 illustrates the use of a mask to increase the spectral resolution.

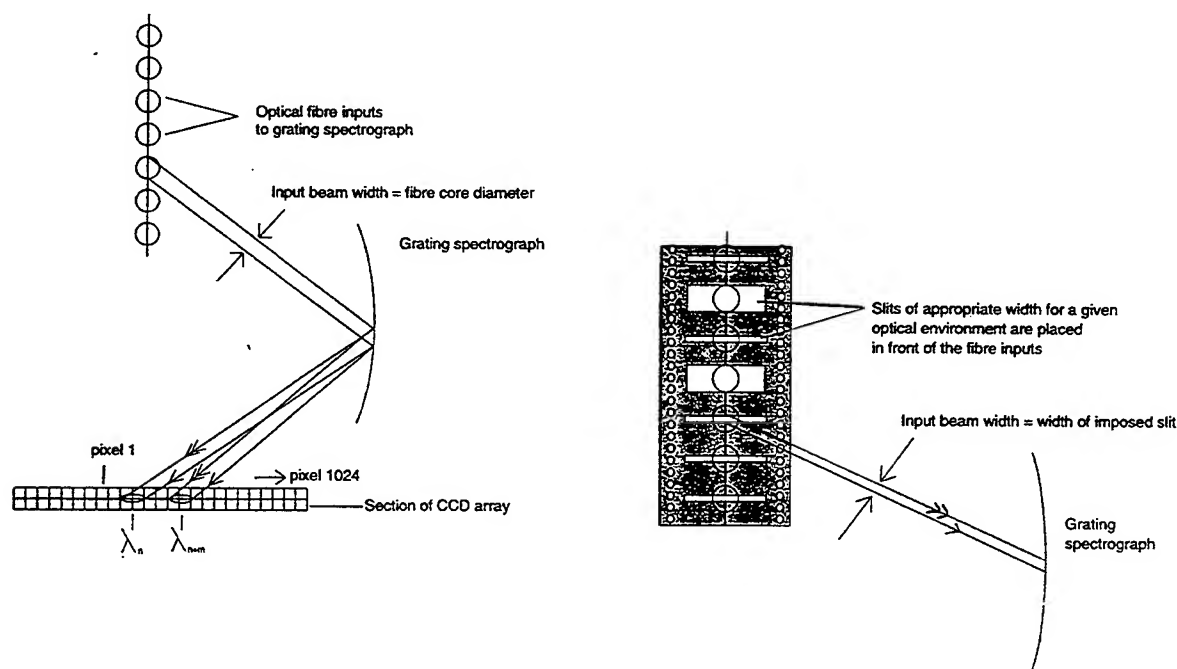


Figure 2.1: Increasing the spectral resolution by changing the effective imaging aperture.

2.4 Advantages of the instrument

- The SUMOSS optical sensors are aligned on a horizontal plane, so that measurements of AOPs and IOPs can be related to one another directly;
- Signals from all sensors can be collected on the CCD array simultaneously, allowing measurement of AOPs and IOPs with no time lag;
- The exposure time can be increased for small signals, and a number of readings can be integrated, improving the S:N ratio;
- The core of the instrument can be used with any optical sensor from which the output is carried by optical fibres: rather than measuring vector irradiance, one could, for example, measure scalar irradiance at two different depths (giving $a(\lambda)$ according to Gershun's equation).

3 THE TIDAL CYCLE EXPERIMENT

The SUMOSS was first deployed in the field on July 20th 1996, off Warsash Pier, which is located at the confluence of the river Hamble with Southampton Water (UK). This is a macrotidal estuary, with extensive mudflats both up- and downstream, optically dominated by resuspended sediments and benthic phytoplankton, and gelbstoff. Optical profiles were taken hourly, along with measurements of current, incident solar power (400nm to 700nm), temperature and salinity, and filtrations for sediments and chlorophyll. Samples of filtered and preserved unfiltered water were also taken. Inorganic and organic fractions of suspended sediments were determined by weighing and ashing the filter papers according to the method described by Shimwell⁵. Chlorophyll concentrations were determined fluorometrically.

Some of the data from this experiment are presented in this section. We stress that the SUMOSS sensors have not yet been calibrated, and the data are shown only as a qualitative indication of the instrument's performance.

3.1 Transmission and scatter data

The inorganic, organic and total suspended particulate matter (SPM) concentrations were plotted against laser transmission (fig. 3.1) and forward scatter to give preliminary field calibration curves. The regression coefficients were statistically insignificant, the best correlation being that between forward scattering and inorganic sediment concentration ($r_{inorg} = 0.44$), however the dataset was very small, and many more data are required for field calibration in the complex estuarine environment.

The time series of suspended sediments and laser transmission and scattering (figure 3.1) shows that the instrument behaves as expected: as turbidity increases (sediments are resuspended), the transmission decreases and scattering increases.

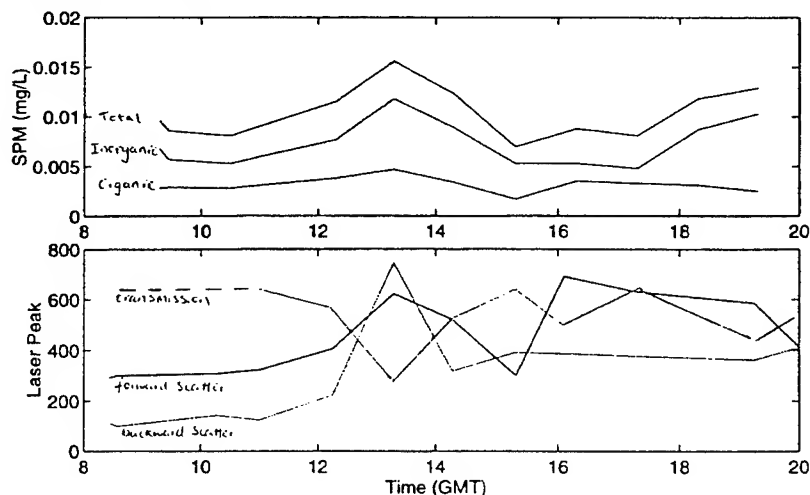


Figure 3.1: total, inorganic and organic suspended particulate matter time series (top), and laser transmission, forward scatter and backward scatter time series, at 0.5m depth.

3.2 Irradiance and reflectance data

3.2.1 Irradiance spectra

Figure 3.2 shows the effects of depth on downwelling irradiance. The subsurface downwelling spectrum is very similar to the incident sunlight spectrum (not shown); as the light travels through the water column a combination of water, gelbstoff, organic and inorganic particulates attenuate the blue and red ends of the spectrum. Much spectral detail is lost with depth, and several wavelengths are absorbed particularly strongly (440nm, 390nm) as can be seen in the reflectance spectrum (fig. 3.3). These data have yet to be analysed.

3.2.2 Reflectance spectrum

Figure 3.3 shows the reflectance spectrum calculated from the irradiance at 0.5m depth (of which the downwelling signal is shown in fig. 3.2). The peak in the red ($\sim 685\text{nm}$) appears consistently in all reflectance spectra for the tidal cycle experiment. It is postulated that this peak is caused by chlorophyll fluorescence; analysis to ascertain the cause of the spectral detail seen here has yet to be performed.

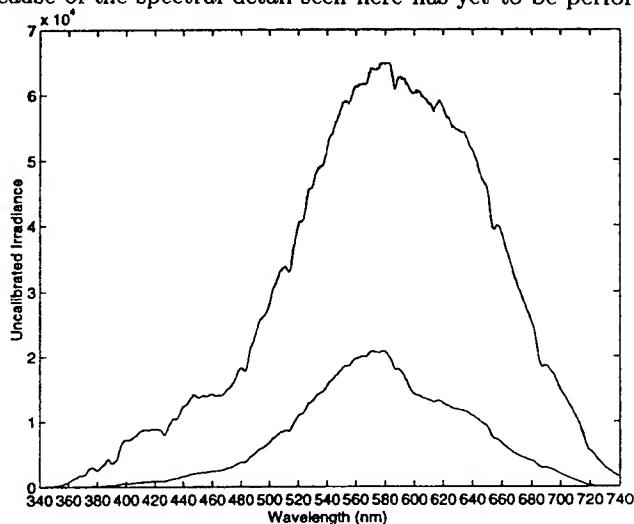


Figure 3.2: Downwelling irradiance, at 0.5m and 2.0m.

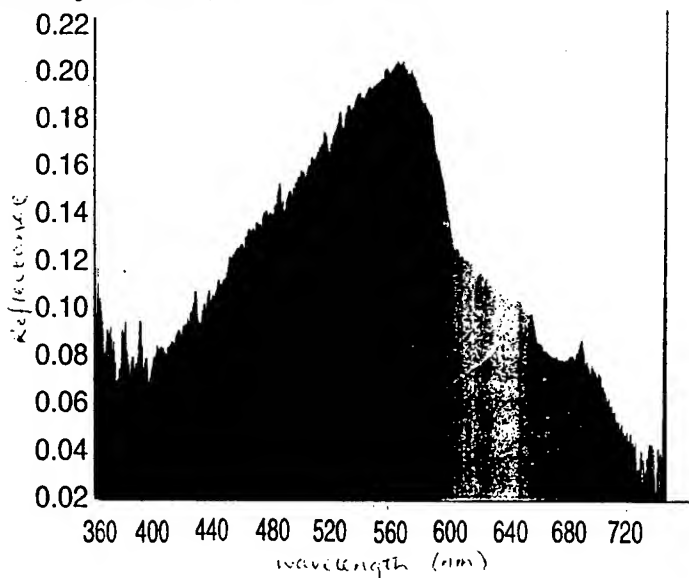


Figure 3.3: Reflectance spectrum calculated from the up- and downwelling irradiance spectra in figure 3.1, 0.5m.

3.3 Reflectance ratio and chlorophyll concentration over the tidal cycle

The reflectance ratio ($R_{448} : R_{550}$) varied approximately inversely with chlorophyll content over the tidal cycle (fig. 3.4), both at the surface and at depth, however the correlation between the $R_{448} : R_{550}$ and chlorophyll content was poor, and much work is required to relate the optics to the oceanography of this area.

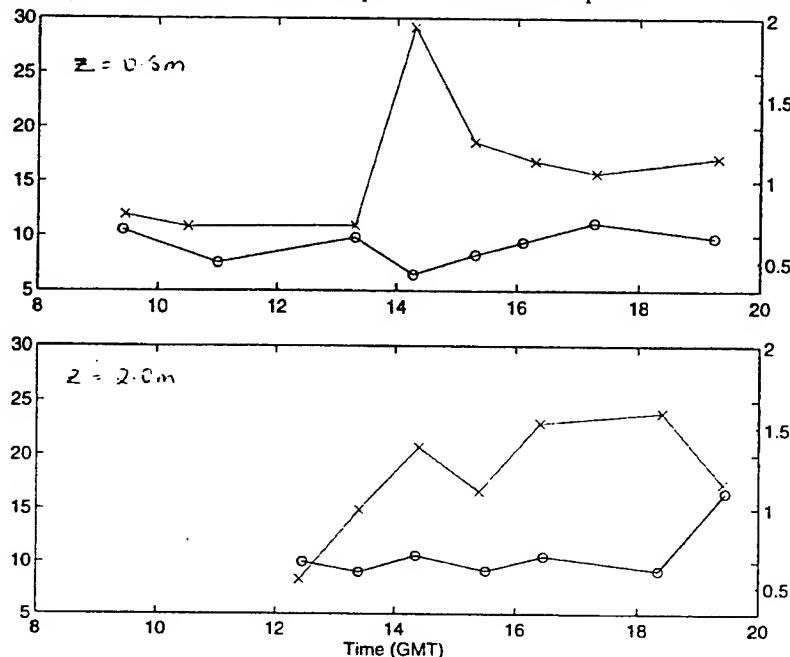


Figure 3.4: Time series of chlorophyll concentration ('x', in mgL^{-1}) and reflectance ratio R_{448}/R_{550} ('o'), for 0.5m (above) and 2.0m (below).

4 CONCLUSIONS AND FURTHER WORK

4.1 Instrument calibration

A laboratory calibration of the SUMOSS transmissometer and nephelometer is currently underway. A range of glass microspheres, clays, dyes and phytoplankton cultures is being used. Further fieldwork will include seawater filtrations to add to the field calibration already obtained.

The irradiance sensors will be radiometrically calibrated at Plymouth Marine Laboratory. Wavelength calibrations have been carried out using emission lines from a mercury lamp.

4.2 Modelling

The SUMOSS presents a range of modelling problems: The acceptance angles of the nephelometer channels are large ($\sim 30^\circ$), and these must be converted into values of $\beta_{4\Omega}$; the actual transmission and scattering values must then be used to find the absorption coefficient $a(\lambda)$; these parameters can then be used to test radiative transfer models (Mobley, Morel, Stavn etc.).

4.3 Conclusions

The instrument developed for measuring *in situ* IOPs and AOPs has performed well in its first field trial, and will provide a source of optical modelling parameters, as well as calibration data for the new, higher spectral resolution satellites (SeaWiFS, MeRIS, MOS). The instrument will also provide an opportunity to explore the spectral variation of attenuation in turbid coastal waters.

5 REFERENCES

- ¹ H.T. Hochman *et al*, "Interpretation of the coastal zone color scanner signature of the Orinoco River plume", *J. Geographical Research*, Vol. 99, no. C4, pp. 7443-7455, 1994.
- ² M. Mayo, "Determination of suspended sediment concentrations from CZCS data", *Photogrammetric Engineering and Remote Sensing*, Vol. 59, no. 8, pp. 1265-1269, 1993.
- ³ R. Aguirre-Gomez, Thesis, Department of Oceanography, University of Southampton, 1996.
- ⁴ K.L Carder *et al*, "Marine humic and fulvic acids: Their effects on remote sensing of ocean chlorophyll", *Limnology and Oceanography*, Vol. 34, no. 1, pp. 68-81, 1989.
- ⁶ S. Shimwell, Thesis, Department of oceanography, University of Southampton, 1995.

Poster Session:
In-Situ and Remote Sensing Sensors and Systems

A polychromatic *in situ* transmissometer for measurements
of suspended particles and yellow substance in water

H. Barth, R. Reuter, U. Stute

Carl von Ossietzky Universität Oldenburg, Fachbereich Physik, D-26111 Oldenburg

ABSTRACT

Hydrographic conditions are often characterised by large amounts of dissolved and particulate matter. These substances influence the optical properties of seawater, and the radiative transfer in the water column. The attenuation coefficient is an optical parameter which depends sensitively on suspended and dissolved substances.

An instrument has been developed for measuring spectral attenuation coefficients over a wavelength range from 370 to 730 nm. The optical path length can be set between zero and 400 mm, which allows an application in a wide range of turbidity. The variable path length enables a calibration of the instrument during *in situ* measurements, which makes it suitable for long-term applications where signals from conventional instruments would degrade due to biofouling of optical windows. From the data, the concentration and size distribution of suspended particles, and the concentration of dissolved organic matter are derived in real time. Algorithms based on Monte Carlo methods are available for a specific evaluation of non-chlorophyllous particles and phytoplankton. Results of field applications are reported.

1. INTRODUCTION

Optical parameters have met the interest of oceanographers and limnologists for a long time.¹ Devices which measure optical data are utilised to classify water masses on the basis of inherent optical properties and to obtain information on dissolved organic substances (denoted as yellow substance or gelbstoff) or particulate matter. The most prominent instrument of that kind is the *in situ* transmissometer, which measures the intensity loss of a near-parallel light beam along a light path r in water, yielding data on the total attenuation coefficient c .² The wavelength-dependent coefficient c of Lambert's law $dI/I = -cdr$ is a composite of several terms which describe absorption and scattering by molecules and particles:

$$c(\lambda) = c_w(\lambda) + c_{pp}(\lambda) + c_{tp}(\lambda) + a_d(\lambda) \quad [1/m] \quad , \quad (1)$$

where the indices w , pp and tp and d refer to contributions from water, phytoplankton, transparent particles, and dissolved organic matter. The term $a_d(\lambda)$ is the gelbstoff absorption coefficient; scattering of this material is negligible, and only absorption needs to be considered. In addition to temperature and salinity, attenuation has been utilised with some success as a parameter to classify water types, although it is not a conservative property of seawater. Attempts have been made to estimate the concentration of dissolved or suspended matter empirically³ and analytically^{4,5,6} from attenuation data, but relations which connect attenuation coefficients to substance concentrations hold in limited regions only. However, it is obvious from these findings that attenuation measurements in spectrally resolved form^{7,8,9} are a prior condition for a data interpretation.

In this paper, we report on the new transmissometer PAAL (Polychromatic Attenuometer with Adjustable Path Length), which has been designed to overcome these limitations. Calibration is done *in situ* using a light path with variable length, with the further advantage of making the instrument suitable for applications in waters with a wide range of attenuation characteristics. Algorithms have been developed for the interpretation of data in terms of attenuating substances. During measurements, the concentrations of gelbstoff and suspended particulates are derived and displayed e.g. as depth profiles in real time. A more sophisticated algorithm can be utilised with stored data to differentiate suspended matter specifically into phytoplankton and non-chlorophyllous particles.

2. THE INSTRUMENT

PAAL is a hydrographic probe designed to collect spectra of attenuation coefficients in the visible wavelength range. It can be used as a component of probing systems for depth-profiling use, or as a towed instrument for time-series measurements. The prototype consists of a cylindrical probe housing 470 mm long and 110 mm in diameter, with two separate optical windows in the bottom for light beam transmission into the water and back into the instrument. A motor-driven retroreflector can be set manually via telemetry or automatically at distances between near-zero and 200 mm from these windows (Fig. 1), which allows to set the optical path length up to 400 mm. Maximum depth of operation for the prototype is 3000 m. The main housing contains a flash lamp as the light source and an optical setup to produce collimated light beams for the sample and reference signal detection. Signals are simultaneously measured in spectrally resolved form by use of two miniaturised grating polychromators and transmitted to the board unit via single conductor cable.

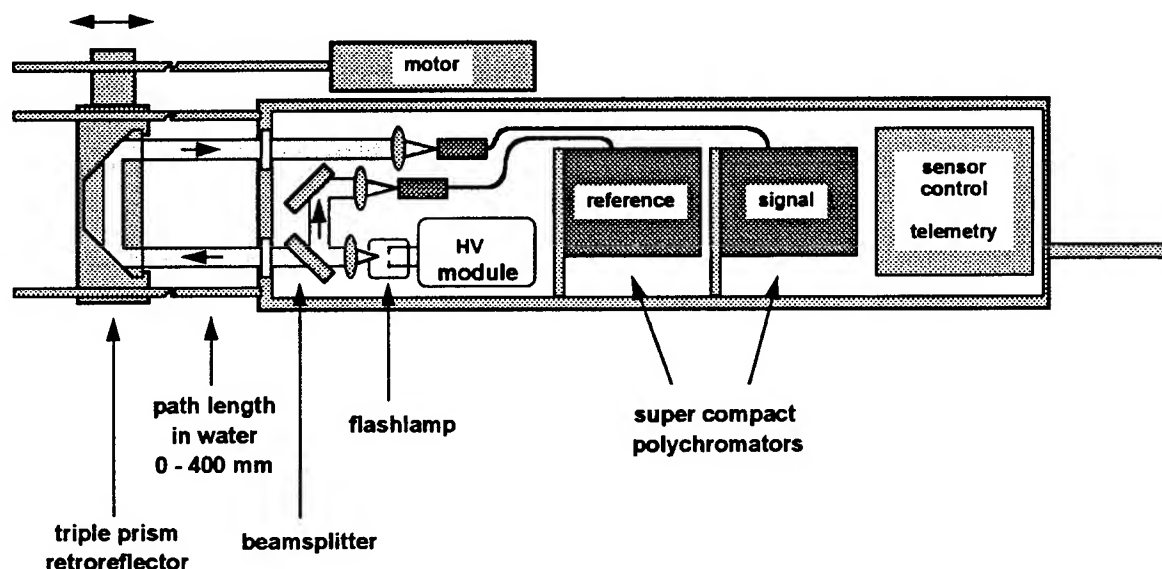


Fig. 1: Schema of the polychromatic attenuometer with adjustable path length.

2.1. Optical path length and self-calibration procedure

To achieve optimum performance, the path length r in water needs to be carefully adopted to the expected range of attenuation coefficients: for a good dynamics of the signal and hence high sensitivity of the instrument, r should be in the order of the inverse attenuation coefficient c . A value of $r = 1$ cm is often required in estuaries and tidal flats with large amounts of suspended matter, while $r = 1$ m would be a suitable value in clear waters. To allow for an easy adaptation of the path length in water to a wide span of optical characteristics of the water, a movable retroreflector mounted on a threaded rod and driven by a DC motor is part of the instrument.

The instrument is calibrated *in situ* with signal readings I_1 and I_2 at two different optical path lengths in water, yielding $c(r_2 - r_1) = \ln(I_1 / I_2)$. Instrumental factors like spectral characteristics and reflection losses cancel out. This holds also for the effect of optical windows contaminated due to bacterial films or other matter, which often occurs during *in situ* operation. A calibration routine is performed prior to each measurement. Depth profiles are initiated by setting the retroreflector to its near-zero distance position and reading the signal intensity. Then the path length in water is set to a position where the signal intensity is about 50% of its initial maximum value, which is near the optimal path length for the given optical conditions. In very clear waters, the path length is set to its maximum value. During moored applications, measurements can be performed at selectable time intervals and initiated with the same calibration routine, which allows long-term measurements with high stability of the data that are difficult to realise with conventional instruments.

3. SUBSTANCE SPECIFIC ATTENUATION SPECTRA

When compared with instruments for single wavelength operation, the rationale of a multispectral transmissometer lies in the information content of the entire attenuation spectrum, from which substance specific features can be extracted (Eq. 1). In a second step, these features can then be related to relevant parameters, like e.g. the concentration of absorbing or scattering matter, if such relations exist and hold with sufficient accuracy.

Within the accuracy of the instrument, the attenuation coefficient of water c_w is independent of salinity and temperature. Therefore, a spectrum of purified water, free of dissolved organic matter and particles due to active carbon and membrane filtration, is subtracted from the total spectrum $c(\lambda)$ as a first step of the data interpretation. With these assumptions, Eq. (1) can be written as

$$c(\lambda) - c_w(\lambda) = \alpha c_{pp}^*(\lambda) + \beta c_{tp}^*(\lambda) + \gamma a_d^*(\lambda) \quad [1/m], \quad (2)$$

where the terms with asterisk denote dimensionless spectral functions related to specific substances or substance classes as defined previously. They are denoted as basic spectra in the following. The goal of the data interpretation is to determine the preceding factors α , β and γ , which describe the relative contributions of individual substances to the entire spectrum: these factors contain information on the substance concentration.

3.1. Transparent particles

The term transparent particles is used here to describe the various kinds of hydrosols with low and spectrally unspecific absorption characteristics. They include e.g. suspended mineral particles, organic detritus, and bacteria. Their size distribution covers several orders of magnitude, ranging from less than 100 nm to up to millimetres. This size range is optically effective and can contribute to the attenuation of light;¹⁰ it differs from the 0.45 μm boundary practically used in biological oceanography to separate dissolved and particulate matter. The size distribution function is given by $n_{tp}(r) = dN_{tp}/dr$, with N_{tp} the total number of particles per unit volume in the given size range. It has been shown in many experiments that the size distribution of hydrosols in the optically effective size range can often be well described by Junge's law

$$n_{tp}(r/r_0) = b (r/r_0)^{-c_j} \quad (3)$$

with the Junge coefficient c_j ranging between about 3 and 5. r_0 is an arbitrary particle radius, and b a concentration-dependent parameter. Then, the spectral attenuation coefficient $c_{tp}^*(\lambda)$ of transparent particles in Eq. (2) follows another hyperbolic law:^{7,10,12,11}

$$c_{tp}^*(\lambda) = \lambda^{3-c_j} \quad (4)$$

The refractive index relative to water can vary from $n = 1.05$ for biogenic particles to 1.20 which is representative of minerals. Its actual value determines the height of the attenuation coefficient, but not its spectral shape according to Eq. (4), if particles follow a Junge distribution.

3.2. Phytoplankton

An essential characteristic of phytoplankton is its absorption due to chlorophyll *a* and other pigments, which is dominant at blue and red wavelengths.^{12,13} Plankton-specific absorption coefficients, refractive indices, and the size distribution determine the spectrum of the attenuation coefficient c_{pp} ^{7,10}. Depending on the values of these parameters, various kinds of curves can be obtained.¹⁴ Therefore, a basic spectrum $c_{pp}^*(\lambda)$ for the attenuation coefficient of phytoplankton cannot be given in a simple analytical form as in Eq. (4) for transparent particles and must be calculated as a function of these parameters.

Phytoplankton biomass is commonly described by the cellular chlorophyll *a* content. However, degradation products of chlorophyll *a* such as phaeopigments cannot be distinguished from intact chlorophyll *a* in *in vivo* absorption measurements. Also, the specific cellular chlorophyll *a* content of different species can vary by one order of magnitude. Due to this, the interpretation of attenuation coefficients in terms of the phytoplankton concentration is subject to uncertainties.¹⁵

3.3. Gelbstoff

Gelbstoff is a pool of organic molecules of natural origin with very broad molecular size distribution. In a good approximation, the absorption coefficient can be sufficiently well represented by an exponential function $\exp\{-s\lambda\}$, where the parameter *s* is virtually constant in the 300-600 nm range. In oceanic waters, *s* takes on values of $0.014 \pm 0.002 \text{ nm}^{-1}$ typically.¹⁶ At wavelengths of above 600 nm, gelbstoff absorption is low and mostly negligible and needs to be considered only in terrestrial waters where gelbstoff concentrations are high.

For convenience, the basic spectrum

$$a_d^*(\lambda) = \exp\{-s(\lambda - \lambda_0)\} \quad (5)$$

is normalised to unity at $\lambda_0 = 450 \text{ nm}$ wavelength.

4. DATA INVERSION IN REAL TIME

The interaction of light with spherical particles is fully described by the Mie theory. The calculation of attenuation coefficients is strongly facilitated with particles having low refractive index *n* relative to the surrounding medium. Then, van de Hulst's approximation¹⁷ holds for the efficiency factor *Q_{att}* of a non-absorbing spherical particle:

$$Q_{att}(\rho) = 2 - (4/\rho) \sin \rho + (4/\rho)^2 (1 - \cos \rho) \quad \text{with} \quad \rho = \frac{4\pi r}{\lambda}(n-1),$$

where *r* is the particle radius and λ the wavelength of light in the surrounding medium. The approach to realise a fast algorithm for a data interpretation in real time does not allow to distinguish between phytoplankton and transparent particles. Therefore, particulate matter is described by a single size distribution *n_p* and a basic spectrum *c_p^{*}* of the same form as given in Eq. (3)-(4). Eq. (2) becomes:

$$c(\lambda) - c_w(\lambda) = \delta c_p^*(\lambda) + \gamma a_d^*(\lambda), \quad (6)$$

The spectral attenuation coefficient $c_p = \delta c_p^*$ of particles is then

$$c_p(\lambda) = \int_{r_{\min}}^{r_{\max}} n_p(r) Q_{att}(r, \lambda) \pi r^2 dr.$$

The integral must be calculated numerically, since it has no analytical solution. Considering the Junge distribution, Eq. (3), and transforming to the size parameter $\alpha = 2\pi r/\lambda = \rho/2(n-1)$, yields:

$$c_p(\lambda) = b \frac{\lambda^{3-c_j}}{(2\pi r_0)^{3-c_j}} \frac{\alpha_{\max}^{2-c_j}}{\alpha_{\min}^{2-c_j}} \int_{\alpha_{\min}}^{\alpha_{\max}} \pi Q_{att}(\alpha) d\alpha.$$

The spectral dependence of *c_p* is given by the factor λ^{3-c_j} , which is equivalent to the basic spectrum. The concentration-dependent parameter is:

$$\delta = \frac{b}{(2\pi r_0)^{3-c_j}} \frac{\alpha_{\max}^{2-c_j}}{\alpha_{\min}^{2-c_j}} \int_{\alpha_{\min}}^{\alpha_{\max}} \pi Q_{att}(\alpha) d\alpha$$

The integral
$$R(c_j) = \int_{\alpha_{\min}}^{\alpha_{\max}} \alpha^{2-c_j} \pi Q_{att}(\alpha) d\alpha$$

must be solved numerically. A hyperbolic fit yields $R(c_j) = 677917 c_j^{-10.11} + 0.5$, with $\alpha_{\min} = 0.01$ and $\alpha_{\max} = 200$, if a refractive index $n = 1.16$ is adopted.

Evaluation of the unknown parameters c_j , δ and γ in Eq. (6), which characterise gelbstoff and suspended particles, is done with attenuation measurements at three wavelengths, which are significantly different in terms of gelbstoff and particle attenuation. In the examples reported here, attenuation coefficients at 394, 504, and 776 nm wavelengths have been selected from the entire spectrum, which results in three independent equations (6). The linear parameters δ and γ are separated into two equations and substituted into the third one, which results in an expression of the type $\left| \{c(\lambda) - c_w(\lambda)\} - f(c_j) \right| = \min$. A value of c_j is found by minimising the left hand side with a number of subsequent measurements. Finally, δ and γ are determined by matrix diagonalization. With δ and c_j , the total particle volume - i.e. the seston volume, is calculated by integrating the size distribution:

$$V_p = \frac{4}{3} \pi \int_{r_{\min}}^{r_{\max}} n_p(r) r^3 dr \quad (7)$$

5. INVERSION OF SPECTRA WITH MONTE CARLO METHODS

The *off line* analysis of stored spectra allows a more detailed data interpretation, with algorithms that require higher computing time. It is then possible to distinguish phytoplankton with absorbing pigments and transparent particles. Moreover, no pre-defined refractive index n of particles is assumed. Instead, an optimum value shall be found by the algorithm itself. Pigment absorption of phytoplankton is taken into account with a particle index of refraction in its complex form:

$$m(\lambda) = n(\lambda) - i n'(\lambda)$$

Then, van de Hulst's efficiency factor for absorbing particles²⁰

$$Q_{att}(\varepsilon, \rho) = 2 - 4e^{-\rho \tan \varepsilon} \sin(\rho - \varepsilon) \frac{\cos \varepsilon}{\rho} - 4e^{-\rho \tan \varepsilon} \cos(\rho - 2\varepsilon) \frac{\cos^2 \varepsilon}{\rho^2} + 4 \frac{\cos^2 \varepsilon}{\rho^2} \cos 2\varepsilon$$

can be utilised, with $\rho = \frac{4\pi r}{\lambda} (n-1) = 2\alpha(n-1)$ and $\varepsilon = \arctan \frac{n'}{n-1}$.

Particle sizes can cover a range from about 1 μm , which is typical of picoplankton, to up to several 100 μm . Nanoplankton with diameters of 2-20 nm generally dominates the total biomass. In many cases, the size distribution can be well described by a Gaussian function with a peak diameter at about 10 μm . For simplicity, this is approximated by a monosuspension with a particle number $N_{pp}(r_0)$ per unit volume at an arbitrary particle size r_0 in this range. The optimum value of r_0 for a given spectrum is estimated by the algorithm.

With this assumption, the attenuation coefficient c_{pp} of phytoplankton becomes

$$c_{pp}(\lambda) = N_{pp} Q_{att}(r_0, n, n', \lambda) \pi r_0^2$$

The imaginary part n' of the refractive index is related to the intracellular absorption coefficient a_{pig} with $n' = a_{pig} \lambda / 4\pi$. The absorption coefficient can be written as $a_{pig} = a_{pig}^* C_{pig}$, with a_{pig}^* the specific intracellular absorption coefficient given as m^2/kg and C_{pig} the intracellular chlorophyll a concentration given as kg/m^3 . It follows for the chlorophyll a concentration due to N phytoplankton particles in the water column:

$$\text{chl } \underline{a} = \frac{4}{3} \pi N r_o^3 C_{pig} \quad (8)$$

A spectrum of the specific absorption coefficient a of *in vivo* algae is given by Smekot-Wensierski¹⁵, which is assumed to well approximate the intracellular absorption coefficient a_{pig} . The real part of the refractive index is limited to the interval 1.038 .. 1.060, the intracellular chl \underline{a} concentration C_{pig} to 2 .. 14 kg/m³.¹⁸

The basic gelbstoff spectrum is given in Eq. (5). The exponential parameter s is set to 0.014 nm⁻¹. Transparent particles are again assumed to be Junge distributed, Eq. (3), with Eq. (4) as the basic spectrum. Values of the Junge coefficient c_j are limited to the interval 3.3 ... 5.0. The calculation of attenuation coefficients c_{tp} follows the same lines as described in sect. 4 for c_p .

In the forward direction, the attenuation coefficients of gelbstoff, transparent particles and phytoplankton can be calculated on the basis of parameters which determine their basic spectra and the concentration-dependent parameters given in Eq. (2). The inverse method, i.e. the evaluation of these parameters from a measured spectrum, is based on a similarity analysis: The optimum parameter set minimises the deviation between a measured and a reconstructed spectrum. This is done by searching for a minimum of the deviation function

$$D = \left\| c(\lambda) - c_w(\lambda) - \alpha c_{pp}^*(\lambda) - \beta c_{tp}^*(\lambda) - \gamma a_d^*(\lambda) \right\|$$

using a Monte Carlo routine, i.e. by subsequently selecting random values of parameters within their pre-defined intervals. The resulting value of D is stored together with the set of parameters used for its calculation. To find "good" values for non-linear parameters like c_j , random numbers are generated from an adaptively confined interval, which is necessary to find the absolute minimum of the deviation function. These adaptive interval restrictions are generated from the best 20 parameter sets which were stored.

6. RESULTS

The application of the data inversion method in real time as described in sect. 4 is demonstrated with a depth profile in the German Bight near the island Helgoland on May 27, 1994. The water column is well stratified, with a thermocline at 7 m depth separating warm surface water with low salinity from deeper cold water with higher salinity; below 15 m depth and extending to the bottom, a third water type with lower temperature is found (Fig. 2). The gelbstoff absorption coefficient in the near-surface water layer is about a factor of two higher than at depths below 7 m (Fig. 2). The depth profile of total particle volume (seston), derived according to Eq. (7), yields low values in the upper layer, a strong increase at the thermocline, and a further monotonic increase in the bottom layer (Fig. 3). The Junge coefficient c_j of the particle size distribution is about 3.7 between the surface and 15 m depth (Fig. 3). This result is near the value of c_j which is often found^{7,12} in marine waters. In the bottom layer, c_j decreases monotonically between 15 m depth and the bottom. Apparently, the shape of the size distribution is constant in both water types of the upper water column, but flatter near the bottom due to the presence of larger particles.

Substance-specific contributions to a reconstructed spectrum are shown in Fig. 4. and Fig. 5. The spectrum is taken from the measured data set in Figs. 2 and 3, from the German Bight. The data of the attenuation spectrum shown in Fig. 4 are reconstructed with the real time data inversion method, and in Fig. 5 with the Monte Carlo routine. Suspended particles are the dominant feature of the spectrum. With the real time data inversion the spectral contributions of the algae and transparent particles are added and the particulate matter represents the spectral dependence of both. The Monte Carlo data inversion allows to discriminate the algae and the transparent particles (Fig.5).

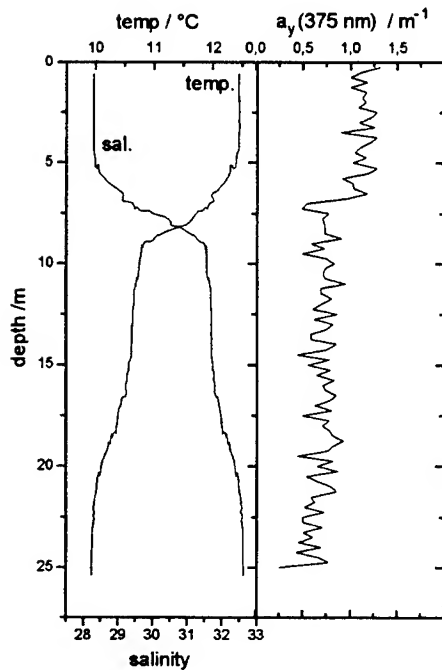


Fig. 2: Depth profiles of temperature, salinity and gelbstoff absorption coefficient $a_d(375\text{nm})$ in the German Bight, $54^{\circ}10'\text{N}$, $8^{\circ}05'\text{E}$, on May 27, 1994.

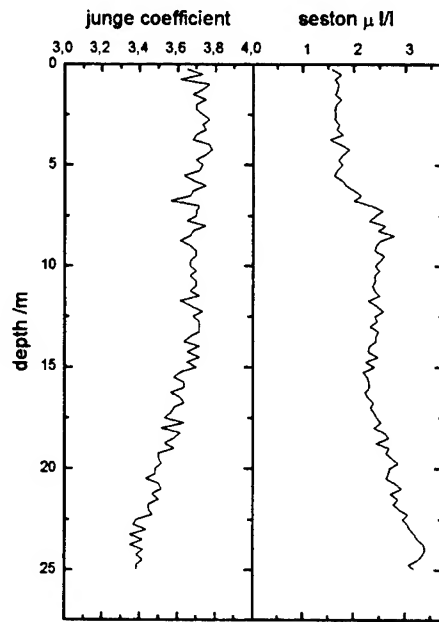


Fig.3: Depth profiles of the total particle volume and the Junge coefficient c_j derived in real time, at the same position as given in Fig.1.

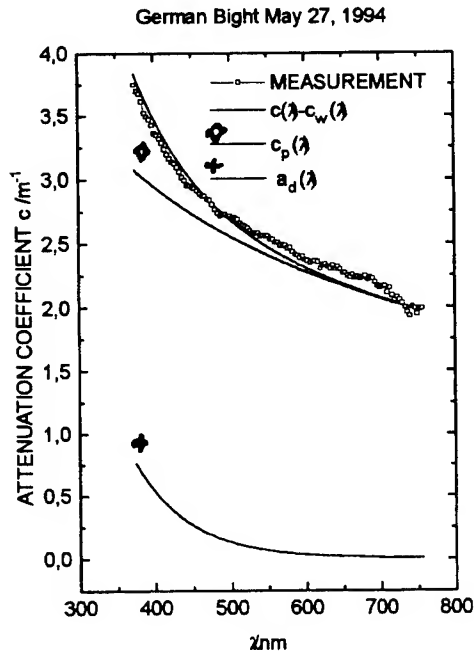


Fig. 4: A spectral attenuation coefficient taken from the data set in Figs. 2 and 3. The reconstruction is done with the real time routine.

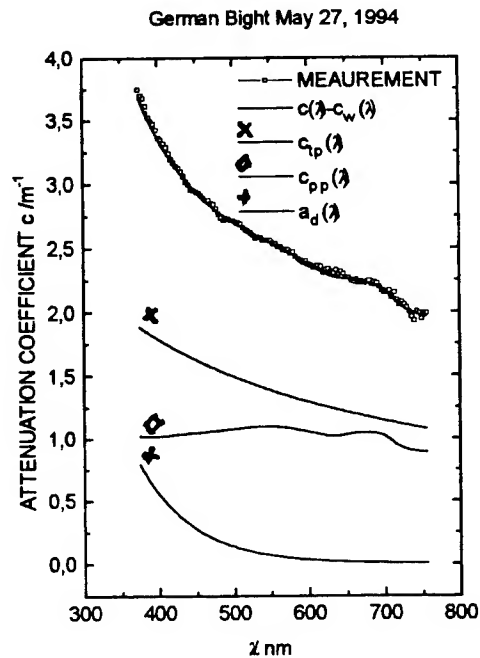


Fig. 5: The same measurement as in Fig. 4. The spectrum is reconstructed with the Monte Carlo method

7. CONCLUSIONS

The transmissometer PAAL is suitable to measure spectra of the attenuation coefficient between the near ultraviolet and the far red with high spectral resolution. The built-in sensor calibration is important, if attenuation coefficients shall be derived with high stability and without biodegradation in moored applications.

Algorithms have been developed which demonstrate the information content of attenuation spectra. This opens a way to interpret attenuation coefficients in terms of absorbing and scattering matter in the water column, which is of primary relevance in marine biology and chemistry.

When performing depth profiles, a fast routine allows to derive specific data of the gelbstoff absorption coefficient, the total particle volume, and the shape of the size distribution, which is assumed to be of the hyperbolic type. Plankton blooms, which follow other types of size distributions, cannot be specifically identified in this profiling mode of operation. A more sophisticated Monte Carlo calculus, that can be used on stored data, allows to discriminate phytoplankton from other types of suspended matter. The same algorithm can be used e.g. in time series measurements on moored stations, if high data rates are not required, to derive detailed information on suspended particles and dissolved organic matter in time steps of minutes, that cannot be obtained with other methods.

8. ACKNOWLEDGEMENTS

The development of the Polychromatic Attenuometer with Adjustable Path Length has been financially supported by the Federal Ministry of Research and Technology, Bonn, within the Eureka Programme Euromar-MERMAID. The PAAL was developed in cooperation with Meerestechnik Elektronik, Trappenkamp. Measurements on board the research buoy META I were made possible by the GKSS Research Centre Geesthacht, and measurements on board the research vessel Victor Hensen were enabled by the Alfred Wegener Institute for Polar and Marine Research, Bremerhaven. Their support is gratefully acknowledged.

9. REFERENCES:

- ¹ N.G. Jerlov, "Marine Optics" (Elsevier, Amsterdam, 1976).
- ² Where possible, the notation follows recommendations given in A. Morel and R.C. Smith, "Terminology and Units in Optical Oceanography", *Marine Geodesy* **5**, 335-349 (1982)
- ³ G. Krause and K. Ohm, "A method to measure suspended load transports in estuaries," *Estuar. Coast. Shelf Sci.* **19**, 611-618, 1984
- ⁴ Kitchen, J.C., J.R.V. Zaneveld and H. Pak, "Effect of particle size distribution and chlorophyll content on beam attenuation spectra," *Appl. Opt.* **21**, 3913-3918, 1982.
- ⁵ P. Diehl and H. Haardt, "Measurement of the Spectral Attenuation to Support Biological Research in a 'Plankton Tube' Experiment", *Oceanol. Acta* **3**, 89-96 (1982)
- ⁶ Spinrad, R. W. "Use of specific beam attenuation coefficient for identification of suspended particulate material," in *Ocean Optics VIII*, M. A. Blizard, Ed., pp. 135-140, (SPIE Vol. 637, Bellingham, Washington, 1986),
- ⁷ B. Lundgren, "Spectral Transmittance Measurements in the Baltic", Copenhagen University, Institute of Physical Oceanography, Report No. 30, Nov. 1976, 38 pp
- ⁸ H. Haardt, P. Diehl and B. Knoppers, "Messungen des spektralen Attenuationskoeffizienten an Latexsuspensionen, Phytoplanktonkulturen und natürlichen Wasserproben aus der Ostsee", Report No. 52, Sonderforschungsbereich 95, Kiel University, Dec. 1979, 62 pp.
- ⁹ M.J. Borgerdon, R. Bartz, J.R.V. Zaneveld and J.C. Kitchen, "A modern spectral transmissometer," in *Ocean Optics X*, R.W. Spinrad, Ed., pp. 373-385 (SPIE Vol. 1302, Bellingham, Washington, 1990) 664 pp.
- ¹⁰ A. Morel, "Diffusion de la lumière par les eaux de mer. Résultats expérimentaux et approche théorique," in *Optics of the Sea (Interface and in-water transmission and imaging)*, AGARD Lecture Series No. 61, 3.1.1 - 3.1.16, 1973.
- ¹¹ R. Reuter, "Characterization of marine particle suspensions by light scattering. II. Experimental Results," *Oceanol. Acta* **3**, 325-332, 1980
- ¹² F.H. Farmer, O. Jarrett Jr. and C.A. Brown Jr., "Visible absorbance spectra: a basis for in situ and passive remote sensing of phytoplankton concentration and community composition," NASA Technical Paper 2094, Feb. 1983, 32 pp.
- ¹³ W.V. Smekot-Wensierski, B. Wozniak, H. Graßl and R. Doerffer, "Die Absorptionseigenschaften des marinen Phytoplanktons" GKSS Research Centre Geesthacht, Report No. GKSS 92/E/105, 112 pp., 1992
- ¹⁴ A. Morel and A. Bricaud, "Theoretical results concerning the optics of phytoplankton, with special reference to remote sensing applications," in *Oceanography from Space*, J.F.R. Gower, Ed., pp. 313-327 (Plenum Publishing Corporation, 1981).
- ¹⁵ H. Haardt and H. Maske, "Variability of excitation, emission, and absorption spectra normalized to the chlorophyll concentration," in *The Use of Chlorophyll Fluorescence Measurements from Space for Separating Constituents of Sea Water*, GKSS Research Centre Geesthacht, Vol. II, Appendix 16, 48 pp., ESA Contract No. RFQ 3-5059/84/NL/MD, Dec. 1986
- ¹⁶ A. Bricaud, A. Morel und L. Prieur, "Absorption by dissolved organic matter (yellow substance) in the UV and visible domains", *Limnology and Oceanography* **26**, 43-53, 1981.
- ¹⁷ H.C. van de Hulst, "Light Scattering by Small Particles" (Wiley & Sons, New York, 1957), 470 pp.
- ¹⁸ Y.H. Ahn, A. Bricaud and A. Morel, "Light backscattering efficiency and related properties of some phytoplankters," *Deep Sea Research* **39**, 1835-1855 (1992)

NEW INSTRUMENT FOR SIMULTANEOUS MEASUREMENT OF THE DAYLIGHT FIELD'S OPTICAL PROPERTIES ABOVE AND UNDER WATER

K. Bochter, C. Wallhäußer

DLR, Institute of Optoelectronics, P.O.Box 1116,
D-82230 Wessling, Germany

ABSTRACT

Sequential measurements of the light field above and under water are affected by changes in the ambient light field. For correlated measurements, a new instrument is being developed, based on an imaging spectrometer with a "flat field" grating. Nine optical fibers connected to different light collectors are attached to the entrance slit. A slow scan camera equipped with a cooled area array CCD allows the simultaneous recording of all nine spectra in the range from 400 nm to 850 nm. The glass fibers are distributed into two groups. Two fibers are relayed to a unit measuring the downwelling vector irradiance and upwelling radiance above the water to determine the remote sensing reflectance and to detect light level changes. The remaining seven fibers are connected to a submersible unit measuring the light field parameters necessary to compute the *in situ* absorption spectrum of the water column, the change of mean cosine with depth, the Q-factor and other important apparent optical properties.

Keywords: Spectrometer, irradiance collectors, calibration, absorption, mean cosine, water, ground truth, remote sensing

1. INTRODUCTION

Optical methods play an important role in quickly deriving quantitative information on water quality parameters of inland lakes and oceans. With remote sensing wide spread areas can be studied. For this purpose the German Aerospace Research Establishment (DLR) operates three airborne sensors, the imaging spectrometer ROSIS¹, and the line scanners DAIS² and DAEDALUS³. Data validation of these and also of satellite-based instruments is improved⁴, if ground truth measurements are available. This was the motivation to construct a shipborne spectral radiometer, allowing to combine remote sensing information with measurements just above and inside the water column. To evaluate spectral light conditions and to characterize water constituents a variety of parameters is recorded. The mechanical construction of the instrument and signal linearity tests are completed. A procedure for absolute radiometric calibration of all light collectors is now being developed in order to provide reference data for atmospheric correction and to compute *PAR*, the photosynthetically available radiation.

2. INSTRUMENT DESCRIPTION

2.1 Design considerations and overview

As our experience showed, the success of a cruise can be spoiled if spectra necessary to compute optical properties of the light field are not measured simultaneously. Passing clouds can change illumination conditions within seconds making it nearly impossible to receive correct results from sequential recordings. Thus we choosed a design that allows the coincident measurement of two above water and seven under water light field parameters by using an imaging spectrometer with an attached slow scan CCD camera. The light collectors are connected to the spectrometer by means of fiber optical cables.

This approach is best suited to estimate the in-water spectral absorption coefficient from only irradiance measurements via the Gershun equation⁵:

$$a(\lambda, z) = - \frac{1}{E_0^-(\lambda, z)} \cdot \frac{dE^-(\lambda, z)}{dz} \quad (1)$$

Here $E^-(z) = E_d^-(z) - E_u^-(z)$ is the net vector irradiance and $E_0^-(z)$ the scalar irradiance ("vector" means cosine-weighting, "scalar" means equal weighting of the directions from which radiation impinges on a collector, "-" refers to under water properties).

The absorption coefficient is the only inherent optical property extractable from passive measurements. One of the early instruments to evaluate the Gershun equation is reported by Højerslev⁶. He obtained the derivative $dE^-(z)/dz$ by recording a depth profile. Under stable light conditions and with a calm sea surface *in situ* estimation of $a(z)$ was possible. To our knowledge the first instrument that records all required quantities simultaneously was MARAS⁷. It measures E^- at two depths and E_u^- at a position inbetween using six miniature collectors. An L_u^- sensor is attached too.

Small collector diameters are required to avoid self-shading for downward looking collectors^{8, 9}. Therefore we applied Højerslev's concept⁶ of measuring E^- and E_0^- . In contrast to 2π - collectors no light shields are necessary and sufficient miniaturization is possible. The angular response of the collector developed by Højerslev is proportional to $1 + \cos\theta$, i.e. the signal is a linear combination of scalar and vector irradiance with equal weighting. Looking upward, such a sensor provides a signal proportional $E_0^- + E^-$. Looking downward means that θ turns to $\theta + 180^\circ$ and $\cos\theta$ changes sign. In this case the collector's signal is proportional to $E_0^- - E^-$. Using a pair of collectors at the same depth looking in opposite directions, it is possible to compute E_0^- by adding and E^- by subtracting the signals.

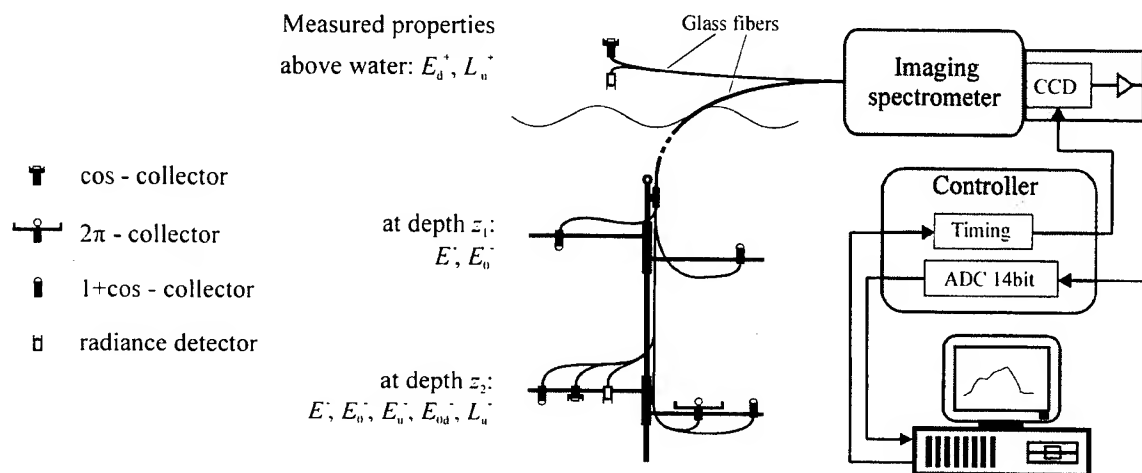


Fig. 1: Schematic diagram of the concept of the instrument

Tab. 1: Optical properties derivable with the instrument

remote sensing reflectance	$R_{RS} = L_u^+ / E_d^+$
vector irradiance reflectance	$R = E_u^- / E_d^-$
Q-factor	$Q = E_u^- / L_u^-$
mean cosine	$\bar{\mu} = E^- / E_0^-$
depth derivative of mean cosine	$d\bar{\mu} / dz$
up - and downwelling parts of $\bar{\mu}$	$\bar{\mu}_u, \bar{\mu}_d$
absorption coefficient	a
backscatter coefficient	$b_b \approx f a / R$ *
attenuation coefficients for	
- net vector irradiance	$K_E = (E^-)^{-1} dE^- / dz$
- scalar irradiance	K_0
- up and downwelling irradiances	K_u, K_d, K_{0u}, K_{0d} **
- upwelling radiance	k_l **

* depending on water type and illumination conditions¹⁰

** from depth profile

Figure 1 illustrates how the collectors are positioned. Above water L_u^+ and E_d^+ are measured. To evaluate Gershun's equation two pairs of 1+cos - collectors are used to obtain E_0^- and E^- at two different depth. Spacing between the two working planes can be varied from 30 cm to 150 cm to adapt to different water turbidities. At z_2 measurement of E_u^- provides the computation of E_d^- . Additionally downwelling scalar irradiance and upwelling radiance are recorded. At present the cable length of the submersible unit is 25 m, manufacturing of an extension is possible.

Table 1 shows a list of inherent and apparent optical properties like remote sensing reflectance, irradiance reflectance, mean cosine of the light field, and the coefficients of absorption, backscattering and diffuse attenuation, that can be computed from the instrument's spectra. All properties corresponding to a certain depth can be derived from one CCD exposure with the exception of the diffuse attenuation coefficients for up- and downwelling irradiances. These can be received from a depth profile. Additional information for modelling light fields are obtained by $d\bar{\mu} / dz$.

2.2 Collectors and fiber optical cables

The different types of irradiance collectors were constructed by using a strongly scattering but not absorbing (i.e. a white translucent) diffuser positioned in front of the glass fiber. Insensitivity against degradation by solar UV-radiation, no embedment of dirt at its surface, wavelength independent scattering characteristics and neglectable fluorescence are important attributes the diffuser must have. Only teflon¹¹, plexiglass¹² and ceramic⁷ are known to be more or less suited. For best machining and light throughput we selected plexiglass GS072 (Röhm). To obtain well-defined angular response, the design of the diffusers and the cos - collectors' light shields was optimized. The machining precision of these parts must be within some 10 µm.

To measure the angular response the collectors were rotated in a collimated beam of white light by means of a step motor. Thereby the signals were recorded automatically every 0.9° with a photodiode. As the angular characteristics depends on the surrounding medium, the E_d^+ sensor was optimized in air, the others under water. We simulated the sensor's accuracy under real light field conditions by computing irradiance errors ϵ with¹³:

$$\epsilon = \frac{\sum_i V(\theta_i) \bar{L}(\theta_i) \sin \theta_i \Delta \theta}{\sum_i w(\theta_i) \bar{L}(\theta_i) \sin \theta_i \Delta \theta} - 1 \quad (2)$$

where $V(\theta_i)$ is the normalized signal of the different types of collectors recorded at the discrete angular values θ_i and $w(\theta_i)$ is their idealized response. Two measured radiance distributions¹⁴, a strongly peaked and a wide spread, nearly asymptotic one, were selected for the simulations and azimuthally averaged to render $\bar{L}(\theta_i)$. Computed irradiance errors are accounted for in the radiometric calibration procedure. Further improvement can be obtained by measuring the wavelength dependency of the relative errors. The sensors were tested for long-time signal drifts under water. After 20 hours deviations were less than 1 %.

1+cos - collector: Figure 2 shows the optimized version and its angular response. The diffusers shape is a hemisphere with 3 mm radius. Light impinging from behind is enhanced by a free space between the hemisphere and the mounting. Also displayed are the normalized angular responses of E_0^+ and E^- . The second sensor looking in the opposite direction, which is necessary to obtain these properties, was simulated by shifting the collector's response curve by 180°. E_0^+ was computed by adding the shifted curve to the unshifted, E^- by subtracting it. Since the angular response errors of E^- and E_0^+ are similar in magnitude at all angles of incidence, the influence of the light field's shape on E^- and E_0^+ is expected to be of the same amount, leaving computed α unaffected. For both above-mentioned light fields the simulated irradiance errors in E_0^+ are about 1 % larger than the corresponding errors in E^- . Changing the radiance distribution from peaked to asymptotic shape results in about 0.15 % deviation in both E^- and E_0^+ .

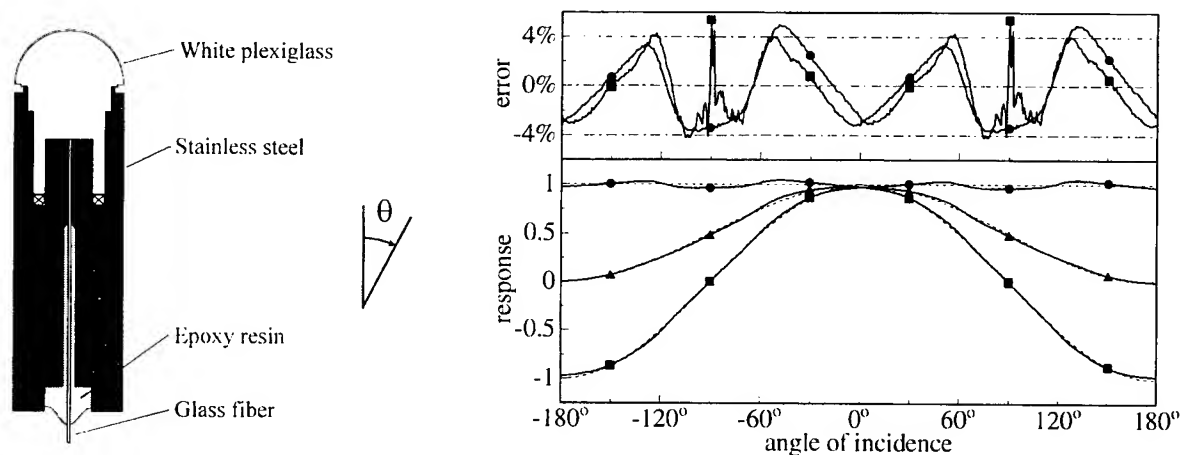


Fig. 2: Outline drawing of the 1+cos-collector and its angular response (Δ), computed angular responses of E^- (\blacksquare) and E_0^+ (\bullet) and their error curves (dashed lines are ideal responses)

cos - collectors: These are 12 mm in diameter. Light stops are constructed according to Smith's proposal¹² to increase the collecting efficiency at large angles of incidence. The angular response accuracy of the submerged version is better than $\pm 2\%$ at

angles between 0° and 63° and better than $\pm 10\%$ up to 87° . Simulating up- and downward looking gives 0.7 % deviation for the peaked and half as much for the asymptotic light field. The irradiance error between the two radiance distributions is 0.5 % for both up- and downward looking cases. For the air-optimized version the accuracy is better than $\pm 1.3\%$ at angles between 0° and 70° and better than $\pm 10\%$ up to 85° .

2 π - collector: To get equal response for all angles the diffuser shape is a sphere⁷ with 3 mm radius. The end of the glass fiber is located within the sphere, about 1.5 mm from the back. Distinct sensitivity cut down at the edge of the field of view is obtained by a large light shield of 10 cm diameter. The angular response accuracy of the collector is better than $\pm 1\%$ between 0° and 75° , decreasing to - 5 % at 83° , where the light stop begins shading. The irradiance error between up- and downward looking is 2.5 %, the influence of the light field's shape is neglectable.

The sensors are connected with the spectrometer by two different kinds of fiber optics. Between the diffuser and the instrument housing the light is guided by PCS fibers of low OH⁻ type, with a numerical aperture NA = 0.4, for best transmission. Fiber diameter is 300 μm for upward and 600 μm for downward looking collectors. To adapt to the spectrometer's numerical aperture quartz/quartz fibers with NA = 0.22, 200 μm diameter and 2 m length are used within the housing. By combining a high NA cable with firmly mounted low NA fibers acting as mode strippers it was intended that the signals become independent on bending the support line. That is true for the 300 μm fibers. No change in signal could be detected whether the 25 m cable was spooled or straight. However, the amount of light carried through the 600 μm fibers is altered by 5 %. This problem can be avoided by hanging the support line overboard while recording a depth profile, thereby keeping the amount of bending constant.

2.3 The spectrometer unit

A bundle of four quartz/quartz fibers is coupled to the 600 μm , and one fiber to the 300 μm PCS fibers. In this way the weak signals of the downward looking sensors are magnified by a factor of 4 through binning the respective CCD lines. The other ends of the quartz/quartz fibers are stacked and cemented on a 50 μm slit. Between fibers belonging to different collectors darkened fiber fragments of the same diameter are inserted. The slit is mounted on a $f = 140$ mm spectrograph CP 140-202 (Instruments S.A.) which is equipped with a holographic "flat field" grating. A 1:1 image of the entrance slit is produced on the focal plane, thereby forming wavelength splitted light stripes separated by means of the mentioned dark fibers. Figure 3 shows an image taken with the attached CCD detector TH 7895A (Thomson Semiconductors). This sensor consists of 512×512 pixels of 19 μm edge length. Wavelength is recorded from 400 nm to 850 nm. Since the grating's astigmatismus correction is insufficient, the wavelength resolution depends on the vertical position of the light stripe. It varies from 3 nm in the central area to 9 nm at positions which are only 3 mm outside the center. Within a stripe it is almost constant. The middle region with the high wavelength resolution is used by the E_d^+ and L_u^+ collectors. Their signals remain constant during lowering, whereas the signals of the submersible unit decrease exponentially. Therefore the E_d^+ sensor's diffusor is made of a less translucent plexiglass and the L_u^- detector is provided with an aperture stop, damping the signals by a factor of about 20. This allows longer exposure times when the under water light signals become weak.

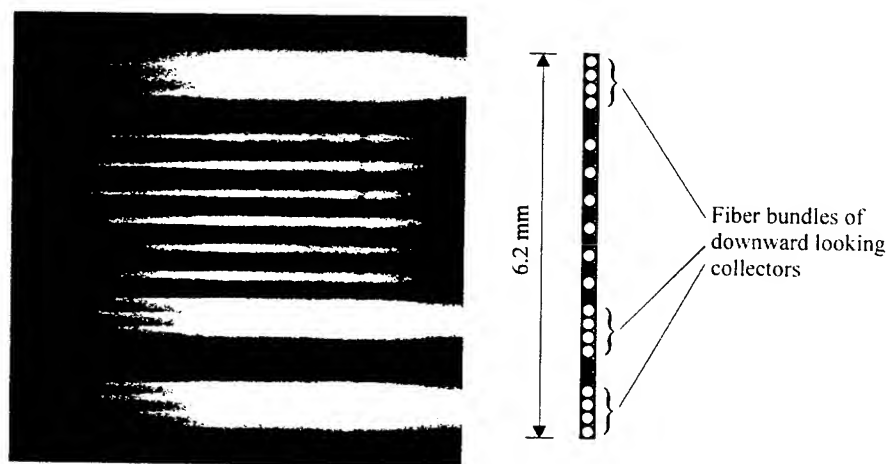


Fig. 3: CCD image showing 9 separated spectra (left), fiber stack at the slit position (right)

The slow scan camera was supplied by the company Schneider Systemtechnik, Germany. During readout of the full frame CCD, when the generated electrons are transported through the image zone with 1 MHz pixel clock, a mechanical shutter keeps the CCD dark and prevents the smearing of the signals. Digitizing is done with 14 bit resolution. To reduce electronic noise, pixels of each wavelength channel within a stripe are binned together on the CCD. Electrons contributing to the output signal are not only generated by impinging light but also by thermal effects resulting in large dark signals of the binned stripes at longer exposure times. Therefore a Peltier cooler was installed which lowers the CCD temperature by about 35 K, allowing exposure times up to 15 s.

3. CALIBRATION

3.1 Slow scan camera and spectrometer inherent effects

For correcting dark signals the CCD detector is provided with masked reference pixels. A dark model is established that correlates the dark signals of pixels within a light stripe to the reference pixels on both sides. The measured correlation was strictly linear. Two exposures of 50 ms and 15 s with closed shutter are sufficient to derive coefficients for dark correction at all other exposure times. The procedure must only be repeated from time to time when ambient temperature changes markedly. Nonlinearity of the CCD camera with changing light intensities but constant exposure time of 100 ms was analyzed by positioning a chopper wheel with 20 windows in the measuring light beam. Closing the windows one by one reduced the light throughput in steps of 5 %. Triggering the camera with the chopper wheel and synchronizing exposure time with rotation frequency ensured that no light entered the spectrometer when the shutter opened or closed. The measured linearity depends on the amount of pixel-lines binned to a stripe and is within ± 0.5 %. Correction is made by a polynomial fit. The performance of the camera was also tested by keeping the illumination constant but varying the exposure times. The deviations were negligible.

Small amounts of cross talk among the light stripes (worst case 1 % at the infrared and blue end of the spectra, 0.2 % from green to red for adjacent stripes) are caused by the grating. As the signal values of different collectors can differ strongly, a large dynamic range is necessary. Therefore the measured cross talk from one light stripe to the others is corrected for. Thereby the correction for diffusely scattered light is included.

3.2 Absolute radiometric calibration

In the following a procedure is described by which all collectors can be related to a gauged irradiance standard. This standard is used to calibrate the L_u^+ sensor. Combining the sensor with a white reflectance standard positioned in front of its lense gives a device with cosine weighting of incident radiance, from which the E_d^+ and E_u^+ collectors are calibrated. For the under water collector the result must be multiplied with the wavelength dependent immersion factors^{11,12}. The next steps are carried out in the natural environment of the submersible unit, e.g. in the light field of a lake. As the signals of the different sensors must be intercompared, this *in situ* calibration gives best performance. The collectors are lowered twice to the same depth, first all looking upward and then all looking downward. Within this short period of time stable light conditions are necessary. All required information is obtained by the two recordings. From the calibrated cos - collector's data E_d^- and E_u^- are obtained. Subtracting the signals of each up- and downward looking gives results proportional to E^- which are calibrated by comparing them to $E_d^+ - E_u^+$. Adding the signals of the 1+cos - collectors provides calibrated E_0^+ , which is then used to calibrate the 2π - sensor.

For under water calibration of the L_u^- sensor the reflectance standard is replaced by a white teflon disk. The signal of the radiance sensor looking downward on the disk is compared to the upward looking cos - collector. The disk is calibrated to the standard in air anticipating that the reflectance of teflon changes only negligible when it is submerged. Another way to calibrate the L_u^- sensor is to estimate its immersion effect. The same experimental arrangement can be used as with the cos - collector, only changing the illumination from collimated to diffuse. Both methods incorporate some uncertainties. Comparison is planned.

Once the required coefficients are established, radiometric calibration is carried out more easily by checking each sensor with the irradiance standard for signal deviations. A highly automated software written with LabVIEW® (National Instruments) is being developed to support all calibration steps, wavelength calibration and also recognizing the light stripe's boundaries on the CCD.

4. DISCUSSION

The signals of 2 above water and 7 under water sensors, split to 512 wavelength channels, provide extensive data sets relevant to remote sensing of water color, modelling the water column's light field and deriving its constituents by optical means. With a cable length of 25 m the instrument is designed for inland lake and costal zone applications but can also be used in the open ocean. Measuring all parameters simultaneously makes the device insensitive to changes of radiation impinging on the water

surface during exposure. Changes of above water illumination during recording a depth profile can be accounted for by the E_d sensor. Focusing effects of surface waves may influence the light intensities at the two working planes of the submergible unit differently, undermining the advantages of coincident measurement. If this problem arises, time averaging of the signals will help.

One remark must be made in deriving the absorption coefficient from the measured quantities. It is essential to know at what depth between the upper and lower working plane $E_0(z)$ must be evaluated to use it in Gershun's law. The scalar irradiance can vary markedly between z_1 and z_2 in some wavelength regions whereas in others the depth difference may be just enough to evaluate the signal differences in E . Deriving a is also affected by changes in the angular distribution of the light field within the regarded depth interval. As the distance of the working planes is variable with our probe, a future goal is to take data series and see whether extrapolation to zero spacing and deriving algorithms to select the adequate $E_0(z)$ is possible for different water types.

In the last decade bio-optical models have been developed to relate reflectance and diffuse attenuation coefficients to inherent optical properties and water constituents. Only little work has been done on the evaluation of $\bar{\mu}$ and $d\bar{\mu}/dz$ which are computable from the measured spectra. The sun beam spreads through scattering by suspended particles and water molecules. Thus $d\bar{\mu}/dz$ should give a rather accurate possibility for estimating the scattering coefficient b . However, the angular distribution of the under water light field is also influenced by absorption. But knowing a , it is expected to obtain a better approximation of b rather than estimating it from diffuse attenuation coefficients only. To decrease influence of the ship's shadow on the measurements, a 4 m long outrigger is installed on the bow of a research vessel operating at Lake Constance.

5. ACKNOWLEDGEMENTS

The authors are grateful to M. Schroeder for encouraging the work, and to H. van der Piepen, P. Gege, the other members of the institute's remote sensing group and to J.H.M. Hakvoort from GKSS, Geesthacht for helpful discussions. Many thanks also to E. Schneider from the company Schneider Systemtechnik for his support of the project.

6. REFERENCES

1. B. Kunkel, F. Blechinger, D. Viehmann, H. van der Piepen and R. Doerffer, "ROSIS imaging spectrometer and its potential for ocean parameter measurements (airborne and spaceborne)," *Int. J. Remote Sensing* **12**(4), 753-761 (1991)
2. P. Strobl, A. Nielsen, F. Lehmann, R. Richter and A. Müller, "DAIS data quality assesment, first results from the 1995 evaluation campaigns," *Proc. 2nd International Airborne Remote Sensing Conference and Exhibition*, San Francisco, Vol. II, 325-334, June 1996
3. V. Amann, "Airborne remote sensing at DLR," *Airborne Multispectral Applications...Worldwide, Daedalus Special Compendium*, Daedalus Enterprises, Inc., P.O. Box 1869, Ann Arbor, MI 48106 USA, 12-15, June 1996
4. P. Gege, *Water analysis by remote sensing: A model for the interpretation of optical spectral measurements*, thesis, ESA-TT-1324, July 1995
5. E. Aas, "Two-stream irradiance model for deep waters," *Appl. Opt.* **26**, 2095-2101 (1987)
6. N.K. Højerslev, "A spectral light absorption meter for measurements in the sea," *Limnol. Oceanogr.* **20**, 1024-1034 (1975)
7. K.D. Moore, E. O'Mongain, S. Plunkett, R. Doerffer and M. Bree, "In situ marine spectral radiometer using frame addition techniques and its calibration," *Proc. SPIE*, Vol. 2048 (*Underwater Light Measurements*), 153-165 (1993)
8. H.R. Gordon and K. Ding, "Self-shading of in-water optical instruments," *Limnol. Oceanogr.* **37**, 491-500 (1992)
9. J. Piskozub, "Effects of surface waves and sea-bottom on self-shading of in-water optical instruments," *Proc. SPIE*, Vol. 2258 (*Ocean Optics XII*), 300-308 (1994)
10. H.R. Gordon, O.B. Brown and M.M. Jacobs, "Computed relationships between the inherent and apparent optical properties of a flat homogeneous ocean," *Appl. Opt.* **14**, 417-427 (1975)
11. J.H. Morrow, M.S. Duhig and C.R. Booth, "Design and evaluation of a cosine collector for a SeaWiFS-compatible marine reflectance radiometer," *Proc. SPIE*, Vol. 2258 (*Ocean Optics XII*), 879-886 (1994)
12. R.C. Smith, "An under water spectral irradiance collector," *J. Marine Res.* **27**, 341-351 (1969)
13. J.L. Mueller and R.W. Austin, Ocean optics protocols for SeaWiFS validation, revision 1, *NASA Tech. Memo. 104566* Vol. 25. S.B. Hooker and E.R. Firestone, Eds., NASA Goddard Space Flight Center, Greenbelt, Maryland, 66 pp (1995)
14. J.E. Tyler, "Radiance distribution as a function of depth in an underwater environment," *Bull. Scripps Inst. Oceanogr.* **7**, 363-411 (1960), Table 4 and 16

Hi-Star: A spectrophotometer for measuring the absorption and attenuation of natural waters *in-situ* and in the laboratory.

E.J. Bruce¹, M. Borgerson¹, C. Moore¹, and A. Weidemann²

¹WET Labs, Inc., 620 Applegate Street, Philomath, OR 97370 USA.

²Naval Research Laboratory, Stennis Space Center, MS 39529 USA.

ABSTRACT

A new submersible spectrophotometer with 3.3 nm spectral resolution throughout the visible range, 400 - 730 nm, has been developed for the Navy. Within the sample chamber, the Hi-Star incorporates an optical configuration similar to that of the existing WET Labs ac-9 dual path absorption and attenuation meter. The absorption path includes a reflective tube to collect the scattered light throughout the sample volume while the attenuation path uses conventional transmissometer optics. The Hi-Star uses fiber optics to couple a single white light source into the two sample optical paths and a reference path. The absorption and attenuation receivers consist of primary collection optics which couple the light into two spectrometers. A third spectrometer is used to directly measure the light from the reference path. Data collected from the absorption and attenuation paths are subsequently reference normalized to correct for changes in the lamp output over time. The Hi-Star is designed to be used either in a continuous flow mode or with discrete samples in cylindrical cuvettes, thus making it suitable for both laboratory or field applications.

We show preliminary data collected with the Hi-Star instrument both in the laboratory and *in-situ*. Laboratory tests will include determination of basic instrument coefficients and determination of the mean scattering error for the absorption measurement. Field results are also presented using the instrument in both bench-top and *in-situ* profiling operation modes.

Keywords: absorption, attenuation, measurements, instrumentation, spectrophotometer

1. INTRODUCTION

During the past ten years substantial effort has been expended in the development of new sensors for determination of the *in-situ* spectral absorption and attenuation coefficients of natural waters. Methodologies employed included the isotropic absorption meter¹, the diffuse source attenuation meter², a fiber coupled, ship based spectrophotometer³, and the reflective-tube absorption meter⁴.

In 1993 WET Labs, Inc. produced the ac-9, the first commercial product for *in-situ* determination of the spectral absorption and attenuation coefficients at nine wavelengths. This instrument coupled two collimated white light sources with a filter wheel to produce dual beams which propagated through a fixed pathlength. The attenuation receiver employed conventional collimating optics⁵ while the absorption beam used the reflective-tube and a large area receiver⁶. The ac-9 has provided an important link between inherent optical property measurements and physical and biological processes occurring within the water column⁷. The instrument has demonstrated the special considerations required for temperature and salinity in performing *in-situ* determinations of the absorption and attenuation parameters⁸. And it has shown good agreement with conventional filter pad methodologies in determination and discrimination of biological components within the water (Ivey, J.E., personal communications).

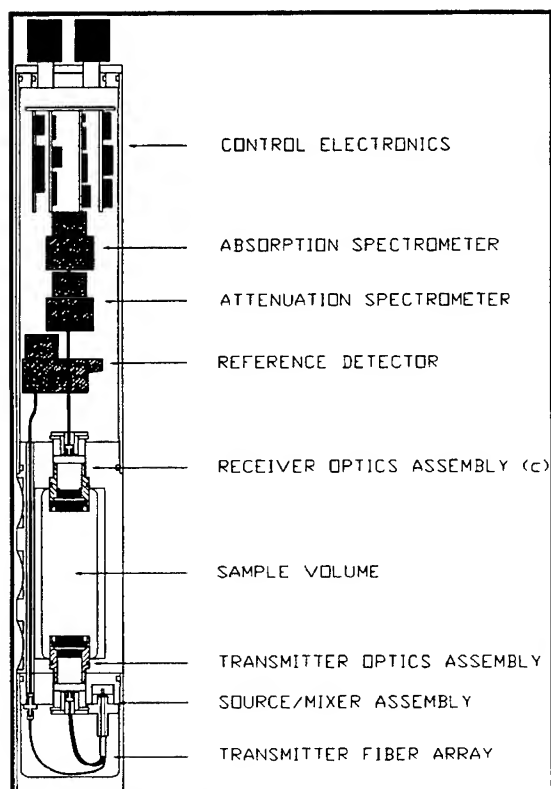
Over the past three years the ac-9 has been applied in numerous applications including ground truthing for remote sensing, fine scale vertical structure and dynamics studies, and *in-situ* chemical analysis. While these uses of the instrument clearly demonstrated the importance and potential of measuring spectral inherent optical properties, they also pointed to the instrumental limitations of the device. In short, they created a need for a technological evolution which would incorporate higher spectral resolution, lower power consumption, improved stability, more compact packaging, and greater flexibility in deployment.

In response to these requirements we have developed the Hi-Star. The Hi-Star is an underwater spectrophotometer designed to measure the absorption and attenuation coefficients of water samples. High resolution is obtained by collecting light

transmitted through the sample path and coupling it into a fiber-coupled miniature spectrometer. The Hi-Star has a 3.3nm spectral resolution throughout the visible range, from 400 to 730nm. Here we present an overview of the instrument design, including a discussion of the optical layout and the electronics. Data is presented from a profiling deployment in Eastsound, Washington. We also show data collected using the Hi-Star in the laboratory, including a dilution series of polymer microspheres and a sample phytoplankton culture.

2. INSTRUMENT DESIGN

Instrument Layout



The Hi-Star can be broken down into four main components: the yoke, the transmitter pressure can, the receiver pressure can, and the flow assembly (see Figure 1). The yoke is designed as the main mounting block for all of the transmit and receive optics. The yoke is machined from a single block of aluminum, thus significantly increasing the overall mechanical stability of the instrument. The transmitter is comprised of a fiber coupled source and collimating optics. The receiver optics, three fiber-coupled miniature spectrometers, and the control electronics are all housed within the receiver pressure can. The center of the yoke serves as the sample volume. A flow assembly, which slides into place within the center of the yoke, contains both the absorption flow cell and the attenuation flow cell. A similar sample cell has been designed to hold two 10cm cylindrical cuvettes, allowing the user to perform measurements of absorption and attenuation in the laboratory with discrete samples.

Optics

In order to minimize the overall dimensions of the instrument, reduce the power consumption, and limit the amount of heat generated by the instrument, the Hi-Star utilizes fiber optics to separate the light from a single source. Three miniature spectrometers are used to receive the transmitted light, separate the white light into its spectral components, and measure the relevant intensities. Figure 2 shows the basic optical layout.

Figure 1. Hi-Star instrument layout.

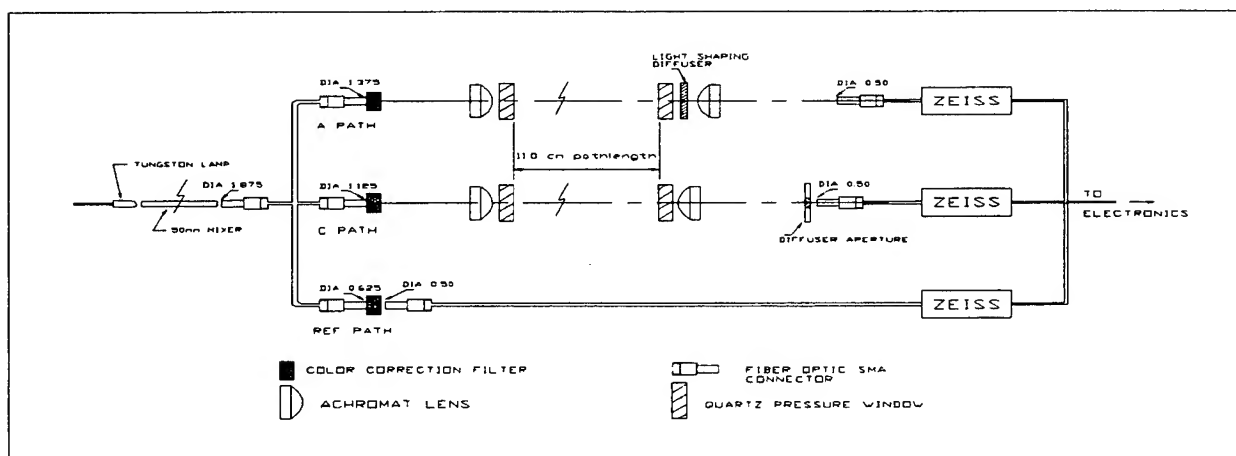


Figure 2. Optical layout of the Hi-Star showing the three main optical paths: absorption, attenuation, and reference.

The white light source is a tungsten miniature lamp which operates at about 2600 Kelvin. The lamp is mounted within the yoke, allowing the heat generated by the 2.5 watt bulb to be dissipated easily. In order to eliminate imaging of the filament structure, the bulb is frosted and a 50mm square optical mixer is coupled directly to the lamp. The output of the mixer is coupled to a trifurcated silica fiber bundle, which splits the light into three paths: the absorption sample path, the attenuation sample path, and the reference path. The fiber bundle is designed to balance the amount of light coupled into each path based on optical losses specific to each path's configuration.

A glass color correction filter is used at the output of each leg of the fiber bundle in order to balance the relative levels of intensity from the blue to the red regions of the spectrum. This is important because it allows us to use a constant integration time when collecting data from the spectrometer's photodiode arrays. The light for the absorption and attenuation sample paths is collimated using 40mm achromat lens before it travels through a 11cm sample path. The absorption path contains a quartz tube in the flow cell which effectively reflects scattered light, based on the principle of total internal reflection, to the receiver optics.

The absorption receiver is comprised of a Light Shaping Diffuser mounted directly behind the pressure window and a 30mm achromat lens to collect the diffused light and concentrate it upon the receive fiber bundle of the spectrometer. The attenuation receiver uses a 30mm achromat lens to focus the collimated light down to a diffuser aperture. The spectrometer input fiber bundle is mounted directly behind the diffuser aperture at a distance that maximizes the amount of light collected based on the fiber optic's numerical aperture and core diameter. Hi-Star uses three miniature spectrometers, one for each of the three optical paths to receive the transmitted light and separate the light into it's spectral components using a grating blazed at 340nm. The spectrometer uses a 256 pixel photodiode array to measure the light intensity from 300 to 1150nm with a resolution of 3.3nm. The Hi-Star electronics selects the pixels corresponding to the 400 to 750nm range and processes the output.

Electronics

The Hi-Star uses a 16-bit microprocessor to control the three miniature spectrometers. The spectrometers are sampled in an interleaved high-speed sequence which collects and digitizes over 100 pixels of data from each of the three spectrometers in approximately 9 milliseconds. The amount of time between spectrometer samples, the integration time, is controlled to a fraction of a microsecond by an internal hardware timer in the CPU. The readout sequence is an uninterrupted sequence of processor instructions which maintains timing accurate to a within a few nanoseconds for each collection cycle.

The miniature spectrometers used by the Hi-Star are serial clocked devices. Each spectrometer transfers the stored charge from the photodiode array to an amplifier which converts the charge to an output voltage. The Hi-Star electronics integrates these output voltages and holds the integrated peak value until it is digitized by an 16-bit A/D converter. The low-noise design of the Hi-Star electronics results in output values which typically have short-term noise of less than two to three counts or about 200 microvolts. A block diagram of the electronics is show in Figure 3.

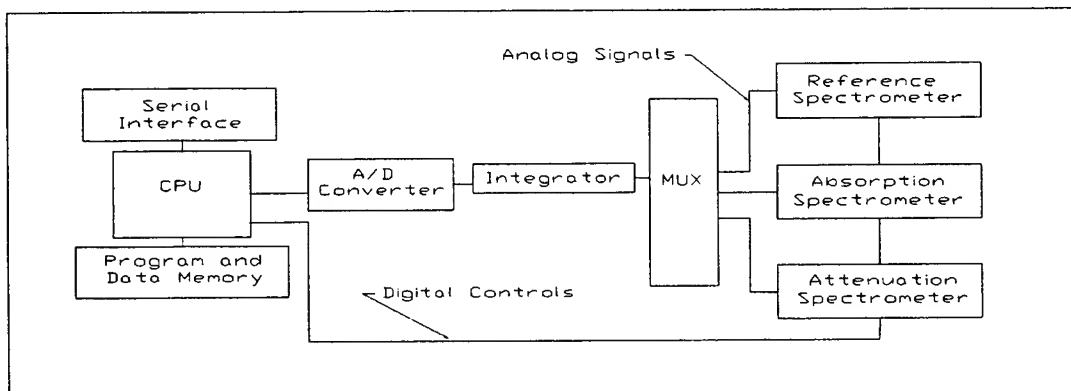


Figure 3. Block Diagram of the Hi-Star Electronics. This diagram shows the relationship between the spectrometers and the CPU.

In order to reduce thermal problems and long-term drift, the Hi-Star uses the same integrator and A/D converter for all three spectrometer channels. The three spectrometers are clocked in a round-robin fashion: Pixel 1 from each of the three spectrometers, then pixel 2, pixel 3, etc. This ensures that all pixels from the three spectrometers have the same integration time and that the spectrometers start and stop integrating photons within 24 microseconds of each other. This interleaved sampling ensures that the three spectrometers are sampling the same water sample and removes any short-term variations in the lamp output, since the reference is sampled at the same time as the signal channels.

The Hi-Star operating firmware clocks out unused pixels, but does not integrate or digitize the values. This reduces the time required to collect the data. Since the processor cannot be interrupted during the data collection, it is helpful to reduce the sampling time so that other time critical events, such as real-time clock ticks and serial input, will be disrupted to the minimum extent possible.

Performance Characteristics

In order to accurately determine the behavior of the Hi-Star in the field, the instrument was characterized for: a) the scattering error in the absorption measurement, b) precision, c) instrumental temperature compensation, and d) short term stability.

In order to accurately measure absorption using a measurement of the transmitted light it is necessary to collect all of the light scattered throughout the sample volume. The reflective tube absorption measurement collects scattered light, however, a certain percentage of the photons never make it to the detector. Losses occur when photons in the flow cell are scattered at angles greater than the critical angle. Photons are also lost at the interface of the flow cell and the receive optics. In order to characterize the Hi-Star's absorption measurement, a dilution series was performed using 5.01 micron polymer microspheres. Figure 4 shows the result of this characterization experiment. Since the amount of scattered light collected at the absorption receiver is dependent on the collection efficiency of the diffuser, the specified diffuser angle of the Light Shaping Diffuser used in the Hi-Star becomes a critical factor. Tests with higher diffuser angles (10° through 20°) have revealed improved collection efficiency, however, the overall throughput of light is significantly reduced resulting in increased levels of noise. The calculated scattering error with the instrument's current optics configuration results in approximately a 35% scattering error.

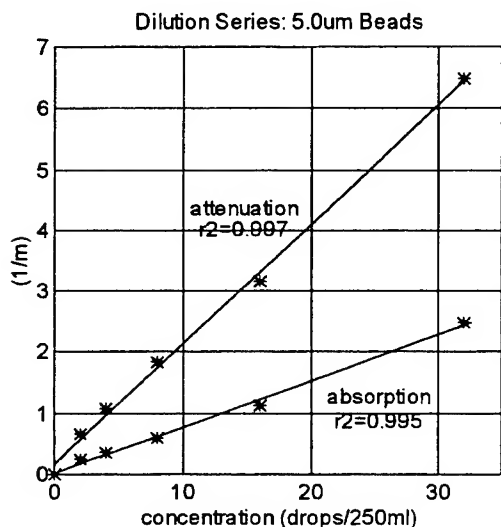


Figure 4. Dilution series of 5.0um polymer spheres.

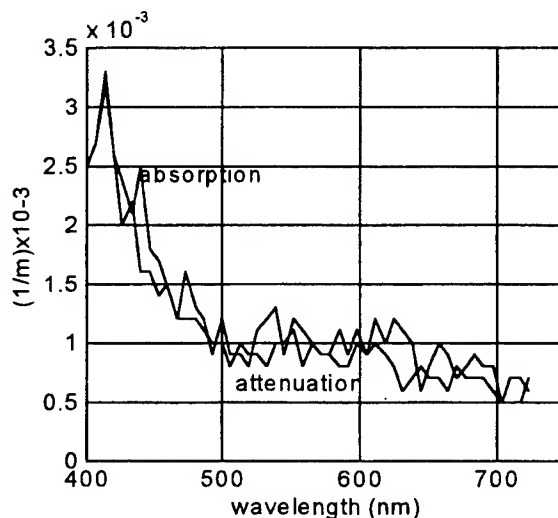


Figure 5. Measured precision of both the absorption and attenuation signals.

The measured precision of the Hi-Star was determined by calculating the standard deviation of 30 spectra with a 1 second time constant. The resulting precision versus wavelength is plotted in Figure 5 for both the absorption and attenuation

paths. The precision is not as high in the blue region of the spectra compared to the precision from 500 to 730nm, which averages a value of 0.0008 m^{-1} , because of the absolute decrease in intensity of the white light source in this portion of the spectra.

In order to characterize the effects of temperature the Hi-Star was placed in a temperature bath with the sample flow volume sealed and filled with Argon to prevent any moisture from condensing on the windows. The water in the temperature bath was gradually reduced from approximately 30 degrees Celsius to 7 degrees Celsius while data was collected. In order to compensate the instrument for temperature effects experienced in the natural ocean environment, a linear temperature correction algorithm based on the temperature calibration tests is applied in the Hi-Star's software program.

With the temperature compensation algorithm applied, the short term stability of the Hi-Star is improved. Data was collected over 15 hours and averaged over 20 samples, resulting in a 4 second time constant. The average deviation for each channel was less than 0.002 m^{-1} over the entire time interval.

3. DATA

The Hi-Star was deployed in the field during August 1996, in Eastsound, Washington. The instrument was used in a profiling mode of operation using a Seabird pump to continuously flow water through the sample volume of the Hi-Star. Figure 6 shows some of the data collected during a 30 meter cast. The first plot shows a plot of the absorption coefficient at 677nm. The second plot shows consecutive absorption spectra collected through the first layer, indicated by the label 'Depth1' in the profile plot. The third plot shows consecutive absorption spectra collected through the second layer, indicated by the label 'Depth2' in the profile plot. The chlorophyll absorption peak appears at about 677nm.

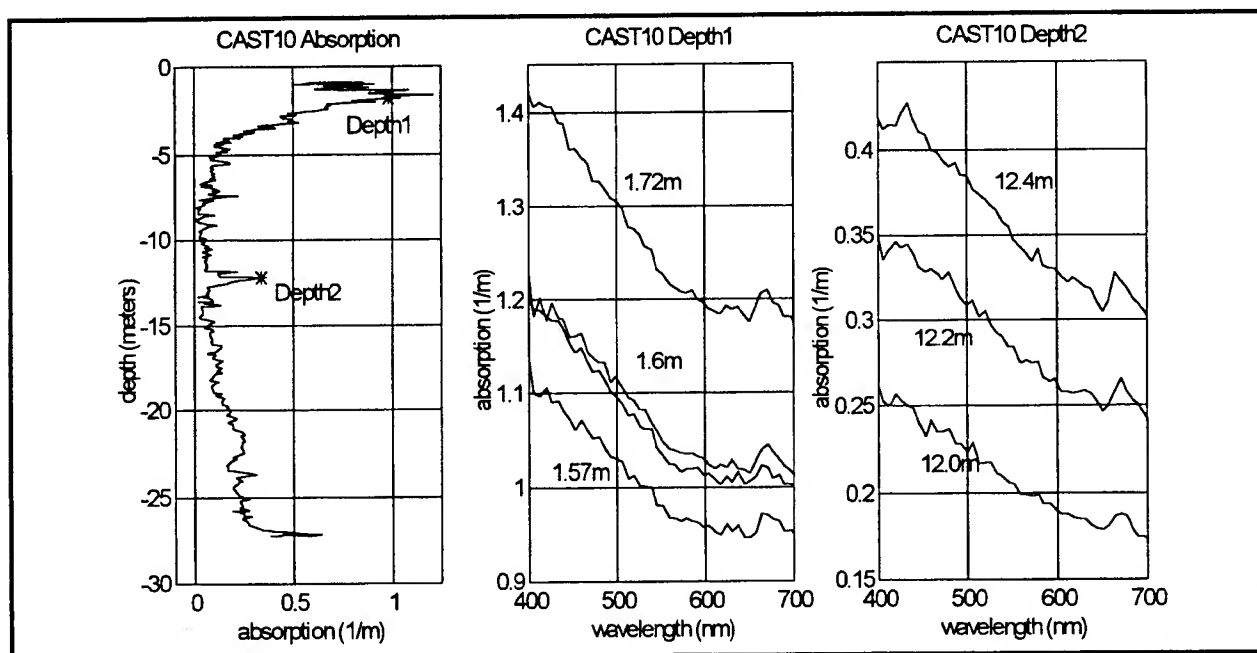


Figure 6. Profile of the absorption coefficient at 677nm during a cast in the Eastsound, Wa (left). Consecutive absorption spectra through the first layer at 1.7 meters, depth1 (center) and the second layer at 12.4 meters, depth2 (right).

The absorption of several different phytoplankton species were measured in the laboratory using a 10cm cylindrical cuvette. Figure 7 shows a set of measured absorption spectra for a sample collected at a 200msec sample rate (5 spectra/second). An initial scattering correction was performed by subtracting a baseline absorption measured at 730nm, assuming that there is no absorption by phytoplankton at this wavelength.

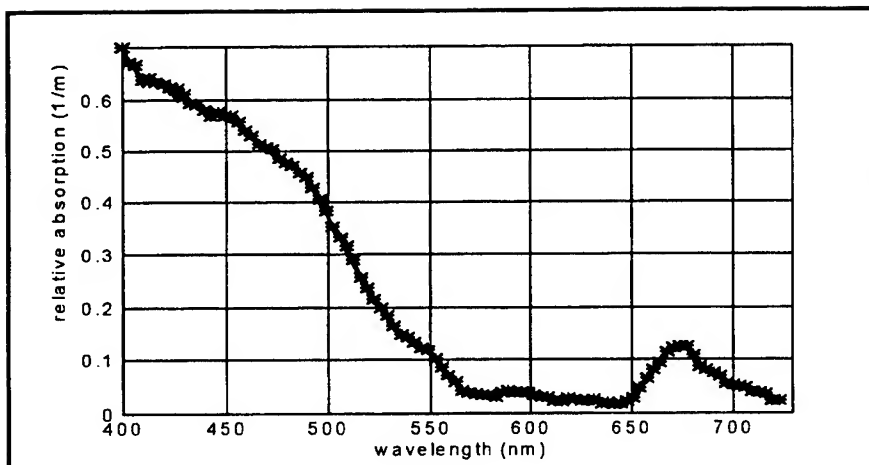


Figure 7. Measured absorption spectra for a phytoplankton laboratory culture: Prymnesiophyceae *Isochrysis galbana*. The plot contains a set of consecutive spectra taken at a 200msec sample rate. This data was collected using a 10cm cylindrical cuvette in the Hi-Star's sample path.

4. DISCUSSION

The initial characterization of the Hi-Star has proven to be comparable to the existing WET Labs ac-9. The precision of the instrument is approximately 0.003 m^{-1} in the blue and 0.001 m^{-1} in the green and red regions of the spectrum. The scattering error in the absorption measurement is about 35% with the current configuration, however, we intend to improve this by using a higher angle Light Shaping Diffuser. In order to accomplish this we will need to increase the absolute amount of light energy in the 400 to 450nm range, by using a higher temperature tungsten source or by further improving our fiber optic mounting to allow for a more efficient coupling of the lamp to the three optical paths. The short term stability of the instrument after temperature corrections are applied results in a 0.002 m^{-1} deviation over 15 hours.

5. ACKNOWLEDGMENTS

We would like to thank Jennifer Crain and Alice Murphy of Oregon State University, Oceanography Department for providing us with phytoplankton cultures for sampling. We would also like to thank Percy Donaghay of the University of Rhode Island for providing us with the opportunity to collect data in the field.

6. REFERENCES

1. E.S. Fry and G.W. Kattawar, "Measurement of the absorption coefficient of ocean water using isotropic illumination," *Ocean Optics IX, Proc. SPIE* **925** 142-148 (1988).
2. J.H.M. Hakvoort, A.E.R. Becker, and J. Krijgsman, "An instrument to measure *in situ* visible light absorption in natural waters," *Ocean Optics XII Proc. SPIE* **2258**, 77-88 (1994).
3. Saito, A. Nishimoto, Y. Kakui, and M. Nanjo, "*In situ* spectral absorption profiler using optical fibers," *Ocean Optics XII Proc. SPIE* **2258**, 67-76 (1994).
4. J.R.V. Zaneveld, R. Bartz, & J.C. Kitchen, "A reflective-tube absorption meter", *Proc. SPIE* **1302** (Ocean Optics X), 124-136 (1990).
5. J.R.V. Zaneveld and R Bartz, "Beam attenuation and absorption meters" *Ocean Optics VII Proc. SPIE* **489**, 318-324 (1984).
6. C. Moore, J.R.V. Zaneveld, J.C. Kitchen, "Preliminary results from an in-situ spectral absorption meter," *Ocean Optics XI, Proc. Soc. Photo-Optical Instrum. Eng. (SPIE)*, Vol. 1750, pp. 330-337, 1992.
7. C.S. Roesler and J.R.V. Zaneveld, "High-resolution vertical profiles of spectral absorption, attenuation and scattering coefficients in highly stratified waters," *Ocean Optics XII Proc. SPIE* **2258**, 309-319 (1994).
8. W.S. Pegau and J.R.V. Zaneveld, "Temperature dependent absorption of water in the red and near-infrared portions of the spectrum," *Limnol. Oceanogr.* **38**, 188-192 (1993).

Measurements of the attenuation coefficient of a lidar in the Southern California Bight

James H. Churnside

NOAA Environmental Technology Laboratory
325 Broadway, Boulder, Colorado 80303

ABSTRACT

Measurements were made of the attenuation coefficient of the National Oceanographic and Atmospheric Administration (NOAA) lidar from a ship in the Southern California Bight in September 1995. The region from about 5 m to about 30 m in depth was covered. The laser was linearly polarized, and the receiver was operated with the same polarization, the orthogonal polarization, and a polarization angle of 45 degrees, so that the first three Stokes parameters of the scattered light can be estimated.

KEYWORDS: Ocean Optics, Lidar, Optical Attenuation

1. INTRODUCTION

The NOAA R/V *David Starr Jordan* was operated for three weeks in September 1995 with a lidar mounted on the flying bridge and directed down into the water. It was located at a height of 10.3 m above the water, and directed outward at an angle of 15°. During a portion of this cruise, lidar and in-situ measurements were made on a rectangular grid of 4 by 6 stations. The area covered was in the Southern California Bight, generally between San Diego and San Clemente Island.

The lidar source was a frequency-doubled, Q-switched Nd:YAG laser, linearly polarized parallel to the plane of incidence. The receiver consisted of a lens that collected the scattered light onto a microchannel plate detector. An interference filter was placed in front of the detector to limit background light. A rotatable polarizer in front of the filter was used to make measurements of the parallel-polarized return, the perpendicular-polarized return, and the 45°-polarized return at each station. The detector was triggered to begin each measurement at a depth of 10 m, and useful signal was generally received down to a depth of 30 to 40 m. The detector output was passed through a logarithmic amplifier and this signal was digitized and stored in the computer. About 1000 lidar pulses of each polarization were recorded at each station. The lidar parameters are presented in Table 1.

Table 1. Lidar transmitter and receiver parameters.

Transmitter	Wavelength	532 nm
	Pulse Length	15 nsec
	Pulse Energy	67 mJ
	Pulse Repetition Rate	10 Hz
	Beam Divergence	43 mrad
Receiver	Aperture Diameter	17 cm
	Field of View	26 mrad
	Optical Bandwidth	10 nm
	Electronic Bandwidth	100 MHz
	Sample Rate	1 GHz

Two packages with in situ optical measurements were lowered into the water at each station. One was a NOAA package that included a Sea Tech 25-cm transmissometer and a Chelsea Aquatrak fluorometer. The other was a Scripps

package that included a Biospherical Instruments underwater radiometer, a second Sea Tech 25 cm transmissometer, a WetLabs Wetstar fluorometer, and a Sea Tech light scattering sensor belonging to NOAA.

2. LIDAR DATA

In homogeneous water, the return signal from a lidar will experience an exponential decrease with propagation distance that is in addition to the geometric loss.¹⁻⁴ For a nadir-pointing lidar, the signal can be represented as

$$S(z) = C \frac{\exp(-2\alpha z)}{(z + nh)^2}, \quad (1)$$

where S is the signal at a particular depth, C is a parameter that depends on the geometry and lidar parameters, α is the lidar attenuation coefficient, z is depth, h is the height of the lidar above the water, and n is the index of refraction of water. Note that C is $(nh)^2$ times the signal at the surface, and has units of $V\ m^2$.

A typical lidar trace is presented in Figure 1. This particular shot was for a parallel polarization. The detector was triggered at a depth of 10 m. There is some ringing of the signal when the detector is first turned on, and this region was not used in the analysis. The peak at about 17 m is an artifact of the trigger circuit; it is consistent throughout the data and was also not used in the analysis. The smooth line is a fit of Eq. 1 plus a background component to the data using three points along the curve. For this case, the amplitude parameter C was $4.73\ mV\ m^2$, the lidar attenuation coefficient was $0.109\ m^{-1}$, and the background level was $2.22 \times 10^{-4}\ V$, which corresponds to 6.9 dB in the figure. The data and the curve agree fairly well. This agreement was typical, and suggests that the lidar attenuation coefficient was not a strong function of depth in this region.

Data were collected in 1-minute segments. A portion of that time was used for data storage and a background light measurement. This left 500 lidar pulses of useful data from each segment. Two segments of each polarization were recorded at each station. For each lidar pulse, the return waveform was analyzed to obtain the three parameters. The background levels were small and very consistent from pulse to pulse. The amplitude varied significantly from pulse to pulse because of surface losses. The average variability for all stations was 35%, with individual values ranging from 27% at station 11 to 46% at station 9. However, the mean values over 1000 pulses should be accurate to about 1%, assuming that the fluctuations of the surface are independent from pulse to pulse.

Figure 2 is a plot of the average returns for each of the stations, plotted as a function of the longitude at the

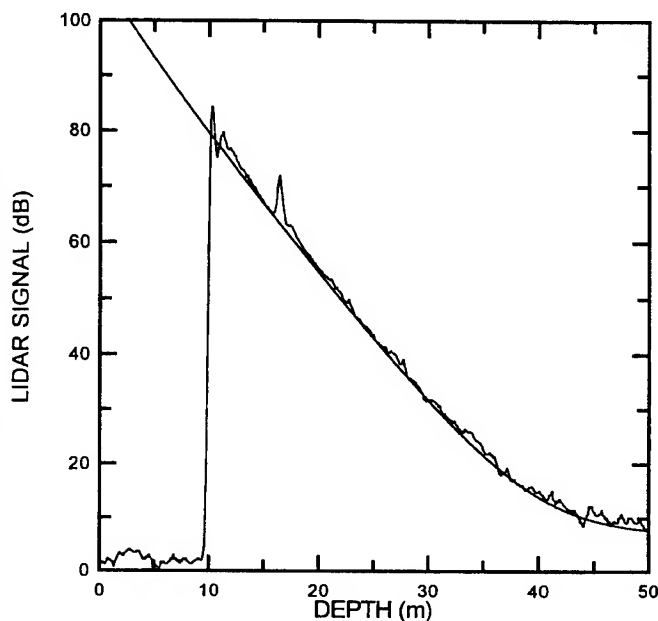


Figure 1 Typical lidar trace and a smooth fit that includes geometric and exponential losses of signal.

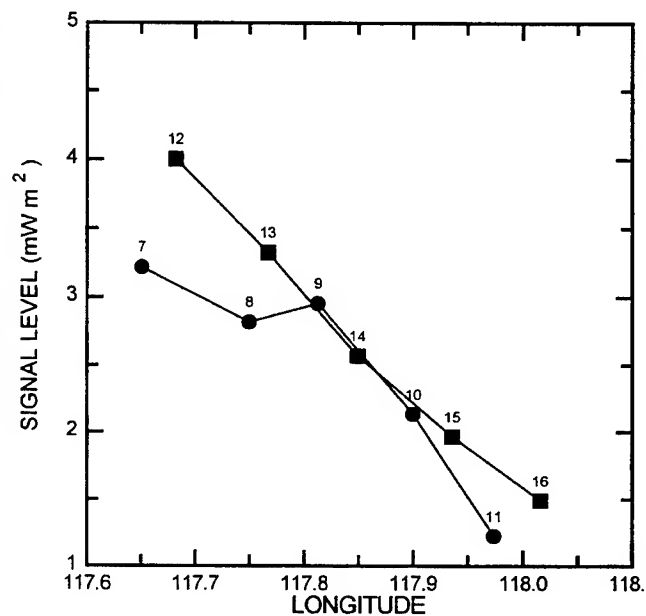


Figure 2 Signal amplitude, C , as a function of longitude for stations 7-11 in the first transect (circles) and stations 12-16 in the second transect (squares).

station. This quantity is the total return; it is the sum of the co-polarized and the cross-polarized values. Each of the two transect lines is shown with a different symbol. The signal level generally decreases with increasing longitude, which implies that the signal is decreasing as the distance from shore increases. This seems like a reasonable trend. One would expect that there would be more scattering particulates nearer to the coastline. The two transect lines have very similar values, and both show the same trend.

The pulse-to-pulse fluctuations in the inferred attenuation coefficient were much smaller, with an average value of 6.8% for the 10 stations. Figure 3 is a plot of the attenuation coefficients for the co-polarized return as a function of the signal level. There is a general trend of decreasing attenuation with increasing signal level, with the notable exception of station 12. This trend seems to imply that the particles in the water are getting bigger as the signal level increases. If the particle size distribution were the same, signal level and attenuation would both increase with increasing numbers of particles. If the number density of particles were constant, increasing particle size would lead to greater backscatter, which implies larger signal level, and also would lead to implies smaller attenuation of the signal.

Figure 4 is a plot of the attenuation coefficient for the cross-polarized return as a function of that for the co-polarized return. The dashed line is a linear regression, which is

$$\alpha_x = 1.15\alpha_{co} - 0.0126, \quad (2)$$

From this, we infer that the attenuation at the two polarizations is about the same. To look at this another way, we calculated the average difference between the co-polarized and the cross-polarized attenuation coefficients and got a result of $1.56 \times 10^{-4} \pm 3.49 \times 10^{-3}$. Thus, there is no statistically significant difference between the two components down to a confidence level of 3.5%.

The near equality of the attenuation coefficient for the co-polarized return and the cross-polarized return is somewhat surprising. One might expect that multiple scattering would remove photons from the co-polarized component of the beam and add them to the cross-polarized component as the beam propagates down through the water. This mechanism would tend to make the co-polarized attenuation greater than the cross-polarized attenuation. This does not seem to be happening to any significant extent.

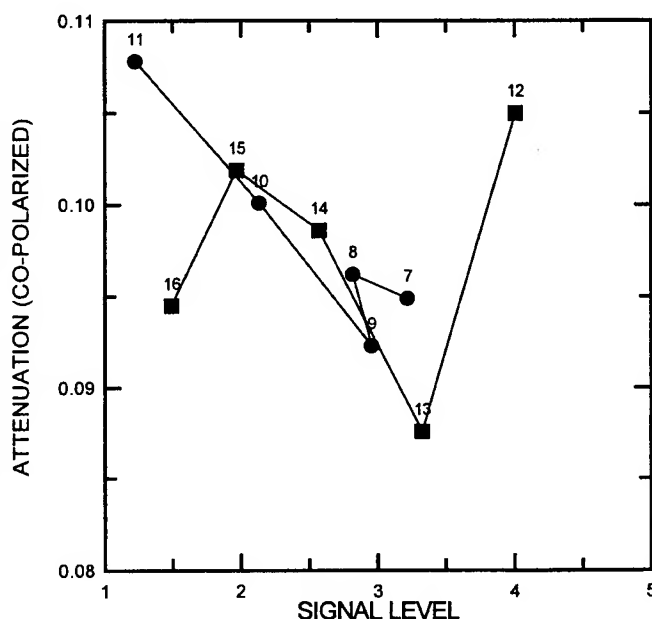


Figure 3 Attenuation coefficient α as a function of the signal level for stations 7-11 in the first transect (circles) and stations 12-16 in the second transect (squares).

more scattering at small angles in the forward direction, which

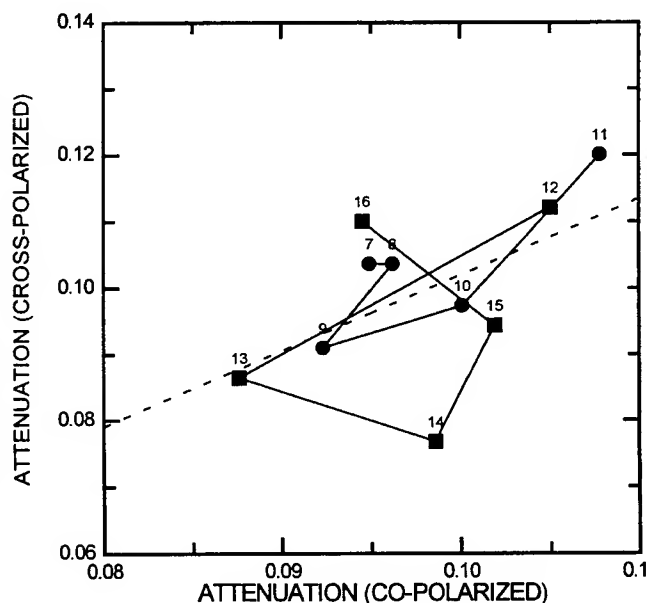


Figure 4 Attenuation coefficient of the cross-polarized lidar return as a function of coefficient for the co-polarized return. Stations are labeled as in Figure 3.

3. TRANSMISSOMETER DATA

The transmission of the water was measured directly using a SeaTech transmissometer with a 25-cm path length. This instrument measures the transmission at a wavelength of 660 nm. For comparison with our lidar system, we use the results of an empirical relationship by Voss⁵

$$c(532\text{nm}) = 1.18 c(660\text{nm}) - 0.419, \quad (3)$$

where c is the beam attenuation coefficient (in m^{-1}) inferred from the transmissometer. The transmissometer does not measure beam attenuation coefficient exactly, however, because of difficulties in rejecting light scattered at very small angles. It actually has a field of view of about 31 mrad, which between the beam divergence angle and receiver field of view of our lidar. For this reason, we might expect there to be some degree of correlation between the beam attenuation coefficient, c , as measured by this instrument and the attenuation coefficient of our lidar.

Figure 5 is a plot of the beam attenuation coefficient, as measured by the SeaTech transmissometer at a depth of 20 m, and the lidar attenuation coefficient for the co-polarized signal at the 10 stations where measurements were made. The correlation, about 88%, is clear from the figure. The dashed line is the best fit line through the points, and is given by

$$\alpha = 0.223c + 0.0686. \quad (4)$$

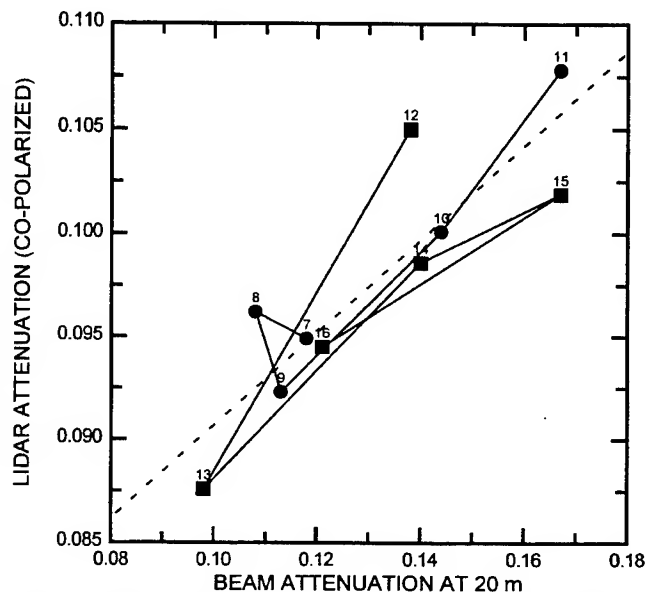


Figure 5 Attenuation coefficient for the co-polarized lidar return as a function of the beam attenuation coefficient measured at a depth of 20 m. Stations are labeled as in Fig. 4.

It is interesting that, despite the good correlation between the lidar attenuation coefficient and the measured beam attenuation coefficient, the slope of the line relating them is not unity; α seems to vary much less than c .

4. SUMMARY

The attenuation coefficients of a lidar were measured from a ship at four stations within the Southern California Bight. The attenuation coefficient generally decreased with increasing signal level, suggesting a greater degree of scattering at angles near zero and 180 degrees. There was no significant difference between the attenuation of the co-polarized return and the cross-polarized return. Finally, we noticed that the lidar attenuation was very well correlated with the beam attenuation coefficient as measured by a SeaTech transmissometer, although the slope of the linear relationship was not unity.

5. ACKNOWLEDGMENTS

This document has been generated as part of a joint NOAA-DOD - Advanced Sensor Applications Program. Thanks to Jim Wilson for lidar construction and testing, Slava Tatarskii for lidar software, Dan Higgins for data processing software, Ken Bliss for collecting transmissometer data, and the officers and crew of the R/V *David Starr Jordan* for their excellent support during the cruise.

6. REFERENCES

1. H.R. Gordon, "Interpretation of airborne oceanic lidar: effects of multiple scattering," *Appl. Opt.* **21**, 2996-3001 (1982).
2. O.K. Steinvall, K.R. Koppari, and U.C. Karlsson, "Airborne laser depth sounding system: system aspects and performance," in *Ocean Optics XII*, Jules S. Jaffe, Editor, Proc SPIE 2258, 392-412 (1994).
3. G.R. Fournier, D. Bonnier, and J.L. Forand, "Underwater laser imaging system with large field of view," in *Ocean Optics XII*, Jules S. Jaffe, Editor, Proc SPIE 2258, 413-421 (1994).
4. V.I. Feigels and Yu.I. Kopilevich, "Applicability of lidar remote sensing methods for vertical structure investigation of ocean optical properties distribution," in *Ocean Optics XII*, Jules S. Jaffe, Editor, Proc SPIE 2258, 449-457 (1994).
5. K.J. Voss, "A spectral model of the beam attenuation coefficient in the ocean and coastal areas," *Limnol. Oceanogr.* **37**, 501 (1992).

The Modular Optoelectronic Scanner MOS: a study of its capabilities for optically active parameter estimation
by means of an ocean colour model.

P. Cipollini¹, G. Corsini²

¹ James Rennell Division for Ocean Circulation, Southampton Oceanography Centre
European Way, Southampton SO14 3ZH, UK

Tel. +44-1703-596405 – Fax +44-1703-596400 – E-mail: cipo@soc.soton.ac.uk

² Department of Information Engineering, University of Pisa

Via Diotisalvi 2, I-56126 Pisa, Italy

Tel. +39-50-568511 – Fax +39-50-568522 – E-mail: gcorsini@iet.unipi.it

ABSTRACT

The Modular Optoelectronic Scanner (MOS) is the first spaceborne ocean colour sensor to become available after a ten-year gap and has already attracted the interest of many scientists. This paper deals with a computational study of MOS spectral capabilities by means of a reflectance model. The model, briefly recalled, has been updated with a review of the most recent results concerning the parameterization of the optically active parameter (OAP) inherent properties (absorption and backscattering coefficient). A first-order parameterization of chlorophyll fluorescence around 685 nm has also been introduced. A large number of reflectance curves are generated with the model, using different distributions of the OAP concentrations to simulate various types of waters. The reflectance curve sets are then integrated over the MOS spectral bands, and a regression analysis is performed to find the coefficients of multilinear algorithms for the parameter estimation. The results highlight the effectiveness of MOS spectral bands in attempting a separation of the optically active parameters in different waters. Nevertheless, the strong dependence of the results on the model input parameter distributions makes further studies needed in order to find robust algorithms to be applied in practice.

Keywords: Remote sensing, ocean colour, optically active parameters, reflectance model, bio-optical algorithms, MOS.

1. INTRODUCTION

Remote sensing of ocean colour allows the estimation of productivity in the oceans on a global scale, through the observation of phytoplankton pigments; in principle, optical remote sensing techniques should also permit an estimation of the coloured fraction of the dissolved organic matter ('yellow substance'), which is a very important reservoir of reduced carbon. As a consequence of these capabilities, the new generation of ocean colour sensors is regarded by the scientific community as a decisive tool for a better understanding of the mechanisms which regulate the absorption of carbon by the oceans, thus affecting the global balance of this element in the atmosphere and eventually the global climate. In addition to its intrinsic global value, such a tool turns out to be extremely useful also for coastal and regional studies, in all those cases where the biological activity and the overall water quality of a smaller area have to be assessed.

The Modular Optoelectronic Scanner^{1,2} (MOS) is the first spaceborne ocean colour sensor (now followed by the Ocean Colour and Temperature Sensor on the ADEOS satellite) since CZCS failed in 1986. Although its envisaged applications include land observation, MOS has been especially designed for the observation of the oceans, and its eight channels in the visible spectrum have been selected to gather spectral information where it is more useful for the estimation of the optically active components (OAPs) found in the water body. It is thus interesting to verify MOS potential for the separation of the three classes of OAPs³ (phytoplankton, non-chlorophyllous particles and dissolved organic matter) on the basis of their spectral signature. Additionally, it is worth studying which are the most appropriate algorithms for parameter retrieval and how they vary depending on type of water, even for coastal environments and case II waters⁴. This purpose is achieved in the present paper with a computational method involving the use of a model of ocean colour, by which it is possible to simulate realistic reflectance curves over many different types of waters. First of all, a description of some of the MOS main characteristics is given in section two. Then the methodology and the reflectance model we use for the computational study are described in section three. Section four presents some results, which are discussed in section five.

2. THE MOS INSTRUMENT

The MOS spectrometer is a multispectral imaging spectrometer operating in narrow spectral bands in the visible (VIS), near infrared (NIR) and short-wave infrared (SWIR). Two MOS instruments have been developed by the Institute for Space Sensor Tecnology at the Deutsche Forschungsanstalt für Luft- und Raumfahrt (DLR) in Berlin. The first MOS is on board the Indian Remote Sensing Satellite IRS-P3 which was launched on 21 March 1996; as of October 1996 this instrument is successfully gathering data (A. Neumann, pers. comm.), and has already entered its Cal/Val phase. The other MOS is on board the PRIRODA module which was launched on 23 April 1996 and docked with the Russian space station MIR on 26 April 1996. The main characteristics of the two MOS instruments are summarized in table I. It can be seen that the instrument itself consists of three separate spectrometers (modules), MOS-A, MOS-B and MOS-C (the latter is a line camera only present on MOS on IRS-P3), which have also separate optical systems. MOS-B is the spectrometer whose bands of 10 nm width are optimized for the observation of the oceans and coastal zones (as well as for some secondary measurements in the NIR as vegetation signature), while MOS-A is an atmospheric spectrometer with four very narrow (1.4 nm) channels in the O₂ absorption band at 760 nm, which permits the estimation of the aerosol optical depth and thus the correction of the effects of aerosol in the other channels. Figure 1 shows the MOS channels in the visible and in part of the near infrared, with a reflectance curve representative of case-1 waters superimposed.

TABLE I - Main characteristics of the MOS instrument

Optical principle	2 pushbroom imaging spectrometers: MOS-A (NIR) and MOS-B (VIS) + CCD line camera MOS-C (SWIR) on IRS-P3 only
Spectral range	MOS-A: 755 to 768 nm; MOS-B 408 to 1010 nm; + MOS-C 1500 to 1700 nm on IRS-P3 only
number of channels	17 (PRIRODA), 18 (IRS-P3) of which: 4 MOS-A, 13 MOS-B and 1 MOS-C
number of pixels per row	420 MOS-A, 384 MOS-B, 299 MOS-C
swath width	85 km (PRIRODA), 200 km (IRS-P3)
pixel size	650 m (PRIRODA), 500 m (IRS-P3)
DeltaL/L	<1% (VIS/NIR), 2% (SWIR)
Quantization	12 bit (PRIRODA), 16 bit (IRS-P3)
In-flight Calibration	internal lamps + sun calibration

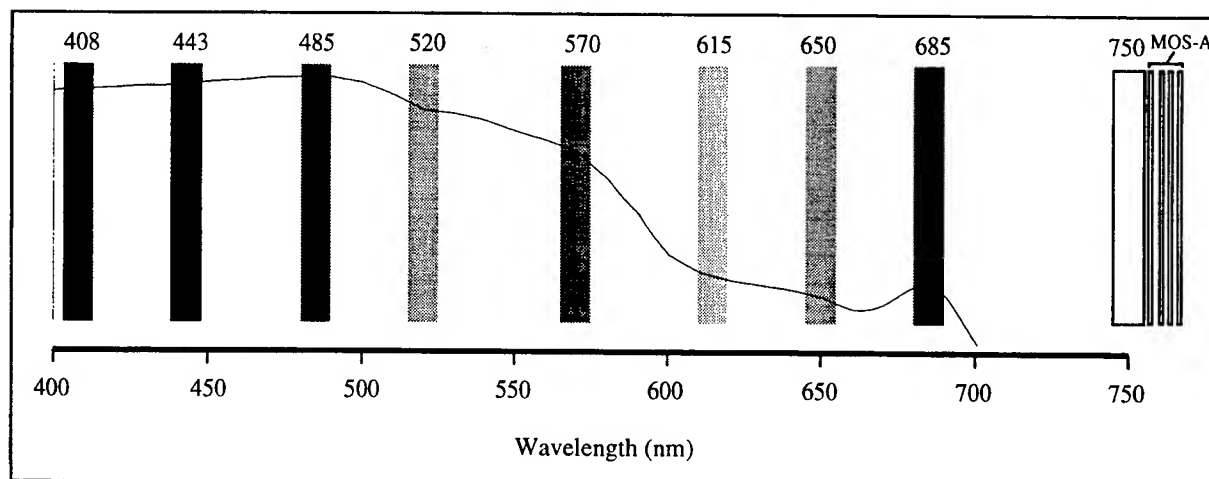


Figure 1. - MOS channels in the visible and in part of the near infrared, with a typical case-1 water reflectance curve superimposed

3. METHODOLOGY AND MODEL

The computational method adopted for the study is in three steps: first, we simulate reflectance spectra over a large number of values of the optically active parameter concentrations, using a model of ocean colour; then, the reflectance curves are integrated over the bands of the sensor. The third step is a regression analysis between the integrated reflectances and the corresponding values of the optically active parameter concentrations, which yields the algorithms for the concentration retrieval. The value of the correlation coefficient for an algorithm is a measure of the (theoretical) effectiveness of that algorithm in estimating the parameter.

The ocean colour model was originally derived from the one by Sathyendranath et al.³, and is of the general form:

$$R(\lambda) = f(C, X, Y) \quad (1)$$

where $R(\lambda)$ is the reflectance just below the sea surface⁴, C is the concentration of chlorophyll-a and phaeopigments in the phytoplankton and thus a measure of phytoplankton concentration itself (mg m^{-3}), X is the concentration of non-chlorophyllous particles expressed in terms of their backscattering coefficient at 550 nm (m^{-1}) and Y is the concentration of yellow substance expressed in terms of the absorption due to this component at 440 nm (m^{-1}). Wavelength λ goes from 400 to 700 nm in steps of 2 nm.

The reflectance is approximately proportional to the ratio of the backscattering and absorption coefficients of the water body⁴; these are then expressed as the sum of the partial contributions due to the water itself and to the three groups of optically active parameters. We have taken the absorption and backscattering of pure sea water from Smith and Baker⁵. The absorption of phytoplankton has been modeled as in a recent study by Bricaud et al.⁶ to take account of the flattening of the absorption spectra with increasing C . The absorption due to non-chlorophyllous particles has been modeled as an exponential⁷ with slope equal to -0.011 nm^{-1} and specific absorption coefficient at 440 nm equal to 0.042^3 . For yellow substance the absorption is the classical exponential with slope equal to -0.014 nm^{-1} used by Sathyendranath et al.³. As regards the backscattering by non-chlorophyllous particles, we have adopted a λ^{-1} dependence³, but with a backscattering ratio of 2% in accordance with Morel^{8,9}.

We have used the backscattering coefficient of phytoplankton to introduce into the model the phenomenon of chlorophyll fluorescence around 685 nm. On the basis of some measurements by Ahn et al.¹⁰ we have modeled that coefficient as a constant baseline plus a narrow gaussian curve peaked at 685 nm and with standard deviation of 10 nm. The amplitude of the gaussian is such that the overall peak of the coefficient is ten times the baseline. The expression for the constant baseline is¹¹:

$$b_{\text{bph-baseline}} = 0.002 \cdot 0.30 \cdot C^{0.62} \quad (2)$$

in which we assume a backscattering ratio of 0.2% for phytoplankton alone⁹. It is acknowledged that further studies are needed for an accurate reproduction of chlorophyll fluorescence in reflectance models, so our approach is just meant as a first-order parameterization.

With the model, we have generated a large number of reflectance curves extracting the input triplets at random. We have chosen a lognormal distribution¹² for C , and we have assumed a similar distribution for the other two parameters as well. We have chosen four different sets (which are shown in table II) both for the mean values μ and standard deviations σ of the parameter decimal logarithms, and for the correlation r between $\log(C)$ and $\log(X)$ and between $\log(C)$ and $\log(Y)$. The values for the sets have been chosen on the basis of an analysis of the CZCS global composite pigment map histogram¹³, except set 4 (Lognorm_2) which is somewhat arbitrary. The sets are representative of open 'case-1' ocean (set 1), upwelling areas (2), case1+case2 (most general case) (3) and turbid case2 waters (4). Figure 2 gives an example of some reflectance curves obtained from the model with the set of distributions Lognorm_1_2 (set 3)

TABLE II - Distribution sets used for the computational study

statistics	set 1 Lognorm_OPEN	set 2 Lognorm_UPW	set 3 Lognorm_1_2	set 4 Lognorm_2
$\mu_{\log C}, \sigma_{\log C}$	-0.86, 0.3	-0.04, 0.35	-0.83, 0.45	0.0, 0.5
$\mu_{\log X}, \sigma_{\log X}$	-1.21, 0.3	-0.98, 0.35	-0.57, 0.45	0.0, 0.5
$\mu_{\log Y}, \sigma_{\log Y}$	-1.75, 0.3	-1.52, 0.35	-1.05, 0.45	-0.5, 0.5
$r_{\log C \log X}, r_{\log C \log Y}$	0.8, 0.8	0.8, 0.8	0.8, 0.8	0.5, 0.5

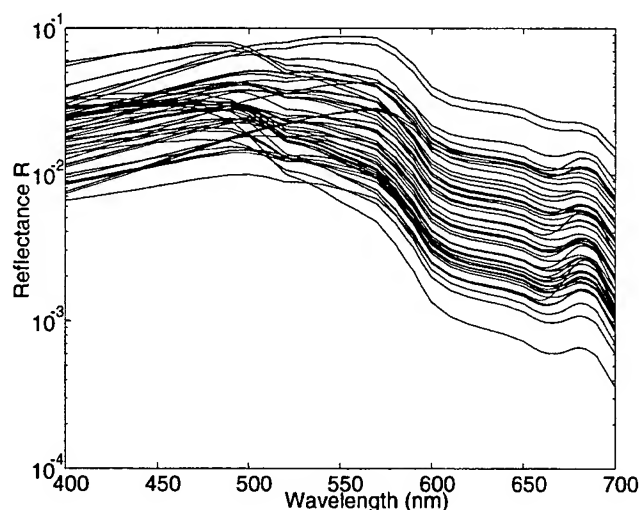


Fig. 2 - Example of reflectance curves generated by the model with the distribution set Lognorm_1_2, corresponding to a general case1 + case2 water type

4. BIO-OPTICAL ALGORITHMS

For each one of the distribution sets in table II, we have simulated 5000 reflectance curves, which have then been integrated over the eight MOS bands in the visible. After that, the form of the algorithms has to be selected in order to be able to perform the regression analysis.

The most general form of the algorithms which we have considered is the multilinear one:

$$\log(OAP) = a_0 + \sum a_i \log(R_i) \quad (3)$$

where OAP indicates one of the optically active parameters, R_i is the reflectance in the i -th band of the sensor and \log is the decimal logarithm. The common reflectance ratio algorithms are also encompassed by the above equation, however it seems interesting to see what happens if we try to use the full spectral information given by the sensor, apart from radiometric considerations (i.e. the signal to noise ratio in some spectral bands can be low and prevent the use of those bands in a practical case) and considerations on sensitivity (i.e. such multilinear algorithms can be very strongly dependent on the particular distribution used).

The results for MOS and for the four different sets of concentration distributions are presented in figure 3. The extremely close to unity values for the correlation coefficient r between the logarithms demonstrate the (theoretical) spectral effectiveness of the instrument. The only case in which such an hyperspectral analysis gives a significantly lower value of r is the retrieval of $\log C$ in the case2 study (set Lognorm_2). From the plots in figure 3 it is clear that the coefficients are highly sensitive with respect to the particular distributions used. This fact and the above mentioned constraints on signal to noise ratio make further studies necessary to find robust algorithms to be used in a practical case. Anyway, the observation of how the coefficients change can already give some suggestions on which bands are the most useful in view of the operational algorithms. For the estimation of non-chlorophyllous particles, for instance, it seems a good idea to try to use the spectral information in nearly all the bands, given the regular behaviour of the coefficients (alternatively positive and negative). The high values of r , and the low variability of the a_0 coefficient for this parameter, indicate that non-chlorophyllous particles are the easiest parameter to estimate in a completely general case. This is in agreement with the findings by Sathyendranath et al.³. Conversely, for phytoplankton the trend of the coefficients would suggest the use of spectral information in the blue and blue-green region, and particularly the use of band 2 to band 3 ratio in a simpler algorithm. The results for yellow substance are not so clear, and show high values of the coefficients in the red channels, where the spectral signature of this component is weaker instead. All the results, however, reinforce the well known concept³ that specialized regional (and seasonal) algorithms, selected for each particular application, perform much better than global algorithms. Detailed studies of the variability of the coefficients will be the object of a future paper.

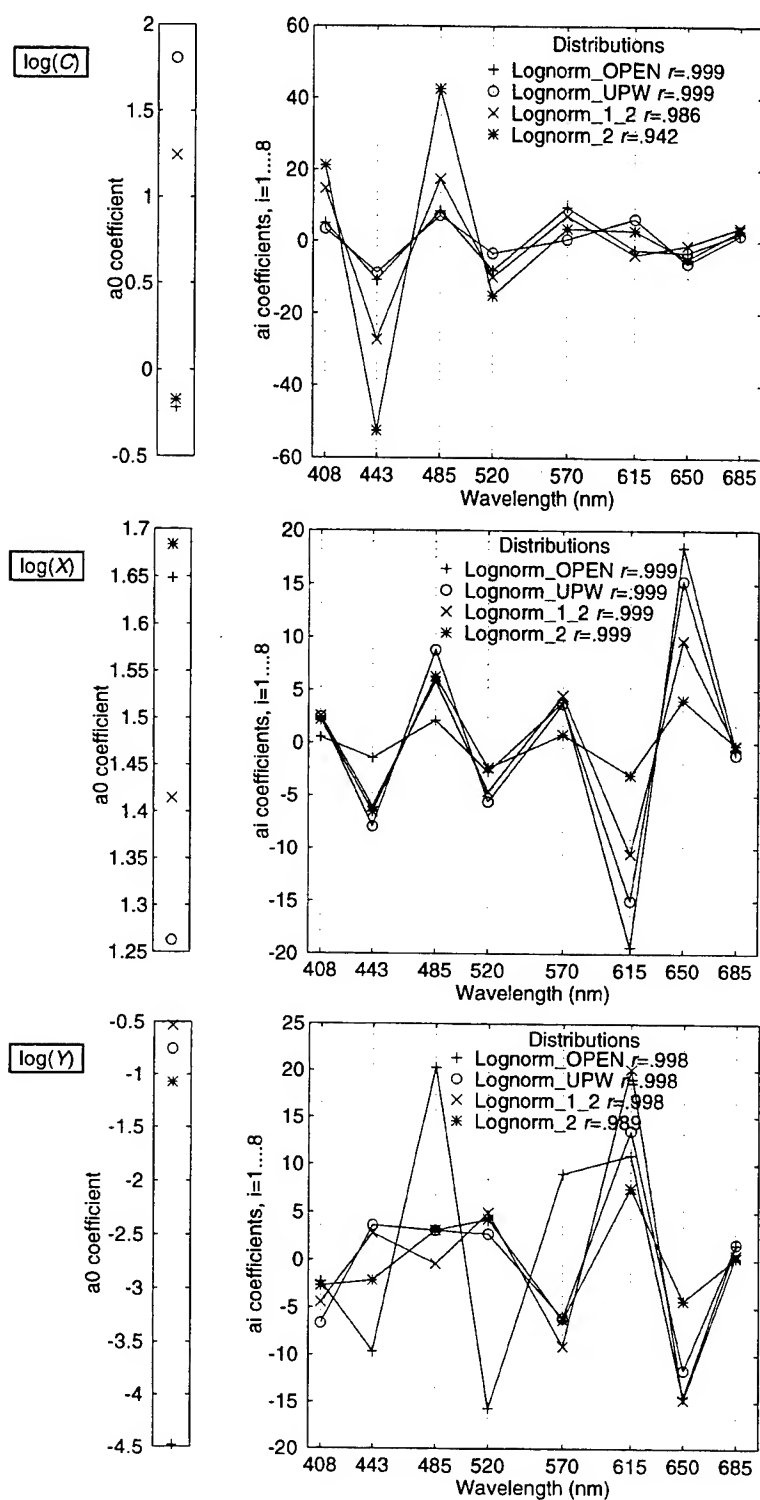


Figure 3 Plot of the coefficients in the multilinear algorithms for $\log(C)$ (upper panel), $\log(X)$ (middle panel), $\log(Y)$ (lower panel), for the different distributions used in the work. Each legend reports also the corresponding values of the correlation coefficient r between the logarithm of the optically active parameter and the linear combination of $\log(R_i)$, for each one of the distribution sets used

5. DISCUSSION AND CONCLUSIONS

The approach we have used permits an evaluation of the sensor spectral performance on the basis of its spectral response alone, once we are confident that the model used produces realistic reflectance curves.

From the results we can assess the theoretical capability of MOS channels to recover enough spectral information for a separate estimation of the concentration of the three optically active parameter groups. Some problems are still present for the estimation of phytoplankton in very turbid case2 waters.

All the algorithms found are very sensitive to changes in the distributions of the model input parameters, although some common features can be spotted in the coefficients. As a consequence, the algorithms presented are just meant as an indication of the instrument spectral capability. Further studies are needed to find a set of robust regional algorithms (using a subset of the spectral bands and taking account of all the radiometric considerations) which can be applied in practice (these studies will be carried out in the Cal/Val phase within a SOC/DLR co-operation). Nevertheless, from the results presented in this work MOS appears to be a very promising instrument.

6. ACKNOWLEDGEMENTS

The authors thank Andreas Neumann of DLR for providing useful information about such an interesting instrument, the first one after a ten-year gap in ocean colour sensors. Paolo Cipollini is funded by the Commission of the European Communities through a Research Training Fellowship (HCM contract no. ERBCHBGCT930440). Giovanni Corsini is funded in the framework of the OMEGA Project (MAST-III Project no. MAS3CT950001)

7. REFERENCES

1. G. Zimmermann et al. "MOS-PRIRODA - An imaging spectrometer for ocean remote sensing," *Proc. SPIE*, vol. 1937, pp. 201-206, 1993.
2. A. Neumann, "Spaceborne imaging spectrometers for ocean colour remote sensing: MOS-PRIRODA and MOS-IRS," *NASA Multisensor Ocean Colour Workshop*, February 1995.
3. S. Sathyendranath, L. Prieur and A. Morel, "A three-component model of ocean colour and its application to remote sensing of phytoplankton pigments in coastal waters," *Int. J. Rem. Sens.*, **10**(8), 1373-1394, 1989.
4. A. Morel and L. Prieur, "Analysis of variations in ocean colour," *Limn. Oceanogr.*, **22**(4), 709-722, 1977.
5. R. C. Smith, and K. S. Baker, "Optical properties of the clearest natural waters," *Appl. Opt.*, **20**(2), 177-184, 1981.
6. A. Bricaud, M. Babin, A. Morel and H. Claustre, "Variability in the chlorophyll-specific absorption coefficients of natural phytoplankton: Analysis and parameterization," *J. Geophys. Res.*, **100**(C7), 13321-13332, 1995.
7. C. S. Roesler, M. J. Perry and K. L. Carder, "Modeling in situ phytoplankton absorption from total absorption spectra in productive inland marine waters," *Limn. Oceanogr.*, **34**(8), 1510-1523, 1989.
8. A. Morel, "Diffusion de la lumière par les eaux de mer, résultats expérimentaux et approche théorique," in *Optics of the Sea, AGARD Lect. Ser.*, vol. 61, pp. 3.1.01-3.1.76, Advisory Group for Aeronautical Research and Development, NATO, Brussels, 1973.
9. A. Morel, "Optical modeling of the upper ocean in relation to its biogenous matter content (case I waters)," *J. Geophys. Res.*, **93**(C9), 10749-10768, 1988.
10. Y.-H. Ahn, A. Bricaud and A. Morel, "Light backscattering efficiency and related properties of some phytoplankters," *Deep-Sea Res.*, **39**(11/12), 1835-1855, 1992.
11. H. R. Gordon and A. Morel, "Remote assessment of ocean colour for interpretation of satellite visible imagery, a review," in *Lecture notes on Coastal and Estuarine Studies*, 114 p., Springer-Verlag, New York, 1983.
12. J. W. Campbell, "The lognormal distribution as a model for bio-optical variability in the sea," *J. Geophys. Res.*, **100**(C7), 13237-13254, 1995.
13. P. Cipollini, "Valutazione delle prestazioni di sensori per il telerilevamento del mare mediante un modello di riflettanza," (Evaluation of performances of ocean colour sensors by means of a reflectance model), Ph.D. thesis (in Italian), 131 pp., University of Pisa, Italy, 1996.

Remote sensing of a pigment patch in the southeastern Bering Sea

Richard F. Davis, Gordana Lazin, Jasmine Bartlett, and Áurea Ciotti

Center for Environmental Observation Technology and Research
Department of Oceanography, Dalhousie University
Halifax, Nova Scotia, Canada B3H 4J1

Phyllis Staben

National Oceanic and Atmospheric Administration
Pacific Marine Environmental Laboratory
7600 Sand Point Way NE, Seattle, WA 98115-0070

ABSTRACT

As a component of a NOAA program studying lower trophic level dynamics in the southeastern Bering Sea, 7 flights were performed in a NOAA P3 aircraft over the southeastern Bering Sea during April and May, 1996, collecting ocean color data with a multichannel radiometer. A research vessel operating on the Bering Sea shelf found a patch of increased chlorophyll concentration at approximately 56° N, 166° W. The increased chlorophyll concentration was clearly noticeable during subsequent overflights, both visually and in the real-time radiometer data. One flight was dedicated to delineating patch size. By then the patch had grown to be approximately 100 by 200 km in size, oriented roughly NW-SE, just southeast of the Pribilof Islands, tracking SE to NW. On April 28 96 the patch edge passed over a bio-physical mooring equipped with in situ spectral absorption meters and fluorometers. Estimates of pigment concentration at this mooring, increased 12 fold in 6 hours with the passage of the feature. A drifter monitoring ocean color released near the mooring also detected the patch.

Keywords: remote sensing, Bering Sea, moorings, drifters

1. INTRODUCTION

A particular strength of optical instruments is their ability to collect data from remote regions, such as the southeastern Bering Sea. The Bering Sea is not always a friendly or cost effective place to visit. However, it is home to the world's largest single-species fishery, making it economically important. For this reason, NOAA funds the Fisheries Oceanography Coordinated Investigations (FOCI) to study lower trophic level dynamics in the region. FOCI has deployed moorings equipped with optical instruments in the southeastern Bering Sea since 1993. Time series of bio-physical data indicate that the greatest source of variability in phytoplankton biomass is advection past the moorings and not local production¹. During the 1996 field year we made a concerted effort to gain some insight into the spatial scales of variability of phytoplankton biomass. Toward this end, we complemented the usual mooring deployments with overflights by a NOAA P3 aircraft ("Miss Piggy") carrying a spectral radiometer, and we also deployed ocean color monitoring (OCM) drifters from a NOAA research vessel (R/V Miller Freeman) close to the moorings. One interesting feature elucidated by all of the optical instruments involved in this study was a large patch of water containing high pigment concentration that translated from southeast to northwest past one of the moorings.

2. INSTRUMENTATION AND METHODS

2.1 Aircraft

The NOAA P3 carried a Satlantic, Inc., SeaWiFS Aircraft Simulator (SAS-II) multichannel radiometer. The SAS-II measured both downwelling irradiance ($Ed(\lambda)$) and upwelling radiance ($Lu(\lambda)$) in 7 channels (412, 443, 490, 555, 670, 683, and 780 nm; 10 nm FWHM). Data were collected at a rate of 10 Hz and then averaged over 1 s, which, at a typical speed of 370 km hr⁻¹, represented approximately 100 m. Nominal field of view for the radiance sensors was 3.3°. At the standard flight altitude of 300 m this gave a footprint of ~18 x 100 m. The plane also carried a large suite of meteorological instruments whose values were recorded every second.

Radiances measured by the airborne radiometer ($Lu(\lambda)$) were converted into water-leaving radiances ($Lw(\lambda)$) using the method of Lazin *et al.*² with one modification. The conversion of $Lu(\lambda)$ into $Lw(\lambda)$ is dependent on the amount of sea-surface reflected sky light. Instead of assuming a ratio of diffuse (i.e., sky light) to global irradiance ($R_{diff} = E_{sky}/E_{gl}$) based on the ambient cloud cover, we used the National Solar Radiation Data Base³ (NSRDB) for Kodiak, AK, to develop an empirical relationship between R_{diff} and the ratio of E_{gl} at all sky covers (SC) to E_{gl} for clear skies ($R_{gl} = E_{gl}(SC)/E_{gl}(0)$). It should be noted that Kodiak is not one of the NSRDB primary stations, so irradiance values are from models based on meteorological observations and statistical relationships for the region.

We sorted all of the daytime data ($n=130117$) by zenith angle. Mean clear-sky global irradiance ($E_{gl}(0)$) for 1° zenith angle bins was produced by averaging all global irradiance values within that bin when SC was equal to 0. E_{gl} was divided by the appropriate $E_{gl}(0)$ for that zenith angle to produce R_{gl} . R_{diff} is simply the ratio of diffuse irradiance to total irradiance. We then averaged R_{gl} and R_{diff} into 1° zenith angle bins and 1 tenth sky cover bins. The results of regressing the mean R_{diff} against the mean R_{gl} is shown in Figure 1. The slope of the line is -1.35 ± 0.02 and the intercept is 1.53 ± 0.02 .

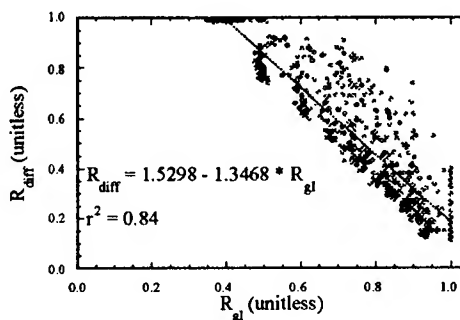


Figure 1. Results of linear regression of the ratio of global irradiance to the corresponding clear-sky global irradiance versus the ratio of diffuse to global irradiance. Each point represents the mean of all data points falling into a 1° zenith angle bin and 1 tenth sky cover bin.

The SAS-II measured global irradiance ($Ed(\lambda)$). In order to generate the clear-sky irradiance, we ran the spectral irradiance model of Bird and Riordan⁴ at 5 minute intervals, using meteorological parameters measured aboard the aircraft to produce clear-sky spectral irradiance ($E_{mod}(\lambda)$). Dividing measured $Ed(\lambda)$ by $E_{mod}(\lambda)$ and then using that ratio in the regression gave us an estimate of R_{diff} . We then multiplied R_{diff} by $Ed(\lambda)$ to obtain an estimate of the diffuse skylight at one second intervals.

The estimated water leaving radiances were converted into estimates of pigment concentration using a relationship similar to that published by Mitchell⁵:

$$\log_{10}[\text{chl } a + \text{pheo}] = 0.446 - 1.86 * Lu(488)/Lw(560). \quad (1)$$

In our case, the wavelengths are 490 and 555 nm, and we used water leaving radiances, not in-water radiances, so, combined with natural variability in the relationship between radiance ratios and pigment concentrations, the pigment estimates reported should be treated as approximate. However, trends in the data should not be affected.

2.2 Mooring

Mooring 2 was at $56^\circ 52'N$, $164^\circ 03'W$, mooring 3 at $56^\circ 04'N$, $166^\circ 14'W$. The moorings were instrumented with WetLabs *in situ* spectral absorption meters (a-3) and non-spectral miniature fluorometers. The a-3 measures absorption at 650, 676, and 710 nm⁶. Absorption data collected hourly from the a-3 were converted into pigment concentrations according to Davis *et al.*¹. The fluorometers recorded voltages every 15 min. The fluorometers were calibrated in the lab using 2 different species of phytoplankton (*Isochrysis galbana* and *Thalassiosira weissflogii*) at 2 different temperatures (22° and 2° C). A subsample of the culture was cycled through the fluorometer using a SeaBird pump and voltages recorded. Prolonged pumping did not significantly change fluorescence readings. The subsample was serially diluted and voltages recorded until the fluorometer could no longer register a change in the pigment concentration. Voltage was regressed against chlorophyll concentration to obtain a calibration factor. It is important to note that the calibration factor changed both as a function of species and temperature, with species having the greatest variability. For example, one fluorometer had a calibration factor for *I. galbana* at 22° of 13.4 and at 2° of 16.0. For *T. weissflogii* the same fluorometer had calibration factors of 22.4 and 18.9, respectively. The room temperature calibration factor is different by 40% between the 2 species. Also note that the direction of change in the calibration factor with change in temperature is different for the 2 species. While

fluorometers are very sensitive and relatively inexpensive, attempts to convert their output into pigment estimates must be made with care. For this extended abstract, an average calibration factor is used to keep all reported values in the same units.

2.3 Drifter

The OCM drifter was a WOCE-type drifter manufactured by MetOcean and drogued at 25 m. Besides position and time, it measured $Ed(\lambda)$ in 1 channel (490 nm; 10 nm FWHM) and $Lu(\lambda)$ in 7 channels (412, 443, 490, 510, 555, 670, and 683 nm; 10 nm FWHM). It also recorded sea-surface temperature. The drifter collected data at a rate of 40 samples per hour and transmitted hourly averages to the ARGOS satellite every 90 s.

The radiance sensors on the OCM drifter are ~45 cm beneath the sea-surface. We used published attenuation coefficients for clean water⁷ and for varying chlorophyll concentrations⁸ to propagate the radiances to the sea-surface. Chlorophyll estimates came from the moorings. As expected, this exercise changed the radiance values very little. Radiances were then transmitted across the air-sea interface using the value of 0.544⁹.

Emergent radiances estimated from the OCM drifter data were converted into estimates of pigment concentration by the relationship of D.K. Clark reported in Müller-Karger et al¹⁰:

$$[\text{chl } a + \text{pheo}] = 5.56 * ((Lw(\lambda_1) + Lw(\lambda_2))/Lw(\lambda_3))^{-2.252}, \quad (2)$$

where $\lambda_1 = 443$, $\lambda_2 = 510$, and $\lambda_3 = 555$ nm. Again, pigment estimates should only be considered as approximate.

3. RESULTS AND DISCUSSION

A patch of water with relatively high pigment concentration was discovered on 25 Apr 96 (day 116) by researchers aboard the Miller Freeman at 56° 03'N, 166° 20'W. They radioed the aircraft with the SAS aboard and directed it to fly over. At that time surface chlorophyll from discrete samples was 4.3 mg m⁻³, while surrounding waters had chlorophyll concentrations less than 1 mg m⁻³. Pigment concentration estimated from the SAS was ~2.9 mg m⁻³ in the patch and ~1.4 mg m⁻³ for surrounding waters.

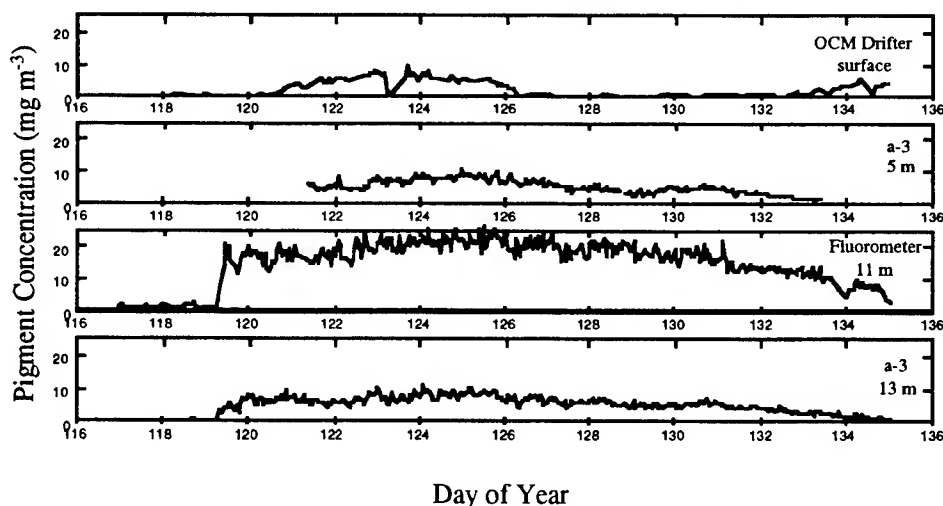


Figure 2. Time series of data from various optical platforms deployed in the southeastern Bering Sea. The fluorometer data has been hourly averaged. The upper panel shows drifter data. The other panels from optical instruments at mooring 3.

A few hours after the overflight an OCM drifter was released next to mooring 3. Initial pigment estimates from radiance ratios were consistent with values measured from the ship (0.39 mg m⁻³ vs 0.48 mg m⁻³, respectively). The

drifter initially moved northwest for ~14 days, then moved inshore and reversed direction. By 50 days later it had returned to very close to its starting position. On 9 May 96 (day 130), the date of the patch delineation flight, it was ~50km away from the mooring, still outside the patch but starting its southward journey.

By 9 May 96 (day 130) the patch had translated northwest ~75 km (~5 km d⁻¹ or 6 cm s⁻¹), passing over mooring 3 (Figure 2). The size of the patch was estimated to be approximately 200 km by 100 km. Its speed and direction were consistent with mean water flow on the outer Bering Sea shelf¹¹. The 11 m fluorometer and 13 m a-3 clearly showed the edge of the patch passing over the mooring on day 119. Pigment estimates from the 11 m fluorometer increased 12 fold in 6 hours. The drifter moved south and intercepted the patch on day 120.

4. CONCLUSIONS

- A suite of optical instruments measuring a range of bio-optical parameters (*in situ* absorption, fluorescence, subsurface radiance and emergent radiance) all detected a patch of water containing high concentrations of pigments.
- Not only did they detect the patch, but, except for the fluorometer, they also returned estimates of pigment concentration within about 30% of each other. Given what is known about the physiology of phytoplankton fluorescence, its lack of agreement is not too surprising. Still, trends are clear in all of the data.
- Autonomous optical instruments can provide reasonable estimates of pigment concentration in regions of the ocean that are logistically difficult to access.

5. ACKNOWLEDGMENTS

We would like to thank N. Bond for cheerfully coordinating the aircraft logistics, C. DeWitt, D. Dougherty, and B. Parker for mooring deployment/recovery, and the crews of Miss Piggy and the Miller Freeman for their hard work and support. This work was supported by NOAA contract 40ABNR600758 to RFD, and NSRC Research Partnerships. AMC was also supported by CNPq (Brazil). CEOTR publication no. 6.

6. REFERENCES

1. R.F. Davis, C.C. Moore, J.R.V. Zaneveld, and J.M. Napp, "Reducing the effects of fouling on chlorophyll estimates derived from long-term deployments of optical instruments," *J. Geophys. Res.*, accepted (1996).
2. G. Lazin, R.F. Davis, A.M. Ciotti, and M.R. Lewis, "Ocean color measurements from low flying aircraft: Atmospheric and surface glint correction," *Ocean Optics XIII, Proc. Soc. Photo-Opt. Instrum. Eng.* this volume.
3. National Renewal Energy Laboratory, "User's Manual: National Solar Radiation Data Base (1961-1990), Version 1.0", National Climatic Data Center (1992).
4. R.E. Bird and C. Riordan, "Simple solar spectral model for direct and diffuse irradiance on horizontal and tilted planes at the earth's surface for cloudless atmospheres," *J. Clim. Appl. Met.* **25**, 87-97 (1986).
5. B.G. Mitchell, "Predictive bio-optical relationships for polar oceans and marginal ice zones," *J. Mar. Sys.* **3**, 91-105 (1992).
6. J.R.V. Zaneveld, R. Bartz, and J.C. Kitchen, "Reflective-tube absorption meter.," *Ocean Optics X, Proc. Soc. Photo-Opt. Instrum. Eng.* **1302**, 124-136 (1990).
7. R.C. Smith and K.S. Baker, "Optical properties of the clearest natural waters (200-800 nm)," *Appl. Opt.* **20**(2), 177-184 (1981).
8. A. Morel, "Optical modeling of the upper ocean in relation to its biogenous matter content (Case I waters)," *J. Geophys. Res.* **93**, 10749-10768 (1988).
9. R.W. Austin, "Gulf of Mexico, ocean-color surface-truth measurements," *Boundary-layer Meteorol.* **18**, 269-285 (1980).
10. F.E. Müller-Karger, C.R. McClain, R.N. Sambrotto, and G.C. Ray, "A comparison of ship and coastal zone color scanner mapped distribution of phytoplankton in the southeastern Bering Sea," *J. Geophys. Res.* **95**(C7), 11483-11499 (1990).
11. L.K. Coachman, "Circulation, water masses, and fluxes on the southeastern Bering Sea shelf," *Cont. Shelf Res.* **5**, 23-108 (1986).

An instrument for underwater high angular resolution volume scattering function measurements*

Paul W. Dueweke, Jay L. Bolstad, Donald A. Leonard, Harold E. Sweeney
EOO, Inc., 269 N. Mathilda Ave., Sunnyvale, CA 94086

Philip A. Boyer, Erik M. Winkler
Global Associates, Ltd., 7600 Leesburg Pike, Falls Church, VA 22043

ABSTRACT

A prototype instrument for *in situ* measurements of the volume scattering function (VSF) and the beam attenuation of water has been built and tested in the EOO laboratory. The intended application of the instrument is the enhancement of Navy operational optical systems for finding and imaging underwater objects such as mines. A description of the apparatus that was built and preliminary laboratory data will be presented. The instrument measures the VSF, $\beta(\theta)$, near the optical axis in both the forward and back directions from $\sim 0.2^\circ$ off axis to $\sim 5^\circ$ in 0.1° steps and at side angles of 45° , 90° , and 135° . A diode-pumped, frequency-doubled, Nd:YAG laser provides the 532 nm light. This is the most used wavelength for underwater optical systems. The forward and back scattered light is collected and focused to a plane where scattering angles in the water are mapped onto concentric rings. At this focal plane, a conical reflector compresses the annular optical data onto a line along the cone axis where it is read by a MOS linear image array providing over 500 separate angular measurements. The beam attenuation coefficient, c , is also measured by means of a unique dual path configuration.

Key Words: polar nephelometer, scattering coefficient, volume scattering function, beam attenuation coefficient, underwater scattering, forward scattering, back scattering, linear array, optical compression, ocean water optical properties

1. OBJECTIVE

The overall objective of our work is to develop an instrument for *in situ* measurement of the VSF (β) and the beam attenuation coefficient (c) in a wide variety of ocean water types. The conceptual design of such an instrument may at first appear straightforward, however engineering the capability of *in situ* determination of β and c can be quite difficult, as the recent survey by Mobley¹ indicates. Only a few one-of-kind instruments have been built for *in situ* measurement, and field measurement of β and c are not routinely made, especially by Navy operational personnel.

2. DESIGN OBJECTIVES AND SPECIFICATION

The instrument measures β vs. scattering angle over a small range of forward scatter (FS) angles near 0° and back scatter (BS) angles near 180° and at three discrete angles in between. In addition, it measures c for two different path lengths in the same water so that window degradation can be monitored and corrected for. The specification is presented in Table 1.

Function	measurement of VSF (β) and beam attenuation coefficient (c)
Dynamic Range	β : 10^{-4} to $10^4 \text{ m}^{-1} \text{sr}^{-1}$ c : 0.05 to 2 m^{-1}
β Angular Measurements	0.1° to 5° in 0.1° increments 175.0° to 179.9° in 0.1° increments 45° , 90° , and 135° each over $\pm 5^\circ$ range
Wavelength	532 nm
Integration Time	≥ 0.1 sec
Depth	surface to 200 m
Calibration	double path continuous

Table 1: Nephelometer System Specification

* Sponsored by NAVSEA under contract number N00024-95-C-4045.

3. APPROACH

3.1 Forward and Back Scatter

The beam from a 5 mW, CW, diode-pumped, frequency-doubled, Nd:YAG laser is used to illuminate two separate columns of the subject water as shown in the schematic overview of Figure 1. Along the longer water column, a lens collects the light scattered backward toward the laser. This light is focused to the focal plane of the lens. At this plane, the lens is operating as a perfect angle-to-position transducer. Thus any radius from the optical axis at the lens focus maps back to a unique angle emitted from the water column.

The nephelometer focuses the lens on an object at infinity as shown in Figure 2. Each bundle of rays at the same angle comprises a parallel beam and has an object at infinity. The image of each of these parallel bundles is an annular ring in the focal plane of the lens. Thus radii in the image plane map to angles incident on the lens. Figure 3 shows four light rays coming from a cylindrical scattering volume at a single scattering angle but at four widely different azimuth angles, one in each quadrant. All four of the rays fall on the same radius in the focal plane, however the quadrant into which each was emitted is preserved.

The same thing is happening along the shorter water column, but the lens there collects the light scattered in the forward direction. Likewise, those forward scattering angles are mapped on to radii at the focal plane of that lens. For example, any light scattered at an angle of one degree will be brought to focus in a single ring around the unscattered central disk. Any light scattered at two degrees will form another concentric ring outside the first one, and so on. Thus the distance from the center of the image is directly proportional to the scattering angle, and the total power falling in that annular ring is proportional to the scattering coefficient for that angle. Forward and back scattering at angles down to a fraction of a degree from the axis and out to several degrees can be measured with this technique.

Having produced such an angular dependent image, the straightforward approach would be to detect the image with a CCD 2-D image array, partition the million or so pixels into concentric rings, and thereby determine scattered light optical power vs. scattering angle. This was the original detection concept of the nephelometer. Although this is feasible, there are some severe problems associated with the software to do the partitioning, the timing to transform the square grid pattern into concentric rings, the long readout time of such an array, and test and evaluation of a device that is totally dependent on software for troubleshooting.

We chose to instead compress each of the concentric rings onto a point by means of a reflecting, internal, 45° cone². Points along the axis of the cone map to concentric rings in the plane normal to the axis and through the apex of the cone as shown in Figure 4. We placed a CMOS linear array along this axis and were able to read out scattering intensity vs. angle simply by measuring signal output vs. linear array pixel. Using a half cone with a linear array along the optical axis throws away half of the scattered light, but signal is not a limiting characteristic of this design. Figure 5 illustrates the transformation of angle to point-on-a-line. The vertical dashed line is the virtual focus where the annular rings analogous to those in Figure 3 would form if the light were not intercepted by the half cone and focused on the linear array. The half cone is essentially an optical condenser placed in front of the focus to condense an areal image into a linear image.

We digitized each array output 100 times per second in synch with the 50 Hz laser pulse repetition frequency. Fifty of the digitized array data sets (every other set) represented the scattering levels with the laser ON. Alternating fifty data sets represented the optical background with the laser OFF. The ON data was summed pixel by pixel for, say, one second of data. The OFF data was similarly summed. The ON data set minus the OFF data set represents the scattering vs. angle (i.e., the VSF) for a one second period.

This was done for both the forward and the back scatter directions. Forward scatter data was measured between approximately 0° and 5° and summed at 0.1° increments. Back scatter data was measured between approximately 180° and 177° and summed at 0.1° increments.

3.2 Side Scatter

A similar technique was used to measure scattering at large angles, however choosing just three angles and not having to resolve small angular differences around those angles made the problem much easier. An aspheric lens whose axis was oriented at the desired scattering angle with a detector at the focus of the lens would collect scattered light in a narrow cone of ± 2 or 3 degrees. We chose to do this at 45°, 90°, and 135° with respect to the incident beam direction (calling that 0°). We perform this side scattering measurement along the longer backscatter water column because the beam intensity there is greater, the length of the column that could be collected by each lens is longer, and geometric constraints are reduced. The space between each collecting lens and the water was filled with glass to reduce interface problems of passing light from a high index volume to air at large angles of incidence.

3.3 Beam Attenuation Coefficient

The beam attenuation coefficient, c , can be determined simply by measuring the intensity of the laser beam incident into the water and ratioing it to the intensity of the laser beam after it traverses the water and has experienced attenuation. Portions of the illuminating beams which transmit through either the forward or back scatter volume without being scattered or absorbed are focused into fiber optic bundles which transmit the light to a pair of detectors. In the same way, portions of the incident beams are transmitted by a second pair of fiber optic bundles to the same pair of detectors where they are appropriately time multiplexed and ratioed to determine the beam attenuation coefficients.

The reason for the two beams is to minimize the effect of dirty windows to the extent that window fouling is the same for both paths. Let the ratio of the signals from each path be given by $I/I(0) = W \exp(-cL)$ where I is the intensity after traversing the path, $I(0)$ is the initial intensity, W is the window loss, c is the beam attenuation coefficient and L is the path length. An equation is thus obtained for each optical path which can be solved simultaneously to eliminate W and obtain c .

3.3 Computer and Data Acquisition

The laser is pulsed at 50 Hz with a 50% duty cycle. Thus each laser ON and OFF time is 10 msec long. A two-channel, 18-slot chopper wheel multiplexes the beam attenuation coefficient data and is the master timer for the laser pulses, the linear array readout, and other data readout. All data is digitized and processed by an on line PC.

The sequence starts with a chopper timing pulse which commands the laser ON. Near the end of the laser ON period, the forward scatter array is read out and then the back scatter array is read. The beam attenuation and the side scatter data is read at the end of each linear array readout. Then the chopper commands the laser OFF, and the above sequence repeats to measure the background levels.

Every desired time resolution period (e.g., one second), the array fields are summed and processed with the appropriate signal and angle calibration coefficients to calculate the VSF and the beam attenuation coefficient. Figure 6 is a photograph of the entire polar nephelometer except for the computer.

4. DATA

Preliminary data, without absolute calibration, has been obtained for the VSF and the beam attenuation sensors.

4.1 Volume Scattering Function

Using bottled "distilled" water, data was obtained in the laboratory simultaneously with both the forward scatter and back scatter optical compression cone receivers. Relative angular calibration was achieved for both receivers by means of insertion of opal glass plates in the beam. No absolute calibration has yet been attempted. The data is shown in Figure 7 overlain on the published data of Petzold³ and in detail in Figures 8 and 9. The laboratory points were normalized to the Petzold data at 3 degrees for "off shore" California water.

Reasonably good qualitative agreement with Petzold is noted for the forward scatter. Our forward scatter data is limited to angles of 1 degree or greater because of inadequate spatial filtering in the forward scatter receiver of the 2 milliradian laser beam. In the future we will incorporate a spatial filter to enable forward scatter measurements much closer to 2 milliradians.

The backscatter data shows a steeper slope than other published available data such as the open circle data in Figure 9 from Maffione and Honey⁴. The reason for this difference will be investigated. Absolute calibration between the forward scatter and back scatter receivers is also planned for future work.

4.2 Beam Attenuation Coefficient

The sensitivity of the instrument to determine the beam attenuation has been tested by the insertion of a glass plate in the laser beam in the water. The Fresnel loss due to the mismatch of the index of refraction of glass relative to water produces a loss of $\approx 1\%$, or an equivalent extinction of 0.05 m^{-1} . This has been measured with the instrument and a standard deviation of approximately 10% or $\pm 0.005 \text{ m}^{-1}$ was obtained.

5. REFERENCES

1. C. D. Mobley, "Light and Water, Radiative Transfer in Natural Waters," Academic Press, p. 100, 1994.
2. J. Wu, J. Wang and P. Hays, "Performance of a circle-to-line optical system for a Fabry-Perot interferometer: a laboratory study," *Applied Optics*, **33**, 7823 (1994).
3. T. J. Petzold, "Volume Scattering Function for Selected Ocean Water," Scripps Institution of Oceanography Report 72-78, October 1972.
4. R. A. Maffione and R. C. Honey, "Instrument for measuring the volume scattering function in the backward direction," *SPIE Vol. 1750 Ocean Optics XI*, p 15 (1992)

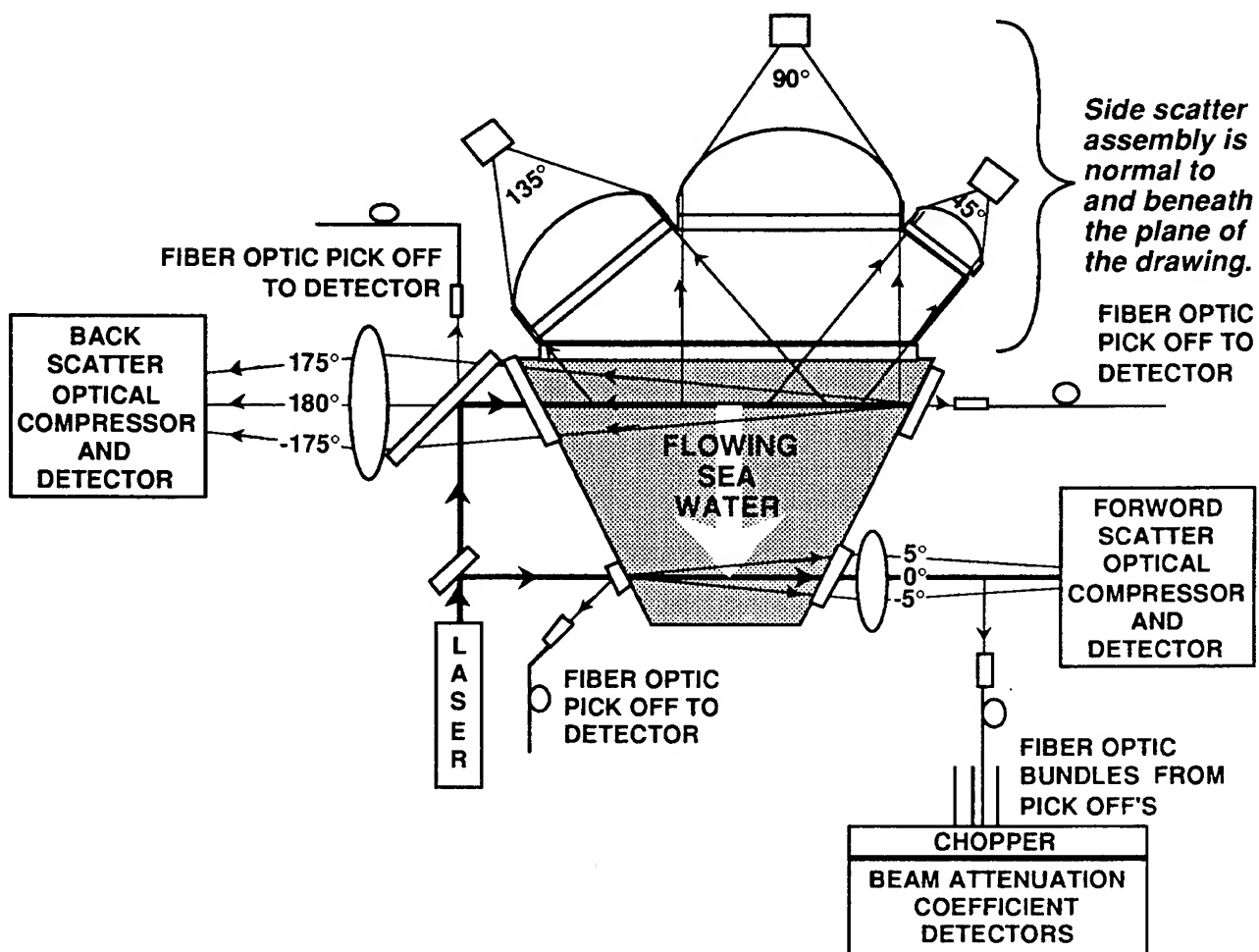


Figure 1: Schematic Overview of Polar Nephelometer

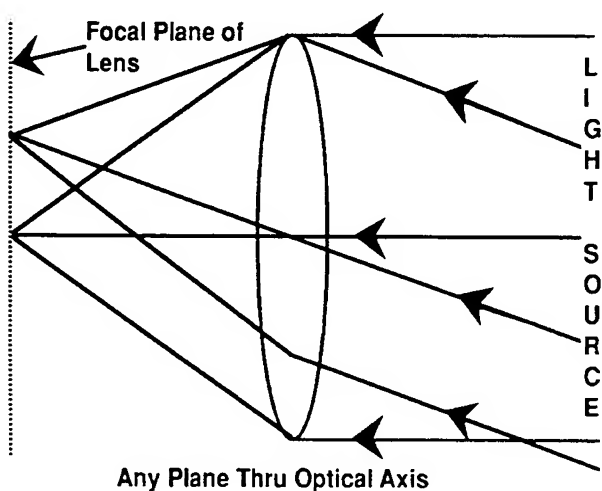


Figure 2: Lens Transforms Angles to Positions

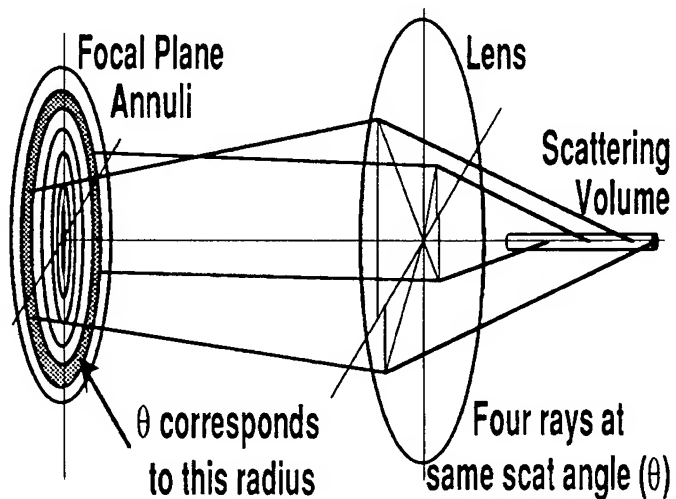


Figure 3: Rays at Same Angle Transform to One Annulus

Figure 4:
Optical Condensing 45° Half
Cone with MOS Linear Array
Along Cone Axis

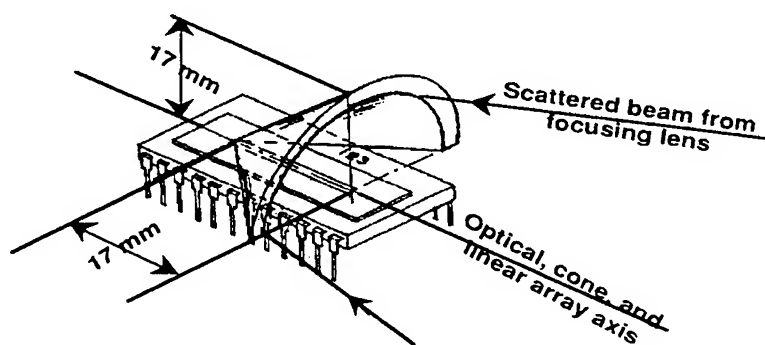


Figure 5:
Transformation of Two
Scattering Angles to Two
Points on a Line

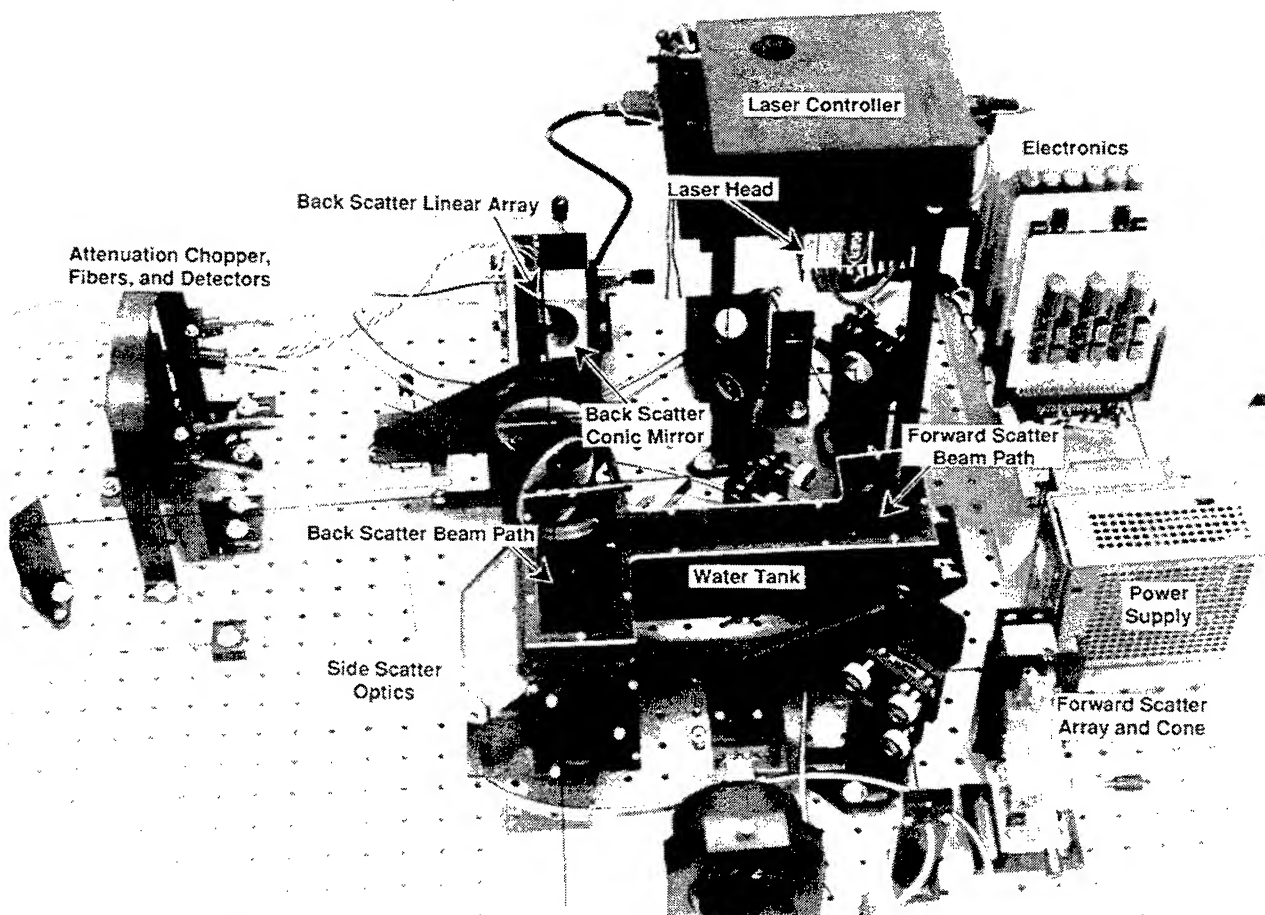
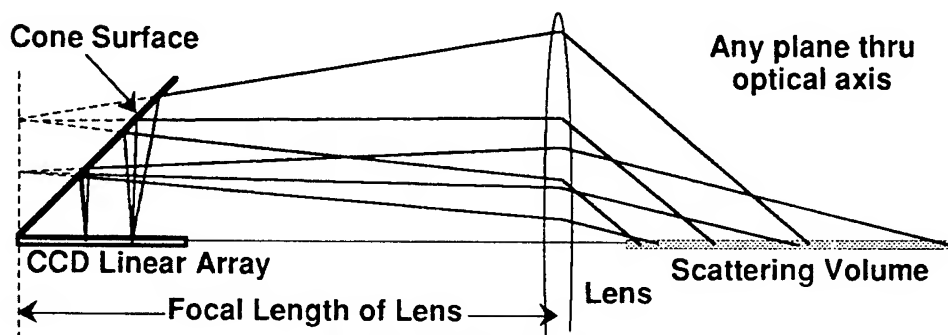


Figure 6: Polar Nephelometer Setup in Lab (computer is missing from photo)

VOLUME SCATTERING FUNCTION

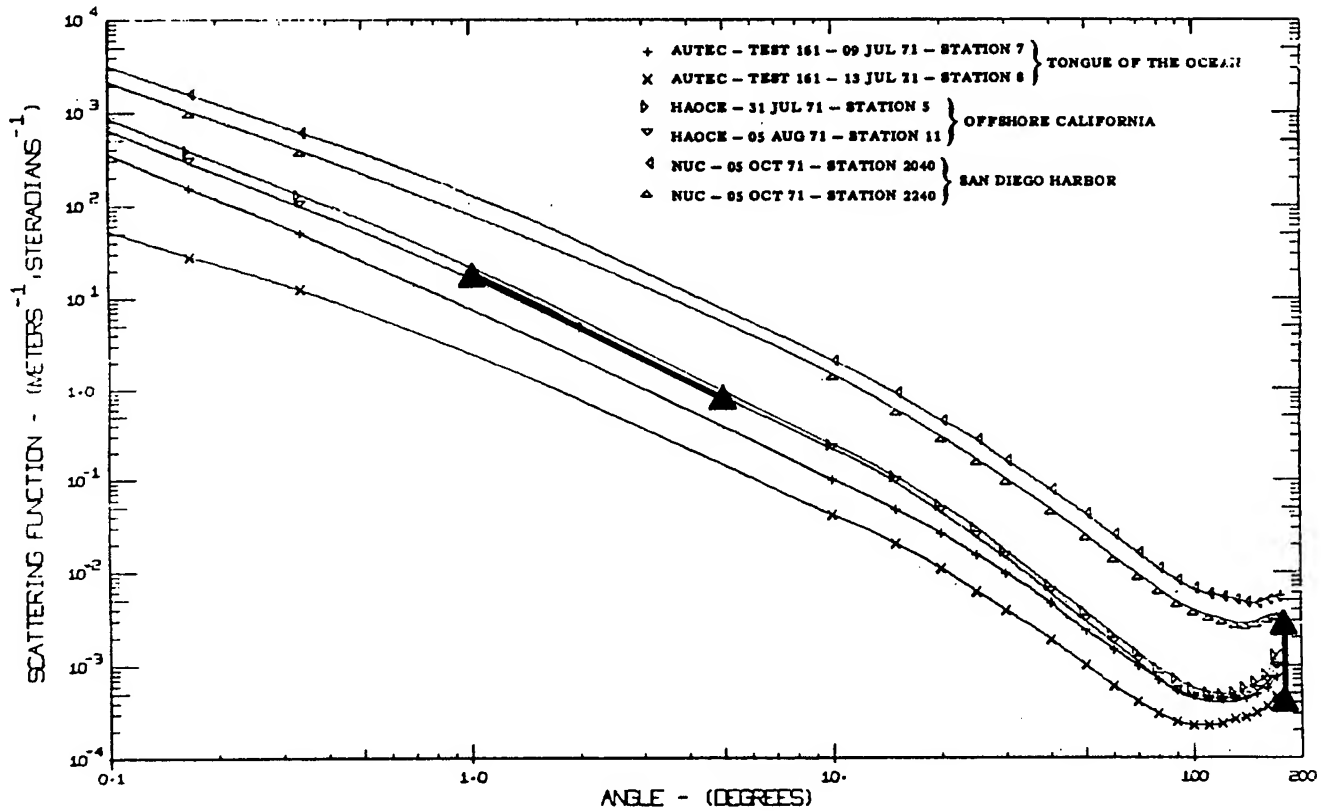


Figure 7: VSF from Petzold Report with Present Data Overlaid (heavy lines between triangles)

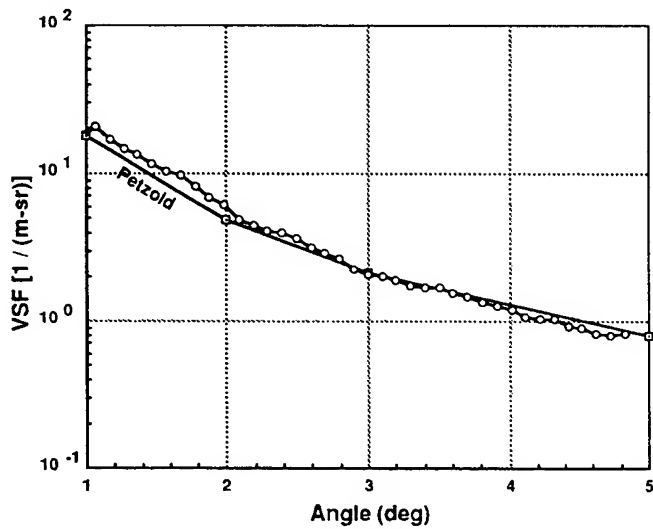


Figure 8: Forward Scatter VSF Data Plotted with Petzold (offshore California) Data

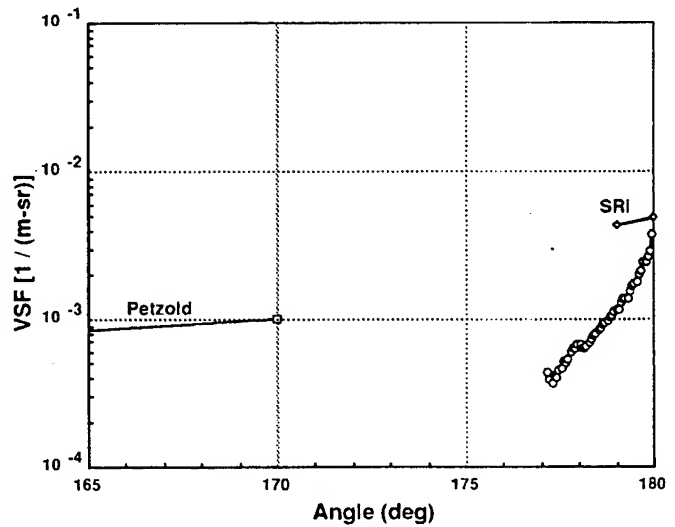


Figure 9: Back Scatter VSF Data Plotted with Petzold (offshore California) and SRI (Monterey Bay) Data

Submersible UV-B spectroradiometer using an acousto-optic tunable filter

Egorov V.G., Nalivaiko S.E., Pavlenko V.S., Rzshevsky O.S., Gordon E.B.

Institute for Energy Problems of Chemical Physics (Branch) RAS, Chernogolovka, Moscow Region, Russia, 142432;

Cooper L.W., Grebmeier J.M., Shugart L.R.,

Oak Ridge National Laboratory, Oak Ridge, Tennessee, USA, 37831-6038.

ABSTRACT

Measurements of solar irradiance in the UV-B region are complicated by large (orders of magnitude) variance in radiation fluxes over it. Normally, measurement requires use of double monochromators with high ($> 10^6$) spectral contrast. We have successfully tested a narrow bandwidth (0.3 nm) acousto-optic tunable filter (AOTF) with low ($\sim 10^4$) spectral contrast. The conditions for deployment were use of (i) a double - beam scheme with simultaneous recording of illumination in measuring and reference channels; and (ii) the intrinsic property of the AOTF to be a neutral filter outside of its passband. To apply the necessary contrast the background intensity determined in the reference channel was subtracted from intensity in the measuring channel. Two identical solar-blind photomultipliers in photon-counting regime were used. The integral solar intensity was averaged over the whole period of spectral record in order to shorten the period of time required for measurement at each wavelength. Formulae determining the spectroradiometer sensitivity and resolution, as well as comparison with US commercial instrument (Biospherical Instruments, Inc.) are presented. The testing was undertaken during US-Russian work at Kasitsna Bay, Alaska, in 1995, where additional genetic and cytological studies of the UV-B radiation impact on marine organisms were made.

Keywords: acousto-optic tunable filter, UV-B spectroradiometer, underwater solar spectra.

1. INTRODUCTION

Quantitative information on the extent of UV-B damage has been obtained by calculating biodoses of UV-B radiant energy. This damage is defined as the temporal and spectral integration of the incident irradiance with appropriate convolutions for the specific spectral response function or action spectrum. Action spectra vary significantly for different biological organisms, therefore the most reliable estimates for biodoses are obtained by carrying out spectrally-resolved UV-B insolation measurements. It is for this reason that spectral resolved devices were used when the U.S. National Science Foundation UV monitoring network was created¹. The strong spectral dependence of biological responses necessarily restricts the optimal spectral width of measurement, but in any case where a large dynamic range of irradiances is measured, there is also a high demand for spectral contrast (the ratio of transmittance within and outside the pass band). Otherwise even a small portion of long wavelength radiation passed through the apparatus will result in spurious photodetector illumination that is greater than the short wavelength radiation being measured. Based upon these considerations, a goal of measuring spectral widths not to exceed 1 nm was linked to a maximum contrast of 10^9 at the 1% illumination level².

Normally, double grating monochromators are used for spectral-resolved measurements both on the surface^{1,2} and underwater³. Possessing some obvious advantages, in particular, of providing necessary resolution and contrast, double monochromators are relatively large in size, but sensitive to vibrations, which complicates their use in field conditions; in addition, they are comparatively expensive. Therefore, the idea of designing an insolation meter by using an acousto-optic tunable filter (AOTF)^{4,5} as a wavelength dispersion unit, seemed attractive. Such filters possess spectral capabilities comparable with double monochromators, and can resolve rather narrow transmission bandwidths. In addition, an AOTF has no moving parts, is more compact and less expensive than comparable grating monochromator systems. However, the simple substitution of a traditional monochromator by an AOTF is undesirable in view of its rather low, ($1-3 \cdot 10^4$), spectral contrast, which arises from imperfections of the polarizer optical elements and crystal. At a total radiation flux in the UV-B region of $2 \cdot 10^{-4}$ W/cm² and given a contrast of 10^4 , background illumination will amount to $2 \cdot 10^{-8}$ W/cm², which is significant relative to the radiation intensity measured within a 1 nm band width at 300 nm ($\sim 10^{-8}$ W/cm²).

These difficulties were resolved in our instrument development and testing by the simple means of altering the measuring technique, and taking advantage of some peculiarities of acousto-optic filters. The possibilities of this approach were demonstrated earlier⁴ during investigations of the spectra of incident solar radiation in the UV-B region, as well as by us in measuring the depth dependence of sea water transmittance in visible light bands⁶. The work described here is divided into a description of the UV-B solar irradiance meter that we have designed on the basis of an acousto-optic filter, as well as details of the measurement technique, and the results of field testing of the apparatus.

2. SCHEMATIC OF UNDERWATER IRRADIANCE METER

The design of the spectroradiometer and its basic elements are shown in Fig.1. It is covered by a water-tight case for submersion. An on-board unit is connected by cable. This on-board section includes the computer, pulse counters, frequency tunable HF excitation generator, and the DC current power supply. The elements of the measuring section are located in the water-tight box, and include the quartz window with Lambert diffuser.

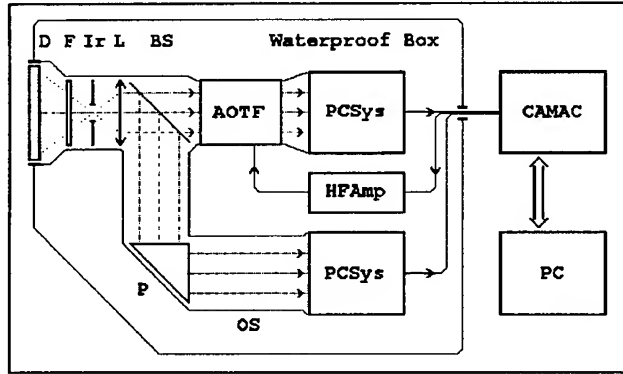


Fig. 1. Device schematic: D - input diffuser, F - broadband UV filter, L - collimating lens, BS - beam splitter, P - prism, HF Amp - high frequency amplifier, PCSys - photon counting system.

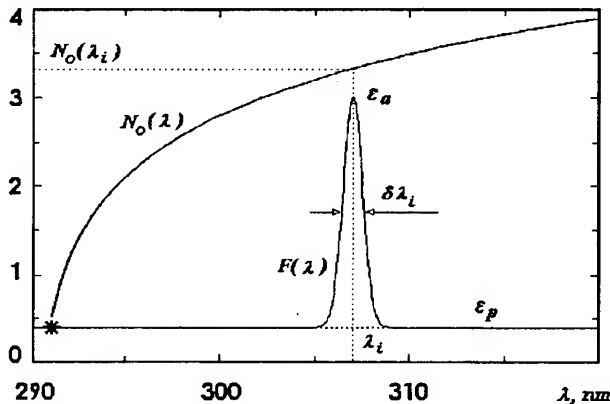


Fig. 2. Vertical axis - irradiance, arb. units.
 $N_0(\lambda)$ - the spectral irradiance at the entrance diffuser,
 $F(\lambda)$ - the transmittance of AOTF in "active" mode.

measurements. The number of photons incident on the beam splitter (BS) is determined as $\alpha(\lambda)N(\lambda, t)$, where $\alpha(\lambda) = \eta(\lambda)G(\lambda)/4\pi$, $\eta(\lambda)$ is the total transmittance of diffuser and UV filter, $G(\lambda)(\text{sr}\cdot\text{cm}^2)$ is the geometrical extent of the entrance lens. The part r of this beam (r is the coefficient of BS reflection) splits out and entirely impact the reference channel PMT, the rest being directed into AOTF.

Neglecting the dark pulses (for photomultipliers used, this value was less than 10 pulses/s), the photon counting rates in the measuring channels are linked with the irradiance function by the following relations:

$$n_r(t) = rT(t) \int \alpha(\lambda) N_0(\lambda) S(\lambda) d\lambda \quad (1)$$

for the reference channel, and

$$n_p(t) = (1-r)T(t)\epsilon_p \int \alpha(\lambda) N_0(\lambda) S(\lambda) d\lambda \quad (2)$$

for the principal channel in the "passive" mode of AOTF. Here $S(\lambda)$ (pulses/photon) is the quantum efficiency of photocathodes, assumed to be the same for both photomultipliers; integration is performed over the whole band of PMT sensitivity.

The on-board section controls meter operation, and gathers and processes data. As indicated on the schematic, the submersible section of the spectrometer is a two-beam optical design with a reference channel. For this reason the spectrometer is provided with a double channel photodetection system including two UV photomultipliers (PMT) operating in photon counting mode.

Without high-frequency (HF) excitation, the AOTF is in a passive non-dispersive mode, with its transmittance solely controlled by the transparency of crossed polarizers and small light depolarization scattering in the crystal. In this case it is essentially a neutral filter with a transmittance of ϵ_p independent of wavelength over the whole spectral band (see Fig.2).

In active mode, i.e. with HF excitation the AOTF transmittance sharply increases in the narrow band $\delta\lambda_i$ to attain the maximal value ϵ_a near λ_i value determined by HF excitation frequency. It is important everywhere, beyond the transmittance band $\delta\lambda_i$, transmittance remains to be equal to ϵ_p .

The ratio ϵ_a/ϵ_p , referred to as spectral contrast, is the most important parameter of the apparatus - it determines the degree of suppressing the broadband background illumination, and its typical value is $\sim 10^4$.

3. THE MEASURING PROCEDURE

The measurement procedure is based on the assumption that the measured spectral function of the flux of light incident on the diffuser $N(\lambda, t)$ (photon/cm²·nm·s), can be represented as a product $N(\lambda, t) = N_0(\lambda)T(t)$, the $N_0(\lambda)$ function being the goal of measurements and representing the time averaged spectral distribution at a given depth, and the $T(t)$ function determining temporary variations of $N(\lambda, t)$ i.e. due to solar shimmers, so the value of $T(t)$ averaged over large period of time is equal to unity.

Generally, the separation of these variables is possible only in the absence of the significant spectral transformations that can result from atmospheric variations during spectrum

The radiation passed through the AOTF in "active" mode can be represented by the sum of two parts (Fig.2). One component is selectively extracted by AOTF at a given wavelength λ_i , and another coincides with that passing through AOTF in "passive" mode. Therefore, one can write for "active" mode:

$$n_a(\lambda_i, t) = n_p(t) + \alpha(\lambda_i)(1-r)T(t)N_0(\lambda_i)S(\lambda_i) \int F(\lambda)d\lambda \approx n_p(t) + \alpha(\lambda_i)(1-r)T(t)N_0(\lambda_i)S(\lambda_i)\varepsilon_a\delta\lambda_i \quad (3)$$

where $F(\lambda)$ is the spectral function of the AOTF transmittance, with its maximal value $\varepsilon_a \equiv F(\lambda_i)$. It is worth noting that ε_a , $S(\lambda_i)$ and $\delta\lambda_i$ values depend on wavelength. One easily obtains from formulae (1) and (2) the ratio of counting rates to be

$$n_p(t)/n_r(t) = \varepsilon_p(1-r)/r \equiv k \quad (4)$$

and k is properly constant, affected by the parameters of the apparatus. In addition, one can derive from expression (3) after allowing for (1), (2) and (4):

$$N_0(\lambda_i)T(t) = (n_a(\lambda_i, t) - kn_r(t))\Phi(\lambda_i)^{-1} \quad (5)$$

where $\Phi(\lambda_i) = \alpha(\lambda_i)(1-r)S(\lambda_i)\varepsilon_a(\lambda_i)\delta\lambda_i$ is the apparatus spectral function, which along with k value can be determined in advance; the physical sense of $\Phi(\lambda_i)$ (pulses·cm² nm / photon) is the spectral sensitivity of the apparatus as a whole. The value of any N_0 function being sought at $\lambda = \lambda_i$ can be derived by averaging the expression (5) over long period of time sufficient for holding the condition $\langle T(t) \rangle \approx 1$. Thus one can derive

$$N_0(\lambda_i) \approx \langle (n_a(\lambda_i, t) - kn_r(t)) \cdot \Phi(\lambda_i)^{-1} \rangle_t \quad (6)$$

where τ reflects the average over the time of measurement. After allowing for the fact that the $\Phi(\lambda_i)$ function and, as seen from the formulae (1-3), the ratio $n_a(\lambda_i, t)/n_r(t)$ do not depend on time, let us rewrite the last expression as

$$N_0(\lambda_i) \approx (n_a(\lambda_i)/n_r - k) \Phi(\lambda_i)^{-1} \cdot \langle n_r(t) \rangle_t \quad \text{or} \quad N_0(\lambda_i) \approx (n_a(\lambda_i)/n_r - k) \Phi(\lambda_i)^{-1} \cdot N_r/\tau \quad (7)$$

where N_r is the total number of pulses in the reference channel. The choice for t value is rather important, since it defines the accuracy for evaluating $N_0(\lambda)$ function; it is seen from (7) that the time Δt_i for measurement at a spectral point λ_i does not define this accuracy, at least, not explicitly. The $T(t)$ function behavior studied in a set of papers, see for example, ⁷, gives maximal characteristic times of irradiation variation up to 1s in dependence on the kind of rough sea - due to ripple or windy conditions. Therefore the time of the whole spectrum record, τ , should comprise about several decades seconds so $\Delta t_i \ll \tau$.

Expression (7) therefore represents the working formula for calculating the $N_0(\lambda)$ function on the base of $n_a(\lambda_i, t)$, $n_r(t)$ and N_r/τ which in turn provides information on the apparatus parameters k and $\Phi(\lambda)$.

4. APPARATUS ELEMENTS AND CALIBRATION

1. Photomultipliers. We used UV solar-blind PMT having tellurium-cesium photocathodes, with quantum efficiency values of $1 \cdot 10^{-2}$, and the long-wavelength sensitivity border of 0.1% of the maximal value being near 365 nm. The dark current of these PMT amounts to $2 \cdot 10^{-11}$ A, with amplitude discrimination that corresponds to the counting rate less than 10 pulses/s.

2. The photon counting system consists of two independent photodetectors loaded by coaxial HF cables; the limiting photon counting rate for this system is $2 \cdot 10^8$ pulses/s, which corresponds to maximum radiation flux of $\sim 10^{15}$ photon/s.

3. Acousto-optical tunable filter. The co-linear UV-AOTF has 6 mm diameter entrance window, provided with quartz polarizers. The spatial filter, located between AOTF and PMT, brings about the maximum attainable AOTF contrast value, which, according to manufacturer specifications, amounts to $2.7 \cdot 10^4$ at the polarized light wavelength of 325 nm, assuming a transparency band width of $\delta\lambda \approx 0.23$ nm and transmittance coefficient of the transparency band of ≈ 0.25 . The ε_a and ε_p values calculated from these data for nonpolarized light are ≈ 0.125 and $\approx 4.6 \cdot 10^{-6}$ respectively. The HF excitation tuning within 115 - 133 MHz is corresponded to optical ranges of 290-320 nm.

4. The spectroradiometer wavelength calibration was carried out using a model DRS-50-1 low pressure mercury lamp emission spectrum. The accuracy of wavelength reproducibility was not worse than 0.1 nm. Thus the maximum number of recorded spectral points was chosen so that distance between each should be less than the instrumental spectral resolution. In the 290-320 nm range, up to 327 spectral points could therefore be recorded, with the resolutions of about 0.12 nm.

5. Calibration of the absolute sensitivity was accomplished by conventional technique ² through use the emission spectrum of a model TRU 1100 tungsten lamp with the brightness temperature of 2350° C.

5. SPECTRAL MEASUREMENTS PROCEDURE

Due to some constructional peculiarities which will improved in the future, the acousto-optic tunable filter we used could operate permanently in active mode not more than 0.1s with the relative pulse duration being ≥ 4 . Therefore we have applied the periods of active and passive modes $\Delta t_i \leq 0.1$ s and $\geq 3\Delta t_i$ respectively. (As a general case, the Δt_i value can vary for different parts of spectral region, depending on light intensity and one can reduce Δt_i at greater intensity).

The number of pulses in the principal channel, N_{ai} , and in the reference channel, N_{ri} , are measured simultaneously in a time of Δt_i . Consequently, the ratio of these two variables is equal to the ratio of the counting rates in the corresponding channels, $N_{ai}/N_{ri} \equiv n_a(\lambda_i)/n_r$, and formula (7) can be rewritten as

$$N_0(\lambda_i) \approx [N_{ai}(\lambda_i)/N_{ri} - k] \cdot \Phi(\lambda_i)^{-1} \cdot N_r / \tau. \quad (8)$$

with the N_r value is accumulated over the whole time of the spectrum measurement, τ . The array of points, $\{N_{ai}, N_{ri}, \lambda_i\}$, together with N_r/τ ratio value are saved as a spectral data file. Given the value of k and $\Phi(\lambda_i)$ values calculated in advance by the approximating function, these data enable to calculate the irradiance at a given depth.

Radiometer operation is supported by the computer software with a menu-driven interface, and the real-time information necessary for on-line control of measurements is provided. The total time for spectral measurements within 290-320 nm waveband, assuming a scan of λ_i with steps of $\sim \delta\lambda$, i.e. about 0.25 nm, amounts to about 1 minute.

6. THE SPECTRAL IRRADIANCE LIMIT LEVEL MEASURED

Let us consider the irradiance limit value, $N_0(\lambda_i)_{\min}$, under circumstances when the absolute statistical error is comparable to the measured $N_0(\lambda_i)_{\min}$ value itself. In this instance, to obtaining $N_0(\lambda_i)_{\min}$ formula (8) can be re-written:

$$N_0(\lambda_i) = \frac{N_{ai}(\lambda_i) - kN_{ri}}{N_{ri}} \cdot \Phi(\lambda_i)^{-1} \cdot \frac{N_r}{\tau}$$

The difference $N_{ai}(\lambda_i) - kN_{ri} = N_{fi}(\lambda_i)$ is the calculated number of pulses corresponding to the $N_0(\lambda_i)$ value in a time of Δt_i . During tuning to the short-wavelength region of UV-B the $N_{ai}(\lambda_i)$ value decreases, and $N_{fi}(\lambda_i)$ drops in accordance with the spectral irradiance curve $N_0(\lambda_i)$. At some wavelength $N_{fi}(\lambda_i)$ becomes close to its deviation, i.e. $N_{fi}(\lambda_i) \approx \sigma(N_{fi}(\lambda_i))$, which corresponds to a measuring error of 100%. Let us take advantage of the circumstance, that the nonequality $N_{fi}(\lambda_i) \ll N_{ai}(\lambda_i) \ll N_{ri}$, holds for our apparatus near $N_0(\lambda_i)_{\min}$, i.e. $N_{fi}(\lambda_i)$ is the little difference of two large values, as this take place, $N_{ai}(\lambda_i) \approx kN_{ri}$, and $N_{ai}(\lambda_i) \gg k^2 N_{ri}$ can be assumed. Thus one can write

$$\sigma(N_{fi}(\lambda_i)) = \sigma(N_{ai}(\lambda_i) - kN_{ri}) \approx \sqrt{\sigma^2(N_{ai}) + k^2 \sigma^2(N_{ri})} \approx \sqrt{N_{ai} + k^2 N_{ri}} \approx \sqrt{N_{ai}(\lambda_i)} \approx \sqrt{kN_{ri}}, \quad \text{i.e.}$$

$N_{ai}(\lambda_i) - kN_{ri} \approx \sqrt{kN_{ri}}$, or for the counting rate

$$\frac{n_{ai}(\lambda_i)}{n_{ri}} - k \approx \sqrt{\frac{k}{n_{ri} \Delta t_i}}. \quad (9)$$

At this point, the measured limit spectral irradiance can be simplified by considering the statistical character of measurements, and after simplification written as

$$N_0(\lambda_i)_{\min} \approx \sqrt{\frac{k}{n_{ri} \Delta t_i}} \cdot \Phi(\lambda_i)^{-1} \cdot \frac{N_r}{\tau}. \quad (10)$$

For quantitative estimates let us transform n_r from formula (1). We take advantage of the weak dependence of $\alpha(\lambda_i)$ and $S(\lambda_i)$ on wavelength and assume them to be constant, equal to the values averaged over measured spectrum; let us also suppose $T(t)=1$. We accept the integration domain to coincide with UV-B band, then $n_r \approx r\alpha SE$, where $E = \int N_0(\lambda) d\lambda$ is the total flux of UV-B light incident on the entrance diffuser. Thus,

$$N_0(\lambda_i)_{\min} \approx \sqrt{\frac{\varepsilon_p \cdot E}{\alpha(1-r) \cdot S \cdot \Delta t_i}} \cdot \frac{1}{\varepsilon_a(\lambda_i) \cdot \delta\lambda_i} \quad (11)$$

Another restriction is the presence of PMT dark pulses. As noted previously, the counting rate for dark pulses is $n < 10s^{-1}$. By analogy, for limit value of $N_{fi}(\lambda_i)$, one can write down: $N_{fi}(\lambda_i) = N_{ai}(\lambda_i) - kN_{ri} \approx n_d \cdot \Delta t_i$ or

$$\frac{n_{ai}(\lambda_i)}{n_{ri}} - k \approx \frac{n_d}{n_{ri}} \quad (12)$$

and the corresponding irradiance level is:

$$N_0(\lambda_i)_{\min} \approx \frac{n_d}{\alpha(1-r) \cdot S \cdot \varepsilon_a(\lambda_i) \cdot \delta\lambda_i} \quad (13)$$

At $\Delta t_i \approx 1s$, $\varepsilon_a(\lambda_i)\delta\lambda_i \approx 2.8 \cdot 10^{-2} \text{ nm}$ and the irradiance level inherent to, for example, $E \approx 3 \cdot 10^{14} \text{ photon/cm}^2 \cdot s \cdot \text{nm}$, one will obtain for both limits the value $N_0(\lambda_i)_{\min} \approx 4.7 \cdot 10^9 \text{ photon/cm}^2 \cdot s \cdot \text{nm}$, or $\sim 3 \cdot 10^{-9} \text{ W/cm}^2 \cdot \text{nm}$.

7. SPECTRORADIOMETER FIELD TESTING

Testing the UV spectroradiometer was carried out during joint American-Russian scientific field studies at the University of Alaska's Kasistna Bay Laboratory on April 1-14, 1995.

The on-board part of the spectroradiometer, consisting of the CAMAC equipment, the HF generator and the controlling IBM-compatible computer, was operated from a small boat. The submersible part of the apparatus was connected to the former with a 25

m long cable. Sea conditions were calm during all measurements and the field tests were carried out under full sun and cloudy conditions. For the most part spectra were recorded in the UV-B spectral region of 290-330 nm.

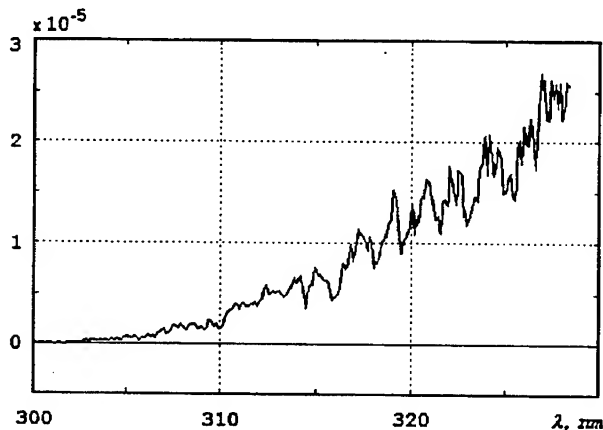


Fig.3. The spectral irradiance (W/cm² nm) on the surface recorded with maximal spectral resolution. The averaging number at each spectral point was 5. The local time: 3.05 p.m., April 07, 1995.

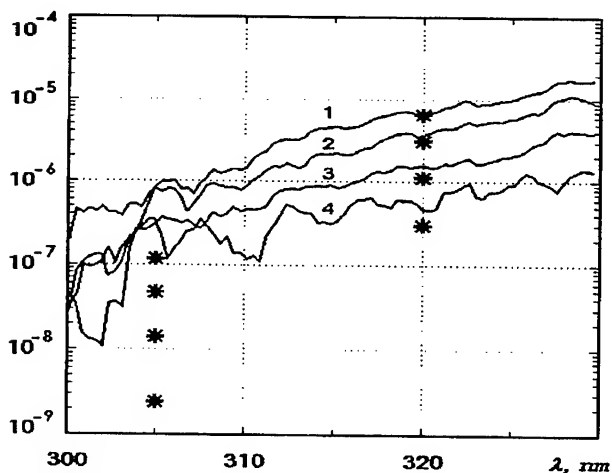


Fig.4. The comparison of the measurements made by the spectroradiometer and the PUV-500A apparatus. The data from PUV-500 are plotted by (*). Depths were: 1 - 0.2 m, 2 - 1m, 3 - 2m, 4 - 4m.

¹⁰ (and C.R.Booth, personal communication). At 320 nm, the coincidence of absolute irradiance values measured by both radiometers can be considered to be satisfactory, while at 305 nm the irradiance values measured by the PUV-500A are by factor of 3 less than those determined by our apparatus. The cause of this discrepancy is not known at this time.

9. CONCLUSION

The data we obtained using the PUV-500A provide a good fit with simulations obtained by a model that uses plane-parallel discrete ordinates radiative transfers methodologies (Stamnes et al., as applied by C.R.Booth, Biospherical Instruments). The NASA DISCORT model ¹⁰ also indicates close agreement with our measurements.

These field tests, as well as the conclusion of theoretical analyses, indicate promise for the development of a sturdy spectrometer suited for wide use in field measurements, including those under water and air. We encountered no problems from

In the example provided, the irradiance spectrum was recorded on the water surface and the maximum number of spectral points is shown. In this instance, the Fraunhofer structure is distinct. During our measurements, the solar zenith angle was about 65°. Total ozone content was at 400±30 DU.(TOVS satellite data from the Climate Analysis Center /MNC/NWS/NOAA; and obtained from a global image for dates of measurement ⁸).

The total time for recording spectra at this maximum resolution is rather long: for 327 spectral points with 5 measurements at a point, the time required exceeds 10 minutes. In weather conditions typical to Alaska in April, this could result in some distortions of the spectra recorded, since the radiance spectrum during measurements could vary depending upon cloud thickness. As a result we decrease the number of spectral points to 109 with an average of five measurements at each point.

Because of relatively low water transparency, we confined ourselves to measurements at shallow depths from 0.2 to 4 m, and over this depth, the integral irradiance in UV-B region decreased by about an order of magnitude. An example of the underwater irradiance spectra, measured at different depths, is provided in Fig. 4.

As can be seen from Fig.4, irradiance near 300 nm vanishes. Some ambiguities in irradiance are related to photon counting statistics, but these can be avoided by increasing the time of measurement at each spectral point. Measurement noise, related to shimmers on the diffuser surface, are completely removed by using the two - channel technique, brought about in our spectroradiometer. The total number of data files recorded during the time of field tests exceeds 30.

8. CROSS - CALIBRATION

A cross - calibration was provided by simultaneous measurements using our spectroradiometer and the Profiling Ultraviolet Radiometer System PUV-500A manufactured by Biospherical Instruments Inc., San Diego, California ⁹. This apparatus measures irradiance in a set of spectral bands centered at 308, 320, 340 and 380 nm. The values of irradiance are averaged over 1 nm and are saved as data files. Although the PUV-500A was supplied with an interference filter centered at 308 nm, data at that apparent waveband are referred to as data at 305 nm, based other comparative studies

mechanical vibrations and swinging, while demonstrating high spectral resolution, reliability of spectral calibration, high flux sensitivity and performance, particularly where fast wavelength tuning is necessary.

10. ACKNOWLEDGMENTS

The authors wish to thank Dr. C.R.Booth (Biospherical Instruments Inc.) for useful and interesting discussions and assistance with interpretation of the field test and cross-calibration. We also thank Drs. V.Voloshinov, U.Kalinnikov and V.Yepihin for useful consultations.

Financial support was provided by the U.S. Department of Energy, through the Office of Health and Environmental Research, and the Newly Independent States-Industry Partnering (NIS-IPP) Program. Oak Ridge National Laboratory is managed by the Lockheed Martin Energy Research Corporation for the U.S. Department of Energy under contract DE-AC05-96OR22464 .

11. REFERENCES

1. C.R.Booth, T.B.Lucas, T.Mestechkina, J.R.Tusson IV, D.A.Neuschuler, and J.H.Morrow. "NSF Polar Programs UV Spectroradiometer Network 1991 - 1993 Operations Report". (Prepared for Antarctic Support Associates and the National Science Foundation by Biospherical Instruments Inc.), pp.138 - 140.
2. R.L.McKenzie, P.V.Johnston, M.Kotcamp, A.Bittar, and J.D.Hamlin. "Solar ultraviolet spectroradiometry in New Zealand: instrumentation and sample results from 1990". *Applied Optics*, **31**, No.30, 6501-6509 (1992).
3. R.C.Smith, B.B.Prezelin,... "Ozone Depletion:Ultraviolet Radiation and Phytoplankton Biology in Antarctic Waters", *Science*, **255**, pp. 952 - 959, 1992.
4. I.B.Belikov, V.B.Voloshinov, V.N.Parygin, "Acousto-optical filtration of electromagnetic radiation in ultraviolet region", *Pisma v jurnal technicheskoi fiziki*, **14**(7), pp. 645-650, 1988.
5. P.Katska, "AOTF overview: past, present and future", *SPIE*, **735**, pp.-28, 1987.
6. Report about joint Russian- US expedition to the Black Sea, Gelendjik, 1984.
7. A.I.Sudbin, *Ocean Optics*, v.1, pp. 293-306, Science, Moscow, 1983.
8. Dr. C.R.Booth, private communication.
9. C.R.Booth, J.H.Morrow, and D.N.Neuschuler, "A New Profiling Spectroradiometer Optimized for the Use in the Ultraviolet", *SPIE*, **1750**, pp. 354-365, 1992.
10. N.A.Krotkov, A.P.Vasilkov, "Ultraviolet radiation in the atmosphere - ocean system: a model study.", *SPIE* **2049**, pp. 244-255, 1993.

SeaWiFS ocean color products and services at the
NASA Goddard Distributed Active Archive Center (DAAC)

Rebecca A. Farr ¹, Ravi Kartan ², Angela W. Li ³ and Robert B. Simmon ²

¹ George Mason University, Fairfax, VA 22030, ² Research & Professional Services, Riverdale, MD 20737; ³ Research & Data Systems Corp., Greenbelt, MD 20770;

ABSTRACT

Sea-Viewing Wide instantaneous Field-of-View Sensor (SeaWiFS) ocean color data will be archived at the Goddard DAAC in early 1997. The Goddard DAAC has been designated the primary archive for all SeaWiFS data. Almost all authorized SeaWiFS users will access SeaWiFS data via the Goddard DAAC Ocean Color Data and Resources web page. New interfaces and services are being developed by the Goddard DAAC Ocean Color Data Support Team on the Ocean Color website to support the SeaWiFS community following launch:

A new SeaWiFS WWW Browser will allow users to browse and order SeaWiFS data via the Web. This Browser will incorporate all necessary elements for SeaWiFS data ordering, including password controls, subsetting, coincident search and visual browse.

Users will also find SeaWiFS ancillary data, software routines, SeaWiFS data products specifications, an order form for the SeaWiFS Technical Memoranda, as well as direct links to the "Dear Colleague" letter and other documents and software on the SeaWiFS Project homepage.

Other ocean color products available at the Goddard DAAC Ocean Color website include the following: New HDF versions of CZCS data files, including browse images and a collection of regridded global composites designed for interdisciplinary study. New CZCS read and visualization software are available. A bibliography of ocean color research papers, several previously rare hardcopy documents, and a periodic ocean color newsletter are also available via the Web. The website also contains a collection of several new educational resources for ocean color educators and students.

Being the main source of SeaWiFS data and consolidating ocean color data, documents, software, and points of contact from several other sources all at one convenient location, the Goddard DAAC hopes to become an important nexus for the entire global ocean color community.

The Ocean Color Data and Resources webpage can be found at <http://daac.gsfc.nasa.gov> under "Ocean Color". Contact the Goddard DAAC Ocean Color Data Support Team about additional ocean color information and SeaWiFS support.

KEYWORDS:

ocean color, SeaWiFS, CZCS, bio-optics, Distributed Active Archive Center, data

1. INTRODUCTION

Sea-Viewing Wide instantaneous Field-of-View Sensor (SeaWiFS) ocean color data will be archived at the Goddard DAAC in early 1997. The Goddard DAAC has been designated the primary archive for all SeaWiFS data. Launch is now scheduled for March 1997, with data flow commencing in May, following a 45-60 day orbit-raising period. Approximately 10 gigabytes of data will be ingested into the Goddard DAAC daily. We anticipate distributing approximately 40 gigabytes per day to authorized users.

Almost all authorized SeaWiFS users will access SeaWiFS data via the Goddard DAAC Ocean Color Data and Resources web page. New interfaces and services are being developed by the Goddard DAAC Ocean Color Data Support Team on the Ocean Color website to support the SeaWiFS community following launch. In addition to SeaWiFS data, the Goddard DAAC website will also offer numerous documents, ancillary data and late breaking news.

Authorized SeaWiFS users will browse and order SeaWiFS data via a new SeaWiFS WWW Browser. This Browser will incorporate all necessary elements for SeaWiFS ordering, including password controls, subsetting, coincident search and visual browse. The SeaWiFS Browser is currently under development and is being adapted from the CZCS Browser which opened in February 1996. The SeaWiFS Browser became partially operational on September 30, 1996 and will continue to be developed throughout the winter.

2. THE SEAWIFS BROWSER

Like the WWW CZCS Browser, the SeaWiFS Browser search engine uses the same logic as the original CZCS browser and is based on three simple lookup tables for latitude, longitude and date of data file acquisition. Each individual SeaWiFS data file in the archive is given an index number which maps directly to the lookup tables and corresponding browse files. In the latitude and longitude lookup tables, all the indices of the files are stored in two degree spatial bins. When a user enters spatial and time ranges of interest, the software first finds all files that fall into the two degree latitude bins specified and then flags those files. This is repeated for the longitude and date. The three lists of flagged files are then compared to find those files common to all three lists. These files are then used to generate the final list of "hits": all unique files which satisfy the user's search criteria exclusively.

The SeaWiFS Browser search engine is written in PERL which is a more natural language for HTML programming and more robust for string manipulation. The PERL program creates HTML documents on the fly, reading different user input parameters. Depending on the user's input, the program executes commands such as "display the image" or "view the previous or next image in the search result list". An order file is generated for insertion into the DAAC's order processing system. This engine can quickly and accurately search the entire SeaWiFS database. For CZCS, the engine returns a list of all 59,337 Level 2 files in the archive in approximately 5 seconds, including transfer time back and forth over the network. By using the NCSA visualization software called Browse-O-Rama, we are able to provide visualization of the HDF browse files without creating an additional collection of GIF or TIFF images of the data. The Browser works for all HDF data and has been adapted to several different datasets already.

3. USING THE SEAWIFS BROWSER

The SeaWiFS WWW Browser may be found on the Goddard DAAC home page in the Data Section under Visual Search at

<http://daac.gsfc.nasa.gov>

To access the SeaWiFS Browser, you will be asked to enter your name and SeaWiFS password. These passwords are provided only to authorized SeaWiFS users who have completed a SeaWiFS user survey. The Goddard DAAC asks that all authorized SeaWiFS user please submit a SeaWiFS Survey prior to launch. The Goddard DAAC is using the SeaWiFS survey information to determine the support and equipment requirements for the SeaWiFS program. In compliance with OrbImage's decision to release the first three month's of data freely to the public, the SeaWiFS Browser password function will be disabled during the first 90 days of data collection.

On the first page of the SeaWiFS Browser you will be asked to select Level 1A individual scenes, Level 2 individual scenes or Level 3 composites. Selecting Level 1A or 2 will bring you to a "Map" page where you click on two corner points to draw a rectangle of your choice on the map of the world to specify your latitude and longitude coordinates. Forms on the same page allow you to manually enter exact coordinates, if wanted, and to define the date range of interest. Selecting the Level 3 products takes you to the Level 3 selection page, which allows you to specify date ranges only, since these data are global. The page may be cleared at any time and new criteria entered. Select the "Start Search" button to send a query to the search engine. This will take you to the "Results" page where a list of files which fit the specified criteria is shown.

Clicking on any filename on the "Results" page sends you to the "Viewing" page where you will see a GIF image of the HDF browse file, its exact area of coverage on a global map, if not a level 3 file, and some of the metadata associated with that file. You may save the GIF image to your own machine using the "save file" function of your browser. Click the "Order" button to add this file to your order and proceed to the next file in the list or click on "Next" to view the next file without ordering the present one. Click on the filename at the top of the page to download the digital HDF browse file itself. Click on the "Additional Information" link to see a complete list of the metadata associated with each file.

Use the "Next File" and "Previous File" buttons on the "Viewing" page to step through the Results list, viewing each file in turn and ordering those desired. You may also return to the "List" page at any time and view any file on the list out of sequence. Click on the "New Search" button to abort this search and go back to the Map page to start a new search session. You may order all files in the results list with out viewing them by selecting the "Order All" button. When you are satisfied that you have added all the files you want to your order, close the browse session by selecting the "Submit Order" button.

This sends you the "Order" page where you must specify the type of data desired. You may order multiple products in the same browse session. For SeaWiFS, the following products are available:

For Level 1A:

- Level 1A LAC
- Level 1A GAC
- Level 1A HRPT
- Level 1A LAC Browse
- Level 1A GAC Browse
- Level 1A HRPT Browse
- Ancillary data that map to those files

For Level 2:

- Level 2 GAC
- Level 2 GAC Browse
- Ancillary data that map to those files

For Level 3:

- Level 3 binned products
- Level 3 standard mapped image, chlor_a
- Level 3 standard mapped image, CZCS_pigment
- Level 3 standard mapped image, nLw_555
- Level 3 standard mapped image, tau_865
- Level 3 standard mapped image, K_490
- Level 1A files that were used to create those Level 3 files

On the "Order" page, you must also specify the medium type and format desired, as follows:

Medium:

- FTP
- 8MM-8200 tape
- 8MM-8500 tape
- 4MM-60 METER tape
- 4MM-90 METER tape

Format:

- TAR
- DD

Select the "Continue" button to see a list of the files you have requested. Selecting the "Continue" button again will bring you to the next and final "Shipping" page where you must enter your shipping information to complete the request. This completes the order file and the system shows you a "Confirmation" page verifying your request and giving you a unique request number for reference. Your data request enters the DAAC system that night at local midnight. It is then placed into the job queue, processed in turn and shipped to the address specified in your browse session.

As an alternative to manually requesting data via the Browser, The Goddard DAAC also offers standing orders or data subscriptions. Contact the Goddard DAAC Ocean Color Support Team for assistance in setting up a standing order.

4. ADDITIONAL PRODUCTS AND SERVICES

On the Goddard DAAC Ocean Color page, in addition to SeaWiFS data, users will also find SeaWiFS ancillary data, software routines, SeaWiFS data products specifications, an order form for the SeaWiFS Technical Memoranda, as well as direct links to the "Dear Colleague" letter and other documents and software on the SeaWiFS Project homepage. Although at present, only the abstracts are available on-line, it is also possible to order all of the SeaWiFS Technical Memoranda from the Ocean Color website.

Other ocean color products designed to augment and assist SeaWiFS research are also provided on the Goddard DAAC Ocean Color website. The entire CZCS data collection has been brought to the web via the CZCS Browser. New SEADAS-compatible HDF versions of Level 1A and 2 CZCS data files are now available on anonymous ftp, including browse images. A new collection of regridded Level 3 global composites designed for interdisciplinary study has also been created. New CZCS read and visualization software are available. A bibliography of ocean color research papers, several previously rare hardcopy documents, including the PC-SEAPAK User's Guide and a periodic ocean color newsletter are also available via the Ocean Color website.

Being the main source of SeaWiFS data and consolidating ocean color data, documents, software, and points of contact from several other sources all at one convenient location, the Goddard DAAC hopes to become an important nexus for the entire global ocean color community. We have established an Earth Interactions Journal (EIJ), several bulletin boards for researchers in other communities and can offer these and other web publishing services to the ocean color community as well.

5. THE OCEAN COLOR DATA SUPPORT TEAM

Contact the authors, who comprise the Goddard DAAC Ocean Color Data Support Team, about these services, more ocean color data and information and additional SeaWiFS support:

Rebecca Farr
Lead, Ocean Color Data Support Team
(George Mason University)
301-614-5381
farr@daac.gsfc.nasa.gov

Angela Li
Programmer
(Research & Data Systems Corp.)
301-614-5253
li@daac.gsfc.nasa.gov

Ravi Kartan
Programmer
(Research & Professional Services)
301-614-5200
kartan@daac.gsfc.nasa.gov

Robert Simmon
Web Editor
(Research & Professional Services)
301-614-5316
simmon@daac.gsfc.nasa.gov

Code 902, Distributed Active Archive Center
Goddard Space Flight Center
Greenbelt, MD 20771

The SeaShark and Starfish operational data processing schemes for AVHRR and SeaWiFS

R.J. Flowerdew, A.M. Corlyon, W.A.D. Greer, S.J. Newby, and C.P. Winder

The VEGA Group plc
2 Falcon Way, Shire Park, Welwyn Garden City, Herts, U.K., AL7 1TW

ABSTRACT

SeaShark is an operational software package for processing, archiving and cataloguing AVHRR and SeaWiFS data using an operator friendly GUI. Upon receipt of a customer order, it produces standard AVHRR data products, including Sea Surface Temperature (SST) and it has recently been modified to include SeaWiFS level 2 data processing. This uses an atmospheric correction scheme developed by the Plymouth Marine Laboratory, U.K. (PML) that builds upon the standard Gordon and Wang approach to be applicable over both case 1 and case 2 waters. Higher level products are then generated using PML algorithms, including chlorophyll *a*, CZCS-type pigment, K_d , and suspended particulate matter (SPM). Outputs are in CEOS-compatible format. The software also produces Fast Delivery Products (FDPs) of chlorophyll *a* and SST.

These FDPs are combined in the StarFish software package to provide maps indicating potential location of phytoplankton and the preferred thermal environment of certain pelagic fish species. Fishing vessels may obtain these maps over Inmarsat, allowing them to achieve a greater efficiency hence lower cost.

Keywords: AVHRR, SeaWiFS, image processing, SeaShark, Starfish, atmospheric correction, SST, chlorophyll

1. INTRODUCTION

In this paper, we present details about the SeaShark operation satellite data software processing package, and in particular, recent enhancements made to process SeaWiFS data through to level 2 geophysical products. SeaShark is a relative of the European Space Agency's Shark processing software, which is used to process AVHRR data, but it has two principal enhancements. Firstly, the graphical user interface (GUI) has been redeveloped and much of the underlying processing code has been improved or rewritten. Secondly, the package has been extended to be capable of processing SeaWiFS data.

In the next section, we discuss SeaShark in more detail, and in section 3, we look at the algorithms underlying the SeaWiFS level 2 products. The StarFish system – a potential beneficiary of SeaShark – is outlined in section 4.

2. SEASHARK PROCESSING SOFTWARE

We discuss firstly the way the software is constructed to achieve flexibility, simplicity of use, and upgradeability, and secondly the principal products produced by the SeaShark processing software.

2.1. Code

SeaShark is written in C++ with a Motif GUI, running on SUN workstations under Solaris 2.4. The GUI allows the operator to initiate product generation, manipulation, and archiving: a typical view of the GUI is shown in Figure 1. Output products may be displayed for quality-checking purposes. The system is robust to errors, which may be corrected interactively. A flexible object-oriented approach has allowed VEGA to develop a tool for handling data from the two imaging sensors that exploits similarities between the systems and yet fully accommodates their individual characteristics. The software may readily be extended to handle new satellites in the series, or even other sensors such as OCTS on the Japanese ADEOS series of satellites.

The operator may work with SeaShark directly, generating products in interactive mode, or prepare a series of jobs for automated processing in batch mode. Products may be archived and catalogued, with dissemination to customers on exabyte tape, or via file transfer protocol. The system has reporting facilities to monitor usage and to provide information for customer billing.

After a new raw image is placed into the import directory, the software automatically recognises its existence, and begins processing. Bad lines are detected, and the image is quality checked. Navigation is performed using an orbit model, or, in the case of SeaWiFS, using the (global positioning system) GPS data. The operator may choose to check the navigation of the image, displaying it on the console, and adjusting if desired. The coastline, political boundaries, or a latitude/longitude grid may be displayed as an image overlay. Normally, the data is processed through to a level 1 archive image, which is

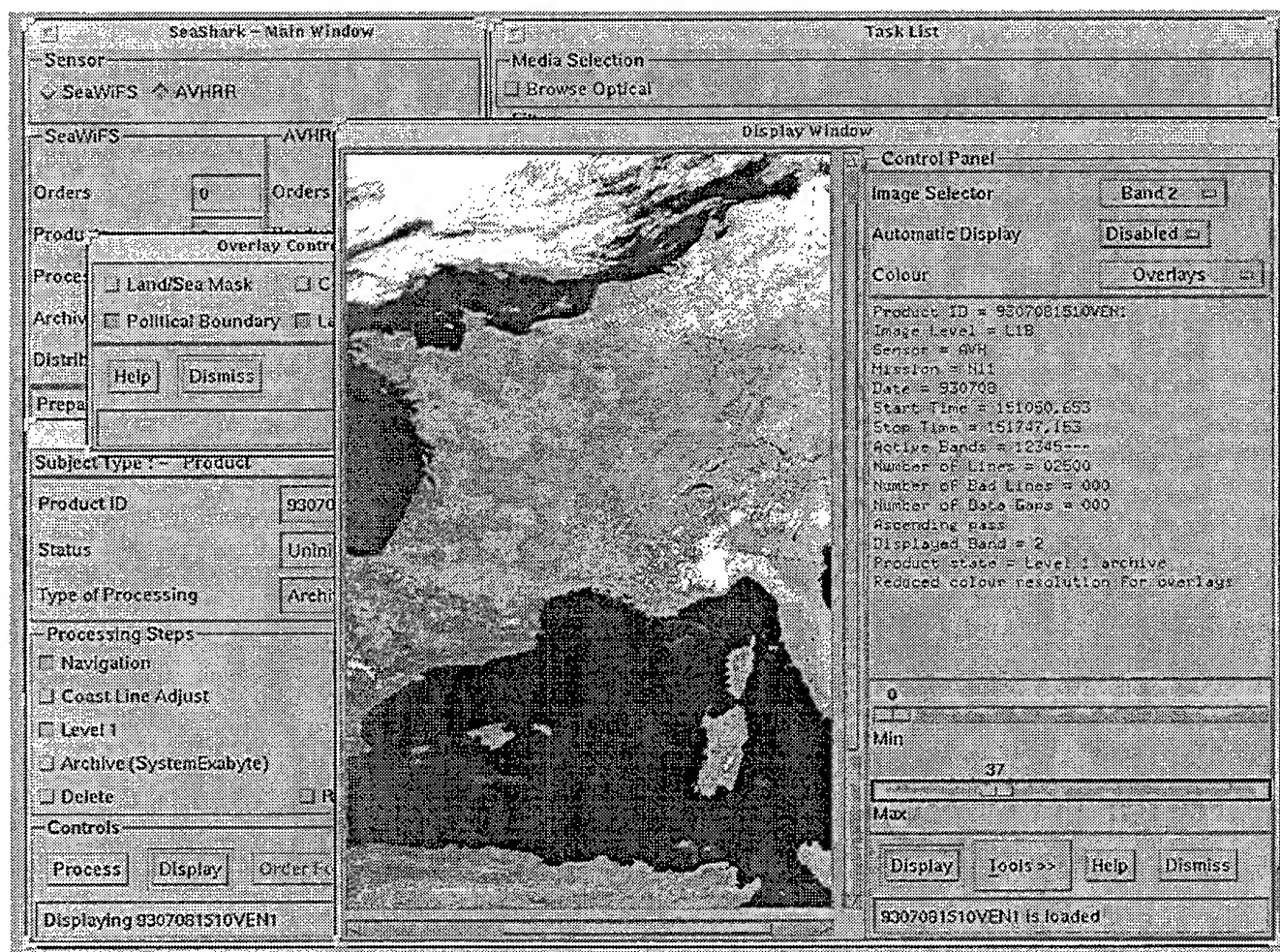


Figure 1. Some of the elements of the SeaShark GUI

then stored on exabyte tape. SeaShark provides tape handling facilities for this. In addition to the internal level 1 archive format, the image is also available as a "PostScript QuickLook" for printing out on an appropriate printer, or as a raster QuickLook colour composite that may be viewed using widely available utilities such as *xview* or *imagetool*.

On receipt of an order, the operator either retrieves the appropriate archive from tape, or finds it on hard disk. If required, the system will readily handle orders for fragments of the image. The order is entered, and will be processed and distributed without the need for further intervention unless an error condition occurs.

Each of the major processing routines is contained within SeaShark as a separate executable, called from the GUI, and returning error messages in a log that is interpretable by the GUI. This scheme has the advantage that new executables may readily replace existing ones, facilitating the rapid upgrade of algorithms if so required. Providing that the interface structure is preserved, new modules could be added by the user.

2.2. Products

SeaShark produces three sorts of product: archive, distribution, and fast delivery. The first is an internal format, used for the long term storage of satellite data, and forming the basis for generation of the remaining two sorts. The distribution products are in CEOS or CEOS-derived format; usually they constitute large portions of a satellite pass. The fast delivery product is for use when the turnaround time needs to be small. Generally, these are smaller (for example, 1000×1000 km) so that less processing is required. A single fast delivery product from AVHRR may be produced within a few minutes of the data reaching the computer system, whilst a SeaWiFS chlorophyll *a* product will take about $\frac{3}{4}$ hr (depending on computer specification) because of the computational demands of the atmospheric correction.

Typical products available from SeaShark are shown in Table 1. Since the package is undergoing continuous development, new products may be added, especially if there is a particular user-driven requirement.

AVHRR radiances are calibrated according to NOAA¹, subsequent revisions and Holben *et al.*²; SeaWiFS radiances are calibrated according to the methods described in the SeaWiFS Technical Report Series^{3,4}. The AVHRR SST algorithm is based on the split-window technique developed by McClain *et al.*⁵. An example of the NDVI algorithm is given in Huete⁶. The SeaWiFS algorithms are described in more detail in section 3.2.

<i>Product</i>	<i>SeaWiFS</i>	<i>AVHRR</i>
formatted Level 1	calibrated radiances	calibrated radiances (SHARP format)
formatted Level 2	water-leaving radiances	sea surface temperature (SST)
	chlorophyll <i>a</i>	vegetation index (NDVI)
	CZCS-type pigment	
	suspended particulate matter	
	coccolithophore	
	carotenoid	
	K_d	
	photosynthetically available radiation	
fast delivery	chlorophyll <i>a</i>	SST
		NDVI

Table 1. Typical products available from SeaShark.

3. SEAWIFS ALGORITHMIC BASIS

3.1. SeaWiFS atmospheric correction

The determination of the effects of the atmosphere are very important in the measurement of ocean colour from space. The method used within SeaShark is a PML-developed enhancement to the technique described by Gordon and Wang⁷. The latter is limited to case 1 (open ocean) waters because of the assumption of zero water leaving radiance in the 0.7-1.0 μm wavelength range, whereas there is a requirement for processing over case 2 (coastal) waters.

This has been addressed more recently by authors such as Land and Haigh⁸, and Moore *et al.*⁹. The latter technique is appropriate for use within an operation processing scheme, where computationally intensive methods are inappropriate because of the volume of data that must be handled. Briefly, the algorithm⁹ preprocesses the satellite data stream to establish the nature of the underlying water. This is done by deriving an Ångström-type exponent from the Rayleigh-corrected reflectances in bands 7 and 8, and using it to calculate a 'predicted' reflectance for band 6. If the difference between this and the actual Rayleigh-corrected reflectance exceeds a predetermined threshold (dependant upon the scene geometry), the underlying water is deemed to be case 2. A bright pixel model is then used to compare the measured reflectances with tabulations of known reflectance and suspended particulate matter (SPM) levels across SeaWiFS bands 6 to 8, and the estimated SPM contribution to reflectance is determined. This effects of the latter may then be corrected, and the corresponding concentration output. A flag is set to distinguish between case 2 sediment waters and case 2 gelbstoff waters.

A Gordon and Wang type scheme⁷ may now be used to perform the atmospheric correction, using either the unaltered case 1 reflectances, or the corrected case 2 reflectances.

3.2. SeaWiFS geophysical product generation

The result of the atmospheric correction is the production of water leaving radiances over the ocean, and zero values with a land flag set over land. The water leaving radiances may be processed into geophysical products, examples of which are shown in Table 1. The chlorophyll *a* and CZCS-type pigment ratio algorithms are based upon Aiken *et al.*¹⁰, with the coefficients contained in configuration files to allow for algorithmic tuning – a feature of all the geophysical product processing code. Carotenoid is derived using a band ratio algorithm of a similar form to the chlorophyll *a* algorithm. K_d (water clearness) is derived from three band ratios dependant upon the level of chlorophyll in the water¹¹.

The SPM and coccolithophore products are both derived from the Moore *et al.*⁹ atmospheric correction process. If a band ratio threshold is met, indicative of coccolithophore characteristics, then the SPM is regarded as being coccolithophore. Photosynthetically active radiation (PAR) is derived from tabulations based on Gregg and Carder¹² dependant upon the derived aerosol optical thickness, an Ångström-type exponent, and the total integrated column ozone concentration, and corrected for the illumination and viewing geometries and the Earth-Sun distance.

4. STARFISH

Ocean colour images are potentially valuable to the fishing industry – plankton are at the bottom of the food chain in the marine world and areas rich in plankton will indicate the likely locations of certain fish stocks. SST is currently used by fishing vessels – the detection of thermal fronts and water currents helps to locate particular fish species. Certain fish species have very specific requirements. For example, albacore prefer the thermal front between clear, warm offshore water

and the turbid, colder but nutrient-rich coastal waters¹³. The additional information about the chlorophyll level within the ocean provided by ocean colour sensors may be usefully combined with SST data to indicate likely fishing grounds for different species¹⁴.

The StarFish system uses fast delivery products of chlorophyll *a* and SST to generate maps of potential fish locations, which may be transmitted directly to vessels via Inmarsat, allowing them to improve their operating efficiency. Whilst vessels may be able to fish more efficiently, they may also fish with greater discrimination, thus reducing the problem of over-quota dumping. Ideally, fish location systems should be combined with vessel tracking systems, since much of the required hardware is common to both applications. This would have the dual benefit of decreasing the cost to the fishing company, whilst allowing the authorities to police fisheries more effectively. In Europe, a draft regulation has recently been submitted to the Council of Ministers requiring member states to use vessel monitoring systems to monitor fisheries.

5. CONCLUSION

The SeaShark processing software is due to go into service shortly with the European Space Research Institute (ESRIN) at their network of ground stations. It is simple to use, robust, and capable of handling operational demands, and is available for academic or commercial use. Potentially, it may be extended to process OCTS data from ADEOS, or other data from similar Earth Observation Satellites. Furthermore, it may be tuned to the needs of individual users.

6. ACKNOWLEDGMENTS

The development of SeaShark has been funded primarily by the European Space Research Institute and the VEGA Group plc. The scientific support of Drs Jim Aiken and Gerald Moore of PML is gratefully acknowledged, as is the development work of Trevor Barker, James Rickards, David Palmer, John Treloar, Roger Price, Jasen Mitchell, Claire Aspell and Michael Lever.

7. REFERENCES

- ¹ W. G. Planet, "Data extraction and calibration of TIROS-N/NOAA radiometers", *NOAA Tech. Memo. NESS 107 - Rev. I*, October 1988.
- ² B. N. Holben, Y. J. Kaufman, and J. D. Kendall, "NOAA-11 AVHRR visible and near-IR in-flight calibration", *Int. J. Rem. Sens.*, **11**, 1511-1519, 1990.
- ³ R. A. Barnes, A. W. Holmes, W. L. Barnes, W. E. Esaias, C. R. McClain and T. Svitek, "SeaWiFS prelaunch radiometric calibration and spectral characterization", *NASA Tech. Memo. 104566*, Vol. 23, 1994.
- ⁴ C. R. McClain, K. Arrigo, W. E. Esaias, M. Darzi, F. S. Patt, R. H. Evans, J. W. Brown, C. W. Brown, R. A. Barnes and L. Kumar, "SeaWiFS Algorithms, Part 1", *NASA Tech. Memo. 104566*, Vol. 28, June 1995.
- ⁵ E. P. McClain, C. C. Walton, L. L. Stowe, "CLAVR, cloud/clear algorithms and non linear atmospheric corrections for multichannel sea surface temperatures", *Fifth conference on satellite meteorology and oceanography*, 3-7 September 1990.
- ⁶ A. R. Huete, "Soil influences in remotely sensed vegetation-canopy spectra", *Theory and applications of optical remote sensing*, G. Asrar, 107-141, John Wiley and Sons, New York, 1989.
- ⁷ H. R. Gordon, H. R. and M. Wang, "Retrieval of water-leaving radiance and aerosol optical thickness over the oceans with SeaWiFS: a preliminary algorithm", *Appl. Opt.*, **33**(3), 443-453, 1994.
- ⁸ P. E. Land and J. D. Haigh, "Atmospheric correction over case 2 waters with an iterative fitting algorithm", *Appl. Opt.*, **35**(27), 5443-5451, 1996.
- ⁹ G. F. Moore, J. Aiken, S. J. Lavender and H. Botrell, "The atmospheric correction of water colour and the quantitative retrieval of biogeochemical variables in case 2 waters: application to MERIS", submitted to *Int. J. Rem. Sens.*
- ¹⁰ J. Aiken, G. F. Moore, C.C. Trees, S. B. Hooker and D. K. Clark, "The SeaWiFS CZCS-type pigment algorithm", *NASA Tech. Memo. 104566*, Vol. 29, June 1995.
- ¹¹ G. F. Moore, *personal communication*.
- ¹² W. W. Gregg and K. L. Carder, "A simple spectral solar irradiance model for cloudless maritime atmospheres", *Limnol. Oceanogr.*, **35**(8), 1657-1675, 1990.
- ¹³ J. J. Simpson, "Remote sensing and geographical information systems: their past, present and future use in global marine fisheries", *Fish. Oceanogr.*, **1**(3), 238-280, 1992.
- ¹⁴ A. F. G. Fiúza, "The use of remotely sensed data for operational fisheries oceanography", *Proceedings of the ocean climate data workshop*, edited by J. Churgin, Goddard Space Flight Center, 18-21 February, 1992.

Influence of late-summer storms on the horizontal variability of phytoplankton pigment determined by Coastal Zone Color Scanner images in the Gulf of St. Lawrence, Canada

César Fuentes-Yaco^a, Alain F. Vézina^b, Michel Gosselin^a, Yves Gratton^c and Pierre Larouche^b

^a *Dépt. d'Océanographie, UQAR, 310 allée des Ursulines, Rimouski (Québec) Canada G5L 3A1*

^b *Maurice Lamontagne Institute, DFO, P.O. Box 1000, Mont-Joli (Québec) Canada G5H 3Z4*

^c *INRS-Océanologie, 310 allée des Ursulines, Rimouski (Québec) Canada G5L 3A1*

ABSTRACT

The western Gulf of St. Lawrence (GSL) is characterized by high, persistent phytoplankton production and functions as the principal supplier of phytoplankton biomass for the central and eastern Gulf. The main objective of this study was to report on the evolution of a wind-induced phytoplankton bloom in this region. We used Coastal Zone Color Scanner images taken on 20, 22, 28, and 30 August 1980 to calculate phytoplankton pigment concentration, sea surface temperature and water reflectance fields. We coupled the satellite information with storm track, wind, air temperature, and bright sunshine data. A strong storm blew over the Gulf between 15 and 17 August, triggering upwelling and mixing processes that presumably made high nutrient concentrations available in the euphotic layer. High atmospheric pressure and southwesterly winds between 18 and 25 August allowed air and water temperatures to rise, stabilizing the water column and stimulating phytoplankton growth. A northern storm between 25 and 27 August associated with clear weather and low temperatures between 28 and 30 August, coinciding with the bloom decline. Water-normalized reflectance values suggested that the estuarine region was characterized by diatoms, the western-central GSL by a mixed composition of diatoms/small flagellates/coccolithophorids, and the eastern-central region by coccolithophorids and small flagellates. These blooms may be critical for fish recruitment. Cooling and warming of the water column by meteorological events seem to be intermittent but frequent at this time of year. The resulting nutrient input may support phytoplankton blooms of intensities similar to or higher than those recorded during spring in the western region of the Gulf.

Keywords: CZCS, phytoplankton, storms, remote sensing, upwelling, wind, Gulf of St. Lawrence.

1. INTRODUCTION

The Gulf of St. Lawrence (GSL) (Figure 1) is influenced by atmospheric and oceanic forcings ¹. During summer, frequent storms cross the Gulf from west to east or northeast with their centres lying over the Gulf, having a maximum incidence over the Gaspé Peninsula and Magdalen Shallows ². The surface circulation in the western Gulf in spring and summer is mainly driven by the buoyancy outflow from the estuarine waters of the St. Lawrence Estuary via the Gaspé Current ¹, but in late summer/early fall, the westerly winds become important, ^{3,4} promoting productivity of the system. Wind-driven upwelling have been documented in the northern Gulf ⁵ but their effect on production have not been directly observed.

Alongshore westerly winds at the mouth of the Lower St. Lawrence Estuary (LSLE) can also drive upwellings⁶ that enrich the Gaspé Current and stimulate its productivity. Studies using Coastal Zone Color Scanner (CZCS) images of the Gulf have shown high phytoplankton biomasses within the western Gulf in late summer and early fall⁷. The purpose of this study was to determine the influence of late summer/early fall storms on phytoplankton production in the western GSL.

2. METHODOLOGY

Meteorological time series for August 1980 for several regions of the GSL (Figure 1) were compared with the satellite information. The storm trajectories were identified using the map of principal cyclone displacement (*Mariners Weather Log*; NOAA, 1991) and atmospheric pressure maps (1000 mb) from the Atmospheric Environment Services (AES), Department of Environment, Canada. Wind and air temperature data come from a statistical model developed by the AES Scientific Services Division, which uses hourly information from land-based stations and ship measurements to extrapolate the most probable values over open-water sectors. Hours of bright sunshine recorded by the AES were used as indicators of light availability. CZCS images taken on 20, 22, 28, and 30 August 1980⁸ were used to calculate phytoplankton pigments (chlorophyll *a* plus phaeophytin) and reflectance. The methodology used has been described in a previous study⁷. Sea surface temperature (SST) was calculated from data contained in channel six of the CZCS, using the scale present in the raw files to transform gray levels into temperature (°C)⁹. The different phytoplankton groups were determined by analyzing the water reflectance in combination with the chlorophyll pigment patterns. The spectral range of the reflectance was used as an indicator of different optical qualities that could be attributed to specific phytoplankton groups¹⁰ and was then used to tentatively identify western GSL species by comparing our results with data from previous studies^{11,12}.

3. RESULTS AND DISCUSSION

3.1 Meteorological and oceanographic data

Between 15 and 17 August, the strongest storm of the month crossed the central GSL. The wind direction changed from northeasterly to northwesterly and wind speeds were up to 10 m s^{-1} for at least 24 h. From 18 to 25 August, a high pressure system with sunny days and rising air temperatures was accompanied by southwesterly winds with speeds generally below 5 m s^{-1} (Figure 2). The thermal channel data also showed sea surface temperature decreasing in the Gulf from west to east (Figure 3 *a, b*). From 26 to 29 August, the GSL was affected by the passage of another pressure system, but its main track was over northern Québec. Northwestery winds dominated over the Gulf from 27 to 29 August, but with lower velocities than during the southern storm (Figure 2). The storm was followed by moderate to high levels of bright sunshine but with slightly cooler air temperatures. The SST image of 28 August showed cooling of the surface layer, especially in the estuary and the Gaspé Current as well as in the eastern Gulf and Jacques-Cartier Strait (Figure 3 *c*). These cooling patterns intensified on 30 August, with upwelling patches seen along the south coast of Anticosti Island and the north shore of Jacques-Cartier Strait

(Figure 3 *d*). Both SST images taken during the northern storm indicate Ekman upwelling along the south shore of Anticosti Island, which has been previously observed with Advanced Very High Resolution Radiometer images ¹. Similarly, our study showed that the wind speed and direction during both storms were sufficient to force Ekman upwelling along the south shore of Anticosti Island following the first storm.

3.2 Phytoplankton pigment response

For the first time in the GSL, satellite images have been used to evaluate the mesoscale response of phytoplankton pigment to storms. On 20 August, the bloom started with a structure south of Anticosti Island (Figure 4 *a*) and two days later extended toward the Magdalen Shallows (Figure 4 *b*). On 28 and 30 August the bloom declined; relatively high biomass levels were still measured in warmer water patches in the central Gulf (Figure 4 *c, d*). In the LSLE, high phytoplankton pigments coincided with the coolest waters (Figures 3 *d* and 4 *d*, respectively). The reflectance data suggested contrasting optical characteristics of the eastern and western Gulf regions that could be linked to the pigment features. The values generally discriminate the diatoms in the Gaspé Current, the mixed flagellates in Anticosti Gyre and Honguedo Strait, and the coccolithophorids in eastern central GSL waters. The association of high biomasses and warm temperatures on the first two images can be explained as the result of phytoplankton growth concurrent with stabilization of the surface layer. The high irradiance and low wind conditions lasted several days, allowing the mixed layer enough time to warm and blend slightly, producing water column stratification. The pattern of the bloom decline on the second pair of images reinforces the association of phytoplankton development and warm temperatures. Except for the estuary, pigment levels fell in the cooler nearshore areas, probably due to upwelling of deeper chlorophyll-poor waters. These high chlorophyll and warm water patches were probably dominated by dinoflagellate communities. Shipboard observations confirm that dinoflagellates, particularly *Gyrodinium aureolum*, can dominate at this time ¹². In addition to production stimulation by buoyancy flow ¹ and coastal upwelling along the north shore ^{5,6}, the kinds of meteorological events we describe here might stimulate production over the western Gulf. Freshwater runoff is unlikely to be responsible for these phytoplankton blooms, since the runoff in the Gaspé Current is at its lowest at the end of summer ³. These blooms may be critical for fish recruitment, particularly herring. Since they spawn in the summer, the phytoplankton bloom following larval production may be more important than the one occurring before the larval release ¹³. Cooling and warming of the water column seems to be intermittent but frequent, and the resulting nutrient input may support strong phytoplankton blooms in the western region of the Gulf. This in turn may justify a reconsideration of the general concept of spring bloom-driven recruitment in the St. Lawrence ecosystem.

4. ACKNOWLEDGEMENTS

The authors thank M. Besner for the meteorological statistical model data and L. Devine Castonguay for improving the figures and the English. The Universidad Nacional Autónoma de México, the Université du Québec à Rimouski, and the Québec government provided scholarships to C.F.Y. during his Ph. D. studies.

5. REFERENCES

1. V.G. Koutitonsky and G.L. Bugden, "The physical oceanography of the Gulf of St. Lawrence: A review with emphasis on the synoptic variability of the motion". In: *The Gulf of St. Lawrence: small ocean or big estuary?* (Therriault, J.-C., ed.). Canadian Special Publication of Fisheries and Aquatic Sciences **113**, pp. 57-90 (1991).
2. M.C. Piccolo and M.I. El-Sabh, "Cyclone climatology of southeastern Canada", *Climatological Bulletin* **27** (3), 81-95 (1993).
3. G. Mertz, V.G. Koutitonsky, and Y. Gratton, "On the seasonal cycle of the Gaspé Current". In: *The Gulf of St. Lawrence: small ocean or big estuary?* (Therriault, J.-C., ed.). Canadian Special Publication of Fisheries and Aquatic Sciences **113**, pp. 149-152 (1991).
4. C. Fuentes-Yaco, A.F. Vézina, P. Larouche, Y. Gratton, and M. Gosselin, "Phytoplankton pigment in the Gulf of St. Lawrence, Canada, as determined by the Coastal Zone Color Scanner. Part 2. Multivariate analysis". *Continental Shelf Research*, (in press).
5. M.-C. Bourque, and D.E. Kelley, "Evidence of wind-driven upwelling in Jacques-Cartier Strait". *Atmosphere-Ocean* **33**, 621-637 (1995).
6. M. Couture, *Les remontées d'eau froide à l'embouchure de l'estuaire maritime du Saint-Laurent*. M. Sc. thesis, Université du Québec à Rimouski, Rimouski, Québec, Canada, 115 p., 1989.
7. C. Fuentes-Yaco, A.F. Vézina, P. Larouche, C. Vigneau, M. Gosselin, and M. Levasseur, "Phytoplankton pigment in the Gulf of St. Lawrence, Canada, as determined by the Coastal Zone Color Scanner. Part 1. Spatio-temporal variability". *Continental Shelf Research*, (in press).
8. C. Fuentes-Yaco, P. Larouche, A. Vézina, C. Vigneau, and M. Gosselin, "Catalogue of phytoplankton pigment images from the Gulf of St. Lawrence: Coastal Zone Color Scanner data from 1979 to 1981". *Canadian Data Report of Hydrography and Ocean Sciences* **135**, v + 91 p., 1995.
9. S.P. Williams, F.F. Szajna, and W.A. Hovis, *Nimbus 7 Coastal Zone Color Scanner (CZCS) Level 1 data product user's guide*. NASA Technical Memorandum 86203, 52 p., 1985.
10. M. Viollier and B. Sturm, "CZCS data analysis in turbid coastal water". *Journal of Geophysical Research* **89** (D4), 4977-4985 (1984).
11. M. Levasseur, L. Fortier, J.-C. Therriault, and P.J. Harrison, "Phytoplankton dynamics in a coastal jet frontal region". *Marine Ecology Progress Series* **86**, 283-295 (1992).
12. D. Blasco, L. Bérard-Therriault, M. Levasseur, and E.G. Vrieling, "Temporal and spatial distribution of the ichthyotoxic dinoflagellate *Gyrodinium aureolum* Hulburt in the St. Lawrence, Canada". *Journal of Plankton Research*, (in press).
13. Y. de Lafontaine, S. Demers, and J. Runge, "Pelagic food web interaction and productivity in the Gulf of St. Lawrence: A perspective". In: *The Gulf of St. Lawrence: small ocean or big estuary?* (Therriault, J.-C., ed.). Canadian Special Publication of Fisheries and Aquatic Sciences **113**, pp. 99-224 (1991).

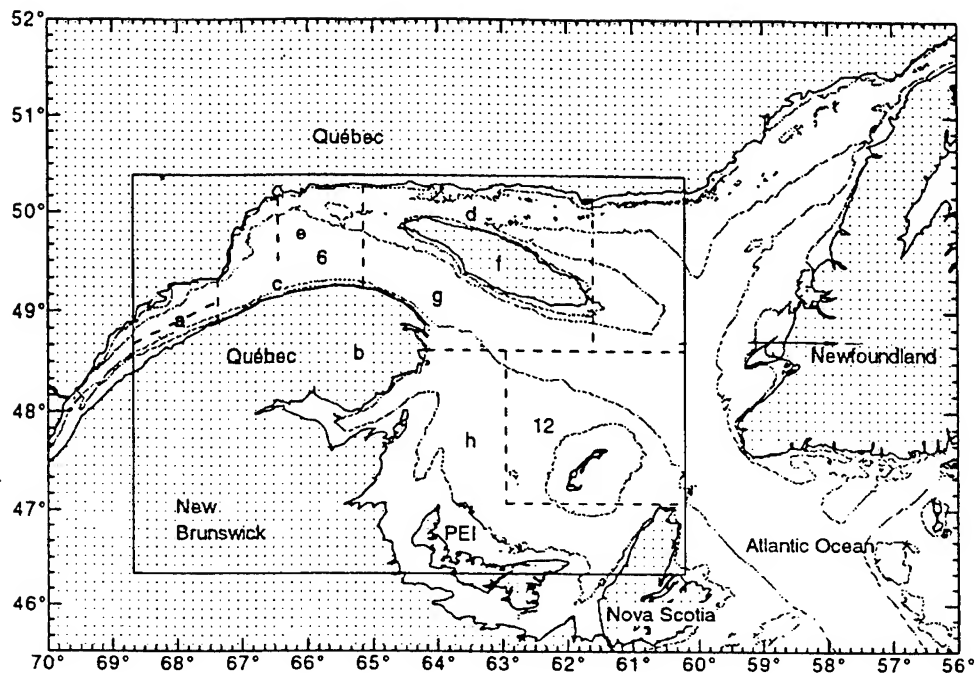


Figure 1. The Gulf of St. Lawrence; the inset rectangle indicates the area covered by the satellite images. The 50 and 200 m isobaths are shown. Wind regions are designated by dashed lines, only regions 6 and 12 are discussed. The letters refer to the regions mentioned in the text. a: Lower St. Lawrence Estuary, b: Gaspé Peninsula, c: Gaspé Current, d: Jacques-Cartier Strait, e: Anticosti Gyre, f: Anticosti Island, g: Honguedo Strait, h: Magdalen Shallows.

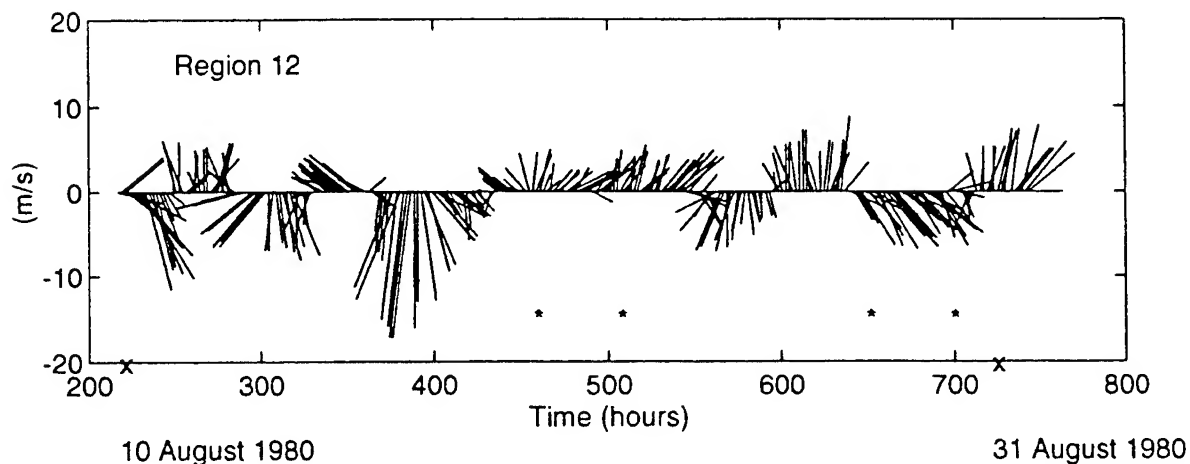


Figure 2. Wind in the central region of the Gulf of St. Lawrence between the 10 and 31 August 1980. Vectors are in m s^{-1} (north positive), showing the direction in which the wind is blowing. Sticks are drawn at two-hour intervals, asterisks indicate dates of CZCS images.

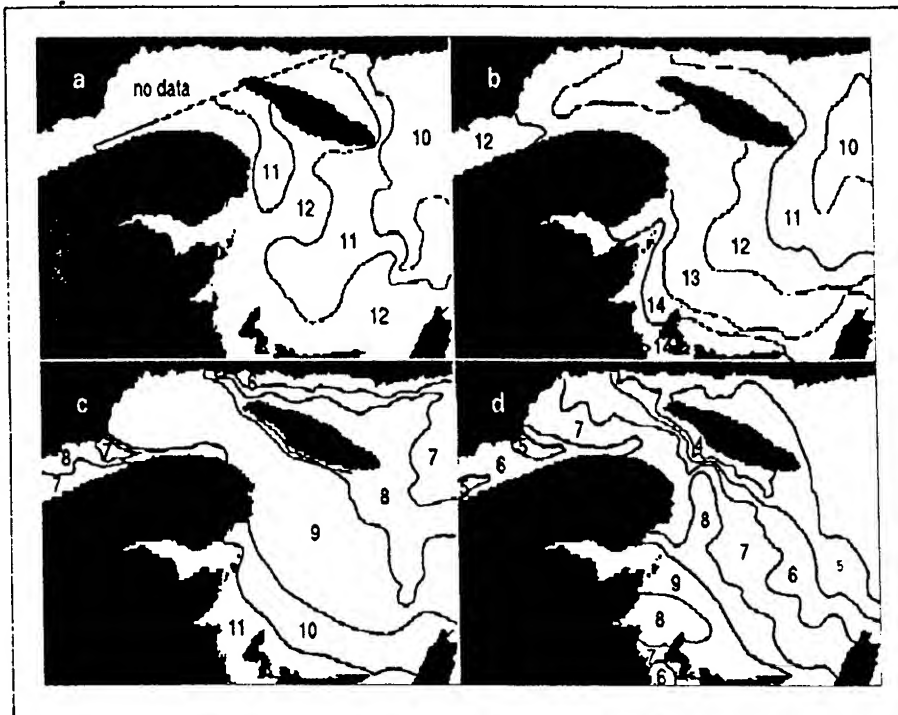


Figure 3. Sea Surface Temperature (degree Celcius)
a) 20, b) 22, c) 28, and d) 30 August 1980

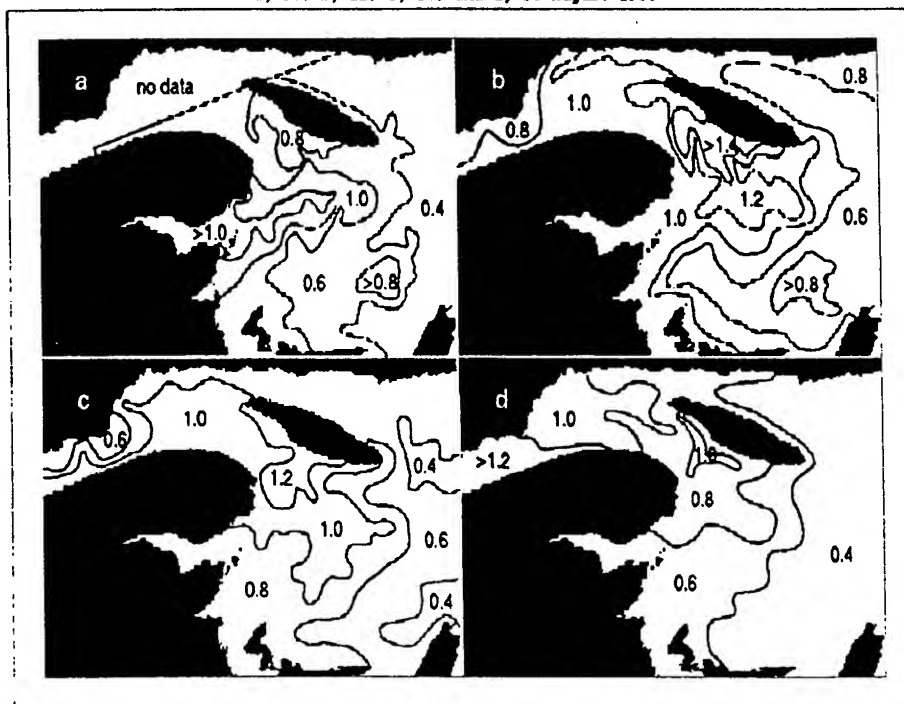


Figure 4. Chlorophyll a plus Phaeophytin (mg m^{-3})
a) 20, b) 22, c) 28, and d) 30 August 1980

Submarine lidar for the detection of chemical pollutants on the seafloor

Stefan Harsdorf, Manfred Janssen and Rainer Reuter

Carl von Ossietzky Universität Oldenburg, Physics Department
26111 Oldenburg, Germany

ABSTRACT

Ship accidents may cause containers and chemical pollutants to be released into the sea. For the recovery of a container or a non-mixing chemical on the seafloor, a fast and small-scaled location of such objects is an essential condition. Because of high turbidity in most coastal regions and the character and behaviour of sinking chemicals, conventional video cameras are often unsuitable. Therefore, a new optical instrument is to be developed which allows the inspection of objects on the seafloor with range gated video images, and a detection of substances by remotely measuring fluorescence on the seafloor and in the water column. It will be applied as the payload of a remotely operated vehicle (ROV) that is also equipped with other chemical and acoustical sensors for seawater analysis. Experiments in the laboratory have been carried out successfully, and first steps have been taken to realise a prototype.

The submarine lidar is an instrument which allows to record contrast enhanced images of containers on the seafloor, and to detect, locate, and classify the discharge of chemicals. Besides this application, it can be used for environmental monitoring, pipeline inspection, and oceanographic survey.

Keywords: seafloor imaging, range gating video, fluorescence lidar

1. INTRODUCTION

In coastal zones with high ship traffic, oil pollution may occur because of accidents and illegal discharges. Since 1993, the German Ministry of Transport has operated an airborne fluorescence lidar for maritime surveillance of the German responsibility areas in the North Sea and the Baltic Sea.¹ This fluorescence lidar is used to detect, identify, and quantify oil spills on the water surface, and to measure maritime parameters such as phytoplankton blooms.

Another approach to detect substances in the sea with remotely using lasers is the shipboard lidar. This type of instrument has been successfully installed on board RV "Polarstern" for measurements of turbidity, yellow substances and phytoplankton while the ship is on its way. It allows depth-resolved profiles to be derived down to 40 m water depth with 10 cm resolution, depending on the seawater turbidity.² Experience gained with this instrument, especially the collecting performance of a lidar at short distances,³ are fundamental for the design of the submarine lidar system.

Besides this, accidents of ships with chemical cargo have led to strong impacts on the marine ecosystem and to risks for pollution control and clean-up teams in recent years. In order to protect environment and people, a fast detection, location and identification of chemical pollutants in the sea is necessary. In accordance with the variety of substances and their properties, and of the individual water bodies and their optical characteristics, on the other hand, a number of strategies for different situations seem to be inevitable, including special equipment for the control of chemicals at sea.

Recent research has shown that remote sensing of swimming chemicals is applicable in the same way as for the detection of oil spills. However, optical remote sensing is limited by the penetration depth of light into the water, if underwater objects are concerned. In this paper, we present a new laser-based instrument, which has been especially designed for the inspection of lost cargo, and detection and classification of hazardous substances on the seafloor also in turbid coastal waters.

2. OBJECTIVES

Beside sonar, conventional video cameras are the standard tools for underwater imaging. In water, acoustic instruments possess a larger range than optical instruments. Because of the lower frequencies compared to light waves, the acoustical image resolution is mostly not high enough to detect e.g. leaks in sunken tanks and containers. Normally dissolved chemicals are neither detectable by standard video nor by sonar techniques. Pools of sunken chemicals on the sediment can hardly be seen on video images taken from above. Especially on coarse-grained sediment the contour of a sinker bubble adapts to the ground so that the low gradient of the index of refraction is mostly insufficient to provide a sufficient contrast in such images. By accidents ship cargo can be damaged, get lost and sink in the sea, and chemicals may spread on the seafloor because of leaks. In order to be prepared for such events and to react efficiently, the German Ministry of Transport intends to operate an ROV based sensor system in the North Sea and in the Baltic Sea. Essential requirements are the detection and inspection of lost cargo and the identification of toxic chemicals on the seafloor and in the water column in real time.

Because of the variety of possible scenarios, the system consists of several sensors developed by different institutions. The instruments use various chemical and physical principles and can be mounted to the ROV as the need arises.

3. METHOD

The submarine lidar is a combination of a fluorescence lidar and a range gating video camera. It is the payload of an ROV, realised by Mariscope, Kiel, Germany, which is also the platform for additional sensors, such as CTD, transmissometer, and pH probes, as shown in Figure 1. The system is specified for a maximum operation depth of 300 metres, with 3 kn maximum speed for application in regions with tidal currents.

The range gating video camera is able to take contrast enhanced images from the seafloor.⁴ Therefore it is used to search for and - in case of success - to inspect lost containers on the ground.

The fluorescence lidar is used to detect chemicals which are normally invisible on video images. The analysis of fluorescence spectra allows a classification of substances.

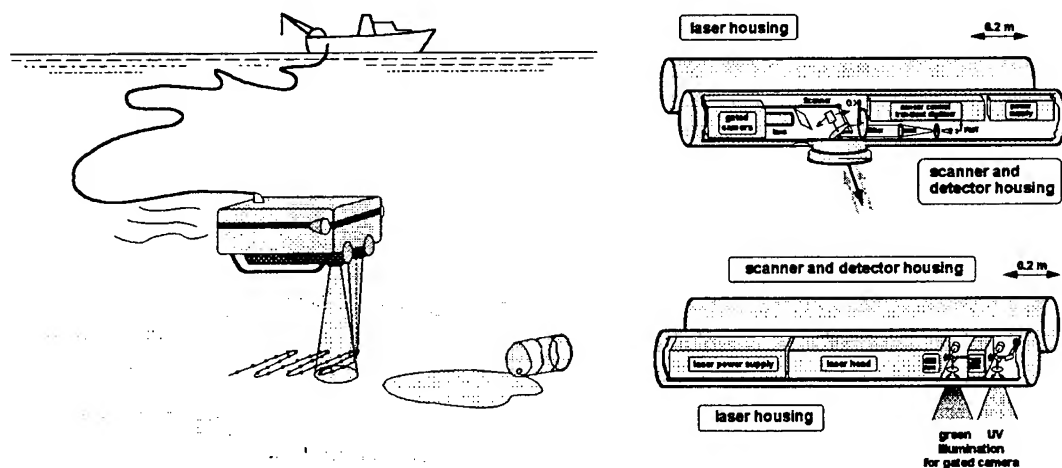


Figure 1: The submarine lidar system as a payload of an ROV

The submarine lidar is a remote sensing instrument. So data from the seafloor are remotely recorded, without any damage to the ecosystem. An altitude of a few metres above ground prevents sediment from rising and reducing visibility. In case of toxic substances spread out on the seafloor a contamination of the system is mostly avoided.

3.1 Range gating video

The submarine lidar uses the 2nd harmonic of a Nd:YAG laser (533 nm, 4 ns, 160 mJ) to illuminate the seafloor. Elastically scattered and reflected light is collected with a gateable intensified CCD camera. The exposure time of the camera is given by the gate-on period of the image intensifier. The beam divergence of the laser is the same as the camera field of view. Following Jaffe and Dunn⁵ the image is composed of a linear superposition of three different components, i.e. backscattering from the water body and from the target, and light backscattered by the target and forward scattered by the water body.

The first component does not include any information about the object. Because of the use of a short pulsed laser and according to the concept of lidar, it reaches the camera prior to the other two components. The minimum gate time of 5 ns allows to fade out the backscattered light from the water column, and to record only the light reflected by the object. This results in a contrast enhanced video image.

The second component consists of the light following the direct trace from the target to the detector without any scattering in the intervening water. Therefore, this component forms a sharp image of the observed object. The image quality is only influenced by the optical transfer function (OTF) of the CCD camera system.⁶

The third component consists of the light which is reflected by the object and then forward scattered in the water between object and camera. It hits the detector at the same time as the second component. Therefore it is not possible to separate the remaining two components by their time of flight. The result is a target image with reduced contrast. It can be calculated as a convolution of the second component and a function representing the optical characteristics of the water. The recorded image is modulated by the OTF of the water and the CCD camera system.

3.2 Fluorescence lidar

Upon detection of an object the 3rd harmonic Nd:YAG laser pulse (355 nm, 4 ns, 60 mJ) is applied with its original 0.5 mrad beam divergence, and the emission response of the water body between ROV and seafloor and of the seafloor itself is recorded at variable wavelengths between 380 and 700 nm with a PMT and a transient recorder with 500 Mhz sampling rate. This allows a maximum depth resolution of approximately 0.2 metre. The spatial resolution of approximately 0.36° is realised by a two-dimensional scanner. The analysis of time-resolved signals at specific emission wavelengths permits the detection, the exact location, and at least a classification of substances seeping out from a container.

Fluorescence signals from substances dissolved in the water column can be interpreted in the same way. Non-fluorescent substances in the water influence the penetration depth of fluorescence lidar due to absorption losses at the excitation wavelength. It has been reported recently that this effect can be utilised to indirectly estimate the concentration of non-fluorescent substances in the water column.⁷ The potential of this method will be investigated with lidar in more detail.

3.3 Technical layout

A schematic drawing of the submarine lidar is shown in Figure 1. The housing consists of two titanium cylinders, which contain the Nd:YAG laser as the light source, the gated camera and the detection unit of the fluorescence lidar, respectively. Since signals measured with lidar and gated camera originate from distances of a few metres only, electromagnetic interference produced by the pulse laser is very critical. The concept of separate cylinders for the laser and the detector assembly, which is most sensitive to interference, reduces this disturbing noise.

The laser has a pulse energy of 160 mJ at 532 nm and of 60 mJ at 355 nm, with a pulse duration of 4 ns. The use of tilting mirrors allows to realise several illumination modes which are specific to the fluorescence lidar and the gated video camera.

The fluorescence lidar detector consists of a telescope with 50 mm free aperture. The wavelength selection is made with a filter wheel, consisting of a 180 degree circular variable interference filter for the 400 to 700 nm wavelength range with ~15 nm resolution, and four interference filters which transmit between 355 and 400 nm. The laser induced emission is detected with a fast PMT and recorded by a pc card transient recorder with 8 bit

resolution and 500 MHz sampling rate. To enhance the dynamic range an 80 dB high speed logarithmic amplifier compresses the PMT signals before digitization with the transient recorder.

The submarine lidar is controlled by a miniature PC which selects the different sampling modes, operates the transient recorder and organizes the data transfer between the lidar and the deck unit on board the ship.

4. PRELIMINARY RESULTS IN THE LABORATORY

The two main objectives of the first phase of the project have been to prove the physical principle as well as to show the possibility of a technical realisation of an underwater lidar. Experiments in the laboratory have been done using a tank of 10 m length, 0.45 m width, and 0.45 m depth. On one side of the tank a quartz window is integrated as the interface between lidar and water column. To simulate underwater measurements, a laboratory version of the lidar has been realised, and different components such as lasers and receivers have been tested. The remote detection and classification of substances and objects has been investigated.

4.1 Contrast enhanced images

The OTF is a well defined measure for the performance of an imaging system. It can be calculated as the Fourier transform of the point spread function (PSF) of the system. As a complex function the OTF can be expressed as the product of the modulation transfer function (MTF) and the phase transfer function (PTF). In most cases of application the PSF is approximately a symmetric function so that the PTF describing phase shifts of single spatial frequencies could be ignored. The MTF represents the reduction of the amplitudes of the different spatial frequencies. The MTF of the different imaging systems realised in the laboratory has been measured using a method proposed by Sitter, Goddard, and Ferrel.⁸

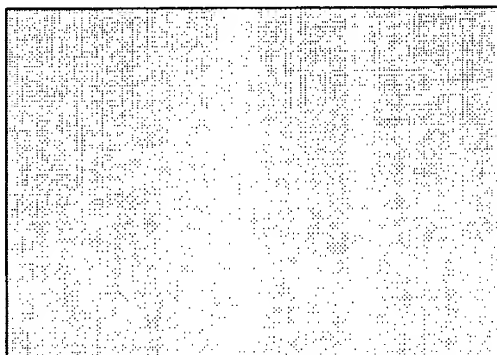


Figure 2: Target at 10 m distance with gate = ∞

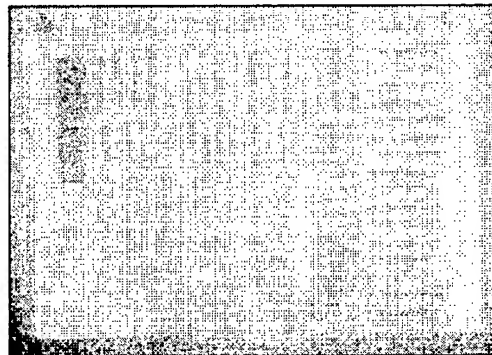


Figure 3: Target at 10 m distance with gate = 5 ns

Figures 2 and 3 show images of a test pattern in turbid water. In both cases the distance between camera and target was 10 m. As illumination source the green light of the Nd:YAG laser has been used. Figure 2 shows the image recorded with an exposure time of the camera which has been much longer than the pulse length and the time of flight of the laser light in the water. Therefore no gating effect is used, and the result is equivalent a conventional underwater video image. In figure 3 the same experiment has been repeated with a gate-on time of 5 ns. The delay between laser emission and gate was chosen so that the light backscattered by the target has reached the camera within the gate-on time. The light backscattered by the water column was not recorded. The images in figure 2 and figure 3 demonstrate the contrast enhancement of a range gating imaging camera. The MTF have been calculated to quantify this effect: figure 4.

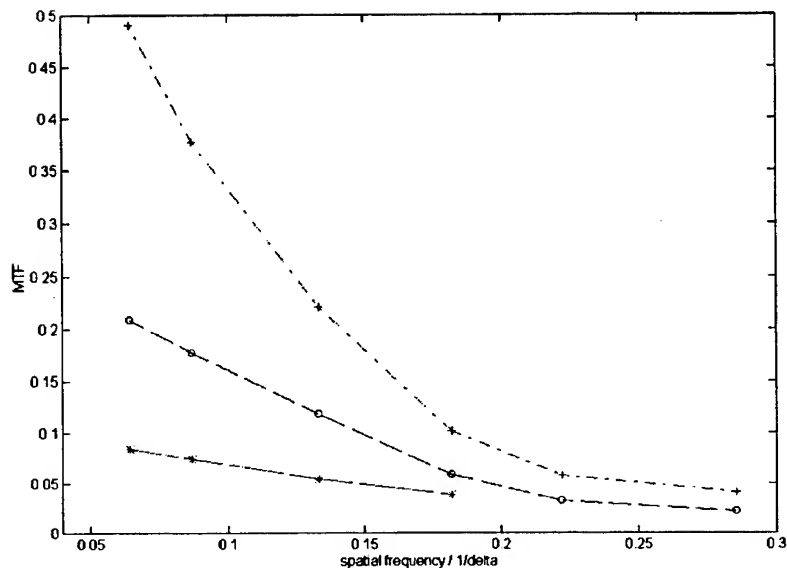


Figure 4: MTFs of figure 2 (*), figure 3 (o) and of a test pattern image in pure water (+)

The spatial frequencies are measured in units $1/\delta$ where δ is the distance between two neighbouring pixels of the image. According to Nyquist's theorem the maximal detectable frequency can therefore be $0.5/\delta$. The lowest curve in figure 4 belongs to the image shown in figure 2, and the medium curve has been calculated from the image in figure 3. The upper curve results from a image of the test pattern in 10 m distance taken in pure water with a gate of 5 ns. The effect of the water column can be neglected in this case, and in first approximation the MTF can be regarded as the MTF of the CCD camera system itself. It therefore represents an upper limit for possible MTFs and with it image quality.

Current research includes the application of the MTF for contrast enhancement, and of standard edge detection algorithms to emphasize the contours of objects within the seafloor image.

4.2 Fluorescence lidar spectra

The laboratory version of the fluorescence lidar has been realised using the components described in section 3.3 with exception of the telescope and the wavelength filters. The filter wheel has been replaced by a monochromator. A Schmidt-Newton type reflecting telescope with a mirror diameter of 150 mm has been used to collect the light. Between telescope and monochromator a 389 nm cut-off filter and a 10% neutral density filter were situated. Fluorescence has been induced by the 355 nm Nd:YAG laser beam.

Figure 4 to figure 7 show fluorescence lidar spectra measured with the laboratory version of the lidar. The distance is estimated as the product of the light speed c in the medium water and the time of flight in nanoseconds. A factor 0.5 must also be added because of the concept of lidar. So 10 ns correspond to ~ 0.1 m. Distance resolution is $(c * 2 \text{ ns})$, and wavelength resolution is 5 nm. The color code for the intensity is additionally plotted in figure 5. Colors are linear interpolated in figure 4 to 7. Spectra are averaged over 10 measurements.

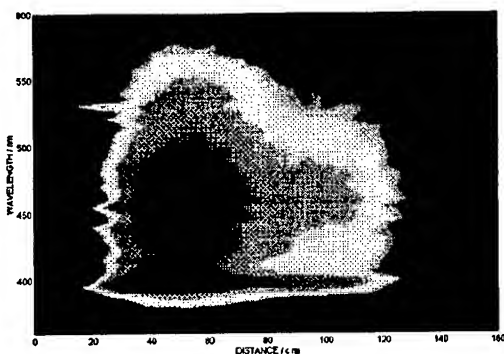


Figure 4: Lidar signal of clear water

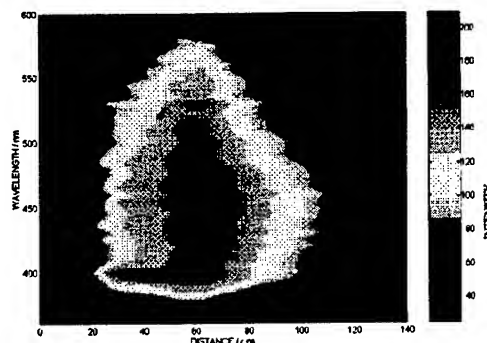


Figure 5: Lidar signal of a strongly fluorescent sinker at 4 m distance in clear water

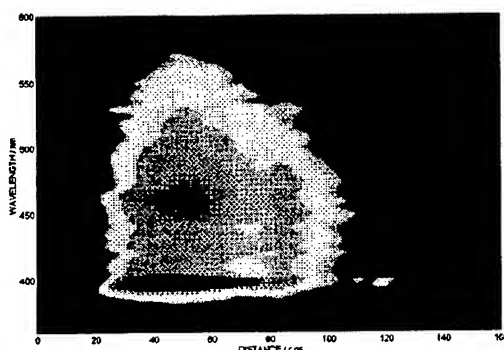


Figure 6: Lidar signal of a strongly fluorescent sinker at 7 m distance in clear water

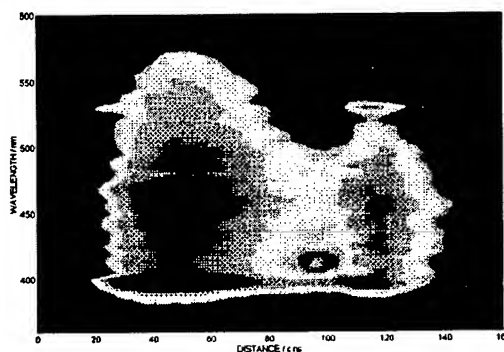


Figure 7: Lidar signal of a strongly fluorescent sinker at 9 m distance in clear water

Figure 1 presents the spectra of a 10 m water column. Raman scattering at 400 nm and yellow substance fluorescence with a maximum at 450 nm can be seen. The sensitivity function of the telescope³ and attenuation of the laser beam are responsible for the intensity distribution over distance. In figure 5, 6, and 7 a quartz cuvette with ~ 15 ml of a strongly fluorescent chemical (diethyl phenyl malonate) is placed at different distances in the tank (4 m, 7 m, and 10 m). From the spectra begin and end of the water column as well as the position of the chemical can be easily derived. Substances with a weaker fluorescence do not lead to local maxima but to a change in the slope.

The lidar spectra are convolved with the laser pulse width and fluorescence lifetime of substances. Future research will concentrate upon the deconvolution to enhance distance resolution and the development of algorithms for the automatic derivation of fluorescence spectra from different distances.

5. ACKNOWLEDGMENTS

The authors gratefully acknowledge the financial support of this project by the DLR Project Executive Department Environmental Protection and Technologies, Bonn, on behalf of the Federal Ministry for Research and Technology (BMBF), Germany. Furthermore, the authors wish to thank Mr. Frank Ahrenberg and Mr. Jörg Niehus for their work with the range gating video camera and the calculation of the MTF.

6. REFERENCES

1. R. Reuter, H. Wang, R. Willkomm and K. Loquay, "A laser fluorosensor for maritime surveillance: measurement of oil spills", *EARSeL Advances in Remote Sensing* 3(3), 152-169 (1995)
2. R. Reuter, R. Willkomm, G. Krause and K. Ohm, "Development of a shipboard lidar: technical layout and first results", *EARSeL Advances in Remote Sensing* 3(3), 15-25 (1995)
3. K. Ohm and R. Willkomm, "Collecting performance of a lidar at short distances", *EARSeL Advances in Remote Sensing* 3(3), 26-31 (1995)
4. L. H. Gilligan, "Range gated underwater viewing", *SPIE Vol. 980 Underwater Imaging* (1988)
5. J. S. Jaffe and C. Dunn, "A model-based comparison of underwater imaging systems", *SPIE Vol. 925 Ocean Optics IX*, 344-350, 26-31 (1988)
6. J. C. Feltz and M. A. Karim, "Modulation transfer function of charge-coupled devices", *Applied Optics*, 29(5), 717-722, (1990)
7. K.-H. Mittenzwey, G. Sinn, N. Roof and S. Harsdorf, "Improved lidar method for monitoring surface waters: experiments in the laboratory", submitted to *Int. J. Remote Sensing* (1996)
8. D. N. Sitter et al., „Method for the measurement of the modulation transfer function for sampled imaging systems from bar-target patterns", *Applied Optics* 34,(4), 746-751 (1995)

Simultaneous retrieval of oceanic and atmospheric properties using satellite remote sensing measurements

Th. Heinemann and J.Fischer

Freie Universität Berlin, Institut für Weltraumwissenschaften
Fabeckstrasse 69, 14195 Berlin, Germany

ABSTRACT

The retrieval of oceanic and atmospheric constituents from satellite measurements is usually performed separately. Near infrared radiances measured from satellites above open oceans contain only information on atmospheric parameters. Ocean colour is measured in the visible. In order to perform an atmospheric correction the information on the atmosphere has to be extrapolated from the near infrared to the visible. Due to multiple scattering effects this extrapolation is subject of large errors. To overcome the problem a retrieval algorithm was developed which uses measurements in the visible as well as in the near infrared, to perform the atmospheric correction and to derive oceanic properties in one step. This algorithm is based on a Neural Network. The method was compared to a nonlinear regression scheme handling visible and near infrared channels independently.

Upward nadir radiances in the spectral bands of SeaWiFS were simulated by an ocean-atmosphere radiative transfer model for a set of open ocean waters and atmospheric conditions. The two algorithms were initialized and tested with these data in order to perform the retrieval of phytoplankton concentration and aerosol optical depth.

A stability analysis has been applied to all results. Aerosol optical depth can be retrieved well by a linear regression scheme. For the phytoplankton retrieval the results for the Neural Network are more accurate and more stable according to randomly distributed errors. The regression method is less sensitive to correlated errors such as surface pressure changes but the higher stability according to noise still recommends the use of the Neural Network.

Keywords: atmospheric correction, SeaWiFS, neural network, phytoplankton, aerosol optical depth

1. INTRODUCTION

Estimating the temporal and spatial distribution of marine phytoplankton on a global scale is the major aim of the new generation of satellite ocean colour sensors, such as SeaWiFS, OCTS and MERIS. Since the atmospheric scattering and absorption dominates the signal at the satellite over the ocean, a very accurate atmospheric correction of ocean colour data is mandatory. The most variable scattering constituent in the atmosphere is aerosol. The retrieval of aerosol properties is not only a part of the atmospheric correction, but also important for climate studies. Aerosol retrieval over ocean surfaces is usually performed in the red and near infrared spectral region, where the water leaving radiance is negligible. For the atmospheric correction, results obtained in this spectral domain have to be extrapolated to the green and blue channels which are used for the retrieval of the oceanic properties. Information about the atmosphere in the visible channels is not used.

Analytical linearizations to perform an atmospheric correction are not sufficient due to the strong multiple scattering effects especially in the blue (mainly by the interaction between Rayleigh scattering and aerosol scattering). Statistical and semi statistical retrieval schemes using inverse modelling or look up tables² based on radiative

transfer calculations have been proposed to perform the retrieval of ocean constituents from satellite measurements. We tried to describe the large simulated data sets by a small number of parameters.

A method of data approximation was tested which uses the radiances in the visible and in the infrared to perform an atmospheric correction and to retrieve phytoplankton simultaneously. This purely statistical method based on a neural network was compared to a semi statistical method using regression schemes. The regression method first performs the atmospheric correction and then retrieval of ocean properties.

2. SIMULATION OF RADIANCES AT TOP OF ATMOSPHERE

For more than 1000 different combinations of oceanic and atmospheric conditions, upward nadir radiances at top of atmosphere for the eight SeaWiFS channels were simulated. These data are referred as *training data*. The simulations were performed with the radiative transfer model MOMO.³ MOMO is a coupled ocean atmosphere model based on the matrix operator theory. Comparisons with an ocean-atmosphere Monte Carlo model as well as comparisons with airborne measurements are showing very good agreement. An ocean surface can be considered. The type and concentration of atmospheric aerosols and of oceanic plankton are introduced by their optical properties extinction coefficient, single scattering albedo and phase function.

All simulations are performed twice. First with the complete ocean atmosphere model to simulate radiances as measured by a satellite and then with a black ocean (no water leaving radiance) to calculate the atmospheric path radiances. Radiances in the sunglint area are excluded.

The optical properties of aerosols are calculated by Mie calculations. The size distributions and complex refractive indices are taken from WCP-112.¹ The absolute amount of aerosol is given by their total optical depth at 550nm. As vertical profile an exponential decrease of the extinction from the ocean surface to the tropopause was assumed. 90% of the aerosols are below 2500m.

A flat water surface was used for all simulations. The ocean water body for the simulations is homogeneous with a depth of 75m. Only scattering and absorption by pure water and phytoplankton is considered. Optical properties of phytoplankton are calculated according to Morel and Gentili 1991.⁴ The phase function is taken from Petzold 1980.⁵

The variable parameters of the simulations are the total aerosol optical depth, the aerosol type and the phytoplankton concentration. Aerosol type variations are performed by mixing up maritime and continental standard aerosols. The three variable parameters are randomly distributed within a given range. The aerosol optical depth varies between 0.0 and 0.5. Aerosol type variations were performed between 100% maritime and 100% continental aerosol. For the phytoplankton the concentration range is 0.01 to 1.5 $\mu\text{g/l}$. A more realistic probability distribution of the variable parameters will surely improve the reliability of the obtained results and error ranges.

Two additional sets of radiative transfer simulations with the ocean atmosphere model have been performed to obtain test data sets for the retrieval algorithms: For the test of the algorithm performance under perfect conditions 400 cases were simulated without any additional changes. The surface pressure was increased to 1025hPa for 600 cases. This change includes an increase in the Rayleigh scattering and in the absorption due to atmospheric oxygen in SeaWiFS channel 7.

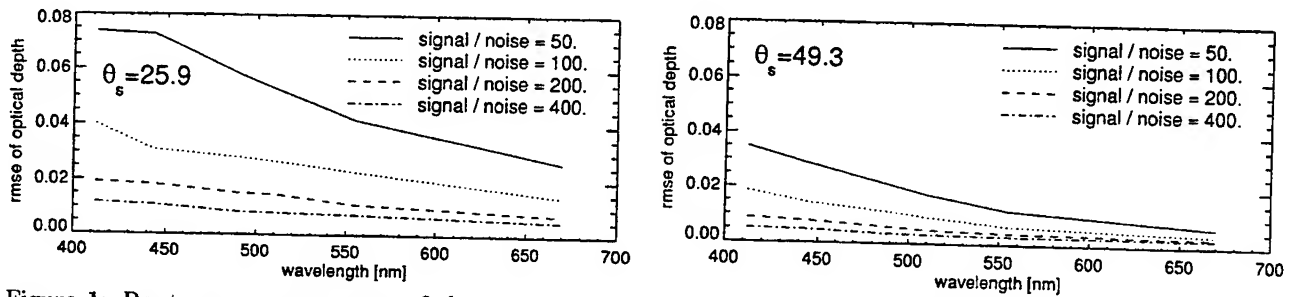


Figure 1: Root mean square error of the aerosol optical depth retrieval by a linear regression; 4 different noise levels; left: sun zenith 25.9°, right: sun zenith 49.3°

3. ALGORITHM DEVELOPMENT

3.1. Regression scheme

The determination of phytoplankton concentrations by a regression of the ratio between the water leaving radiances of two channels in the visible range (blue green ratio) from satellite data requires an atmospheric correction of both channels. The satellite radiance L_{sat} is described by the following expression:

$$L_{sat} = L_A + L_r + L_w T \quad (1)$$

Where $L_A = L_a + L_{ar}$ is the sum of multiple scattering aerosol path radiance L_a and interaction effects of aerosol and Rayleigh scattering L_{ar} . L_r is the multiple scattering Rayleigh path radiance in absence of aerosol. The diffuse transmittance factor of the atmosphere can be expressed as a function of sun zenith angle θ_s , the diffuse transmission by air molecules T_R and the aerosol optical depth τ_a .

$$T = e^{-\tau_a C_t} T_R \quad (2)$$

with

$$C_t = \frac{c_0}{\cos \theta_s} - c_1 \quad (3)$$

The diffuse aerosol transmittance factor C_t depends on the phase function and on the strength of multiple scattering. It is considered constant in this study for given sun zenith angle θ_s and wavelength λ .

In order to derive $L_w(\lambda)$ from satellite measurements $L_r(\lambda)$ and $C_t(\lambda)$ as well as $L_a(\lambda)$ and $\tau_a(\lambda)$ for every case must be known. The Rayleigh path radiance L_r is the top of atmosphere radiance for a clear sky over black ocean and can be estimated for a given surface pressure. The development of retrieval methods for $\tau_a(\lambda)$ and $L_a(\lambda)$ and the determination of C_t is described in the following subsections.

3.1.1. Linear regression of the aerosol optical depth $\tau_a(\lambda)$ It has been shown by Fischer et.al.⁶ that the aerosol optical depth at 550nm can be derived from the radiances in SeaWiFS channel 7 and 8 by a linear regression scheme. A previous subtraction of Rayleigh path radiances is not required for this method. In this paper the linear regression approach is applied to the retrieval of the spectral aerosol optical depth. Fig.1 shows the noise dependence of the root mean square error (rmse) of aerosol optical depth. Two different sun zenith angles are displayed.

3.1.2. 2-dimensional regression of the aerosol path radiance $L_a(\lambda)$ Since the multiple scattering effects in channel 7 and 8 are small, a linear approach for the retrieval of the aerosol optical depths is justified. Due to

multiple scattering effects the relation between aerosol optical depth $\tau_a(\lambda)$ and aerosol path radiance $L_a(\lambda)$ in the green and blue channels is nonlinear. Therefore a two dimensional quadratic regression has been performed to describe the relationship between $L_a(\lambda)$, the path radiance in channel 7 ($L_A(765nm) = L_{sat} - L_r$) and the ratio of the path radiances in channel 7 and channel 8 ($\epsilon = L_A(765nm)/L_A(865nm)$). In this description $L_A(765nm)$ bears mainly the information about the absolute aerosol concentration, while ϵ describes the aerosol type. The results indicate an unambiguous derivation of $L_a(\lambda)$ except for high sun zenith angles ($\theta_s > 70^\circ$).

3.1.3. Determination of the transmittance factor C_t and the phytoplankton concentration A first guess phytoplankton concentration retrieval is performed for the visible SeaWiFS channels by a quadratic regression of the phytoplankton concentration c versus $L_w(\lambda)$. Equation (1) is used to calculate $L_w(\lambda)$ from the satellite radiances L_{sat} . For this approach L_A and τ are retrieved as described before. The factor C_t is varied in order to minimize the rmse of the retrieved phytoplankton concentrations versus the phytoplankton concentrations used for the simulations.

The $\tau(\lambda)$, $L_a(\lambda)$ and $C_t(\lambda)$ are used (equation (1)) to calculate the water leaving radiances for all channels in the visible. This completes the atmospheric correction. Now a simple regression to a blue green ratio (channel 2, 443nm and channel 5, 555nm) is performed to retrieve the phytoplankton concentration.

3.2. Neural network

neural networks are statistical tools to perform nonlinear function approximations. In present geo-sciences several types of nets are applied to many different purposes. We used a simple one (hidden) layer backpropagation network to describe the nonlinear relation between top of atmosphere radiances in 4 different SeaWiFS channels on the one side and aerosol optical depth and phytoplankton concentration on the other side.

For the calculation of the activation of all neurons we used a *sigmoide* function.⁷ All links between input and hidden and between hidden and output layer are defined. The hidden layer consists of 14 neurons. The input data for the network are the *reduced* radiances $L_A = L_{sat} - L_r$ in channel 7, 2 and 5 as well as the ratio of L_A in channel 7 and channel 8 ($\epsilon = L_A(765nm)/L_A(865nm)$). Two output neurons according to the aerosol optical depth and the phytoplankton concentration are defined. A specific neural network is trained for every simulated sun zenith angle. Since the aerosol retrieval by the neural network showed less performance than the linear regression (see below), the nets were optimized for the retrieval of phytoplankton concentration.

4. RESULTS

The performance of the two different approaches to perform an atmospheric correction and to derive the phytoplankton are tested with the two simulated test data sets.

The aerosol optical depth can be retrieved with high accuracy and low noise sensitivity by the linear regression approach (see Fig.1). The results obtained by the neural network are less accurate for this purpose. A neural network performs a nonlinear approximation of the relation between input and output data. Usually an approximation with a higher order is more sensitive to small deviations and errors in the input data than a linear approach. It is not useful to apply a neural network to a simple linear relation such as the retrieval of aerosol optical depth.

For the phytoplankton concentration retrieval a nonlinear procedure following three steps must be applied to extract the information by a regression scheme. Here the approximation by a neural network is very promising. Fig.2 shows a scatterplot of phytoplankton concentrations retrieved from simulated top of atmosphere radiances (test data) versus the phytoplankton concentrations used to simulate these radiances. The rmse of the neural network scheme is lower for all given sun zenith angles. Especially for higher phytoplankton concentrations the neural

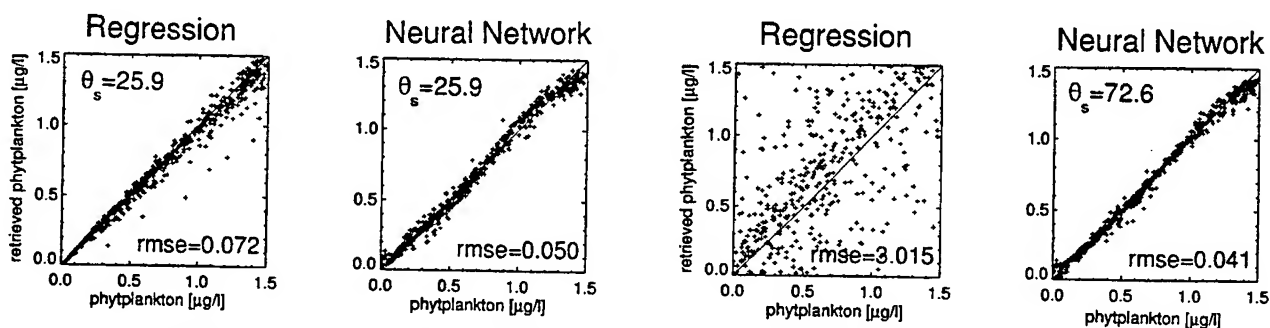


Figure 2: Scatterplot of the phytoplankton concentration versus the phytoplankton concentration retrieved by the neural network or by the regression scheme; left: sun zenith 25.9° , right: sun zenith 72.6°

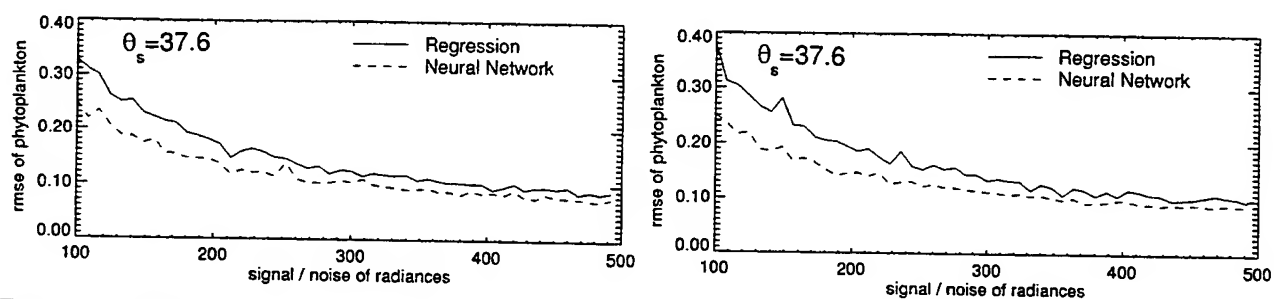


Figure 3: a:(left) Root mean square error of the phytoplankton retrieval for the two methods b:(right) Root mean square error of the phytoplankton retrieval for an uncertainty in the surface pressure of 12hPa

network is more accurate. Due to problems in the determination of L_A (see above) the retrieval of phytoplankton by the regression scheme is not possible for large sun zenith angles. The neural network shows even for those sun angles a high performance.

A typical problem for a neural network algorithm is the high sensitivity to errors in the input data. To test the sensitivity of the two algorithms we added to the 400 test cases a noise according to different signal to noise ratios. In Fig.3a the rmse of the phytoplankton retrieval is displayed as a function of the introduced noise. The neural network is not more sensitive to noise than the regression scheme.

Surprisingly the physical knowledge introduced in the regression scheme by equation (1) does not increase the performance significantly against the purely statistical neural network. The network cannot only use the near infrared channels for the atmospheric correction, but can also obtain information on the atmosphere from the channels in the visible. In addition the neural network can describe higher orders of nonlinearity than the quadratic regression. This feature is necessary for the purposes of a nonlinear atmospheric correction.

The previous tests were performed with data of the same type used for the development of the algorithms. A typical error source for the atmospheric correction of ocean colour data is an uncertain knowledge of the surface pressure. We tested the algorithms with data simulated for a 12hPa higher surface pressure. Introducing an error that influences the simulated channels in a correlated manner (like the pressure change) is more difficult to handle by the neural network than by the regression scheme. Without noise the performance of the regression is higher than that of the neural network for this case. An adding of instrumental noise to the radiances affects more the regression more than the neural network (see Fig.3b). Though the neural network retrieval scheme is more reliable when more realistic measuring conditions are introduced.

5. CONCLUSION AND OUTLOOK

Statistical analysis of nadir satellite radiances can be used to develop retrieval schemes for aerosol optical depth and phytoplankton concentrations over open oceans. A linear regression scheme describes well the relation between the satellite radiances in the near infrared channels and the aerosol optical depth. The retrieval of oceanic components like the phytoplankton contents is much more difficult to perform by a regression algorithm. Several steps are necessary to perform an atmospheric correction of the channels in the visible using the atmospheric information from the channels in the near infrared.

The atmospheric correction of ocean colour data can be improved if the information from channels in the visible and in the near infrared is used. A neural network is a tool to handle highly nonlinear correlations between several parameters. It is a suitable method to describe large data sets by a small number of parameters. In this study the neural network performance was at least as high as the performance of the regression scheme. Even though both approaches have substantially room for improvements.

For the application of these methods to satellite data the whole range of satellite viewing geometries must be covered. More aerosol types, especially background aerosol, desert dust and stratospheric aerosol should be introduced, to study their effects on the retrieval. Further error sources like surface roughness and systematic calibration errors must be considered, too. A combination of the regression scheme and the neural network might also improve the performance. A neural network is able to handle highly correlated information, which allows us to use all channels of the ocean colour sensors in one retrieval scheme. Though more complex water structures including gelbstoff and suspended matter can be investigated by this method.

6. REFERENCES

- [1] World Climate Programme, *A preliminary cloudless standard atmosphere for radiation computation*, WMO/TD-No.24, Geneva, (1986)
- [2] H. Gordon and M. Wang, "Retrieval of water leaving radiance and aerosol optical depth over the oceans with SeaWiFS: a preliminary algorithm", *Applied Optics*, Vol. 33, No. 3, pp. 443-452, (1994)
- [3] F. Fell, J. Fischer, D. Buckton "Validation of a numerical model for computing atmospheric and underwater light fields", Final Report - Mast II MAS2-CT92-0020, CEC, (1995)
- [4] A. Morel and B. Gentili, "Diffuse reflectance of oceanic waters: its dependence on on Sun angle as influenced by the molecular scattering contribution", *Applied Optics*, Vol. 30, No. 30, pp. 4427-4438, (1991)
- [5] T.J. Petzold, "Volume scattering functions for selected natural waters", SIO Ref. 72-78, (Scripps Institution of Oceanography, San Diego, Calif.), (1972)
- [6] J. Fischer, T. Heinemann, R. Preusker, "Retrieval of aerosol properties from MERIS and SeaWiFS measurements", submitted to: *Journal of Geophysical Research*, (1996)
- [7] P. Rojas, *Theorie der neuronalen Netze*, Springer-Verlag, Berlin, (1993)

A bio-optical time series collected in coastal waters for SeaWiFS calibration and validation: large structure shadowing considerations

Edward Kearns

Computer Sciences Corporation
National Data Buoy Center
Stennis Space Center, MS 39529

Rodney Riley

Computer Sciences Corporation
National Data Buoy Center
Stennis Space Center, MS 39529

Catherine Woody

National Oceanic and Atmospheric Administration
National Data Buoy Center
Stennis Space Center, MS 39529

ABSTRACT

A suite of bio-optical sensors is to be deployed by the National Data Buoy Center (NDBC) in coastal waters in anticipation of the launch of the SeaWiFS instrument aboard the SeaStar satellite. Surface-referenced solar irradiance, upwelling radiance, chlorophyll concentration, pressure, temperature, conductivity, and oxygen concentration will be measured at depth. Hourly reports of time averages of these quantities will be made available through GOES satellite messages which will be disseminated through normal NDBC data channels as well as through the Internet in near-real time. High resolution (6 Hz) time series data will be collected for post-processing to evaluate the hourly measurements. These data will provide valuable ground-truth information for SeaWiFS calibration. The bio-optical sensors and the data recording and transmission systems have been installed for field testing at the Army Corps of Engineers facility in Duck, North Carolina. The final installation of the sensor system has been delayed by damage suffered by the targeted platform (Ambrose Light Tower in the New York Bight) as well as by a review of sensor mounting strategies inspired by a tower shadowing study conducted by NDBC.

Radiometric measurements taken by NDBC near the Apache 990 oil production platform located in the northern Gulf of Mexico show evidence of significant shadowing effects from such large (≈ 24 m square, elevation 22.0 m) ocean structures. Approximations derived from the least-squares fit of an analytical function to data collected during overcast conditions indicate that distances from the structure of greater than 100 m must be achieved to avoid any shadowing effects.

Keywords: bio-optical, radiometric, time series, shadow, shadowing, structure, SeaWiFS, validation

1 INTRODUCTION

As a part of the calibration/validation efforts related to NASA's SeaWiFS ocean color sensor system which will be mounted upon the SeaStar satellite, NDBC has been tasked with the design, deployment, and operation of a bio-optical sensor system in coastal (case II) waters. The system consists of instruments at three levels: at the 0⁺ m level, it includes a Satlantic MVD above-water cosine irradiance sensor, standard NDBC meteorological and wave package; at 5 m depth, a Satlantic OCI-200 cosine irradiance sensor, Satlantic OCR-200 radiance sensor, Sea-Bird SBE 16-03 conductivity and temperature sensors, and Viatran pressure transducer; at 9 m depth, a Satlantic OCI-200 cosine irradiance sensor, Satlantic OCR-200 radiance sensor, Sea-Bird SBE 16-03 conductivity and temperature sensor, Sea-Bird SBE 23B Beckman dissolved oxygen sensor, Viatran pressure transducer, WETLabs AC-9 chlorophyll absorption sensor, and a WETLabs fluorometer. The means and standard deviations of the data from each sensor (sampled each hour for 3 minutes at 6 Hz) will be transmitted hourly through the GOES satellite. The raw data will be recorded on a hard disk for later retrieval and subsequent post-processing to evaluate the hourly measurements.

The bio-optical sensor suite has been deployed on an easily maintainable trolley/track mounting system at the Army Corps of Engineers pier at Duck, NC since late October, 1996. This test deployment will allow NDBC to establish the reliability of the sensors, system software and hardware, satellite transmission hardware, and data handling systems prior to the final deployment. The original target platform for the final deployment of the system was Ambrose Light Tower, located 8 miles outside of New York Harbor. This tower was severely damaged by a collision with a tanker on October 5, 1996, and consequently will not be used as the deployment platform. An alternate deployment site and platform is under investigation; platform considerations have also been influenced by the results of a recent shadowing study conducted by NDBC.

In anticipation of the deployment of the bio-optical sensor system at Ambrose Light (a darkly colored four-pile structure with an approximately 35 m × 35 m platform mounted 20.6 m above mean low water), NDBC undertook a study to estimate the effects that such a sizable structure would have upon radiometric measurements taken nearby. This platform shadow study was conducted at the Apache 990 oil rig (also a four pile structure, painted bright yellow, measuring approximately 24 m × 24 m with its main deck located 22.0 m above mean low water) in the Gulf of Mexico on July 31 and August 1, 1996. This platform approximated the size and shape of Ambrose Light tower while providing convenient access from the NDBC facilities that are located on the Gulf Coast of Mississippi. The platform shadowing study has produced significant results that will affect the final design of the NDBC bio-optical sensor system mounting scheme, and may have important implications for any radiometric measurements taken near large ocean platforms. A discussion of the experiment and its results will comprise the bulk of this report.

2 METHODS

The instrumentation used for the NDBC platform shadowing experiment consisted of two sets of Satlantic radiometers (each set consisting of one upward-looking cosine collector which measures downwelling irradiance, and one downward-looking narrow field-of-view collector which measures upwelling radiance) mounted inside floating PVC frames that were tethered by lines to the tower and a research vessel. The depth of the radiometers could be set at either 1, 3, or 5 meters. One set of radiometers was kept as a reference some distance (far field) from the ship and tower, while the other (the so-called test set) was moved in prescribed increments from the far field toward the tower. The data from each set of radiometers were collected continuously and simultaneously upon a PC on board the ship. Irradiance and radiance measurements were taken for the 412.8, 443.5, 490.2,

509.2, 555.4, 665.6, and 683.5 nm wavelengths.

The basic method used to infer the effect of the platform shadow upon the irradiance and radiance measurements was simply to use the reference data to remove any effects other than the platform shadow (including varying sun angle, clouds, and surface conditions) from the data collected by the test radiometers as they were drawn towards the platform. Data that were collected when the radiometers were in motion, i.e. being pulled by the lines towards the platform or ship, were of poor quality, presumably due to the motion of the radiometers as they passed horizontally through the water. These data were deleted from the record. The radiometers were halted for several minutes at prescribed distances from the leg of the platform, during which time they sampled the ambient light field at 6 Hz. This high sampling rate (relative to surface waves) allows the effects of wave focusing to be averaged out of the data. This was accomplished through the application of a median filter of 5s width, which has the desired quality of suppressing any spikes in the time-series data. The mean and standard deviation of the difference of the filtered test and reference signals were computed for each prescribed distance from the platform. These differences were then recast as percentages of the difference at the far field position. A hyperbolic tangent function (actually $y(x) = A(1 - B \tanh(Cx))$) was fit in a least-squares sense to the averaged data for each iteration. It was desired that this simple model of the decay of the effect of platform shadow with increasing distance from the tower could then be used to estimate the far field values given the values collected near the tower leg.

Each iteration of the experimental procedure was necessarily classified as sunny or overcast. On overcast days, the downwelling radiance is entirely comprised of diffuse skylight (indirect, scattered light), the magnitude of which is highly dependent on the percentage of unobstructed sky which may be seen by the radiometer. While on sunny days the platform will still obscure a similar portion of skylight, the contribution to total irradiance from this indirect source was found to be a fraction (< 20%) of that of the direct insolation.

3 DATA

The data collection suffered from a few technical difficulties and cloud conditions, resulting in several casts that were not very instructive. For example, the radiometers were not level for one cast, another cast's test data was contaminated by electronic noise, and another cast started under cloudy conditions but was exposed to direct sunlight as the instrument neared the tower. Nevertheless, adequate examples of the effects of the platform shadow were recorded for both sunny and overcast conditions.

A representative cast from both a sunny and overcast day are depicted in this section. For the sake of brevity, only the downwelling irradiance ($E_d(\lambda)$) at $\lambda = 443.5\text{nm}$ will be discussed; the results from the measurements of upwelling radiance ($L_u(\lambda)$) and from other wavelengths are not significantly different than those for $E_d(443.5)$. Figure 1 shows the reference radiometers' raw measurements of E_d versus time; Figure 2 shows the corresponding values for the test radiometers. The sunny day's data are represented by crosses, and the overcast day's data by circles. The gaps in the data record are those time periods during which the radiometers were in transit to the next prescribed distance. The varying magnitude of E_d under sunny conditions, primarily caused by passing clouds, is troublesome since it is desired to examine the effects of the platform shadow when there is direct sunlight. Therefore, all reference E_d with a magnitude of $< 38 \mu\text{Wm}^{-2}$ (points) and the corresponding test E_d data (points) will not be considered, while those records with a magnitude greater than this threshold (crosses and circles) will be used to compute the average values at each distance from the platform leg.

Figure 3 depicts a hyperbolic tangent function (solid curve) that was fit to the differences' per cent change from the far field values for E_d on the overcast data (upper panel) and sunny day (lower panel). The per cent change is plotted against the distance from the platform leg. The mean value for the time period at each distance is represented by a circle, and the standard deviation by a vertical line. A reasonable fit of this function was achieved for the overcast data, and may be expressed as $y(x) = 24.859(1 - 1.064 \tanh(0.070x))$, where y is the

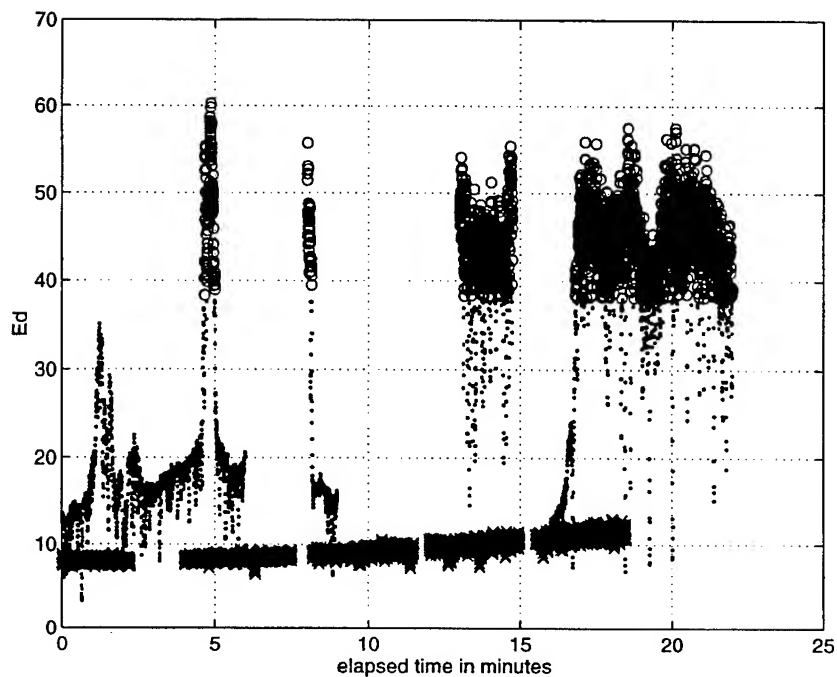


Figure 1: The reference downwelling irradiance $E_d(443.5nm)$ in μWcm^{-2} versus time in minutes during sunny (crosses, lower values) and overcast conditions (circles, higher values) are both shown on the same axes. Unused cloudy data are denoted by points. The distance from the tower decreases with increasing time.

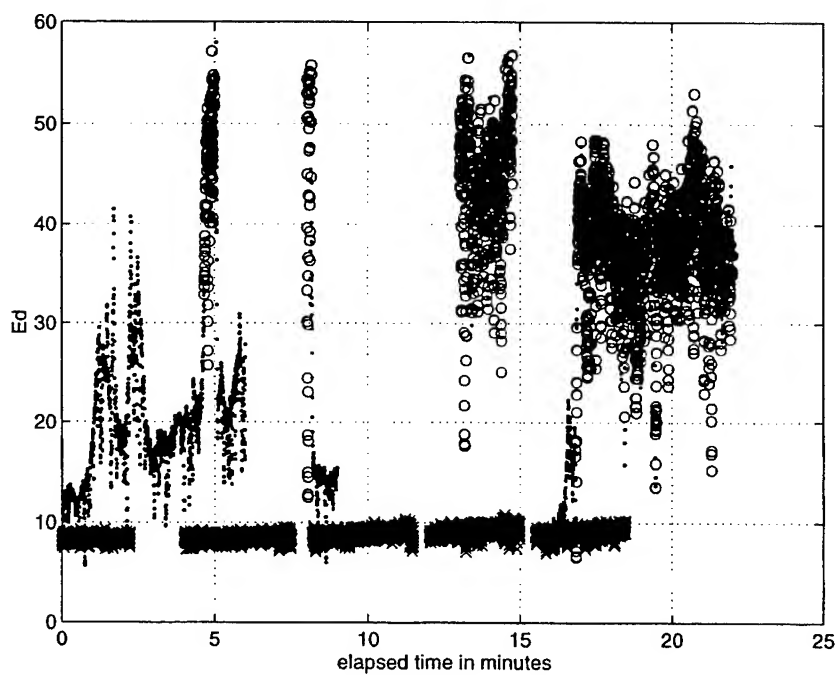


Figure 2: The test downwelling irradiance is displayed in a fashion identical to that of Figure 1.

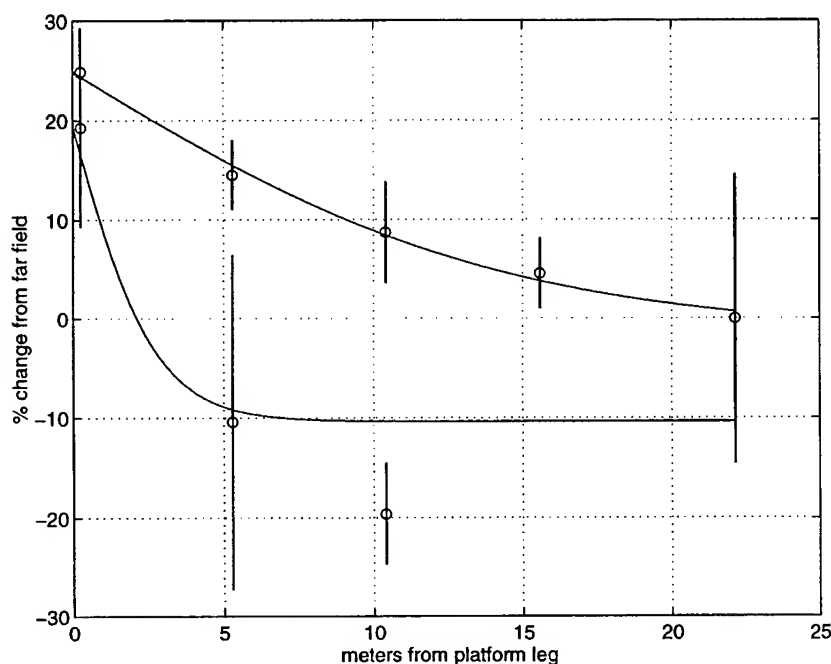


Figure 3: The means (circles) and standard deviations (vertical line) of E_d under overcast (upper curve) and sunny (lower curve) conditions are plotted against the distance from the platform leg. Least-squares fits of a hyperbolic tangent function are also shown.

percentage change from the far field, and x is the distance from the tower in meters. The fit of this curve for the sunny data is not reasonably determined.

4 DISCUSSION

During overcast conditions, it is readily apparent that the platform structure has a large influence on the available light reaching the radiometers. Since the curve in the upper panel of Figure 3 never flattens completely, the light field at distances of $> 20\text{ m}$ from the platform leg cannot be considered to be truly representative of far field conditions. This is due to the large amount of skylight blocked by the sizable structure; this skylight is the principal component of available irradiance on overcast days. It should be noted that the strength of the shadow's effect under these overcast conditions is in keeping with the results of the Monte Carlo simulations reported by Gordon.¹ In an attempt to empirically estimate the necessary distance to avoid the tower shadowing effects, it is possible to determine the point at which the fitted tanh curve is essentially flat (having a slope of less than 0.00001 m^{-1}) which is indicative of far field conditions. Though it is but a crude estimate, the slope function $dy/dx = (24.859)(1.064)(0.070)\text{sech}^2(0.070x)$ achieves this condition at $\approx 96\text{ m}$.

The effects of the platform shadow under sunny conditions have not been clearly demonstrated by the shadow experiment. While there is a discernible effect at the platform leg, at distances $> 5\text{ m}$ from the platform the effects, if any, are more difficult to resolve due to the greater variability in the signal as well as the effects of reflection from the tower (manifested by the 10–20 coarse spatial resolution used in this experiment further hindered the accurate determination of any shadow effects. Gordon¹ estimated a minimum separation for negligible shadowing effects, under sunny skies, to be $0.75/K_d$, where K_d is the wavelength-dependent attenuation coefficient. Secchi disk

measurements taken during the experiment at the Apache 990 platform provide a rough estimate of $K_d = 0.20 m^{-1}$ (using $K_d = 1.44/z$);² the limit of the shadow effect (exclusive of reflection) under sunny skies could thus be estimated to be about 3.75 m.

5 CONCLUSIONS

NDBC has designed and is testing a bio-optical sensor system for the calibration and validation of the SeaWiFS sensor in coastal (case II) waters. This system will provide hourly measurements in near-real time of surface-referenced solar irradiance, upwelling radiance, chlorophyll concentration, pressure, temperature, conductivity, and oxygen concentration. While the original plans for this sensor system called for its installation on an offshore light tower, a study conducted by NDBC of the shadowing effect from such a structure indicates that large towers may be a source of considerable error in radiometric measurements taken nearby. A minimum separation between the radiometers and the Apache 990 oil production platform for the avoidance of any shadowing effects was estimated to be approximately 100 m. Though not a comprehensive investigation of tower shadowing, this experiment has demonstrated that caution must be exercised when performing radiometric measurements near large structures.

6 ACKNOWLEDGMENTS

This work is supported by NASA grant S-12895F. The authors wish to thank Rick Nash, Jim Patterson, Richard Burgess, Dave Brown, and Fred Tagge of Computer Sciences Corporation, Ltjg. Brett Taft of the United States Coast Guard, the captain and crew of the R/V Tommy Munro, and the Apache Corporation for their assistance in the NDBC platform shadow experiment.

7 REFERENCES

- [1] Gordon, H.R., (1985) "Ship perturbation of irradiance measurements at sea 1: Monte Carlo simulations", *Applied Optics*, **24**(23), 4172-4182.
- [2] Kirk, J.T.O., *Light and photosynthesis in aquatic ecosystems*, Cambridge University Press, London, 1983.

Ocean color measurements from low flying aircraft: Atmospheric and surface glint correction

Lazin, G., Davis, R.F., Ciotti, A.M. and Lewis, M.R.

Department of Oceanography, Dalhousie University
Halifax, NS, Canada B3H 4J1

ABSTRACT

Optical properties of sea water, such as water leaving radiance, contain valuable information about constituents of the aquatic system. Airborne remote sensing provide access to synoptic data over large spatial scales, even under cloudy conditions. However, in addition to the desired water-leaving radiance, the upwelling radiance measured aboard the aircraft contains contributions from atmospheric scattering and from reflection from the sea surface. Here, we discuss atmospheric and surface correction methodologies. Our goal was to develop a simple operational correction method for data collected during low-altitude flights that would apply to different atmospheric conditions. Remote ocean color data were collected from a low flying NOAA P3 aircraft in the southeastern Bering Sea in April and May 1996. Shipboard observations of upwelling radiance just below the sea surface made during aircraft overflights were used as sea-truth observations. Our simple method performed well, but still has to be tested with independent data.

Keywords: airborne remote sensing, atmospheric correction, sky glitter

1. INTRODUCTION

Aircraft have become an important platform for remote sensing of ocean color. Unlike satellite-based measurements, airborne remote sensing can be used under cloudy conditions. However, when compared to satellites, the methodologies for interpretation of aircraft data are not as widely validated in the scientific community. The basic difference between the correction algorithm for airborne ocean color and for satellite is that airborne methods include only a part of the atmosphere that depends on the flight altitude. At present, few attempts have been made to assess methodologies for aircraft data applications in ocean color analysis^{1,2}. The model proposed by Guzzi *et al.*,¹ based on an approximate solution of the radiative transfer equation, seems to perform good atmospheric corrections, however, it is too complicated for our operational needs. Therefore, we developed a simple parameterization for removing both atmospheric and surface effects from the airborne upwelling radiance using sea-truth measurements. This method was developed with, and was applied to a data set collected during two flights performed on April 1996, in the southeastern Bering Sea. Further work will be dedicated to test the method with complementary data from the same experiment, retrieving water leaving radiance from aircraft data for flights over optical drifters.

2. MEASUREMENTS

Remote ocean color data were collected from a low flying NOAA P3 aircraft in the southeastern Bering Sea in April and May 1996. Measurements were carried out from altitudes between 150 and 300 meters. Airborne upwelling nadir radiance ($Lu(\lambda)$) and downwelling global irradiance ($Ed(\lambda)$) data were collected with a Satlantic SeaWiFS Aircraft Simulator (SAS-II). The instrument collects data at seven spectral bands, 10nm wide, centered at 412, 443, 490, 555, 670, 683 and 780 nm. Optical data were sampled 10 times per second, averaged over 1 s, and merged with navigational instruments. A suite of meteorological parameters were collected during the flights. Shipboard observations of upwelling radiance 45 cm below the sea surface were made at the same wavebands, using a Satlantic Tethered Spectral Radiometer Buoy (TSRB) deployed from the R/V Miller Freeman during aircraft overflights. Chlorophyll samples, collected at the same time, were analyzed fluorometrically aboard the ship. A total of five flights were analyzed: three under fairly clear sky conditions and two under overcast skies.

3. ATMOSPHERIC CORRECTION

The upwelling spectral radiance sensed at altitude h by a sensor pointed to the sea surface is given by:

$$L_u(\lambda, h) = L_r(\lambda, h) + L_a(\lambda, h) + T(\lambda, h)L_{sun-g}(\lambda) + t(\lambda, h)[L_w(\lambda) + L_{sky-g}(\lambda)] \quad (1)$$

where the terms are:

L_r	radiance scattered into the field of view of the sensor by molecules (Rayleigh scattering)
L_a	radiance scattered by aerosols
L_{sun-g}	direct sun radiance reflected from the sea surface into the field of view of the sensor
L_{sky-g}	diffuse sky radiance reflected from the water surface into the field of view of the sensor
L_w	radiance backscattered out of the water
$t(\lambda, h)$	diffuse transmittance of the atmospheric layer between the surface and level of observation
$T(\lambda, h)$	direct transmittance of the atmospheric layer between the surface and level of observation

3.1 Estimation of the terms

The atmospheric scattering for molecules and for aerosol are defined through the respective phase functions. The molecular phase function is given by the classical Rayleigh function³. For the aerosol phase function, we used a two-term Henyey-Greenstein function, with parameters for marine aerosol proposed by Gordon⁴ ($a=0.985$, $g_1=0.713$ and $g_2=-0.759$). The Rayleigh scattering, which contributes primarily in the blue part of the spectrum, was taken into account. The estimated radiance scattered by aerosol is an order of magnitude less than the measured signal and therefore was neglected ($L_a \sim 0$).

The spatial distribution of the direct radiance reflected by the sea surface (sun glitter) into the field of view of the sensor, depends on the sea surface state. It can be determined by a relation proposed by Cox and Munk⁵ as a function of the wind speed and viewing geometry. It was estimated that the effect of direct sun glitter was negligible for our overflights (solar zenith angle=40°, wind speed 6 ms⁻¹, and nadir view of sensor).

The diffuse transmittance for the upwelling radiance $t(\lambda, h)$ was calculated from optical depths $\tau(\lambda, h)$ of atmospheric constituents according to Gordon and Morel⁶. The molecular optical depth, as a function of flight altitude, was obtained through relations proposed by Van Stokkom and Guzzi⁷:

$$\tau_R(\lambda, h) = H_R(h) \cdot 0.0088\lambda^{-4.15+0.2\lambda} \quad [\lambda(\mu\text{m})]$$

where

$$H_R(h) = 1 - \exp(-0.1188h - 0.00116h^2) \quad [h(\text{km})]$$

The absorption optical depth of water vapor and ozone² for the atmospheric layer between the sensor and sea surface, was estimated to be extremely low and also negligible. The aerosol optical depth was estimated from a model^{8,9} for aerosol extinction in a marine boundary layer. The model calculates size distribution of sulfate aerosol as a function of measured relative humidity, and from there, the extinction coefficients, single scattering albedos and asymmetry parameters. The maximum attenuation of upwelling signal was estimated to be 2%. Therefore the atmospheric layer was assumed transparent and we set the diffuse and direct transmittance⁶ equal to 1.

Using these simplifying assumptions equation 1 becomes:

$$L_u(\lambda, h) = L_r(\lambda, h) + L_{sky-g}(\lambda) + L_w(\lambda) \quad (2)$$

and we concluded that the main source of observed glitter comes from the diffuse skylight reflected from the surface.

4. SKY GLITTER PARAMETERIZATION AND RESULTS

Diffuse radiance reflected from the sea surface, $L_{sky-g}(\lambda)$, was calculated from equation 2, using upwelling radiance measured from aircraft, calculated Rayleigh scattering radiance, and water leaving radiance computed from the TSRB measurements. In order to obtain water leaving radiance at the surface ($L_w(\lambda)$) from upwelling radiance measured at the depth of 45 cm, the in-water signal was propagated to the surface and transmitted through the air sea interface¹⁰. The spectral in-water diffuse attenuation coefficient was estimated from the chlorophyll values measured during the overflights¹¹.

Sky glitter radiance, calculated for all overflights, was then related to the diffuse sky irradiance $E_{diff}(\lambda)$ at the sea surface, via a linear relationship (Figure 1):

$$L_{sky-g}(\lambda) = f \times E_{diff}(\lambda)$$

It was assumed that the sky-glitter is independent of the sea surface state since the difference between the reflectance of a flat and ruffled sea surface is negligible for diffuse radiance⁵. Since downwelling diffuse irradiance was not measured during the flights, it was estimated in one of two ways. For cloudless days, the ratio of diffuse to global irradiance was calculated from a solar spectral irradiance model¹², using the meteorological parameters measured on the aircraft. For completely overcast days, it was assumed that 90% of the measured global irradiance was diffuse¹³. The slope, f , which is the ratio of upwelling radiance originating from diffuse skylight reflected from the surface, to the downwelling diffuse irradiance, was validated by comparison with a parameterization given by Bukata³ where f is expressed as:

$$f = \rho_0 \frac{L_{d-sky}(0^\circ)}{E_{diff}}$$

where $L_{d-sky}(0^\circ)$ is downwelling zenith sky radiance, and $\rho_0 = 0.0212$ is the Fresnel reflectivity for vertical incidence. The value of f estimated here is in agreement with $\frac{L_{d-sky}(0^\circ)}{E_{diff}}$ measurements¹³.

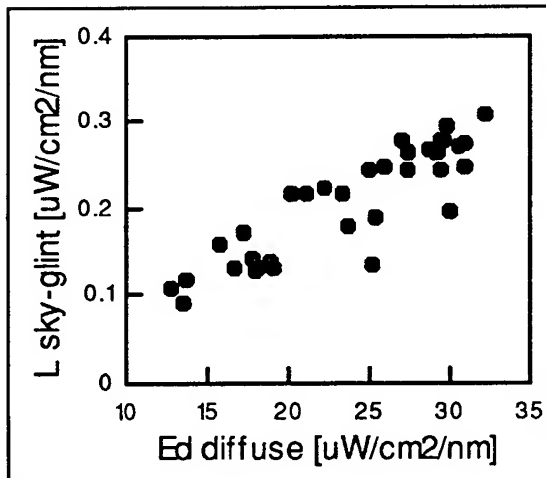


Figure 1. Relationship between downwelling diffuse sky irradiance at the sea surface and sky glitter. $L_{sky-g} = 0.0087 \cdot E_{diff}$.

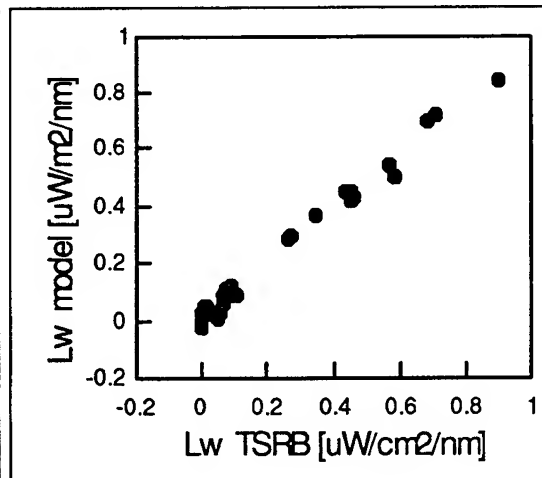


Figure 2. Comparison of water leaving radiance predicted from model and those estimated from ship measurements.

The slope f was then used in the model to predict water leaving radiances:

$$L_w(\lambda) = L_u(\lambda) - L_r(\lambda, h) - 0.0087 \times E_{diff}(\lambda)$$

The correlation coefficient between measured water leaving radiance and those predicted by the model is 0.99 with root mean square error of 0.03 (Figure 2) for both sunny and cloudy days. Although the parameterization seems to perform atmospheric correction of the data well, we realize that further validation of the model is necessary on an independent set of data.

5. CONCLUSION AND FUTURE WORK

In the atmospheric correction for low flying (150-300m) aircraft data we included Rayleigh scattering only, and considered that the atmospheric layer between the surface and level of observation was transparent.

Outside the direct sun glitter region, the primary source of glitter is diffuse skylight reflected from the sea surface. The observed sky glitter was related to the downwelling diffuse skylight via a linear relationship.

The simple parameterization developed removes sky glitter from the upwelling signal efficiently, and it was equally successful for sunny and cloudy days.

Regarding operational use of aircraft ocean color data, proper corrections would have to include measurements of diffuse sky irradiance or downwelling zenith sky radiance.

The proposed method will be tested against independent data set, by retrieving water leaving radiance from aircraft data for other flights, and comparing them with data collected by optical drifters deployed during the same experiment.

6. ACKNOWLEDGMENTS

This project was funded by NOAA contract 40ABNR600758, Naval Research Laboratory, NASA, and NSERC.

Special thanks to Dr. Qiang Fu, Nick Bond, Jasmine Bartlett, and Jeff Wong

7. REFERENCES

1. Guzzi, R., Rizzi, R., Zibordi, G., "Atmospheric correction of data measured by a flying platform over the sea: elements of a model and its experimental validation", *Appl. Optics* **26**, 3043-3051, 1987
2. Zibordi, G., Maracci, G., Schlittenhardt, "Ocean colour analysis in coastal waters by airborne sensors", *Int. J. Remote Sensing* **11**, 705-725, 1990
3. Bukata, P. B., Jerome, H. J., Kondratyev, K. Y., Pozdnyakov, D. V., *Optical properties and remote sensing of inland and coastal waters*, CRC Press, Boca Raton, 1995
4. Gordon, H. R., Clark, D. K., Brown, J. W., Brown, O. B., Evans R. H., Broenkow, W. W., "Phytoplankton pigment concentration in the Middle Atlantic Bight: comparison of ship determination and CZCS estimates", *Appl. Optics* **22**, 20-36, 1983

5. Cox, C, Munk, W., "Measurement of the roughness of sea surface from photographs of the sun's glitter", *J. Opt. Soc. America* **44**, 838-850, 1954
6. Gordon, H. R., Morel, A. Y., "Remote assessment of ocean color for interpretation of satellite visible imagery", A review in *Lecture notes on coastal and estuarine studies*, R. T. Barber, C. N. K. Mooers, M. j. Bowman, B. Zeitschel Ed., Springer-Verlag, New York, 1983
7. Van Stokkom, H. T. C., Guzzi, R., "Atmospheric spectral attenuation of airborne remote-sensing data: Comparison between experimental and theoretical approach", *Int. J. Remote Sensing* **5**, 925-938, 1984
8. Wong, J., Dalhousie University, Halifax, personal communication, 1996
9. Winter, B., *Light scattering by a sea salt aerosol layer*, Ms. thesis, Dalhousie University, Halifax, 1994
10. Austin, R. W., "The remote sensing of spectral radiance from bellow the ocean surface", In *Optical aspects of oceanography*, ed. N. G. Jerlov & E. S. Nielsen, pp 317-344, Academic Press, London, 1974
11. Morel, A., "Optical modeling of the upper ocean in relation to its biogenous matter content (Case I waters)", *J. Gophy. Res* **93**, 10749-10768, 1988
12. Gregg, W. W., Carder, K. L., "A simple spectral solar irradiance model for cloudless maritime atmospheres", *Limn. Ocea.* **35**, 1657-1675, 1990
13. Walker, R. E., *Marine Light Field Statistics*, John Willey & Sons Inc. , New York, 1994
14. Iqbal, M., *An introduction to solar radiation*, Academic Press, New York, 1983
15. Kirk, J. T. O., *Light and photosynthesis in aquatic ecosystems*, Cambridge University Press, Cambridge, 1983
16. Mobley, C. D., *Light and Water; Radiative transfer in natural waters*, Academic Press, San Diego, 1994
17. Plass, G. N., Kattawar, G. W., Guinn, J. A., "Radiance distribution over a ruffled sea: contributions from glitter, sky, and ocean", *Applied Optics* **15**, 3161-3165, 1976
18. Zibordi, G., Maracci, G., "Determination of atmospheric turbidity from remotely-sensed data", *Int. J. Remote Sensing* **9**, 1881-1894, 1988

Field evaluation of anti-biofouling compounds on optical instrumentation

Scott McLean and Bryan Schofield

Satlantic Inc., Halifax, Nova Scotia, Canada, B3K 5X8

Giuseppe Zibordi

Space Applications Institute, Joint Research Center, Ispra, 21020, VA, Italy

Marlon Lewis

Department of Oceanography, Dalhousie University, Halifax, Nova Scotia, Canada, B3J 1R2

Stanford Hooker

NASA Goddard Space Flight Center, Greenbelt, MD, USA, 20771

Alan Weidemann

Naval Research Laboratory, Stennis Space Center, MS, USA

ABSTRACT

Biofouling has been a serious question in the stability of optical measurements in the ocean, particularly in moored and drifting buoy applications. Many investigators coat optical surfaces with various compounds to reduce the amount of fouling; to our knowledge, however, there are no objective, in-situ comparative testing of these compounds to evaluate their effectiveness with respect to optical stability relative to untreated controls.

We have tested a wide range of compounds at in-situ locations in Halifax Harbour and in the Adriatic Sea on passive optical sensors. Compounds tested include a variety of TBT formulations, antifungal agents, and low-friction silicone-based compounds; time-scales of up to four months were evaluated. The results of these experiments are discussed.

1. HALIFAX HARBOUR EXPERIMENT

1.1 Objective

The objective of the Halifax Experiment was to evaluate several commercially available anti-biofouling compounds for their effectiveness and stability when exposed to high productivity seawater. This experiment is unique in that the effectiveness of these types of compounds has never been evaluated in a quantitative method which preserves the in-water optical properties of the fouling organisms.

1.2 Experimental Setup

Test samples consisting of glass and acrylic, coated with various test compounds, were placed in Halifax Harbour for several months and periodically removed for evaluation. For the in-situ component, the sample holders suspended eleven test samples at a depth of one meter on a floating dock in 8 meters of water 10 meters from a 1.1 meter diameter untreated sewer outlet which provided a nutrient rich environment for the experiment.

The in-situ sample holders held the test sample (a 2 inch diameter acrylic or glass substrate) with the anti-biofoulant coated side exposed to the seawater. The substrate was held in place with a delrin faceplate (which was also coated) as it would be on a typical Satlantic OCR-100 radiance sensor. A plug blocked the back of the window from being exposed to the

water. A photo of the mounted sample holders can be seen in Figure 1. The sample holders were transferred the 50 meters from the in-situ site to the sample evaluation system in a transfer tank filled with seawater to ensure that the fouling organisms were kept alive during transfer and evaluation.

The sample evaluation system was designed to repeatedly assess the biofouling of each sample using a method that would simulate the field environment¹. Thus the system has five objectives: 1) keep the fouling organisms alive, 2) maintain the in-situ optical properties of the organisms, 3) evaluate the change in radiance (relative to an unfouled sample) measured by a detector array while viewing a lambertian source (simulating the upwelling radiance distribution of the ocean), 4) allow the evaluation to be repeated frequently with minimal setup time, and 5) allow the samples to be installed and removed such that measurements were repeatable without realignment.

The system consisted of a 450 liter fiberglass tank, a radiance source and an immersed radiance detector array. The tank was fitted with a 12 liter per minute filtration system using a double diaphragm pump and a 5 micron filter cartridge. This prevented the tank water from becoming contaminated between evaluations. The tank and fixtures were coated with flat black paint to prevent light from reflecting surfaces from biasing the test results. The radiance



Fig. 1. Sample holder with 11 test windows at in-situ experiment site.

source consisted of a 1.2 meter optical rail mounted parallel to the tank's water surface. The rail held a 250W HLX halogen lamp and an alignment laser. Mounted in the center of the optical axis of the rail, and directly over the test radiance sensor, was a 50 cm standard reflectance target which acted as a near lambertian source. The target was mounted at 45 degree angle to both the lamp and the instrument. This unconventional configuration permitted accurate and repeatable alignment.

To produce the lambertian source, the standard reflectance target was placed normal to the optical axis of the illuminating lamp. By leaving the target at 45 degrees, the variation across the target from the edge closest to the lamp to the edge farthest from the lamp is about 50% (at a lamp to target center distance of 200cm), which was sufficient since the detector viewing geometry was constant through the experiment. The detector system for this experiment was a

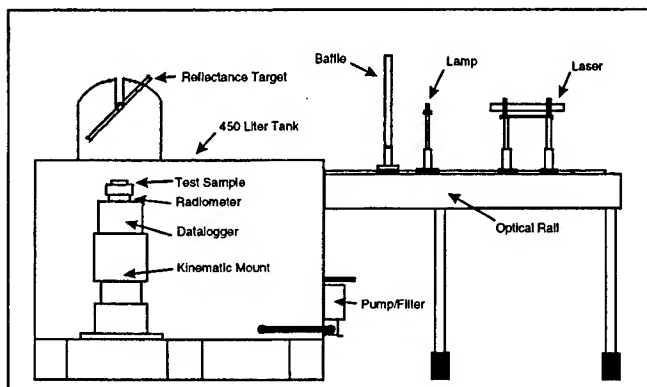


Fig. 2. Sketch of sample evaluation setup.

seven channel radiance sensor (OCR-100) with the same wavelengths as a standard Satlantic OCM-II buoy (412, 443, 490, 510, 555, 670 and 683nm). The radiometer was held at the bottom of the tank viewing the reflectance target in a kinematic mount. Test samples were placed over the radiometer face for evaluation.

1.3 Test Sample Compounds

Nine sample compounds were identified for initial testing, of which five were selected for the actual in water testing. These compounds are listed in Table 1.

All coatings were applied to a disk of acrylic substrate to pre-screen them for suitability in this test. Test criteria included spectral absorption, adhesion and surface quality. All samples were scanned in a digital Cary14 spectrophotometer and evaluated². The results are summarized below.

Manufacturer	Product Name	Product Type (application method)	Sample Code Glass, Acrylic
Extensor AB	Prop-N-Drive	TBT Fluorocarbon (spray)	AG, AA
Tempo Products Company	Clear Anti-Fouling Paint #6993	TBT Methacrylate (spray)	BG, BA
Chemtronics Inc	Konform SR2000	Silicone (spray)	CG, CA
Kiss-Cote Inc	Kiss Cote #1083	Silicone Polymer (wax)	DG, DA
Tempo Products Company	Clear Anti-Fouling Paint #6993	TBT Methacrylate (spray)	EG, EA
M.G. Chemicals	Silicone Conformal Coating	Silicone (spray)	FG, FA
Oceanographic Industries	custom product	TBT time release module (ring)	GG, n/a
ITW Philadelphia Resins	Classic Yacht	TBT Methacrylate (spray)	HG, HA
Glasgow Marine Technology Center	proprietary compound	Ablative compound (gel)	n/a
US Navy	OMP-10	TBT Methacrylate (vacuum bake)	n/a

Table 1 - Test Compounds

- The Classic Yacht compound was selected after a recommendation from Dennis Clark (NOAA/NESDIS) and Tom Dickey (UCSB) as a clear, spray-on anti-biofouling compound. This compound contains Tributyltin (TBT) which is an effective anti-biofoulant used in the Navy OMP-8 compound. The commercial application for this compound is an outboard motor anti-biofoulant. This coating forms a very thick, uniform layer when sprayed.
- The Tempo #6993 is the Tempo Products version of the Classic Yacht. Two different spray cans were available for testing. Both tested the same, only one was be used. This forms a much harder, thinner coating than the Classic Yacht.
- The Extensor TBT Fluorocarbon compound was sprayed on a test sample, only to find that the compound was actually an opaque white, not clear as indicated on the label. This compound also failed the adhesion test - instead of scratching, it peeled up. This compound was eliminated from the testing.
- The OMP-10 compound currently used by the US Navy is very similar to the OMP-8 compound tested by SeaTech in 1987³. Two windows were sent to NRL for coating. These were not returned; again it was not selected for further testing.
- The Oceanographic Industries compound is a proprietary mixture of a TBT anti-biofoulant packed around small plastic beads. The resulting solid is machined to fit over the face of a sensor such that it does not block the view of the sensor. The time release of the anti-biofoulant is designed to keep the two inch window clear for 4-6 months. This system is used by Francisco Chavez (Monterey Bay Aquarium Research Institute). The appealing feature of this system is that the optical path is not obstructed as is the case for the coatings.
- The Glasgow Marine Technology Center compound was being studied by Chelsea Instruments. Windows were sent to Chelsea to be coated, but the samples were not made available. More details on the compound revealed that it was probably not useful for absolute radiometric instrumentation due to its ablative nature. The coating was also described as a soft gel-like coating which did not sound robust enough for oceanographic sensors. Chelsea is currently pursuing another compound.
- Kiss-Cote is a non-toxic compound recommended by Jim Aiken (Plymouth Marine Laboratory). This compound provides an extremely hard and slick surface which prevents organisms from attaching. Based on a silicone polymer, this compound is most commonly used for coating racing yachts. This compound is applied like a wax and forms a very thin, hard coating which has no detectable absorption over 400-700nm.
- The Konform was initially selected since it is used as a conformal coating for electronics in high humidity conditions to prevent growth of organisms using an anti-fungal agent. The coating is a clear spray and it was thought that it may prevent organisms from attaching to the windows. This compound was eliminated from testing after it failed a pre-screening test due to high blue absorbance. The compound also showed poor adhesion to acrylic.
- The M.G. Chemicals Silicone Conformal Coating was thought to be similar to the Konform but it does not have any unusual absorbance characteristics. Its adhesion to the acrylic was much better.

Once the coatings were pre-screened, the experimental samples were coated. Both the faceplate and window of the test sample were coated. All compounds (except the Oceanographic Industries ring) were applied to both glass and acrylic windows.

For controls an uncoated substrate of glass and acrylic was kept dry, in the lab and used only in the test tank (identified as samples ZG and ZA respectively). Another set of uncoated glass and acrylic substrates was placed in-situ (identified as samples XG and XA respectively).

1.4 Sample Evaluation

For evaluation, the samples were removed from the sample holder plugs and immersed in the evaluation tank carefully as not to disturb the fouling organisms. The sample window holders were placed over the face of the immersed radiance sensor viewing the lambertian target above for measurement. By using this radiance sensor to measure the target radiance with the uncoated lab control window (ZG or ZA) (at time t_n) and sample window (at time t_n), the difference ratio $R(t_n) = ([\text{sample-control}]/\text{control})$ becomes the amount of signal degradation caused by the fouling and the coating on the window. The original measurement of the unfouled window (at time t_0) and the coated window (at time t_0) give $R(t_0) = ([\text{control-sample}]/\text{control})$. The amount of fouling absorption was evaluated as $F(t_n) = ([R(t_0) - R(t_n)]/R(t_0)) \times 100\%$.

Water samples were taken each day the test samples were removed for evaluation. Pigments were determined fluorimetrically after extraction in 90% acetone.

1.5 Results

The experiment was run from September 15th through December 21st, 1995. The experiment began with a 48 hour presoak where the samples were immersed in filtered seawater to check their short term stability before moving to the in-situ site. All samples changed less than 1% during the presoak, except the Classic Yacht which changed 2-3% on both substrates. All of the samples were placed in the in-situ site on September 18th. During the experiment, the repeatability of the measurements (using the lab controls) was within $\pm 2\%$.

Pigments varied from 11ug/l to 1.5ug/l during the experiment as can be seen in Figure 3.

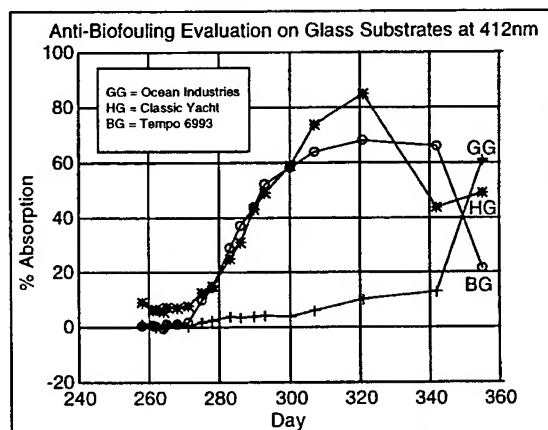


Fig. 4. Three heavily biofouled test samples on glass substrates.

be seen in Figure 4 (the 412nm channel on is shown in all figures as this was the worst case, the glass and acrylic substrates performed similarly so only glass is shown), the TBT formulations performed poorly on both window types, fouling up to 85%. Even worse, after about two months, the fouling organisms began to slough off these samples causing changes of up to 40%. The Oceanographic

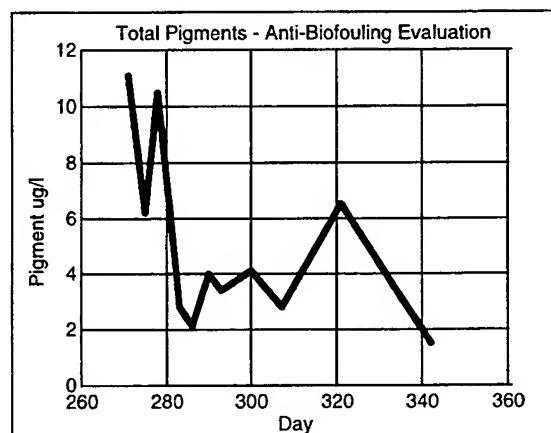


Fig. 3. Pigment concentration during the experiment.

The results of the experiment are quite surprising⁴. As can

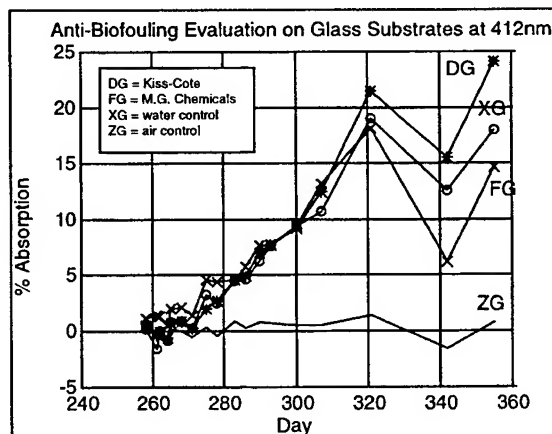


Fig. 5. Four test samples (including controls) on glass substrates.

Industries anti-fouling ring performed quite well for almost 3 months with about 10% fouling, after which it must have run out of its time release capabilities, as it began fouling rapidly (see sample GG, Figure 4). Kiss-Cote and the uncoated samples performed the best, fouling 15-25% in four months, with the uncoated samples having slightly better performance than Kiss-Cote (see Figure 5). The M.G. Chemicals conformal coating also did quite well, actually out-performing uncoated glass. Both uncoated glass and uncoated acrylic performed about the same.

2. ADRIATIC SEA EXPERIMENT

2.1 Objectives

A joint effort of the Marine Environment Unit (Space Applications Institute - European Commission Joint Research Center (JRC)) and Goddard Space Flight Center (NASA) completed a second experiment in Case-I waters in the Adriatic Sea. The purpose of this experiment was to evaluate the short-term (a few weeks) biofouling effects on underwater optical radiometers. This effort was devoted to evaluating the capability of Kiss-Cote #1083 (one of the compounds also tested in the Halifax Experiment) as an anti-biofouling agent for glass. Kiss-Cote was selected for this experiment because of its non-toxic nature and its high transmittance in the visible wavelengths.

This experiment was performed at the Acqua Alta oceanographic tower of the Italian National Research Council. The tower is located in 17m of water approximately 16km off the coast of Venice in the North Adriatic Sea. From June 19 to July 09, 1996, two Satlantic OCR-200 radiometers and 38 glass samples were suspended on the tower at a depth of 6m (see Figure 6). One of the radiometers was coated with Kiss-Cote, the other was untreated. Data from the two radiometers and other ancillary sensors was recorded during the experiment on a Satlantic STORE-120 module. The 38 glass samples (using the same glass material as the radiometers) were placed on a

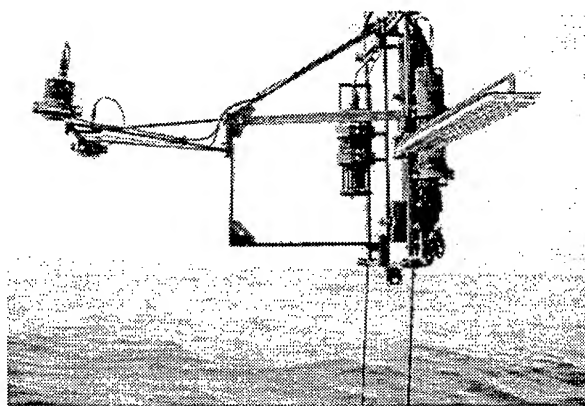


Fig. 6. Adriatic Experiment instrumentation on Aqua Alta. OCR-200's on left, bar with 38 glass samples in foreground, STORE-120 and ancillary sensors in background.

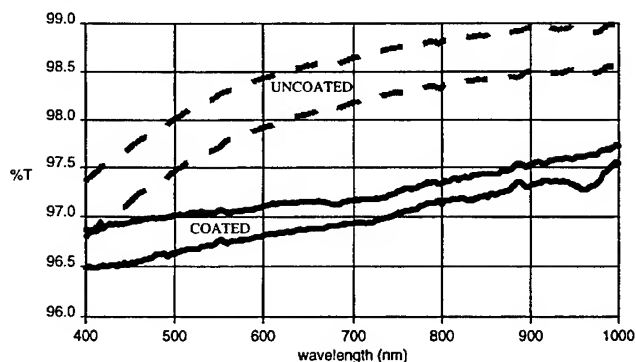


Fig. 7. Two coated and two uncoated glass samples scanned wet after three weeks in the Adriatic Sea

bar and sealed so only the coated face was exposed. 19 of the glass samples were coated with Kiss-Cote, the other 19 were left untreated. Both the glass samples and the two radiometers face downwards as they would in normal operation. During the experiment the measured total pigment concentration was about $0.2\mu\text{g/l}$.

2.2 Results

The experiment site was revisited after 8 days, 13 days, 14 days and 21 days. The sample bar was removed and samples were scanned with 2nm resolution in a Perkin-Elmer Lambda-12 spectrophotometer. For these measurements the

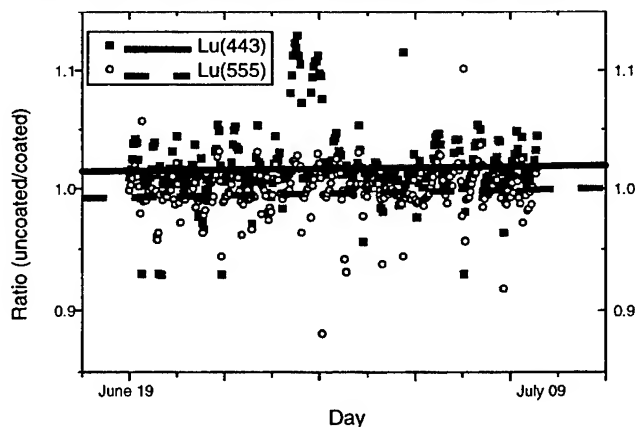


Fig. 8. Two channels of radiometer data ratioed uncoated/coated radiance for duration of experiment and regression lines showing less biofouling in uncoated samples.

samples were dried before measuring, and were contaminated by dried salts, thus this data is not presented here. At the end of the experiment (after 21 days) the samples were scanned wet by inserting them in a cuvet of 0.22 μ m filtered seawater. The results of two samples of each coated and uncoated is shown in Figure 7. These results indicate that the uncoated glass performed better than the Kiss-Cote treated samples, particularly in the red.

Data was also collected from the two OCR-200 radiance sensors submerged on the tower. The units were scheduled to record at 10 minute intervals an average of 64 samples for 14 hours a day for three weeks. These results are shown in Figure 8 for two of the seven channels in the radiometers (Lu443 and Lu555). The data is shown as the ratio of the uncoated radiance sensor over the coated radiance sensor. The scatter in the data is likely due to the difference in the light fields between the radiometers, spaced about one meter apart, due to wave focusing and shadowing of the instruments during the afternoon. A regression of all the data points is represented by a solid line for Lu443 and a dashed line for Lu555. The uncoated/coated ratio increases for Lu443 about 1.5% during the experiment and about 2% for Lu555. These results are consistent with those shown in Figure 7 and the results obtained in the Halifax Experiment.

3. SUMMARY

From the test results of the Halifax Experiment it is clear that TBT formulations, directly applied to the window are ineffective as anti-biofoulants, and, in fact, appear to promote the growth of fouling organisms. It is suspected that the surface roughness of these coatings (which when sprayed on were rougher than all the others) had more effect than the actual composition of the coatings. This is consistent with the results obtained from the uncoated glass and the Kiss-Cote which had the smoothest surfaces. Both the Adriatic Experiment and the Halifax Experiment showed that fouling for short periods (3 weeks) is on the order of a few percent for very smooth surfaces, even in high pigment waters. Experiments continue by other investigators, Dennis Clark (NOAA/NESDIS) is currently working on a copper/stainless steel anti-biofoulant ring which may prove to have even better performance. Satlantic is also working on a system to prevent fouling on uplooking sensors.

4. ACKNOWLEDGEMENTS

Funding for the Halifax Experiment was provided by the Tactical Oceanographic Warfare Office, Naval Research Laboratory under contract N00014-94-C-6002. The authors would like to thank Dirk van der Linde (JRC) for his contribution to the field measurements in the Adriatic Sea and Mike MacDonald for the pigment analysis of the Halifax Experiment samples.

5. REFERENCES

1. McLean, S.D. (1995) Optical surface anti-biofouling experiment: Experiment plan. Satlantic Technical Report 95-002, 12pp.
2. Spinrad, R.W. (1987) Testing of Optical Properties and Development of Application Procedure for OMP-8 Antifoulant on Submersible Optical Surfaces. SeaTech Reference Technical Report 8701, 44pp.
3. McLean, S.D. (1995) Optical surface anti-biofouling experiment: Test sample pre-screening. Satlantic Technical Report 95-001, 25pp.
4. The daily absorption tables for each wavelength have been placed on an FTP site at Dalhousie University. This information is public access. The data is arranged in seven tab delimited ASCII data files FOUL412.DAT through FOUL683.DAT. Each one contains each sample's absorption since the test initiation. The data files can be accessed by using FTP to connect to **predator.ocean.dal.ca** the username is **anonymous** and the password is your name. The path for the data files is **/pub/scott/biofoul**.

OCEAN OPTICS IN THE CALIFORNIA CURRENT: OBSERVATIONS AND THEORY

B. Greg Mitchell, P. J. Flatau, Mati Kahru, and Curt Mobley⁺
Scripps Institution of Oceanography
University of California, San Diego
La Jolla, California 92093-0218

⁺Sequoia Scientific, Inc.
9725 SE 36th Street, Suite 308
Mercer Island, WA98040

ABSTRACT

We present a combined analysis of apparent optical properties and inherent optical properties of the California Current based on multi-instrument bio-optical measurements during the California Cooperative Oceanic Fisheries Investigation (CalCOFI) cruises. Detailed radiative transfer modeling is employed and radiance and irradiances for the model are derived and compared to measured values. Bio-optical parameterizations for the California Current are developed and compared to existing parameterizations for Case 1 waters. Discrepancies between absorption parameterizations are discussed.

Key words: CalCOFI, optics, absorption, remote sensing, California Current

1 INTRODUCTION

Apparent optical properties (AOP) in the ocean (e.g. diffuse attenuation coefficients, reflectance) depend on variations in inherent optical properties (IOP) including the absorption and scattering due to phytoplankton, and other particles, colored dissolved organic matter (cDOM) and on the boundary conditions of radiometric forcing, including atmospheric conditions, solar zenith angle, the underwater radiance distribution and bottom reflection. An adequate description of ocean optics and the goal of optical closure require detailed measurement complemented by radiative transfer modeling. This paper presents a combined analysis of AOP and IOP of the

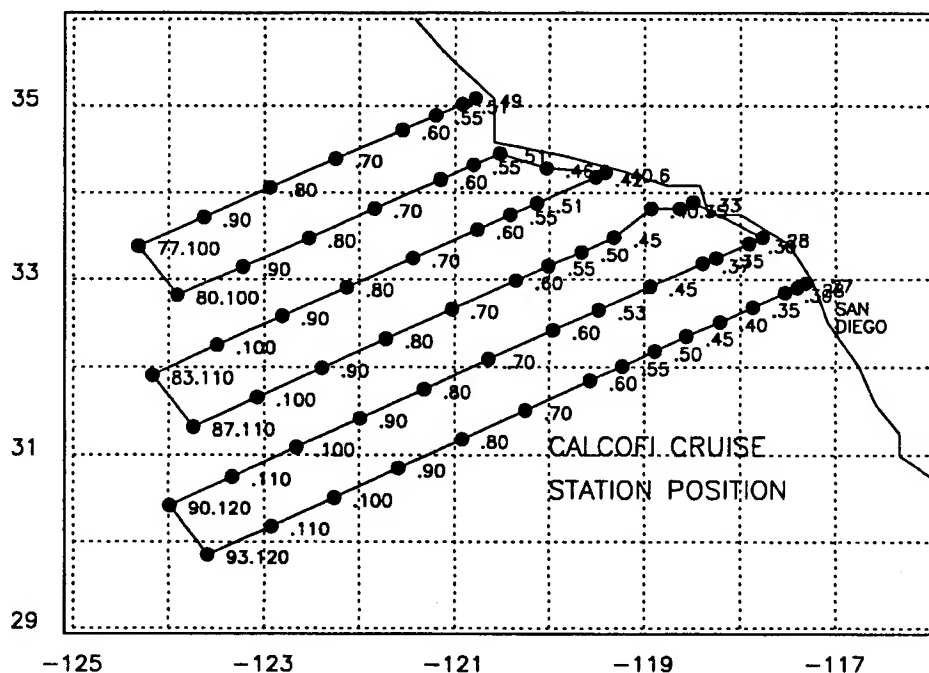


Figure 1: Station positions along the CalCOFI grid from line 77 north of Point Conception to line 93 off San Diego.

California Current based on multi-instrument bio-optical measurements during CalCOFI cruises and a detailed modeling study.

1.1 CalCOFI and Bio-optical Properties of the California Current

The California Cooperative Oceanic Fisheries Investigations (CalCOFI) region (Fig. 1) encompasses the full dynamic range of temperate coastal and open ocean trophic structure. CalCOFI Reports provide information on the biological and physical status of the region. For example Hayward et al⁹ report on a transient state of the California current in 1994-1995. Mantyla et al¹³ report on primary production and chlorophyll relationships, derived from ten years of CalCOFI measurements. Mean transport of mass, heat, salt and nutrients has been studied²⁵ for the volume defined by the modern (1984-1987) CalCOFI surveys (Fig. 1). Phytoplankton distributions in the North Pacific Ocean including the California Coastal Current have been reported by Ondrusek et al.²²

The California Current region has been studied extensively with respect to its bio-optical properties²⁸ and almost half of the observations for NASA's CZCS Global Processing algorithm were collected in the Pacific off Baja California or the Gulf of California. Pioneering work on scattering phase functions²⁴ diffuse attenuation, and reflectance¹ have been carried out in this region. Several studies have focused on the details of the absorption coefficients^{15,30} and one of the first experiments on "optical closure" was carried out in waters off San Diego.²⁰ Mueller and Lange²¹ discuss a provisional analysis of satellite ocean color imagery and profiles of spectral irradiance and Chl-a fluorescence of the Northeast Pacific Ocean including the California Current system. The large historical background of optical measurements in the region, and the large dynamic range of pigment and particle concentrations, make this an ideal location to study the optical properties of Case 1 waters in detail. We have implemented a detailed optical sampling program as part of the quarterly CalCOFI cruises which occupy the stations shown in Figure 1.

During 3 years of sampling we have completed more than 300 optical stations and participated in 12 cruises. Surface chlorophyll values range four orders of magnitude (0.05 – 500mg/m³) for the stations we have occupied. The focus of the work has been to acquire spectral irradiance and radiance profiles and to support the in-water measurements with detailed analyses of pigments, and measurements of the absorption coefficients for particulate and soluble fractions.

1.2 Radiative transfer models - matching IOP with AOP

For the special condition of large optical depth of a homogeneous layer it is possible to derive an expression for the rate at which the diffuse attenuation coefficient for vector irradiance approaches its asymptotic value. Thus, it is possible to define the relationship between single scattering properties and irradiances.^{33,6,31} For example, it can be shown that the asymptotic diffuse coefficient K_d and ω are related

$$K_{\infty}/c = 1 - 0.52\omega - 0.44\omega^2 \quad (1)$$

This theoretical expression can be inverted to show that, in principle, the vertical structure of the absorption, scattering, attenuation, and backscattering coefficients can be derived from the vertical structure of the scalar and vector irradiances and the nadir radiance.³³ The approach has great merit as it offers semi-analytical insight to the inverse problem. However, the assumptions of a diffuse regime and a homogeneous water layer limit this approach.

We have therefore used a computationally intensive approach by employing a plane parallel multistream radiative transfer model¹⁸ to match IOP with AOP. This approach gives us the capability to define arbitrary vertical distributions of single scattering properties (IOP) and also to derive absolute values of the radiance field or directional water-leaving reflectance.

2 METHODS

2.1 Basic relationships

Among the AOP of most interest to ocean scientists are the spectral diffuse attenuation coefficient, the irradiance reflectance, and the remote sensing reflectance (K , R , and R_{rs} , respectively). Numerous prior studies have shown how K , R , and R_{rs} depend on the IOP. In particular, for Case 1 waters, absorption coefficients are a dominant terms. The spectral absorption properties of dissolved and particulate matter may be partitioned into several components:

$$a(\lambda) = a_w(\lambda) + a_p(\lambda) + a_s(\lambda) \quad (2)$$

$$a_p(\lambda) = a_{ph}(\lambda) + a_d(\lambda) + a_i(\lambda) \quad (3)$$

where the subscripts w , p , ph , d , s and i denote water, particulates, phytoplankton, detrital particulates, soluble (gelbstoff) and inorganic particulates, respectively. An analogous set of equalities may be written for the beam attenuation (extinction) and total scattering coefficients, c and b . For oceanic water types with little terrestrial influence (Case I), the phytoplankton and detrital particulates are key variables (Smith and Baker, 1978) and the water coefficients are constant and suspended inorganic particles are negligible. The sum $a_p = a_{ph} + a_d$ or $a_{ph}(\lambda)$ are often normalized for convenience by pigment concentration (e.g. chl + phaeo or chl- a) to give the pigment specific absorption coefficients:

$$a_p(\lambda) = a_p^*(\lambda)[\text{chl} + \text{phaeo}] \quad (4)$$

$$a_{ph}(\lambda) = a_{ph}^*(\lambda)[\text{chl} - a] \quad (5)$$

2.2 In situ data collection and water sampling

Our data set includes measurements from two WetLabs AC9s, a Biospherical Instruments MER 2040, beam c(660) with a Seatech transmissometer, and discrete measurements of spectral absorption at 1 nm resolution for particulate (a_p) and soluble (a_s) material. The AC-9 absorption and attenuation meter concurrently determines the spectral transmittance and spectral absorption of water for nine channels in the range 410-850 nm with a bandpass at 10 nm per channel. The MER2040 measures downwelling irradiance and upwelling radiance covering 340-700 nm for 13 channels with 10 nm bandpass. Conductivity and temperature sensors (SeaBird), the Seatech transmissometer, and a Wetlabs fluorometer are integrated to the MER2040 data stream. A Wetlabs Modular Data and Power System (MODAPS) provides power and data acquisition for all instruments on the profiling package. Water samples were collected from a General Oceanics rosette consisting of 24 ten liter bottles, a CTD, transmissometer, and fluorometer. Samples from the water bottles were taken for determination of a_p , a_s , and chlorophyll.

2.3 Spectral measurements of absorption

Estimates of the absorption of particles (a_p) were made by concentrating the particles on Whatman GF/F filters under low vacuum pressure. The samples were scanned 300-800 nm in a dual beam spectrophotometer (Varian Cary 1) using a blank filter saturated with filtered sea water as the reference. Procedures for sample preparation, data acquisition, and data processing followed the Quantitative Filter Technique of Mitchell.¹⁴ Absorption of soluble material (a_s) was determined by filtering the seawater through 0.2 μ m pore size polycarbonate filters. The filters were first rinsed several times with MilliQ (Millipore Corporation) water to minimize contamination by the filters. The samples were run on the Cary 1 spectrophotometer in 10 cm quartz cuvettes from 300-800 nm with MilliQ water as the reference. We attempted to maintain the reference and sample cells at room temperature using a temperature controlled circulating bath interfaced to circulating flow cuvette holders. Residual temperature artifacts are often noted from 650-750 nm,²³ so the value at 600 nm was used as a null point.

2.4 Chlorophyll determination

Samples were collected on GF/F filters, extracted in 90% acetone for 24 hours at 4C in the dark, and chlorophyll concentrations were determined by the fluorometric method¹⁰ using a Turner Designs fluorometer. Procedures followed the standard CalCOFI protocols.³²

2.5 Hydrolight model

The numerical radiative transfer model used in this study is a slightly modified version of Hydrolight 3.0 code.¹⁶ We have found that sky radiance boundary conditions, including specifications of clouds, are important for proper in-water irradiance modeling. Therefore, we investigated the model of Brunger and Hopper⁴ for the average anisotropic sky radiance (or intensity) as a function of the position of the Sun, the diffuse fraction k , and the atmospheric clearness index k_t . The complete range of sky conditions from clear to turbid to overcast is covered. We have tested (not reported here) sensitivity of in-water fluxes to choice of k and k_t . We have found that zenith position and cloud cover play an important role in modeling results. A simple spectral solar irradiance model for cloudless maritime was employed,⁸ complemented by a cloudy sky model.¹² A separate user-supplied function $chlz(z)$ estimated the chlorophyll concentration at geometric depth z using a spline interpolation and CalCOFI measurements. Then the bio-optical models of Morel (1991)¹⁸ and Gordon and Morel (1983)⁷ were used to convert the chlorophyll concentration into a and b values. Pure sea water absorption and scattering coefficients are determined from the data of Smith and Baker (1981).²⁹ Twelve model wavebands were specified 335 – 345, 375 – 385, 390 – 400, 407 – 417, 438 – 448, 450 – 460, 485 – 495, 505 – 515, 527 – 537, 550 – 560, 565 – 575, 660 – 670 to correspond with MER channels.

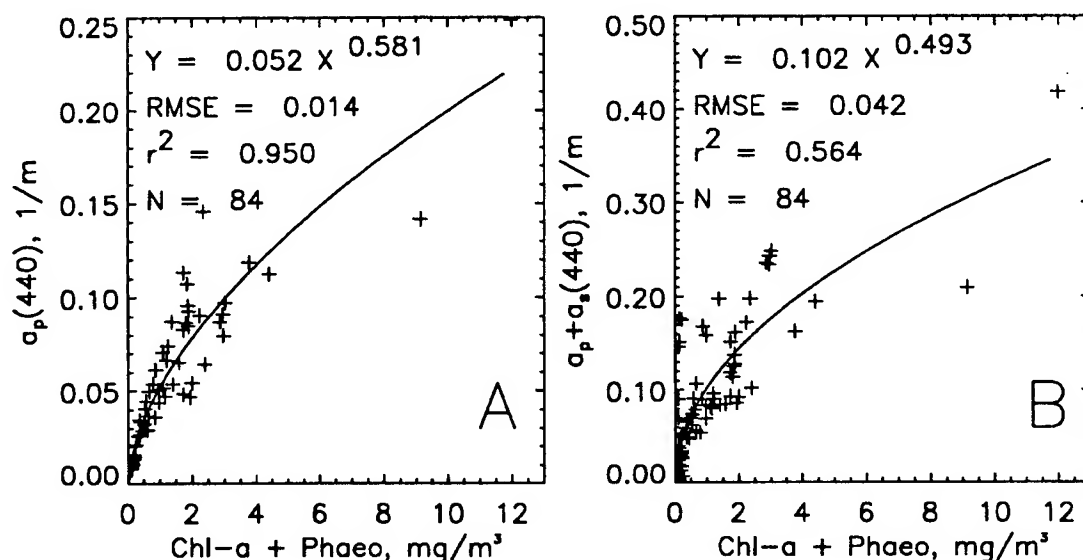


Figure 2: (A) Correlation between pigment (chl-a+phaeo) and the particle absorption at 440 nm. (B) Correlation between pigment (chl-a +phaeo) and the sum of particle and soluble absorption at 440 nm.

3 RESULTS

3.1 Bio-optical models of California Current Case 1 waters

We have developed a version of the bio-optical model for Case 1 water based on measured chlorophyll and published parameterizations.^{27,17,2} Also, we have developed absorption parameterizations based on *in situ* chlorophyll, a_p and a_s measurements (c.f. Figure 2). These models have been used in numerical sensitivity studies and will be reported in an extended publication.

3.2 Modeling results

Data collected for latitude 29.51.4N, longitude 123.35.6W at station 93.120 was modeled using Hydrolight.¹⁶ The station was occupied commencing at 1838 UTC with up and downcasts separated by about 10 minutes. The winds were southerly with wind speed of 5 kn. The atmospheric pressure was 1018.9 hPa and the Secchi depth was 41m. Thin clouds were observed. *In situ* water was collected at 2, 27, 54, 110, and 154 meters. Comparison of the model results to observation is given in Figure 3. While we observe reasonable agreement between observations and model output

of E_d and L_u , there are notable issues which must be considered. Rarely does one have ideal sky conditions when operating at sea, and the 30% high cirrus cloud condition observed at this station is a typical good situation. The consequence for this station is that the downcast had about 20% lower irradiance than the upcast but this was not modeled explicitly. Also there was a cloud anomaly at about 12 m depth on the upcast. Surface illumination forcing, together with possible near surface effects from the ship shadow, bubbles, foam, wave focusing, etc. may be responsible for some anomalies in the example. These are realistic issues which challenge accurate retrieval of R_{rs} and L_u from measurements alone. There are remaining inconsistencies due to the bio-optical model which has highly parameterized particulate and cDOM absorption components based on the Morel model for Case 1 waters. Figure 3B shows that our measurement of the non-water absorption ($a_p + a_s$) is in good agreement with the Morel model from 350-450 nm but diverges significantly at longer wavelengths where the Morel model over estimates $a_p + a_s$. We believe the high estimates of the Morel model are physically impossible at the red absorption peak where a_s is negligible and a_p is extremely well correlated to chlorophyll.^{30,15,2} Errors in the Morel absorption model, when it is applied to total water attenuation coefficients, are relatively unimportant at wavelengths longer than 600 nm since water absorption greatly dominates $a_p + a_s$. However, as indicated in our example for 440 and 555 nm (Figure 2A), the excess absorption per unit pigment of the Morel model may result in stronger attenuation of the Hydrolight modeled E_d and L_u fields (e.g. larger slope of the $\ln(L_u)$ or $\ln(E_d)$ vs depth).

4 DISCUSSION

Absorption by dissolved material has been considered less significant for Case 1 waters^{11,3} but this is not a reasonable assumption.^{26,5} Figure 2 shows $a_p(440)$ is much better correlated to chl+phaeo than is the sum $a_p(440) + a_s(440)$. The good correlation between a_p and pigment concentration is the basis for most bio-optical parameterizations. However, a_s is not well correlated with total particulate absorption, or pigment, and will thus pose a challenge for ocean color algorithms and bio-optical parameterizations.

The parameterizations of a_p and a_s as a function of chlorophyll for the Hydrolight model were chosen to be based on Morel.¹⁹ Thus, the a_p shape function is dependent on the Prieur et al parameterization derived from a fitting to spectral K , R and chlorophyll data. Measurement of a_s was generally not done for most cruises, so the parameterizations for a_s also are not based on a concurrent data set with the K and R data. The laboratory determinations that we perform for a_p and a_s also have a set of issues that must be considered. Our correction for the pathlength amplification factor for the a_p measurements on GF/F filters is largest in weakly absorbing regions, and the instrument noise is also largest in this domain, so the errors of the method are largest from 575-650 nm. Furthermore, we have chosen to normalize our raw a_s at 600 nm, which may lead to underestimates of the true values. The issues of methodology, treatment of blanks, null value normalization, pathlength amplification, and storage of preparations for determinations of a_p and a_s are still unresolved within the community and require more focused attention before a

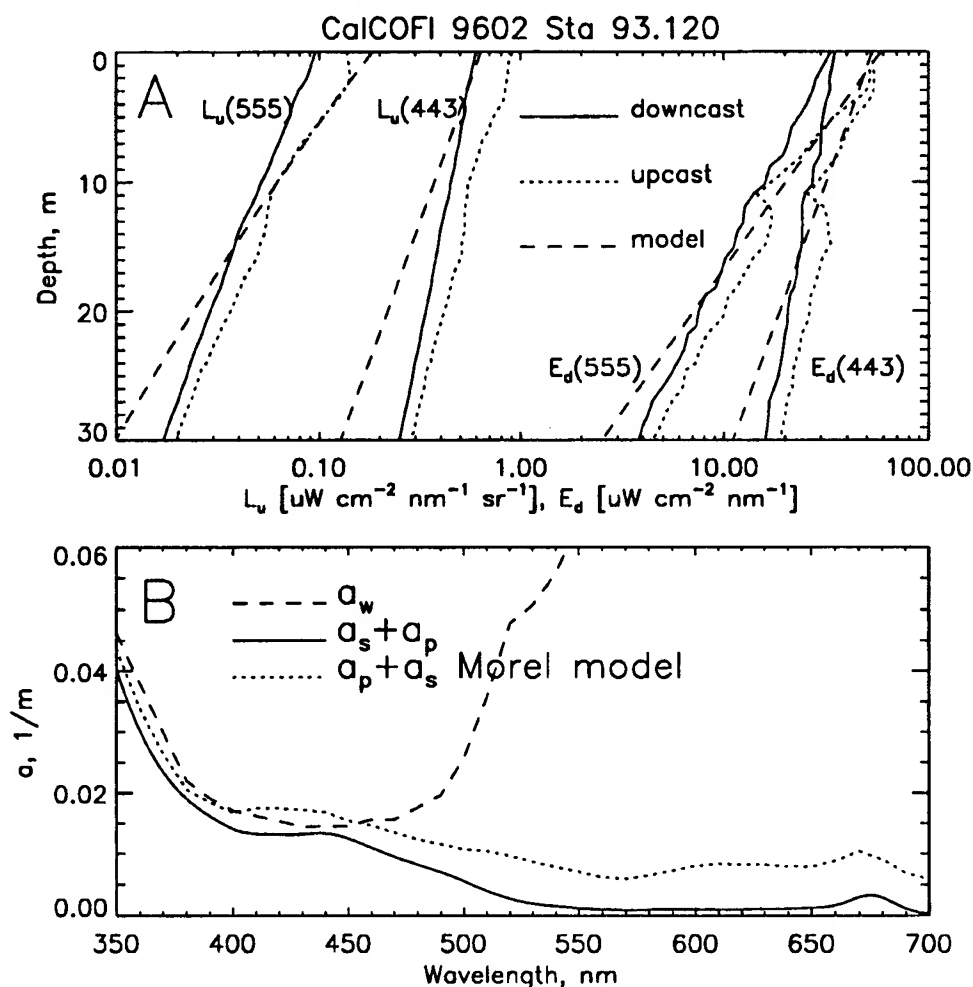


Figure 3: (A) Comparison of measurement at CalCOFI 9602 station 93.120 with radiative transfer calculations based on the Hydrolight code for 2 wavelengths (443 and 555 nm). The left half of the panel depicts nadir upwelling radiance, while the right half depicts downwelling irradiance. R_{rs} can be calculated from these measurements. Dashed lines are model data; solid lines are the downcast; dotted lines are the upcast. (B) Comparison of the Morel¹⁹ bio-optical model for $a_s + a_p$ (based on our measured chl-*a*+phaeo), and our direct laboratory estimates of $a_s + a_p$ for the mixed layer at the same station. Absorption by pure water is shown for comparison. The value of chl was 0.08 mgm^{-3} .

consensus will be attained. What we do see, quite clearly in Figure 3B, is that direct methods for estimating $a_p + a_s$ are not in agreement with one of the leading parameterizations. When the Hydrolight model is run, discrepancies that are dependent on parameterizations should be expected, and the discrepancies we note in Figure 3A between measured and model output are consistent with overestimates of the $a_p + a_s$ when the Morel¹⁹ parameterization is used.

5 Acknowledgments

Greg Mitchell has been supported in part by ONR N000014-91-J-1186 and NASA (NAGW-3665) grants. P. J. Flatau is supported in part by the Office of Naval Research Young Investigator Program and DuPont Corporate Educational Assistance. The existence and high quality of the CalCOFI data is made possible by the efforts of many members of the Marine Life Research Group (MLRG).

6 REFERENCES

- [1] R. W. Austin and T. J. Petzold. *The determination of the diffuse attenuation coefficient of sea water using the Coastal Zone Color Scanner*, pages 239–256. 1981.
- [2] A. Bricaud, M. Babin, A. Morel, and H. Claustre. Variability in the chlorophyll-specific absorption coefficients of natural phytoplankton: analysis and parameterization. *J. Geophys. Res.*, 100(C7):13321–13332, 1995.
- [3] A. Bricaud, A. Morel, and L. Prieur. Absorption by dissolved organic matter of the sea (yellow substance) in the uv and visible domains. *Limnol Oceanogr*, 26:43–53, 1981.
- [4] A.P. Brunger and F.C. Hooper. Anisotropic sky radiance model based on narrow field of view measurements of shortwave radiance. *Sol. Energy*, 51(1):53–64, 1993.
- [5] K. L. Carder, R. G. Steward, G. R. Harvey, and P. B. Ortner. Marine humic and fulvic acids: Their effects on remote sensing of ocean chlorophyll. *Limnology and Oceanography*, 34(1):68–81, 1989.
- [6] P. W. Francisco and N. J. McCormick. Chlorophyll concentration effects on asymptotic optical attenuation. *Limnology and Oceanography*, 39(5):1195–1205, 1994.
- [7] H.R. Gordon and A.Y. Morel. *Remote assessment of ocean color for interpretation of satellite visible imagery: A review*, volume 4, page 114. Springer-Verlag, Berlin, West Germany, 1983.
- [8] W. W. Gregg and K. L. Carder. A simple spectral solar irradiance model for cloudless maritime atmospheres. *Limnology and Oceanography*, 35(8):1657–1675, 1990.

- [9] T. L. Hayward, D. R. Cayan, P. J. S. Franks, R. J. Lynn, A. W. Mantyla, J. A. McGowan, P. E. Smith, F. B. Schwing, and E. L. Venrick. The state of the California current in 1994-1995: A period of transition. *California Cooperative Oceanic Fisheries Investigations Reports*, 36:19-39, 1995.
- [10] O. Holm-Hansen, C. J. Lorenzen, R. W. Holmes, and J. D. H. Strickland. Fluorometric determination of chlorophyll. *J. Cons. Perm. Int. Explor. Mer.*, 30(1):3-15, 1965.
- [11] N. K. Horjeslev. *On the origin of yellow substnce in the marine environment*, pages 39-56. Kobenhavns Universitet, 1980.
- [12] F. Kasten and G. Czeplak. Solar and terrestrial radiation dependent on the amount and type of cloud. *Sol. Energy*, 24(2):177-189, 1980.
- [13] A. W. Mantyla, E. L. Venrick, and T. L. Hayward. Primary production and chlorophyll relationships, derived from ten years of CalCOFI measurements. *California Cooperative Oceanic Fisheries Investigations Reports*, 36:159-166, 1995.
- [14] B. G. Mitchell. *Algorithms for determining the absorption coefficient of aquatic particles using the quantitative filter technique (QFT)*, volume 1302, page 137. SPIE, 1990.
- [15] B. G. Mitchell and D. A. Kiefer. Chlorophyll a specific absorption and fluoescence excitation spectra for light-limited phytoplankton. *Deep-Sea Research Part A Oceanographic Research Papers*, 35(5):639-664, 1988.
- [16] Curtis D. Mobley. *Light and water : radiative transfer in natural waters*. Academic Press, San Diego, 1994.
- [17] A. Morel. Optical modeling of the upper ocean in relation to its biogenous matter content (case I waters). *J. Geophys. Res.*, 93(C9):10749-10768, 1988.
- [18] A. Morel. Light and marine photosynthesis: A spectral model with geochemical and climatological implications. *Progress in Oceanography*, 26(3):263-306, 1991.
- [19] A. Morel and B. Gentili. Diffuse reflectance of oceanic waters: its dependence on Sun angle as influenced by the molecular scattering contribution. *Appl. Opt.*, 30(30):4427-4438, 1991.
- [20] A. Morel, K.J. Voss, and B. Gentili. Bidirectional reflectance of oceanic waters: a comparison of modeled and measured upward radiance fields. *J. Geophys. Res.*, 100(C7):13143-13150, 1995.
- [21] J. L. Mueller and R. E. Lange. Bio-optical provinces of the Northeast Pacific Ocean: A provisional analysis. *Limnology and Oceanography*, 34(8):1572-1586, 1989.
- [22] M. E. Ondrusek, R. R. Bidigare, S. T. Sweet, D. A. Defreitas, and J. M. Brooks. Distribution of phytoplankton pigments in the North Pacific Ocean in relation to physical and optical variability. *Deep-Sea Research Part A Oceanographic Research Papers*, 38(2):243-266, 1991.

- [23] W. S. Pegau and J. R. V. Zaneveld. Temperature dependent absorption of water in the red and near-infrared portions of the spectrum. *Limnology and Oceanography*, 38(1):188–192, 1993.
- [24] T. J. Petzold. Volume scattering functions for selected ocean waters. *SIO*, 72-78(8):79, 1972.
- [25] D. Roemmich. Mean transport of mass, heat, salt and nutrients in southern California [USA] coastal waters: Implications for primary production and nutrient cycling. *Deep-Sea Research Part A Oceanographic Research Papers*, 36(9):1359–1378, 1989.
- [26] C. S. Roesler, M. J. Perry, and K. L. Carder. Modeling in situ phytoplankton absorption from total absorption spectra in productive inland marine waters. *Limnology and Oceanography*, 34(8):1510–1523, 1989.
- [27] S. Sathyendranath, L. Prieur, and A. Morel. A three-component model of ocean colour and its application to remote sensing of phytoplankton pigments in coastal waters. *Int. J. Remote Sens.*, 10(8):1373–1394, 1989.
- [28] R. C. Smith and K. Baker. The bio-optical state of ocean waters and remote sensing. *Limnology and Oceanography*, 23(2):247, 1978.
- [29] R.C. Smith and K.S. Baker. Optical properties of the clearest natural waters (200–800 nm). *Appl. Opt.*, 20(2):177–184, 1981.
- [30] H. M. Sosik and B. G. Mitchell. Light absorption by phytoplankton, photosynthetic pigments and detritus in the California Current System. *Deep-Sea Research Part I Oceanographic Research Papers*, 42(10):1717–1748, 1995.
- [31] Zheng Tao, N.J. McCormick, and R. Sanchez. Ocean source and optical property estimation from explicit and implicit algorithms. *Appl. Opt.*, 33(15):3265–3275, 1994.
- [32] E. L. Venrick and T. L. Hayward. Determining chlorophyll on the 1984 calcofi surveys. *Cal-COFI Reports*, XXV:74–79, 1984.
- [33] J. R. V. Zaneveld. An asymptotic closure theory for irradiance in the sea and its inversion to obtain the inherent optical properties. *Limnology and Oceanography*, 34(8):1442–1452, 1989.

The WET Labs ac-9: field calibration protocol, deployment techniques, data processing and design improvements.

C. Moore & E.J. Bruce

WET Labs Inc., Philomath, OR 97370 USA

W.S. Pegau

College of Oceanic and Atmospheric Sciences, Oregon State University, Corvallis, OR 97331 USA

A. Weidemann

Naval Research Laboratory, Stennis Space Center, MS 39529 USA

ABSTRACT

The WET Labs ac-9 has been used by scientists world wide to collect absorption and attenuation measurements for over three years. The ac-9 provides measurements of the *in-situ* spectral signatures of particulate and dissolved material using a dual source nine wavelength filter wheel transmitter with reflective tube absorption optics and a conventional transmissometer configuration. Since the ac-9 was introduced, much effort has been expended in establishing workable protocols for instrument calibration, deployment and data processing. In addition, considerable effort has been placed in design improvements, enhancing reliability, stability and ease of use. From these efforts a protocol document was produced which provides detailed instructions for operation, deployment and data processing and an overview of the instrument evolution since it's original introduction as a product. An overview of the protocol document is presented in order to familiarize the reader with critical issues associated with meter usage and proper handling of data.

Keywords: ac-9, absorption, attenuation, spectrophotometer

1. INTRODUCTION

The ac-9 is a spectral, beam absorption and attenuation meter used for the *in situ* determination of inherent optical properties in natural waters. Using dual sources coupled with a single filter wheel, the meter provides concurrent determination of the absorption and attenuation coefficients at nine wavelengths spanning from 400 nm to 715 nm. Since initial delivery, approximately 80 more units have been used in applications ranging from tow-yos to long term moorings. As more researchers used the meter, questions as to proper usage, data integrity and post processing requirements quickly exceeded the scope of the original user manual. In response to this need for more information WET Labs, Inc. produced a new protocol document. This paper provides an overview of the protocol and delineates the salient issues involved with proper usage of the instrument. Researchers wishing for more detailed information should contact WET Labs, Inc. for a copy of the full protocol document. (www.wetlabs.com)

The protocol for ac-9 usage breaks down into three primary sections. We discuss basic operation and deployment issues. We discuss the ac-9 laboratory and field calibration. We delineate the steps for processing and correction of the data obtained by the instrument.

2. ac-9 OPERATION

2.1 Mounting

The ac-9 contains two optical paths that are sensitive to lateral and torsional stresses. To ensure that the unit functions properly, it is important to minimize stresses when mounting the unit to a frame. If possible the ac-9 should be mounted upright. It is preferable to rest the bottom of the ac-9 on the cage framework and attach both the upper and lower housings to the vertical framework of the cage

2.2. Plumbing & Tubing

It is important to ensure good flow through the ac-9 flow tubes. The flow rate through the instrument should be kept above 1 liter/min. The pump for the ac-9 should be placed above the upper set of nozzles of the ac-9 flow tubes. It is required that the pump pull the water through the tubes rather than push it through. It is critical that all plumbing help move bubbles out of the system.

2.3 Deployment

The ac-9 is used in a variety of deployment modes. Each of these methods requires some consideration in how best to optimize results from the meter. Table 1. summarizes the primary considerations with each of these applications

Moorings	Towed Bodies	Underway/Bench-top	Profilers
<i>Anti-fouling</i>	<i>Mounting</i>	<i>Keep the meter within specified temperature range</i>	<i>Mounting</i>
<i>Warm-up</i>	<i>Flow</i>	<i>Initial purge</i>	<i>Pre-purge</i>
<i>Ground loops</i>	<i>Pre-purge</i>	<i>Watch for bubbles</i>	<i>Free-fall descent</i>
<i>Plumbing</i>	<i>Consider time constants</i>		<i>Time constants and spatial resolution</i>
<i>Post calibration</i>	<i>Protect the meter</i>		<i>Care of meter between casts</i>
<i>Power consumption and battery life</i>			

Table 1. - Summarization of special considerations for various deployment methods.

3. ac-9 CALIBRATION

3.1. WET Labs Calibration Procedures

The standard ac-9 calibration procedures at WET Labs include: a series of characterization tests to confirm the instrument's performance is within factory specifications, temperature calibration, pure water calibration and an air calibration.

Factory Pre-calibration Procedures

Before undergoing temperature tests and calibration the meter is subjected to a series of tests to determine basic operational integrity. These include:

- *12 hour burn-in*
- *Optical throughput tests*
- *Minimum and maximum signal determination*
- *Shock and vibration tests*
- *Precision tests*

Factory Temperature Calibration

During the temperature calibration of the ac-9, the instrument's temperature coefficients are determined. The temperature coefficients provide a correction factor for temperature for each channel of the ac-9. The temperature calibration data is also used to identify unusual instrument performance issues causing the output of the meter to change dramatically as a function of temperature. Figure 1. shows a typical example of ac-9 absorption and attenuation at 488nm

plotted versus internal instrument temperature, both uncorrected and corrected. The internal temperature range for this meter, stated on its Calibration Sheet, is 11 to 39 degrees Celsius.

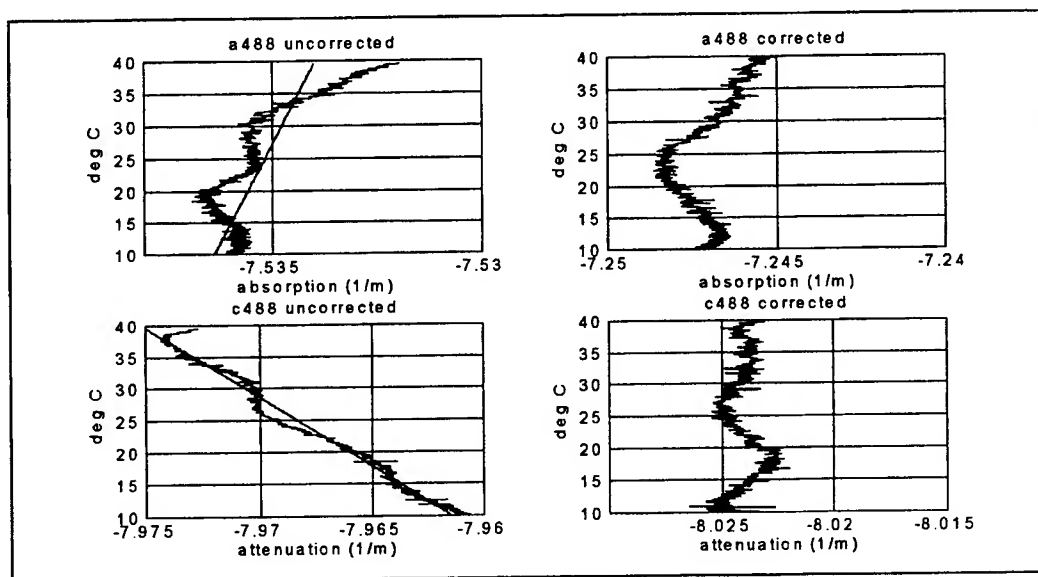


Figure 1. Typical ac-9 temperature calibration data. The uncorrected data is collected to determine the temperature coefficients (K_t). The corrected data is obtained in a second temperature cycle to verify the temperature corrections, which are automatically applied in WETView.

Factory Water Calibration

The purpose of the WET Labs water calibration is to determine the offset values of absorption and attenuation that result in a 0.00 m^{-1} reading with pure water in the sample volume of the flow tubes. These water offset values are listed on the Calibration Sheet and included in the device file for each meter's new calibration.

Factory Air Calibration

The purpose of the WET Labs air calibration is to determine the offset values of absorption and attenuation that result in 0.000 m^{-1} readings with air in the sample volume of the flow tubes. These air offset values are listed on the Calibration Sheet and are included in the air tracking device file for each meter's new calibration.

3.2. Air Tracking

Air tracking is primarily intended to be used to monitor offsets in the instrument's output due to changes in the optical system caused by shipping or mounting of the instrument to a cage or other deployment package. Air tracking can also be used to monitor instrument drift over extended periods of time. Air tracking involves the collection of data with the ac-9 in air using WETView and the air CAL file. Output collected following the Air Tracking Protocol are considered the Air Tracking Offsets. These offset values are an indication of changes in the optical throughput of the instrument since the factory air calibration and can be used in certain situations to correct data collected using the ac-9.

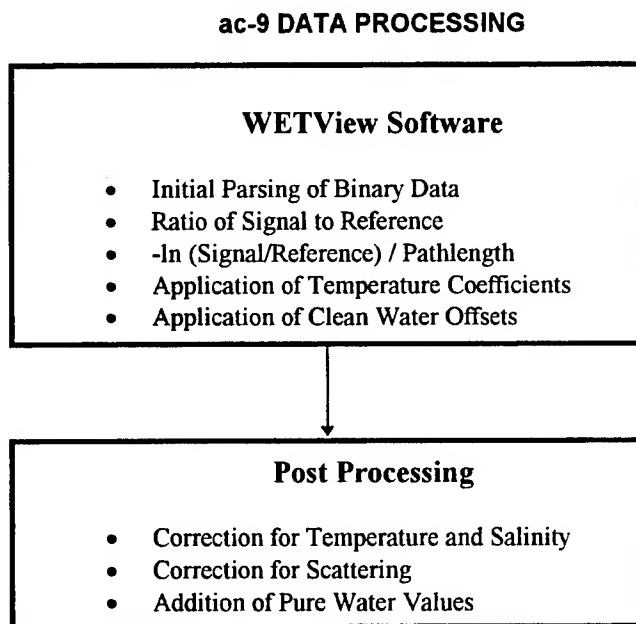
3.3. Field Water Calibration

Maximum accuracy of measurements is obtained by performing water calibrations of the ac-9 in the field. Field water calibrations can remove the effects of small misalignments of the optical system caused by shipping or mounting of the instrument on a cage or other deployment package. When a reliable source of optically clean water is available, water

calibrations are easy to perform in the field. The concept behind the water calibrations is simple. The idea is to provide the instruments with a source of clean, bubble-free water which can be used as a reference value. This is the same concept used when the factory offset values are determined. Clean water can be produced in the lab and transported to the ship or a portable system can be constructed for shipboard use.

4. ac-9 DATA PROCESSING

An ac-9 acquires raw values representing light losses of a light beam propagating through a fixed path of water. In order to convert these values into meaningful units and to correct for instrument and environmental factors associated with the measurements, several processing steps are required. The following flow chart provides an overview of these steps.



4.1. WETView Calculations

WETView is the basic WET Labs software package used to collect and process data from the ac-9. WETView reads in the raw binary data from the ac-9 and then parses the data. The parsed data contains digitized signal values for signal and reference levels for each channel. WETView then applies an algorithm which: converts signal and reference values into terms of uncorrected inverse meters; applies a linear temperature correction; applies clean water offsets supplied from the instrument's device file which provide a value referenced against clean water.

4.2. Temperature and Salinity Corrections

Water in the red and near-infrared portions of the spectrum is subject to changes in absorption as a function of temperature¹. These effects must be accounted for before applying scattering corrections to the data. Data may need to be corrected for a second salinity effect². The effect is due to the difference in the index of refraction between fresh and saline water which cause changes in the reflectance at the windows of the instrument. Figure 2. shows a dissolved phase profile taken from an ac-9. The plot shows the uncorrected values as well as the corrected values for temperature and salinity.

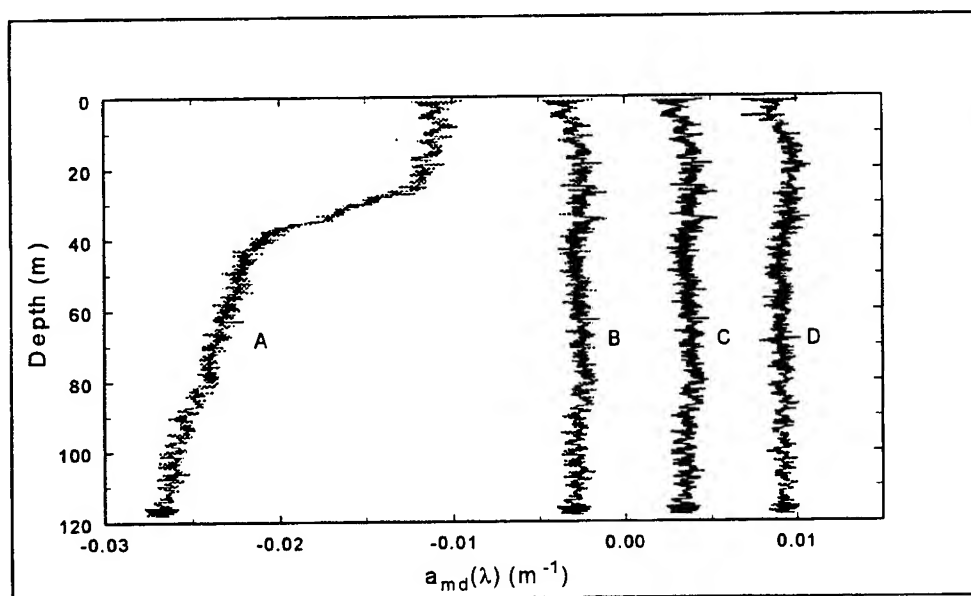


Figure 2. The application of temperature and salinity corrections to a gelbstoff profile. Line A is the raw $a(715)$. Line B has the temperature correction applied. Line C includes the temperature and salinity corrections. Line D is the absorption coefficient at 650 nm, given to provide a reference profile. Note both temperature and salinity corrections are necessary to provide a profile with positive absorption values².

4.3. Scattering Corrections

Reflecting tube absorption meters and spectrophotometers do not collect all of the light scattered from the beam. The uncollected scattered light causes the instrumentation to overestimate the absorption coefficient. There are several schemes to correct absorption measurements for scattering errors. The three methods most commonly used include:

- 1) subtraction of a reference wavelength where the absorption is assumed to be zero.
- 2) removal of a fixed proportion of the scattering coefficient
- 3) use of a reference wavelength to determine the proportion of the scattering coefficient to be subtracted from the signal³.

Each of these methods require different assumptions and ancillary measurements.

4.4. Addition of Pure Water Values

Since the ac-9 measurements are referenced to optically pure water, it is necessary to add the optical properties of the reference water to arrive at the total absorption or attenuation coefficient. Many sources are available for the absorption coefficient of pure water, however large differences in the absorption coefficient of water exist between the various authors. We recommend using the absorption coefficients reported by Pope⁴ for wavelengths less than 700 nm. For wavelengths in the near infrared we recommend the values of Kou et al⁵.

5. ACKNOWLEDGEMENTS

Initial development work for the ac-9 was performed under the aegis of NRL Contract Number N00014-96-C-6002. Percy Donaghay and Mike Twardowski of the University of Rhode Island provided significant contributions in development of the operational and calibration protocol.

6. REFERENCES

1. W.S. Pegau, and J.R.V. Zaneveld, "Temperature dependence of the absorption coefficient of pure water in the visible portion of the spectrum", *Ocean Optics XII Proc.*, Soc. Photo-Optical Instrum. Eng. (SPIE), in press, 1994.
2. W.S. Pegau, D. Gray, and J.R.V. Zaneveld, "Absorption of visible and near-infrared light in water: the dependence on temperature and salinity", pre-print submitted to *Applied Optics*, 1996.
3. J.R.V. Zaneveld, J.C. Kitchen, C. Moore, The scattering error correction of reflective-tube absorption meters, *Ocean Optics XII Proc. SPIE 2258*, 44-55 (1994).
4. Pope, R.M., "Optical absorption of pure water and sea water using the integrating cavity absorption meter", Ph.D. Thesis. (Texas A & M, College Station, TX, 1993).
5. Kou, L., D. Labrie, and P. Chylek, "Refractive indices of water and ice in the 0.65 to 2.5 μm spectral range", *Appl. Opt.*, **32**, 3531-3540. (1993)

Modulated Pulse Lidar for Enhanced Underwater Detection

L. Mullen and V. M. Contarino

Naval Air Warfare Center Aircraft Division
22541 Millstone Road
Patuxent River, Maryland 20670-5304

ABSTRACT

Past laboratory experiments established the ability of the modulated pulse lidar system to improve underwater target contrast. Due to the limitations of the laboratory environment in assessing the performance of the new detection scheme, a system was designed and constructed for use in an ocean experiment which was carried out in December, 1995. Results from the field test confirm the capability of modulated pulse lidar to reduce backscatter clutter and enhance underwater target contrast. In addition, the existence of microwave subcarrier interference effects confirmed that the microwave signal integrity was maintained throughout the range of measurements.

Keywords: lidar, radar, laser radar, ocean remote sensing, optical modulation

2. INTRODUCTION

Conventional air-to-underwater lidar systems are contrast limited in the detection of small, shallow underwater targets. This is due to the backscatter of the transmitted optical beam from water particles within the receiver field of view. In response to this shortcoming, a modulated pulse lidar detection scheme has been developed by combining the sophisticated modulation, detection and signal processing techniques of radar with the underwater transmission capability of lidar. This work focuses on evaluating the ability of this new technique to reduce backscatter clutter and to improve the detection sensitivity of underwater targets.

The feasibility of this novel detection scheme was investigated through laboratory experiments. An ocean mass simulator was designed and constructed to test the effect of the water on a modulated optical pulse¹. An analytical model based on the ocean mass simulator was developed to predict experimental outcomes. The results of the theoretical study and corresponding laboratory experiments confirmed the ability of the hybrid detection scheme to reduce backscatter clutter and improve the contrast of underwater targets².

The laboratory experiments combined with the analytical considerations provide a basis for understanding the benefits of the new detection scheme. Specifically, use of the modulated pulse lidar detection scheme has resulted in a decrease in backscatter clutter and a corresponding enhancement of underwater target contrast over the conventional, unmodulated lidar system. However, the complexities involved with the transport of light through water cannot be completely represented in these preliminary studies. Furthermore, the geometrical differences between the laboratory and actual lidar system measurements must be accounted for when evaluating the new detection scheme. Therefore, a modulated pulse lidar system was constructed with the aim of performing experiments in a true ocean setting. These experiments were carried out in December, 1995 at the Atlantic Undersea Test and

Evaluation Center on Andros Island, Bahamas. In the following section, we describe the goals of the experiments, including parameters which were varied to evaluate the sensitivity of the hybrid system relative to conventional lidar. Next, we discuss experimental results obtained in the ocean field test, followed by conclusions and topics for future investigation.

3. MODULATED PULSE LIDAR OCEAN EXPERIMENT

For the modulated pulse lidar detection scheme to succeed in the lidar environment, the microwave signal encoded on the optical carrier should endure minimal distortion as it travels through the water. Therefore, mechanisms which affect the dispersion of the modulated optical signal in water must be identified. An ocean field test was designed and conducted to validate the benefits of the hybrid detection scheme and to identify those variables which affect the encoded microwave signal.

In order to thoroughly address these objectives, a set of independent and dependent variables was defined. Three types of independent variables were identified:

- i. those which could be controlled during experimentation, namely the receiver field of view, the transmitter beam divergence, the target size and the target depth;
- ii. those which were fixed due to the location of the field test, including the water depth, the water clarity, and the platform altitude; and
- iii. those which varied randomly and were not controllable, specifically the sea surface fluctuations.

The dependent variables were: the lidar and radar relative amplitudes of the target echoes, the backscatter signal levels, and the target contrasts.

The next step in the design of the ocean experiment was to establish the experimental goals. The ultimate goal of the experiment was to study the sensitivity of the hybrid detection scheme as a function of the independent and dependent variables. Thus, three successive goals were established for the ocean experiment:

- i. The first and most crucial objective was to design and assemble a modulated pulse lidar system which could operate effectively in the ocean environment.
- ii. The second goal was to utilize the system to determine how well the integrity of the microwave subcarrier is preserved as it travels through water.
- iii. The final aim was (1) to evaluate experimentally how parameters and variables affect the sensitivity of the hybrid system, and (2) to compare the results with those predicted by analytical studies.

In the following section, the design and characterization of the modulated pulse lidar system for ocean experimentation is discussed.

4. EXPERIMENTAL SETUP

To attain the first experimental goal, a modulated pulse lidar system was designed and constructed. The block diagram of the system is shown in Fig. 1. The transmitter requirements include a blue-green wavelength to minimize absorption in the water, high peak power (>10 kW), a 7-20 nsec pulsewidth, and a stable microwave modulation. The transmitter developed which met these specifications consists of a laser oscillator, an optical amplifier and a frequency doubler. The critical component is the oscillator, an optical cavity containing a flashlamp-pumped Nd:YAG rod, a 3 GHz

phase modulator and a passive Q-switch. This configuration produced 3 GHz modulated, 6-20 nsec, 10 kW peak power, blue-green optical pulses.

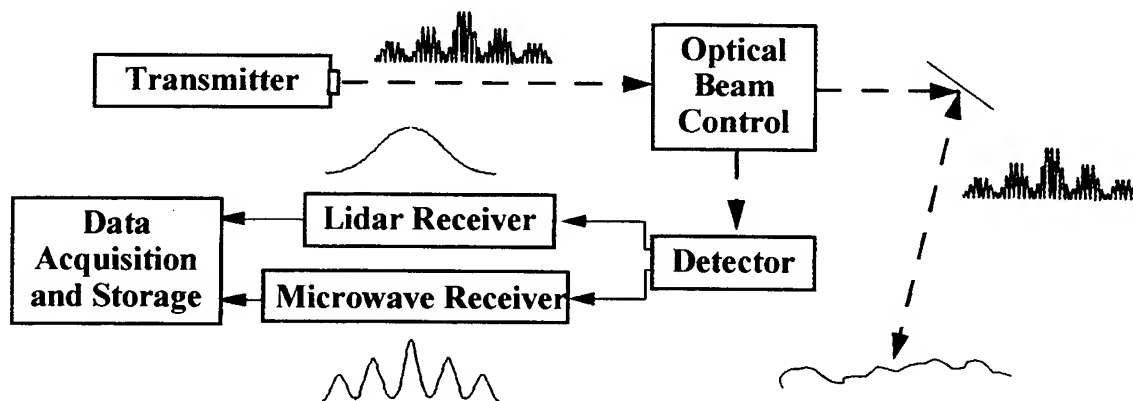


Fig. 1. Block diagram of the modulated pulse lidar system.

The transceiver, which includes the optical beam control and detector, must provide beam divergence and receiver field of view regulation. The constructed transceiver included optics to vary the beam divergence from 1 to 40 mRad, and a variety of irises for a 10 to 50 mRad field of view range. The detector requirements include a large bandwidth to recover the modulation encoded on the optical carrier, in addition to a large active area, high gain, and low noise to enhance the signal level. The detector chosen is the intensified photodiode (IPD) fabricated by Intevac³. This device has a 50 mm² active area, a 10³ gain, and a 1 GHz 3 dB bandwidth.

The output of the IPD was split into its high frequency (3 GHz radar signal) and low frequency (100 MHz lidar pulse envelope) components by use of a bias tee network. The microwave envelope was then amplified, filtered by a 3 GHz bandpass filter, and detected by a Schottky diode. The lidar and modulated pulse lidar returns were digitized at a 1 GHz sampling rate by two separate channels of a digitizing oscilloscope. The digitized signals were displayed simultaneously on the scope monitor. An external computer controlled the data collection and storage.

The constructed system was assembled inside a tower located approximately 1 mile from shore at the Atlantic Undersea Test and Evaluation Center. The optical signal was transmitted through a window to an outside mirror which was positioned to reflect the transmitted light to the water surface. The water return signal was reflected off an adjacent mirror and recovered by the transceiver. A pulley system was constructed to raise and lower circular plywood targets in the water. The entire system operated effectively and provided echoes with good signal-to-noise and stability. In the following section, the results obtained with this system are discussed.

5. EXPERIMENTAL RESULTS

In the following paragraphs, the ocean experimental results are presented in accordance with the previously outlined experimental goals. First, the integrity of the recovered microwave signal is examined. Second, the ability of the modulated pulse lidar detection scheme to reduce backscatter clutter and to enhance target contrast is discussed.

5.1. Microwave subcarrier fading

The preservation of the frequency and phase of the microwave envelope is critical to the performance of the modulated pulse lidar system. If the microwave subcarrier integrity is preserved, multipaths in the return signal from objects which are large compared to the modulation wavelength produce a cancellation, and subsequent fading, of the microwave subcarrier. Experimental evidence of this microwave subcarrier fading is shown in Table 1, where the measured radar-to-lidar target return ratio as a function of target size and depth and receiver field of view is shown. It is evident that the largest decrease (approximately 7 dB) in the signal ratio occurs as the target size increases relative to the microwave wavelength. These results indicated that the propagation through water did not affect the integrity of the microwave subcarrier.

Beam Divergence		Wide (40 millirad)	
Field of View		Narrow (10 millirad)	Wide (50 millirad)
Target Depth	Target size	-	-
3 m	0.15 m	-1.10	-1.15
	0.5 m	-7.96	-8.17
5 m	0.15 m	-1.18	-4.03
	0.5 m	-8.59	-9.75

Table 1. Radar-to-lidar target return ratio (in dB) as a function of target size, target depth, and receiver field of view.

5.2. Clutter reduction and contrast enhancement

Prior theoretical and laboratory studies predicted that the hybrid detection scheme suppresses the backscatter clutter and therefore enhances the contrast of small, shallow underwater targets. To test this premise, the lidar and radar backscatter signal levels were measured simultaneously. The optical pulse was transmitted at a slight angle to the water surface to minimize surface reflections. A representative sample of the measured return signal is displayed in Fig. 2. Since the surface return is absent, the steadily rising segment of the backscatter signal represents the pulse as it enters the water. The peak occurs when the entire pulse has entered the water. The signal subsequently decays exponentially due to absorption and scattering of the optical beam by the water column. For the narrow beam divergence experiment, the radar backscatter signal level is decreased by 9 dB relative to the lidar backscatter magnitude. The difference in the backscatter amplitudes is expected to expand as the beam footprint increases to that which is typical in an aerial lidar system.

To evaluate the lidar and radar target contrasts, two different footprint-to-target size ratios were obtained by using a large beam divergence (0.5 m footprint radius) in combination with two different target sizes (0.15 and 0.5 m radii). In addition, with each scenario, the receiver field of view was varied from narrow (10 milliradians) to wide (50 milliradians) to determine its effect on the target contrast. Although the target contrast is obtained by measuring the target return-to-background ratio, the shallow water depth at the test site prohibited the quantification of this information. However, results indicated that the hybrid system produced an improvement in target contrast when the 0.15 m target was detected with a wide beam divergence and a narrow field of view. A sample of the lidar and radar returns obtained with this set of parameters is shown in Fig. 3. This figure clearly demonstrates that the contrast

of the radar target return is improved as compared to the corresponding lidar return. This contrast enhancement is credited to the reduction in microwave backscatter.

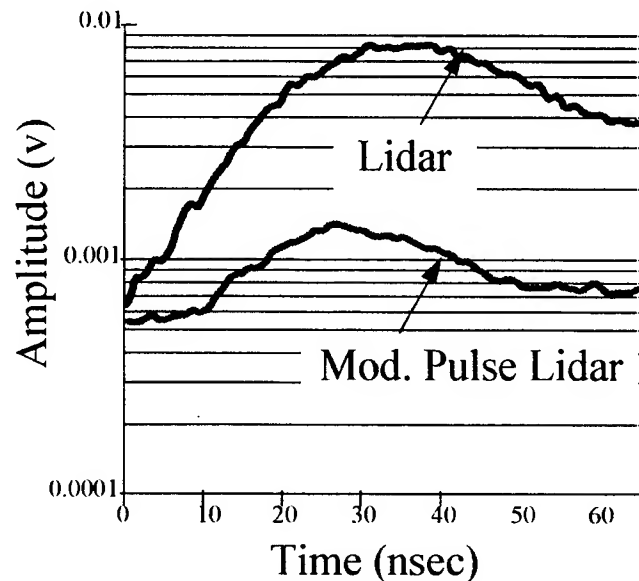


Fig. 2. Comparison of lidar and modulated pulse lidar backscatter signal returns obtained with the following set of variables: narrow beam divergence (1 milliradian), and wide field of view (50 milliradians). The modulated clutter is suppressed by 9 dB relative to the unmodulated lidar return.

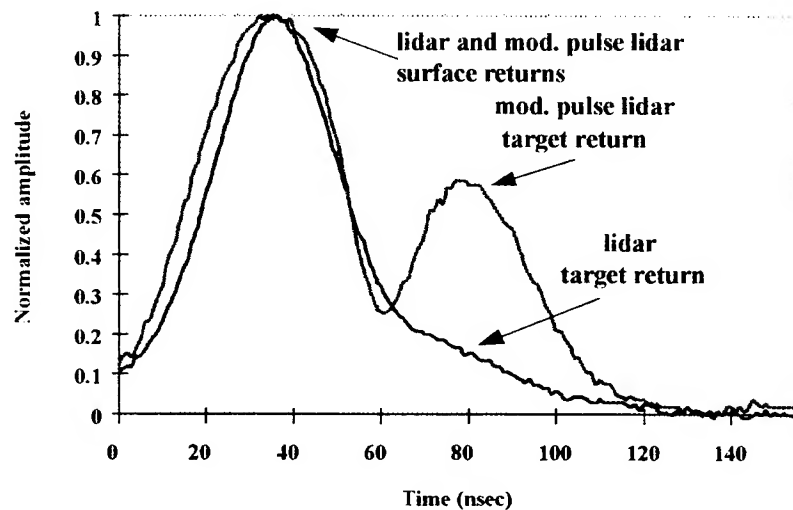


Fig. 3. Lidar and modulated pulse lidar echo returns obtained with the following set of parameters: 0.15 m target at 5 m depth, wide beam divergence (40 milliradians), and narrow field of view (10 milliradians). The contrast of the modulated pulse lidar target return is improved relative to that of the lidar return due to the backscatter clutter reduction.

6. CONCLUSIONS AND FUTURE WORK

Due to the limitations of the laboratory environment, a system was designed and constructed to evaluate the performance of the modulated pulse lidar detection scheme in the ocean environment. The system generated and detected high-power, microwave-modulated, blue-green optical pulses. Various experiments were performed with this system to evaluate the relative sensitivity of modulated pulse lidar to conventional, unmodulated lidar as a function of system and environmental variables. The experimental results led to the following conclusions:

- i. The microwave envelope remained coherent throughout the range of measurements.
This is a prerequisite to the introduction of more sophisticated detection and signal processing techniques to future modulated pulse lidar systems.
- ii. The modulated pulse system reduces backscatter clutter which limits the contrast of underwater targets.
- iii. The backscatter reduction produced by the hybrid detection scheme enhances the contrast of small, shallow underwater targets relative to conventional lidar.

Thus, the evaluation of the modulated pulse lidar detection scheme from theory, to laboratory experiments, to ocean experiments has provided insight into the possibilities of the new technique to enhance the sensitivity of lidar in the detection of underwater objects. Future work includes developing a Monte Carlo model for the modulated pulse lidar system to predict future experimental results. A multiple modulation frequency system is being developed, and a tank experiment will be conducted to evaluate the new system as a function of water clarity and sea surface effects.

7. REFERENCES

1. L. Mullen, P. R. Herczfeld, and V. M. Contarino, "Analytical and Experimental Evaluation of an Optical Fiber Ocean Mass Simulator," *IEEE Microwave and Guided Wave Letters*, **Vol. 4**, No. 1, pp. 17-19, 1994.
2. L. Mullen, A. Vieira, P. R. Herczfeld, and V. M. Contarino, "Application of Radar Technology to Aerial Lidar Systems for Enhancement of Shallow Underwater Target Detection," *IEEE Transactions on Microwave Theory and Techniques*, **Vol. 43**, No. 9, pp. 2370-2377, 1995.
3. R. La Rue, J. Edgecumbe, G. Davis, S. Gospe, V. Aebi, "High quantum efficiency photomultiplier with fast time response," *SPIE Photodetectors and Powermeters*, **Vol. 2022**, pp. 64-73, 1993.

A method for removing a majority of the error in PUV attenuation coefficients due to spectral drift in response with depth in the water column

Karen W. Patterson and Raymond C. Smith

Institute for Computational Earth Systems Science
and Department of Geography
University of California Santa Barbara
Santa Barbara, California 93106

Charles R. Booth

Biospherical Instruments, Inc.
5340 Riley Street
San Diego, California 92109

ABSTRACT

It is well known that ultraviolet (UV) radiation has the potential to cause significant damage to living organisms. Generally, shorter UV wavelengths have the potential to do exponentially more damage than longer wavelengths (i.e. Setlow¹). Therefore, in calculating biological doses of radiation to marine organisms, even small spectral variations in recorded UV irradiances can propagate into large errors.

The PUV instrument made by Biospherical Instruments, Inc. is a commonly used filter-based radiometer used to measure UV radiation in the water column. It has long been known that the signal from the PUV becomes increasingly weighted by longer wavelengths with increasing depth in the water column.² This is due to the increased attenuation of shorter UV wavelengths as compared to longer UV wavelengths in the water column.

Presented here is a method of removing the majority of the spectral drift effect from the UV attenuation coefficients calculated from PUV data for biogenic waters. Chlorophyll and dissolved organic matter (DOM) are allowed to vary independently with depth in a simple high-resolution spectral model for a variety of atmospheric total ozone concentrations and solar zenith angles. To investigate the magnitude of errors and possible corrections, attenuation coefficients are calculated using the estimated PUV spectral response function for each channel and for 1nm model wavebands at 305, 320, 340 and 380nm. The same process was conducted for clear water. Differences between the PUV-weighted attenuation coefficients and corresponding model attenuation coefficients for clear water and biogenic waters are used to develop a fairly simple method of eliminating a large portion of the spectral drift effect in attenuation coefficients calculated from PUV data.

Keywords: PUV, spectral drift, ultraviolet, UV

1. INTRODUCTION

The capabilities of ultraviolet (UV) wavelengths of radiation to do damage to living organisms has been well documented. This knowledge in conjunction with indications of decreasing global ozone (increasing UV radiation) has spawned greater interest in the measurement of UV radiation in a variety of environments. The PUV (Profiling Ultraviolet Radiometer) made by Biospherical Instruments, Inc. is a filter-based radiometer used to measure UV radiation in the marine environment. The PUV has four UV channels and a broadband PAR photosynthetically active radiation channel. The effective bandwidths and spectral centers of the four UV channels are determined from the intersection of the estimated spectral response of the instrument² (Figure 1) and the solar spectrum. The UV channels are effectively ~10nm wide centered on 305, 320, 340 and 380nm. The filter combination in the shortest wavelength channel of the prototype PUV instruments resulted in a center wavelength close to 308nm and "308" was used as the channel reference. Changes in the filter design of this channel for production instruments resulted in a center wavelength closer to 305nm and the channel has been subsequently renamed and will be referred to as the 305 channel³.

In calculating the biological dose of UV radiation for marine organisms, a spectrally accurate and consistent dataset is essential. Biological weighting functions are often strongly a function of wavelength with shorter UV wavelengths having the potential to do much more damage than longer UV wavelengths (i.e. Setlow¹). As depth

increases in the water column, shorter UV wavelengths are generally attenuated faster than longer wavelengths. As the shorter UV wavelengths attenuate faster, the effective central wavelength of the PUV channels shifts to longer wavelengths and the effective bandwidth decreases.² Since the shorter UV wavelengths have the potential to do more damage and are also more strongly attenuated in the water column, small variations in the effective central wavelength and/or bandwidth of the PUV channels can lead to significant errors in the calculation of biological UV dose.

Accurate calibration is equally critical. Relating to both spectral consistency and accurate calibration is the issue of the consistency of the estimated spectral response functions between PUV instruments. Filters used in the PUV instruments vary slightly in their spectral transmission from instrument to instrument.² Thus, two PUV's calibrated at the surface may give slightly different readings at depth due to slight variations in the filter transmission spectra. In the method presented for removing the majority of spectral drift from PUV data, spectral drift will be defined as a deviation of modelled attenuation coefficients weighted by the estimated PUV response function for each channel from the monochromatic modelled attenuation coefficient at 305, 320, 340 and 380nm. By doing this, variations in the filter transmission spectra between instruments and changing effective central wavelengths will be put on common ground.

2. METHOD

In biogenous ocean waters, the total attenuation coefficient as a function of wavelength ($K_{TOT}(\lambda)$) is the sum of attenuation due to seawater ($K_{SW}(\lambda)$), chlorophyll and related pigments ($K_{CHL}(\lambda)$), and dissolved organic matter ($K_{DOM}(\lambda)$) which are the dominant attenuators of UV radiation. All three generally attenuate stronger at shorter UV wavelengths (Figure 2). Since the spectral attenuation coefficient curves for these three variables have slightly different shapes, one approach to removing the spectral drift from PUV data would be to 1) estimate CHL and DOM from PUV profiles, 2) estimate spectral drift from these estimates of CHL and DOM and 3) adjust attenuation coefficients calculated from PUV data accordingly. Using this type of spectral drift correction could result in large errors unless accurate independent profiles of CHL and DOM are collected in conjunction with each PUV profile. This will become clear in the following paragraphs.

Even in pure seawater, spectral drift occurs with increasing depth in the water column as shorter UV wavelengths are attenuated out of the water column faster than longer UV wavelengths (Figure 3). Since CHL and DOM also attenuate more strongly at shorter UV wavelengths than at longer UV wavelengths, spectral drift can be expected to occur faster for larger attenuation coefficients. Similarly, for larger attenuation coefficients, larger spectral drift adjustments to attenuation coefficients calculated from PUV data are necessary as the relative difference in the strength of attenuation as a function of wavelength increases.

In order to do a spectral drift correction based on estimates of CHL and DOM from PUV profiles accurately, without independent measurements of CHL and DOM, it is necessary to start making estimates and spectral drift adjustments at the ocean surface where the calibration is known and work down into the water column making adjustments at every step. For instruments such as the PUV which only measure downwelling irradiance, the accuracy of calculated attenuation coefficients generally decreases near the surface due to increasing wave action effects. Errors in spectral drift adjustments made near the surface accumulate as depth increases.

A second approach would be to estimate spectral drift based on the magnitude of the attenuation coefficient and the pattern of spectral drift in clear water. The behavior of attenuation coefficients in pure seawater can be modelled (Figure 3). We also know that increasing CHL and/or DOM will increase $K_{TOT}(\lambda)$ and the amount of spectral drift correction needed to be applied to attenuation coefficients calculated from PUV measurements. Thirdly, the detection limit of the instrument will limit how far the effective central wavelength of each channel can shift.

All modelled data are used in this paper due to the fact that full spectral datasets are not available at the same time and depth resolutions as PUV datasets. The surface model used, including attenuation through the air-sea interface, is a modified version of the model by Gregg and Carder⁶. Modifications include using: 1) the Modtran 3 extraterrestrial solar spectrum summed to 1nm resolution, 2) extinction coefficients for maritime aerosols of d'Almeida et al.⁷ and 3) ozone absorption coefficients derived from Molina and Molina⁸ below 350nm. These modifications were made in order to expand the range of the model to 280-700nm and to simplify aerosol computations. All model runs presented here are for clear skies, flat seas, 80% surface relative humidity and a surface temperature of 294.1K, which are average values for the Southern California Bight. In-water spectra were calculated at 1nm spectral resolution and at 1m depth intervals using the method of Baker and Smith⁵. For statistical validity, ozone

and solar zenith angle were allowed to vary randomly from 250-350DU and 0-80° respectively in the surface model. The ozone range encompasses ranges typically seen in the Southern California area. Solar zenith angles above 80° were eliminated since both the model and PUV measurements start to become suspect at high solar zenith angles. Random profiles of CHL ranging from 0.2, 0.4 and 0.6 µg/l were used for the calculation of $K_{CHL}(\lambda)$. According to the equations of Baker and Smith⁵,

$$K_{DOM}(\lambda) = k_d(380nm) \text{Exp}[-0.014(\lambda - 380nm)]. \quad (1)$$

Here, the terms $k_d(380nm)$ and the concentration of DOM (D) are combined as a single term $K_{DOM}(380nm)$ and is allowed to vary randomly with depth from 0.2, 0.4 and 0.6 m⁻¹. The ranges of CHL and $K_{DOM}(380nm)$ were taken from chlorophyll samples and the 380 channel of PUV profiles collected in the Southern California Bight during the BURNM (Biological effects of Ultraviolet Radiation on Natural Mortality) cruises of 1993-1995. With three range categories for each of CHL and $K_{DOM}(380nm)$ and 100 model runs for each range combination, there were a total of 900 model runs. From the spectra at each depth, attenuation coefficients were calculated for 1nm bandwidths centered on 305, 320, 340 and 380nm (collectively referred to as K_{mono}) and for spectra weighted by the estimated PUV spectral response function for each channel (collectively referred to as K_{PUV}) down to the detection limit of the instrument (assumed to be .01 µW cm⁻² nm⁻¹ here).

Unlike reality, spectral drift can be calculated in modelled biogenous waters and is equal to $K_{PUV} - K_{mono}$. Similarly, $K_{SW,PUV} - K_{SW,mono}$ would be the spectral drift in modelled clear seawater. The percent spectral drift error can be calculated by dividing $K_{PUV} - K_{mono}$ by K_{mono} (Figure 4). When spectral drift occurs, the absolute value of $K_{PUV} - K_{mono}$ generally increases as K_{PUV} increases. A perfect spectral drift correction factor will be able to account for all of the variation in $K_{PUV} - K_{mono}$ with depth in the water column. Initially, $K_{PUV}(K_{SW,PUV} - K_{SW,mono})$ was plotted against $K_{PUV} - K_{mono}$ to determine if there was any correlation between the clear water spectral drift weighted by the magnitude of K_{PUV} and the actual spectral drift in modelled biogenous waters (Figure 5). The two are significantly correlated, but the axes are on different scales and small non-linearities are apparent. Since the non-linearities are small, a first order spectral drift correction factor can be developed by calculating a least squares linear fit to the modelled values plotted in Figure 5. The spectral drift correction factor is now

$$F_D = A + BX \quad (2)$$

$$X = K_{PUV}(K_{SW,PUV} - K_{SW,mono})$$

where A and B are as listed in Table 1.

An important note here is that K_{PUV} and $K_{SW,PUV}$ were paired up based on being at the same percent of surface irradiance, not the same geometrical depth. This was done so that the detection limit for each channel was reached at the same time in clear water and in biogenous water.

3. RESULTS

K_{PUV} values were corrected by subtracting off F_D values. Now plotting $(K_{PUVcorrected} - K_{mono})/K_{mono}$ against K_{PUV} (Figure 6) shows a marked decrease in scatter as compared to the same plot before subtracting F_D from K_{PUV} (Figure 4). Also note that much of the scatter in $(K_{PUVcorrected} - K_{mono})/K_{mono}$ is now more centered about zero. The improvement is most marked in the 305 and 320 channels which are often the most important channels in calculating biological UV dose. Large improvements can also be seen in the mean and standard deviation of $K_{PUVcorrected} - K_{mono}$ as compared to $K_{PUV} - K_{mono}$ (Table 2). After correction, the mean is much closer to zero and standard deviation is reduced by 57-66%.

4. DISCUSSION

One of the initial constraints in the development of a spectral drift correction factor for data we have collected with the PUV is that we often have very little in the way of independent measurements of atmospheric and water column variables which can affect the magnitude of and rate at which spectral drift occurs. A second major constraint is that the surface waters are often difficult to characterize optically due to wave action. Thirdly, calibration is only known at the surface. The second and third constraints combined eliminate the possible use of iterative techniques involving estimates of CHL and DOM from measured PUV profiles to estimate spectral drift error.

The method developed here for reducing the spectral drift in PUV attenuation coefficients is based on a couple of assumptions. First, seawater, CHL and DOM are the primary attenuators in the water column. Second, variations in the shape of the irradiance curve just below the sea surface are minimal in the UV region for variables other than atmospheric ozone concentration and solar zenith angle.

One major advantage of this method over other possible methods of spectral drift correction is that little a priori knowledge about the region in which data are collected is required. Other than the PUV data, a general knowledge of the CHL ranges in the water column is the only critical additional piece of information required. Ozone concentration ranges can be estimated from PUV surface unit data; $K_{DOM}(380nm)$ ranges can be estimated by calculating attenuation coefficients for the 380 channel of PUV data; and solar zenith ranges can be calculated from the timestamps of PUV profiles.

Given a PUV dataset, the percent of surface irradiance can be approximated by dividing underwater unit values at depth by surface unit values collected at the same time. This eliminates the problem of having to know the near surface waters well. Using the ozone concentration estimated from surface unit data and the solar zenith angle calculated from the timestamp of each profile, $K_{SW,PUV}$ and $K_{SW,mono}$ can be modelled and F_D can be calculated using the polynomial curve fit parameters determined through a method like the one described here.

Visual analysis of plots of K_{PUV} versus $(K_{PUV} - K_{mono})/K_{mono}$ (Figure 4) and K_{PUV} versus $(K_{PUVcorrected} - K_{mono})/K_{mono}$ (Figure 6) along with broad statistical analysis of $K_{PUV} - K_{mono}$ and $K_{PUVcorrected} - K_{mono}$ (Table 2) indicate a significant reduction in spectral drift in the modelled dataset. The reduction of spectral drift was most pronounced in the 305 and 320 channels which are often most critical in the calculation of biological UV dose. These results indicate that a majority of the spectral drift error can be removed from the UV channels of the BURNM PUV dataset, resulting in a more spectrally consistent dataset.

5. ACKNOWLEDGMENTS

This work was supported by National Aeronautics and Space Administration Grant NAGW290-3 and Environmental Protection Agency fellowship number U-914954-01-0. Although the research described in this article has been funded wholly or in part by the United States Environmental Protection Agency under assistance agreement number U-914954-01-0 to Karen W. Patterson, it has not been subject to the Agency's peer and administrative review and therefore may not necessarily reflect the views of the Agency and no official endorsement should be inferred.

6. REFERENCES

1. R. Setlow, "The wavelengths in sunlight effective in producing skin cancer: a theoretical analysis," *Proceedings of the National Academy of Science, U.S.A.*, **71**, 3363-3366 (1974).
2. C.R. Booth, J.H. Morrow and D.N. Neuschuler, "A new profiling spectroradiometer optimized for use in the ultraviolet," SPIE Vol. 1750, *Ocean Optics XII*, pp. 354-365 (1992).
3. J.T.O. Kirk, B.R. Hargreaves, D.P. Morris, R.B. Coffin, B. David, D. Fredrickson, D. Karentz, D.R.S. Lean, M.P. Lesser, S. Madronich, J.H. Morrow, N.B. Nelson and N.M. Scully, "Measurement of uv-b radiation in two freshwater lakes: an instrument intercomparison," *Ergebnisse der Limnologie*, **43**, 71-99 (1994).
4. R.C. Smith and K.S. Baker, "Optical properties of the clearest natural waters (200-800 nm)," *Applied Optics*, **20**, 177-184 (1981).
5. K.S. Baker and R.C. Smith, "Bio-optical classification and model of natural waters. 2.," *Limnology and Oceanography*, **27**, 500-509 (1982).
6. W.W. Gregg and K.L. Carder, "A simple spectral solar irradiance model for cloudless maritime atmospheres," *Limnology and Oceanography*, **35**, 1657-1675 (1990).
7. G.A. d'Almeida, P. Koepke and E.P. Shettle, *Atmospheric Aerosols: Global Climatology and Radiative Characteristics*, A. Deepak Publishing, Hampton, VA (1991).
8. L.T. Molina and M.J. Molina, "Absolute absorption cross sections of ozone in the 185- to 350-nm wavelength range," *Journal of Geophysical Research*, **91**, 14501-14508 (1986).

List of Symbols

λ	wavelength (nm)
SW	clear seawater
CHL	chlorophyll and related pigments
DOM	dissolved organic matter
$K_{SW}(\lambda)$	clear seawater component of spectral attenuation coefficient (m^{-1})
$K_{CHL}(\lambda)$	component of spectral attenuation coefficient due to chlorophyll and related pigments (m^{-1})
$K_{DOM}(\lambda)$	component of spectral attenuation coefficient due to dissolved organic matter (m^{-1})
$K_{TOT}(\lambda)$	total spectral attenuation coefficient (sum of SW, CHL and DOM components) (m^{-1})
K_{PUV}	attenuation coefficients in biogenous waters calculated from model spectra weighted by the estimated PUV spectral response function for each UV channel (m^{-1})
K_{mono}	attenuation coefficients in biogenous waters calculated from un-weighted model spectra for 1nm bandwidths centered on 305, 320, 340 and 380nm (m^{-1})
$K_{SW,PUV}$	PUV-weighted attenuation coefficients in modelled clear seawater (m^{-1})
$K_{SW,mono}$	un-weighted attenuation coefficients in modelled clear seawater (m^{-1})
F_D	spectral drift correction factor
$K_{PUVcorrected}$	PUV-weighted attenuation coefficients in biogenous waters corrected by subtracting off F_D

Table 1: Linear fit parameters for F_D .
 $F_D = A + B[K_{PUV}(K_{SW,PUV} - K_{SW,mono})]$

λ	A	B
305	-8.95×10^{-5}	3.798
320	-4.55×10^{-6}	5.305
340	0.00139	11.14
380	-0.000753	11.21

Table 2: Mean and standard deviation for
 $K_{PUV} - K_{mono}$ before and after correction of K_{PUV} .

λ	$K_{PUV} - K_{mono}$		$K_{PUVcorrected} - K_{mono}$	
	Mean	St. Dev.	Mean	St. Dev.
305	-0.0211	0.0124	-2.27×10^{-9}	0.00449
320	-0.0205	0.0195	-6.33×10^{-8}	0.00663
340	-3.07×10^{-4}	0.00406	1.60×10^{-7}	0.00177
380	0.00629	0.00308	1.38×10^{-7}	0.00126

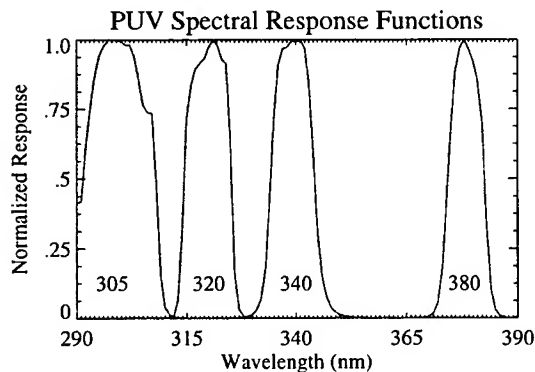


Figure 1: Estimated spectral response of the PUV UV channels normalized to 1 at the wavelength of maximum response of each channel.

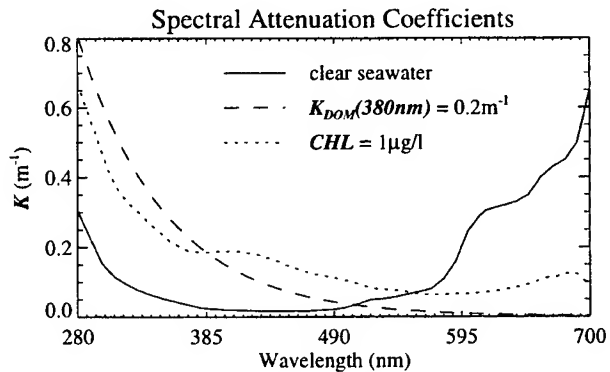


Figure 2: Attenuation coefficients for clear water,⁴ DOM and CHL.⁵

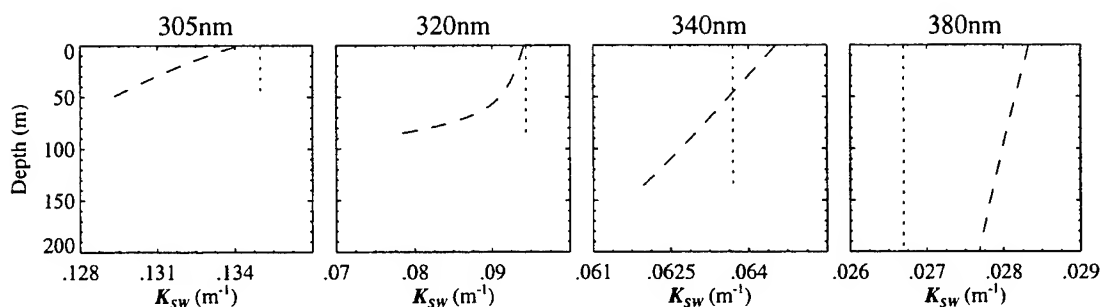


Figure 3: Modelled attenuation coefficients for clear seawater with ozone = 300DU and 0° solar zenith angle. The dotted line represents K_{mono} and the dashed line represents K_{PUV} .

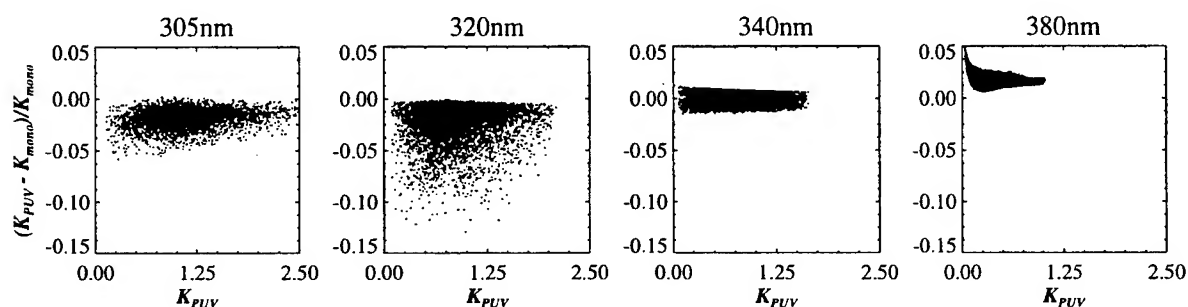


Figure 4: K_{PUV} vs. spectral drift error normalized to K_{mono} . Spectral drift error is negative where K_{PUV} is more weighted by longer wavelengths than K_{mono} .

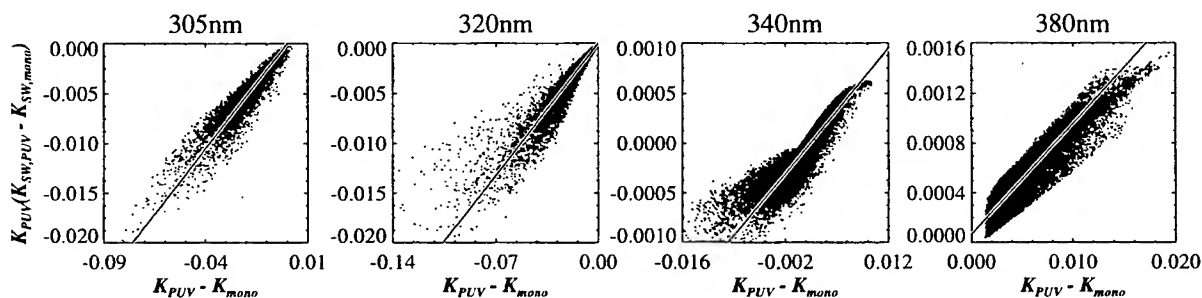


Figure 5: Spectral drift error vs. K_{PUV} -weighted clear water spectral drift error. A least squares linear fit line is also plotted for each channel.

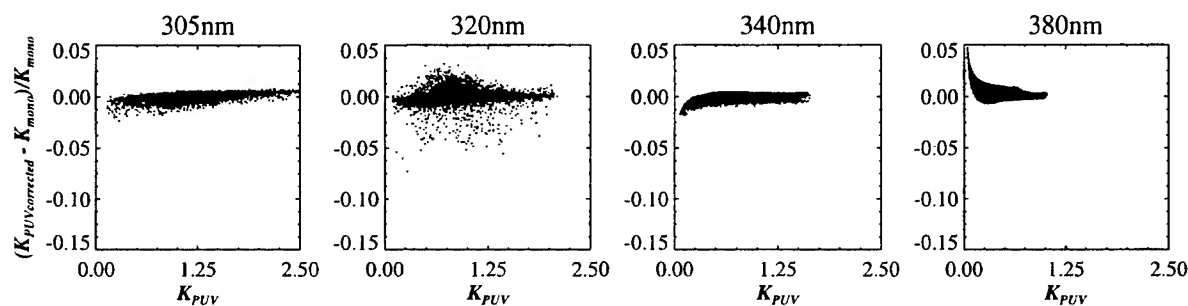


Figure 6: K_{PUV} vs. spectral drift error normalized to K_{mono} after correcting K_{PUV} by subtracting F_D .

The relationship between remote sensing reflectance and optically active substances in Case 1 and Case 2 waters.

David A. Phinney, Douglas I. Phinney and Charles S. Yentsch
Bigelow Laboratory for Ocean Sciences, McKown Point, W. Boothbay Harbor, ME, USA 04575

ABSTRACT

Remote sensing reflectance, as the ratio of upwelling radiance to downwelling irradiance (L_u/E_d), was measured in a variety of oceanographic regimes representing Case 1 and Case 2 waters during 6 cruises in 1995-1996 using a Satlantic TSRB II buoy. The dataset includes reflectance in seven bands (406, 412, 443, 490, 510, 555, and 665nm), CDOM and particulate absorption, chlorophyll concentration and total suspended solids from the coastal and offshore waters of the Arabian Sea, coastal waters and deep basins of the Gulf of Maine and clear shallow waters of the Dry Tortugas in the Florida Keys. Chlorophyll concentrations vary by two orders of magnitude (0.2 - 20 $\mu\text{g/L}$), k values vary by one order of magnitude (0.1-1 m^{-1}) and yellow substance absorption ranged from near zero in the oligotrophic offshore waters of the Indian Ocean to $> 5 \text{ m}^{-1}$ in the freshwater outflow from the rivers of the southern Gulf of Maine

Buoy data were reduced to one minute averages, with the in-air downwelling irradiance data corrected for refraction/reflection at the air-sea interface as a function of sun angle and propagated to the depth of the upwelling sensor (0.7m) before the ratio of L_u/E_d was calculated for each band. Stations were classified on the basis of the shape and amplitude of the spectral reflectance curves. Modeled curves developed from the concentrations of optically active substances showed good agreement with measured curves. CZCS-like band ratio algorithms for chlorophyll performed very well in Case 1 waters ($r^2 > 0.9$ for offshore Gulf of Maine stations), but high CDOM concentrations invalidate these algorithms.

Keywords: reflectance, absorption, inherent optical properties, phytoplankton, remote sensing

2. INTRODUCTION

Early estimates of spectral reflectance at the ocean surface were often a secondary product of submersible spectroradiometer profiles performed to measure the attenuation coefficients of downwelling irradiance (or radiance) and upwelling radiance, K_d and K_u (Tyler and Smith, 1970). New instruments have been introduced which specifically attempt to measure so-called 'remote sensing reflectance' above, or just below, the sea surface. We have used a tethered buoy system (Satlantic TSRB II) which measures downwelling irradiance above water and upwelling radiance below water at seven wavelengths matched to the SeaWiFS sensor while floating away from the ship to avoid shadowing effects (Voss, et al., 1986).

The buoy was deployed during 6 cruises in 1995-1996 in an attempt to relate remote sensing reflectance just below the surface to concentrations of optically active substances in Case 1 and Case 2 ocean waters as part of our ocean color algorithm development efforts. The cruises included the Arabian Sea during spin-up of the Southwest Monsoon (June/July, 1995), the following autumn inter-

monsoon (Sept/Oct, 1995), two cruises to Stellwagen, Jordan and Wilkinson Basins in the Gulf of Maine (March and April, 1995), coastal Gulf of Maine to the outflows of the Merrimack, Piscataqua, Saco, Kennebec and Sheepscot Rivers during spring runoff (May, 1996) and the clear shallow waters off the Dry Tortugas in the Florida Keys National Sanctuary (July, 1995). A total of 54 stations were obtained, 25 in Case 1 and 29 in Case 2 waters.

3. METHODS

Station data were collected in 1995-1996 during two cruises in the Arabian Sea, two cruises to the deep basins of the Gulf of Maine and one cruise to the outflows of five rivers in the southern Gulf of Maine during spring runoff. Coastal stations were spaced 4-5km apart along straight line transects from the head of the estuaries to the 100m isobath. Temperature, salinity and *in-situ* fluorescence were profiled at all stations using a CTD/fluorometer package. Discrete water samples were obtained using Niskin bottles from depths to 75m, deeper at Arabian Sea stations. Aliquots of sample were filtered through Millipore HA 0.45µm filters and analysed for chlorophyll fluorimetrically by the method of Yentsch and Menzel (1963). Total suspended solids (TSS) samples were collected on preweighed Watman GFF filters, dried and reweighed by the method of Strickland and Parsons (1972). Spectral particulate absorption (a_p 350-750nm) samples were filtered through Whatman GFF filters and analysed using a Bausch and Lomb dual beam spectrophotometer by the method of Yentsch and Phinney (1989). Dissolved yellow substance absorption (a_y 200-750nm) samples were filtered using 0.22µm Millipore Sterivex-GS cartridges and stored in amber glass bottles. Spectral measurements were obtained using 10cm quartz cuvettes in a dual beam spectrophotometer with 0.22µm filtered Nannopure water in the reference cell (Phinney and Yentsch, 1986). A Satlantic TSRB II reflectance buoy was also deployed for 15 minutes at each station to obtain measurements of surface incident solar irradiance (E_{da}) and upwelling radiance (L_{uw}) at seven wavelengths (406, 412, 443, 490, 510, 555 and 665nm).

4. POST-PROCESSING

Raw irradiance and radiance counts were processed through Satlantic's ASCIICON program to derive calibrated engineering units of $\mu W \text{ cm}^{-2} \text{ nm}^{-1}$ and $\mu W \text{ cm}^{-2} \text{ nm}^{-1} \text{ sr}^{-1}$, respectively. These 6Hz data were minute averaged, and E_{da} for each wavelength processed for refraction and losses due to surface reflection as a function of solar zenith angle calculated by date, time and latitude of each deployment. Finally, values of a_p^* ($\mu g/L \text{ Chl}$) and surface chlorophyll concentration were used to attenuate irradiance to the depth of the upwelling sensor (0.7m) to determine E_{dw} . Remote sensing reflectance at each wavelength was calculated as the ratio L_{uw}/E_{dw} .

Spectral absorption values of pure water (a_w) at 5nm intervals were taken from Prieur and Sathyendranth (1981). Particulate absorption (a_p) measured by the filter pad technique were corrected for β and calculated by:

$$a_p \text{ (m}^{-1}\text{)} = 2.3 * OD_s * (\pi r^2/V) * 100 \quad (1)$$

where OD_s is the b corrected optical density in suspension, πr^2 is the area of particles on the filter pad and V is the volume filtered in milliliters. Dissolved yellow substance absorption was calculated by:

$$a_y (m^{-1}) = 2.3 * OD (10cm^{-1}) * 10 \quad (2)$$

from the 10cm cuvette measurements.

5. RESULTS

Remote sensing reflectance spectra were sorted according to increasing R_{443} and grouped into classes of similar spectral shape with class number increasing with increasing short wavelength absorption. Average curves and reflectance values are presented in Figure 1. All classes converge at 555nm with strong differences in the blue part of the spectrum, except Classes II and III even though the average concentration of chlorophyll varies from 1 μ g/L in Class II to 4 μ g/L in Class III.

Example stations for each class were selected in order to compare the concentrations of optically active water column materials. Reflectance spectra, concentrations of chlorophyll and total suspended solids (TSS) and absorption coefficients for these stations are given in Figure 3. An excellent spectral match can be seen between the average classes and the example stations. Total suspended solids and a_y decrease by two orders of magnitude from Class VI to I with chlorophyll increasing geometrically from Class I to II, then decreasing and becoming variable, presumably due to light limitation in the increasingly darker waters. The sum of chlorophyll and TSS correlates well with a_{p400} .

Spectral absorption coefficients for each class are shown in Figure 3. Dissolved substances dominate absorption below 555nm in Classes IV - VI, but are similar to particulates in Classes I - III (note changes in the coefficient axis to provide resolution). Total absorption curves (seven bands) for the example stations are shown in Figure 4.

6. DISCUSSION

In-water spectral reflectance is an apparent optical property that is closely correlated to the inherent optical properties (Gordon, et al., 1988; Roesler and Perry, 1995; Zaneveld, 1995). IOP's are the basis of optical algorithms that permit the retrieval of concentrations of optically active substances which are ecologically important from remotely sensed ocean color. This approach has been shown to be practical in Case 1 waters where water and phytoplankton are the primary absorbers. However, in Case 2 waters where dissolved materials and non-absorbing particulates are found in high concentrations, these algorithms fail.

The present dataset demonstrates that dissolved yellow substance absorption is the major competitor with chlorophyll for short wavelengths of light in ocean waters. While total suspended solids concentrations may be high, their contribution to total absorption is low. Rather, TSS is important to reflectance in terms of scattering. Figure 5 shows the effect of high concentrations of CDOM and TSS on a simple two band ratio algorithm for estimating chlorophyll concentration. The top panel shows a typical relationship for Gulf of Maine offshore waters (Case 1) where TSS is less than 1mg/L and a_{y400} is on the order of 0.1 (m^{-1}). The bottom panel highlights these data among points for the entire dataset with Class VI points to the extreme left and Arabian Sea/Florida Keys data at lower right. The large

group of points remaining are the coastal GOM points during spring runoff with TSS > 1mg/L and moderate to high ($a_{y400} = 0.2-2.0 \text{ m}^{-1}$) yellow substance concentrations.

7. SUMMARY

We have developed a dataset of spectral reflectance and optically active substances for Case 1 and Case 2 waters which will be useful for testing ocean color algorithms, particularly in severe Case 2 waters with high concentrations of non-absorbing particles and dissolved substances. It has also been useful for defining operational limits for Case 1 and Case 2 waters on the basis of the shape of the spectral reflectance curve and concentrations of non-chlorophyll containing substances. Namely, we suggest that Case 1 waters are indicated when spectral reflectance at 400nm is greater than or equal to 555nm. At TSS > 1.0mg/l and/or $a_{y400} > 0.2 \text{ (m}^{-1}\text{)}$, Case 2 waters are indicated by $R_{rs400}/R_{rs555} < 1$. Separate algorithms will be required to improve the accuracy of retrieved concentrations of substances from Case 2 waters that will utilize both the shape and magnitude of the surface reflectance spectra.

8. ACKNOWLEDGEMENTS

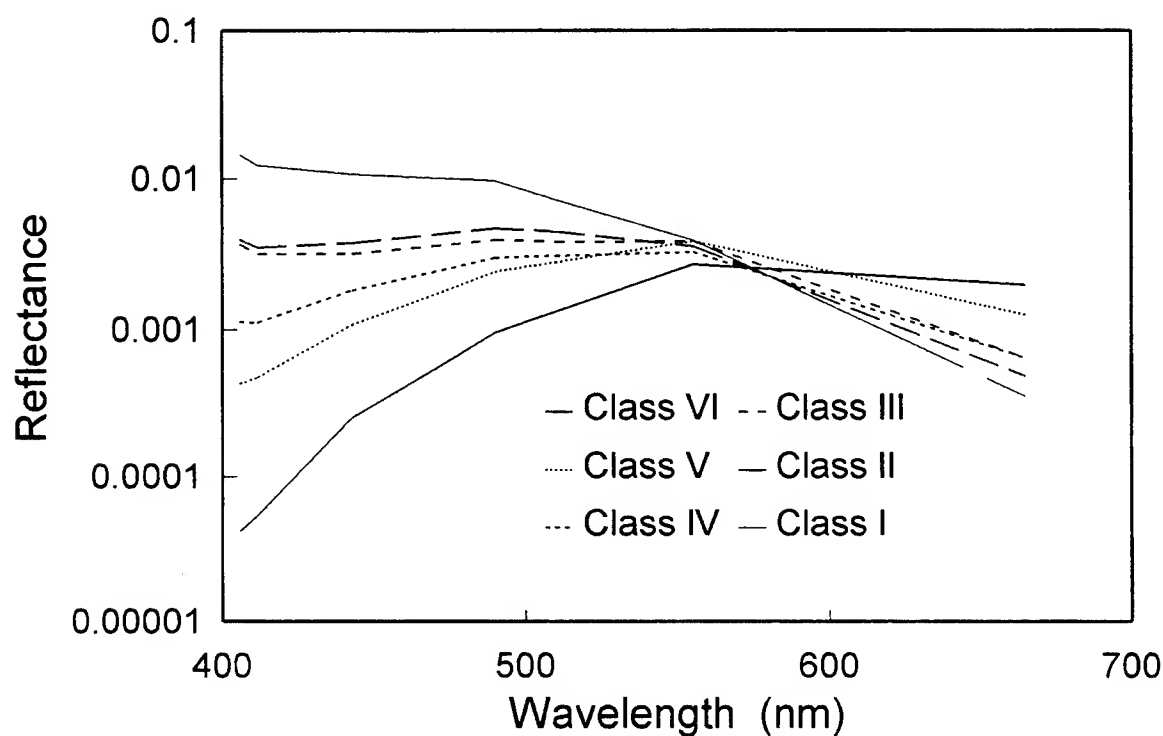
The authors wish to thank S.Ackleson, J. Brown, S. Sherman and S. Woodman for their assistance. This work was supported by grants from the Regional Marine Research Program for the Gulf of Maine (UM-S262), Office of Naval Research (N00014-94-1-0298 and N00014-95-1-0460) and NASA (NAGW-4672).

9. BIBLIOGRAPHY

- Gordon, H.R., O.B. Brown, R.E. Evans, J.W. Brown, R.C. Smith, K.S. Baker and D.C. Clark. 1988. "A semianalytic model of ocean color." *J. Geophys. Res.*, 93: 10909-10924.
- Phinney, D.A. and C.S. Yentsch. 1986. "On the contribution of particles to blue light attenuation in the sea." *J. Plank. Res.*, 13 (Supl.): 143-152.
- Roesler, C.S and M.J. Perry. 1995. "In situ phytoplankton absorption, fluorescence emission and particulate backscattering spectra determined from reflectance." *J. Geophys. Res.*, 100: 13279-13294.
- Strickland, J.D.H. and T.R. Parsons. 1972. "The determination of the weight of microscopic particles in seawater." In: A Practical Handbook for the Analysis of Seawater, Fisheries Research Board of Canada, Ottawa, pp.181-184.
- Tyler, J.E. and R.C. Smith. 1970. Measurements of Spectral Irradiance Underwater, Gordon and Breach, NY, 103 pp.
- Voss, K.J., J.W. Knowlton and G.D. Edwards. 1986. "Ship shadow effects on apparent optical properties." In: Ocean Optics VIII, Proc. SPIE 637, M.A. Blizard (ed.), pp. 186-190.

- Yentsch, C.S. and D.W. Menzel. 1963. "A method for the determination of phytoplankton chlorophyll and phaeophytin by fluorescence." *Deep Sea Res.*, 10: 221-231.
- Yentsch, C.S. and D.A. Phinney. 1989. "A bridge between ocean optics and microbial ecology." *Limnol. Oceanogr.*, 34: 1698-1709.
- Zaneveld, J.R.V. 1995. "A theoretical derivation of the dependence of the remotely sensed reflectance of the ocean on the inherent optical properties." *J. Geophys. Res.*, 100: 13135-13142.

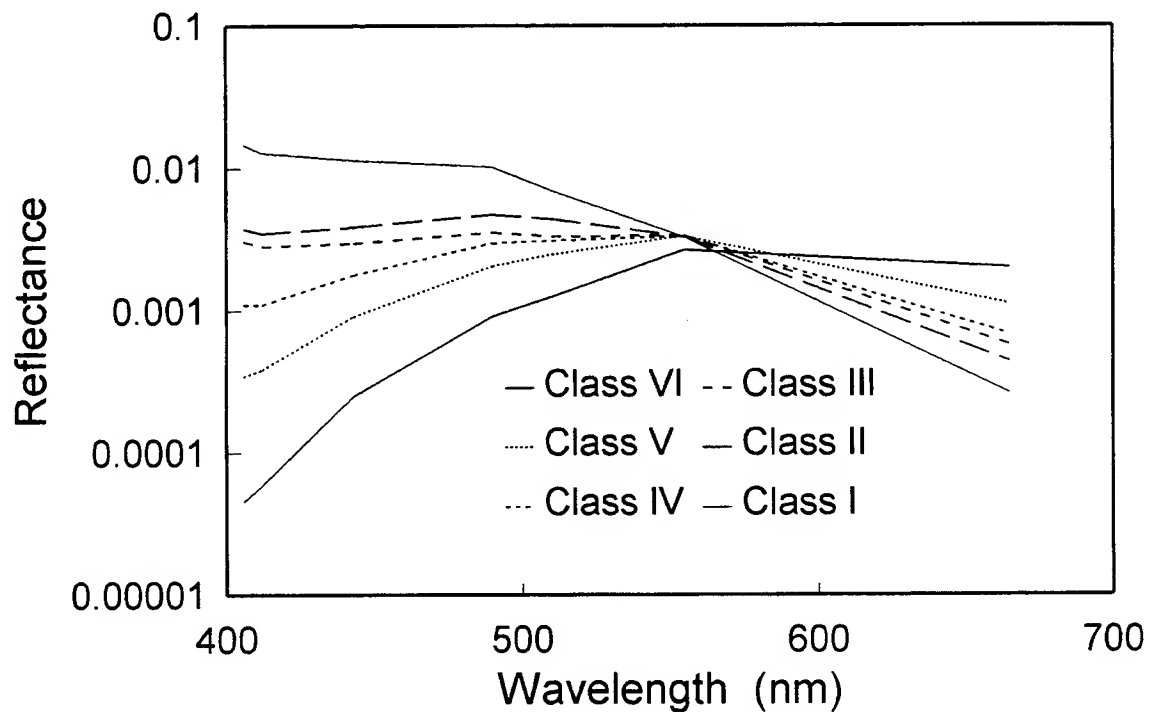
Spectral Classes



Wavelength	Class VI	Class V	Class IV	Class III	Class II	Class I
406	0.00004	0.00043	0.00112	0.00365	0.00390	0.01443
412	0.00005	0.00047	0.00112	0.00315	0.00348	0.01227
443	0.00025	0.00107	0.00181	0.00316	0.00372	0.01074
490	0.00096	0.00240	0.00299	0.00393	0.00465	0.00967
510	0.00131	0.00278	0.00306	0.00382	0.00443	0.00724
555	0.00272	0.00383	0.00326	0.00383	0.00356	0.00392
665	0.00199	0.00125	0.00065	0.00064	0.00049	0.00036

Figure 1. Top: Average spectral classes of remote sensing reflectance developed from database of 54 stations. Bottom: Table of reflectance values as a function of wavelength.

Example Stations



Class	Chl (ug/l)	TSS (mg/l)	aw400 (m-1)	ap400 (m-1)	ay400 (m-1)
VI	2.40	3.86	0.018	0.326	3.105
V	3.40	2.48	0.018	0.222	1.081
IV	1.43	1.66	0.018	0.081	0.667
III	5.41	0.81	0.018	0.117	0.138
II	1.23	0.08	0.018	0.034	0.115
I	0.44	0.03	0.018	0.018	0.023

Figure 2. Spectral reflectance of example stations for classes of Figure 1 with concentrations of optically active constituents.

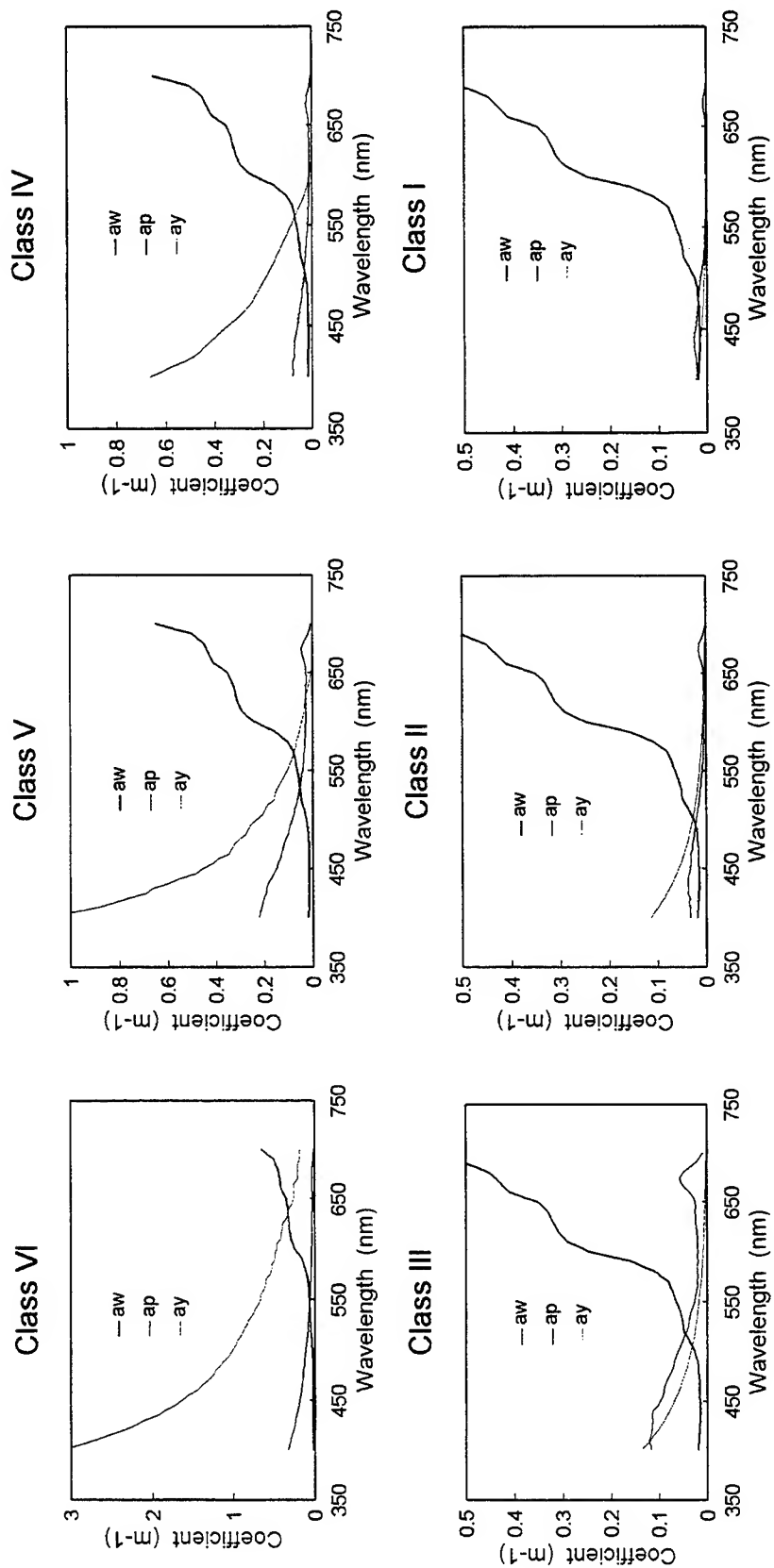


Figure 3. Spectral curves of absorption of pure water, particulates and dissolved yellow substances for the example stations in Figure 2.

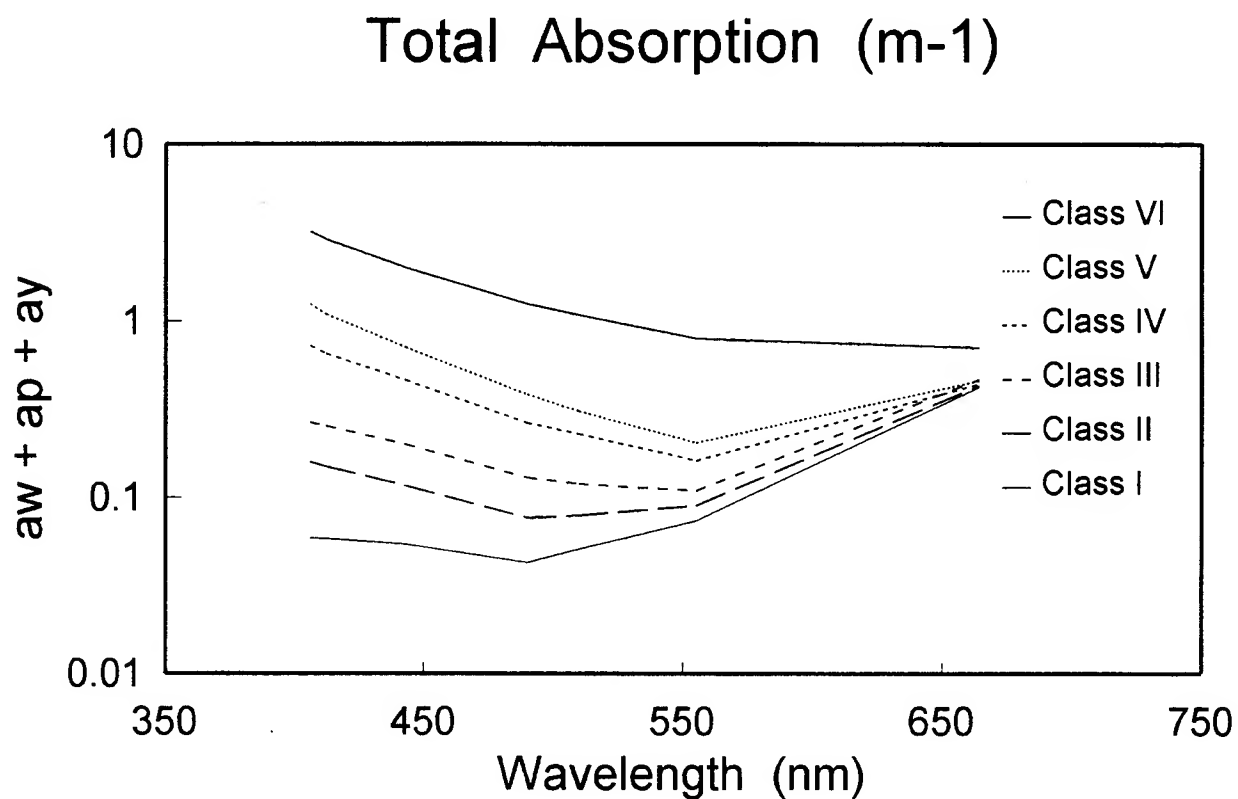
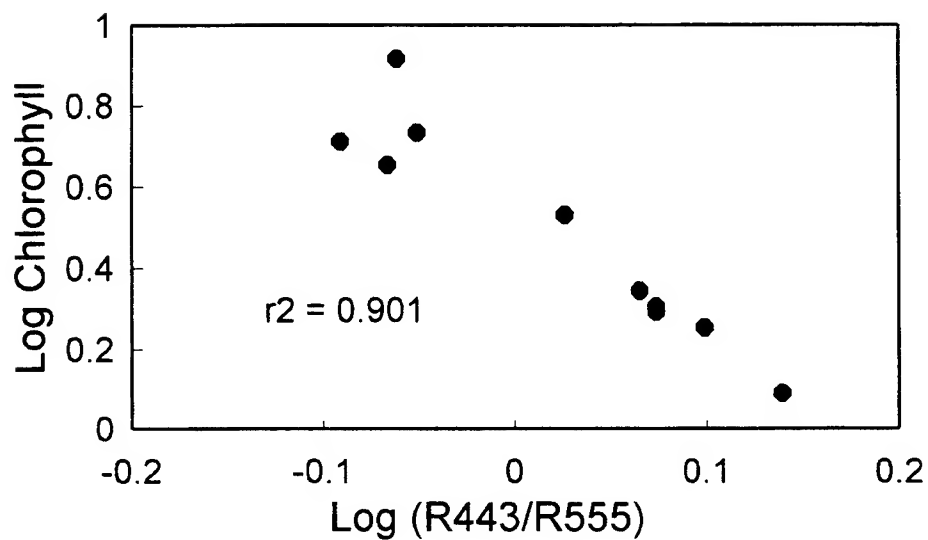


Figure 4. Total absorption of optically active water column constituents from example stations in Figure 3.

Deep Basins - GOM



Entire Dataset

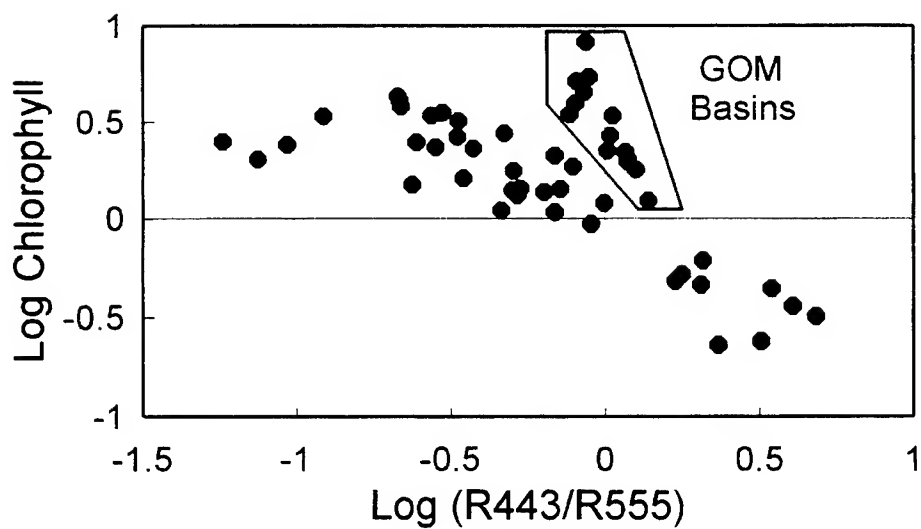


Figure 5. Top: Relationship between two band algorithm and chlorophyll for open waters of the Gulf of Maine. Bottom: Same plot for entire dataset with GOM points highlighted, Class VI points to far left.

Algorithms for path radiance and attenuation to provide color-corrections for underwater imagery, characterize optical properties and determine bottom albedo

Patty Pratt
Kendall L. Carder
David K. Costello
Zhongping Lee

Department of Marine Science
University of South Florida
140 7th Avenue South
St. Petersburg, FL 33701-5016

ABSTRACT

There is growing interest in the development and utilization of optical instrumentation to measure water properties of coastal waters for ground-truthing satellite data. Current methods for determining above-water remote-sensing reflectance assume vertical homogeneity in the water column. In cases where in-water vertical structure and bottom reflectance confound standard algorithms, new methods must be developed to incorporate inhomogeneities. This paper addresses the available avenues for characterizing optical properties, color-correcting underwater imagery and determining bottom albedo values. The method begins by deriving backscatter from remote-sensing reflectance data collected near the red end of the visible spectrum near the surface where bottom reflectance is negligible and path radiance is maximal. Measured upwelling radiance is divided by measured downwelling irradiance yielding underwater remote sensing reflectance values. The backscattering coefficient is then modeled for each wavelength and the path radiance calculated and removed using measured attenuation coefficients. The above values are used to reduce the algorithm to an equation for bottom albedo by removing the bias associated with path radiance and the filter effects associated with the water path to and from the bottom. The calculated bottom reflectance is needed to interpret and correct above-water remote-sensing reflectance and satellite imagery. The results are illustrated using comparisons of color-corrected and non-color-corrected *in-situ* imagery of specific corals and their immediate surroundings. Imagery of a coral scene at various altitudes is also presented to illustrate spectral changes due to changes in thickness of the water column between the camera and the bottom.

Keywords: bottom albedo, remote sensing reflectance, underwater imagery, color-correction, optical properties, ground-truthing

1. INTRODUCTION

Multi-spectral satellite imagery provides valuable information for determining water properties of various oceanic environments. Oligotrophic, optically deep waters are well described by standard ocean-color algorithms; however, neritic, optically shallow waters require a more complex analysis of the hyperspectral spectral signature of upwelling radiance. As new models of hyperspectral interpretation evolve to explicitly include the additional parameters associated with these waters, new in-water applications are emerging. Bottom classification, man-made object detection and determination of health status of marine organisms can be enhanced by hyperspectral, airborne and spaceborne sensor data. In return, in-water measurements of inherent and apparent optical properties can provide periodic spatial ground-truthing of sensors and algorithms.

Bottom reflectance, terrigenous run-off and suspended sediments are major factors in the overall upwelling radiance signal. A model for the interpretation of remote-sensing reflectance R_{rs} , developed by Lee *et al*¹ is utilized to characterize the various additional parameters needed to assemble a comprehensive algorithm useful in a variety of marine environments, including neritic waters. Remote sensing is generally thought of as above-water data acquisition from satellite or airborne sensors; however the term can apply to imagery data collected by unmanned vehicles as they are also at a significant distance from their targets. In this study, field measurements of in-water remote-sensing reflectance were made along with multi-spectral imaging over a reef bottom. The various data presented in this paper were collected using the USF Optics Group's ROSEBUD remotely operated vehicle (ROV) equipped with a bio-optical underwater package also

developed at USF.^{2,3,4,5} The package includes two hyperspectral (512 channel) radiometers, a multi-spectral (6-channel), intensified bottom imaging camera, a high resolution color video camera and a laser range finder for determining precise altitude. Other instruments providing simultaneous data were a Sea-tech optical backscatter meter, OBS, a Falmouth CTD, a Sea-tech transmissometer and a Wetlabs Wet Star fluorometer. Utilizing the measurements from these instruments and components of the hyperspectral remote-sensing algorithm bottom albedo is first derived hyperspectrally and then applied in a color correction for bottom imagery.

2. THEORY

2.1 Background Theory

Deconvolution of the hyperspectral the remote sensing reflectance at various altitudes within the coastal water column is performed following the model described by Lee *et al.*¹ To begin, R_{rs} , at some depth, z , in the water column is defined as

$$R_{rs}(z) = \frac{L_u(z)}{E_d(z)}, \quad (1)$$

where L_u is the upwelling radiance and E_d is the downwelling irradiance. Note that for R_{rs}^w above the water column an air-sea interface factor must be added to the equation..

2.2 Deriving backscatter

Morel and Prieur⁶ found that the reflectance ratio, R , is dependent on the ratio of backscattering to the absorption coefficient (b_b/a) and proportional to the function, f , that depends on the radiance distribution and volume scattering function of the water. This equation was simplified ultimately by Gordon *et al.*⁷ to

$$R_{rs} \approx f \frac{b_b}{a}, \quad (2)$$

where f was averaged for all sun angles to be approximately 0.33 and valid only when $b_b/a \ll 1$. To minimize the effects of bottom reflectance, b_b is approximated at the surface at the wavelength of 660 nm where, because of water absorption, any contribution from bottom reflectance would be minimal. This value is used to estimate b_b over the visible spectrum through the relationship

$$b_b(\lambda) = b_b(660) \left(\frac{660}{\lambda} \right)^y, \quad (3)$$

where y is a value from 0.5 to 1.0 as in Carder and Steward.⁸

2.3 Path radiance and bottom reflectance terms

Path radiance in an optically shallow water column is less than that of deep by waters by an amount that is exponentially proportional to the total depth of the water column. For the moment, assuming a black, totally absorbing bottom layer,

$$R_{rs}^{path} \approx 0.093 \left(\frac{b_b}{a + b_b} \right) \left[1 - \exp(-3.2(K_d \bar{\mu}_d)z) \right], \quad (4)$$

where K_d is the spectral diffuse attenuation coefficient, $\bar{\mu}$ is the average cosine of the downwelling solar irradiance, and z refers to the altitude of the desired R_{rs}^w measurement. The coefficient in the exponent is derived by Lee *et al.*¹ Assume now, that path radiance is negligible, for example the sensor is near the bottom, and that the bottom is a Lambertian reflector. The sole contributor to R_{rs}^w is bottom reflectance,

$$R_{rs}^{htm} \approx \frac{\rho}{\pi} [\exp(-2.6(K_d \bar{\mu})z)], \quad (5)$$

where ρ = bottom albedo. The coefficient in the exponent is the for the path elongation for photons in a round trip.

2.4 Solving for bottom albedo

Combining Eq. (4) and Eq. (5), an equation for R_{rs}^w at any altitude in the water column is given. Subsequently, the equation can be solved for bottom albedo,

$$\rho \approx \left[R_{rs}^w - 0.093 \left(\frac{b_b}{a + b_b} \right) [1 - \exp(-3.2(K_d \bar{\mu})z)] \right] / \left[\frac{1}{\pi} [\exp(-2.6(K_d \bar{\mu})z)] \right]. \quad (6)$$

The upwelling radiance, L_u , of bottom imagery can be corrected by dividing the effective, L_u^g , of a gray card reflector and compensating for the interval between the reflector and the bottom.

$$L_u = \pi \frac{L_u^g}{R_g} \frac{\rho}{\pi} [\exp(1.5(K_d \bar{\mu})z)], \quad (7)$$

R_g is the percentage reflectance of the gray card reflector. Solving for bottom albedo for imagery is as follows.

$$\rho = \frac{(L_u - L_u^{path}) R_g}{L_u^g} [\exp(1.5(K_d \bar{\mu})z)]. \quad (8)$$

3. FIELD MEASUREMENTS

The Coastal Benthic Optical Properties, CoBOP, is funded by the Office of Naval Research and is focused on the optical properties of reef environments. In August of 1995, the ROSEBUD ROV was deployed in the Dry Tortugas (24.5° N and 82.9° W). Data collected from this research cruise from 8/22 and 8/24 are presented in this paper. The primary instruments for collecting radiometric measurements were 512-channel Spectrix radiometers (model # 299 & 302). The Spectrix is triggered by the operator of the ROV at each desired 3 dimensional location, activating both the upwelling and downwelling radiometers. The images were collected using an intensified spectral imaging camera (Xybian IMC-301-blue) and corrected for exposure times. Bottom albedo's were then derived quantitatively and qualitatively. Particle backscatter was measured with the Sea-tech OBS, an instrument not well understood at this time. Relatively, the optical backscatter on 8/24 was about 50% higher than 8/22. The absorption coefficient was measured from water samples using the filter pad method developed by Mitchell and Kiefer.⁹ Altitudes of coral imagery were calculated using geometric ratios based on the separation of two collimated laser beams directed toward the bottom within the known field of view angle of the bottom imaging camera.

4. METHOD

R_{rs}^w from Eq. (1) was calculated for each Spectrix scan and is shown separately for both days in figures 1a & 3a. Each scan is calibrated by subtracting the instrument dark current and corrected with a spectral response. The spectral diffuse attenuation coefficient for spectral downwelling plane irradiance, K_d , was calculated using downwelling irradiance, E_d ,

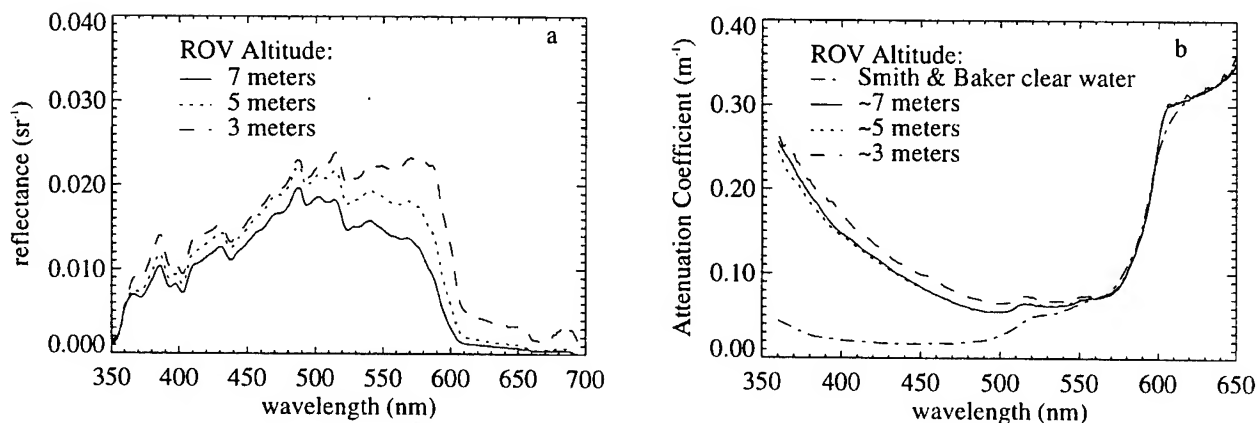


Figure 1. Results of underwater radiometric measurements collected during COBOP 1995 data acquisition, used to calculate bottom albedo. (a) Remote sensing reflectance measured *in-water* during a vertical downcast on 8/22. (b) Respective diffuse attenuation coefficients, K_d values, for each interval of the vertical downcast.

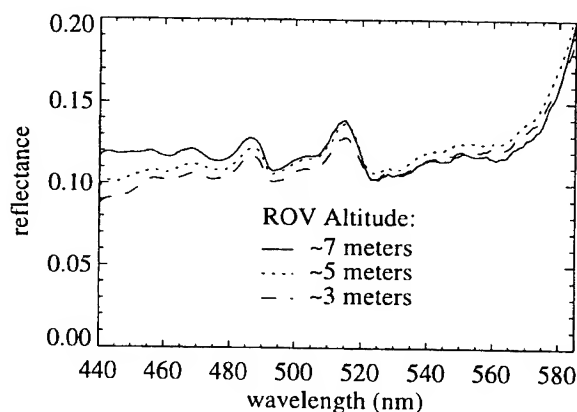


Figure 2. Calculated bottom albedo for the COBOP 1995 vertical downcast using the results shown in figures 1a & 1b. The bottom type for this albedo is mixed coral, algae and sand.

values at sequential depths in the vertical downcast ($K_d = [\ln(E_d/E_{d_0})]/\Delta z$). Each interval was assigned a respective K_d , see figures 1b & 3b. The average cosines were computed using Radtran¹⁰ for the times of each collection. The backscatter was derived using a near surface sample of R_{rs}^w at 660 nm and then distributed over the visible spectrum using Eq. (3). Each component is then placed into Eq. (6) and the spectral curve analyzed. The near bottom imagery was corrected using Eq. (8) to process the image resulting in a pictorial description of bottom albedo.

5. RESULTS AND DISCUSSION

5.1 Results and applications of bottom albedo

The albedos in figures 2 & 4 show good support for the hyperspectral algorithm¹ used. For the three different altitudes on 8/22, the albedo remains virtually constant. Through most of the optical "water window", the curves show good correlation. A comparison between the two days over similar coral bottom show approximately the same values for bottom albedo. The peaks in the curves at 486 and 515 likely indicate coral fluorescence signatures are present in the bottom reflectance albedo measurements. It is possible that the peak near the red end is also showing coral fluorescence:

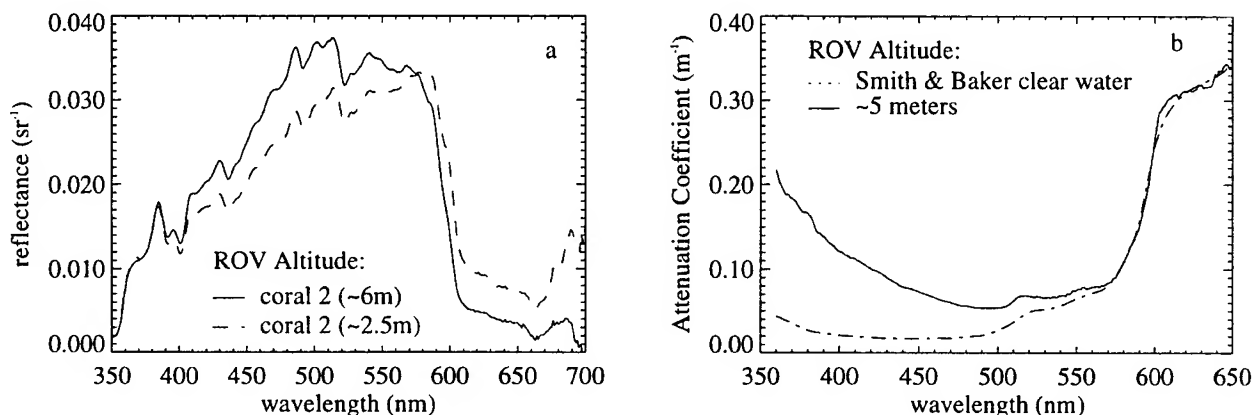


Figure 3. Results of underwater radiometric measurements collected during COBOP 1995 data acquisition, used to calculate bottom albedo. (a) Remote sensing reflectance measured *in-water* for two altitudes over same coral scene 8/24 (includes coral 2 as referenced in text). (b) Diffuse attenuation coefficients, K_d values.

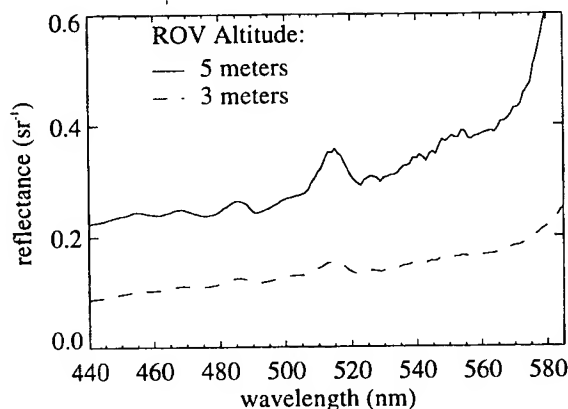


Figure 4. Calculated bottom albedo (see text) for COBOP 1995 tagged coral transect using the results shown in figures 3a & 3b. The knobby amorphous coral on the right is *Meandrina Meandrites* (C-17 during the mission and coral 2 in post-processing). The bottom type in the background for this albedo includes large patches of sand.

however, more data is needed for verification. Toward the blue end of the curve the broad band peak apparent in the 8-22 albedos could be the result of gelbstoff fluorescence. Here the correlation of the curves appears to diverge which illustrates the importance of the CDOM fluorescence term that is considered in the model, but not included in this demonstration of bottom albedo. The lower altitude albedo curve of 8-24 does not fall exactly on the albedo curve of the higher altitude and, since the spectral shape is consistent, could demonstrate the effects of self-shading or a similar phenomenon. An alternate explanation is that a greater percentage of sand is present in the field of view at the higher altitude.

Generally speaking, the bottom albedos derived by this method appear to be consistent to first order approximations and provide useful information for correcting underwater imagery. Direct quantitative measurements of backscatter at all altitudes in the water column are needed to improve the accuracy of the derived bottom albedo. It is probable that this parameter causes much of the signal distortion when attempting to deriving water column properties and bottom types from above-water R_{rs}^w measurements. In addition, effects of coral fluorescence (refer to figure 5d) and water Raman scattering are integral parts of the spectral shape of the apparent bottom albedo and must be considered before conclusions can be made.

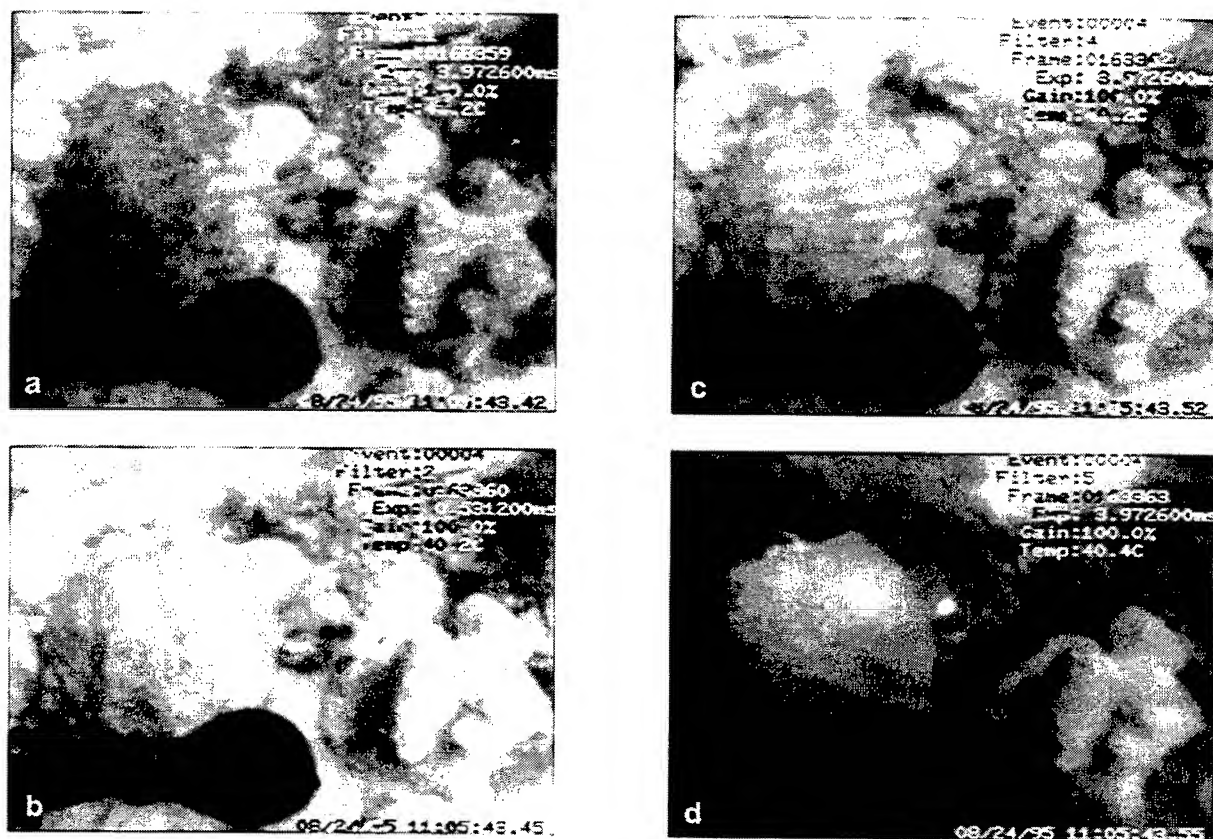


Figure 5. Imagery collected with the Multi-spectral imaging camera (see text). The coral specimen on the right is *Meandrina Meandrites*. Exposure times are listed in the upper right-hand text on the images. (a) Filter 1 refers to a wavelength at 460 nm with a 20 nm FWHM bandwidth. (b) Filter 2 refers to a wavelength at 520 nm with a 20 nm FWHM bandwidth. (c) Filter 4 refers to a wavelength at 620 nm with a 20 nm FWHM bandwidth. (d) Filter 5 refers to a wavelength at 685 nm with a 30 nm FWHM bandwidth. The two bright spots near the center of the image are the laser range finders used to calculate altitudes.

5.2 Results of color-corrected imagery.

RGB color composite images were produced using three monochromatic bands of the Xybion multi-spectral imaging camera. The blue band is centered on 460 nm (figure 5a), the green band at 520 nm (figure 5b) and 620 nm (figure 5c) for the red, each with FWHM bandwidth of 20 nm. The amorphous knobby coral situated on the right in figures 5 a-d is identified as *Meandrina Meandrites* (referred to coral 2 in this paper and coral 17 during the 1995 reef transect analysis). Each band was separately corrected for the exposure time (located on the figures) by dividing the image values with the reference target. The results of the comparison between a processed and non-processed coral scene show significant differences. As expected, the color-corrected image reveals the dominant red coloration that depicts the presence of algal symbionts known to exist in the tissues of the corals and in the surrounding substrate. Other image comparisons were made of this same scene at various heights above the bottom. Consistent color changes are observed and the images become progressively darker with reduced bottom reflectance with altitude. The white elliptical shape in individual bands of these images are the fluorescent tags used to mark the target corals.

This type of image color correction could assist in techniques for discovering man-made objects on the ocean floor. Through stereoscopic and cross-covariance of sequential imagery, which is inherently collected with a moving camera, it is possible to add a third physical dimension (height) to the spectral shape obtained by this method. This would improve

automated mapping and target recognition capabilities. For specific applications such as bottom classification, reef health, and target identification, imagery becomes an important part of the assessment package.

6. CONCLUSIONS

Tracking health and changing compositions of benthic organisms in the reef environment is necessary for environmental management of coastal habitats. The combined technologies of satellite and in-water remote sensing will aid in data calibration and algorithm validation. It is essential to first address the research necessary to provide accurate assessment of the optical properties of the water column. For determining bottom albedo, multi-spectral optical backscatter, absorption, and attenuation need to be quantified. Commercial instruments that make these type of measurements have become available and are being integrated into our underwater vehicle instrument package. They will be used to verify the K_d 's and eliminate uncertainties in the bottom albedo algorithm (Eq. (6)). An integrated GPS tracking system for the ROV has also been implemented, allowing relatively precise positions to be recorded during deployment. Especially for coastal environments, automated imaging systems could serve as an efficient low-cost alternative for traditional data acquisition methods, while providing greater local coverage. With this ability to collect more in-situ data in a shorter time period, and with robust algorithm development tailored to specific environments, routine ground-truthing of satellite data is possible.

7. ACKNOWLEDGEMENTS

The authors wish to express appreciation and gratitude for the financial support for this project provided by the Office of Naval Research through grants N00014-95-1-0578 and N00014-96-1-5013. The authors wish to thank Tom Peacock for helpful discussions throughout the course of this study.

8. REFERENCES

1. Z. Lee, K. L. Carder, S. K. Hawes, and R. G. Steward, "Model for the interpretation of hyperspectral remote-sensing reflectance," *Appl. Opt.* **33**(24), 5721-5732 (1994).
2. D. K. Costello, K. L. Carder, R. F. Chen, T. G. Peacock, and N. S. Nettles, "Multi-spectral imagery, hyperspectral radiometry, and unmanned underwater vehicles: Tools for the assessment of natural resources in coastal waters," *SPIE Visual Communications and Image Processing*, Vol. 2501, pp. 407-415 (1995).
3. D. K. Costello and K. L. Carder, "Using unmanned vehicle systems for ground-truthing oceanographic satellite data," *Proc. AUUS Intelligent Vehicles: Systems, Technology and Information Resources*, (1994).
4. D. K. Costello, I. I. Kaminer, K. L. Carder and R. Howard, "The use of unmanned vehicle systems for coastal ocean surveys: Scenarios for joint underwater and air vehicle missions," *Proc. International Program in Undersea Robotics & Intelligent Control (URIC)*, (1995).
5. D. K. Costello and K. L. Carder, "New Instrumentation and platforms for subsurface optical measurements," *SPIE Ocean Optics XII*, Vol. 2258, (1994).
6. A. Morel and L. Prieur, "Analysis of variations in ocean color," *Limnol. Oceanogr.* **22**, 709-722 (1977).
7. H. R. Gordon, O. B. Brown, and M. M. Jacobs, "Computed relationship between the inherent and apparent optical properties of a flat homogeneous ocean," *Appl. Opt.* **14**, 417-427 (1975).
8. K. L. Carder and R. G. Steward, "A remote-sensing reflectance model of a red tide dinoflagellate off West Florida," *Limnol. Oceanogr.* **30**, 286-298 (1985).
9. B. G. Mitchell and D. A. Kiefer, "Chl a specific absorption and fluorescence excitation spectra for light limited phytoplankton," *Deep-Sea Res.* **35**, 635-663 (1988).
10. W. W. Gregg and K. L. Carder, "A simple spectral solar irradiance model for cloudless maritime atmospheres," *Limnol. Oceanogr.* **35**, 1657-1675 (1990).

Influence of ship shadow on underwater irradiance fields

Saruya, Y., *T. Oishi, **M. Kishino, *Y. Jodai, *K. Kadokura, *A. Tanaka.

* School of Marine Science and Technology, Tokai Univ.,
Orido 3-20-1, Shimizu City, Shizuoka Pref., Japan, Postal Code 424

** Institute for Physical and Chemical Research,
Hirosawa 2-1, Wako City, Saitama Pref., Japan, Postal Code 351-01

ABSTRACT

The underwater irradiance measurements are usually carried out from a ship, so that it is easy to imagine that the data is affected by the shadow due to a ship.

The simple algorithm to compute the 3 dimensional underwater irradiance fields was developed based on the forward Monte Carlo method, by assuming that the infinitely thin and totally absorbing disk (ship) exists at the air-sea interface. The model was confirmed by the field experiment, and found the good agreement with observed irradiance fields. According to the computations, it was found that the influence of the shadow on downward and upward irradiances appear in different manner. That is, the downward irradiance affected by the disk (ship) appears in downward with respect to the direction of the direct of the sun light. On the other hand, it appears in upward in the case of upward irradiance. As the result, it is predicted that the overestimate (near the sea surface) and underestimate regions of irradiance reflectance are formed.

2. INTRODUCTION

The underwater irradiance is one of the important parameters with respect to Optical Oceanography, for instance, ocean color remote sensing, and the photosynthesis of phytoplankton and so on. However, the irradiance measurements are usually carried out from a ship. So the influence of the ship shadow on underwater irradiance fields is the inevitable problem, in particular near the sea surface.

As far as the authors know, the first study of this problem was done by Aas (1969)¹. He calculated the influence of the ship shadow and pointed out that the error in clear weather with the sun are less than 10%, while the error in cloudy weather may reach 20% depending on depth. The Monte Carlo simulation performed by Gordon (1985,1992)^{1,2} evaluated how to influence measurements of irradiance by the ship shadow. He also shows that under the overcast condition, upward irradiance is effectively influenced by the ship shadow. Helliwell et al. (1990)⁴ evaluated the shadow problem by the Finite Difference method. Further, they confirmed the result of simulation by the radiance and irradiance measured by CID (Change Injection Device). Zibordi and Ferrari (1995)⁵ were discussed instrument self-shading by comparison between the experimental and theoretical data of upward radiance and irradiance.

The purpose of this study is to develop the numerical tool and analyses the nature of the ship shadow in water.

3. CALCULATION METHOD AND FIELD EXPERIMENT

3.1 Algorithm for computing the influence of the ship shadow based on the forward Monte Carlo method

The radiative transfer calculation by using Monte Carlo method is based on the phenomenological behavior, i.e. travelling, scattering and absorption of photon. Following large number of photon, we are able to obtain average light fields. We developed the modified forward Monte Carlo method to handle the influence of the shadow due to the ship on irradiance fields.

We consider that the medium has absorption and scattering properties, and the disk is irradiated by only parallel beam for simplicity. In this situation, photons, which irradiate the area except the disk, propagate following the given absorption and scattering probabilities. Probability speaking, on the other hand, photons which fall onto the disk also propagate with the same absorption and scattering probability as photons irradiating out side of the disk. Since these photons are trapped by the disk, as the results the disk

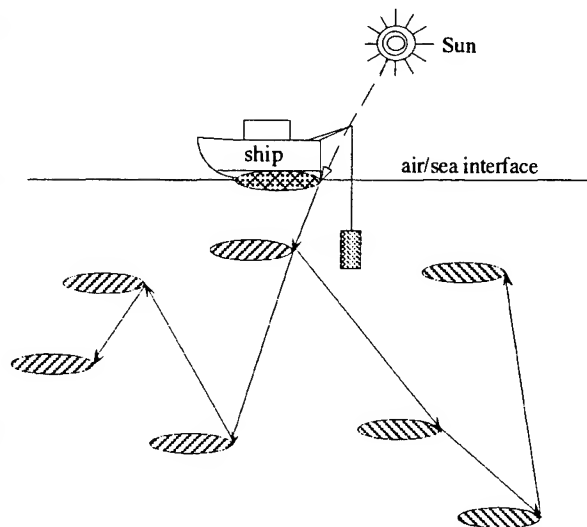


Fig. 1 Concept for computing the influence of ship shadow on underwater light fields based of the forward Monte Carlo method.

forms the shadow region. In other word, following the movement of the disk as if it behaves like a photon with negative energy, we are able to obtain the irradiance of the shadow region by subtracting from the true irradiance fields (See Fig.1).

3.2 Field validation of the model

The field experiment to validate the model was made by observing the vertical profile of E_d and $L(\pi)$ at different distance, 2m interval, from the moored ship, SeaTec II owned by Oki SeaTec Co., Japan. The lengths of SeaTec II are 30m(L), 13m(W) and 5.5m(H). SeaTec II has the bottom with black paint and has 0.8m of draft. So it is considered to be suitable for our model. The sea bottom with clay was about 30m in depth. Further, the distance from the coast to the ship was 300m, so that there is no interfere from the coast. (Fig. 2)

The experiment was carried out on 16 and 17 May., 1996 in Utiura bay ($N35^{\circ}01' \cdot E138^{\circ}54'$) and the weather condition was clear with the wind speed of 3-7m/s and overcast with 8-9m/s, respectively. The line of 40m was stringed between SeaTec II and the anchored floating buoy. The irradiance and nadir radiance measurements were made by PRR600 from the edge of the ship side to 20m away along the line with 2m interval. The PRR610 was used for monitoring the irradiance condition on the deck. This data was used for correcting the measured underwater irradiance. The wavelength of the observed downward irradiance and nadir radiance were 412, 433, 490, 510, 555 and 665nm, respectively.

4. COMPARISON

4.1 Estimation of parameters

In order to compute the underwater irradiance field, the inherent optical properties, a and $\beta(\theta)$, and the boundary conditions at the air-sea interface and the bottom are required. The symbols which are used in this paper are summarized in Table 1. We assumed that totally absorbing bottom (no-reflection) is located at 30m below the sea surface and the sea surface is irradiated by only the sun, of which latitude and azimuth are ϕ and ζ , respectively.

We measured the volume scattering function from 10-160 deg. at 5 wavelength in the visible range of spectrum. The shape of the scattering functions were very similar to that of San Diego Harbor water obtained by Petzold (1971)⁶. So we used his phase function for the present study. The a and b , when the experiments were carried out, were determined so as to fit with the far most vertical profiles of not only E_d but also E_u , where we assumed there were no influence of the ship shadow. We observed $L(\pi)$, so that $L(\pi)$ were converted to E_u in order to compare with the computed E_u using the following scheme.

Aas (1987)⁷ applied the Hojorslev's radiance distribution model⁸, which was derived from the observed radiance distribution in asymptotic region, to estimate μ_u , and found that the model can be applicable for near the sea surface.

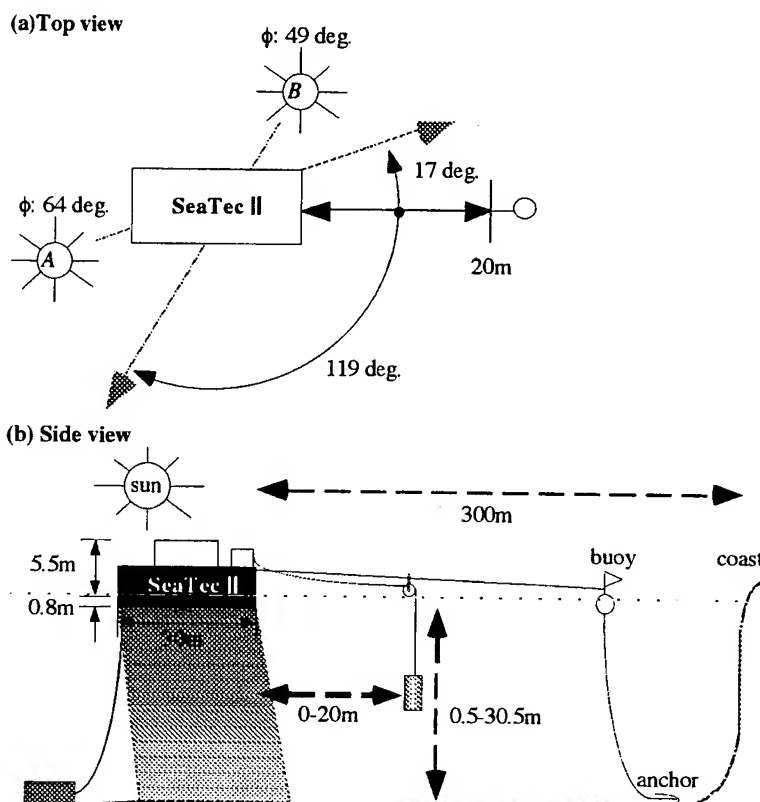


Fig. 2 Schematic diagram of experimental set up.

Table 1 Symbol descriptions

a	absorption coefficient
b	scattering coefficient
c	beam attenuation coefficient $c = a + b$
$\beta(\theta)$	scattering function
$L(\theta)$	radiance
E_d	downward vector irradiance
E_{d_0}	downward scalar irradiance
L_u	upward radiance
E_u	upward vector irradiance
	upward scalar irradiance
R	reflectance
ω	albedo $\omega = b / c$
ϕ	sun latitude angle (degree)
ζ	sun azimuth angle (degree)
μ_u	upward averaged cos $\mu_u = E_u / E_{d_0}$

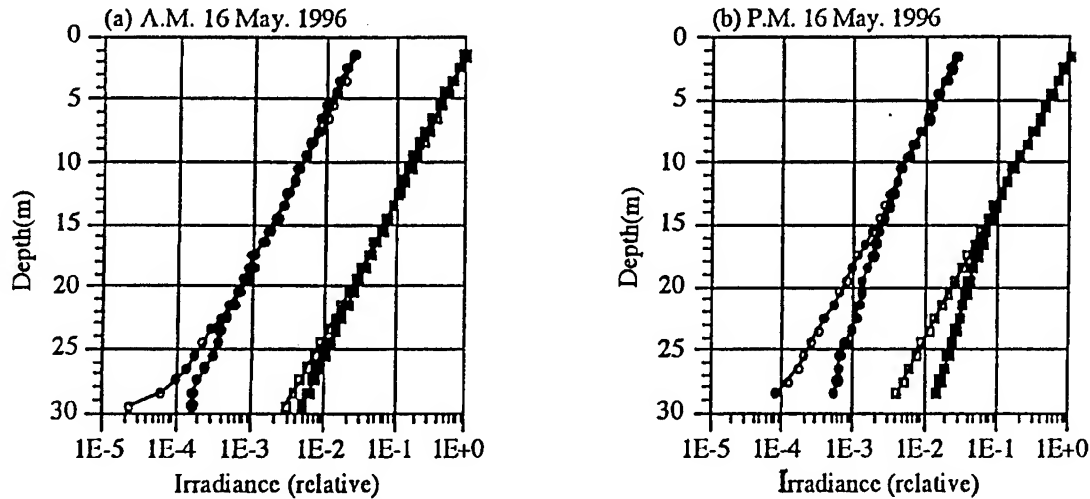


Fig.3 Comparison of measured and calculated irradiance fields using estimated a and b . The symbols corresponding to $E_{d,\lambda}$ (depth, wavelength) are ; Measured $E_d(z,412)$: —■—, Measured $E_u(z,412)$: —●—, Estimated $E_d(z,412)$: —□—, Estimated $E_u(z,412)$: —○—

$$L(\theta) = L(\pi) \cdot \frac{1 + \alpha}{1 - \alpha \cdot \cos \theta} \quad (1)$$

with

$$\alpha = \frac{L(\pi/2)}{L(\pi)} - 1 \quad (2)$$

Here, θ is the polar angle. Integrating eq.(1) with the definition of scalar and vector irradiance, and taking the ratio of these parameters, we are able to express the upward average cosine as follow

$$\mu_u = \frac{E_u}{E_{u0}} = \left(1 - \frac{\ln \rho}{\rho - 1} \right) / \ln \rho \quad (3)$$

Here, $\rho = \alpha + 1$.

Aas' result implies that we are able to estimate the upward radiance distribution, if we could obtain or estimate μ_u . Thus, we calculate μ_u by the Monte Carlo computation using the estimated a and b , and convert the vertical profile of $L(\pi)$ to that of E_u . The a and b are determined by repeating above procedure until the difference between the observed and the calculated irradiance fields become minimum. The optimized irradiance fields by above procedure are shown in Fig.3 together with measured one, where the estimated a and b are 0.15 and 0.45 (m^{-1}), respectively.

4.2 Validation of the model with experiment

Using the a and b which were determined by the scheme described in Section 4.1, the underwater irradiance fields around the ship were computed by the modified forward Monte Carlo method which is also described in Section 3.1. In this section, we will compare observed irradiance fields with computed ones. As an example, we discuss E_d and E_u only for 412nm case which were observed on 16 May., because of limited space.

Fig.4-(a) and -(b) show the observed downward and upward irradiance fields, respectively, when the sun located the opposite side of the observation line, indicated by A in Fig.2. Fig.4-(c) and -(d) are the same as Fig.4-(a) and -(b) when the sun irradiated the line from the side indicated by B. As shown in Fig.4-(a) and -(b), it is clear that the ship affects on not only downward but also upward irradiance fields. On the other hand, when the sun irradiates the line from the side, the influence of the ship shadow is much smaller (the contour lines are almost parallel). It is difficult to see the influence of the ship shadow on the light fields by irradiance level, so that the following quantity is introduced;

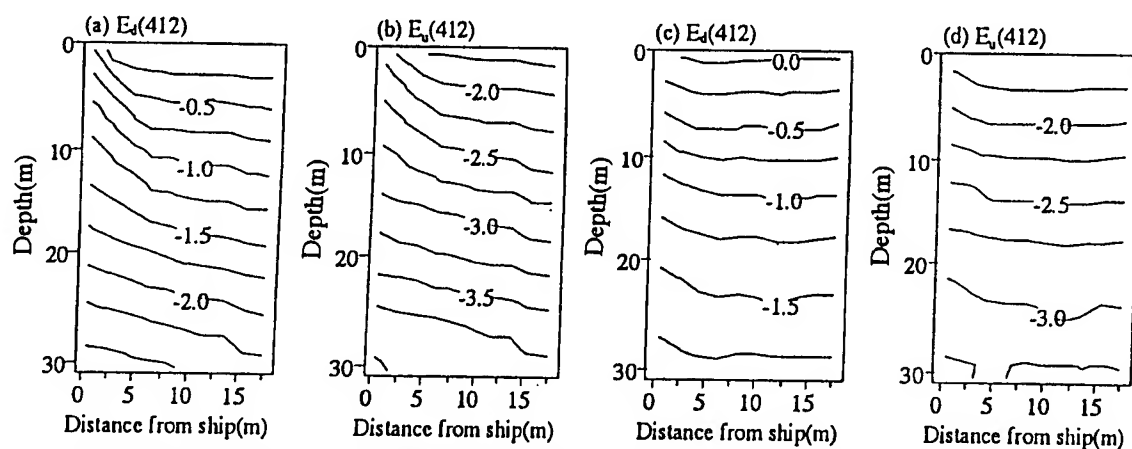


Fig.4 Vertical distribution of the observed irradiance fields as a function of distance from the ship side. (a) and (b) are the case when the sun locates at *A*, and (c) and (d) are the case of *B* in Fig.2

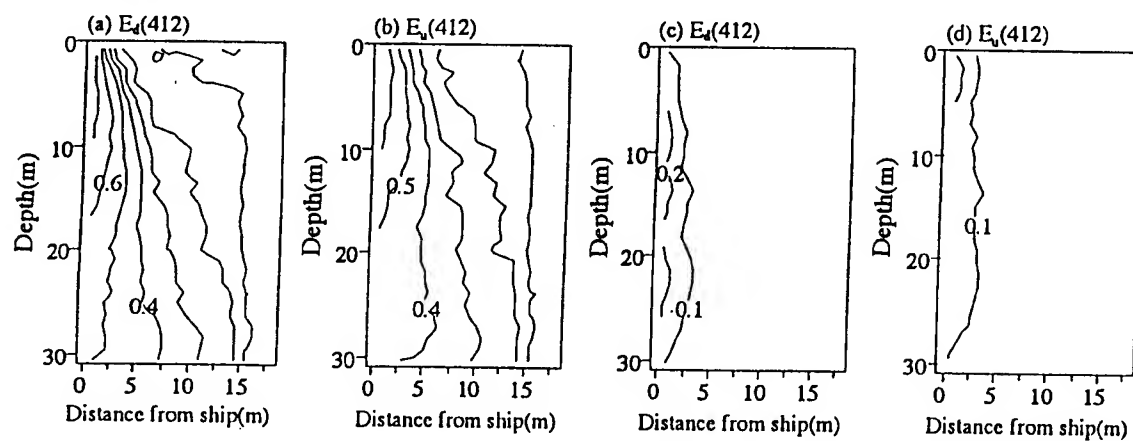


Fig.5 The error contour maps of Fig.4.

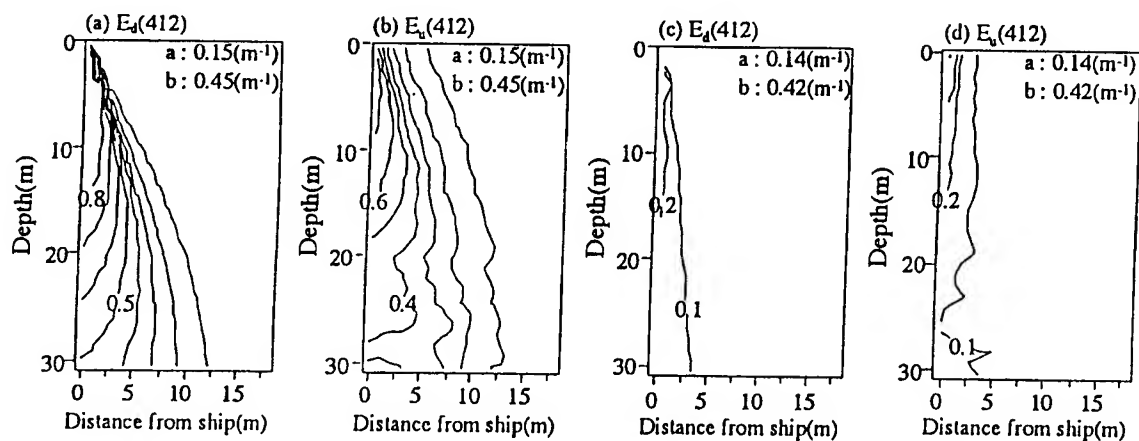


Fig.6 The error contour maps using estimated *a* and *b* of Fig.4.

$$\varepsilon = \frac{E_{true} - E_{cal. or obs.}}{E_{true}} \quad (5)$$

where E_{true} is the true or far most measured irradiance and $E_{cal. or obs.}$ is the computed or observed irradiance at given positions. Fig.5-(a) and -(b) show the error contour maps of Fig.4-(a) and -(b), respectively. It can be easily notice that the error of measured E_d due to the shadow is very large near the ship, and it decrease steeply as a function of distance from the ship. On other hand, the error of E_u is smaller than that of E_d near the ship, but not negligible. Further, the error decreases as a function of distance but not as steeply as the case of E_d . In other words, the relatively large region is affected by the ship on E_d and E_u . Fig.5-(c) and (d) are the same error contour map of Fig.4-(c) and -(d), respectively. The error regions irradiating observed line from side are much smaller than the former cases. The 10% error line is about 3m from the ship side.

Fig.6 is the computed error contour map based on our model using estimated a and b, 0.15 and 0.45(m^{-1}) for Fig.6-(a) and -(b), 0.14 and 0.42(m^{-1}) for Fig.6-(c) and -(d), respectively. The error of computed E_d and E_u due to the shadow is large as similar as the observed ones (See Fig.5-(a)). The gradient of the contour becomes smaller as a function of depth. In the case of E_u it is apparent that the influence of the ship shadow appears lager area than that of E_d near the sea surface. There is the disagreement near the sea surface in E_d . The moored ship has the height of 5.5m, so that it forms the shadow at the sea surface, and the sky light irradiates the shadow area as well. These factors are considered to be the reasons of this disagreements. When the sun irradiates the observation line from the side, the computed measurements errors for E_d and E_u have good agreements with observed ones (See Fig.6). Considering the imperfection of the model we can conclude that our model expresses the nature of ship shadow in water properly.

5. DISCUSSION

Irradiance reflectance, R, is one of important parameters for ocean color remote sensing. The computed error contour map concerned with R around the ship which is circular in ship is presented in Fig.7. It can be seen that the influence of the ship shadow on R is categorized into two types. Thus, one is the underestimate region which appears around the ship near the seasurface. The other is the overestimate region which

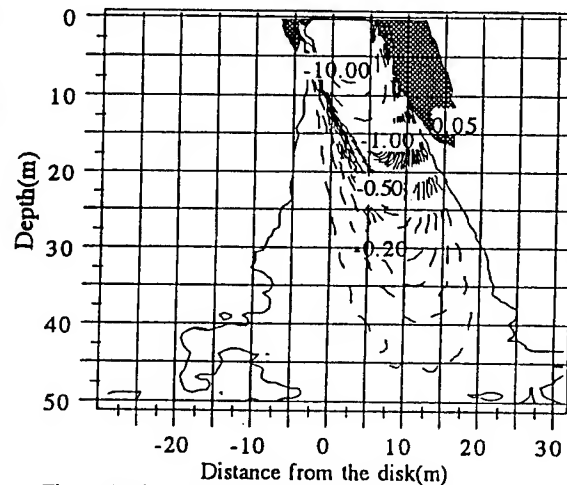


Fig.7 Vertical cross section of error contour map for R due to ship shadow, for which a, ζ and ω are 0.4 (m^{-1}), 60(deg.) and 0.8, respectively.

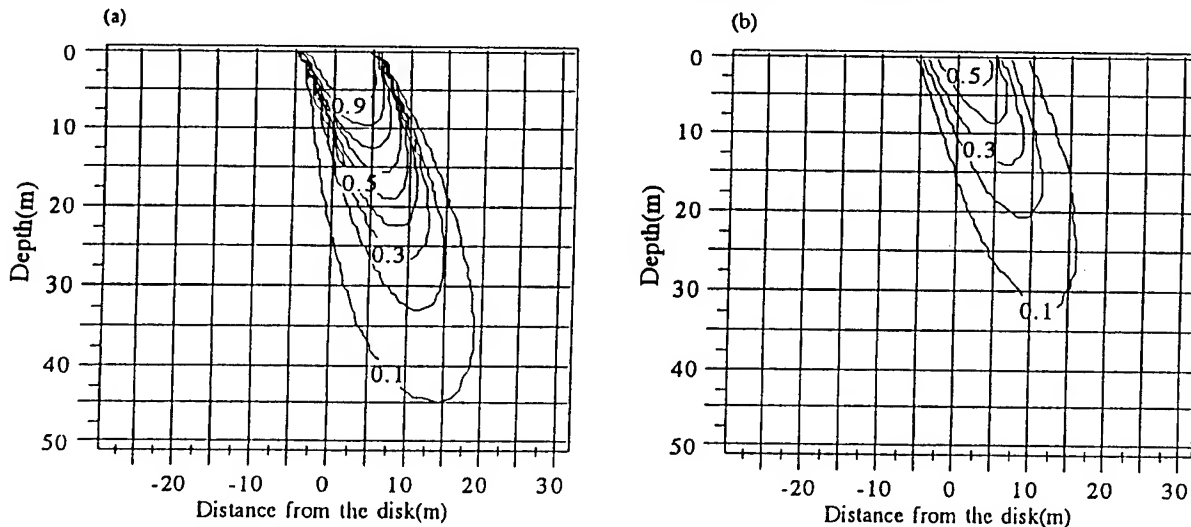


Fig.8 Vertical cross section of error contour map due to ship shadow, for which a, ζ and ω are 0.4 (m^{-1}), 60(deg.) and 0.8, respectively. (a): E_d (b): E_u

appears below the ship.

Fig 8-(a) and -(b) show the error contour map of E_d and E_u , respectively. The error region of E_d occurs in downward with respect to the direction of the sun light, and there is very little influence of the shadow near the sea surface. On the other hand, in the case of E_u , the error region appears in upward. In other word, the influence of the shadow appears in different manner, so that the underestimate region is formed near the sea surface. E_u has the smaller influence than E_d , since the scattering process develop. As the result, the overestimate region is formed along the direction of the sun light.

The relations between the ship size and the irradiance measurement error at the different position from the ship side was also investigated (See Fig.9). All parameters are normalized by the optical length. In order to simplify the situation, the disk is the circular in shape and the sun latitude is 90 deg. At the edge of ship side, the measurements error of E_u is smaller than E_d . However, it is not negligible error (See Fig.9-(b)). On the other hand, when the position is 5 away from the ship side, the relation of error between E_d and E_u reverses, i.e. E_u has the large error due to scattering (See Fig.9-(b)). Further, in both cases, the errors increase as function of ship size, and finally converge. That is, it is expected that the measurement errors of E_d and E_u do not change if the disk is large enough.

6. ACKNOWLEDGMENTS

The authors would like to express their thanks to Oki SeaTec Co., Japan, for giving the permission to use their experimental site, SeaTec II, and to H. Emoto and M. Taguchi for their help. Their thanks go also to K. Yajima and Y. Suzuki, Tokai Univ., for their back up

7. REFERENCES

- 1.E. Aas, "On submarine irradiance measurements", Rep. Inst. Geophy. Univ. Oslo, **6**, pp. 17-23, 1969
- 2.H.R. Gordon, "Ship perturbation of irradiance measurements at sea. 1: Monte Carlo simulations", *App. Opt.*, **24**, pp. 4172-4182, 1985
- 3.H.R. Gordon and K. Ding, "Self-shading of in-water optical instruments", *Limnol. Oceanogr.*, **37**, pp. 491-500, 1992
- 4.W.S. Helliwel, G.N. Sullivan, B. Macdonald and K.J. Voss, "Ship shadowing: model and comparisons", *Ocean Optics X*, R.W. Spinrad, **1**, **302**, pp. 55-71, SPIE, Bellingham, 1990
- 5.G. Zibordi and G.M. Ferrai, "Instrument self-shading in underwater optical measurements: experimental data", *App. Opt.*, **34**, pp. 2750-2754, 1995
- 6.T.J. Petzold, "Volume scattering function for selected ocean water", Scripps institution of oceanogr. visibility lab., SIO Ref., pp. 72-78, 1972
- 7.E. Aas, "The light absorption coefficient of clear water", Rep. Inst. Geophy. Univ. Oslo, pp. 17, 1987
- 8.B. Lundgren and N.K. Hojerslev, "Daylight measurements in the Sarugasso Sea", Rep. Inst. Phys. Oceanogr. Univ. Copenhagen, **14**, pp. 44, 1971

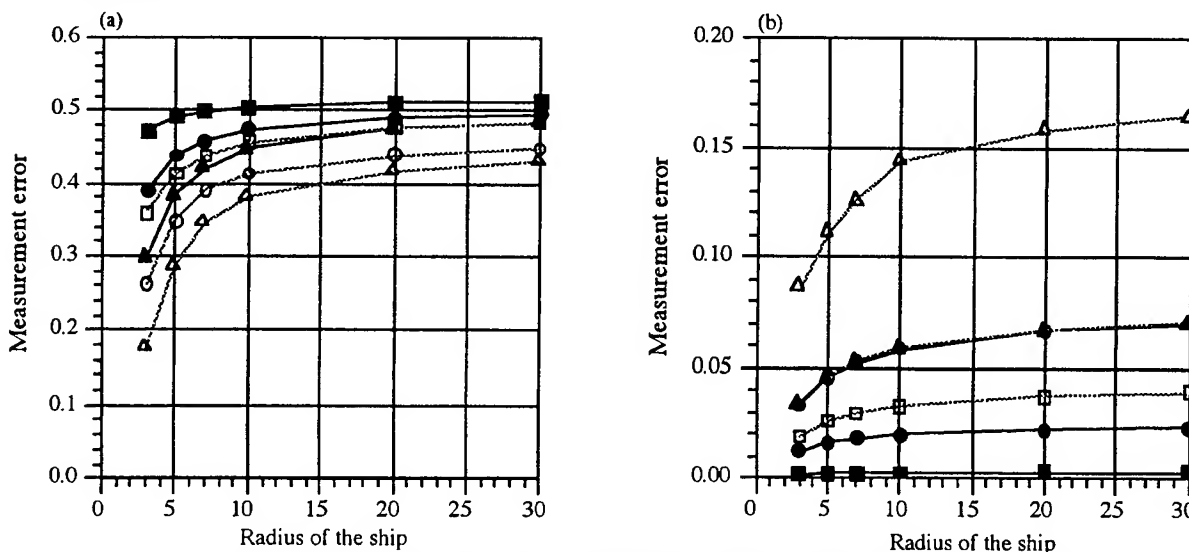


Fig.9 The relation between ship size and the measurement error at different water depth. The symbols corresponding to $E_{d,u}$ (distance from the ship side, optical depth) are ;
 $E_d(0,5)$: —■—, $E_d(0,10)$: —●—, $E_d(0,15)$: —▲—, $E_u(0,5)$: —□—, $E_u(0,10)$: —○—, $E_u(0,15)$: —△—

Development of bio-optical algorithm for ocean color remote sensing in the sub-Arctic North Pacific Ocean

Sei-ichi Saitoh*, Takako Miyoi*, and Motoaki Kishino**

*Faculty of Fisheries, Hokkaido University, Hakodate, Hokkaido 041, Japan

**The Institute of Physical and Chemical Research, Wako, Saitama 351-01, Japan

ABSTRACT

Sub-Arctic North Pacific Ocean is one of the highest biological productivity regions in the world. The quantitative assessment of phytoplankton production in this region is very important to estimate global primary production. Primary objective of this study is to validate and to develop bio-optical algorithm for new series ocean color sensors, such as Ocean Color and Temperature Scanner(OCTS) on ADEOS and Sea-viewing Wide Field-of-view Sensor (SeaWiFS) on SeaSTAR in the sub-Arctic North Pacific Ocean. We measured bio-optical parameters, which include upwelled spectral radiance, downwelled spectral irradiance, phytoplankton pigments (fluorometric technique), and general oceanographic parameters. Selected study areas were (1)155° E meridional transect, (2)180° meridional transect, (3)Gulf of Alaska, (4)eastern Bering Sea, and (5)southwest area of St. Lawrence Is. in 1995 and 1996. By using data sets gathered by field observation, we examined two kinds of bio-optical algorithms, Coastal Zone Color Scanner (CZCS)-type algorithm and OCTS-type algorithm which were generated by two visible bands and three visible bands respectively. As a result, OCTS-type algorithm has relatively good regression comparison with CZCS-type algorithm.

Keywords: bio-optical algorithm, ocean color, remote sensing, OCTS, CZCS, SeaWiFS, North Pacific, Bering Sea

1. INTRODUCTION

Sub-Arctic North Pacific Ocean is one of the highest biological productivity regions in the world. The quantitative assessment of phytoplankton production in this region is very important to estimate global primary production. Empirical and semi-empirical in-water algorithm for ocean color remote sensing has been accumulated through the studies for Coastal Zone Color Scanner (CZCS) in the past¹⁻⁴. Recently, Kishino et al.⁵ proposed new in-water algorithm for new series ocean color sensor, Ocean Color and Temperature Scanner(OCTS) on ADEOS⁶.

Primary objective of this study is to validate and to develop bio-optical algorithm for new series ocean color sensors, such as OCTS on ADEOS and Sea-viewing Wide Field-of-view Sensor(SeaWiFS) on SeaSTAR⁷ in the sub-Arctic North Pacific Ocean. We measured bio-optical parameters, which include upwelled spectral radiance, downwelled spectral irradiance, phytoplankton pigments (fluorometric technique) and general oceanographic parameters. Selected study areas were sub-Arctic North Pacific Ocean and Bering Sea in 1995 and 1996.

By using data sets gathered by field observation, we examined two kinds of bio-optical algorithms, CZCS-type algorithm and OCTS-type algorithm, which were generated by two visible bands and three visible bands respectively.

2. METHODS

2.1 Field observation

Data sets for this study were collected during four cruises to sub-Arctic North Pacific Ocean and Bering Sea. 65 bio-optical stations occupied during the four cruises, a total of 42 stations were considered to have reliable data for interpretation of the optical properties in surface waters (Table 1). Criteria for inclusion of stations included negligible ship-shadow effects, relatively constant solar irradiance and sufficient illumination for irradiance and radiance measurements with in the subsurface layer. Selected study areas were (1)155° E meridional transect, (2)180° meridional transect, (3)Gulf of Alaska, (4)eastern Bering Sea, and (5)southwest area of St. Lawrence Is. in 1995 and

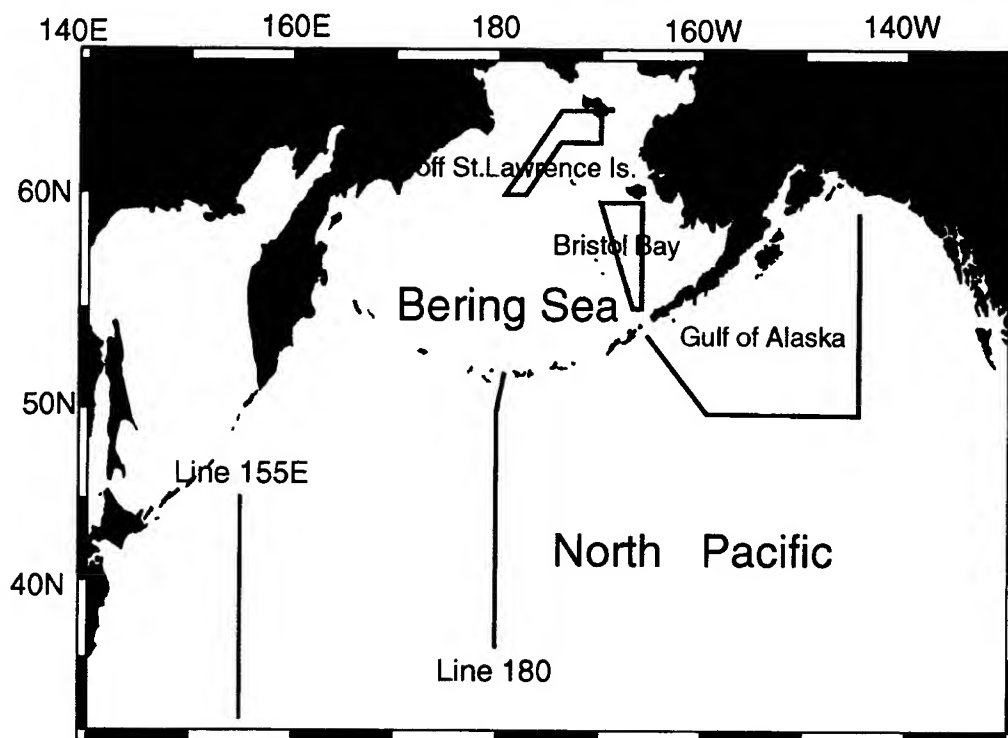


Figure 1 Map of the field observation areas and lines in North Pacific and Bering Sea

Table 1. Summary of field observation and number of bio-optical data

Study Area	Period		Ship	No. of Observation	No. of Adoption
	Days	Year			
North Pacific					
155° E Line	November 5-11	1995	T/S Oshoro Maru	7	2
	June 5-12	1996	T/S Hokusei Maru	7	6
	June 23-29	1996	T/S Hokusei Maru	9	7
180° Line	June 9-21	1995	T/S Oshoro Maru	6	5
Gulf of Alaska	July 1-12	1995	T/S Oshoro Maru	7	5
Bering Sea					
Bristol Bay	July 19-24, 31	1995	T/S Oshoro Maru	17	7
off St. Lawrence	July 24-29	1995	T/S Oshoro Maru	12	10
Total				65	42

1996. (Figure 1).

Sea water samples were collected by using a bucket from 0 m surface and by using Niskin bottles (1.71 l) mounted on the CTD rosette sampling system from some subsurface depths (shallower 200 m). Water samples (200 ml) were filtered through a Whatman GF/F filter on board. Filtered samples were put into glass vials containing 10ml of N,N-dimethylformamide, for extraction of chlorophyll a, after that stored in a freezer. Chlorophyll a and phaeopigments were determined by the fluorometric method⁸ with the Turner Designs Fluorometer at the laboratory.

Upwelled spectral radiance (\mathbf{Lu}), and Downwelled spectral Irradiance (\mathbf{Ed}), profile samples were measured with spectroradiometer MER-2020A (Biospherical Instruacts Inc.), which have the seven wave lengths : 412, 443, 490, 510, 555, 565 and 683 nm..

2.2 Bio-optical Algorithms

Normalized water leaving radiance is defined as follows:

$$\mathbf{nLw}(\lambda) = \frac{(1.0 - \mathbf{r_w})}{\mathbf{n}^2} [\mathbf{Lu}_1(\lambda) \times \exp\{\mathbf{Ku}(\lambda) \times \mathbf{Z}_1\}] \quad (1)$$

where, $\mathbf{r_w}$ is the reflectance from air to water and fixed 0.02, and \mathbf{n} is the refraction index and fixed 1.334. Here \mathbf{Ku} is the diffuse attenuation of upwelled spectral radiance, defined as

$$\mathbf{Ku}(\lambda) = \frac{1}{(\mathbf{Z}_2 - \mathbf{Z}_1)} \ln \left\{ \frac{\mathbf{Lu}_1(\lambda)}{\mathbf{Lu}_2(\lambda)} \right\} \quad (2)$$

where \mathbf{Z}_1 , \mathbf{Z}_2 are the upper and lower depth (m) and \mathbf{Lu}_1 and \mathbf{Lu}_2 are upwelled spectral radiance at \mathbf{Z}_1 and \mathbf{Z}_2 respectively.

The water-leaving radiance calculated by equation (1) and (2) using optical data measured by means of MER-2020A.

In this study, we estimated the three kinds of algorithms, which are using relationship between the ratio of radiance in different wave lengths and each of the pigments.

$$\langle \mathbf{C} \rangle = \mathbf{a} \left(\frac{\mathbf{L}_i}{\mathbf{L}_j} \right)^b \quad (3)$$

$$\langle \mathbf{C} \rangle = \mathbf{a} \left(\frac{\mathbf{L}_i + \mathbf{L}_j}{\mathbf{L}_k} \right)^b \quad (4)$$

$$\langle \mathbf{C} \rangle = \mathbf{a} \left(\frac{\mathbf{L}_i}{\mathbf{L}_k} \right)^b \left(\frac{\mathbf{L}_j}{\mathbf{L}_k} \right)^c \quad (5)$$

where $\mathbf{L}_i, \mathbf{L}_j, \mathbf{L}_k$ are upwelled spectral radiance of each wave length and $\mathbf{a}, \mathbf{b}, \mathbf{c}$ are the regression coefficient and $\langle \mathbf{C} \rangle$ is the concentration of pigments (chlorophyll a and phaeopigments) or the concentration of chlorophyll a. Equation (3) is CZCS-type algorithm by Gordon et al.¹. Equation (4) and (5) are OCTS Standard (OCTS-type) algorithms proposed by Kishino et al.⁵.

We examined two kinds of bio-optical algorithms for pigment and chlorophyll a. Pigment algorithm includes CZCS-type algorithm and OCTS-type algorithm which were generated by two visible bands and three visible bands

respectively. Chlorophyll a algorithm are generated by using only OCTS-type three visible bands model. Statistical analysis was carried out for two regions, North Pacific (17 stations) and Bering Sea (25 stations) (Table 1).

3. RESULTS AND DISCUSSION

Results of the statistical analysis of the relationship between ratios of upwelled spectral radiance and the sum of phytoplankton pigment concentration or chlorophyll a concentration are summarized in Table 2.

Table 2. Results of the statistical analysis

	Area	Wave length		a	b	c	R ²
Pigments							
this study	Bering Sea	443/555		0.8539	-1.2583		0.72
this study	Bering Sea	443/510	490/510	0.3889	-1.6757	-1.6864	0.74
this study	North Pacific	443/555		1.5310	-0.7504		0.69
this study	North Pacific	443/510	490/510	2.9713	1.0266	-5.2046	0.73
Kishino	Japan	443/520	490/520	1.5680	-2.0790	-3.4980	0.90
Gordon	case 1 water	443/550		1.0544	-1.7100		0.96
Gordon	case 1+2 water	443/550		0.8905	-1.3300		0.91
Chl.a							
this study	Bering Sea	(510+555)/490		0.2075	3.3754		0.66
this study	Bering Sea	412/490	510/490	0.4632	-0.6993	4.8012	0.76
this study	North Pacific	(510+555)/490		0.4839	1.9755		0.70
this study	North Pacific	412/490	510/490	1.0824	0.8578	3.9206	0.76
Kishino	Japan	(520+565)/490		0.2818	3.4970		0.95

3.1 Pigment algorithm

(1) Two bands model

General bio-optical algorithms¹ (equation(3)) were made of form using relationship between the ratio of Lu(443)/Lu(550) and the pigment concentration. The relationship between pigments and ratio of Lu from our study and the algorithm of Gordon, et al.¹ are presented in Figure 2. There is good agreement for data sets in Bering Sea (Figure 2(A)), but some disagreement appears in North Pacific (Figure 2(B)). By using Gordon et al.¹ algorithm for estimating pigment concentration, the results would be underestimated in North Pacific. A deference of "bio-optical provinces"⁹ between North Pacific and Bering Sea would be considered.

(2) Three bands model

The correlation value of three bands model is greater than that of two bands model in both regions (Table 2). Estimated values in Bering Sea would be overestimated and estimated value in North Pacific would be underestimated when the algorithm of Kishino et al.⁵ (equation(4)) is applied.

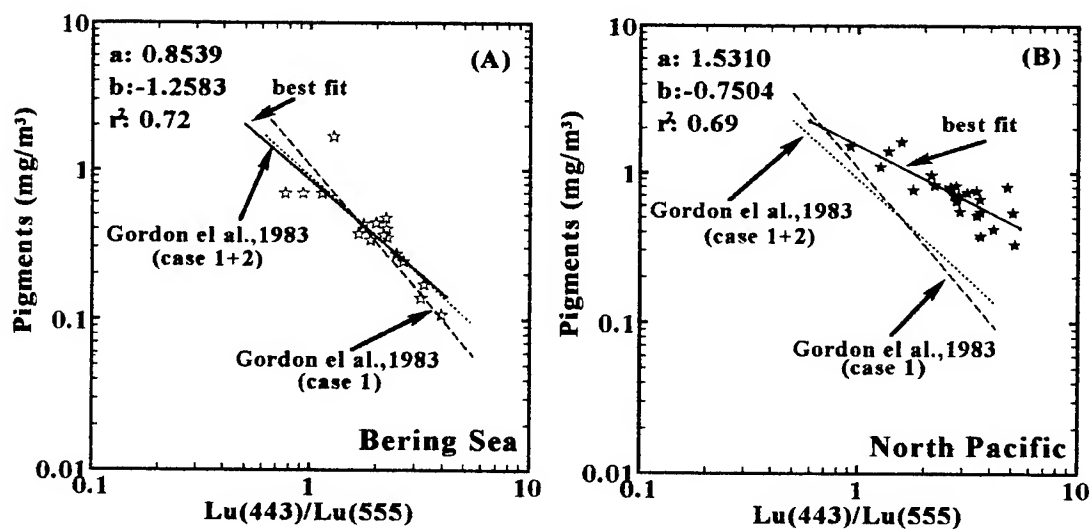


Figure 2. Relationship between ratios of upwelled spectral radiance and total pigments. Results are compared to the best fit regression results of Gordon et al.¹.

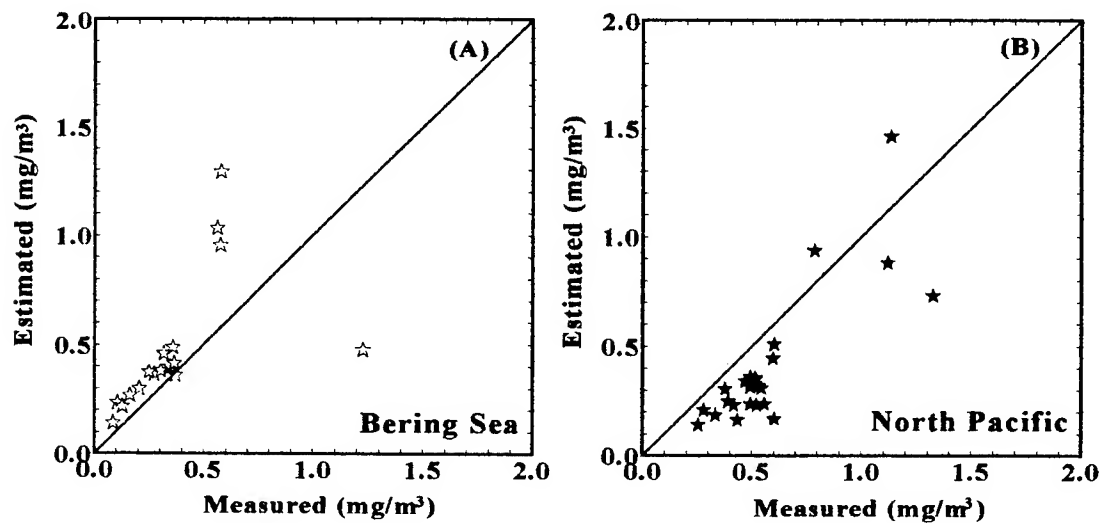


Figure 3. Relationship between measured chlorophyll a values and estimated chlorophyll a values by using the algorithm of Kishino et al.⁵ (equation(4) : $C = a \left[\frac{Lu(520)+Lu(565)}{Lu(490)} \right]^b$, C is the chlorophyll a concentration).

3.2 Chlorophyll a algorithm

The correlation value of equation (5) is greater than that of equation (4) model in both regions (Table 2). The relationship between measured values and estimated values using the algorithm of Kishino et al.⁵ (equation(4) : $C = a \{ [Lu(520)+Lu(565)]/Lu(490) \}^b$, C is the chlorophyll a concentration) are presented in Figure 3. Estimated chlorophyll a values in Bering Sea would be overestimated and estimated chlorophyll a values in North Pacific would be underestimated when the algorithm of Kishino et al.⁵ is applied. A difference of wave lengths between bio-optical measurement (510nm and 555nm) and wave lengths of OCTS (520nm and 565nm) would be considered.

4. CONCLUDING REMARKS

We examined two kinds of bio-optical algorithms for total pigments and chlorophyll a. Pigment algorithm includes CZCS-type algorithm and OCTS-type algorithm which were generated by two visible bands and three visible band respectively. As a result, OCTS-type algorithm has relatively good regression comparison with CZCS-type algorithm. However, there is a difference of wavelength between bio-optical measurement (555nm) and OCTS (565nm). Mitchell and Holm-Hansen¹⁰ pointed out that the ratio $Lu(560)/Lu(550)$ ranges from about 0.85 to 1.15 from oligotrophic to eutrophic waters. We are continuing to gather bio-optical parameters using new spectroradiometer PRR-600 (Biospherical Instruments Inc.) which has same wave lengths of OCTS in the same region. We will compare of this results and results from new data sets in future study.

5. ACKNOWLEDGEMENTS

We thanks to T. Ishimaru and S. Satoh for their kind providing optical instrument MER-2020A in the study period. This work was supported in part by the Grant-in-Aid for Science Research from Ministry of Education, Science, Sports and Culture, Japan (No.08456092).

6. REFERENCES

1. H. R. Gordon, D. K. Clark, J. W. Brown, O. B. Brown, R. H. Evans, and W. W. Broenkow, "Phytoplankton Pigment concentrations in the Middle Atlantic Bight: comparison of ship determinations and CZCS estimates", *Appl. Opt.*, Vol. 22, pp. 20-36, 1983.
2. H. R. Gordon, O. B. Brown, R. H. Evans, J. W. Brown, R. C. Smith, K. S. Baker and D. K. Clark, "A Semianalytic Radiance Model of Ocean Color", *J. Geophys. Res.*, Vol. 93, pp. 10909-10924, 1988.
3. S. Sugihara and M. Kishino, "An Algorithm for Estimating the Water Quality Parameters from Irradiance Just below the Sea Surface", *J. Geophys. Res.*, Vol. 93, pp.10875-10862, 1988.
4. B. G. Mitchell, "Predictive bio-optical relationships for polar oceans and marginal ice zones", *J. Mar. Sys.*, Vol.3, pp. 91-105, 1992.
5. M. Kishino, T. Ishimaru, K. Furuya, T. Onishi and K. Kawasaki, *Development of underwater algorithm* (in Japanese), 90pp., Institute of Physical and Chemical Research, Wako, Saitama, 1995.
6. S. Saitoh, OCTS on ADEOS, in Ed. by M. Ikeda and F. W. Dobson, *Oceanographic Application of Remote Sensing*, CRC Press, 473-480. 1995.
7. S. B. Hooker and W. E. Esaias, An overview of the SeaWiFS Project, *Eos*, Transactions, American Geophysical Union, 74, 245-246, 1993.
8. T. R. Persons, Y. Maita and C. M. Lalli, *A Manual of Chemical and Biological Methods for Seawater Analysis*, Pergamon Press, Oxford, pp.173, 1984.
9. J. L. Mueller and R. E. Lange, "Bio-optical provinces of the Northeast Pacific Ocean: A provisional analysis", *Limnol. Oceanogr.*, Vol. 34, pp.1572-1585, 1989.
10. B. G. Mitchell and O. Holm-Hansen, "Bio-optical properties of Antarctic Peninsula waters: differentiation from temperate ocean models", *Deep-Sea Res.*, Vol.38, pp.1009-1028, 1991.

The SeaWiFS Quality Monitor - a portable field calibration light source

Ping-Shine Shaw and B. Carol Johnson

Optical Technology Division
National Institute of Standards and Technology
Gaithersburg, MD 20899 USA

Stanford B. Hooker

NASA/Goddard Space Flight Center, Code 970.2
Greenbelt, MD 20771 USA

Don Lynch

Reyer Corporation, 11847-B Lime Plant Road
New Market, MD 21774 USA

ABSTRACT

A portable and stable source, the Sea-viewing Wide Field-of-view Sensor (SeaWiFS) Quality Monitor, has been developed for use as a field instrument. The source can be used with either radiance- or irradiance-measuring sensors to transfer the laboratory calibration to the field so that the stability of the sensors can be monitored during the experiment. Temperature-controlled silicon photodiodes with colored glass filters are used to monitor the stability of the SeaWiFS Quality Monitor.

Keywords: calibration, field instrument, portable source, radiometric source, SeaWiFS

1. INTRODUCTION

Oceanographic field studies are an essential component of the Sea-Viewing Wide Field-of-View Sensor (SeaWiFS) Calibration and Validation Program.^{1,2} Ocean-color data collected during cruises will be used to assist in the analysis of the data collected by the SeaWiFS satellite, with the ultimate goal to improve the atmospheric correction and bio-optical algorithms. The quality of these ocean-color data is critical to the success of the SeaWiFS project, and protocols have been established for the measurements.³ To ensure data quality, each marine radiometer is generally calibrated before and after the field experiment. Ideally, the stability of the calibration should be monitored during the cruise. Because on-board calibration facilities are difficult to realize in practice, current investigative cruises rely on the manufacturer's calibration data or pre- and post-cruise calibration data. Considering the severe environmental changes encountered by marine radiometers, especially during shipment, the stability of the radiometer is in question and that, in turn, raises the concern that the data are not accurate enough for the success of the project.

In response to the requirement to monitor the stability of the marine radiometers, the National Institute of Standards and Technology (NIST) along with National Aeronautics and Space Administration's Goddard Space Flight Center

(NASA/GSFC), jointly developed a portable field light source, the SeaWiFS Quality Monitor (SQM). The goals were to produce a uniform large-area light source that is stable when used on board ships or other field platforms (e.g. aircraft), affordable to the relevant scientific community, and otherwise practical for field use. Because the stability of the marine radiometers over long time intervals is critical to the field experiments, the stability of the SQM was the key parameter. To utilize the SQM, the radiance or irradiance responsivity of the marine radiometer is first measured in the laboratory using calibration sources (e.g., integrating sphere, irradiance standard lamp, or diffuse plaque and standard lamp). At the same time, the signal levels corresponding to these calibration values are transferred to the SQM by making measurements with the marine radiometers and the SQM. Then the SQM and the marine radiometers are sent to the field experiment and the SQM is used to monitor the stability of the sensors.

A prototype SQM has been built and used on the second and third Atlantic Meridional Transect experiments as well as at the fifth SeaWiFS Intercalibration Round-Robin Experiment.⁴ This prototype source includes three temperature stabilized, filtered photodiodes so that the stability of the SQM can be monitored at all times. The 20 cm diameter exit aperture is a plastic diffuser that is protected by a glass window. An adaptor plate, customized for each class of marine radiometers, mounts to the exit aperture. The adaptor plate is designed so that the position of the radiometer is reproducible with respect to all six degrees of freedom. Because the exit aperture is a diffuser, the SQM can be used with radiance or irradiance sensors. The relative spectral shape of the SQM source (including the diffuser) corresponds to an apparent blackbody temperature of about 2250 K as measured at seven wavelengths using two radiometers. The radiance variability over a circle of 15 cm in diameter is no larger than 4% (peak-to-valley). The optical design of the SQM resulted in an aspect

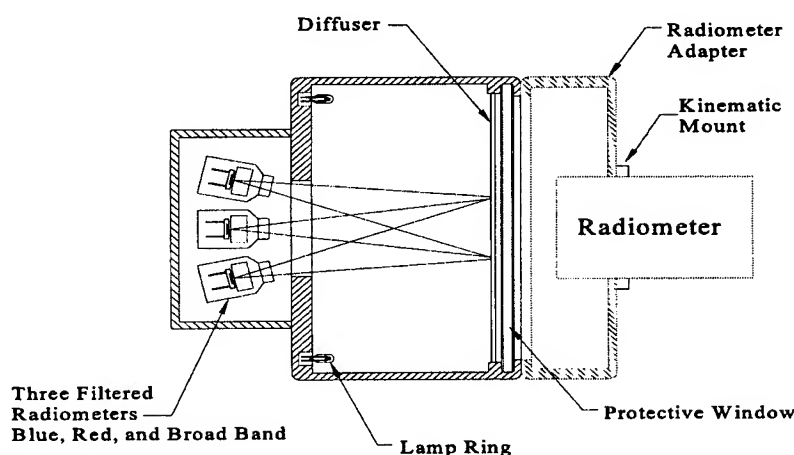


Figure 1. Simplified schematic of the SQM Prototype.

ratio (diameter/length of lamp chamber) of two, so compared to traditional radiance calibration standards, the SQM is compact. Rugged construction and consideration of the marine environment resulted in a stable and portable device.

2. SQM PROTOTYPE

The basic design of the SQM is shown in Fig. 1. Additional details and complete description of the modeling of the radiometric output are discussed elsewhere.⁵ Briefly, the source consists of a ring of 16 miniature quartz-halogen lamps. Eight are 5.0 V at 3.45 A lamps, and eight are 4.2 V at 1.05 A lamps. Each set of lamps are connected in series and operated by separate precision current sources; normal operation provides three different output levels. The 3.2-mm-thick plastic diffuser, which serves as the exit aperture, is about 12 cm from the plate containing the ring of lamps. The three monitor silicon photodiodes are mounted behind small apertures in the center of the lamp mounting plate and three different glass

filter combinations are located between the apertures and each photodiode in order to limit the spectral coverage. The filters and photodiodes are temperature stabilized at 35 °C using a single thermoelectric cooler, a calibrated thermistor, and a commercial temperature controller. The measured photocurrents are converted to voltages using a custom amplifier circuit based on the design used in the NIST standard detectors. The result is stable and precise monitoring of the SQM in the red, blue, and broad-band/visible spectral region. The diffuser and the lamp ring assembly are enclosed in a cylindrical housing made of bead-blasted aluminum so that the diffuse component of the reflectance is significant. This cylindrical structure is sealed using o-rings to protect the light source from the environment.

Because the lamps are enclosed in the cylindrical housing, the equilibrium temperature of the SQM at 22 °C is high, about 50 °C. A fan assembly mounted to the rear of the SQM is used to cool the device and under normal laboratory conditions the temperature is about 30 °C. A closed-loop electrical heater, which is independent of the other control systems, can be used to maintain the SQM at a fixed temperature, thus decreasing the time required to reach thermal equilibrium when the lamps are turned on.

The radiometer adaptor, which is painted black, satisfies the kinematic mounting requirements for the marine radiometers. It also eliminates stray light from the environment, so that the field tests could occur outdoors under full solar illumination if necessary. The effect of the adaptor on the output of the SQM is not a factor in the calibration chain, since the adaptor is in place for all measurements with the SQM and the marine radiometers. The assembled SQM and adaptor is shown in Fig. 2. Because the reflectance of the front face of the marine radiometers may change during the field experiment, with a concomitant change in the signals measured by the SQM monitor photodiodes and perhaps the marine radiometer as well, a set of fiducial "radiometers" were produced. These fiducials simply consist of cylinders made from white plastic or aluminum. The aluminum was painted with a diffuse black paint and one end of the cylinder was covered with a clear glass plate in order to simulate the glass window on actual radiometers. The fiducials are kept clean and are not exposed to the environment. Normal operation consists of recording the signal on the SQM monitor photodiodes using the fiducials, followed by measurements with the marine radiometers.

The two power supplies for the two lamp sets in the SQM are stabilized precision current sources. The design of each system is similar to the automated current control of standard lamps described by Walker and Thompson.⁶ In this method, the current through each set of eight lamps is measured using an accurate 0.5 Ω shunt resistor. If the current is not at the desired value, the power supply is adjusted via voltage programming. Both lamp systems are controlled with a single computer program, and the two power supplies as well as a digital voltmeter with an eight-channel multiplexer are interfaced to the computer using the IEEE GPIB interface protocols. A 16-bit D/A, which resides on a slot in the computer, is used to convert the programming voltage to an analogue signal. The digital voltmeter measures the voltages across the shunt resistors, the output of the three monitor photodiodes, and the resistance of two thermistors, one attached to each of the shunt resistors. All data are recorded in an ASCII file along with the current time, day, and year. Ancillary data from the SQM can also be collected using the SQM "deckbox". This unit attaches to auxiliary connections on the SQM so that the voltage across each of the 16 lamps can be recorded manually. The temperature of the SQM, as measured by three thermistors integrated into the cylindrical housing and the detector assembly, can also be recorded using the SQM deckbox. These data were found to be useful during testing of the SQM prototype. Finally, an automated timer circuit records elapsed lamp operating time.

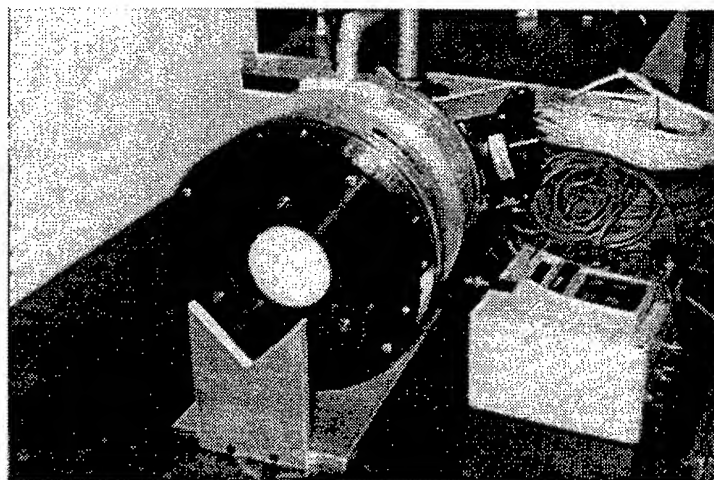


Figure 2. SQM prototype with radiometer adaptor

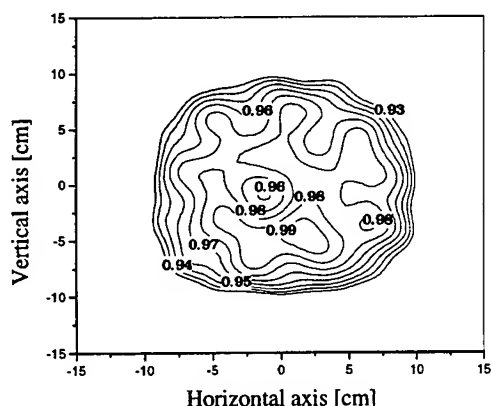


Figure 3. Measured uniformity at 412 nm during the development of the SQM.

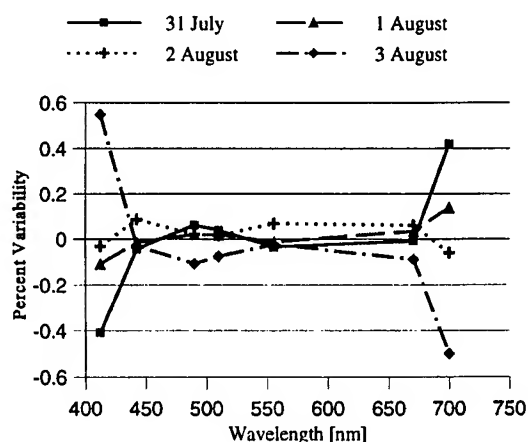


Figure 4. Variability of an irradiance sensor over a four-day interval when monitored using the SQM.

3. PERFORMANCE OF THE SQM PROTOTYPE

Figure 3 shows the radiance uniformity, normalized to the maximum value, of the SQM prototype as measured with the SeaWiFS Transfer Radiometer at 412 nm (see Ref. 4 and references therein). In the central area of the exit port, a 4% uniformity is achieved within an area with a diameter of 15 cm. Because the radiometers are kinematically mounted to the SQM, the effect of this non-uniformity is negligible.

The stability of the SQM prototype was measured during a four-day interval by monitoring the output of radiance and irradiance ocean-color sensors. On each day, the SQM was turned on and allowed to stabilize. The signals from the SQM photodiodes were recorded in one computer file as described above, and the signals from the test radiometers were recorded by a second computer using the normal data acquisition software. These radiometers are designed to record downwelling irradiance or upwelling radiance at seven wavelengths. The stability of the SQM as measured using the SQM monitor photodiodes and the black fiducial attached to the SQM is given in Table 1. The stability of the test radiometers is illustrated in Fig. 4 for the down-welling irradiance radiometer. The daily results for the SQM indicate a stability of about 0.1% or better, while the test radiometer results varied by up to 1%.

Table 1. Variation from the mean for the SQM monitor photodiodes.

	31 July	1 August	2 August	3 August
Blue Monitor	-0.037%	0.025%	-0.027%	0.039%
Red Monitor	0.073%	0.000%	0.017%	-0.090%
Broad Band Monitor	0.029%	0.004%	0.009%	-0.041%

4. CONCLUSION

We have designed, constructed, and tested a portable field source that is a prototype for general field use in support of SeaWiFS calibration and validation. This large-area source is simple in construction, stable, portable, and suitable for monitoring sensor stability during a field experiment. Laboratory tests demonstrated the ability to monitor changes in the calibration coefficients of marine radiometers at about the 0.1% level. This result is very satisfactory given that the combined standard uncertainty in the absolute radiometric calibration of the marine radiometers is typically between 1% and 2%. Monitoring of the ocean color sensors using the SQM during field experiments will greatly improve the reliability of these

ocean color data.

REFERENCES

1. S.B. Hooker and W.E. Esaias, *EOS, Trans. Am. Geophys. Union*, **74**, 241 (1993).
2. C.R. McClain, W.E. Esaias, W. Barnes, B. Guenther, D. Endres, S.B. Hooker, B.G. Mitchell, and R. Barnes, SeaWiFS Calibration and Validation Plan, *SeaWiFS Technical Report Series, NASA Tech. Memo. 104566*, Vol. 3, 41pp (1992).
3. J.L. Mueller and R.W. Austin, Ocean Optics Protocols for SeaWiFS Validation, Revision 1, *SeaWiFS Technical Report Series, NASA Tech. Memo. 104566*, Vol. 25, 67pp (1992).
4. The Fifth SeaWiFS Intercalibration Round-Robin Experiment, July 22 - 30, 1996, in preparation for submission to the *SeaWiFS Technical Report Series, NASA Tech. Memo. 104566*.
5. P.S. Shaw, B.C. Johnson, S.B. Hooker, and D. Lynch, The SeaWiFS Quality Monitor, in preparation.
6. J.H. Walker and A. Thompson, *J. Res. Natl. Inst. Stand. Technol.* **99**, 255 (1994).

Oceanographic Bio-Optical Profiling System II

Raymond C. Smith and David W. Menzies

Institute for Computational Earth System Science
University of California at Santa Barbara
Santa Barbara, CA. 93106

Charles R. Booth

Biospherical Instruments Inc.
5340 Riley Street
San Diego, California 92110

ABSTRACT

A second generation Bio-Optical Profiling System (BOPS) has been designed, built and used extensively at sea. The BOPS-II is an oceanographic instrument used to measure in-water optical, biological and physical properties in support of interdisciplinary programs. Significant advances beyond BOPS-I include: a depth capability of 500 m; more rapid data acquisition for higher water column resolution; lower inherent dark signal giving greater sensitivity; and greater multicomponent capability, permitting a wide range of additional sensors. The BOPS-II has a proven record of reliability supporting sampling strategies using ship, mooring, aircraft, and satellite optical sensors for ocean research. Rather than an article about a newly designed instrument, this is a report of an instrument and its optical calibration that has been used routinely for nearly a decade, often in the most extreme environments of the world's oceans. An example of optical calibration history is included since calibrations are among the most important aspects of ocean optical measurements, whether in support of a single field experiment or of long-term data collection. The BOPS instrument has served as a model for new generations of optical profiling sensors.

Keywords: optical, ocean color, instrumentation, long-term, time-series

1. INTRODUCTION

Oceanographic Bio-Optical Profiling Systems (BOPS) have been used for over a decade in support of interdisciplinary ocean research. The BOPS¹ was originally designed to: (1) permit the rapid acquisition of data so as to accommodate shipboard "synoptic" sampling, (2) provide an instrument platform for interdisciplinary sampling using ancillary instrumentation, and (3) measure parameters necessary for bio-optical and satellite ocean color research. As used here, interdisciplinary (optics, physics, chemistry, biology) sampling implies close coupling and a common scientific focus for each discipline as distinct from multidisciplinary where frequently samples taken for each discipline are separated in space and/or in time. The BOPS-II design builds upon the original philosophy but makes use of recent technical advances to significantly enhance at sea performance.

Bio-optics is a term coined² to represent the mechanistic coupling of dissolved and suspended biogenetic material in ocean waters and corresponding ocean optical properties. Given concentrations of these materials, optical properties can be estimated (direct problem) or conversely, ocean optical properties can be used to infer constituents and concentrations of biogenetic material within the water column (indirect problem)³. The use of optical sensors to determine proxy estimations of pigment biomass and phytoplankton production is now widely accepted in oceanography where optical sensors have been deployed on a variety of platforms (ships, moorings, aircraft, satellites). Bio-optical techniques are increasingly important for studies aimed at advancing our understanding of global ocean processes since they permit sampling of biological parameters over space and time scales that would otherwise be impracticable⁴.

The Joint Ocean Flux Study (JGOFS) is one recent example of an international, interdisciplinary research project with a global perspective. The long-range goals of JGOFS are: "1) To evaluate and understand on a global scale the processes controlling the time-varying fluxes of carbon and associated biogenic elements in the ocean, and 2) To develop

the capability to predict the response of oceanic biogeochemical processes to climate change" ⁵. A common theme of JGOFS and related studies is to understand the processes and controls governing phytoplankton production and the fate of related biogenic materials in the sea. Bio-optical processes are a recognized component of such research because only satellite observations permit global coverage ^{4,6}.

Oceanographic time series programs such as the Hawaii Ocean Time-series (HOT) ⁷, Bermuda Atlantic Time-series Study (BATS) ⁸, and the Palmer Long-Term Ecological Research (Palmer LTER) ⁹ are examples of programs designed to gain a comprehensive understanding of habitat variability in key locations and to provide the long-term observations necessary to put human induced change into perspective with respect to natural variability. Optical observations play an important role in these long-term programs by permitting rapid proxy estimation of biological parameters, and BOPS-like instruments have been used in both BATS and Palmer LTER as routine water column profiling instruments. In addition, the Palmer LTER BOPS-II rosette provides twelve 5 or 12 liter 'clean' water samples for biological and chemical analysis.

High quality optical surface data, in conjunction with the next generation of ocean color satellite sensors (e.g., SeaWiFS, OCTS, MODIS, etc.) ¹⁰, will provide proxy estimation of pigment biomass across a range of space/time scales and with a higher accuracy than would otherwise be possible. SeaWiFS workshops and proceedings ¹¹⁻¹⁴ have detailed science objectives and requirements for contemporaneous surface calibration/validation and bio-optical algorithm development for the SeaWiFS and related ocean color projects. Mueller and Austin (Table 1) ¹⁴ present a summary of these requirements. The BOPS-II was designed to complement ocean color satellite observations and operate within the optics protocols necessary to optimize the usefulness of SeaWiFS data. Table 1 summarizes the SeaWiFS requirements which can be met using the BOPS-II.

Related scientific objectives influencing the design and construction of optical profiling systems include: the quantitative description and predictive modeling of upper ocean radiant energy balance; the description and prognostic modeling of the coupling between physical forcing and the dynamics of chlorophyll variation; and the description and modeling of ocean optical variability as a function of relevant physical and biological processes. These efforts require bio-optical characterization of large ocean areas.

In addition to the scientific objective of acquiring data synoptically from multiple platforms, there are operational constraints imposed by the interdisciplinary nature of oceanographic programs which define requirements for a BOPS-like instrument. These criteria include: 1) rapid measurement of important optical, biological and physical parameters to accommodate limited ship-board "wire time"; 2) compatibility of the data acquisition system with conventional cables and winches of the oceanographic fleet; 3) robustness to permit the system to be handled and launched even in rough seas; 4) rosette to collect "clean" water samples for chemical and biological analysis; 5) real time display of profile data for optimum selection of discrete water samples at depth; and 6) computer interface for rapid preliminary data reduction at sea for timely comparison with contemporaneous remotely sensed and other shipboard data sets. In short, BOPS is an interdisciplinary (optical, physical, chemical, biological) analogue to the conventional physical oceanographic Conductivity-Temperature-Depth (CTD) system.

2. BIO-OPTICAL PROFILING SYSTEM

The Bio-Optical Profiling System II (BOPS-II) is an integrated data collection and analysis system designed to provide rapid and accurate measurement of the variability of ocean optical and ancillary properties in the upper 500 meters of the ocean (Fig.1). It is a redesign of the original BOPS ¹ which was made compatible with the first ocean color satellite (Coastal Zone Color Scanner, CZCS) for the Warm Core Rings Program ¹⁵. Table 2 lists current instrument components of BOPS-II while Figure 2 is a block diagram showing the relationship of the underwater unit to the shipboard deck unit and the computer system. The physical layout of optical sensors includes downwelling irradiance sensors whose top profile is above the top of the water bottles and out and away from the cable termination (a potential source of shadowing). The physical sensors are in a plane at the bottom of the package to minimize interference with temperature and salinity sensors in order to optimize their data on the descending profile. The stand and the protective ring at the top of the package provide important protection from inadvertent bumping the side of the ship and for attaching handling lines during instrument deployment and retrieval during rough seas. For Antarctic work aboard the R/V Polar Duke, the BOPS-II has been deployed from the ships stern both because the A-frame provides the longest reach away from the ship and for

protection and stability in stormy weather.

2.1. Optical components

While the BOPS-II has been periodically upgraded, within the constraints of resources and a demanding field deployment schedule, many components of this system are nearly a decade old. More recent systems are described in Sect. 2.3 below. A primary objective of this article is to describe a field-proven instrument, illustrate the robustness of a system that has been used for over 1600 casts mostly in the Southern Ocean under extreme environmental conditions, and to document the optical calibration history, and hence optical precision and accuracy, over time.

The central components of the underwater BOPS-II are two MER-2040 microprocessor controlled spectroradiometers. Each MER can digitize up to 64 analog and 3 frequency inputs, so many additional sensors can be added including scalar irradiance, transmissometers and fluorometers. The optical sensors of the MER-2040 are based on arrays of solid-state photodetectors. Each photodetector assembly is composed of a high shunt resistance, blue enhanced silicon photodetector hermetically packaged with its own custom narrow-band interference filter. Blocking filters are added to reduce stray light levels, typically to values below the sensitivity detection levels of the sensors. Each detector is connected to an electrometer amplifier with sensitivity optimized for wavelength and geometrical configuration. This array of detector assemblies with amplifiers is scanned under microprocessor control at a rate of approximately one channel per millisecond.

The current optical characteristics of the BOPS-II were selected to meet SeaWiFS requirements (Table 1) including accurate cosine response and quantitative measure of the immersion effect¹⁶. The irradiance detector arrays view the inside of a cosine corrected optical collector. To test the cosine response of the design, a MER-2040 was placed on an automated rotating arm in a water-tight test tank equipped with nonparallel sides. A collimated beam was positioned to fill the collector at the precise center of rotation of the assembly. Under computer control, the instrument is rotated in 5° increments from +90° to -90° "zenith" angles and the response from each channel recorded relative to the source. The cosine response of the instrument agrees with the cosine rule within ± 5% out to angles of 75° and ± 10% to 85°. Immersion coefficients used in the calibrations are those from tests conducted at Biospherical Instruments on MER Series spectroradiometers. The immersion coefficient of the collector was determined experimentally from irradiance measurements made in air and under water¹⁶. The instrument was carefully positioned in a test tank beneath a calibration lamp fixture. Readings from the lamp were recorded in air and at 5 cm depth increments both during filling and emptying the tank. Following SeaWiFS protocols¹⁷, these data were used to measure the attenuation coefficient for the water used in the test and to solve for the immersion coefficient at each wavelength. BSI currently offers collectors with more accurate fidelity to a cosine response.

The radiance array consists of a cluster of "Gershun Tube" radiance collectors which view the upwelling radiance through an acrylic pressure window. The radiance collector array was designed with a half-angle field of view of 10.2° in water and 13.7° in air with later versions reduced to 10.0° field of view in water.

A maximum of eight MER-2040s can be networked into the same data stream and synchronously sampled on a single serial data port. In the case of the BOPS-II configuration, two profiling MER-2040 spectroradiometers interface with a MER-2020 with a MER-2040 EPROM serving as an above water sensor with 4 channels of downwelling irradiance (410, 441, 488, and 560nm). In addition, a sub-surface floater¹⁸ containing a MER-2020 with a MER-2040 EPROM has been used to provide the downwelled spectral irradiance just below the surface, $E_d(0^-, \lambda)$, at 5 wavelengths, and the upwelled radiance about a meter below the surface, $L_u(1m)$, at 5 wavelengths including 683nm. This floater uses a 50m kevlar conducting tether and floats away from the ship to avoid ship shadow problems. This component of the BOPS-II will be particularly useful for satellite comparisons with SeaWiFS and other ocean color satellite sensors. As the floater requires extra time to deploy, it is deployed when sampling constraints allow sufficient time and remains deployed perhaps for an entire day.

The BOPS is extensible in that auxiliary instruments may be interfaced. For instance, a transmissometer,¹⁹ accurately measuring beam transmission in a 25 centimeter water path, uses a modulated light emitting diode (660nm) and a synchronous detector. This instrument contains stable temperature compensated electronics and provides data with an error of less than 0.5% transmission. Also, a scalar irradiance quantum meter²⁰ is used to measure photosynthetically

active radiation (PAR). Scalar irradiance PAR is the number of photosynthetically active photons arriving at a point from all directions within the wavelength band 400-700nm.

2.2 MER-2040 Hardware and Software

To accommodate the wide dynamic range encountered in the ocean, the signals are digitized by a data acquisition system composed of a 14 bit analog to digital converter (ADC) with a computer controlled input amplifier with selectable gain ranges of 1, 16 and 256, yielding a dynamic range of approximately four million to one. To compensate for the small temperature sensitivities inherent in silicon detectors and amplifiers, temperature sensors located in close proximity to the detectors and amplifiers are digitized.

A design feature of the MER-2040 has allowed us to modify the electronics module within the General Oceanics Rosette so as to allow better firing of the water bottles. A simple circuit is used which permits bottles to be tripped within 1 sec of a computer keystroke and which provides a signal change within the data stream confirming the tripping of each bottle. Eliminating the need to halt the winch at each sample depth has significantly simplified and speeded up our profiling. The UCSB software searches for the change in voltage level and prints out a confirmation line with depth in addition to other parameters for output onto water sample worksheets.

The microprocessor within each of the BOPS MER units is programmed for flexibility. The surface computer sends information to each unit specifying which channels to sample, the order of sampling, and the gain to use for each channel. The frequency counting channels are also programmed to select the number of cycles of each signal to count. Commands are sent to specify whether multiple scans of the programmed analog channels are to be averaged and the time interval between the start of each sampling. Another command allows multiple repeats of each sampling suite to proceed automatically. The result is that multiple instruments can be configured so that all sample synchronously and store their averaged data internally until the data are requested by computer command. If a different number of channels is requested in each instrument, the number of scans that are averaged can be specified so that each instrument takes the same time for completion. Thus not only would the sample start time be synchronized, but also the sampling time window. For example, the MER-2040 with irradiance sensors on both ends measures 36 channels 10 times during each programmed sampling window. The other unit, having scalar irradiance and radiance channels, measures 15 channels but does so 24 times. The modified MER-2020 surface unit (running at half the clock rate) measures 9 channels but averages 35 scans.

We have carried out tests to show that each instrument can complete all required sampling at our desired rate of three times per second. The frequency counting circuitry uses the sine-wave signal from the Sea-Bird temperature and conductivity probes to gate on, and then off, the counting of a 6 MHz reference frequency for a specified number of cycles. By measuring the cycle period (as distinct from the frequency), the necessary high resolution is retained even though the sampling window is less than 350 ms.

With each MER unit programmed to complete its analog and frequency sampling within a selected time and programmed to start each sampling at a given time spacing, the surface computer needs only to request a data scan from each unit as it becomes available. The sampling interval is also dependent on the speed of the surface computer which must retrieve each scan of data from all instruments, combine the strings and write to a data file, as well as display selected parameters in a real-time graphic display. With a data rate of 3 scans per second, we use a lowering speed of about 25 m/s through the euphotic zone (1% PAR depth) to assure sufficient data for accurate determination of the diffuse attenuation coefficients. Winch speed can then be increased to roughly 35 m/s for the remainder of the cast. Although most casts have little detectable irradiance below 200 m, we continue to 500 m, or 10 m above the bottom, in order to obtain a fuller hydrographic data set with the CTD and other sensors on the BOPS-II. On a profile to 200 m, 1600 data frames are typically recorded on both the down- and up-casts.

The BOPS-II is operated over a three conductor armored cable with power and data on separate conductors. Before transmission, each data frame is encoded with a start byte, instrument status and identification byte, and a checksum for verification of proper transmission. The readings of each optical sensor are then transmitted up the cable to the deck unit via asynchronous serial communications using an RS-232 interface. The system is limited to cable lengths less than 1000 meters on a standard CTD cable.

The current shipboard components of the system include a constant current power supply for the underwater system, a 486 microprocessor with 6 MB RAM, a 2 GB disk drive, a high resolution graphics display system, printer and tape backup system. The system also makes use of a third MER-2040 mounted shipboard for reference recording of incident irradiance above the surface to correct for changing atmospheric conditions during a vertical profile.

2.3 MER-2040 Series Instrument Evolution

The MER-2040 has evolved significantly since it was originally deployed on the BOPS-II. The optics have been expanded and the MER is available with up to 13 channels of downwelling irradiance, $E_d(\lambda)$, and 13 channels of either upwelling radiance, $L_u(\lambda)$, or upwelling irradiance, $E_u(\lambda)$. A special version of the MER called the MER-2048 is available featuring 13 channels of downwelling irradiance and seven channels each of both upwelling radiance and irradiance. Optimized for use into the ultraviolet region of the spectrum, the cosine collector on this 2040 series instrument has been redesigned to use a quartz-backed, vacuum-formed Teflon® diffuser. A modified version of the collector optimized for use in air is used on the MER-2041 Surface Reference Radiometer. Although the exterior dimensions have not changed, internally the newest MER features a low noise, 16 bit, bipolar analog-to-digital converter for data acquisition as well as eight digital I/O ports. Communications can be performed over a four conductor, 1000 m serial cable or using FSK over up to 10 km armored (single or multiple conductor) coax cable. In addition to those listed for the BOPS, the Remote Data Spooler (RDS) option for the MER-2040 affords operation with up to four additional serial-output instruments such as the WETLabs' AC-9, and the newest generation of intelligent rosette, such as those manufactured by General Oceanic or Sea-Bird Electronics.

2.4. Biological components

Chlorophyll and related pigments are the dominant absorbing constituents in the upper layers of productive ocean waters, and are therefore a key link in the bio-optical description of these waters^{21,22}. In addition, chlorophyll is used as a measure of phytoplankton biomass and is the pigment that has the primary influence on ocean color and hence CZCS imagery²³⁻²⁶. BOPS-II uses a fluorometer for the continuous measure of chlorophyll and a rosette sampler to obtain discrete water samples from depth. The discrete water samples are used to obtain an extracted chlorophyll concentration, which is used to calibrate the fluorometer profile²⁷ as well as provide samples for analysis such as nutrients, primary production, dissolved gases, and microbiological parameters.

A fluorometer excites chlorophyll fluorescence in the blue and senses the output in the red region of the spectrum, providing a continuous measure of chlorophyll fluorescence as BOPS-II is lowered through the water column. After viewing vertical structure of chlorophyll fluorescence, beam transmittance, temperature and a selected irradiance channel in real time on the "down cast", the 12 bottle rosette is used to sample at representative depths on the "up cast" both for calibration of the fluorometer and to sample specific features and/or optical depths for use by other disciplines. A molecular oxygen probe²⁸ provides a profile of the dissolved oxygen.

2.5. Physical components

The BOPS-II contains temperature, conductivity and depth sensors in order to provide an accurate physical description of the water column. The Sea Bird temperature probe sensing element is a glass coated thermistor bead with an absolute accuracy of $\pm 0.01^\circ\text{C}$ and a useable resolution of better than 0.0001. The conductivity sensing element²⁹ is a two-terminal platinum electrode flow through cell with an absolute accuracy of 0.001 Siemens/meter and a usable resolution of better than 0.0001. The frequency output from these sensors is measured using the period averaging inputs of the MER-2040. Period averaging preserves the inherent accuracy of the sensors while permitting sampling rates of several per second.

Each of the MER-2040s comprising BOPS-II is equipped with a pressure transducer. One uses a quartz frequency output transducer (Paroscientific) with a 6.21MPa full scale with a typical accuracy of 0.01%. The output from this is digitized using the MER period averaging interface. The second unit is equipped with a strain gauge transducer with a similar full scale. Angle sensors on 2 axes are included to measure the package orientation during profiles.

2.6. Data Processing, Instrument Calibration and Error Analysis

BOPS data processing, calibration and binning have been discussed elsewhere³⁰⁻³³. Specific consideration has been given over the years to particular topics to be considered for the processing of in-water spectral irradiance data such as the influence of: the air-water interface³⁴, ship shadow effects^{18,35,36} and surface albedo³⁷⁻³⁹. For BOPS-II, calibrations have been supplied by Biospherical Instruments Inc. upon delivery of the MERs while subsequent calibrations have been performed at the UCSB Ocean Optics Calibration Facility.

Each of the sensors on the BOPS (Table 2) has its own calibration procedure which is used to achieve and maintain the performance specifications as listed in Table 3. For example, the spectral irradiance arrays are calibrated using an FEL 1000 watt standard of spectral irradiance⁴⁰. The radiance calibrations have used both a 20 inch integrating sphere and, more recently, 24 inch Spectralon® diffuse reflectance plaque. Our normal procedure, when logistics permit, is to calibrate both before and after each cruise. An eight year calibration history of the spectral downwelling irradiance channels on the BOPS-II is shown in Figures 3. These figures illustrate several points regarding calibration maintenance of an optical field instrument over time. (1) Wavelength channels which 'degrade' become obvious outliers (Fig. 3a), can be 'flagged' as problem channels and subsequently replaced (e.g. channels 410 nm and 520 nm were replaced prior to our 1992 field work). Identifying and replacing degrading components is a critical reason to maintain a protocol of periodic calibration. (2) Even though subjected to periodic transportation (by air and ship) between Santa Barbara and Palmer Station, Antarctica and to intense usage in often extreme environmental conditions, the mean drift of the calibration (stable channels) over time is negligible and the scatter is less than a few percent (Fig. 3b). (3) A calibration in the field was made in 1993 by transporting calibrated lamps and an optical bench to Palmer Station. The result of this effort was inconclusive because of the potential that the calibration lamps themselves may be more susceptible to change with shipment across the ocean than the optical components to be calibrated. Also, quality space for optical calibration with appropriate light baffles, etc. is difficult to achieve in the field. (4) In early 1995 the sensor head was rebuilt, and some channels added or replaced. (5) The 'optical train' including cosine collector, filters, photodiode, amplifier and analog to digital conversion circuitry is a robust system that, with periodic calibration, can maintain stability within a percent or so over relatively long times and harsh working conditions. Finally, and this is a key point, repeated, periodic recalibration is an essential element of meeting the optical protocols for time-series observations and to support the calibration/validation of the next generation of ocean color satellite sensors.

The cosine response and immersion coefficients, which allow transfer of an air calibration to an underwater calibration, were determined as described above (Sect. 2.2). We tested and found that there was no observed depth dependence, caused by temperature changes, for the irradiance sensors. Bandwidth and wavelength accuracy of the MER Spectroradiometer were determined by comparison with a double grating monochromator and are listed in Table 2.

The transmissometer calibration is checked by first carefully cleaning the windows, and then comparing the output voltage in air with the "air calibration" provided by the manufacturer. This instrument calibration also can be checked occasionally, since the optical properties of ocean waters can be constant over large areas when below the euphotic zone. In the North Pacific, during a 6 week period with more than 40 casts into the same 200 meter water, the beam transmittance repeated to within $\pm 0.02\%$.

Fluorescence, as measured on the BOPS instrument, is a relative indicator of chlorophyll concentration. The rosette sampler is then used to obtain water samples from depths of interest, and the chlorophyll concentration of these discrete samples is determined fluorometrically in a laboratory calibrated fluorometer²⁷. These discrete values of chlorophyll, which can be determined to $\pm 15\%$, are then used to calibrate the continuous fluorescence trace.

3. DISCUSSION

An exciting aspect of oceanography is the capability to view, via satellites, large areas of the oceans synoptically. The perspective provided by aircraft and satellite data is giving insight into a wide range of research areas⁴¹ including the study of physical and biological processes on space and time scales previously unattainable. The next generation of ocean color satellite sensors¹⁰ will carry this effort through the next decade. The new satellite technology has required a new approach to obtaining shipboard biological and optical data in order to provide both "synoptic" shipboard data as well as contemporaneous surface information for calibration/validation of aircraft and satellites. The versatility and flexibility of

the BOPS-like instrument has provided one successful approach as evidenced by its use in a variety of programs including Warm Core Rings⁴²⁻⁴⁵, the Optical Dynamics Experiment (ODEX)⁴⁶, Watercolors⁴⁷⁻⁵¹, Biowatt^{22,52-57}, Icecolors⁹⁰⁻⁵⁸⁻⁶⁰, the Long-Term Ecological Research Program (Palmer LTER)^{9,61-63}, the Bermuda Atlantic Time Series (JGOFS/BATS)^{36,64} and the Tropical Ocean-Global Atmosphere/Coupled Ocean Atmosphere Response Experiment (TOGA/COARE)⁶⁵. Careful and periodic optical calibration is an essential element of an ocean optics field program. The Bio-Optical Profiling System II, including its calibration history, is a robust interdisciplinary oceanographic instrument capable of providing accurate and precise optical data over long time periods.

5. ACKNOWLEDGEMENT

The contributions of Karen Baker and Kirk Waters (UCMBO) as well as M. Elston and John Morrow (BSI) are acknowledged. Support for design, construction, and maintenance of the BOPS-II are from the National Aeronautics and Space Administration Grants NSG6-14 and NAGW 290 (RCS). Support for use of the BOPS-II in the Palmer LTER program is provided by the National Science Foundation, Office of Polar Programs DPP90-11927 (RCS).

6. REFERENCES

1. R. C. Smith, C. R. Booth, and J. L. Star, "Oceanographic bio-optical profiling system," *Appl. Opt.*, **23**, 2791-2797 (1984).
2. R. C. Smith and K. S. Baker, "Optical classification of natural waters," *Limnol. Oceanogr.*, **23**, 260-267 (1978).
3. R. W. Preisendorfer "Hydrologic optics: Volume I. Introduction," (U.S. Department of Commerce, Washington, 1976)
4. R. C. Smith, O. B. Brown, F. E. Hoge, K. S. Baker, R. H. Evans, R. N. Swift, and W. E. Esaias, "Multiplatform sampling (ship, aircraft, and satellite) of a Gulf Stream warm core ring," *Appl. Opt.*, **26**, 2068-2081 (1987).
5. D. M. Butler, R. E. Hartle, M. Abbott, R. Cess, R. Chase, P. Chistensen, J. Dutton, L.-L. Fu, C. Gautier, J. Gille, R. Gurney, P. Hays, J. Hovermale, S. Martin, J. Melack, D. Miller, V. Mohnen, and et. al. "From Pattern to Process: The Strategy of the Earth Observing System," EOS Science Steering Committee Report Volume II, (NASA, 1988)
6. T. D. Dickey and D. A. Siegel, Eds "U.S. Joint Global Ocean Flux Study - Bio-optics in U.S. JGOFS," U.S. JGOFS Planning Report Number 18, December 1993, (US JGOFS Planning and Coordination Office, Woods Hole, Mass. 02543, 1993) (180 pages). Report of the Bio-optics Workshop, Boulder, CO, 17-18 June 1991 plan.
7. D. M. Karl and R. Lukas, "The Hawaii Ocean Time-series (HOT) program: Background, rationale and field implementation," *Deep-Sea Res.*, **43 II**, 129-156 (1996).
8. A. F. Michaels and A. H. Knap, "Overview of the US JGOFS Bermuda atlantic time-series study and the hydrostation S program," *Deep-Sea Res.*, **43 II**, 157-198 (1996).
9. R. C. Smith, K. S. Baker, W. R. Fraser, E. E. Hofmann, D. M. Karl, J. M. Klinck, L. B. Quetin, B. B. Prezelin, R. M. Ross, W. Z. Trivelpiece, and M. Vernet, "The Palmer LTER: A long-term ecological research program at Palmer Station, Antarctica," *Oceanography*, **8**, 77-86 (1995). Palmer LTER Contribution #78.
10. W. Esaias, G. Feldman, R. Frouin, W. Gregg, S. Hooker, and C. McClain "Ocean color multisensor data evaluation and utilization plan," (Godard Space Flight Center, Washington, DC) (xx pages)
11. B. G. Mitchell, W. F. Esaias, G. Feldman, R. G. Kirk, C. R. McClain, and M. R. Lewis, "Satellite ocean color data for studying oceanic biogeochemical cycles," *National Telesystems Proceedings Conference*, (Atlanta, Georgia, 1991) p. 283-287
12. J. A. Yoder and H. Fukushima "Satellite Ocean Color," A Joint US-Japan Seminar program held at the East-West Center in Honolulu, Hawaii, 7-10 May, 1991: Final Report: 10 July 1991, (1991) (26 pages)
13. S. B. Hooker, C. R. McClain, and A. Holmes, "Ocean color imaging: CZCS to SeaWiFS," *Marine Technology Society Journal*, **27**, 3-15 (1993).
14. J. L. Mueller and R. W. Austin, in: "Volume 25, Ocean Optics Protocols for SeaWiFS Validation, Revision 1," S. B. Hooker, E. R. Firestone, and J. G. Acker, Eds., Vol. 25. (*SeaWiFS Technical Report Series; NASA Technical Memorandum 104566*, (NASA/GSFC, Code 970.2, Greenbelt, MD 20771, 1995) p. 1-67
15. T. Joyce and P. Wiebe, "Warm core rings of the Gulf Stream," *Oceanus*, **26**, 34-44 (1983).

16. R. C. Smith, "An underwater spectral irradiance collector," *J. Mar. Res.*, **27**, 341-351 (1969).
17. J. L. Mueller and R. W. Austin "Volume 5, Ocean optics protocols for SeaWiFS validation," *SeaWiFS Technical Report Series; NASA Technical Memorandum 104566*, Vol. 5, (1992) (46 pages)
18. K. J. Waters, R. C. Smith, and M. R. Lewis, "Avoiding ship-induced light-field perturbation in the determination of oceanic optical properties," *Oceanography*, **3**, 18-21 (1990).
19. R. Bartz, J. R. V. Zaneveld, and H. Pak, "A transmissometer for profiling and moored observations in water," *Proc. SPIE Ocean Opt.* **V**, **160**, 102-108 (1978).
20. C. R. Booth, "The design and evaluation of a measurement system for photosynthetically active quantum scalar irradiance," *Limnol. Oceanogr.*, **19**, 326-335 (1976).
21. K. S. Baker and R. C. Smith, "Bio-optical classification and model of natural waters. 2," *Limnol. Oceanogr.*, **27**, 500-509 (1982).
22. R. C. Smith, J. Marra, M. J. Perry, K. S. Baker, E. Swift, E. Buskey, and D. A. Kiefer, "Estimation of a photon budget for the upper ocean in the Sargasso Sea," *Limnol. Oceanogr.*, **34**, 1673-1693 (1989).
23. W. A. Hovis, D. K. Clark, F. Anderson, R. W. Austin, W. A. Wilson, E. I. Baker, D. Ball, H. R. Gordon, J. L. Mueller, S. F. El-Sayed, B. Sturm, R. C. Wrigley, and C. S. Yentsch, "Nimbus-7 Coastal Zone Color Scanner: System Description and Initial Imagery," *Science*, **210**, 60-63 (1980).
24. H. R. Gordon, D. K. Clark, J. L. Mueller, and W. A. Hovis, "Phytoplankton pigments from the Nimbus-7 Coastal Zone Color Scanner: comparisons with surface measurements," *Science*, **210**, 63-66 (1980).
25. W. H. Wilson, R. C. Smith, and J. W. Noltan "The CZCS Geolocation Algorithms," SIO Ref. 81-32., (University of California, San Diego, Scripps Institution of Oceanography, Visibility Laboratory, La Jolla, California, 1981)
26. H. R. Gordon and A. Y. Morel "Remote Assessment of Ocean Color for Interpretation of Satellite Visible Imagery, A Review, *Lect. Notes on Coastal and Estuarine Stud.*" **4**. ((Springer-Verlag, New York, 1983) (114 pages)
27. R. C. Smith, K. S. Baker, and P. Dustan "Fluorometer techniques for measurement of oceanic chlorophyll in the support of remote sensing," SIO Ref. 81-17, (Visibility Laboratory, Scripps Institution of Oceanography, Univer. of Calif., San Diego, La Jolla, 1981) (14 pages)
28. J. W. VanLandingham and M. W. Greene, "An in situ molecular oxygen profiler: a quantitative evaluation of performance," *Marine Technology Society Journal*, **5**, 11-23 (1971).
29. A. M. Pederson and M. C. Gregg, "Development of a small *in-situ* conductivity instrument," *IEEE J. Oceanic Eng.*, **OE-4**, 69 (1975).
30. R. C. Smith and K. S. Baker, "The analysis of ocean optical data," *Proc. SPIE Ocean Opt.* **VII**, **489**, 119-126 (1984).
31. R. C. Smith and K. S. Baker, "Analysis of ocean optical data II," *Proc. SPIE Ocean Opt.* **VIII**, **637**, 95-107 (1986).
32. J. C. Sorensen, M. C. O'Brien, D. Konnoff, and D. A. Siegel, "The BBOP data processing system," *SPIE12*, **2258**, 539-546 (1994).
33. D. A. Siegel, D. Konnoff, M. C. O'Brien, J. Sorensen, and E. Fields "BBOP sampling and data processing protocols," US JGOFS Planning Report #19, (US JGOFS Planning Office, Woods Hole, MA, 1995) (77 pages)
34. K. S. Baker and R. C. Smith, "Irradiance transmittance through the air-water interface," *Proc. SPIE Ocean Opt.* **X**, **1302**, 556-565 (1990).
35. H. R. Gordon, "Ship perturbation of irradiance measurements at sea. 1: Monte Carlo simulations," *Appl. Opt.*, **24**, 4172-4182 (1985).
36. C. T. Weir, D. A. Siegel, D. W. Menzies, and A. F. Michaels, "In situ evaluation of a ship's shadow," in: *Case studies for SeaWiFS calibration and validation, Part 3, SeaWiFS Technical Report Series; NASA Technical Memorandum 104566*, S. B. Hooker, E. R. Firestone, and J. G. Acker, Eds., Vol. 27, (NASA/GSFC, Code 970.2, Greenbelt, MD 20771, 1995) p. 25-33
37. H. R. Gordon and M. M. Jacobs, "Albedo of the ocean-atmosphere system: influence of sea foam," *Appl. Opt.*, **16**, 2257-2260 (1977).
38. R. W. Preisendorfer and C. D. Mobley, "Albedos and glitter patterns of a wind-roughened sea surface," *J. Phys. Oceanogr.*, **16**, 1293-1316 (1986).
39. K. Patterson, P. L. Handley, and R. C. Smith, "Palmer LTER: Open water PUV albedo measurements (submitted)," *Antarct. J. U. S.* (1996)

40. R. Stair, W. E. Schneider, and J. K. Jackson, "A new standard of spectral irradiance," *Appl. Opt.*, **2**, 1151 (1963).
41. W. E. Esaias, "Remote sensing in biological oceanography," *Oceanus*, **24**, 32-38 (1981).
42. T. Joyce, R. Backus, K. S. Baker, P. Blackwelder, O. Brown, T. Cowles, R. Evans, G. Fryxell, D. Mountain, D. Olson, R. Schlitz, R. Schmitt, P. Smith, R. C. Smith, and P. Wiebe, "Rapid evolution of a gulf stream warm-core ring," *Nature*, **308**, 837-840 (1984).
43. O. B. Brown, R. H. Evans, J. W. Brown, H. R. Gordon, R. C. Smith, and K. S. Baker, "Phytoplankton blooming off the U.S. east coast: A satellite description," *Science*, **229**, 163-167 (1985).
44. R. C. Smith and K. S. Baker, "Spatial and temporal patterns in pigment biomass in gulf stream warm-core ring 82B and its environs," *J. Geophys. Res.*, **90**, 8859-8870 (1985).
45. J. K. B. Bishop, R. C. Smith, and K. S. Baker, "Springtime distribution and variability of biogenic particulate matter in Gulf Stream warm-core ring 82B and surrounding N.W. Atlantic waters," *Deep-Sea Res.*, **39**, S295-S325 (1992).
46. R. C. Smith and K. S. Baker "Optical Dynamics Experiment (ODEX) III Cruise 10 October 1982 - 17 November 1982, Vol. 5: BOPS Vertical Cast Measurements, UCMBO Data Report," SIO Ref. 87-23., (University of California, San Diego, Scripps Institution of Oceanography, La Jolla, California, 1987)
47. R. C. Smith, R. R. Bidigare, B. B. Prezelin, K. S. Baker, and J. M. Brooks, "Optical characterization of primary productivity across a coastal front," *Mar. Biol.*, **96**, 575-591 (1987).
48. R. C. Smith, B. B. Prezelin, R. R. Bidigare, and K. S. Baker, "Bio-optical modeling of photosynthetic production in coastal waters," *Limnol. Oceanogr.*, **34**, 1524-1544 (1989).
49. O. Schofield, B. B. Prezelin, R. C. Smith, P. Stegmann, N. B. Nelson, M. R. Lewis, and K. S. Baker, "Variability in spectral and nonspectral measurements of photosynthetic light utilization efficiencies," *Mar. Ecol. Prog. Ser.*, **78**, 253-271 (1991).
50. R. R. Bidigare, B. B. Prezelin, and R. C. Smith, "Bio-optical models and the problems in scaling," in: *Primary Productivity and Biogeochemical Cycles in the Sea*, P. G. Falkowski, Ed., Vol. 43, (Plenum Press, New York, 1992) p. 175-212
51. O. Schofield, B. B. Prezelin, R. R. Bidigare, and R. C. Smith, "In-situ Photosynthetic quantum yield. Correspondence to Hydrographic and optical variability within the Southern California Bight," *Mar. Ecol. Prog. Ser.*, **93**, 25-37 (1993).
52. R. R. Bidigare, R. C. Smith, K. S. Baker, and J. Marra, "Oceanic primary production estimates from measurements of spectral irradiance and pigment concentrations," *Global Biogeochem. Cycles*, **1**, 171-186 (1987).
53. R. R. Bidigare, J. Marra, T. D. Dickey, R. Iturriaga, K. S. Baker, R. C. Smith, and H. Pak, "Evidence for phytoplankton succession and chromatic adaptation in the Sargasso Sea during spring 1985," *Mar. Ecol. Prog. Ser.*, **60**, 113-122 (1990).
54. D. A. Siegel, R. Iturriaga, R. R. Bidigare, R. C. Smith, H. Pak, T. D. Dickey, J. Marra, and K. S. Baker, "Meridional variations of the springtime phytoplankton community in the Sargasso Sea," *J. Mar. Res.*, **48**, 379-412 (1990).
55. R. C. Smith, K. J. Waters, and K. S. Baker, "Optical variability and pigment biomass in the Sargasso Sea as determined using deep sea optical mooring data," *J. Geophys. Res.*, **96**, 8665-8686 (1991).
56. J. Marra, T. Dickey, W. S. Chamberlin, C. Ho, T. Granata, D. A. Kiefer, C. Langdon, R. C. Smith, K. S. Baker, R. Bidigare, and M. Hamilton, "Estimation of seasonal primary production from moored optical sensors in the Sargasso Sea," *J. Geophys. Res.*, **97**, 7399-7412 (1992).
57. K. J. Waters, R. C. Smith, and J. Marra, "Phytoplankton production in the Sargasso Sea as determined using optical mooring data," *J. Geophys. Res.*, **99**, 18385-18402 (1994).
58. R. C. Smith, B. B. Prezelin, K. S. Baker, R. R. Bidigare, N. P. Boucher, T. Coley, D. Karentz, S. MacIntyre, H. A. Matlick, D. Menzies, M. Ondrusek, Z. Wan, and K. J. Waters, "Ozone depletion: Ultraviolet radiation and phytoplankton biology in Antarctic waters," *Science*, **255**, 952-959 (1992).
59. B. B. Prezelin, N. P. Boucher, and R. C. Smith, "Marine primary production under the influence of the Antarctic ozone hole: Icecolors '90," in: *Ultraviolet radiation in Antarctica: Measurements and biological effects*, C. S. Weiler and P. A. Penhale, Eds., Vol. 62, (1994) p. 159-186. Icecolors Contribution #5.
60. K. M. Crocker, M. E. Ondrusek, R. L. Petty, and R. C. Smith, "Dimethylsulfide, algal pigments and light in an Antarctic *Phaeocystis* sp. bloom," *Marine Biology*, **124**, 335-340 (1995).
61. R. C. Smith, K. S. Baker, K. K. Hwang, D. Menzies, and K. J. Waters, "Palmer LTER: Hydrography and optics within the peninsula grid, November '91 cruise," *Antarct. J. U. S.*, **27**, 250-253 (1992). Palmer LTER Contribution #10.

62. R. C. Smith, H. Dierssen, and M. Vernet, "Phytoplankton biomass and productivity to the west of the Antarctic peninsula," in: *Foundations for Ecological Research West of the Antarctic Peninsula*, R. M. Ross, E. E. Hofmann, and L. B. Quetin, Eds., Vol. 70, *AGU Antarctic Research Series*, (1996) Palmer LTER Contribution #77.
63. R. C. Smith, K. S. Baker, and M. Vernet, "Seasonal and interannual variability of phytoplankton biomass west of the Antarctic Peninsula (in press)," *Journal of Marine Systems*, (1996) Palmer LTER Contribution #99.
64. D. A. Siegel, A. F. Michaels, J. C. Sorensen, M. C. Obrien, and M. A. Hammer, "Seasonal variability of light availability and utilization in the Sargasso Sea," *J. Geophys. Res.*, **100**, 8695-8713 (1995).
65. D. A. Siegel, J. C. Ohlmann, L. Washburn, R. R. Bidigare, C. Nosse, E. Fields, and Y. Zhou, "Solar radiation, phytoplankton pigments and the radiant heating of the Equatorial Pacific warm pool," *J. Geophys. Res.*, **100**, 4885-4891 (1995).



Figure 1. Photograph of the Bio-Optical Profiling System underwater unit.

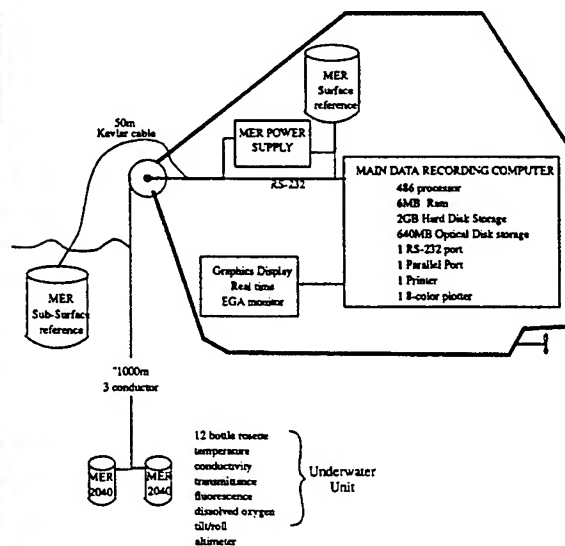


Figure 2. Schematic diagram of the BOPS integrated system showing the principal components of the underwater and the deck units connected by means of a hydrowinch and slip-rings.

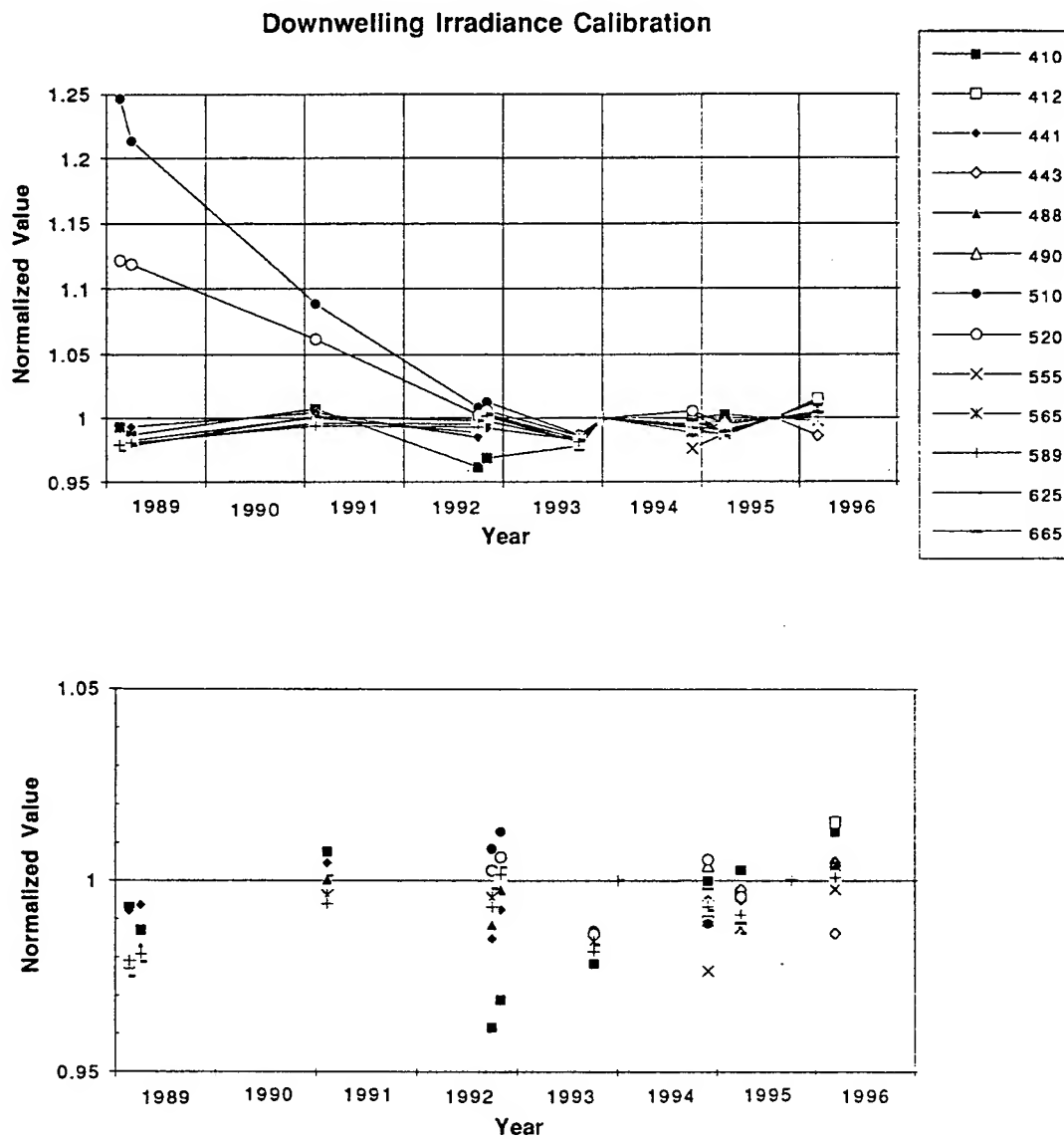


Figure 3. The eight year calibration history of the downwelling unit (MER8714) of the Bio-Optical Profiling System II in normalized units versus time. The top panel shows data on channels which prematurely degraded and were replaced. The lower panel displays an expanded scale for the remaining channels.

Table 1. Observation requirements for Calibration/Validation, Algorithm Development, and Supporting Science for SeaWiFS. The observations indicated under Calibration/Validation and Algorithm Development are considered Core measurements of the SeaWiFS Project.

Observation	Calibration Validation	Algorithm Development	Supporting Science	BOPS-II
Optical Observations				
Incident Spectral Irradiance-Ed,(0,-)	X	X		+
Downwelled Spectral Irradiance-Ed,Z	X	X		+
Upwelled Spectral Radiance-Lu,Z	X	X		+
Spectral Solar Atmos. Trans (Ta)	X	X		-
Sea State photograph	X	X		-
Wind Velocity	X	X		-
Drifting Buoy Optics			X	-
Upwelled Spectral Irradiance-Eu,Z			X	+
Spectral Beam Attenuation Coefficients			X	x
Spectral Absorption coefficient			X	a
Red beam attenuation			X	+
<i>In situ</i> Fluorescence Profile			X	+
Sky Radiance			X	-
Submerged Up Radiance Distribution			X	-
Spectral Backscattering coefficient b_b			X	x
Spectral Volume Scat. Function			X	x
Biological/Chemical/Physical Observations				
Phyto. Pig (Fluor. Tech.) Chlor. and Phaeo.		X		w
Phytoplankton Pigments (HPLC ¹)		X		w
Total Suspended Matter (TSM) Conc.		X		w
Dissolved Colored Organic Material		X		w
Aerosol samples			X	-
Primary Productivity (^{14}C , O_2)			X	w
Temperature and Salinity Profiles			X	+
Phycobilipigments (mg/m^3)			X	w
Particle absorption coefficient			X	w
Detritus absorption coefficient			X	w
Phytoplankton absorption coefficient			X	w
Organic Suspended Matter Conc.			X	w
Inorganic Suspended Matter Conc.			X	w
New Production (^{15}N)			X	w
Coccolith Concentration			X	w
Humic and Fluvic Acids			X	w
Microphotometric particle absorption			X	w
Particle fluorescence spectra			X	w
Sinking Flux/Sed. Traps			X	-
Particle size spectra			X	w
Total Dissolved Organic Carbon			X	w
Airborne Fluorescences			X	-
Airborne Radiances			X	-
Phytoplankton species counts			X	w
Grazing Losses			X	w

¹High Performance Liquid Chromatography

x = can be added

+ = now

a = from g... relate.; not accurate

w = potential-using discrete water sample

- = not applicable

Table 2. Instrument components of BOPS underwater unit.

Instrument	Manufacturer	Property Measured
spectroradiometer (MER-2040)	Biospherical Instruments, Inc.	downwelling irradiance upwelling irradiance upwelling radiance chlorophyll fluorescence band scalar irradiance spectral PAR
transmissometer	SeaTech, Inc.	beam transmittance at 660nm
fluorometer	SeaTech, Inc.	chlorophyll fluorescence
ocean thermometer (SBE 3)	Sea-Bird Electronics, Inc.	temperature
conductivity meter (SBE 4)	Sea-Bird Electronics, Inc.	conductivity (salinity)
oxygen probe (SBE 13-01)	Sea-Bird Electronics, Inc.	dissolved oxygen
pressure gauges		depth
quartz strain	ParoScientific SensoTec	
rosette (twelve 5 or 12 liter)	General Oceanics	discrete water samples
AccuStar electronic	Schaevitz	tilt and roll
altimeter	DataSonics	distance from the bottom

Table 3. Performance Specifications for the Bio-Optical Profiling System (BOPS)

<p>Spectroradiometer (Spectral Irradiance): Downwelling Irradiance: 410,412,441,443,488,490,510, 520,555,565,589,625,665nm Upwelling Irradiance: 410,441,488 520 565 589,625nm Upwelling Radiance: 410,441,488,520,565,625,chl fluorescence Bandwidth: 50% points +5nm, -5nm; 1% points +15nm, -20nm Wavelength Accuracy: ± 2nm Radiometric Accuracy: 5% Stray light: <0.01% 40nm from peak; <0.0001% 100nm from peak</p>	<p>Temperature Sensor: Accuracy: $\pm 0.01^{\circ}\text{C}$ Long term stability: $\pm 0.003^{\circ}\text{C}$ per 6 month Resolution: .0001$^{\circ}\text{C}$</p>
<p>Scalar Irradiance: Downwelling Scalar Irradiance: 410, 441, 488, 520, 565nm Equal Quantum Response (PAR): 400-700nm</p>	<p>Conductivity Sensor: Accuracy: 0.001 Siemens/m Long term stability: 0.0003 Siemens/m per month Resolution: .000001 S/M</p>
<p>Data Acquisition Systems: Analog Channels per MER-2040: 56 A/D Conversion: float (12 bit mantissa, 4 bit exponent); integer (16 bit) Frequency Channels per MER-2040: 3 Frequency Conversion: integer (24 bit)</p>	<p>Tilt/Roll: Range: $\pm 45^{\circ}$ Accuracy: $\pm 1^{\circ}$</p>
<p>Data Transmission: RS-232: 9600 baud (up to 38,400 baud) Maximum Cable Length: 1000 meters 3 conductor armored cable Acquisition, Process, Transmit Time: 2.5 msec/channel at 9600baud</p>	<p>Transmissometer: Wavelength: 660nm Pathlength: 25cm Accuracy: $\pm 0.5\%$</p>
<p>Depth Sensor (ParoScientific): Range: 0-600m Pressure Accuracy: $\pm 0.04\%$ at 250m Depth resolution: 0.1m Other: includes internal temperature sensor</p>	<p>Oxygen Sensor: Range: 0 - 15ml/l Resolution: 0.01 ml/l Time Response: 10 seconds</p>
	<p>Data Recording & Control Computer: Processor: 486 Storage: 2GB disks; 650 MB optical disk Memory: 6MB RAM</p>

LASER LINE SCAN FLUORESCENCE AND MULTI-SPECTRAL IMAGING OF CORAL REEF ENVIRONMENTS

Strand, M.P., NSWC Coastal Systems Station, Panama City, FL 32407; Coles, B.W., Raytheon Co., Tewksbury, MA 01876; Nevis, A.J., NSWC Coastal Systems Station, Panama City, FL 32407; Regan, R., Raytheon Co., Tewksbury, MA 01876

During the summer of 1996 a series of field trials were conducted in the Florida Keys and Bahama Islands to evaluate the ability of a unique laser line scan system to measure and map the fluorescent characteristics of coral reef environments. Typical fluorescence maps that were obtained are presented and compared with monochrome and RGB color images of the same reefs. The monochrome images were obtained with the laser line scan system simultaneously with the fluorescent maps. The RGB images, which were also obtained with the laser line scan system, were recorded in the same location on a subsequent trial.

The data used to create the images that are presented in this extended abstract were collected with a specially configured laser line scan system, a simplified optical schematic of which is presented in Figure 1. The fundamental difference between the sensor used on this program and the sensor used in more conventional laser line scan systems, such as the CSS/Raytheon EOID Sensor or the Raytheon LS-4096, is the fact that the sensor used in this program has four separate receivers. Each receiver consists of a rotating optical assembly, a controllable aperture assembly, a photo-multiplier tube (PMT), a preamplifier and signal conditioning electronics, and an analog-to-digital converter (ADC). As shown in Figure 1, all four of the rotating optical assemblies, plus the rotating mirror that is used to deflect the outgoing laser beam, are attached to a single drive shaft which assures their mechanical synchronization.

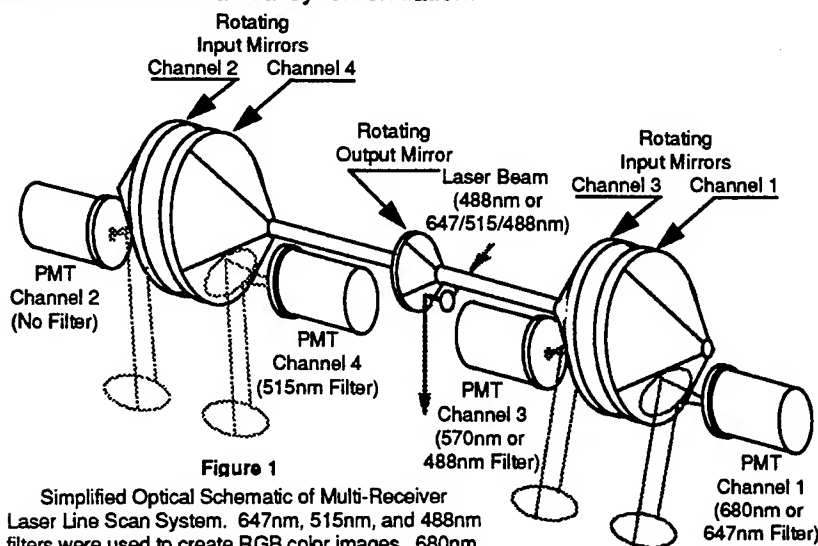


Figure 1

Simplified Optical Schematic of Multi-Receiver Laser Line Scan System. 647nm, 515nm, and 488nm filters were used to create RGB color images. 680nm, 515nm, and 570nm filters were used to investigate biological fluorescence phenomena.

Each of the receivers' rotating optical assemblies can be fitted with optical interference filters and other optical elements, such as polarization analyzers, which allow various aspects of the reflected light field to be evaluated. In a conventional laser line scan system, the receiver is used to measure the magnitude of the reflected light field and the receiver is therefore fitted with no filter or with a filter whose center wavelength matches the wavelength of the outgoing laser light. The use of an optical filter in this case helps reduce the undesirable energy due to ambient sunlight or auxiliary luminaires that may be mounted on the deployment platform.

During the CoBOP Program the multi-receiver laser line scan system was used to investigate biological fluorescence by using a short wavelength laser and fitting the receivers with optical filters whose center wavelengths correspond to known fluorescence wavelengths. An Argon Ion laser whose output was tuned to 488nm was used as the stimulating light source and three of the receivers were fitted with interference filters. A 680nm (20nm FWHM) filter was installed in channel #1, a 570nm (40nm FWHM) filter was installed in channel #3, a 515 nm (20nm FWHM) filter was installed in channel #4, and channel #2 was left open without any filter.

When the system is used to create color images the Argon Ion laser is replaced with an Argon/Krypton mixed gas laser which provides simultaneous outputs at 647nm (red), 515nm (green), and 488nm (blue). Matching filters, with 6nm FWHM bandwidths, are then added to three of the four receivers and the data required to produce RGB color images can be collected.



Figure 2a. Monochrome Image

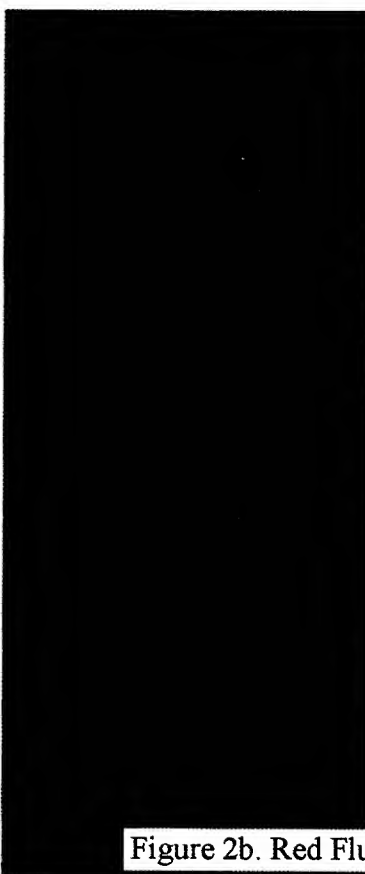


Figure 2b. Red Fluorescence

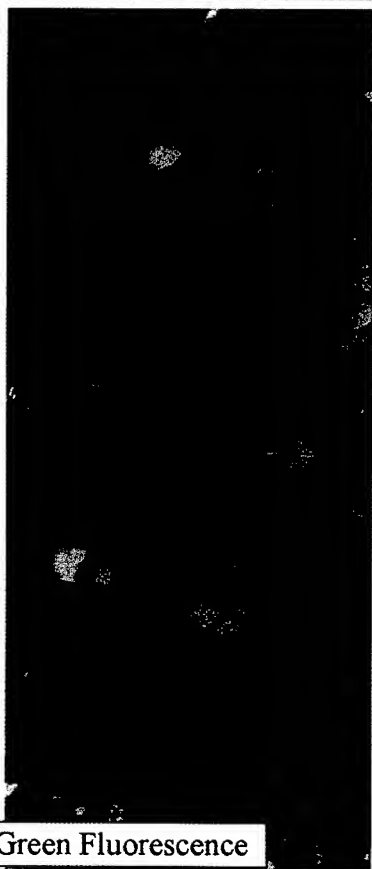


Figure 2c. Green Fluorescence

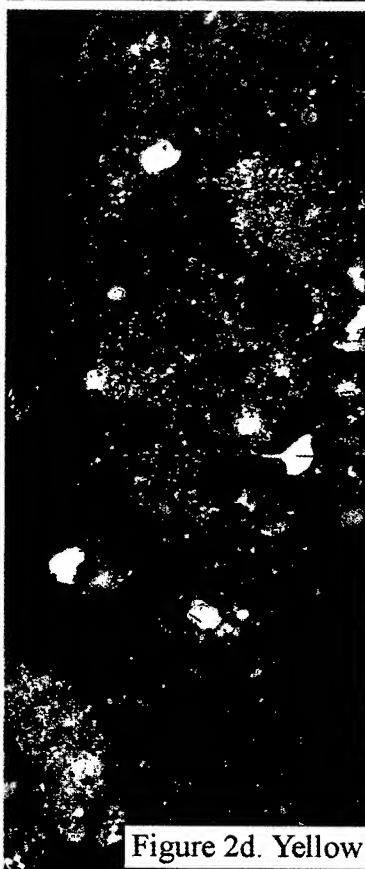


Figure 2d. Yellow Fluorescence

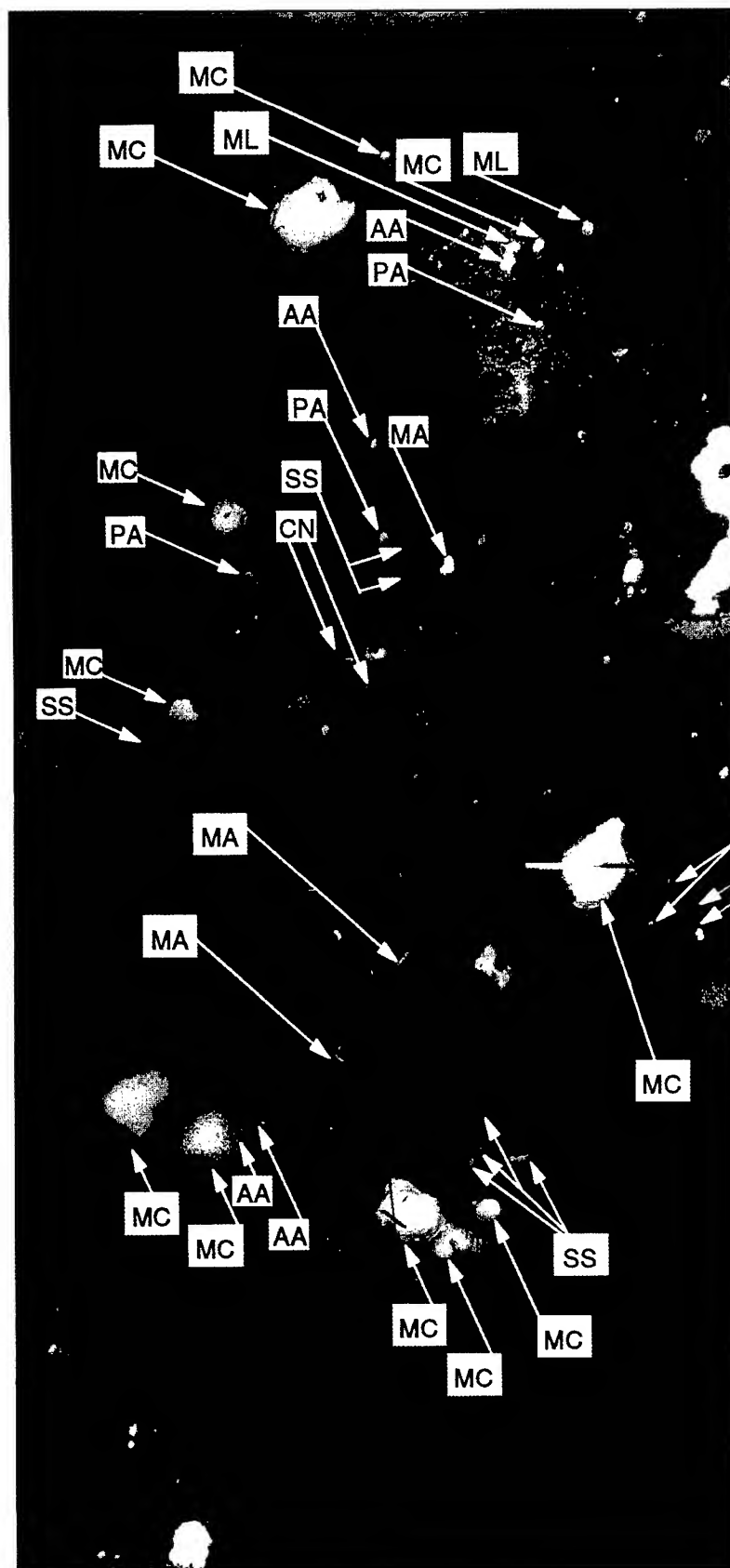


Figure 2e. Pseudocolor fluorescence image created by combining figures 2b, 2c, and 2d.

CN	Colpophyllia natans
ML	Mycetophyllia lamarckiana
MC	Montastrea cavernosa
MA	Montastrea annularis
MiA	Millipora alcicornis
Sc	Scolymia sp.
SS	Siderastrea siderea
LC	Leptoseris cucullata
AA	Agaricia agaricites
PA	Porites asteroides
MF	Mycetophyllia ferox

Figure 2. Fluorescence Imaging Laser Line Scan (FILLS) imagery of a coral reef near Logger Head Key in the Dry Tortugas, showing (a) monochrome image from the unfiltered channel, (b) red fluorescence image (680 nm filter, 20 nm FWHM), (c) green fluorescence image (515 nm filter, 20 nm FWHM), (d) yellow fluorescence image (570 nm, 40 nm FWHM), and (e) pseudocolor fluorescence image, with coral species identification. The species identification was by divers (Dr. Charles Mazel of MIT and Dr. Michael Lesser of UNH) guided by the FILLS pseudocolor image. The pseudocolor image was formed by mapping the red, green, and yellow fluorescence signals to red, green, and blue, respectively.

Figure 3a. Monochrome Image

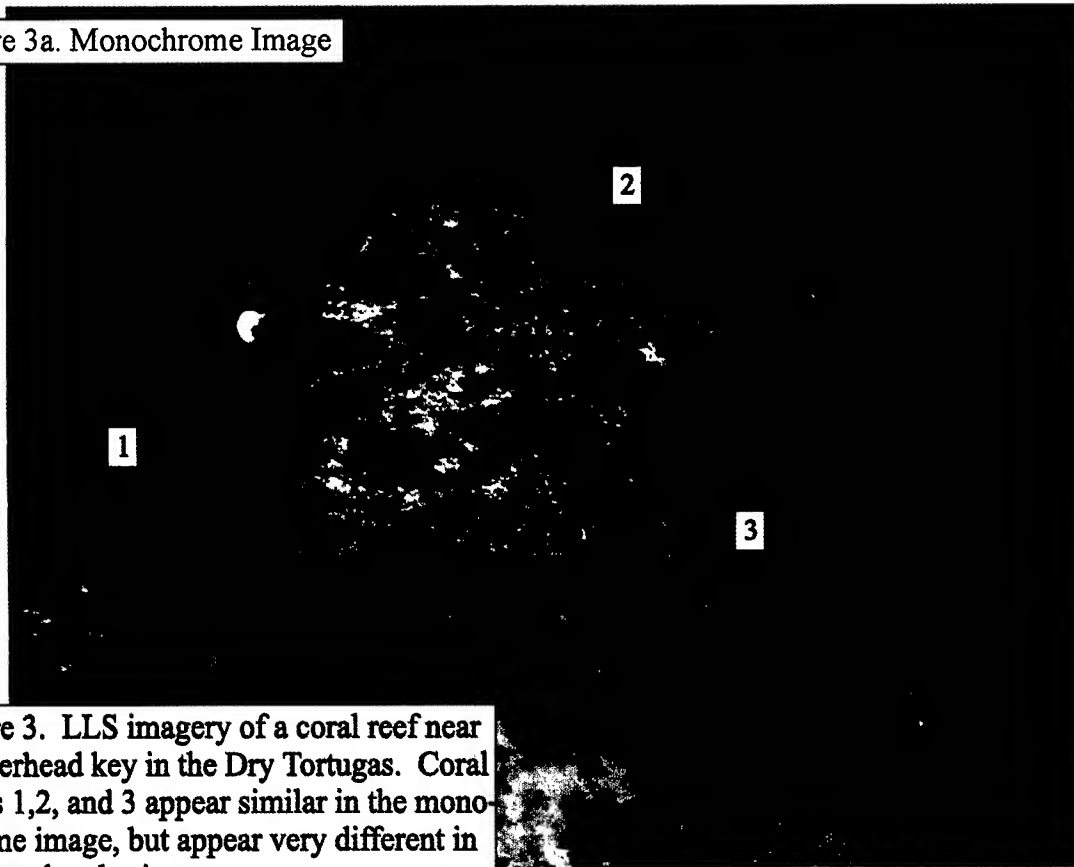


Figure 3. LLS imagery of a coral reef near Loggerhead key in the Dry Tortugas. Coral heads 1,2, and 3 appear similar in the monochrome image, but appear very different in the pseudocolor image.

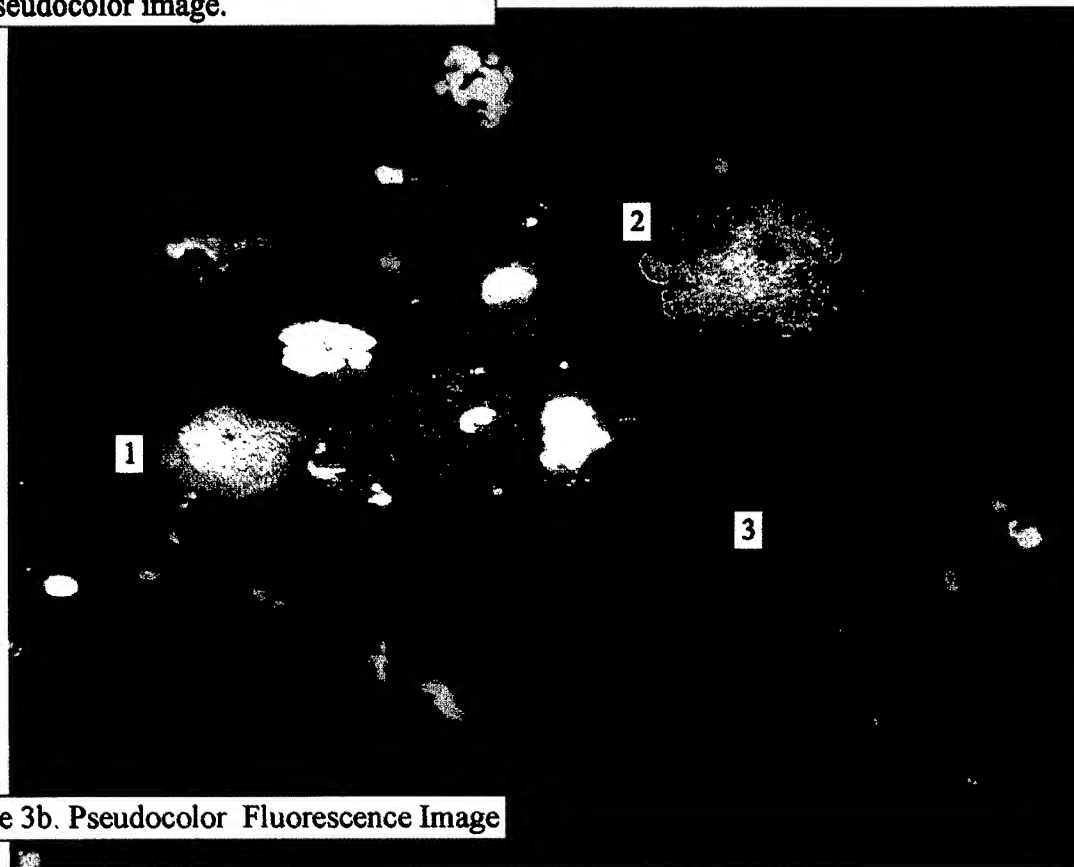


Figure 3b. Pseudocolor Fluorescence Image

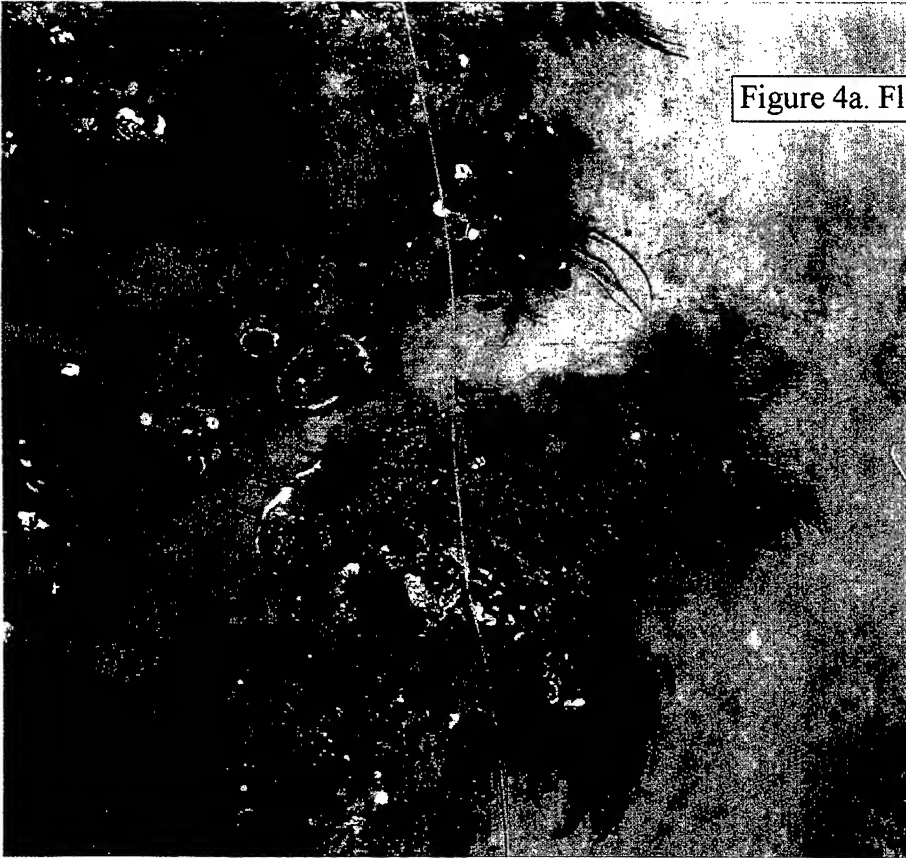


Figure 4a. Fluorescence Image

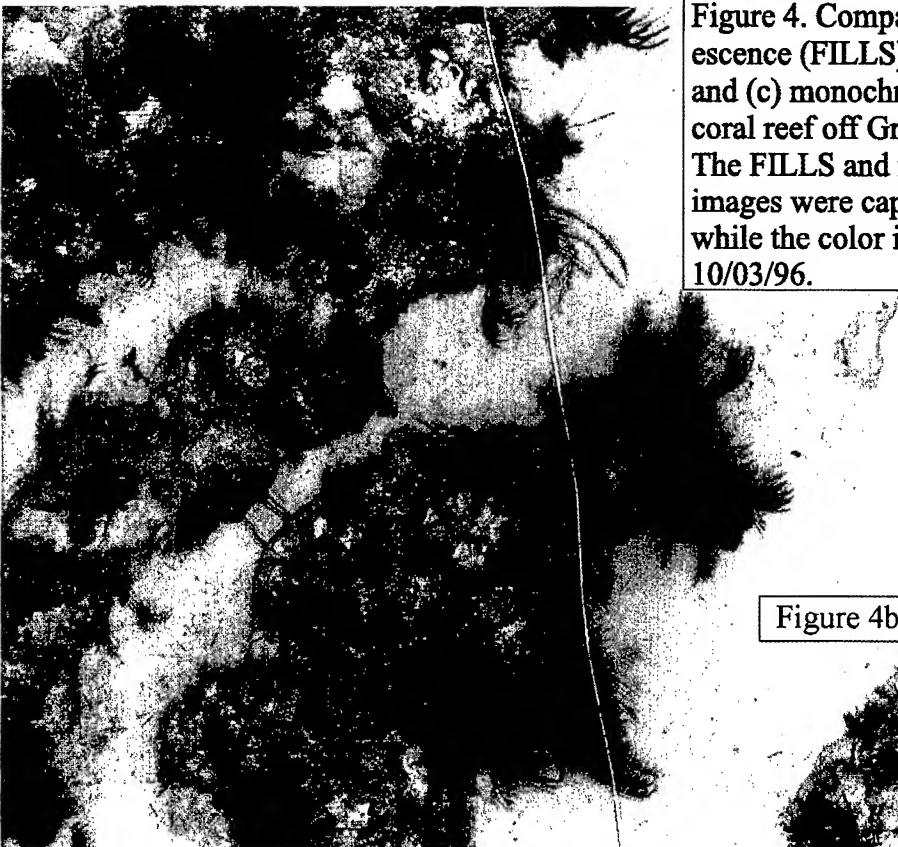


Figure 4b. RGB Color Image

Figure 4. Comparison of (a) fluorescence (FILLS), (b) RGB Color, and (c) monochrome images of coral reef off Grand Bahama Island. The FILLS and monochrome images were captured 06/27/96 while the color image was captured 10/03/96.

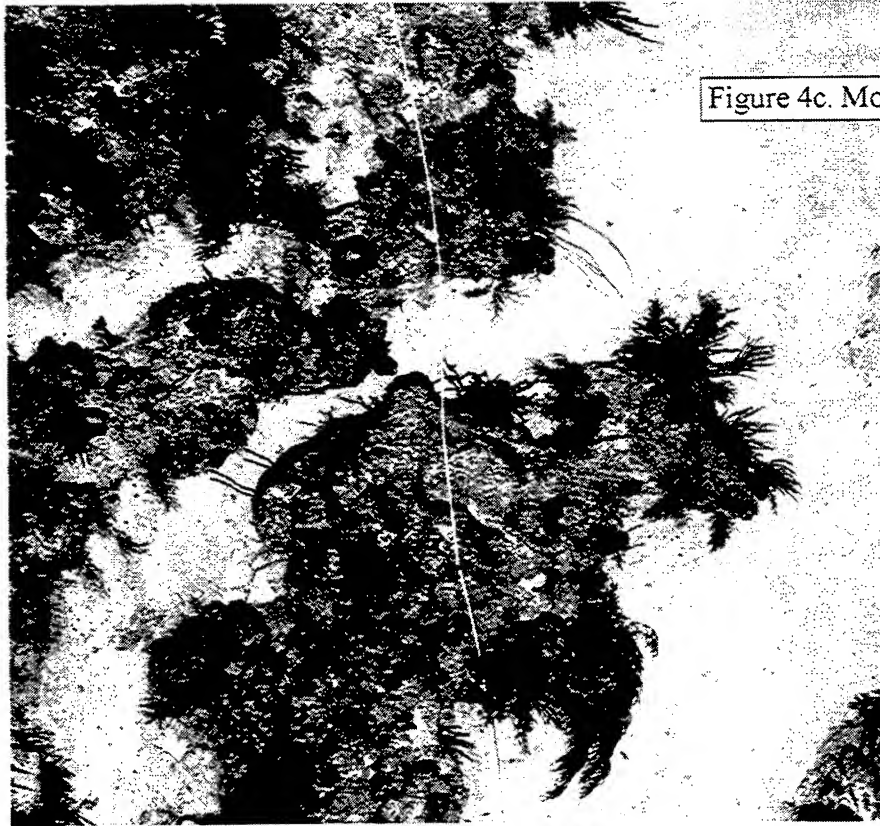


Figure 4c. Monochrome Image

Previous programs, the results of which have been reported and discussed in other forums, have demonstrated the capability of laser line scan systems to produce images of submerged objects with greater resolution and dynamic range, and at longer physical ranges than is possible with competing techniques. These standard laser line scan systems produce visual representations of the desired target by measuring the magnitude of the monochromatic light reflected from various closely spaced points on the target.

But elastic, or linear, reflectance is only one aspect of the light field produced by the interaction of the incident laser light and the submerged target. The images presented in this abstract demonstrate that the quantity and quality of target related information produced by a laser line scan system can be increased dramatically by evaluating other linear and non-linear, or elastic and inelastic, characteristics of the light field. Colorful RGB images, for example, can be produced by illuminating the object with a multi-colored laser and simultaneously monitoring the magnitude of the reflected light at three coordinated wavelengths. The color images produced in this manner have been shown to be very realistic and could be produced at a range that was 8-10 times greater than the range at which a three chip color CCD television camera was able to produce useful color information.

These images also demonstrate conclusively that inelastic, or trans-spectral, phenomena such as fluorescence can also be used to great benefit. Fluorescence maps can be produced that describe, on a point-by-point basis, the fluorescent characteristics of large and small individuals within a relatively large, panoramic field of view. While the importance and application of these fluorescence maps is just beginning to be explored, the intimate connection of fluorescence with key biological processes makes the potential utility of FILLS imagery appear to be particularly tantalizing. Possible applications of these new image forms include wide area evaluation and assessment of specie diversity and distribution, the study of inter-relationships between species and individuals, evaluation and mapping of the health and biological vigor of coral reef communities, and the possible localization and identification of pollutants and other negative stress factors.

The authors would like to thank all who provided financial, material, moral, intellectual, and physical support for these field trials, including the Office of Naval Research, the Coastal Benthic Optical Properties (CoBOP) participants, Harbor Branch Oceanographic Institution, Raytheon Electronic Systems, NSW Coastal Systems Station, and others.

Long Time-Series of Turbid Coastal Water using AVHRR: an Example from Florida Bay, USA

R. P. Stumpf and M. L. Frayer
U.S. Geological Survey
Center for Coastal Geology
600 Fourth Street South
St. Petersburg, Florida 33701 USA

ABSTRACT

The AVHRR can provide information on the reflectance of turbid case II water, permitting examination of large estuaries and plumes from major rivers. The AVHRR has been onboard several NOAA satellites, with afternoon overpasses since 1981, offering a long time-series to examine changes in coastal water. We are using AVHRR data starting in December 1989 (with plans to extend the record backward), to examine water clarity in Florida Bay, which has undergone a decline since the late 1980's. The processing involves obtaining a nominal reflectance for red light (AVHRR channel 1 at 580-680 nm) with standard corrections including those for Rayleigh and aerosol path radiances. Established relationships between reflectance and the water properties being measured in the Bay provide estimates of diffuse attenuation and light limitation for phytoplankton and seagrass productivity studies. Processing also includes monthly averages of reflectance and attenuation. The AVHRR data set describes spatial and temporal patterns, including resuspension of bottom sediments in the winter, and changes in water clarity. The AVHRR also indicates that Florida Bay has much higher reflectivity relative to attenuation than other southeastern US estuaries.

Keywords: AVHRR, attenuation, turbidity, time series, case II water, Florida Bay

1. INTRODUCTION

The Advanced Very High Resolution Radiometer (AVHRR) on the NOAA polar-orbiting meteorological satellites has provided almost daily imagery at a 1 km pixel size for over 15 years. In oceanography, the sensor has had primary importance for looking at sea surface temperature. While the visible bands on the instrument were designed for cloud and land studies, they have shown utility in documenting bright features in the ocean. Examples include coccolithophore blooms¹, cyanobacteria blooms², and sediment-laden river plumes and estuaries.³⁻⁵

Coastal estuaries are under extreme stress due to changes in runoff and nutrient loads that result from increasing population and changing landuse. Florida Bay, at the southern tip of Florida, USA (Figure 1), has seen dramatic environmental changes in the last decade; these changes follow years of water management of the Everglades, the dominant source of fresh water for the Bay. A major dieoff of seagrass started in the late 1980's, which was closely followed by a decline in water clarity because of increased sediment resuspension (of sediments formerly stabilized by seagrasses) and from algal blooms⁶⁻⁸. Turbid water reduces light levels, causing stress on seagrasses, which may result in a self-reinforcing cycle where additional dieoffs occur resulting in further resuspension. Documentation of change over the last several years, and conditions prior to new management of water flow through the Everglades, will help significantly in documenting future change.

With the launch of new ocean color instruments, such as OCTS (ocean color temperature sensor) and SeaWiFS (sea wide field-of-view sensor), the coastal oceanographic community will have powerful tools for documenting water quality in the future. However, many management and scientific studies require information on existing and past conditions as well as on the variability of the system. The AVHRR provides a tool for documenting turbid conditions over a long record with morning passes since 1979 and afternoon passes starting in 1981. The AVHRR also provides information on case II waters, where the coastal zone color scanner (CZCS) was least

effective. However, overlap between early AVHRR and late CZCS imagery (through 1986) may provide some comparative analyses in less turbid case II waters.

This paper shows example information on water clarity collected by the AVHRR for Florida Bay over a seven-year time period. Relationships between the satellite reflectance and variables measured by field programs, in particular the diffuse attenuation coefficient, provide a means of expanding measurement programs by providing additional spatial and temporal resolution and by permitting extrapolation of current field efforts backwards in time.

2. PROCESSING

2.1 Satellite Imagery

The AVHRR collects data in two reflected-light bands, channel 1 in the red at 580-680 nm and channel 2 in the near-infrared at 720-1000 nm. Thermal bands provide data used to extract sea surface temperature. Because the instrument was designed for observation of land and clouds it is relatively insensitive; 1 count corresponds to a radiance of $0.5 \text{ W m}^{-2} \text{ sr}^{-1} \text{ um}^{-1}$ in channel 1 and $0.3 \text{ W m}^{-2} \text{ sr}^{-1} \text{ um}^{-1}$ in channel 2. In the red band, this is about an order of magnitude less sensitive than CZCS. As a result, the AVHRR is a "brown water" instrument-- effective for water color only in case II waters.

The data set used here extends from December 1989 to the present. Sources include the NOAA National Climatic Data Center, the Louisiana State University Earth Scan Lab, and the University of South Florida/Florida Department of Environmental Protection Joint-Use Facility. Over 600 mostly cloud-free scenes are used from some 1500 scenes processed. At the present, the analysis uses only the afternoon satellites, NOAA-11 from 1989 to 1994 and NOAA-14 starting in January 1995. NOAA-12 provided morning passes during this time, but these were not used because of present uncertainties in sensor calibration.

While each AVHRR sensor is calibrated before launch, the lack of onboard calibration for reflected light raises concerns for post-launch calibration and sensor deterioration. Post-launch calibration has been examined through determination of the absolute calibration at a particular time against aircraft⁹ and through determination of relative calibration using fixed desert targets that would have minimal change.^{10,11} The calibration uses the equation:

$$L_s(\lambda) = G(\lambda)(N(\lambda) - N_0(\lambda)) \quad (1)$$

where L_s is the radiance at the satellite, λ is the spectral band, N is the count value, N_0 is the offset (count value for zero radiance), and G is the calibration slope. We have used N_0 of 40 for both channels of NOAA-11, and 41 for both channels of NOAA-14. The values of G used here in units of $\text{W m}^{-2} \text{ sr}^{-1} \text{ um}^{-1}$ are 0.5496 and 0.3364 for NOAA-11 bands 1 and 2, respectively, and 0.5778 and 0.4007 for NOAA-14 bands 1 and 2. NOAA-11 was a nearly stable sensor after launch, while NOAA-14 has shown deterioration. NOAA-14 degradation is not yet incorporated into our processing (this will require reprocessing of data with a degradation term in G). A gradual deterioration results in the "true" December 1996 values being 1.077 times those reported here¹¹.

The reflectance of the water R_w (which includes the bottom where the water is optically shallow) is

$$R_w = \frac{\pi L_w(\lambda)}{E_d(\lambda)} \quad (2)$$

where L_w is the water-leaving radiance, E_d is the downwelling irradiance entering the water, and λ is the spectral band. L_w and R_w refer to values above the water surface. R_w is approximated by R_d , which is the Rayleigh and aerosol corrected channel 1 reflectance:

$$R_d = R_c(\lambda_1) - Y R_c(\lambda_2) \quad (3)$$

with subscripts 1 and 2 denoting channels 1 and 2 and:

$$R_c(\lambda) = \frac{\pi L_s(\lambda)/E_o(\lambda) - \pi L_r(\lambda)/E_o(\lambda)}{(1/r^2)T_o(\lambda)T_l(\lambda)\cos\theta_o} \quad (4)$$

where L_s is the radiance measured at the satellite, L_r is the Rayleigh radiance, E_o is the solar constant, and r is the normalized earth-sun distance, θ_o is the solar zenith angle, and T_o and T_l are the transmission coefficients for sun-to-earth and earth-to-satellite respectively. This model follows the one used for CZCS¹² and is described in more detail in Stumpf¹³.

Most of Florida Bay is shallow with depths of < 2 m. Because of the shallow and highly variable bathymetry that has not been resurveyed in over 100 years, corrections for bottom reflectance have been problematic and have not been implemented yet. This is a minimal problem in winter as the high sediment load tends to result in an optically deep water column. During the summer, contamination by bottom reflectance is a problem and reflectances tend to be brighter than is appropriate.

2.2 Field Methods

Field ecologists in the area document light attenuation using scalar radiometers measuring photosynthetically active radiation (PAR). For comparisons, we have taken profiles of scalar irradiance (E_o) at 0.25 m increments from 0.25 m depth to the bottom (typically 2 m). The diffuse attenuation (K) is determined from regression $\ln(E_o)$ against depth. Stations also include Secchi disk depth, which in the winter is often shallower than the bottom, to tie in with a comprehensive volunteer monitoring program as well as early measurements. Reflectance values to match K are determined by finding the median of the 3x3 block of pixels around the sampling station within 4 hours of overpass. The range of reflectances in the 3x3 block provides a crude approximation of the spatial variance. The range of K values is modest, so linear regression is best for the relationship between R_d and K (Figure 2), rather than the semi-analytic logistic equation $R_d \sim F/(1+G/K)^{14}$.

3.0 RESULTS

Reflectance and K show a strong relationship in Florida Bay. The positive relationship corresponds to a system that is dominated by scattering. The amount of reflectance in Florida Bay is far greater for a given attenuation than that determined for MobileBay¹⁴, which is more typical of southeast river-dominated estuaries. This suggests minimal absorption in Florida Bay by either dissolved pigments (CDOM) or by particulate-based pigments such as iron. Florida Bay also has carbonate sediments rather than the siliceous sediments found throughout the eastern US.

The type of patterns in the Bay can be represented by several sites (Figure 3). Twin Key basin and Butternut Key represent endpoints of water clarity in the Bay. Butternut Key, in the northeastern Bay, is in a region that has sparse seagrass and fine sediment. During the winter, high winds associated with the passage of cold fronts result in extensive resuspension. (For reference, these reflectances are typically higher than those observed in the Mississippi River plume.) Twin Key is a sheltered basin in the central bay with dense seagrass beds and more rocky material. This area has shown only a slight indication of higher reflectance in 1995-1996. In the early 1990's, Rankin Lake more closely resembled Twin Key in the presence of seagrass. With dieoffs, the water showed a significant increase in brightness and a deterioration in water clarity recognized and documented by the entire Florida Bay community.

Several research and monitoring programs have been operational in the Bay for a number of years. Everglades National Park and Florida International University have operated a monthly monitoring program of the Bay since about 1991, and the Florida Department of Environmental Protection and The Nature Conservancy began an additional comprehensive program in 1994. Measurement systems have varied considerably, making integration of the different data sets problematic. While the local community describes the Bay as having exceptionally clear water before the seagrass dieoffs, only limited data sets are available for documentation. The AVHRR can

provide a standard record over the last decade and permit extrapolation of existing data on water clarity into the past in order to describe the entire bay prior to the seagrass dieoffs. This effort at expanding the AVHRR time series will be conducted jointly with the NOAA Coastal Services Center (J. Brock and K. Waters). Ultimately, intercomparison of AVHRR with OCTS and SeaWiFS will permit a continuous record of water clarity from the past well into the future.

REFERENCES

1. Ackleson, S.G. W.M. Balch, and P.M. Holligan, "AVHRR observations of a Gulf of Maine coccolithophore bloom", *Photogram. Engr. & Remote Sensing*, **55**, pp. 473-474, 1989.
2. Kahru, M., and O. Rud, "Monitoring the decadal-scale variability of cyanobacteria blooms in the Baltic Sea by satellites", *Proc. Third Conference on Remote Sensing for Marine and Coastal Environments*, Vol. II, pp. 76-83, 1995.
3. Stumpf, R.P. and J.R. Pennock, "Calibration of a general optical equation for remote sensing of suspended sediments in a moderately turbid estuary", *Jour. Geophys. Res. - Oceans*, **94**, pp. 14363-14371, 1989.
4. Walker, N.D., G.S. Fargion, L.J. Rouse, and D.C. Biggs, "The great flood of summer 1993: Mississippi River discharge studied", *Eos, Trans., American Geophys. Union*, **75**, pp. 409,414-415, 1994.
5. Stumpf, R.P., G. Gelfenbaum, and J.R. Pennock, "Wind and tidal forcing of a buoyant plume, Mobile Bay, Alabama", *Continental Shelf Research*, **13**, pp. 1281-1301, 1993.
6. Robblee, M.B., T.B. Barber, P.R. Carlson, Jr., M.J. Durako, J.W. Fourqurean, L.M. Muehlstein, D. Porter, L.A. Yarbro, R.T. Zieman, and J.C. Zieman, "Mass mortality of the tropical seagrass *Thalassia testudinum* in Florida Bay (USA)" *Marine Ecology Progress Series*, **71**, pp. 297-299., 1991.
7. Phlipps, E.J., T.C. Lynch, and S. Badylak, "Chlorophyll *a*, tripton, color, and light availability in a shallow tropical inner-shelf lagoon, Florida Bay, USA", *Marine Ecology Progress Series*, **38**, 1995.
8. Fourqurean, J.W., R.D. Jones, and J.C. Zieman, "Processes influencing water column nutrient characteristics and phosphorus limitation of phytoplankton biomass in Florida Bay, FL, USA: inferences from spatial distributions", *Estuarine, Coastal and Shelf Science*, **36**, pp. 295-314, 1993.
9. Abel, P, and B. Guenther, "Calibration results for NOAA-11 AVHRR Channels 1 and 2 from congruent path aircraft observations", *Jour. Atmospheric and Oceanic Tech.*, **10**, pp. 493-508, 1993.
10. Rao, C.R.N. and J. Chen, "Inter-satellite calibration linkages for the visible and near-infrared channels of the Advanced Very High Resolution Radiometer on the NOAA-7, -9, and -11 spacecraft", *Intl. J. Remote Sensing.*, **16**, pp. 1931-1942, 1995.
11. Rao, C.R.N. and J. Chen, "Post-launch calibration of the visible and near-infrared channels of the Advanced Very High Resolution Radiometer on the NOAA-14 spacecraft", *Intl. J. Remote Sensing.*, **17**, pp. 2743-2747, 1996.
12. Gordon, H.R., D.K. Clark, J.W. Brown, O.B. Brown, R.H. Evans, and W.W. Broenkow, "Phytoplankton pigment concentrations in the Middle Atlantic Bight: comparison of ship determinations and CZCS estimates", *Applied Optics*, **22**, pp. 20-36, 1983.
13. Stumpf, R.P., "Remote sensing of water quality in coastal waters", *Proc. Remote Sensing of Marine and Coastal Environments, SPIE 1930*, pp. 293-305, 1992.
14. Stumpf, R.P., and J.R. Pennock, "Remote estimation of the diffuse attenuation coefficient in a moderately turbid estuary", *Remote Sensing of Environment*, **38**, pp. 183-191, 1991.
15. Stumpf, R.P., "Retrospective and future studies of coastal water clarity and sediment loads" *Proc. Third Conference on Remote Sensing for Marine and Coastal Environments*, Vol. 1, pp. 128-139, 1995.

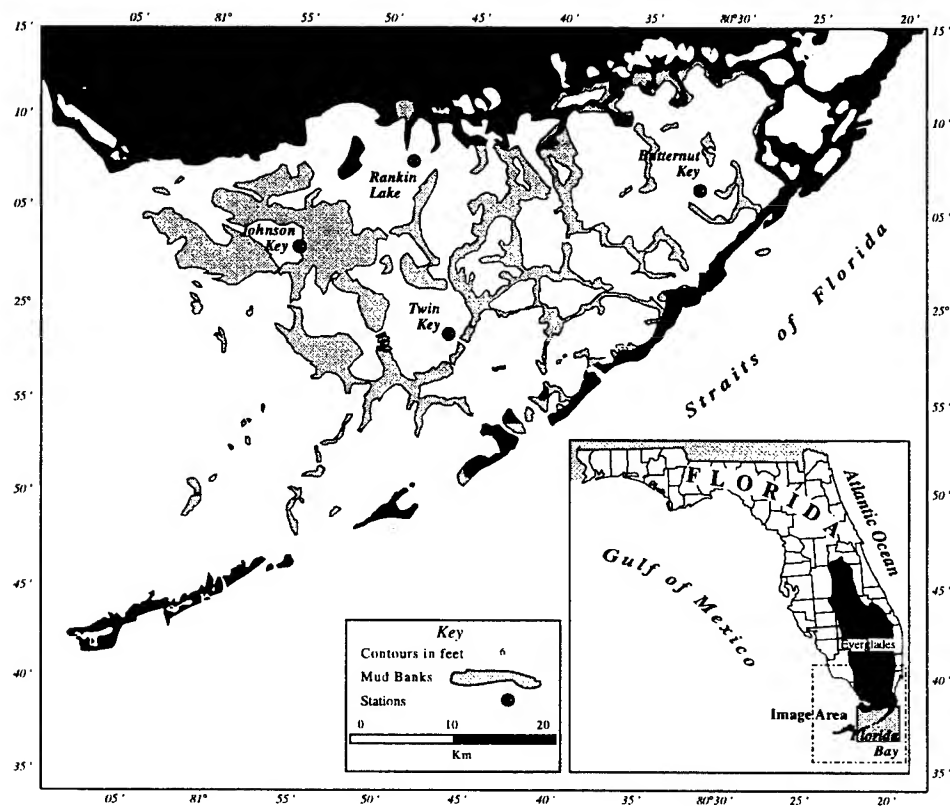


Figure 1. Location of Florida Bay with sample stations marked.

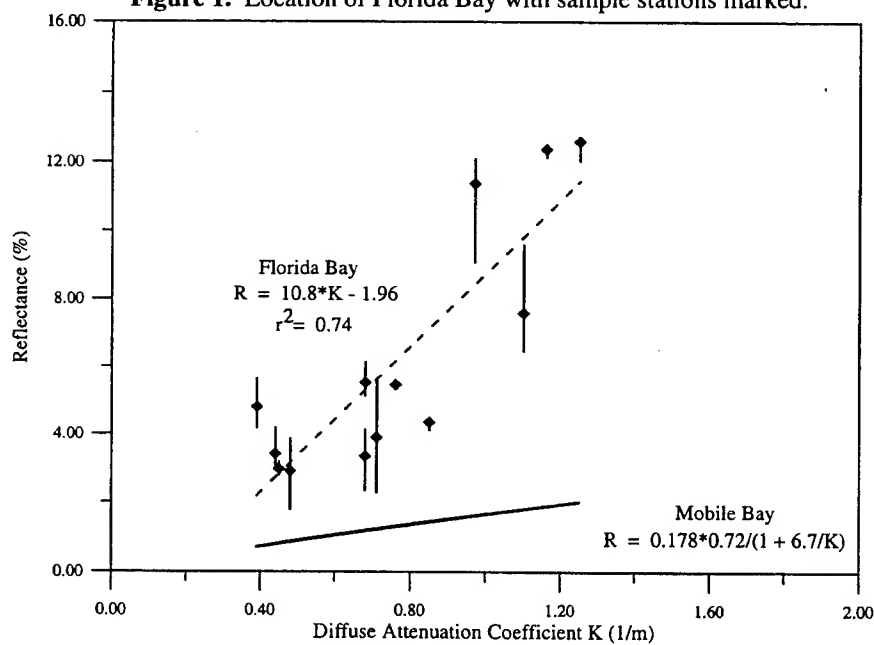


Figure 2. Data and Relationship between AVHRR reflectance and diffuse attenuation (K) for PAR in Florida Bay. The relationship for Mobile Bay is shown for reference.

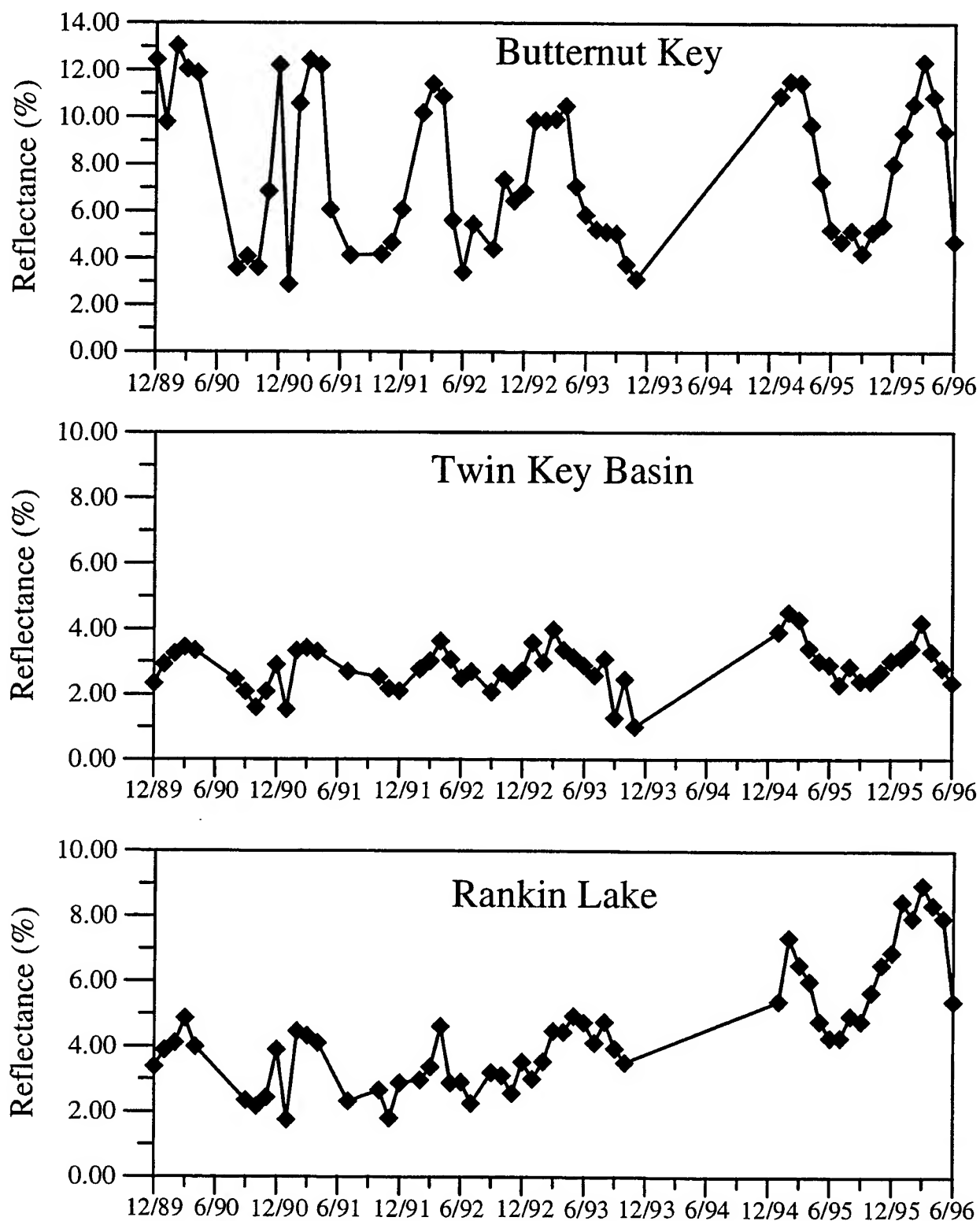


Figure 3. Monthly means of reflectance for Butternut Key, Twin Key, and Rankin Lake stations (Figure 1). In a typical month about 5-8 images were available. During 1994, afternoon satellites were not operational. The low reflectance in January 1991 may result from anomalously low winds during that month.

The valuation of perspective application of LIDAR methods for sea monitoring.

Igor V. Aleshin*, Vadim K. Goncharov**, Vladimir G. Lyskov*, Eugene A. Tsvetkov.*

*S.I. Vavilov State Optical Institute, 3 Pochtamskaya st., St. Petersburg, 190000, Russia.

**Krylov Shipbuilding Research Institute, 44 Moskovskoe shosse, St. Petersburg, 196158, Russia

ABSTRACT.

The materials of settlement valuations and experimental data about structures oil product's discharging and depth its finding can be used for valuation of opportunity and conditions of application of air laser methods to detection and classification of oil pollution at operations of deposits of oil in shelf zone. The theoretical estimations of opportunity realization of air LIDAR systems in view of oil distribution features in sea are adduced. It's shown, that in processes of decomposition its space structure changes, and the floating drops can be formed the optical contrast layers in waters near to the "sea - atmosphere" interface. The estimations of optical systems permits to generalize about reality of development two-frequent LIDAR system, containing two channels, one of which measures the fluorescence of organic substances located in thicker water, and second - combinational scattering of light by molecules of water.

KEY WORDS: lidar methods, oil pollution, index of color, sea monitoring.

1. FLUORIMETRY OF OIL OR OIL PRODUCTS IN SEA.

It is well-known, that the most the effective method of crude oil or oil production (OP) detection from underwater source is the fluorescent method. Optical properties of emulsion and solution, contained oil products in sea water, depends not only on concentration or composition, but also on temperature of water, sea and weater conditions, flows and others. Some researches stress the additional dependance upon time of spill existance, structure and particle size, which are dispersion system^{1,2,3}. The problem of underwater spills detection in sea by means of airborne lidar system incomparable complicated. The principle disturbance of to detection OP spills in sea are dissolved organic matter (DOM), which optical properties are coincide.

It is very difficult problem of the optical distant control of the crude oil (or oil products) discharges from the underwater oil pipelines or wells in the oil mining regions on depth 50 - 100 m and it is impossible to solve it at present. Nevertheless it is possible to offer the means of this problem solving. In this study on base of the theoretical and experimental investigations² it was showed that after discharge the OP "cloud" came to the surface and divided into separate clusters in accordance with oil drops sizes. These OP drops clusters are being transfered by sea currents and dispersed by turbulent movements. Under certain conditions the OP drops clusters are able to emerge near by sea surface and its concentration are able to be sufficiently large and its are able to form the surface slicks which are accessible for discovery by various optical instruments. As it was showed in¹⁰ the maximum of OP drop sizes distribution corresponded to the drops with 0.4...0.5 mm diameter.

The condition of slick with minimum sizes formation on the sea surface as result of impulsive discharge is formed by formula²:

$$Q \geq 2\pi \cdot \epsilon \cdot \gamma \cdot \delta_1 \cdot K_z^{0.5} \cdot h^{1.5} \cdot w^{0.5},$$

where: Q - volume of OP discharge.

h - depth of OP discharge.

w - velocity of OP drop emerging, which is depended upon its sizes.

K_z - turbulent diffusivity coefficient in vertical direction.

γ - specific weight of sea water.

ε - horizontal and vertical turbulent diffusivity coefficients ratio.

δ₁ - minimum OP slick thickness which defines its arise conditions.

This formula shows the OP drops sizes increase accompanied by its emerging. Velocities increase makes easier the slick formation. Namely for the slick with minimum sizes arise it is necessary the lesser OP discharge volume. It is necessary to take into consideration, that another important circumstance is the slick existence time. Because of the air and water temperature the intensity of the crude oil light fractions evaporation and heavy fractions oxidation decreases. That is way the natural self-liquidation processes of OP slick are delayed to a marked degree and stopped in general.

The research of fluorescent characteristics dissolved organic matter and OP in marine water were conducted beside of authors and have allowed to determine the characteristic properties of fluorescent fields of these substances and attributes of them distinction. The reviews of these data are adduced in ^{1,5}. The fluorescence of these substances are stacked in spectral band $\Delta\lambda \approx 100$ nm. At use of such method the summary fluorometer signal is determined by sum of light flows $P_{\Sigma} = P_{\Sigma}^{(DOM)} + P_{\Sigma}^{(OP)}$. The problem consists of in division of these components, even if the requirements of quantitative determinations of concentration OP or DOM are not included. The main problems, which arise at determination by air lidar systems (irrespective of principles their work) OP in arctic seas, are common for such systems and found out processes such, as:

- Multifoldness of objects in real conditions and their status. On data of laboratory researches ⁶ the fluorescent bands of dissolved and emulsified OP are considerably distinguished.

- Form of solution OP fluorescence band poorly depends on as initial sample and is stable on time ⁶.

- For emulsified samples of OP the dependence of intensity and forms of fluorescence bands from state initial OP and its "age" is observed.

- Experimental research data about the behaviour of OP spills in sea conditions are absent.

- Influence some conditions, for example, of ice thickness and morphology on structure of OP spills, is not investigated.

The optical methods of fluorescent signals OP and DOM division are based on distinction of optical properties of these two kinds of substances, including various spectral bands of excitation and fluorescence. Obviously, that the most effective method of division of signals in such fields is multifrequently laser fluorimetry. The application of this method were suggested some authors, for example ¹. On our opinion, application as source laser on copper vapour is optimum, since it provides the wide set of generated lines (17 waves lengths) in interval UV and visible range: from 262 nm (average power 270 mW) to 510.6 and 578.2 nm (about 2000 mW) ⁷. Duration of impulse 10-15 ns, frequency 10 kHz. The application one of scanning method allows to adapt the system to sea condition observing.

The valuation of molecular spectroscopy fluorescent method sensitivity to concentration OP in laboratory conditions ⁸ gives the significances in interval 0.0001 ... 0.1 mg/l. However presence in marine environment DOM, distribution of which on depth non-uniformly, gives that the real sensitivity of method (on results of our experiments ²) is defined just by these effects and in conditions of our experiments (Black sea) and made 18...60 mg/l in nearsurface layers to depth 15 m and 0.3...0.5 mg/l on depth more 30...40 m.

The simplified kind of air lidar equation is possible to be presented in following form:

$$P_{\phi_{\Sigma}}^{(imp)} = P_0^{(imp)} S_{\phi_{\Sigma}} \frac{A}{(Hh+z)^2} \frac{c\Delta t}{2} F(\sigma_s z, \sigma_{\phi_{\Sigma}} z, \alpha\theta) \exp[-(\chi_s + \chi_{\phi_{\Sigma}}) \frac{c\Delta t}{2}] \int \tau_s^{(s)} \tau_{\phi_{\Sigma}}^{(s)} \tau_s^{(M)} \tau_{\phi_{\Sigma}}^{(M)} \quad (1)$$

where: $P_{\phi_{\Sigma}}^{(imp)}$ - power of accepted fluorescent pulsing signal,

$P_0^{(imp)}$ - power of exiting light,

z - depth of strobing layer,

A - area of receiver,

$S_{\phi_{\Sigma}}$ - fluorescent section, $S_{\phi_{\Sigma}} = s_{\phi_{\Sigma}} \cdot C \cdot V$, with $s_{\phi_{\Sigma}}$ - specific section, C - concentration and V - volume of fluorescent substance),

H - height of flight,

c - speed of light,

$F(\dots)$ - integrated function, dependent from "cloud" size and optical properties of environment, (is tabulated in ¹¹).

$a\theta$ - angular size of object (in our case $a\theta \rightarrow \infty$, $F \rightarrow 1$).

σ - scattering coefficient.

χ - absorption coefficient

τ - optical density of layers of marine water, atmosphere at distribution excitation or fluorescent light.

n - refractive index.

Δt - duration of light pulse.

To take into account real conditions the formula is simplified and in final kind, as is shown in ⁶, the lidar system is permitted not only to find out fluorescent layers by impurity, but also to evaluate the size of concentration. Really, at use of two-frequent lidar in consideration are introduced 4 signals, which are determined by fluorescence of organic substances and combinational scattering on two waves lengths is entered.

The substance of reliability problem is reduced to following phenomena. Except for discussed kind of basic handicaps, connected with nature of processes in nature, on character and level of signals can influence by handicaps, connected with other effects of natural processes. For example, the influence of cloudness, low transparency of all site, on which light stretched. In such situation it is possible the fluorescent object omission, large flight height and series other ones happens. The program for board computer complex, ensuring control of operating modes of instruments and choosing by operator optimum (from point of sight of maximum of reliability of results) flight regimes and work of instruments ⁹ is developed.

2. LASER SPECTROZONAL SYSTEM.

The principles of spectrozonal systems on passive principle are in detail considered in series of work, for example ^{12,13}. The "Index of Colour" as the characteristics of marine environments condition receives the recognition in physical oceanography. A long time "Index of colour", are carried out supervision for conditions of seas and lakes¹. In two-flow approximation theoretically this quantity presents the characteristics of pigment concentration in sea water ¹³. The application of active laser systems for ecological sea monitoring is of interest from point of sight of operative local analysis of situation (relatively the small dependence on weather conditions, accuracy of coordinat, operational receiving data, etc.). However, use of one-frequent laser as source of illumination limits the opportunities of monitoring only by fixing of phenomenon of change of optical properties of environment.

The multispectral illumination, which by certain image chooses the lengths of waves, permits to identify the kind of impurity - "painted" throwing off, area of distribution pigments of natural organic origin, or terrigenic substances. In majority of tasks the decision of this problem is determining process.

At use of two-frequent laser ¹⁴ with radiation waves λ_1 and λ_2 attitudes of capacities accepted radiation, normalized on capacity radiatin of each length of wave ¹¹, the index of colour equation take a view:

$$P_{\lambda_1} / P_{\lambda_2} \approx P_{0\lambda_1} / P_{0\lambda_2} \times \exp[2(\chi_{\lambda_2} - \chi_{\lambda_1})l].$$

To similar kind of dependence present the valuations on data ¹² in view of features of water radiance distribution. Given ¹¹ for valuation of errors, arising at using of this formula, it is possible to show, that in (1) the attitude

$$F(\sigma_{\lambda_1 Z}, a\theta) / F(\sigma_{\lambda_2 Z}, a\theta)$$

little depends on the length of wave l and is possible to be thought of constant value near to 1.

The consideration of features of work active spectrozonal system, in which as the source of illumination is applied the two-frequent laser, permits to generalize that such system provides the identification not only of "painted" areas, but hydromecanical disturbance of marine environment. Obviously, that the conclusion about properties of system with two-frequent illumination and its technical opportunities is possible to be made on results of its tests in marine conditions. The experimental installation was designed for placing on board of flying laboratory ².

Photometer on active principle:

- The source of radiation	The pulsed Cu-laser.
- Wave length of radiation	510.6 and 578.2 nm.
- The average capacity, accordingly, W.	3.2 and 1.8
- The radiation instability	3.. 4 %.
- Angle of beam	6 mrad.
- The pulsed frequency	7.. 10 kHz.
- The duration of pulses	20 ns.
- The receiver	Objective on Cassaigren scheme.
- The objective diameter (working)	200 mm.
- The angle of field of sight	2.5 °.

Optical axis of active system is tilted under angle of 7° ahead, on direction of flight, with the purpose of reduction of influence by radiation components, which reflected from sea surface. With this purpose the strobing of receiver were entered.

The optical systems and recording instruments were placed on board of flying laboratory and permitted to conduct the synchronous supervision of variability of signals in conditions of minimum influence from radiation, which are scattered by underlying layers of atmosphere. The chosen region of researches - coastal zone by extent about 15 miles - began on distance of 1 mile from coast-line and included the sites, where the significant gradients of optical properties were observed. The flight height of laboratory were 200 m, speed - 100 m/s. Whole flying by extent 25 km is broken on sections by extent of 4 km. Each readout is removed through 100 m of flight (1s). The first sections relates to aquatorium with relatively uniform properties. The next section is the frontal zone with sharp gradients of optical properties, and on subsequent sections the variability of signals determined heterogeneity of optical properties of environment, is marked.

At stable sea surface irradiant during the experiment the variability of signals is determined by random character of distribution of optical characteristics of environment. Therefore at analysis of data the statistical methods of signals processing were applied. Each sample of signals during post-processing is considered as the quasistationary realization of random process. The trend of signals is remote. Then improved records were used for account of cross-correlation functions (CCF) of signals and their direct comparison. Form CCF of signals of active system in this experience testifies about insignificant degree of correlation. The results of account CCF of signals, relating to various flying sections are adduced on drawings 1 - 3. On first section the characteristic scale heterogeneity, significance CCF in maximum more than 0.85 - 0.9. On next sections it is possible to note the characteristic phenomenon - more "high-frequency" character of process, less on scale and less the significance CCF in maximum. In series of cases may be seen absence of expressed maximum, that is characteristic of uncorrelated processes. The opportunities of optical methods can be extended not only at the expense of round-the-clock application optical monitoring, but also opportunities of identification of impurity or kind of processes, description of their space-temporary variability.

Obviously, that the adduced results of our supervision can not apply for on completeness, their purposes was the desire to draw attention on expansion of remote monitoring's marine environment by optical methods.

3. ACKNOWLEDGEMENTS

Special thanks to ONREUR Visiting Scientists Program for assistance and support in participation in the Conference.

4. REFERENCES.

1. "Дистанционные методы исследования океана". Сб. статей. Издательство ИПФ АН СССР, г. Горький, 1987г.
2. В.К. Гончаров, В.Г. Лысков. Исследование особенностей распространения нефти в морской среде и условий ее всплытия на поверхность. Океанология, т. 33, № 6, 1993 г., с. 856- 862.

3. Океанографическая энциклопедия. "Гидрометеиздат", Л., 1974 г.
4. Б.Я. Гайцхоки. Тело распределения яркости в море подо льдом. Сб. "Оптика моря и атмосферы", СО АН СССР, г. Красноярск, 1990 г.
5. Г.С. Карабашев. Флуоресценция в океане. "Гидрометеиздат", Л., 1987 г.
6. Аброскин А.Г., Нольде С.Е., Фадеев В.В. и др. Определение концентрации эмульгированно-растворенных в воде нефтей методом лазерной флуориметрии. ДАН СССР, 1987 г.
7. И.Л. Ловчий. "Управление характеристиками излучения лазеров на парах меди". Автореферат диссертации на соискание ученой степени к.ф.-м. наук. ГОИ, 1995 г.
8. "Спектроскопические методы определения следов элементов". Сб. под ред. Дж. Вайнфорднера. "Мир", М., 1979 г.
9. В.И. Фейгелс. Автореферат диссертации на соискание ученой степени кандидата технических наук. ЛИТМО, 1989 г.
10. Goncharov V.K., Lyskov V.G. Investigation of the oil spreading in the deep sea and search for method of discover the oil pollution under sea surface. Proceeding of SPIE. Ocean Optics XII, 1994, vol.2258, pp.797-803.
11. Долин Л.С., И.М. Левин. Справочник по теории подводного видения. ("The references book on theory underwater vision.") Л. Гидрометеиздат, 1991, 229 с.
12. Remote sensing in meteorology, oceanography and hydrology. Ed. A.P.Cracknel. ELLIS HORWOOD LIMITED, New York, 1981.
13. И.В. Алешин, В.Г.Лысков, В.Н.Писарев, Е.А.Цветков. Фотометрия оптических полей поверхностных слоев моря. (Photometry of optical fields of surface layers of sea.) " The Optical Journal " (Russia), 1993, №12.
14. John F. Potter. Two-frequency lidar inversion technique. Appl.Opt. V26, ы7,1987, p1250-1256.

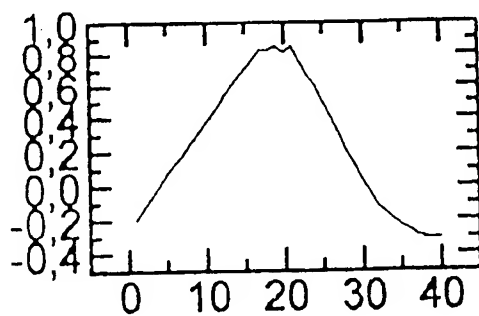


Figure 1.

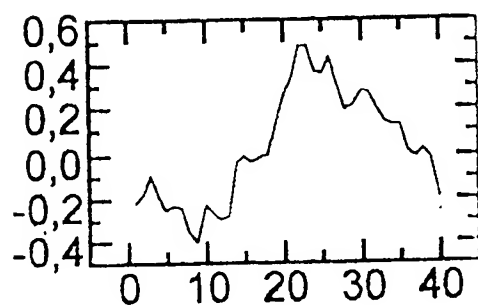


Figure 2

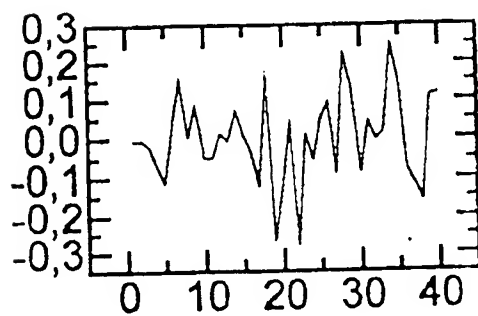


Figure 3

The generation of high resolution ocean colour information from 5 particular bands
(a case 2 water approach)

Marcel R. Wernand, Susan J. Shimwell*, Jan C. de Munck

Department of Physical Oceanography, Netherlands Institute for Sea Research (NIOZ), PO Box 59, 1790AB Den Burg,
Texel, The Netherlands

* Department of Oceanography, University of Southampton, Southampton Oceanography Centre, Waterfront Campus,
European Way, Southampton, SO14 3HZ, England, UK

ABSTRACT

Ground truth measurements are necessary for the validation of remotely sensed data. Rapid ship or aircraft spectral measurements of the upwelling and downwelling (ir)radiance are needed to determine the reflectance of the water column as well as to intercalibrate with satellite sensors. Inter calibrations are hindered by the application of different instruments with varying spectral bands.

It has been found that high resolution ocean colour data (case2) do not contain more information on water quality than data from a limited amount of spectral bands. However the positioning of these spectral bands over the visible spectrum should be correctly chosen. The present work uses a reconstruction technique which would enable simple optical instruments with 5 specific bands to be used to determine water quality parameters and to validate satellite data even if the sensors differ in central wavelengths. It is shown that when an optical data bank (ODB) of high resolution spectra (400-720 nm) of a specific sea area is available it is possible to reconstruct complete reflectance spectra, accurate to within 1 %, out of the reflectance measured in 5 bands. Such an ODB could contain subsurface or airborne reflectance (or normalised radiance) data. The reconstruction technique used is based upon a multiple regression analysis (MRA) of the ODB. To validate this full reflectance spectrum reconstruction method spectral data collected with different radiometers in different locations were successfully regenerated from 5 specific bands (412, 492, 556, 620 and 672 nm). Another advantage of the reconstruction technique is the storage of high resolution spectral data by means of only 5 bands. It is proposed that airborne spectral reflectance measurements could stay limited to only 5 specific spectral bands.

Keywords: ocean colour, remote sensing, reflectance, spectral bands, reconstruction of spectra, multiple regression analysis, optical databank

1. INTRODUCTION

New ocean colour sensors can differ in number of wavebands as well as in wavelength with both previous and future sensors. At present only those instruments with a high number of spectral bands could overlap the spectral bands of the different airborne and space borne sensors. It has been shown by various authors using principal components analysis (PCA) that 3 components explain most of the variation observed in the spectral signature of the visible reflectance spectrum in natural waters (Gower et al 1984, Fischer 1985, Sathyendranath et al 1989, Hinton 1991, Marees and Wernand 1991, Gitelson et al 1993). A linear transformation technique for the complete retrieval of solar irradiance spectra (400 - 720 nm) by means of 3 bands was used by Spitzer and Wernand (1986) and was found to be accurate to within 10 %. The optimum number of wavebands required to show most of the information contained in a full spectrum was found to be 9 for an airborne sensor monitoring inland waters (Dekker et al 1991, 1992). Sathyendranath et al (1987) also showed in their 3-component model of ocean colour that with only 5 selected channels there was no significant loss in the information that could be retrieved from their modelled spectra. The 5 key-wavelengths they used were 400, 440, 520, 565, 640 nm. It should be possible to reconstruct a complete spectrum from a few specific wavebands. This has been attempted previously by Mayo et al (1993) by using a different technique to the one that is presented here. They reconstructed a complete normalised radiance spectrum derived from the CZCS bands by using a kriging interpolation method. It is shown here that if an ODB of high resolution reflectance spectra (400 - 720 nm) of a specific sea area exists it is possible to fully reconstruct these and new spectra by a 5-band approach. The technique used here is based upon multiple regression analysis (MRA). A minimum of 5 key bands were chosen as independent variables in the MRA technique; 412, 492, 556, 620 and 672 nm (incl. 4 SeaWiFS bands). These were found to give good results.

2. INSTRUMENTS AND DATA COLLECTION

Data collection was performed in Dutch and Belgian coastal waters and in the Dover Strait (Area A, Fig. 1) during four seasons in 1993. The total suspended matter concentration ranged between 1 mg/l and 66 mg/l and chlorophyll-a concentrations were observed to vary from 0.3µg/l to 30µg/l.

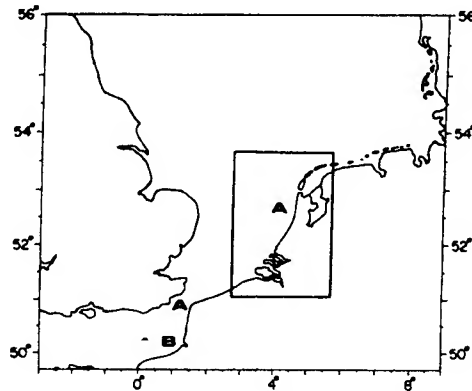


Fig. 1. The North Sea and English Channel. The spectral data were collected in the area marked with an A. Spectra that were used for reconstruction were collected with a different radiometer in the area marked B.

Two PR-650 SpectraColorimeters (Photo Research) were employed for the spectral downwelling irradiance and upwelling radiance measurements. This instrument has a spectral range from 380 - 780 nm with a FWHM of 8 nm and a spectral accuracy of 2 nm. The wavelength resolution is less than 3.5 nm / pixel. The detector is a self-scanned 128-element diode array.

Ship borne spectral data were collected at 119 stations from a height of 4 metres above sea level. For the downwelling irradiance (E_d) a cosine head was mounted on the instrument. The radiance (L_u) was measured through an objective lens with a 1° field of view. To minimise direct surface reflectance the instrument was tilted 20° off nadir away from the sun during measurements. Both E_d and L_u were measured simultaneously. All measurements were performed between 9.30 h and 16.30 h local time. Weather conditions varied from full overcast to bright skies. Variation in wave height was in the order of 0 to 2 metres.

A single measurement was accumulated 4 times and 3 measurements were taken at each station. The measurements were then averaged. The diffuse spectral reflectance R was calculated from the ratio of the upwelling radiance and downwelling irradiance using:

$$R(\lambda) = Q \cdot L_u(\lambda) / E_d(\lambda) \quad (1)$$

where $R(\lambda)$ is the diffuse spectral reflectance, $L_u(\lambda)$ is the upwelling spectral radiance, $E_d(\lambda)$ the downwelling spectral irradiance and Q could vary between π and 2π where in this case Q was chosen to be 5 as was suggested for nadir and near-nadir viewing angles (see Austin 1980 and Kirk 1994). In Fig. 2 the reflectance is shown for all the stations.

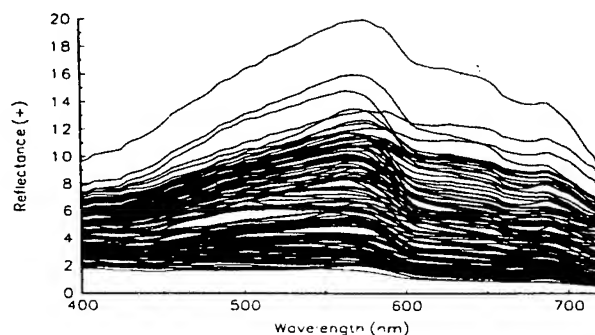


Fig. 2. The reflectance spectra for the ODB which were measured at 119 stations in area A (Fig. 1).

3. METHODS

The idea underlying the proposed reconstruction technique is to express the full reconstructed spectrum $R(\lambda)$ as a linear combination of a constant and the reflectance at points where the spectrum is known:

$$R(\lambda) = b_0(\lambda) + \sum_{i=1, I} b_i(\lambda) R(\mu_i) \quad (2)$$

Here, the functions $b_i(\lambda)$ are derived from the optical data bank (ODB) and $\mu_1, \mu_2, \dots, \mu_I$ are the wavelengths where the spectrum is known.

When it is attempted to reconstruct a spectrum $R_k(\lambda)$ of the ODB itself using Equation (2), an error $\epsilon_k(\lambda)$ will remain:

$$R_k(\lambda) = b_0(\lambda) + \sum_{i=1, I} b_i(\lambda) R_k(\mu_i) + \epsilon_k(\lambda), \quad k = 1, \dots, K. \quad (3)$$

In our application the number of points I equals 5 and the number of spectra in the ODB is K and equals 119. The functions $b_i(\lambda)$ are determined by a multiple regression analysis. It is required that the sum of squared errors $\sum \epsilon_k^2(\lambda)$ is as small as possible, for each wavelength λ . For this purpose Eq. (3) is expressed in matrix form, as follows. With

$$A = \begin{matrix} 1 & R_1(\mu_1) & \dots & R_1(\mu_I) \\ 1 & R_2(\mu_1) & \dots & R_2(\mu_I) \\ \dots & \dots & \dots & \dots \\ 1 & R_K(\mu_1) & \dots & R_K(\mu_I) \end{matrix}, \quad \mathbf{b}(\lambda) = \begin{matrix} b_0(\lambda) \\ b_1(\lambda) \\ \dots \\ b_I(\lambda) \end{matrix} \quad \text{and} \quad \mathbf{r}(\lambda) = \begin{matrix} R_1(\lambda) \\ R_2(\lambda) \\ \dots \\ R_K(\lambda) \end{matrix} \quad (4)$$

equation (2) can be expressed as $\mathbf{r}(\lambda) = A \mathbf{b}(\lambda) + \epsilon(\lambda)$ and for $\mathbf{b}(\lambda)$ it is found

$$\mathbf{b}(\lambda) = (A A^T)^{\text{inv}} A \mathbf{r}(\lambda) \quad (5)$$

With this equation for $\mathbf{b}(\lambda)$ and with $\mu_1 = 412 \text{ nm}$, $\mu_2 = 492 \text{ nm}$, $\mu_3 = 556 \text{ nm}$, $\mu_4 = 620 \text{ nm}$ and $\mu_5 = 672 \text{ nm}$, we computed the numbers of table (1) which are shown graphically in Fig. 3. Using this table and equation (2) any spectrum can be reconstructed of which only $R(\mu_1), \dots, R(\mu_5)$ have to be measured.

	b0	b1 (412 nm)	b2 (492 nm)	b3 (556 nm)	b4 (620 nm)	b5 (672 nm)
400 nm	0.092644	1.099933	-0.09268	-0.00922	0.083177	-0.09766
420 nm	-0.05271	0.916038	0.075304	-0.01018	-0.00302	0.00975
440 nm	-0.10173	0.646618	0.392782	-0.0997	0.082318	-0.03549
460 nm	-0.08723	0.372728	0.700702	-0.12042	0.101425	-0.04832
480 nm	-0.03489	0.119206	0.927145	-0.07259	0.063668	-0.04069
500 nm	0.018229	-0.06039	0.987759	0.084353	-0.05687	0.052795
520 nm	0.04237	-0.1117	0.770187	0.307217	0.018604	0.01552
540 nm	0.039403	-0.12478	0.47735	0.636132	-0.03178	0.039934
560 nm	0.000061	0.034573	-0.11905	1.091447	0.014107	-0.01919
580 nm	0.026719	0.057311	-0.36937	1.070214	0.4088	-0.1812
600 nm	-0.00216	0.065534	-0.13299	0.21947	1.16801	-0.31556
620 nm	0	0	0	0	1	0
640 nm	-0.00023	-0.03936	0.033377	-0.05112	0.848697	0.2088
660 nm	-0.02983	-0.04617	0.104507	-0.11788	0.410075	0.64614
680 nm	-0.02112	0.117242	-0.19487	0.120563	-0.05369	1.021293
700 nm	-0.22263	0.240766	-0.22374	0.023645	0.030069	0.948429
720 nm	-0.48275	0.415441	-0.33785	0.221446	-1.00017	1.690322

Table 1. The regression coefficients at a 20 nm wavelength interval to be used for the reconstruction of unknown spectra with given wavelengths. This table can be used in combination with equation (2).

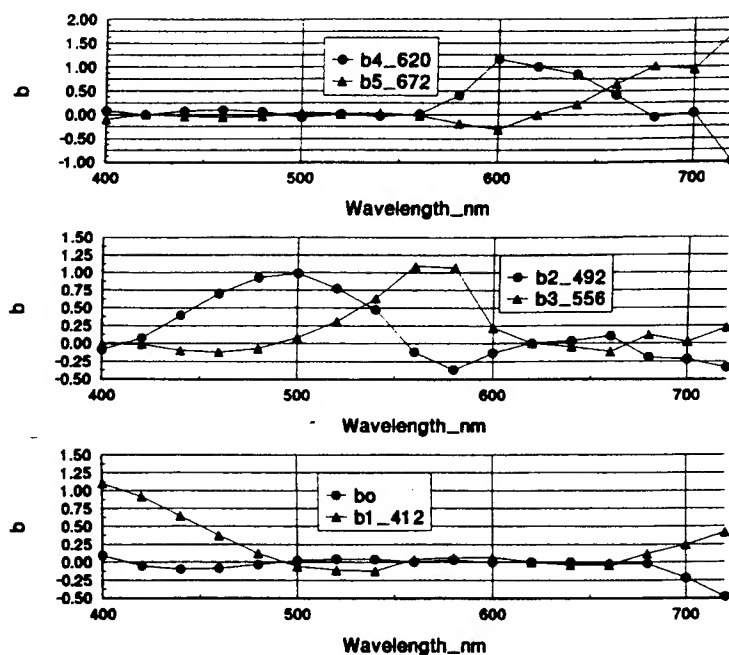


Fig. 3. Spectral behaviour of the regression coefficients b_0 to b_5 of table 1 between 400 and 720 nm.

4. RESULTS OF RECONSTRUCTION OF SPECTRA

The reconstruction technique was first applied to a set of reflectance spectra collected in the same area and with the same instrument as those spectra contained within the ODB. However to ensure independence this set of test spectra was not included in the ODB. The measured spectra (solid lines) and reconstructed spectra (symbols) are shown together in Fig. 4.

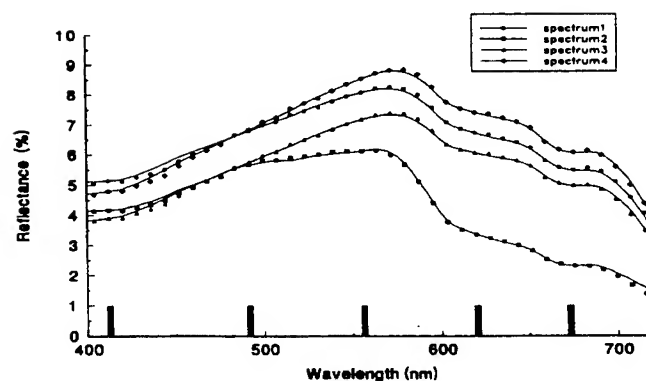


Fig. 4. Measured (solid lines) and reconstructed (symbols) reflectance spectra from area A (Fig. 1). The bars represent the wavebands (412, 492, 556, 620 and 672 nm) used to derive the regression coefficients.

The technique reconstructs spectra to within 1% for the majority of the wavelength range 400 - 720 nm. Around 450 nm and at the end of the spectrum reconstruction is within 4%. In order to investigate the capabilities of this technique further, sets of spectra collected in different areas and with a different radiometer were reconstructed. Data were available from the coast of Northern France which were collected with a Spectron Engineering SE-590 multispectral radiometer in March and May 1992. The SE-590 measures in 252 bands over a spectral range of 360 nm to 1110 nm with a FWHM of 10 nm and a spectral accuracy of 3 nm. The first set of data was collected in March from coastal waters 15 miles south-west of the Baie de Somme. The dissolved and particulate constituents of the water here were substantially different from those in the area where the spectra for the ODB were collected. Exceptionally high reflectances of up to 30% were observed, (Fig. 5), because the inorganic component of the suspended material consisted mainly of fine chalk particles (less than .4 μm). The chlorophyll-a concentration measured from water samples taken at the same time was 8 $\mu\text{g/l}$ at spectrum 1 and decreased to 1 $\mu\text{g/l}$ at spectrum 4. The actual total suspended particulate matter concentration determined gravimetrically from water samples only varied from 3 mg/l at spectrum 1 to 5 mg/l at spectrum 4. Fig. 5 also shows the reconstructed spectra of region B using the ODB of reflectance data collected in region A. The reconstruction is again accurate to within 1% for all wavelengths and for spectra of varying magnitude except for the region around 580 nm where the accuracy is within 4%.

A further set of reflectance spectra was available from the French coast within 5 miles of the Baie de Somme estuary which was collected in May 1992. Here the water quality was again different with higher levels of organic material. The concentrations of chlorophyll-a ranged from 3 to 14 $\mu\text{g/l}$, and the total suspended matter concentrations ranged from 3 mg/l to 9 mg/l. The measured and reconstructed spectra are shown in Fig. 6.

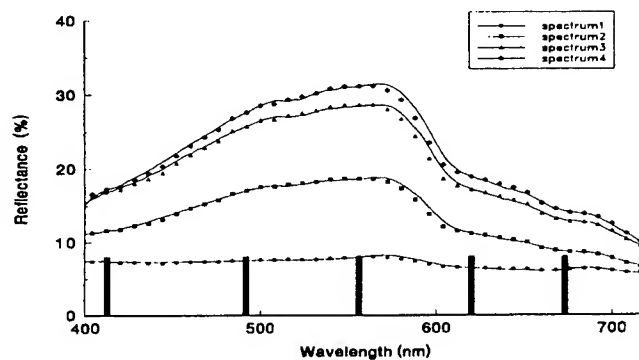


Fig. 5. Measured (solid lines) and reconstructed (symbols) reflectance spectra from coastal waters 15 miles south-west of the Baie de Somme (Area B, Fig. 1). The bars represent the wavebands (412, 492, 556, 620 and 672 nm) of the ODB of reflectance data, collected in area A, used to derive the regression coefficients.

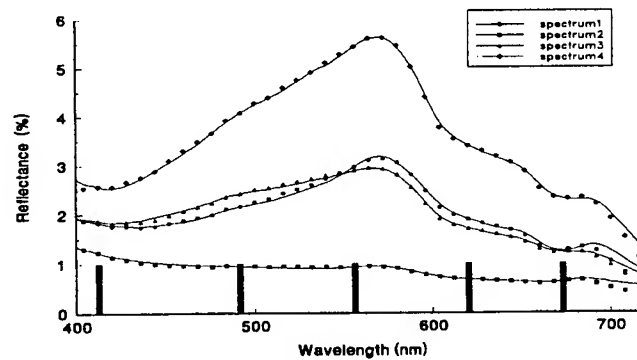


Fig. 6. Measured (solid lines) and reconstructed (symbols) reflectance spectra from coastal waters within 5 miles of the Baie de Somme (Area B, Fig. 1). The bars represent the wavebands (412, 492, 556, 620 and 672 nm) used to derive the regression coefficients.

The reconstructions are accurate in all wavelengths apart from above 700 nm where there is a decline in accuracy. This effect was emphasised when a set of spectra from inside the Somme estuary (May 1992) was reconstructed (Fig. 7).

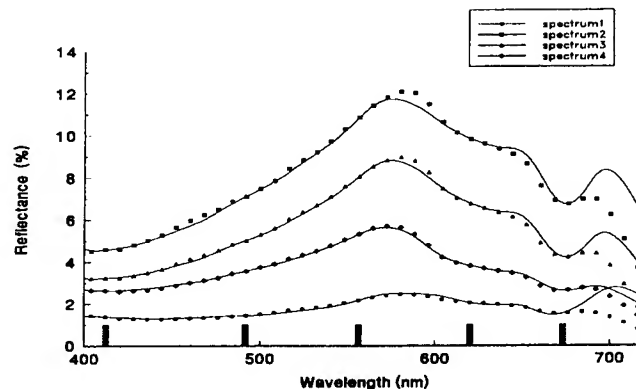


Fig. 7. Measured (solid lines) and reconstructed (symbols) reflectance spectra from the Somme Estuary (Area B, Fig. 1). The bars represent the wavebands (412, 492, 556, 620 and 672 nm) used to derive the regression coefficients.

It can be seen that there is a large reflectance peak at around 700 nm in the measured spectra, caused by a shift in the 685 nm fluorescent signal, and this peak is not reproduced in the reconstructed spectra. The reason for this is that there were no spectra having such optical signatures in the ODB of spectra.

5. CONCLUSION

This 5-band reconstruction method of full spectra by means of multiple regression techniques seems to be an accurate and promising method to aid the validation of remotely sensed data. This implies that ground truth radiometers developed nowadays do not need constant adjustment of their spectral performance if new satellite sensors are introduced. However one should take notice that the reconstruction does not add any extra value to the 5-band spectral signature of the investigated water type. In other words this means that the composition of the particulate and dissolved matter is embedded in the reflectance behaviour within the 5 used spectral bands. Furthermore this implies that the information derived from case 2 water reflectance spectra is limited.

Those waters with exceptionally high chlorophyll concentrations, showing a shift in the fluorescence peak, will be hard to reconstruct, at that particular waveband, if there are no representative spectra in the ODB. The ODB in this study contains only spectra from case 2 waters and it is essential that it is enlarged to include data from waters with a different composition. Care should be taken that all spectral signatures are equally represented.

Notice the use of the 620 nm band in the MRA which was necessary for accurate reconstruction. In the design of future airborne band (imaging-) radiometers one should consider this extra band.

It is proposed that future work should concentrate on the optimum position for the bands within the visible spectrum and to what extent the FWHM of the key-wavelengths can be enlarged in order to encompass any variation at a discrete waveband and if one should incorporate an extra waveband beyond 700 nm. Another aspect of the described MRA method should involve airborne high resolution spectra and under water spectra.

6. ACKNOWLEDGEMENTS

The spectra in the ODB were collected from the research vessel "Pelagia" of the Netherlands Institute for Sea Research, during cruises within the Particulate Matter North Sea programme (PMNS), in conjunction with National Institute for Coastal and Marine Management (RIKZ), University of Groningen. The reconstructed spectra from the French coast were collected during cruises on board the British research vessel "Challenger" and French research vessel "Cote de Normandie" within the MAST CEC funded FLUXMANCHE programme co-ordinated by the University of Southampton. We like to thank the participants of both programs for their assistance in data collection. The Spectron SE-590 was loaned by the NERC Equipment Pool for Field Spectroscopy, University of Southampton. Special thanks goes out to the captain and crew of the R.V. Pelagia for their pleasant co-operation during the PMNS cruises.

7. REFERENCES

1. Austin R. W., "Gulf of Mexico, ocean-colour surface-truth measurements", *Boundary-Layer Meteorology* **18**, 269 - 285, (1980).
2. Dekker A. G., Malthus T. J., Wijnen M. M., and Seyhan E., "A multi-sensor approach to spectral signature analysis of inland waters", *Proceedings of the 5th International Colloquium, Physical measurements and Signatures in Remote Sensing* (1991).
3. Dekker A. G., Malthus T. J., Wijnen M. M., and Seyhan E., "Remote sensing as a tool for assessing water quality in Loosdrecht lakes", *Hydrobiologia* **233**: 137 - 159, (1992).
4. Fischer J., "On the information content of multispectral radiance measurements over an ocean", *International Journal of Remote Sensing*, Vol. **6**, No 5, 773 - 786, (1985).
5. Gitelson A., Garbuzov G., Szilagyi F., Mittenzwey K. H., Karnieli A., Kaiser A., "Quantitative remote sensing methods for real-time monitoring of inland water quality", *International Journal of Remote Sensing*, Vol. **14**, No 7, 1269 - 1295, (1993).
6. Gower J. F. R., Lin S., Borstad G. A., "The information content of different optical spectral ranges for remote chlorophyll estimation in coastal waters", *International Journal of Remote Sensing*, Vol. **5**, No 2, 349 - 364, (1984).
7. Hinton J. C., "Application of eigenvector analysis to remote sensing of coastal water quality", *International Journal of Remote Sensing*, Vol. **12**, No 7, 1441 - 1460, (1991).
8. Kirk J.T.O., *Light & photosynthesis in aquatic ecosystems*. Cambridge University Press, Cambridge: 144 - 151. ISBN 0 521 45966 4, (1994).
9. Mayo M., Karnieli A., Gitelson A., Ben-Avraham Z., "Determination of suspended sediment concentrations from CZCS data", *Photogrammetric Engineering & Remote Sensing*, Vol. **59**, no. 8, 1265 - 1269, (1993).
10. Marees G., Wernand M. R., "Interpretation of optical remote sensing data over coastal waters", *Internal report Netherlands Remote Sensing Board*. No. 91 - 27, ISBN 90 54 11006 6, (1991).
11. Sathyendranath S., Prieur L., Morel A., "An evaluation of the problems of chlorophyll retrieval from ocean colour, for case 2 waters", *Advances in Space Research*, Vol. **7**, No. 2, (2)27-(2)30, (1987).
12. Sathyendranath S., Prieur L., Morel A., "A three-component model of ocean colour and its application to remote sensing of phytoplankton pigments in coastal waters", *International Journal of Remote Sensing*, Vol. **10**, no. 8, 1373 - 1394, (1989).
13. Spitzer D., Wernand M. R., "Assessment of solar irradiance spectra", *Applied Optics*. Vol. **25**, No. 15, 2466, (1986).

N.B.: An extended form of this paper has been accepted (1994) for publication by the *International Journal for Remote Sensing* under a different title.

A System for Maritime Surveillance Aid

Kazuo Yamamoto*, Kimio Yamada* and Nobuo Kiriya†

* Electronic Navigation Research Institute, Ministry of Transport

† Ship Research Institute, Ministry of Transport
6-38-1 Shinkawa Mitaka-shi, Tokyo 181, Japan

ABSTRACT

A system to aid maritime surveillance is being studied to search for small floating objects like a life raft or to detect oil spill more reliably and efficiently. The system consists of sensors, an image processor and a display so as to reject unnecessary noise in the sea surface images, and then to detect and identify the objects to be searched. This paper describes the optical sensor system with an infrared camera and a TV camera. The infrared camera detects 3 - 5 μm waveband by 512×512 solid state sensing elements. The system was used to gather images on different sea areas in summer and winter by aircraft and on the ground. Typical images are presented to demonstrate the validity of the sensor system to search for small floating objects. The influences of air and water temperature, weather and observation altitude upon the images are discussed. Image processing techniques like filtering or image superposition are also described to suppress noise.

keywords: Maritime surveillance, Search and rescue, Infrared camera, Noise suppression, Image processing

1. Introduction

Search and rescue or environmental surveillance on the sea is performed visually and by radar in Japan. However, visual surveillance is deteriorated by inclement weather and sea condition. Present radar surveillance is greatly influenced by undesired echo (clutter) from precipitation or sea. SAR (Synthetic Aperture Radar) was introduced to enhance the detection performance of conventional radars¹. Several sophisticated surveillance systems with multiple sensors were presented to deal with these problems². However, most of these systems are heavy and expensive. We are in the process of exploring the framework of a system for maritime surveillance aid. In this system, we place emphasis on a function to reject unnecessary noise included in the surveyed images, detect searching objects, identify, map and display the objects.

In this paper, the outline of the maritime surveillance aid is presented. The optical sensor system which consists of an infrared (IR) camera and a high resolution TV camera was constructed. Ground measurement and flight measurement were conducted using the system. Small boats were mainly surveyed to evaluate the detection performance of these cameras.

Typical images are presented to describe the performance of these cameras and to examine a proper altitude for the measurement. The influence of air and water, temperature, weather condition and sunlight reflection upon the images is discussed. Several image processing techniques are also presented to develop a procedure to suppress unnecessary noise.

2. The outline of the surveillance aid

The primary goal of this study is to develop a procedure to suppress unnecessary noise included in the images and to detect objects, and then to identify, map and display them. The surveillance aid must satisfy the following requirements:

1. The sensor can detect small and non-conductive objects like a life raft with the diameter of 3m.
2. The system can reject or suppress noise in the image like whitecaps or sunlight reflection from the sea.
3. The system can identify the searching object automatically.
4. The system can give alarm and display a clear image of the object so that the personnel can make final identification.

The principle of the surveillance aid is illustrated in Fig.1 The system consists of image sensors, a data recording equipment, a data processing equipment and a display. The image sensors consist of an infrared (IR) camera and a visible ray camera (TV camera). The data recording equipment stores video (NTSC) information and digital images. The data processing equipment suppress the noise and identifies the object to be searched.

As a first step in developing the total system, we constructed an optical sensor system. The system consists of an IR camera, a visible ray camera (TV camera), video recorders and an A/D converter (a video capture board). The IR camera (MITSUBISHI IR-M500) can detect 3 - 5 μm infrared by 512 \times 512 PtSi Schottky-Barrier elements. This element is reported to have a wide dynamic range³, which is important for our application. The field time is 1/60 second. The IR camera (FLIR 2000HP SAFIRE) which can detect 8 - 12 μm infrared, was also used to compare the images from these cameras. A high resolution 3CCD TV camera (SONY XC-003) was introduced to obtain reference images. Fig.2 shows these cameras, where 8 - 12 μm IR camera is packaged in a 15-inch spherical enclosure (turret). Images from these cameras are recorded by two Hi-8 video recorders and are converted into the digital information to store in a disk. The sensor system is installed on a twin turbo-prop aircraft (Beechcraft B-99) to look down the sea.

3. Measurement

3.1. Ground Measurement

The optical sensor system was placed on the cape Kan-non-zaki, which is about 60 meter high above sea level and is 12 miles south to Yokohama. From Kan-non-zaki, the Uraga channel which is the entrance of the Tokyo bay can be surveyed. The width of the channel is about 6 nautical miles. The vessels were observed there in summer and winter.

Fig.3(a) shows the image of vessels measured by 3 - 5 μm IR camera (IR-M500 : IR camera 1). Fig.3(b) is the image from 8 - 12 μm IR camera (2000HP : IR camera 2). Both images were gathered in June. The field of vision is about 14° by 11° for IR camera 1 and 28° by 16.8° for IR camera 2. Although the vision of each camera is different, the visibility of each camera can be compared by these figures. A fishing boat, displayed in the center of the figure is about 7 to 8 meters in length. The contour of the boat in Fig.3(a) is clearer than that in Fig.3(b) because the sensing device of IR camera 1 has a higher resolution than that of IR camera 2. The figure also demonstrates, that IR information can penetrate thin smoky or foggy atmosphere, since buildings and chimneys at the opposite shore are displayed clearly on IR images, although they were unable to be seen visually.

Fig.4 is the IR image recorded in November evening by IR camera 1. Vessels looked vague in the figure. The image from IR camera 2 on the other hand, remained clear in the same environment although the image is

not presented here. Generally, it is known that the solar energy is dominant in 3 - 5 μm waveband. This fact and above phenomenon suggest that the image from IR camera 1 may be easily affected by sunlight reflection. However, this problem can be avoided to some extent by using a low pass IR lens filter and will be described in the next section.

3.2. Flight Measurement

Fig.5 is the image measured by the CCD camera. This image was collected in July by the west coast of Kyusyu, the southern main island of Japan at the altitude of 6500 ft. Flight speed at the measurement was about 130 knots. The temperature was about 35°C°, and the water temperature was about 25°C°. The field of view with the standard 50mm lens at that altitude was about 530 × 410 m. 4 fishing boats, the size of which is about 8 × 3 m, were displayed. There were glittering spots on the upper right portion by sunlight reflection. Measurement was made in different altitude to examine a proper altitude for surveillance. Higher altitude flight makes the image recognition difficult. Lower altitude flight makes the surveillance area narrower. We noted the number of pixels constituting an object to decide surveillance altitude. The number of pixels of a fishing boat was counted on Fig.5. Approximately 170 pixels were used to represent the 8 × 3 m boat in the whole image including 428000 pixels, which means that about 50 pixels will be used in a life raft with the diameter of 3 m. It has been shown that the contour of the boat could fairly be drawn by 50 pixels. Thus, we can say that this sensor system will detect the life raft by 6500ft flight, although of course, further work is necessary to decide a most suitable altitude to identify an object.

Fig.6 shows the IR image measured by IR camera 1 by the coast of Hokkaido, the northern main island of Japan at the altitude of 6500ft in January. Flight speed at the measurement was about 130 knots. The temperature was about -15°C°, while the water temperature was about 5°C°. It was expected that the IR image observed in winter was clearer than that in summer because the high temperature and humidity in Japan will attenuate IR energy. However, the image in winter tended to be degraded. This is because the sensing device of IR camera 1 has a temperature dependency and must be calibrated often in cold environment.

Fig.6 shows that boats were displayed dark on brighter background because the water was warmer than the air in this measurement. This figure implies that the contrast between the object and sea may be reversed, or in the worst case, the object will not be detected in the image depending on the water and atmospheric temperatures. We have to take this fact into account in the process of identifying an object.

4. Introduction of image processing techniques to suppress noise

Several filtering techniques were examined to construct a proper procedure for noise suppression. Fig.7 is the IR image measured by the coast of Kyusyu in summer. (The CCD image corresponding to Fig.7 was depicted in Fig.5.) The altitude of the measurement was 6500ft. There are 4 fishing boats in lower right portion on the figure. White spots caused by sunlight reflection did not appear in the IR image because the 3.8 μm IR filter was added on the IR lens. But 4 boats looked vague because the filter attenuated the IR energy.

The threshold method, which is one of the simple filtering techniques to reject darker portions in an image, was imposed on Fig.5 to yield Fig.8. 4 boats were extracted by this process. However, there were several white spots on the upper right portion on the figure due to sunlight reflection. So, another process must be added to enhance the contrast between the objects and noise.

We tried to superpose two images from different sensors. A portion including 4 boats shown by a dotted rectangle in Fig.7 was cut, and underwent 50 percent transparent process. The portion was then superposed on the image from CCD camera, Fig.5. Fig.9 is the combined image where the superposed image is shown inside the

dotted rectangle, while original CCD image remains outside the rectangle. The glittering by sunlight reflection has been suppressed in the rectangle, since this process averages two images. The brightness of 4 boats became dark, while the background was darker than the boats, which facilitates a boat identification. Superposition of the several images, taken successively by one sensor may also suppress clutter just like the synthetic aperture technique if a proper period for data acquisition is established⁴. However the information like a precise aircraft location and the attitude is essential for the successful image superposition. Close study is being done to obtain the information simply.

5. Conclusion

A system for maritime surveillance aid is now under study. The outline of the system is presented. The optical sensor system, which is a part of the total system was constructed. The system consists of a CCD camera and an infrared (IR) camera to gather sea surface images. Measurement was made both on the ground and by air. The analysis of the measured images showed that the optical sensor system can penetrate foggy atmosphere and that it can detect a life raft with the diameter of 3 m at the altitude of 6500ft. The influence of sunlight reflection on the IR image was also discussed.

Several image processing techniques were introduced and examined to find out a proper procedure to suppress unnecessary noise in the image. Then, several filtering techniques have demonstrated to serve for noise reduction, although they were not always valid in all noise in the images. Another methods, such as the aperture synthesis and the histogram analysis are now being studied to avoid these difficulties.

6. references

1. H. Shinohara et al., "An X-Band SAR System for a Light Airplane," Technical Report of IEICE Japan Vol. SANE92-53, pp.7-14, Nov.1992. (Japanese).
2. Aerojet ElectroSystems, "AIREYE Multi-Sensor Data Manage Systems," AIREYE System Catalog, (Approved for release by US Coast Guard letter DTCG 23-80-20012), Dec.1985.
3. J.Silverman, J.M.Mooney, V.E.Vicks, "Display of wide dynamic range infrared images from PtSi Schottky barrier cameras," Opt.Eng. 29(2), pp.97-104, Feb.1990.
4. J.W.Coltman and A.E. Anderson, "Noise limitations to resolving power in electronic imaging," Proc.IRE, 858, May 1960

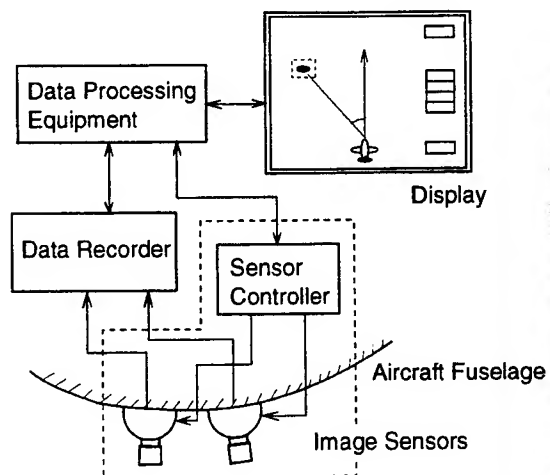


Fig.1 The principle of the surveillance aid

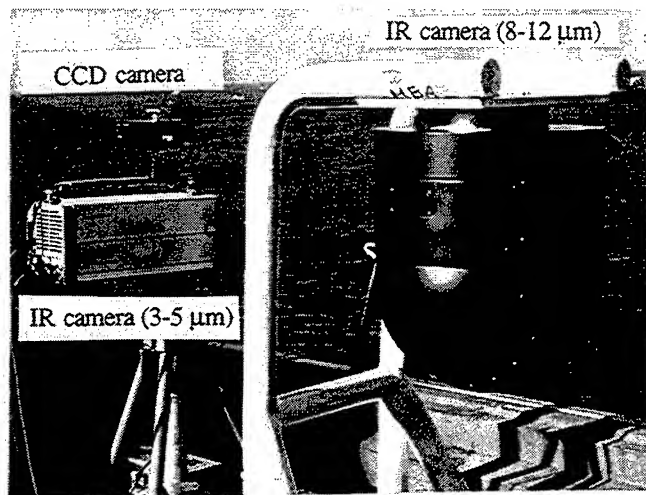
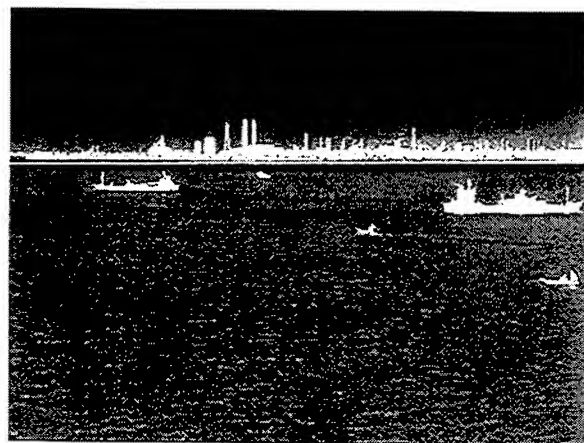
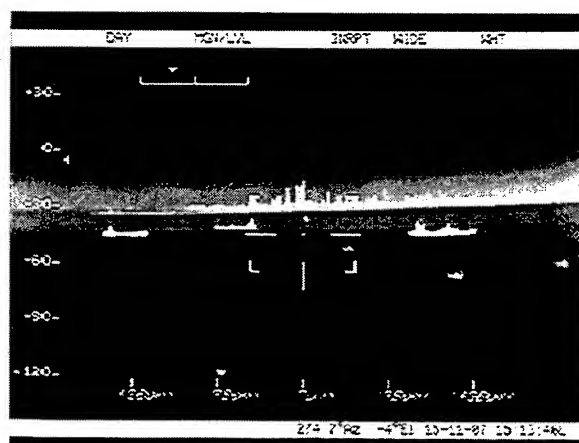


Fig.2 The optical sensor system



(A) The image by 3-5 μm IR camera
Fig.3 IR images measured at the Uraga Channel (Ground measurement in June)



(B) The image by 8 - 12 μm IR camera

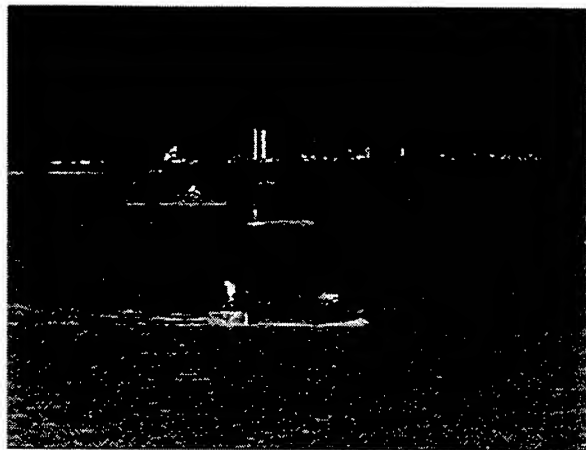


Fig.4 IR image at the Uraga Channel
(Ground measurement in November)

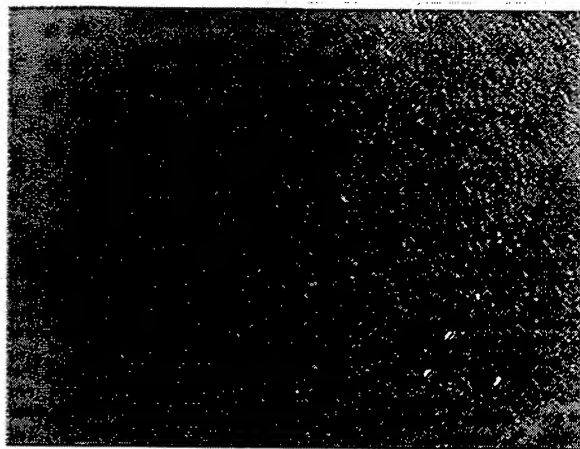


Fig.5 CCD image in Kyushu
(Flight measurement in July)

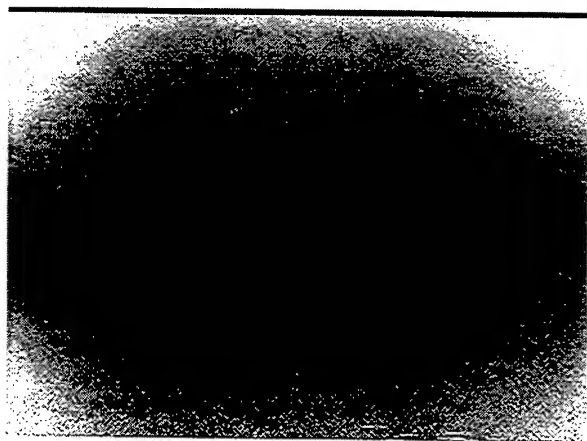


Fig.6 IR image in Hokkaido
(Flight measurement in January)

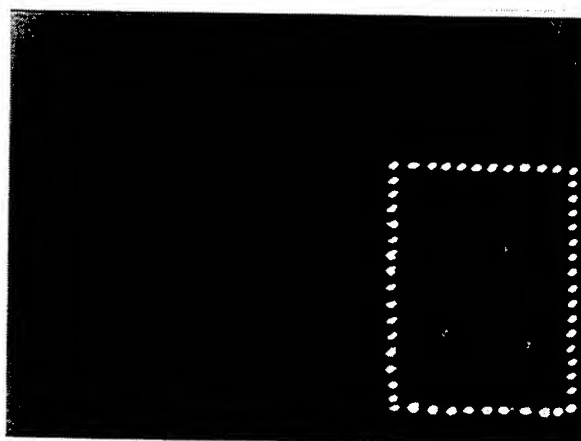


Fig.7 IR image in Kyushu
(Flight measurement, corresponding to Fig.5)



Fig.8 The threshold method
(Fig.5 was processed to suppress noise)

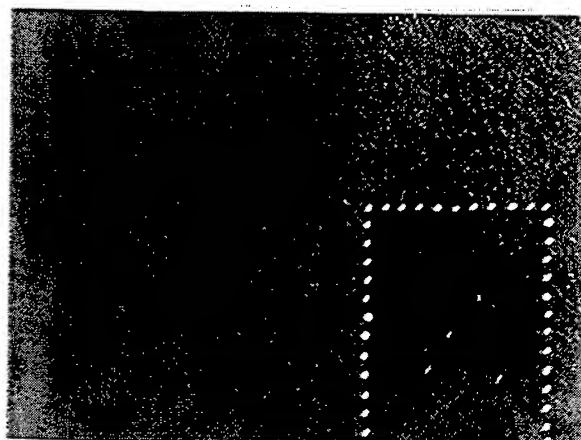


Fig.9 Superposed Image
(Fig.4 + Fig.7 : in the dotted rectangle)

VARIATION OF AEROSOL OPTICAL THICKNESS AND MOISTURE CONTENT OF THE ATMOSPHERE IN THE AREA OF CANARY ISLANDS

Zuev, V.E., Kabanov, D.M., and Sakerin, S.M.
 Institute of atmospheric optics,
 1 Akademicheskii avenue, Tomsk, Russia, 634055
 E-mail: zuev@iao.tomsk.su

The aerosol optical thickness (AOT) and the columnar water vapor (CWV) of the atmosphere are the most important characteristics determining the radiation flux transformation.

This paper summarized the results of investigations of the short-period variability of spectral AOT (0.37-1.06 μm) and CWV obtained during the four marine expeditions in the region of Canary Islands.

From the geophysical standpoint this subtropical area of the Atlantic Ocean is of our main interest because it is located in an outlying area of dust emission from Western Sahara. Practical significance of this area is conditioned by active anthropogenic pollution, namely, a large number of health resort, an area of intensive fishery, navigation and so on.

Instruments, operating instructions for measurement, calibration as well as separate results were published in the previous papers [1-3 et al.].

Main parameters of a sun-photometer (in a variant of 1995):

Field of view angle, deg.	0.75
Number of spectral channels	12
Maxima (and half widths) of light filters	370 (22) 409 (30) 425 (13)
transformation, nm	439 (6) 485 (7) 514 (22)
	553 (8) 638 (5) 673 (10)
	870 (11) 940 (10) 1061 (19)
Error of photometric measurements, %	1
Time of single measurement series, min	1 - 2

The areas of investigations in various expeditions are illustrated in Fig. 1, and the parameters of the data obtained are given in Table 1.

Table 1

N	Expedition	Period of investigation	Quantity of spectral channels of AOT	Quantity of measurement s days	Quantity of measurement s series	Quantity of hourly average significances of AOT
1.	40-th cruise of the R/V "Akademik Vernadsky"	12/05/89-12/14/89	4	9	52	30
2.	43-th cruise of the R/V "Akademik Vernadsky"	07/04/91-08/03/91	6	29	347	162
3.	The B/H "Esperanza del Mar"	05/01/94-05/22/94	11	19	2750	151
4.	35-th cruise of the R/V "Akademik Mstislav Keldysh"	01/29/95-02/01/95 04/0/95-04/12/95	11	7	1638	57

The atmospheric transmission was measured in different synoptic situations, seasons, and after the Mt. Pinatubo eruption (July 1991). A direct consequence of the above research is a relatively large range of variability of atmospheric optical thickness (AOT).

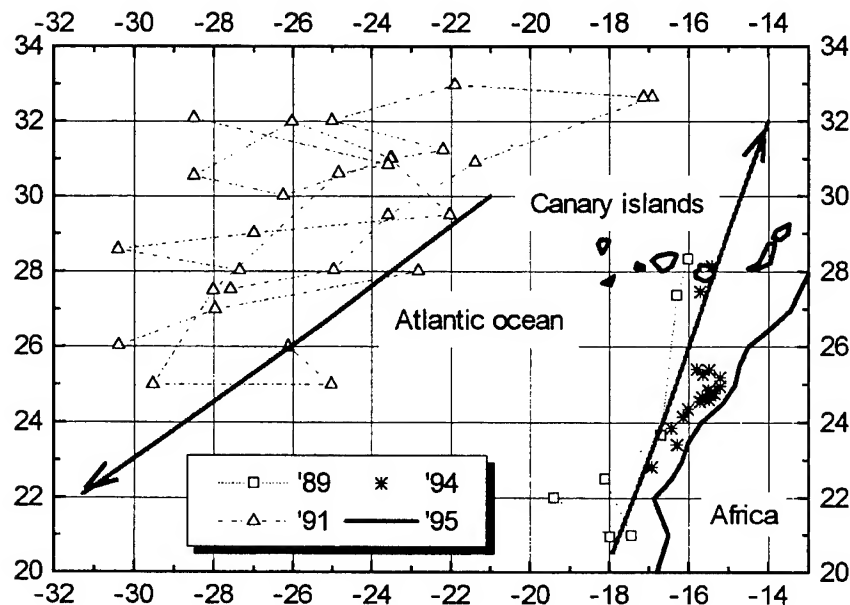


Fig. 1. Map of investigation regions.

From the statistical data (Table 2 and Figure 2) it follows that the most transparent atmosphere was during 40-th cruise of R/V in December 1989. During this period of investigations the mean values of AOT (about 0.06) were consistent with the conditions of the open ocean [1-3]. Frequent transfers of cold air from the northwest of the Atlantic ocean during winter period contributed to clearing the atmosphere from the influence of continental dust escapes. During spring and summer expeditions of 1994 and 1995 the nearness to the northwestern shore of Africa shows itself constantly as the increased values of AOT. Minimal values of aerosol turbidity did not go below the mean values of τ_{λ}^a for December 1989. The effect of the dust escapes from the West Africa on the sea atmosphere can be followed, for example, from the 1994 data. Table 2 shows a separate data array for the conditions of the increased dust turbidity during several days at the beginning of the cruise (designed by 1994*).

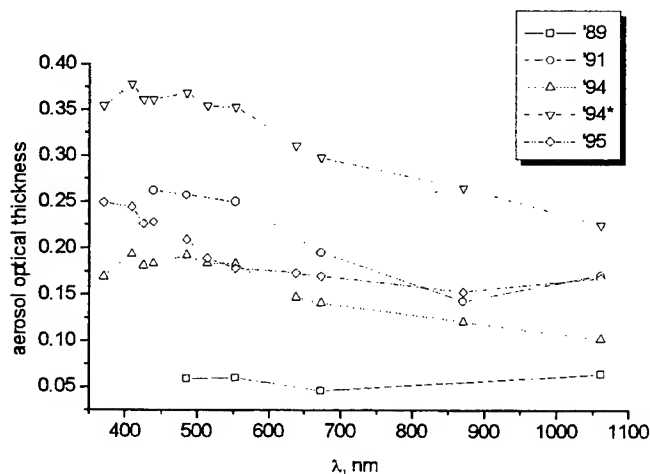


Fig. 2. Spectral dependences τ_{λ}^a for different expeditions.

Table 2

τ_{λ}^a	1989	1991	1994	1994*	1995	Total (without 1991)
	Mean Min - Max V					
370			<u>0.169</u> 0.06-0.74 0.98	<u>0.354</u> 0.24-0.74 0.55	<u>0.249</u> 0.09-0.43 0.56	
409			<u>0.193</u> 0.07-0.77 0.88	<u>0.378</u> 0.21-0.77 0.53	<u>0.244</u> 0.09-0.43 0.54	
425			<u>0.181</u> 0.07-0.75 0.90	<u>0.361</u> 0.25-0.75 0.53	<u>0.226</u> 0.08-0.41 0.54	
439		<u>0.262</u> 0.09-0.835 0.65	<u>0.183</u> 0.07-0.75 0.89	<u>0.361</u> 0.25-0.74 0.53	<u>0.228</u> 0.09-0.41 0.53	
485	<u>0.059</u> 0.03-0.1 0.45	<u>0.257</u> 0.08-0.83 0.66	<u>0.192</u> 0.08-0.77 0.85	<u>0.368</u> 0.25-0.77 0.54	<u>0.209</u> 0.08-0.38 0.52	<u>0.171</u> 0.03-0.77 0.85
514			<u>0.183</u> 0.08-0.75 0.87	<u>0.354</u> 0.23-0.75 0.56	<u>0.189</u> 0.08-0.35 0.52	
553	<u>0.06</u> 0.04-0.11 0.44	<u>0.250</u> 0.09-0.81 0.66	<u>0.183</u> 0.07-0.76 0.88	<u>0.353</u> 0.23-0.76 0.56	<u>0.178</u> 0.07-0.32 0.51	<u>0.159</u> 0.04-0.78 0.87
638			<u>0.147</u> 0.04-0.7 1.05	<u>0.311</u> 0.19-0.70 0.62	<u>0.173</u> 0.06-0.32 0.54	
673	<u>0.046</u> 0.02-0.09 0.62	<u>0.195</u> 0.04-0.74 0.82	<u>0.141</u> 0.04-0.69 1.07	<u>0.298</u> 0.17-0.69 0.65	<u>0.170</u> 0.06-0.32 0.55	<u>0.127</u> 0.02-0.69 1.01
870		<u>0.143</u> 0-0.66 1.06	<u>0.121</u> 0.03-0.64 1.17	<u>0.265</u> 0.15-0.64 0.71	<u>0.153</u> 0.04-0.29 0.60	
1061	<u>0.064</u> 0.02-0.11 0.48	<u>0.171</u> 0.03-0.68 0.84	<u>0.102</u> 0.01-0.55 1.20	<u>0.225</u> 0.14-0.55 0.71	<u>0.168</u> 0.04-0.31 0.63	<u>0.109</u> 0.01-0.55 1.01
α	0.64	0.91	0.84	0.57	0.51	0.73
W			<u>1.233</u> 0.93-1.83 0.17		<u>1.150</u> 0.90-1.63 0.22	<u>1.211</u> 0.90-1.83 0.19

In contrast to the AOT values, the relative spectral behavior during the dust escapes varies slightly. The mean values of the Angström coefficient α , characterizing the spectral behavior ($\tau_{\lambda} = \tau_{1.0} \cdot \lambda^{-\alpha}$), in all the cases were within 0.5 to 0.7. Such a behavior of α is caused by the fact that both under the conditions of transparent sea atmosphere and during the dust escapes the large particles (salt or dust) play a decisive role, which resulted in neutralization of the AOT spectral behavior.

The measurements of 1991 began within three weeks after the Mt. Pinatubo eruption. The influence of volcanic aerosol manifested itself mainly in the short-wave spectral range. The mean values of α increased up to 0.9, characterizing the increase (manifestation) of the contribution of finely divided stratospheric aerosol.

A qualitative analysis of time dependencies of τ_{λ}^a has shown that the main variations occur during several days under the influence of large-scale circulation processes. The coefficient of AOT variations V (the ratio of root-mean-square deviations to mean values) are within the limit of 40-70%. Intrusion of high-power dust escapes results in the increase of variation coefficients up to 80-120%.

The histograms of repetitions of the values of $\tau_{0.55}^a$ and α (without designations of 1991) are given in Fig. 3. The common property of histograms is an asymmetric form with a more delayed decrease to the field of large values.

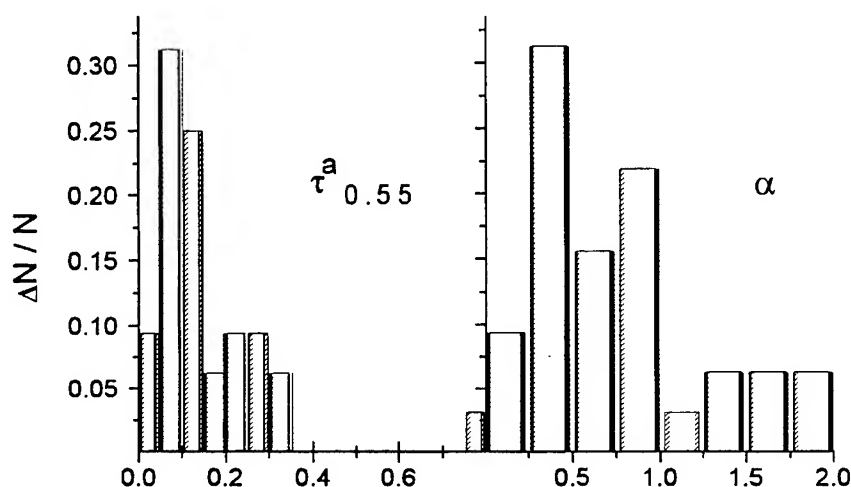


Fig. 3. Frequency of occurrence graphs of $\tau_{0.55}^a$ and coefficient α .

The estimates of diurnal variability of normalized values of AOT (Fig. 4a) illustrated the increase of turbidity from the morning to the noon (by 10%) and then the decrease by the evening (to 30%).

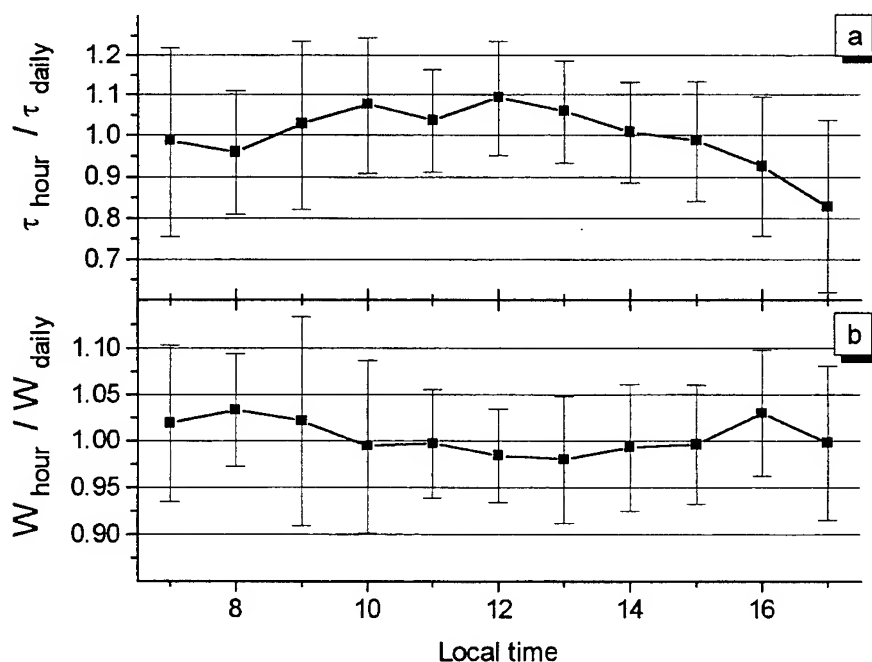


Fig. 4. The relative diurnal run of $\tau_{0.55}^a$ and W .

The measurements of atmospheric transmission in the range of water vapor absorption band $0.94 \mu\text{m}$ have made it possible to analyze the variation of the columnar water vapor of the atmosphere W . Although the area being studied refers to the subtropics, the measured CWV during the warm period turned out to be rather low and with small variations (the mean value is 1.21 g/cm^3 , the variations coefficient is 19%). Analysis of the radiosounding data in the 1994 expedition has shown that a characteristic property of vertical distribution of water vapor in this region is the extreme decay of CWV up to the altitudes of 1-1.5 km. Figure 5 shows a typical humidity profile during the research period.

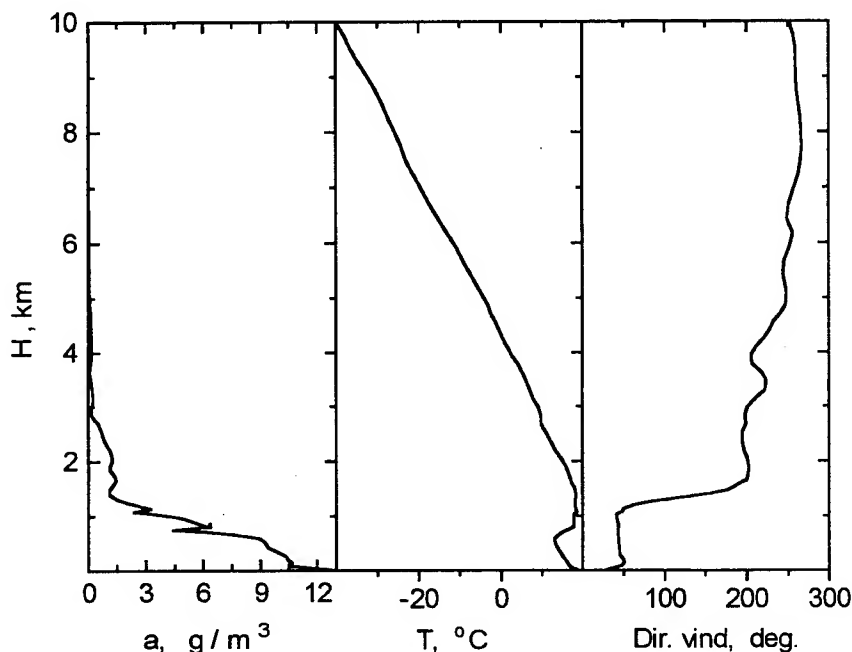


Fig. 5. Typical vertical profiles of meteorological parameters in the troposphere.

A regular component in the diurnal variability is not manifested practically. From the data of Fig. 4b one can follow the availability of two weak maxima. At about 8:00 AM and 4:00 PM and the minimum at noon. However, the total amplitude of the average diurnal variations W does not exceed 5%.

The calculations of the cross-correlation coefficients show the availability of a close relationship τ_{λ}^a for different wavelengths ($R \approx 0.9-1.0$) and the lack of dependence on meteorological parameters in the adjacent to water layer. Above the level of significance (0.277) there exists only the correlation with absolute humidity - 0.34. Weak negative correlation (up to -0.56) appears between τ_{λ}^a and the coefficient α (the increase of AOT is often accompanied by the decrease of α).

Referents

1. G. Korotaev, S. Sakerin, et al. *J. Atm. Ocean Tech.* 10, 5, 752-735, 1993.
2. D.M. Kabanov, S.M. Sakerin. *Atmos. Oceanic Opt.* 8, No6, 442-446, 1995.
3. S.M. Sakerin, D.M. Kabanov, V.V. Polkin. *Atmos. Oceanic Opt.* 8, No12, 1767-1777, 1995.

Poster Session: Process Studies

Chlorophyll maximums controlled by under water current and solar irradiation

Ichio Asanuma, Kazuhiko Matsumoto, Takeshi Kawano, Chizuru Saitoh

Marine Research Department, Japan Marine Science and Technology Center
2-15, Natsushima, Yokosuka, Japan, 237

Marlon R. Lewis, and Scott D. McLean

Department of Oceanography, Dalhousie University
Halifax, Nova Scotia, B3H 4J1, Canada

ABSTRACT

Through the bio-optical measurement over the equatorial warm water pool, we could discuss the vertical structure of the chlorophyll maximum. The chlorophyll-a from the surface to the top of the chlorophyll maximum layer was expressed as the inverse function of photosynthetically available radiance (EdPAR). The chlorophyll-a from the bottom of chlorophyll maximum layer to 150 m was expressed as logarithm function of EdPAR.

As we could observe the different current streams within the surface mixed layer by the ship-mounted ADCP, we could make a new hypothesis on the generation of chlorophyll maximum layer in the warm water pool. As the top portion of the chlorophyll maximum layer is in the east-north-east current and the nitrate in this layer is depleted, it is supposed the chlorophyll maximum to be maintained by the reproduction. As the deeper portion of the chlorophyll maximum layer was on the top of the north-west current and it was just above the nitracline, it is supposed the chlorophyll maximum to be maintained by the new production.

Keywords: phytoplankton, chlorophyll, chlorophyll maximum, warm water pool, nutrients, nitrate, current profile, photosynthetically available radiance.

1. INTRODUCTION

On the western equatorial Pacific, there is the warm water pool through the year from the north of Papua New Guinea to Kiribati Islands, sometimes to the eastern side of the international date line. The warm water pool is a heat storage, where the upper mixed layer to 120 to 150 m keeps temperature 29 to 30 °C. Also the warm water pool is a heat source, which produces a train of Rossby waves disrupting the normal circulation patterns.¹ In the warm water pool, the westward south equatorial current is observed in the surface layer, and the east-ward equatorial under current is observed under the south equatorial current.² Pickard et al. pointed out that the thermocline in 150 to 200 m inhibits a vertical transfer of water properties between the well-mixed and homogeneous surface layer and the deep water in the western equatorial Pacific.² Lewis et al. reported a large fraction of the solar flux into the warm water pool because of a shallow mixed layer and optically clear.³

In the western tropical Pacific, it is known as one of oligotrophic water and the water with a deep chlorophyll maximum. Pak et al. summarized the hypotheses for the chlorophyll maximum of (1) accumulation of cells at a density discontinuity due to decrease in sinking, (2) differential grazing pressure, and (3) a physiological adaptation of the cells to the light conditions.⁴ Siegel et al. demonstrated a clear coupling between upper ocean biogeochemical processes and upper ocean heating rates for the warm water pool.⁵ Pena et al. estimated the new production resulting from vertical turbulent fluxes of nitrate base on fluxes of heat at the sea surface in the oligotrophic water.⁶

The mechanisms of the deep chlorophyll maximum related to the nutrients supplement are still in discussion.

We have repeated the bio-optical cruise over the warm water pool since 1992. There was a contrast in a vertical distribution of phytoplankton in the water column between the warm water pool and the equatorial upwelling.

Although the eastern end of the warm water pool varied to the Kiribati Island in the La Nina stage or to the eastern

side of the international date line in the El Ninos, the general vertical distribution of chlorophyll-a and nutrients were similar in the warm water pool. In this report, we discuss the mechanism of the deep chlorophyll maximum from our measurement including chlorophyll-a concentration, nutrients, optical properties, and currents in the water column.

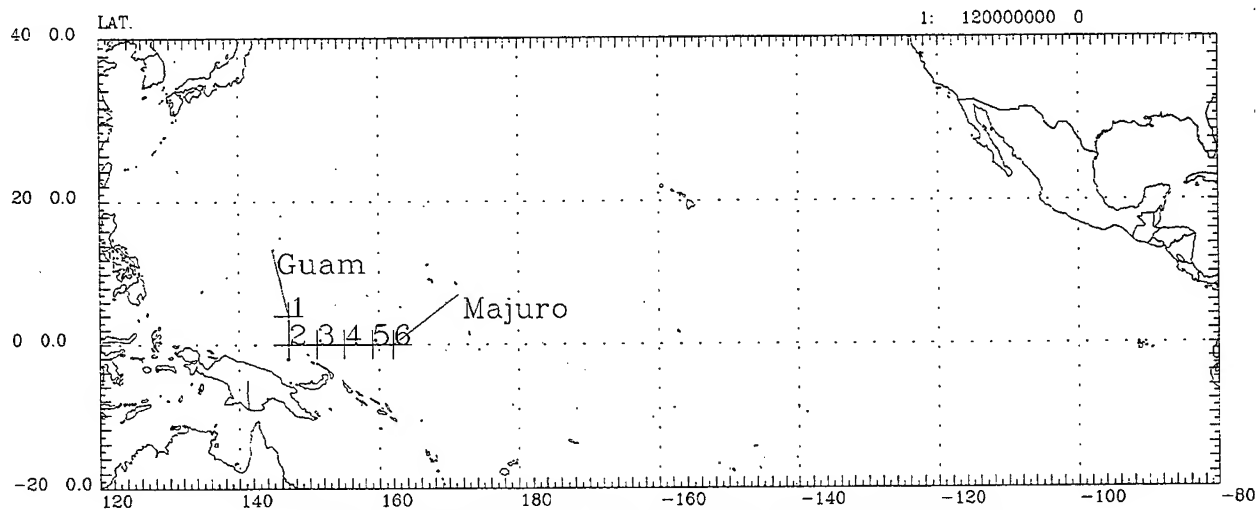


Fig.1 Cruise Track by R/V Kaiyo from Dec.24 of 1995 to Jan.3 of 1996.

2. METHODS

Fig.1 shows the cruise track of our bio-optical cruise using the research vessel Kaiyo from December 24, 1995 to January 3, 1996. We have conducted measurement and sampling at each station from 10:00 to 12:00 in local time daily with assuming the synchronized observation with the ocean color sensors on the satellite, although which were not available at that time.

2.1 Water sampling and chlorophyll-a concentration

We sampled the water from the surface using a sampling bucket, from the water column using niskin bottles attached along the Kevlar rope. Samples were filtered by Nuclear pore filter, of which pore size is $0.4 \mu\text{m}$, and soaked by Dimethyl-form-amid (DMF) in the freezer for more than 24 hours. Pigment concentrations were determined by the fluorometric determination using Turner fluorometer, by the spectrophotometric determination¹⁷ using Shimadzu spectrophotometer, and by the high performance liquid chromatography (HPLC) determination using Waters HPLC system to keep consistency of pigment analysis among different methods. For all layers at all stations, the fluorometric determination was used to determine concentrations of chlorophyll-a and pheopigment.

2.2 Photosynthetically available radiance measurement

We deployed the SeaWiFS Profiling Multichannel Radiometer System (SPMR, Satlantic Inc.). It consists of two separate instrument packages, one that floats just below the sea-surface, and one that profiles in a free-fall mode through the water column. Each of two sensors has 13 downwelling irradiance channels (Ed), and upwelling radiance channels (Eu). The 13 wavelengths are 375, 412, 443, 490, 510, 520, 532, 555, 565, 590, 670, 683, and 700 nm. The photosynthetically available radiance (EdPAR) was computed with integrating $\text{Ed}(z, \lambda)$ for all wavelength.

2.3 Current profiling

A ship mounted acoustic doppler current profiler (ADCP, RD instruments) was operated during the cruise. In this cruise, sampling depth was set from 16 m to 500 m with a sampling interval of 4 m along the depth. Data were sampled every one minute. Moving average was applied to data to reduce a noise of measurement.

2.4 CTD profiling

A CTD (SBE19 SEACAT profiler, Seabird Electronics, Inc.) with a fluorometer (Seatech Inc.) and a transmissometer (25cm at 650 nm, Seatech Inc.) was operated to get vertical profiles of temperature, salinity, fluorescence, transmittance at each station. The vertical profiles of fluorescence, which is almost corresponding to a vertical distribution of chlorophyll-a, were used to decide the sampling depth by Niskin bottles. The density profiles were computed from depth, temperature, and salinity after measurement.

2.5 Nutrients analysis

Nutrients analyses were conducted on Bran+Luebbe continuous flow analytical system (Model TRACCS 800, 4 channels) to get concentrations of Nitrate (NO_3), Nitrite (NO_2), Phosphate (PO_4), Silicate (SiO_4). The water was drawn from the Niskin bottles and immediately put into the analysis on board. As the water in the warm water pool is a nutrient depleted one, we prepared two reference for analysis of Nitrate to get higher accuracy in a low concentration. One is in the lower concentration, less than $10 \mu\text{M/l}$, and the other one is in the higher concentration, greater than $10 \mu\text{M/l}$.

3. RESULTS

In the warm water pool, we had 6 stations at $4\text{N} \ \& \ 147\text{E}$, along the equator at 151E , 155E , 159E , and 162E . Fig.2 and Fig.3 are plots of vertical profiles at 151E (St.3, Dec.,27 1995, 10:00-12:00) and 155E (St.4, Dec.,28 1995, 10:00-12:00), which are representing characteristics of the warm water pool in this cruise.

Fig.2-1 and Fig.3-1 show concentration of chlorophyll-a, concentration of nutrients, NO_3 , NO_2 , PO_4 and SiO_4 , and EdPAR%. A percentage of EdPAR (EdPAR%) at the depth relative to the EdPAR at the surface was plotted on the log scale, so as to show a big dynamic range where EdPAR decreases exponentially in the water. The nutrients were plotted also on the log scale, so as to express details of vertical distribution of NO_3 , especially for a nutrient depleted water in the surface layer.

Fig.2-2 and Fig.3-2 show vertical profiles of temperature and salinity, which are measured by CTD, and a vertical profile of density, which is computed from CTD measurement.

Fig.2-3 and Fig.3-3 show vertical profiles of current, which is measured by a shipboard ADCP, in east-west component, north-south one, and vertical one.

3.1 Chlorophyll maximum

At St.3, Fig.2-1, a concentration of chlorophyll-a was $0.1 \mu\text{g/l}$ in the surface, increased to $0.3 \mu\text{g/l}$ from 30 m to 60 m, decreased to $0.28 \mu\text{g/l}$ at 70 m, increased to $0.3 \mu\text{g/l}$ to 90 m, and decreased gradually to $0.0 \mu\text{g/l}$ at 190 m. At St.4, Fig.3-1, a concentration of chlorophyll-a was $0.12 \mu\text{g/l}$ in the surface, increased to $0.3 \mu\text{g/l}$ from 15 m to 50 m, decreased to $0.25 \mu\text{g/l}$ at 70 m, increased to $0.3 \mu\text{g/l}$ at 95 m, and decreased gradually to $0.0 \mu\text{g/l}$ at 200 m. Although St.3 showed 10 m deeper chlorophyll maximum layer than St.4, both chlorophyll maximum layer were about 40 m in depth.

3.2 Temperature and salinity

At St.3, Fig.2-2, the surface temperature was 30°C , was from surface to 80 m, and decreased to 28.5°C from 80 m to 115 m, which was the bottom of surface mixed layer. The thermocline was from 115 m to 350 m judging from CTD profile. At St.4, Fig.3-2, the surface temperature was 30°C from surface to 80 m, and decreased to 28.5°C from 80 m to 125 m. The thermocline was also from 125 m to 350 m. There were a slightly difference in the depth of surface mixed layer between two stations. There were a difference in the salinity between two stations. St.3 showed a lower salinity from the surface to 20 m, and from 40 m to 80 m less than St.4. There was a difference in the density, where St.3 showed a lower density in the surface mixed layer, but the densities in both stations were almost same in the thermocline.

3.3 Nutrients

St.3, Fig.2-1, showed a clear nitracline, NO_3 , from 95 m to 135 m, and the nitrate was equal or less than a detection limit of $0.02 \mu\text{M/l}$ in the surface mixed layer. St.4, Fig.3-1, showed a clear nitracline from 80 m to 110 m, and the nitrate was equal or less than detection limit in the surface mixed layer. The phosphate and the silicate

increased from the surface to 120 m. The nitrite showed a peak just beneath the nitracline, where it is supposed that the activity of a bacterium showed a high consumption of oxygen from the nitrate. The nitrite was under the detection level from the surface to the top of the nitracline, and below 150 m where chlorophyll-a was almost missing. In this cruise, we did not have measurement of ammonia and bacterium.

3.4 Photosynthetically available radiance

On Fig.2-1 and Fig.3-1, EdPAR% showed a moderate slope on the log scale from the surface to 25 m, a little higher slope from 25 m to 110 m, and a higher slope from 110 m and deeper. The attenuation coefficients of EdPAR, which were computed as a ratio of EdPAR along the depth, was 0.2 to 0.3 m⁻¹ from the surface to 25 m, 0.05 to 0.09 m⁻¹ from 25 to 110 m, and less than 0.03 m⁻¹ along the depth from 110 m and deeper. The three layers of the attenuation coefficients are corresponding to the surface water which shows a lower chlorophyll-a concentration, the water including chlorophyll maximum which shows a higher chlorophyll-a concentration, and the deep water which shows a lower chlorophyll-a concentration. When we define the chlorophyll maximum layer as the half of concentration between surface and maximum, the chlorophyll maximum layer was observed from 10 to 0.3 % of EdPAR%.

3.5 Current profile

On Fig.2-3 and Fig.3-3, vertical profiles of components of current are plotted. The solid line shows the east (+) or west (-) component, the dashed line shows the north (+) or south (-) component, and the small dashed line shows the up (+) or down (-) component. Fig.2-3 and Fig.3-3 showed similar profiles. There was the east-north-east flow from the surface to 60 m with a speed of 1 kt. From 60 m to 90 m, the east component changed to the west component, although there remains the north component in constant along the depth. From 90 m to 140 m, there was north-west component with a speed of 1 kt. From 140 m to 160 m, the west component changed to the east component as much as the surface. For both stations, the vertical components were not clear, but there was a down ward component from surface to 60 m at St.3., and the upward component from 90 m to deeper at St.4.

4. DISCUSSIONS

The chlorophyll maximum layer at both stations were observed in the surface mixed layer. From the surface to the top of the chlorophyll maximum layer, the concentration of chlorophyll-a was gradually increased along the depth. A vertical distribution of chlorophyll-a, Chl-a(z), could be expressed as an inverse function of EdPAR%, EdPAR%(z), as follows;

$$\text{Chl-a}(z) = C_1 \text{EdPAR}\%(z)^{-C_2} \quad \dots (1),$$

where C1 and C2 are constants for these stations. At this depth, phosphate and salinity increased with the increase of chlorophyll-a along the depth, but it was difficult to give concentrations of chlorophyll-a from both factors.

From the top of chlorophyll maximum layer to the middle of the chlorophyll maximum layer, the concentration of chlorophyll-a decreased as a function of EdPAR% to 80 m. And the concentration of chlorophyll-a increased again from 80 m to 90 or 100 m. This deeper chlorophyll maximum was observed at the top of the nitracline. Then the concentration of chlorophyll-a decreased along the depth as a function of EdPAR%, although there was a sufficient nitrate. The vertical profile of chlorophyll-a from the bottom of the chlorophyll maximum layer to 150 m, Chl-a(z), could be expressed by the next equation;

$$\text{Chl-a}(z) = C_3 \log(\text{EdPAR}\%(z)) \quad \dots (2),$$

where C3 is the constant at these stations.

The chlorophyll maximum from 50 to 100 m is the phenomenon, which could not be explained by equations (1) or (2). We could discuss this chlorophyll maximum layer from the vertical profile of current, because of the lower concentration within the chlorophyll maximum is corresponding to the depth where the east component changed to the west component. It means that the top portion of the chlorophyll maximum layer and the bottom portion of the

chlorophyll maximum layer was located between two different water mass.

As the nitrate was not detected at the top portion of the chlorophyll maximum, we could suppose the chlorophyll maximum to be maintained by a reproduction, where nitrogen from ammonium may be a major source for the reproduction.

In the lower portion of the chlorophyll maximum layer, the chlorophyll maximum is maintained by the new production with the sufficient supply of nitrate at the top of nitracline.

5. CONCLUSION

Through the bio-optical measurement over the equatorial warm water pool, we could discuss the vertical structure of the chlorophyll maximum layer. The chlorophyll-a from the surface to 50 or 60 m, which is corresponding to the water with a low chlorophyll-a concentration in the surface and to the top of the chlorophyll maximum layer, was expressed as the inverse function of EdPAR%. The chlorophyll-a from 100 or 110 to 150 m, which is corresponding to the water from the bottom of chlorophyll maximum layer to the water with a low chlorophyll-a concentration, was expressed as logarithm function of EdPAR%.

As we could observe the different current streams within the surface mixed layer by the ship-mounted ADCP, we could make a new hypothesis on the generation of chlorophyll maximum layer in the warm water pool. The chlorophyll maximum layer is separated into two parts by the different current streams. The top portion of the chlorophyll maximum layer is in the east-north-east current. As the nitrate in this layer is depleted, it is supposed the chlorophyll maximum to be maintained by the reproduction, where nitrogen from the ammonium is the major source for the reproduction. The deeper portion of the chlorophyll maximum layer was on the top of the north-west current. The peak of the north-west current is corresponding to the top of the thermocline and the nitracline. As the deeper portion of the chlorophyll maximum layer was observed just above the nitracline, it is supposed the chlorophyll maximum to be maintained by the new production.

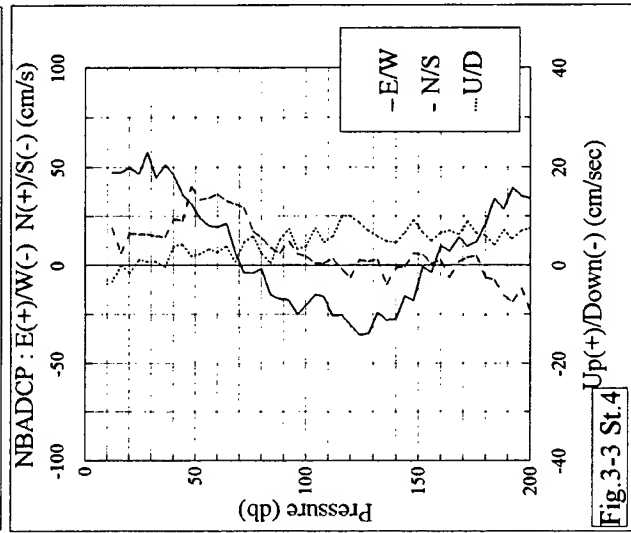
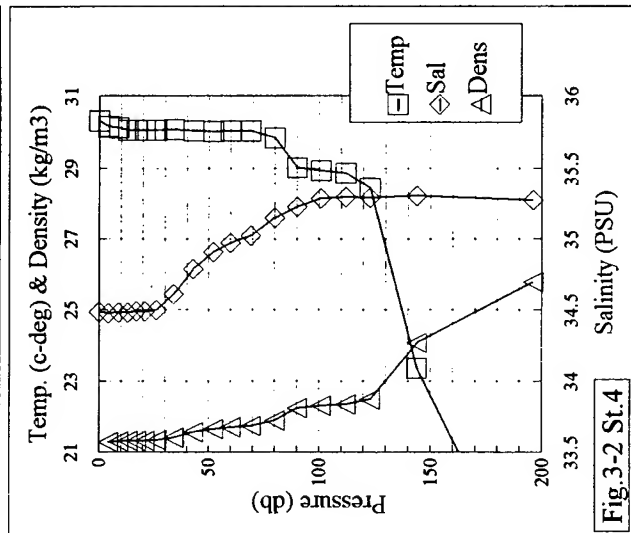
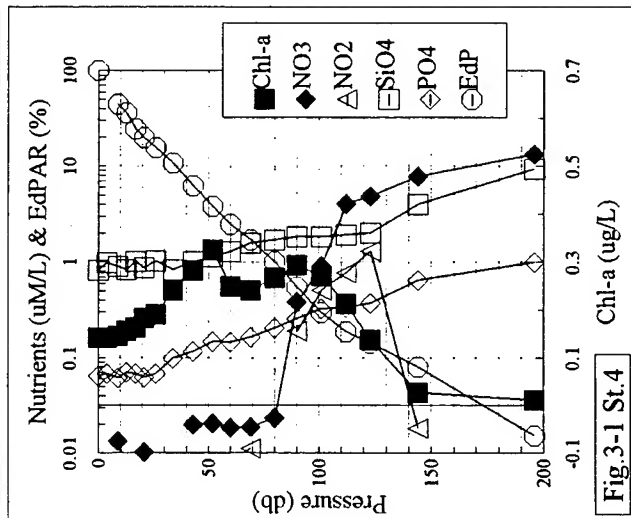
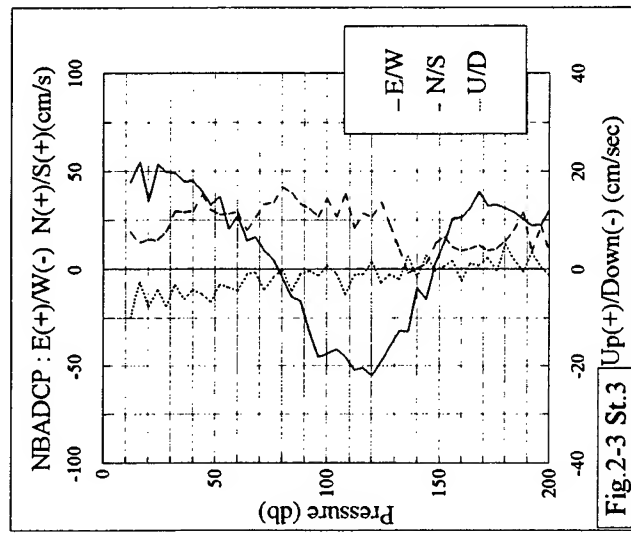
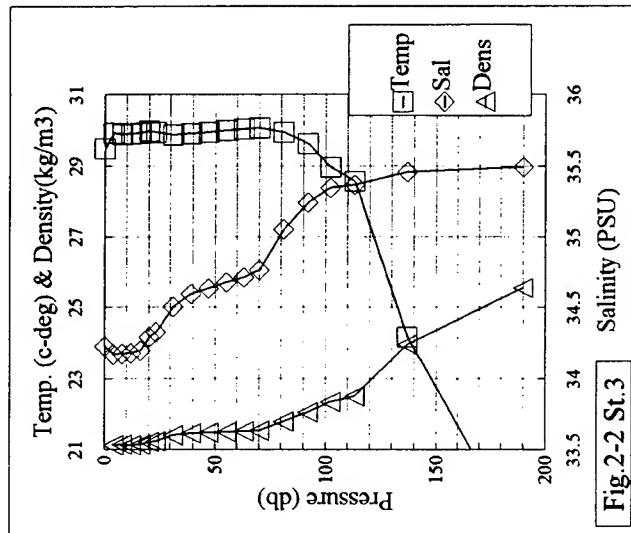
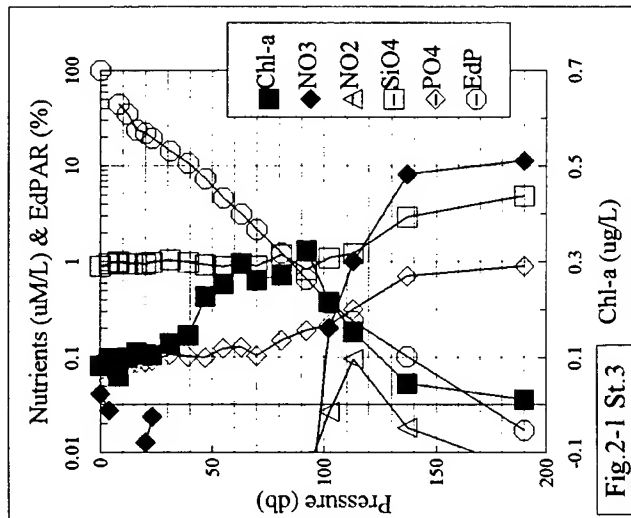
6. ACKNOWLEDGEMENTS

Authors wish to thank Capt. Ishida and his crews of the R/V Kaiyo for the water sampling and measurement.

7. REFERENCES

1. Wells, N., *The Atmosphere and Ocean: A Physical Introduction*, Taylor & Francis, London and Philadelphia, 347pp, 1986.
2. Pickard, G.L., and W.J. Emery, *Descriptive Physical Oceanography: An Introduction*, Pergamon Press, 249pp, 1982.
3. Lewis, M.R., M.E. Carr, G.C. Feldman, W. Esaias, and C. McClain, Influence of penetrating solar radiation of the heat budget of the equatorial Pacific Ocean, *Nature*, 347, 543-545, 1990.
4. Pak, H., D.A. Kiefer, and J.C. Kitchen, Meridional variations in the concentration of chlorophyll and microparticles in the North Pacific Ocean, *Deep-Sea Res.*, 35, 7, 1151-1171, 1988.
5. Siegel, D.A., J.C. Ohlmann, L. Washburn, R.R. Bidigare, C.T. Nossé, E. Fields, and Y. Zhou, Solar radiation, phytoplankton pigments and the radiant heating of the equatorial Pacific warm pool, *J.G.R.*, 100, C3, 4885-4891, 1995.
6. Pena, M.A., M.R. Lewis, & J.J. Cullen, New production in the warm waters of the tropical Pacific Ocean, *J.G.R.* 99, C7, 14255-14268, 1994.
7. Moran, R., Formulae for Determination of Chlorophyllous Pigments Extracted with N,N-Dimethylformamide, *Plant Physiol.*, 69, 1376-1381, 1982.

This research is partly supported by the special coordination fund of the Science and Technology Agency of Japan.



Ground truthing modeled k_{PAR} and on deck primary productivity incubations with *in situ* observations

Richard T. Barber, Lisa Borden and Zackary Johnson

Duke University, Nicholas School of the Environment, Marine Laboratory
135 Duke Marine Lab Road, Beaufort NC 28516

John Marra and Carol Knudson
Lamont-Doherty Earth Observatory of Columbia University
Palisades NY 10964

Charles C. Trees
San Diego State University, Center for Hydro-Optics and Remote Sensing
San Diego CA 92182

ABSTRACT

The Arabian Sea Process Study carried out on six cruises in 1995 provided observations that make possible the ground truthing of model estimates of k_{PAR} and on deck productivity incubations with direct k_{PAR} observations and *in situ* productivity incubations. The Morel 1988 optical model did a good job of reproducing the observed values (Obs. = $0.994 \text{ Modeled} + 0.004$; $r^2 = 0.75$). Comparison of on deck and *in situ* depth profiles suggested that on deck incubators received more irradiance across the entire light gradient. This subsidy in E_0 apparently came from efficient absorption of reflected light and low angle sunlight by small (30 x 20 x 20 cm) incubators. When depths were recalculated taking into account the irradiance subsidy, profiles of productivity as a function of depth determined by on deck incubations were essentially identical to *in situ* profiles.

Keywords: primary productivity, irradiance, k_{PAR} , *in situ* incubation, Arabian Sea, areal productivity, productivity methods, modeled k_{PAR} , extinction models, optical models

1. INTRODUCTION

In situ primary productivity incubations are less prone to several kinds of systematic errors than on deck incubations because *in situ* photosynthesis is driven by a real oceanic light gradient over a known depth gradient. However, *in situ* primary productivity determinations are costly in ship time because they require about 20 - 30 hours on station, and each station must start at 2 - 3 hours before dawn. The time on station and required phase lock with the light cycle make *in situ* incubations incompatible with most general purpose oceanographic cruises.

Calculation of vertical profiles and areal productivity rates from on deck incubations requires an independent estimate of extinction, k_{PAR} , to assign percent light depths. The on deck method measures carbon uptake in a series of incubators in which each incubator reduces light to a fixed percent of the incident light, or to a given "percent light level".¹ To calculate areal productivity, it is necessary to assign a depth to each percent light level and integrate the carbon uptake profile. Assignment of depths to percent light levels is frequently problematic.

2. BACKGROUND

Analysis of on deck estimates of primary productivity in the equatorial Pacific made from a variety of ships in the 1980's showed that the process of determining k_{PAR} and assigning a depth to each percent light level was the largest source of variation in estimating primary productivity.² This was true regardless of whether *in situ* radiometry or a Secchi disk was used. Secchi disk readings are known to vary systematically with sea state, wind speed and ship size,³ but subsurface irradiance measurements (in the 1980's) were not standardized and, even now, reliable results require experienced personnel. Multi-purpose survey cruises on which primary productivity has been measured usually have not had a dedicated optics technician on board.

To eliminate individual, ship and cruise dependent sources of variability in the estimation of k_{PAR} and assignment of light depths, Barber and Chavez² used André Morel's optical model⁴ that estimates the profile of light extinction based on a profile of extracted chlorophyll concentrations. An advantage of using the Morel model to estimate k_{PAR} and assign light depths is that it is possible to reprocess productivity and chlorophyll data from a variety of sources and eliminate one major source of systematic error. This is useful for asking interannual and decadal questions about changes in productivity, but one particularly important application of this procedure is to reprocess productivity estimates from various ships and cruises for testing satellite algorithms of primary productivity.

3. MODELED VERSUS OBSERVED k_{PAR}

There have been few opportunities to test model estimates against direct measurements of k_{PAR} ; the US JGOFS Arabian Sea Process Study provided such an opportunity. Two kinds of direct measurements of k_{PAR} are available to ground truth the model estimates. The Lamont-Doherty Earth Observatory (LDEO) method measured subsurface irradiance with Biospherical Instruments QSP-200 PAR sensors and data loggers attached to the line of the *in situ* primary productivity array at 3 or 4 depths and deployed from before dawn to after dark. The Center for Hydro-Optics & Remote Sensing of San Diego State University (CHORS) method used a Biospherical Instruments MER-2040 deployed at local noon to determine the irradiance profile. Morel model estimates are made with the optical model program provided by André Morel (Laboratoire de Physique et Chimie Marines, Villefranche-sur-mer, France). The productivity procedures followed JGOFS protocols⁵; see also <http://www1.whoi.edu/eqpac-docs/proto.html>.

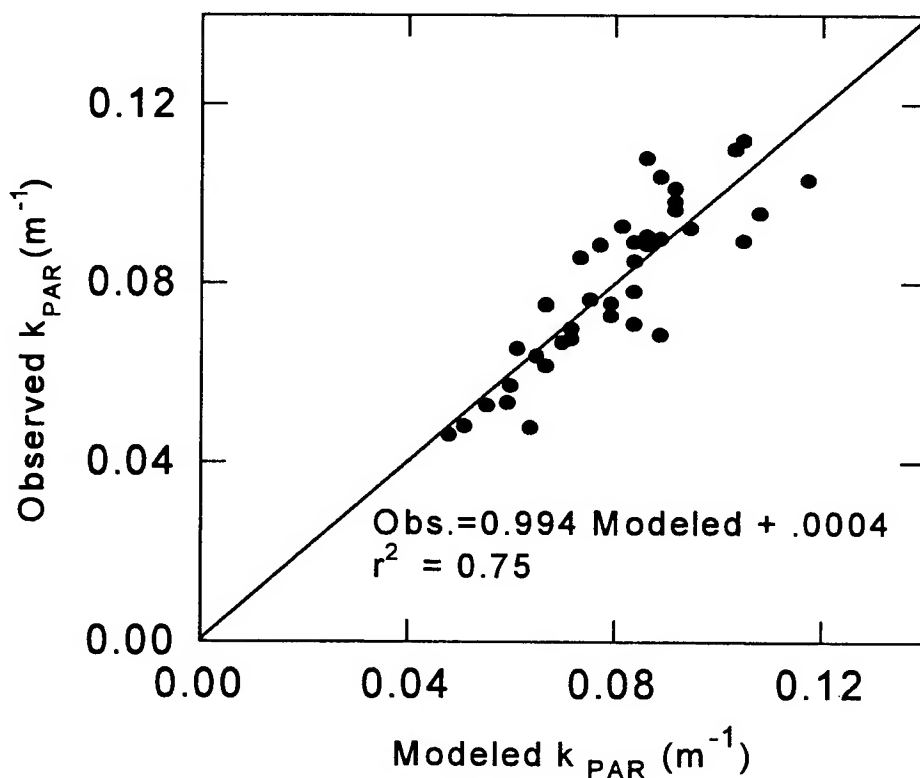


Fig. 1. Regression of LDEO observed k_{PAR} vs modeled k_{PAR} for Arabian Sea Process Cruises 1, 2, 4, 5, 6 and 7.

How does modeled k_{PAR} compare with observed k_{PAR} ? As shown in Fig. 1 the Morel model does a good job of reproducing the LDEO estimates of k_{PAR} . The slope is about 1.0, the intercept about zero and the r^2 is highly significant. For the CHORS estimates r^2 was about the same (0.73), but the slope was somewhat higher (Obs. = 1.165 Modeled = 0.0121).

4. IN SITU VERSUS ON DECK PRODUCTIVITY

On the Arabian Sea Process Study simultaneous on deck and *in situ* incubations were carried out on water drawn from the same sample bottle and treated identically except for the incubation procedure. When on deck carbon fixation values from the southern US JGOFS transect (See Marra *et al.*, this volume for the location of the transect) were plotted as depth profiles using the depths determined by the Morel model and compared with *in situ* profiles, the on deck values had a consistent depth offset of about +9m (see Figs. 2 - 4, profiles on the left labeled 1st Iteration). In determining this offset, we assume that equal production levels are the result of equal light availability. The offset consistently occurs throughout the water column indicating a systematic error. Since we have independently verified that there is no systematic error with the Morel model determined attenuation coefficients (Fig. 1), the only remaining variable that influences the determined light depth is the incubator light percentage,

$$\frac{E_{OD}}{E_{-o(in situ)}} = e^{-kz} \quad (1)$$

where E_{OD} is the on deck incubator irradiance, $E_{-o(in situ)}$ is the *in situ* surface irradiance, $\frac{E_{OD}}{E_{-o(in situ)}}$ is the nominal incubator light percentage, k is the Morel determined attenuation coefficient, and z is the corresponding light depth. On the left side of Figs. 2-4, we have used nominal incubator light percentages to determine light depths utilizing equation (1) by solving for z ; that is, we used the transmittance of the incubator and assumed incoming irradiance was equal to the incoming *in situ* irradiance. Using these assumptions, we get a consistent depth offset of +9m. We can calculate the error of our nominal light percentages with the offset of +9m between the *in situ* and on deck production values using equation (2),

$$E'_{OD} = E_{OD} e^{-k_{PAR}(z'-z)} \quad (2)$$

where E_{OD} is the irradiance for a given on deck nominal incubator light percentage, E'_{OD} is the irradiance estimated from the *in situ* production curve, k_{PAR} is the mean attenuation coefficient for the water column, z is the apparent light depth calculated using equation (1), and z' is the depth of the corresponding *in situ* production value. Taking the depth of the same production value on the *in situ* production curve as indicative of the true light field, $(z'-z)$ becomes -9m; that is, the on deck productivity values should be shifted 9m towards the surface. Note that depth is defined as decreasing towards the surface. Utilizing the mean cruise PAR attenuation coefficient k_{PAR} of 0.08m^{-1} , the ratio of E'_{OD} (irradiance estimated from the *in situ* production curve) to nominal E_{OD} reduces to,

$$\frac{E'_{OD}}{E_{OD}} = e^{-k_{PAR}(z'-z)} = e^{-0.08(-9)} = 2.05 \quad (3)$$

This suggests that the on deck incubators are actually receiving 205% of the nominal light percentage values. Thus, the nominal light percentage values used to calculate the depth profiles given on the left hand side of Figs. 2-4 of:

93, 75, 44, 27, 14, 7, 4 and 1% of $E_{-o(in situ)}$ (1st Iteration)

are recalculated actually to be:

191, 154, 90, 55, 29, 14, 8, 2% of $E_{-o(in situ)}$ (Recalculated)

The Morel model was rerun using the original observed chlorophyll profile and the new light percent values to recalculate correct depths for the new light percent values. In Fig. 2 - 4 on deck profiles with recalculated depths are shown together with *in situ* profiles in the three pairs of profiles on the right. Obviously, the recalculated profiles agree more closely with observed *in situ* profiles of carbon uptake.

The source of the irradiance subsidy for this particular design of on deck incubator is easily explained. In the Arabian Sea Process Study the on deck method was changed by the introduction of small incubators (that were each constructed of different materials to achieve proper spectral balance). The on deck incubators were small Plexiglas boxes (about 30x20x20 cm) mounted approximately 25 cm apart on a table on the fantail of the ship. It appears that the small incubators were functioning to some degree like 4π collectors efficiently absorbing through the side panels both light reflected off the deck and low angle solar irradiance. Using small incubators each made of different color Plexiglas was a good way to achieve spectral accuracy, but the large surface to volume ratio made the small incubators into overly efficient light absorbers.

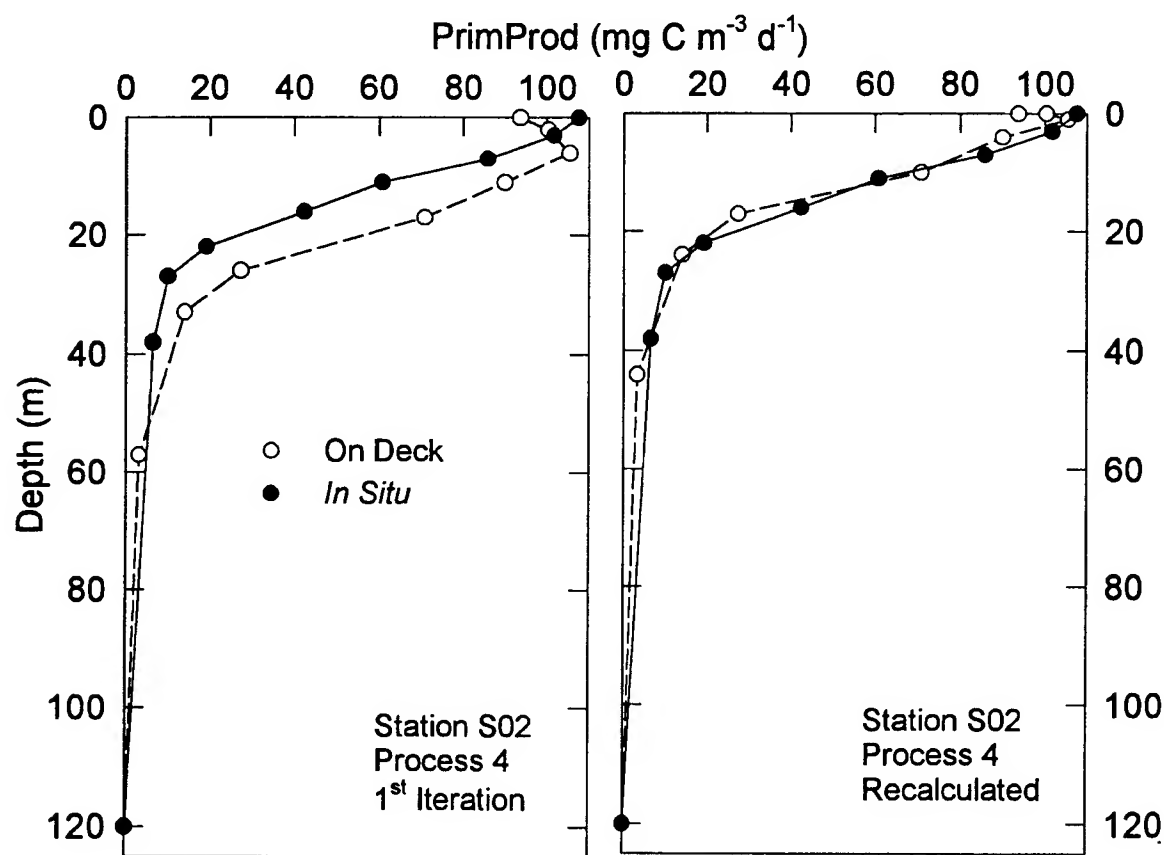


Fig. 2. Vertical profiles of on deck and *in situ* primary productivity. The pair of profiles on the left assumes that E_{OD} and $E_{o(in situ)}$ were equal. The pair of profiles on the right assumes that E'_{OD} was 2.05 times $E_{o(in situ)}$; therefore, each on deck productivity value was plotted at a shallower depth.

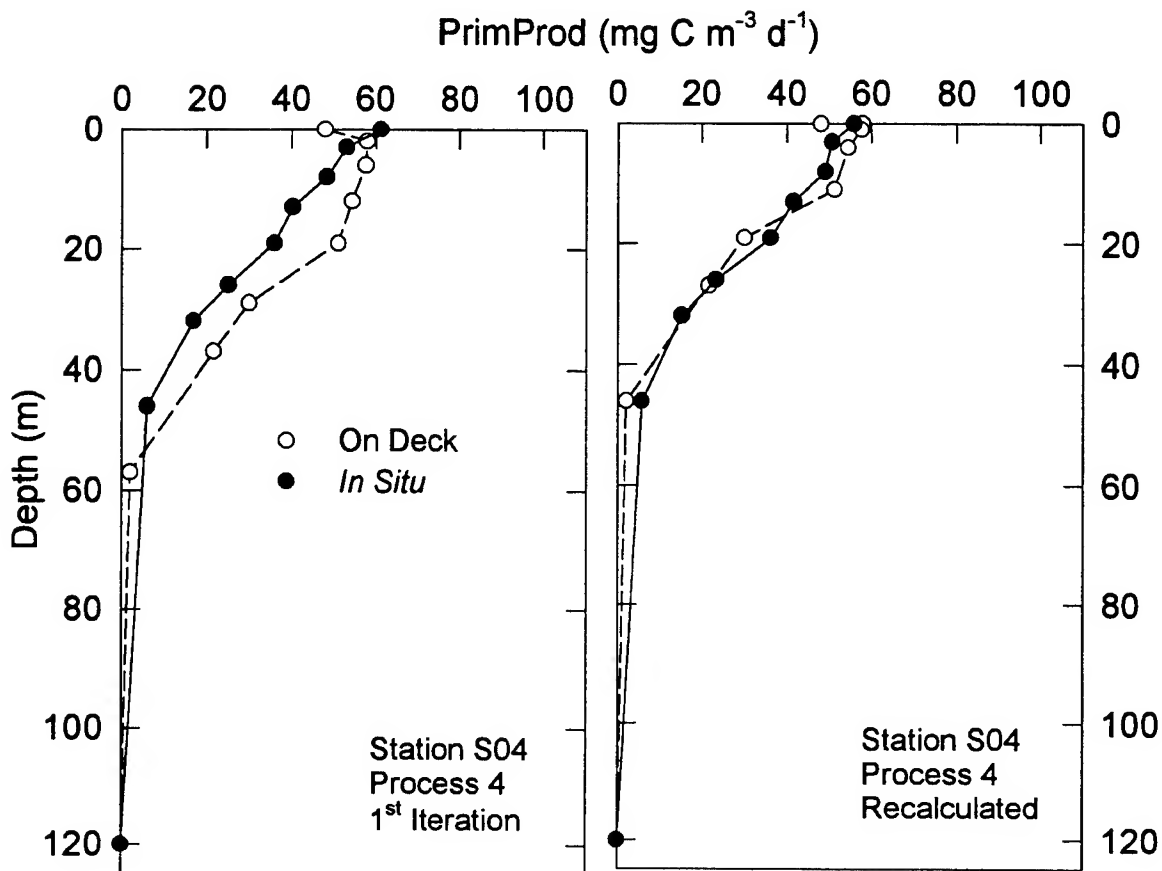


Fig. 3. Vertical profiles of on deck and *in situ* primary productivity. The pair of profiles on the left assumes that E_{OD} and $E_{o(in situ)}$ were equal. The pair of profiles on the right assumes that E'_{OD} was 2.05 times $E_{o(in situ)}$; therefore, each on deck productivity value was plotted at a shallower depth.

5. CONCLUSIONS

1. The Morel (1988) model is effective for estimating k_{PAR} and assigning light depths using observed chlorophyll profiles. In particular, the model is an efficient and accurate way to reprocess historical on deck incubation data to make basinwide or global comparisons.
2. The new design of small, spectrally adjusted on deck incubators used in the Arabian Sea Process Study were subject to systematic error because they efficiently absorbed reflected and low angle irradiance. When appropriate corrections were made for the additional irradiance, on deck profiles were essentially identical to *in situ* profiles.
3. On deck incubation methods can provide accurate estimates of primary productivity, but ground truthing with *in situ* methods is necessary for each on deck incubation protocol.

6. ACKNOWLEDGMENTS

This is U. S. JGOFS Contribution 338. It was supported by NSF Grant OCE-9312355.

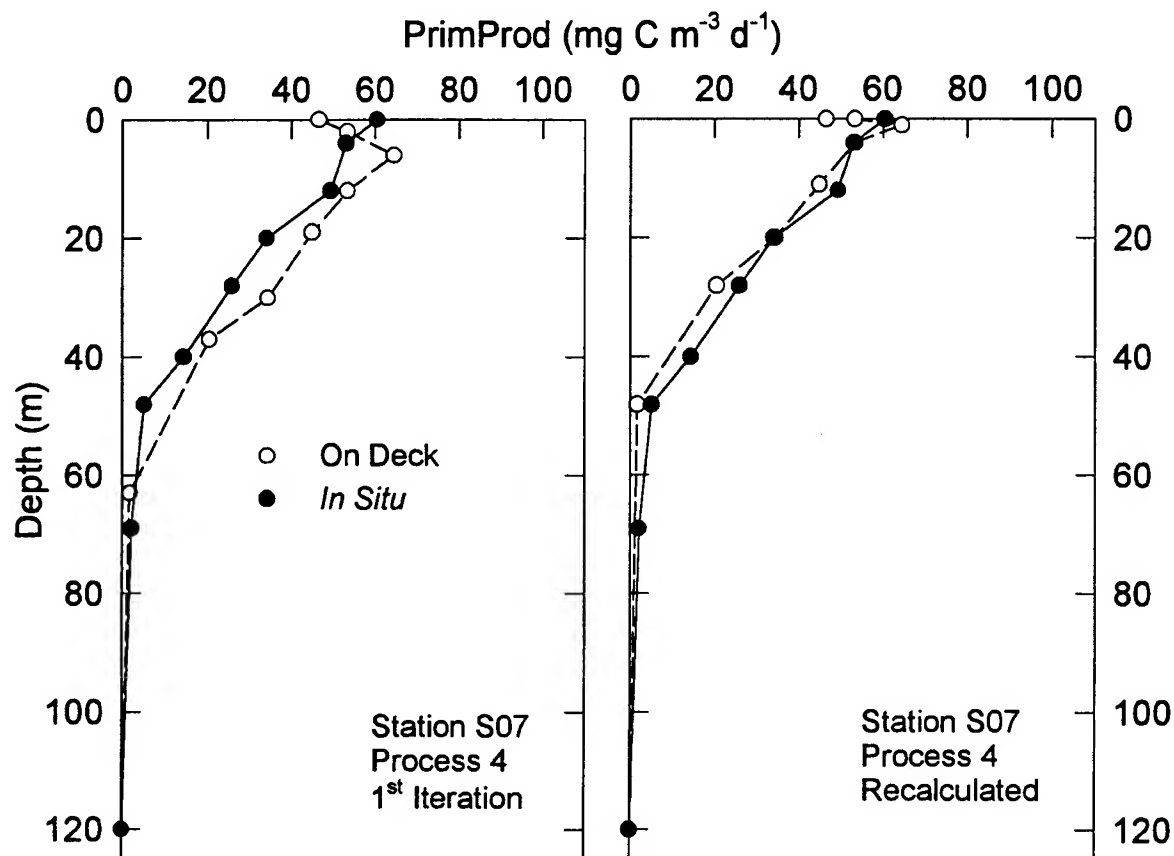


Fig. 4. Vertical profiles of on deck and *in situ* primary productivity. The pair of profiles on the left assumes that E_{OD} and $E_{o(in situ)}$ were equal. The pair of profiles on the right assumes that E'_{OD} was 2.05 times $E_{o(in situ)}$; therefore, each on deck productivity value was plotted at a shallower depth.

7. REFERENCES

1. Ryther, J. H., J. R. Hall, A. K. Pease, A. Bakun and M. M. Jones (1966) Primary production in relation to the chemistry and hydrography of the western Indian Ocean. *Limnol. Oceanogr.*, 11:371-380.
2. Barber, R. T. and F. P. Chavez (1991) Regulation of primary productivity rate in the equatorial Pacific Ocean. *Limnol. Oceanogr.*, 36:1803-1815.
3. Priesendorfer, R. W. (1986) Secchi disk science: Visual optics of natural waters. *Limnol. Oceanogr.*, 31:909-926.
4. Morel, A. (1988) Optical modelling of the upper ocean in relation to its biogenous matter content (Case I waters). *Journal of Biophysical Research*, 93:10749-10768.
5. Barber, R. T., M. P. Sanderson, S. T. Lindley, F. Chai, J. Newton, C. C. Trees, D. G. Foley and F. P. Chavez (in press) Primary productivity and its regulation in the equatorial Pacific during and following the 1991-92 El Niño. *Deep-Sea Research II*.

PUMP-DURING-PROBE FLUOROMETRY OF PHYTOPLANKTON: GROUP-SPECIFIC PHOTOSYNTHETIC CHARACTERISTICS FROM INDIVIDUAL CELL ANALYSIS

Chekalyuk, A.M., Olson, R.J., Sosik, H.M.
Woods Hole Oceanographic Institution, Woods Hole, MA 02543, USA

ABSTRACT

Saturating-flash fluorescence techniques are used to monitor the state of the photosynthetic apparatus in phytoplankton under natural conditions. At present these are bulk water measurements, which produce estimates of average properties of all the fluorescent particles present in a sample. Here we describe an improved approach for single-cell measurements of phytoplankton.

We have combined individual-cell "pump-during-probe" (PDP) measurements of chlorophyll (Chl) fluorescence induction on the time scale of 30 to 100 microseconds [1, 2] with flow cytometric (FC) characterization of each cell, to obtain population-specific photosynthetic characteristics. The results provide information about the potential quantum yield of photochemistry (Φ_p), the fraction of functional reaction centers (f), and the functional absorption cross section for photosystem 2 (σ_{PS2}).

Key words: phytoplankton, photosynthesis, fluorescence, technique, pump-during-probe, induction

1. CHL FLUORESCENCE INDUCTION AND PHOTOSYNTHETIC CHARACTERISTICS

The biophysical background of the PDP approach is discussed in [1, 2]. To a first approximation, fluorescence induction at the time scale of 30-100 μ s under supraoptimal light intensity I can be described as

$$\Phi_f(t) = (\Phi_m^{-1} - (\Phi_m^{-1} - \Phi_o^{-1}) e^{-\alpha t})^{-1}, \quad (1)$$

where Φ_o and Φ_m are initial and maximum values of Chl fluorescence yield, and α is the rate constant of closing of PS2 reaction centers (RCs, $\alpha = \sigma_{PS2} I$). The magnitudes of Φ_m , Φ_o and α can be retrieved using nonlinear regression of a measured PDP induction curve to equation (1), and the photosynthetic characteristics can be estimated as

$$\Phi_p = (\Phi_m - \Phi_o) / \Phi_m, \quad f = (\Phi_{p_{max}}^{-1} - 1) / (\Phi_p^{-1} - 1), \quad \sigma_{PS2} = \alpha / I. \quad (2)$$

The maximum PS2 photochemistry efficiency for phytoplankton, $\Phi_{p_{max}}$, is known to be 0.65 [3].

2. THE EXPERIMENTAL TECHNIQUE

We measure the time course of chlorophyll fluorescence yield during a 100 μ s excitation flash provided by a weak 488 nm argon ion laser whose beam passes through an electro-optical modulator, while a strong laser beam for measuring conventional FC parameters is blocked by an electromechanical shutter (Figs. 1, 2). A cell detector based on an infrared diode laser triggers the PDP and subsequent FC measurements. Since both analog and photon counting detection techniques are used, cells ranging in size from $<0.7 \mu$ m (prochlorophytes) to $>30 \mu$ m can be assayed.

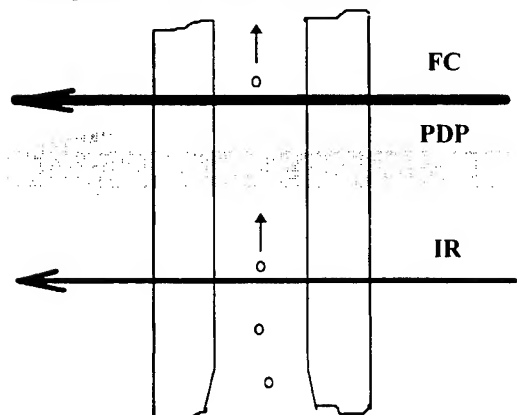


Fig 1. Schema of the flow cell with the IR, PDP and FC laser beams.

The optical setup (Fig. 2) includes an Ar ion laser (488 nm, 350 mW), splitters S1 and S2 (20% transmission), an electro-mechanical shutter (100 μ s opening time) which is normally closed to prevent distortions in PDP induction, an electro-optic modulator (1 μ s opening time) which produces a 100- μ s PDP pulse, and an infrared (785 nm, 50 mW) laser. Spherical lenses (L1, L2, $f = 80$ and 100 mm) and cylindrical lenses (L3-L10, $f = 50$ mm) are used to shape the beams.

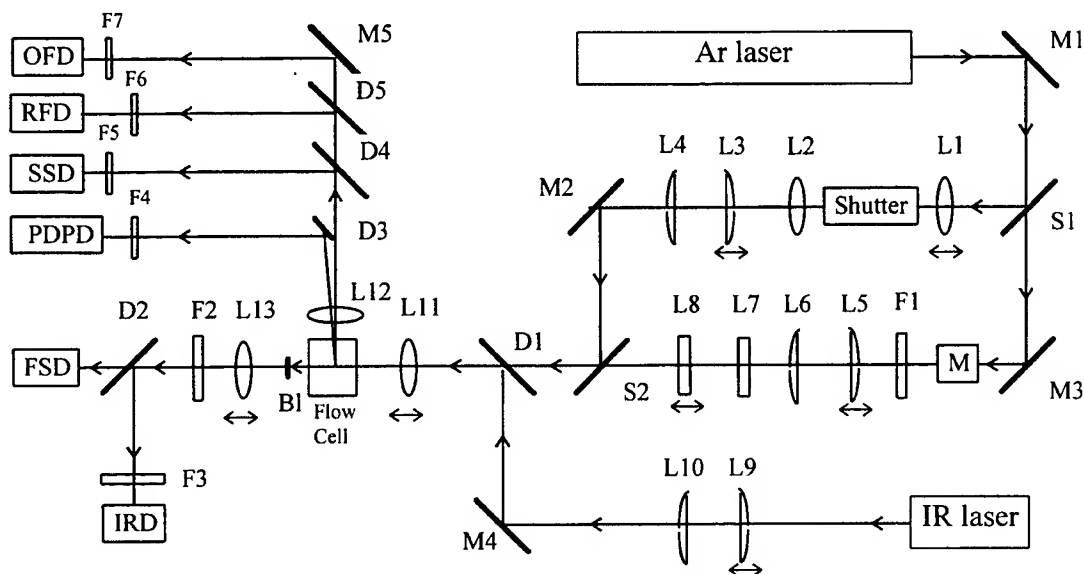


Fig. 2 Schema of the optical part of the PDP flow cytometer.

The achromatic lens L11 ($f = 38$ mm) provides focusing of the IR, PDP and conventional FC beams as presented in Fig.1. Lenses L7 and L8 increase the vertical divergence of the PDP beam, resulting in vertical widening of the PDP laser spot in the flow cell and an almost rectangular PDP "pulse" with opening of the modulator. Translations of L3, L5 and L8 allow independent adjustment of the horizontal size of the PDP and FC laser spots. Dichroic filter D1 serves to direct the IR beam to the flow cell. Lens L12 (from a Becton-Dickinson FACScan) and spherical lens L13 ($f = 30$ mm) are used for collection of side and forward optical signals from the the flow cell. Blue and IR forward scattered (FS) signals are split by dichroic filter D2 and detected by a photodiode (FSD) and an avalanche photodiode (IRD), respectively. Neutral density filters F1 and F2 are used for adjustment of the PDP beam and FS signals to appropriate levels. Dichroic filters D3, D4, D5, and a mirror M5 provide splitting of the side optical signals and, after filtering with F4, F5, F6 and F7 filters, direction to PMT detectors for PDP (PDPD), side scattering (SSD), red fluorescence (RFD), and orange fluorescence (OFD).

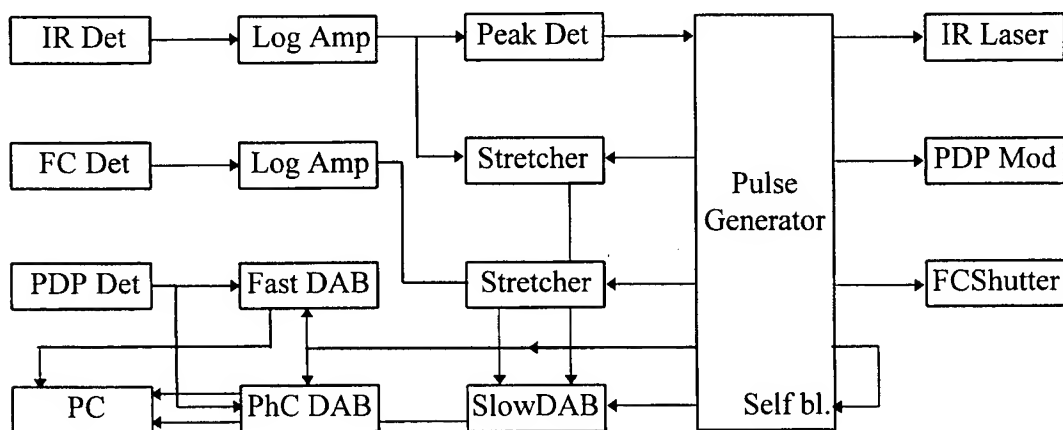


Fig. 3 Simplified schema of the PDP FC electronics.

A simplified schema of PDP FC electronics is presented in Fig. 3. It consists of the IR triggering channel, a conventional FC measuring part, and the PDP measuring channel. Since FC channels for measuring forward scattering, side scattering, orange and red fluorescence are almost identical, we show just one "FC" channel in Fig. 3. 4.5-decade logarithmic amplifiers (Log Amp) are used to maximize the dynamic range in both IR and FC channels. Stretcher modules catch and hold the peak amplitudes of cell-produced pulses in IR and FC channels. An 8-channel 100-KHz ADC computer board (Slow DAB) measures these amplitudes on triggering from a timing pulse generator. This generator also provides resets of the stretchers after each measuring cycle, self-blocking to avoid triggering by new cells during event processing, blocking the IR laser to reduce background when measuring the PDP and FC response, pulsed opening of the PDP modulator (PDP Mod) and the FC beam shutter (FC shutter), and triggering of data acquisition in the PDP channel. This channel includes a PMT (PDP Det), a 60-Mhz analog ADC (Fast DAB) and time-resolved photon counting (PhC DAB, 2- μ s resolution) boards installed (along with the Slow DAB) in a 100-MHz Pentium personal computer (PC). Fig. 4 shows a timing diagram of the system.

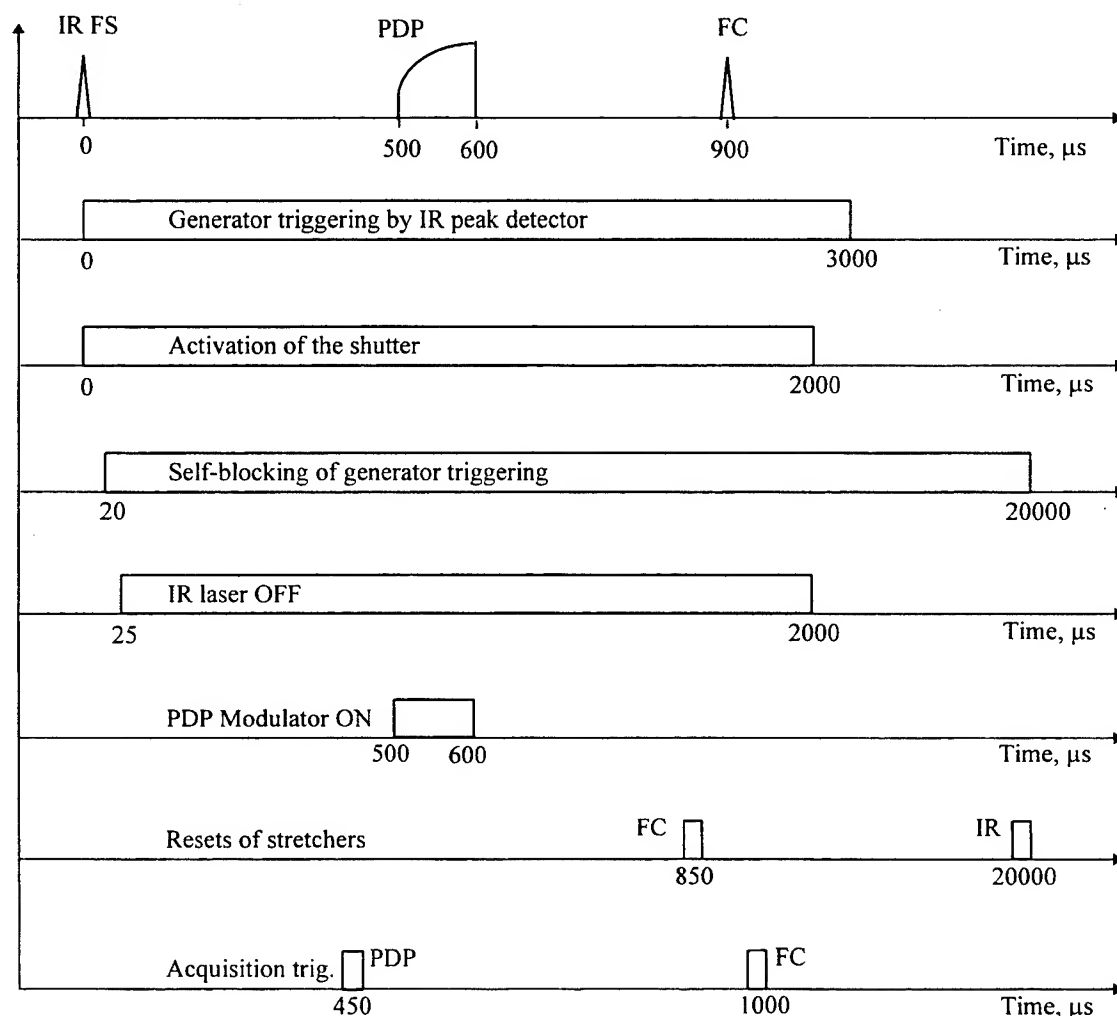


Fig. 4 Timing diagram of the PDP electronics.

A specially developed data acquisition software runs under Windows and allows real-time control of Fast DAB, Slow DAB, PhC DAB, and storage of both the PDP induction curve and FC data for each cell in the PC memory and on the hard drive. Due to substantial amount of information to be acquired (about 1.6 Kbyte per cell), we use a CD recording system for permanent data storage after finishing the measurement. Typically we accumulate 1,000 to 25,000 events from each sample. An analysis of conventional FC data allows specification of cells or cell groups in the sample for retrieving individual or group-specific photosynthetic characteristics. In analog mode, either individual cell curves (for cells $> 5 \mu\text{m}$) or curves averaged over a group of cells can be reconstructed; in photon counting mode data from hundreds to thousands of cells are accumulated for each PDP induction curve.

We measure the fluorescence time course of red-fluorescing latex microspheres, added to the sample, to monitor the shape of the excitation "pulse", i.e. the light intensity profile in the PDP area within the core of the flow cell. The PDP induction curves are then normalized to this profile to compensate for deviations from the "ideal" rectangular shape. The intensity of the PDP laser beam was adjusted with neutral-density filters (F1 in Fig. 2) to obtain cell fluorescence rise times of approximately 30-100 μs , and the rate of sample introduction was adjusted to ensure that only one cell was in the PDP beam at any given time.

3. LABORATORY TESTS OF THE PDP APPROACH

The results of preliminary laboratory tests of the PDP approach were presented in (Olson et al. 1995, 1996). In particular, for six species of phytoplankton grown under different conditions of light intensity and nutrient depletion, estimates of the quantum yield of photochemistry in PS2 by PDP measurements made on individual cells were well correlated with estimates derived from DCMU-enhancement measurements of bulk samples (Fig. 5). Part of the measurements was made with a microscope-based PDP system (Olson et al. 1995, 1996). No obvious differences were observed between the two PDP instruments or among the six species tested. These results indicate that the microscope- and flow cytometer-based PDP techniques, applied to individual cells, provide reliable information about the photosynthetic characteristics of phytoplankton.

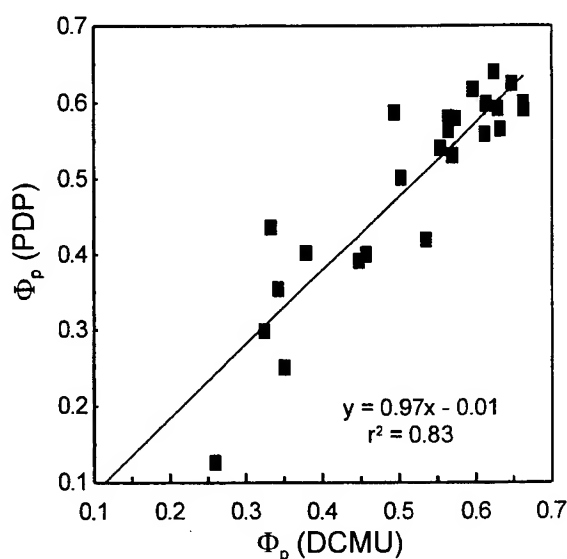


Figure 5. Correlation between PDP-based estimates of Φ_p and estimates derived from bulk measurements of DCMU enhancement of fluorescence.

We have recently tested the use of a compact solid-state green laser (100 mW, 532 nm) in the PDP FC system. Although we observed an apparent decrease in the efficiency of Chl fluorescence excitation (due to the lower absorption cross-section as compared to the blue region of the spectrum), the green laser appeared to be suitable for both FC and PDP measurement of relatively big ($>1 \mu\text{m}$) cells. In Fig. 6 we present results of a sample containing a mixture of *Dunaliella tertiolecta* (5-7 μm cells, DT) and *Nannochloris* sp. (2-3 μm cells, N). 1- μm red beads (BD) were used for monitoring the PDP profile in the flow cell. This profile was used to normalize PDP intensity profiles for the two species (panel B in Fig. 6). Processing of the PDP induction curves (see Fig. 6-C) was done based on equations (2). Due to unfavorable nutrient conditions both species indicated moderate photosynthetic performance:

	DT	N
Φ_p	0.51	0.38
f	0.56	0.32

In fact, just one third of PS2 reaction centers were active in the case of *Nannochloris* sp., and about 50% for *Dunaliella tertiolecta*.

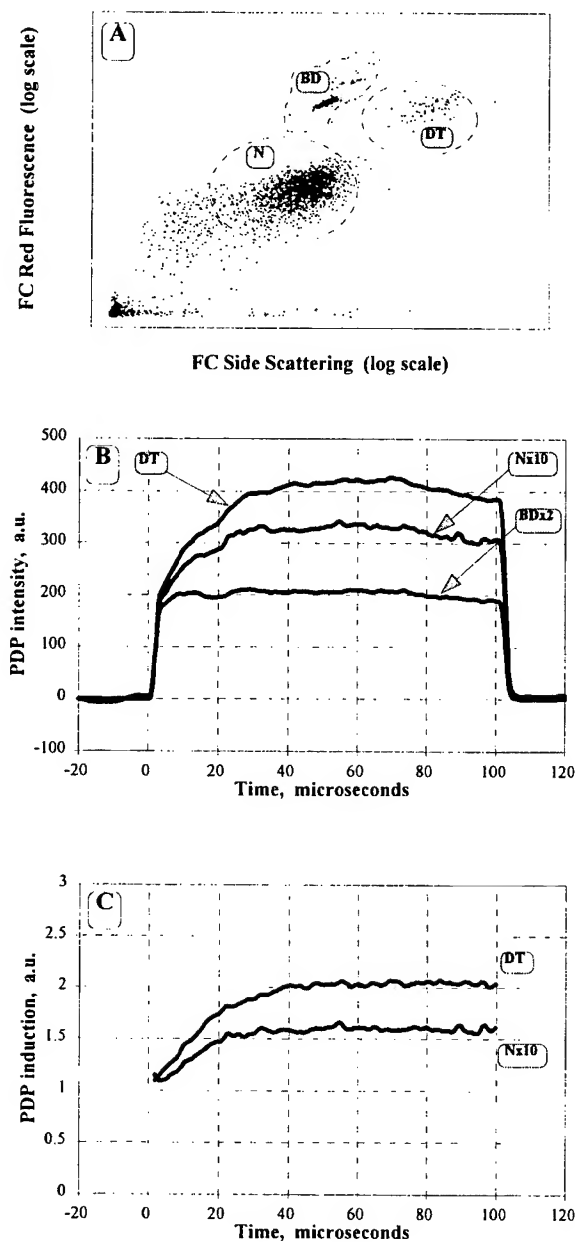


Fig. 6 PDP FC measurement of a mixture of *Dunaliella tertiolecta* (DT) and *Nannochloris* sp. (N), and 1- μ m red beads (BD). The solid-state green laser (100 mW, 532 nm) was used. Panel A: FC red fluorescence vs. FC side scattering (5,000 events); B: PDP intensity profiles for different sample components, reconstructed based on individual PDP curves; panel C: PDP induction curves for two species, obtained by normalizing corresponding PDP intensity profiles to BD PDP profile.

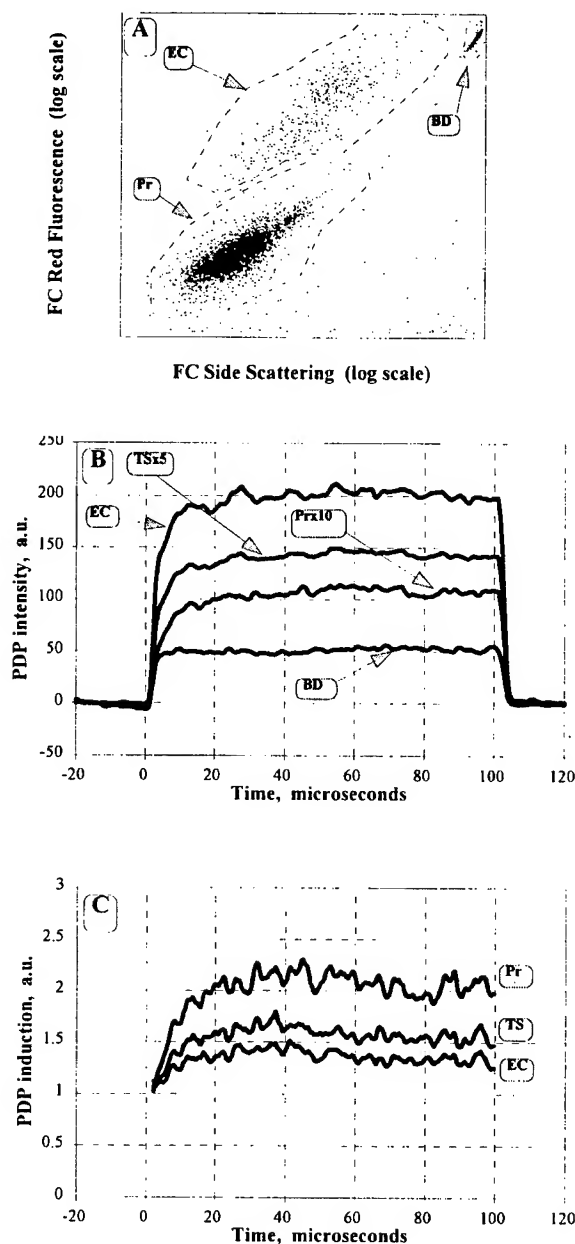


Fig. 7 Analysis of group-specific PDP induction curves for a natural sample of sea water (279 Oceanus Cruise, June 1996, Gulf Stream, Chl maximum at 80 m). Panel A: prochlorophytes (Pr) and small eukaryotic phytoplankton (EC) are well defined along with 2- μ m Nile Red beads. Panel B: PDP intensity profiles for different sample components. Panel C: PDP induction curves for two phytoplankton groups (Pr and EC) and a curve averaged over these two groups (TS).

4. FIELD APPLICATION

The operation of the PDP flow cytometer was tested at sea during R/V Oceanus cruise 279 (June 1996). An example of group-specific PDP induction curves for natural populations is presented in Fig. 7. Note the change in relative intensity of red fluorescence per particle between beads and phytoplankton cells in the FC (upper panel) and PDP (middle panel) modes. This can be explained by strong saturation of Chl phytoplankton fluorescence in the powerful FC laser beam. Normalization of the group-specific PDP induction profiles to the PDP profile for beads (middle panel) allows us to obtain the phytoplankton group-specific PDP induction curves (lower panel) and photosynthetic characteristics presented in the table:

	Prochlorophytes	Eukaryotic cells	Total sample
PS2 efficiency, Φ_p	0.52	0.31	0.42
Fraction of active RCs, f	0.59	0.27	0.43
Abs. cross-section, a.u.	0.16	0.11	0.14

The photosynthetic functional state of the smallest phytoplankton cells (**Pr**) appeared to be better than that of the larger eukaryotic group (59% vs. 27% of functional RCs) in the same sample, and the TS column indicates intermediate values, as would be obtained with techniques based on bulk measurements. This example illustrates how group-specific analysis of photosynthetic characteristics can improve evaluation of the "health" of the phytoplankton community.

5. CONCLUSION

By combining pump-during-probe measurements of individual phytoplankton cells with conventional flow cytometric measurements of light scattering and fluorescence, we can obtain information about the photosynthetic characteristics of different groups of cells in natural populations. This capability will be valuable in investigations of the regulation of phytoplankton growth and productivity; for example, it should help to elucidate the responses of phytoplankton of different size classes to nutrient limitation.

6. REFERENCES

1. Olson, R.J., A.M. Chekalyuk, and H.M. Sosik. "Phytoplankton photosynthetic characteristics from fluorescence induction assays of individual cells." *Limnol. Oceanogr.* **41**: 1253-1263 (1996).
2. Olson, R.J., A.M. Chekalyuk, H.M. Sosik, and M.Yu. Gorbunov. "Pump-during-probe technique for measuring photosynthetic characteristics of individual algal cells using flow cytometry and microfluorometry". In *"Photosynthesis: from light to biosphere"*, P. Mathis (ed.), Kluwer Acad. Publ., Dordrecht/Boston/London, Proc. of the X Int. Photosynthesis Congress, Montpellier, France, 20-25 Aug. 1995, **5**: 743-748 (1995)
3. Kolber, Z.S., and P.G. Falkowski. "Use of active fluorescence to estimate phytoplankton photosynthesis in situ." *Limnol. Oceanogr.* **35**: 72-79 (1993)

ABSTRACT

Using a highly resolved LTER data base collected near Palmer Station, Antarctica, from 1991-1994, the variability in the column photosynthetic cross section (Ψ^* , $\text{m}^2 \text{ g Chl } a^{-1}$) was analyzed. For the whole dataset, Ψ^* had an average value of $0.0695 \text{ m}^2 \text{ g Chl } a^{-1}$ but extreme values extended over a 50-fold range (0.009 - $0.488 \text{ m}^2 \text{ g Chl } a^{-1}$). A six-fold variation in Ψ^* was observed with time of year and was strongly associated with the high seasonality in incident irradiance characteristic of these polar sampling sites. Variability in daily incident irradiance as influenced by cloudiness and variation in chlorophyll content were responsible for an additional two-fold variation in Ψ^* . Finally, the taxonomic dependency of Ψ^* was demonstrated for the first time. For identical chlorophyll content and surface irradiance, mean Ψ^* value of $0.114 \pm 0.051 \text{ m}^2 \text{ g Chl } a^{-1}$ were recorded for diatom blooms and $0.053 \pm 0.011 \text{ m}^2 \text{ g Chl } a^{-1}$ for cryptophyte-dominated populations. Results illustrate the validity of Ψ^* -based approaches for estimating primary production for the Southern Ocean but emphasize the need to address taxon-specific photophysiology to better estimate primary production on smaller spatio-temporal scales.

Keywords: Antarctic, marine primary production, bioptical models

1. INTRODUCTION

The column photosynthetic cross section Ψ^* , ($\text{m}^2 \text{ g Chl } a^{-1}$) is defined as^{1,2} :

$$\Psi^* = \frac{39 P}{Q_{\text{PAR}}(0^+) \langle \text{Chl} \rangle}$$

where the surface irradiance $Q_{\text{PAR}}(0^+)$ is expressed into its energy equivalent ($\text{kJ m}^{-2} \text{ d}^{-1}$), P ($\text{gC m}^{-2} \text{ d}^{-1}$) is the column integrated (down to 0.1% of $Q_{\text{PAR}}(0^+)$) primary production rates, $\langle \text{Chl} \rangle$ ($\text{g Chl } a \text{ m}^{-2}$) is an estimate of areal chlorophyll a and the constant value of 39 corresponds to the kilojoules of chemical energy stored by the photosynthetic fixation of 1 g C.

For various trophic situations in temperate and tropical oceans, it was observed^{1,3} that Ψ^* varies by $\pm 50\%$ (at one standard deviation) around a central value of $0.07 \text{ m}^2 \text{ g Chl } a^{-1}$. The relative stability of this biogeochemical index is of great hope in view of deriving primary production rates from synoptic measurements of chlorophyll (remote sensing) and estimates of surface irradiance. For the Southern Ocean, documentation of phytoplankton distribution, *in situ* rates of primary production and associated photophysiological efficiency have been generally lacking. Therefore, the accuracy of bio-optical algorithms for prediction of Antarctic primary production on different time and space scales remains uncertain and the problem of specific parametrization relevant to polar latitudes has to be addressed.

As part of the Palmer Long Term Ecological Research (LTER) program⁴, a large data base of primary production, algal pigmentation, and incident irradiance was acquired over a three-year period (1991-1994) from late to early winter for a coastal Antarctic region⁵. Even though the sampling stations were in shallow waters, analyses shows that Case I water predominated for most of the samples collected and enabled us to make comparisons relevant to the high nutrient, often low biomass waters of the Southern Ocean⁶. Using this highly-resolved data set, the column photosynthetic cross section has been derived for 151 sample dates and the sources of variability have been assessed as a function of season, cloudiness, as well as phytoplankton biomass and taxonomic dominance.

2. RESULTS AND DISCUSSION

The frequency distribution of Ψ^* for the whole data set and using irradiance measurements (Figure 1A) was found to be non-normally distributed, with a median of $0.088 \text{ m}^2 \text{ g Chl } a^{-1}$ and an average of $0.109 \text{ m}^2 \text{ g Chl } a^{-1} \pm 0.075$. This average value corresponds to what is considered as an upper limit for Ψ^* ^{1,3}. The range of variation at one standard deviation

extend over a factor 5.4 (compared to 3-fold for temperate and tropical area) and the extreme values recorded in this studies extend over a 50-fold range ($0.009\text{--}0.488 \text{ m}^2 \text{ g Chl } a^{-1}$).

If the data set is restricted to a period of two months centered around the summer solstice (removing seasonal effect) (November 21 - January 21), the frequency distribution of Ψ^* (for clear sky condition, modeled using standard conditions², in order to remove cloudiness effect) is normal (Figure 1B): the median ($0.060 \text{ m}^2 \text{ g Chl } a^{-1}$) nearly equals the average ($0.064 \text{ m}^2 \text{ g Chl } a^{-1} \pm 0.027$). The range of variation at one standard variation is now 2.5 which is below the range reported for a compilation of data from various provinces³. But, even with the seasonality and cloudiness removed, significant variability still exists in Ψ^* . This variability is likely due to biology and to the possible variations in phytoplankton biomass and photo-physiology.

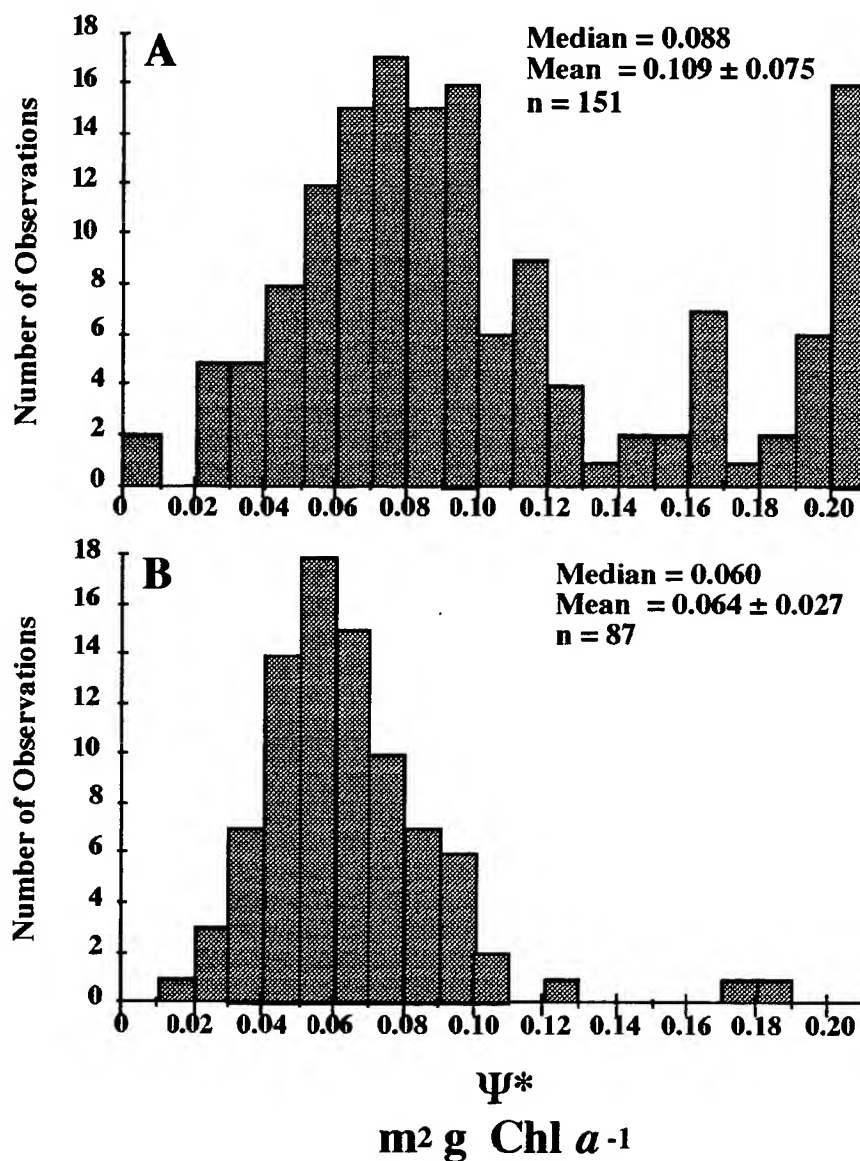


Figure 1 : Frequency distribution of Ψ^* at Palmer station, Antarctica. **A** For the whole data set. **B** For clear-sky conditions only (removing cloudiness effect) and for a two-months period around the summer solstice (removing seasonal effect).

Considering all profiles where a single taxon contribute to more than 50% of the chlorophyll biomass, Ψ^* (computed for clear sky conditions) for diatoms was greater than that for cryptophytes by 77 % (t-test, $p < 0.001$) and greater than that for nanoflagellates by 60 % (t-test, $p < 0.02$) (Table 1). But such comparisons suffer from the possible interference of seasonality in surface light or from some biomass effect. Therefore, the data set was restricted to the period around the summer solstice (November 21-January 21) and the samples were partitioned according to a mean chlorophyll content (Chl) threshold of $2 \text{ mg Chl } a \text{ m}^{-3}$. In order to deal with quasi-monospecific populations, only those data where a single taxonomic group contribute to more than 70% of the chlorophyll biomass were considered. Using such restrictions, the data set is limited, however, it clearly shows two main results. (1) For diatom-dominated communities, when Chl increased by a factor 7 (from 1.1 to $7.3 \text{ mg Chl } a \text{ m}^{-3}$) Ψ^* decreased by a factor 1.7 (test t, $p < 0.02$) (Table 1). Such a reduction in Ψ^* associated with increasing chlorophyll biomass is higher than expected from modeled results², which predict a reduction in Ψ^* of only ca. 10 % for the same biomass range. For cryptophyte-dominated communities, the range of chlorophyll concentration investigated here is only 3 (from 1.3 to $3.9 \text{ mg Chl } a \text{ m}^{-3}$) and an associated reduction of a 1.5 factor (test t, $p < 0.02$) is also observed. (2) Ψ^* for diatoms was 2.15 times higher than for cryptophytes ($p < 0.001$) when Chl was lower than $2 \text{ mg Chl } a \text{ m}^{-3}$, and 2 times higher when was greater than $2 \text{ mg Chl } a \text{ m}^{-3}$. Therefore we can conclude that, for the same amount of chlorophyll in the water column and for the same incident irradiance, daily integrated primary production is depressed by a factor two when cryptophytes replace diatoms.

Table 1: Influence of chlorophyll concentration and phytoplankton community structure on Ψ^* (for clear-sky conditions) at Palmer station, Antarctica.

TAXONOMIC GROUP		Ψ^*	n
<i>Taxonomic group contribution > 50% of <Chl></i>			
no Chl <i>a</i> threshold	Diatoms	0.094 ± 0.041	51
no Chl <i>a</i> threshold	Cryptophytes	0.053 ± 0.017	31
no Chl <i>a</i> threshold	Flagellates	0.059 ± 0.035	16
<i>Taxonomic group contribution > 70% of <Chl>¹</i>			
< $2 \text{ mg Chl } a \text{ m}^{-3}$	Diatoms	0.114 ± 0.051	6
< $2 \text{ mg Chl } a \text{ m}^{-3}$	Cryptophytes	0.053 ± 0.011	13
> $2 \text{ mg Chl } a \text{ m}^{-3}$	Diatoms	0.068 ± 0.020	14
> $2 \text{ mg Chl } a \text{ m}^{-3}$	Cryptophytes	0.034 ± 0.013	3

¹ For the period November 21 to January 21, only (to remove the seasonal influence).

3. CONCLUSIONS

Analysis of the variability of Ψ^* has highlighted the importance of incident light variations, driven by seasonality and cloudiness. The remainder of the variability (more than a factor of 2) can be explained by changes in phytoplankton composition and associated photophysiology. It was indeed very clear from this study that the water column efficiency in trapping and converting solar energy into organic matter is greater when diatoms dominate the community as compared to cryptophytes or other flagellate species. This observation is restricted to the present data set but it nevertheless emphasizes the need to account for taxonomic differences in the development of future biooptical models, if the goal is improved accuracy in primary production estimates.

4. ACKNOWLEDGMENTS

This study was supported by National Science Foundation grant DPP 90-901127 to B. B. Prézélin. H. Claustre received a NATO grant as part of his sabbatical in B. B. Prézélin laboratory.

5. REFERENCES

1. Morel, A., "Available, usable, and stored radiant energy in relation to marine photosynthesis," *Deep Sea Res.*, **25**, 675-688 (1978).
2. Morel, A., "Light and marine photosynthesis : a spectral model with geochemical and climatological implications," *Progr. Oceanogr.*, **26**, 263-306 (1991).
3. Platt, T., "Primary production of the ocean water column as a function of surface light intensity : algorithms for remote sensing," *Deep Sea Res.*, **33**, 149-163 (1986).
4. Smith R. C., K. S. Baker, W. R. Fraser, E. E. Hofman, D. M. Karl, J. M. Klinck, L. B. Quetin, B. B. Prézelin, R. M. Voss, W. Z. Trivelpiece, and M. Vernet, "The palmer LTER : A long-term ecological research program at Palmer Station, Antarctica," *Oceanography*, **8**, 77-86 (1996).
5. Moline, M.A., and B. B. Prézelin, "Palmer LTER 1991-1994: Long-term monitoring and analyses of physical factors regulating variability in coastal Antarctic phytoplankton biomass, *in situ* productivity and taxonomic composition over subseasonal, seasonal and interannual time scales," *Mar. Ecol. Prog. Ser.*, in press.
6. Claustre, H., Moline, M.A., Prézelin, B.B., "Variability in the column photosynthetic cross section for Antarctic coastal waters," *J. Geophys. Res.*, in press.

Variability of remote sensing reflectance and absorption spectra in the western Arabian Sea

R.W. Gould, Jr.
Planning Systems, Inc., Slidell, LA 70458

R.A. Arnone
NRL Code 7240, Stennis Space Center, MS 39529

D.A. Phinney
Bigelow Laboratory for Ocean Sciences, West Boothbay Harbor, ME 04575

C.O. Davis
NRL Code 7212, Washington, D.C. 20375

ABSTRACT

The coherence between particulate absorption spectra (measured with a spectrophotometer) and remote sensing reflectance spectra (Rrs -- measured with a field spectroradiometer) is investigated for twelve stations from different water masses in the western Arabian Sea during the post-southwest monsoon time period (September/October 1995). The application of derivative analysis, which has been previously employed on absorption spectra, is extended to Rrs spectra to assess whether the pigment composition of a water mass can be remotely estimated. Preliminary analyses show promise, but comparisons with coincident HPLC data are required to validate the approach. In addition, reflectance from high concentrations of suspended sediments in turbid, coastal waters may overwhelm the pigment signals in the Rrs spectra, but additional measurements and analyses are required in Case II waters.

Physical characterization of the stations using temperature and salinity compare favorably with an optical characterization using scattering and absorption. Multivariate clustering techniques were employed on the derivative spectra of Rrs, particulate absorption, and AC9 total absorption to group the stations. Results from the three different input data sets agree favorably as well, with low, moderate, and high chlorophyll stations clustering separately. Spectrophotometric and AC9 measurements of absorption are compared with model absorption values from the SeaWiFS bio-optical model. At 440 nm, AC9 values exceed the spectrophotometer values which exceed the model values.

Keywords: remote sensing, reflectance, Arabian Sea, absorption, SeaWiFS, pigments

1. INTRODUCTION

Remote sensing reflectance (Rrs) can be used to estimate the bio-optical properties of a water column; when measured from a satellite we can obtain a rapid, synoptic assessment of the chlorophyll concentration, absorption (a), and scattering (b) coefficients over broad regions. We examine the variability of shipboard measurements of Rrs spectra, particulate absorption spectra, AC9 absorption spectra, and temperature/salinity at twelve stations in the Arabian Sea from cruise TN051 on the R/V Thomas Thompson in September/October 1995, during the post-southwest monsoon time period. The stations were selected to cover a wide variety of water masses where we had coincident data from all instruments (Figure 1). The Rrs spectra were incorporated into the proposed SeaWiFS bio-optical model¹ to derive estimates of a and b for comparison with measured values. In addition, we employed derivative analysis to examine the coherence between the absorption and Rrs spectra, to assess whether we can derive an estimate of water column pigment composition remotely from hyperspectral reflectance measurements.

2. METHODS

An Analytical Spectral Devices dual-channel fiber optic field spectroradiometer was used to collect the Rrs spectra. The bio-optical model provides an estimate of backscattering (b_b). These values were converted to total scattering (b) using a relationship derived from Petzold data². A WetLabs AC9 meter operated in flow-through mode provided continuous measurements of beam attenuation and absorption at nine wavelengths; scattering was calculated from the difference. The AC9 data presented here have not been post processed for scatter corrections. Particulate filter pad absorption was measured spectrophotometrically every two hours along the cruise track. Temperature and salinity were recorded by the ship's continuous flow-through system.

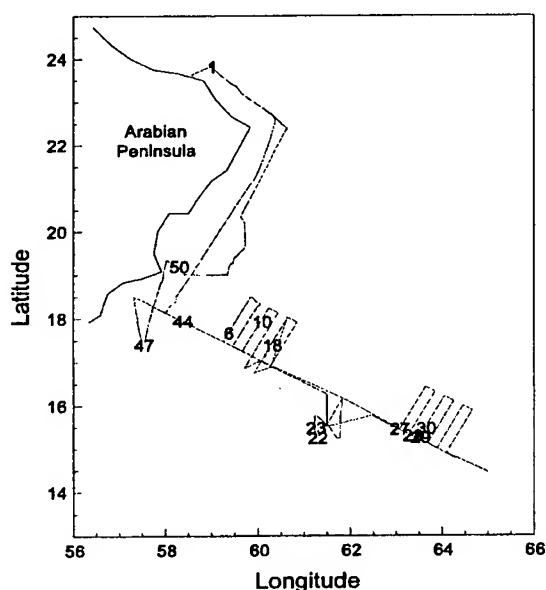


Figure 1. Station locations.

Figure 3. Measured chlorophyll was derived fluorometrically (chlorophyll + phaeopigments³); modeled chlorophyll was derived from the SeaWiFS bio-optical algorithm using the Rrs spectra collected with a field spectroradiometer. The modeled and measured values agree well at measured chlorophyll values less than about 1 $\mu\text{g/l}$, but for the two stations with higher concentrations (stations 47 and 50), the model results significantly underestimate the measured values.

The magnitude of the 4th derivative of the particulate absorption spectrum at 675 nm can be also be used to estimate the chlorophyll *a* concentration⁴. Measured chlorophyll is plotted against the 4th derivative of the filter pad absorption spectra in Figure 4. An R^2 value of 0.76 is obtained from linear regression; this compares with an R^2 value of 0.79 reported previously⁴.

3. PHYSICAL/OPTICAL STATION CHARACTERIZATION

A standard T/S plot of surface data defines the physical characterization of the twelve stations analyzed from cruise TN051 (Figure 2A). Station 1, located in the Persian Gulf, was warm and saline. At the other extreme were the cooler, less saline coastal upwelling stations 47 and 50, and station 6 from the nearshore radiator pattern. The remaining stations cluster together with similar temperatures and salinities, with stations 10 and 18 somewhat more saline than the rest. Modeled scattering vs. absorption at 443 nm is shown in Figure 2B. Estimates of total scattering and absorption coefficients were modeled using Rrs spectra coupled with the proposed SeaWiFS bio-optical model. Stations 1, 6, 47, and 50 are again distinct, with higher absorptions than the other stations. Station 10 is characterized by the lowest modeled absorption and scattering values. The remaining stations cluster together with similar optical characteristics. The physical characterization and the modeled optical characterization yield fairly similar station groupings.

4. COMPARISON OF MEASURED AND MODELED BIO-OPTICAL DATA

Measured and modeled chlorophyll values are shown in

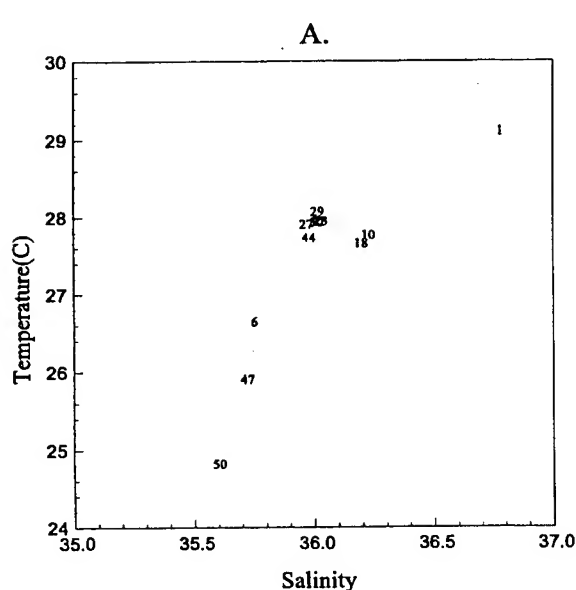


Figure 2A. T/S distribution of surface data.

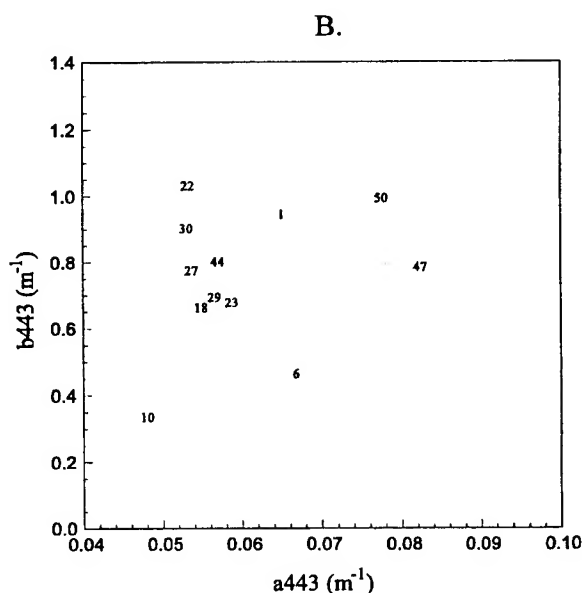


Figure 2B. Modeled *b* vs. *a* at 443 nm.

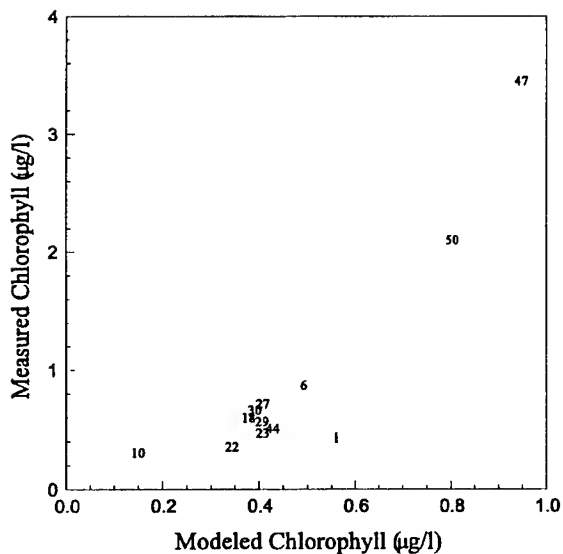


Figure 3. Measured vs. modeled chlorophyll.

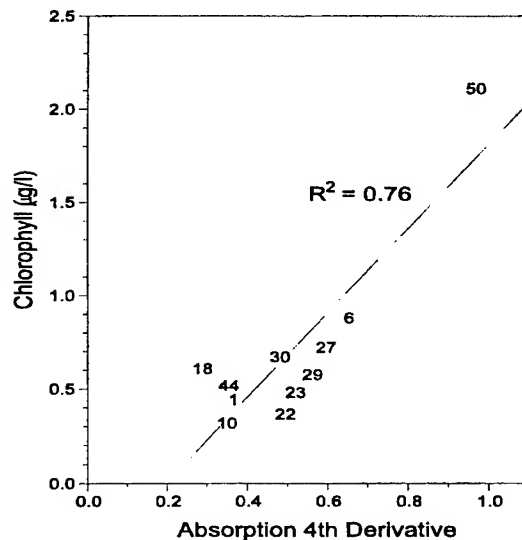


Figure 4. Measured chlorophyll vs. absorption 4th derivative.

The absorption coefficient was measured both spectrophotometrically and with an AC9 which employs a reflecting tube technique; it was also modeled using the SeaWiFS algorithm. Figure 5 is a comparison of the measured and modeled values at 440 nm. In Figure 5A, spectrophotometrically-measured particulate absorption (phytoplankton and detrital components) is plotted against total absorption (phytoplankton, detrital, dissolved, water components) derived from the SeaWiFS bio-optical model. The dissolved absorption component should be relatively minor at these open-ocean stations; pure water absorption is also very low at 440 nm (0.0083 m^{-1}). Even with dissolved and water components added in, modeled values underestimate measured values. Spectrophotometrically-measured particulate absorption vs. total absorption measured with an AC9 meter is shown in Figure 5B. AC9 values do not have pure water absorption values added back in. They are about 2-5 times larger than the spectrophotometric values. AC9 values also overestimate modeled values by about 4-8 times. In

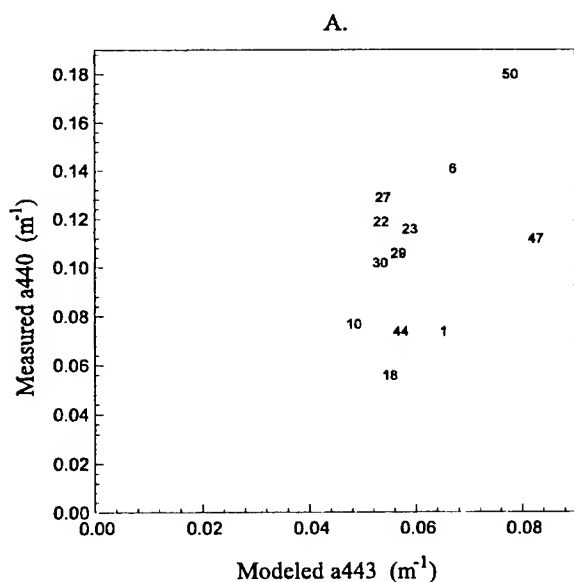


Figure 5A. Spectrophotometrically-measured particulate a vs. modeled total a.

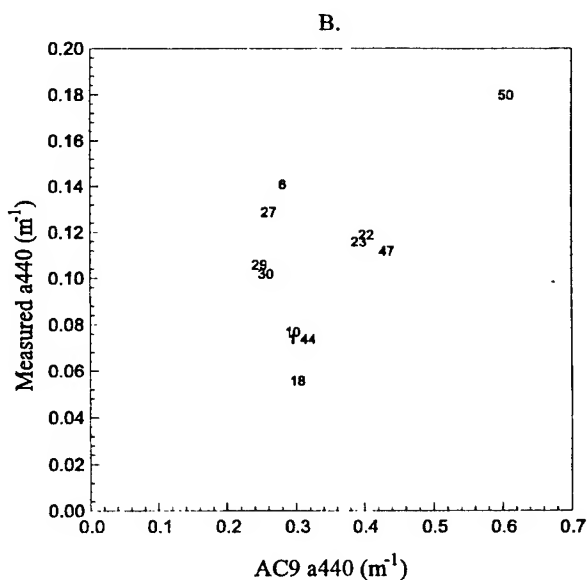


Figure 5B. Spectrophotometrically-measured particulate a vs. AC9 a.

summary, if we assume the spectrophotometric absorption measurements represent the "true" values, AC9 measurements at 440 nm overestimate and model values underestimate the true values.

5. CLUSTER ANALYSIS

A cluster analysis was performed on three optical data sets to group stations and to determine whether the choice of input data affected the resulting station clusters. The 2nd derivatives of the Rrs, filter pad absorption, and AC9 absorption spectra were derived for each of the twelve stations. The derivative data were then incorporated into a K-means centroid cluster analysis. This method produces a grouping of stations (observations) with a minimized within-cluster sum-of-squares⁵. Three seed stations were selected based on low, moderate, and high chlorophyll values (stations 10, 30, and 47 were used, respectively). The clustering procedure was performed three times with different input derivative spectra (either Rrs, absorption, or AC9 data), thereby producing three different cluster groupings. The clustering of the derivative data groups stations with similar curve shapes, i.e., stations with similar peaks and shoulders in absorption. Thus, subtle differences which might not be discernible in the raw spectra are enhanced by taking the derivative. The objective here is to determine whether the different data sets produce similar station groupings. Although there were some differences in the station groupings depending on which data set was used in the cluster analysis, the results were fairly similar. For the cluster results based on the 2nd derivative of the particulate absorption spectra, the Persian Gulf station and the nearshore stations that were not in upwelled water grouped in cluster 1 (stations 1, 10, 18, 44). In cluster 2 are the farthest offshore stations (22, 23, 247, 29, 30), and in cluster 3 are station 6 and the high chlorophyll upwelling stations near the coast (47, 50).

6. DERIVATIVE ANALYSIS

Previous work by Bidigare et al.⁴ suggested that the 2nd derivative of the absorption spectrum can be used as a qualitative indicator of the pigments present in a sample, while the 4th derivative data might be a more quantitative measure of pigment concentrations. Here we extend the application of derivative analysis from absorption spectra to Rrs spectra, to assess whether we can derive an estimate of the presence/concentration of individual pigments in the water column from remote measurements of reflectance. In Figure 6A, the particulate filter pad absorption is shown overlaid with its 2nd derivative, for station 23. Note that the minima in the derivative spectrum correspond to peaks and shoulders in the absorption spectrum, indicating higher absorption by individual pigments at those wavelengths. The strong absorption maximum and derivative minimum at 675 nm is due to chl *a* absorption. The Rrs spectrum from the same station is overlaid with its second derivative in Figure 6B. Although the curve is generally featureless, the derivative analysis enhances the subtle dips in the curve. Because absorption and reflectance are inversely related (low reflectance at a wavelength indicates enhanced absorption), we are

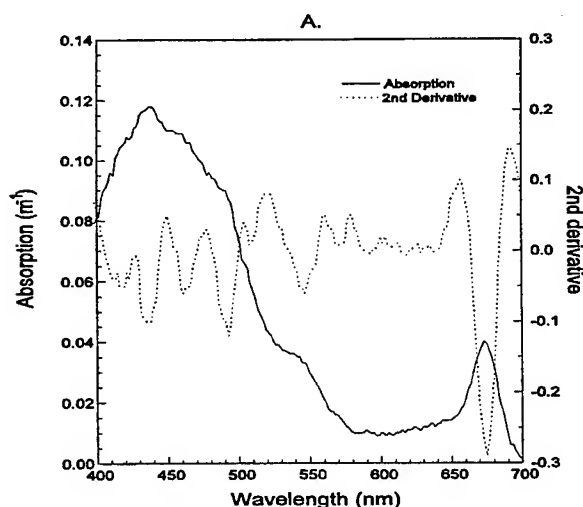


Figure 6A. Particulate absorption and 2nd derivative vs. wavelength.

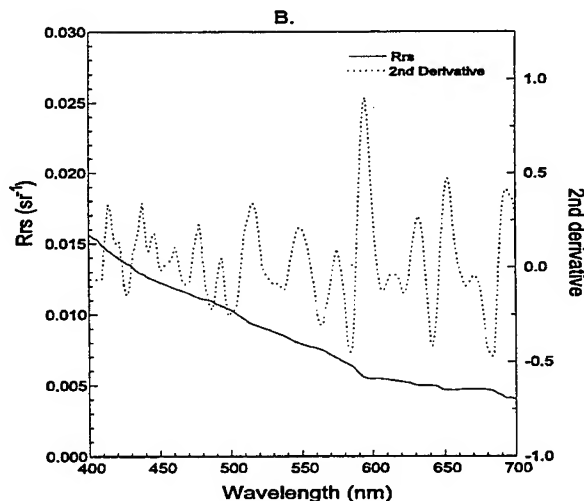


Figure 6B. Rrs and 2nd derivative vs. wavelength.

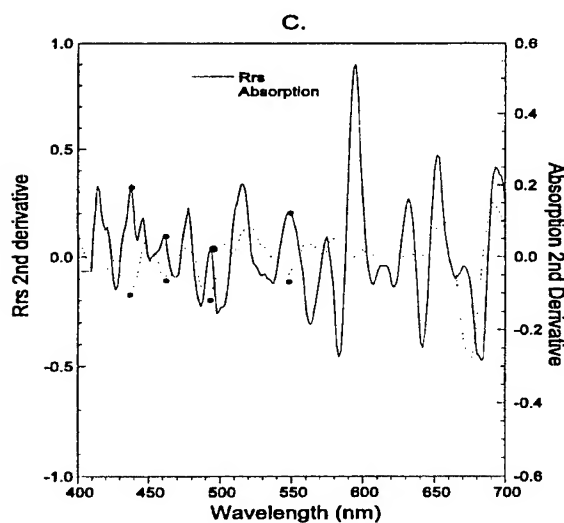


Figure 6C. Rrs and absorption 2nd derivatives vs. wavelength.

individual pigments to the Rrs derivative maxima is valid, we should be able to predict pigment variations at the stations. Coincident HPLC data are required to verify the predictions.

interested in the dips in the Rrs curve, rather than the peaks as with the absorption curve. Thus, maxima in the Rrs derivative spectrum should correspond to minima in the absorption derivative spectrum. However, the minimum in the Rrs derivative curve at 682 nm corresponds to chl *a* fluorescence rather than absorption. Rrs and absorption 2nd derivatives vs. wavelength are plotted together in Figure 6C. Note that the main absorption minima correspond to Rrs maxima, as expected, denoted by the black circles on the figure. Note the offset between chl *a* absorption at 675 nm (blue curve) and chl *a* fluorescence at 682 nm (red curve).

In Figure 7, one station from each of the three cluster groups above (stations 10, 30, and 50) is plotted to determine whether the patterns observed in Figure 6 are consistent. Absorption derivatives are shown in Figure 7A. Note the similarities in the locations of the minima in the derivative spectra. Rrs derivatives are shown in Figure 7B. Note the consistency in the locations of the derivative maxima, but the variations in amplitude. The assignment of individual pigments to the absorption derivative minima and to the Rrs derivative maxima is tentative and based on pigment absorption maxima in Bidigare et al.⁴ and Hoepffner & Sathyendranath⁶. If the assignment of

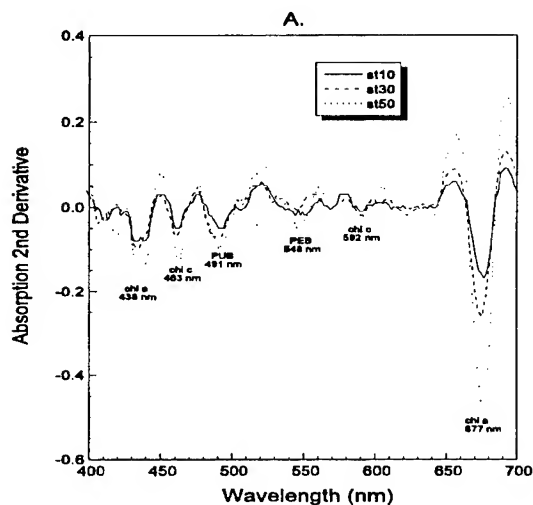


Figure 7A. Absorption 2nd derivative vs. wavelength, station comparison.

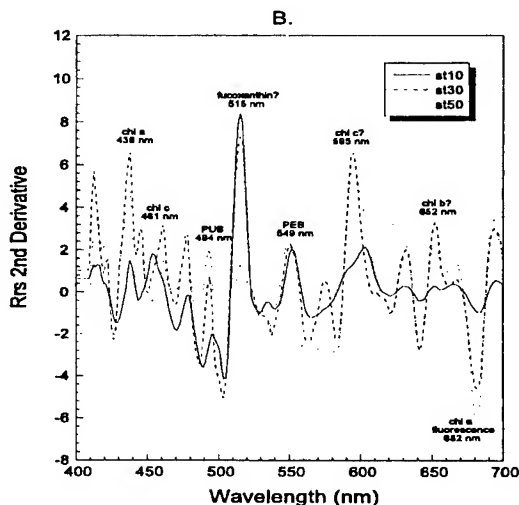


Figure 7B. Rrs 2nd derivative vs. wavelength, station comparison.

7. SUMMARY

- Physical characterization of Arabian Sea stations based on temperature and salinity compare favorably with an optical characterization based on scattering and absorption.

- At 440 nm, absorption measurements with an AC9 meter exceeded spectrophotometric measurements which in turn exceeded model estimates based on the proposed SeaWiFS bio-optical algorithm.
- Multivariate cluster analyses of derivative spectra of Rrs, particulate absorption, and AC9 absorption yield fairly consistent station groupings related to station location and chlorophyll concentration.
- Derivative analysis of Rrs spectra shows promise as a tool to remotely estimate the pigment composition of water masses.

8. ACKNOWLEDGMENTS

The authors thank C. Wood and S. Ladner for assistance with data and image processing. This research was funded under the ONR/NRL Forced Upper Ocean Dynamics Accelerated Research Initiative, Program Element 0601153N.

9. REFERENCES

1. K.L. Carder, S.K. Hawes, and Z. Lee, "SeaWiFS algorithm for chlorophyll *a* and colored dissolved organic matter in subtropical environments," *J. Geophys. Res.*, submitted.
2. T.J. Petzold, "Volume Scattering Functions for Selected Ocean Waters," SIO Ref. 72-78, 1972.
3. C.S. Yentsch and D.W. Menzel, "A method for the determination of phytoplankton chlorophyll and phaeophytin by fluorescence," *Deep-Sea Res.*, **10**, 221-231, 1963.
4. R.R. Bidigare, J.H. Morrow, and D.A. Kiefer, "Derivative analysis of spectral absorption by phytoplankton pigments, *SPIE Ocean Optics IX*, Vol. 925, pp. 101-108, 1988.
5. J.A. Hartigan and M.A. Wong, "Algorithm AS 136: A K-means clustering algorithm," *Applied Statistics*, **12**, 61-75, 1979.
6. N. Hoepffner and S. Sathyendranath, "Determination of the major groups of phytoplankton pigments from the absorption spectra of total particulate matter," *J. Geophys. Res.*, **98**(C12), 22789-22803, 1993.

Modeling the environmental/optical relation in near shore regions

Donald R. Johnson
Roger W. Meridith

Naval Research Laboratory
Stennis Space Center, Mississippi 39509

ABSTRACT

Fresh water runoff into the ocean from rivers and estuaries contains colored dissolved organic matter (CDOM) that strongly affects optical absorption. If conservative mixing occurs between these fresh water plumes and the surrounding high salinity/low CDOM oceanic waters, then a linear relationship should exist between salinity and optical absorption, enabling remote mapping of the plume's dispersion. In this study we test this relationship in the near shore region with optical absorption and salinity time series taken during four different experiments in separate locations and separate seasons. Our conclusion is that in very near shore regions, away from the immediate river runoff, the conservative mixing relationship is easily violated.

1. INTRODUCTION

Because of the highly variable nature of near shore hydrodynamics, it is imperative that methods for synoptically mapping these areas using aircraft or satellite be developed. One method that has recently demonstrated high potential, at least with river plume tracing, involves the relationship between optical absorption and salinity¹. The concept is fairly straight forward: fresh water outflow from rivers and estuaries contains high quantities of colored dissolved organic matter (CDOM), or gelbstoff, that affect optical absorption and hence the spectral radiance reaching remote sensing platforms. If this fresh water is conservatively (i.e., linearly) mixed with surrounding oceanic waters of high salinity and low CDOM, and if that inverse linear relationship can be determined, then sea surface salinity can be mapped using remotely sensed spectral radiance. Or, conversely, mapping salinity remotely via microwave radiometry² can provide a means to estimate the optical character of the water.

Naval oceanographic interests have recently tended to focus in the near shore region, where coastal buoyancy layers with alongshore jets are formed from river/estuary plumes, and are ubiquitous to coasts with moderate to high runoff. This low salinity water is found trapped against the coast (<10 km) by pressure gradients and the earth's rotation. Observations indicate that the associated jet can provide an effective means of transporting suspended material and CDOM long distances from their sources. We would expect that the linear relationship under these conditions would break down when a third water mass is intermittantly introduced. This could happen by upwelling or by vertical mixing of deeper waters to the surface, or by horizontal advection of another water mass with a different CDOM/salinity ratio. It can also happen by biological changes and by non-linear flocculation

of CDOM as the water ages. In this study, we have sought to determine something of the limits of the salinity/optical absorption relationship in the near shore regions at moderate distances from fresh water sources. Four field experiments over the past two years (1994-1996) were the basis of our effort. These experiments involved a larger look at the relationships between environmental forcing (i.e., winds, currents, waves, water mass character) and the optical nature of the water column in shallow water. For the present study, however, we have chosen to focus specifically on the relationship between salinity and optical absorption.

2. OBSERVATIONS AND METHOD

Figure 1 shows the location of three sites where observations were made for 2-3 week periods during 1994-1996. At one of the sites (Hamlet's Cove), observations were made during a summer and a winter period. Table 1 provides a listing of some of the experimental conditions. In each experiment, time series of salinity were obtained from moored Seabird SEACAT thermosalinographs, and concomitant time series of optical absorption were obtained with moored WetLabs AC-9 meters. The SEACATs sampled temperature and salinity at 1 minute intervals; the AC-9s sampled 9 channels of absorption and total attenuation at 10 minute intervals (5 minute intervals during COPE 96). Absorption measurements were corrected for scattering. After the first experiment (Hamlets-summer), it was found that the best salinity/optical absorption fit occurred at the shortest wavelength absorption channel, 412 nanometers. This, then became the standard for comparison of the other experiments.

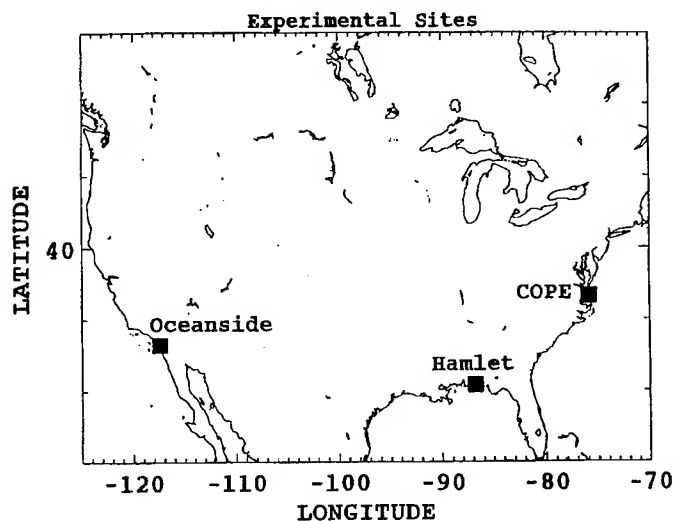


Figure 1

Three of the experiments took place in the summer-fall season, from August to late October, while the fourth experiment took place in the late winter (February/March). The Hamlet's Cove summer and winter experiments were conducted at the same location. Although this location was approximately 25 km from a relatively minor estuary at Destin, Florida, there were still readily identifiable pulses of low salinity water which invaded the mooring site. In the COPE 96 experiment (Chesapeake Bay Outflow Plume Experiment), we moored the instruments approximately 25 km south of the bay's entrance, and near shore. Due to recent hurricane activity nearby, there was an unusually large outflow of river water during that experiment. In contrast the Oceanside experiment was conducted near a seasonally dry river during a relatively dry season. It also was the only experiment shown with the sensors situated near the bottom instead of near the surface.

Table 1: Experimental Sites & Conditions

Experiment	Date	Background	Weather	Water Depth	Sensor Depth
Hamlet-Summer	6-14 Aug 94	sandy beach ~25 km from estuary	very mild	7 m outside bar	near-surface
Hamlet-Winter	28 Feb -17 Mar 95		stormy	5 m outside bar	near-surface
Oceanside	15-28 Oct 95	kelp beds ~15 km from dry estuary	very mild	15 m	near-bottom
COPE 96	14-27 Sep 96	nearshore plume of Chesapeake Bay	mild/stormy	9 m	near-surface

In order to extract the linear relationship between salinity and optical absorption at 412 nm, a first order polynomial fit was made to predict salinity from the a412 time series. The rms difference between the observed salinity and the predicted salinity gives "rms error." The percent "rms variance explained" is the rms error divided by the rms variance of the observed salinity curve.

3. RESULTS

In order to provide a visual comparison of the salinity/optical absorption (a412) relationship, each of the time series was normalized between zero and one, with the salinity time series *inverted*, and the results presented in Figures 2a-2d. In the Hamlet's Cove-summer experiment (Fig. 2a), the visual relationship is remarkably good. Sharp pulses of high and low salinity waters lasting one or two hours passed by the mooring, and were picked up in the a412 optics. In contrast, however, during the winter experiment at the same location, equally large pulses in salinity were not matched by a412. Referring to Fig. 2b, it seems clear that the general low frequency trend in salinity and a412 were similar during the winter experiment but the strong high frequency pulses did not match. Part of the reason may be provided by an examination of the mixing conditions during the two experiments. In Fig. 3, a comparison of the significant wave height (SWH) during each of the above experiments is given. Clearly the summer experiment took place during very mild conditions, contrasting with two large storm events that took place during the winter experiment. In this shallow water, with little vertical density difference during winter, it seems clear that bottom water, with its detrital and sediment content, probably mixed into the surface layer, changing the salinity/a412 ratio. Curiously, however, pulses of estuarine water "fronts" were seen passing through, but with the wrong relationship (not inverse). In Fig. 4, a time-expanded version of salinity, alongshore currents, a412 and b412 (scattering) is presented for two of these fronts. In the salinity/alongshore current time series (upper-Fig.4) two fronts are clearly visible, corresponding closely to the semi-daily tidal events. In the corresponding a412 time series (middle-Fig. 4), the first of these pulses is visible, but not with the inverse relationship to salinity. The second of the pulses is absent, but replaced with "noisy" events. In the b412 scattering time series (bottom-Fig.4), there is little variation during the first frontal passage, but large variation during the second passage. This would imply that the strong mixing event (beginning at "day" 10 in Fig. 3) brought up water with a different salinity/a412 ratio -

sediment/detrital suspension, not CDOM, was an important component of this ratio.

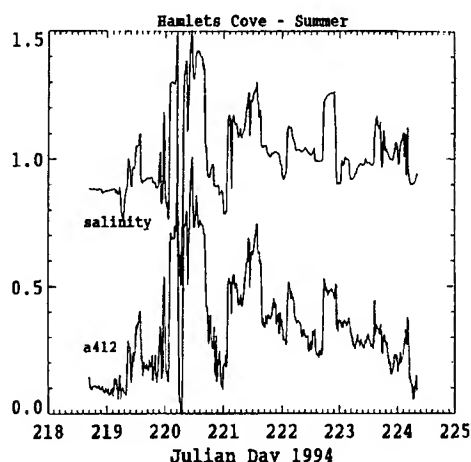


Figure 2a

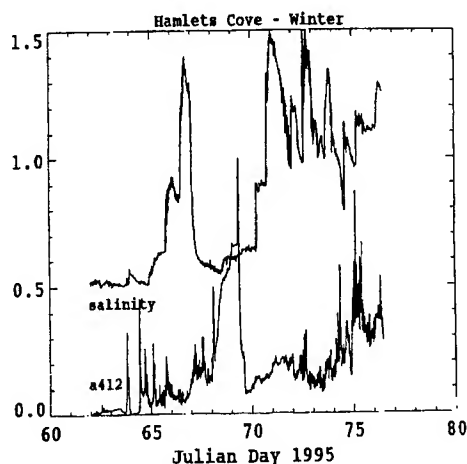


Figure 2b

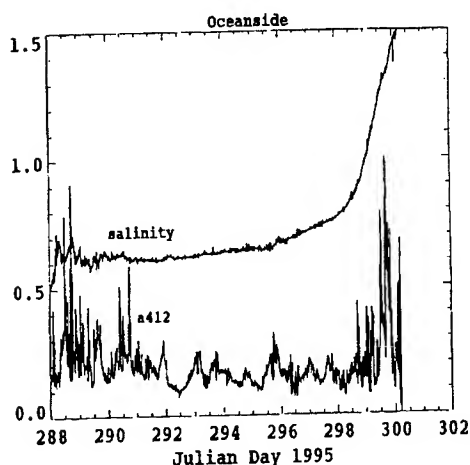


Figure 2c

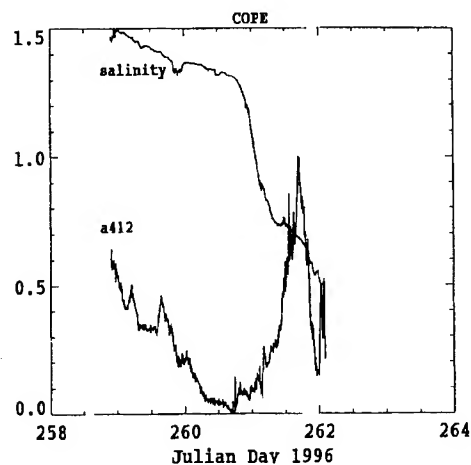


Figure 2d

The only one of the four experiments where we show near-bottom observations is presented in Fig. 2c (Oceanside, California). This experiment was done in approximately 15 m of water at a distance approximately 5 km from shore in comparison to the Hamlet's Cove experiments at about 0.2 km from shore. Except for the sudden decrease in salinity and increase of a412 near day 298, there is little relationship between the two curves. This might be expected since there is probably considerable elapse of time between generation of low salinity water in the near shore region and its arrival at the mooring site. In addition, there was a strong nepheloid layer of detritus in closer to shore (not shown) which advected past the mooring site in response to tidal currents and alongshore wind events. This would indicate that there is little conservative mixing relationships between salinity and optics at this location.

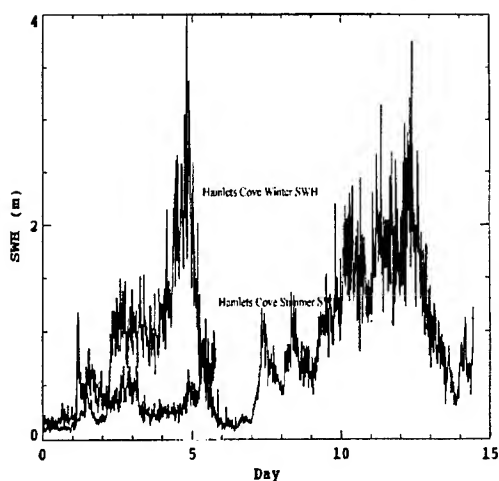


Figure 3: Significant WaveHeight comparison for the summer and winter at Hamlet's Cove.

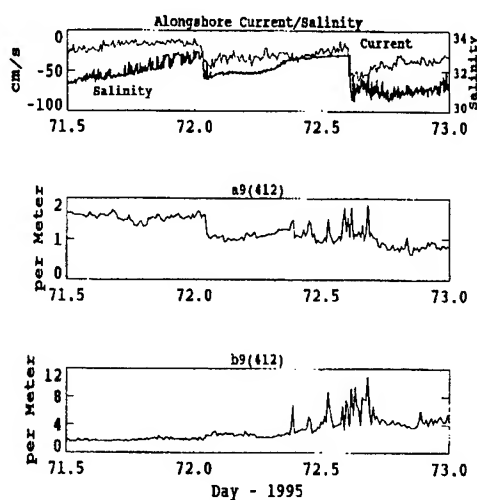


Figure 4: alongshore currents/salinity optical absorption and scattering during winter at Hamlet's Cove.

Figure 2d shows the salinity/a412 relationship in the Chesapeake Bay outflow plume. It was anticipated that this experiment would show the strongest relationship since it involves fresh waters dispersing directly into continental shelf waters. However, in Fig. 2d, the inverse salinity/a412 relationship is only seen in the first half of the record (to day 261). After that the relationship is

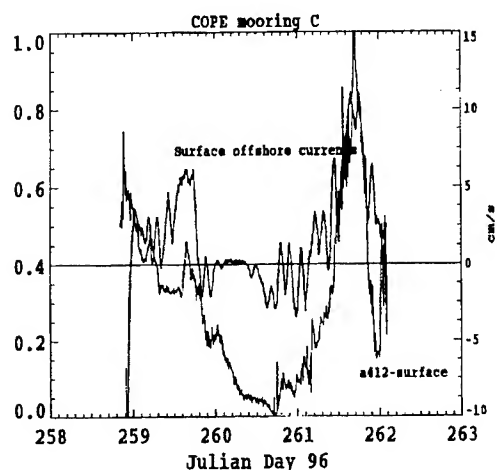


Figure 5: Time series of a412 and offshore currents (positive) showing influence of bottom water on a412.

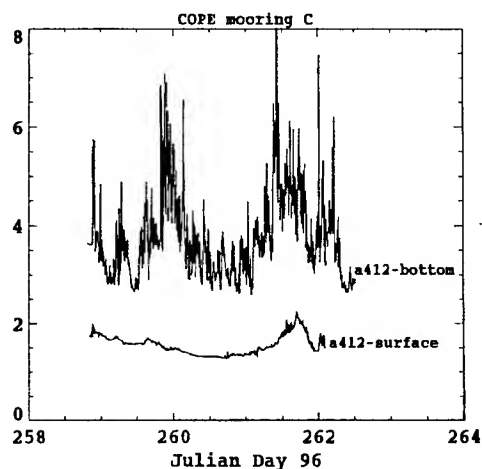


Figure 6: Bottom (upper curve) and surface (lower curve) a412 during COPE 96.

inverted. This site was about 2 km from shore and responded quickly to wind events. On day 261, an upwelling (northward) wind event occurred which pushed surface water offshore. In Fig. 5, the

a412 time series is shown together with the offshore surface current time series. The clear coincidence between the upwelling event (positive offshore surface current) and the increase in a412 is evident. Fig. 6 indeed shows significantly larger a412 deeper in the water column.

Table 2 summarizes the attempt to predict salinity from optical absorption (a412) using a linear relationship:

Table 2

	Hamlet-Summer	Hamlet-Winter	Oceanside	COPE 96
rms error	+/- 0.4 ppt	+/- 1.29 ppt	+/- 0.4 ppt	+/- 2.63 ppt
% rms variance explained	87%	4%	41%	32%

4. CONCLUSIONS

Our goal in this study was to examine the simple relationship between optical absorption in the channel most sensitive to CDOM, and salinity, using time series from moored instruments. It was reasonable from the outset that this relationship would only hold when conservative mixing of fresh water outflow with oceanic waters occurred. We have found that, in well defined situations where linear horizontal mixing is appropriate, this is indeed the case. But when a third water mass enters, it is also quite clear that the ratio between salinity and optical absorption is disturbed. In shallow water, this third water mass is easily obtained by storm events which mix bottom water upward or by upwelling events which advect it upward. Other water masses which advect horizontally into the area must also be considered. It is indeed possible that other optical channels may have sensitivity to detritus which will enable the distinction, but at present the methodology is not clear. We expect that the ability to determine salinity from optics (or optics from salinity) will be possible, but there needs to be much effort placed in the distinction of detritus from CDOM.

Acknowledgements: We appreciate the support from the Naval Research Laboratory under the Littoral Optical Program. Discussions with Alan Weidemann and Robert Arnone were extremely helpful.

5. REFERENCES

1. K. L. Carder, R. G. Steward, R. F. Chen, S. Hawes, and Z. Lee, "AVIRIS calibration and application in coastal oceanic environments: tracers of soluble and particulate constituents of the Tampa Bay coastal plume," *Photogr. Eng. & Remote Sensing*, Vol. 59, pp.339-344, March 1993.
2. B. M. Kendall, "Remote sensing of the Chesapeake Bay plume salinity via microwave radiometry," in *Chesapeake Bay Plume Study: Superflux 1980*, NASA Conference Publication 2188, NOAA/NEMP III 81 ABCDFG 0042, January 1980.

Modeled Inherent Scattering Properties of Small Light-Limited Phytoplankton: Implications for Deep Phytoplankton Size Class Distributions

Z. I. Johnson*

Botany Department and Marine Laboratory, Duke University
135 Duke Marine Lab Rd., Beaufort, NC, 28516-9721 USA

ABSTRACT

Small phytoplankton ($<2\mu\text{m}$), ubiquitous throughout the world's oceans, numerically dominate many open ocean ecosystems with increasing importance towards the base of the euphotic zone. As an example, light-limited deep secondary chlorophyll maxima are usually dominated by small phytoplankton species. Theoretical models describing light-particle interactions predict that small particles scatter light less efficiently than their larger counterparts. To investigate a possible relationship between the dominance of small phytoplankton in light-limited situations and efficiency predictions, a light scattering efficiency model based on Mie theory as approximated by Van de Hulst is used to determine scattering efficiency as a function of size. This scattering efficiency model, which approximates light-phytoplankton interactions by considering phytoplankton as homogeneous spheres, is driven by the spectral light field from an observed deep ($\sim 135\text{m}$) phytoplankton population dominated by small phytoplankton. This deep secondary chlorophyll maximum is discussed as an example of a highly efficient small phytoplankton population at the threshold of the euphotic zone which could benefit as a result of its size distribution.

Keywords: phytoplankton, Mie scattering, light limitation, secondary chlorophyll maximum, scattering efficiency

1. INTRODUCTION

Small phytoplankton, dominant in the upper layers of nutrient-limited open ocean areas¹ in part due to advantages in nutrient uptake kinetics afforded by large surface area to volume ratios² may be increasingly important in terms of community structure towards the base of the euphotic zone.³ Given a typical tropical structure of increased nutrients towards the base of the euphotic zone coincident with the thermocline / pycnocline (ex. figure 5), the surface area / volume ratio - diffusion argument⁴ advantage for small phytoplankton would suggest that other factors besides nutrient limitation could become important at depth. Various suggestions have been offered to account for small phytoplankton dominating these light-limited regimes including increased absorption ability due to reduced package effect of pigments⁵ and pigment complementations that are optimized for the spectral distribution of light at deep depths.⁶ While these possibilities may be important in determining the size distribution of organisms in open ocean areas with depth, other factors such as light-phytoplankton interactions (absorption + scattering) may also be at work.

Here I describe simulated deep ocean light field interactions with ideal spheres as models of small spherical phytoplankton as a framework for understanding picoplankton-light interactions in the deep ocean. This is performed by coupling a Van de Hulst⁷ scattering model as an approximation of theoretical Mie scattering⁸ to a spectral distribution of the underwater light field as measured at deep small phytoplankton dominant stations. The scattering model then calculates spectrally weighted scattering efficiencies as a function of diameter (size). These scattering properties are discussed in terms of ecological implications for the size distribution of phytoplankton at depths where light limitation is extreme.

2. MODEL

The actual spectral distribution - Van de Hulst scattering coupled model is a C language program which is available upon request from ZI Johnson.

2.1 Radiation Transfer

The radiation transfer input to the Van de Hulst scattering model is a simple spectral characterization of the light field based on direct measurement of the light field. Specifically, transmission, T over depth interval a to b for wavelength λ was calculated as,

* Other author information: Email: zij@acpub.duke.edu; Telephone: 1-919-504-7641; Fax: 1-919-504-7648

$$T_{a,b,\lambda} = 100 * \frac{\Phi_{b,\lambda}}{\Phi_{a,\lambda}} \quad (1)$$

where $\Phi_{x,\lambda}$ is the photon flux density at depth x for wavelength λ . Total PAR (photosynthetic active radiation, 400-700nm) transmission at depth, z , was calculated as the integrated photon flux density at depth divided by the integrated surface photon flux density. $\Phi_{x,\lambda}$ were directly measured using a Bio-spherical Instruments, Inc. Multichannel Environmental Radiometer with an on-deck correction for changes in the surface light field during the measurement process.⁹ Seven wavelengths were measured corresponding to SeaWiFS absorptions bands, namely, 405, 410, 442, 489, 508, 555, and 666nm. Wavelength inputs for the scattering model not directly measured were extrapolated from measured data using linear interpolation.

2.2 Van de Hulst Scattering Model

The Van de Hulst scattering model is used to determine the scattering efficiency, the ratio of scattered light to light impinging on a projected area of particle, of a homogeneous spherical particle. The Van de Hulst model is based on the Van de Hulst⁷ approximation as applied to Mie theory.⁸ This is chosen over the more rigorous exact Mie solution because it is less complex and consequently less computationally intensive. Further, it has been shown that for the range of optical properties covered by phytoplankton, the Van de Hulst approximation is adequate.¹⁰ The Van de Hulst scattering model has as its raw inputs ρ (eq 2) and $\tan \xi$ (eq 3).

$$\rho = 2\alpha(n-1) \quad (2)$$

$$\frac{n'}{n-1} = \tan \xi \quad (3)$$

The first parameter is a dimensionless phase lag term which is composed of α , a dimensionless length scale term (composed of λ and sphere diameter, d), and n , the real portion of the refractive index. The second term is the ratio between the imaginary and real minus one portions of the refractive index. Equations one and two are the parameters, which are simple functions of m ($m = n - in'$), λ , and d (the diameter of the sphere), which comprise the true inputs for the Van de Hulst⁷ efficiency equations for absorption (eq 4), attenuation (eq 5), and scattering (eq 6).

$$Q_a(\rho) = 1 + \frac{e^{-2\rho \tan \xi}}{\rho \tan \xi} + \frac{e^{-2\rho \tan \xi}}{2\rho^2 \tan^2 \xi} + \frac{1}{2\rho^2 \tan^2 \xi} \quad (4)$$

$$Q_c(\rho) = 2 - 4e^{-\rho \tan \xi} \left[\left(\frac{\cos \xi}{\rho} \right) \sin(\rho - \xi) + \left(\frac{\cos \xi}{\rho} \right)^2 \cos(\rho - 2\xi) \right] + 4 \left(\frac{\cos \xi}{\rho} \right)^2 \cos 2\xi \quad (5)$$

$$Q_b(\rho) = Q_c(\rho) - Q_a(\rho) \quad (6)$$

Since the spectroradiometry data has light as a function of wavelength and the refractive index is assumed to stay constant and independent of d and λ , the absorption efficiency equation can be re-termed to be a sole function of diameter for a particular wavelength by substituting the right hand side of equation 7 for all ρ in equation 4 (eq 8). A similar re-termining is performed on equation 5 and 6 (not shown).

$$\rho = 2 \frac{\pi d}{\lambda} (n-1) \quad (7)$$

$$Q_{a,\lambda}(d) = 1 + \frac{\lambda e^{-4(\pi d(n-1)/\lambda) \tan \xi}}{2\pi d(n-1) \tan \xi} + \frac{\lambda^2 e^{-4(\pi d(n-1)/\lambda) \tan \xi}}{8(\pi d(n-1))^2 \tan^2 \xi} + \frac{\lambda^2}{8(\pi d(n-1))^2 \tan^2 \xi} \quad (8)$$

It is the absorption and attenuation efficiency equations that have been retermed for d that are used to calculate the scattering efficiency as with equation 6.

2.3 Combined Model

The Van de Hulst model, with appropriate constants, is driven by spectral availability of light. For each wavelength a scattering efficiency is calculated for each particle size of interest, typically 0-30 μm in diameter with 0.1 μm steps. Scattering efficiencies for each diameter are then combined using a weighted mean based on relative availability of each wavelength at the depth of interest (eq 9). The final output is a weighted mean scattering efficiency for each diameter step and depth, $\bar{Q}_{b,d,z}$.

$$\bar{Q}_{b,d,z} = \frac{\int_{400}^{700} \Phi_{z,\lambda} Q_{b,d,z,\lambda} d\lambda}{\int_{400}^{700} \Phi_{z,\lambda} d\lambda} \quad (9)$$

Spectroradiometry data was selected based on the occurrence of a deep (~135meters) secondary peak in the fluorescence profile (see section 4), indicative of increased phytoplankton biomass in extremely low light levels. Values for the refractive index, were taken from Bricaud et al.¹¹ and Morel et al.⁶. n values used ranged from 1.038-1.05. n' values used range from 0.002-0.02. These values were chosen because they correspond to the *Synechococcus* and *Prochlorococcus* that are common in deep waters. While it has been shown that the refractive index values are spectrally dependent, here I use a mean constant value for the model because spectral values were not available, and the model is focused on determining the relative changes in scattering efficiency in terms of the diameter of particle.

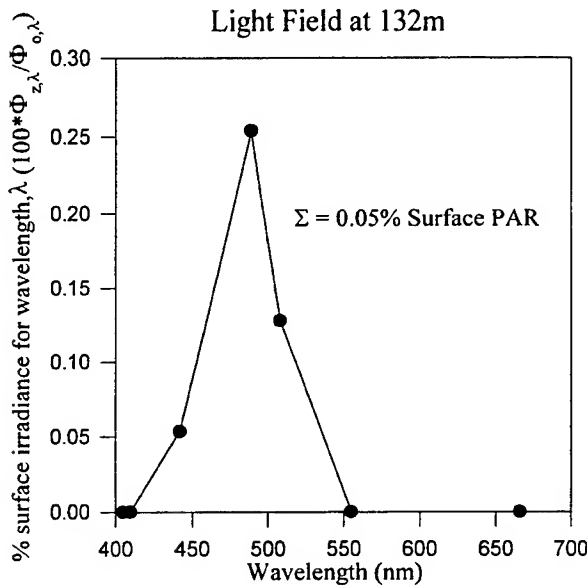


Figure 1: Measured spectral quality of light field at 132m. Data courtesy of C Trees (CHORS).

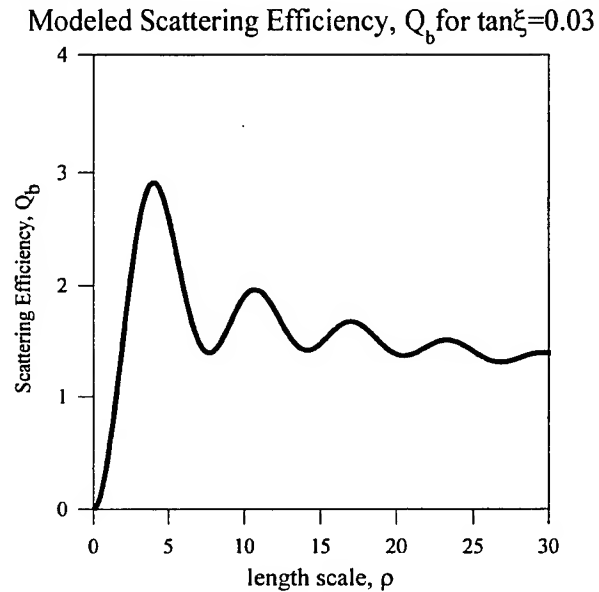


Figure 2: Modeled scattering efficiency for $\tan\xi=0.03$ as a function of length scale, ρ

3. MODEL OUTPUT

Model output was generated for several scenarios with varying refractive indices, spectroradiometry profiles, and depths of interest. Here I have chosen $m = 1.05 - 0.01i$ and $z = 132$, with spectroradiometry data from the Arabian Sea (see section 4) as a representative example for discussion.

The spectroradiometry input data at $z=132$ shows a clear peak in transmission around 490nm (figure 1). All longer wavelengths have been absorbed due to high attenuation coefficients of water at longer wavelengths.¹² Wavelengths shorter than 490nm are also depleted in part due to water absorption, but also due to inelastic scattering processes and phytoplankton absorption corresponding to the Soret chlorophyll absorption band. The resultant transmission peak at 490nm represents a minimum in attenuation for combined water and phytoplankton, which dominate the optical properties in this type of region.¹³

The Van de Hulst scattering model was evaluated in terms of wavelength specific output and spectrally weighted values. Comparisons of the scattering efficiency function with previously reported values are in agreement (data not shown).^{14,10} The generalized function shape of the scattering efficiency vs. diameter is a rapid initial increase to a peak followed by a decreasing oscillatory motion around the asymptotic value (figure 2). The location of the scattering efficiency peak is wavelength and refractive index dependent, hence each will modify the exact magnitude and position of peaks in the generalized curve. The spectral nature of the scattering efficiency can be seen for a constant diameter and refractive index (figure 3). This curve agrees with previous spectral scattering efficiency determinations with diameter and refractive index held constant.¹¹

Using the spectral availability of light, the spectrally weighted mean scattering efficiency can be determined for a particle size range at a particular depth for a refractive index. Using the depth of a deep secondary chlorophyll maximum as an indicator of an area where small phytoplankton are dominant, scattering efficiency vs. diameter was determined for a unique refractive index. The refractive index of $m = 1.05 - 0.01i$ was taken from Morel et al.⁶ as a representative value for the *Prochlorophytes* that dominate this deep fluorescence peak (see below). The spectrally weighted mean scattering efficiency vs. diameter (figure 4) is similarly shaped to a non-spectrally weighted curve (figure 2) except that the secondary peaks have been dampened giving an initial rapid increase to a peak followed by a decay to a steady state value. Also, the steady state value of \bar{Q}_b for large diameters is not constant across the model runs (figure 2, 4), because it is highly dependent on the absorption portion of the refractive index, n' . For no absorption, ($Q_c = Q_b$), the Q_b value oscillations dampen and approach the value of two as the diameter increases.

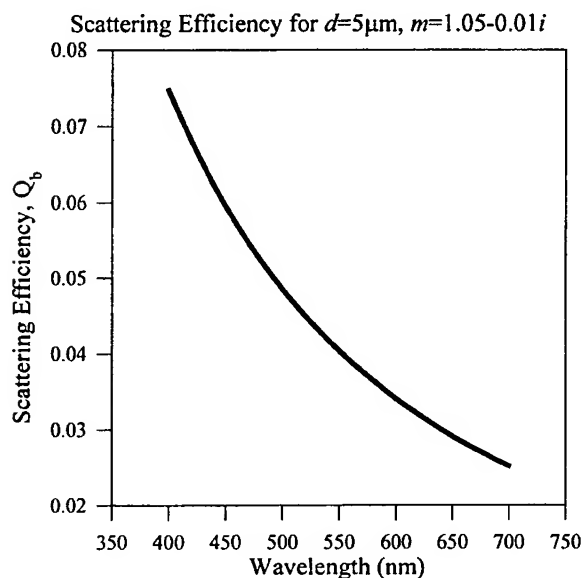


Figure 3: Modeled spectral scattering efficiency for $d=5\mu\text{meters}$ and $m=1.05-0.01i$. Note the strong spectral nature of the curve.

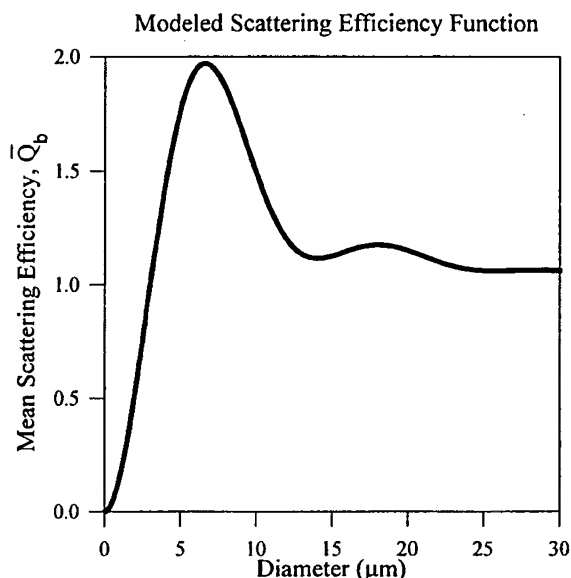


Figure 4: Spectrally weighted mean scattering efficiency as a function of particle diameter at 132m and $m=1.05-0.01i$.

4. CASE STUDY

During the US JGOFS Arabian Sea process cruises (1994-1996), a deep secondary fluorescence maximum was observed at several station locations found in the oligotrophic portion of the central Arabian Sea. This secondary chlorophyll maximum was most pronounced during the NE monsoon period around January, but was found throughout the year. Subsequent examination revealed that this deep secondary chlorophyll maximum was dominated almost exclusively by *Prochlorococcus spp.* as elucidated by the dominance of di-vinyl chlorophylla through HPLC and by flow cytometric signatures.¹⁵ This paper is not focused on the description of the phenomenon. However, several useful parallels between the presence of the deep picoplankton population and the above-described model are apparent. I have selected one station as representative of the phenomenon to detail these analogies.

The station, located at N°10.0896 E°64.9829 was sampled for chlorophyll and irradiance at approximately noon on 11 November 1995. As was typical throughout the region for this time of year, the station was characterized by a strong chlorophyll maximum at the base of the euphotic zone where nutrients started to increase and oxygen decreased rapidly (figure 5). Also typical of the secondary chlorophyll maximum stations was a secondary peak in the fluorescence coincident with the transition layer between the oxic/anoxic regions. Percent total surface irradiance at the depth of the secondary fluorescence maximum (132m) was ~0.05%, well below the classically defined euphotic zone depth ($\approx 1\%$) of 84meters. Hence, while nutrients are high, light levels are extremely low suggesting light-limitation. If light is limiting and there are adequate nutrients immediately above the deep population maximum, there must be an additional advantage such as predator avoidance due to anoxic conditions at that water column location. Regardless, the deep peak must be extremely efficient if photosynthetically active.

These deep phytoplankton, presumed to be light-limited because their photosynthetic response is exclusively on the linear portion of a PvsE curve, must be well adapted to survive in an extremely low light level environment. In fact, for a similar station the initial slope of a PvsE curve is $0.26 \text{ mg C mg Chl}^{-1} \text{ hr}^{-1}$ with I_k at $17 \mu \text{Ein m}^{-2} \text{ sec}^{-1}$. What adaptations enable these phytoplankton to survive with orders of magnitude less light than chlorophyll maximum populations? One line of evidence centers around the size of the dominant phytoplankton in these deep secondary fluorescence peaks. Because the phytoplankton at the secondary peak are small, they are afforded certain inherent advantages with phytoplankton-light interactions. In addition to small phytoplankton exhibiting minimal package effects⁵ and optimized pigment complementation⁶, inherent physical interactions between light and phytoplankton may be important.

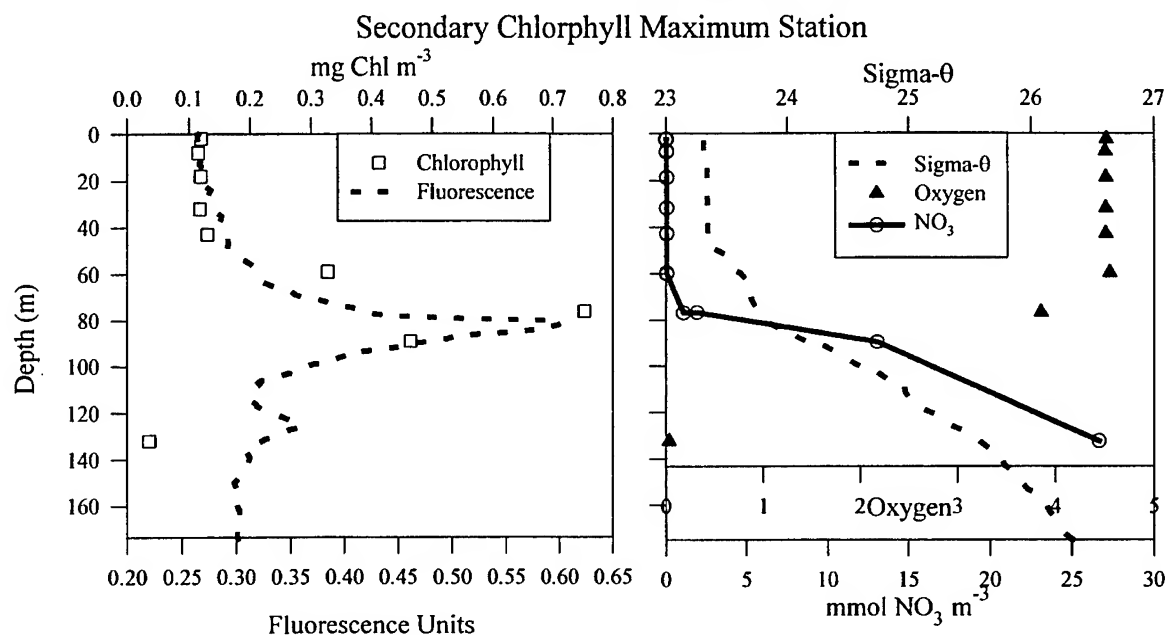


Figure 5: Biological and physical characteristics of the secondary chlorophyll maximum station in the Arabian Sea at $N^{\circ}10.09$ $E^{\circ}64.98$. Fluorometry data courtesy of C Trees (CHORS).

From the model derived above, size is shown to profoundly influence the behavior of light-particle interactions. With the spectral input of light, the Van de Hulst scattering model suggests a sharp increase in scattering efficiency from 0 to $5.5 \mu \text{meters}$ in diameter where a peak in scattering efficiency occurs (figure 4). Subsequently, scattering efficiency drops-off and reaches a stable value of ~ 1.1 at approximately $10 \mu \text{meters}$. From an anthropocentric point of view, a phytoplankter trying to optimize its light capturing ability by minimizing the scattering efficiency should be to the left of the value of 1.1 on the ascending portion of the scattering efficiency curve. For a phytoplankter, this translates into a size range that is less than $2.6 \mu \text{meters}$ in diameter. Further, since the slope of this portion of the curve is quite steep, small decreases in diameter will result in relatively large decreases in scattering efficiency; a decrease in scattering efficiency from a typical $2 \mu \text{meters}$ diameter dinoflagellate to a typical $1.2 \mu \text{meters}$ diameter *Synechococcus* cell to a typical $0.6 \mu \text{meter}$ diameter *Prochlorococcus* cell is 57% and 73%, respectively. To a phytoplankter under extreme light limitation, such differences represent a huge influence in the amount of light that is scattered; at the secondary chlorophyll peak dominated exclusively by *Prochlorophytes*, cell density was $< 26,000 \text{ cell ml}^{-1}$, and assuming a completely non-columnar light-field and a typical diameter for *Prochlorococcus* the average distance between particles over all angles is greater than the expanse of the secondary peak. Thus, a scattered photon is a lost photon.

The model assumes that the refractive index remains constant over different size ranges. In fact, the refractive index has been shown to vary substantially, both spectrally and with different types of cells from different size classes. The imaginary portion of the refractive index which corresponds to absorption properties is particularly variable between taxa. A comparison of scattering efficiency curves for $m = 1.05 - 0.01i$, a typical value for *Prochlorococcus* and $m = 1.05 - 0.003i$, a typical value for *Synechococcus*⁶ reveals that the peak height and location is variable because of the large changes in the refractive index due to absorptive property differences. For the larger *Synechococcus* cells with the smaller n' , the scattering

efficiency peak is moved to the right by 0.4 μ meters (data not shown). This may be another evolutionary mechanism whereby larger light-limited phytoplankton alter their refractive index through cellular composition changes to compensate for their larger size.

Several problems exist in the derived model describing scattering efficiency as a function of diameter. Refractive indices are assumed to remain constant over a wide size range, when definite differences exist. Refractive indices are also assumed to be spectrally independent, when clearly phytoplankton pigments can markedly influence the absorptive and scattering properties of the cell. Finally, the derivation of the scattering model uses the Van de Hulst approximation which can lead to errors in determining attenuation, scattering, and absorption efficiencies.¹⁶

5. CONCLUSIONS

Despite some shortcomings, the simple scattering efficiency model has some interesting implications: (1) Size is an important factor in influencing scattering efficiency. In very low light regimes selective pressure could favor smaller phytoplankton due to reduced scattering efficiency. (2) To overcome scattering efficiency selective pressure due to size considerations, refractive indices may be selected for which minimize scattering efficiency for a given size. (3) Phytoplankton may have inherent physical characteristics beyond pigment complementation that optimize the phytoplankton-light interactions in an extremely light limited situation.

6. ACKNOWLEDGEMENTS

I would like to thank RT Barber for critical reading of an earlier version of this manuscript, R Olson and A Shalapyounok (WHOI) for Prochlorophyte numbers, and C Trees (SDSU-CHORS) for providing fluorometry and spectroradiometry data for the Arabian Sea secondary chlorophyll maximum station. This is a US JGOFS contribution supported by NSF Grant OCE-9312355.

7. REFERENCES

1. G. R. DiTullio, D. A. Hutchins, and K. W. Bruland, "Interaction of iron and major nutrients controls phytoplankton growth and species composition in the tropical North Pacific Ocean," *Limno. and Oce.*, **38**(3), p.495-508, 1993.
2. S. W. Chisholm, "Phytoplankton Size," in *Primary Productivity and Biogeochemical Cycles in the Sea*, P. G. Falkowski and A. D. Woodhead ed., p.213-237 Plenum Press, New York, 1992.
3. J. B. Waterbury, S. W. Watson, F. W. Valois, and D. G. Franks, "Biological and ecological characterization of the marine unicellular cyanobacterium *Synechococcus*," in *Can. Bul. of Fish. Aq. Sci.*, **214**, T. Platt and W. Li ed., p.71-210 1986.
4. R. J. M. Hudson and F. M. M. Morel, "Iron transport in marine phytoplankton: Kinetics of cellular and medium coordination reactions," *Limno. and Oce.*, **35**(5), p.1002-1020, 1990.
5. A. Morel and A. Bricaud, "Theoretical results concerning light absorption in a discrete medium, and application to specific absorption of phytoplankton," *Deep-Sea Res.*, **28a**(11), p.1375-1393, 1981.
6. A. Morel, Y.-H. Ahn, F. Partensky, D. Vaultot, and H. Claustre, "Prochlorococcus and Synechococcus: A comparative study of their optical properties in relation to their size and pigmentation.," *J. of Mar. Res.*, **51**(3), p.617-649, 1993.
7. H. C. Van de Hulst, *Light Scattering by Small Particles*, John Wiley and Sons, NY, 1957.
8. G. Mie, "Beitrage zur Optik truber Medien, speziell kolloidalen Metall-losungen," *Annalen der Physik*, **25**, p.377-445, 1908.
9. C. Trees, personal communication.
10. A. Morel, "Optics from the single cell to the mesoscale," in *Ocean Optics*, **25**, R. W. Spinrad, K. L. Carder and M. J. Perry ed., p.93-106 Oxford Univeristy Press, New York, 1994.
11. A. Bricaud, A.-L. Bedhomme, and A. Morel, "Optical Properties of diverse phytoplankton species: experimental results and theoretical interpretation," *J. of Plank. Res.*, **10**(5), p.851-873, 1988.
12. A. Morel and L. Prieur, "Analysis of variations in ocean color," *Limno. and Oce.*, **22**(4), p.709-722, 1977.
13. A. Morel, "Optical Modeling of the Upper Ocean in Relation to Its Biogenous Matter Content (Case I Waters)," *J. of Geophys. Res.*, **93**(C9), p.10749-10768, 1988.
14. J. T. O. Kirk, *Light and Photosynthesis in Aquatic Ecosystems*, Cambridge University Press, NY, 1994.
15. R. Goericke, L. Campbell, H. Liu, A. Shalapyounok, and R. Olson, personal communication.
16. D. Deirmendjian and R. J. Clasen. (United States Air Force Project Rand, Santa Monica, 1962).

Phytoplankton quantum yield measured on minute time scales *in situ*

Gary J. Kirkpatrick¹, Daniel Kamykowski² and Robert E. Reed²

¹Mote Marine Laboratory, 1600 Ken Thompson Parkway, Sarasota, FL 34236

²North Carolina State University, Department of Marine, Earth and Atmospheric Sciences,
PO Box 8208, Raleigh, NC 27695-8208

ABSTRACT

We measure simultaneously, on sub-minute time scales, the downwelling irradiance spectra and the vertical attenuation spectra for downwelling irradiance of a contained phytoplankton culture while the culture is exposed to the full spectrum of an *in situ* light treatment. This technique incorporates miniature, fiber optic spectrometers (Ocean Optics, Inc.) and twin Self-contained, Underwater Photosynthesis Apparatus (SUPA). One SUPA serves as the reference, with filtered culture media in the exposure chamber. The other SUPA contains the phytoplankton sample in the exposure chamber. Using the assumptions that irradiance reflectance is small (<5%) in the SUPA and that upwelling vertical attenuation equals downwelling vertical attenuation in the culture, it is possible to approximate the flux absorbed by the phytoplankton by the product of downwelling irradiance and downwelling vertical attenuation. The concurrent measurements of net carbon uptake and net oxygen production in SUPA, each minute, support calculations of net quantum yield of the phytoplankton *in situ*. Results from a field study using the red tide organism *Gymnodinium breve* illustrate the ability to quantify the effects high, fluctuating irradiance exposure near the surface.

Keywords: *in situ* quantum yield, attenuation spectra, phytoplankton, fiber-optic spectrometer, *Gymnodinium breve*, SUPA

1. INTRODUCTION

Bio-optical models of primary production require knowledge of the operational quantum yield of photosynthesis.¹ Quantum yield is highly variable,²⁻⁶ dependent upon species and history of exposure to environmental conditions. Absorbed quanta (AQ) and photosynthetic yield (P) are needed to compute quantum yield directly. Presently the AQ must be estimated using irradiance spectra calculated or measured at the depth of interest, and using absorption spectra determined in the laboratory after samples of phytoplankton have been removed from the environment of interest and prepared for analysis. Additionally, the absorption spectra are measured using scanning monochrometers that expose the sample to sequential, narrow wavebands of light. The presumption that absorption spectra measured in laboratory spectrophotometers accurately represent absorption characteristics *in situ* is not well founded at present. Cullen and Lewis⁷ suggest that the application of remote sensing to productivity measurements lacks an understanding of the response of phytoplankton to high and fluctuating irradiance experienced in the surface layer, a particularly problematic issue since this is where the strongest impacts occur on remote sensing reflectance. Many bio-optical models estimate gross production and therefore do not account for the concurrent energy costs of cellular metabolism and behavior.⁸ Eventually, net production will be required for modeling carbon flux on a global scale.

Kuhl and Jorgensen⁹ demonstrated the feasibility of using fiber-optic spectrometers to measure spectral irradiance in the aquatic environment. Recently, two miniature, fiber optic, CCD spectrometers (Ocean Optics, Inc.) have been fitted, in a trial configuration, to the Self-contained Underwater Photosynthesis Apparatus (SUPA).¹⁰ Tests have demonstrated a unique ability to measure vertical attenuation spectra, of phytoplankton culture contained within one of the SUPA exposure chambers relative to filtered medium in the other chamber under full-spectrum irradiance exposure, that complement SUPA's proven ability to measure photosynthetic carbon uptake and oxygen production of the contained culture on minute time scales *in situ*.

2. METHODS

2.1 Instrument

For this study, the SUPA consisted of twin one-liter, quartz-dome chambers (Fig. 1), each with a set of sensors including temperature, pH, dissolved oxygen and spectral irradiance, and a single data acquisition and control computer. A slow-speed stirring paddle maintained a homogeneous distribution of the phytoplankton sample. The pH and reference electrode were a unique design (Innovative Sensor, Inc.) that allowed them to operate pointing upward; the dissolved oxygen electrode operated in the pulsed mode to reduce stirring requirements. The spectral irradiance sensors were based on dual Ocean

Optics, Inc., miniature, fiber-optic spectrometers. Teflon disks, 0.8 mm thick, positioned in the center and just above the surface of the each exposure chamber baseplate, served as the downwelling irradiance collectors.

These collector disks were viewed from below by 200 μm diameter, silica (HOH) optical fibers (0.22 NA). The optical configuration of the fiber-optic spectrometer included a grating with 600 lines mm^{-1} and an 1100 element CCD. This configuration provided a spectral range from 350 to 890 nm with an optical resolution of approximately 10 nm and a pixel resolution of approximately 0.5 nm. The serial stream of 1100 analog output signals were digitized to 12 bits and averaged with either 35 or 8 other spectra depending on the shutter period of either 66 msec or 264 msec respectively.

Approximately 6 averaged spectra were stored to disk each minute. The spectral irradiance sensors was calibrated against a calibrated fiber optic spectrometer (Analog Spectral Devices, Inc., LabSpec) under solar irradiance.

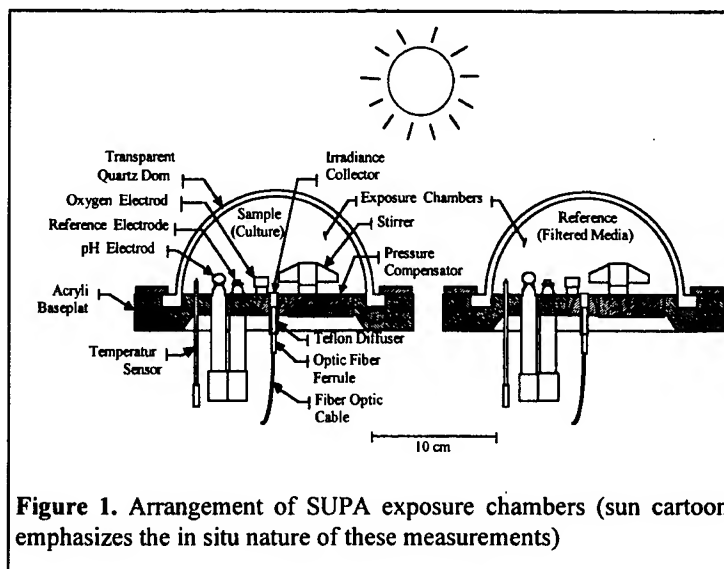


Figure 1. Arrangement of SUPA exposure chambers (sun cartoon emphasizes the in situ nature of these measurements)

2.2 Field experiment

A batch culture of the red tide dinoflagellate *Gymnodinium breve* was grown in f/2 media¹¹, at 25 °C, under approximately 60 $\mu\text{mol m}^{-2} \text{sec}^{-1}$ scalar irradiance (PAR). One SUPA exposure chamber was filled with the culture which had reached a chlorophyll *a* concentration of approximately 50 $\mu\text{g l}^{-1}$. The other SUPA chamber was filled with the filtrate from filtration of an aliquot of the culture through glass-fiber filters (Whatman, GF/F) using < 75 mmHg vacuum. Additionally, a 20 l collapsible polyethylene bag with a quartz window on the top side was attached to the SUPA at the same level as the SUPA exposure chamber. This bag was also filled with the red tide culture and samples were withdrawn periodically through tubing connected from the bag to the SUPA exposure chamber and from the exposure chamber to the dock. Aliquots of these periodic samples were filtered using GF/F filters and the phytoplankton absorption spectrum determined using the quantitative filter technique (QFT).^{12,13} The apparatus was suspended at a depth that ranged from 0.5 m and 1 m, depending on the tide. Measurements began at approximately 2200 hrs and continued for 36 hours. Data from the daylight period of the first day are considered in this paper. The sky was nearly cloudless on the morning of the first day resulting in irradiance exposure well above the desired levels. The exposure level was reduced by suspending a layer of neutral density screening above the SUPA at approximately 0925 hrs.

2.3 Calculations

The spectral irradiance data were binned into one minute intervals to match the data period of the SUPA productivity measurements (recorded once per minute). The vertical attenuation coefficient for downwelling irradiance within the sample exposure chamber attributable to the phytoplankton cells ($K_{dph}(\lambda, t)$) was calculated from:

$$K_{dph}(\lambda, t) = -\frac{d \ln E_d(\lambda, t)}{dz} \cong \frac{\ln E_{dr}(\lambda, t) - \ln E_{ds}(\lambda, t)}{r} \quad (1)$$

where $E_{dr}(\lambda, t)$ is the spectral (λ) downwelling irradiance at time t in the SUPA exposure chamber with filtered media (reference), $E_{ds}(\lambda, t)$ is the spectral downwelling irradiance at time t in the SUPA exposure chamber with phytoplankton (sample) and r is the radius of the SUPA dome. With the assumption that irradiance reflectance was small (<5%) and the vertical attenuation coefficient for upwelling irradiance equaled that for downwelling irradiance within the SUPA exposure chambers, Kirk¹⁴ provided an approach for calculating quanta absorbed by the phytoplankton within the SUPA sample exposure chamber (AQ_{ph}) such that:

$$AQ_{ph}(t) \cong \int_{400}^{700} K_{dph}(\lambda, t) \cdot E_{dr}(\lambda, t) d\lambda . \quad (2)$$

It should be emphasized that the configuration of the twin SUPA chambers with filtered culture media in the reference chamber made it possible to assume that the difference in downwelling irradiance between two chambers was due to phytoplankton, the absorption by water being approximately the same in both chambers. The operational quantum yield of photosynthesis ($\phi_{O_2}(t)$) was calculated using the relationship:

$$\phi_{O_2}(t) = \frac{P_{O_2}(t)}{AQ_{ph}(t)} \quad (3)$$

where $P_{O_2}(t)$ is the SUPA-measured rate of oxygen evolution at time t

3. RESULTS

Net oxygen evolution increased rapidly in the early morning, reaching maximal rates by 0900 hrs (fig. 2). A period of rapidly increasing irradiance between 0900 and 0925 did not yield commensurately higher productivity. After the neutral density screen was placed over the instrument the oxygen evolution rates were maintained until approximately 1100 hrs. when the turbidity of the water surrounding the SUPA increased (data not shown). This turbidity increase was apparent in a shift to more green irradiance spectra and a sharp decline in AQ_{ph} . Additionally, the irradiance exposure throughout the morning and early afternoon was a least twice the preparatory, laboratory growth irradiance level even with the neutral density screen. The culture apparently was stressed by these irradiance levels as the cells in the polyethylene reservoir bag gradually settled or swam to the bottom of the bag, resulting in reduced cell counts (from 9×10^6 to 5×10^6 cells l^{-1}) and chlorophyll content (from 50 to 30 $\mu g\ l^{-1}$) in the SUPA as the day progressed. By mid-afternoon the oxygen evolution rate had reached zero and continued to decrease to a basal respiration rate in the dark that was stable through the night.

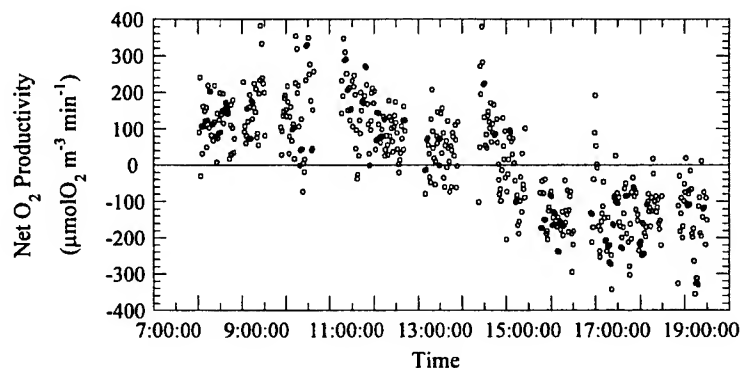


Figure 2. SUPA-measured net oxygen productivity. Gaps in the dataset correspond to the times when discrete culture samples were removed from the SUPA exposure chamber, interfering with the productivity measurements.

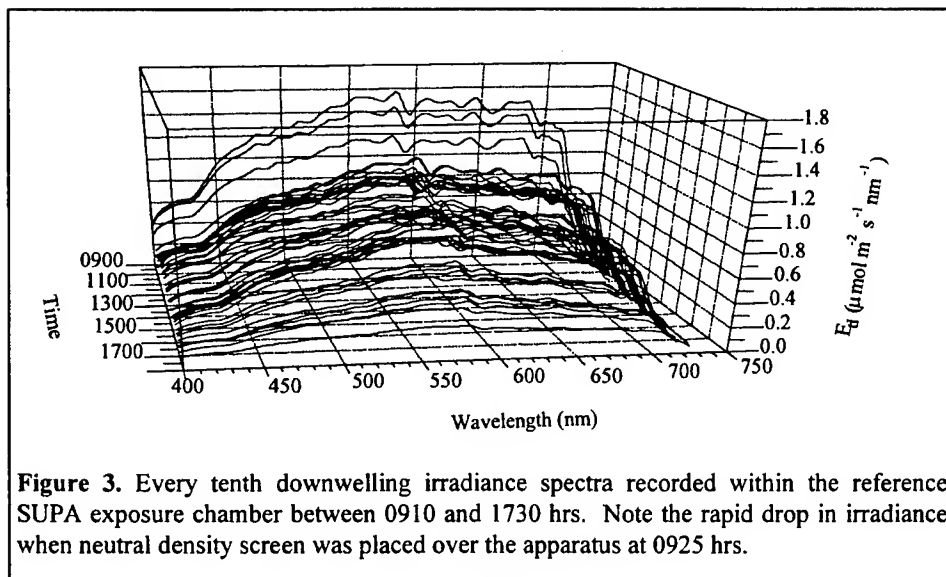


Figure 3. Every tenth downwelling irradiance spectra recorded within the reference SUPA exposure chamber between 0910 and 1730 hrs. Note the rapid drop in irradiance when neutral density screen was placed over the apparatus at 0925 hrs.

The irradiance exposure fluctuated widely due to the passage of thunderstorms, the change in water turbidity and the application of the neutral density screen (fig 3). A few

irradiance spectra were considered outliers resulting from shading due to dock pilings (early and late in the day) and personnel on the dock. These outliers were easy to detect, often in groups over several minutes, from the significant (>10%) difference between the reference and sample chamber readings. Discounting the outliers, the shape of the vertical attenuation spectra (fig. 4) were consistent through the day and the variation in magnitude correlated well with the variation of chlorophyll *a* concentration in the exposure chamber.

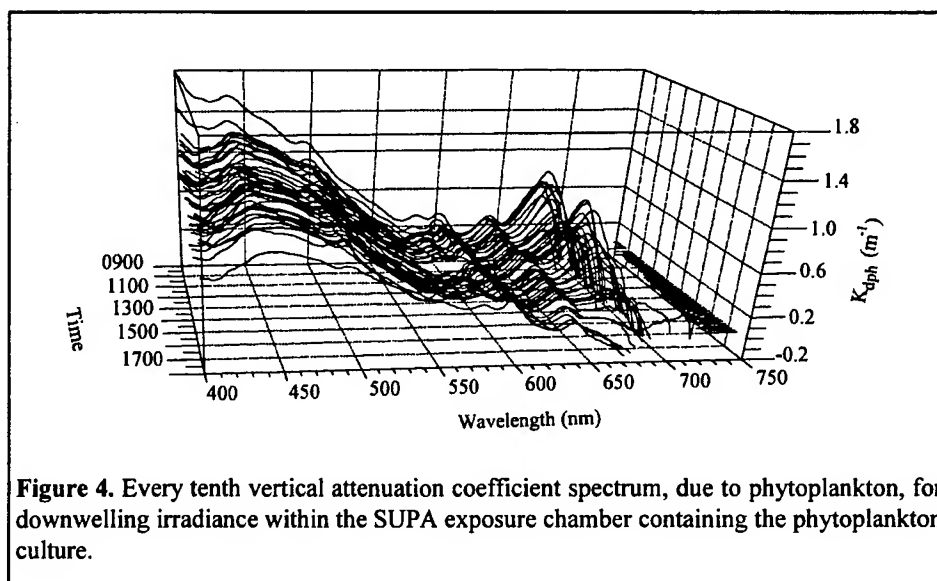


Figure 4. Every tenth vertical attenuation coefficient spectrum, due to phytoplankton, for downwelling irradiance within the SUPA exposure chamber containing the phytoplankton culture.

Shoulders in the attenuation spectra matched the shoulders in the absorption spectra obtained by the QFT (Fig. 5). The shoulder at 466 nm is less pronounced in the SUPA attenuation spectra than in the QFT absorption spectra, and the shoulders

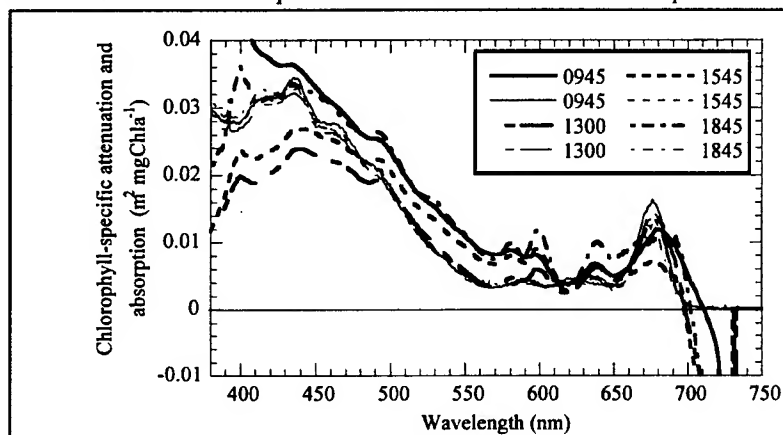


Figure 5. Comparisons, at the indicated times, of SUPA-measured vertical attenuation coefficient for downwelling irradiance versus absorption spectra obtained using the quantitative filter method on discrete samples. Thick lines, K_{dph} ; thin lines, ap .

absorption spectra peaks and other extended periods when the attenuation spectra peaks are significantly lower than the absorption spectra peaks. These long-period trends suggest processes within the culture are responsible for some of the variability. Negative attenuation is also apparent in the spectra of figure 4 between approximately 700 nm and 740 nm. This has been tentatively identified as fluorescence.

The net quantum yield of oxygen evolution measured for this *in situ* culture was within the expected range of values and was related to the AQ_{ph} (Fig. 6). The relationship to AQ_{ph} was consistent through the morning, but net quantum yield began decreasing in the early afternoon and continued downward through the rest of the day. The magnitude of *in situ* irradiance during the middle of the day was higher than growth irradiance in the laboratory. This *in situ* light stress may have inhibited

and peaks at 495, 590, and 639 nm are more pronounced in the attenuation spectra. Generally, the magnitudes of the attenuation spectra and absorption spectra match well, but there is more variability in the attenuation spectra throughout the day. The attenuation spectra are considerably different than the absorption spectra at the 678 nm absorption peak. Some of this variability is due to the decreasing signal-to-noise ratio resulting from the rapid decrease of irradiance reaching the instrument with increasing wavelength in this part of the spectrum. However, this variability is not simply noise due to low signal strength. There are consistent trends, for extended periods, where the 678 nm peaks in the attenuation spectra match the

or damaged the photosynthetic system thus reducing oxygen production, and requiring enhance metabolic use of oxygen to counteract the effects of the stress. The decrease of cell count in the reservoir bag from the late morning through the rest of the day suggests that the cells were avoiding the high irradiance by moving to deeper water (bottom of the reservoir).

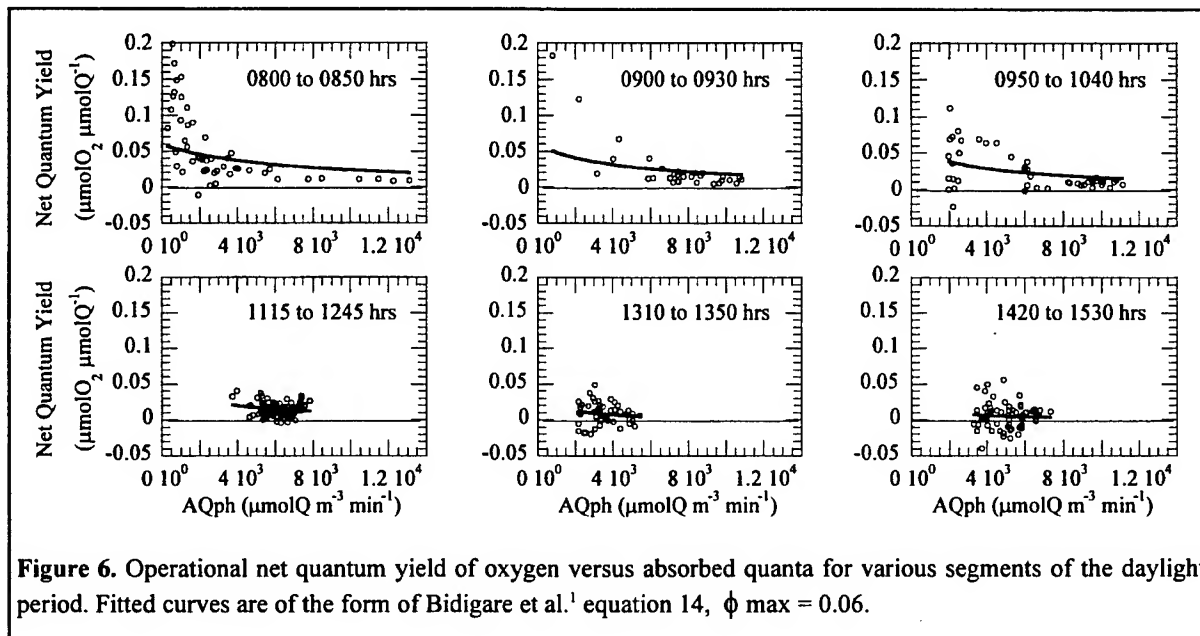


Figure 6. Operational net quantum yield of oxygen versus absorbed quanta for various segments of the daylight period. Fitted curves are of the form of Bidigare *et al.*¹ equation 14, $\phi_{\text{max}} = 0.06$.

4. DISCUSSION

Several improvements are planned to reduce some of the variability in the attenuation spectra. These include frosted domes to increase the similarity of the light field diffuseness in the exposure chambers, more extensive calibration measurements, more care in the selection of deployment site to avoid interference from surrounding structures and increased sample averaging with outlier removal. With these improvements, the time course of attenuation spectra variation and quantum yield will readily be measured over multi-day deployments. This is a particularly useful capability for investigations of the photophysiology and migration behavior of the surface-dwelling red tide organism, *Gymnodinium breve*. Spectral attenuation and fluorescence emission measurements will permit estimates of the light energy budget in an investigation of the partitioning of energy by bloom-forming dinoflagellates with different vertical migration strategies. Kamykowski *et al.*¹⁵ describe a metabolism and photoacclimation biophysical model of dinoflagellate swimming behavior that incorporates a "metabolism-influenced" response.

Millie *et al.*¹⁶ applied fourth derivative analysis to optical density spectra from laboratory, light treatment experiments to identify regions of the spectra that responded significantly to different light exposures. Changes were related to HPLC derived photosynthetic and photo-protective pigments. The combination of our ability to subsample the SUPA culture for HPLC pigment analysis with the ability to measure attenuation spectra *in situ* will extend this experiment to short time scales in the natural water column.

The variability of quantum yields must be described to verify and refine bio-optical production models. Operational quantum yields in natural populations and in cultures vary with light exposure, nutrient availability, temperature exposure and growth phase.²⁻⁶ SUPA now provides a capability to directly measure quantum yield allowing manipulative studies on populations with a known history *in situ* to develop a submodel for quantum yield.

5. CONCLUSION

The good resemblance between the SUPA-derived vertical attenuation spectra and the particulate absorption spectra obtained using the quantitative filter method suggest the SUPA approach is providing spectra that are useful for computing absorbed

quanta. The operational quantum yield values determined with this method compared favorably to results from other accepted methods. The approach is seen as a means to extend laboratory techniques to *in situ* studies. Doing so will establish the links between processes elucidated in the laboratory and how those processes behave *in situ* to produce the observed results in natural populations.

6. ACKNOWLEDGEMENTS

The authors wish to thank Dr. Robert Euwema and Maxim Eckmann for their tireless efforts developing a set of software to acquire, store and process the spectrometer and SUPA data. This research was supported by NASA grant NAGW-3575 (GJK, DK), ONR AASERT grant N00014-93-1-1156 (RER) and the William G. Selby and Marie Selby Foundation.

7. REFERENCES

1. Bidigare, R.R., B.B. Prezelin and R.C. Smith, "Bio-optical models and the problems of scaling," *Primary Productivity and Biogeochemical Cycles in the Sea*, P. G. Falkowski and A. Woodhead, Editors, 175-212, Plenum Press, New York, 1992.
2. Cleveland, J. S., M. J. Perry, D. A. Kiefer, and M. C. Talbot, "Maximum quantum yield of photosynthesis in the northwestern Sargasso Sea," *J. Mar. Res.*, **47**, 869-886, 1989.
3. Kolber, Z., K. D. Wyman and P. G. Falkowski, "Natural variation in photosynthetic energy conversion efficiency: a field study in the Gulf of Maine," *Limnol. Oceanogr.*, **35**, 72-79, 1990.
4. Schofield, O., B. B. Prezelin, R. R. Bidigare and R. C. Smith, "In situ photosynthetic quantum yield. Correspondence to hydrographic and optical variability within the southern Californian bight," *Mar. Ecol. Prog. Ser.*, **78**, 253-271, 1993.
5. Sosik, H. M. and B. G. Mitchell, "Effects of temperature on growth, light absorption, and quantum yield in *Dunaliella tertiolecta* (chlorophyceae)," *J. Phycol.*, **30**, 833-840, 1994.
6. Kroon, B. M. A., "Variability of photosystem II quantum yield and related processes in *Chlorella pyrenoidosa* (Chlorophyta) acclimated to an oscillating light regime simulating a mixed photic zone," *J. Phycol.*, **30**(5), 841-852, 1994.
7. Cullen, J. J. and M. R. Lewis, "Biological processes and optical measurement near the sea surface: Some issues relevant to remote sensing," *J. Geophys. Res.*, **100**(C6), 13,255-13,266, 1995.
8. Geider, R. J., "Respiration: Taxation without representation," *Primary Productivity and Biogeochemical Cycles in the Sea*, P. G. Falkowski and A. Woodhead, Editors, 47-67, Plenum Press, New York, 1992.
9. Kuhl, M. and B. B. Jorgensen, "Spectral light measurements in microbenthic phototrophic communities with a fiber-optic microprobe coupled to a sensitive diode array detector," *Limnol. Oceanogr.*, **37**, 1813-1823, 1992.
10. Kirkpatrick, G.J., T.B. Curtin, D. Kamykowski, M.D. Feezor, M.D. Sartin and R.E. Reed, "Measurement of photosynthetic response to euphotic zone physical forcing," *Oceanogr.*, **3**(1), 18-22, 1990.
11. Guillard, R. R. L. and J. H. Ryther, "Studies of marine planktonic diatoms. I. *Cyclotella nana* Hustedt and *Detonula confervacea* (Cleve) Gran," *Can. J. Microbiol.*, **8**, 229-239, 1962.
12. Mitchell, B.G., "Algorithms for determining the absorption coefficient for aquatic particulates using the quantitative filter technique," *Ocean Optics X*, Richard W. Spinrad, Editor, Proc. SPIE 1302, 137-148, 1990.
13. Cleveland, J. S. and A. D. Weidemann, "Quantifying absorption by aquatic particles: A multiple scattering correction for glass-fiber filters," *Limnol. Oceanogr.*, **38**(6), 1321-1327, 1993.
14. Kirk, J. T. O., *Light and photosynthesis in aquatic ecosystems*, 293-305, Cambridge University Press, Cambridge, 1994.
15. Kamykowski, D., H. Yamazaki, A. K. Yamazaki and G. J. Kirkpatrick, "A comparison of how different orientation behaviors influence dinoflagellate trajectories and photoresponses in turbulent water columns," *The Physiology and Ecology of Harmful Algal Blooms*, D. M. Anderson, A. D. Cembella and G. M. Hallegraeff, Editors, Springer-Verlag, In press.
16. Millie, D. F., G. J. Kirkpatrick and B. T. Vinyard, "Relating photosynthetic pigments and *in vivo* optical density spectra to irradiance for the Florida red-tide dinoflagellate, *Gymnodinium breve* Davis," *Mar. Ecol. Prog. Ser.*, **120**, 65-75, 1995.

Measurements of photo-physiological parameters and primary production
in the Central North Pacific Ocean

Michael E. Ondrusek and Robert R. Bidigare

University of Hawai'i, Department of Oceanography, Honolulu, HI 96822

ABSTRACT

The North Pacific Central Gyre is one of the largest homogenous bodies of water on Earth. Phytoplankton distributions appear to remain relatively constant for thousands of kilometers throughout the year. However, recent studies conducted at Station ALOHA as part of the Hawaii Ocean Time-series (HOT) program reveal significant seasonal and interannual variability in phytoplankton biomass and production rates. Despite the high resolution sampling performed at the HOT site, spatial and temporal variations in phytoplankton pigment biomass are difficult to resolve. This will require remote sensing platforms such as moorings and satellites. *In situ* measurements of the photo-physiological parameters necessary to bio-optically model primary production rates are an essential element for the interpretation of data that will result from the HOT and MOBY moorings and the SeaWiFS and OCTS satellite sensors. We participated in a transect cruise in the North Pacific Ocean from Station ALOHA to the CLIMAX site to document the spatial variability of photo-physiological parameters and to determine if the conditions at the HOT site are representative of the central gyre and, in particular, are comparable to the CLIMAX site. We measured the light limited rate of photosynthesis (α), the irradiance at which photosynthesis becomes light saturated (E_k), the maximum rate of photosynthesis (P_{max}), the phytoplankton spectral absorption coefficient (a_{ph}^*), and the maximum quantum yield of photosynthesis (Φ_{max}). The photosynthetic parameters were similar at the HOT and CLIMAX locations, however a diatom bloom at intermediate stations resulted in a doubling of P_{max} , α , and Φ_{max} . If these variations in photosynthetic parameter estimates are not accounted for when modeling production rates for the diatom-dominated stations, then carbon uptake estimates would be underestimated by 2-fold. This study demonstrates the need for temporally dynamic algorithms that account for variations in phytoplankton composition and physiology.

Keywords: P vs. E, North Pacific Central Gyre, phytoplankton, quantum yield, absorption coefficient

1. INTRODUCTION

There are numerous versions of absorption- and photosynthesis vs. irradiance (P vs. E)-based models to bio-optically estimate primary production rates and all require some knowledge of the photosynthetic parameters P_{max} , α , and E_k .¹ For P vs. E models, E_k can be used to predict the light level at which photosynthesis rates drop below P_{max} . For absorption-based models, it is necessary to know the efficiency at which absorbed quanta are converted into carbon (Φ) under various light regimes.² Photosynthetrons provide a means of rapidly measuring quasi-instantaneous photosynthetic rates and how they vary as a function of growth irradiance. From these data, the photosynthetic parameters described above can be estimated as long as care is taken in relating the spectral light field in the photosynthetron to that in the field. In this report we describe variations in photosynthetic parameters measured on a cruise in the North Pacific Central Gyre. Knowledge of the magnitude and variability of these parameters is essential for developing robust light-pigment models for use in estimating production rates with data acquired via remote sensing.

2. METHODS

2.1 Sample collection

We participated in an ALOHA-CLIMAX transect cruise between 8-16 July 1996 aboard the R/V *Moana Wave*. Four evenly spaced stations were occupied beginning at Station ALOHA (22.75°N, 158.37°W) and ending at Station CLIMAX (28.00°N, 155.41°N). Experiments were performed using

clean techniques as described in the U.S. JGOFS protocols. Water was collected using 10 liter Go-Flo bottles on a kevlar line with Teflon messengers. Samples were collected daily from depths of 0 m, 45 m, 75 m, and 100 m, at 1330 hr (local time).

2.2 P vs. E measurements

From each depth, twenty-eight 20 ml-borosilicate scintillation vials were filled with seawater and spiked with approximately 11.5 μCi of ^{14}C sodium bicarbonate. Duplicate sub-samples of the tracer solution were collected daily to determine the activity of tracer added. Two vials were processed for T_0 counts and two vials were incubated in the dark. The tracer uptake in the dark controls were subtracted from the P vs. E rates to correct for dark uptake. The twenty-four remaining samples were incubated under twenty-four different light levels in one of four identical photosynthetrons. Each photosynthetron was illuminated with two 250 watt ENH lamps (Vantage Lighting, CA). The beam passed through a heat shield gel (ROSCO thermashield) to remove infrared light and then through a 2.54 cm copper sulfate solution producing a blue spectral quality of light that resembles the *in situ* light field. After the copper sulfate solution, the beam of light passes through neutral density filters which produce twenty-four different levels of photosynthetically available radiation (E_{PAR} , 0 - 1500 $\mu\text{Ein m}^{-2} \text{s}^{-1}$). The light enters the samples through the bottom of the scintillation vials which are set in a black aluminum cooling block. The 0 m and 45 m samples were cooled using pumped surface seawater. The two deeper samples were cooled with a refrigerated water bath. The samples were incubated for one hour. The spectral quality of the light was measured with a SpectraScope fiber optic probe attached to a S1000 spectrometer (Ocean Optics, Inc.). E_{PAR} was measured in each sample before each experiment with a Biospherical Instruments QSL-100 PAR meter. The start time for the incubations was when the lamps were switched on and the stop time was when the lamps were switched off.

2.3 Sample processing

Each sample of known volume was filtered through a 25 mm GF/F filter, acidified with 1 ml 10% HCl for 24 hrs and then fixed with 10 ml Aquasol II. The activities of the samples were counted initially and then recounted after 2 weeks. The counts after two weeks were used in the calculations (HOT protocols). The carbon uptake for each sample was calculated using the following equation:

$$P = (g \text{ C g Chl}^{-1} \text{ hr}^{-1}) = ([\text{DIC}] * ^{14}\text{C}_{\text{POC}} * 1.05) (^{14}\text{C}_{\text{DIC added}} * \text{incubation time} * g \text{ Chl})^{-1} \quad (1)$$

P vs. E curves are defined by the data points using a non-linear best fit solution to equation 2.^{3,4}

$$P = P_{\text{max}} * \tanh(E_{\text{PAR}} E_k^{-1}) * \exp(-\beta * (E_{\text{PAR}} - E_t)) \quad (2)$$

P_{max} is the Chl-specific maximum rate of photosynthesis ($g \text{ C g Chl}^{-1} \text{ hr}^{-1}$) measured in the photosynthetron and E_k ($\mu\text{Ein m}^{-2} \text{s}^{-1}$) is the saturation parameter for photosynthesis. The expression, $\exp(-\beta * (E_{\text{PAR}} - E_t))$, is a photoinhibition term, where $-\beta$ is the negative slope of the P vs. E curve encountered under high light levels and E_t is the light level at the onset of photoinhibition.

2.4 Production rate calculations

Photosynthesis rate, as computed using an absorption-based model,² is dependent on the quantum efficiency (Φ , mol C Ein^{-1}), Chl concentration, growth irradiance, and the spectrally-weighted Chl-specific absorption coefficient ($a_{\text{ph}} *$):

$$P = \Phi * E_{\text{PAR}} * \text{Chl} * \overline{a_{\text{ph}}} * \quad (3)$$

where Φ is parameterized according to the equation given below.²

$$\Phi = \Phi_{\text{max}} * (E_k E_{\text{PAR}}^{-1}) * \tanh(E_{\text{PAR}} E_k^{-1}) \quad (4)$$

In this study α_{ph} was estimated using the spectral reconstruction technique⁵ and the spectral irradiance distribution measured in the photosynthetron.

3. RESULTS

The photosynthetic parameters determined in this field study are summarized in Table 1. In the transect from Station ALOHA to Station CLIMAX, several trends are evident. Despite slightly higher values of P_{max} and α for each depth at Station CLIMAX relative to that measured at Station ALOHA, most of the variability observed at each site is consistent with photoadaptation.⁶ P_{max} and E_k decrease with increasing depth while α and Φ_{max} increase with increasing depth. At the intermediate stations, P_{max} also decreases with depth, however the 5 and 45 m values are approximately twice those measured at Stations ALOHA and CLIMAX. The highest P_{max} value ($9.93 \text{ g C g Chl}^{-1} \text{ hr}^{-1}$) was measured at the 24.6°N station. At the intermediate stations, α does not show the same pattern with depth as observed at the outer stations. At the intermediate stations, α values are approximately twice those measured at Stations ALOHA and CLIMAX with a maximum value of $0.030 \text{ g C g Chl}^{-1} \text{ hr}^{-1} (\mu\text{Ein m}^{-2} \text{ s}^{-1})^{-1}$ measured at 45 m of the 24.6°N station. E_k values measured at a given depth do not vary appreciably with respect to latitude. Maximum quantum yield values generally increase with increasing depth with the exception of the maximum value of $0.046 \text{ mol C Ein}^{-1}$ measured at 45 m of the 24.6°N station.

Based on pigment profiles (data not shown), the conditions at Stations ALOHA and CLIMAX were consistent with and representative of typical oligotrophic conditions in the North Pacific Central Gyre.^{7,8} Chl concentrations were low in surface waters ($<0.1 \text{ mg m}^{-3}$) and gradually increased to maximum concentrations at 100 m ($0.2 - 0.3 \text{ mg m}^{-3}$). At the intermediate stations, there is a second chlorophyll maximum at 45 m with concentrations twice those measured at 45 m at Station ALOHA and Station CLIMAX. Prokaryotic pigment marker concentrations (divinyl chlorophyll *a* and zeaxanthin) measured at a given depth did not vary with respect to latitude. By comparison, fucoxanthin concentrations (diatom marker) increased by up to 20-fold at depths of 5 and 45 m sampled at the intermediate stations; other eukaryotic phytoplankton pigment markers did not show latitude-dependent variations. The presence of a diatom bloom at the intermediate stations was confirmed by light microscopy (R. Scharek, per. comm).

4. DISCUSSION

At present, we have not determined what caused the diatom bloom encountered along the transect. Most likely there was an increase in nutrient supply from below the mixed layer or an increase in iron from the deposition of atmospheric dust.^{9,10} The nitrate plus nitrite values are depleted ($<0.01 \mu\text{M}$) in the mixed layer of all stations. Concentrations start to increase at shallower depths at the 24.6°N station (80 m) relative to that observed at the other stations ($<110 \text{ m}$), possibly indicating a recent mixing event. Meteorological data may help clarify the physical processes that triggered the diatom bloom. We have also not been able to resolve the temporal and spatial extent of the bloom, but we can estimate some limits for these scales. We know that the latitudinal extent of the bloom was constrained between Station ALOHA and Station CLIMAX and extended at least the distance between the two intermediate stations. The bloom lasted at least one week since elevated fucoxanthin concentrations were encountered on the transect back to Hawai'i. The temporal and spatial scales of such a bloom could be resolved using ocean color imagery. Even though the pigment concentrations were higher at the 26.4°N site than at the 24.6°N , the elevated α and Φ_{max} values at 24.6°N suggest that this station may have had higher growth rates and was at the beginning or middle phase of bloom formation while the bloom at 26.4°N bloom may have already peaked.¹¹

We modeled the production rates at Station ALOHA and the 24.6°N station using the absorption-based and P vs. E models described above. First we calculated production rates using the photosynthetic

Table 1. Photosynthetic parameters determined for natural populations of phytoplankton from the ALOHA-CLIMAX cruise (units: P_{\max} = g C g Chl⁻¹ hr⁻¹; α = g C g Chl⁻¹ hr⁻¹ (μ Ein m⁻² s⁻¹)⁻¹; E_k = μ Ein m⁻² s⁻¹; \overline{aph}^* = m² mg Chl⁻¹; Φ_{\max} = mol C Ein⁻¹)

Date	Depth (m)	Latitude (°N)	Longitude (°W)	P_{\max}	α	E_k	\overline{aph}^*	Φ_{\max}
07/09/96	5	22.75	158.00	3.46	.007	484	.018	.009
07/09/96	45	22.75	158.00	3.48	.011	325	.015	.017
07/09/96	75	22.75	158.00	2.19	.014	157	.011	.030
07/09/96	100	22.75	158.00	1.27	.012	106	.011	.026
07/10/96	5	24.57	157.00	9.01	.021	424	.023	.021
07/10/96	45	24.57	157.00	7.01	.030	234	.015	.046
07/10/96	75	24.57	157.00	2.38	.021	113	.012	.042
07/10/96	100	24.57	157.00	1.37	.013	106	.011	.026
07/11/96	5	26.38	156.17	9.93	.015	662	.018	.019
07/11/96	45	26.38	156.17	6.88	.025	272	.018	.032
07/11/96	75	26.38	156.17	2.11	.021	101	.013	.039
07/11/96	100	26.38	156.17	1.44	.018	80	.011	.038
07/12/96	5	28.00	155.41	5.55	.011	513	.015	.016
07/12/96	45	28.00	155.41	4.12	.016	250	.014	.027
07/12/96	75	28.00	155.41	2.96	.015	199	.013	.026
07/12/96	100	28.00	155.41	1.87	.019	98	.013	.034

parameters measured at each station, then recalculated the production rate at the 24.6°N station using the photosynthetic parameters measured at Station ALOHA. This was done to assess the error produced when typical values for photosynthetic parameters are used as constants to model productivity over large temporal or spatial scales. When using the higher Φ_{\max} measured at the 24.6°N station, absorption-based model estimates were 2.6-fold higher than when Φ_{\max} values from Station ALOHA were used in the calculation. Use of the higher P_{\max} values measured at the 24.6°N station in the P vs. E model yielded daily production rates which were 2.7-fold higher than that obtained using the P_{\max} values measured at Station ALOHA. This may seem obvious, however, many studies have used Φ_{\max} and P_{\max} values measured at one location as values for computing production rates at different locations or at the same location at different times.

A large number of P vs. E responses using photosynthetrons have been determined for the equatorial Pacific, California coastal waters, and the Atlantic.^{6,12,13} However, prior to this study, comparable measurements have not been published for Hawaiian waters or the North Pacific Central Gyre. Some efforts have been made to parameterize P vs. E relationships when modeling global rates of primary production. The most accurate estimates of primary production will probably come from local investigators using regional parameterizations over time and space. Each investigator can ground truth their estimates and work on scales small enough to modify, when necessary, the parameter inputs to accommodate local variations in the phytoplankton community (e.g., like the diatom bloom described here). From the small amount of data obtained in this study, a regression of surface Chl concentration vs. P_{\max} yielded a coefficient of determination of 0.85. Future production estimates may be confounded by the fact that other groups of phytoplankton with different physiological parameters (e.g., *Trichodesmium*) also form blooms in the central gyre leading to increases in surface pigment biomass. Based on its unique optical properties, however, it should be possible to distinguish diatom and *Trichodesmium* blooms.

More effort is required for distinguishing phytoplankton community composition from space.

5. CONCLUSIONS

The North Pacific Central Gyre is usually considered as a homogeneous, barren oceanic region with little temporal and spatial variability in phytoplankton biomass and production rates. Recently, we have seen in HOT deep sediment trap collections, increases in pigment flux which are associated with surface diatom blooms. In the future, such blooms should be resolved via the increased availability of satellite and mooring sensors. We made P vs. E measurements in the vicinity of the Hawaiian Islands in an effort to determine the variability of photosynthetic parameters and were very fortunate to have encountered a large diatom bloom. The values of the photosynthetic parameters remained fairly constant for the typical oligotrophic conditions which are normally encountered over most of the North Pacific Central Gyre. When bloom events occur the parameters must be scaled appropriately to ensure accurate estimates of primary production. The photosynthetic parameter estimates measured in this study will improve our ability to model phytoplankton production in the North Pacific, especially when diatom bloom events are observed via remote sensors. The importance of such events in the global carbon cycle will be improved with the increased availability of remote sensing data.

6. ACKNOWLEDGMENTS

We wish to acknowledge the NOAA/EOS/MOBY project of D. Clark and Dr. Barbara Prezelin for their assistance in constructing the photosynthetrons. We gratefully acknowledge Dr. D. Karl and all the HOT personnel for allowing us to participate on the transect cruise and for their assistance in collecting the data. This research was supported by NASA grant NAGW-3439 (RRB) and NSF grant OCE-9315311 (RRB). This is U.S. JGOFS Contribution No. 340.

7. REFERENCES

1. R. R. Bidigare, B. B. Prezelin, and R. C. Smith "Bio-optical models and the problems of scaling," *Primary Productivity and Biogeochemical Cycles in the Sea*, P. G. Falkowski and A. D. Woodhead, eds., 175-212, Plenum Press, New York (1992).
2. D. A. Kiefer and B. G. Mitchell, "A simple, steady state description of phytoplankton growth based on absorption cross section and quantum efficiency," *Limnology and Oceanography* **28**, 770-776 (1983).
3. A. T. Jassby and T. Platt, "Mathematical formulation of the relationship between photosynthesis and light for phytoplankton," *Limnology and Oceanography* **21**, 540-547 (1976).
4. P. J. Neale and P. J. Richerson, "Photoinhibition and the diurnal variation of phytoplankton photosynthesis - I. Development of a photosynthesis-irradiance model from studies of in situ responses," *Journal of Plankton Research* **19**(1), 167-193 (1987).
5. R. R. Bidigare, M. E. Ondrusek, J. H. Morrow, and D. A. Kiefer, "In vivo absorption properties of algal pigments," *Proc. SPIE Ocean Opt. X* **1302**, 290-302 (1990).
6. J. J. Cullen, M. R. Lewis, C. O. Davis, and R. T. Barber, "Photosynthetic characteristics and estimated growth rates indicate grazing is the proximate control of primary production in the equatorial Pacific," *Journal of Geophysical Research* **97**, 639-654 (1992).
7. M. E. Ondrusek, R. R. Bidigare, S. T. Sweet, D. A. Defreitas and J. M. Brooks, "Distribution of phytoplankton pigments in the North Pacific Ocean in relation to physical and optical variability," *Deep-Sea Research* **38**, 243-266 (1991).
8. R. M. Letelier, R. R. Bidigare, D. V. Hebel, M. Ondrusek, C. D. Winn, and D. M. Karl, "Temporal variability of phytoplankton community structure based on pigment analysis," *Limnology and Oceanography* **38**, 1420-1437 (1993).
9. R. R. Bidigare, J. Marra, T. D. Dickey, R. Iturriaga, K. S. Baker, R. C. Smith, and H. Pak, "Evidence for phytoplankton succession and chromatic adaptation in the Sargasso Sea during springtime 1985," *Marine Ecology Progress Series* **60**, 175-211 (1990).
10. J. H. Martin and others, "Testing the iron hypothesis in ecosystems of the equatorial Pacific Ocean," *Nature* **371**, 123-129 (1994).

11. R. M. Kudela and F. P. Chavez, "A novel approach to estimating new Production: use of the quantum yield of nitrate uptake," *Proc. SPIE Ocean Opt. XIII*, This issue.
12. B. B. Prezelin, R. R. Bidigare, H. A. Matlick, M. Putt, and B. V. Hoven, "Diurnal patterns of size-fractionated primary productivity across a coastal front," *Marine Biology* **96**, 563-574 (1987).
13. B. B. Prezelin, M. Putt, and H. E. Glover, "Diurnal patterns in photosynthetic capacity and depth-dependent photosynthesis-irradiance relationships in *Synechococcus* spp. and larger phytoplankton in three water masses in the Northwest Atlantic Ocean," *Marine Biology* **91**, 205-217 (1986).

Nora Sadoudi¹, Marcel Babin^{1,2}, Karima Allali¹, Mike Behrenfeld³, Hervé Claustre¹ and André Morel¹

¹Lab. de Physique et Chimie Marines, U. Pierre et Marie Curie and CNRS, BP 8, 06230 Villefranche-sur-Mer, France

²ACRI S.A., BP 234, 260 Route du Pin Montard, 06904 Sophia Antipolis, France

³Oceanographic and Atmospheric Sciences Division, Brookhaven National Laboratory, Upton, New York 11973, USA

INTRODUCTION

Laboratory experiments already showed that the most significant photoacclimation strategy deployed by *Prochlorococcus* sp. would consist of changing the number of photosynthetic units per cell¹ and, thereby, the minimal turnover time for *in vivo* electron transport from water to CO₂ (τ). As a result, the saturation parameter E_k , would tightly covary with growth irradiance. Also, because the zeaxanthin cellular content in *Prochlorococcus* sp. is quite stable, the ratio of zeaxanthin-to-dv-chl a would also covary with irradiance. A study in the Atlantic Ocean already showed that, to some extent (i.e. by a factor of 3), the maximum quantum yield of carbon fixation, $\phi_{C\max}$, is proportional to the ratio of non-photosynthetic pigments (mostly zeaxanthin) to all phytoplankton pigments (hereafter denoted the "non-photosynthetic pigment index; NPP index")². In turn, the NPP index is linearly correlated with the mean irradiance in the mixed layer. The present study aims at documenting the above mentioned relationships in the equatorial and sub-equatorial Pacific, where prokaryotic photoautotrophs dominate the phytoplankton community.

2. MATERIAL AND METHODS

Data were collected in the equatorial Pacific during the OLIPAC (JGOFS-France) cruise, in November 1994. Sampling was conducted along 150° W, from 16° S to 1° N. For each seawater sample, the following variables were measured: nanomolar concentration of NO₂ and NO₃, pigment composition using HPLC, *in vivo* light absorption by phytoplankton, photosystem 2 energy conversion efficiency (F_v/F_o) measured by FRR fluoremetry, and physiological parameters derived from P vs. E experiments. The maximum quantum yield of carbon fixation was derived from the following expression:

$$\phi_{C\max}^n = \alpha^B / (12000 \tilde{a}_n^*)$$

where α^B is the chl a -specific initial slope of the P vs. E curve, \tilde{a}_n^* is the mean specific absorption coefficient weighted by spectral values of irradiance in incubators and 12 000 is the molar weight (mg) of carbon. The subscripts $n = ph$ or ps and account for all phytoplankton pigments and photosynthetic pigments only, respectively. The saturation parameter E_k is obtained from the ratio P_{\max}^B / α^B , where P_{\max}^B is the maximum carbon fixation rate. Some data collected during the FLUPAC (JGOFS-France) cruise were also included in data interpretation. FLUPAC was conducted in October 1994 along two transects: 165°E, from 20°S to 6°N, and Equator from 167°E to 150°W.

3. RESULTS AND DISCUSSION

The thickness of the upper mixed layer (Z_m) increased when going from 16°S to 1°N, while that the euphotic layer (Z_e) decreased (Figs. 1 and 2). The total chl a concentration (dv-chl a + chl a) showed a maximum around 80 m at 11°S, which progressively broadened in the equatorial zone (Fig. 3). The NPP index had the highest values at 16°S where the mean irradiance in the mixed layer is also the highest (Fig. 4). Both $\phi_{C\max}^{ph}$ and $\phi_{C\max}^{ps}$ increased with depth along the transect (Fig. 5) but the latter showed higher values at the surface layer. The parameter F_v/F_o (Fig. 6) exhibit the same tendency as $\phi_{C\max}^{ps}$. The Fig. 7 shows variations in E_k . The highest value were recorded at 16°S near the surface. A tight relationship between E_k and the mean irradiance in the mixed layer is shown in Fig. 8.

E_k variations may be predicted from Z_e and Z_m when trying to estimate primary production from ocean color, at least in systems where prokaryotes dominate the phytoplankton community.

5. REFERENCES

1. M. Babin, N. Sadoudi, L. Lazzara, J. Gostan, F. Partensky, A. Bricaud, M. Veldhuis, A. Morel and P. G. Falkowski, "Photoacclimation strategy of *Prochlorococcus* sp. and consequences on large scale variations of photosynthetic parameters, (this meeting).
2. M. Babin, A. Morel, H. Claustre, A. Bricaud, Z. Kolber and P. G. Falkowski, "Nitrogen- and irradiance-dependent variations of the maximum quantum yield of carbon fixation in eutrophic, mesotrophic and oligotrophic marine systems", *Deep-Sea Res.* (in press).
3. Z. Kolber and P. G. Falkowski, "Use of active fluorescence to estimate phytoplankton photosynthesis *in situ*", *Limnol. Oceanogr.* 38, 1646-1665 (1993).

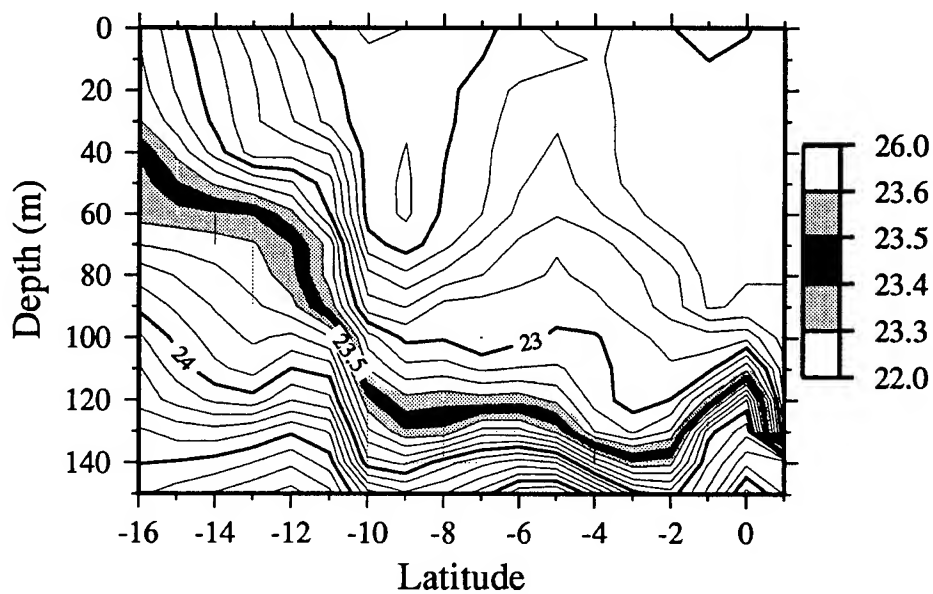


Figure 1. Vertical distribution of density excess.

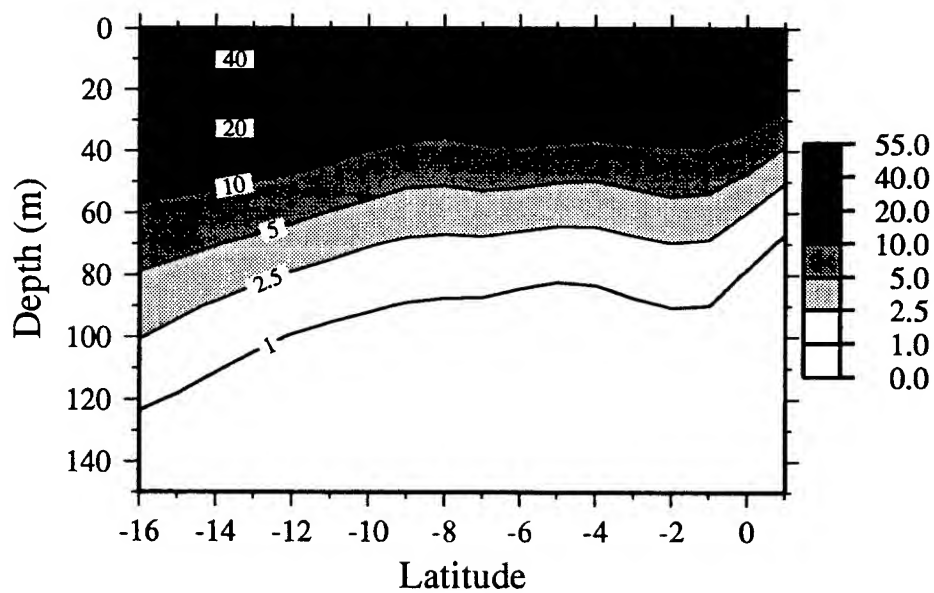


Figure 2. Vertical distribution of the photosynthetically available radiation (relatively to surface value).

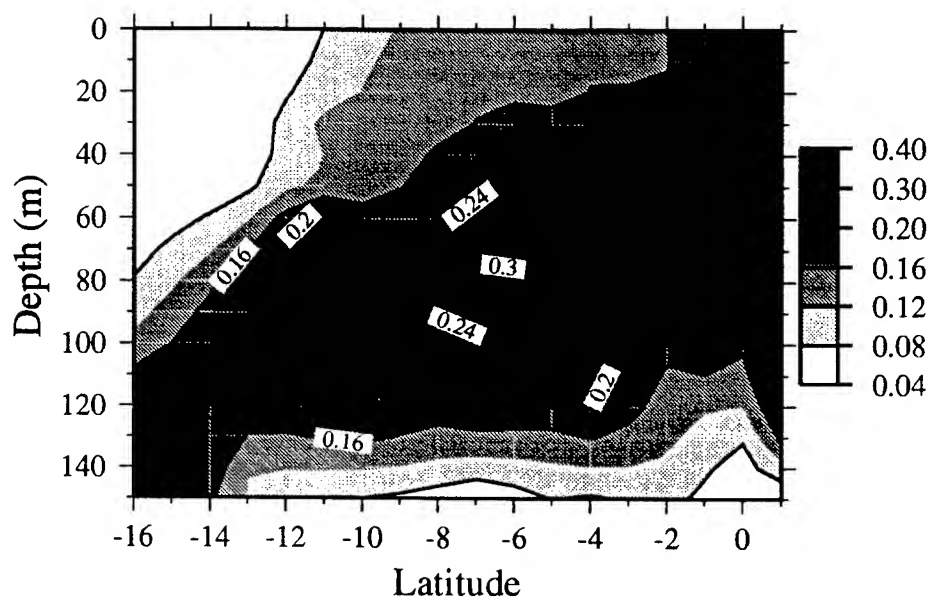


Figure 3. Vertical distribution of Chla + DV-Chla concentration.

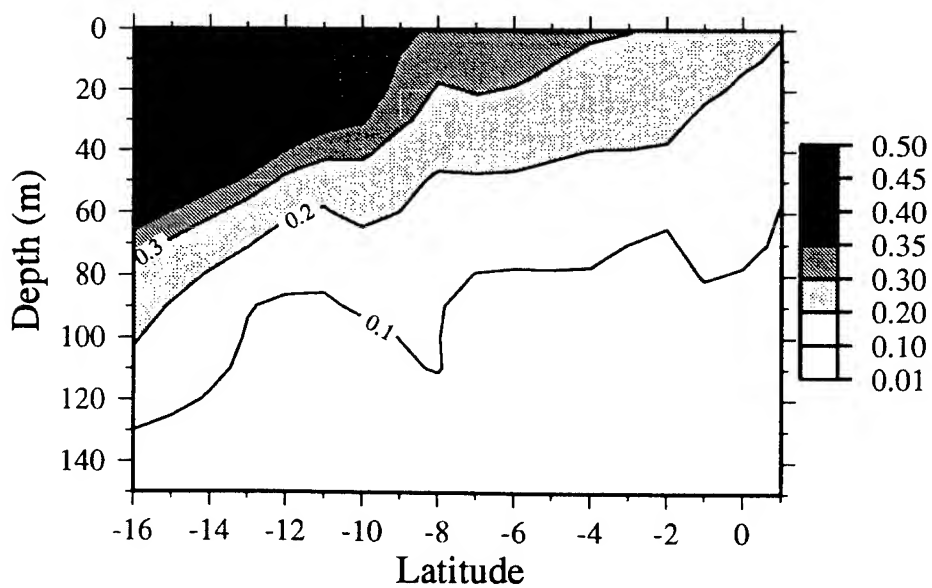


Figure 4. Vertical distribution of the non-photosynthetic pigment index, defined as the mass ratio of non-photosynthetic pigments (zeaxanthin, diadinoxanthin, diatoxanthin and B-carotene) to all phytoplankton pigments.

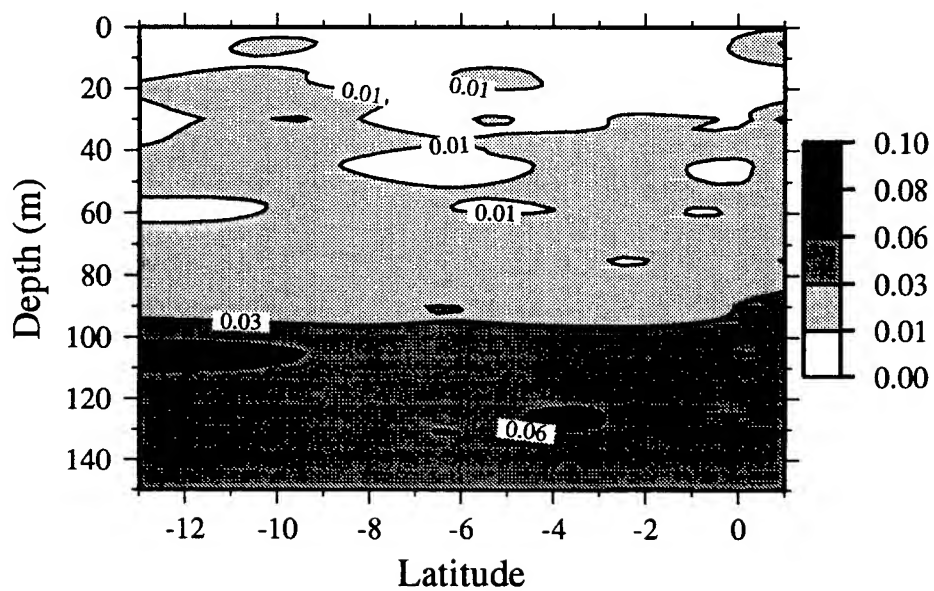
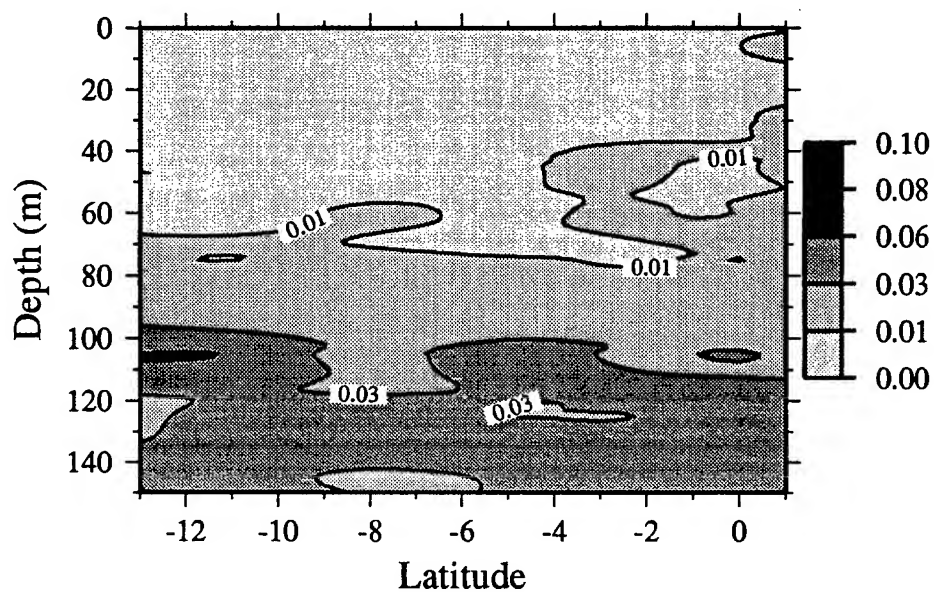


Figure 5. Vertical distribution of the maximum quantum yield ($\text{mol C (mol quanta)}^{-1}$)
(5A. ϕ_{cmax}^{ph} and 5B. ϕ_{cmax}^{ps})

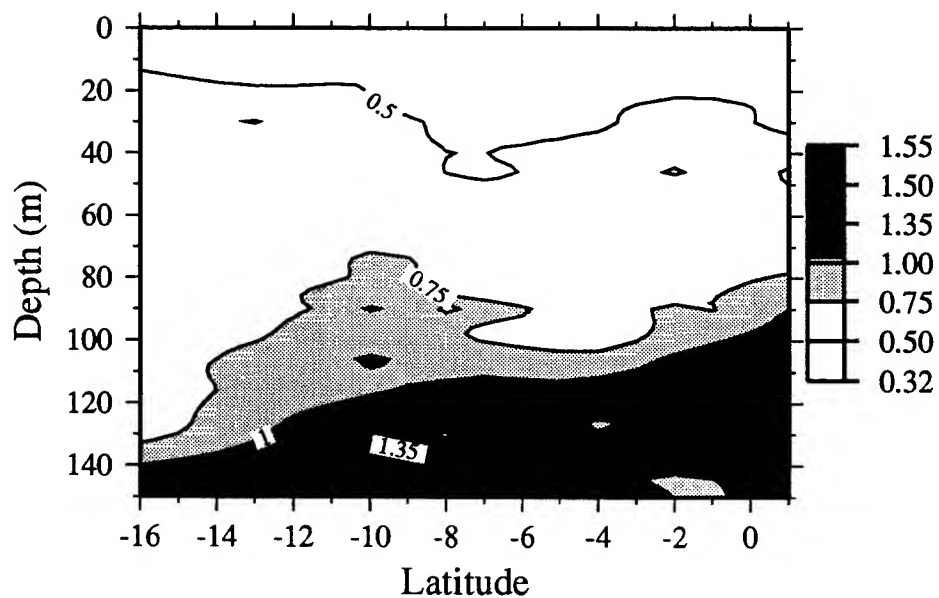


Figure 6. Vertical distribution of variable fluorescence obtained from FRR Fluorometry (F_v/F_o).

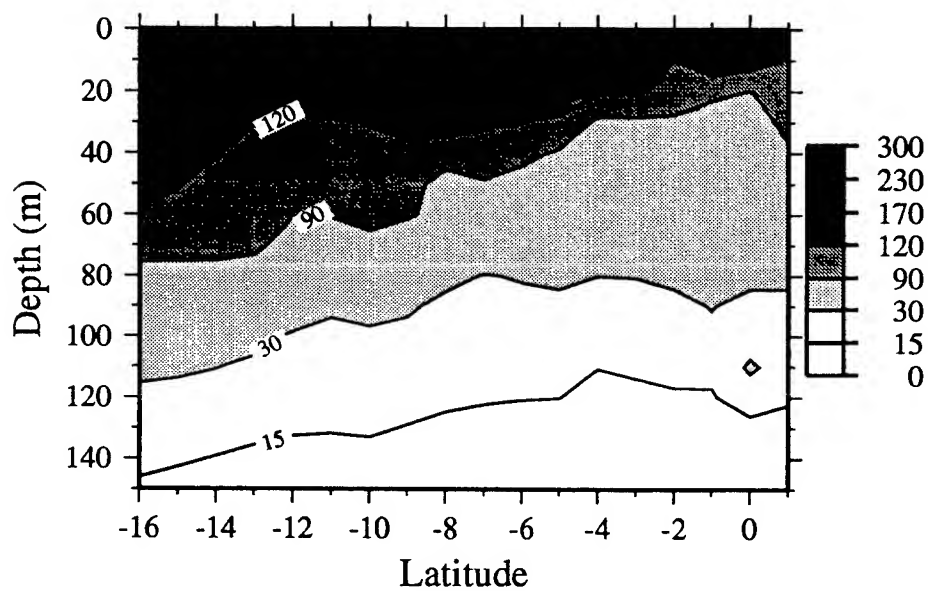


Figure 7. Vertical distribution of the saturation parameter (E_K $\mu\text{mol quanta m}^{-2}\text{s}^{-1}$).

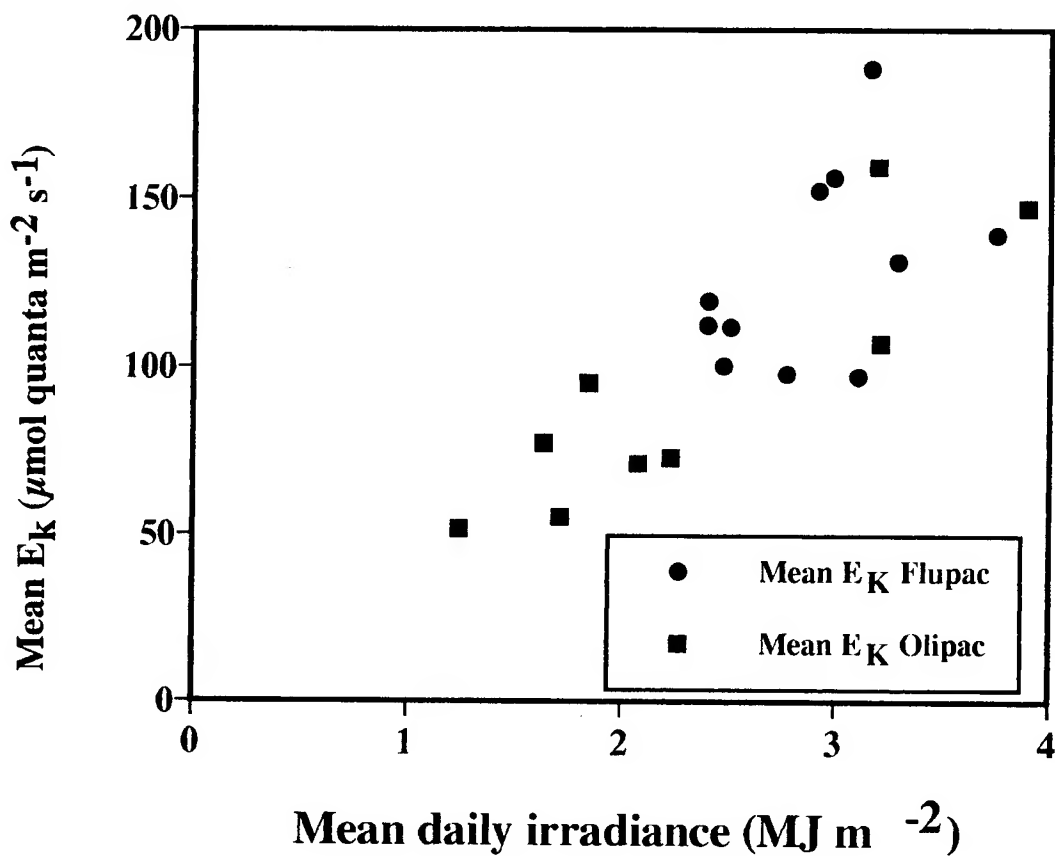


Figure 8. Relationship between the mean E_K and the mean daily irradiance in the mixed layer. Additional data are included from a cruise (FLUPAC) conducted in the same area one month before OLIPAC.

A high throughput volume particle in-flow imaging system

Sieracki, C. K. and Sieracki, M. E.,

Bigelow Laboratory for Ocean Sciences
West Boothbay Harbor, Maine, USA,
04575-0475. 207-633-9600

ABSTRACT

The Bigelow Lab in-flow particle imaging and analyzing system was designed with a 3 micrometer resolution and a maximum particle size of 1mm, making it useful for studying marine particles well beyond the useful range of conventional flow cytometers. This system allows the user to continuously monitor phytoplankton and particulate matter in underway water or sampled water over long periods of time. When particle fluorescence is detected, the fluorescence and image data is acquired, stored, and presented to the user in scattergram and image form. While this system emulates conventional flow cytometers, it has a flow rate twenty times greater, making it useful for studies of sparse larger phytoplankton. It also provides images of each cell event, making it useful for particle classification. Because of these features, this system allows rapid analysis of particles which affect optical variability and photophysiological processes. The entire system is inexpensive, compact and PC-based and uses a novel binary optical element to increase the imaged volume. We present data from samples from cruises and from locally sampled water.

KEYWORDS: Binary optics, imaging flow cytometer, phytoplankton

SYSTEM DESCRIPTION

Figure 1 is an illustration of the Bigelow In-Flow Particle Imaging and Analyzing System (BIF-PIAS). The fluid under investigation is drawn into the low fluorescence flow chamber where it is illuminated with 440 nm light from an Hg arc lamp. The system PMT monitors fluorescence emissions from 500 to 800 nm. The presence of any particle fluorescence emissions causes the system to strobe a light emitting diode which reduces the effects of motion and captures an image of the flow chamber on the video camera. The video camera signal is then captured by the PC framegrabber. The PC simultaneously measures the peak fluorescence emission associated with the passing particle. The computer software then studies the resulting image and extracts the subimage of the particle in the main image. This subimage is stored as part of an image collage of all particles. The software also measures the cell size from the image. Cell size, fluorescence and area information is stored in Excel spreadsheets for later study.

A binary optical element is used to increase the amount of fluid in the flow chamber that is in focus each instant^{1,2}. This is accomplished by stretching the objective lens' depth of focus by a factor of 5. The result is that the system flow throughput is 1 ml/minute, 20 times that of a conventional flow cytometer. Figure 2 is a photograph of the binary optical element. Rings in the photo show where the glass of the element changes thickness.

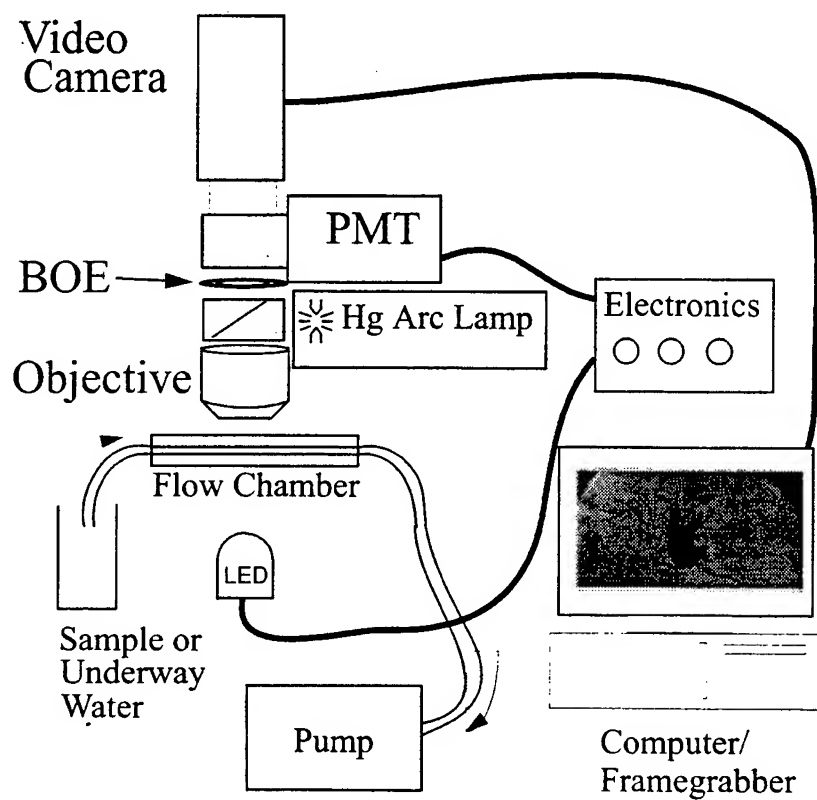


Figure 1.BIFPIAS System Diagram

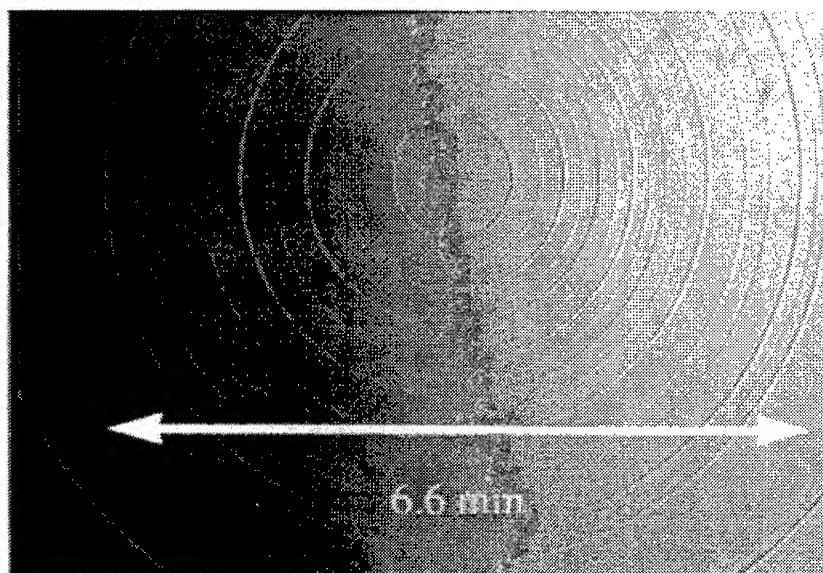


FIGURE 2. Binary optical element used in the BIFPIAS to increase the imaged volume

METHODS

Underway measurements were conducted on sea water from the sea chest on two separate cruises (R/V Edwin Link - Tropical waters or R/V Argo Maine-Gulf of Maine waters). In both cases, the sea chest was 2 meters below the waterline. The water was drawn through the imaging chamber with a peristaltic pump at 1ml/minute. This rate was verified with periodic measurements of the flow. As particles were imaged, they were sized by computing the number of pixels that were above the threshold values set by the user. Pixel size was previously calibrated by imaging a calibrated microscope reticle. Using this information, it was possible to compute the area of the particle imaged. This same information was used to compute the particle's equivalent spherical diameter. Particle fluorescence was measured by measuring the peak voltage from the system PMT. Size, fluorescence and event time information was stored in Excel files for later analysis. Chamber fouling was observed while sampling in coastal regions. This problem was alleviated by hourly 5 minute chamber purges with chlorine bleach.

When bottle cast or dock sample water was analyzed by the system, the water was placed into a beaker and drawn through the flow chamber at 1 ml/minute. Again, size, fluorescence and event time information was stored in Excel files for analysis.

All data and images were later studied for the presence of air bubbles and chamber fouling that may have affected the total particle count and measured particle size. Erroneous data was removed prior to final analysis.

RESULTS

Normalized Particle Size Distributions for Different Marine Regions

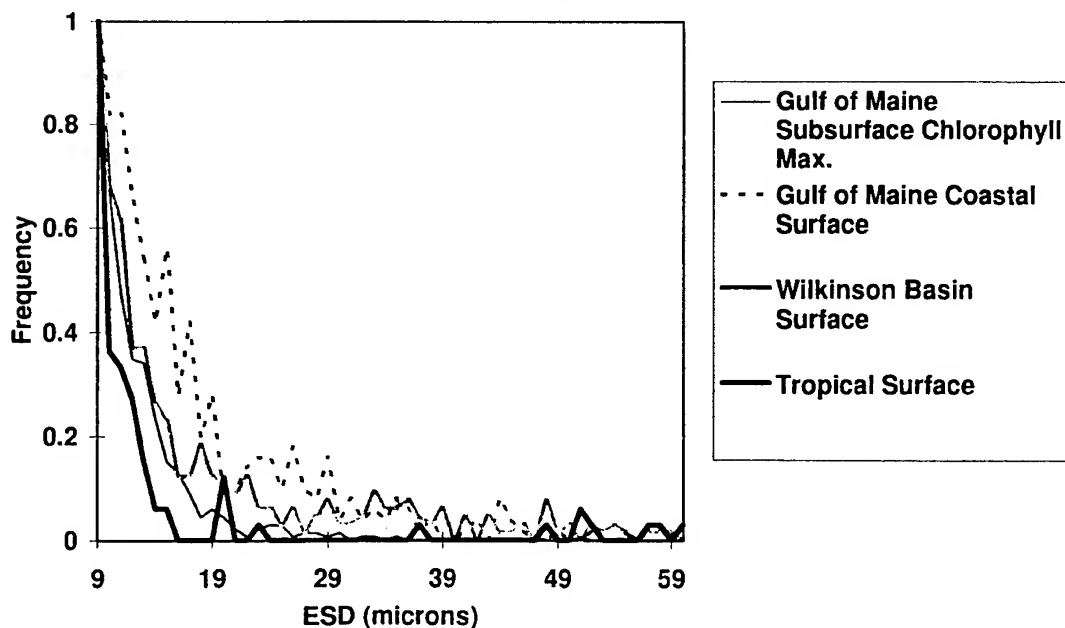


FIGURE 3. Large particle size distributions from various marine regions as measured by the BIFPIAS.

Particle size distributions from various marine regions were measured with the BIFPIAS and the results are shown in Figure 3. These results show size distributions up to 60 μm equivalent spherical diameter (ESD) for best comparison. The CoBOP '96 (tropical) plot shows a distribution skewed towards smaller particles with some larger particles also present. The sub-surface chlorophyll maximum (SCM) Gulf of Maine plot also shows a distribution which is skewed towards smaller cells but with few larger particles. Both DEPSCoR '96 (Gulf of Maine) surface plots show the presence of larger particles (larger diatoms and *Ceratium*), however, the Gulf of Maine temperate coastal surface plot shows the highest presence of cells in the range of 10 to 30 micrometers. This is due to a high concentration of smaller diatom chains in the coastal region of the Penobscot Bay.

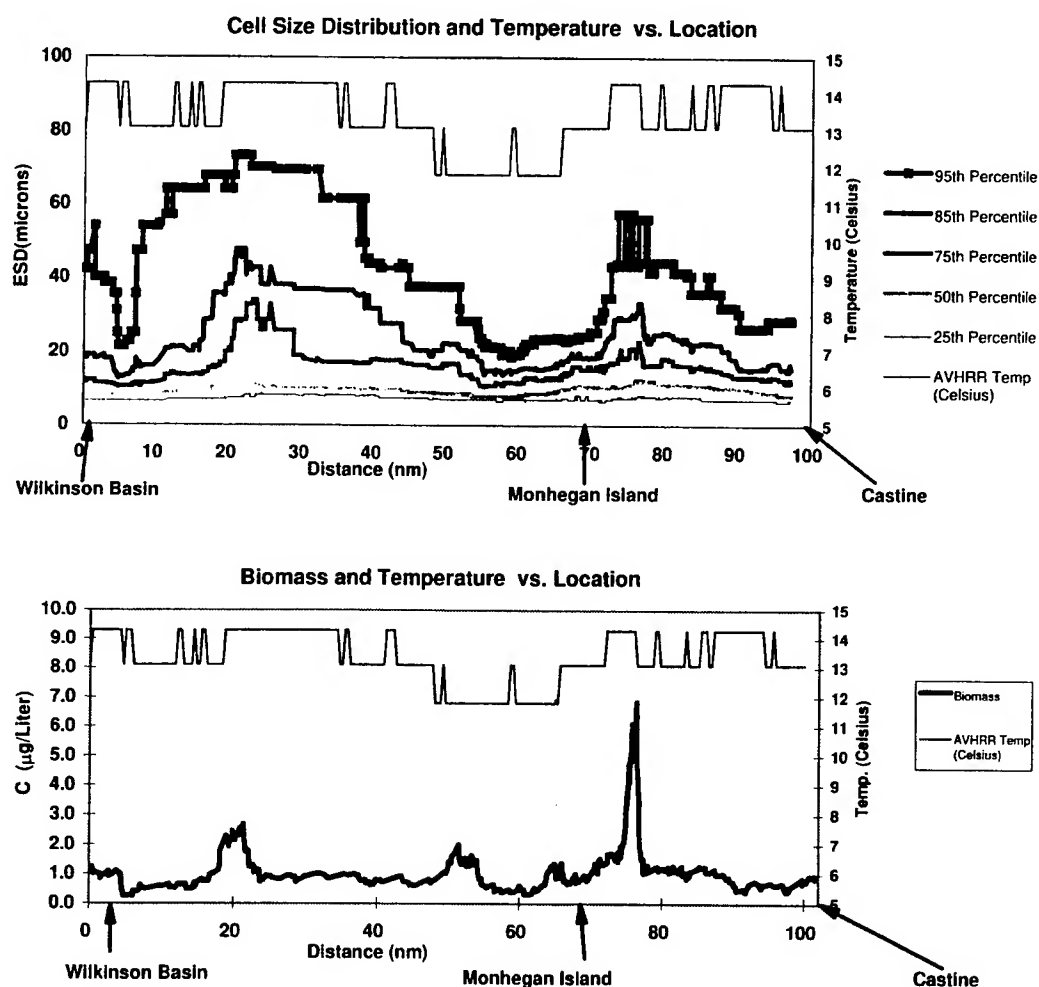


FIGURE 4. Continuously measured biological data taken with the BIFPIAS along the transect from the Central Gulf of Maine to Castine, Maine.

Figure 4 demonstrates the ability of the BIFPIAS to continually monitor the cell size distribution for particles from 10 μm to 1000 μm . Both plots describe particle properties measured along the transect from the central Gulf of Maine to Castine, Maine. The top plot shows the percentage of cells which fall below a certain ESD for each location. Superimposed on this plot is the jagged temperature as read off of an AVHRR satellite image. The satellite image was taken within a week of the inbound cruise leg. There is a strong correlation between the cell size distribution and temperature. The biomass trace in the bottom plot shows the computed carbon per liter of underway water as measured by the BIFPIAS³. Again there is a strong correlation between biovolume and satellite-measured temperature.

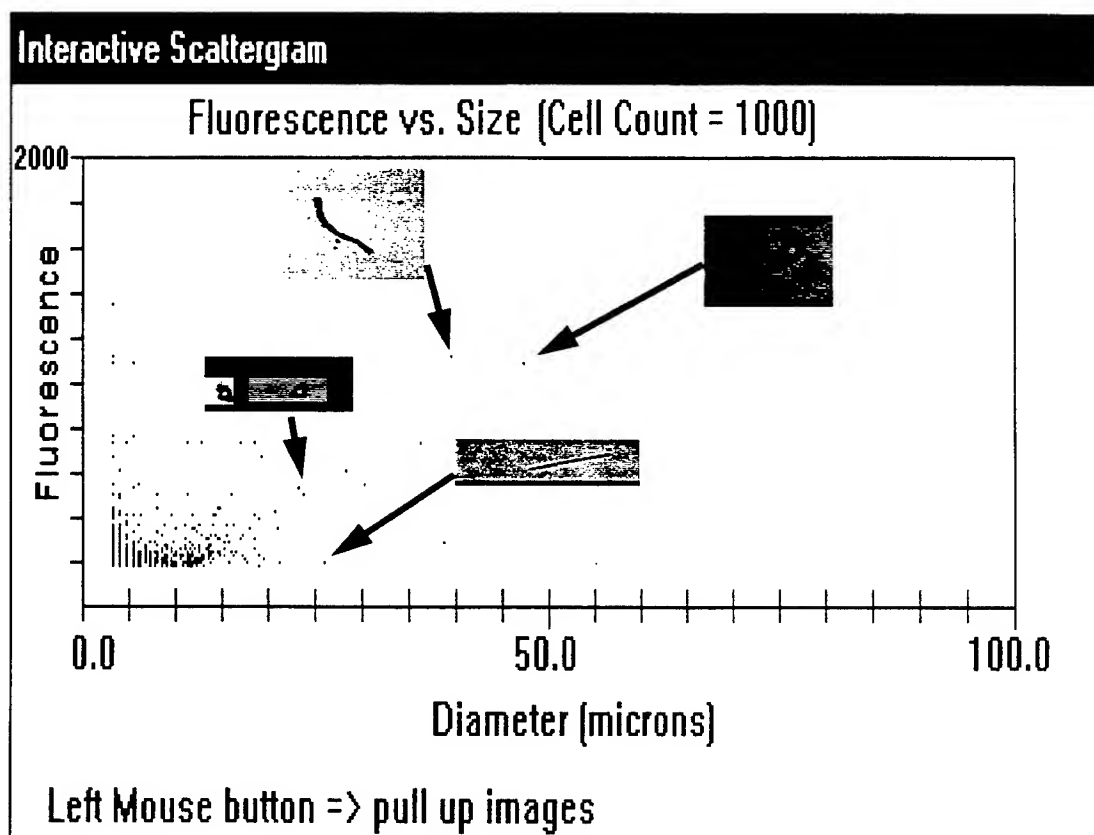


FIGURE 5. The BIFPIAS interactive scattergram allows the user to select particle events from the flow cytometer scattergram and call up the corresponding particle images. In this image, four particle regions have been selected, as indicated by the arrows.

The scattergram shown in Figure 5 illustrates two qualities of the BIFPIAS: 1) the user may use the flow cytometer scattergrams and interactively click on dots on the scattergram to pull up images of those particles represented by those dots and 2) the system operates much like a conventional flow cytometer except for the fact that it operates over a different particle size range (up to 1000 μm). This scattergram was generated by sampling 60ml of dock water from the Department of Marine Resources (West Boothbay Harbor, Maine) with the BIFPIAS. It shows a general increase of fluorescence with particle size and also a decrease of cell counts with size.

SUMMARY

- The BIFPIAS is able to continuously image particles and monitor particle Size Distributions while underway.
- At station particle analysis is also possible
- The Binary Optical Element increases the system flow throughput and still allows analysis of particles from 10 μm to 1000 μm .
- BIFPIAS particle size range extends well beyond that of conventional flow cytometers.
- The flow rate is also much greater than with conventional flow cytometers (1ml/minute)
- The interactive scattergram allows for taxonomic particle identification

ACKNOWLEDGMENTS

The authors wish to thank Dr. Charles Yentsch of Bigelow Laboratory for assistance in system design and testing. Research funding was received from Office of Naval Research grant number N000-14-94-1-0972.

REFERENCES

- 1 C. K. Sieracki, "An experimental and computational study of binary optical elements for aberration correction in three dimensional fluorescence microscopy," Ph.D. dissertation (Dartmouth College, Hanover, NH, 1995).
- 2 C. K. Sieracki, C. G. Levey, and E.W. Hansen, "Simple binary optical elements for aberration correction in confocal microscopy," *Optics Letters* **20**(10), pp. 1213-1215, (1995).
- 3 P. G. Verity, C.Y. Robertson, C. R. Tronzo, M. G. Andrews, J. R. Nelson and M. E. Sieracki, "Relationships between cell volume and the carbon and nitrogen content of marine photosynthetic nanoplankton," *Limnol. Oceanogr.* **37**(7), pp. 1434-1446 (1992).

Satellite Assessment of Hurricane-Induced Ocean Turbidity for the Southern U.S. Coastline

Kirk Waters

TPMC, NOAA Coastal Services Center,
2234 South Hobson Ave.
Charleston, SC, 29405-2413

John Brock

NOAA Coastal Services Center,
2234 South Hobson Ave.
Charleston, SC, 29405-2413

Ajit Subramaniam

TPMC, NOAA Coastal Services Center,
2234 South Hobson Ave.
Charleston, SC, 29405-2413

Richard Stumpf

USGS Center for Coastal Geology
600 Fourth St. South
St. Petersburg, FL 33701

Edward Armstrong

TPMC, NOAA Coastal Services Center,
2234 South Hobson Ave.
Charleston, SC, 29405-2413

Keywords: AVHRR, turbidity, hurricane

ABSTRACT

Advanced Very High Resolution Radiometer images before and after three hurricanes were processed to estimate the reflectance difference between visible and near-infrared bands. The reflectance difference provides a measure of the turbidity in the water column. The images were compared to examine the influence of hurricanes on coastal waters. Hurricanes were found to increase turbidity in a large area, with the greatest impact to the right side of the hurricane track.

1. INTRODUCTION

Advanced Very High Resolution Radiometer (AVHRR) images acquired prior to and just after the landfall of hurricanes along the southeastern U.S. and Gulf of Mexico coasts have been processed to depict ocean turbidity due

to suspended particles. The images were processed using the algorithms of Stumpf and Pennock^{1,2} to depict the reflectance difference of the visible and near-infrared channels after correction for atmospheric Rayleigh scattering. The ratio of the reflectance difference after the hurricane and before the hurricane were calculated and could be used as a proxy measure of the relative impact of a hurricane on coastal waters.

Three hurricanes are presented: Hugo in 1989 (Figure 1); Opal in 1995 (Figure 2); and Fran in 1996 (Figure 3). Hugo and Fran made landfall in South and North Carolina respectively. Both hurricanes impacted Long Bay and Onslow Bay. Opal made landfall along the Florida panhandle in the Gulf of Mexico. These three hurricanes illustrate both the similarities and differences in impact that hurricanes have on coastal waters.

2. REFLECTANCE DIFFERENCE ALGORITHM

The reflectance difference was calculated from AVHRR bands 1 (visible, 580-680 nm) and 2 (near-infrared, 725-1100 nm). The Rayleigh scattering is estimated based on the sun-earth-satellite viewing geometry and is subtracted from both bands. The remaining band 2 reflectance is assumed to represent the aerosol scattering contribution and is subtracted from the Rayleigh corrected band 1. This assumption involves both a very low water-leaving radiance in the near infrared and a maritime aerosol type with an angstrom coefficient of zero^{1,2}. Thus, the water reflectance difference is:

$$R_d = R_c(\lambda_1) - Y \cdot R_c(\lambda_2)$$

where $R_c(\lambda)$ is the Rayleigh corrected reflectance for band x and Y is the aerosol color ($=1.0$).

3. HURRICANE DESCRIPTIONS

The following three hurricanes were selected for several reasons: 1) Hugo was a major hurricane in the area of the authors, 2) Opal had a dramatic effect on the turbidity, and 3) Fran was simply a very recent hurricane. In addition, imagery was available showing relatively clear coastlines within 24 hours of hurricane landfall. All of the post hurricane images shown here are less than 24 hours from the time of hurricane landfall.

3.1. Hurricane Hugo

Hurricane Hugo made landfall on September 21, 1989 at near Charleston, SC as a category 4 hurricane with maximum sustained winds of 120 knots. The red line in Figure 1 indicates the track of the eye of the storm. Six days prior to the storm (Figure 1a) the reflectance difference in the ocean was fairly low, indicating relatively clear water. After the passage of the Hugo (Figure 1a), the turbidity increased dramatically to the right of the eye (Figure 1c). Relatively little impact is seen to the left. The highest ratio of reflectance after/before is seen in Long Bay. The ratio also has an interesting feature with respect to rivers. There is normally a river plume of turbid water from Cape Fear at the northern end of Long Bay. The ratio shows a decrease where the plume runs, suggesting that the river runoff did not have as large an increase in turbidity as the areas where bottom sediment resuspension had occurred.

3.2. Hurricane Opal

Hurricane Opal made landfall near Pensacola, FL on October 4, 1995 with category 4 hurricane with sustained winds of 130 knots. As with Hugo, the turbidity was relatively low prior to Opal (Figure 2a) followed by a large increase in turbidity after the Opal (Figure 2b). Again the highest relative increase (Figure 2c) is to the right of the hurricane eye track and is primarily in the bays. The ratio of turbidity for Opal is much higher than it was for Hugo, although the wind strengths were approximately the same. This may be a combination of slightly lower initial turbidity and perhaps a difference in the sediment type. The raised turbidity significantly decreased by October 9th.

3.3. Hurricane Fran

Hurricane Fran made landfall near Wilmington, NC on September 5, 1996 with 100 knot winds as a category 3 hurricane. As with Opal and Hugo, the turbidity prior to Fran (Figure 3a) is low and increases after Fran (Figure 3b). The highest relative increases (Figure 3c) are seen in the bays near the hurricane track. In contrast to Hugo and Opal, there is a significant increase in the turbidity on both sides of the eye. With Hugo, there were no large bays to the left of the hurricane, but with Opal there was a large bay to the left. However, the bay to the left of Opal is fed directly by the Mississippi river and had a higher initial turbidity. While Fran had significant effect to the left of the hurricane, the majority of the change was still to the right side.

4. DISCUSSION AND CONCLUSIONS

These three hurricanes illustrate some expected effects of hurricanes on coastal waters. In all cases the water clarity has decreased due to resuspension of sediments from the shallow bottom. Since the strongest winds of a hurricane are in the northeast quadrant, the highest turbidity increase on the right hand side of the hurricane track is in good agreement. The high turbidity areas are the nearby bays, as we expect from wave focusing effects and the general expectation of higher erosion rates.

While the basic expectations of hurricane effects hold true, there are differences that are revealed by the satellite data. Although Hugo and Opal had similar wind speeds, the turbidity due to Opal was much higher, both in a relative and absolute sense. It is difficult to know the exact reasons for this, though the differences in geomorphology, sediment type, and hurricane track are likely candidates. Opal meandered within the gulf before making landfall, thus stirring the water off the coast for longer. Although Fran was a slightly weaker hurricane than Hugo, its impact on the relative turbidity was slightly higher. Where they made landfall is probably the largest factor in this difference, since Fran passed over two bays, one on either side of the eye.

Examining the turbidity in this manner allows us a synoptic view of where sediment has been mobilized. There is a potential to combine estimates of mobilized sediment with models of current movement, providing estimates of sediment transport. This would be useful for many applications, including beach renourishment projects and determining areas where the bathymetry is likely to have changed dramatically, requiring new surveys for coastal navigation. The increased turbidity may impact seagrass beds by reducing the light available for photosynthesis or loss of bottom sediment and increased wave action may be simply uproot them. Shellfish and other filter feeders may also be affected by higher sediment loads.

5. REFERENCES

1. R.P. Stumpf and J.R. Pennock, "Calibration of a general optical equation for remote sensing of suspended sediments in a moderately turbid estuary," *Journal of Geophysical Research*, **94**(C10), 14363-14371, 1989
2. R.P. Stumpf and J.R. Pennock, "Remote estimation of the diffuse attenuation coefficient in a moderately turbid estuary," *Remote Sensing of the Environment*, **38**, 183-191, 1991

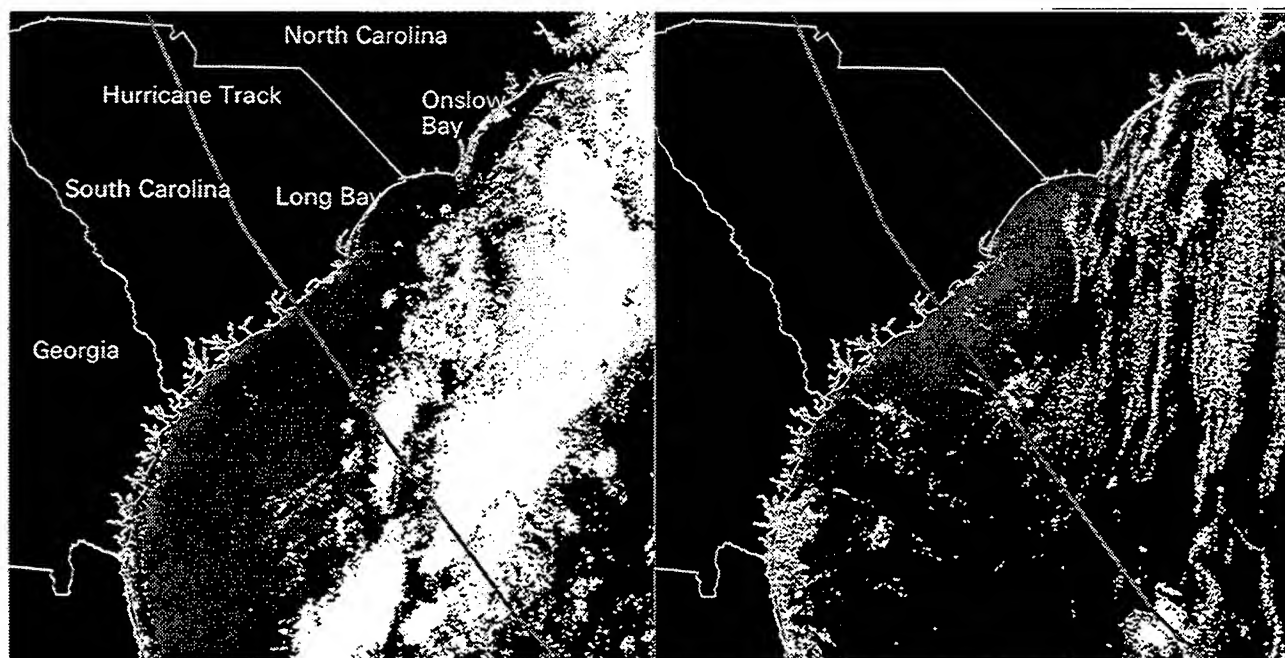
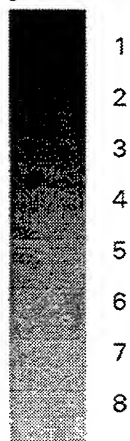


Figure 1a. The reflectance difference before hurricane Hugo, Sept. 15, 1989 is shown.

Figure 1b. The reflectance difference after hurricane Hugo, Sept. 22, 1989 is shown.

Percent Reflectance Difference
(Figures 1a and b)



Ratio (Figure 1c)

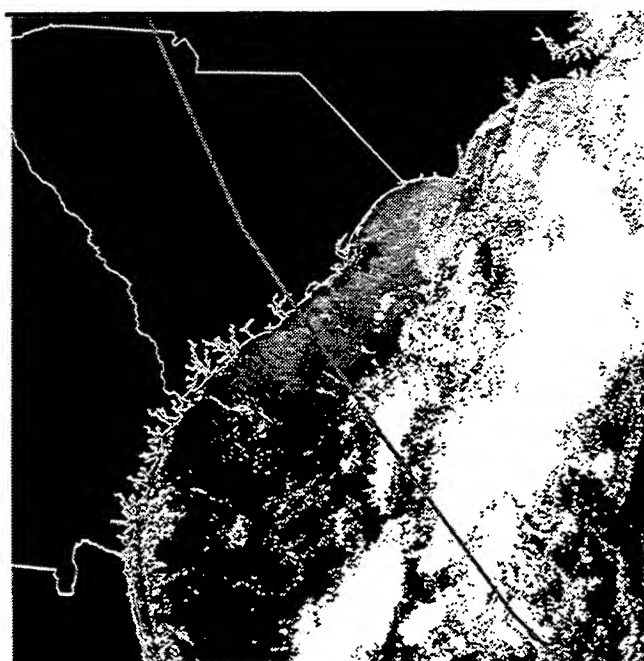
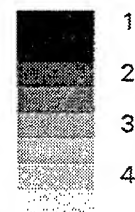
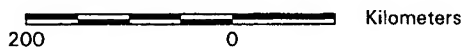


Figure 1c. The Ratio of the reflectance difference before and after hurricane Hugo is shown (after/before).

Scale



1 : 7000000

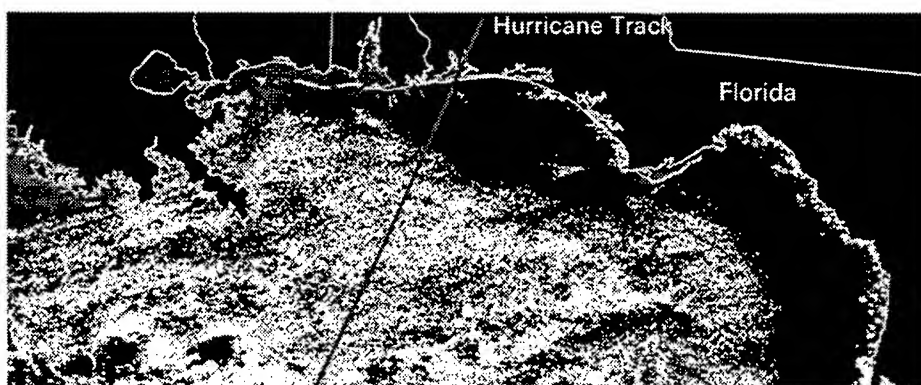


Figure 2a. The reflectance difference before hurricane Opal, Sept. 29, 1995 is shown.

Percent Reflectance Difference
(a and b)

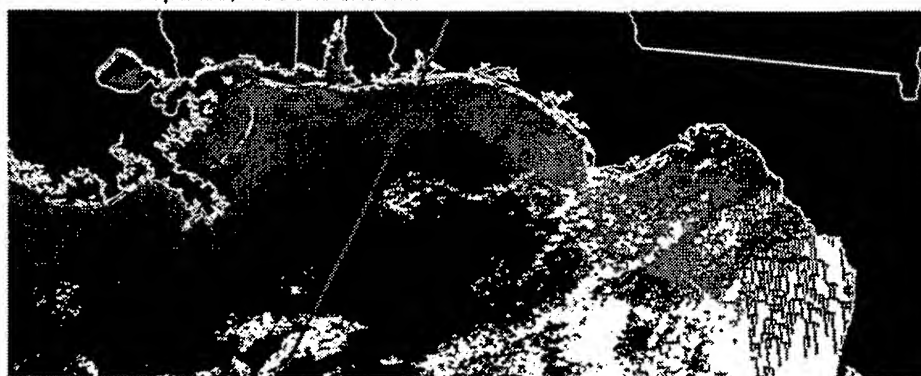
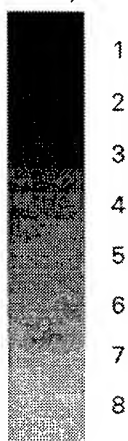


Figure 2b. The reflectance difference after hurricane Opal, Oct. 5, 1995 is shown.

Ratio (Figure 2c)

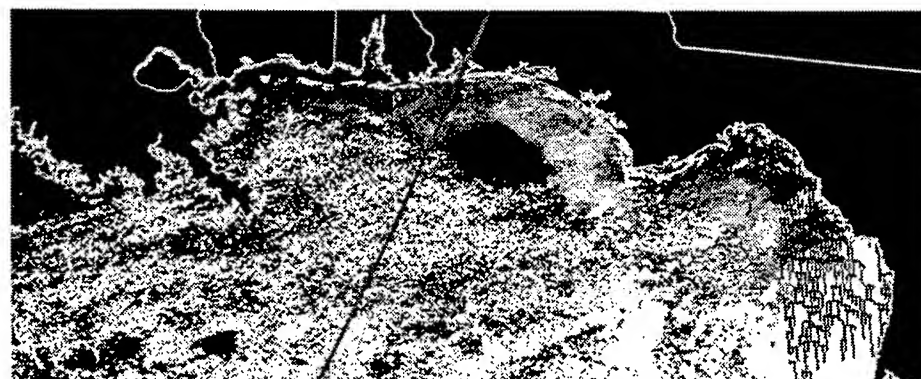
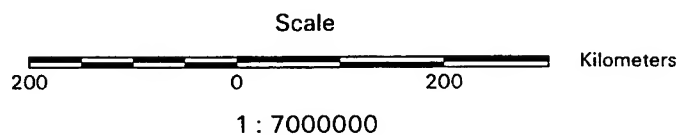


Figure 2c. The ratio of the reflectance difference before and after hurricane Opal is shown (after/before). Note that the greyscale for this figure has a greater dynamic range than figures 1c and 3c.



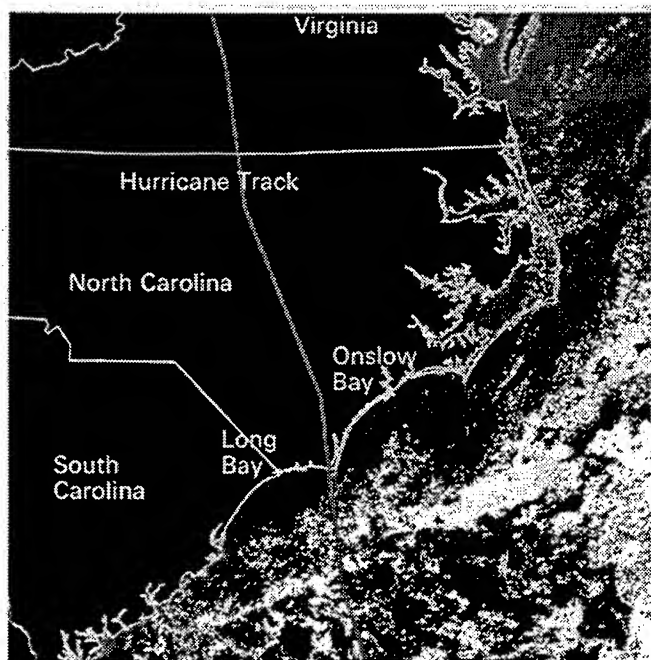


Figure 3a. The reflectance difference before hurricane Fran, Aug. 29, 1996 is shown.

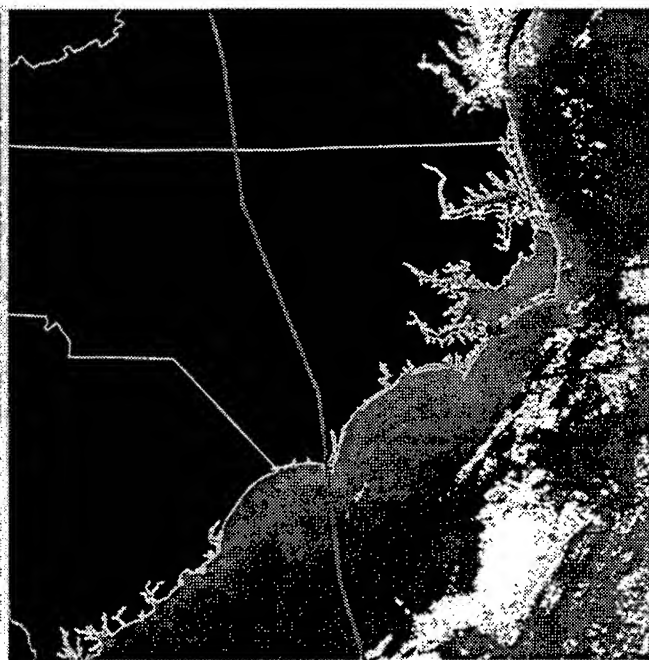
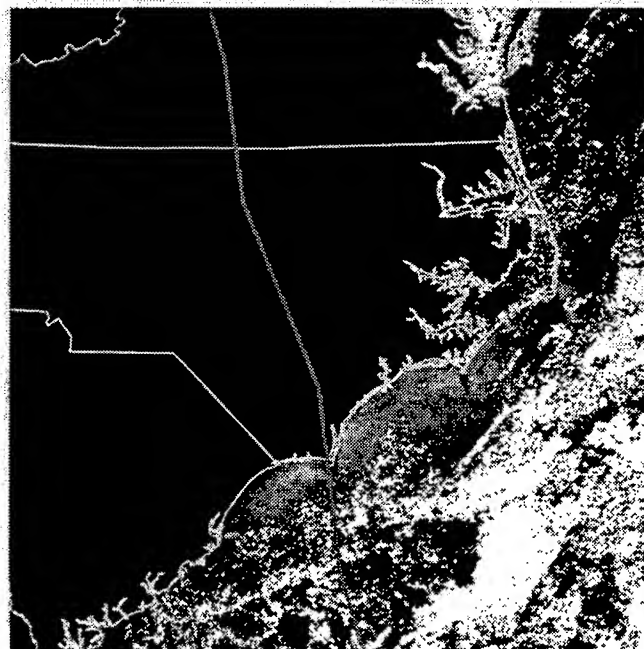
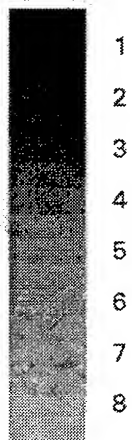


Figure 3b. The reflectance difference after hurricane Fran, Sept. 6, 1996 is shown.

Percent Reflectance difference
(Figure 3a and b)



Ratio (Figure 3c)

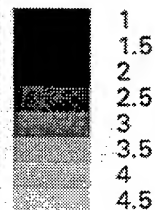
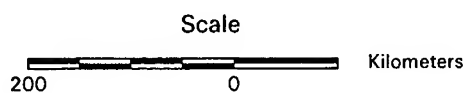


Figure 3c. The Ratio of the reflectance difference before and after hurricane Fran is shown (after/before).



1 : 7000000

Solitary coastal lee waves observed from space

Quanan Zheng, Xiao-Hai Yan, Vic Klemas, and Zongming Wang
Graduate College of Marine Studies, University of Delaware, Newark, Delaware USA 19716

Chung-Ru Ho, and Nan-Jung Kuo
Department of Oceanography, National Taiwan Ocean University, Keelung, Taiwan 20224

ABSTRACT

Alternating dark-bright patterns along the coast on Landsat MSS and the ERS-1 SAR images were recognized to be the image of a coastal lee wave. Such waves are called coastal lee waves because they occur along the lee side of the coast. The first case was noted in the offshore area of the Delaware Bay in the Middle Atlantic Bight shown as a wave-like cloud pattern on MSS images taken in December 14, 1975. The second case was detected by the ERS-1 SAR shown on the image of the Taiwan Strait taken on December 8, 1994. The average wavelength is 2 km, ranging from 0.3 km to 4.2 km. The crest lines with length from 20 km to more than 100 km are generally parallel to the coastline. The horizontal distribution range is a band 20 km wide, 20-100 km offshore. The vertical extent of the disturbance reaches from the ocean surface to the top of cumulus. The waves manifest solitary characteristics. The seasonal land-breeze circulation is being proposed as a major generation mechanism for the observed lee waves.

Keywords: coastal lee waves, satellite images, remote sensing, atmospheric waves, coastal ocean

1. INTRODUCTION

Lee waves are a type of atmospheric internal gravity waves, which occur in the lower layer of the atmosphere and are generated by an obstacle to air flow. Mountain lee waves generated by isolated mountain obstacles on the lee side of mountains are a typical example of atmospheric lee waves and have been intensively studied^{1,2}. Lee waves analogous to mountain lee waves but caused by an isolated linear island have recently been observed using an ERS-1 (European Remote Sensing satellite) synthetic aperture radar (SAR) image³. From an ERS-1 SAR image of the North Sea, a nonlinear wave disturbance was identified in the marine atmosphere 30 km offshore in the German Bight⁴.

The atmospheric lee waves under investigation is characterized by their occurrence being associated with the coastal environment, a transition region between marine and terrigenous air masses. In this case, the obstacle to air flow is no longer from a mountain nor from an island. The waves occur in the form of wave packets along the lee side of the coast, no matter whether it is a plain coast or hilly coast. The wave crest lines are nearly parallel to the coastline and over a hundred kilometers long. Satellite images also provide evidence that the vertical disturbance height caused by this kind of lee wave may reach to the top of cumulo-stratus clouds, about 3000 m above sea level. According to the close association of its occurrence with the coast, a unique feature, we define this kind of lee wave as a coastal lee wave.

2. COASTAL LEE WAVES IN THE MIDDLE ATLANTIC BIGHT

A group of wavelike cloud patterns occurring in the offshore region of the Middle Atlantic Bight was imaged by the NASA ERTS-1 MSS on December 14, 1975. The center of the images was located at 38°58'N 74°1'W, about 100 km offshore from the Delaware Bay mouth. A partially enlarged false color composite image produced with bands MSS 7, 5, and 4 is shown as Figure 1. One can see that alternative dark-bright cloud patterns occurred in the offshore region of about 50 km from the Delaware Bay mouth. According to the definition given in the Introduction, we affirm that these cloud patterns represent the signature of coastal lee waves in the lower atmosphere. The waves occurred in the form of a packet with a total of 15 visible waves arrayed over a band of about 20 km wide. The average wavelength measured along profile B-B' is 0.94 ± 0.51 km, ranging from 0.30 to 2.05 km. The length of the wave crest lines, which appeared as bold bright lines generally parallel to the coastline, is as long as 80 km. The clouds are cumulo-strati, and the cloud top height was estimated at about 3 km above sea level (Moran, et al., 1991).

Examining the traverse structures of wavelike patterns along four profiles A-A', B-B', C-C', and D-D' marked in Figure 1, we found that all the waves occurred in a packet, which occupied a limited space less than 20 km wide. More interesting is the fact that the amplitudes of the waves grew gradually from the rear to the front of the packet, but leading waves near the cloud front in the first three profiles had been broken. The wavelengths, i.e., the spatial separations between two solitary waves, also increased gradually from about 0.3 km in the rear to about 2 km in the front. This dependence of the wavelength on the amplitude, in fact, implies the amplitude-dependence of the phase speed, which is a unique feature of solitary waves. A comparison of the theoretical result with measurements taken from profile B-B' shows that the theoretical curves fit the measurements quite well. This good agreement of measurements with the theoretical predictions reveals a significant property of coastal lee waves, i.e., under certain conditions, coastal lee waves may exhibit pronounced solitary wave characteristics.

In order to clarify the conditions for occurrence of the land breeze, monthly mean data of the land and ocean temperatures in the study area were collected in 1975 and early 1976. In December 1975 and January 1976, the monthly mean ocean surface temperature was 8°C higher than that of the land indicating a favorable condition for generating strong seasonal land breezes.

3. COASTAL LEE WAVES IN THE TAIWAN STRAIT

The ERS-1 SAR image was taken on December 8, 1994, at 6:26:43 GMT. The coverage of the image is a square area with one side 100 km wide centered at 25°38'27" N, 119°38'41" E. A processed image is shown in Figure 2. The imaged area is a portion of the coastal and offshore region of Fujian Province, China, the northwest part of the Taiwan Strait.

According to field observations, the land-sea temperature was 4° C at imaging time. It was a favorable condition for the establishment of the land breeze circulation (Simpson, 1994). In fact, an offshore wind of 1.5 - 3.5 m/s confirmed that the land breeze had occurred. Meanwhile, the coastal lee wave was generated together with the land breeze.

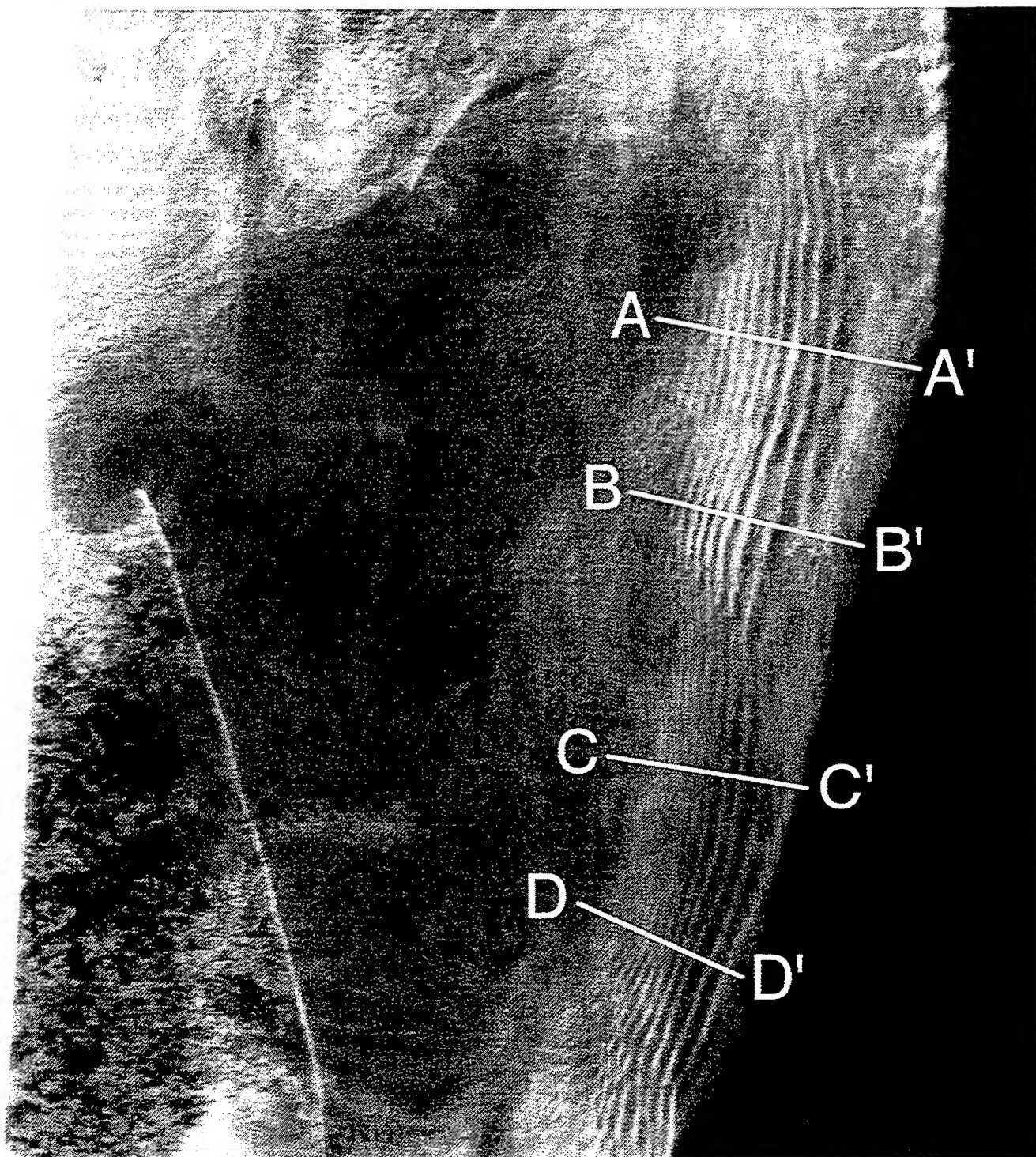


Figure 1. A false color composite ERST-1 MSS image of the Middle Atlantic Bight. Three bands used for the composite are MSS 7 as red, MSS 5 as green, and MSS 4 as blue. Original images coded E-2326-14542-7,-5, and -4 were acquired on December 14, 1975. The wave-like cloud patterns are the signature of coastal lee waves.

The alternative dark-bright patterns also belong to three packets of solitary coastal lee waves. One can see that they are distributed in a band with an offshore width of 20 - 40 km. The first packet on the upper-right corner of Figure 5 contains 6 solitons with a spatially variable wavelength: the average wavelength of 1.7 km measured along the line marked by A-A', and 2.7 km along line B-B'. The second packet, which is close to center-right, contains 10 solitons with the average wavelength of 4.2 km measured along line C-C'. The third packet on the lower-left corner contains 17 solitons with the average wavelength of 2.0 km measured along line D-D'. The crest length of the solitons is about 20 - 40 km.

4. CONCLUSIONS

The coastal lee waves exhibit the following general characteristics:

1) The average wavelength is 2 km ranging from 0.3 km to 4.2 km. The crest lines, with lengths from 20 km to more than 100 km, are generally parallel to the coastline. The horizontal distribution range is a band 20 km wide, 20 - 100 km offshore. The vertical disturbance extent reaches from the sea surface to the top of cumulus clouds.

2) Unlike the mountain lee waves, coastal lee waves are the travelling waves. Their behavior can be described by two layer model theory. The phase speed of the wave, therefore, depends on the lower layer depth. The lower layer depth decreases to zero at the cold front, so that the phase speed also gradually tends towards null. Thus, the coastal lee wave never propagates far from the coast, but appears to be "trapped" by the coast.

3) Coastal lee waves exhibit some solitary features: they occur in the form of packets containing 6 - 20 solitons. The leading solitons have larger wavelengths, implying that their phase speed depends on their amplitudes. This agrees with predictions by solitary wave theory.

4) The land breeze circulation, which is driven by the land-sea temperature difference, is suggested to be a major mechanism for generating coastal lee waves. The offshore distribution and the modulated spatial structure of coastal lee waves in the three observed cases coincide with features of the land breeze described by Simpson⁵. All the three observed cases occurred in the mid-latitudes (25° - 40° latitude) during the local early winter. The land-sea temperature difference reaches the maximum value during that season and constitutes favorable conditions for generating the seasonal land breeze, providing further evidence for the proposed generation mechanism.

5. ACKNOWLEDGEMENTS

The authors would like to express their thanks to Zhouwen Yu and Runheng Huang for providing weather maps and GMS satellite images; to Norden E. Huang for valuable discussions on small wave spectra, and to Harald Frick for assistance in data processing. The work in UD is supported by the ONR Physical Oceanography and Environmental Optics Program under grant N00014-95-1-0065, and partly supported by the NOAA Sea Grant Program through grants NA16RG0162-03 and NA56RG0147. The work in NTOU is supported by the grant Taiwan NSC 85-NSPO(A)-OCI-09-02.

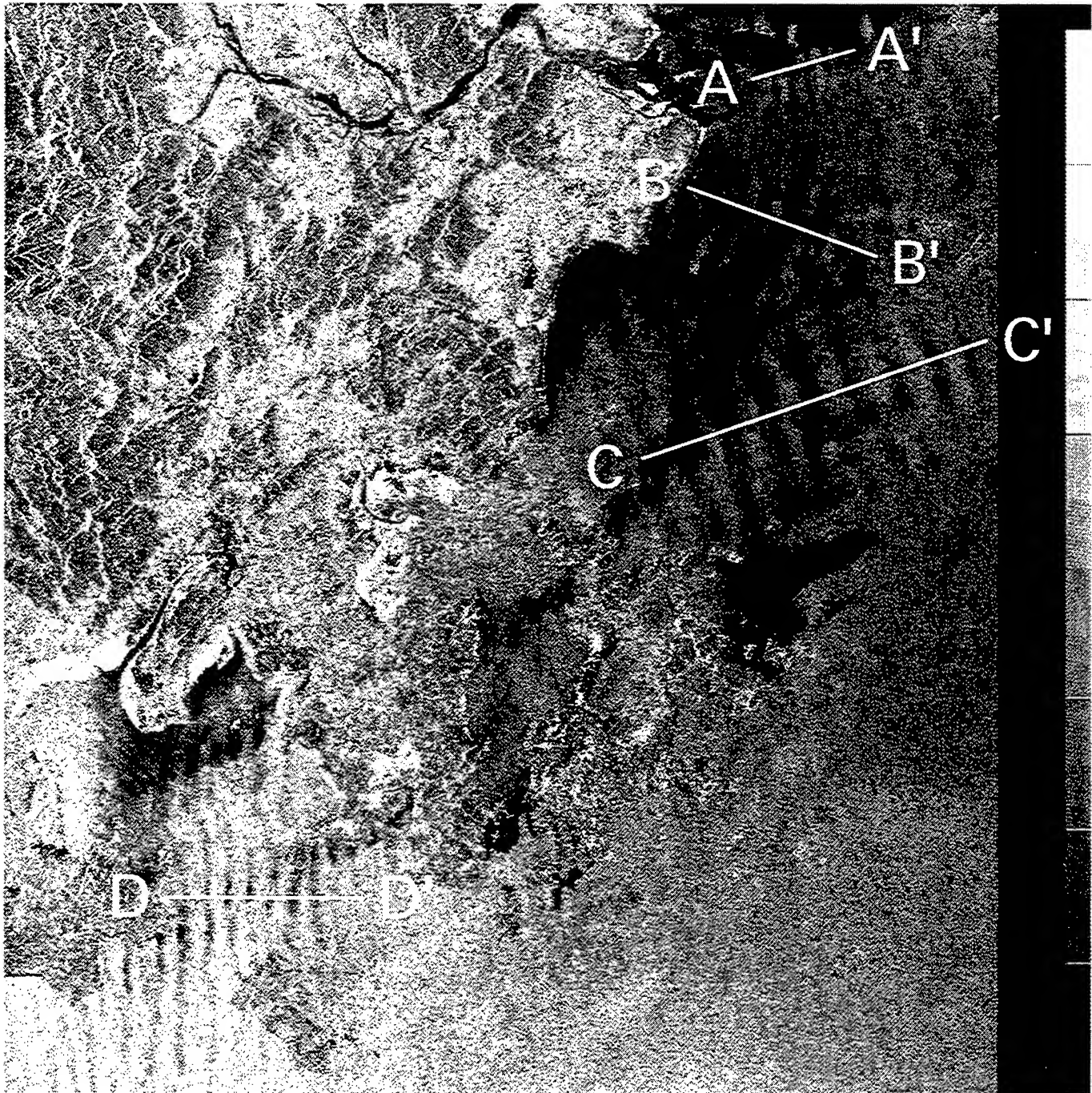


Figure 2. ERS-1 SAR image of the western side of Taiwan Strait acquired on December 8, 1994, at 6:26:43 GMT. The image covers an area of 100 km x 100 km, centered at 25°38'27" N, 119°38'41" E with a scale 1 : 560,000. Alternative dark-bright patterns along the coast represent solitary coastal lee waves.

6. REFERENCES

1. E. E. Gossard and W. H. Hooke, *Waves in the Atmosphere*, Elsevier Scientific Publishing Co., New York, pp. 1-456, 1975.
2. S. Panchev, *Dynamic Meteorology*, D. Reidel Publishing Co., Boston, pp. 1-360, 1985.
3. P. W. Vachon, O. M. Johannessen, and J. A. Johannessen, "An ERS 1 synthetic aperture radar image of atmospheric lee waves," *J. Geophys. Res.*, 99, 22,483-22,490, 1994.
4. W. Alpers and G. Stilke, "Observation of a nonlinear wave disturbance in the marine atmosphere by the synthetic aperture radar aboard the ERS 1 satellite," *J. Geophys. Res.*, 101, 6513-6525, 1996.
5. J. E. Simpson, *Sea Breeze and Local Winds*, Cambridge University Press, Cambridge, pp. 1-234, 1994.

Author Index

- Aas, Eyvind, 138
 Abbott, Mark R., 216
 Ackleson, Steven G., 326
 Adams, James T., 54
 Aguirre-Gómez, R., 344
 Aleshin, Igor V., 802
 Allali, K., 179, 880
 Alvarez-Borrego, Saul, 502, 585
 Antoine, David, 101
 Armstrong, Edward, 543, 892
 Arnone, Robert A., 222, 850
 Arst, Helgi, 477
 Asanuma, Ichio, 828
 Ayoub, L. M., 338
 Babin, Marcel, 314, 880
 Balch, William M., 260
 Ballesterio, Daniel, 570
 Barber, Richard T., 260, 302, 834
 Barnard, Andrew H., 585
 Barth, H., 622
 Bartlett, Jasmine S., 592, 654
 Beckert, Marko, 526
 Behrenfeld, Mike, 880
 Berthon, Jean-François, 353, 401
 Berwald, Juli, 66, 455
 Besiktepe, Sukru, 560
 Bidigare, Robert R., 260, 874
 Bissett, W.P., 358
 Blanco-Sequeiros, Alberto, 477
 Blough, Neil V., 132
 Bochter, K., 631
 Bogucki, Darek, 49
 Bolstad, Jay L., 658
 Booth, Charles R., 737, 777
 Borden, Lisa, 834
 Borgerson, Mark J., 637
 Bowers, D. G., 532
 Bowers, Todd E., 320
 Boxall, Simon R., 148, 344, 520
 Boyer, Philip A., 658
 Boynton, G. Chris, 10
 Bricaud, Annick, 179, 314
 Brock, John, 543, 892
 Brody, E. A., 308, 375
 Bruce, Elizabeth J., 637, 725
 Buckton, D., 72
 Byfield, Valborg, 148
 Caporelli, Elizabeth A., 308, 375
 Carder, Kendall L., 160, 358, 483, 579, 753
 Chavez, Francisco P., 471
 Chekalyuk, Alexander M., 840
 Churnside, James H., 643
 Ciotti, Áurea M., 272, 380, 654, 703
 Cipollini, P., 648
 Claustre, Herve, 179, 846, 880
 Coles, B. W., 790
 Contarino, V. M., 731
 Cook, Jeremy, 148
 Cooper, L. W., 664
 Corlyon, A. M., 674
 Corsini, G., 648
 Costello, David K., 579, 753
 Cullen, John J., 272, 380
 Cunningham, Alex, 198
 Dana, David R., 154
 Danaher, Seán, 72
 Darecki, Mirosław, 386
 Davies, James E., 95
 Davis, Curtiss O., 160, 850
 Davis, Richard F., 272, 654, 703
 de Haan, J. F., 392
 de Munck, Jan C., 808
 Dekker, A. G., 392, 440
 Dickey, Tom D., 254
 Dierssen, Heidi M., 204
 Doerffer, Roland, 435
 Dolin, Lev S., 60
 Domaradzki, Andrzej, 49
 Dowell, Mark, 353, 401
 Dueweke, Paul W., 658
 Egorov, V. G., 664
 Emery, Yves, 210
 Ershova, Svetlana, 167
 Falkowski, Paul G., 314
 Farr, Rebecca A., 670
 Fearn, Peter R., 408
 Fell, Frank, 78
 Fischer, Jürgen, 691
 Flatau, Piotr J., 414, 714
 Flowerdew, R. J., 674
 Fournier, Georges R., 32
 Franks, P. J. S., 278
 Frayer, M. L., 796
 Frew, Brian J., 566
 Fry, Edward S., 210
 Fuentes-Yaco, César, 678
 Gallie, E. A., 417
 Garver, S. A., 308
 Gege, Peter, 423
 Gerth, Monika, 526
 Goncharov, Vadim K., 802
 Gong, Gwo-Ching, 429
 Gordon, E. B., 664
 Gordon, Howard R., 10, 246
 Gosselin, Michel, 678
 Gostan, Jacques, 314
 Gould, Richard A., Jr., 222, 549, 850
 Gratton, Yves, 678
 Grebmeier, J. M., 664
 Greer, W. A. D., 674
 Grossi, Stefania, 353, 401
 Haigh, Joanna D., 609
 Hakvoort, Hans, 435
 Haltrin, Vladimir I., 185, 597

- Hargreaves, B. R., 338
 Harsdorf, Stefan, 684
 Heinemann, Thomas, 691
 Hetscher, M., 234
 Hirawake, Toru, 296
 Ho, Chung-Ru, 898
 Hoepffner, Nicolas, 284, 353, 401
 Højerslev, Niels K., 138
 Holligan, Patrick M., 554
 Hoogenboom, H. J., 392, 440
 Hooker, Stanford, 708, 772
 Hou, Weilin, 579
 Hu, Chuanmin, 266
 Hull, Patricia G., 448
 Irwin, Brian D., 538
 Ishimaru, Takashi, 296
 Ishizaka, J., 173
 Iturriaga, Rodolfo H., 455
 Ivey, James E., 489
 Jaffe, Jules S., 278
 Janssen, Manfred, 684
 Jodai, Y., 461, 760
 Johnson, Donald R., 856
 Johnson, Zachary, 260, 302, 834, 862
 Jones, B. H., 254
 Jones, Ken, 198
 Jogan, Laurie A., 320
 Kabanov, D. M., 821
 Kadokura, K., 760
 Kahru, Mati, 714
 Kamykowski, Dan, 514, 868
 Kartan, Ravi, 670
 Kattawar, George W., 54, 597
 Kawaguchi, So, 495
 Kawano, Takeshi, 828
 Kawasaki, K., 173, 466
 Kearns, Edward, 697
 Kennedy, Clark D., 185
 Kiefer, Dale A., 66
 Kinkade, C., 302
 Kiriya, Nobuo, 815
 Kirk, John T. O., 192
 Kirkpatrick, Gary J., 514, 868
 Kishino, Motoaki, 173, 296, 461, 760, 766
 Klemas, V., 898
 Knudson, Carol, 834
 Kopelevich, Oleg V., 167
 Kowalczyk, Piotr, 386
 Kratzer, Suzanne, 603
 Krawczyk, H., 234
 Kudela, Raphael M., 471
 Kuo, Nan-Jung, 898
 Kusaka, K., 173
 Kutser, Tiit, 477
 Kyewalyanga, Margaret N., 290
 Ladner, Sherwin, 549
 Land, Peter E., 609
 Lara-Lara, Ruben, 502, 585
 Larkin, David, 284
 Larouche, Pierre, 678
 Latasa, Mikel, 260
 Lazin, Gordana, 654, 703
 Lazzara, Luigi, 314
 Leathers, R. A., 21
 Lee, Zhongping, 160, 358, 483, 753
 Leonard, Donald A., 658
 Letelier, Ricardo M., 216
 Levin, Iosif M., 228
 Lewis, Marlon R., 380, 703, 708, 828
 Li, Angela W., 670
 Lohrenz, Steven E., 489
 Lynch, Don, 772
 Lynch, Mervyn J., 95, 408
 Lyskov, Vladimir G., 802
 Maass, Heidi, 538
 Mäekivi, Sirje, 477
 Maffione, Robert A., 16, 154
 Mahapatra, Kedarnath, 495
 Mankovsky, Viktor I., 560
 Marra, John, 302, 834
 Maske, Helmut, 502, 585
 Matsumoto, Kazuhiko, 828
 Matsumura, Satsuki, 495
 Matulewski, Ken M., 489
 Mazel, Charles H., 240
 McBride III, Walton E., 185
 McCormick, Norman J., 21
 McKee, David, 198
 McLean, Scott, 708, 828
 Menzies, Dave W., 777
 Meridith, Roger W., 856
 Michaels, Anthony F., 308
 Mishonov, Alexey V., 560
 Mitchel, B. G., 714
 Mitchelson-Jacob, E. G., 532
 Miyoi, Takako, 173, 766
 Mobley, Curtis D., 16, 66, 331, 714
 Moline, Mark, 846
 Moore, C., 637, 725
 Moore, Karl D., 246
 Morel, André, 101, 108, 314, 880
 Morinaga, Tsutomu, 296
 Morris, D. P., 338
 Mueller, James L., 160, 502, 585
 Mullen, L., 731
 Nalivaiko, S. E., 664
 Neale, Patrick J., 272
 Nelson, N. B., 308, 375
 Neumann, Andreas, 234
 Nevis, Andrew J., 790
 Newby, S. J., 674
 O'Brien, M. C., 308, 375
 O'Mongain, Eon, 72
 Oishi, T., 461, 760
 Olson, Robert J., 840
 Ondrusek, Michael E., 874
 Ozsoy, Emin, 560
 Partensky, Frederic, 314
 Patch, J. S., 358
 Patterson, Karen W., 737
 Pavlenko, V. S., 664
 Peacock, Thomas G., 160, 483
 Pegau, W. Scott, 320, 502, 508, 585, 725
 Phinney, David A., 120, 743, 850

Phinney, Douglas I., 743
 Platt, Trevor, 26, 290, 538
 Pratt, Patty D., 753
 Preusker, René, 78
 Prezelin, Barbara, 846
 Quinby-Hunt, Mary S., 448
 Ranheim, Robert, 543
 Redalje, Donald G., 489
 Reed, Robert E., 514, 868
 Regan, Richard F., 790
 Reuter, Rainer, 622, 684
 Riley, Rodney, 697
 Robinson, I. S., 570, 614
 Roesler, Collin S., 380
 Rzshevsky, O. S., 664
 Sadoudi, Nora, 314, 880
 Saitoh, Chizuru, 828
 Saitoh, Sei-ichi, 173, 766
 Sakerin, S.M., 821
 Saruya, Y., 461, 760
 Sathyendranath, Shubha, 26, 290, 538
 Satoh, Hiroo, 173, 296
 Schofield, Bryan, 708
 Schreurs, R., 392
 Schwarz, Jill, 614
 Senga, Yasuhiro, 495
 Shaw, Ping S., 772
 Shifrin, Kusiel S., 90
 Shimwell, Susan J., 520, 808
 Shugart, Lee R., 664
 Siegel, David A., 308, 375
 Siegel, Herbert, 234, 526
 Sieracki, C. K., 886
 Sieracki, M. E., 886
 Simmon, Robert B., 670
 Smith, P. S. D., 532
 Smith, Raymond C., 204, 737, 777
 Solov'ev, Mark V., 560
 Sonek, Gregory J., 455
 Sorensen, Jens C., 308
 Sosik, H. M., 840
 Spinrad, Richard W., 2
 Stabeno, Phyllis, 654
 Stavn, Robert H., 38
 Steward, Robert G., 160, 483
 Stramski, Dariusz, 49, 66
 Strand, Michael P., 790
 Stuart, Venetia, 538
 Stumpf, Richard P., 796, 892
 Stute, U., 622
 Subramaniam, Ajit, 543, 892
 Sweeney, Harold E., 658
 Sydor, Michael, 222
 Tanaka, A., 760
 Terrie, Gregory E., 549
 Tett, Paul B., 603
 Trees, Charles C., 260, 302, 834
 Trundle, K. J., 614
 Tsvetkov, Evgeny A., 802
 Tyrrell, Toby, 554
 Ulloa, Osvaldo, 284
 Valdez, Eduardo, 502, 585
 Veldhuis, Marcel, 314
 Vezina, Alain F., 678
 Vladimirov, Vladimir L., 560
 Vodacek, Anthony, 132
 Volten, H., 392
 Voss, Kenneth J., 246, 266, 566
 Wallhäußer, C., 631
 Walzel, Th., 234
 Wang, Zongming, 898
 Waterman, Talbot H., 115
 Waters, Kirk, 543, 892
 Weeks, Alison R., 344, 570, 614
 Weidemann, Alan D., 38, 185, 320, 489, 597, 637, 708, 725
 Wernand, Marcel R., 520, 808
 Wilton, R., 603
 Winder, C. P., 674
 Winkler, Erik M., 658
 Woody, Catherine, 697
 Wozniak, Stawomir B., 84
 Yamada, Kimio, 815
 Yamamoto, Kazuo, 815
 Yan, Xiao-Hai, 898
 Yentsch, Charles S., 120, 743
 Zaneveld, J. Ronald V., 49, 502, 585
 Zhang, Tianming, 10
 Zheng, Quanan, 898
 Zibordi, Giuseppe, 708
 Zimmerman, Richard C., 331
 Zolotov, Ilja G., 90
 Zolotukhin, Igor V., 228
 Zuev, Vladimir E., 821